

AD-A134 151

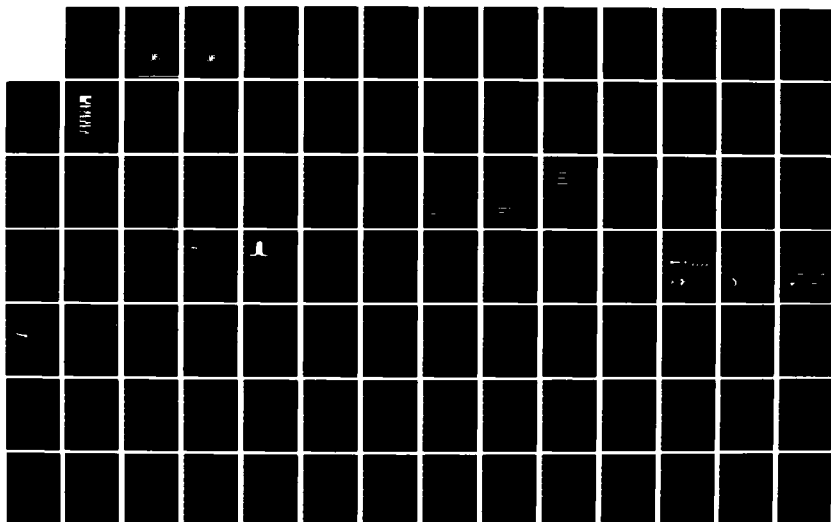
SYMPOSIUM ON NUMERICAL AND PHYSICAL ASPECTS OF
AERODYNAMIC FLOWS (2ND) 17-20 JANUARY 1983(U)
CALIFORNIA STATE UNIV LONG BEACH T CEBECI 1983

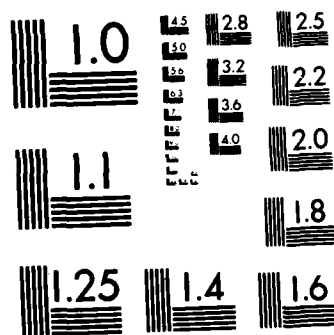
1/5

UNCLASSIFIED

F/G 20/4

NL





MICROCOPY RESOLUTION TEST CHART
NATIONAL BUREAU OF STANDARDS-1963-A

Second Symposium on

NUMERICAL AND PHYSICAL ASPECTS OF AERODYNAMIC FLOWS

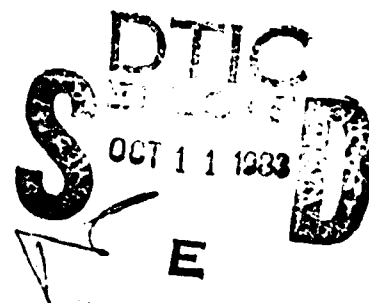
17-20 January 1983

CALIFORNIA STATE UNIVERSITY, LONG BEACH
CALIFORNIA



DTIC FILE COPY

This document has been approved
for public release and sale; its
distribution is unlimited.



83 10 04 002

AD-A134232

Second Symposium on
NUMERICAL AND PHYSICAL ASPECTS
OF AERODYNAMIC FLOWS

17-20 January 1983

CALIFORNIA STATE UNIVERSITY, LONG BEACH
CALIFORNIA



This document has been approved
for publication by the
distribution committee

Second Symposium on
**NUMERICAL AND PHYSICAL ASPECTS
OF AERODYNAMIC FLOWS**

17-20 January 1983

PREFACE

This volume contains the papers presented at the second symposium on Numerical and Physical Aspects of Aerodynamic Flows, held at the California State University, Long Beach, from 17 to 20 January 1983. The symposium was organized with an emphasis on the calculation of flows of relevance to aircraft, missiles and ships. The subject of viscous/inviscid interactive calculation procedures is especially contentious at the present time, with many groups and individuals working in this area. As a consequence, the greatest proportion of time was made available for this subject with six sessions devoted to the numerical procedures and to the related experimental investigations. Three-dimensional boundary layer and inviscid flows constitute the remaining four sessions and are each essential components for the understanding and a priori calculation of wings, ship hulls and other

aerodynamic and hydrodynamic shapes. It is hoped that this volume will be of value to researchers, engineers and designers, and, in particular, will provide a better understanding of aerodynamic flows and the development of related calculation methods.

The symposium was made possible by the financial support provided to the California State University in part by the National Science Foundation, Naval Air Sea Systems Command, U.S. Army Research Office, NASA Ames and NASA Langley, and by the cooperation of the authors, session chairmen, participants and colleagues at the University. Particular thanks are due to Professors James H. Whitelaw of Imperial College, Keith Stewartson of University College, Mr. Dennis Bushnell of NASA Langley and Professor Hillar Unt of the University.

Accession For	
NTIS GRA&I	<input checked="" type="checkbox"/>
DTIC TAB	<input type="checkbox"/>
Unannounced	<input type="checkbox"/>
Justification	<i>per</i>
By	
Distribution/	
Availability Codes	
Dist	Avail or/or Special
A	

Tuncer Cebeci
Long Beach, California
January 1983



TABLE OF CONTENTS

Session 1, Measurements and Calculations of Interactive Flows

Time-Dependent Finite-Difference Simulation of Unsteady Interactive Flows, G.S. Deiwert and H.E. Bailey **AD-P004929**

Navier-Stokes Solution of Shock Boundary-Layer Interactions at Transonic Speed, Y. Tassa and D. Shuster

A Direct Method for the Solution of Unsteady Two-Dimensional Incompressible Navier-Stokes Equations, K.N. Ghia, G.A. Osswald and U. Ghia **AD-P004930**

Global Solution Procedures for Incompressible Laminar Flow with Strong Pressure Interaction and Separation, S.G. Rubin and D.R. Reddy **AD-P004931**

Computation of Flow Past a Hypersonic Cruiser, J.S. Shang and W.L. Hankey **AD-P004934**

Session 2, Measurements and Calculations of Interacting Flows

Numerical Solutions of Spatially Periodic Boundary Layers, O.R. Burggraf

Asymptotic Theory of Turbulent Wall Jets, R.E. MeInik and A. Rubel

On the Coupling of Boundary Layer and Euler Equation Solutions, E.M. Murman and T.R.A. Bussing

Interactive Separation From a Fixed Wall, L.L. van Dommelen and S.F. Shen **AD-P004932**

Session 3, Measurements and Calculations of Interactive Flows

The Interaction Between a Steady Laminar Boundary Layer and an Oscillating Flap: The Condensed Problem, P.W. Duck **AD-P004933**

Application of Unsteady Laminar Triple-Deck Theory to Viscous-Inviscid Interaction From an Oscillating Flap in Supersonic Flow, M.-K. Huang and G.R. Inger **AD-P004934**

A Study of Non-Unique Solutions of the Two-Dimensional Boundary-Layer Equations at Laminar Separation and Reattachment Points, M. Drela and W.T. Thompkins, Jr. **AD-P004935**

Measurements and Calculations of a Separating Boundary Layer and the Downstream Wake, D. Adair, B.E. Thompson and J.H. Whitelaw **AD-P004936**

(Why?) A Finite-Element Algorithm for the Parabolic Navier-Stokes Equations, A.J. Baker **AD-P004937**

Keynote Lecture 1: Wing Design and Analysis - Your Job, A.M.O. Smith **AD-P004938**

Session 4, Measurements and Calculations of Interactive Flows

Numerical Viscid-Inviscid Interaction in Steady and Unsteady Flows, J.-C. LeBalleur **AD-P004939**

Computation of Transonic Viscous-Inviscid Interacting Flow, D.L. Whitfield, J.L. Thomas, A. Jameson and W. Schmidt **AD-P004940**

Airfoil Flow Field Calculations with Coupled Boundary Layer/Potential Codes, J.D. Murphy and L.S. King

Viscous-Inviscid Matching Using Higher-Order Shear-Layer Equations, P. Bradshaw, M.J. Kavanagh and D. Hobbs **AD-P004941**

A Comparison Between the Predicted and Experimental Characteristics of a NACA 643-418 Aerofoil at Low Reynolds Numbers, P.M. Render and J.L. Stollery **AD-P004942**

Session 5, Measurements and Calculations of Interactive Flows

A Survey of Recent Work on Interacted Boundary Layer Theory for Flow With Separation, H. McDonald and W.R. Briley **AD-P004943**

An Interactive Approach to Subsonic Flows with Separation, T. Cebeci and R.W. Clark **AD-P004944**

A Calculation Method of Leading Edge Separation Bubbles, C. Gleyzes, J. Cousteix, J.L. Bonnet **AD-P004945**

Prediction of Subsonic Separation Bubbles on Airfoils by Viscous-Inviscid Interaction, O.K. Kwon and R.H. Pletcher **AD-P002 944**

Session 6, Measurements and Calculations of Interactive Flows

Theoretical and Experimental Dynamic Stall, Investigations on a Rotor Blade Tip, W. Geissler **AD-P002 950**

Unsteady Viscous Transonic Flow Computations Using the LTRAN2-NLR Code Coupled with Green's Lag-Entrainment Method, R. Houwink **AD-P002 945**

Viscous/Inviscid Interaction Analysis of Asymmetric Trailing-Edge Flows, V.N. Vatsa and J.M. Verdon **AD-P002 946**

Measurements of Attached and Separated Turbulent Flows in the Trailing-Edge Regions of Airfoils, A. Nakayama **AD-P002 947**

Numerical Simulation of Turbulent Trailing Edge Flows, C.C. Horstman **AD-P002 948**

Keynote Lecture 2: Problems Associated with the Aerodynamic Design of Missile Shapes, Jack N. Nielsen **AD-P002 949**

Session 7, Subsonic Wings

Effect of Roughness on Three-Dimensional Turbulent Boundary Layers, P.A. Krogstad and T.K. Fannelop **AD-P002 952**

Three-Dimensional Wake of a Swept Wing, J. Cousteix, G. Pailhas and B. Aupoix *Supers*

Three-Dimensional Boundary-Layer Calculations on Wings, Starting from the Fuselage, J.P.F. Lindhout, B. van den Berg, A.C. de Bruin

The QuasiSimultaneous Calculation of Strongly Interacting Viscous Flow Around an Infinite Swept Wing, A.E.P. Veldman and J.P.F. Lindhout

Session 8, Transonic Wings

Transonic Small Disturbance Calculations Including Entropy Corrections, M. Hafez and D. Lovell **AD-P002 953**

The Efficient Solution of Transonic Wing Flow Fields, T.L. Holst and N.R. Subramanian **AD-P002 953**

Transonic Flowfield Computation Using a Modified Shock-Point Operator, L.T. Chen **AD-P002 954**

Viscous-Inviscid Interactions with a Three-Dimensional Inverse Boundary-Layer Code, L. Wigton and H. Yoshihara **AD-P002 955**

Session 9, Missiles

An Inviscid Computational Method for Tactical Missiles, A.B. Wardlaw, F.P. Baltakis, J.M. Solomon and L.B. Hackerman *Supers*

Store Separation at Transonic Speeds, S.S. Stahara **AD-P002 956**

Navier-Stokes Computational Study of the Influence of Shell Geometry on the Magnus Effect at Supersonic Speeds, W.B. Sturek, D.C. Mylin, B. Guidos, C.J. Nietubicz *Supers*

Development of Boundary Layers and Separation Patterns on a Body of Revolution at Incidence, H.U. Meier, H.P. Kreplin, H. Vollmers **AD-P002 957**

Calculation of Boundary Layers and Separation on a Spheroid at Incidence, V.C. Patel and J.H. Baek **AD-P002 958**

Session 10, Ships

Structure of the Turbulent Shear Flow in Ship Boundary Layers, A. Yücel Odabasi and M.E. Davies

Stern Boundary-Layer Flow on Two Three-Dimensional Bodies Having Elliptical Transverse Cross-Sections, T.T. Huang, N.C. Groves and G.S. Belt **AD-P002 959**

Calculation of Three-Dimensional Boundary Layers Around Ship Hull Forms, S. Soejima **AD-P002 960**

Calculations of Thick Boundary Layers Using a Streamline Curvature Method, L.-E. Johansson and L. Larsson **AD-P002 962**

SESSION 1

TIME-DEPENDENT FINITE-DIFFERENCE SIMULATION OF UNSTEADY INTERACTIVE FLOWS

George S. Deiwert* and Harry E. Bailey*

NASA Ames Research Center, Moffett Field, California 94035

Abstract

The solution of the time-dependent, Reynolds-averaged, Navier-Stokes equations for unsteady, interacting flows by finite-difference algorithms is discussed. Specific examples include 1) unsteady transonic flow over a thick biconvex airfoil, 2) determination of buffet boundaries for a transonic lifting airfoil, 3) the simulation of aileron buzz and 4) dynamic stall. Algorithms considered include explicit methods, mixed (or hybrid) methods, and fully implicit methods. Consideration of time scales for computational stability, computational accuracy, and physical accuracy and the use of time-dependent adaptive meshing to realize computational efficiency are also discussed.

Introduction

During the past decade, advances in computer hardware and numerical methods have permitted the development of computer programs capable of simulating unsteady interactive flows. The physical realism of the simulated unsteady flows has been validated by comparison with experimental measurements. The promising results obtained so far, coupled with continued improvements in both computer performance and algorithm efficiency, encourage further development of these methods and their implementation to study unsteady, interactive aerodynamic flows.

This paper reviews the development of time-dependent numerical simulations of unsteady interactive flows of an aerodynamic nature. It focuses primarily on compressible flows at flight Reynolds numbers and noniterative schemes based on the Navier-Stokes equations. In the following sections the governing equations are outlined, time and length scales are discussed, and numerical methods currently in use are reviewed. A selection of computed results and their comparison with experiment are presented, followed by some concluding remarks.

Governing Equations

The equations of motion for continuous fluid mechanics are the Navier-Stokes equations. For many flows of aerodynamic interest, these equations can be greatly simplified, for example, for inviscid flows (Euler equations), irrotational flows (potential equations), or simple thin shear layers (boundary-layer equations). For unsteady interactive flows, however, such simple uncouplings are not possible and the full form of the equations is generally considered. Interactions between the inviscid external flow and the viscous wall-bounded flow are typified by

rapid thickening of the shear layer with strong streamline curvature. This is often accompanied by separation or flow reversal. Streamwise pressure gradients can be quite large and shock waves may exist that penetrate the shear layer. In addition, interaction between two viscous-dominated flows occurs at the trailing edge of bodies or between elements of multielement configurations. Here two (or more) shear layers, with different upstream histories, interact and form a complex shear layer. Further complexity exists at flight Reynolds numbers in the form of turbulence, which extends the range of length and time scales that require consideration.

For unsteady interactive flows of aerodynamic interest, some simplification of the full Navier-Stokes equations for compressible flow can be made. One is to time-average the equations over a time-scale that is small compared with the aerodynamic time-scale for unsteady flow, yet large compared with the time-scale of the turbulent eddies. This results in the Reynolds-averaged form of the Navier-Stokes equations which contain Reynolds-stress terms that must be modeled empirically. Another simplification that is sometimes used is the thin-shear-layer approximation. Here, all streamwise- and cross-derivatives of the viscous, as well as turbulent stress terms, are neglected. The momentum equation across the shear layer is still retained, however, so that the critical coupling between the wall-bounded shear flow and the inviscid external flow is not lost.

It is generally convenient to cast the equations in conservation-law form to facilitate the capture of discontinuities and so that global conservation of the dependent variables can be easily maintained. The conservative form of the differential equations avoids fictitious sources along discontinuities and permits the numerical attainment of the weak solution to the equations. It is highly desirable to write the equations for a body-oriented coordinate system so that the description and modeling of Reynolds stress terms in the wall-bounded shear layers are not unnecessarily complex and so that empirical models developed for thin shear layers can be easily used and modified. There are two possible ways to write equations for generalized geometries while maintaining strong conservation-law form. One is to write the equations in integral form, using Cartesian momentum components, Cartesian space coordinates, and contravariant velocity components. These equations are applied to volume elements of arbitrary shape and are commonly referred to as the finite-volume formulation.¹⁻¹⁰ The other way to write the equations is to use Cartesian momentum components and contravariant velocity components and transform the space coordinates to a generalized system. When the Navier-Stokes equations in conservation-law form are transformed from the Cartesian coordinates to arbitrary curvilinear coordinates, they do not generally retain the conservation-law form; however, following the method proposed by Viviani,¹¹ they can again be put in conservation-law form.

*Research Scientist.

This paper is declared a work of the U.S. Government and therefore is in the public domain.

AD P001929

The two-dimensional, Reynolds-averaged, Navier-Stokes equations for compressible flow are written below in strong conservative form in generalized coordinates as

$$\frac{\partial q}{\partial t} + \frac{\partial(E - E_v)}{\partial \xi} + \frac{\partial(F - F_v)}{\partial \eta} = 0$$

where

$$q = \frac{1}{J} \begin{pmatrix} \rho \\ \rho u \\ \rho v \\ e \end{pmatrix}, \quad E = \frac{1}{J} \begin{pmatrix} \rho U \\ \rho u U + \xi_x P \\ \rho v U + \xi_y P \\ (e+p)U - \xi_t P \end{pmatrix},$$

$$F = \frac{1}{J} \begin{pmatrix} \rho V \\ \rho u V + \eta_x P \\ \rho v V + \eta_y P \\ (e+p)V - \eta_t P \end{pmatrix}, \quad E_v = \frac{1}{J} \begin{pmatrix} 0 \\ \xi_x \tau_{xx} + \xi_y \tau_{xy} \\ \xi_x \tau_{yx} + \xi_y \tau_{yy} \\ \xi_x \beta_x + \xi_y \beta_y \end{pmatrix}$$

$$F_v = \frac{1}{J} \begin{pmatrix} 0 \\ \eta_x \tau_{xx} + \eta_y \tau_{xy} \\ \eta_x \tau_{yx} + \eta_y \tau_{yy} \\ \eta_x \beta_x + \eta_y \beta_y \end{pmatrix}$$

and

$$U = \xi_t + \xi_x u + \xi_y v$$

$$V = \eta_t + \eta_x u + \eta_y v$$

$$\tau_{xx} = \lambda(u_x + v_y) + 2\mu u_x$$

$$\beta_x = \frac{\gamma K}{Pr} e_{I_x} + u \tau_{xx} + v \tau_{xy}$$

$$\tau_{xy} = \tau_{yx} = \mu(u_y + v_x)$$

$$\beta_y = \frac{\gamma K}{Pr} e_{I_y} + u \tau_{yx} + v \tau_{yy}$$

$$\tau_{yy} = \lambda(u_x + v_y) + 2\mu v_y$$

$$e_I = e/p - \frac{1}{2}(u^2 + v^2)$$

The coordinates ξ and η are generalized curvilinear, whereas the dependent variables, u and v , are Cartesian velocity components corresponding to the x and y directions, respectively. The metric terms relating Cartesian space to the generalized curvilinear space are given by

$$\xi_x = J \eta_y, \quad \eta_x = -J \xi_y$$

$$\xi_y = -J x_\eta, \quad \eta_y = J x_\xi$$

$$\xi_t = -x_t \xi_x - y_t \xi_y, \quad \eta_t = -x_t \eta_x - y_t \eta_y$$

$$\frac{1}{J} = x_\xi y_\eta - x_\eta y_\xi$$

The Reynolds stresses and turbulent heat-flux terms have been included in the stress tensor and heat-flux vector by using the eddy-viscosity and eddy-conductivity concept, whereby the coefficients of viscosity and thermal conductivity are the sum of the molecular (laminar) part and an eddy (turbulent) part:

$$\mu = \mu_l + \mu_t$$

$$\lambda = \lambda_l + \lambda_t$$

$$\kappa = \kappa_l + \kappa_t$$

It is also possible to model the Reynolds stresses directly rather than relating them to the mean field gradients via an eddy-viscosity concept, but this has received little attention to date for unsteady interactive flows.

The accuracy of numerical simulations with the Reynolds-averaged, Navier-Stokes equations depends principally on the accuracy of the turbulence modeling. The eddy coefficients are given by empirical expressions which can range from fairly simple algebraic expressions, based on mixing-length concepts, to fairly complex expressions, based on empirical transport equations, to determine length and velocity scales. Most unsteady interactive computations to date (except some used only to approach a steady state in a timewise manner) have relied on the simpler algebraic expressions for eddy viscosity and a constant turbulent Prandtl number to determine eddy conductivity. These algebraic models are developed from boundary-layer concepts and in general have not been validated for other than thin shear layers. In recent work by Shamroth,¹² a differential expression for turbulent kinetic energy combined with an algebraic length scale to describe the eddy viscosity was used to study subsonic flow over an oscillating airfoil where the influence of viscous/inviscid interactions is small.

Time and Length Scales

To simulate unsteady flows, it is necessary to know what time and length scales are important and thus require resolution. Time scales exist

that range from the very short periods associated with the high-frequency dissipative turbulence structure (the Kolomogorov microscale) to the very long times associated with slow-moving signals propagating along upstream characteristic paths in a transonic flow field. (For example, pressure waves propagate upstream at a speed equal to $(1 - M_\infty)a$, which for Mach numbers close to unity can be quite slow.) Length scales exist that range from the very small microscale structure of the dissipative turbulent eddies to the very long scales that extend from the aerodynamic body to the outer boundaries of the computational control volume. Many unsteady flows of aerodynamic interest have important time and length scales that are somewhere in the middle of this vast range, and numerical schemes can be selected such that they neglect the very short scales yet remain sufficient to resolve the scales of concern.

Strong interactive effects occur when the range of flow conditions and airfoil motion parameters produces unsteady, shock-induced, boundary-layer separation, trailing-edge separation, or various combinations of interactions that result in separation-induced transonic flutter, buffet, aileron buzz, and dynamic stall. In the absence of forced motions, the characteristic speed that drives the unsteady behavior is the free-stream velocity (U_∞), and the characteristic length is the body-length scale (L) or separation scale (S). A nondimensional frequency parameter (Ω) can be defined that describes the characteristic time scale as $\Omega = fL/U_\infty$, where f is the dimensional frequency of unsteady motion. For forced frequencies, such as occur with propellers and helicopter rotors, the dominant driven frequency is sinusoidal, with higher harmonics becoming important as the blades pass through the trailing vortices of the preceding blades. These flows are characterized by a nondimensional frequency parameter defined as $k = \omega c/2U_\infty$, where ω is the circular frequency and c is the chord of the airfoil section.

An important consideration concerns how high the frequencies f or $\omega/2\pi$ can be, relative to the mean frequency f_T of the turbulent eddies, for realistic simulations with the Reynolds-averaged equations. For the concept to be valid, the averaging time interval must be long compared with the characteristic time f_T^{-1} of the principal turbulent eddies and short compared with the characteristic time f^{-1} of the unsteady mean flow. Hence, f should be much smaller than f_T . In order to obtain a perspective on this question, Chapman¹³ assembled some relevant data for unsteady aerodynamic flows. These are reproduced in Fig. 1, which maps typical unsteady aerodynamic flow and turbulent eddy domains as functions of nondimensional frequency parameter Ω and flight Mach number M_∞ . The lines representing the mean frequency of the turbulent eddies are based on flat-plate experiments and correspond to $f\delta/U_\infty = 0.2$, the experimentally observed mean turbulent-burst period. Also shown are domains representative of airfoil buffet, wing buffet, leading-edge separation, vortex shedding behind bluff bodies, supercritical diffuser stall, low-speed diffuser transitory stall, dynamic stall, transonic wing rock, and unsteady boundary-layer experiments.¹⁴ Almost all of the frequencies of these unsteady aerodynamic flows are one to two orders of magnitude

smaller than f_T . The two open circle points in Fig. 1 represent airfoil buffeting and aileron buzz for which frequencies the Reynolds-averaged equations have provided good simulations when using turbulence models developed for steady flows. The unsteady frequencies in these cases are two orders of magnitude less than f_T . At the highest frequencies tested, the usual steady-flow turbulence models supported accurate descriptions of the time-varying changes in amplitude and phase of the velocity profiles and turbulence intensity. Thus, for these frequencies, just one order of magnitude less than f_T , the Reynolds-averaged equations are adequate for unsteady simulation; hence, for many unsteady flows of practical aerodynamic interest their validity can be expected. A partial explanation for this fortunate situation can be seen as follows: Although the average frequency of the large-scale eddies passing a given point on a surface is f_T , the average frequency of eddies passing a given spanwise station on an airfoil, say with a span of one chord length, would be of the order of $100 f_T$. For such conditions, the Reynolds concept for time-averaging may be realistic for frequencies f of the order f_T . However, for highly three-dimensional flows with large spanwise variations, f may need to be much smaller than f_T for realistic simulations with the Reynolds-averaged equations.

Another important consideration concerns the ability of the Reynolds-averaged Navier-Stokes equations to simulate unsteady flows with a wide range of frequency spectra, such as can occur in rotating machinery or helicopter rotors in which the multiple elements, each of which generates and interacts with vortices, induce higher harmonics. Applications to date have been conducted for two-dimensional flows without the complications of three-dimensional effects, free-stream turbulence, airfoil vibrations, or structural oscillations. These have resulted in essentially cyclic unsteadiness with a single narrow-band frequency. It is well known from experimental observations that many flows have complexities resulting in broader-band

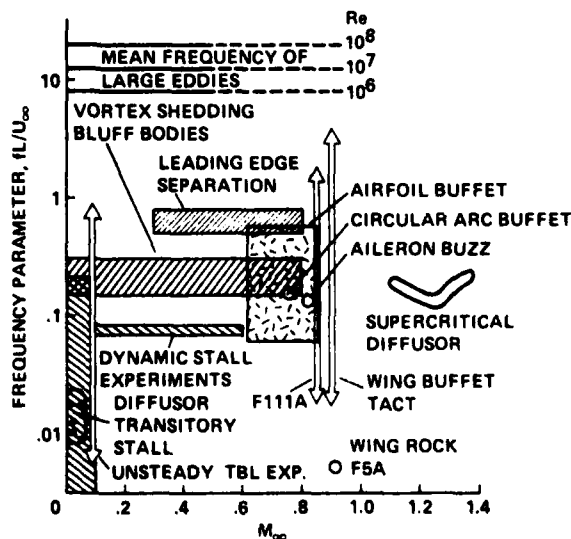


Fig. 1 Comparison of frequency range of unsteady flows with mean frequency of large-scale turbulent eddies.¹³

distributions of frequencies. A capability to simulate these types of flow would permit the study, for example, of unsteady inlet flows feeding into compressors, compressor stall, certain flutter problems, gust loading, and wing buffet. Such unsteady flow simulations would probably necessitate removal of the Reynolds-averaging restriction and use instead a large-eddy simulation scheme in which only the fine-scale turbulence associated with dissipation would be empirically modeled. Such computations which are not yet feasible with today's algorithms and computers, must await a later generation of computational power and sophistication.

To determine finite-difference solutions to the Reynolds-averaged equations, a computational grid must be constructed about the aerodynamic shape of interest. The grid must be capable of resolving all the essential length scales and at the same time be efficient so as not to over resolve the flow field and saturate computer storage systems and processing times. Stretching and clustering of grid points are used extensively and dynamic remeshing during transient phases of the solution is desirable to ensure adequate resolution of high gradient regions.

The primary variable determining the required minimum number of grid points is the boundary-layer thickness, δ . This thickness can be estimated from flat-plate, turbulent boundary-layer behavior as $\delta = 0.37 L / Re_x^{1/2}$. For steady attached turbulent boundary layers, the well-known "law of the wall" describes the boundary-layer behavior near the body surface. In interactive regions, however, the log-law region of the turbulent boundary layer can be annihilated, and it is necessary to resolve the boundary layer to the scale of the viscous sublayer, if accurate simulations of separation and surface shear are to be expected. To ensure this resolution, the first grid line off the surface should lie within the sublayer where the velocity varies linearly with distance from the surface (i.e., $u^+ = y^+$ where $u^+ = u/u_\tau$, $y^+ = \eta u_\tau / \nu$, and $u_\tau = (\tau_w / \rho_w)^{1/2}$). This occurs for values of $y^+ \approx 8$ and can be estimated from the free-stream Reynolds number and body length scale by $\Delta \eta_{min} \approx 0.08L / (Re)^{1/2}$, where $\Delta \eta_{min}$ is the distance away from the body surface to $y^+ \approx 8$. From this first point, additional grid lines can be distributed away from the body, with exponentially increased spacings to a distance somewhere just outside the boundary layer. An external grid can be further constructed to extend the computational field to the outer edge of the computational control volume, again using either geometric or algebraic progressions to increase grid spacings away from the body.

Unsteady flows typically contain regions of high gradients that move about in space; shock waves and shear layers, for example. Resolution of these high-gradient regions requires a tight clustering of grid lines, and efficient use of grid lines is best achieved by moving or adapting the clustered grid with the moving region. Fortunately, in many instances, this can be realized by adapting just one family of grid lines, for example lines of constant η for shear layers and lines of constant ξ for shocks normal to the streamwise direction. When there

are interacting shocks that result in structures not aligned with a principal coordinate, the problem of adaptive meshing becomes much more cumbersome and complex. Unsteady interactive computations with completely general adaptive meshing of this kind have not yet been attempted. Examples of one coordinate adaptive meshing for shocks are given by MacCormack and Baldwin,⁷ Schiff,¹⁵ and Deiwert,⁹ and examples for near-wake flows (moving shear layers) by Deiwert.¹⁰ Note that in the equations presented in the previous section the time-varying metrics have been included to facilitate adaptive meshing.

Numerical Methods

Finite-difference methods for solving the Reynolds-averaged, Navier-Stokes equations can be classified by type: explicit, implicit, or some hybrid combination of the two. Explicit methods offer the advantage of low cost per step and ease of formulation and computer programming. Associated with them are time-step stability constraints based on convection of signals (the Courant condition) and on diffusion of signals (the viscous-stability condition). The Courant condition restricts the time-step Δt to values less than $\Delta x / (U + a)$, where Δx is the mesh spacing and $(U + a)$ is the local convection speed in the x-direction plus the local speed of sound. A similar restriction exists for the y-direction (or ξ and η directions). The viscous-stability condition restricts the time-step to values less than $\Delta x^2 / 2\nu$ (or $\Delta y^2 / 2\nu$, etc.). If these time-step constraints are compatible with the unsteady frequency of the flow being computed (i.e., if Δt from stability considerations is not orders of magnitude less than f^{-1}), then explicit methods are a good choice. Examples of an explicit method used to compute unsteady transonic flow past an airfoil section are given in Refs. 1-3; the method is of the Lax-Wendroff¹⁶ type and solves the equations in the finite-volume formulation.

Generally, however, at the high Reynolds numbers associated with actual flight conditions, the shear layers are so thin and require such finely spaced meshes that the time constraints imposed by both the Courant condition and the viscous-stability condition are prohibitively small. To circumvent this problem, either semi-implicit schemes are used (e.g., MacCormack¹⁷), whereby the diffusion-dominated regions are treated implicitly and the convective dominated regions explicitly, or fully implicit schemes are used for the entire flow field (e.g., Beam and Warming¹⁷ and Briley and McDonald¹⁸). The MacCormack hybrid scheme requires the solution of simple tridiagonal matrices for the viscous terms and characteristic equations for some of the convective terms in the diffusion-dominated regions, and retains an explicit formulation for convective-dominated regions. Because of the programming logic required to hybridize the method, it is difficult to vectorize this procedure for modern array processors. The fully implicit method of Beam and Warming requires the solution of block-tridiagonal matrices, and hence requires more computation per grid point per time-step than the hybrid method on the average, but is readily vectorized when approximate factorization of the differencing operators

is used. The MacCormack hybrid method still requires satisfaction of a Courant condition for stability. Since this is based on the convective-dominated flow regime, where mesh spacings are large relative to the diffusion-dominated regime, the time-steps are not restrictive for unsteady flow computations. The fully implicit method of Beam and Warming is neutrally stable and has no formal time-step constraint. However, when artificial dissipation is included to make the scheme robust, stability time-constraints dependent on both the coordinate transformation and the mean-flow variation occur. Because there is yet no straightforward way to estimate these constraints, the solutions must be monitored for violation of the stability condition. This is generally done by tracking the development of the residuals at each step of the solution.

An important consideration concerns the frequency range supported by a finite-difference solution method. Finite grids can support only a finite number of frequencies in a discrete Fourier series. Higher frequencies than the grid will support are aliased to lower frequencies. For example, on an equispaced grid of n points, $k = n/2$ harmonics of the form e^{ikx} can be accurately supported. Frequencies higher than k reappear as lower frequencies. In unsteady flows with moving shocks, high frequencies are continually generated by nonlinear convective interactions. For example, the product of waves $e^{imx} e^{inx}$ arises due to terms such as uU and vU , and these produce two harmonics, a lower one proportional to $m - n$ and a higher one proportional to $m + n$. The numerical problem that occurs in this situation has been described by Mehta and Lomax¹⁹ and is illustrated in Fig. 2 (taken from their paper). Schematically, amplitude is shown as a function of wave number. The frequencies to the right of the mesh cutoff line are subgrid frequencies that alias back to the low-frequency range and introduce numerical error. This error can be sufficient to cause numerical instability. Artificial numerical dissipation is generally introduced to remove the high-frequency terms before significant aliasing occurs. Additionally, mesh clustering is generally used in the vicinity of shocks where high-frequency terms are generated, and this reduces the magnitude of aliasing that would otherwise occur on a coarse grid.

A second consideration concerns the use of shock-capturing methods to describe a discontinuity as it moves about in the mesh. When such a technique is used, the shock profile is "smeared"

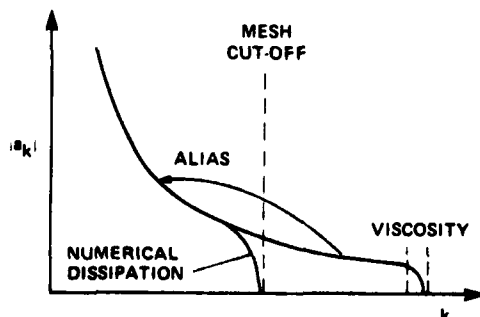


Fig. 2 Numerical dissipation of subgrid amplitudes.¹⁹

over a few mesh points. For most applications, the shock strength and location are adequately represented and in fact, for shock/boundary-layer interactions the smeared shock structure in the interaction region is preferred to a discontinuous representation. Alternatively, shock-fitting may be esthetically more attractive in the inviscid regions. However, shock-capturing is practically more advantageous, with no real loss of accuracy near the body, although it must be recognized, of course, that shocks really are essentially discontinuities in the exterior flow field.

A third consideration concerns the computation of turbulence or, rather, the effect of turbulence. No real attempt is made to resolve the full range of scales inherent in a turbulent shear flow, nor is there any attempt to account for the inherent three-dimensional structure of turbulent fields. There is, however, an interaction between the numerical procedures and the computation of turbulence effects. Two different issues are involved. One is the manner in which the subgrid scales are accommodated and the other is the manner in which the turbulence model is implemented. Subgrid scales are continually generated by the larger scale structure by means of nonlinear wave interactions in the convective terms. Numerical control of the subgrid energy production is achieved by the addition of dissipation, either through approximations to spatial derivatives or by artificial terms. In either instance, the dissipation is arbitrary to the extent that it must lie within the error band of the large-scale resolution and it must prevent the accumulation of energy in the highest frequencies supported by the mesh. This artificial dissipation is not related to the eddy viscosity that is empirically modeled and must not be of comparable order. Nonetheless, even though its detailed form is somewhat arbitrary, its presence is essential to prevent the flow of subgrid scale energy to the large-scale terms where it would not have physical meaning.

The second interaction is more subtle and is related to the manner in which the turbulence model is incorporated into the computer code. Although the analytical form of a given eddy-viscosity model is well described, its implementation and the means by which certain key parameters (particularly length scales) are evaluated are not clear. Every code developer practices the art of model implementation. The numerical effect of the complete model is the sum of all its parts, including grid-distribution effects, metric evaluation techniques, difference approximations, and the adaptation of "thin-shear-layer" models to describe complex shear layers. Because the models are empirical, a wide degree of freedom is often exercised in their implementation. The accuracy of the models with all these ingredients is difficult to evaluate and the final assessment of the method must be based on comparisons with experiments and benchmark computations.

Results

We mention here five examples of unsteady interactive flow which have been computed: 1) flow past a biconvex airfoil; 2) buffet boundaries; 3) aileron buzz; 4) stall boundaries;

and 5) dynamic stall. In each case the flow is transonic and there are in each instance some experimental results with which comparisons are made. In each of the five cases the time scale of interest is narrow-banded and is long compared with the mean frequency of the turbulent eddies.

Biconvex Airfoil

First, the experiments of McDevitt et al.,²⁰ in which the transonic flow past an 18%-thick, biconvex, circular-arc airfoil at zero angle of incidence was investigated, are considered. The circular arc was placed in a high-Reynolds-number channel with walls contoured to match streamlines predicted from a transonic Navier-Stokes code.⁶ Both Mach number and Reynolds number were varied. At a Mach number of 0.72, the flow was steady, the viscous/inviscid interaction was somewhat weak, and flow separation occurred just ahead of the trailing edge. At a Mach number of 0.783, the flow was quasi-steady, and the viscous/inviscid interaction was strong and resulted in shock-induced separation well ahead of the trailing edge, with reattachment in the wake of the airfoil. At Mach numbers in between these values, the flow was observed to be highly unsteady, with shock waves and separation points oscillating fore and aft with a dimensionless frequency of $\Omega = 0.49$ (Ref. 21).

Levy,²² using a code written by Deiwert⁸ based initially on the explicit MacCormack method and subsequently the hybrid MacCormack method,⁹ simulated the same flow conditions and observed the same cyclic behavior for the same Mach number range as was observed experimentally. The computed frequency of the oscillations and the magnitude of the shock excursions agreed remarkably well with experimentally measured values. Shown in Fig. 3 are the Reynolds-number and Mach-number domains for which the flow was observed to be weakly interacting, steady; strongly interacting, quasi-steady; or strongly interacting, unsteady. Experimentally, as Mach number is increased, the onset of unsteady-flow regime occurs for Mach numbers near 0.76;

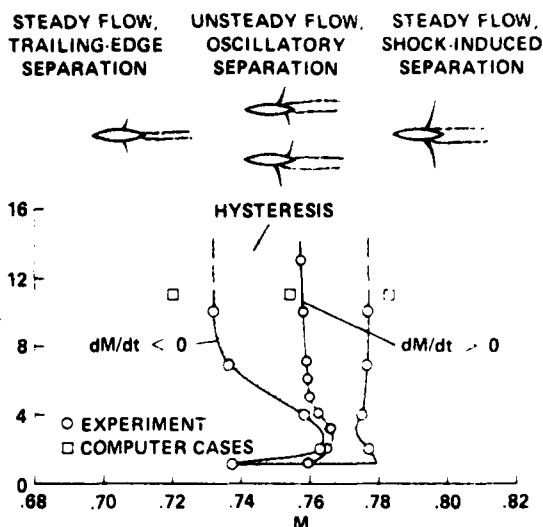


Fig. 3 Experimental flow domains for 18% circular-arc airfoil.²⁰

it terminates at values near 0.78. As Mach number is decreased, the unsteady regime persists down to values near 0.73. The hysteresis region showing this difference in the unsteady flow domain with increasing and decreasing Mach numbers is shaded in Fig. 3. The computations of Levy are for fixed Mach numbers of 0.72, 0.754, and 0.783, all for a Reynolds number of 11×10^6 . These Mach numbers are denoted by the square symbols in the figure. For the Mach number 0.72, the computed flow is steady as observed in the experiment; for 0.754, it is unsteady; and for 0.783, it is quasi-steady; again as observed experimentally.

Figure 4 shows a comparison of computed and measured surface-pressure distributions for the three computed cases. Mean experimental results are denoted by the circular symbols and mean computed results by the solid line. The amplitude and range of the unsteady pressure variation is

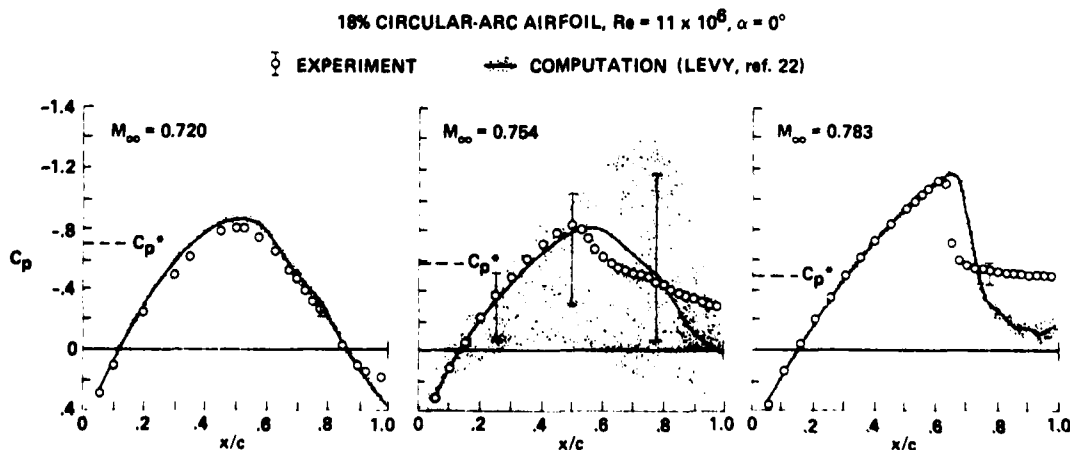


Fig. 4 Pressure distributions over 18% circular-arc airfoil.

indicated by vertical bars for experiment and by shaded regions for the computation. For the Mach-number-0.72 case, the agreement between computation and experiment is excellent except for disparities near the trailing edge where the flow has separated. For 0.754, the pressure distributions are highly unsteady. The amplitude of both the experimental and computed oscillations are quite similar, with the computed oscillations showing somewhat greater excursions on the high-pressure side. For Mach number 0.783, the agreement ahead of the shock is excellent, but the computation predicts a strong, nearly normal shock as opposed to the weak, oblique shock observed experimentally. Subsequent studies²³ suggest that the strong-shock solution is the result of improper downstream boundary conditions on pressure and that if experimentally observed pressures are imposed at the downstream boundary, the weak-shock solution will be realized. The amplitude of the pressure oscillation in this quasi-steady flow is the same for both computation and experiment.

Figure 5 shows a comparison of the surface-pressure variation with time at four different locations on the airfoil: at the midchord on both the upper and lower surface and at 77.5% chord on both upper and lower surface. The oscillations on the upper and lower surfaces are a half period out of phase with each other. The frequency of the computed and measured oscillations agrees to within 20%. It is of special interest to note the agreement between some of the details of the pressure oscillations. For example, at the midchord position, both experimental and computed pressures show a very rapid rise and then a slower, almost exponential-like decay. At the 77.5% position, the pressure

rise is less rapid and there is almost a pressure plateau, with fine-scale structure, before a decay to a pressure minimum again. Some of this fine-scale structure is indicated in the computed results, as well as in the experiments.

Finally, in Fig. 6 is shown a comparison of experimental shadowgraph pictures and computed Mach contours over the upper aft portion of the airfoil at four different times during one period of oscillation. Except for the difference between a weak experimental shock wave and a strong computed shock wave, as noted earlier, the agreement between measured and computed flow-field features is excellent.

Buffet Boundaries

Another unsteady flow application of the same code used above was the determination of buffet boundaries for the Korn 1 airfoil.²⁴ Figure 7 shows a lift-drag polar and a lift curve for the Korn 1 supercritical airfoil for a nominal Mach number of 0.75. The computations, performed for angles of incidence ranging from -1.54° to 4.34° , are compared with the experimental data of Kacprzynski and Ohman.²⁵ The computed drag polar indicates the onset of buffet somewhat after maximum lift has been realized; it is illustrated by two different C_L -vs- C_D branches for angles of 3.25° and 4.34° . The lift and drag vary periodically along the branch corresponding to the particular angle of incidence. Other angles of incidence greater than 3° (not shown) would exhibit different paths of periodic variation. The lift curve indicates that the onset of buffet occurs at an angle of incidence of nearly 3° to the free stream. Here, for a given incidence, the minimum and maximum lift values define a buffet envelope. The computations were performed assuming free boundaries at the nominal wind-tunnel test conditions and no adjustments were made to account for Mach-number or flow-angularity corrections caused by wall interference. Neglecting Mach-number corrections, comparisons with the lift-curve data suggest equivalent angle-of-attack corrections of about -0.3° and -1.3° for the 6% and 20.5% wall-porosity experiments, respectively. This compares with corrections of -0.89° suggested by the experimental investigators in a subsequent study.²⁶

Aileron Buzz

Another unsteady phenomenon, this time associated with a moving boundary, is represented by the performance characteristics of the aileron of a P-80 aircraft. This configuration was exhaustively investigated experimentally in the mid-1940's by Erikson and Stephenson.²⁷ The flow has been simulated by Steger and Bailey,²⁸ using the fully implicit algorithm of Beam and Warming²⁹ and a method that couples the solution of an ordinary differential equation describing the motion of the aileron with the flow-field solution. The interrupted shock-wave motion over the aft portion of the airfoil causes a shift in phase of the aerodynamic hinge moment with respect to the movement of the aileron, thereby exciting an oscillation of the aileron (buzz) in one degree of freedom. In the experiment, for a Mach number of 0.82 and an angle of incidence to the free stream of -1.0° , the initially undeflected aileron was released (i.e., the one degree of freedom was made available) and it would oscillate 22.2° about a mean

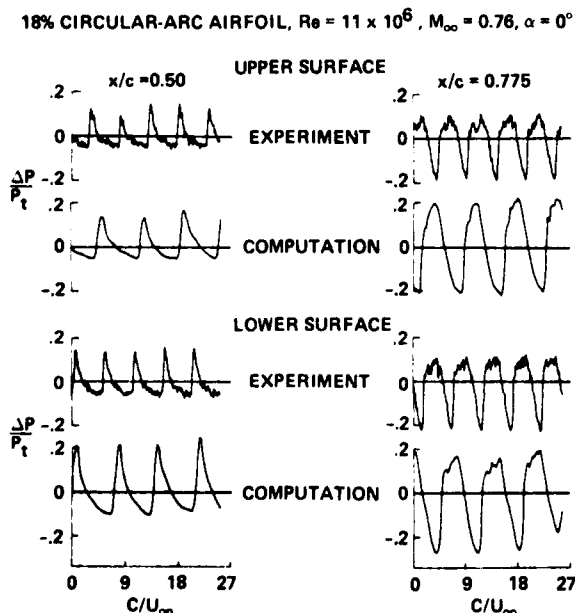


Fig. 5 "Buffeting" flow, surface-pressure time histories for 18% circular-arc airfoil.²⁴

18° CIRCULAR-ARC AIRFOIL, $Re = 11 \times 10^6$, $M_\infty = 0.76$
(SEEGMILLER et al., ref 21)

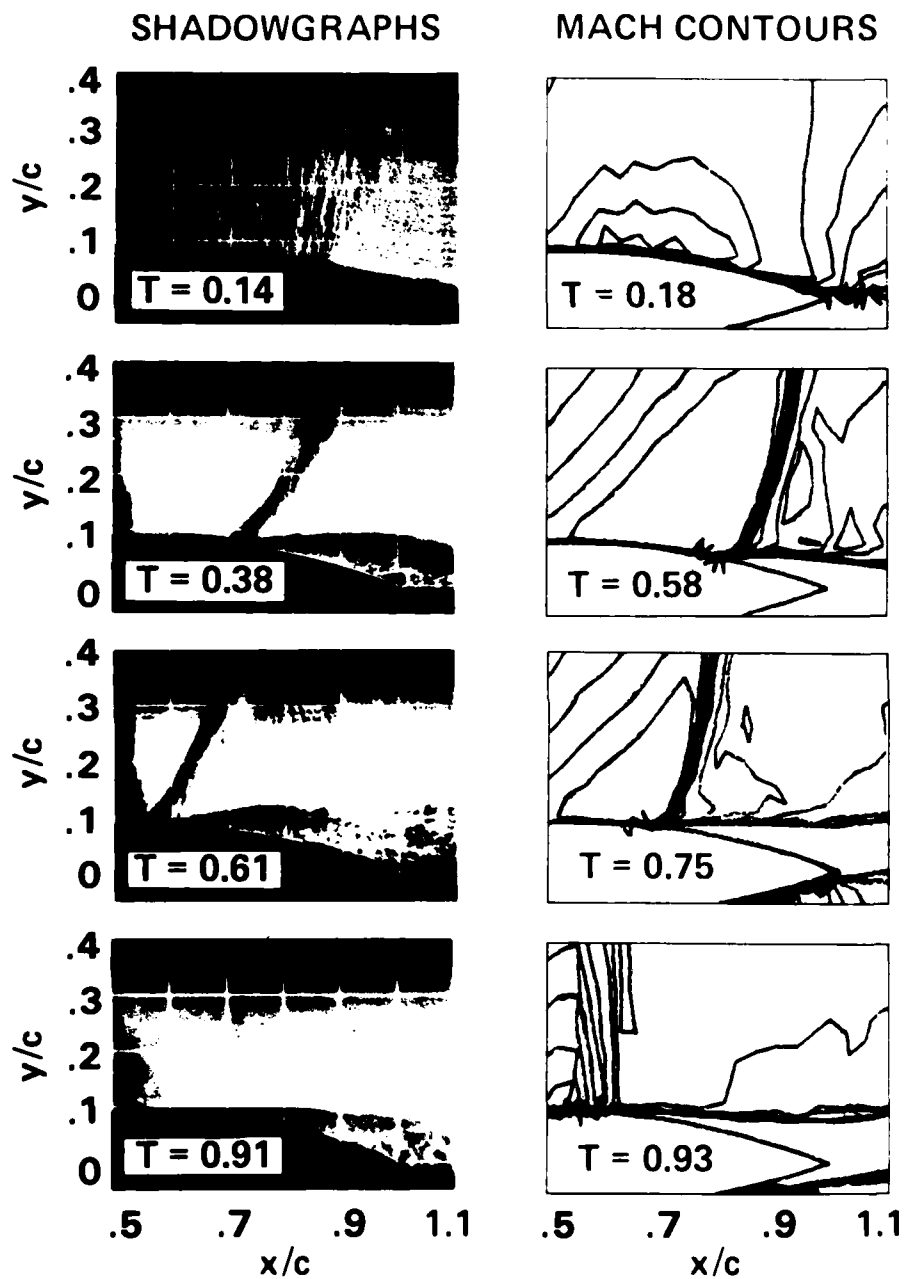


Fig. 6 Comparison of shadowgraphs and Mach contours for 18° circular-arc airfoil.¹⁹

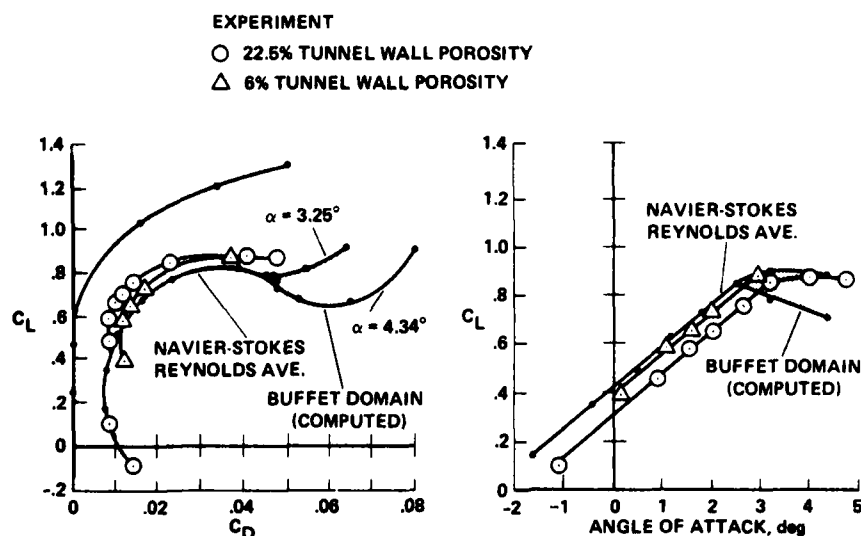


Fig. 7 Computed and measured transonic drag polar and lift curve for a supercritical airfoil.²⁴

incidence of -1.1° at a frequency of 22.2 Hz. Computationally, this unsteady behavior was not obtained for an initially undeflected aileron, but when the aileron was released from an initial position of 4° , it experienced oscillations of 18.4° about a mean incidence of -3.0° at a frequency of 21.2 Hz. Similar computations for an airfoil angle of incidence of -1.0° were made for a free-stream Mach number of 0.79; they showed that even with an initial deflection of 4° , the oscillations would damp out in a few cycles. The

results of these computations compared with experiment in Fig. 8, which shows both the buzz boundary as a function of free-stream Mach number and airfoil angle of incidence, and aileron deflection angles as a function of time for free-stream Mach numbers of 0.79 and 0.82 for the airfoil at an incidence of -1.0° . Shown in Fig. 9 are computed Mach contours for both the upper and lower deflection limits of the buzz cycle. Note particularly the relative positions of the upper and lower surface shocks in each of these limiting configurations.

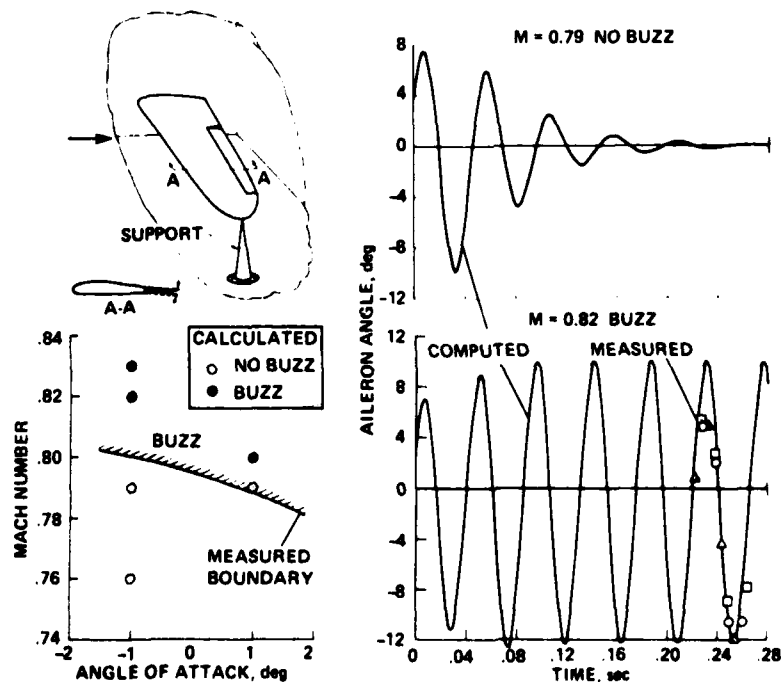


Fig. 8 Computed and measured characteristics of transonic aileron buzz.²⁴

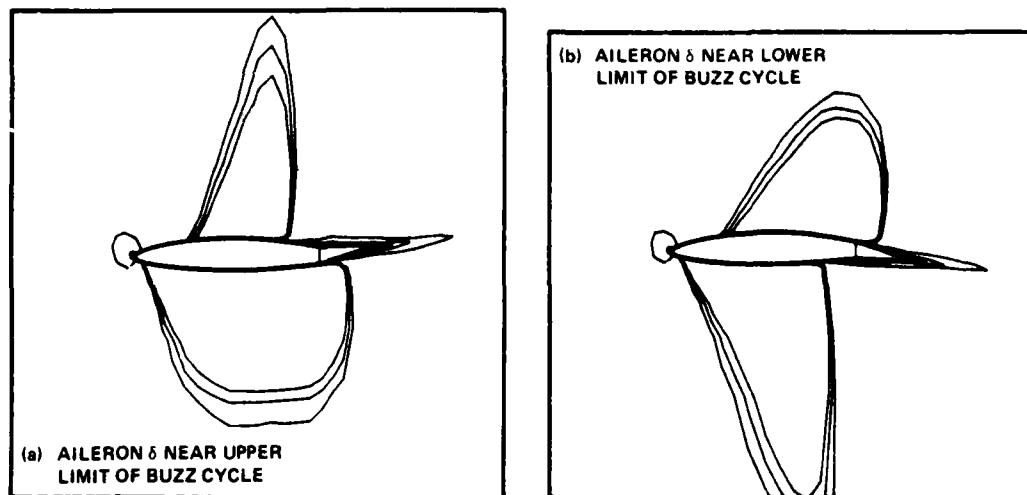


Fig. 9 Mach number contours of flow fields for transonic aileron buzz: $M = 0.82$, $\alpha = -1.1^\circ$

Stall Boundaries

A fourth example is the computation of the stall boundary of a given airfoil. Levy and Bailey,²⁹ using both the hybrid MacCormack algorithm and the fully implicit Beam and Warming algorithm, performed a series of computations for a wide range of Mach numbers and angles of

incidence for both a NACA 65-213 airfoil (the P-80 airfoil section) and the Korn 1 supercritical airfoil. Shown in Fig. 10 is the boundary for the onset of unsteady flow as a function of lift coefficient and free-stream Mach number for the Korn 1 section. Comparison with experimental data of Ohman et al.³⁰ for the same configuration show generally good agreement, especially for the higher values of Mach number and lower lift coefficients,

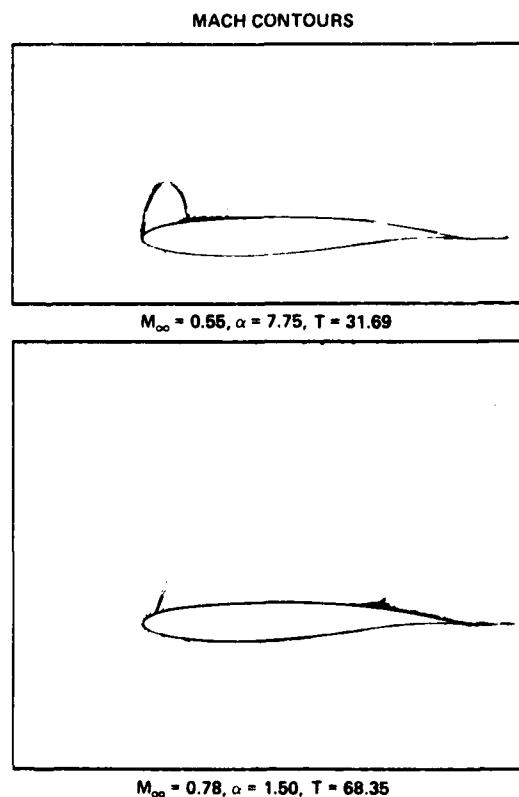
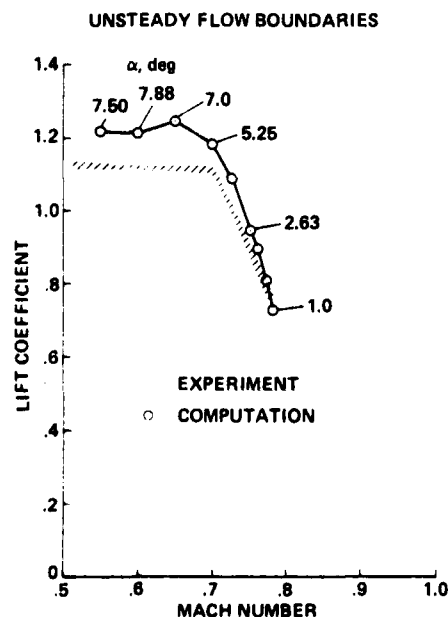


Fig. 10 A performance characteristic in maneuver of Korn-1 airfoil at $Re = 21 \times 10^6$

values of Mach number and lower lift coefficients, where the shock-wave system determines a buffet-onset boundary. For the lower Mach numbers and high lift coefficients (corresponding to high angles of incidence), the stall boundary is similar to that of classical low-speed trailing-edge separation, as opposed to shock-wave/boundary-layer interactions. This is illustrated by the computed Mach contours for both a high-incidence and low-incidence configuration in the figure.

Dynamic Stall

Several studies of dynamic stall have been performed using the compressible Navier-Stokes equations. In most instances the implicit method of Briley and McDonald⁸ was used to study flows with free-stream Mach numbers low enough so that there were no regions of supersonic flow and hence no shock/boundary-layer interactions. Included in these works are the laminar dynamic stall studies of Gibelings et al.¹¹ and of Sankar and Tassa,¹² and the turbulent dynamic stall studies of Shamroth and Gibelings¹³ and of Tassa and Sankar.¹⁴ Shamroth¹² also used a one-equation, differential eddy-viscosity model to study an oscillating airfoil without stall.

More recently, Chyu and Kuwahara¹⁵ used the Beam and Warming implicit method to study the transonic flow over an oscillating airfoil with shock-induced separation. Both the full Navier-Stokes equations and the thin-layer approximation were considered. Shown in Fig. 11 is a comparison of computed and experimental mean-value pressure distributions over an NACA 64A010 airfoil section that is oscillating between 3° and 5°. These results indicate a significant influence of cross- and transverse-shear terms in the full Navier-Stokes equations and suggest the importance of their inclusion to realize good agreement with the experimental oscillating airfoil data. In view of the relatively coarse streamwise grid spacing used in the computations and corresponding

lack of resolution of the additional shear terms relative to the thin-layer terms, the reason for the significant difference observed for the two computations is not completely clear. Even though the additional terms were included in the equations, any finite-difference evaluation of them with the coarse grid considered should result in negligibly small values. Studies by other investigators (e.g., Degani and Steger¹⁶ and Hung and Kurasaki¹⁷) indicate that these terms are negligible and do not influence the flow-field solution.

Concluding Remarks

In the preceding sections some of the considerations and problems associated with numerically simulating unsteady interactive flows of aerodynamic interest have been discussed. Attention was focused on solutions to the time-dependent, compressible, Reynolds-averaged, Navier-Stokes equations, using empirical eddy-viscosity models to account for the effects of turbulence. The importance of writing the equations in strong conservation-law form for a generalized body-oriented coordinate system was pointed out. Some considerable discussion of time and length scales inherent in the class of flows considered was given. To date, simulations have been performed for unsteady flows with narrow frequency bands. The treatment of many flows with broad-band unsteadiness has not been attempted yet and poses a serious challenge to state-of-the-art methods. The numerical schemes used to solve the governing equations were classified as explicit, implicit, or hybrid, and all were seen to have associated time-step constraints for numerical stability. There is some degree of choice in the implementation of turbulence models in the computational algorithms, and the final evaluation of an algorithm including the model must be based on comparisons with experiment and benchmark computations. Several examples of simulated unsteady interacting flows were given covering such aerodynamic phenomena as buffet, stall, and aileron buzz. In each case good agreement with experimental data was found, thus increasing our confidence in our ability to simulate numerically these complex flows.

References

- ¹MacCormack, R. W., "The Effect of Viscosity in Hypervelocity Impact Cratering," AIAA Paper 69-354, Jan. 1969.
- ²MacCormack, R. W. and Baldwin, B. S., "A Numerical Method for Solving the Navier-Stokes Equations with Application to Shock-Boundary Layer Interactions," AIAA Paper 75-1, Jan. 1975.
- ³Baldwin, B. S., MacCormack, R. W., and Delwert, G. S., "Numerical Techniques for the Solution of the Compressible Navier-Stokes Equations and the Implementation of Turbulence Models," AGARD-LS-73, Computational Methods for Inviscid and Viscous Two- and Three-dimensional Flow Fields, Feb. 1975.

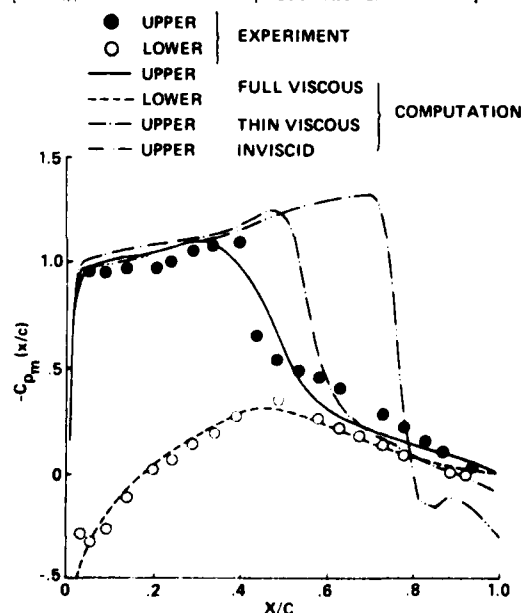


Fig. 11 Mean value of unsteady pressure over oscillating NACA 64A010 airfoil.

⁶McCormack, R. W., "A Rapid Solver for Hyperbolic Systems of Equations," Lecture Notes in Physics, Vol. 54, A. I. van de Vooren and P. J. Zandbergen, Eds., Springer-Verlag, New York, 1976, pp. 307-317.

⁷McCormack, R. W., "An Efficient Explicit-Implicit-Characteristic Method for Solving the Compressible Navier-Stokes Equations," SIAM-AMS Proceedings, Vol. 11, 1978, pp. 130-155.

⁸Deiwert, G. W., "Numerical Simulation of High Reynolds Number Transonic Flows," AIAA Journal, Vol. 13, 1975, pp. 1354-1359.

⁹Deiwert, G. S., "Computation of Separated Transonic Turbulent Flows," AIAA Journal, Vol. 14, 1976, pp. 735-740.

¹⁰Deiwert, G. S., "On the Prediction of Viscous Phenomena in Transonic Flows," Transonic Flow Problems in Turbomachinery, T. C. Adamson and M. F. Platzer, Eds., Hemisphere Publishing Corp., 1977, pp. 371-391.

¹¹Deiwert, G. S., "Recent Computation of Viscous Effects in Transonic Flow," Lecture Notes in Physics, Vol. 59, A. I. van de Vooren and P. J. Zandbergen, Eds., Springer-Verlag, New York, 1976, pp. 159-164.

¹²Deiwert, G. S., "Computation of Turbulent Near Wakes for Asymmetric Airfoils," Viscous and Interacting Flow Field Effects, K. H. Bronau and H. U. Meier, Eds., Proceedings of the 4th U. S. Air Force and the Federal Republic of Germany Data Exchange Agreement Meeting BMVg-FBWT 79-31, 1979, pp. 455-467; also NASA TM-78581, 1979.

¹³Viviani, H., "Conservation Forms of the Gas Dynamics Equations," Recherche Aerospaciale, Vol. 1, 1974, pp. 153-158.

¹⁴Shamroth, S. J., "A Turbulent Flow Navier-Stokes Analysis for an Airfoil Oscillating in Pitch," Unsteady Turbulent Shear Flows, R. Michel, J. Cousteix, and R. Houdeville, Eds., Springer-Verlag, New York, 1981, pp. 185-196.

¹⁵Chapman, D. R., "Computational Aerodynamics Development and Outlook," AIAA Journal, Vol. 17, 1979, pp. 1293-1313.

¹⁶Michel, R., Cousteix, J., and Houdeville, R., Eds., Unsteady Turbulent Shear Flows, Springer-Verlag, New York, 1981.

¹⁷Schiff, L. B., "A Numerical Solution of the Axisymmetric Jet Counterflow," Lecture Notes in Physics, Vol. 59, A. I. van de Vooren and P. J. Zandbergen, Eds., Springer-Verlag, New York, 1976, pp. 391-397.

¹⁸Lax, P. and Wendroff, B., "Systems of Conservation Laws," Communications in Pure and Applied Mathematics, Vol. 13, 1960, pp. 217-237.

¹⁹Beam, R. M. and Warming, R. F., "An Implicit Factored Scheme for the Compressible Navier-Stokes Equation," AIAA Journal, Vol. 16, 1978, pp. 393-402.

²⁰Brilov, W. R. and McDonald, H., "Solution of the Multidimensional Compressible Navier-Stokes Equations by a Generalized Implicit Method," Journal of Computational Physics, Vol. 24, No. 1, Aug. 1977, p. 372.

²¹Mehta, U. and Lomax, H., "Reynolds Averaged, Navier-Stokes Computations of Transonic Flows - The State-of-the-Art," D. Nixon, Ed., Transonic Aerodynamics, AIAA, New York, 1982; also M. Summerfield, Ed., Progress in Astronautics and Aeronautics, Vol. 81, AIAA, New York, 1982, pp. 297-375.

²²McDevitt, J. B., Levy, L. L., and Deiwert, G. S., "Transonic Flow about a Thick Circular-Arc Airfoil," AIAA Journal, Vol. 14, 1976, pp. 606-613.

²³Seegmiller, H. L., Marvin, J. G., and Levy, L. L., "Steady and Unsteady Transonic Flows," AIAA Journal, Vol. 16, 1978, pp. 1262-1270.

²⁴Levy, L. L., "Experimental and Computational Steady and Unsteady Transonic Flows About a Thick Airfoil," AIAA Journal, Vol. 16, 1978, pp. 564-570.

²⁵Coakely, T. J. and Bergmann, M. Y., "Effects of Turbulence Model Selection on the Prediction of Complex Aerodynamic Flows," AIAA Paper 79-0070, Jan. 1979.

²⁶Deiwert, G. S. and Bailey, H. E., "Prospects for Computing Airfoil Aerodynamics with Reynolds Averaged Navier-Stokes Codes," NASA CP-2045, 1978.

²⁷Kacprzynski, J. J. and Ohman, L. H., "Wind Tunnel Tests of a Shockless Lifting Airfoil No. 1," National Research Council of Canada, NAE Project Rept. 5x5/0054, 1972.

²⁸Kacprzynski, J. J., "A Second Series of Wind Tunnel Tests of the Shockless Lifting Airfoil No. 1," National Research Council of Canada, NAE Project Rept. 5x5/0062, 1972.

²⁹Erikson, A. L. and Stephenson, I. D., "A Suggested Method of Analyzing for Transonic Flutter of Control Surfaces Based on Available Experimental Evidence," NACA RM-A7F30, 1947.

³⁰Steger, J. L. and Bailey, H. E., "Calculation of Transonic Aileron Buzz," AIAA Journal, Vol. 18, 1980, pp. 249-255.

³¹Levy, L. L. and Bailey, H. E., "Computation of Airfoil Buffet Boundaries," AIAA Journal, Vol. 19, 1981, pp. 1488-1490.

³²Ohman, L. H., Kacprzynski, J. J., and Brown, D., "Some Results from Tests in the NAE High Reynolds Number Two-dimensional Test Facility on 'Shockless' and Other Airfoils," Canadian Aeronautics and Space Journal, Vol. 19, 1973, pp. 297-312.

³³Gibeling, H. J., Shamroth, S. J., and Eiseman, P. R., "Analysis of Strong-Interaction Dynamic Stall for Laminar Flow on Airfoils," NASA CR-2969, 1978.

³⁴Sankar, N. L. and Gass, Y., "Reynolds Number and Compressibility Effects on Dynamic Stall of a NACA 0012 Airfoil," AIAA Paper 80-0610, Jan. 1980.

¹³Shumroth, S. J. and Gibeling, R. J., "Analysis of Turbulent Flow about an Isolated Airfoil Using a Time-Dependent Navier-Stokes Procedure," AGARD Specialists Meeting on Boundary Layer Effects on Unsteady Airloads, Aix-en-Provence, Sept. 1980.

¹⁴Tassa, Y. and Sankar, N. L., "Dynamic Stall of an Oscillating Airfoil in Turbulent Flow Using Time Dependent Navier-Stokes Solver," Unsteady Turbulent Shear Flows, R. Michel, J. Cousteix, and R. Houdeville, Eds., Springer-Verlag, 1981, pp. 185-196.

¹⁵Chyu, W. J. and Kuwahara, K., "Computations of Transonic Flow over an Oscillating Airfoil with Shock-Induced Separation," AIAA Paper 82-350, Jan. 1982.

¹⁶Degani, D. and Steger, J. L., "A Computational Comparison between Navier-Stokes and Thin Layer Equations for Separated Supersonic Flow," Submitted to AIAA Journal.

¹⁷Hung, C. M. and Kurasaki, S. S., "Thin-Layer Approximation for Three-Dimensional Supersonic Corner Flows," AIAA Journal, Vol. 18, Dec. 1980, pp. 1544-1546.

NAVIER-STOKES SOLUTION OF SHOCK BOUNDARY-LAYER INTERACTIONS AT TRANSONIC SPEED

Y. Tassa and D. Shuster
Lockheed-Georgia Company
Marietta, Georgia

Abstract

In this paper we will compare numerical solutions of the Reynolds averaged Navier-Stokes equations to experimental data for flows over airfoils at transonic speed in which a shock wave interacts with, and causes separation of, a turbulent boundary layer. The numerical solutions will be generated using Lockheed-Georgia Navier-Stokes code which we have been developing over the past several years. We'll describe some of the features of the code. An algebraic turbulence model is used to describe the Reynolds shear stress. The 2-D Navier-Stokes equations are written in a strong conservation form in a curvilinear coordinate system. The computational plane is obtained using grid generation based on the Thompson et al. approach. The numerical scheme is based on an Alternating Direction Implicit (ADI) procedure.

Convergence to steady state is accelerated by the use of a variable time step determined by the local Courant number. The far-field boundary conditions are based on the appropriate characteristics combination of the dependent variables.

Two basic geometries will be analyzed, the NACA64A010 airfoil and LG4-612 supercritical airfoil. Detailed numerical results will be obtained for both geometries at various freestream Mach numbers, angles of attack and Reynolds number. Cases will include both mild and strong separated regions. Numerical results will be compared to an extensive set of experimental data which includes wall pressure distributions, velocity profiles and Mach number contours.

A DIRECT METHOD FOR THE SOLUTION OF UNSTEADY
TWO-DIMENSIONAL INCOMPRESSIBLE NAVIER-STOKES EQUATIONS

K.N. Ghia, G.A. Osswald and U. Ghia

Department of Aerospace Engineering and Applied Mechanics
University of Cincinnati
Cincinnati, Ohio

Abstract

The unsteady incompressible Navier-Stokes equations are formulated in terms of vorticity and stream function in generalized curvilinear orthogonal coordinates to facilitate analysis of flow configurations with general geometries. The numerical method developed solves the conservative form of the transport equation using the alternating-direction implicit method, whereas the stream-function equation is solved by direct block Gaussian elimination. The method is applied to a model problem of flow over a back-step in a doubly infinite channel, using clustered conformal coordinates. One-dimensional stretching functions, dependent on the Reynolds number and the asymptotic behavior of the flow, are used to provide suitable grid distribution in the separation and reattachment regions, as well as in the inflow and outflow regions. The optimum grid distribution selected attempts to honor the multiple length scales of the separated-flow model problem. The asymptotic behavior of the finite-differenced transport equation near infinity is examined and the numerical method is carefully developed so as to lead to spatially second-order accurate wiggle-free solutions, i.e., with minimum dispersive error. Results have been obtained in the entire laminar range for the backstep channel and are in good agreement with the available experimental data for this flow problem.

1. Introduction

The accurate simulation of moderately high-Reynolds number viscous flows in and around complex internal configurations of importance in turbomachinery applications, poses a formidable task. The flow fields for these complex configurations may involve any or all of the following features, namely, unsteadiness, three-dimensionality, geometrical complexities, streamwise separation, recirculation, compressibility, turbulence, etc. For accurate prediction of aerodynamic losses and heat-transfer rates in such configurations, it is important that the viscous flow field be predicted correctly. The present study is directed towards accurate simulation of viscous flows involving streamwise separation and unsteadiness, in addition to other features that may be present in the flow.

For viscous flows in configurations of practical interest, the Reynolds number is generally quite high. Nevertheless, the classical boundary-layer theory is inadequate for prediction of such flows as they contain regions of separated flow, massive blowing, etc., where the boundary layer is sufficiently displaced from the body surface so as to alter the inviscid pressure distribution significantly. For this class of problems, where a

significant displacement effect prevails, two viable approaches are available for predicting the viscous flow fields. (i) The first method is based on an inviscid-viscous strong interaction analysis based on localized-flow regions, whereas (ii) the second method consists of using, in the entire region of interest, a single set of equations which have the necessary mutual dependence between the inviscid and the viscous flow built into them. Recently, Davis and Werle [1] have reviewed the progress of the strong-interaction analysis, which is useful in describing a large class of boundary-layer departure flows. The theoretical basis for the various strong-interaction models lies in the multi-structured asymptotic analyses [see 2-6]. In these analyses, the subscale flow structure embedded under the boundary layer-like region is considered rigorously and the strong-interaction approach is formally shown to provide an exact representation of the flow for asymptotically large Reynolds numbers. In the flow field of interest, as the displacement-interaction effects become significant, the 'triple-deck' theory aids in establishing the relative orders of the length scales required for the adjustment of a classical boundary layer as it enters a region of strong interaction and separation. However, for complex internal flows at finite Reynolds number, the prevailing flow may differ significantly from the predictions of the strong-interaction model.

The second class of methods used in obtaining solutions for internal flows, in which viscous phenomena considerably alter the inviscid pressure field, is the fully viscous analysis. In these analyses, a single set of equations, valid in the entire flow field, is used, thus avoiding the need for dividing the flow field into inviscid and viscous regions. Of the three prominent approaches available in this category, two are based on reduced forms of the Navier-Stokes equations, whereas the third uses the complete Navier-Stokes equations. (i) In the first approach, the time-dependent thin-shear-layer equations are used (Steger [7]) to successfully compute separated flows; this approach has been widely used. Rubin and co-workers have also calculated separated flows using the steady thin-layer form of the Navier-Stokes equations with the streamwise pressure-gradient term represented by a forward-difference approximation. The results obtained using this approach have been summarized by Rubin [10]. (ii) In the second approach, the complete pressure interaction is included by using a Poisson equation for pressure, in lieu of the continuity equation. This has been termed a semi-elliptic formulation by U. Ghia et al. [8] who employed it to successfully compute separated flow inside a doubly infinite channel with an asymmetric constriction using primitive variables. Recently, K. Ghia and U. Ghia [9] have proposed yet another semi-elliptic formulation for

* This research was supported, in part, by AFOSR Grant No. 80-0160 and, in part, by NASA Lewis Grant No. NSG-3267.

compressible viscous flow, which efficiently computes separated flow. (iii) Finally, separated, internal flows are calculated using the complete Navier-Stokes equations by many researchers (see, e.g. [11-14]). With this last approach, it is possible to compute flows with large separated regions, where shear layers are not necessarily aligned with any one of the coordinates. Moreover, since the solution of the complete Navier-Stokes equations are generally based on the time-dependent equations, both unsteady as well as steady solutions can be determined numerically by explicit or implicit methods.

In general, implicit numerical methods display improved stability characteristics as compared to explicit methods, at the expense of increased arithmetic-operations count. Therefore, an implicit method for the solution of algebraic equations is recommended whenever the step-size limitation imposed by the stability requirement for an explicit-method is significantly less than the step-size limitation imposed by the time-scale resolution of the physical problem. Furthermore, the presence of multiple scales in a separated flow contributes to increased stiffness of the nonlinear system of discretized algebraic equations, and may also suggest the use of implicit solution techniques. Recently, Osswald and Ghia [14] have developed a direct method for the solution of two-dimensional, unsteady, incompressible Navier-Stokes equations in generalized orthogonal coordinates. This unsteady analysis was formulated using the derived variables, namely, vorticity ω and stream function ψ . In this method, the stream function equation was solved using a block Gaussian elimination (BGE) technique. This direct Dirichlet Poisson solver in generalized orthogonal coordinates is very accurate and efficient, with computational gains of an order of magnitude over the corresponding iterative schemes. In a recent review of fast solvers for elliptic equations, Stüben [15] has shown that the Dirichlet Poisson problem with a (256, 256) grid in Cartesian coordinates required one to two orders of magnitude higher computing time when solved by iterative schemes such as the alternating-direction implicit (ADI) method and the successive over relaxation (SOR) method, respectively, as compared to the time required by a direct solver such as that of Buneman. The efficiency and accuracy of the fast solvers make them very well suited for the solution of the Poisson equation in the unsteady analysis of flows using the complete Navier-Stokes equations.

The primary objective of the present study is to provide an accurate and efficient direct method for the solution of two-dimensional unsteady incompressible Navier-Stokes equations using orthogonal curvilinear coordinates. To achieve this goal, it was decided to refine the method developed by Osswald and Ghia [14] by incorporating in it the following improvements which could lead to a more realistic simulation of physical problems and increase the accuracy and efficiency of the overall solutions:

- i. For a class of internal-flow configurations, with the length in the streamwise dimension very large compared to the length in the normal dimension, an estimate is made of all the local scales of the flow problems in order to provide a clustered grid distribution which honors these individual scales.

- ii. With the aid of an estimate of the asymptotic metric coefficients, a reduced form of the governing equations are obtained near infinity and the numerical solutions of these equations are used to provide consistent inflow and outflow boundary conditions.
- iii. The separated-flow model problem selected is one for which reliable experimental data are available, so that the results obtained using the present analysis can be meaningfully assessed by comparison with these data.

2. Governing Equations in Generalized Orthogonal Coordinates

A considerable number of numerical simulations of 2-D, laminar incompressible viscous flows have been obtained using the vorticity-stream function (ω, ψ) system. There are definite advantages as well as disadvantages in using this system as compared to the primitive-variable (u, v, p) system. In this study, it has been preferred to employ the (ω, ψ) system. The form of the governing differential equations and the notations used parallel the study of Osswald and K. Ghia [14]. The conservation form of the two-dimensional, unsteady, incompressible Navier-Stokes equations, in terms of the vorticity ω and the stream function ψ , consist of a temporally parabolic-spatially elliptic vorticity-transport equation

$$\frac{\partial \omega}{\partial t} + \nabla \cdot (\omega \vec{v}) = \frac{1}{Re} \nabla^2 \omega, \quad (2.1)$$

together with an elliptic Poisson equation for the stream function

$$\nabla^2 \psi = -\omega. \quad (2.2)$$

Here, Re is the Reynolds number of the flow and the stream function is defined through the relation

$$\vec{v} = \nabla \psi \times \vec{k}, \quad (2.3)$$

where \vec{k} is the unit vector normal to the plane of the flow and \vec{v} is the total velocity vector. A general orthogonal curvilinear coordinate system (ξ^1, ξ^2) is used in this study to provide non-uniform surface-oriented coordinates for arbitrary geometries. The new (ξ^1, ξ^2) coordinates can be related to the inertial Cartesian coordinate system (x^1, x^2) by an admissible coordinate transformation $\xi^i(x^1, x^2) \leftrightarrow x^j(\xi^1, \xi^2)$, $i, j=1, 2$. In this coordinate system, Eqs. (2.1) and (2.2) take the following form:

$$\begin{aligned} \frac{1}{\sqrt{g}} \frac{\partial \omega}{\partial t} + \frac{1}{\sqrt{g}} \left(\omega \frac{\partial \psi}{\partial \xi^1} \right) - \frac{1}{\sqrt{g}} \left(\omega \frac{\partial \psi}{\partial \xi^2} \right) \\ = \frac{1}{Re} \left[\frac{1}{\sqrt{g}} \left(\frac{\partial^2 \omega}{\partial \xi^1^2} \right) + \frac{1}{\sqrt{g}} \left(\frac{\partial^2 \omega}{\partial \xi^2^2} \right) \right] \end{aligned} \quad (2.4)$$

and

$$\frac{1}{\sqrt{g}} \left(\frac{\partial^2 \psi}{\partial \xi^1^2} \right) + \frac{1}{\sqrt{g}} \left(\frac{\partial^2 \psi}{\partial \xi^2^2} \right) = -\omega. \quad (2.5)$$

Here, g_{ij} are the elements of the covariant metric tensor and are defined as

$$g_{ij} = \sum_{k=1}^2 \left(\frac{\partial x^k}{\partial \xi^i} \right) \left(\frac{\partial x^k}{\partial \xi^j} \right), \quad (2.6a)$$

and g is the determinant of the metric tensor.

Since the (ξ^1, ξ^2) coordinate system is assumed orthogonal in the present study,

$$g_{12} = g_{21} = 0, \quad (\text{Orthogonality Condition})$$

so that

$$g = g_{11} g_{22}, \quad \text{and} \quad \frac{g_{11}}{\sqrt{g}} \frac{g_{22}}{\sqrt{g}} = 1. \quad (2.6b,c)$$

For a general orthogonal coordinate transformation, the metric coefficients \sqrt{g} , g_{11}/\sqrt{g} and g_{22}/\sqrt{g} will be functions of both ξ^1 and ξ^2 , so that Eqs. (2.4) and (2.5) are, in general, not separable. For orthogonal coordinates, the metric elements are related to the scale factors as $\sqrt{g_{11}} = h_1$ and $\sqrt{g_{22}} = h_2$; hence, the metric coefficient g_{11}/\sqrt{g} and g_{22}/\sqrt{g} can be written as

$$\frac{g_{11}}{\sqrt{g}} = \sqrt{\frac{g_{11}}{g_{22}}} = \frac{h_1}{h_2} \quad \text{and} \quad \frac{g_{22}}{\sqrt{g}} = \sqrt{\frac{g_{22}}{g_{11}}} = \frac{h_2}{h_1}. \quad (2.6d,e)$$

These ratios in Eq. (2.6d,e) represent the aspect ratio of a general curvilinear element in the physical plane corresponding to an infinitesimal square element in the transformed plane. Also, the elemental area dA in the physical plane is related to the corresponding area in the transformed plane as $dA = \sqrt{g} d\xi^1 d\xi^2$.

Use of Eqs. (2.4) and (2.5), together with appropriate boundary conditions for ω and ψ can lead to the formulation of an appropriate boundary-value problem for the flows. However, the discussion on the boundary conditions will be deferred until the model flow problem to be analyzed has been selected. The governing Eqs. (2.4) and (2.5) form a coupled set of nonlinear equations and the numerical method used to obtain their solutions is discussed next.

3. Numerical Analysis of the Discrete Equations

3.1 Preliminaries

The coordinate transformation referred to in Section 2 is so chosen as to transform the physical region R to a unit square in the computational plane (ξ^1, ξ^2) . A uniform $(N+1, M+1)$ finite-difference grid Δ is used and is defined as

$$\Delta = \{(\xi_i^1, \xi_j^2) : \xi_i^1 = i(\Delta\xi^1), \xi_j^2 = j(\Delta\xi^2); \\ 0 \leq i \leq (N+1), 0 \leq j \leq (M+1)\} \quad (3.1)$$

with

$$\Delta\xi^1 = \frac{1}{N+1} \quad \text{and} \quad \Delta\xi^2 = \frac{1}{M+1}.$$

Thus, the region R is comprised of $(N+1)$ and $(M+1)$ computational intervals along the ξ^1 and ξ^2 coordinate directions, respectively. The cell aspect ratio β in the computational plane is given as $\beta = (\Delta\xi^1/\Delta\xi^2)$, and is maintained constant. For convenience, the following nomenclature is introduced for the metric coefficients:

$$G = \sqrt{g}, \quad G_{11} = g_{11}/\sqrt{g} = \sqrt{g_{11}/g_{22}}, \\ G_{22} = g_{22}/(\sqrt{g} \beta^2), \quad G_{22} = \sqrt{g_{22}}/\sqrt{g_{11}} \quad (3.2)$$

The spatial derivatives are approximated by appropriate finite-difference quotients, using at most three grid points in a given direction. Keeping the spatial differences compact facilitates the implementation of the boundary conditions to second-order accuracy and aids in the overall stability of the algorithm. Consequently, central differences are used for both convective and diffusive derivatives in the governing equations. It is significant to note that, in this study, even with central-difference approximations for all spatial derivatives, no artificial dissipation is added to dampen the high-frequency errors, but the latter are carefully annihilated through appropriate resolution of the various length scales of the problem.

3.2 Alternating-Direction Implicit (ADI) Method for Transport Equation

The conservative form of the two-dimensional vorticity-transport Eq. (2.4) is differenced using a uniform $(N+1, M+1)$ grid Δ defined by Eq. (3.1) and the resulting nonlinear algebraic equations are solved using the ADI technique as described by Osswald and K. Ghia [14]. In this method, the transport equation at time level t_{n+1} is discretized with the stream function being frozen at the time level t_n . Due to this linearization, the formal temporal accuracy of the scheme is $O(\Delta t_n)$. For spatial discretization, a typical computational cell is shown sketched in Figure 1. For consistent differencing of the conservation form of the differential equations, the metric coefficients $(G_{11})_{i,j}$ and $(G_{22})_{i,j}$ are evaluated at the staggered half-grid point locations, whereas the metric coefficient $G_{i,j}$, the solution field functions $\omega_{i,j}$, $\psi_{i,j}$ and the source term $S_{i,j}$ are evaluated at the cell corners. The ADI form of the discrete equations is arrived at by approximate factorization, which simplifies the computational algorithm to a sequence of the one-dimensional solution processes. First, the intermediate vorticity field $\omega_{i,j}^*$, with its appropriate boundary conditions, is described by a tridiagonal-matrix problem. Similarly, the final vorticity $\omega_{i,j}^{n+1}$, with its own boundary conditions, forms a second tridiagonal-matrix problem. These matrix problems are solved sequentially using the Thomas algorithm, which is a special form of the direct Gaussian elimination procedure. This calculation requires $[28(N \cdot M) + 24(N)]$ floating-point

multiplications. The solution of the discrete transport equation provides a transient flow simulation with a formal truncation accuracy of $O[(\Delta \xi_1)^2, (\Delta \xi^2)^2]$

3.3 Block Gaussian Elimination (BGE) Method

For the solution of the discrete Poisson problem on a rectangular domain, considerable effort has been focused on the efficient direct methods of Buneman and Hockney as presented in References [16-19] using Cartesian coordinates. Schumann and Sweet [20] extended Buneman's cyclic-reduction technique to include a very special class of separable non-Cartesian coordinates, whereas Schwarztrauber [21] has provided the extension of Buneman's method to treat the general separable elliptic equation. For the discrete Poisson problem in completely general orthogonal coordinates, Osswald and K. Ghia [14] have provided the highly competitive direct block Gaussian elimination (BGE) method, which is accurate and efficient and is briefly summarized next.

3.3.1 The Matrix Dirichlet Poisson Problem in Generalized Orthogonal Coordinates

The Dirichlet Poisson problem is formulated using a general scalar field function ϕ in some arbitrary orthogonal curvilinear coordinate system (ξ^1, ξ^2) such that

$$\frac{\partial}{\partial \xi^1} \left(\frac{g_{22}}{\sqrt{g}} \frac{\partial \phi}{\partial \xi^1} \right) + \frac{\partial}{\partial \xi^2} \left(\frac{g_{11}}{\sqrt{g}} \frac{\partial \phi}{\partial \xi^2} \right) = \sqrt{g} s(\xi^1, \xi^2) \quad \text{in } R \quad (3.3a)$$

$$\text{with } \phi = d(\xi^1, \xi^2) \quad \text{on } \partial R. \quad (3.3b)$$

In this equation, $s(\xi^1, \xi^2)$ is the known source term and $d(\xi^1, \xi^2)$ represents the given Dirichlet boundary conditions. Use of the grid Δ and central-difference approximations for the spatial derivatives appearing in Eq. (3.3a) results in the discretized equation

$$\begin{aligned} & G_{22B_{i-1,j}} \phi_{i-1,j} + G_{11_{i,j-1}} \phi_{i,j-1} \\ & - (G_{22B_{i-1,j}} + G_{11_{i,j-1}} + G_{11_{i,j}} + G_{22B_{i,j}}) \phi_{i,j} \\ & + G_{11_{i,j}} \phi_{i,j+1} + G_{22B_{i,j}} \phi_{i+1,j} \\ & = (\Delta \xi^2)^2 G_{i,j} s_{i,j} \end{aligned} \quad (3.4)$$

The Dirichlet boundary conditions are given as

$$\phi_{i,j} = d_{i,j} = d(\xi_i^1, \xi_j^2) \quad \text{on } \partial \Delta. \quad (3.5)$$

The formal truncation accuracy of Eq. (3.4) is $O[(\Delta \xi^1)^2, (\Delta \xi^2)^2]$. Equation (3.4) can be written symbolically in matrix-vector form as

$$A P = S \quad (3.6)$$

The coefficient matrix A in Eq. (3.6) is a symmetric $(N \times N)$ block-tridiagonal matrix of the form

$$A = \begin{bmatrix} A_1 & B_1 & 0 & 0 & \dots & 0 & 0 \\ B_1 & A_2 & B_2 & 0 & & 0 & 0 \\ 0 & B_3 & A_2 & B_2 & & 0 & 0 \\ & & & & & & \\ & & & & & B_{N-1} & A_N \end{bmatrix} \quad (3.7a)$$

where the individual blocks A_i and B_i are square $(M \times M)$ submatrices dependent only upon the metric coefficients of the transformation given in Eq. (3.2). In particular, the diagonal blocks of A are the symmetric $(M \times M)$ tridiagonal matrices given as

$$A_i = \begin{bmatrix} a_{i,1} & G_{11_{i,1}} & 0 & 0 & 0 & 0 \\ G_{11_{i,1}} & a_{i,2} & G_{11_{i,2}} & 0 & 0 & 0 \\ 0 & G_{11_{i,2}} & a_{i,3} & G_{11_{i,3}} & 0 & 0 \\ & & & & & \\ & & & & & G_{11_{i,M-1}} & a_{i,N} \end{bmatrix} \quad (3.7b)$$

where the diagonal elements of A_i are given as

$$a_{i,j} = -(G_{22B_{i-1,j}} + G_{11_{i,j-1}} + G_{11_{i,j}} + G_{22B_{i,j}}). \quad (3.7c)$$

Further, the off-diagonal blocks of A are the $(M \times M)$ diagonal matrices given as

$$B_i = \begin{bmatrix} G_{22B_{i,1}} & & & & \\ & G_{22B_{i,2}} & & & \\ & & G_{22B_{i,3}} & & \\ & & & & \\ & & & & G_{22B_{i,M}} \end{bmatrix} \quad (3.7d)$$

To arrive at the form of the matrix-vector equation represented by Eq. (3.6), the unknown solution field $\phi_{i,j}$ has been arranged as a block-vector P such that the individual block entries of P are the column vectors of the matrix $\phi_{i,j}$. This is expressed as

$$P = (P_1, P_2, \dots, P_N)^T \quad (3.8a)$$

where

$$P_i = (\phi_{i,1}, \phi_{i,2}, \dots, \phi_{i,M})^T \quad (3.8b)$$

Thus, the column vector P contains a total of $(N \cdot M)$ unknowns. Similarly, the source vector S is given as

$$S = (S_1, S_2, \dots, S_N)^T \quad (3.9a)$$

where

$$S_i = (q_{i,1}, q_{i,2}, \dots, q_{i,M})^T \quad (3.9b)$$

with

$$\begin{aligned} q_{i,j} = & (\Delta \xi^2)^2 G_{i,j} s_{i,j} - \delta_{i1} G_{228,0,j} d_{0,j} \\ & - \delta_{iN} G_{228,N,j} d_{N+1,j} - \delta_{1j} G_{11,i,0} d_{i,0} \\ & - \delta_{Mj} G_{11,i,M} d_{i,M+1} \end{aligned} \quad (3.9c)$$

Here, δ_{ki} is the Kronecker delta function.

Equation (3.7) shows that each diagonal block element A_i of the matrix Dirichlet Poisson operator A is itself diagonally dominant. Also, since the metric coefficients of Eq. (3.2) are always positive for any admissible coordinate transformation, each block element A_i will be negative definite and, consequently, nonsingular. Such a symmetric block-tridiagonal matrix, whose diagonal blocks are tridiagonal submatrices and whose off-diagonal blocks are diagonal submatrices is very well suited for efficient direct inversion by the BGE technique of Osswald and K. Ghia [14] as described next.

3.3.2 The BGE Technique for the Dirichlet Poisson Problem

The block Gaussian elimination technique is a direct extension of the Gaussian elimination procedure to matrices whose individual elements are themselves matrices or blocks. The efficiency of the block elimination approach is enhanced when the block matrix is sparse. The BGE technique provides the effective inversion of an $(N \cdot M \times N \cdot M)$ matrix through the actual inversion of a predetermined sequence of N $(M \times M)$ submatrices; the choice $M \leq N$ leads to the best computational efficiency. Thus, BGE may be viewed as a "multi-level" technique since it reduces the level of the matrix problem to a series of N $(M \times M)$ subproblems.

The BGE approach naturally divides itself into two separate calculation phases. In the first phase, a sequence of N $(M \times M)$ matrices is formed and individually inverted by simple scalar-Gaussian elimination. This phase is the most time-consuming part of the calculation and the multiplication count performed shows that approximately $[\frac{1}{2}(N)(M)^3 + 2(N)(M)^2 - \frac{1}{2}(M)^3]$ floating-point multiplications are required to complete this phase for the Dirichlet Poisson operator of Eq. (3.7a). Fortunately, this preliminary phase need be executed only once for a given coordinate choice, its result being permanently stored as a series of coefficient matrices for later use in the second phase of the block-elimination procedure.

The second phase consists of the actual solution of the block matrix problem given by Eq. (3.6) for a prescribed source term S through a set of recursion relationships. These recursion relationships use the coefficient matrices precalculated in phase one and require approximately $[2(N)(M)^2 + 2(N)(M) - (M)^2]$ floating-point multiplications. This count shows that the second phase of the procedure is, by far, less time-consuming.

Indeed, it is precisely because only the second phase of the BGE procedure need be repeated to solve Eq. (3.6) for various source terms that reasonable computational efficiency may be expected. This is particularly true in the context of an unsteady Navier-Stokes calculation during which the Dirichlet stream-function Poisson problem must be solved many times in a given coordinate system for a progression of updated source terms.

It is important to note that the difference between the technique of Osswald and K. Ghia [14] described above and the block-Gaussian elimination algorithm given by Dorr [17] is the recognition of the natural splitting of the BGE method into two separate phases. Indeed, it is precisely this splitting which allows the block-Gaussian elimination procedure to remain competitive with other techniques available for the solution of the Dirichlet Poisson problem for the stream function ψ .

In view of this discussion, it should be stated that the combined ADI-BGE method developed here is very well suited for studying unsteady flows governed by the unsteady Navier-Stokes equations; it is also useful in obtaining time-asymptotic solutions of the steady Navier-Stokes equations.

4. Model Problem for Incompressible Separated Flow

The separation phenomena caused by abrupt changes in flow geometries in internal flows are well known. Any insight gained for this class of separated flows will lead to improved analyses, and will aid in developing effective design tools. In general, separated flows become unstable at relatively moderate Reynolds number and an unsteady analysis which can accurately predict these types of flows would be most desirable. The flow over a backward facing step inside a channel has been used by many investigators as a model problem for viscous separated flow, due to the simplicity of the geometry. Careful experimental data [22, 23] as well as theoretical analyses [24, 25] are available for this flow. Hence, this configuration has also been used in the present study of incompressible separated flow.

4.1 Details of Geometry and Transformations

Figure 2 shows the configuration of a backward facing step inside a doubly infinite channel. For brevity, the configuration will be referred to as a backstep channel. The origin of the physical-plane coordinates is placed at the location of the step transition. The channel height at the outlet is chosen as the reference length L_r , and the mean outflow velocity is taken as the reference velocity, U_r . Therefore, the Reynolds number is defined as $Re = \rho U_r L_r / \mu$. Clearly, this flow

configuration has a geometric similarity parameter H as shown in Fig. 2. Here, H is the ratio of the throat opening or pre-transition channel height to the post-transition channel height and may be viewed as a throttling mechanism for reference outflow conditions. The mean velocity U_{in} at inlet is related to the outflow velocity by the relation $U_{in} = U_r / H$. Thus, for fixed outflow conditions, diminishing the throat opening, i.e. decreasing H , will increase the mean inflow velocity, and subsequently, produce a larger separated flow field

at fixed Re. Hence, similarity for the backstep channel requires not only Reynolds number equality, but also equality of the throat opening ratio H, which is bounded between 0 and 1.

4.1.1 Conformal Transformation - T_B

The "natural" coordinate system for the backstep channel is obtained using an analytical conformal transformation. This coordinate transformation is not only convenient to align the boundaries of the channel with the new curvilinear coordinates, but also allows accurate implementation of the boundary conditions while maintaining formal second-order spatial accuracy. The desired conformal transformation T_B is given by the relation

$$z = \frac{1}{2} \{ \ln[U + (U^2 - 1)^{1/2}] - H \ln[V + (V^2 - 1)^{1/2}] \} . \quad (4.1a)$$

The various quantities appearing in this equation, as well as those used in subsequent definitions, are given as

$$U = \frac{2W - (k+1)}{(k-1)} , \quad V = \frac{(k+1)W - 2k}{(k-1)W} , \quad W = e^{-\zeta} ,$$

$$k = \left(\frac{1}{H}\right)^2 , \quad \zeta = -1 + i\eta^2 , \quad z = x + iy \quad \text{and} \quad i = \sqrt{-1} . \quad (4.1b)$$

This transformation maps the doubly infinite backstep channel geometry of Fig. 2 onto a doubly infinite strip $\{-1, -2\} \leq \eta^2 \leq 1$ in the conformal (η^1, η^2) plane. An additional transformation is needed to make the domain in the η^1 direction bounded for computational purposes.

4.1.2 Grid-Clustering Transformation - T_C

A second transformation is used to map this doubly infinite strip in the (η^1, η^2) plane onto a unit square in the computational domain R. Here, two independent one-dimensional stretching transformations are used to provide the desired grid clustering in the boundary layers and separated regions of the flow field. The use of two separate 1-D stretching transformations provide the flexibility needed to resolve the multiple scales of this flow problem. These grid-clustering transformations are given as

$$\xi^1 = \frac{1}{2} \left[\tan^{-1} \left(\frac{\eta^1 - x_1}{D_1} \right) + \tan^{-1} \left(\frac{\eta^1 - x_2}{D_2} \right) \right] + \frac{1}{2} , \quad (4.2a)$$

$$\xi^2 = \left[2 \tan \left(\frac{1}{2c} \right) \right]^{-1} \tan \left(\frac{\eta^2 - \frac{1}{2}}{c} \right) + \frac{1}{2} . \quad (4.2b)$$

The parameters x_1 and x_2 represent the two η^1 locations where grid points are to be clustered in the streamwise direction, while the parameters D_1 and D_2 control the degree of this clustering. Similarly, the parameter c controls the degree of grid-point clustering in the normal direction. The degree of clustering can also be interpreted in terms of a stretching ratio SR, e.g., for the normal-coordinate clustering, $SR = \frac{d(\xi^2)}{d(\eta^2)} \approx 2 = 0.1$.

4.1.3 Combined Transformation - $T = T_B \cdot T_C$

The metric coefficients given in Eq. (3.2) can now be determined for the overall coordinate transformation, which is obtained by combining the transformations T_B and T_C given in Eqs. (4.1) and (4.2). The metric coefficients become

$$G = h^2 \gamma_1(\eta^1) \gamma_2(\xi^2) , \quad (4.3a)$$

$$G_{11} = \gamma_1(\eta^1) / \gamma_2(\xi^2) , \quad (4.3b)$$

and

$$G_{22} = \gamma_2(\xi^2) / \gamma_1(\eta^1) . \quad (4.3c)$$

The quantities $\gamma_1(\eta^1)$ and $\gamma_2(\xi^2)$ are defined as

$$\gamma_1(\eta^1) = 2\pi / \left[\frac{D_1}{2 + (\eta^1 - x_1)^2} + \frac{D_2}{(D_2)^2 + (\eta^1 - x_2)^2} \right] ,$$

$$\gamma_2(\xi^2) = 2c \tan \left(\frac{1}{2c} \right) / \left\{ 1 + \left[2 \left(\xi^2 - \frac{1}{2} \right) \tan \left(\frac{1}{2c} \right) \right]^2 \right\}$$

and h is the scale factor of the conformal transformation given as

$$h = \left| \frac{dz}{d\zeta} \right| . \quad (4.4c)$$

For the overall transformation given in Eq. (4.3), γ_1 is a function of η^1 only and γ_2 depends only on ξ^2 . In this sense, the coordinate transformation is considered separable. Indeed, this was expected because of the choice of the individual transformations T_B and T_C . However, it should be noted that the analysis developed here is valid even when the coordinate transformation is merely orthogonal, i.e., neither conformal nor separable in the sense just stated.

4.2 Selection of Transformation Parameters to Resolve Multiple Scales

For the backstep channel geometry as shown in Fig. 2, the region extending from slightly upstream of the backward facing step to the furthest reattachment point is referred to as the "transition" region. In this region, convection dominates over diffusion. On the other hand, the regions upstream and downstream of this "transition" region become increasingly diffusion-dominated as the inlet and outlet sections at $\pm \infty$ of the channel are approached. In an experimental study of the "transition" region of the backstep channel geometry, Armaly and Durst [23] have shown the existence of one or more separation bubbles in the channel, for a fixed value of H , as the value of Re is increased gradually. If such a separated flow has to be computed accurately, the scaling in the normal direction is no longer of $O(Re^{-1/2})$. As given in References [3, 4], at high Re , the correct scaling for the separated flow around the separation points is of $O(Re^{-3/8})$ in the streamwise direction and $O(Re^{-5/8})$ in the normal direction.

In the grid clustering transformation T_C , five

parameters x_1 , x_2 , D_1 , D_2 and SR are embedded in Eq. (4.4). These parameters facilitate, to a reasonable extent, the desired grid clustering in the physical plane to resolve the multiple scales of this separated-flow model problem. To resolve the scales in the streamwise direction near the separation points, the parameters D_1 and D_2 are

chosen to provide the desired grid clustering around the proper locations x_1 and x_2 , such that the separation scales of $O(\text{Re}^{-3/8})$ in the streamwise direction are appropriately resolved. The mathematical expressions which determine these four parameters are given as

$$x_1 = \frac{\ln(k)}{\pi}, \quad (4.5a)$$

$$x_2 = x_1 + c_1 \left[\frac{\ln(W_{x_0})}{\pi} - x_1 \right], \quad (4.5b)$$

$$D_1 = x_1 / \tan[2\pi m_1 \Delta\xi^1 - 1 + \tan^{-1}(\frac{x_2 - x_1}{D_2}) - \tan^{-1}(\frac{x_2}{D_2})] \quad (4.5c)$$

and

$$D_2 = (x_2 - x_1) / \tan[2\pi(m_2 - m_3 \Delta\xi^1)] . \quad (4.5d)$$

Here, m_1 is an integer denoting the number of $\Delta\xi^1$ -intervals placed on the step height BO and m_3 is the total number of $\Delta\xi^1$ intervals between the inflow boundary and point O . The quantity m_2 is taken to be $1/2$ in order to map the points B and O onto mid-points of $\Delta\xi^1$ intervals; this allows for circumventing the singularity in the metric coefficients at these corner points. The values selected for m_1 and m_3 are such that the resulting overall grid satisfies two requirements. First, between the corner point B and the reattachment point x_0 , the streamwise grid spacing is required to be nearly uniform as the distance $B-x_0$ is a measure of the convection scale. Second, the near-infinity diffusion scale must also be resolved. Hence, the grid is stretched in the streamwise direction only after the flow has become diffusion dominated.

In the normal direction, the parameter SR aids in resolving the scales of $O(\text{Re}^{-5/8})$ around the lower and upper separation points as well as the wall shear layers. The actual choice of a particular grid for a given configuration is arrived at by numerical experiments with the grid generator in which the various parameters are so selected as to yield the desired grid. The grid distributions used in this study will be presented in the next section.

4.3 Asymptotic Flow Near Channel Infinities

The analysis to be presented here is valid for a class of internal flow problems in which the normal coordinate η^2 is bounded and, asymptotically at $\eta^1 = \pm\infty$, the configurations have straight inflow and outflow sections, with any desired shape of the connecting transition section. The grid-clustering transformation T_C was selected so as to map the inflow and outflow boundary conditions at $\pm\infty$ to the finite values $\xi^1 = 0$ and $\xi^1 = 1$, respectively,

in the computational coordinates. Consequently, $1/\eta^1$ becomes a small parameter in the proximity of the inflow section, where $\xi^1 = 0$, and near the outflow section, where $\xi^1 = 1$. With the use of a small parameter defined as

$$\varepsilon = \frac{1}{\eta^1}, \quad (4.6)$$

Osswald [26] has determined the scale factor h near the inflow and outflow sections and has shown that

$$\text{As } \eta^1 \rightarrow -\infty: h = H - H \cos(\pi\eta^2) \left(\frac{k-1}{2k}\right) e^{\pi/\varepsilon} + O(e^{\pi/\varepsilon})^2, \quad (4.7a)$$

and

$$\text{As } \eta^1 \rightarrow +\infty: h = 1 - \cos(\pi\eta^2) \left(\frac{k-1}{2}\right) e^{-\pi/\varepsilon} + O(e^{-\pi/\varepsilon})^2. \quad (4.7b)$$

Thus, the backstep channel approaches a straight channel near the inflow and outflow sections in an exponential manner. Near these sections, the function γ_1 of Eq. (4.4a) takes the form

$$\gamma_1 = \frac{2\pi}{D_1 + D_2} \left(\frac{1}{\varepsilon}\right)^2 - \frac{4\pi(x_1 D_1 + x_2 D_2)}{(D_1 + D_2)^2} \left(\frac{1}{\varepsilon}\right) + O(1), \quad (4.8)$$

whereas the function γ_2 of Eq. (4.4b) remains unaffected. Considering only the leading term in

Eq. (4.8) yields $\gamma_1 = \Gamma_\infty \left(\frac{1}{\varepsilon}\right)^2$, where $\Gamma_\infty = \text{const.}$

This asymptotic behavior of γ_1 is representative of the wide class of internal flow problems referred in the beginning of this subsection.

The grid-clustering transformation T_C maps the region $-\infty < \eta^1 < \infty$ onto the interval $[0,1]$ in the ξ^1 direction in such a manner that η^1 approaches infinity like $1/\varepsilon$. Hence, the metric coefficients given in Eq. (4.3) take the form

$$G = h_\infty^2 \Gamma_\infty \gamma_2 \left(\frac{1}{\varepsilon}\right)^2 - O\left(\frac{1}{\varepsilon}\right), \quad (4.9a)$$

$$G_{11} = \frac{\Gamma_\infty}{\gamma_2} \left(\frac{1}{\varepsilon}\right)^2 - O\left(\frac{1}{\varepsilon}\right), \quad (4.9b)$$

and

$$G_{22} = \frac{\gamma_2}{\Gamma_\infty} (\varepsilon)^2 + O(\varepsilon^3), \quad (4.9c)$$

$$\text{where } h_\infty = \lim_{\xi^1 \rightarrow 0,1} [h] \text{ and } \Gamma_\infty = \lim_{\eta^1 \rightarrow \pm\infty} \left[\frac{\gamma_1}{(\eta^1)^2} \right] = \frac{2\pi}{D_1 + D_2}. \quad (4.10a,b)$$

In light of this analysis, near upstream and downstream infinity, the governing differential equations (2.4-2.5) take the following form

$$\left[\frac{\varepsilon^2}{h_\infty^2 \gamma_2} + O(\varepsilon^3) \right] \frac{\partial}{\partial \xi^1} \left[\frac{\gamma_2 \varepsilon^2}{\gamma_1} \frac{\partial \psi}{\partial \xi^1} + O(\varepsilon^3) \frac{\partial \psi}{\partial \xi^1} \right] + \left[\frac{\varepsilon^2}{h_\infty^2 \gamma_2} + O(\varepsilon^3) \right] \frac{\partial}{\partial \xi^2} \left[\frac{\gamma_2}{\gamma_1} \frac{\partial \psi}{\partial \xi^2} - O\left(\frac{1}{\varepsilon}\right) \frac{\partial \psi}{\partial \xi^2} \right] = -\dots \quad (4.11a)$$

$$\begin{aligned}
& \frac{\partial}{\partial t} + \left(\frac{\varepsilon^2}{h_{\infty}^2 \gamma_2} + O(\varepsilon^3) \right) \left[\frac{\partial}{\partial \xi^1} \left(\omega \frac{\partial \psi}{\partial \xi^2} \right) - \frac{\partial}{\partial \xi^2} \left(\omega \frac{\partial \psi}{\partial \xi^1} \right) \right] \\
& = \frac{1}{\text{Re}} \left[\frac{\varepsilon^2}{h_{\infty}^2 \gamma_2} + O(\varepsilon^3) \right] \frac{\partial}{\partial \xi^1} \left[\frac{\gamma_2 \varepsilon^2}{2} \frac{\partial \omega}{\partial \xi^1} + O(\varepsilon^3) \frac{\partial \omega}{\partial \xi^1} \right] \\
& + \frac{1}{\text{Re}} \left[\frac{\varepsilon^2}{h_{\infty}^2 \gamma_2} + O(\varepsilon^3) \right] \frac{\partial}{\partial \xi^2} \left[\frac{\gamma_2 \varepsilon^2}{2} \frac{\partial \omega}{\partial \xi^2} - O(\varepsilon^3) \frac{\partial \omega}{\partial \xi^2} \right],
\end{aligned} \quad (4.11b)$$

Since η^1 is a function of ξ^1 only,

$$\frac{\partial}{\partial \xi^1} (\varepsilon^2) = -2\varepsilon^3 \frac{d\eta^1}{d\xi^1} = -2\varepsilon^3 \gamma_1 = -2\gamma_{\infty} \varepsilon + O(\varepsilon^2),$$

and

$$\frac{\partial}{\partial \xi^2} \left(\frac{1}{\varepsilon^2} \right) = 0. \quad (4.12a,b)$$

Thus, Eqs. (4.11) simplify to the following form near the channel inflow and outflow sections:

$$\frac{\partial \omega}{\partial t} = \frac{1}{\text{Re} h_{\infty}^2 \gamma_2} \frac{\partial}{\partial \xi^2} \left[\frac{1}{\gamma_2} \frac{\partial \omega}{\partial \xi^2} \right] + O(\varepsilon), \quad (4.13a)$$

and

$$\frac{1}{h_{\infty}^2 \gamma_2} \frac{\partial}{\partial \xi^2} \left[\frac{1}{\gamma_2} \frac{\partial \psi}{\partial \xi^2} \right] = -\omega + O(\varepsilon). \quad (4.13b)$$

It is observed that Eqs. (4.11) are ξ^2 -diffusion dominated near channel inflow and outflow sections. The most significant terms, namely, those of $O(1)$ as well as $O(\varepsilon)$ are associated with the ξ^2 -diffusion operator, whereas the convection terms are of $O(\varepsilon^2)$ and the ξ^1 -diffusion terms are of $O(\varepsilon^3)$. If terms of $O(\varepsilon)$ are to be considered negligible in the asymptotic equations (4.12), η^1 must be large enough such that $\eta^1 \sim O(1/\varepsilon)$. For large η^1 , the present class of geometrical configurations are such that $x^1 \sim \eta^1$. Hence, there exist regions of $O(1/\varepsilon)$ in the physical plane near the inflow and outflow boundaries in which the flow simply diffuses in the ξ^2 -direction normal to the channel walls. These regions isolate the infinity boundaries from the convection-dominated transition region since any disturbance entering these regions is totally damped within the regions. Equations (4.13) enable plane Poiseuille flow to be established near the inlet and outlet sections, without any special treatment of the interior difference operators at these boundaries.

4.4 Boundary and Initial Conditions

To maintain consistent second-order spatial accuracy of the overall solution, the wall vorticity boundary conditions must also be implemented with second-order spatial accuracy. The earlier analysis of K. Chia et al. [27] was generalized by Osswald [26] to provide the second-order accurate form of the wall-vorticity boundary condition. This analysis expands the function $\partial \psi / \partial \xi^2$ at the mid-point of a boundary cell using a Taylor's series expansion in terms of the function

and its derivatives at the boundary itself. The consistent treatment of the higher derivatives of $\partial \psi / \partial \xi^2$ at the boundary, including the use of the reduced form of the governing equation (2.5), leads to the desired expression for the wall vorticity. Thus, the boundary conditions on the lower wall $\xi^2 = 0$ are

$$\begin{aligned}
& (\Delta \xi^2)^2 [3G_{L+1} \omega_L + G_{L+1} \omega_{L+1}] \\
& = 8 G_{L+1} \frac{[\psi_{L+3} - 3\psi_{L+2} - 21\psi_{L+1} + 23\psi_L]}{24} \\
& - (\Delta \xi^2)^2 \frac{\partial}{\partial \xi^1} [G_{22} \frac{\partial \omega}{\partial \xi^1}]_{L+1} + O(\Delta \xi^2)^4 \quad (4.14a)
\end{aligned}$$

$$\text{and } \psi_L = 0. \quad (4.14b)$$

A similar expression can be obtained for the vorticity at the upper wall $\xi^2 = 1$, where the stream function $\psi_U = 1$.

The boundary conditions for ω and ψ at inflow and outflow sections are determined from the asymptotic form of the governing differential equations. These are obtained from Eqs. (4.13) as

$$\frac{\partial \omega}{\partial t} = \frac{1}{\text{Re} h_{\infty}^2 \gamma_2} \frac{\partial}{\partial \xi^2} \left[\frac{1}{\gamma_2} \frac{\partial \omega}{\partial \xi^2} \right], \quad (4.15a)$$

$$\frac{1}{h_{\infty}^2 \gamma_2} \frac{\partial}{\partial \xi^2} \left[\frac{1}{\gamma_2} \frac{\partial \psi}{\partial \xi^2} \right] = -\omega. \quad (4.15b)$$

For consistency with the numerical solutions in the interior, numerical rather than analytical solutions of the steady form of Eqs. (4.15) are used to provide the boundary conditions for ω and ψ at inflow and outflow sections. The appropriate wall boundary conditions for these asymptotic equations are obtained from Eqs. (4.14) by dropping out the ξ^1 -derivative term. Equations (4.15a,b) were solved simultaneously using a block Gaussian elimination method, which in effect is identical to solution by a modified Thomas algorithm for this coupled set of equations.

For the initial conditions, the flow inside the backstep channel was assumed, everywhere, to consist of the numerical solution of the steady form of Eqs. (4.15) obtained at $\eta^1 \rightarrow \pm \infty$. In the physical plane, this corresponds to parabolic velocity distributions at $x^1 \rightarrow \pm \infty$, while in the region of the backstep, these are scaled by the conformal-transformation scale factor. This procedure avoids discontinuities in the initial conditions at the backstep.

5. Results for Backstep Channel

The unsteady Navier-Stokes analysis and solution procedure discussed in sections 2 and 3 are applied to the flow in a doubly infinite backstep channel. This separated flow problem has been classified by Kumar and Vajnik [28] to have a streamwise length scale L_x of $O(\text{Re})$ and, in the limit of high Reynolds number, is governed by parabolic equations. This implies that the upstream influence is confined to a relatively short distance,

whereas the extent of the region of downstream influence increases with Re . The singularity at the sharp convex corner, as well as the difficulties associated with the simulation of high- Re flows, have been circumvented in the present analysis by exercising care in the formulation of the discretized problem. Hence, the results obtained are anticipated to be accurate. For all of the flow configurations listed in Table 1, the predicted results have asymptoted to steady state.

5.1 Quality of Grid

Application to flow configurations for which experimental data are available, together with the fact that the Navier-Stokes equations (2.4)-(2.5) asymptote to the diffusion-dominated equations (4.15) near the inflow and outflow boundaries, aided in the choice of appropriate values for the parameters m_1 and m_3 . Numerical experiments with various grids for these configurations enabled careful examination of the length scales near the separation points, as well as the near-infinity scale. This latter scale is assumed to be correctly represented if the flow solution in the interior smoothly approached the inflow and outflow boundary values. This requires that grid points be appropriately distributed in the diffusion-dominated regions near these boundaries. The degree to which the ϵ^2 -diffusion coefficient $G_{11}/(Gr\epsilon)$ dominates over the convection coefficient G in the grid cells adjacent to these boundaries provides a quantitative measure of the appropriateness of the near-infinity grid-point distribution. Hence, a quantity Q is defined as

$$Q = \frac{\text{convection}}{\epsilon^2 - \text{diffusion}} \bigg|_{\text{near infinity}} = \max \left[\frac{Re}{G_{11} N, j} \right] \quad (5.1)$$

and is required to be as small as possible near $\epsilon^1 = 0$ and 1. In the present study, Q was monitored for each grid distribution used and maintained to be of $O(10^{-3})$ or less. Two typical distributions with (85,33) and (195,33) grid points used in some of the present computations are shown in Figs. 3a and 3b.

5.2 Criterion for Steady State, Accuracy and Computational Efficiency

The steady state results were generated, wherever possible, as the time-asymptotic limit of the unsteady analysis. The criterion used to define the steady state is given as

$$\left| \frac{f_{i,j}^{n+1} - f_{i,j}^n}{f_{i,j}^{n+1} \Delta t} \right|_{\max} < \epsilon_f \quad \text{with} \quad \epsilon_f = 10^{-4} \quad (5.2)$$

where f represents either u or v , and the subscript \max denotes the maximum value encountered in the grid L . It was observed that, in general, u converged much more rapidly than v . Much before this criterion was satisfied everywhere, the flow in the "transition" region settled at its steady state values, while the flow in the regions near the outflow boundary continued to adjust at rather slow rates until it finally satisfied Eq. (5.2). Hence, the calculations were continued for almost twice as many characteristic time units as those required for steady state to be achieved in the transition

region. In each case, the numerical procedure continued to yield consistent and stable solutions.

Central differences are used throughout the flow field, so that the overall accuracy of the present method is $O(\Delta t, (\Delta \epsilon^1)^2, (\Delta \epsilon^2)^2)$. By satisfactorily resolving the multiple scales present in the problem, the resulting solutions are totally wiggle-free.

The relative computational efficiency of the present algorithm was measured in terms of the CPU time τ required to advance the solution by one time step per spatial grid point, i.e.,

$$\tau = \frac{\text{CPU seconds}}{\text{number of mesh points} \times \text{number of time steps}}$$

where τ represents the "computational effort." For the present algorithm, $\tau = 2.67 \times 10^{-4}$ seconds for the AMDAHL 470V/7 computer. The corresponding value for the implicit method of Beam and Warming [29] is 4.4×10^{-4} seconds for the compressible Navier-Stokes equations using the CDC 7600 computer.

5.3 Comparison of Steady State Flow Results with Experimental Data

Table 1 shows the eight flow configurations which have been analyzed in the present study. These include the configurations for which experimental data are available from Denham and Patrick [22] or Armaly and Durst [23]. The published experimental data provide one or more of the following results

- i. streamline contours;
- ii. velocity profiles at various streamwise locations using Cartesian coordinates;
- iii. locations of separation and reattachment points.

Although not presented here, the present streamline contours for the configurations with $Re = 146$ and 458 were compared with those of Denham and Patrick [22] and the agreement was very good for $Re = 146$ but, for $Re = 458$, the predicted results showed a higher value of the reattachment length L_1 than the corresponding measured value. This discrepancy is attributed to differences in the flow conditions just upstream of the backstep. In the present calculations, the flow exhibits a nearly-parabolic velocity distribution almost up to the backstep. This is not the case in the experiments where the backstep channel was devised by placing an appropriately shaped ramp on the lower wall of the channel. This destroys the symmetric parabolic velocity distribution and the flat portion of the ramp is not long enough for the symmetry to be restored by the time the flow reaches the backstep.

Comparison of the velocity profiles at various streamwise locations in the physical plane involves interpolation of the predicted results at points other than the computational points. The process has a tendency to degrade the accuracy of the results. Hence, the comparison of velocity profiles has been avoided in the study.

The separation bubble off the backstep is characterized by the length of this eddy, i.e., by the corresponding reattachment length. This reattachment length is plotted versus Re in Fig. 4a.

with the throat-opening ratio as a parameter. The present results show higher values of this reattachment length as compared to the experimental data of Denham and Patrick [22]. The discrepancy is maximum for $Re = 458$. Again, this is attributed to the differences in the flow conditions just upstream of the backstep where the experimental data of Denham and Patrick [22] show significant departure from a symmetric parabolic distribution. The device used to produce the backstep geometry distorts the flow in such a manner that the velocity near the lower wall upstream of the backstep is higher than that for a parabolic distribution. Due to this higher energy of the fluid in this region, the flow reattaches in a shorter distance than that predicted by the present calculations where the flow remains nearly parabolic just upstream of the backstep. The experimental data of Armaly and Durst [23] for $H = 0.5148$ are also plotted in Fig. 4a; the results of the present analysis are somewhat different in character as compared to this data. Armaly and Durst have predicted the laminar-flow regime to end at $Re = 600$, i.e., at $Re_D = 1200$, so that a slight further increase in Re is observed to lead to the onset of the transition regime characterized by a sharp decrease in the reattachment length as shown in Fig. 4a. Their experimental results for the location and the extent of the recirculation regions on the two walls are shown in Fig. 4b. It is seen from this figure that separation on the upper wall first occurs at $Re_D = 1014$ and further increase of Re causes the upper-wall separation point to shift upstream towards the backstep. On the other hand, the results of the present analysis show that the upper-wall separation point continues to shift downstream and away from the backstep even for $Re = 507$ and 600 , which correspond, respectively, to $Re_D = 1014$ and 1200 . Thus, it appears that according to the present predictions, this flow configuration with $Re_D = 1200$ is still in the laminar regime. It should be noted that, in the present analysis, the boundary conditions were placed at true infinities and the diffusion-dominated regions of $O(1/\epsilon)$ near infinities serve to totally diffuse any disturbances that enter these regions. It is possible that factors normally affecting transition may have triggered it early in the experiments. Further numerical experiments are planned to investigate this issue.

Armaly and Durst [23] had shown the existence of similarity between their experiments and those of Denham and Patrick [22] by plotting the reattachment length versus the Reynolds number, using the step height as the characteristic length. The results are shown in Fig. 4c, along with the results obtained from the present analysis. Because the upper-wall separation bubble continues to exist in the present computations even at $Re_D = 600$, the structure of the separated flow according to the present predictions is considerably different from that of Armaly and Durst [23]. Hence, the present results for configurations with $H = 0.51485$ should not show similarity with those of Denham and Patrick [22] who observed only a single separation bubble on the lower wall. The mechanism controlling the dynamics of the separation bubbles in the case with two separation bubbles is indeed different from that with only one separation bubble caused by the separating shear layer at the step. In fact, Denham and Patrick felt that, in their experiments for the configuration with $Re_D = 916$, the flow was only

marginally stable. The present results show that the appearance of the upper-wall separation bubble is marked by an abrupt decrease in the slope of the curve of h_1/h_2 vs. Re_D ; nevertheless, this slope remains positive.

5.4 Steady-State Results for Various Backstep Flow Configurations

The steady-state results are presented here for flow configurations I, II, IV and VII with Re_D of 1800, 292, 916 and 1014, respectively. Figure 5 (a through d) shows the streamline contours for these configurations. As seen in Fig. 5a, configuration I with $Re_D = 1800$ is the one with the smallest separation bubble and, hence, relatively simple to compute. This configuration was used by Rubin and Khosla [30] in the development of their coupled strongly implicit method. Figures 5b and 5c show the streamline contours for configuration II with $Re_D = 292$ and configuration IV with $Re_D = 916$, respectively. These configurations were used by Denham and Patrick [22] in their experimental study. As expected, the length of the separation bubble grows with increase in Re . Finally, the streamline contours are presented for configuration VII with $Re_D = 1014$ in Fig. 5d. This configuration was used by Armaly and Durst [23] in their study. To the authors' knowledge, the present results constitute the first detailed results computed for this flow problem showing a separation bubble on the upper wall. The shear layer separating off the backstep dips down and attaches to the lower wall, causing sharp changes in the flow and, consequently, the separation bubble at the upper wall.

The corresponding vorticity contours for these four configurations are shown in Figs. 6a through 6d. As anticipated, a heavy concentration of contour lines occurs near the sharp-convex corner, an indication of the presence of high velocity gradients in this region of maximum generation of vorticity. In the "transition" region, the vorticity contours are swept downstream by the stronger convection effects.

Figures 7a through 7d provide the transverse profiles of the total velocity vector, along ξ^2 lines, at selected streamwise locations. A region of reversed flow is observed downstream of the step near the lower wall for all of these configurations. Configuration VII with $Re_D = 1014$, shown in Fig. 7d, exhibits a large region of reversed flow near the upper wall also.

5.5 Transient Results for Backstep Flow Configuration VIII

The transient results for flow configuration VIII with $Re_D = 1200$ are presented in Figs. 8. Starting from time $t = 0$, four values of the characteristic time, namely, 4, 40, 112 and 421, are chosen to depict the time history of the flow as it approaches steady state. The flow in the transition region reaches close to its steady-state value at about $t = 76$, but the adjustments taking place near the outflow boundary require $t = 421$ in order to satisfy the steady-state criterion of Eq. (5.2). Figures 8a through 8d show the streamline contours of this transient flow as it reaches steady state, whereas Figs. 9a through 9d show the vorticity contours. The shedding of vortices at the sharp convex corner leads to additional separation bubbles at the lower wall. The strong

adverse pressure gradient resulting from the sudden expansion near the backstep also causes separation on the upper wall. Armaiv and Durst [23] had observed additional separation bubbles, in the transition regime of Re , downstream of the main bubble on the lower wall. Figures 8a and 8b also show such bubbles in the transient steps; but, according to the present prediction, these bubbles do not persist in the steady state. The vorticity contours shown in Fig. 9b exhibit the occurrence of the bursting phenomenon which may be partially responsible for the decay of the additional bubbles at the lower wall. Finally, the transverse profiles of the total velocity vector, along ξ -lines, at selected streamwise locations, are shown in Fig. 10. Two regions of strong reversed flow are observed both on the lower and the upper walls.

6. Conclusion

An analysis has been developed, using the unsteady Navier-Stokes equations in generalized curvilinear coordinates, to study 2-D incompressible separated flows. The discretized problem is formulated using central differences for the spatial derivatives, thus avoiding artificial viscosity. The ADI method has been used to solve the transport equation, whereas the BGE method is used to solve the Dirichlet Poisson problem. The overall accuracy of the numerical solution is $O(\Delta t, (\Delta \xi^1)^2, (\Delta \xi^2)^2)$.

The numerical method developed is applied to the separated flow inside a backstep channel. The results of the present analysis are verified extensively by comparison with the available experimental data for Re_s ranging from 72 to 565. For the configurations with only one separation bubble at the lower wall, there exists a similarity with respect to the backstep channel geometry. Hence, the reattachment length L_1/h_s of the primary separation bubble on the lower wall, for various geometries, collapses into a single curve when plotted versus Re_s . On the other hand, the configurations with an additional separation bubble at the upper wall show a marked change in the reattachment length L_1 of the lower-wall separation bubble. To the authors' knowledge, similar results have not been previously reported in the literature.

The unsteady analysis provides an accurate and efficient determination of the transient flow in the backstep channel. The shedding of vortices at the corner of the step, the formation of additional separation bubbles at the lower wall, the occurrence of the upper-wall separation bubble and the bursting phenomenon are observed in the present results which provide the detailed time-dependent structure for this flow. The analysis of this separated flow in the transitional regime of Re appears feasible with this unsteady analysis.

References

1. Davis, R.T. and Werle, M.J., (1981), "Progress on Interacting Boundary-Layer Computations at High Reynolds Number," Proceedings of First Symposium on Numerical and Physical Aspects of Aerodynamic Flows, Long Beach, California.
2. Stewartson, K., (1974), "Multistructured Boundary Layers on Flat Plates and Related Bodies," Advances in Applied Mechanics, Academic Press, Inc., Vol. 14, pp. 145-239.
3. Sochev, T.N., (1972), "On Laminar Separation," Mechanika Zhidkosti i Gaza, No. 3, pp. 47-59.
4. Messiter, A.F., (1975), "Laminar Separation: A Local Asymptotic Flow Description for Constant Pressure Downstream," in Flow Separation, AGARD Conf. Proceedings on Flow Separation, CP 168.
5. Smith, F.T., (1977), "The Laminar Separation of an Incompressible Fluid Streaming Past a Smooth Surface," Proc. Roy. Soc. A 356, p. 443.
6. Smith, F.T., (1979), "Laminar Flow of an Incompressible Fluid Streaming Past a Bluff Body, The Separation, Reattachment, Eddy Properties and Drag," J. Fluid Mech., Vol. 92, Part 1, pp. 171-205.
7. Steger, J., (1978), "Implicit Finite-Difference Simulation of Flow About Arbitrary Two-Dimensional Geometries," AIAA Journal, Vol. 16, No. 7, pp. 679-686.
8. Ghia, U., Ghia, K.N., Rubin, S.G. and Khosla, P.K., (1981), "Study of Separated Flow in a Channel Using Primitive Variables," International Journal of Computers and Fluids, Vol. 9, pp. 123-142.
9. Ghia, K.N. and Ghia, U., (1982), "Semi-Elliptic, Globally-Iterative Analysis for Two-Dimensional Subsonic Internal Viscous Flows," presented at NASA-Lewis Workshop on Computational Fluid Mechanics, Cleveland, Ohio, October 2-21.
10. Rubin, S.G., (1982), "Incompressible Navier-Stokes and Parabolized Navier-Stokes Solution Procedures and Computational Techniques," VKI Lecture Notes for Series on Computational Fluid Dynamics.
11. Briley, W.R., (1971), "A Numerical Study of Laminar Separation Bubbles Using the Navier-Stokes Equations," Journal of Fluid Mechanics, Vol. 47, Pt. 4, pp. 713-736.
12. Ghia, U., and Davis, R.T., (1974), "Navier-Stokes Solutions for Flow Past a Class of Two-Dimensional Semi-Infinite Bodies," AIAA Journal, Vol. 12, No. 12, pp. 1659-1665.
13. McDonald, H., Shamroth, S.J. and Briley, W.R., (1982), "Transonic Flows with Viscous Effects," in Transonic, Shock and Multi-Dimensional Flows: Advances in Scientific Computing, Editor: R.E. Meyer, Academic Press.
14. Osswald, G.A. and Ghia, K., (1981), "Study of Unsteady Incompressible Flow Using Nonuniform Curvilinear Grids, Time Marching and a Direct Method," Multigrid Methods, NASA CP-2202, Oct.
15. Stüben, K., (1982), "On the Construction of Fast Solvers for Elliptic Equations," VKI Lecture Notes, Brussels, Belgium, March 29-April 2.
16. Buzbee, B.L., Golub, G.H. and Nielson, C.W., (1970), "On Direct Methods for Solving Poisson's Equations," SIAM J. Numer. Anal., Vol. 7, pp. 627-657.

17. Dorr, F.W., (1970), "The Direct Solution of the Discrete Poisson Equation on a Rectangle," SIAM Review, Vol. 12, pp. 248-263.
18. Sweet, R.A., (1973), "Direct Methods for the Solution of Poisson's Equation on a Staggered Grid," Journal of Computational Physics, Vol. 12, pp. 422-428.
19. Sweet, R.A., (1974), "A Direct Method for the Discrete Solution of Separable Elliptic Equations," SIAM J. Numer. Anal., Vol. 11, pp. 506-520.
20. Schumann, U. and Sweet, R.A., (1976), "A Direct Method for the Solution of Poisson's Equation with Neumann Boundary Conditions on a Staggered Grid of Arbitrary Size," J. Comp. Physics, Vol. 20, pp. 171-182.
21. Schwarztrauber, P.N., (1974), "A Direct Method for the Discrete Solution of Separable Elliptic Equations," SIAM J. Numer. Anal., Vol. 11, pp. 1136-1150.
22. Denham, M.K. and Patrick, M.A., (1974), "Laminar Flow over a Downstream-Facing Step in a Two-Dimensional Flow Channel," Trans. Instrn. Chem. Engrs., Vol. 52, pp. 361-367.
23. Armaly, B.F. and Durst, F., (1980), "Reattachment Length and Circulation Regions Downstream of a Two-Dimensional Single Backward Facing Step," Momentum and Heat Transfer Processes in Recirculating Flows, HTD-Vol. 13, ASME, New York, New York, pp. 1-8.
24. Roache, P.J. and Mueller, T.J., (1970), "Numerical Solutions of Laminar Separated Flows," AIAA Journal, Vol. 8, No. 3, pp. 530-538.
25. Gosman, A.D. and Pun, W.M., (1973), "Lecture Notes for Course Entitled: Calculation of Recirculating Flow," Heat Transfer Report HTS/74/2, Imperial College, London, England.
26. Osswald, G.A., (1983), "Internal Viscous Flow Simulation Using a Direct Unsteady Incompressible Navier-Stokes Procedure and Generalized Orthogonal Coordinates," Ph.D. Dissertation, University of Cincinnati, Cincinnati, Ohio.
27. Ghia, K.N., Hankey, W.L., and Hodge, J.K., (1977), "Study of Incompressible Navier-Stokes Equations in Primitive Variables Using Implicit Numerical Technique," AIAA Paper No. 77-648, also, AIAA Journal, Vol. 17, No. 3, pp. 298-301, 1979.
28. Kumar, A. and Yajnik, K., (1980), "Internal Separated Flows at Large Reynolds Number," Journal of Fluid Mechanics, Vol. 97, Pt. 1, pp. 27-51.
29. Beam, R.M. and Warming, R.F., (1982), "Implicit Numerical Methods for the Compressible Navier-Stokes and Euler Equations," VKI Lecture Notes, Brussels, Belgium, March 29-April 2.
30. Rubin, S.G. and Khosla, P.K., (1981), "Navier-Stokes Calculations with a Coupled Strongly Implicit Method - I, Finite Difference Solutions," Computers and Fluids, Vol. 9, pp. 163-180.

TABLE 1. PARAMETERS FOR VARIOUS FLOW CONFIGURATIONS

CONFIGURATION	H	h_s	Re	Re_D	Re_S	L_1	L_4	L_5	(L_5-L_4)	Reference
I	0.90000	0.10000	900	1800	100	0.69	--	--	--	Rubin & Khosla [30]
II	0.66667	0.33333	146	292	72	1.69	--	--	--	Denham & Patrick [22]
III			250	500	125	2.50	--	--	--	
IV			458	916	229	3.91	--	--	--	
V	0.51485	0.48515	150	300	141	3.23	--	--	--	Armaly & Durst [23]
VI			300	600	283	4.96	4.05	7.32	3.27	
VII			507	1014	478	6.08	4.70	11.45	6.75	
VIII			600	1200	565	6.39	4.97	12.96	7.99	

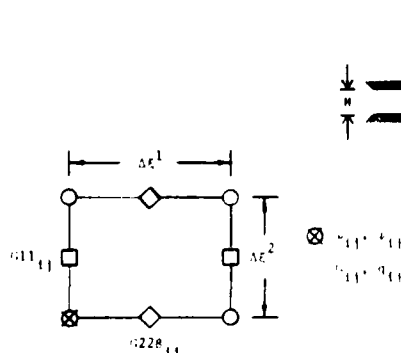


Fig. 1. Typical Computational Cell and Location of Variables

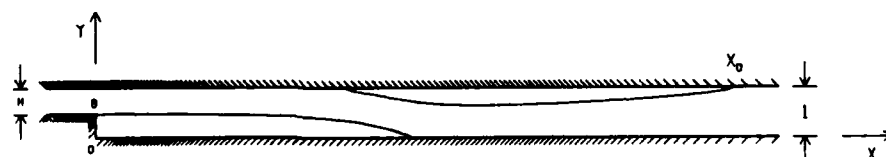


Fig. 2. Backstep Channel Geometry

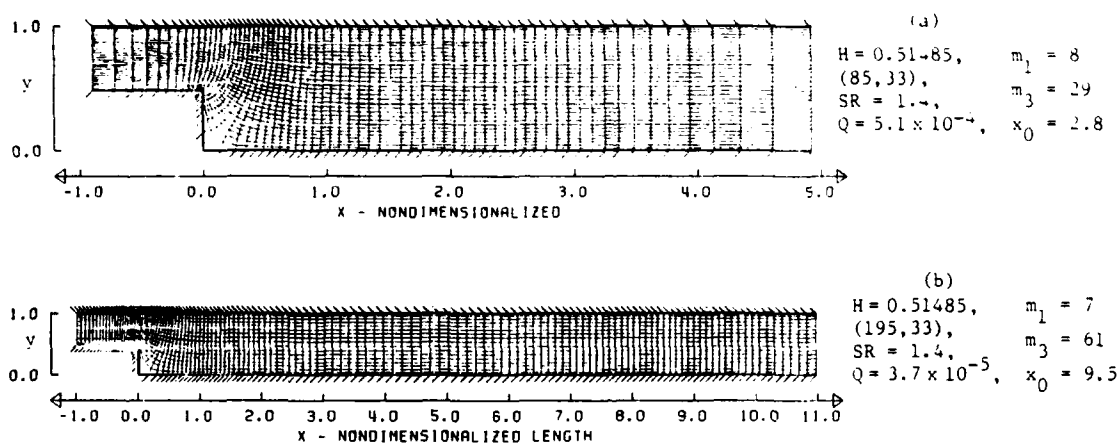


Fig. 3. Typical Grid Distributions.

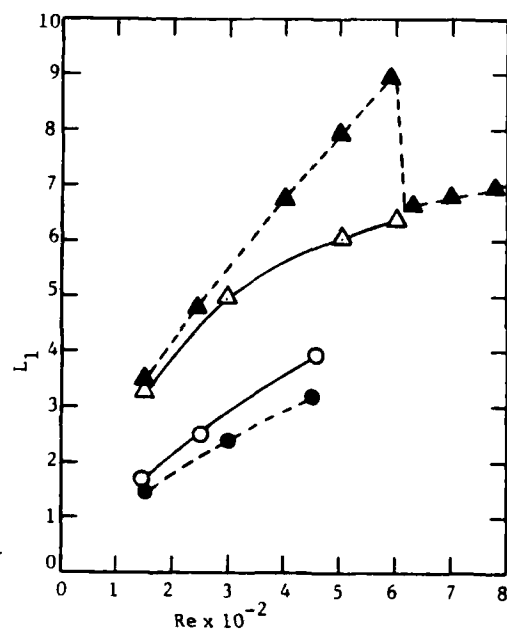


Fig. 4a. Reattachment Length of Separation Bubble on Lower Wall.

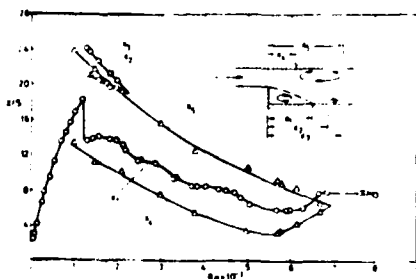


Fig. 4b. Circulation Regions at the Upper and Lower Walls. (After Ref. 23)

LEGEND FOR FIGURES 4a AND 4c

Ref.	Present	Denham & Patrick [22]	Armaly & Durst [23]
H			
0.51485	—△—	—●—	—▲—
0.06667	—○—	—●—	
0.90000	□		

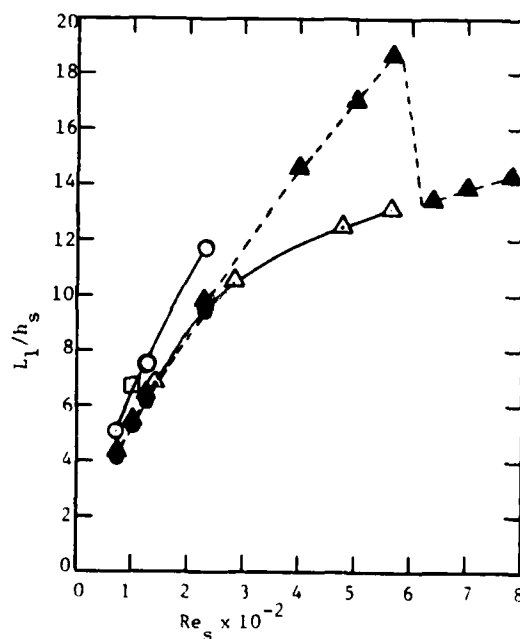


Fig. 4c. Similarity Study for Reattachment Length.

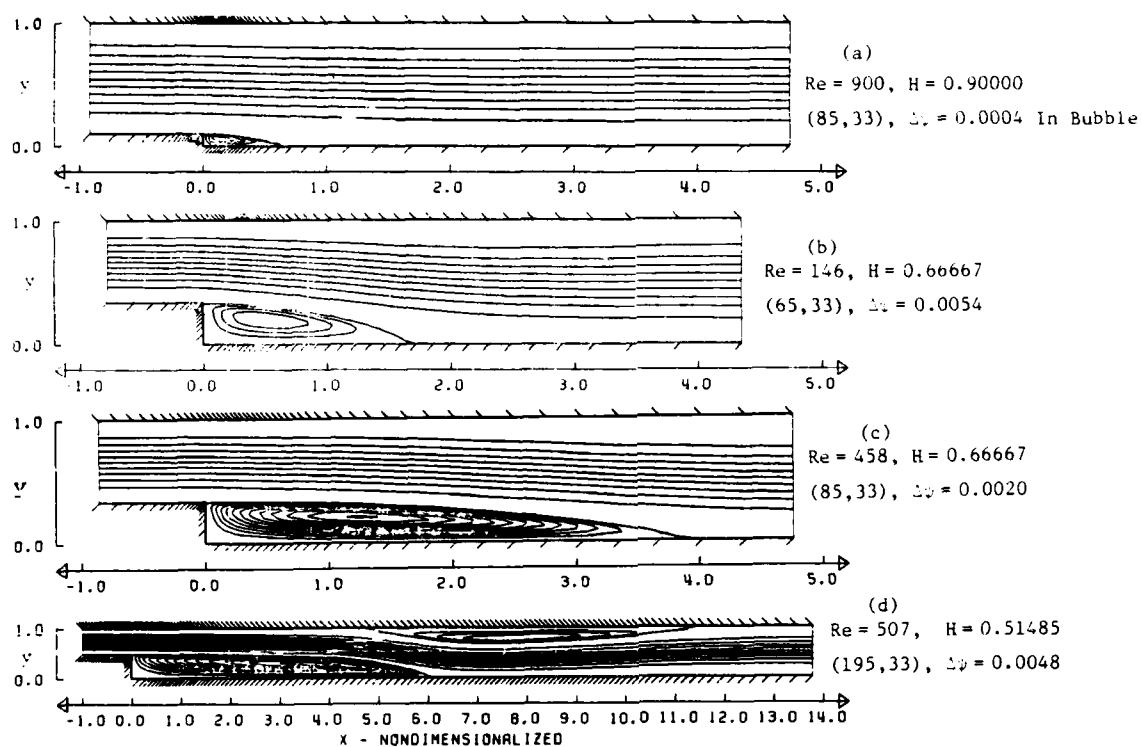


Fig. 5. Steady-State Stream-Function Contours; $\Delta y = 0.1$.

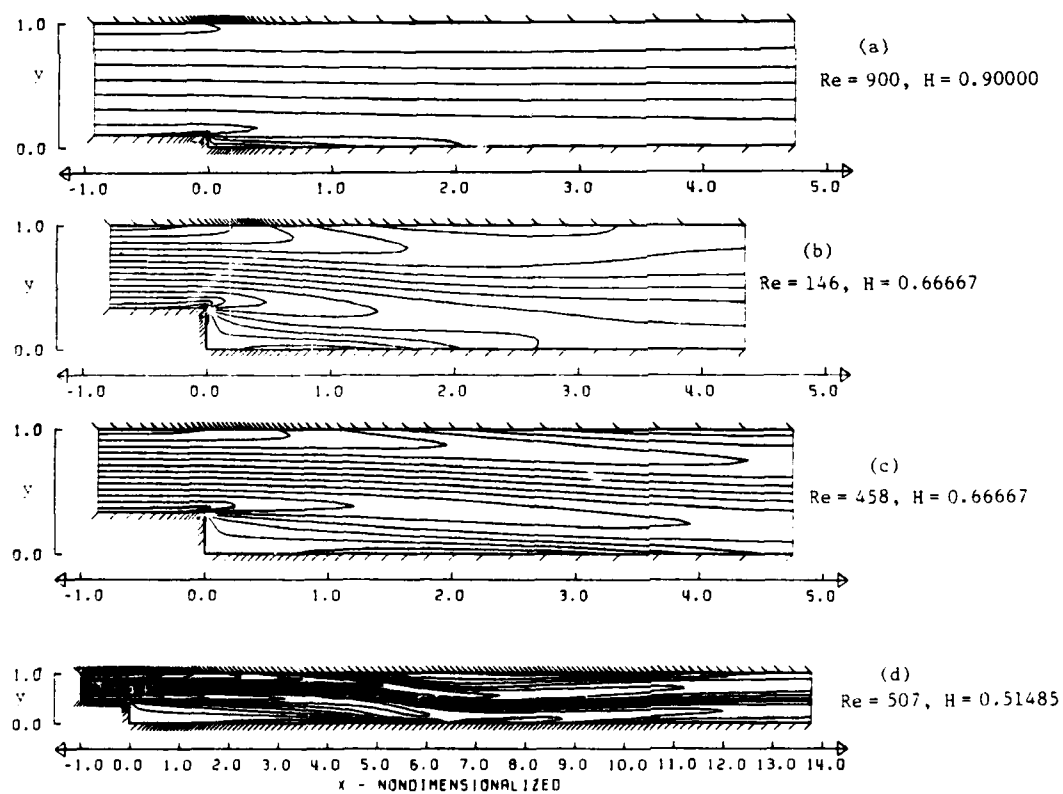


Fig. 6. Steady-State Vorticity Contours; $\Delta x = 2.0$.

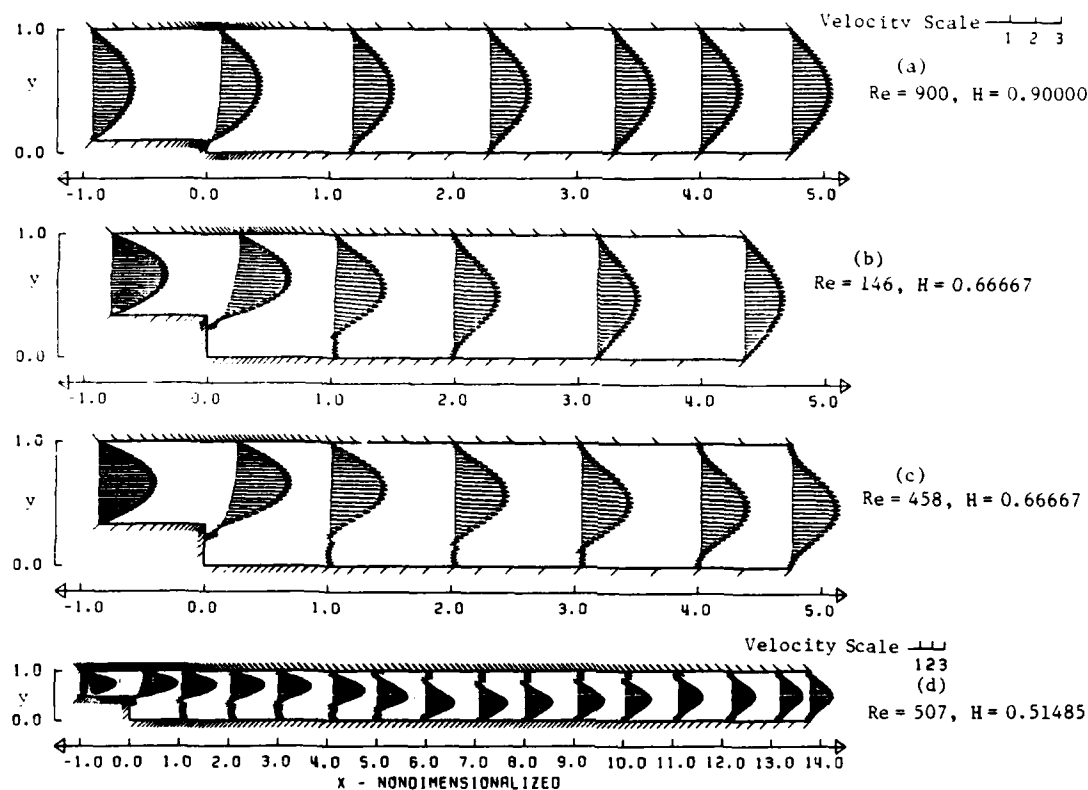


Fig. 7. Steady-State Total-Velocity Vectors.

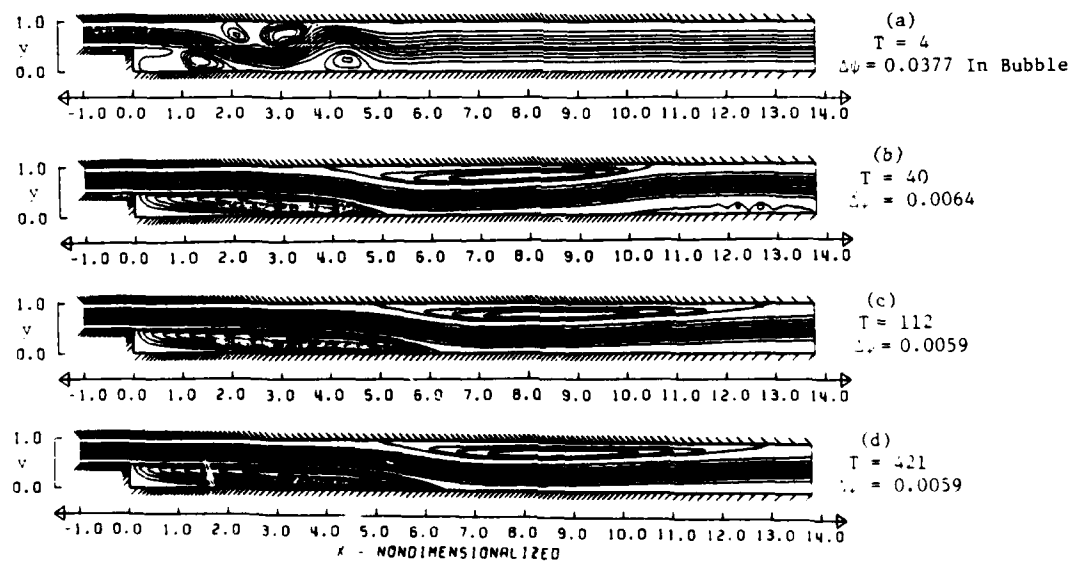


Fig. 8. Transient Stream-Function Contours for $Re = 600$; $\Delta t = 0.1$.

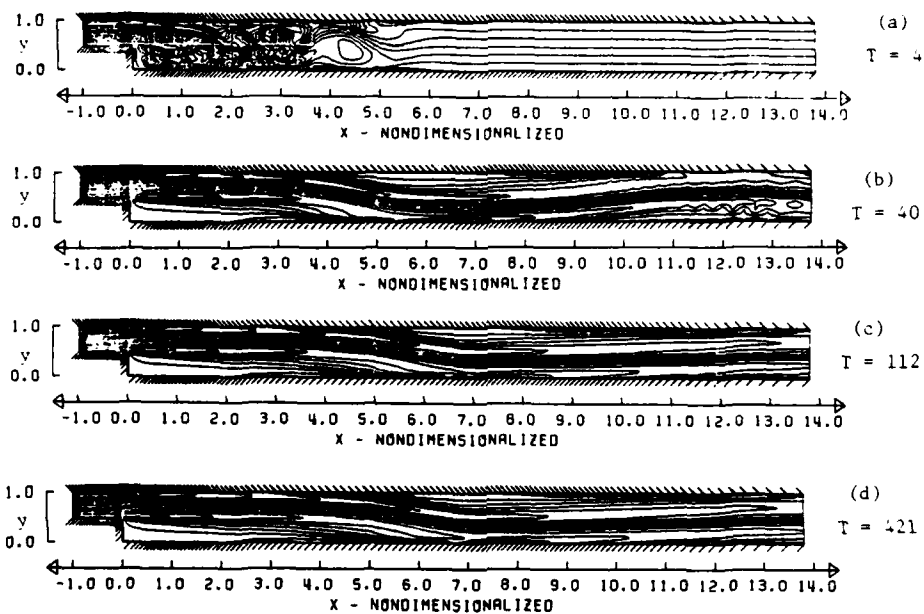


Fig. 9. Transient Vorticity Contours. $Re = 600$; $\Delta\omega = 2.0$.

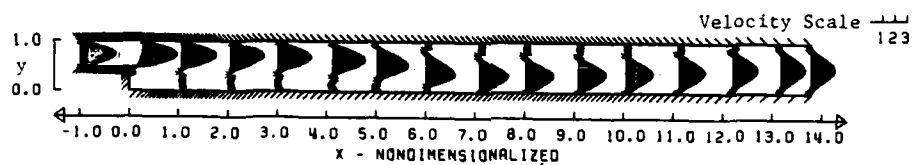


Fig. 10. Steady-State Total Velocity Vectors. $Re = 600$.

GLOBAL SOLUTION PROCEDURES FOR INCOMPRESSIBLE LAMINAR FLOW
WITH STRONG PRESSURE INTERACTION AND SEPARATION

S.G. Rubin and D.R. Reddy
Department of Aerospace Engineering and Applied Mechanics
University of Cincinnati
Cincinnati, Ohio

Abstract

Global or relaxation formulations for the reduced form of the Navier-Stokes equations, frequently referred to as parabolized Navier-Stokes (PNS), are presented. Difference procedures and relaxation solutions for the (u,v,p) system are presented. The continuity equation is satisfied exactly at each grid point and a poisson pressure equation is not required explicitly. The development of a second composite (U,ψ,G) velocity relaxation procedure for the primitive variable equations is also discussed. For the (u,v,p) system, several model problems, e.g., finite flat plate, trough, boattail and airfoil, are considered. Strong pressure interaction is evident in each case and axial flow separation occurs for several of the problems. The questions of accuracy, stability, convergence rate, and implied difference forms of the pressure and vorticity equations are addressed.

1. Introduction

Conventional methods for the numerical solution of the primitive variable form of the incompressible (elliptic) Navier-Stokes or ("semi-elliptic") parabolized Navier-Stokes (PNS) equations are such that the velocity components, u,v , are determined from the momentum equations, and the pressure p is obtained from the differential poisson equation derived from the momentum equations. The equation of continuity is not evaluated explicitly but is satisfied indirectly through the poisson equation and pressure boundary conditions. Since this procedure differs markedly from most inviscid, boundary layer and triple deck formulations, an alternate development that more closely follows these asymptotic theories is considered here for the evaluation of viscous interacting flows at large Reynolds numbers.

In the present paper, the authors continue the line of thought first presented for the PNS system in references [1-3]. The analysis is developed in greater detail here and in [4, 5]. The questions of global stability of the relaxation procedure, the resulting difference forms of the pressure and vorticity equations, accuracy and rate of convergence, are examined more critically. Comparisons are given with triple deck and interacting boundary layer solutions for trailing edge and trough configurations; solutions are also obtained for boattail and airfoil geometries. The effects of strong pressure interaction and/or flow separation are evident in each of these problems. The majority of the solutions are for laminar flow conditions; however, several results have been obtained with the Cebeci-Smith two layer eddy viscosity closure model.

The objective of the present development is the solution of the PNS system by direct application of the momentum and (first-order) continuity equations. The formulation does not require the second-order differential form of the poisson pressure solver. A global line relaxation procedure is developed for (u,v,p) or a composite [6, 7] (U,ψ,G) system. For non-separated flows only p or ψ are stored during the relaxation process. For separated flows, (u,v) or (U) is required only in regions of reversed flows. This significantly reduces computer storage requirements.

2. Governing Equations

We consider here the reduced set of PNS equations (1, 2) written in two-dimensional or axisymmetric body fitted conformal coordinates. The equations in general orthogonal coordinates are given in [3]. As discussed for cartesian coordinates in [2, 3], for incompressible flow a consistent PNS approximation allows for the neglect of all axial (ξ) diffusion terms as well as all diffusion effects in the normal (η) momentum equation. Normal diffusion can be included in the η -momentum equation; however, for consistency these terms have generally been neglected. Numerical tests with and without these terms have confirmed the validity of this approximation for several of the problems considered herein.

(i) (u,v,p) :

continuity

$$(hh_3u)_\xi + (hh_3v)_\eta = 0 \quad (1a)$$

ξ -momentum

$$(hh_3u^2)_\xi + (h^2uv)_\eta + uvh_3h_\eta - v^2h_3h_\xi = -hh_3p_\xi + V \cdot T/R_e \quad (1b)$$

$$\text{where } V \cdot T = [h_3(hu)_\eta/h^2]_\eta \quad (1c)$$

η -momentum

$$hh_3p_\eta = - (hh_3uv)_\xi - (hh_3v^2)_\eta - uvh_\xi + u^2h_3h_\eta \quad (1d)$$

The cartesian coordinates $\xi = \xi(x,y)$, $\eta = \eta(x,y)$ are related to the (x,y) physical coordinates through the transformation $\tau = f(z)$ or $z = F(\tau)$ where $\tau = \xi + i\eta$ and $z = x + iy$. The metric h is defined by

- This research was supported by the Air Force Office of Scientific Research under Grant No. 80-0047.

$$h = f'(z) = (x_1^2 + y_1^2)^{1/2} = (x_n^2 + y_n^2)^{1/2}$$

The metric $h_3 = y$, where $\epsilon = 0$ for two-dimensions and $\epsilon = 1$ for axisymmetry. The metric h and all derivatives are evaluated with second-order difference formulas. In the axial and normal momentum equations (1b, 1c), the metric h and derivatives of h are assumed to be at most of order one. For geometries with larger curvature the complete expression for $V \cdot T$ may be required in (1b) and the viscous effects in (1d) may become important. The full Navier-Stokes equations or a more appropriate non-conformal coordinate mapping may then be required, see [6, 7].

(ii) (U, ϵ, G) :

In the composite velocity development described in [6, 7], an "inviscid" pseudo-potential ϵ , "viscous" velocity U and "inviscid" Bernoulli pressure G , replace (u, v, p) , i.e.,

$$u = U(1 + \epsilon_\epsilon)/h = U u_\epsilon$$

$$v = \epsilon_\eta/h$$

$$G = p/\epsilon + (u_\epsilon^2 + v^2)/2 - G_\infty$$

The equations become

continuity

$$(h_3 U \epsilon_\epsilon)_\epsilon + (h_3 v)_\eta + (h_3 U)_\xi = 0 \quad (2a)$$

ξ -momentum

$$u_\epsilon + \epsilon [hh_3 u_\epsilon^2 (U^2 - U)]_\epsilon + [hh_3 u_\epsilon v (U - 1)]_\eta / h^2 h_3 + u_\epsilon v h_\eta (U - 1) / h^2 + u_\epsilon u_{\epsilon\epsilon} (U - 1) / h = -G_\epsilon / h + V \cdot T / R_\epsilon \quad (2b)$$

η -momentum

$$G_\eta = - (U - 1) \cdot (u_\epsilon^2 / 2)_\eta - u_\epsilon^2 u_{\eta\eta} / h \quad (2c)$$

This multiplicative composite velocity development is patterned after matched asymptotic viscous-inviscid flow theory. For inviscid irrotational flows, $U \equiv 1$; (2a) then reduces to the potential equation and (2b,c) lead to the Bernoulli equation, $G = 0$. For boundary layer problems, $u_\epsilon, u_{\epsilon\epsilon}$ for $\epsilon_\epsilon, \epsilon_{\epsilon\epsilon}$ and G are specified with boundary layer edge conditions and (2a,b) combine to determine (U, v) . Interacting boundary layer theory combines elements of both limits, so that (2a,b) form a coupled system for (U, ϵ) , with G prescribed. The equations (1) or (2) contain all the terms appearing in each layer of the triple deck structure [3].

The present investigation concentrates on the (u, v, p) formulation described by equations (1). Composite solutions have already been discussed for

the full Navier-Stokes equations in [6, 7]. Analysis of the PNS equations with the composite system is in progress and results with this formulation shall be presented in a future paper.

3. Difference Equations

In the previous analyses [1-3], it was shown that if the system (1) was forward marched in the boundary layer sense, i.e., backward differences are applied for all ξ derivatives in non-separated regions, the elliptic pressure interaction would not be properly represented and therefore the exponentially growing Lighthill departure solutions would appear for step sizes $\Delta \xi > (\Delta \xi)_{\min}$. For cartesian coordinates, from [2, 3], we find that $(\Delta \xi)_{\min} = \frac{2}{3} y_M$, where y_M is the location of the outer boundary $y = y_M$. Only for $y_M \gg 1$ are accurate solutions possible with forward marching.

If global relaxation or multiple sweep marching is used, i.e., all ξ derivatives of velocities are backward differenced in non-separated regions, but some form of forward differencing is applied for p_ξ in (1a), the elliptic pressure interaction is recovered and the departure free limit $\Delta \xi > (\Delta \xi)_{\min}$ is removed. Solutions can then be obtained for $\Delta \xi \rightarrow 0$, see [2, 3]; the numerical procedure is consistent and any desired degree of accuracy can be specified. Finally, in order to circumvent the pressure singularity at separation, the p_ξ term must also allow for a local as well as a spatial interaction. For example, central differencing fails in this regard and, as discussed in [2, 3], is unstable globally. Forward differencing of p_ξ satisfies all constraints and moreover is consistent with the eigenvalue analysis of Vigneron et al. [9] which shows that for incompressible flow ($M \rightarrow 0$), there should not be any forward marched component of the p_ξ term; i.e., $\epsilon = 0$ in his analysis. Forward differencing and global relaxation was first applied successfully in [1-3] for several model incompressible flow problems. The extension to compressible flows is discussed for a conical geometry in [2] and for flows with axial flow separation and strong pressure interaction in [10]. More detailed discussion and results are given in [3, 4].

The difference scheme used in [1-3] was developed from the following discrete grid:

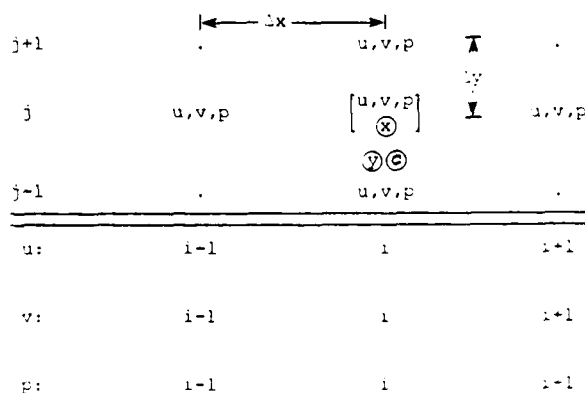


Figure 1: Difference Grid I.

The continuity, x and y momentum equations are centered at \odot , \otimes and \odot , respectively and the difference equations given for a uniform mesh in cartesian coordinates are as follows.

continuity, centered at $(i,j-\frac{1}{2})$:

$$\frac{u_{i,j} - u_{i-1,j} + u_{i,j-1} - u_{i-1,j-1}}{2\Delta x} + \frac{v_{i,j} - v_{i,j-1}}{\Delta y} = 0 \quad (3a)$$

x-momentum, centered at (i,j) :

$$u_{i,j} \left(\frac{u_{i,j} - u_{i-1,j}}{\Delta x} \right) + v_{i,j} \left(\frac{u_{i,j+1} - u_{i,j-1}}{2\Delta y} \right) + \frac{p_{i+1}^{n-1} - p_i^{n-1}}{\Delta x} = \frac{1}{\text{Re}} \left(\frac{u_{i,j+1} - 2u_{i,j} + u_{i,j-1}}{\Delta y^2} \right) \quad (3b)$$

y-momentum, centered at $(i,j-\frac{1}{2})$:

$$-\frac{p_{i,j} - p_{i,j-1}}{\Delta y} = \left(\frac{u_{i,j} + u_{i,j-1}}{2} \right) \left(\frac{v_{i,j} - v_{i-1,j} + v_{i,j-1} - v_{i-1,j-1}}{2\Delta x} \right) + \left(\frac{v_{i,j} + v_{i,j-1}}{2} \right) \left(\frac{v_{i,j} - v_{i,j-1}}{\Delta y} \right) \quad (3c)$$

The equations are shown here in non-conservative form as this simplifies the subsequent discussion of the linear system. In fact, for most calculations conservative equations were considered. All quantities are evaluated at the n th iteration level except p_{i+1}^{n-1} , which is evaluated at the previous iteration. For separated flows the convective terms are upwinded and u_{i+1}^{n-1} , v_{i+1}^{n-1} terms are also required at level $n-1$. The difference equations (3) are first-order accurate, i.e., $O(\Delta x, \Delta y^2)$.

An alternate and more accurate derivation of the equations and interpretation of "forward" differencing for p_i is given below for cartesian coordinates. This system was considered initially for inviscid flows [4] and resembles a slightly different development proposed by Israeli [8]. Consider the staggered difference grid as shown:

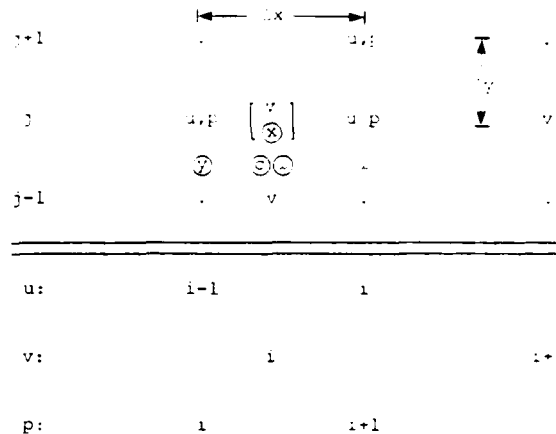


Figure 2: Difference Grid II

The appropriate difference equations, also shown in non-conservative form, are now centered at somewhat different \odot , \otimes , \odot locations.

continuity, centered at \odot is the same as (3a):

$$\frac{u_{i,j} - u_{i-1,j} + u_{i,j-1} - u_{i-1,j-1}}{2\Delta x} + \frac{v_{i,j} - v_{i,j-1}}{\Delta y} = 0 \quad (4a)$$

x-momentum, centered at \otimes :

$$\begin{aligned} & \left(\frac{u_{i,j} + u_{i-1,j}}{2} \right) \left(\frac{u_{i,j} - u_{i-1,j}}{\Delta x} \right) \\ & + v_{i,j} \left(\frac{u_{i,j+1} - u_{i,j-1} + u_{i-1,j+1} - u_{i-1,j-1}}{4\Delta y} \right) \\ & + \frac{p_{i+1}^{n-1} - p_{i,j}}{\Delta x} \\ & = \frac{1}{\text{Re}} \left(\frac{u_{i,j+1} - 2u_{i,j} + u_{i,j-1} + u_{i-1,j+1} - 2u_{i-1,j} + u_{i-1,j-1}}{2\Delta y^2} \right) \end{aligned} \quad (4b)$$

y-momentum, centered at \odot :

$$\begin{aligned} & -\frac{p_{i,j} - p_{i,j-1}}{\Delta y} \\ & = \left(\frac{u_{i,j} + u_{i-1,j}}{2} \right) \left(\frac{v_{i,j} - v_{i-1,j} + v_{i,j-1} - v_{i-1,j-1}}{2\Delta x} \right) \\ & + \frac{1}{4} (v_{i,j} + v_{i-1,j} + v_{i,j-1} + v_{i-1,j-1}) \\ & \cdot \left(\frac{v_{i,j} - v_{i,j-1} + v_{i-1,j} - v_{i-1,j-1}}{2\Delta y} \right) \end{aligned} \quad (4c)$$

In this formulation full second-order accuracy is achieved. The primary modification of the system (3) is the averaging of the y -derivative terms in the momentum equations. The unknown pressure p_i is also shifted one point to the left of that given by the formulation (3). This interpretation is more accurate and is consistent with the character of the interactive solutions as will be seen for the trailing edge problem to be discussed in a following section.

A third system of equations, which also provides second-order accuracy has been proposed by Israeli [8]. The staggered u, v grid is then of the form:

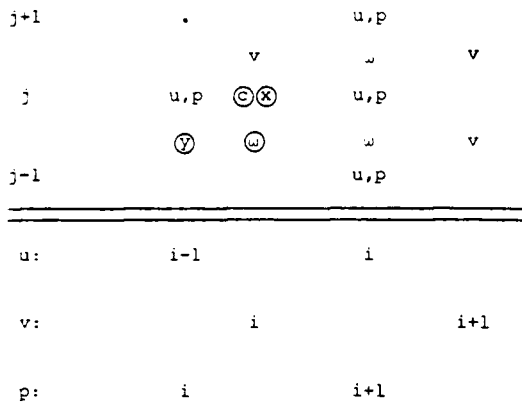


Figure 3: Difference Grid III.

The equations are only slightly modified from those of (4); however, the y boundary condition for v must be treated somewhat differently.

- (i) Definition of vorticity and vorticity transport equation:

If the nonlinear coefficients u and v are assumed constant and the pressure is eliminated from (4a, 4b), the following difference equation is obtained, in the inviscid limit, for the vorticity transport [4]:

$$u \left(\frac{\omega_{i,j} - \omega_{i-1,j}}{\Delta x} \right) + v \left(\frac{\omega_{i,j+1} - \omega_{i,j-1}}{4\Delta y} \right) = O(\Delta x^2, \Delta y^2) \quad (5a)$$

where

$$\omega_{i,j} = \frac{v_{i+1,j} - v_{i,j}}{2\Delta x} - \frac{u_{i,j} - u_{i,j-1}}{\Delta y} \quad (5b)$$

This corresponds to defining ω at the location ω shown in Figure 2 and centering (5a) at location ω . Both expressions (5a) and (5b) are second-order accurate. The difference equation obtained by replacing $\omega_{i,j}$ terms in (5a) with the formula (5b) is exactly that resulting from the elimination of the pressure in (4a) and (4b) except for the

vv_{xy} term in vv_y ; however, with the definition (5b) the error in this expression is $O(\Delta x^2, \Delta y^2)$, so that second-order accuracy is retained in the difference approximation of the vorticity transport equation, see [4]. Similar results can be obtained with the scheme proposed by Israeli in Figure 3.

If (5b) and the continuity equation (3a) are combined to eliminate either u or v terms, for $\omega = 0$ we recover a nine-point second-order accurate difference formula for either $\nabla^2 u = 0$ or $\nabla^2 v = 0$. In fact, inviscid irrotational flows can be solved numerically with (5b) and (3a), in lieu of the potential equation $\nabla^2 \phi = 0$. This is a result of backward differencing of u_x in the continuity equation and, as seen in (5b), forward differencing of v_x in the definition of vorticity. One boundary condition is satisfied for u (left boundary) and one for v (right boundary). This is a direct result of the differencing procedure applied for the u, v, p primitive variable system; i.e., backward differences for velocities (in non-separated regions) and "forward" pressure differences as interpreted in Figure 1 (first-order accuracy) or Figure 2 or 3 (second-order accuracy). Further details of this analysis are given in [4].

- (ii) Difference equation for pressure:

In a similar manner, the effective poisson difference equation for the pressure can be obtained by $(x\text{-mom})_{i,j} - (x\text{-mom})_{i-1,j} + (y\text{-mom})_{i,j+1} - (y\text{-mom})_{i,j} = 0$. This equation is of the form (see [4] for derivation)

$$\sigma p_{i,j+1} - [(p_{i,j}^{n-1} + p_{i,j}) + 2\sigma(p_{i,j})] + \sigma p_{i,j-1} + p_{i+1,j}^{n-1} + p_{i-1,j} = f_{i,j}(u,v) \quad (6a)$$

where $\sigma = (\Delta x / \Delta y)^2$.

In order to recover the more conventional line relaxation form of the difference equation, Israeli [5] has shown that if a source term $S_{i,j}$ is introduced in the x -momentum equation (3b or 4b), we obtain

$$\sigma p_{i,j+1} - 2(1+\sigma)p_{i,j} + \sigma p_{i,j-1} + p_{i+1,j}^{n-1} + p_{i-1,j} = \bar{f}_{i,j}(u,v) \quad (6b)$$

where $S_{i,j} = S_{i-1,j} - p_{i,j}^{n-1} + p_{i,j}$.

This is equivalent to introducing an iterative "time" derivative into the relaxation process. Israeli [5] has also introduced an overrelaxation parameter ω as a mechanism to improve convergence rate. Our experience has not led to a marked improvement in convergence for the nonlinear system (4) with overrelaxation. Therefore, all solutions depicted herein are for the first-order system (5a) or the second-order system (5b) with $\omega = 1$. Multi-grid procedures have been applied

for convergence acceleration when fine meshes are required, see [4].

It should be reiterated here that although a poisson-like relaxation scheme can be inferred, boundary conditions are prescribed for p only at the outer (y) boundary and downstream (x) boundary; also, the pointwise continuity equation is satisfied exactly. As noted in the introduction, this is in sharp contrast with conventional solution procedures that use the poisson form of the pressure equation with full Neumann boundary conditions and only indirectly satisfy the pointwise continuity equation.

4. Consistency and Convergence

In order to complete the analysis of the relaxation technique discussed herein, two questions are posed. Does the prescribed differencing procedure capture the elliptic pressure interaction in each sweep of the iteration cycle, and what are the convergence properties of the global relaxation process. The first question has been addressed in [1-3] and as discussed in section 3, the departure effect is circumvented and the elliptic interaction is captured with the forward pressure differencing of (3b) or (4b). As shown in [4], the introduction of the source terms $S_{i,j}$ provides increased numerical damping and enhances the stability properties in each marching step.

The second question is considered in detail in reference [4]. The primary conclusions are presented here. Although the forward pressure differencing eliminates the inconsistency found with single sweep procedures, so that $\Delta\epsilon$ can be made arbitrarily small, the departure limit $\Delta x > 2y_M/\pi$ appears indirectly as a factor affecting convergence of the global relaxation procedure.

It can be shown from a linear global stability analysis that central differencing of p_x is unstable [2-4], but with forward differencing of p_x , as in (3b), the iteration technique is unconditionally stable. The maximum eigenvalue is given [3, 4] as

$$\lambda = 1 - c_1 \tau^2 \left(\frac{\Delta x}{y_M}\right)^4 N_x^2$$

or

$$\lambda = 1 - c_1 \left(\frac{\tau \Delta x}{y_M}\right)^2 \left(\frac{x_M}{y_M}\right)^2$$

where c_1 is a constant of order one, y_M is the outer y boundary, x_M is the outer x boundary, and N_x is the number of x grid points; i.e., $N_x = x_M/\Delta x$. Therefore for $\frac{\tau \Delta x}{y_M} \ll 1$ or $\Delta x \ll \frac{y_M}{\tau}$, $\lambda \rightarrow 1$ and the convergence rate will deteriorate. For $\left(\frac{\tau \Delta x}{y_M}\right) \ll 1$ and N_x fixed, convergence is very slow as $\lambda \rightarrow 1 - \left(\frac{\tau \Delta x}{y_M}\right)^2$. Although the departure limit $\frac{\tau \Delta x}{2y_M} > 1$ is no longer a stability limitation, the condition $\frac{\tau \Delta x}{y_M} \ll 1$ is a convergence limit. For

coarser grids, e.g., $\frac{\tau \Delta x}{y_M} \approx \frac{1}{2}$, convergence is quite rapid. For finer grids, SOR or multigrid acceleration has been considered [4, 5].

The outer pressure boundary condition must be prescribed at a location beyond the extent of the interaction zone of influence, e.g., triple deck. The pressure boundary condition can be fixed during each sweep of the global procedure. This value will remain unchanged if the outer boundary is sufficiently far from, and unaffected by, the viscous interaction; alternatively, the pressure boundary condition can be updated prior to each sweep in order to account for viscous displacement effects. In conformal body fitted or streamline coordinates, this should be unnecessary. Unlike interactive boundary layer theory, where the outer pressure boundary value requires a local interactive treatment in order to circumvent the separation point singularity, a fixed outer pressure condition is acceptable with the PNS formulation. The normal momentum equation reflects the outer inviscid or interactive behavior and the separation singularity is automatically suppressed.

To summarize, if p_x is treated explicitly or central differenced, the global procedure is unstable; if p_x is backward differenced, departure solutions appear for $\Delta x \rightarrow 0$. With "forward" differencing all iterative procedures are stable and the global marching problem is well-posed.

5. Boundary Conditions

For the finite-difference grids of Figures 1 or 2 the appropriate boundary conditions are specified as follows in the transformed body fitted coordinate system:

At a surface $y = 0$ ($j = 0$), the velocities $u = v = 0$; at a symmetry line $y = 0$ ($j = 0$), the velocities satisfy $u_y = v = 0$.

At the outer boundary $y = y_M$ ($j = M$), where y_M lies outside of the extent of the interaction zone, e.g., triple deck, $p = p_\infty$, $u = u_\infty$ and a boundary condition on v is not required.

At the inflow boundary $x = 0$ ($i = 1$), $u = u(0, y)$, and $v_x(0, y) = 0$. For inviscid regions, where $u = u_\infty$, $v_x = 0$ is a zero vorticity condition and for viscous regions $v_x = 0$ is equivalent to a boundary layer approximation. The velocity v should not be specified at the inflow. This leads to inviscid vorticity production and has a destabilizing effect on the global iteration procedure. The flow pressure is not prescribed and with the formulation of Figure 2 is unknown and a result of the calculation procedure.

Finally, the only boundary condition required at the outflow is the pressure or equivalent pressure gradient. This of course reflects the elliptic pressure interaction.

b. Solutions

Five model problems have served as test cases for the global PNS formulation described herein. For each geometry there is a region of strong pressure interaction and in several cases axial flow separation occurs. The test problems include (1) the trailing edge of a flat plate, (2) the Carter-Wornom [12] trough, (3) a boattail configuration, (4) a NACA 0012 airfoil at zero incidence (laminar), and (5) the NACA 0012 airfoil at zero incidence (turbulent).

(i) Trailing Edge

Solutions for the trailing edge geometry are given in Figures (4a, 4b). The agreement with the interacting boundary layer results of [11] are quite good. The finest grid includes (161×121) mesh points for (x, y) , respectively. The coarsest grid was (41×121) and full convergence required only several global iterations. If the calculation was run on the finest grid alone, convergence was still not achieved after several hundred iterations. With a multigrid technique [4], full convergence to $O(10^{-4})$ for the maximum error in successive iterations was achieved in approximately ten to fifteen global iterations. The outer boundary y_M was chosen to lie outside the triple deck extent. If y_M violated this condition, the calculation diverged. The calculation was relatively insensitive to y_M when this condition was satisfied.

The solutions for pressure and skin friction, both defined with triple deck normalization [11] are shown for $Re = 10^5$. It is significant that the skin friction (velocity profile) is relatively insensitive to the grid and appears to be quite acceptable even on some of the coarser meshes. On the other hand, the pressure is extremely grid sensitive and requires the finest mesh in order to accurately represent the triple deck interaction. With the difference grid of Figure 1, the minimum pressure occurs one grid point downstream of the trailing edge. With the grid of Figure 2 this pressure value is correctly obtained at the trailing edge.

(ii) Trough

The solutions for the trough geometry $[y_b(x) = \varepsilon \operatorname{sech} 4(x - 2.5)], (0 \leq x \leq \infty)$ are shown in Figures (5a, 5b). Values of $\varepsilon = -0.015$ [3, 4] and $\varepsilon = -0.03$ were considered. Only the latter results are presented here. Solutions were obtained for Reynolds numbers up to $Re = 3.6 \times 10^5$. Again, the agreement with the interacting boundary layer solutions is quite good. The insensitivity of C_f and the sensitivity of p to the grid is also evident for this example. As the Reynolds number was increased, more smoothing was required on the coarser grids in order to achieve convergence to the prescribed tolerance. The outer undisturbed pressure boundary condition was held fixed at $y = y_M$ throughout the computation. There were no difficulties at separation or reattachment points. As with the trailing edge problem, full convergence with the multi-grid iteration procedure was achieved in ten to fifteen global iterations. For the finest grid (241×121) mesh points were evaluated.

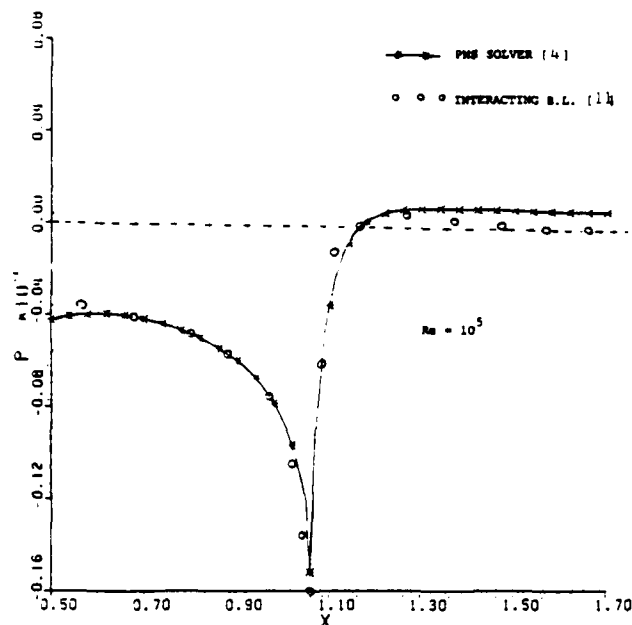


Figure 4a. Trailing Edge Pressure Distributions
PNS Solver.

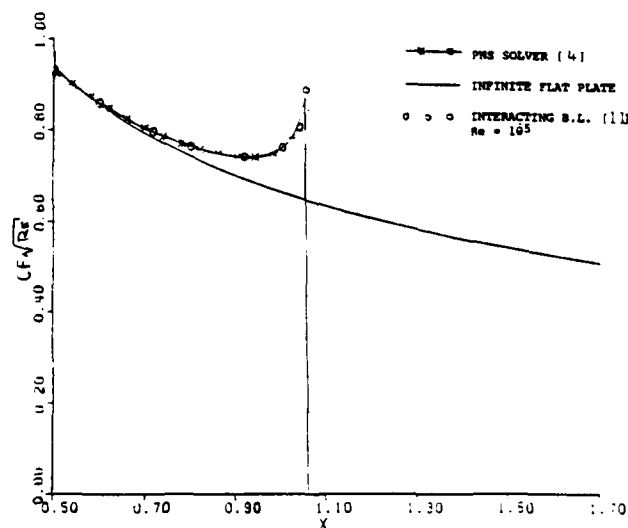


Figure 4b. Trailing Edge Skin Friction Solutions
PNS Solver.

(iii) Boattail

Laminar flow solutions for the boattail geometry of Figure 6 are shown in Figures (7a, 7b, 7c). The grid is generated with the Schwarz-Christoffel mapping routine of Davis [13]. These results are in good agreement with full Navier-Stokes solutions obtained with the composite (u, v, G) equations as reported in [3, 7]. For $Re = 6000$, based on maximum radius, with a juncture angle of 12 degrees a sizable separation bubble is obtained. All velocities are stored in the recirculation region. The relaxation process is slower than for the trailing edge or trough geometries; however, convergence to 10^{-4} for the maximum error in pressure is obtained in approximately 35 iterations. As the Reynolds number or corner angle is increased, the rate of convergence decreases and the multi-grid procedure also deteriorates. Further analysis of this behavior is required. Some improvement has been observed with the source correction of (5b).

Solutions have also been obtained for turbulent flow conditions. The Cebeci-Smith two layer viscosity model has been applied to close the system. Although this may not be an accurate approximation in the recirculation region, it does serve to give a qualitative picture of the flow. A Reynolds number of $Re = 5 \times 10^5$ based on maximum body radius has been specified. The effective turbulent Reynolds number is of course much lower and the separation region is considerably smaller than that obtained for the laminar flow at $Re = 6000$. These results are discussed in greater detail and figures are presented in [4].

(iv) Airfoils: laminar and turbulent

The flow over NACA 0012 and 12% thick Joukowski airfoils has been evaluated with global PNS relaxation. Analytic or conformal mapping [13] is used to generate the requisite metric functions for the system (1), Figure 8. Solutions have been obtained for fully laminar conditions for $Re = 2000$ to 7500. Recirculation is evident for the Joukowski airfoils for $Re > 2000$. For the NACA 0012 configuration, separation is not evident for $Re \leq 5000$. Typical laminar solutions are shown in Figures (9a, 9b). The laminar stagnation point results are also in close agreement with the familiar Navier-Stokes (boundary layer) values [4].

Triple deck analyses have recently been presented for separation on cusped and sharp trailing edge airfoils [14, 15]. Estimates of incipient separation as a function of Re are in qualitative agreement with the present numerical solutions, and the flow behavior near the wedge-like trailing edge is also reasonable, see Figure 10. Further comparisons are given in [4].

Finally, for $Re = 5 \times 10^5$, transition to turbulent flow conditions is assumed at $x/c = 0.32$. The two layer eddy viscosity model should be representative of the turbulent flow behavior as separation does not occur even for this very large value of Re [16]. Comparisons with experimental results and earlier calculations [16] are quite reasonable, see reference [4].

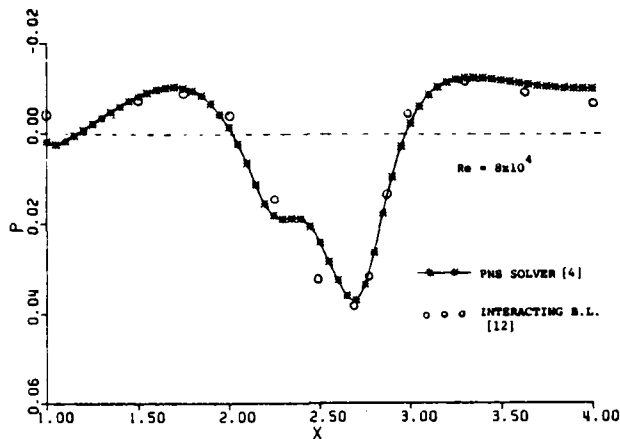


Figure 5a. Trough Skin-Friction Solutions
PNS Solver: $\epsilon = -0.03$.

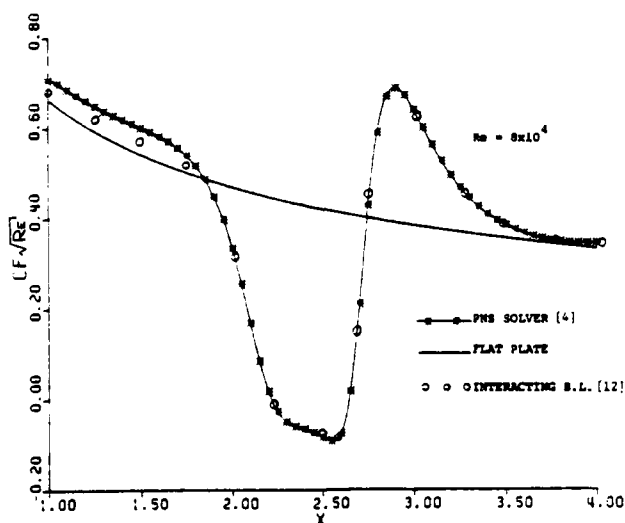


Fig. 5b. Trough Pressure Solutions PNS Solver:
 $\epsilon = -0.03$.

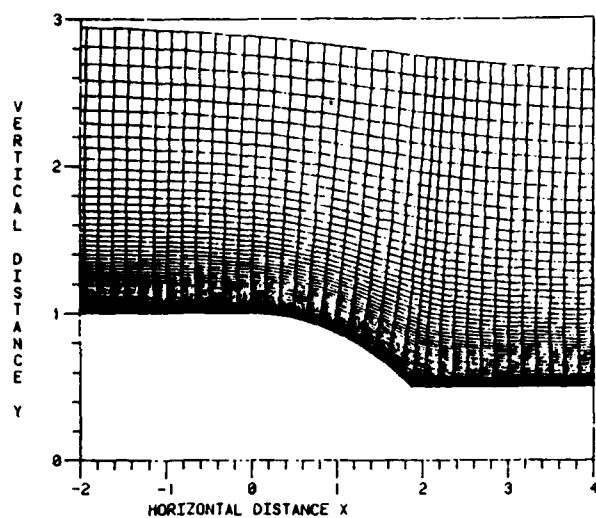


Figure 6. Boattail (BETAC = 15 Deg) Grid Near the Corner.

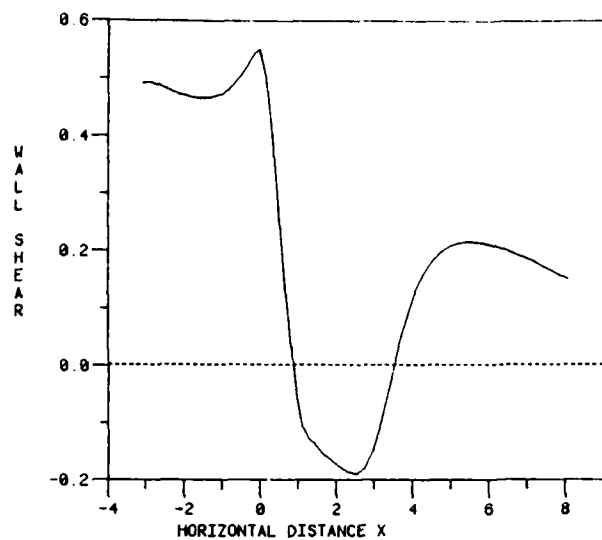


Figure 7b. Boattail (BETAC = 15 Deg) Laminar Flow $Re = 1000$.

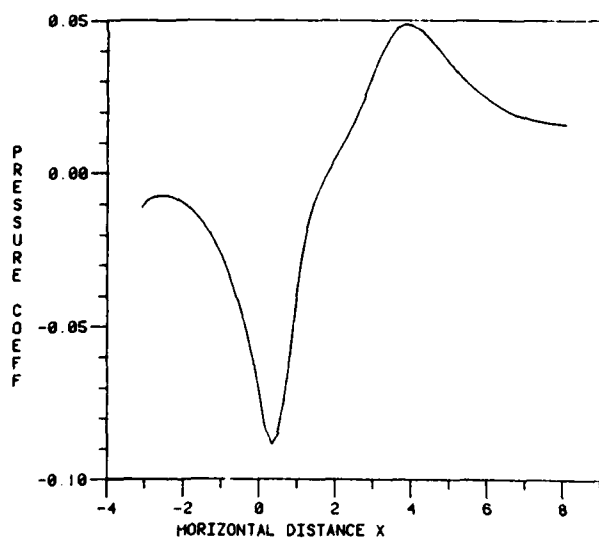


Figure 7a. Boattail (BETAC = 15 Deg) Laminar Flow $Re = 1000$.

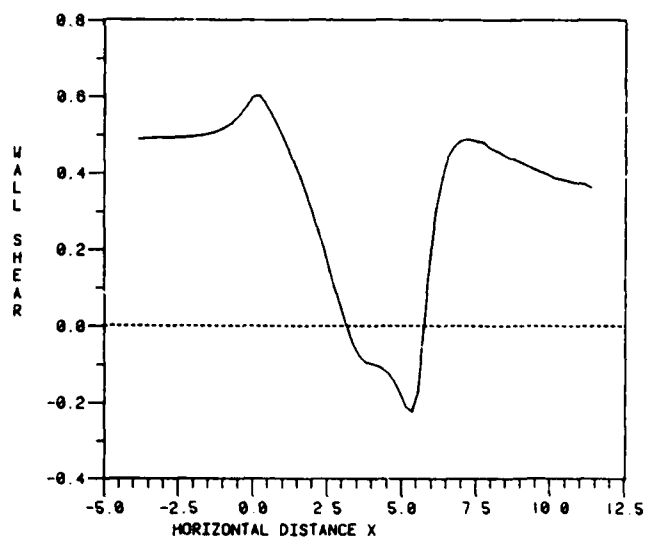


Figure 7c. Boattail (BETAC = 6 Deg) Laminar Flow $Re = 6000$.

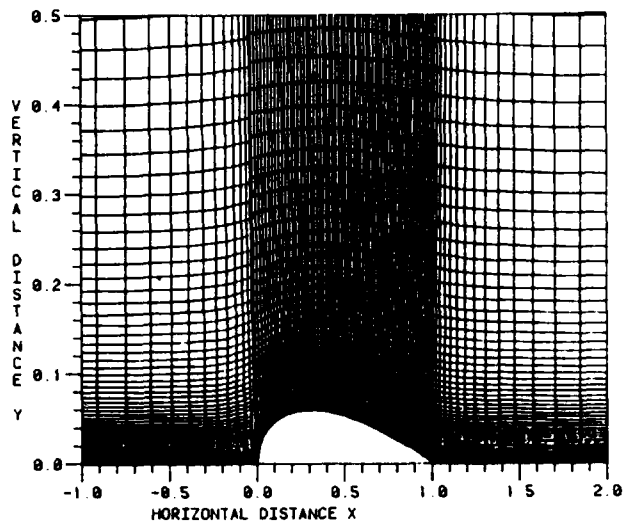


Figure 8. NACA 0012 Airfoil Grid Close to the Body.

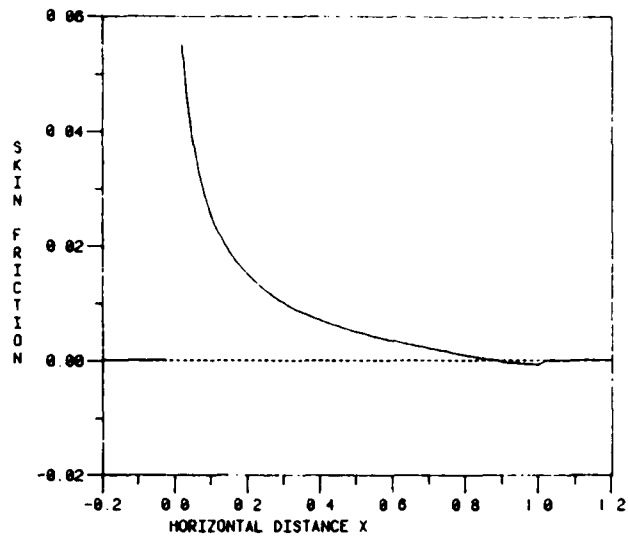


Figure 9b. NACA 0012 Airfoil Laminar Flow (Re = 12,500).

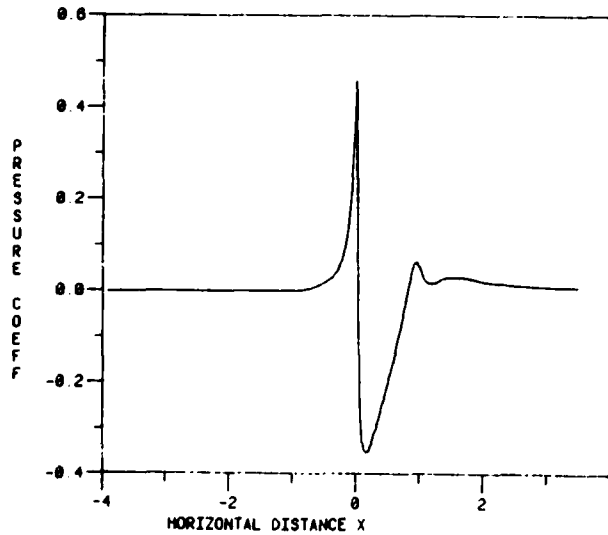


Figure 9a. NACA 0012 Airfoil Laminar Flow (Re = 12,500).

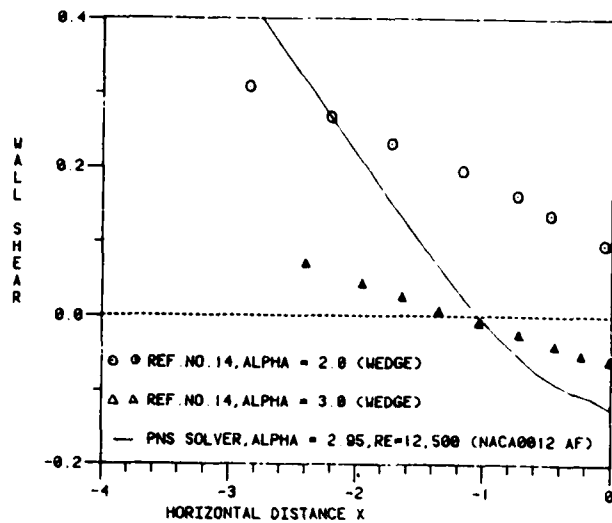


Figure 10. Trailing Edge Results in Triple Deck Scalings.

7. Summary

A global or relaxation procedure for the PNS system of equations has been developed. First and second-order accurate formulations have been presented. In the latter case, a staggered grid is considered and the unknown pressure is evaluated one grid point upstream of the velocity. In the former case, a forward pressure difference is implied. The effective difference forms of the vorticity transport and poisson pressure equations have been derived and results of global stability and convergence analyses have been reported.

Solutions have been obtained for laminar and turbulent flows where strong pressure interaction and/or axial flow separation occurs. The full elliptic pressure interaction is accurately evaluated and with the local pressure interaction there is no separation singularity. Procedures for increasing convergence rates have been examined, e.g., multi-grid; however, further analysis is still necessary, see [4].

Significantly, the differential form of the poisson pressure equation is not required explicitly and the local continuity equation is satisfied exactly at all points.

References

1. Rubin, S.G. and Lin, A. (1980), "Marching with the PNS Equations," *Israel J. of Technology*, **18**, pp. 21-31.
2. Rubin, S.G. (1981), "A Review of Marching Procedures for PNS Equations," 1st Symposium on Numerical and Physical Aspects of Aerodynamic Flows, Long Beach, CA, Springer-Verlag.
3. Rubin, S.G. (1982), "Incompressible Navier-Stokes and PNS Solution Procedures and Computational Techniques," VKI Lecture Notes, Brussels, Belgium; also, to appear in part, in "Recent Advances in Numerical Methods for Fluids," Pineridge Press, 1983.
4. Rubin, S.G. and Reddy, D.R. (1983), "Relaxation Analysis for the PNS Equations," in preparation.
5. Israeli, M. and Lin, A. (1982), "Numerical Solution and Boundary Conditions for Boundary Layer Like Flows," 4th ICNMF, Aachen, West Germany, Springer-Verlag.
6. Khosla, P.K. and Rubin, S.G. (1982), "A Composite Velocity Procedure for the Compressible Navier-Stokes Equations," AIAA Paper No. 82-0099.
7. Rubin, S.G. and Khosla, P.K. (1982), "A Composite Velocity Procedure for the Incompressible Navier-Stokes Equations," 4th ICNMF, Aachen, West Germany, Springer-Verlag.
8. Israeli, M. (1982), Private Communication.
9. Vigneron, Y. et al. (1978), "Calculation of Supersonic Viscous Flow over Delta Wings with Sharp Supersonic Leading Edges," AIAA Paper No. 78-1137.
10. Khosla, P.K. and Lai, H. (1983), "Global PNS Solutions for Subsonic Strong Interaction Flows," submitted for 9th AIAA CFD Conference, Danvers, Mass.
11. Davis, R.T. and Werle, M. (1981), "Progress on Interacting Boundary Layer Calculations at High Reynolds Numbers," 1st Symposium on Numerical and Physical Aspects of Aerodynamic Flows, Long Beach, CA, Springer-Verlag.
12. Carter, J. and Wornom, S. (1975), "Solutions for Incompressible Separated Boundary Layers Including Viscous-Inviscid Interaction," NASA SP-347.
13. Davis, R.T. (1980), "Numerical Methods for Coordinate Generation Based on a Schwarz-Christoffel Mapping Technique," VKI Lecture Notes, Brussels, Belgium, Hemisphere Press.
14. Smith, F.T. and Merkin, J.H. (1982), "Triple-Deck Solutions for Subsonic Flow Past Humps, Steps, Concave or Convex Corners and Wedged Trailing Edges," *Computers and Fluids*, **10**, pp. 7-25.
15. Cheng, H.K. and Smith, F.T. (1982), "The Influence of Airfoil Thickness and Reynolds Number on Separation," *ZAMP*, **33**, pp. 151-180.
16. Von Doenhoff, A.E. (1940), "Investigation of the Boundary Layer About a Symmetrical Airfoil in a Wind Tunnel of Low Turbulence," NACA Wartime Report L-507.

W. L. HAN-CHANG
Air Force Wright Aeronautical Laboratories
Wright-Patterson Air Force Base, Ohio

Abstract

Numerical simulations of a hypersonic cruiser were accomplished by means of the mass-averaged Navier-Stokes equations at a nominal Mach number of six and a Reynolds number of fifteen million. The computations of flow at the zero and ten degree angles of attack were performed on a CRAY-1 computer utilizing a grid consisting of over 56,000 points. The present results adopting a branch-cut mesh system yielded superior numerical resolution over the previous solution using a wrap-around grid distribution. Numerical results are presented showing the detailed flow field structure, density and vorticity distribution, and velocity field. These results indicate that the wing-fuselage configuration investigated generates an unfavorable interference factor.

Nomenclature

c	speed of sound
Def	deformation operator
D	Van Driest's damping factor
e	specific internal energy
F, G, H	vector fluxes
J	Jacobian of coordinate transformation
L	length scale of eddy viscosity model
M	Mach number
n	outward normal
p	static pressure
Pr	Prandtl number, 0.72
Pr _t	turbulent Prandtl number, 0.9
r	radius of ogive forebody, 0.598 cm
Rey	Reynolds number based on running length
T	temperature
t	time
U	dependent variables $U(\phi, \psi, \chi, \eta, \zeta)$
u, v, w	velocity components in Cartesian frame
x, y, z	coordinates in Cartesian frame
α	angle of attack
δ_{ij}	Kronecker delta
ϵ_{ij}	eddy viscosity coefficient
$\bar{x}, \bar{y}, \bar{z}$	transformed coordinate
μ	molecular viscosity coefficient
ρ	density
τ	stress tensor
ω	vorticity vector

Subscripts

∞	free stream condition
o	stagnation condition
b	surface condition

1. Introduction

Aerodynamic interference around the juncture of the wing and fuselage is a direct consequence of three-dimensional inviscid and viscous interaction.^{1,2,3} Until the early seventies, numerical analyses for wing-body interference were exclusively restricted to small disturbance schemes or panel methods.^{4,5} In this mode of investigation, numerical analysis was used as an extension of analytic

research. The uniqueness of the solution was ensured by imposing certain constraint such as the Kutta condition. The achievement was very significant, however directly usable results contained ambiguities. As computational aerodynamics made substantial progress, solutions of the quasi-linear potential equation⁶ and Euler equations became achievable^{5,6,7}. The most recent efforts using the Euler equations which admit vorticity probably reflect the current state-of-the-art in solution development. However, the inviscid-viscous interaction around the wing-fuselage configuration remain unresolved.

In the past few years, numerical simulations of the wing-body combination by means of the parabolized Navier-Stokes and the mass-averaged Navier-Stokes equations were attempted. In particular, Venkatapathy, Rakich and Tannehill⁸ used a parabolized Navier-Stokes code to calculate the supersonic, viscous laminar flow around the space shuttle orbiter forebody. Their solution contained the complex flow structure that developed near the wing-body region, and a multi-vortex pattern was observed. On the other hand, the present author also attempted to simulate numerically the flow field around a hypersonic cruiser by means of the mass-averaged Navier-Stokes equations. Both investigations indicated that the local grid system played a very important role in resolving the flow field around the wing-body juncture in that the geometric singularities were presented. The appropriate selection of the coordinate system became critical. The main thrust of the current effort is to explore an alternative grid system.

The investigated wing-fuselage configuration is comprised of a tangent-ogive forebody and a sharp leading edge delta wing with a sweepback angle of 70° (Figure 1). The geometric singularities at the wing-fuselage junctions and the wing tip are all curvature induced, being consequence of joining piecewise continuous body surfaces. In principle, the homeomorphism can not be maintained in the coordinate transformation to facilitate the computation. In the early effort, a wrap-around coordinate system was adopted with some numerical rounding of the sharp edges. Basically, it was an O-O type grid which thus offered the most efficiency in terms of computational effort for a given resolution.⁹ However, the O-O type grid around the wing tip caused serious numerical difficulties.⁹ In the present analysis, a branch cut was incorporated for the body-oriented coordinate system. The mesh system can be identified as the H-H type (Figure 2). The branch cut is performed along the upper and the lower wing surface. This particularly chosen coordinate system essentially eliminates all of the geometric singularities of wing-body configuration for the present numerical simulation.

Computations were performed for flow fields around a hypersonic cruise vehicle at a Mach number of 6.2 and a Reynolds number of 14.6 million. One of the computations was conducted for the flow

* Aerospace Engineer

**Tech Manager

AD P001931

without incidence. The other was performed for the oncoming stream with a ten degree angle of attack. The present numerical effort investigates the intricate viscous-inviscid interaction around the wing-body configuration. More importantly, the present analysis attempts to assess the feasibility of obtaining the numerical predictions of flows around a three-dimensional aircraft configuration by means of the mass-averaged Navier-Stokes equations. Special attention is focused on the treatment of the geometrical singularities frequently encountered in aircraft configurations. Thus, a criterion is established for the choice of coordinates for future full-scale aircraft numerical simulations. Numerical results are first verified by comparing with both the static and the impact pressure measurements under identical freestream conditions⁵. Then the flow field structure is delineated by presenting the density contours, the cross flow velocity distribution, and the streamwise vorticity formation.

II. Analysis

Governing Equations

The time dependent, three-dimensional Navier-Stokes equations in mass-averaged variables and in the transformed space (ξ, η, ζ) can be given as³

$$\begin{aligned} \frac{\partial U}{\partial t} + \left(\begin{matrix} \xi_x \\ \xi_y \\ \xi_z \end{matrix} \right) \left(\frac{\partial F}{\partial \xi}, \frac{\partial G}{\partial \xi}, \frac{\partial H}{\partial \xi} \right) + \left(\begin{matrix} \eta_x \\ \eta_y \\ \eta_z \end{matrix} \right) \left(\frac{\partial F}{\partial \eta}, \frac{\partial G}{\partial \eta}, \frac{\partial H}{\partial \eta} \right) \\ + \left(\begin{matrix} \zeta_x \\ \zeta_y \\ \zeta_z \end{matrix} \right) \left(\frac{\partial F}{\partial \zeta}, \frac{\partial G}{\partial \zeta}, \frac{\partial H}{\partial \zeta} \right) = 0 \end{aligned} \quad (1)$$

where the dependent variables are $U(\rho, \rho u, \rho v, \rho w, \rho e)$. The system is in the so-called chain rule conservation law form^{11,12}. The Navier-Stokes equations in this particular form is more computationally efficient in comparison to both the strong and the weak conservative forms¹². The flux vectors F , G , and H are simply the Cartesian components of the continuity, momentum, and energy equations.

$$F = \begin{pmatrix} \rho u \\ \rho u^2 - \tau_{xx} \\ \rho uv - \tau_{xy} \\ \rho uw - \tau_{xz} \\ \rho eu - \gamma \left(\frac{u}{Pr} + \frac{\epsilon}{Pr_t} \right) \frac{\partial e}{\partial x} - (u\tau_{xx} + v\tau_{xy} + w\tau_{xz}) \end{pmatrix} \quad (2-1)$$

$$G = \begin{pmatrix} \rho v \\ \rho uv - \tau_{yx} \\ \rho v^2 - \tau_{yy} \\ \rho vw - \tau_{yz} \\ \rho ev - \gamma \left(\frac{v}{Pr} + \frac{\epsilon}{Pr_t} \right) \frac{\partial e}{\partial y} - (u\tau_{yx} + v\tau_{yy} + w\tau_{yz}) \end{pmatrix} \quad (2-2)$$

$$H = \begin{pmatrix} \rho w \\ \rho uw - \tau_{zx} \\ \rho vw - \tau_{zy} \\ \rho w^2 - \tau_{zz} \\ \rho ew - \gamma \left(\frac{w}{Pr} + \frac{\epsilon}{Pr_t} \right) \frac{\partial e}{\partial z} - (u\tau_{zx} + v\tau_{zy} + w\tau_{zz}) \end{pmatrix} \quad (2-3)$$

where, the component of shear stress is defined by

$$\tau_{ij} = (\mu + \epsilon) (\text{Def } \bar{u})_{ij} - \left[\frac{2}{3} (\mu + \epsilon) (\nabla \cdot \bar{u}) + p \right] \delta_{ij} \quad (3)$$

The closure of the system of equations is achieved by introducing the Baldwin-Lomax turbulence model¹³ with a minor modification and by assigning a turbulent Prandtl number of 0.9. Specifically the Baldwin-Lomax turbulence model is found to be Mach number sensitive¹⁴. A constant in the outer layer is altered from a value of 1.5 to 2.0. The new constant (0.0336), twice the magnitude of Clauser's constant (0.0168), has been selected based on several bench mark calculations of turbulent flows over a flat plate at supersonic Mach numbers. For the skin friction coefficient prediction, the new constant used in the eddy viscosity model results in a better agreement with experimental data. The two-layer eddy viscosity model is given by

Inner region:

$$\epsilon = \rho (0.4LD)^2 |\omega| \quad (4-1)$$

where ω is the vorticity of the flow field

$$\omega = \frac{1}{2} \nabla \times \bar{u} \quad (4-2)$$

In the present formulation, the Van Driest damping factor, D is given as

$$D = 1 - \exp \left[- \left(\frac{\rho_b |\omega_b|}{\mu_b} \right)^{1/2} L/26 \right] \quad (4-3)$$

For the present analysis, an asymptotic length scale formula developed for an earlier investigation of a three-dimensional corner configuration is adopted for the wing-fuselage juncture region¹¹:

$$L = 2yz/[y+z+(x^2+y^2)^{1/2}] \quad (4-4)$$

Outer region:

The outer layer is basically the law of the wake including the intermittency correction by Klebanoff¹³.

$$\epsilon = 0.0336 \rho F_{\text{wake}} / [1 + 5.5(0.3L/L_{\text{max}})^6] \quad (4-5)$$

The associated boundary condition for the present investigation are straight forward. The initial condition is assigned the freestream value for the entire computational domain excluding only the surface nodes. On the solid body contour, the no-slip condition for velocity components, and the isothermal and ortho-isobaric conditions are imposed for temperature and pressure respectively. Since the attached bow shock wave isolates the interacting flow domain, the upstream and far field conditions require that the flow remains unperturbed. For the on-coming stream with an angle of attack, the x and y component of velocity assign the values of

$u_\infty \cos \alpha$ and $u_\infty \sin \alpha$, respectively, while the z component of velocity vanishes. The present analysis takes advantage of the property of symmetry with respect to the y axis (Figure 2). Only a half cross-flow plane is evaluated at the plane of symmetry. A reflection condition is applied which insists that the z component of velocity be equal to zero. The usual no-change condition is imposed at the far downstream boundary. For the supersonic problem this boundary condition is known to be well-posed and stable. In essence, we have

Initial condition

$$U(0, \xi, \eta, \zeta) = U_\infty \quad (5-1)$$

upstream ($\xi=0$) and far field condition ($\eta=1$)

$$U(t, 0, \eta, \zeta) = U(t, \xi, 1, \zeta) = U_\infty \quad (5-2)$$

on solid contour

$$u, v, w = 0 \quad (5-3)$$

$$T_b = 278^\circ K \quad (5-4)$$

$$\bar{n} \cdot \nabla p = 0$$

$$\text{where } \bar{n} = \nabla(x_b, y_b, z_b) / |\nabla(x_b, y_b, z_b)| \quad (5-5)$$

symmetry condition ($\zeta=0, \zeta=1$)

$$\frac{\partial U}{\partial \zeta} = 0, w = 0 \quad (5-6)$$

downstream condition ($\xi=1$)

$$\frac{\partial U}{\partial \xi} = 0 \quad (5-7)$$

Coordinate System and Grid Generation

For the present investigation, in spite of the highly swept wing the leading edge is still supersonic. Thus numerically rounding the wing tip will alter the shock structure from an attached shock wave to a bow shock wave³. Meanwhile, the rapid metric variations around the wing tip cannot be eliminated completely. A better choice of coordinate systems becomes necessary. A new coordinate system with a branch cut along the wing surface may alleviate the difficulty. Particularly, in view of the fact that the leading edge of the wing in the limit sharpens to a cusp, the coordinate system with a branch cut can describe this unique characteristic easily. In essence, branch cuts are performed along the upper and lower wing surfaces and the cuts are extended to the outer boundary of the mesh system (Figure 3). The branch cuts are defined by constant values of the transformed coordinate ζ . The spacing between the cuts also represents the finest in the present calculations ($\Delta Y_{\min} = 0.00012$ cm). The wing tip then is defined by the surface nodes and the immediately adjacent nodes upstream of the leading edge. Basically, the branch cuts remove all the geometric singularities at the wing tip and wing-fuselage junctures. This observation is made obvious in Figure 4. The normalized metric value of γ_v is given along a distance, s originating from the upper wing root to the wing tip and terminating at the lower wing root. The maximum value of γ_v for the wrap-around grid is already restrained by the numerically rounding of the wing tip. One notes a jump in the metric variation at the wing tip, where the numerical errors were overwhelming. On the other hand, the same transformation derivation of the branch-cut system is well behavior. It is

obvious that the demanding numerical resolution for a complex three dimensional configuration will require the grid generation and the solving scheme to be tightly integrated in the future.

The necessary but tedious preparation of the mesh point distribution for the rather complex wing-fuselage configuration is provided by a body-oriented homotopy scheme^{5,15}. The coordinate system is constructed by a series of consecutive axial cross sections unevenly spaced to achieve optimal numerical resolution. In each cross-sectional plane, a two-dimensional grid system is established between two control surfaces. The inner surface (Y_1, Z_1)

depicts the body contour. The outer surface (Y_0, Z_0) is chosen to represent the enveloping shock wave. The field points are generated by the interpolation functions:

$$Y = Y_0 \left(\frac{e^{k\eta} - 1}{e^k - 1} \right) + Y_1 \left(1 - \frac{e^{k\eta} - 1}{e^k - 1} \right) \quad (6-1)$$

$$Z = Z_0 \left(\frac{e^{k\eta} - 1}{e^k - 1} \right) + Z_1 \left(1 - \frac{e^{k\eta} - 1}{e^k - 1} \right) \quad (6-2)$$

Since the rather complex three-dimensional body consists of two distinct geometric formations, the inverted wedge wing and the ogive forebody, the orthogonality of coordinates is not enforced. However, along the branch cut the coordinate is merely a mild deviation from the Cartesian frame. The single homotopy scheme is extremely efficient. Grid systems of $31 \times 30 \times 61$ points have been generated and evaluated on a CRAY-1 computer in less than two seconds. Once the coordinates X, Y, Z are generated, the derivatives of coordinate transformation can be evaluated through the Jacobian and its inverse.

III. Solving Scheme and Numerical Procedure

MacCormack's¹⁶ explicit and unsplit algorithm is utilized in the present study to reduce the number of accessions of main memory, thereby developing an efficient data flow of the coding for a vector processor (CRAY-1). For a 3-D factored scheme, a field point requires five accessions of main memory in order to advance one time step in either the predictor or corrector sweep:

$$U^{n+1} = L_z(\Delta t/2) L_y(\Delta t/2) L_x(\Delta t) L_z(\Delta t/2) L_y(\Delta t/2) U^n \quad (7-1)$$

However, the unsplit algorithm requires only one accession of main memory to acquire the same end result:

$$U^{n+1} = [L_z(\Delta t) + L_y(\Delta t) + L_x(\Delta t)] U^n \quad (7-2)$$

In the CRAY-1 computer, which operates on a single memory path, saving on memory loading is substantial. The present effort indicates that the achievable data processing rate is 4.9×10^{-5} (sec/grid points/time step) at a maximum vector length of 61. In comparison with an earlier effort¹⁷, the current development achieves a twenty percent improvement in the data processing rate. Vector processors such as the CRAY-1 and CYBER 203 make the reliable but conditionally stable MacCormack's explicit method attractive. The detailed computer code structure, the numerical efficiency, and the numerical laminar procedure have been described in Reference 19, and therefore, will not be repeated here.

The solution is considered to be converged when the wing surface pressure variation is less than two percent over one half of an elapsed characteristic time (U_∞/L). A total of 1.4 hours of CRAY-1 computer time was required to meet the aforementioned criterion for $\alpha=0$. At the 10° angle of attack, the viscous effects become dominant as the inviscid-viscous interaction intensified. A significant reduction in allowable time step forces additional iterations to be performed to meet the convergence criterion. However, for the 10° angle of attack case, the initial condition is the converged case for $\alpha=0$. In this manner the 10° case required only 40% more total computing time to reach the steady asymptotic state.

IV. Discussion of Results

The present results are given in two groups. In the first group of results, the numerical solutions are presented and compared with experimental data under identical flow conditions. The rest of the discussion concentrates on the delineation of the detailed flow structure around the wing-fuselage configuration at 10° degree angle of attack.

The comparison of static pressure distributions around the wing-body combination either for the zero degree angle of attack or the 10° degree angle of attack with the experimental data of reference 6 agrees very well. Except phase for the known cause of misalignment of the pressure probe, the maximum discrepancy between data⁶ and calculations is confined within a few percent¹⁹. All essential features including the pressure jump across the bow shock are faithfully duplicated.

In Figure 5, comparisons of pitot pressure distributions with data are presented. The pitot pressure is normalized with the freestream stagnation pressure p_{t_∞} (4.1368×10^5 KPA). Thus the normalized pitot pressure attains a value of 0.027 in the freestream. The overall comparison of the data⁶ with the present result is reasonable. The maximum discrepancy between data and present results is around fourteen percent (mostly in the region bounded by the upper wing surface and fuselage). The experimental measurements revealed a much stronger expansion inboard of the wing tip than computations including the inviscid results⁶ for the same configuration. Misalignment of the probe or model could account for some of this discrepancy. However, both the data and numerical results indicate a larger stagnated region in the upper wing-fuselage juncture ($y/r > 0$, $z/r = 1$) than the lower juncture ($y/r < 0$, $z/r = 1$). A rapid expansion jet-like zone at the lower wing tip is also indicated.

In Figure 6, the comparison of total pressure profiles at the 10° angle of attack is presented. The pitot pressure probe is known to be relatively insensitive to the probe alignment with the flow. Excellent agreement between data and present results is clearly evident. Except perhaps in the shock envelope region, the deviation between data and present results is about the range of the data scattering. In short, the specific comparisons of static pressure distributions and pitot pressure profiles indicate that the present results duplicate nearly all the experimental measurements.

The static pressure distributions over the entire span of the wing surface at the zero and ten

degree angle of attack are presented in Figure 7. Numerical predictions at the wing tip and the meridian plane of fuselage agree very well with the inviscid asymptotes. For the flow without incidence, the upper surface pressure maintains the freestream value until about 0.8 of the wing span then increases its value toward the wing-tip. This pressure rise is influenced by the higher pressure level beneath the wing through the thin shear layer over the sharp leading edge. For the lower wing surface a continuous compression toward the wing tip originates at about 0.7 of the wing span. In the lower wing tip region, the surface pressure attains the value equal to the oblique shock of three degree flow deflection. At 10° angle of attack, the pressure distributions over the wing exhibit a similar behavior. The only difference is that at the higher angle of attack, the windward surface pressure distribution reveals three plateaus. The lowest pressure plateau is in the wing-body juncture, then compresses rapidly until the mid-span to reach the second pressure plateau and a final compression toward the wing tip. In the windward leading edge domain, the surface pressure corresponds to the oblique shock value of 13° flow deflection. It is clear that the windward surface pressure of the wing body is always lower than the value if the wing were exhibited alone. The cross feeding over the wing leading edge through the thin shear layer between leeward and windward surface and the expansion from wing tip to wing root over the windward wing reduces substantially the lift generated by the wing.

In Figure 8, the circumferential surface pressures of the wing-body combination are presented. In addition the circumferential surface pressure over cylindrical forebody is also depicted here for reference purposes. This particular cross flow plane is in the intermediate streamwise location between the ogive forebody and the plane which the wing is first merged with the fuselage. The circumferential pressure is similar to the pressure distribution over a circular cone at angle of attack²⁰. For all the cases considered, the aerodynamic interference in terms of pressure is unfavorable; the leeward pressure is higher and the windward pressure is lower than the forebody alone. Favorable interference is noted in both the leeward and windward wing-body junctures. However, the total contribution to the lift is small. Therefore, the present result at a Mach number of six shows an unfavorable aerodynamic interference for the delta-wedge wing and ogive cylindrical fuselage. The conclusion is consistent to the experimental observations that the compressibility effect and angle of attack reduce the wing-body interference factor from favorable to adverse^{5,21}. For the cases investigated, the wing-body interference factor decreases from the value of 0.64 at zero angle of attack to the value of 0.60 for angle of attack equal to ten degrees.

In order to describe the kinematic structure of the flow over the wing-fuselage at 10° angle of attack, two cross flow patterns depicted W and V velocity components are given in Figures 9 and 10. In Figure 9, the vortical singularity lift off and the flow separation over the leeward side of the forebody are clearly demonstrated. The line of flow separation is at a peripheral location of $\phi = 150^\circ$, which is in perfect agreement with experimental observation²². In Figure 10, the cross flow

velocity distribution over the wing-body combination is given. The flow separation in the windward junction of the wing and fuselage is clearly indicated. Along the windward wing and outboard of the reattachment, a jet-like stream is observed. The presence of a leading edge shock wave is also made evident by the abrupt change in orientation of the cross flow velocity. Since the leading edge is supersonic, the shock wave is attached to the leading edge. No significant upwash around the wing tip is detected. Over the leeward wing-fuselage juncture, the recirculated separated flow is easily detectable. The stream lift off over the leeward wing surface is also obvious. This phenomenon is faithfully depicted around the 0.8 of the span of wing. From the cross flow velocity component, it is easily deduced that a multiple vortex structure exists in the cross flow plane with strong concentrations at both the windward and leeward wing-body junctures, the leeward midspan of the wing and over the leeward fuselage. All of these observations can be confirmed by the computed vorticity distributions at the aforementioned streamwise locations (Figures 11 and 12).

In Figure 13, the leeward surface shear distribution is depicted and the windward surface result is presented in Figure 14. According to the limiting streamline concept²², the separation is a locus of the intersection of a family of limiting streamline. For three dimensional flow separation, the convergence of the limiting streamline represents separation. Then it is clearly indicated that the flow separated from the leeward fuselage near the meridian plane, the wing-fuselage juncture, and the outboard leeward wing surface. Secondary features of the shear distribution adjacent to the location where the wing first emerges from the fuselage on the fuselage surface also are detectable. However, no experimental data are available to make a convincing comparative study. On the windward surface, Figure 14, the surface shear structure is easier to understand. The flow separates along the wind-body juncture and reattaches outboard of the wing root. Outwash around the fuselage due to the angle of attack is also clearly discernible.

In the final figure, density contours ranging from the ogive forebody to the wing-body combination are selectively presented in Figure 15. Two features stand out in this figure, namely, the growth of the enveloping bow shock wave and the distortion of the bow shock due to the wing. The density contours upstream of wing bear the strong resemblance to that of conical flow at an angle of attack². The windward bow shock dominates, then the flow expands rapidly leeward into the aerodynamic shadow. As soon as the wing merges from the fuselage the leading edge shock appears in the windward domain and overwhelms all other features of the flow.

V. Concluding Remarks

The numerical simulations of a hypersonic cruiser were accomplished for the flow without incidence and at ten degree angle of attack. The aerodynamic interference of the ogive cylindrical fuselage and the inverted wedge delta wing was found to be unfavorable.

The selection of a coordinate system for a configuration containing geometric singularities is

demonstrated to be critical. The use of a "branch cut" was found to greatly decrease numerical difficulties. Therefore, the grid generation and the solving procedure can not be treated as separate issues. In our pursuit to simulate the full-scale aircraft by means of segmented or patched computational domains this finding is of vital importance.

References

1. Ashly, H. and Rodden, W.P., "Wing-Body Aerodynamic Interaction," Annual Review of Fluid Mechanics, Vol. 4, 1972, Annual Reviews Inc., Palo Alto, CA, pp 431-472.
2. Loeve, W., "The Calculation of Aerodynamic Characteristics of Wing-Body Combinations at Subsonic Flight Speeds," Lecture notes in physics, Vol. 59, Springer-Verlag, 1976, p 75.
3. Peake, D.J., and Tobak, M., "Three-Dimensional Interactions and Vortical Flows with Emphasis on High Speeds," AGARDograph No. 252, July 1980.
4. Caughey, D.A., and Jameson, A., "Numerical Calculations of Transonic Potential Flow About Wing-Body Combinations," AIAA J. Vol. 17, No. 2, February 1979, pp 175-181.
5. Klopfer, G.H., and Nielson, J.H., "Euler Solutions for Wing and Wing-Body Combination at Supersonic speeds with Leading-Edge Separation," AIAA Preprint 80-0126, AIAA 18th Aerospace Sciences Meeting, Pasadena, CA, January 14-16, 1980.
6. Wang, C.R., Zakkay, V. and Parikh, H., "An Experimental and Analytical Investigation of a Hypersonic Cruising Vehicle at Mach 6," AIAA Preprint 80-0004, AIAA 18th Aerospace Sciences Meeting, Pasadena, CA, January 14-16, 1980.
7. Rizzi, A., "Damped Euler-Equation Method to Computer Transonic Flow Around Wing-Body Combinations," AIAA J. Vol. 20, No. 10, Oct 1982, pp 1321-1328.
8. Venkatapathy, E., Rakich, J.V., and Tannehill, J.C., "Numerical Solution of Space Shuttle Orbiter Flow Field," AIAA Preprint 82-0028, AIAA 20th Aerospace Sciences Meeting, Orlando, FL, January 11-14, 1982.
9. Shang, J.S., "Numerical Simulation of Wing-Fuselage Interference," AIAA Preprint 81-0048, AIAA 19th Aerospace Sciences Meeting, St. Louis, MO, January 12-15, 1981.
10. Eriksson, L.E., "Generation of Boundary-Conforming Grids Around Wing-Body Configurations Using Transfinite Interpolation," AIAA J. Vol. 20, No. 10, Oct 1982, pp 1313-1320.
11. Shang, J.S., Hankey, W.L., and Petty, J.S., "Three-Dimensional Supersonic Interacting Turbulent Flow Along a Corner," AIAA J. Vol. 17, No. 7, July 1979, pp 706-713.
12. Hindman, R.G., "Generalized Coordinate Forms of Governing Fluid Equations and Associated Geometrically Induced Errors," AIAA J. Vol. 20, No. 10, Oct 1982, pp 1359-1367.
13. Baldwin, B.S., Lomax, H., "Thin Layer Approximation and Algebraic Model for Separated Turbulent Flows," AIAA Preprint 78-257, AIAA 16th Aerospace Sciences Meeting, Huntsville AL, January 16-18, 1978.
14. Knight, D.D., "Hybrid Explicit-Implicit Numerical Algorithm for the Three-Dimensional Navier-Stokes Equations," AIAA Preprint 83-223, AIAA 21st Aerospace Sciences Meeting, Reno Nevada, January 10-13, 1983.
15. Eisman, P.R., and Smith, R.E., "Mesh Generation Using Algebraic Techniques," NASA Conference Publication 2166, NASA Langley Research Center, Hampton, VA, Oct 1980, pp 73-120.

16. Shang, J.S., Smith, R.E., and Hankey, W.L., "Flow Oscillations of Spike-Tipped Bodies," AIAA Preprint 80-0062, AIAA 18th Aerospace Sciences Meeting, Pasadena, CA, January 14-16, 1980.
17. McCormack, R.W., "Numerical Solutions of the Interactions of a Shock Wave with Laminar Boundary Layer," Lecture note in physics, Vol. 59, Springer-Verlag, 1976.
18. Shang, J.S., Buning, P.G., Hankey, W.L., and Wirth, M.C., "Performance of a Vectorized Three-Dimensional Navier-Stokes Code on the CRAY-1 Computer," AIAA J. Vol. 18, No. 9, Sept 1980, pp 1073-1079.
19. Shang, J.S., "Numerical Simulation of Wing-Fuselage Aerodynamic Interaction," AIAA Preprint 83-225 AIAA 21st Aerospace Sciences Meeting, Reno, Nevada, January 10-13, 1983.
20. McRae, D.S., and Hunsami, M.Y., "Numerical Simulation of Supersonic Cone Flow at High Angle of Attack," High Angle of Attack Aerodynamics AGARD-CP-247, Oct 1978, pp 23-1, 23-10.
21. Nielsen, J.H., "Nonlinearities in Missile Aerodynamics," AIAA Paper, AIAA 16th Aerospace Sciences Meeting, Huntsville, AL, Jan 16-18, 1978.
22. Moore, F.K., Ed., Theory of Laminar Flows, High Speed Aerodynamics and Jet Propulsion, Vol. IV, Princeton University Press, Princeton, NJ, 1964, pp 387-390.
23. Shang, J.S., and Hankey, W.L., "Numerical Solution of the Navier-Stokes Equations for a Three-Dimensional Corner," AIAA J. Vol. 15, No. 11, Nov 1977, pp 1575-1582.

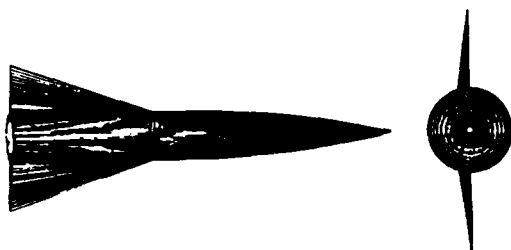


Figure 1 The Wing-Fuselage Configuration

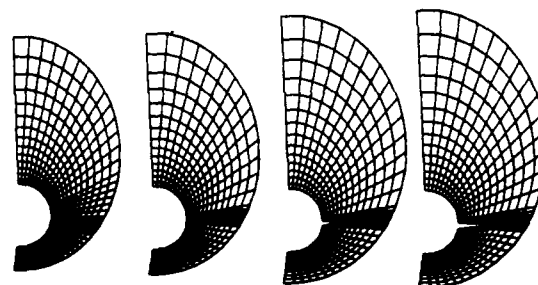


Figure 3 Grid Point Distribution of the Wing-Fuselage Configuration

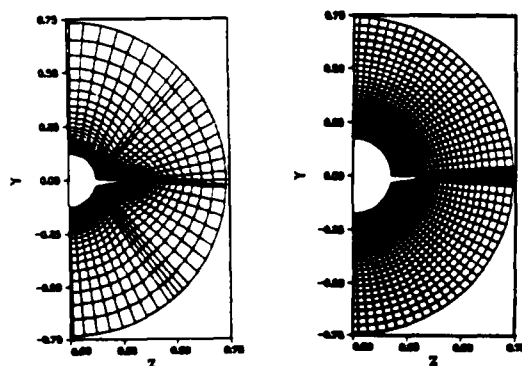


Figure 2 The Wrap-Around and Branch-Cut Mesh System

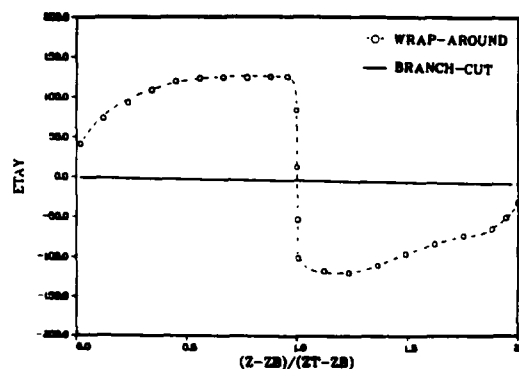


Figure 4 The Metric Variations Along the Wing Surface

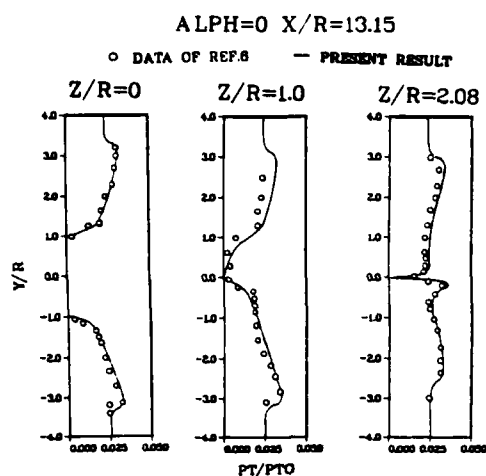


Figure 5 Comparison of the Pitot Pressure Distributions ($\alpha=0$)

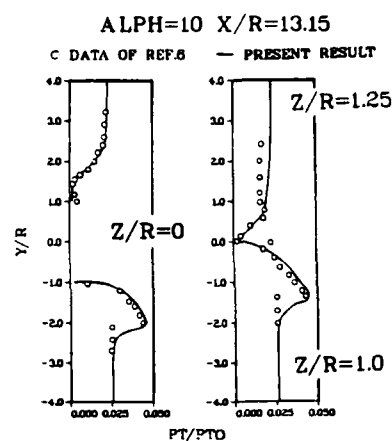


Figure 6 Comparison of the Pitot Pressure Distributions ($\alpha=10$)

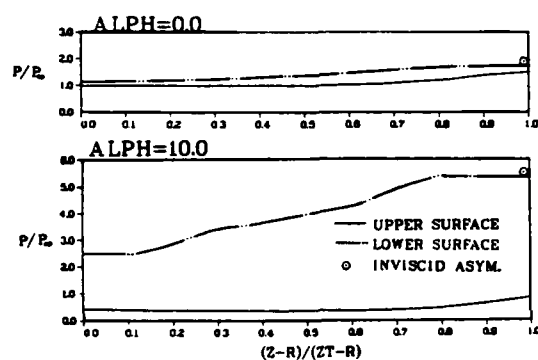


Figure 7 The Pressure Distributions Over the Wing Span

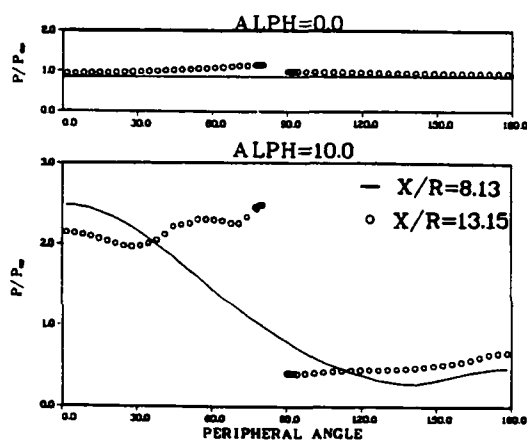


Figure 8 The Peripheral Pressure Distributions Over the Wing-Body Surface

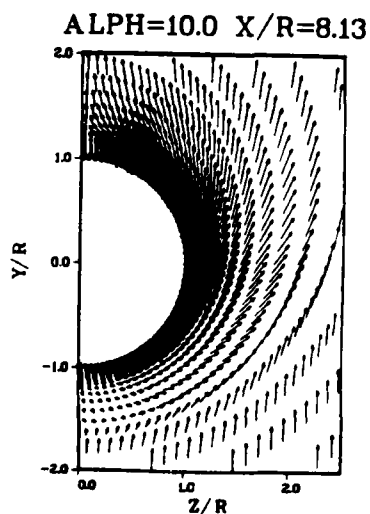


Figure 9 Computed Cross Flow Velocity Field of the Cylindrical Forebody $\alpha=10$

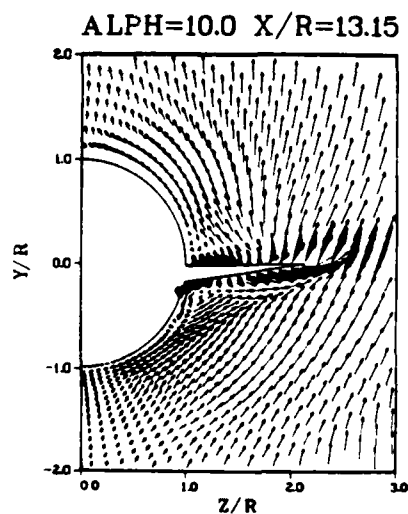


Figure 10 Computed Cross Flow Velocity Field of the Wing-Fuselage $\alpha=10$

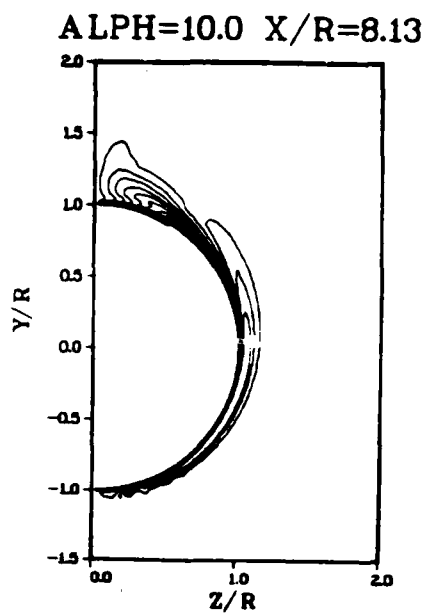


Figure 11 The Vorticity Distribution Over the Cylindrical Forebody $\alpha=10$

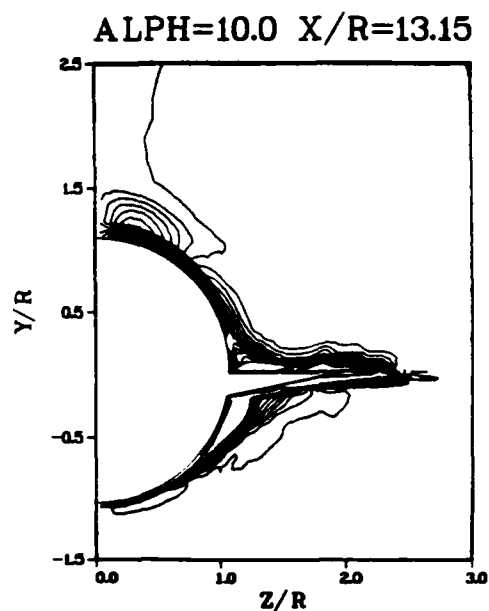


Figure 12 The Vorticity Distribution Over the Wing-Fuselage $\alpha=10$

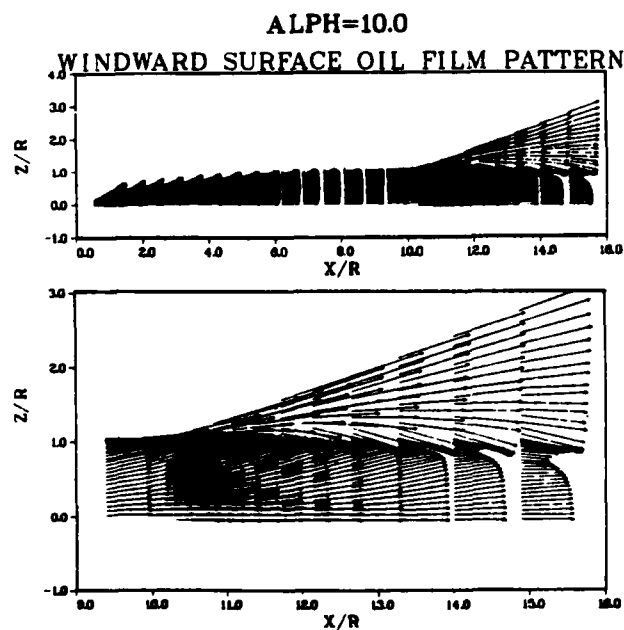


Figure 14 The Surface Shear Map on the Windward Wing-Body Surface

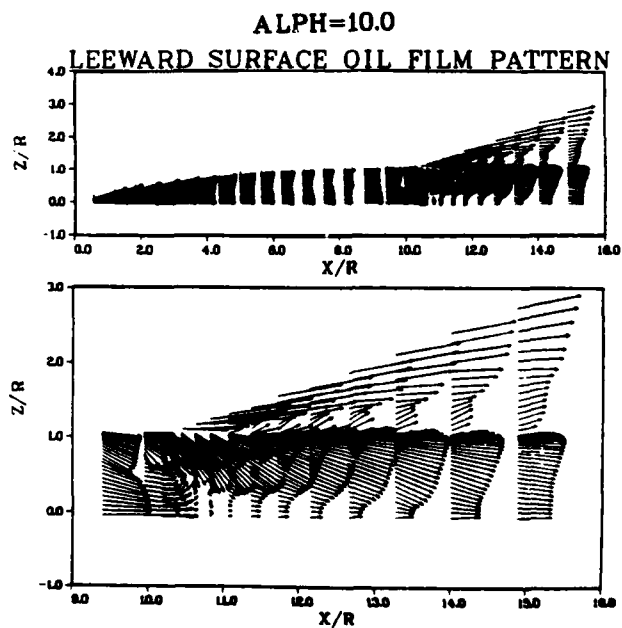


Figure 13 The Surface Shear Map on the Leeward Wing-Body Surface

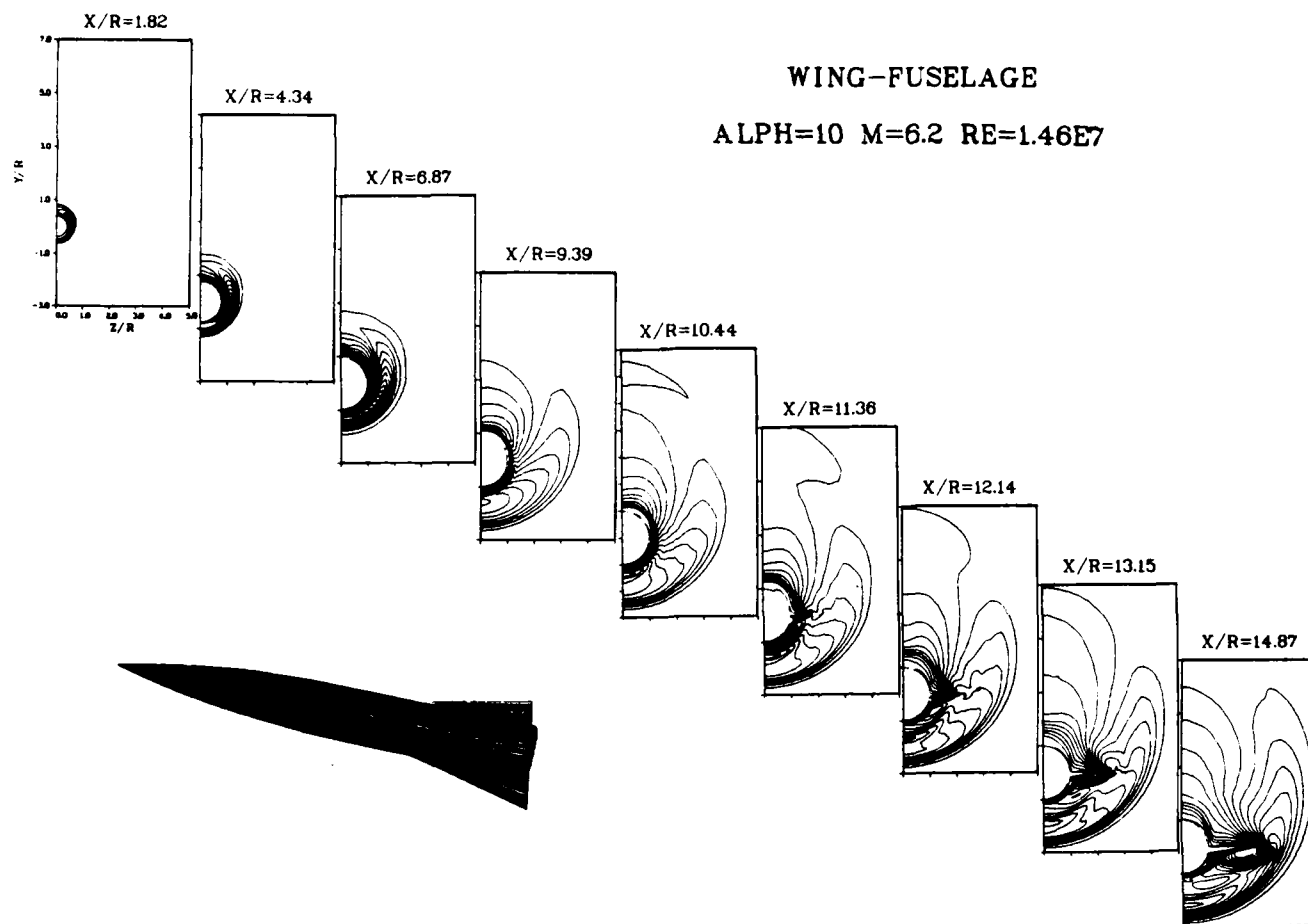


Figure 15 Density Contours Over the Entire Wing-Fuselage Configuration

SESSION 2

NUMERICAL SOLUTIONS OF SPATIALLY-PERIODIC BOUNDARY LAYERS

O. R. Burggraf
The Ohio State University
Columbus, Ohio

Abstract

Spatially periodic viscous flows have a number of diverse applications, among which may be mentioned use as a model for the recirculating eddy in a separated flow, periodic surface roughness in transition studies, and as a device to oxygenate blood in open-heart surgery. Batchelor (1956) considered a circular eddy in his work on the structure of steady recirculating flows. More recently Van Dyke (1981) attacked this problem by the method of series truncation. The present author (1966) studied the same problem by an Oseen-like linearization, and also considered the flow in a square cavity with a sliding lid. An intriguing aspect of the problem is that the vorticity of the inviscid core is an eigenvalue that is determined by the periodicity condition.

In the present study the nonlinear boundary-layer equations are solved by marching forward from an arbitrarily chosen initial state with an assumed value of the core vorticity. For each sweep around the fluid circuit the change of momentum thickness θ (or other thickness scale) varies asymptotically as $N^{1/2}$, where N is the

number of sweeps. The correct value of core vorticity for a periodic flow divides the cases for which θ increases from those for which it decreases (algebraically). The asymptotic state is achieved for N of the order of nine to sixteen sweeps. For noncircular configurations, the marching method breaks down, either due to the separation-point singularity, or through instability at corner points if the pressure gradient is too weak to produce separation. In either case, viscous interaction with the inviscid core is required to smooth out the singularity.

The same problem has been formulated spectrally, in terms of Fourier series in the main-flow direction. This approach guarantees periodicity, and it has been shown previously that the spectral method handles separation without difficulty. The core-vorticity eigenvalue is a novel feature here; it is treated by an iterative procedure. Results of the spectral and marching methods will be compared for the circular eddy and for the unseparated noncircular cases. In addition, spectral results will be presented for a polygonal eddy with flow separation in the corners.

ASYMPTOTIC THEORY OF TURBULENT WALL JETS

R. E. MeInik and A. Rubel
Research & Development Center
Grumman Aerospace Corporation
Bethpage, New York

Abstract

This paper presents a systematic analysis of two-dimensional turbulent wall jets using the method of matched asymptotic expansions. The expansions are carried out in terms of two basic parameters - one the usual Reynolds number, Re , that is taken to be large and the other a small parameter, σ , that is related to the statistical aspects of turbulent flows. The latter parameter scales the turbulence levels in free turbulent flows such as jets and mixing layers which are essentially independent of Re . The σ parameter is a basic turbulence parameter that governs the spreading rate of such flows. The present work is based on a two-equation ($k-\epsilon$) turbulence model, in which the turbulence parameter, σ , can be identified with the model constant C_μ appear-

ing in the turbulent viscosity law. The asymptotic theory for the $k-\epsilon$ model leads to a four-layer description of wall jets. A number of ad-hoc theoretical models previously developed have employed a two-layer description of the turbulent wall jet consisting of an outer free jet patched to an inner wall layer. Although the outer region of the present theory bears some relation to a free jet, there are very important differences. The influence of the wall boundary conditions on the turbulent energy and dissipation extends across the entire outer region and acts to significantly reduce the spreading rate below that of free jets. Our work indicates that this effect accounts for much of the reduced spreading rates observed for wall jets compared to free flows.

ON THE COUPLING OF BOUNDARY LAYER AND EULER EQUATION SOLUTIONS

Earl M. Murman and Thomas R.A. Rusing
Department of Aeronautics and Astronautics
Massachusetts Institute of Technology
Cambridge, Massachusetts

Abstract

The coupling of boundary-layer solutions to potential-flow calculations is relatively well developed and has been called Interacting Boundary-Layer Theory (IBLT) by Melnik (ref. 1). The boundary layer and inviscid potential flow are coupled using displacement thickness concepts. Rather than use the classical approach of modifying the body shape by adding the displacement thickness, Lighthill's (ref. 2) transpiration boundary condition $\partial \psi / \partial n = d(\phi / g \delta^*) / dS$ is applied on the body surface. The potential flow is solved iteratively with boundary-layer calculations being done at intermediate stages of the calculation. Thus the converged result is a solution of both sets of equations. For unseparated flows, direct solutions of the boundary layer are done (ref. 1) while for separated flows, inverse solutions (e.g. refs. 3-5) are required.

The coupling of boundary-layer solutions to solutions of the Euler equations is of increasing interest due to the rapid development of efficient and practical algorithms for the Euler equations (e.g. refs. 6-8). However, the correct coupling conditions for the inviscid and viscous flow are not as well understood as the classical Lighthill (ref. 2) conditions which are restricted to potential flow. The key difference is that potential flow just solves the continuity equation so that coupling only involves the displacement thickness. The Euler equations, however, require the solution of the continuity, momentum, and (usually) energy equations, and coupling must involve displacement, momentum, energy, and other thickness parameters. Thus the transpiration boundary condition must be expanded to include momentum and energy sources on the body together with mass sources.

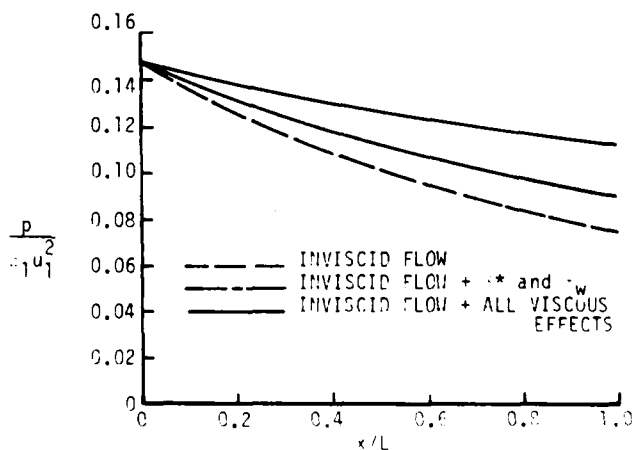
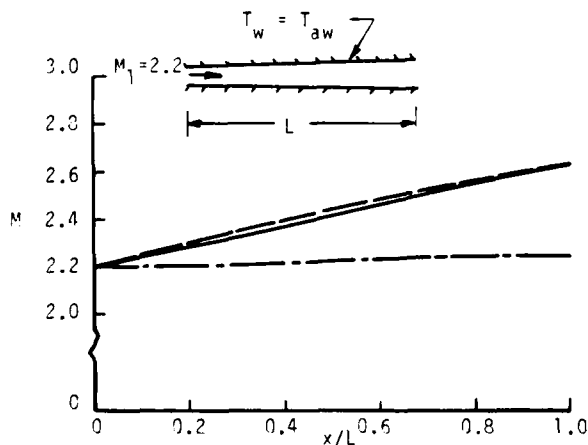
The present authors derived these matching relationships for an internal flow configuration

where the inviscid flow is being treated as one-dimensional. The attached figure shows a calculation for a diverging duct with a turbulent boundary layer. The figure shows that if only the displacement thickness effects are added, the results are substantially different from the complete matching of the viscous flow. Independent of the present investigation, Johnston and Sockel (ref. 9) developed an equivalent analysis of the matching conditions. This paper will present the coupling theory and example calculation to illustrate the effects of the various terms.

This work is being supported by NASA Grant NAG-1-229.

References

1. Melnik, R.E.: Paper 10, AGARD CP 291, 1980.
2. Lighthill, M.J.: JFM 4, 1958.
3. Carter, J.E.: AIAA Paper 79-1450, 1979.
4. Wigton, L.B. and Holt, M.: AIAA Paper 81-1003, 1981.
5. LeBalleur, J.C.: La Recherche Aerospatiale (English ed.) No. 1981-3, pp. 21-45.
6. McCormack, R.: AIAA Paper 69-345, 1969.
7. Jameson, A., Schmidt, W. and Turkel, E.: AIAA Paper 81-1259, 1981.
8. Ni, R.H.: AIAA Paper 81-1025, 1981.
9. Johnston, W. and Sockel, P.: AIAA J. 17:6, pp. 661-663, 1979.



INTERACTIVE SEPARATION FROM A FIXED WALL*

L. L. van Dommelen and S. F. Shen

Sibley School of Mechanical and Aerospace Engineering
Cornell University, Ithaca, NY 14853Abstract

Numerically a solution is sought to describe the separation process from a fixed wall in the interaction region. Introduction of an analytical flow velocity in the external flow insures continuity, irrotationality and the correct asymptotic behaviour. In the boundary layer flow region, a finite difference procedure is employed. This procedure solves diffusion of vorticity rather than of momentum. It retains the full boundary layer equation in the region of reversed flow. The entire boundary layer flow region is mapped onto a finite computational domain in order to eliminate artificial cut-offs. Interactively, the external and boundary layer flows must agree on both boundary layer pressure distribution and displacement effects. This agreement is here achieved by least square minimization of the differences. Preliminary results seem a significant step forward for both accuracy and computational efficiency and flexibility. But though the boundary layer flow results do extend further downstream than previous work by a factor of two, the objective of a solution extending all the way downstream to infinity has not yet been met. In contrast, far upstream the scheme performs excellently.

Setting the Stage

To explain why the fluid dynamic drag does not appear to vanish when the coefficient of viscosity does, the inviscid theory requires Kirchhoff free vortex sheets. Physically, these free vortex sheets ought to correspond to the boundary layer which has lifted off from the wall.

But up to a decade ago there was no known mechanics for the boundary layer to lift off from the wall. A difficulty was the square root singularity in the outer flow at a position of lift off¹:

$$u - i v - u_S - i k [z - x_S]^{1/2}$$

$$z \equiv x + i y \quad (1)$$

with x the coordinate along the wall and y the distance from the wall; " k " is a constant depending on the location of the separation point. For a circular cylinder, k vanishes when separation is located 55 degrees from the forward stagnation point and k is positive if it is located further downstream.

If k does not vanish, it implies on account of the Bernoulli law a severe adverse pressure gradient in the boundary layer immediately upstream of separation:

$$p - p_S - \rho u_S k [x_S - x]^{1/2} (x + x_S) \quad (2)$$

By integrating the momentum equation in Von Mises variables, it may be shown that the boundary layer

particles near the wall simply do not have the kinetic energy to penetrate such an adverse pressure gradient. They would come to a stop and the existence of the boundary layer flow should be expected to terminate in a Goldstein² singularity well upstream of the separation point.

And if separation would indeed occur at a location $k = 0$ where the square root external flow singularity just happens to vanish, the pressure gradient would be favourable in the boundary layer upstream of separation¹. Then the boundary layer particles would reach the separation point with too much velocity to allow their path to deflect significantly away from the wall. At least some retardation of the boundary layer particles near the wall is necessary for them to cause a significant deflection of the boundary layer away from the wall.

To resolve this difficulty, Sychev³ adopted the hypothesis that the actual location of the separation point would depend on the Reynolds number. It would be close to the location of vanishing k on account of the small kinetic energy of the boundary layer particles near the wall, but still at positive k in order for an adverse pressure gradient to be present to retard these particles. His estimates led to the postulate that

$$k \sim Re^{-1/16} K$$

where K would be a constant for which the value remained unknown.

The pressure gradient in the boundary layer upstream of separation would then be favorable for the major part; approximately the one which occurs when separation is exactly located at the position of vanishing k . Only relatively close to the separation point would the non-zero value of k become evident. For, the singular behaviour of the square root singularity Eq. (2) must eventually always dominate the pressure gradient and turn it adverse.

Thus there would be only a relatively short part of the boundary layer in which the pressure gradient is adverse. As a consequence of this short length scale, diffusion effects in the retardation of the boundary layer particles would remain restricted to a thin sublayer of boundary layer particles close to the wall. Except in this "lower deck" close to the wall, all boundary layer particles retain their vorticity throughout the separation process.

It follows that coming out of the lower deck, the boundary layer particles still have the same vorticity they had near the wall before the pressure gradient turned adverse:

$$\omega = \tau_0 \quad (3)$$

if τ_0 denotes the value of the wall vorticity at

*This paper is dedicated to Professor W.R. Sears for his 70th birthday.

the location of vanishing pressure gradient. Equivalently, it is the wall shear at this location, for in boundary layer approximation shear and vorticity are proportional.

Within the lower deck, pressure retardation and diffusion effects work together to give a rapid fall off of the vorticity from its starting value τ_0 . It is the expression

$$v/u = - \int \int \omega_{,x} dy^2 / \int \omega dy,$$

as found from continuity and the definition of the boundary layer vorticity, which relates this rapid vorticity fall off to significant deflection of the boundary layer streamlines away from the wall.

The square root singularity above the separation point occurring in the Kirchhoff description of the external flow, Eqs. (1) and (2), would of course not exist in the actual flow. Sychev argues that when the separating flow is examined sufficiently closely, it is seen that the small but non-zero boundary layer thickness acts to smooth out this singular behaviour. To do so, phenomena on a tiny $O(Re^{-3/8})$ length scale must be resolved.

Thus Sychev postulated that in a region with a typical dimension $O(Re^{-3/8})$ around separation, external and boundary layer flows could exist for which the Kirchhoff singularity Eqs. (1) and (2) in the external flow would be smoothed out by the boundary layer displacement effects. The main source of this displacement effect would be the lower deck of boundary layer particles near the wall.

Essentially, Sychev's separation structure was a generalization of the "triple deck" flow structure discovered earlier by Stewartson⁴ and by Messiter and Enslow⁵ for the flow at the trailing edge of a flat plate.

Sychev's assumption that outer and boundary layer flows would be possible in the interaction region was not trivial: if solutions could exist, they would have to agree on both the boundary layer pressure distribution and the displacement effects. The first attempt to verify the postulate was made when Smith⁶ tried to find numerical solutions for the local irrotational and boundary layer flows in this "interaction region". First, all variables were suitably normalized;

$$\begin{aligned} x &= x_S + \sqrt[3]{8} u_S^{3/2} \tau_0^{-5/4} X \\ y &= \sqrt[3]{8} u_S^{3/2} \tau_0^{-5/4} Y = \sqrt[3]{8} u_S^{1/2} \tau_0^{-3/4} \underline{y} \\ u &= u_S + \sqrt[3]{8} \tau_0^{1/2} U = \sqrt[3]{8} u_S^{1/2} \tau_0^{1/4} \underline{u} \\ v &= \sqrt[3]{8} \tau_0^{1/2} V = \sqrt[3]{8} u_S^{-1/2} \tau_0^{3/4} \underline{v} \\ p &= p_S + \sqrt[3]{8} u_S \tau_0^{1/2} P \\ \kappa &= \sqrt[3]{16} u_S^{-3/4} \tau_0^{-9/8} K \\ \tau_0 &\equiv \sqrt[3]{12} \tau_0 \end{aligned} \quad (4)$$

Here capitals refer to the external flow and italics to the boundary layer flow.

In these normalizations, the lower boundary layer deck satisfies

$$\underline{u}_{,X} + \underline{v}_{,Y} = \underline{\omega}_{,Y} \underline{y} \quad (5a)$$

$$\underline{u}_{,X} + \underline{v}_{,Y} = 0 \quad \underline{\omega} \equiv \underline{u}_{,Y} \equiv \underline{\tau} \quad (5b)$$

$$\underline{\omega}_{,Y} = P_{,X} \text{ at } \underline{y} = 0 \quad (5c)$$

Since by Eq. (4), τ_0 is normalized to unity, the asymptotic behaviour Eq. (3) leaving the lower deck becomes

$$\underline{\omega} \sim 1 \quad \underline{y} \rightarrow \infty \text{ or } X \rightarrow -\infty \quad (5d)$$

The external flow field is described by an complex flow velocity

$$W \equiv V - i U \quad (5e)$$

which should be analytic in the flow region

$$\text{Imag}\{Z\} > 0 \quad Z \equiv X + i Y$$

In order that this irrotational flow field does indeed seem to have the square root Kirchhoff singularity (1) when Z is large,

$$W \sim K Z^{1/2} \quad Z \rightarrow \infty \quad (5f)$$

The Bernoulli law relates the boundary layer pressure to the external flow velocity at the wall as

$$P = -U \quad (5g)$$

Finally, in order that both lower deck and external flow agree on the same deflection of the boundary layer streamlines,

$$v_{Y=0} = \left\{ \frac{v}{u} \right\}_{\underline{y}=\infty} = - \int_0^\infty \underline{\omega}_{,X} d\underline{y} \quad (5h)$$

the latter equality from Eq. (5b), using the asymptotic behaviour Eq. (5d). The X -integral of the displacement velocity (5h) describes the displacement thickness, but this thickness is poorly defined in the present case where vorticity rather than velocity remains finite at large \underline{y} .

The procedure followed by Smith was to try various values for the constant K in the asymptotic behaviour (5f) and see whether for that value a solution could be found iteratively. In the iterative procedure, the boundary layer displacement thickness was found from his guess for the external flow. He then found the corresponding boundary layer pressure distribution by integrating the boundary layer equation. With this new pressure distribution, he updated his external flow, hopefully obtaining a better guess. Using severe underrelaxation, he iterated typically 80 times and tried to find evidence of convergence of the results. For a value $K \approx 0.44$ his results did indeed suggest the existence of a meaningful solution. Apparently, the divergence of the iterative procedure for other values of K would mean that for these values no solution exists. But Smith does not give a discussion why this should be true.

In order to be able to solve the boundary layer flow by a marching procedure, the Reyhner & Flügge-Lotz "approximation" was made to neglect all backward transport of momentum. This involves a finite error, although in many cases it was found that numerically this error is relatively small.

The region of integration of the boundary layer flow was rendered finite in upstream direction by an artificial cut-off at $X=-64$; in downstream direction by one at $X=20$ and in vertical direction by one at $y=500$.

However, with these cut-offs unacceptably high oscillations in the solution occurred. This problem was resolved by the introduction of an artificial "development region" $-4096 < X < -64$ in which the boundary layer displacement thickness was prescribed from a known two term asymptotic expansion valid far upstream. The effect of each of these artifices on the solution had of course to be examined separately.

Basically, Smith's program reconciles the solutions of a simple potential outer flow and a simple parabolic boundary layer equation. For the downstream moving wall case, a similar problem was solved by Van Dommelen and Shen³. With a different numerical procedure, determination of the solution to five digits accuracy took there mere seconds on the IBM 370. The scheme had none of these cut-offs to introduce numerical errors and possible mutual interactions. It could easily be implemented in global programs or generalized to cover the finite Reynolds number case. And the Reyhner & Flügge-Lotz step was not needed.

It is the purpose of the present investigation to extend the procedure of Van Dommelen and Shen toward the fixed wall case. Such a program could be a stepping stone to the upstream moving wall case: there one could not possibly hope to get away with the Reyhner & Flügge-Lotz error!

Outline of the Numerical Procedure

In the previous section, it was seen that the problem for the flow in the interaction region at separation is described by the system of equations (5a) through (5h). Basically, one has to reconcile the local outer and boundary layer flows on both the boundary layer pressure P and displacement effect (5h).

Following the line of the procedure of Van Dommelen and Shen³, it shall be attempted to approximate the external flow velocity as a finite sum of analytical functions. For the preliminary results presented here, this sum was chosen to be of the general form

$$V - iU = K \Delta Z^{1/2} + \frac{1}{2} K Z_0 \Delta Z^{-1/2} + \sum_{n=5}^N A_n \Delta Z^{-n/6} \quad (6)$$

$$\Delta Z \equiv Z - Z_0$$

and Z_0 is a constant with a negative imaginary part which was introduced to keep singularities out of the flow region. Clearly this is about the

simplest possible approximation to describe the correct square root singularity (5f) for large Z .

The summation occurs in inverse powers of $\Delta Z^{1/6}$, since this would reproduce the known next few asymptotic terms^{1,2,3} also correctly. More precisely, correct up to $n=8$ in Eq. (6). For the downstream moving wall case³ the sum was in inverse powers of $\Delta Z^{1/2}$, reflecting the different asymptotic analysis. The summation was in the results presented here truncated at $N=9$. Probably there would be much better representations of the external flow but a search has not yet been made.

When the coefficients A_n in the external flow approximation (6) are arbitrary, the wall pressure distribution and boundary layer displacement effect would not correspond to a possible boundary layer solution. For, when the displacement effect would be used to integrate the boundary layer flow, the resulting boundary layer pressure distribution would in general not be the same as the one of the external flow. Van Dommelen and Shen³ now determined values for the coefficients A_n by least square minimization of this difference in the two results for the pressure distribution. The problem was there simplified by the fact that the boundary layer flow was inviscid and could be solved analytically.

Here however, the boundary layer equation must be integrated numerically. And rather than to prescribe the displacement thickness everywhere, the physics of the problem suggests that the pressure gradient should be described in the attached boundary layer at the upstream end of the interaction region and the displacement velocity in the separating boundary layer at the downstream end. In between, a linear combination of both was prescribed,

$$[1 - \tanh X/2L] P_{,X} + [1 + \tanh X/2L] V \quad (7)$$

where on behalf of typical results the characteristic length L was chosen to be 10. There exists some similarity with the procedure of Veldman³. Occurrence of a Goldstein singularity² would imply infinite displacement velocity, hence is not possible.

Following the procedure for the downstream moving wall³, values for the constants K and A_n in the external flow representation (6) were found from least square minimization of the differences between boundary layer and external flows. Since now both flows agree only exactly on the linear combination Eq. (7), both the differences in pressure gradient and displacement velocity were numerically minimized.

More precisely, using δ_k to denote a difference at an arbitrary collocation point X_k and M_p and M_v for the characteristic magnitudes of pressure gradient and displacement velocity, the minimized quantity was chosen to be

$$\frac{\delta_k^2}{K^2} + \frac{\delta_k^2}{V_k^2} + \frac{\delta_k^2}{P_{,X,k}^2} + \frac{\delta_k^2}{V_k^2} + \frac{\delta_k^2}{M_p^2} + \frac{\delta_k^2}{M_v^2} \quad (8)$$

As collocation points X_k , the X -stations of the

finite difference mesh of the boundary layer integration were used. And on behalf of typical results, the values $M_p=0.1$ and $M_v=0.3$ were chosen.

Iterative Newton minimization of the quantity (8) was performed according to

$$\sum_{m,n} \{ \epsilon_{Pk,A_m} \epsilon_{Pk,A_n} + \epsilon_{V_k,A_m} \epsilon_{V_k,A_n} \} dA_n + \epsilon_{Pk,A_m} \epsilon_{Pk} + \epsilon_{V_k,A_m} \epsilon_{V_k} = 0 \quad (9)$$

if dA_n is the change in the coefficient A_n required to minimize quantity (8). The unknown coefficient K in (6) was here considered equivalent to an unknown A_{-3} .

Summarizing these results, the residuals ϵ_{Pk} and ϵ_{V_k} can be evaluated provided that a way is found to integrate the boundary layer equation subject to prescribing (7). Replacing the A_n -derivatives by simple one-sided differences, the minimization Eq. (9) can then be performed and the external flow (6) and corresponding boundary layer flow found.

Thus the one missing piece is to integrate the boundary layer flow. Briefly, the entire boundary layer flow region was mapped onto a unit square computational domain,

$$0 \leq \alpha \leq 1 \quad 0 \leq \beta \leq 1 \\ \alpha = \alpha(X) \quad \beta = \beta(X, y) \quad (10a)$$

Thus the boundary layer equations (5a,b,c) and (7) become

$$u \frac{\omega}{\alpha} + v \frac{\omega}{\beta^3} \frac{\partial \omega}{\partial \beta} = \frac{\omega}{\beta^3} \frac{\partial^2 \omega}{\partial \beta^2} + \frac{\omega}{\beta^3} \frac{\partial^2 \omega}{\partial \alpha \partial \beta} \quad (10b)$$

$$u = \int \frac{\omega}{\alpha} dy \quad v = - \iint \frac{\omega}{\alpha} d\alpha \quad (10c)$$

$$\frac{\omega}{\alpha} = \frac{\omega}{\alpha^3} \frac{\partial \omega}{\partial \alpha} + \frac{\omega}{\alpha^3} \frac{\partial \omega}{\partial \beta} \quad (10d)$$

$$[1 - \tanh X/2L] \left\{ \frac{\omega}{\alpha^3} \frac{\partial \omega}{\partial \beta} \right\}_{y=0} =$$

$$[1 + \tanh X/2L] \int_0^\infty \frac{\omega}{\alpha} dy = \text{prescribed} \quad (10e)$$

In the vorticity diffusion equation (10b), (10d) standard central differences are used in β -direction. For ω/α backward differences were used with respect to the direction of flow in order to reflect the correct domain of dependence. These one-sided α -derivatives are only first order accurate, but the calculation was repeated at doubled resolution in α -direction and a Richardson extrapolation toward second order accuracy made.

Up to flow reversal, the backward α -derivative allows a single sweep marching downstream. At each computational station α -constant, Newton's method was used to solve the finite difference equations. It works out that this requires the solution of a linear system of equations for the mesh values of the vorticity at that station, but this system proves nearly lower diagonal and may be solved fairly efficiently. Instead, old values

for the velocity components could be used in (10b) and the tridiagonal algorithm would result, but Newton's method converges much better.

Beyond flow reversal, the forward α -derivative in the reversed flow region requires more than a single march downstream. Here the present procedure marches alternatively downstream and upstream, performing at each α -station a single Newton iteration for the values of the vorticity at that station.

In the very first march downstream, initial estimates for the vorticity are obtained. But here the forward α -derivative in the region of reversed flow cannot be evaluated, since as yet no guesses are available for the vorticity at the next station. So, only in this first march, all convection of vorticity in the reversed flow region is neglected. Since the vorticity equation now reduces to

$$\frac{\omega}{\alpha} \frac{\partial \omega}{\partial \beta} = 0 \quad (11)$$

another way to look at it is that the vorticity profile is linearly extrapolated toward the wall. As an alternative for when a previous solution was available, we used

$$\frac{\omega}{\alpha} \frac{\partial \omega}{\partial \beta} = \left\{ \frac{\omega}{\alpha} \frac{\partial \omega}{\partial \beta} \right\}_{\text{old}}$$

The real analogue of the Reyhner & Flügge-Lotz approximation would be to neglect only the α -transport of vorticity, but numerically that proves unstable.

This completes the description of the numerical method except for the mapping of the boundary layer to the computational α, β unit square. But discussion of this mapping can only be meaningful when the known asymptotic properties of the solution are taken into account.

Solution Far Upstream

Far upstream, the boundary layer flow in the interaction region is approximately a uniform shear flow^{4,10}, with unit vorticity, Eq. (5d). Under those conditions, balance of diffusion and convection effects is consistent with a vertical coordinate

$$y = y/|x|^{1/3} \quad (12)$$

The wall boundary condition Eq. (5c) is seen to be consistent with a perturbation expansion

$$\frac{\omega}{\alpha} = 1 + K |x|^{-1/6} \omega_1(y) + K^2 |x|^{-2/6} \omega_2(y) + K^3 |x|^{-3/6} \omega_3(y) + \dots \quad (13)$$

These expansions do qualitatively resemble the classical Goldstein singularity²; but here the acceptable homogeneous solutions ω_n do always blow up exponentially. As a consequence, here the wall shear can be fully determined from the acting boundary layer pressure gradient.

Substitution of the expansion in the boundary layer equations (5a,b,c) yields

$$\begin{aligned}
\omega_1'' &= \frac{2}{6} Y^2 \omega_1' + \frac{1}{3} Y \omega_1 \\
\omega_2'' &= \frac{2}{6} Y^2 \omega_2' + \frac{2}{6} Y \omega_2 + \\
&\quad \frac{3}{6} f_1 \omega_1' + \frac{1}{6} u_1 \omega_1 \\
\omega_3'' &= \frac{2}{6} Y^2 \omega_3' + \frac{3}{6} Y \omega_3 + \\
&\quad \frac{3}{6} f_1 \omega_2' + \frac{2}{6} f_2 \omega_1' + \\
&\quad \frac{2}{6} u_1 \omega_2 + \frac{1}{6} u_2 \omega_1
\end{aligned} \quad (14a)$$

where $\omega \equiv u_n'$ and $u_n \equiv f_n'$. The wall boundary conditions are

$$\begin{aligned}
\omega_1'(0) &= \frac{1}{2} \\
\omega_2'(0) &= \omega_3'(0) = 0
\end{aligned} \quad (14b)$$

The boundary layer displacement effect (5h) is seen to become

$$v = -\frac{1}{6} |x|^{-2/3} \{K|x|^{-1/6} I_1 + K^2|x|^{-2/6} I_2 + K^3|x|^{-3/6} I_3 + \dots\}$$

$$I_n \equiv \int_0^\infty \{2 Y \omega_n' + n \omega_n\} dY \quad (14c)$$

Characteristic of the integrand of these "displacement integrals" I_n is that the two terms separately cannot be integrated, Eq. (16); it is their sum that vanishes sufficiently rapidly at large Y for the integral to converge. This integrand may be recognized in the differential equations (14a) for the ω_n ; it is there proportional to the convective derivative. Thus the rapid vanishing of the integrand in the displacement integrals becomes equivalent to a statement that the viscous effects ω_n' are negligible far from the wall.

Numerically, as long as the viscous forces are not callously over-estimated at large y , the finite difference discretization of the convective terms will display the correct rapid decay. Therefore, using exactly this same discretization, the displacement integrals can meaningfully be evaluated. But for a different discretization, the small numerical error integrated over infinite Y would make the results meaningless. The rule is to keep the discretizations of convective derivative and displacement integrals exactly the same.

This rule generalizes toward the full problem Eqs. (10) that the discretizations of ω_y in the integrals for displacement velocity V and vertical boundary layer velocity component v should be kept identical to the discretization in the convective derivative in (10b). But since the rule is only important at large y , for simplicity in the integrals no reversal of the α -derivative was made in the region of reversed flow.

The differential equation (14a) for the first vorticity perturbation ω_1 may be solved analytically¹⁰. For, when the solution is expanded around the wall, the Taylor series coefficients of the confluent hypergeometric functions may be recognized¹¹. The solution which does not blow up exponentially is

$$\omega_1 = -\left[\Gamma\left(\frac{1}{6}\right)/24^{1/3}\Gamma\left(\frac{2}{3}\right)\right] \underline{u} \left(\frac{1}{6}; \frac{2}{3}; \frac{Y^3}{9}\right) \quad (15a)$$

Its value at the wall is seen to be

$$\omega_1(0) = -\left[\Gamma\left(\frac{1}{3}\right)/6^{1/6}\Gamma\left(\frac{2}{3}\right)\right]^2 \quad (15b)$$

Particularly interesting is the behaviours of the solutions ω_n for large Y . The self-consistent asymptotic form of the f_n is easily found as

$$\begin{aligned}
f_1 &= \frac{4}{3} C_1 Y^{3/2} + \frac{A_1}{3} Y + \frac{B_1}{3} + O(Y^{-3/2}) \\
f_2 &= \frac{C_2}{3} Y \ln Y + \frac{(A_2 - C_2)Y}{3} + 2 \frac{A_1}{3} \frac{C_1}{3} Y^{1/2} + \frac{B_2}{3} \\
&\quad + \frac{2}{3} \frac{B_1 C_1}{3} Y^{-1/2} + O(Y^{-2}) \\
f_3 &= \frac{A_3}{3} Y + 2 \frac{C_1 C_2}{3} Y^{1/2} \ln Y - 4 \frac{C_3}{3} Y^{1/2} \\
&\quad + \frac{A_1 C_2}{3} \ln Y + \frac{B_3}{3} + \\
&\quad \left(\frac{5}{6} A_1^2 - \frac{2}{3} B_2\right) \frac{C_1}{3} Y^{-1/2} + \left(\frac{2}{3} C_1^2 - \frac{1}{2} C_2\right) \frac{B_1}{3} Y^{-1} \\
&\quad + \frac{1}{3} \frac{A_1 B_1 C_1}{3} Y^{-3/2} + O(Y^{-5/2} \ln Y)
\end{aligned} \quad (16a)$$

The vorticity perturbations ω_n follow as the second derivative.

In this asymptotic representation, the constants C_n may be identified as the coefficients of the homogeneous solutions ω_n to the differential equations (14a) while the A_n and B_n are the additional integration constants which appear in the double integration to find the f_n . Numerical values for the constants B_n may be found from integrating the differential equations once in Y direction and collection of the $O(1)$ terms after substitution of the asymptotic behaviour Eqs. (16). This results in

$$B_1 = -1 \quad B_2 = \frac{1}{2} A_1^2 \quad B_3 = \frac{A_1}{3} A_2 \quad (16b)$$

And of course A_1 and C_1 may be found from the known exact solution Eq. (15), most easily from the integral representation of the hypergeometric function¹¹ \underline{u} . The result is

$$\begin{aligned}
C_1 &= \Gamma\left(\frac{1}{6}\right)/2\Gamma\left(\frac{2}{3}\right) \\
A_1 &= 6^{1/3}\Gamma\left(\frac{2}{3}\right)
\end{aligned} \quad (16c)$$

The values of the displacement integrals I_n may be related to the asymptotic expansion (16a) by

means of a partial integration of Eq. (14c):

$$I_1 = -\frac{A_1}{2} \quad I_2 = 2 \frac{C_2}{3} \quad I_3 = \frac{A_3}{2} \quad (16d)$$

Turning now to numerical solution of the differential equations (14a) for the ω_1 , as a first step the semi-infinite Y axis is mapped onto a unit computational interval $0 < \beta < 1$. Of particular interest is here of course the behaviour for large Y . Since from (16a)

$$\omega_1 \sim \frac{C_1}{Y} Y^{-1/2} + \dots$$

mappings that suggest themselves are of the general form

$$1 - \beta \sim Y^{-1/2} \quad Y \rightarrow \infty \quad (17)$$

Indeed, meaningful finite difference quotients are only possible if $\omega(\beta)$ is smooth enough, and Eq. (17) achieves this for large Y .

If first a smoothed power raising operation is defined as

$$Y^{Sp} \equiv (Y^2 + 1)^{p/2} \sim |Y|^p \quad (18)$$

then the chosen mapping was $\beta = 1(Y)$ with the function $1(.)$ defined as

$$1(Y) \equiv \frac{2}{\pi} \arctg(Y^{Sp/2} \tanh Y) \quad (19)$$

It may be verified that this mapping is of the required behaviour (17).

In agreement with the procedure for the full boundary layer equations (10), in the asymptotic differential equations (14a) all 3-derivatives were replaced by centered finite differences. The resulting finite difference equations for ω_1 , ω_2 and ω_3 were solved by the tridiagonal algorithm.

Table 1 compares results for ω_1 with the exact solution, for various number of mesh points. The mapping proves very effective: for only 33 mesh points excellent agreement exists. Similarly the second order and third order wall shear coefficients and displacement integrals show good agreement with results from literature.

This numerical procedure for the flow far upstream generalizes toward the full problem Eqs. (10). First the asymptotic behaviour of ω is determined for large Y . If the large Y expansion (16a) is generalized to finite X , there results

$$\omega \sim 1 + K \frac{C_1}{Y} \Delta Y^{-1/2} + K^2 \frac{C_2}{Y} \Delta Y^{-1} - \frac{1}{2} K^3 \frac{C_1}{Y} \frac{C_2}{Y} \Delta Y^{-3/2} \ln \Delta Y + K^3 \frac{C_3}{Y} \Delta Y^{-3/2}$$

$$+ O(\Delta Y^{-2} \ln^2 \Delta Y)$$

$$\Delta Y \equiv Y - Y_0(X)$$

$$Y_0 \sim K I_1 |X|^{1/6} + \frac{1}{6} K^2 I_2 \ln |X| + o(1) \quad X \rightarrow \infty \quad (20)$$

Again, in order to avoid significant singular behaviour in the vorticity far from the wall

$$1 - \beta \sim Y^{-1/2} \quad Y \rightarrow \infty \quad (21a)$$

and in order to conform with the successful asymptotic calculation far upstream,

$$\beta \sim 1 - |Y/X|^{1/3} \quad X \rightarrow \infty \quad (21b)$$

In order that the mapping $\alpha(X)$ does not introduce significant singular behaviour far upstream, the form of the expansions Eq. (13) for the vorticity requires

$$\alpha \sim |X|^{-1/6} \quad X \rightarrow \infty \quad (21c)$$

The asymptotic behaviour (20) of the vorticity far from the wall may also be used to find suitable representations for the integrals which relate the flow velocity to the vorticity. It may be verified by substitution that possible representations which allow an accurate evaluation by the trapezium rule are given by

$$u = \int \frac{\omega [1-\beta]^2 / \beta}{Y} d\beta \quad (22a)$$

$$v = \int \left\{ \left[\int \frac{\omega}{X} \frac{d\beta}{\beta} \right] \frac{[1-\beta]^2}{\beta} \right\} d\beta \quad (22b)$$

$$v = \int_0^1 \frac{\omega}{X} \frac{d\beta}{\beta} \quad (22c)$$

The reason for the tilde above the vorticity in the integral for u shall be given in the next section.

Solution Far Downstream

Downstream³, the displacement effect of the boundary layer flow grows rapidly: it is seen that the displacement velocity integrates to a displacement thickness

$$Y_0 \sim \frac{2}{3} K X^{3/2} \quad (23)$$

But like far upstream, diffusion can only balance convection in a much thinner layer of typical dimension

$$\Delta Y \sim O(X^{1/3})$$

As a result, diffusion remains restricted to a comparatively thin mixing layer centered around Y_0 , which separates unit vorticity in the main boundary layer above from negligible vorticity in the starting wake below. The general description of this mixing layer is

$$\frac{\omega}{\Delta Y} \sim g'' \left(\frac{\Delta Y}{X} \right)^{1/3} \quad (24a)$$

$$\Delta Y = Y - Y_0(X)$$

The Falkner Skan equation for the similar profile becomes

$$g'''' + \frac{2}{3} g g'' - \frac{1}{3} g'^2 = 0 \quad (24b)$$

The entrainment of this mixing layer is described as the value of the streamfunction at the lower edge. Runge-Kutta integration of the similar profile (24b) gives

$$\underline{y} = C X^{2/3} \Delta y / X^{1/3} + \infty \quad (24c)$$

with $C = 1.258146$ (cf. 1.2521 according to Smith⁶).

To provide this entrained fluid, an influx exists in the starting wake below the mixing layer:

$$\underline{u} = -\frac{3}{2} C K^{-1} X^{-5/6} \quad 0 < \underline{y} < \underline{y}_0 \quad (25)$$

From the Bernoulli law, this implies a pressure distribution

$$P = -\frac{9}{8} C^2 K^{-2} X^{-10/6} \quad (26)$$

And of course this influx generates a reversed wake flow boundary layer near the wall. Its general form is

$$\underline{w} = X^{-7/4} h''(\underline{y}/X^{11/12}) \quad (27a)$$

Runge-Kutta solution of the Falkner-Skan equation

$$24 h''' = 45 C^2 K^{-2} - 2 h h'' - 20 h'^2 \quad (27b)$$

gives for the final value of the wall shear

$$\underline{\tau} = 2.71529 K^{-3/2} X^{-7/4} \quad (28)$$

From this asymptotic character of the flow far downstream, more guidelines follow for the numerical mapping of the boundary layer. For, it must be clear that adequate resolution should be maintained in the relatively thin mixing layer around \underline{y}_0 ; it is in this layer that the important diffusion effects take place. And though the wake flow boundary layer (27) is of secondary importance, meaningful values for the wall shear can only be obtained when enough mesh points are available to describe the vorticity profile.

Pending a better understanding, the present results distribute half of the meshpoints far downstream in the mixing layer and half in the wall layer:

$$\beta = 3[\underline{y}/X^{11/12}] \quad X \rightarrow \infty, \beta < \frac{1}{2}$$

$$\beta = 3[\Delta y/X^{1/3}] \quad X \rightarrow \infty, \beta > \frac{1}{2} \quad (29)$$

A mapping which meets these requirements, and the previous ones (21) was chosen as

$$\alpha = \pi^{-1} \arctg[(X/L)^{51/6} \tanh(X/2L)] + \frac{1}{2}$$

$$\beta = \frac{1}{2} \pi^{-1} \{1 + \tanh(X/2L)\} \arctg(\underline{y}/\delta_w)$$

$$+ \phi(X) \{1 - (\underline{y} - \underline{y}_0^*)/\delta_m\} - 1 - \underline{y}_0^*/\delta_m$$

$$\underline{y}_0^* \equiv \text{Real}\left\{\frac{2}{3} K (Z - Z_0)^{3/2} + K Z_0 (Z - Z_0)^{1/2}\right\}$$

$$\delta = (X/L)^{51/12}$$

$$w$$

$$\delta_m = \left\{\frac{3}{2} + \frac{1}{2} \tanh(X/2L)\right\} (X/L)^{51/3} \quad (30)$$

where the smoothed power raising operation and the function $l[\cdot]$ were defined before, Eqs. (18) and (19), the characteristic length L was again chosen to be 10 and the expression for the function $\phi(X)$ may be found from imposing the requirement $\beta = 1$ at infinite \underline{y} .

In the mixing layer, the characteristic length Δy is much smaller than the penetration \underline{y}_0 away from the wall. Yet this penetration does not dominate the mechanics of the flow on account of Prandtl's transposition theorem. But due to numerical inaccuracy, there is a real chance that relatively small errors arising from this large penetration would seriously disturb the numerical results. Thus a numerical discretization is desired which retains a discrete form of Prandtl's theorem, in which scheme the finite difference equations are exactly independent of the penetration \underline{y}_0^* of the mesh points in the mixing layer. It may be verified by substitution that such independence of \underline{y}_0^* is achieved if in the integral (22a) for the boundary layer velocity component \underline{u} a smoothed representation for the vorticity $\underline{\tau}$ is used:

$$\underline{\tau} = \frac{1}{4} (\underline{\tau}_{j-1} + 2 \underline{\tau}_j + \underline{\tau}_{j+1}) \quad (31)$$

if j is the mesh point index in β -direction.

Results

The Kirchhoff free-vortex sheet description of separated flows was long believed to be physically relevant¹. But it would imply a singularity in the boundary layer pressure distribution at separation which would seem to prohibit the existence of a boundary layer solution.

Only comparatively recently did Sychev³ manage to find a plausible mechanics for the boundary layer flow near separation. In a small "interaction region" around the separation point, boundary layer thickness effects would be sufficient to smooth out the Kirchhoff singularity in the outer flow.

But no analytical proof could be given that indeed a boundary layer flow and outer flow could exist in this interaction region. The non-linearity of the governing flow equations made it appear that a numerical investigation was needed. After artificially restricting the region of boundary layer flow to a finite one and neglecting the backward momentum transport in the region of reversed flow, Smith⁶ could find a definite interaction flow. Plausibly his modifications of the original problem would be of little importance for the existence and character of the solution. And if more than one flow solution could exist, at least his scheme converged to only one.

Here, the existence of an interaction flow is verified with a numerical scheme that conforms more closely to the physical flow. In the method,

the boundary layer equation becomes once more the simple, reliable tool it once was. Motivation was also, to develop a numerical procedure that could handle unsteady flows. There, the wall will in general be in relative motion compared to the position of the separation point. And in particular if the wall moves upstream, the region of reversed flow must be much more important; thus the forward momentum transport should no longer be neglected as it is in Smith's scheme.

To take account of this forward momentum transport in the boundary layer calculation, here a forward convective finite difference is used in the region of reversed flow.

By mapping the boundary layer flow onto a finite computational domain, the computation could be extended infinitely far upstream and away from the wall.

But attempts to continue the boundary layer calculation all the way downstream to infinity were so far unsuccessful. When resolution becomes low, formation of numerical wiggles and lack of convergence resulted. A possible explanation of the breakdown could be a mutual interaction between the various layers in which the lower boundary layer deck divides at the downstream end of the interaction region. If numerical inaccuracy would allow some of the vorticity in the downstream mixing layer to seep through to the starting wake and wake boundary layer, this small vorticity could, integrated over a relatively large boundary layer thickness, seriously disturb the numerical estimates for the flow velocity.

To eliminate the breakdown, here an artificial cut-off was introduced at a downstream location $X = 40$. In any case, this compares favourably with the location at $X = 20$ used by Smith⁶. The present finite difference procedure needs a boundary condition at the reversed flow part of the cut-off in order to replace the missing information about the vorticity further downstream. The choice for this boundary condition was that the vorticity at the next mesh station downstream of the cut-off would exactly conform with the asymptotic behaviour (27a) valid far downstream in the starting wake boundary layer;

$$\frac{\omega}{c+\Delta\alpha} \equiv \frac{\omega}{c} \left[\frac{X_{c+\Delta\alpha}}{X_c} \right]^{-7/4} \quad (32)$$

if "c" denotes the cut-off.

A comparison calculation with the cut-off located at $X = 25$ did not show a significant influence of the cut-off on the boundary layer flow. From a physical point of view, the same separation process should occur independent of small disturbances downstream. The small deviations in wall shear in the reversed flow region are listed in Table 2.

Some example calculations, listed as I, II and III in Table 3 give an impression of the effect of changing the important parameters in the numerical procedure. The results of calculation I are shown graphically in Fig. 1. To avoid losing the upstream part of the curves, they have been plotted against the computational coordinate α rather than the physical coordinate X .

The boundary layer pressure gradient is shown in Fig. 1b. The external and boundary layer flows predict within line thickness the same curves, verifying the effectiveness of the least square minimization. In the present numerical procedure the pressure gradient is always correct far upstream. For the external flow representation Eq. (6) was deliberately chosen to have the

correct square root behaviour in the wall pressure far upstream. And it is this same wall pressure which is prescribed in the boundary layer solution far upstream, Eq. (7). Far downstream, the asymptotic pressure gradient Eq. (26) is shown as the curve labelled t in Fig. 1b.

The boundary layer displacement velocity is shown in Fig. 1c. This velocity represents the X -derivative of the displacement thickness; it is here better defined than the thickness itself. The reason is basically that in the lower deck boundary layer flow the velocity does not remain bounded far from the wall, but only the vorticity, compare Eqs. (5). In a similar way as for the pressure gradient far upstream, the numerical scheme is always correct for the displacement velocity far downstream, Eqs. (6) and (7). Far upstream, the velocity was normalized as

$$v^* = 5 \left| X \right|^{5/6} v \quad (33)$$

In Fig. 1c it is compared with the asymptotic solution Eqs. (14), curves shown as 1, 2 and 3 for increasing order of approximation.

Up to the station indicated by a circle symbol in Fig. 1c, Smith⁶ prescribes his displacement thickness from the two term expansion, curve 2. It is seen that this implies a significant error in the derivative V of the displacement thickness. The test for numerical accuracy reported by Smith varies the displacement thickness by a constant, hence would not alter the derivative. Smith's error in displacement thickness may provide a possible explanation for the differences in wall shear shown in Fig. 1d. Again Smith's results are indicated by the circle symbols.

The Reyhner & Flügge-Lotz "approximation" in Smith's calculation neglects the backward transport of momentum in the reversed flow region. The present results for the wall shear in this region do verify that indeed the resulting error is numerically small, Fig. 1d.

Returning to Table 3, the calculation II estimates the effect of the precise representation Eq. (6) of the external flow on the results. As in calculation I, the three coefficients A_5 , A_6 and A_7 were determined from the known asymptotic behaviour Eqs. (14) far upstream. The value for the constant Z_0 was chosen on a basis of a crude preliminary optimization which is of no further consequence. But while calculation I uses the values of the constants K , A_8 and A_9 to minimize the differences between the external and boundary layer flows in least square sense, instead calculation II uses only K and A_9 .

The difference in outer flow representation does lead to significant deviations in boundary layer pressure gradient, wall shear and displacement velocity. The differences are listed as E(.)

in Table 3 and shown in detail in Fig. 2. But the main effect appears to be an uniform shift of the solution in X-direction. Since the problem Eqs. (5) does indeed not fix an origin to X, the shift is of little importance. Thus both computations do agree excellently on the important variables: the constant K, the maximum boundary layer pressure gradient and the minimum wall shear, compare Table 3. And for each computation individually, the external and boundary layer flows do show excellent agreement; these differences are listed as δ_{\max} in Table 3. Various ways in which the shift may be eliminated suggest themselves, but have not yet been incorporated.

Calculation III examines the influence of halving the resolution in the boundary layer and reducing the location of the downstream cut-off from $X = 40$ to 25. Again no important change in the results occurs.

It is recalled from the introduction that the coefficient K describes the downstream shift of the separation point with decreasing Reynolds number, Eq. (4). All three computations I, II and III yield a value of about 0.41 for this important constant, Table 3. The value given by Smith⁶ was instead "approximately 0.44", but he notes that the second decimal place could easily be altered. Clearly, the present value results from limited data of a still imperfectly understood numerical procedure. On the other hand, the two term asymptotic expansion far upstream, Fig. 1c, does not seem a very good approximation for Smith's development range.

A typical calculation took about 3 minutes on the IBM 370.

Acknowledgement

This research was supported by the Office of Naval Research under contract number N00014-77-C-0033.

1. Thwaites, B., Ed., Incompressible Aerodynamics, Oxford Univ. Press, Oxford, England, 1960, pp. 149-168.

Table 1. Effect of mapping the distance away from the wall onto a finite computational interval examined for the asymptotic expansion Eqs. (14) through (16) valid far upstream. The asymptotic wall shear coefficients $\omega_2(0)$ and $\omega_3(0)$ are compared to those of N. Riley¹⁰; the displacement integrals I_2 and I_3 with results of Melnik and Chow¹⁰; the other values in the last column are exact.

mesh points:	17	33	65	129	257	exact/ reference
$\omega_1(0)$	-2.1678	-2.1571	-2.1547	-2.1541	-2.1540	-2.1539
$I_1 = A_1$	-2.4731	-2.4636	-2.4613	-2.4608	-2.4606	-2.4600
B_1	-1.0499	-1.0123	-1.0029	-1.0007	-1.0002	-1.0000
C_1	-2.0677	-2.0593	-2.0566	-2.0557	-2.0555	-2.0553
$\omega_2(0)$	-0.9143	-0.8987	-0.8951	-0.8943	-0.8941	-0.8940
$\frac{1}{2}I_2 = C_2$	-3.13	-3.20	-3.24	-3.26	-3.26	-3.255
$\omega_3(0)$	-1.2733	-1.2367	-1.2284	-1.2263	-1.2258	-1.2256
$I_3 = A_3$	-17.911	-17.613	-17.551	-17.537	-17.534	-17.408

2. Goldstein, S., "On laminar boundary layer flow near a position of separation", Quart. J. Mech. Appl. Math., Vol. 1, 1948, pp. 43-69.
3. Sychev, V.V., "Laminar separation", Izv. Akad. Nauk SSSR, Mekh. Zhidk. Gaza, Vol. 3, 1972, pp. 47-59.
4. Brown, S.N., and Stewartson, K., "Trailing-edge stall", J. Fluid Mech., Vol. 42, 1970, pp. 561-584.
5. Messiter, A.F., and Enslow, R.L., "A model for laminar boundary layer flow near a separation point", SIAM J. Appl. Math., Vol. 25, 1973, pp. 655-670.
6. Smith, F.T., "The laminar separation of an incompressible fluid streaming past a smooth surface", Proc. Roy. Soc. London A, Vol. 356, 1977, pp. 443-463.
7. Reyhner, T.A., and Flügge-Lotz, I., "The interaction of a shock wave with a laminar boundary layer", Int. J. Nonlinear Mech., Vol. 3, p. 173.
8. Van Dommelen, L.L., and Shen, S.F., "A bifurcation-free interaction solution for steady separation from a downstream moving wall", AIAA paper 82-0347, AIAA Aerosp. Sci. Meet., Orlando, Florida, Jan. 11-14, 1982. To appear in AIAA J.
9. Veldman, A.E.P., "New, quasi-simultaneous method to calculate interacting boundary layers", AIAA J., Vol. 19, 1981, pp. 79-85.
10. Melnik, R.E., and Chow, R., "Asymptotic theory of two dimensional trailing edge flows", Grumman Res. Dept. Report RE-510J.
11. Abramowitz, M., and Stegun, I.A., Handbook of Mathematical Functions, Dover, 1970, pp. 255, 256, 504-509.

Table 2: The effect of the cut-off at the downstream end of the boundary layer calculation. the wall shear is shown for cut-off locations at $X=25.0$ and 39.8 .

X	τ	τ
1.97	-0.0269	id.
3.98	-0.0593	id.
6.09	-0.0753	id.
8.38	-0.0756	id.
11.0	-0.0703	id.
14.2	-0.0562	id.
18.4	-0.0406	id.
25.0	-0.0293	-0.0260
39.8		-0.0127

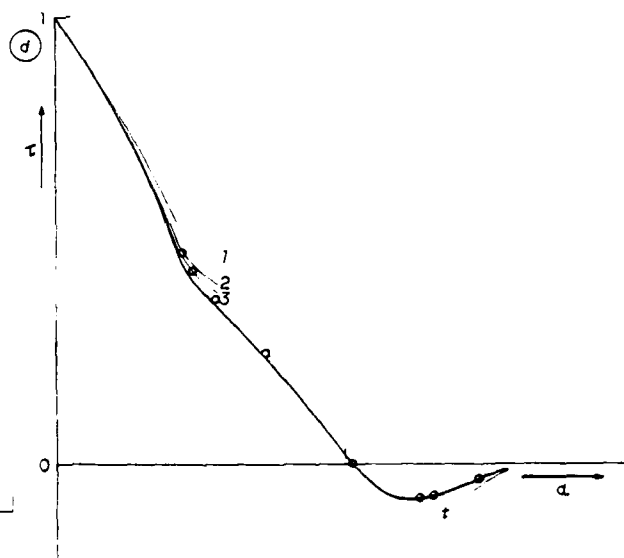
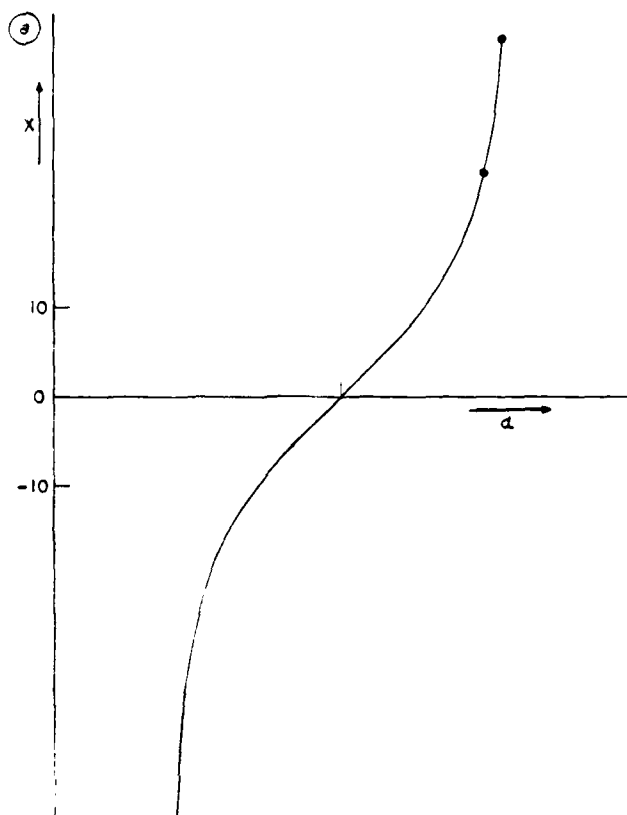
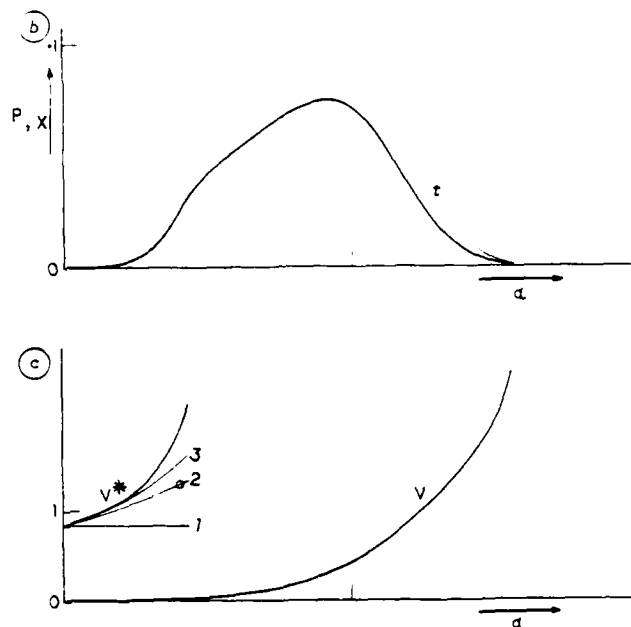


Fig. 1: The boundary layer pressure gradient b , displacement velocity c and wall shear d according to the numerical solution 1 of Table 3. In order to avoid losing the upstream part of the solution, it has been plotted against the computational coordinate a , as defined by Eq. (30); the correspondence with the physical coordinate X is depicted graphically in a . The circle symbols in c and d relate to Smith's calculation⁵. The curves labelled 1, 2 and 3 represent successive approximation levels in the expansion Eqs. (14) through (16) valid far upstream. The curves labelled τ represent the expansions Eqs. (26) and (28) valid far downstream.

Table 3: Three example calculations I, II and III. Tabulated are: the number of mesh points in the finite difference boundary layer calculation and the X-location of the downstream cut-off in this calculation; the constants in the numerical representation Eq. (6) of the external flow; the maximum deviations δ_{\max} in boundary layer pressure gradient and boundary layer displacement velocity between the numerical solutions for the external and boundary layer flows; the maximum deviations $E(\cdot)$ in pressure gradient, displacement velocity and wall shear respectively from the solution I (for case II, the detailed deviations are shown in Fig. 2); the maximum boundary layer pressure gradient and the minimum wall shear.

calculations	I	II	III
mesh	65x33	65x33	33x17
X_{\max}	39.8	39.8	25.0
K	0.40888	0.41089	0.40942
Z_0		-11.24737	
A_5		-0.47354 K	
A_6		-1.09 K ²	
A_7		-3.3737 K ²	
A_8	3.9961- 2.8554i	0.4099- 0.5682i	3.5297- 3.0496i
A_9	-5.6260+ 0.0523i	0	-5.2698+ 1.1634i
$\delta_{\max} P_{,X}$	0.00085	0.0014	0.0010
$\delta_{\max} V$	0.00099	0.00094	0.0011
$E(P_{,X})$	0	0.0055	0.0021
$E(V)$	0	0.058	0.018
$E(\tau)$	0	0.021	0.018
$\max\{P_{,X}\}$	0.075	0.075	0.074
$\min\{\tau\}$	-0.079	-0.078	-0.080

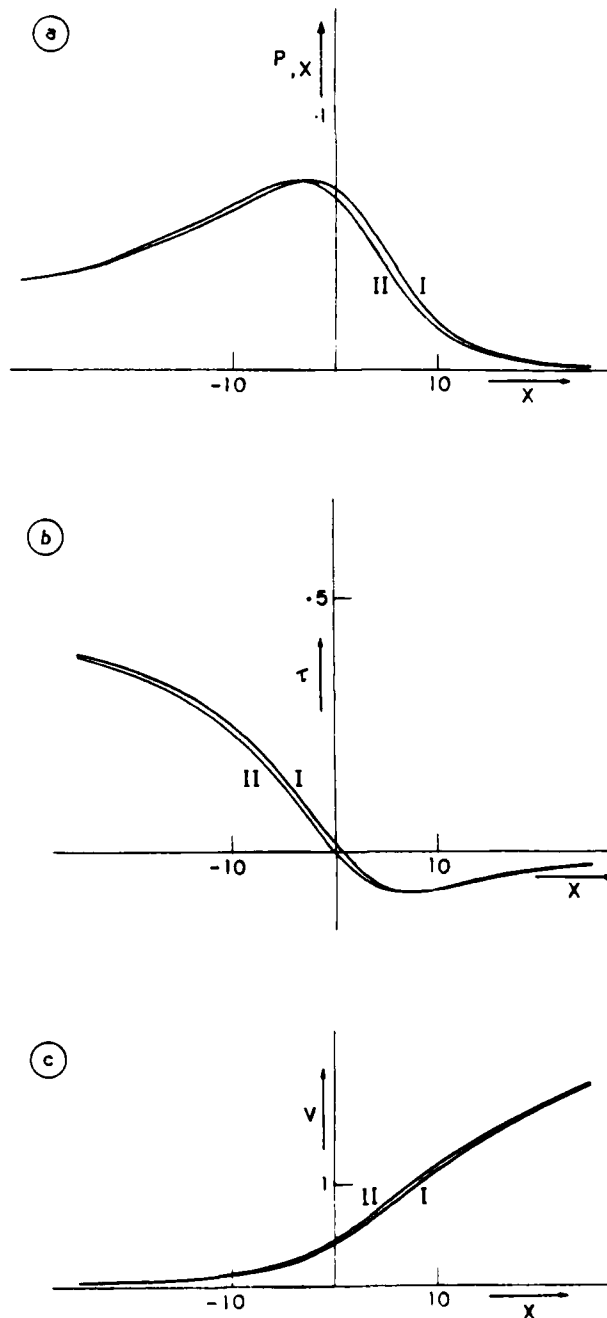


Fig. 2: The relatively large differences $E(\cdot)$ between the solutions labelled I and II in Table 3 arise mainly from an uniform shift in X-direction. The original problem Eqs. (5) is invariant under such a shift.

SESSION 3

THE INTERACTION BETWEEN A STEADY LAMINAR
BOUNDARY LAYER AND AN OSCILLATING FLAP:
THE CONDENSED PROBLEM

P.W. Duck

Department of Mathematics
University of Manchester, England

Abstract

Numerical results are presented for the viscous interaction between a flap performing small amplitude time oscillations, and an otherwise steady, laminar, boundary layer. The method used involves Fourier decomposing the solution in time, a technique which appears to have a number of advantages over more conventional time marching schemes.

I. Introduction

The manner in which a planar boundary layer on a flat plate adjusts to a trailing edge, and the subsequent change in inner boundary conditions from one of no-slip, to one of zero shear, was first considered in the now classical paper of Goldstein¹. It was found that the boundary layer adopted a double structure, close to the trailing edge, with the vertical velocity component developing a singularity of $O(x^{*-2/3})$ downstream of the trailing edge (where x^* is the distance measured from the trailing edge). Stewartson² and Messiter³ found that the order of this singularity could be reduced by studying the immediate neighbourhood of the trailing edge, using the now well-known "triple deck theory". The outcome of this work was a non-linear boundary layer problem (with novel outer boundary conditions), which was subsequently solved by Jobe and Burggraf⁴ for

subsonic flows, and by Daniels⁵ for supersonic flows, using finite difference techniques.

A number of related problems have also been studied using triple deck theory, for instance: flat plates at incidence to the freestream flow⁶, the numerical problem of which was studied by Chow and Melnik⁷ for subsonic flows, and by Daniels⁸ for supersonic flows; oscillating flat plates in subsonic flows^{9,10}; wedged type trailing edges¹¹; the edge effects of a torsionally oscillating finite disk¹². Recently, Smith¹³ has considered the question of catastrophic stall involved with flapped trailing edges (and also asymmetric wedged type trailing edges). Triple deck theory has been utilised in a wide variety of other problems, a comprehensive summary of which is given by Smith¹⁴

The effect of unsteadiness has been incorporated into a number of multi-layer problems involving distorted boundaries^{15,16,17}, but except for the work of Brown and Daniels³ (in which, incidentally, the resulting numerical problem was solved only approximately) and that of Brown and Cheng¹⁰ (which was primarily concerned with a quasi-steady solution), little progress appears to have been made on the effect of unsteadiness on trailing edge classes of flows at high Reynolds number.

In this paper, we shall consider the effect of a small, unsteady trailing edge flap, on an

otherwise steady laminar boundary layer.

II. Mathematical formulation of the problem

We take L to be the chord length of the plate, ρ and ν the density and kinematic viscosity, respectively, of the fluid which has a steady velocity U_∞ far from the plate. Then the dimensional coordinates (origin at the trailing edge) are taken to be Lx and Ly in the streamwise and vertical directions respectively. $U_\infty u$ and $U_\infty v$ are the velocity components in the x and y directions, and the pressure is written as $\rho U_\infty^2 p$.

We introduce a Reynolds number

$$Re = U_\infty L / \nu, \quad (1)$$

which is assumed to be large. Following previous studies involving triple decks, we find it convenient to introduce a small parameter ϵ as follows :

$$\epsilon = Re^{-1/8}. \quad (2)$$

Following Smith¹³, we assume that there is a small flap on the trailing edge, whose streamwise dimension is $O(\epsilon^3 L)$, and with a dimension in the y direction of $O(\epsilon^5 L)$. Supposing this flap to be oscillating with frequency ω , we may then introduce a further dimensionless parameter β_0 by

$$\beta_0^2 = U_\infty / \omega L \quad (3)$$

(a parameter related to the Strouhal number). We shall choose the magnitude of β_0 to be such that

$$\beta_0 = \epsilon \hat{\beta}, \quad \hat{\beta} = O(1). \quad (4)$$

The reason for this particular choice of β_0 will be explained later.

Fig. 1 shows a schematic layout of the structure to the problem. The solution in the upper deck (wherein $y = O(\epsilon^3)$) and the lower deck (wherein $y = O(\epsilon^4)$) follows previous triple deck work, for example Stewartson², and will not be repeated. In the lower deck, we expect the following scalings:

$$(u, v, w, p, x, y) = (\epsilon \lambda_B^{1/4} \hat{u}, \epsilon^3 \lambda_B^{3/4} \hat{v}, \epsilon^2 \lambda_B^{1/2} \hat{p}, \epsilon^3 \lambda_B^{-5/4} \hat{x}, \epsilon^3 \lambda_B^{-3/4} \hat{y}), \quad (5)$$

where λ_B is a measure of the wall shear of the on-coming boundary layer. Note $\lambda_B = 0.3321$ in the case of a Blasius boundary layer. The boundary layer pressure \hat{p} is independent of \hat{y} .

Continuity allows us to introduce a stream-function $\hat{\psi}$ such that

$$\hat{u} = \hat{\psi}_Y, \quad \hat{v} = -\hat{\psi}_X, \quad (6)$$

and the non-linear equation we have to solve is

$$\frac{1}{\beta^2} \hat{\psi}_{Yt} + \hat{\psi}_Y \hat{\psi}_{YX} - \hat{\psi}_X \hat{\psi}_{YY} = \hat{\psi}_{YY} - \hat{p}_X. \quad (7)$$

If we assume that the plate lies along

$$\hat{Y} = \hat{F}(\hat{X}, t), \quad \hat{X} < 0, \quad (8)$$

then we must solve (7) subject to the following boundary conditions

On $\hat{Y} = \hat{F}(\hat{X}, t)$, $\hat{X} < 0$:

$$\hat{\psi} = - \int_{-\infty}^{\hat{X}} \frac{\hat{F}_t(\hat{X}, t)}{\hat{\beta}^2} d\hat{X}, \quad (9)$$

$$\hat{\psi}_Y = 0. \quad (10)$$

As $\hat{Y} \rightarrow \pm \infty$ (for all \hat{X}) :

$$\hat{\psi}_Y \rightarrow \pm \hat{Y} + \hat{A}_\pm(\hat{X}, t). \quad (11)$$

For $\hat{X} > 0$:

$$\begin{aligned} \hat{p}_+(\hat{X}, t) &= \hat{p}_-(\hat{X}, t) \\ \hat{u} &\text{ regular for all } \hat{Y} \end{aligned} \quad (12)$$

where subscripts $+$ and $-$ refer to conditions above and below the plate respectively.

We see that our choice of β_0 leads to a problem in which unsteadiness is important in the lower deck, and hence we may expect the maximum interaction between unsteadiness, inertia terms, and viscous terms. Notice that our choice of order of dimensions of the flap has also been taken in order to coincide with those of the lower deck.

The upper deck then yields a relationship between \hat{P} and \hat{A} . In the particular case of a supersonic freestream flow

$$\hat{P}_{\pm}(\hat{X}, t) = -\hat{A}_{\pm\hat{X}}(\hat{X}, t), \quad (13)$$

whilst for an incompressible flow we obtain

$$\hat{P}_{\pm}(\hat{X}, t) = -\frac{1}{\pi} \int_{-\infty}^{\infty} \frac{\hat{A}_{\pm\xi}(\xi, t)}{\hat{X} - \xi} d\xi \quad (14)$$

However, we shall now assume that the flap has streamwise scale $O(\ell)$, and vertical scale $O(\ell^{1/3})$ relative to the lower deck scales, where $\ell < 1$. We then expect the solution in most of the flowfield to be effectively that of the symmetric flat plate, the numerical solutions of which are given by Jobe and Burggraf⁴ in case of the subsonic flows, and by Daniels⁵ for supersonic flows.

To be rather more precise, suppose these aforementioned studies yield the following:

$$\begin{aligned} \hat{P}_{\pm\hat{Y}\hat{Y}}(\hat{Y} = 0, \hat{X} \rightarrow 0-) &= \tau_0 > 0, \\ \hat{P}_{\pm}(\hat{X} \rightarrow 0\pm) &= P_0 < 0, \\ \hat{P}_{\pm}(0-) &\text{finite, } \hat{P}_{\pm}(\hat{X}) \sim \hat{X}^{-1/3} \text{ as } \hat{X} \rightarrow 0. \end{aligned} \quad (15)$$

Close to the trailing edge, on a scale comparable to the flap, we expect a departure from the results (15). Specifically, we introduce variables as follows

$$\begin{aligned} X &= \hat{X}/\ell, \quad \bar{Y} = \tau_0^{1/3} \ell^{-1/3} \hat{Y}, \\ \bar{\Psi} &= \ell^{-2/3} \tau_0^{-1/3} \hat{\Psi}, \quad P = (\hat{P} - P_0) \ell^{-2/3} \tau_0^{-4/3}, \\ \beta &= \ell^{-1/3} \hat{\beta}. \end{aligned} \quad (16)$$

We shall also assume that the flap shape is defined by

$$\bar{Y} = F(X, t), \quad X < 0. \quad (17)$$

In the upper deck, there is no longer a balance of terms in the momentum equations, which implies that the simple relationship

$$A_{\pm}(X, t) \equiv 0 \quad (18)$$

applies, in place of either (13) or (14), whilst the rescaled problem still satisfies (7)-(12) with the obvious change in notation. As well as being considerably easier to treat numerically, the "condensed problem", as noted by Smith¹³ (who carried out a similar procedure to that described above), is still likely to be a good model of the flow characteristics in the neighbourhood of the trailing edge, even for other, more complicated, pressure/displacement relationships.

The great simplification resulting from (18), is the lack of upstream influence (in the case of non-reversing flows). Notice that, just as in the analogous steady problem¹³, the pressure may not be determined absolutely, but only down to an arbitrary $P_{\pm}(-\infty, t)$. Further, as $X \rightarrow \infty$, $P(X, t) \sim P(X) \sim X^{2/3}$, with the solution taking on the similarity solution of Hakkinen and Rott¹⁸.

We write

$$\begin{aligned} \bar{\Psi} &= X^{-2/3} G(\eta) + \dots, \\ P &= X^{2/3} P_1 + \dots, \end{aligned}$$

with $\eta = \bar{Y}/X^{1/3}$ and

$$G''' + \frac{2}{3}GG'' - \frac{1}{3}G'^2 = \frac{2}{3}P_1,$$

with $G \sim \pm \frac{1}{2} \eta^2 \pm P_1$ as $\eta \rightarrow \pm\infty$. (19)

We now make the following transformations

$$Y = \bar{Y} - F(X, t). \quad (20)$$

$$\psi = \bar{\psi} + \int_{-\infty}^X \frac{F_t(X, t)}{\beta^2} dX \quad (21)$$

(which is the unsteady version of the Prandtl transformation). Substitution of (20) and (21) into (7), again leaves the governing non-linear equation unchanged, with ψ , X and Y replacing $\bar{\psi}$, \bar{X} and \bar{Y} respectively. The boundary conditions (9)-(11) are simplified somewhat however:

On $Y = 0$, $X < 0$

$$\psi = \psi_Y = 0. \quad (22)$$

As $Y \rightarrow \pm\infty$

$$\psi_Y \rightarrow \pm Y \pm F(X, t). \quad (23)$$

The remaining boundary conditions are unaltered.

We now go on to consider a numerical solution to equation (7).

III. Numerical method

We shall from here on assume that $F(X, t)$ is a periodic function of time. To be rather more precise, we set

$$F(X, t) = f(X) \sin t \quad (24)$$

i.e. the flap is oscillating about the zero mean position.

One method to solve equation (7), and associated boundary conditions would be to use a

time marching procedure. However, such techniques have a tendency for requiring lengthy computing times, whilst transient terms are decaying. Further, it is difficult with such solutions to reduce the solution into (for example) steady and unsteady components, in order to gain a deeper insight into the solution.

Instead, we shall pursue a method, similar to that used by Duck¹² (but in a "prescribed pressure" context), in which the solution is expressed in the form of a Fourier series in time. In addition to partly overcoming the difficulties encountered with time marching schemes mentioned above, we shall see that this type of approach allows the exploitation of a number of useful symmetries in this particular problem.

Specifically, we write

$$\begin{aligned} \psi(X, Y, t) &= \sum_{n=-\infty}^{\infty} \psi_n(X, Y) e^{int}, \\ P(X, t) &= \sum_{n=-\infty}^{\infty} P_n(X) e^{int}, \end{aligned} \quad (25)$$

where we must insist that $\psi_{-n}(X, Y)$ is the complex conjugate of $\psi_n(X, Y)$, and similarly we have that $P_{-n}(X)$ is the complex conjugate of $P_n(X)$. Substitution of (25) into (7) yields the following infinite system of equations

$$\begin{aligned} \frac{in}{\beta^2} \psi_{nY} + \frac{1}{1+\delta_{0,n}} [\psi_0 \psi_{nYX} + \psi_{nY} \psi_{0YX} - \psi_0 X \psi_{nYY} \\ - \psi_{nX} \psi_{0YY}] - \psi_{nYYY} + P_{nX} \\ = \sum_{j=-\infty}^{\infty} [\psi_j X \psi_{n-jYY} - \psi_j \psi_{n-jYX}] (1-\delta_{j,0}) (1-\delta_{n,j}) \end{aligned} \quad (26)$$

for $n = 0, \pm 1, \pm 2, \pm 3 \dots$

$$\begin{aligned} \text{Here } \epsilon_{i,k} &= 0, i \neq k \\ &= 1, i = k. \end{aligned} \quad (27)$$

Notice that only $n = 0$ is a non-linear equation, all other values of n correspond to effectively linear equations.

Before proceeding further, we must first consider the transformations (20) and (21) in rather more detail. We have already stated that $F(X,t)$ is the "shape" of the flap. However, since the flap and plate extend only up to $X = 0$, then for $X > 0$, strictly, $F(X,t)$ is undefined. In order to proceed further with our Fourier time decomposition type of approach, and to exploit the method to the full, we must now be specific about $F(X,t)$ in the wake. In fact, for $X > 0$, $F(X,t)$ is arbitrary, and consequently assuming that $F(X,t)$, $X < 0$, is given analytically, we shall use the analytic continuation of $F(X,t)$ into the wake. We may then expect our solution to be as smooth as possible, with a continuous vertical coordinate transformation.

We now consider the boundary conditions to be applied in the wake, assuming $F(X,t)$ to take on the form of (24).

Firstly, since the flap is oscillating about a zero mean position, the conditions above the plate at time t , must correspond to conditions below the plate at time $t + \pi$ and because of condition (12), we must insist that

$$P_+(X,t) = P_-(X,t) = P(X,t) = P(X,t + \pi) \quad \text{for } X > 0, \quad (28)$$

i.e. we must have

$$P_{2n-1}(X) = 0, \quad X > 0, \quad (29)$$

for all n .

Similarly, we must also require

$$\psi_Y(X,Y,t) = \psi_Y(X,-Y,t + \pi). \quad (30)$$

The implication of this statement is that $\psi_{2n}(X,Y)$ is odd about $Y = 0$, whilst $\psi_{2n-1}(X,Y)$ is even about $Y = 0$. Consequently we may halve the domain of Y we need to consider, solving in just $Y \geq 0$. The system (24) must then be solved, subject to the following boundary conditions

$$\psi_n(X,0) = \psi_{nY}(X,0) = 0, \quad X < 0, \quad (31)$$

$$\psi_{2n}(X,0) = \psi_{2nY}(X,0) = 0, \quad X > 0, \quad (32)$$

$$\psi_{2n-1Y}(X,0) = 0, \quad X > 0, \quad (33)$$

$$P_{2n-1}(X) = 0, \quad X < 0, \quad (34)$$

$$\psi_{nY} \rightarrow Y \delta_{n,0} \pm \frac{1}{2i} \delta_{n,\pm 1} f(X) \quad \text{as } Y \rightarrow \infty, \quad (35)$$

whilst upstream/downstream we have

$$\left. \begin{aligned} \psi_n &\rightarrow \frac{1}{2} Y^2 \delta_{n,0} \\ P_{nX}(X) &\rightarrow 0 \end{aligned} \right\} \quad \text{as } X \rightarrow -\infty, \quad (36)$$

$$P_n \sim \delta_{n,0} X^{2/3} \quad \text{as } X \rightarrow +\infty. \quad (37)$$

The next step in the technique is to truncate (23) as follows

$$\begin{aligned} \psi(X,Y,t) &= \sum_{n=-N}^N \psi_n(X,Y) e^{int}, \\ P(X,t) &= \sum_{n=-N}^N P_n(X) e^{int}, \end{aligned} \quad (38)$$

which then reduces (26) to a finite system.

Notice that because of the relationships between $\psi_n(X,Y)$ and $\psi_{-n}(X,Y)$ (and similarly for the pressure and displacement function) we need also only consider $n \geq 0$ in (26).

Next, we apply Crank-Nicholson differencing

to the boundary layer momentum equation (26), with $L_0 \leq X \leq L_1$ in steps of ΔX , and $0 \leq Y \leq Y_\infty$ in steps of ΔY .

For $n = 0$ we choose to evaluate the correction terms to the solution at each iteration, whilst for $n \neq 0$, we choose to evaluate the streamfunction and pressure terms themselves (the reason for this difference being because of the non-linearity of (26) if $n = 0$).

The resulting equation is generally of a banded matrix form, for each n and X , with a right-hand column (due to the pressure term), and may be written schematically as follows

$$A_n x_{j+2} + B_j x_{j+1} + x_j + C_j x_{j-1} + D_j x = R_j, \\ j = 1, \dots, J-2, \quad (39)$$

where x_j relates to the streamfunction at the j^{th} Y station, and x relates to the pressure term. Our iteration procedure for solving (26) was a combination of Newton iteration (for $n = 0$), coupled with back substitution (for $n \neq 0$), the system (39) being solved in all cases by Gaussian elimination.

Notice that in the wake, the situation is slightly different for n odd, since $P_{2n-1}(X) = 0$, $X > 0$. However the system is not over-determined, since we have only one boundary condition on $Y = 0$ (instead of the two for n even). The result of this is that we may set $D_j = 0$, for all j in (39) for n odd, $X > 0$, yielding a truly banded system.

The numerical scheme was then as follows. Using the asymptotic behaviour as $X \rightarrow -\infty$, at $X = L_0$, the solution was then marched forward in X . At each X station, the differenced form of

(26) was solved for $n = 0, 1, 2, \dots, N$, and this was repeated until the maximum change in any of the $\psi_0(X, Y)$, $0 \leq Y \leq Y_\infty$ fell below some prescribed tolerance limit (generally 10^{-7}). Once such convergence at a given X station was obtained, the $X + \Delta X$ station would then be considered. This process was repeated up to and including $X = 0$. However, we require that the $P_{2n-1}(0) = 0$, and in general this will not be achieved. We resolved this discrepancy by simply subtracting $P_{2n-1}(0)$ off the previous $P_{2n-1}(X)$, $X < 0$, yielding a finite value of $P_{2n-1}(L_0) \sim P_{2n-1}(-\infty)$. (Consequently the $P_{2n-1}(-\infty)$ are determined absolutely, it is the $P_{2n}(-\infty)$ that may not be determined). All the latest n even solutions were left unaltered. Restarting the computation at $X = \Delta X$, the marching process was continued, with the appropriate wake boundary conditions on $Y = 0$. Then the solution was marched forward to $X = L_1$, where $L_1 > 1$, by which stage the solution was generally seen to take on the similarity form of Hakkinen and Rott¹⁸.

Several advantages of the Fourier series approach now emerge. Supposing reversed flow does not occur, at any given X station we need only store values of the streamfunction at X , and the preceding X station $X - \Delta X$. In the case of time marching schemes, all the values of the streamfunction for all X at t , and the previous timestep $t - \Delta t$ must be stored, although this advantage of the Fourier time series approach is partly offset because there are $N+1$ modes to be stored, all of which (except $n = 0$) involve complex values. Perhaps, however, the major advantage of the present method over time marching

methods is that we need sweep through the entire flowfield just once.

IV. Results

All calculations were on the following class of flap shape

$$F(X,t) = \frac{\alpha \sin t}{1 + (X - \frac{1}{\sqrt{3}})^2}, \quad X < 0 \quad (40)$$

$$\text{i.e.} \quad f(X) = \frac{\alpha}{[1 + (X - \frac{1}{\sqrt{3}})^2]}, \quad X < 0. \quad (41)$$

Computations were accomplished using 161 points in the lateral (Y) direction, with $0 \leq Y \leq 10$, and 81 points in the streamwise (X) direction, with $-10 \leq X \leq 10$. A uniform grid was employed in both directions. The smaller grid in the Y direction was deliberately chosen because of the sensitivity of the solution, particularly the wall shear, to ΔY (the solution being relatively insensitive to ΔX). Further, generally we took $N = 4$ (i.e. five Fourier modes). A number of control calculations were performed for the larger α computations, using $N = 6$, which resulted in a change in generally no more than the third decimal place of the solution.

Two checks of the numerical scheme are available. Firstly, if $\alpha = 0$, then the similarity solution of Hakkinen and Rott¹⁸ applies uniformly downstream from the trailing edge, with no upstream perturbation of the uniform shear (due to the lack of upstream response). The scheme was found to reproduce these results satisfactorily. Secondly, as $\beta \rightarrow \infty$, the solution is expected to become quasi-steady in form, with the solutions obtained by Smith¹³ applying instantaneously. A number of computa-

tions with large values of β were performed, and the solutions obtained did indeed appear to approach such a limit.

Figs. 2 and 3 show the upper wall shear ($\tau = \psi_{YY}$) and pressure distributions respectively, in intervals of $\pi/2$, commencing at $t = 0$, for the particular example of $\alpha = \beta = 1$. In all cases, the local maximum/minimum of the wall shear is seen to occur at the trailing edge itself, $X = 0$. In fig. 3, the arbitrary additive pressure term (described previously) is taken to be the average of the upper and lower pressure, at $X = -\infty$, at each particular time. Notice that the periodicity of the flow implies $P_-(-\infty, t) = P_+(-\infty, t+\pi)$ and $\tau_-(X, Y=0, t) = \tau_+(X, Y=0, t+\pi)$. Further, as a result of our comments previously, the pressure distribution for $X \geq 0$ at time t , is identical to that at time $t+\pi$.

Fig. 4 shows the variation of wall shear at the point $X = 0$ with time. For $\beta = 1$, the maximum shear is seen to occur slightly before $t = \pi/2$, whilst the minimum shear occurs just after $t = 5\pi/4$. We see that there is a fair degree of departure from the quasi-steady solution, which would possess a maximum at $t = \pi/2$, and a minimum at $t = 3\pi/2$, with $\tau(X=0, Y=0, t=\pi/2) = \tau(X=0, Y=0, t=3\pi/2) = 0$.

Figs. 5, 6, 7 are the corresponding figures for the example $\alpha = 2$, $\beta = 1$. In particular fig. 7 indicates that for a period, the flow is undergoing flow reversal in the region of the trailing edge. Strictly, our numerical scheme is invalid in regions of reversed flow - we have employed a marching scheme in the streamwise direction, which prohibits the propagation of any

flow information upstream. We shall return to a discussion of this point later.

Figs. 8, 9, 10 relate to the case $\alpha = 3$, $\beta = 1$. In fig. 10 we see again that for a period in the cycle, flow reversal occurs. Figs. 11, 12, together with one of the plots in fig. 4, are for the case $\alpha = 1$, $\beta = \frac{1}{2}$, corresponding to a somewhat higher frequency of oscillation than the previous examples. Again, a period of flow reversal at the trailing edge is observed.

Let us now consider this apparent separation in the vicinity of the trailing edge. Similar one-sided separation has been found in other (steady) studies^{7,8}, and it has been argued that this is a condition for the breakdown of the multi-layered structure of the problem, since a form of the Hakkinen-Rott¹³ similarity solution applies locally as $X \rightarrow 0^+$ (as well as $X \rightarrow +\infty$), but this requires $\tau(X = 0^-, Y = 0^+) \geq 0$ both be positive. However our numerical results do indicate that one-sided separation occurs at the trailing edge, and it would appear that it is only truncation error in the numerical scheme that permits us to extend our solution into the wake for such flows.

Indeed, computations involving more severe separations were attempted, but failed to converge. In all cases these calculations stopped at the very first wake station ($X = \Delta X$), suggesting that the failure was not caused by the reversed flow per se, but rather because of a failure in the necessary condition for the Hakkinen-Rott¹³ solution to exist.

However, in a recent study by Smith¹³, the steady analogue of the present problem has been examined, using a numerical scheme that correctly

accounts for the reversal flow regions, and it was found that the flow reattaches very close to the trailing edge, permitting the solution to be continued into the wake. Thus it would appear that for these separated flows, the numerical scheme must correctly account for reversed flow regions. In the case of the Fourier time series method, it is rather unclear how reversed flow regions should be treated, since although the flow may be reversed at certain points in the flow-field at certain times, at other times, the flow will be in the forward direction. This is undoubtedly a restriction on the time series decomposition technique, and work is on hand to resolve this problem.

Acknowledgements

The author wishes to thank Dr. F.T. Smith for suggesting the problem, and Professor O.R. Burggraf for discussions relating to the numerical method.

References

1. Goldstein, S., Proc.Camb. Phil. Soc. 26, 1, 1930
2. Stewartson, K., Mathematika 16, 106, 1969
3. Messiter, A.F., SIAM J. Appl. Math., 18, 241, 1970
4. Jobe, C.E., and Burggraf, O.R., Proc. Roy. Soc. Lond., A340, 91, 1974
5. Daniels, P.G., Quart. J. Mech. Appl. Math. 27, 175, 1974
6. Brown, S.N. and Stewartson, K., Fluid Mech. 42, 561, 1970
7. Chow, R. and Melnik, R.E., Proc. 5th Int. Conf. Num. Meth. Fluid Dyn. 59, 135, Enschede, Netherlands 1976

8. Daniels, P.G., J. Fluid Mech. 63, 641, 1974
9. Brown, S.N. and Daniels, P.G., J. Fluid Mech. 67, 743, 1975
10. Brown, S.N. and Cheng, H.K., J. Fluid Mech. 108, 171, 1981
11. Smith, F.T. and Merkin, J.H., Comput. Fluids 10, 7, 1982
12. Duck, P.W., SIAM J. Appl. Math. 41, 247, 1981
13. Smith, F.T., United Technologies Report UTRC 82-13, 1982
14. Smith, F.T., IMA J. Appl. Math. 28, 207, 1982
15. Duck, P.W., Mathematika 25, 24, 1978
16. Duck, P.W., J. Fluid Mech. 95, 635, 1979
17. Duck, P.W., Z. Angew. Math. Phys. 32, 62, 1981
18. Hakkinen R.J. and Rott, N., AIAA Jnl. 3, 1553, 1965

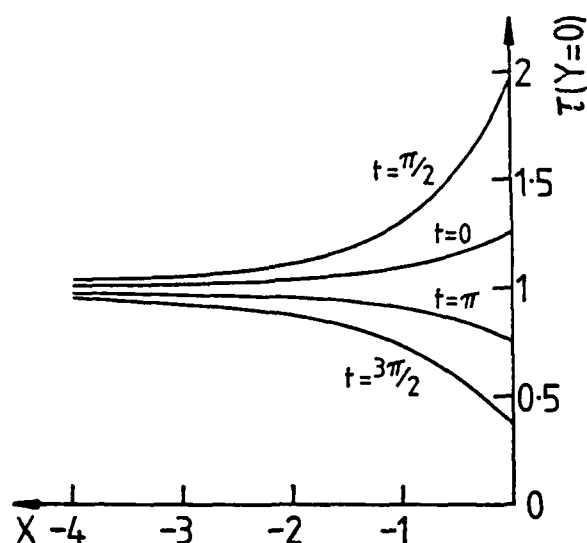


Fig. 2. $\alpha = 1$, $\beta = 1$ upper wall shear stress distributions.

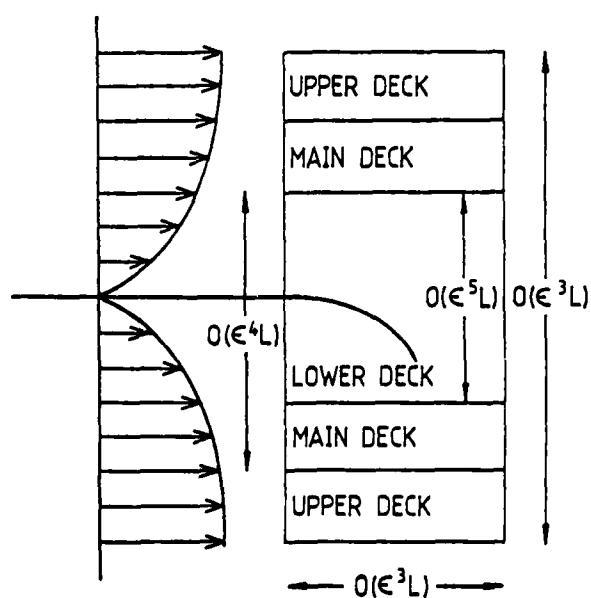


Fig. 3. Layout: the triple deck problem (not to scale).

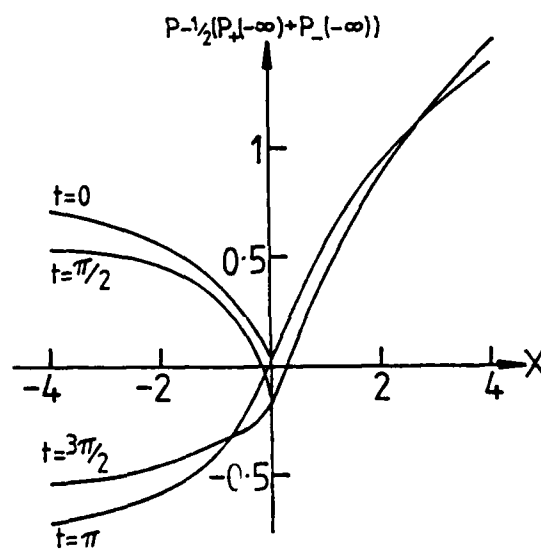


Fig. 4. $\alpha = 1$, $\beta = 1$ upper pressure distributions.

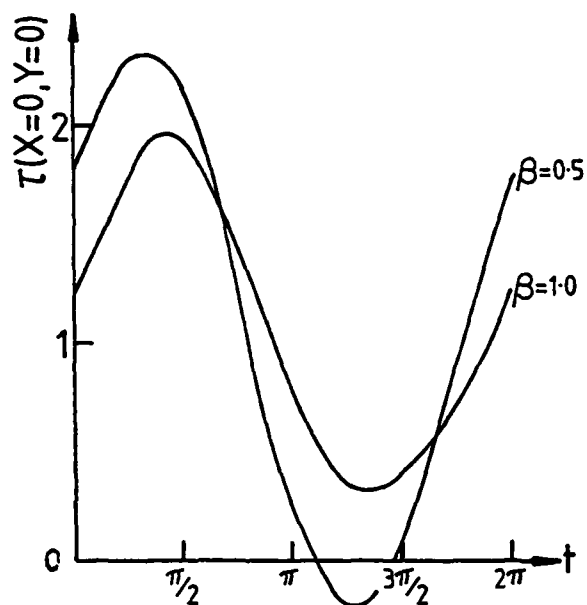


Fig. 4. Variation of upper wall shear at trailing edge with time, $\alpha = 1$.

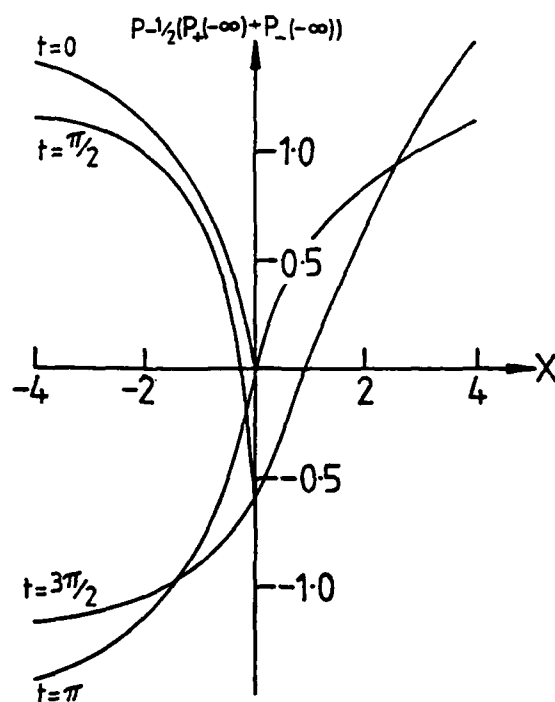


Fig. 6. $\alpha = 2$, $\beta = 1$ upper pressure distributions.

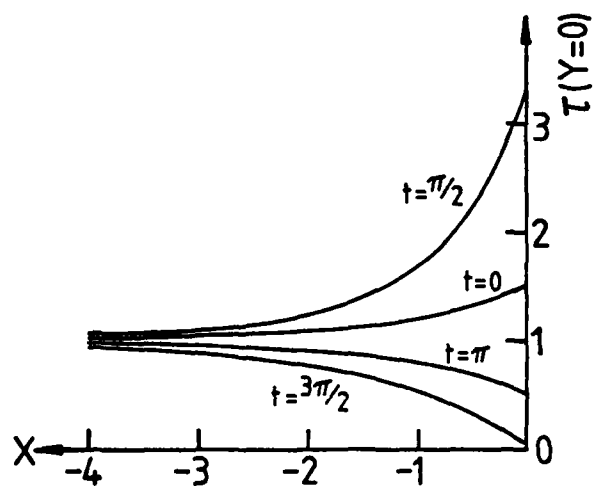


Fig. 5. $\alpha = 2$, $\beta = 1$ upper wall shear stress distributions.

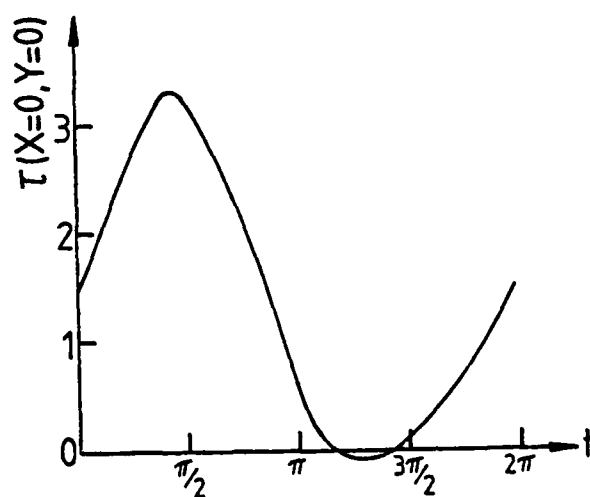


Fig. 7. Variation of upper wall shear at trailing edge with time, $\alpha = 2$, $\beta = 1$.

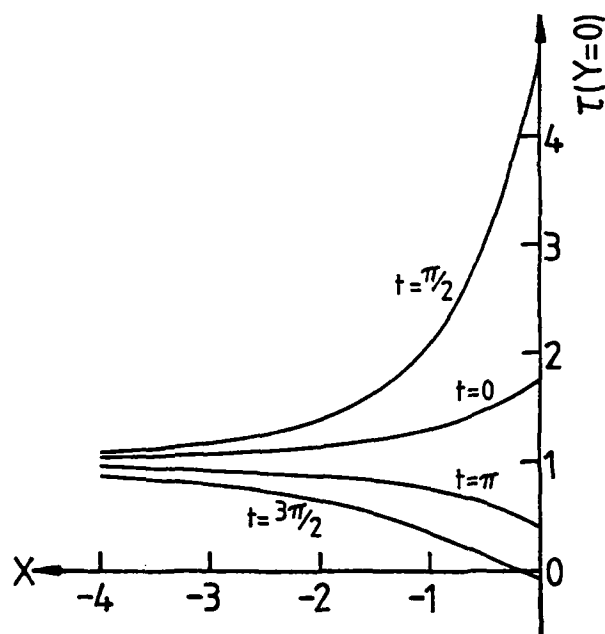


Fig. 8. $\alpha = 3$, $\beta = 1$ upper wall shear stress distributions.

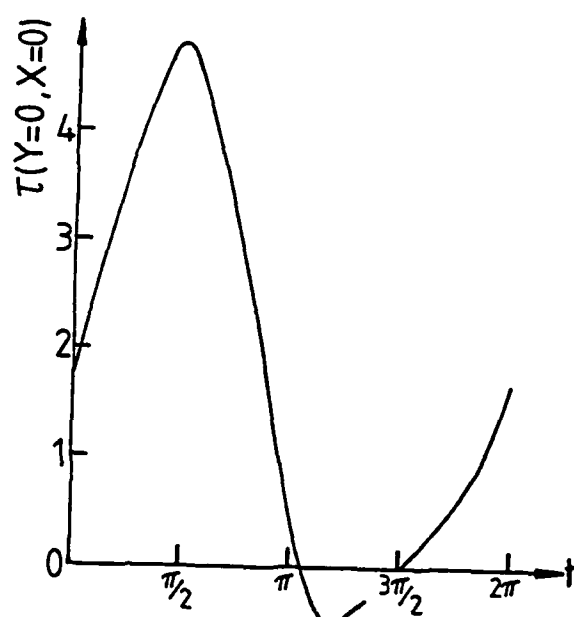


Fig. 10. Variation of upper wall shear at trailing edge with time, $\alpha = 3$, $\beta = 1$.

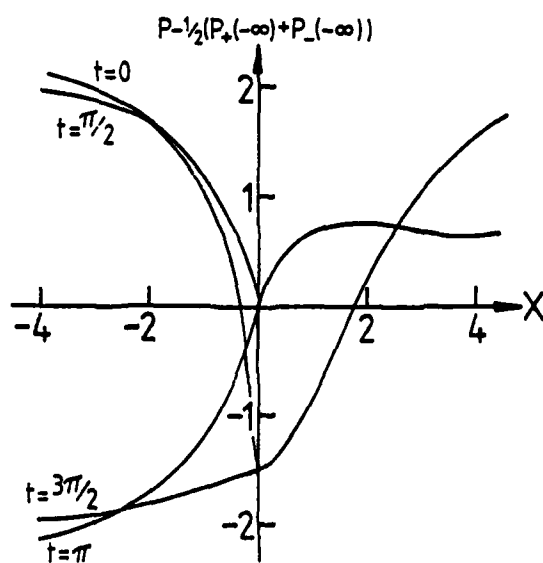


Fig. 9. $\alpha = 3$, $\beta = 1$ upper pressure distributions.

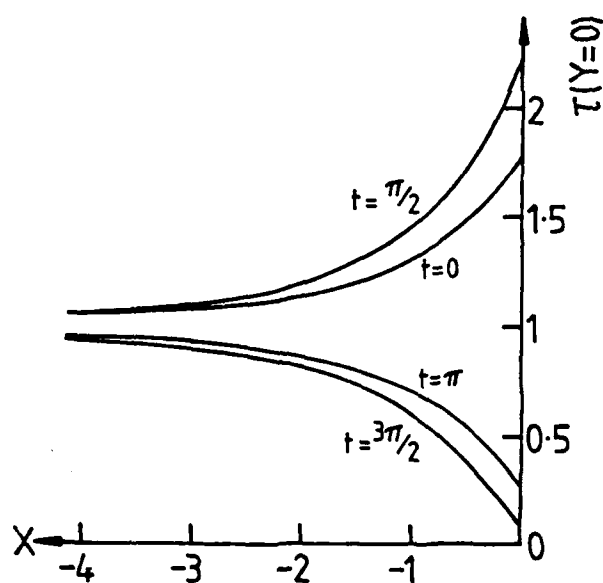


Fig. 11. $\alpha = 1$, $\beta = 1$ upper wall shear stress distributions.

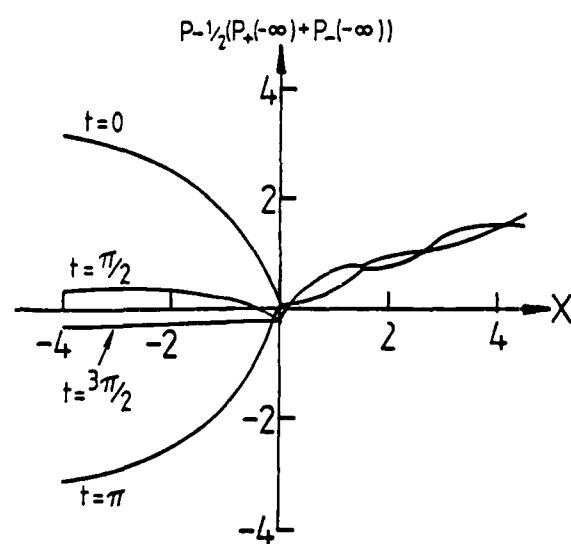


Fig. 12. $\alpha = 1$, $\beta = \frac{1}{2}$ upper pressure distributions.

APPLICATION OF UNSTEADY LAMINAR TRIPLE-DECK THEORY TO VISCOUS-INVISCID INTERACTION FROM AN OSCILLATING FLAP IN SUPERSONIC FLOW

Ming-Ke Huang* and G. R. Inger**
University of Colorado
Boulder, Colorado

Abstract

Unsteady triple-deck theory is applied to analyze the local viscous-inviscid interaction of an idealized oscillating flap with a laminar boundary layer in supersonic flow. For small flap amplitudes and small-to-moderate nondimensional frequencies, linearized analytical solutions by means of Fourier transformation are given for the pressure and shear distributions ahead of and behind the flap hinge. In the supersonic case, the predicted unsteady viscous effects reduce the pressure amplitude and spread it out upstream while causing it to lag the quasi-steady inviscid prediction (flap motion); this also results in an unsteady delay of incipient separation at the hinge to a higher flap amplitude. The unsteady upstream influence of the interaction is found to decrease as the frequency increases. These trends are shown to be in qualitative agreement with available experimental data.

I. Introduction

The formal asymptotic triple-deck theory of unsteady free laminar viscous-inviscid interactions for purely supersonic or subsonic inviscid flow has been developed in general by Ryzhov and Zhuk¹ as an extension of the steady flow theory due to Stewartson and Williams.² Their results for the leading approximation as $Re_L \rightarrow \infty$ indicate that when the reduced frequency ω based on reference length L and freestream velocity $u^*/U^* \leq O(Re_L^{-1/4})$, the explicit unsteady effect remains only in the viscous lower-deck equations, the inviscid disturbance flow in the overlying middle (main) and outer decks being quasi-steady. Schneider³ has also given a fundamental analysis of unsteady disturbances in purely supersonic outer flow for arbitrary amplitudes in which, unlike the aforementioned free-interaction case, the amplitude governs the streamwise interaction scale; he also found that the quasi-steady approximation fails near the wall.

Notwithstanding these general theoretical developments, there has been little application of them to specific problems wherein we can gain a more concrete appreciation for the physics of the unsteady viscous-inviscid interaction process. Accordingly, the present paper describes such an application to a model problem of both practical yet fundamental interest in aerodynamics, namely the unsteady 2-D interaction field produced by an oscillating flap in supersonic flow. The problem is also instructive because it possesses a well-known steady state solution^{4,5} for flow past a corner that permits the new unsteady viscous effects of interest here to be readily displayed.

In Section 2 we outline the general formulation of the problem with its appropriate unsteady

triple-deck scaling. We then treat its application to supersonic flow in Section 3, including a linearized solution for small flap amplitudes. A supporting comparison with experimental results is also given. Section 4 concludes with a discussion on the implications of the present work for future studies.

II. General Triple-Deck Formulation

2.1. General Set-Up

Consider a flow past a plate airfoil with a flap oscillating with frequency ω^* and amplitude α^* , as shown in Fig. 1. The flap is idealized as having a large length compared with the streamwise interaction scale. Suppose that the fluid is Newtonian with constant Prandtl number obeying the Chapman-Rubens viscosity law ($\mu = \text{constant}$) with the wall surface maintained at a constant absolute temperature. For simplicity zero angle of attack is considered, so that a Blasius boundary layer can be assumed on the plate upstream of the leading edge of the control surface. We set up x, y coordinates with the origin at the corner (Fig. 1). In what follows, we denote time, pressure, density, viscosity and temperature by t, p, ρ, μ and T , respectively; u and v are the velocity components in x and y directions, respectively, while the superscript $*$ denotes the original physical variables, the rescaled dimensionless variables being denoted without a star. The subscripts ∞ and w refer to the free stream and the wall conditions, respectively; U_∞^* and M_∞^* are the free stream velocity and Mach number, and L^* is the characteristic length shown in Fig. 1.

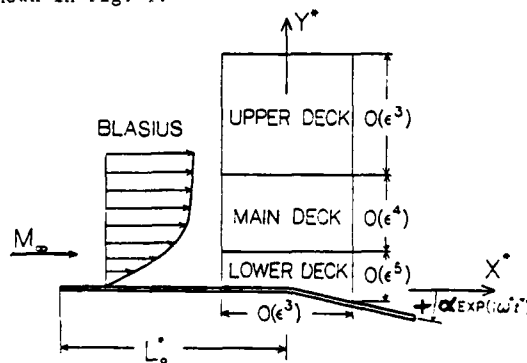


Figure 1. Schematic Triple-Deck Structure near the Leading Edge of the Oscillating Flap

In the region very close to the corner, a local interaction takes place between the viscous layer and the pressure induced in the external flow. The interaction region extends over a streamwise length of order ϵ^3 , where $\epsilon = Re_L^{-1/3}$ is a small parameter and $Re_L = U_\infty^* L^* / \mu^*$ is the free stream Reynolds number which is supposed to be very large. For oscillation frequencies such that $\omega^* L^* / U_\infty^* \leq O(\epsilon^{-2})$ it can be shown that there are three distinct transverse decks in which different physical

*Visiting Associate Professor, Department of Aerospace Engineering Sciences; on leave from Nanjing Aeronautical Institute, People's Republic of China.

**Professor and Chairman, Department of Aerospace Engineering Sciences.

processes dominate¹⁻³ (Fig. 1), as follows. The main deck with thickness of order ε^2 acts as the disturbed rotational inviscid continuation of the upstream boundary layer, the first order solution therein being a simple quasi-steady displacement of the streamlines. The upper deck has a thickness of order ε^3 in which the dominant process is quasi-steady irrotational inviscid flow so that the first order equations are potential disturbance flow equations. The lower deck has a height of order ε^5 and contains an unsteady viscous incompressible disturbance flow. The pressure induced at the base of the upper deck is impressed upon the top of the lower deck, so that the problem reduces to the solution of the unsteady incompressible boundary-layer equations governing the lower deck subject to unusual boundary conditions.

According to Stewartson⁵ and Ryzhov and Zhuk,¹ the suitable scaled variables for the lower deck are $x^* = \varepsilon^5 y$, $y^* = \varepsilon^5 b y$, $(p^* - p_\infty^*)/\rho U_\infty^2 = \varepsilon^2 c p$, $u^* = (\varepsilon d/b) u$, $v^* = (\varepsilon^3 d/a) v$, $\alpha^* = \varepsilon^2 (b/a) \alpha$, $\tau^* = \varepsilon^2 (ab/d) t$ and $\omega^* = \omega/\varepsilon^2 (ab/d)$ with $\omega \leq O(1)$, where the constants a , b , c and d are given in Appendix A, and where $C = \frac{u^* T_\infty^*}{u_\infty^* T_\infty^*}$, $\lambda = 0.3321$ and

$\delta = M_\infty^2 - 1$. The resulting first order lower-deck flow equations are of the nonlinear boundary-layer type

$$\frac{\partial u}{\partial x} + \frac{\partial v}{\partial y} = 0 \quad (1)$$

$$\frac{\partial u}{\partial t} + u \frac{\partial u}{\partial x} + v \frac{\partial u}{\partial y} = -\frac{dp}{dx} + \frac{\partial^2 u}{\partial y^2} \quad (2)$$

with the upstream initial condition

$$\frac{\partial u}{\partial y} \rightarrow 1 \quad \text{as} \quad x \rightarrow \infty \quad (3)$$

Matching with the small disturbance external flow yields the outer boundary condition

$$u \rightarrow y + A(x, t) \quad \text{as} \quad y \rightarrow \infty \quad (4a)$$

where

$$\frac{\partial A}{\partial x} = -p \quad [\text{supersonic wave-like behavior}] \quad (4b)$$

$$\frac{\partial^2 A}{\partial x^2} = -\frac{1}{\pi} \int_{-\infty}^{\infty} \left(\frac{\partial p / \partial \xi}{x - \xi} \right) d\xi \quad [\text{subsonic}] \quad (4c)$$

The inner boundary conditions for zero slip on an impermeable wall are

$$u = 0 \quad (5)$$

$$\left. \begin{aligned} v &= -i\alpha\omega e^{i\omega t} x H(x) \end{aligned} \right\} \text{on } y = -\alpha e^{i\omega t} x H(x) \quad (6)$$

where $H(x)$ is Heaviside's unit function. It should be noted that these equations differ in two respects from the steady case studied by Stewartson^{4,5}: there is a term $\partial u / \partial t$ in the x-momentum equation, and $v \neq 0$ at the wall when $x > 0$ because of the oscillating flap.

2.2. Linearized Version

The foregoing problem is nonlinear and hence difficult to solve analytically, especially for the unsteady case. However, the essential physics may be brought out by considering small amplitude flap oscillations, for which linearized solutions can be

obtained as follows. Assuming that α is sufficiently small, we can expand u , v and p as power series in α ; to the first order (linearized) approximation, this gives

$$u = y + \alpha U(x, y) \cdot \exp(i\omega t)$$

$$v = V(x, y) \cdot \alpha \exp(i\omega t) \quad (7)$$

$$p = P(x) \cdot \alpha \exp(i\omega t)$$

Substituting these into Eqs. (1) and (2) and equating like powers of α yields

$$\frac{\partial U}{\partial x} + \frac{\partial V}{\partial y} = 0 \quad (8)$$

$$i\omega U + y \frac{\partial U}{\partial x} + V = -\frac{dP}{dx} + \frac{\partial^2 U}{\partial y^2} \quad (9)$$

To the same order of approximation the wall boundary conditions (5) and (6) can be shifted to $y = 0$, so that

$$U(x, 0) = xH(x), \quad V(x, 0) = -i\omega xH(x) \quad (10)$$

The remaining boundary conditions are unaltered.

Analytical solutions of this small perturbation problem will be obtained by taking the Fourier transform with respect to x . Thus, for example, if

$$\bar{U}(y, k) = \int_{-\infty}^{\infty} e^{-ikx} U(x, y) dx, \quad (11)$$

then letting $\bar{V} = ikf$, $\bar{U} = -\frac{df}{dy}$ and $\zeta = \zeta_1(\omega + ky)$ where $k\zeta_1 = (ik)^{1/3}$, we find from Eqs. (8) and (9) that the function f satisfies Airy's differential equation

$$\frac{d^4 f}{d\zeta^4} = \zeta \frac{d^2 f}{d\zeta^2} \quad (12)$$

The boundary conditions (10) require that f satisfy

$$f(0) = -\frac{i\omega}{(0 + ik)^3} \quad (13)$$

$$\frac{df}{dy}(0) = -\frac{1}{(0 + ik)^2} \quad (14)$$

A third condition can be obtained by satisfying the x-momentum equation (9) right at the wall; after Fourier transformation, in terms of f this leads to

$$\frac{d^3 f}{dy^3}(0) = -ik\bar{P} \quad (15)$$

where $\bar{P}(k)$ is the wall pressure spectrum. The remaining outer matching conditions of Eq. (4) introduce the specific type of outer flow solution and will be taken up below; regardless of this type, however, we note that either of these conditions implies that the disturbance flow vorticity $\partial(u - y)/\partial y$ [and hence $d^2 f / dy^2$] vanishes as $y \rightarrow \infty$.

Now the general solution of Eq. (12), which vanishes as $\zeta \rightarrow \infty$, is

$$\frac{d^2 f}{dy^2} = B \text{Ai}(\zeta) \quad (16)$$

where Ai denotes the Airy function of the first kind and B is a constant. Following two successive y -integrations of Eq. (16) to obtain f , the two resulting integration constants plus B can be determined in terms of \bar{P} by conditions (13) - (15); the particular value of \bar{P} is then determined for either supersonic or subsonic flow by the transformed outer matching condition (4a) or (4b), respectively. Fourier inversion to the physical plane then completes the solution.

III. Supersonic Solution

The transformed version of the supersonic outer matching condition (4b) is

$$\frac{df}{dy}(\infty) = \frac{\bar{P}}{(0 + ik)} \quad (17)$$

The integration of Eq. (16) plus the four conditions (13), (14), (15) and (17) then yields the pressure spectrum

$$\bar{P} = -\frac{1}{(0 + ik) N(k)} \quad (18a)$$

where

$$N(k) = 1 - \frac{\omega^2}{(\zeta_1 \omega)^2 Ai'(\zeta_1 \omega)} \int_{\zeta_1 \omega}^{\infty} Ai(\zeta) d\zeta \quad (18b)$$

The physical solution now follows by inversion; for example, the complex amplitude of the pressure distribution per unit α is

$$P(x) = \frac{1}{2\pi} \int_{-\infty}^{\infty} e^{ikx} \bar{P}(k) dk \quad (19)$$

The corresponding shear stress along the wall can then be determined by

$$\left(\frac{\partial u}{\partial y}\right)_{y=0} = 1 + \alpha \exp(i\omega t) \cdot \left(\frac{\partial \bar{U}}{\partial y}\right)_{y=0},$$

so that if we let

$$\tau = \frac{\left(\frac{\partial \bar{U}}{\partial y}\right)_{y=0}^{-1}}{\alpha \exp(i\omega t)} = \left(\frac{\partial \bar{U}}{\partial y}\right)_{y=0} \quad (20)$$

be the complex amplitude of the disturbed shear stress per unit α , then

$$\tau(x) = \frac{1}{2\pi} \int_{-\infty}^{\infty} e^{ikx} \left(\frac{\partial \bar{U}}{\partial y}\right)_{y=0} dk \quad (21)$$

Because of the complexity of the function $\bar{P}(k)$ given by Eq. (13), a numerical procedure in general is required to invert the Fourier transform. However, several important physical features of the interaction can be obtained analytically, as follows.

3.1. Upstream Influence

The effective distance of upstream influence in the leading approximation can be obtained by examining the asymptotic behavior of $P(x)$ as $x \rightarrow -\infty$ and calculating the resulting logarithmic decrement. As shown by Lighthill,⁶ this corresponds to that zero k_1 of the function $N(k)$ [Eq. (18b)] in the lower-half complex k -plane having the least value of its imaginary part $-\text{Im}(k_1)$, which means that $P(x)$ decreases by a factor $[\exp \text{Im}(k_1)]$ per unit distance. Now it can be shown that the equation $N(k) = 0$ is exactly that studied by Schneider³; the curve for $M_\infty = \sqrt{2}$ in his Fig. 7(a) can be directly taken over for determination of the present-

ly required logarithmic decrement if its ordinate is interpreted as $-\text{Im}(k_1)$ and its abscissa as $1/\omega^2$. This result is plotted in Fig. 2, from which we can see that the pressure disturbance extends a shorter distance upstream as the frequency is increased.

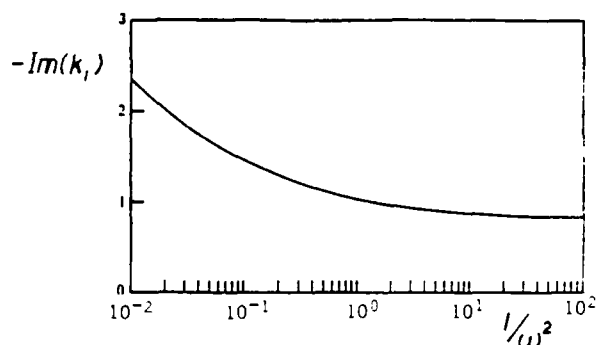


Figure 2. Logarithmic Decrement

3.2. Low-Frequency Behavior

Another interesting aspect of the unsteady interaction is its low-frequency behavior pertaining to small values of ω such that $\omega^2 \ll 1$; this can be obtained systematically by expanding $\bar{P}(k)$ and $(\partial \bar{U} / \partial y)_{y=0}$ as power series in ω . To the second order, we can then get the inversions of the transforms in closed form (see Appendix B) and so obtain the wall pressure and shear stress as

$$P(x) = P_0(x) + i\omega P_1(x) + \omega^2 P_2(x) + \dots \quad (22)$$

$$\tau(x) = \tau_0(x) + i\omega \tau_1(x) + \omega^2 \tau_2(x) + \dots \quad (23)$$

where $P_0(x)$ and $\tau_0(x)$ are the same functions as those given by Stewartson² for steady flow while the remaining functions are defined in the Appendix. Fig. 3 presents the numerical results for P_0 , P_1 and P_2 as functions of x , while Fig. 4 shows τ_0 , τ_1 and τ_2 . We see from Fig. 3 that P_0 , P_1 , $P_2 \rightarrow 0$ as $x \rightarrow -\infty$, and $P_0 \rightarrow -1$, $P_1 \rightarrow 0$, $P_2 \rightarrow 1.38$ as $x \rightarrow +\infty$. These functions are continuous at $x = 0$ due to the presence of viscous effects, whereas they would have a jump across $x = 0$ according to purely inviscid potential theory. Fig. 4 shows that τ_0 , τ_1

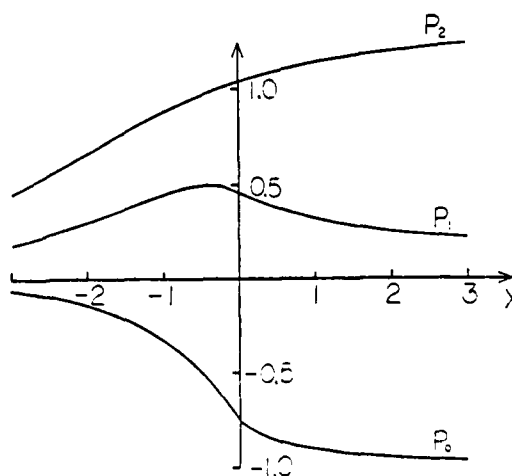


Figure 3. Complex Amplitude of the Pressure Oscillation, $P = P_0 + i\omega P_1 + \omega^2 P_2$

and $\tau_2 \rightarrow 0$ as $x \rightarrow -\infty$, while $\tau_0 \rightarrow 0$, $\tau_1 \rightarrow -1$ as $x \rightarrow +\infty$. We note that the divergence of τ_2 far downstream indicated here is not a physically realistic result but simply implies an ultimate breakdown of the small disturbance approximation due to the unlimited growth in x of the perturbation wall boundary conditions (10) when $\omega \neq 0$; however, this breakdown is well downstream of the main interaction zone $-3 \leq x \leq 2$ around the flap hinge.

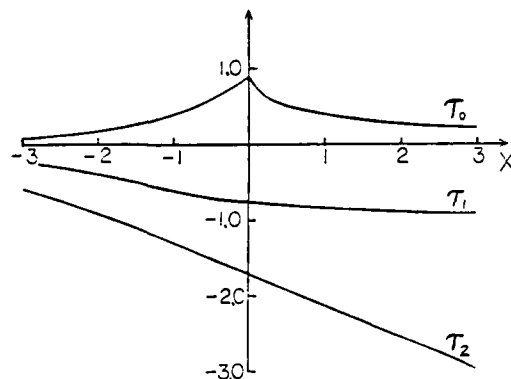


Figure 4. Complex Amplitude of the Disturbed Shear Stress, $\tau = \tau_0 + i\omega\tau_1 + \omega^2\tau_2$

From Eqs. (22) and (23), we may draw some inferences about the effects of frequency upon the amplitudes of the unsteadiness. To the second order in ω , we have

$$\frac{|P| - |P_0|}{|P_0|\omega^2} \approx \frac{P_2}{P_0} + \frac{1}{2} \left(\frac{P_1}{P_0}\right)^2 \quad (24)$$

and

$$\frac{|\tau| - |\tau_0|}{|\tau_0|\omega^2} = \frac{\tau_2}{\tau_0} + \frac{1}{2} \left(\frac{\tau_1}{\tau_0}\right)^2, \quad (25)$$

where Fig. 5 presents the numerical results as functions of x . It is seen that the amplitude of both the pressure and wall shear oscillations decreases when the frequency increases. Likewise the

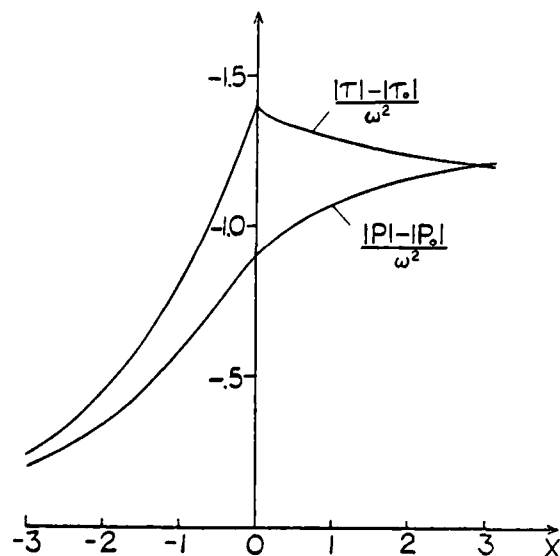


Figure 5. Effects of ω upon the Amplitudes

effects of the frequency upon the phases can be found from Eqs. (22) and (23); letting ϕ denote the phase, we obtain

$$\left(\frac{\tan \phi}{\omega}\right)_{\text{pressure}} \approx \frac{P_1}{P_0} \quad (26)$$

and

$$\left(\frac{\tan \phi}{\omega}\right)_{\text{shear stress}} \approx \frac{1}{\tau_0}, \quad (27)$$

where Fig. 6 presents the results as functions of x . These curves indicate that both the upstream pressure and shear stress responses lag behind the flap movement about the same, the lag growing toward $\phi \rightarrow -\pi/2$ as $x \rightarrow -\infty$. Downstream, the pressure lag is small while the shear stress lag remains significant.

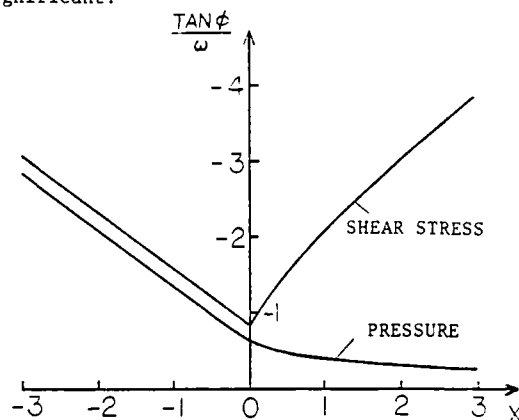


Figure 6. Effects of ω upon the Phases

The aforementioned results are consistent with unsteady linearized supersonic flow theory⁷ as one would intuitively expect it to be modified by viscous effects: the unsteady flow lags the flap motion and reduces the pressure amplitude increasingly with larger frequency, while viscous-inviscid interaction (Fig. 5) spreads out the pressure field upstream of the hinge line and introduces a phase lag that grows with upstream distance. Although experimental data on oscillating flaps in supersonic flow is very sparse, some Swedish test results for a flap on a wing at $M_\infty = 1.31$ quoted by Tijdeman⁸ and illustrated in Fig. 7 also qualitatively support the present theory: this data clearly indicates a flap pressure amplitude level well below inviscid theory with a correspondingly greater phase lag that extends ahead of the flap hinge.

Possible flow separation in the interaction zone near the leading edge of the flap is also of interest. Although actual separation must be excluded from this linearized treatment because of the local breakdown of the small disturbance approximation for shear stress, we may still obtain a rough indication of the conditions leading to the onset of separation. Since the interactive viscous shear field is free from any singularities at its streamwise minimum, we may reasonably adopt the Moore-Rott-Sears ("MRS") criterion⁹ for unsteady flow separation which in the present problem requires that the total wall shear vanish on the instantaneous no-slip wall location. In the linearized approximation, this becomes from (7)

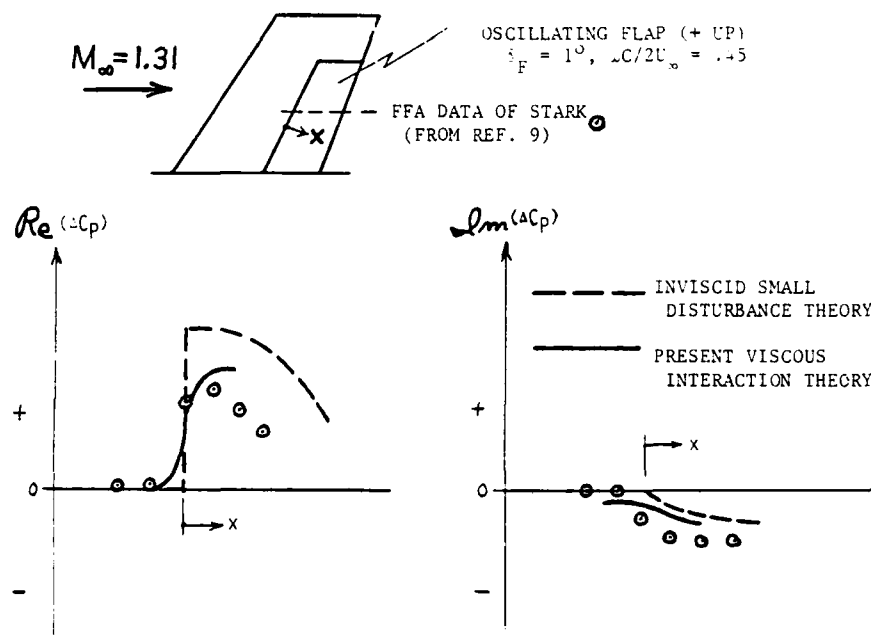


Figure 7. Qualitative Comparison of Theory and Experiment for an Oscillating Flap in Supersonic Flow (schematic)

$$\left(\frac{\partial u}{\partial y}\right)_{y=0} = 1 + \alpha | \tau | e^{i(\omega t + \phi)} = 0 \quad (28)$$

where because of the lagging phase the minimum shear stress does not appear when the flap is deflected at the upper extreme position. The separation condition can also be written as $\alpha | \tau | > 1$. Now excluding the unrealistic far downstream behavior of τ , Fig. 5 shows that minimum $| \tau |$ occurs at the hinge line $x = 0$ with the value

$$| \tau(0) | \approx | \tau_0(0) | = 1.4\omega^2 \quad (29)$$

so that the flap angle α_s at which the separation occurs is roughly

$$\begin{aligned} \alpha_s &= \frac{1}{| \tau_0(0) | = 1.4\omega^2} \approx \frac{4\epsilon^{2/3}}{9\text{Ai}(0)} (1 + 1.5\omega^2) \\ &= 1.1(1 + 1.5\omega^2) \end{aligned} \quad (30)$$

where the value for $\omega = 0$ is just that given by Stewartson^{4,5} for a concave corner in the steady case (note that the α defined by Stewartson is one-half that used here; moreover, we have corrected some numerical inaccuracy in his paper). The above expression predicts that α_s increases with increasing frequency, a result of the fact that in supersonic flow the (negative) unsteady skin-friction disturbance around the hinge line lags the flap motion (Fig. 6). Thus the instantaneous τ_{\min} does not occur at the largest flap deflection (perturbation) and so a slightly higher flap angle can be tolerated than in the quasi-steady ($\omega \approx 0$) case.

IV. Concluding Remarks

Although the present linearized treatment of the disturbance field due to small oscillations of an idealized unbounded flap model introduces unrealistic large x -scale growth of some perturbation properties and is restricted to amplitudes $\alpha^* \lesssim \text{Re}_L^{-1/4}$, the local results in the neighborhood

of the hinge give a good qualitative account of and insight into the dominant unsteady viscous-inviscid interaction effects. The restriction on the permissible reduced frequency to values $k \equiv \omega^* L^*/U^* \lesssim \epsilon^{-2} \leq \text{Re}_L^{1/4}$ in fact embraces much of the low-to-moderate frequency range encountered in aeroelastic problems,¹⁰ so that the quasi-steady approximation for the outer part of any strong local viscous-inviscid interaction regions occurring in this range is indeed often applicable in practice, as are the small $\omega \equiv \epsilon^2 k \ll 1$ expansion analyses used herein.

Owing to the linearized purely supersonic nature of the inviscid flow assumed here, a separate treatment is required of the far more difficult mixed nonlinear problem associated with transonic flow. Indeed, the unsteady transonic triple-deck problem might exhibit a basically different quasi-steady behavior than that treated in the present work.

Appendix A

The Interactive Scaling Constants

$$\begin{aligned} a &= L^* C^{3/3} \epsilon^{-5/4} \delta^{-3/2} (T_w^*/T_\infty^*)^{3/2} \\ b &= L^* C^{5/3} \epsilon^{-3/4} \delta^{-1/2} (T_w^*/T_\infty^*)^{3/2} \\ c &= C^{1/4} \epsilon^{1/2} \delta^{-1/4} \\ d &= L^* U_\infty^* C^{3/4} \epsilon^{-1/2} \delta^{-1/4} (T_w^*/T_\infty^*)^2 \end{aligned}$$

Appendix B

Details of the Low-Frequency Approximation

B.1. Complex Amplitude of Pressure Oscillation

$$P = P_0 + iP_1\omega + P_2\omega^2 + \dots$$

$$P_0 = -\frac{1}{2\pi} \int_{-\infty}^{\infty} e^{ikx} \left\{ \frac{1}{(0+ik)} + \frac{(0+ik)^{1/3}}{\theta^{4/3} - (0+ik)^{4/3}} \right\} dk$$

$$= \begin{cases} -\left\{ 1 - \frac{\sqrt{3}}{2\pi} \int_0^{\infty} \frac{\xi^{1/3} e^{-\theta\xi x} d\xi}{\xi^{8/3} + \xi^{4/3} + 1} \right\} & \text{as } x > 0 \\ -\frac{3}{4} e^{\theta x} & \text{as } x < 0 \end{cases}$$

$$P_1 = \frac{3\theta^{4/3} Ai(0)}{2\pi} \int_{-\infty}^{\infty} \frac{e^{ikx} dk}{(0+ik)^{1/3} [\theta^{4/3} - (0+ik)^{4/3}]^2}$$

$$= \begin{cases} \frac{3\sqrt{3}}{2\pi} \theta^{-2/3} Ai(0) \int_0^{\infty} e^{-\theta\xi x} \frac{1 + 2\xi^{4/3}}{\xi^{1/3}(1 + \xi^{4/3} + \xi^{8/3})^2} d\xi & \text{as } x > 0 \\ \frac{3}{16} (6 - 9\theta x) Ai(0) \theta^{-2/3} e^{\theta x} & \text{as } x < 0 \end{cases}$$

$$P_2 = \frac{3Ai(0) + \theta^{8/3}}{2} I_1 + 9\theta^{4/3} Ai^2(0) I_2$$

where

$$I_1 = \frac{1}{2\pi} \int_{-\infty}^{\infty} \frac{e^{ikx} dk}{(0+ik) [\theta^{4/3} - (0+ik)^{4/3}]^2}$$

$$= \begin{cases} \theta^{-8/3} \left\{ 1 - \frac{\sqrt{3}}{2\pi} \int_0^{\infty} e^{-\theta\xi x} \frac{\xi^{1/3}(2 + \xi^{4/3}) d\xi}{(1 + \xi^{4/3} + \xi^{8/3})^2} \right\} & \text{as } x > 0 \\ \frac{\theta^{-3/3}}{16} (12e^{\theta x} - 9\theta x e^{\theta x}) & \text{as } x < 0 \end{cases}$$

$$I_2 = \frac{1}{2\pi} \int_{-\infty}^{\infty} \frac{e^{ikx} (0+ik)^{1/3} dk}{[\theta^{4/3} - (0+ik)^{4/3}]^3}$$

$$= \begin{cases} \frac{\sqrt{3}}{2\pi} \theta^{-8/3} \int_0^{\infty} e^{-\theta\xi x} \xi^{1/3} \frac{\xi^4 + 3\xi^{8/3} - 1}{(1 + \xi^{4/3} + \xi^{8/3})^3} d\xi & \text{as } x > 0 \\ \frac{9\theta^{-8/3}}{128} [3(\theta x)^2 e^{\theta x} - \theta x e^{\theta x}] & \text{as } x < 0 \end{cases}$$

$$\theta = [-3Ai'(0)]^{3/4} = 0.8272$$

B.2. Complex Amplitude of Disturbed Shear Stress

$$\tau = \tau_0 + i\tau_1\omega + \tau_2\omega^2 + \dots$$

where the Fourier transformations of τ_0 , τ_1 , and τ_2 are

$$\bar{\tau}_0 = \frac{Ai(0)}{Ai'(0)} (ik)^{2/3} \bar{P}_0$$

$$\bar{\tau}_1 = \bar{P}_0 + \frac{Ai(0)}{Ai'(0)} (ik)^{2/3} \bar{P}_1$$

$$\bar{\tau}_2 = -\bar{P}_1 + \frac{Ai^2(0)}{2Ai'(0)} (ik)^{-2/3} \bar{P}_0 + \frac{Ai(0)}{Ai'(0)} (ik)^{-1/3} \bar{P}_2$$

By inversion, we have

$$\tau_0 = \begin{cases} \frac{3\sqrt{3}Ai(0)}{2\pi\theta^{2/3}} \int_0^\infty \frac{e^{-\theta\xi x}(1+\xi^{-1/3}) d\xi}{\xi^{1/3}(1+\xi^{4/3}+\xi^{8/3})} & \text{as } x > 0 \\ \frac{9Ai(0)}{4\theta^{2/3}} e^{\theta x} & \text{as } x < 0 \end{cases}$$

$$\tau_1 = \begin{cases} P_0 + \frac{9\sqrt{3}Ai^2(0)}{2\pi\theta^{4/3}} \int_0^\infty \frac{e^{-\theta\xi x}\xi^{1/3}(1-\xi^{2/3}) d\xi}{(1+\xi^{4/3}+\xi^{8/3})^2} & \text{as } x > 0 \\ P_0 + \left(\frac{3}{2}\right)^4 \frac{Ai^2(0)}{\theta^{4/3}} \theta x e^{\theta x} & \text{as } x < 0 \end{cases}$$

$$\tau_2 = -P_1 - \frac{9Ai^2(0)}{2\theta^{8/3}} [J_1 + J_2] - \frac{3Ai(0)\theta^{-4/3}[3Ai(0) + \theta^{8/3}]}{2} J_3 - 27Ai^3(0) J_4$$

where

$$J_1 = \frac{1}{2\pi} \int_{-\infty}^\infty \frac{e^{ikx} dk}{(0+ik)^{5/3}} = \begin{cases} \frac{3\sqrt{3}}{4\pi} x^{2/3} \Gamma(\frac{1}{3}) & \text{as } x > 0 \\ 0 & \text{as } x < 0 \end{cases}$$

$$J_2 = \frac{1}{2\pi} \int_{-\infty}^\infty \frac{e^{ikx} dk}{(0+ik)^{1/3} [\theta^{4/3} - (0+ik)^{4/3}]} =$$

$$= \begin{cases} \frac{\sqrt{3}}{2\pi} \theta^{-2/3} \int_0^\infty \frac{e^{-\theta\xi x}(1+\xi^{4/3}) d\xi}{\xi^{1/3}(1+\xi^{4/3}+\xi^{8/3})} & \text{as } x > 0 \\ \frac{3}{4} \theta^{-2/3} e^{\theta x} & \text{as } x < 0 \end{cases}$$

$$J_3 = \frac{1}{2\pi} \int_{-\infty}^\infty \frac{e^{ikx} dk}{(0+ik)^{1/3} [\theta^{4/3} - (0+ik)^{4/3}]^2} =$$

$$= \begin{cases} \frac{\sqrt{3}\theta^{-2}}{2\pi} \int_0^\infty \frac{e^{-\theta\xi x}(1+2\xi^{4/3}) d\xi}{\xi^{1/3}(1+\xi^{4/3}+\xi^{8/3})^2} & \text{as } x > 0 \\ \frac{3}{16} \theta^{-2} (2e^{\theta x} - 3\theta x e^{\theta x}) & \text{as } x < 0 \end{cases}$$

$$J_4 = \frac{1}{2\pi} \int_{-\infty}^\infty \frac{e^{ikx}(0+ik) dk}{[\theta^{4/3} - (0+ik)^{4/3}]^3} =$$

$$= \begin{cases} -\frac{3\sqrt{3}}{2\pi} \theta^{-2} \int_0^\infty \frac{e^{-\theta\xi x}\xi^{7/3}(1+\xi^{4/3}) d\xi}{(1+\xi^{4/3}+\xi^{8/3})^3} & \text{as } x > 0 \\ \frac{6}{(4)^4} \theta^{-2} [9(\theta x)^2 e^{\theta x} + 9\theta x e^{\theta x} - 4e^{\theta x}] & \text{as } x < 0 \end{cases}$$

References

- ¹Ryzhov, O.S. and Zhuk, V.I., "Internal Waves in the Boundary Layer with the Self-Induced Pressure," Journal de Mécanique, Vol. 19, 1980, pp. 561-580.
- ²Stewartson, K. and Williams, P.G., "Self-Induced Separation," Proceedings of the Royal Society, Vol. A312, 1969, pp. 181-206.
- ³Schneider, W., "Upstream Propagation of Unsteady Disturbances in Supersonic Boundary Layers," Journal of Fluid Mechanics, Vol. 63, 1974, pp. 465-485.

⁴Stewartson, K., "On Laminar Boundary Layers near Corners," Quarterly Journal of Mechanics and Applied Mathematics, Vol. 23, 1970, pp. 137-152.

⁵Stewartson, K., "On Laminar Boundary Layers near Corners, Corrections and an Addition," Quarterly Journal of Mechanics and Applied Mathematics, Vol. 24, 1971, pp. 387-389.

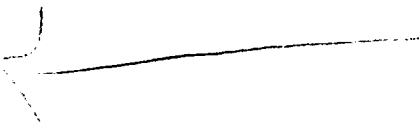
⁶Lighthill, M.J., "On Boundary Layers and Upstream Influence--II. Supersonic Flows Without Separation," Proceedings of the Royal Society, Vol. A217, 1953, pp. 478-507.

⁷Miles, J.W., The Potential Theory of Unsteady Supersonic Flow, University Press, Cambridge, 1959.

⁸Tijdeman, H. and Zwann, R.J., "Unsteady Aerodynamics for Wings with Control Surfaces," AGARD Conference Proceedings, Vol. 80-II, Symposium on Unsteady Aerodynamics for Aeroelastic Analyses, 1971. (See also Zeitschrift für Flugwissen, Vol. 18, 1970.)

⁹Moore, F.K., "On the Separation of the Unsteady Laminar Boundary Layer," Boundary Layer Research, H. Görtler (ed.), Springer-Verlag, Berlin, 1958.

¹⁰Brune, G. and Dusto, A.R., "Slowly-Oscillating Lifting Surfaces at Subsonic and Supersonic Speeds," Journal of Aircraft, Vol. 9, 1972, p. 777.



A STUDY OF NON-UNIQUE SOLUTIONS OF THE TWO-DIMENSIONAL BOUNDARY LAYER EQUATIONS AT LAMINAR SEPARATION AND REATTACHMENT POINTS

M. DRELA

W. T. THOMPSON JR.

Massachusetts Institute of Technology
Cambridge, Massachusetts

Abstract

The possibility of non-unique solutions to the laminar boundary equations in direct problem calculations has been identified for decelerating flow. For flows far from separation or reattachment one solution is physically reasonable and the others unrealistic. As a separation or reattachment point is approached, the multiple solutions approach each other and become identical. Understanding of this behavior allows direct problem calculations through separation, although such calculations are not practical. The computer code used to generate these results was developed to solve compressible, laminar or turbulent boundary layer and free wake problems in direct or inverse mode. The equation formulation uses a variable (scaling based on the local displacement thickness rather than the more common Levy-Lees scaling. Similarity solutions in either primitive variable or stream function form are possible. The resulting equations are solved using a modified Keller's Box scheme in which the energy equation and turbulence modeling equations are solved simultaneously with the continuity and momentum equations. The approach is efficient and robust for all of the variety of test cases examined. The transformations and computational particulars for the direct and inverse modes will be presented. The efficiency and accuracy will be illustrated by few computational examples. A number of examples illustrating the nature of the solutions at separation and reattachment points will be presented.

Introduction

As part of a research program designed to study viscous-inviscid interactions in turbomachinery flow fields, a compressible, two-dimensional boundary layer calculation scheme was developed. The scheme was designed for internal flow applications where separation often occurs at unexpected locations and causes a strong interaction between the boundary layer and the core flow. Since over a large portion of the flow field the boundary layer is usually known to be attached, an efficient scheme should allow easy transition between operation as an inverse or direct solver and accept a wide variation in boundary layer growth rates.

In order to generate a scheme suited to our particular needs, we adopted a number of uncommon but not unique procedures. We based the transformation from physical to computational coordinates directly on the displacement thickness δ^* rather than the more common Levy-Lees type transform. This type transform was used previously by Carter [1] for incompressible flow. Similarity solutions can be obtained in either primitive or stream-function form when the equations are written appro-

priately. A Keller type box scheme was used to solve the system of equations. We solved the continuity-momentum, energy, and turbulence model equations simultaneously rather than by iterating between them. The simultaneous solution of the entire equation system at each marching location leads to an efficient solution scheme in terms of computer time as it appears to have quadratic convergence rate at every point.

With these procedures the distinction between inverse mode and direct mode solutions was limited to a single boundary condition switch, and the ability to easily switch between direct and inverse mode calculations allowed us to study separation and reattachment point behavior in a systematic fashion. During this separation behavior study we were able to uncover what appear to be multiple, non-unique solutions to the boundary layer equations when solving the direct problem for decelerating flow.

In the present paper we present the analysis for the δ^* transformation, and show sample calculations in direct and inverse modes to demonstrate the computational efficiency of the present scheme. We then present a computational experiment to demonstrate that multiple solutions to the boundary layer equations always exist for decelerating flow. Since the multiple solutions always appear to involve reverse flow, we must make some approximation for the upstream momentum convection terms. To do this we introduced a modified Reyhner-Flügge-Lotz approximation. We believe that our basic results are independent of these approximations but are unable to prove this conclusively.

Analysis

Eqs. (1-5) are the two-dimensional, compressible, boundary layer equations written as a first-order system. An eddy viscosity and turbulent Prandtl number have been included to allow for turbulence modeling. Bars denote dimensioned quantities.

continuity:

$$\frac{\partial(\bar{\rho}\bar{u})}{\partial\bar{x}} + \frac{\partial(\bar{\rho}\bar{v})}{\partial\bar{y}} = 0 \quad (1)$$

x-momentum:

$$\bar{\rho}\bar{u}\frac{\partial\bar{u}}{\partial\bar{x}} + \bar{\rho}\bar{v}\frac{\partial\bar{u}}{\partial\bar{y}} = \frac{\partial\bar{\tau}}{\partial\bar{y}} + \bar{\rho}_e\bar{u}_e\frac{d\bar{u}_e}{d\bar{x}} \quad (2)$$

energy:

$$\rho u \frac{\partial \bar{h}}{\partial x} + \rho v \frac{\partial \bar{h}}{\partial y} = \frac{\partial \bar{q}}{\partial y} \quad (3)$$

shear definition:

$$\tau = (\bar{u} + \bar{u}_t) \frac{\partial \bar{u}}{\partial y} \quad (4)$$

\bar{q} definition:

$$\bar{q} = \left(\frac{\bar{u}}{\text{Pr}} + \frac{\bar{u}_t}{\text{Pr}_t} \right) \frac{\partial \bar{h}}{\partial y} + \mu \left(1 - \frac{1}{\text{Pr}} \right) \bar{u} \frac{\partial \bar{u}}{\partial y} \quad (5)$$

With the reference quantities L , ρ_0 , u_0 , T_0 , and $a_0 = \sqrt{\gamma R T_0}$, non-dimensional variables are defined as follows:

$$\Delta = \frac{\delta^*}{L} \sqrt{\text{Re}_0} \quad (6a)$$

$$u = \frac{\bar{u}}{a_0} \quad (6b)$$

$$v = \frac{\sqrt{\text{Re}_0}}{a_0} \left(\bar{v} - \frac{\bar{v}}{\delta^*} \frac{d\delta^*}{dx} \bar{u} \right) \quad (6c)$$

$$h = \frac{\bar{h}}{a_0^2} \quad (6d)$$

$$\tau = \frac{\bar{\tau}}{\rho_0 a_0^2} \sqrt{\text{Re}_0} \quad (6e)$$

$$q = \frac{\bar{q}}{\rho_0 a_0^2} \sqrt{\text{Re}_0} \quad (6f)$$

$$\mu = \frac{\bar{\mu}}{\mu_0} \quad (6g)$$

$$\mu_t = \frac{\bar{\mu}_t}{\mu_0} \quad (6h)$$

$$T = \frac{\bar{T}}{T_0} \quad (6i)$$

This unusual definition of the transformed normal velocity is used because it simplifies the intermediate and final equations. No computational problems are encountered when extracting the physical v velocity from this transformation. Using the displacement thickness, the computational coordinates x and y used in this analysis are defined as:

$$x = \frac{\bar{x}}{L} \quad (7a)$$

$$y = \frac{\bar{y}}{\delta^*} \quad (7b)$$

This coordinate transformation has some definite advantages over the commonly used Levy-Lees transformation. Because the normal coordinate grows as the displacement thickness, grid extension is never necessary, even in separation bubbles and rapidly growing turbulent boundary layers. This transformation is also trivial to invert. With the above definitions, Eqs. (1-5) become:

$$\frac{\partial(\rho u \Delta)}{\partial x} + \frac{\partial(\rho v)}{\partial y} = 0 \quad (8)$$

$$\rho u \Delta \frac{\partial u}{\partial x} + \rho v \frac{\partial u}{\partial y} = \frac{\partial \tau}{\partial y} + \rho_e u_e \Delta \frac{du_e}{dx} \quad (9)$$

$$\rho u \Delta \frac{\partial h}{\partial x} + \rho v \frac{\partial h}{\partial y} = \frac{\partial q}{\partial y} \quad (10)$$

$$\tau \Delta = (\mu + \mu_t) \frac{\partial u}{\partial y} \quad (11)$$

$$q \Delta = \left(\frac{\mu}{\text{Pr}} + \frac{\mu_t}{\text{Pr}_t} \right) \frac{\partial h}{\partial y} + \mu \left(1 - \frac{1}{\text{Pr}} \right) u \frac{\partial u}{\partial y} \quad (12)$$

Eqs. (8-12) are singular at the leading edge, and therefore cannot be used to generate a similarity solution to start streamwise marching. To overcome this problem, the equations are rewritten using the following similarity variables.

$$U = \frac{u}{u_e} \quad (13a)$$

$$V = \frac{v}{u_e} \frac{x}{\Delta} \quad (13b)$$

$$H = \frac{h}{h_e} \quad (13c)$$

$$S = \frac{1}{\rho_e u_e \Delta} \frac{x}{u_e} \tau \quad (13d)$$

$$Q = \frac{1}{\rho_e u_e \Delta} \frac{x}{h_e} q \quad (13e)$$

$$R = \frac{\rho}{\rho_e} \quad (13f)$$

$$M_e^2 = \frac{u_e^2}{T_e} \quad (13g)$$

$$\beta_u = \frac{x}{u_e} \frac{du_e}{dx} \quad (14a)$$

$$\beta_\Delta = \frac{x}{\Delta} \frac{d\Delta}{dx} \quad (14b)$$

The resulting equation set with relevant boundary conditions is:

$$\left(\beta_\Delta + \beta_u (1 - M_e^2) \right) RU + \frac{\partial(RV)}{\partial y} + x \frac{\partial(RU)}{\partial x} = 0 \quad (15)$$

$$\frac{\partial S}{\partial y} - RV \frac{\partial U}{\partial y} + \beta_u (1 - RU^2) = x RU \frac{\partial U}{\partial x} \quad (16)$$

$$\frac{\partial Q}{\partial y} - RV \frac{\partial H}{\partial y} = x RU \frac{\partial H}{\partial x} \quad (17)$$

$$S = \frac{x}{\rho_e u_e \Delta} \left(\mu + \mu_t \right) \frac{\partial U}{\partial y} \quad (18)$$

$$Q = \frac{x}{\rho_e u_e \Delta} \left(\frac{\mu}{\text{Pr}} + \frac{\mu_t}{\text{Pr}_t} \right) \frac{\partial H}{\partial y} + \mu \left(1 - \frac{1}{\text{Pr}} \right) \left(\frac{u_e^2}{h_e} \right) U \frac{\partial U}{\partial y} \quad (19)$$

Boundary conditions:

$$y=0: \quad 1) U = 0 \quad (\text{for boundary layer}) \quad (20a)$$

$$\text{or } S = 0 \quad (\text{for free wake}) \quad (20b)$$

$$2) V = 0 \quad (20b)$$

$$3) H = H_w \quad \text{or} \quad Q = Q_w \quad (20c)$$

$$y=y_e: \quad 4) U = 1 \quad (20d)$$

$$5) H = 1 \quad (20e)$$

Equations (15-20) can also be expressed in terms of a stream function F :

$$RU = \frac{\partial F}{\partial y} \quad (21)$$

$$\begin{aligned} \frac{\partial S}{\partial y} + \left(\beta_\Delta + \beta_u (1 - M_\infty^2) \right) F \frac{\partial U}{\partial y} + \beta_u \left(1 - U \frac{\partial F}{\partial y} \right) \\ = x \left(\frac{\partial F}{\partial y} \frac{\partial U}{\partial x} - \frac{\partial F}{\partial x} \frac{\partial U}{\partial y} \right) \end{aligned} \quad (22)$$

$$\begin{aligned} \frac{\partial Q}{\partial y} + \left(\beta_\Delta + \beta_u (1 - M_\infty^2) \right) F \frac{\partial H}{\partial y} \\ = x \left(\frac{\partial F}{\partial y} \frac{\partial H}{\partial x} - \frac{\partial F}{\partial x} \frac{\partial H}{\partial y} \right) \end{aligned} \quad (23)$$

$$S = \frac{x}{\rho_e u_e \Delta^2} \left(\mu + \mu_t \right) \frac{\partial U}{\partial y} \quad (24)$$

$$\begin{aligned} Q = \frac{x}{\rho_e u_e \Delta^2} \left(\frac{\mu}{Pr} + \frac{\mu_t}{Pr_t} \right) \frac{\partial H}{\partial y} \\ + \mu \left(1 - \frac{1}{Pr} \right) \left(\frac{u_e^2}{h_e} \right) U \frac{\partial U}{\partial y} \end{aligned} \quad (25)$$

Boundary conditions:

$$y=0: \quad 1) U = 0 \quad (\text{for boundary layer}) \quad (26a)$$

$$\text{or } S = 0 \quad (\text{for free wake}) \quad (26b)$$

$$2) F = 0 \quad (26b)$$

$$3) H = H_w \quad \text{or} \quad Q = Q_w \quad (26c)$$

$$y=y_e: \quad 4) U = 1 \quad (26d)$$

$$5) H = 1 \quad (26e)$$

Either formulation can be used. In this study, Eqs. (21-26) were solved, as a matter of personal preference.

Using these equations, the calculation of Falkner-Skan type similarity solutions is straightforward. For similarity, β_u is a constant, and $u_e(x)$ is of the form

$$u_e(x) = C_u x^{\beta_u} \quad (27)$$

Likewise, $\Delta(x)$ is of the form

$$\Delta(x) = C_\Delta x^{\beta_\Delta} \quad (28a)$$

and β_Δ is related to β_u by

$$\beta_\Delta = \frac{1 - \beta_u}{2} \quad (28b)$$

With these definitions, and the assumption that the similarity flow is laminar, equations (24) and (25) can be written as

$$S = \frac{1}{\rho_e C_u C_\Delta^2} \mu \frac{\partial U}{\partial y} \quad (29)$$

$$Q = \frac{1}{\rho_e C_u C_\Delta^2} \frac{\mu}{Pr} \frac{\partial H}{\partial y} + \mu \left(1 - \frac{1}{Pr} \right) \left(\frac{u_e^2}{h_e} \right) U \frac{\partial U}{\partial y} \quad (30)$$

For normal marching calculations, u_e is known and Δ unknown (direct problem), or vice versa (inverse problem). When a similarity solution is being calculated, the global unknown is either C_Δ (direct similarity), or C_u (inverse similarity), with β_u and β_Δ held fixed at their prescribed values. The x -dependent terms are eliminated by setting x equal to zero.

Strictly speaking, similarity solutions exist only for the zero pressure gradient case, since R , ρ_e , μ , M_∞ , and u_e^2/h_e which appear in the equations are all functions of u_e and therefore depend on x if u_e is not constant. In practice, however, all wedge flows with nonzero pressure gradient found in applications have a stagnation point at the leading edge, where the local flow is essentially incompressible. In this region, the troublesome quantities mentioned above are either negligibly small or can be treated as constants. Thus, similarity can be obtained at the leading edge ($x = 0$), or for a point sufficiently close to the leading edge so that stagnation conditions exist within some tolerable error.

Solution Scheme

The finite difference scheme used in this study is a Modified Keller's Box Scheme (Figures 1 and 2). The Standard Keller's Box Scheme was obtained from Cebeci and Smith [2].

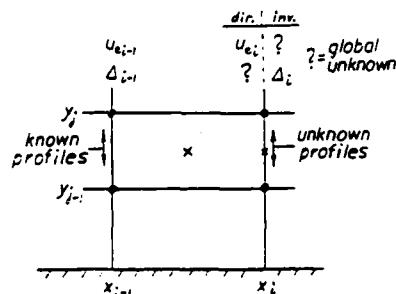


Fig. 1. Standard Keller's Box Scheme.

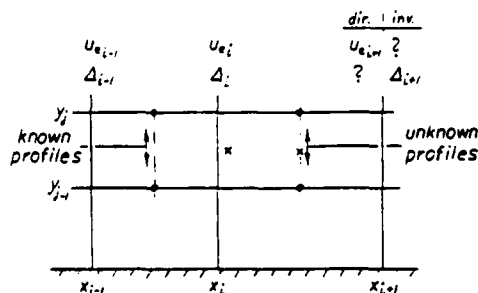


Fig. 2. Modified Box Scheme

The literature is unclear as to how β_u is to be evaluated from u_e . If we specify the gradient parameters (β 's) midway between the two profiles rather than at the profile positions, then streamwise profile oscillations with little tendency to damp out will occur (see Figure 3). This behavior is readily explained by noting that equations (12) and (24) at the wall reduce to

$$\beta_u \approx k(x) \frac{d^2 U}{dy^2} \quad (31)$$

where $k(x)$ is a weak function of x . Since β_u is specified at the box midpoints, equation (31) constrains the average of $d^2 U/dy^2$ between any two successive streamwise stations:

$$\beta_{u, i+1/2} = \frac{k}{2} \left[\left(\frac{d^2 U}{dy^2} \right)_{i+1} + \left(\frac{d^2 U}{dy^2} \right)_i \right] \quad (32)$$

Hence, at the wall, $d^2 U/dy^2$ can have large amplitude excursions with alternating signs and still satisfy the finite difference equations. Figure 3 shows that the velocity profiles do indeed exhibit these fluctuations following a disturbance. The Modified Box Scheme eliminates this problem by calculating the profiles midway between the x stations. Here, β_u is specified at the same position as the profiles:

$$\beta_{u, i+1} = k \left(\frac{d^2 U}{dy^2} \right)_{i+1/2} \quad (33)$$

Thus, the velocity profiles cannot oscillate at the wall because each one is individually constrained (see Figure 4).

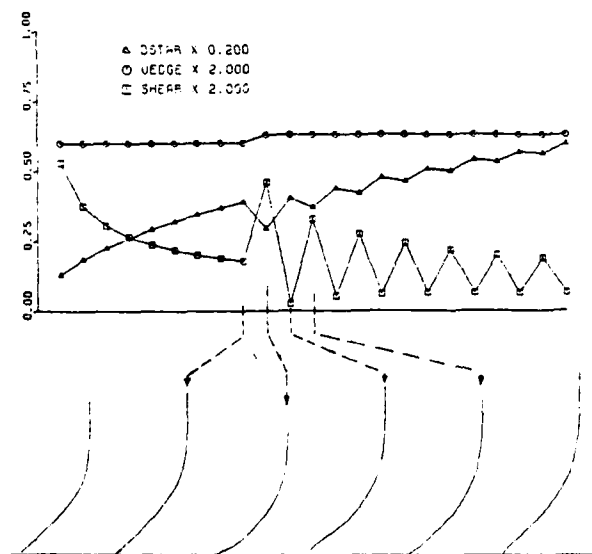


Fig. 3. Response of Standard Box Scheme to 5% edge velocity jump.

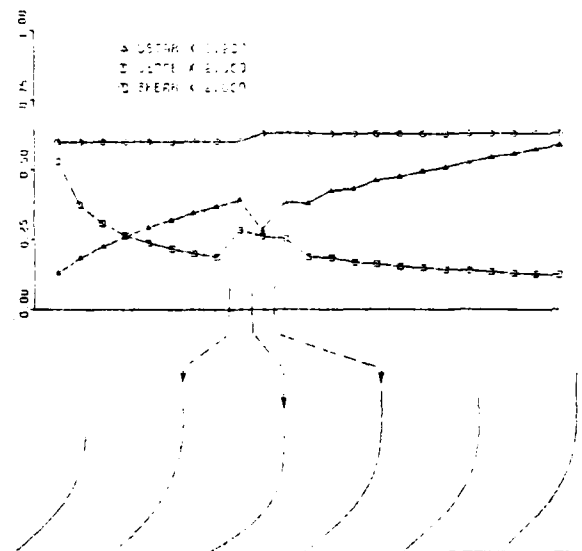


Fig. 4. Response of Modified Box Scheme to 5% edge velocity jump.

Solution Procedure

At each streamwise marching step, there are five unknowns at each y_j station at streamwise station $x_{i+1/2}$: F_j , U_j , H_j , S_j , and Q_j . In addition, there is one global (independent of y) unknown at x_{i+1} : u_{ei+1} , or Δ_{i+1} . It is convenient, however, to treat both of these quantities as unknown when the governing equations are discretized.

Since the discretized equations do not call for u_{ei+1} or Δ_{i+1} , but instead require the midpoint values $u_{ei+1/2}$ and $\Delta_{i+1/2}$, the latter are temporarily taken as the global unknowns while the profiles are calculated. For convenience, the lack of a subscript on a gradient parameter or x will from now on imply $i+1/2$. The gradient parameters are defined as:

$$\beta_u = \frac{\ln (u_e/u_{ei})}{\ln (x/x_i)} \quad (34a)$$

$$\beta_\Delta = \frac{\ln (\Delta/\Delta_i)}{\ln (x/x_i)} \quad (34b)$$

These definitions were chosen because they allow arbitrarily large streamwise steps in similar flows.

After u_e , Δ , and the unknown profiles are calculated, u_{ei+1} or Δ_{i+1} are determined from the following relationships and stored for the next marching step.

$$u_{ei+1} = u_{ei} \left(\frac{x_{i+1}}{x_i} \right)^{\beta_u} \quad (35a)$$

$$\Delta_{i+1} = \Delta_i \left(\frac{x_{i+1}}{x_i} \right)^{\beta_\Delta} \quad (35b)$$

Following common practice, the iterates δF , δH , δS , and δQ are introduced in the linearization and discretization process. The wall shear rate δS_w is introduced at this point since it appears in the linearized expression of the inner viscosity (the Cebeci-Smith two-layer model is used). Together with δS_w , the global iterates $\delta \Delta$ and $\delta \Delta$ are lumped on the righthand side to collectively produce four blocktridiagonal systems with a common coefficient matrix of 5x5 blocks.

$$\begin{bmatrix} \delta F \\ \delta H \\ \delta S \\ \delta Q \end{bmatrix} = \begin{bmatrix} a \\ b \\ c \\ d \end{bmatrix} - \delta u_e \begin{bmatrix} e \\ f \\ g \\ h \end{bmatrix} - \delta \Delta \begin{bmatrix} i \\ j \\ k \\ l \end{bmatrix} - \delta S_w \begin{bmatrix} m \\ n \\ o \\ p \end{bmatrix} \quad (36)$$

Iterates which are not explicitly included in the system are expressed as linear combinations of included iterates. Equations (37-39) are examples of how these combinations are made.

$$\frac{\rho}{\rho_e} = \frac{T_e}{T} = \frac{1 - u_e^2/2h_e}{H - U^2 u_e^2/2h_e} \quad (37a)$$

$$\delta U \frac{\partial R}{\partial U} + \delta H \frac{\partial R}{\partial H} + \delta u_e \frac{\partial R}{\partial u_e} \quad (37b)$$

$$\mu_t = 0.0168 \rho \sqrt{Re_o} \Delta u_e \gamma_{tr} \quad (38a)$$

$$\delta \rho \frac{\partial \mu_t}{\partial \rho} + \delta u_e \frac{\partial \mu_t}{\partial u_e} + \delta \Delta \frac{\partial \mu_t}{\partial \Delta} \quad (38b)$$

$$\beta_u = \frac{\ln(u_e/u_{ei})}{\ln(x/x_i)} \quad (39a)$$

$$\delta u_e \frac{d\beta_u}{du_e} = \delta u_e \frac{1}{u_e \ln(x/x_i)} \quad (39b)$$

After the systems are solved with a block tri-diagonal algorithm, each unknown is expressed as a value r_j minus the global iterates times respective influence coefficients a_j , b_j , c_j , d_j ($j=1, 2, \dots, J$).

$$r_{1j} - \delta u_e a_{1j} - \delta \Delta b_{1j} - \delta S_w c_{1j} \quad (40a)$$

$$r_{2j} - \delta u_e a_{2j} - \delta \Delta b_{2j} - \delta S_w c_{2j} \quad (40b)$$

$$r_{3j} - \delta u_e a_{3j} - \delta \Delta b_{3j} - \delta S_w c_{3j} \quad (40c)$$

$$r_{4j} - \delta u_e a_{4j} - \delta \Delta b_{4j} - \delta S_w c_{4j} \quad (40d)$$

$$r_{5j} - \delta u_e a_{5j} - \delta \Delta b_{5j} - \delta S_w c_{5j} \quad (40e)$$

Since there are three unknowns left, namely δu_e , $\delta \Delta$, and δS_w , three more equations are required. One is obtained from the definition of momentum thickness (by integrating (21)).

$$F_e - F_w = \gamma_e - 1 \quad (41a)$$

$$\delta F_J - \delta F_1 = \gamma_e - 1 - F_e + F_w \quad (41b)$$

Another equation is obtained from the identity

$$S_w = S_1 \quad (42a)$$

$$\text{or } \delta S_w = \delta S_1 \quad (42b)$$

The third equation is determined by whether the direct, inverse, or hybrid problem is being solved.

$$\text{direct: } \delta u_e = 0 \quad (43a)$$

$$\text{inverse: } \delta \Delta = 0 \quad (43b)$$

$$\text{hybrid: } \delta u_e(A) + \delta \Delta(B) = C \quad (43c)$$

Note that the only difference between the direct and inverse calculation modes occurs in this final step. The hybrid mode is extremely useful in viscous-inviscid interaction calculations. By substituting (40a) into (41b) and (40d) into (42b), a simple 3x3 system for the global unknown iterates is obtained.

$$\begin{bmatrix} (a_{11} - a_{1J}) & (b_{11} - b_{1J}) & (c_{11} - c_{1J}) \\ (a_{41}) & (b_{41}) & (c_{41} + 1) \\ (1 \text{ or } 0) & (0 \text{ or } 1) & 0 \end{bmatrix} \times \begin{bmatrix} \delta u_e \\ \delta \Delta \\ \delta S_w \end{bmatrix} = \begin{bmatrix} r_{11} - r_{1J} + \gamma_e - 1 - F_e + F_w \\ r_{41} \\ 0 \end{bmatrix} \quad (44)$$

Because the variations of all quantities are taken into account, the entire system converges quadratically. This property drastically reduces calculation time for flows in which the energy equation and/or turbulence model significantly affect the momentum equation. Figure 5 shows the advantages of taking account of the variation of eddy viscosity for laminar flat plate flow transitioning to fully turbulent flow. The transition was achieved by artificially varying the turbulence intermittency factor in a continuous manner. Note that the higher the Reynolds Number, the stronger the effect of the turbulence on the momentum equation, and the higher the payoff of linearizing the eddy viscosity.

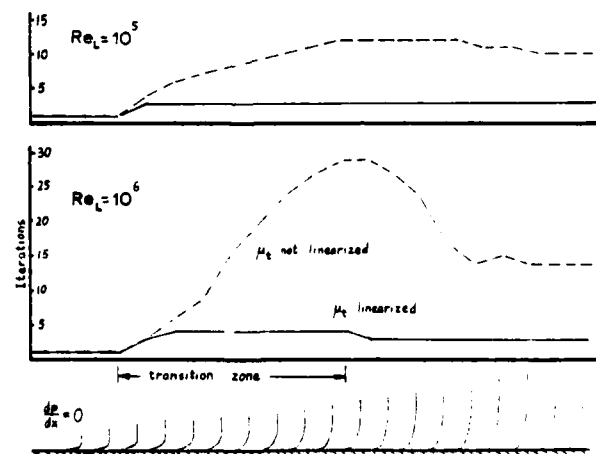


Fig. 5. Effect of linearizing eddy viscosity on the number of iterations per streamwise station. Convergence criterion: $\delta U_{max} < 10^{-5}$

AD-A134 151

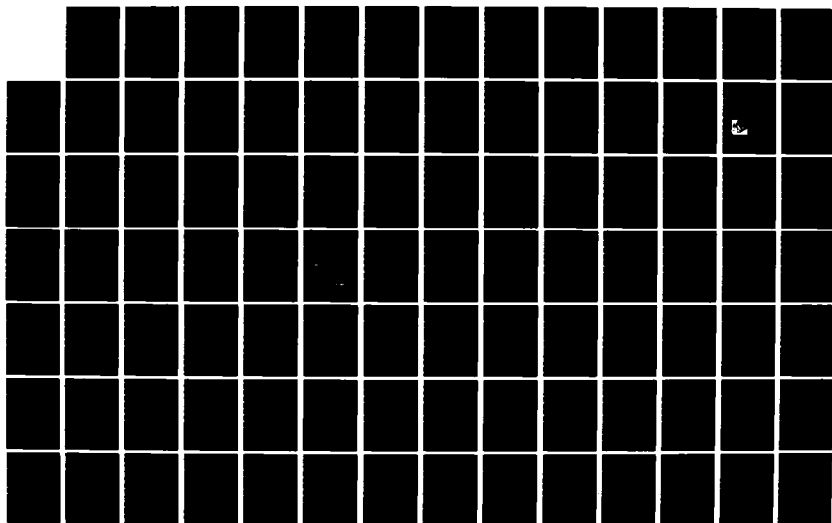
SYMPOSIUM ON NUMERICAL AND PHYSICAL ASPECTS OF
AERODYNAMIC FLOWS (2ND) 17-20 JANUARY 1983(U)
CALIFORNIA STATE UNIV LONG BEACH T CEBECI 1983

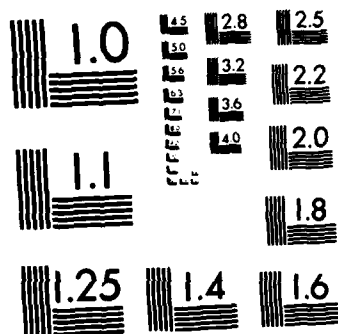
2/5

UNCLASSIFIED

F/G 20/4

NL





MICROCOPY RESOLUTION TEST CHART
NATIONAL BUREAU OF STANDARDS-1963-A

The Reyhner-Flügge-Lotz approximation, which is applied to regions of reverse flow, consists of setting the streamwise convective terms $U(\partial U/\partial x)$ and $U(\partial H/\partial x)$ to zero. This is necessary to avoid growth of numerical errors and to prevent a zone of dependence violation.

All the test cases run indicated that it is possible to retain the momentum convection term $U(\partial U/\partial x)$ in reverse flow simply by eliminating only its contribution to the variable iterates, thus avoiding artificial growth of numerical errors. This convection term is still retained in the residues (i.e. the righthand side of (36)). All results presented in this investigation which involved reverse flow were calculated using this Modified Reyhner-Flügge-Lotz approximation. Of course, setting the variation of any term to zero destroys the quadratic convergence of the overall system. However, the contribution of convection terms is small in separated flow, and as a result the number of iterations per streamwise step rarely exceeded five.

Results and Discussion

To gain confidence in the solution scheme presented here, an inverse calculation using the displacement thickness distribution given by Carter [1] was performed. Figure 6a compares the wall shear calculated with the present method to the values calculated and tabulated by Cebeci [3]. Since Cebeci's calculations were for incompressible flow, a freestream Mach Number of 0.015625 was used to make compressibility effects negligible.

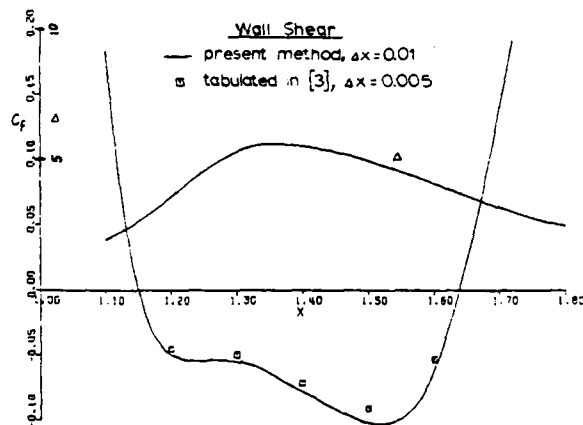


Fig. 6a. Carter's inverse test case.
Fine grid calculation.

Cebeci observed streamwise oscillations inside the bubble for a Δx of 0.005 or larger. The test shown in Figure 6a was performed with a Δx of 0.01 with no indication of oscillations. In an attempt to induce these oscillations, a case with the large Δx of 0.05 was run. Figure 6b shows the computed solution. Again, no oscillations were found, despite the extremely coarse grid.

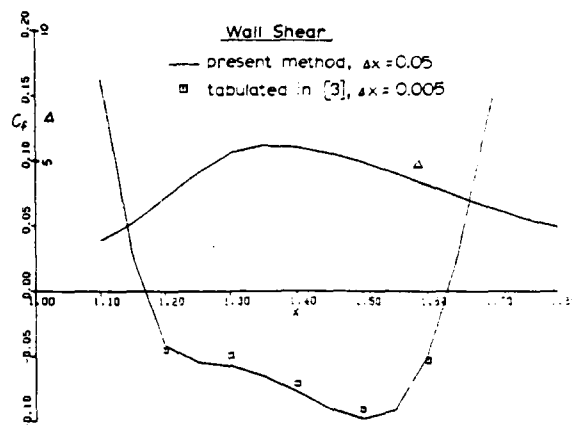


Fig. 6b. Carter's inverse test case.
Coarse grid calculation.

Using the solution scheme presented here it is possible to investigate in detail the relationships between u_e , Δ and wall shear with relative ease, since the calculation mode can be changed from direct to inverse and vice-versa at any marching step.

We first assume that all global quantities at the $i-1$ th and i th stations, and the profiles midway between those two stations are known (see Figure 2). Now consider the usual inverse problem of calculating the u_e and profiles at $x_{i+1/2}$ which correspond to a specified Δ . If this specified Δ is deliberately varied in some systematic manner, a relationship between u_e and Δ (or, equivalently, between β_u and β_Δ) can be determined. Figure 7a shows such a relationship together with the corresponding wall shear at $x_{i+1/2}$. In this case the known upstream profile corresponds closely to the Blasius profile for zero pressure gradient. Several surprising features are apparent:

- 1) When β_u turns out to be negative, (i.e. u_e is less than u_{ei} and an adverse pressure gradient is present) there are two values of Δ and corresponding β_Δ 's which will produce this β_u .
- 2) The smaller Δ always gives a positive wall shear, the larger Δ always gives a negative wall shear.
- 3) There is a minimum permissible β_u and hence a minimum permissible u_e . If a direct problem was being solved and the specified u_e was less than this minimum, no solution to the finite difference equations would exist.
- 4) The minimum u_e occurs when the wall shear equals zero.

Assume now that a direct problem is being solved and that a moderate adverse pressure gradient of -0.16 is specified at $x_{i+1/2}$. Figure 4 clearly shows that two distinct solutions are possible. However, the Δ corresponding to attached flow produces a smooth continuation from the preceding stations, while the Δ corresponding to separated flow is ridiculously large and has a radically different profile from the previous stations (see Figure 7b). Because the initial guesses for Δ and the profiles are obtained by extrapolating from the

two previous stations, the iterative solution scheme in this case always converges on the "reasonable" solution, since it is the one closest to the initial guess.

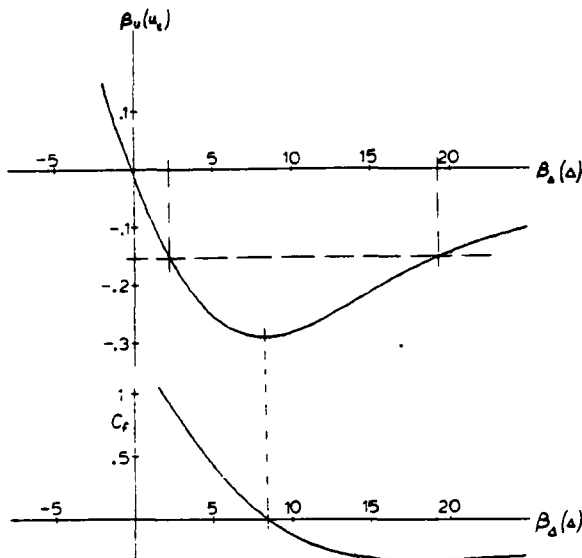


Fig. 7a. Gradient parameter and wall shear relations far from separation.

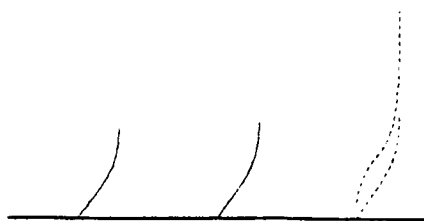


Fig. 7b. Two profiles (dashed) corresponding to the same edge velocity. Upstream profiles are far from separation.

This situation changes significantly if the known upstream profile is close to separation. If the same pressure gradient as in the previous case is specified (Figure 8a), the two possible values of Δ are now quite close together. Furthermore, it is not clear which solution is reasonable and which is not since the two possible profiles are very nearly the same (see Figure 8b). If a direct solution to the specified β_u and corresponding u_e is blindly attempted, the iterative algorithm will wander aimlessly between the two possible values of Δ . Also note that β_u is locally quite insensitive to β_w in contrast to the case in Figure 7a. This implies that the direct problem (convergence to a specified edge velocity) is ill-conditioned near the point of zero wall shear. Of course, it is also possible to specify a value u_e which is below the minimum and therefore has no solution. On the other hand, it is easy to see that the inverse problem is well-conditioned no matter what state the boundary layer is in.

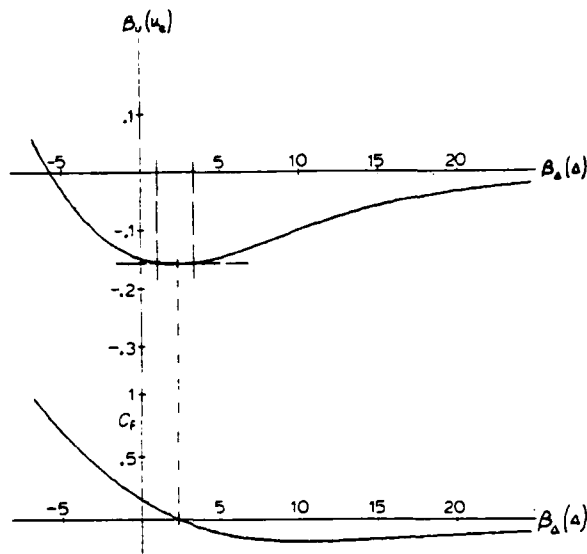


Fig. 8a. Gradient parameter and wall shear relations close to separation.

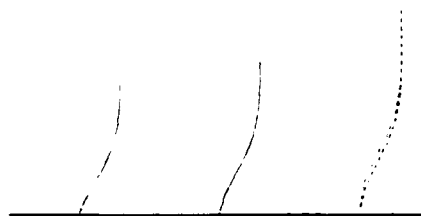


Fig. 8b. Two profiles (dashed) corresponding to the same edge velocity. Upstream profiles are close to separation.

Although the direct problem is ill-conditioned at separation and reattachment, it is not necessarily incomputable. A direct mode solution is performed in the usual manner until the sensitivity of Δ to u_e increases above some value, making direct convergence impossible. The sensitivity can be quantitatively determined from (44). The sensitivity typically rises drastically at the x stations just before separation and reattachment. At these points, the inverse mode is used to determine the relationship between u_e and Δ for the next station. Four values of Δ which bound the two solutions are thus defined. At this point, one branch is chosen, and the inverse mode is used iteratively to converge on the specified u_e . This is done by repeatedly subdividing the interval which contains the correct u_e (see Figure 9).

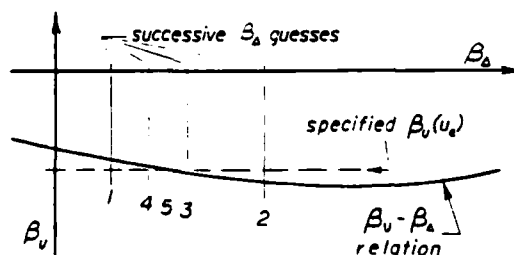


Fig. 9. Direct problem calculation procedure near separation and reattachment.

Once inside the bubble, the direct mode can be marched in the usual way. The iterative procedure must again be used to get past reattachment.

Figure 10 shows a supersonic diffuser with a weak oblique shock impinging on a flat plate boundary layer. Pressure and wall shear measurements were performed by Hakkinen [7] along the bottom wall in the vicinity of the impinging shock. The direct marching procedure described above was carried out using the u_e distribution corresponding to the measured pressure. Because the shock is very weak, stagnation pressure loss was neglected. Liberty was taken in smoothing out the slight noise present in the measurements inside the bubble. Figure 11 shows the calculated Δ and wall shear. The agreement with the measured wall shear is reasonably good.

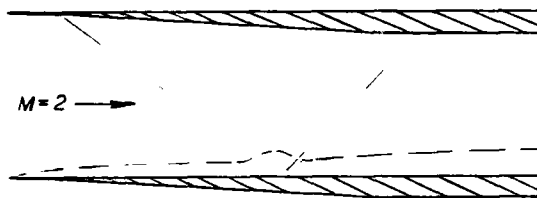


Fig. 10. Supersonic diffuser with shock-boundary layer interaction.

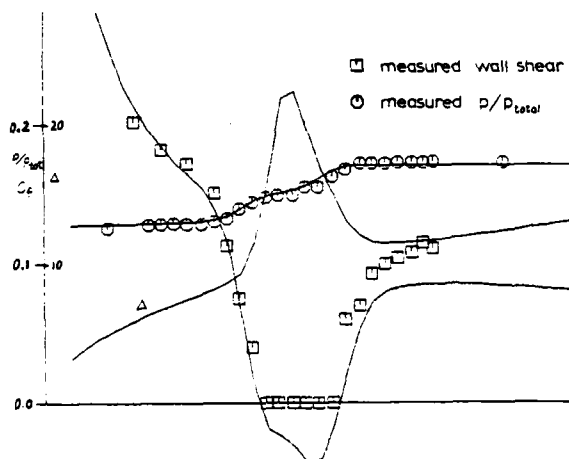


Fig. 11. Direct problem calculation through separation and reattachment. Specified edge velocity is from measured pressure distribution.

It must be stressed that solving direct problems involving separation is generally impractical. Extensive human judgement is necessary in deciding which solution branch to take at each station near separation and reattachment and in smoothing the input u_e distribution. The case presented is merely a curiosity and serves as a demonstration of our ideas about separation point behavior.

The relationships between δ_u and δ_Δ shown in Figures 7 and 8 correspond to a freestream Mach Number of 0.0625, making the flow essentially incompressible. To determine what role compressibility plays in the non-unique character of the direct solutions, tests were also performed for Mach Numbers of 0.8 and 1.5. There was no qualitative change in the δ_u - δ_Δ relationships shown in Figures 7 and 8.

Finally, it must be mentioned we believe that the nonuniqueness of the direct problem is not due to the modified Reyhner-Flügge-Lotz approximation, which is applied in reverse flow regions to avoid zone of dependence violation and to avoid numerical instability. The original Reyher-Flügge-Lotz approximation allowed multiple solutions for all pressure gradients, whereas the modified approximation allows multiple solutions only for adverse pressure gradients. At the separation point where the occurrence of multiple solutions is most important, both solutions approach each other and no upstream momentum convection exists. Further work must be done to assess the role upstream momentum convection plays at separation and reattachment points.

Acknowledgments

This work was supported under NASA Training Grant NGT-22-009-901.

References

- [1] J.E. Carter, "Inverse Solutions for Laminar Boundary-Layer Flows With Separation and Reattachment," NASA TR R-447, 1975.
- [2] J.E. Carter, "Development of a Prediction Method for Transonic Shock Induced Separated Flow," URTC Report R80-915213-4, 1980.
- [3] T. Cebeci, H.B. Keller, and P.G. Williams, "Separating Boundary-Layer Flow Calculations," Academic Press, New York, 1979.
- [4] T. Cebeci and P. Bradshaw, "Momentum Transfer in Boundary Layers," McGraw-Hill, New York, 1977.
- [5] P. Bradshaw, T. Cebeci, and J.H. Whitelaw, "Engineering Calculation Methods for Turbulent Flow," Academic Press, New York, 1981.
- [6] T. Cebeci and A.M.O. Smith, "Analysis of Turbulent Boundary Layers," Academic Press, New York, 1974.
- [7] R.J. Hakkinen, I. Greber, L. Trilling, and S.S. Abarbanel, "The Interaction of an Oblique Shock Wave with a Laminar Boundary Layer," NASA Memo 2-18-59W, 1959.
- [8] H. Schlichting, "Boundary Layer Theory," McGraw-Hill, New York, 1968.

MEASUREMENTS AND CALCULATIONS OF A SEPARATING
BOUNDARY-LAYER AND THE DOWNSTREAM WAKE

D. Adair, B.E. Thompson and J.H. Whitelaw
Imperial College of Science and Technology
Department of Mechanical Engineering
Fluids Section, London SW7 2BX

Abstract

A combination of total-head pressure, static-pressure, hot-wire and flying hot-wire probes have been used to quantify the pressure and velocity characteristics of the flow in the vicinity of a trailing flap whose angle of incidence results in boundary layer separation, a large region of recirculating flow and a curved downstream wake. A two-dimensional form of the time-averaged Navier-Stokes equations has been solved numerically with a finite difference grid obtained by a solution of Laplace equation and the results compared with the measurements. The general flow patterns are well calculated and the results are in close accord in some regions of the flow. In others, including the near-wall region and near wake, significant discrepancies exist and numerical tests suggest that these are due to numerical assumptions although the two-equation turbulence model and related wall functions are also likely to be deficient.

1. Introduction

The paper describes the progress made in a project intended to develop a calculation method, based on the Navier-Stokes equations, to represent the velocity and pressure characteristics of the flow around the trailing edge of airfoils at high angle of incidence. The calculation method is based on the numerical procedure introduced by Gosman and Pun¹ and applied to a range of flow configurations by many authors. Since the calculated results are approximate, measurements of the flow around and downstream of a trailing flap arranged at incidence in order to introduce a large region of recirculation, have been obtained and are compared with calculation in orthogonal curvilinear coordinates on a staggered grid using the corresponding measured boundary conditions.

Most existing methods for the calculation of the flow around airfoils make use of a combination of potential-flow and boundary-layer equations. Inverse procedures become necessary where the angle of incidence is sufficiently great to cause upper-surface separation, and where the region of recirculating flow exceeds a value which remains to be established, the boundary-layer approximations cease to apply and the Navier-Stokes equations are required. The measurements of Nakayama², for example, suggest that the boundary-layer approximations are likely to be adequate for his upper surface flow which separated at around 98° chord. The flow chosen for the present investigation separated some 20cm upstream of the trailing edge of the flap and seemed likely to require consideration of the normal momentum equation and longitudinal diffusion. This supposition is considered here.

The flow over the flap is shown to be two-dimensional, steady and incompressible. As a consequence of the two-dimensionality, the Laplace

equation was solved with the wind tunnel and flap surfaces as boundary conditions and provided lines of constant stream function and velocity potential which represented the grid used in the solution of the Navier-Stokes equations. This coordinate system is orthogonal, requires an assumption for the dividing streamline downstream of the trailing edge and takes no account of the separated flow. Thus, in any region of separated flow, the streamlines are likely to intersect the finite-difference grid at an angle with consequent numerical error for the present hybrid-differencing algorithm. Errors of this type may be avoided by higher order differencing schemes but it is desirable to assess the magnitude of the problem before exploring more complex schemes with their likely convergence penalties.

The solution of time-dependent equations implies the need for a closure assumption to represent the unknown Reynolds stress terms and, in common with many previous investigations of flows which separate from surface discontinuities, a two-equation model has been used. The experimental investigation required approximately half of the present effort and is accordingly described in detail. It made use of a flying hot-wire arrangement to measure the characteristics in the regions of separated and high turbulence intensity flow and the precision and application of the technique are discussed.

The problem of measurements in the separated flows in the vicinity of airfoils at angle of attack has been considered in a number of previous papers among which those of Young et al³, Bachalo and Johnson⁴, Coles and Wadcock⁵, Solignac⁶, Johnson and Spaid⁷ and Nakayama² are worthy of special note in that they made use of either laser-Doppler velocimetry or, as in the third paper, flying-wire anemometry. The laser-anemometry measurements of Simpson et al⁸ and Hastings and Moreton⁹ were also made in turbulent separating boundary layers and are relevant to the present work. Calculations of boundary layers up to separation were considered in the 1968 Stanford Conferences [Coles and Hirst¹⁰] and some further work is referred to by Le Balleur et al¹¹, Bradshaw et al¹², Melnik¹³ and Marvin¹⁴. In general, the calculation efforts which account for regions of separated flow have made use of interactions between solutions of the potential and boundary-layer equations.

Exceptions include Murphy¹⁵, Thompson et al¹⁶, Sugavanam and Wu¹⁷ and Rhie and Chow¹⁸ who solve a form of the Navier-Stokes equations to predict separation. Among the relevant wake studies are those of Andreopoulos and Bradshaw¹⁹, Viswanath et al²⁰, Yu²¹, Hah and Lakshminarayana²² and Baker et al²³; the second includes calculations which compare solutions obtained with the boundary layer equations and the Navier-Stokes equations for a symmetric wake and the second last solves the elliptic Navier-Stokes equations in boundary layer co-ordi-

nates for an asymmetric wake. The final paper solves a parabolised form of the Navier-Stokes equation with a viscous-corrected potential flow solution. In general, present experimental and computational investigations have been concerned with small regions of separated flow and their consequences for the downstream wake.

Our objective is to develop a calculation method but, since this required consideration of a particular flow, the experimental investigation is described next and is followed by a section dealing with the equations, turbulence model, finite-difference assumptions and solution algorithm. The results of the calculation method are presented and compared with the measured values in the fourth section which discusses the precision and implications for future work.

II. Experimental Investigation

The flow configuration is shown on figure 1 and comprised a 1m flat plate with a trailing flap located in the working section of a low speed wind tunnel. The cross-section of the tunnel was 450x300mm and the uniform velocity at exit from the 8 to 1 area contraction was 26.3m/s with an rms of the corresponding fluctuations of 0.24m/s. The flat plate was located at 1 degree incidence and the flap at 17.5 degrees, both with respect to the tunnel coordinates. The boundary layers on the upper surface of the plate and the tunnel roof were subjected to trips, comprising of 1.5mm wire, and located 0.57m from the leading edge. The trailing flap was 250mm long and was connected to the plate by a radius of 812.5mm. This arrangement caused the upper surface boundary layer to separate approximately 200mm upstream of the trailing edge and gave rise to the characteristic boundaries indicated on figure 1.

In the upstream region of the upper surface, for most of the lower surface and for much of the wake, the flow had a preferred direction and comparatively low turbulence intensities. In these regions, it was possible to measure the velocity characteristics with impact probes and, as outlined by Thompson and Whitelaw²⁴, a combination of Pitot tubes, static pressure probes, static wall-pressure taps and hot wires allowed measurements in and around the wall boundary layers. For the results presented here, and away from the separated flow region, a Pitot-static probe of external diameter 2.2mm provided information of the mean velocity and static pressure distributions. Close to the separation region and where the flow angle deviated significantly from that of the surface, a five-hole probe of 2.5mm external diameter guided the use of the Pitot static tube and quantified the flow-angle distribution. Close to the wall, a flattened Pitot tube of 0.45mm external width allowed the measurement of mean velocity with reduced blockage and gradient effects.

In the boundary layers and in the downstream wake, velocity characteristics were determined with single (DISA 55P11) and cross-wire probes (DISA 55P61) linked to anemometers (DISA 55M10) and, through a mini computer (PDP8E) and analogue-to-digital voltage convertor (AD01) to a digital magnetic tape. The wires were calibrated in the free stream of the wind tunnel and digitally linearised on the mini computer with the procedures recommended by Thompson²⁵. The transform

functions used to obtain velocity characteristics from the signal voltage are the same as those described by Ribeiro and Whitelaw²⁶.

Measurements are more difficult in a region of separated flow with laser velocimetry, pulse-wire anemometry and flying-wire anemometry offering different possible advantages. A flying-wire arrangement was selected for the present measurements of velocity characteristics which were supplemented by static-pressure measurements obtained with the five-hole probe. The essential details of the flying-wire mechanism are provided in Table 1. The signals from an encoder, which identified the position of measurement and the probe velocity, and from the anemometer or anemometers were obtained simultaneously and ensemble averaged to within 1.5% with a 95% confidence level. The effective velocity transform equations were similar to those for the stationary wire but modified to take account of the known wire velocity. Further details have been reported by Thompson²⁷.

The two-dimensionality of the flow was examined in several ways. In the upstream boundary layer measurements of wall static pressure, mean velocity profiles and normal stress profiles were identical at any S-location, within experimental error, over more than 90% of the tunnel width. Surface flow visualisation showed that the mean separation line was straight and normal to the flow over the central 140mm of the flap although passive side-wall control vanes were required to achieve this. The flying wire was used to measure mean velocity profiles on the geometric centre-line and 50mm to either side and the results, which were obtained at values of s/c of 0.96, x/c of 1.06 and 1.20, agreed within 1.5% of the local values.

The skin friction coefficient, wall static pressure coefficient, free-stream velocity and static pressure coefficient normalised with the free stream velocity and static pressure at the boundary layer trip are shown in Figure 2. The values of skin friction coefficient were obtained from Clauser charts using $k=0.41$ and $B=5$ which confirmed that a logarithmic region exists in the attached boundary layer prior to separation albeit reducing in width with downstream distance. The influence of the change in wall curvature, at s/c of 0.68, can be seen to have affected the pressure and velocity field some 5% of chord further upstream. The static pressure coefficient varies between the wall and the free stream from just upstream of the curvature and throughout the separated region to the trailing edge.

Figure 2 also shows the momentum thickness and shape factor, calculated with the velocity measured locally at the edge of the boundary layer. Values are presented for the separated region although their applicability is limited since terms in the cross-stream momentum equation are important in this region. It can be seen from the momentum thickness and shape factor that the boundary layer grows rapidly as separation is approached with values of 8mm and 2.7 respectively at the location of mean streamline detachment.

The distribution of static pressure coefficient in the attached boundary layer and wake are shown on figure 3. The magnitude of the cross-stream pressure gradient increases as detachment is approached and at s/c of 0.826, achieves a value

which is approximately 2.6 times that of the longitudinal pressure gradient. The implications of these pressure variations are discussed further in section 4.

The general organisation of the mean velocities in the separated region is represented by the vector and streamline plates of Figure 4. The streamlines were determined by integrating the mean velocity profiles and show the negative velocity region close to the surface and throughout the length of the bubble. The cross-stream velocity in the separated region is larger than the corresponding streamwise velocity particularly in the regions of flow approaching attachment and after separation of the reverse flow boundary layer: they are small, however, compared with the free stream velocity. The negative flow region extends about 25mm beyond the trailing edge after which the shear layers which circumvent the recirculation interact and develop into the asymmetric wake.

Profiles of mean velocity and flow angle are shown on figures 5 and 6 respectively for the region up to separation, in the separated region, and in the wake: it should be noted that the coordinate system has changed at the trailing edge to correspond to the tunnel rather than the body although the flow angle is measured relative to the tunnel throughout. The measurements for the attached boundary layer extend to s/c of 0.87 and measurements with a predominant direction in the wake begin at $x/c=0.016$ although instantaneous flow reversals were still experienced. The intervening region features the recirculation bubble with its maximum 40mm width and 250mm length and negative mean velocities less than 20% of the free stream value. The free shear layer which circumvents the upper boundary of the recirculation region appears to start forming at approximately 7% of chord upstream of the location where the mean streamlines detach from the surface. In the velocity profiles downstream of this and before detachment, the mean velocity gradient across the flow, $\partial U/\partial y$, decreases and then increases at a distance less than 10 per cent of the boundary layer thickness away from the wall. The corresponding kink in the velocity distribution may occur because the mean flow near the wall is deflected outwards around the region of recirculation. The corresponding flow angles in this region indicate the tendency towards separation with the rapid increase in flow angle spreading away from the surface as separation is approached. The velocity profiles in the separated region are characterised by the shear layer at the edge of the recirculation bubble which spreads as the strain rate increases with downstream distance and by the reverse flow boundary layer which begins around the trailing edge and continues towards the location of mean streamline detachment. The flow angle is consistent with the larger transverse velocity directed towards the surface in the lower half of the bubble and particularly in the vicinity of the trailing edge and of the separation of the reverse-flow boundary layer.

The wake can be divided into three regions: the very near wake where negative mean velocities exist, the near wake where the shear layers from the suction and pressure side interact and the far wake where recovery to a fully developed plane mixing layer occurs. The very near wake extends

from the trailing edge to x/c of 0.021 and includes about 12 per cent of the length of the recirculation bubble. The mean velocity remains small inside the bubble after the trailing edge and its direction indicates there is entrainment from the outer forward flowing boundary layer as the rear stagnation point is approached. Downstream of the location where the two shear layers interact, the shape factor asymptotically approaches 1.4 as the momentum thickness decreases at a faster rate than the displacement thickness. Here, the static pressure variation across the boundary layer decreases with downstream distance. At x/c of 0.066 a pressure difference exists between the suction and pressure sides which gradually reduces until they are equal at the end of the near wake at about 20% of chord downstream of the trailing edge. In the far wake, beyond x/c of 0.25, the mean velocity recovers to form a plane mixing layer profile.

III. Computational Investigation

The results discussed here relate to the region of the flow identified by the solution domain of figure 7. Thus, boundary conditions were assigned on all sides of the solution domain and the differential equations solved, in finite-difference form and with a mesh of grid points determined with the aid of a solution of the corresponding potential-flow equations. The equations solved represent mean conservation of mass, momentum, kinetic energy and rate of turbulent dissipation and may be written in the form shown below with the coefficients given in Table 2.

$$\frac{\partial U}{\partial x} + \frac{\partial V}{\partial y} = 0 \quad 1$$

$$U \frac{\partial U}{\partial x} + V \frac{\partial U}{\partial y} = -\frac{1}{\rho} \frac{\partial P}{\partial x} + \frac{1}{\rho} \left(\frac{\partial}{\partial x} \left[(\mu + \mu_t) \frac{\partial U}{\partial x} \right] + \frac{\partial}{\partial y} \left[(\mu + \mu_t) \frac{\partial U}{\partial y} \right] \right) \quad 2$$

$$U \frac{\partial V}{\partial x} + V \frac{\partial V}{\partial y} = -\frac{1}{\rho} \frac{\partial P}{\partial y} + \frac{1}{\rho} \left(\frac{\partial}{\partial x} \left[(\mu + \mu_t) \frac{\partial V}{\partial x} \right] + \frac{\partial}{\partial y} \left[(\mu + \mu_t) \frac{\partial V}{\partial y} \right] \right) \quad 3$$

$$U \frac{\partial k}{\partial x} + V \frac{\partial k}{\partial y} = G_t - \epsilon + \frac{1}{\rho} \left(\frac{\partial}{\partial x} \left[\left(\frac{\mu + \mu_t}{\sigma_k} \right) \frac{\partial k}{\partial x} \right] + \frac{\partial}{\partial y} \left[\left(\frac{\mu + \mu_t}{\sigma_k} \right) \frac{\partial k}{\partial y} \right] \right) \quad 4$$

$$U \frac{\partial \epsilon}{\partial x} + V \frac{\partial \epsilon}{\partial y} = C_{\epsilon 1} \frac{\epsilon}{k} G_t - C_{\epsilon 2} \frac{\epsilon^2}{k} + \frac{1}{\rho} \left(\frac{\partial}{\partial x} \left[\left(\frac{\mu + \mu_t}{\sigma_\epsilon} \right) \frac{\partial \epsilon}{\partial x} \right] + \frac{\partial}{\partial y} \left[\left(\frac{\mu + \mu_t}{\sigma_\epsilon} \right) \frac{\partial \epsilon}{\partial y} \right] \right) \quad 5$$

$$\text{with } \mu_t = C_\mu k^2 / \epsilon \quad 6$$

$$\text{and } G_t = \frac{\mu_t}{\rho} \left[2 \left(\frac{\partial U}{\partial x} \right)^2 + 2 \left(\frac{\partial V}{\partial y} \right)^2 + \left(\frac{\partial U}{\partial y} + \frac{\partial V}{\partial x} \right)^2 \right] \quad 7$$

The use of the $k-\epsilon$ turbulence model represents a compromise between extreme possibilities each with known problems rather than a directly justifiable choice. Algebraically specified length scales are generally unsatisfactory in recirculating flows and Reynolds stress models are more expensive in computer time.

The application of the conservation equations in this form is clearly uneconomic in regions where the boundary-layer assumptions are valid and the solution domain was chosen as a compromise which minimised these regions while allowing specification of boundary conditions, based on experi-

mental knowledge. Thus the upstream boundary corresponds to a location immediately upstream of the influence of boundary-layer curvature where measurements of all properties were available in the boundary layer, except the rate of dissipation which was obtained from the equation

$$\epsilon = C_\mu k' \frac{\partial U}{\partial y} \overline{u'v'}$$

Detailed knowledge of the lower surface boundary layer was used for the upstream boundary conditions of the flow entering the calculation domain from beneath the trailing edge. However, the boundary-layers on the upper and lower surfaces of the wind tunnel were quantified only in terms of a no slip boundary condition and zero normal gradient assumptions were made for k and ϵ . In all cases, interpolation of measurements necessary to determine values at the selected node points and, at some future date, the influence of this interpolation needs to be quantified. In comparison with the other sources of uncertainty discussed in the following paragraphs, it is believed to be unimportant. The downstream boundary was chosen at a location where the flow was presumed to be well approximated by fully developed flow and zero normal gradients were presumed. This assumption needed to be tested and relevant results are reported below

The nature of the streamlines shown on figure 4 suggests that, although a rectangular Cartesian grid could be used to represent the flow, it would lead to a very uneven distribution of calculation accuracy since some gradients would be much better represented than others. To help to overcome this problem, a calculation scheme based on the solution of the potential flow equations was applied to the generation of lines of constant stream function and velocity potential and the intersections were taken as the nodes for the finite difference solution of the conservation equations. The potential flow equations do not take any account of separation and the resulting node distribution was concentrated in this region to ensure that the cell Reynolds numbers were as small as possible. This was essential, since the streamlines could be expected to intersect the cells at angles which could lead to numerical diffusion for those cases where the cell Reynolds number exceeded 121.

The Laplace equations for the velocity potential, ϕ , and stream function, ψ , of an irrotational flow were solved in the inverse form:

$$\frac{\partial^2 x}{\partial \phi^2} + a^2 \frac{\partial^2 x}{\partial \psi^2} = 0 \quad 8$$

$$\frac{\partial^2 y}{\partial \phi^2} + a^2 \frac{\partial^2 y}{\partial \psi^2} = 0 \quad 9$$

$$\text{with } a^2 = \left[\left(\frac{\partial x}{\partial \phi} \right)^2 + \left(\frac{\partial y}{\partial \phi} \right)^2 \right] / \left[\left(\frac{\partial x}{\partial \psi} \right)^2 + \left(\frac{\partial y}{\partial \psi} \right)^2 \right] \quad 10$$

and located the intersections of iso-vorticity and iso-stream function lines. The equations were solved in finite-difference form with the TEACH program operated in a manner similar to that described by Gosman and Johns²⁸. The boundary of the calculation domain was arranged to be coincident with the surface, the tunnel roof, a location upstream of separation selected with experimental

knowledge, and a short distance downstream of the trailing edge with it extended, for this calculation, parallel to the tunnel roof. An orthogonal curvilinear mesh of 48x48 nodes was generated within this domain. The near-wall nodes were linked to the surfaces by normals to the cubic polynomials used to describe the surface shape.

The 48x48 grid, generated as described above, was linked to similar but geometrically expanding rectangular Cartesian grids which were specified to represent the flow stemming from lower surface and in the downstream wake. The resulting grid of 60x60 nodes implied that solutions of the Navier-Stokes equations would be expensive and time consuming. The results described below were, as a consequence, obtained with fewer nodes and these were selected with empirical knowledge of the regions of steep gradients and angled streamlines.

The grid generated in the above manner corresponds to an orthogonal curvilinear system of equations and the conservation equations were, therefore, written in the common form:

$$\begin{aligned} \frac{\partial}{\partial \xi_1} (\ell_2 \rho U_1 \phi) + \frac{\partial}{\partial \xi_2} (\ell_1 \rho U_2 \phi) &= \frac{\partial}{\partial \xi_1} (\ell_2 \Gamma_\phi \frac{\partial \phi}{\partial \xi_1}) + \\ + \frac{\partial}{\partial \xi_2} (\ell_1 \Gamma_\phi \frac{\partial \phi}{\partial \xi_2}) &+ \ell_1 \ell_2 S_\phi \end{aligned} \quad 11$$

and were solved by the central-difference/upwind arrangement, with staggered locations of velocity and scalar quantities, of the TEACH computer program. In this equation ϕ can represent any of the dependent variables of equations 2 to 5, Γ_ϕ the corresponding diffusivity, ℓ_1 and ℓ_2 are the corresponding metric coefficients and ξ_1 and ξ_2 are the coordinates corresponding to the stream function and velocity potential obtained from the solution of equations 8 to 10. The metric coefficients were obtained from this solution with cubic polynomials to connect the constant vorticity or stream function locations, and were incorporated into the finite-difference form using surface integrals to obtain the cell face areas, volumes, arc lengths and radii of curvature in the ξ_1 and ξ_2 directions. The Coriolis and centripetal accelerations, with higher order curvature terms were incorporated in the source term, S_ϕ , as were terms representing dissipation and production of turbulent kinetic energy in the k and ϵ equations.

A typical grid, generated by the above method and used in the solution of equation 11, is shown on figure 7. It comprises 30x30 nodes, selected from the 60x60 mesh initially generated, and led calculation times of around 850s for about 250 iterations required to achieve a convergence criterion of 0.1% of the maximum residual of any dependent variable including the mass flow of the pressure correction equation. Under-relaxation was employed with all equations with maximum under-relaxation factors of 0.5.

It should be noted that in the present orthogonal curvilinear coordinates, the generation term given by equation 7 has the form

$$G_t = \frac{u_t}{\rho} \left[2 \left(\frac{1}{r_1} \frac{\partial U}{\partial \xi_1} + \frac{v^2}{r_1^2} \right) + 2 \left(\frac{1}{r_2} \frac{\partial V}{\partial \xi_2} + \frac{U^2}{r_2^2} \right) + \left(\frac{1}{r_2} \frac{\partial U}{\partial \xi_2} - \frac{U}{r_1} + \frac{1}{r_1} \frac{\partial V}{\partial \xi_1} - \frac{V}{r_2} \right)^2 \right]$$

with r_1 , and r_2 radii of curvature of the stream function and velocity potential lines respectively. It can be expected that this and the second order terms which have been retained in the turbulence conservation equations, will not fully represent the effects of stabilising curvature in the turbulence model but the proposals of previous work, for example those of Launder et al²⁹, Gibson³⁰ and Leschinger and Rodi³¹ have not conclusively been shown to be satisfactory and have not been incorporated.

IV. Calculated Results and Discussion

The calculated mean velocity vectors of figure 8 may be compared with the measurements of figure 3 and are clearly in good qualitative agreement. As quantified in figure 9, mean streamline detachment was calculated to occur at 0.866 rather than the 0.870 of the measurements. The overall size of the reverse flow region is wider by some 10% and extends to a value of x/c of 0.021 rather than the 0.016 of the measurements. The calculations also show that the normal momentum is greater than the longitudinal momentum in the vicinity of separation and in the shear layer surrounding the bubble where the normal pressure gradient has its largest values. Within the bubble, the mean velocity has a maximum value of approximately 20% of the free stream velocity and the normal and longitudinal velocities have similar magnitudes with the former being larger at the beginning and end of the reverse flow boundary.

The free stream velocity and wall pressure distributions are shown on figure 10. The difference between the measured and calculated velocity distribution is consistent with the discrepancy in the size of the recirculation region which may, in part, be due to the inadequate representation of streamline curvature as discussed previously. The pressure distribution is, of course, very different from that obtained from the Laplace equations in the vicinity of the separation region and is in close accord with the measured results except where there are insufficient nodes to represent the stream-wise gradients at the start of curvature.

The distribution of skin friction coefficient of figure 10 is also in good agreement with experiment and was obtained with the aid of the wall functions:

$$\tau_w = \rho C_u \frac{1}{4} \kappa U / \ln(Ey^+)$$

$$\epsilon_w = C_u \frac{1}{4} \kappa^{3/2} / \kappa y$$

$$\left(\frac{1}{r_2} \frac{\partial U}{\partial \xi_2} \right)_w = U/y \ln(Ey^+)$$

with the production of turbulent kinetic energy modified to take some account of the normal stress in the form

$$G_{tw} = \frac{\tau_w}{\rho} \left[\left(\frac{1}{r_2} \frac{\partial U}{\partial \xi_2} \right)_w - \frac{U}{r_1} \right] + \left[\frac{2}{3} \kappa - \frac{u_t}{\rho} \frac{1}{r_1} \frac{\partial U}{\partial \xi_1} \right] \frac{1}{r_1} \frac{\partial U}{\partial \xi_1}$$

These wall functions linked the wall to the finite-difference node closest to it and always located at a value of y^+ less than 50 and greater than 10 with the minimum occurring in the separated region.

The results presented on figures 7 to 10 and discussed above are encouraging and it is essential to determine the extent to which they depend on the numerical detail of the calculations. A partial answer to this question can be provided on the basis of the limited number of tests referred to in the following paragraph. It is clear from the velocity profiles of figure 11 that the calculated wake is wider than it should be and, since experience with the present turbulence model would suggest that it should be slightly narrower, the difference must be associated with numerical inaccuracy. Accordingly the influence of the location of the downstream boundary condition was investigated and shown to be negligibly small and subsequent calculations were performed with the same number of nodes differently located in the solution domain of figure 7 and with smaller numbers of nodes.

With 30x30 nodes and a greater number located away from the near-flap region, the velocity and pressure fields were very similar and this suggested that, although the cell Reynolds numbers in the free stream had magnitudes up to 10^3 , the resulting truncation errors were unimportant. This conclusion was supported by calculations with 20x20 nodes which gave very similar velocity and pressure values away from the surface of the flap: even the velocities in the outer region of the recirculation were little changed although the wake was even wider with this number of nodes. The distribution of nodes, with concentration away from the flap region, gave rise to different near wall values. In particular, the skin-friction was altered by up to 5 and 15% in the boundary layer and separated region respectively by locating the near wall node in the y^+ region between 20 and 90, in contrast to the 10 to 50 range used earlier. Local velocities and pressure coefficients were different by up to 14% and 0.003 with the wall-pressure coefficient showing a maximum difference of 0.0012. These maximum discrepancies occurring in the vicinity of separation.

The influence of the location of the roof and floor of the wind tunnel did not appear to be very great since their representation by the actual and expanded tunnel co-ordinates led to the same wall-pressure coefficient on the flap and to the same size of separation region. Similarly, the location of separation of the mean streamline was always calculated to an accuracy of not less than the distance between grid nodes in the S-direction. The sensitivity of the skin-friction coefficient is, at least in part, due to the use of the law of the wall in regions where it does not strictly apply but it is clear that either more nodes, or a higher order finite-difference scheme is required to represent the gradients in the near-wall and near-wake regions.

Further work is necessary to quantify fully the influence of numerical detail and to separate errors due to numerical, turbulence-model and wall-function assumptions. Measurements, including

more detailed near-wall information, are essential as are numerical procedures such as that of McGuirk et al.³². It is useful to note that ratio of $\partial P/\partial y$ to $\partial P/\partial x$ immediately upstream of separation and in the near wake, defines the need for equations which represent both. In addition, the evaluation of the measured convection terms showed that the y-momentum terms were generally greater than the x-momentum terms in the downstream region of the separation region, of similar magnitude in the central region and smaller in the upstream region, except very close to the wall. Direct evidence of the magnitudes of the diffusion terms cannot be deducted from the present measured results but the calculated results show that they are most important in the vicinity of the edge of the recirculation region and diminish in value towards the free stream and the near wall, although their influence may be outweighed by numerical diffusion in some regions of the flow and particularly in the near wake.

Acknowledgements

The authors gratefully acknowledge support from the Procurement Executive of the Ministry of Defence and from the Northern Ireland Education Department. Dr. M.M. Ribeiro, J. Laker and O. Vis contributed greatly to the development of the flying wire arrangement and Mr. Ken Winter and Dr. B.R. Williams of the Royal Aircraft Establishment to the overall plan of attack and we are glad to record our thanks.

References

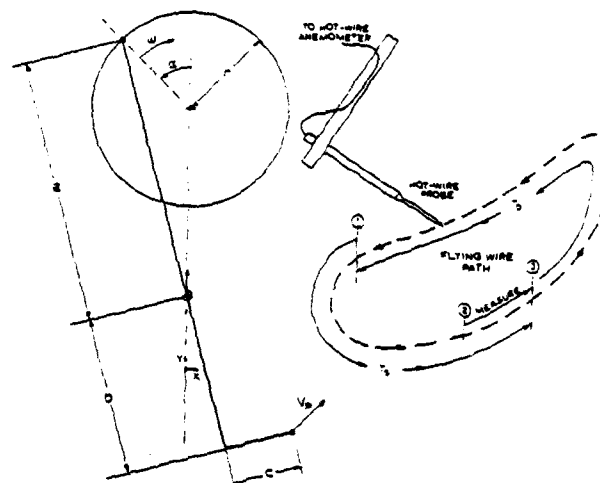
1. A.D. Gosman and W.M. Pun (1973): Calculation of recirculating flows. Imperial College, Mechanical Engineering Dept, Report HTS/73/2.
2. A. Nakayama (1983): Measurements of attached and turbulent separated flows in the trailing regions of airfoils. 2nd Symposium on Physical and Numerical Aspects of Aerodynamic Flows, Long Beach.
3. W.H. Young, J.F. Meyers and D.R. Hoad (1978): A laser velocimeter flow survey above a stalled wing. NASA TP 1266.
4. W.D. Bachalo and D.A. Johnson (1979): An investigation of transonic turbulent boundary layer separation generated on an axisymmetric flow model. AIAA paper 79-1497.
5. D. Coles and A.J. Wadcock (1979): Flying-hot-wire study of flow past a NACA 4412 airfoil at maximum lift. AIAA 17,321.
6. J.-L. Solignac (1980): Experimental study of the separation at the trailing edge of an axisymmetrical contoured after-body. Rech. Aerosp. No. 1980-3.
7. D.A. Johnson and F.W. Spaid (1981): Measurements of the boundary layer and near wake of a supercritical airfoil at cruise conditions. AIAA paper 81-1242.
8. R.L. Simpson, Y.-T. Chew, B.G. Shivaprasad (1981): The structure of a separating turbulent boundary layer. Part 1. Mean flow and Reynolds stresses. J. Fluid Mech. 113, 23.
9. R.C. Hasting and K.G. Moreton (1982): An investigation of a separated equilibrium turbulent boundary layer. Int. Symposium on Applications of Laser-Doppler Anemometry to Fluid Mechanics, Lisbon, Portugal, 11.1.
10. D. Coles and E.A. Hirst (ed.) (1968): Proceedings computation of turbulent boundary layers. ASOFR-IFP-Stanford Conference, Volume 2, Thermosciences Division, Stanford University.
11. J.C. Le Balleur, R. Peyret and H. Viviani (1980): Numerical studies in high Reynolds aerodynamics. Computer and Fluids, 8.
12. P. Bradshaw, T. Cebeci and J.H. Whitelaw (1981): Engineering calculation methods for turbulent flows. Academic Press.
13. R.E. Melnik (1980): Turbulent interactions on airfoils at transonic speeds-recent developments. AGARD CP 291 10-15.
14. J.C. Marvin (1982): Turbulence modelling for computational aerodynamics. AIAA paper 82-0164.
15. J.D. Murphy (1977): An efficient solution procedure for the incompressible Navier-Stokes equations. AIAA 15, 1307.
16. J.F. Thompson, L. Turner, W.S. Long and J.H. Bearden (1979): Numerical solution of the Navier-Stokes equations for arbitrary two-dimensional multi-element airfoils. NASA CP 2045, 183.
17. A. Sugavanam and J.C. Wu (1982): Numerical study of separated turbulent flow over airfoils. AIAA 20, 464.
18. C.M. Rhie and W.L. Chow (1982): A numerical study of the turbulent flow past an isolated airfoil with trailing edge separation. AIAA paper 82-0998.
19. J. Andreopoulos and P. Bradshaw (1980): Measurements of interacting turbulent shear layers in the near wake of a flat plate. J. Fluid Mech. 100, 639.
20. P.R. Viswanath, J.W. Cleary, H.L. Seegmiller and C.C. Horstman (1980): Trailing-edge flows at high Reynolds number. AIAA 18, 1059.
21. J.C. Yu (1981): Mean-flow and turbulence measurements in the vicinity of the trailing edge of an NACA 63₁-012 airfoil. NASA TP 1845.
22. C. Hah and B. Lakshminarayana (1982): Measurements and prediction of mean velocity and turbulence structure in the near wake of an airfoil. J. Fluid Mech. 115, 251.
23. A.J. Baker, J.C. Yu, J.A. Orzechowski and T.B. Gatski (1982): Prediction and measurement of incompressible turbulent aerodynamic trailing edge flows. AIAA 20, 51.
24. B.E. Thompson and J.H. Whitelaw (1983): A turbulent boundary layer approaching separation. Walz-Festschrift Volume, Springer-Verlag.
25. B.E. Thompson (1981): A preliminary evaluation of flying-hot wire instrumentation. Imperial College, Mech. Eng. Dept FS/81/23.
26. M.M. Ribeiro and J.H. Whitelaw (1975): Statistical

cal characteristics of a turbulent jet. J. Fluid Mech. 70, 1.

27. B.E. Thompson (1983): Appraisal of a flying-hot-wire anemometer. To be published in DISA Information.
28. A.D. Gosman and R.J.R. Johns (1979): A simple method for generating curvilinear-orthogonal grids for numerical fluid mechanics calculations. Imperial College, Mech. Eng. Dept, FS/79/23.
29. B.E. Launder, C.H. Pridden and B.I. Sharma (1977): The calculation of turbulent boundary layers on curved and spinning surfaces. J. Fluids Engng, 99, 237.
30. M.M. Gibson (1978): An algebraic stress and heat-flux model for turbulent shear flow with streamline curvature. Int. J. Heat Mass Transfer 21, 1609.
31. M.A. Leschziner and W. Rodi (1981): Calculation of annular and twin parallel jets using various discretization schemes and turbulent model variants. J. Fluids Engng 103, 352.
32. J.J. McGuirk, A.M.K.P. Taylor and J.H. Whitelaw (1981): The assessment of numerical diffusion in upwind-difference calculations of turbulent recirculating flows. Proceedings of Third Symposium on Turbulent Shear Flows, Davis, U.S.A.

TABLE 1

Essential details of the flying-hot wire anemometer



Dimensions:	a	0.160m
	b	0.357m
	c	0.127m
	r	0.04-0.06m
Velocity:	shaft (maximum)	100rad/s
	probe (maximum)	13.5m/s
Calibration range:		0-30m/s
Time in sampling part of cycle		$T_S=0.01s$
Time in dormant part of cycle		$T_D=5s$
Maximum uncertainties:	probe speed	0.04m/s
	flow velocity	$0.012U_{ref}$
	flow angle	0.6degrees

TABLE 2

Turbulence model constants

C_ν	$C_{\epsilon 1}$	$C_{\epsilon 2}$	σ_k	σ_ϵ	κ	E
0.09	1.44	1.92	1.0	1.22	0.4187	9.793

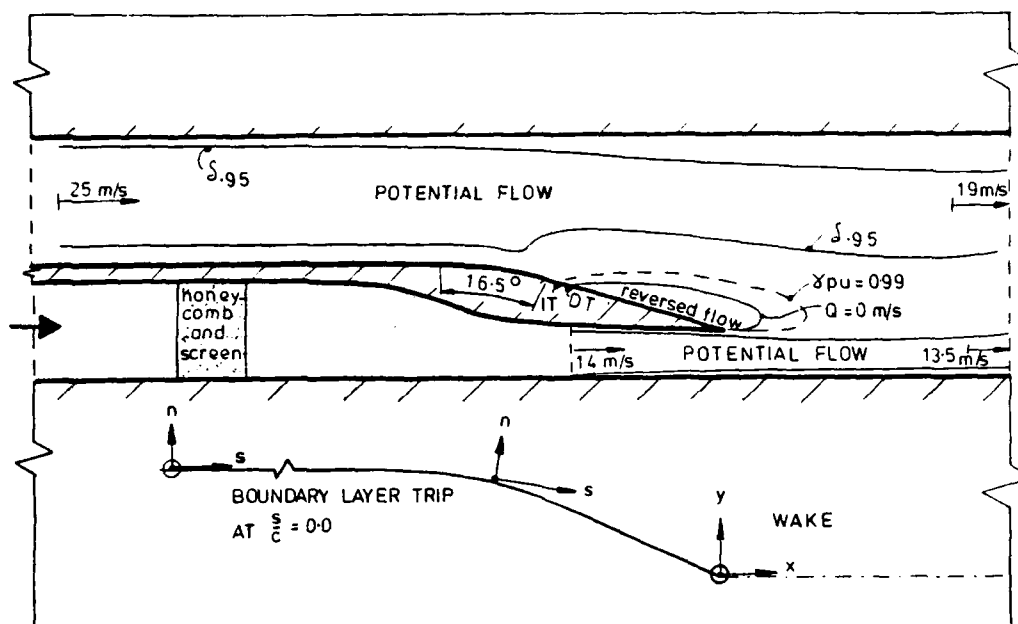


Figure 1. Flow configuration: DT mean streamline detachment; IT incipient separation (1% probability of reversed flow); $Q=0$ line of zero mean velocity; γ_{pu} fraction of time flow is in the downstream direction; $\delta_{0.95}$ boundary layer thickness ($U/U_G=0.95$).

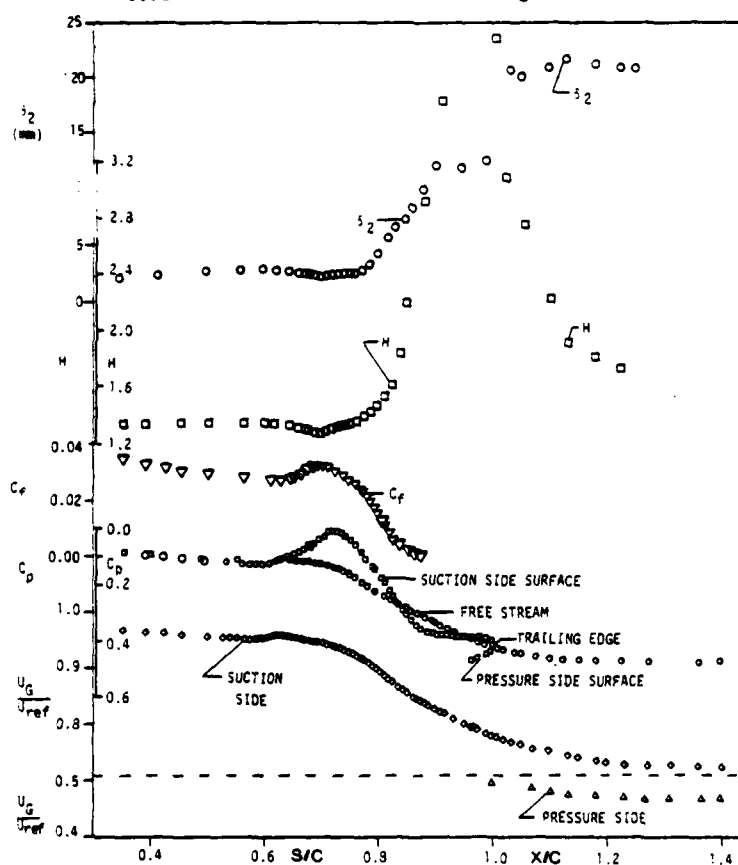


Figure 2. Distributions of momentum thickness, skin friction coefficient, surface and free stream static pressure coefficient and free stream velocity ratio.

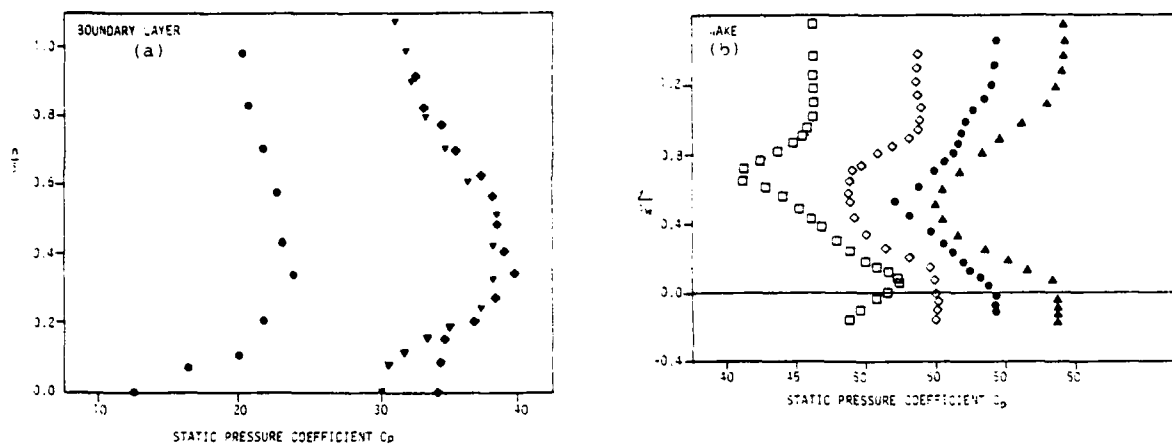


Figure 3. Profiles of static pressure coefficient; (a) s/c of 0.777 \bullet , 0.826 \blacktriangledown , 0.852 \blacklozenge ; (b) x/c of 0.132 \square , 0.181 \diamond , 0.231 \bullet , 0.329 \blacktriangle .

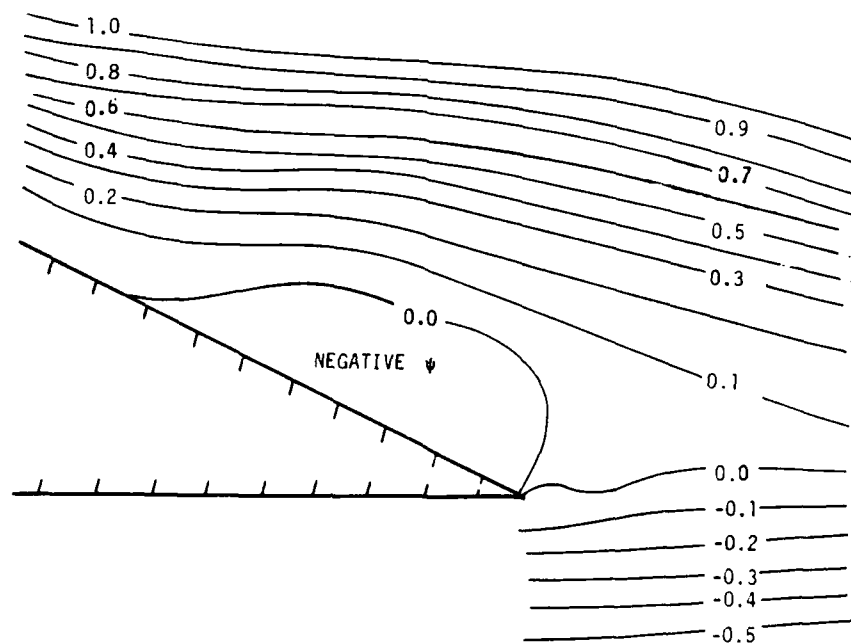
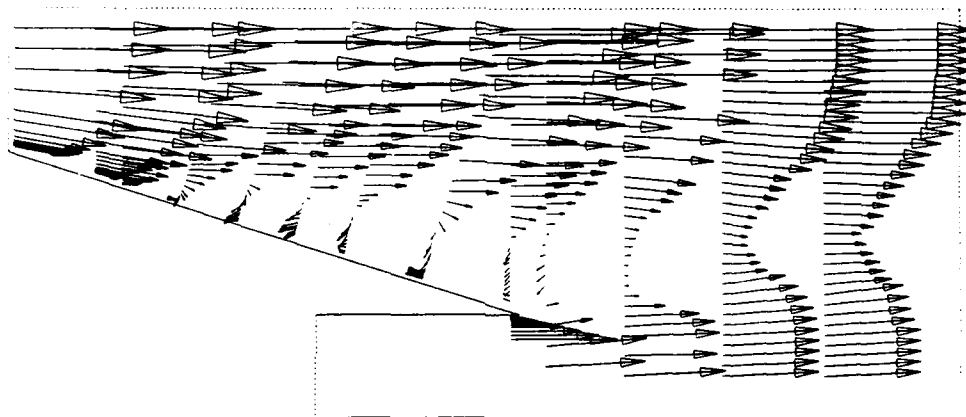


Figure 4 Mean velocity vectors and streamlines in the vicinity of separation

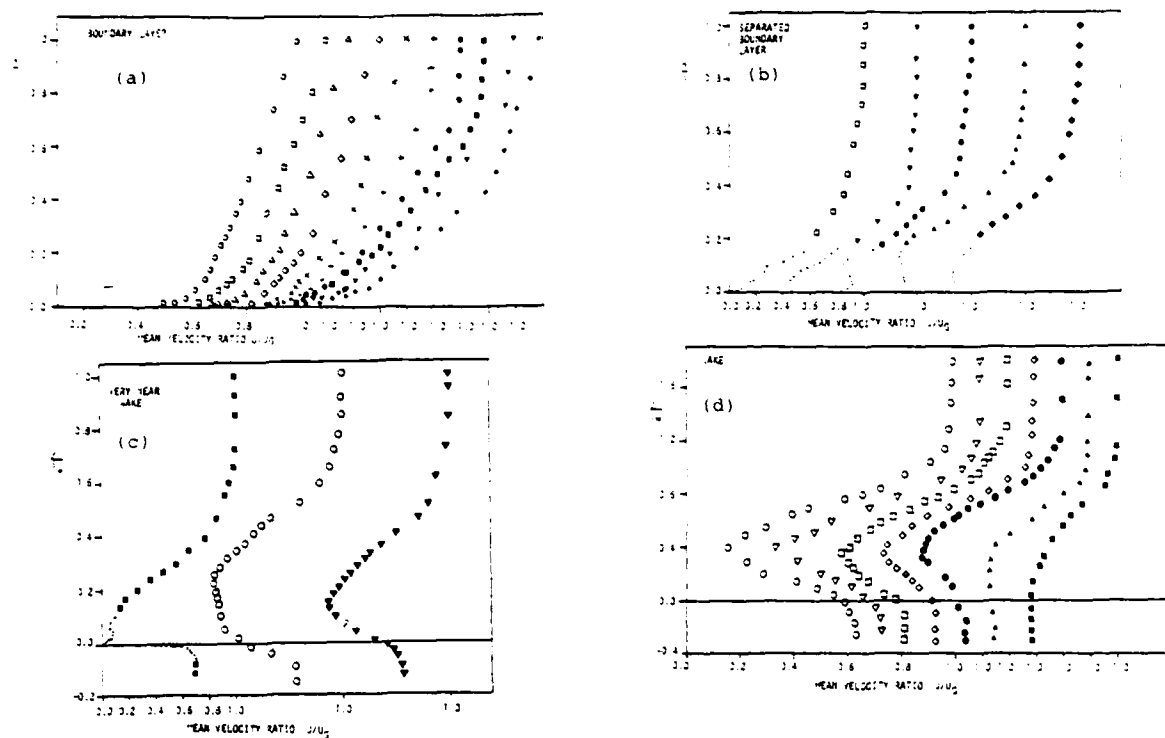


Figure 5. Profiles of mean velocity

- (a) s/c of 0.352 \square , 0.649 \square , 0.668 Δ , 0.695 \diamond , 0.716 \times , 0.757 $+$, 0.777 \bullet , 0.798 \blacksquare , 0.826 ∇ , 0.852 \blacklozenge
 (b) s/c of 0.866 \square , 0.886 ∇ , 0.905 \bullet , 0.968 Δ , 1.000 \blacklozenge
 (c) x/c of 0.000 \blacksquare , 0.006 \square , 0.050 ∇
 (d) x/c of 0.066 \square , 0.099 ∇ , 0.132 \square , 0.181 \diamond , 0.231 \bullet , 0.329 Δ , 0.428 \blacksquare

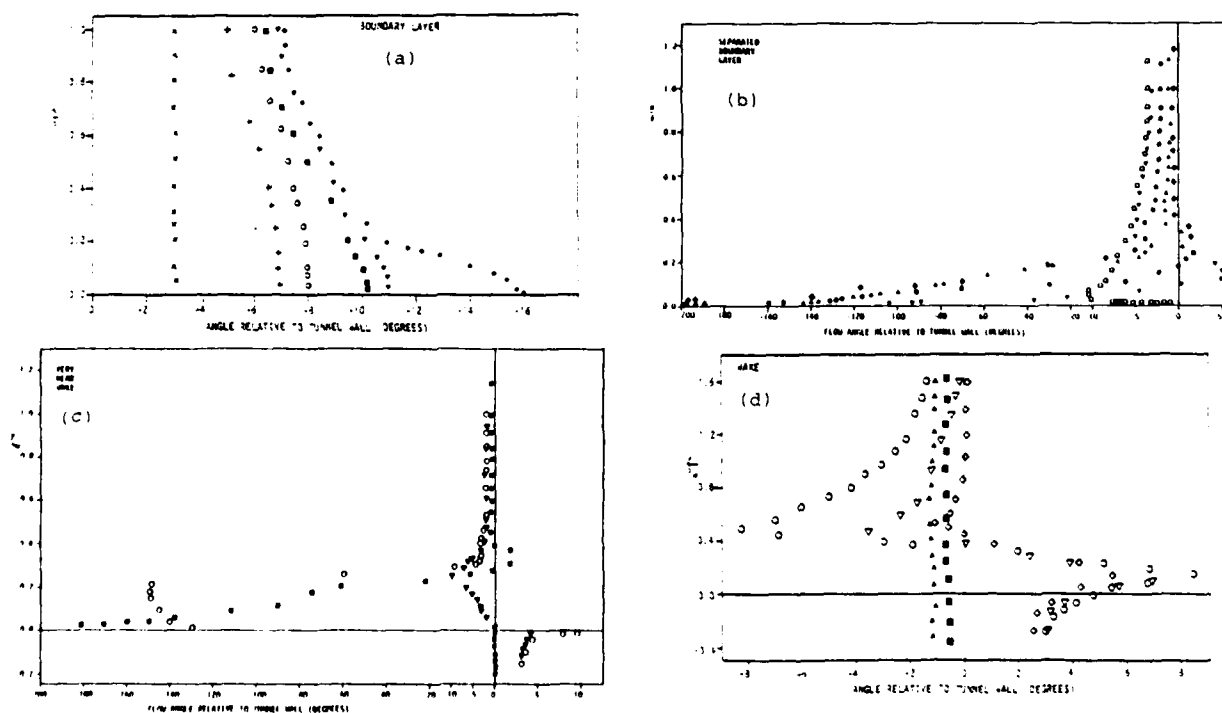


Figure 6. Profiles of flow angle. (Symbols as on figure 5)

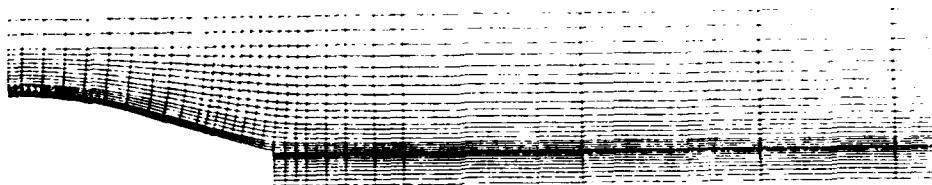


Figure 7. Calculation domain and scalar cell faces

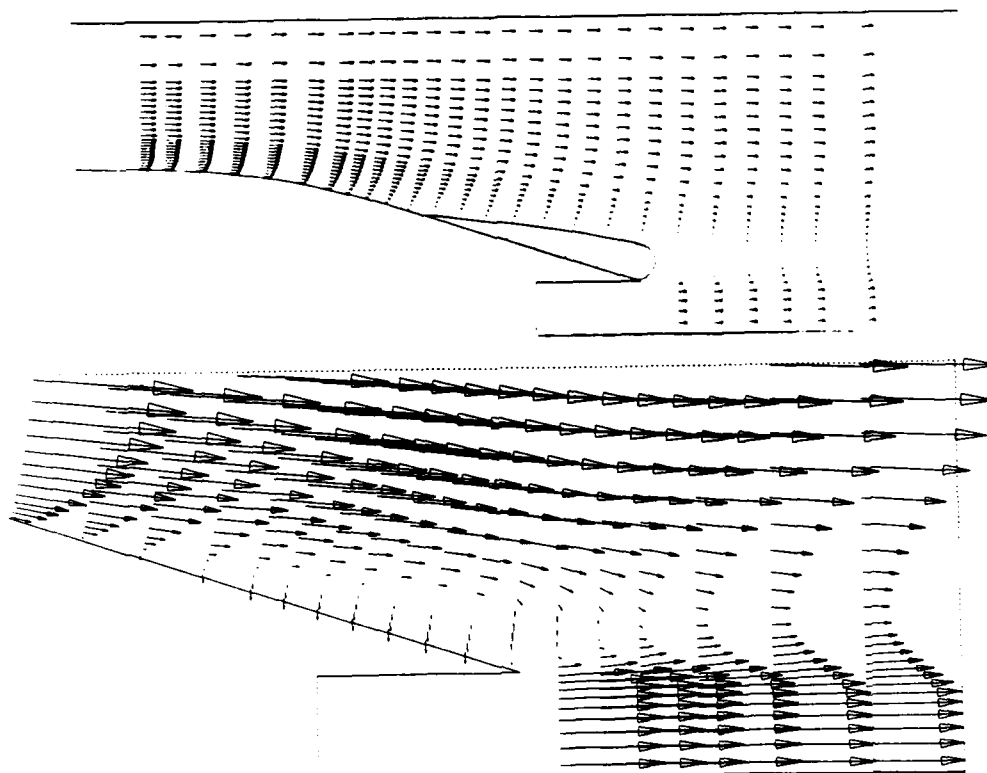


Figure 8. Calculated mean velocity vectors

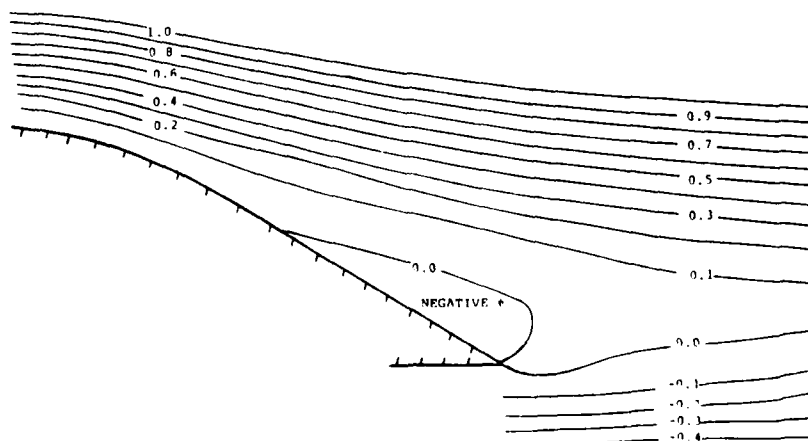


Figure 9. Calculated mean streamlines

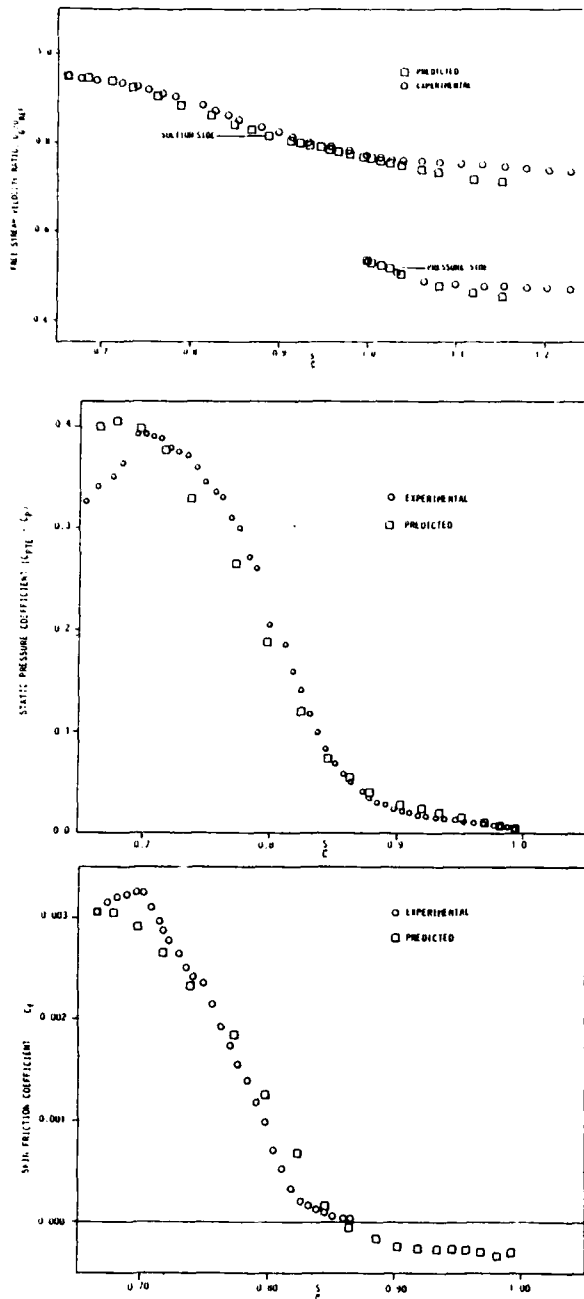


Figure 10. Distributions of experimental and calculated values of free stream velocity, surface static pressure and skin friction coefficient.

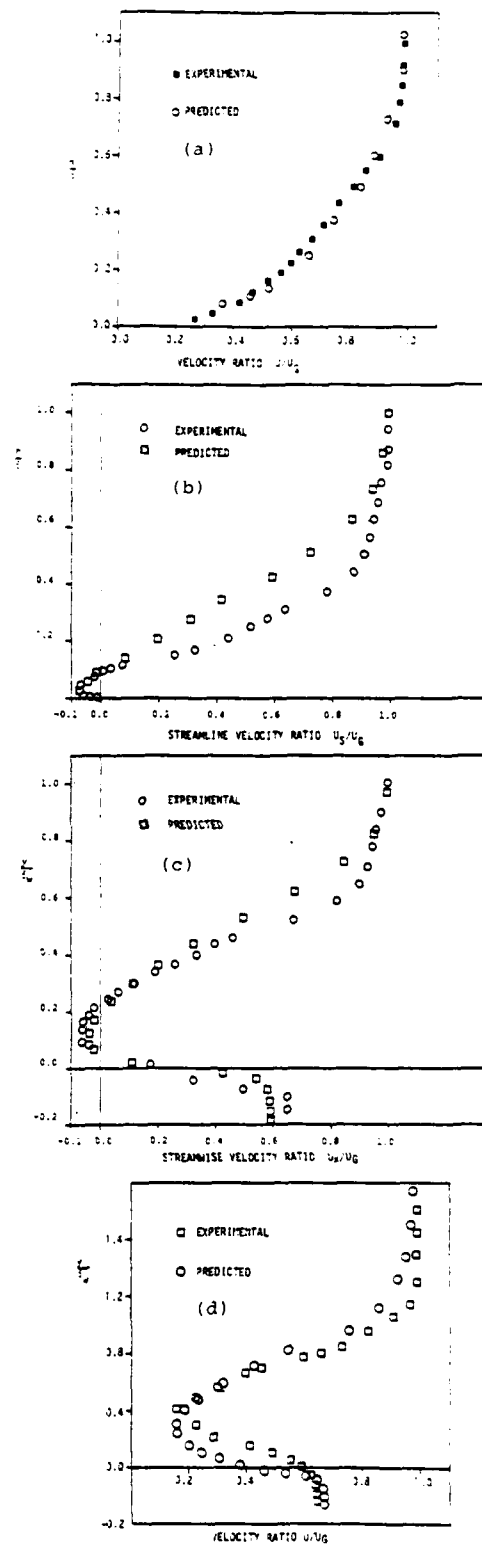


Figure 11. Profiles of calculated and experimental mean velocity; (a) s/c of 0.798; (b) s/c of 0.905; (c) x/c of 0.006; (d) x/c of 0.066

(WHY ?) A FINITE ELEMENT ALGORITHM
FOR THE PARABOLIC NAVIER-STOKES EQUATIONS

A. J. Baker
University of Tennessee
Knoxville, TN USA

Abstract

The three-dimensional Navier-Stokes equations governing steady, turbulent subsonic flows have been simplified into the "parabolic" form using a formal order of magnitude analysis procedure. The results of this analysis confirm that the transverse momentum equations, to first order, govern appropriate pressure distributions, and that the continuity equation governs first order effects of transverse plane velocities. This paper summarizes the identification of a well-posed, initial-boundary value differential equation description, and construction and evaluation of a numerical solution algorithm for the parabolic Navier-Stokes equations in physical variables.

1. Introduction

A wide variety of important aerodynamics problem configurations are characterized by the velocity vector being principally aligned with a single coordinate direction. Provided there is no reversal of this dominant component of velocity, the three-dimensional parabolic Navier-Stokes (PNS) equation system is a candidate for solution of the problem class. A formal order of magnitude PNS analysis confirms¹, in this scenario, that axial diffusion processes are negligible, and that the transverse momentum equations principally govern transverse plane pressure distributions. The continuity equation governs first order effects on momentum. The transverse momentum equation can be combined, using the divergence operator, into a quasi-linear pressure Poisson equation possessing complementary and particular solutions. The boundary conditions for the complementary solution enforce overall ellipticity, while the particular solution yields modifications due to convection, viscosity and Reynolds stress distributions. A turbulence closure model is also required, and the parabolic form of the two-equation turbulence kinetic energy-isotropic dissipation system is assumed the minimum acceptable level of simplicity.

With the basic governing equation system thus defined, construction of a suitable algorithm requires addressing the ordering analysis and the boundary conditions. A primitive variables formulation must rearrange the continuity equation to yield a deterministic system for transverse velocities, cf. Baker et.al.¹, Dodge², Patankar³. Alternatively, a vector potential function can be defined to identically satisfy the continuity equation, and a vorticity equation derived to replace the transverse momentum equations, cf. Briley et.al.⁴, Mikhail et.al.⁵. One dominant factor controlling this basic decision is the boundary condition specifications associated with various solution domains, including flows which are fully bounded, semi-bounded and/or totally nonbounded. This variability suggests retaining the physical variables problem description. For flexibility, and the inherent mathematical robustness of the construction, a finite element penalty function algorithm is appropriate. This paper presents a statement of the algorithm, boundary condition specifications, and the results of computational experiments for a class of problem definitions.

II. Problem Statement

The three-dimensional PNS equation system for the steady, subsonic turbulent flow of an isoeenergetic fluid, to the principal scale of ordering¹, is

$$L(\bar{p}) = \frac{\partial}{\partial x_j} [\bar{\rho} \bar{u}_j] = 0 \quad (1)$$

$$L(\bar{u}_1) = \frac{\partial}{\partial x_1} [\bar{\rho} \bar{u}_1 \bar{u}_1 + \bar{p}] + \frac{\partial}{\partial x_2} [\bar{\rho} \bar{u}_2 \bar{u}_1 + \bar{\rho} \bar{u}_2 \bar{u}_1] - \frac{1}{Re} \frac{\partial \bar{u}_1}{\partial x_2} = 0 \quad (2)$$

$$L(\bar{u}_k) = \frac{\partial \bar{p}}{\partial x_k} + \frac{\partial}{\partial x_2} [\bar{\rho} \bar{u}_k \bar{u}_2] = 0 \quad (3)$$

$$L(k) = \frac{\partial}{\partial x_1} [\bar{\rho} \bar{u}_1 k] + \frac{\partial}{\partial x_2} [\bar{\rho} \bar{u}_2 k + \bar{\rho} \left(C_k \frac{k}{\epsilon} \bar{u}_j \bar{u}_2 \right. \\ \left. - \bar{u}_j \bar{u}_2 \right) \frac{\partial k}{\partial x_j}] + \bar{\rho} \bar{u}_1 \bar{u}_2 \frac{\partial \bar{u}_1}{\partial x_2} + \bar{\rho} \epsilon = 0 \quad (4)$$

$$L(\epsilon) = \frac{\partial}{\partial x_1} [\bar{\rho} \bar{u}_1 \epsilon] + \frac{\partial}{\partial x_2} [\bar{\rho} \bar{u}_2 \epsilon + \bar{\rho} C_\epsilon \frac{k}{\epsilon} \bar{u}_j \bar{u}_2 \frac{\partial \epsilon}{\partial x_j}] \\ + C_\epsilon^1 \bar{\rho} \bar{u}_1 \bar{u}_2 \frac{\epsilon}{k} \frac{\partial \bar{u}_1}{\partial x_2} + C_\epsilon^2 \bar{\rho} \frac{\epsilon^2}{k} = 0 \quad (5)$$

The variables appearing in equations 1-5 have their usual interpretation in fluid mechanics, where superscript bar denotes conventional time averaging⁶, and the cross coupling of fluctuations in density and velocity have been assumed negligible. The tensor index summation convention is implied, with x_1 aligned with the principal flow direction, and $1 \leq j \leq 3$ and $2 \leq (k, l) \leq 3$. The turbulence kinetic energy k is the trace of the Reynolds stress tensor, ϵ is the isotropic dissipation function, and Re is the characteristic Reynolds number.

For the variety of reported results, the Reynolds stress tensor field constitutive model of Baker et.al.¹ has been employed. The PNS ordering analysis indicates the extremum significance of components of $u_i u_j$ is one order smaller than unity. Simplifying the constitutive equation to this order yields

$$\bar{u}_1 \bar{u}_1 = C_1 k - C_2 C_k \frac{k^3}{\epsilon^2} \left[\left(\frac{\partial \bar{u}_1}{\partial x_2} \right)^2 + \left(\frac{\partial \bar{u}_1}{\partial x_3} \right)^2 \right] \\ \bar{u}_2 \bar{u}_2 = C_3 k - C_2 C_k \frac{k^3}{\epsilon^2} \left[\frac{\partial \bar{u}_1}{\partial x_2} \right]^2 \\ \bar{u}_3 \bar{u}_3 = C_3 k - C_2 C_k \frac{k^3}{\epsilon^2} \left[\frac{\partial \bar{u}_1}{\partial x_3} \right]^2$$

$$\begin{aligned}\overline{u_1 u_2} &= -C_4 \frac{k^2}{\varepsilon} \frac{\partial \bar{u}_1}{\partial x_2} \\ \overline{u_1 u_3} &= -C_4 \frac{k^2}{\varepsilon} \frac{\partial \bar{u}_1}{\partial x_3} \\ \overline{u_2 u_3} &= -C_2 C_4 \frac{k^3}{\varepsilon^2} \left[\frac{\partial \bar{u}_1}{\partial x_2} \frac{\partial \bar{u}_1}{\partial x_3} \right] \quad (6)\end{aligned}$$

The coefficients C_α , $1 \leq \alpha \leq 4$, in equation 6 are correlation constants; the standard values are $C_2 = \{0.94, 0.067, 0.56, 0.063\}$.

In the primitive form, equations 1-5 do not represent a well-posed initial-boundary value problem description for the subsonic flow problem class. As a consequence of the ordering, the scalar continuity equation governs both components of velocity in the transverse plane perpendicular to x_1 . As cited in the Introduction, various algorithm constructions have been formulated to address this issue. The approach taken in the present analysis is to employ a finite element penalty function formulation, and to append the order (8) transverse plane momentum equations,

$$L^\delta(\bar{u}_k) = \frac{\partial}{\partial x_1} \left[\bar{\rho} \bar{u}_1 \bar{u}_k \right] + \frac{\partial}{\partial x_2} \left[\bar{\rho} \bar{u}_2 \bar{u}_k - \frac{1}{Re} \frac{\partial \bar{u}_k}{\partial x_2} \right] = 0 \quad (7)$$

to equation 3. Further, equation 3 is rearranged to the pressure Poisson equation.

$$L(\bar{p}) \equiv \frac{\partial}{\partial x_k} L(\bar{u}_k) = \frac{\partial}{\partial x_k} \left[\frac{\partial \bar{p}}{\partial x_k} \right] + \frac{\partial}{\partial x_i} \left[\bar{p} \frac{\partial \bar{u}_k}{\partial x_i} \right] = 0 \quad (8)$$

Equation 8 represents a quasi-linear elliptic boundary value problem, possessing complementary and particular solutions¹. The complementary solution p_c to the homogeneous form of equation 8 is obtained using farfield boundary conditions defined by the exterior flow, or in the fully bounded domain case, by the duct geometry. The particular solution p_p to equation 8 is thus generated using homogeneous Dirichlet boundary conditions where p_c is known. The total three-dimensional pressure field \bar{p} is the sum $p_c + p_p$, which in general requires execution of multiple PNS solutions, in an interaction algorithm construction, to impose p_p axial pressure gradients into the \bar{u}_1 momentum equation solution.

Upon addition of equations 3 and 7, $L(\bar{u}_k) + L^\delta(\bar{u}_k)$ represents a well-posed initial-boundary value problem for \bar{u}_k , upon addition of the order (8²) terms to the appropriate scalar components of the Reynolds stress tensor, which are

$$\overline{u_x u_k} \Big|_{j^2} = -C_4 \frac{k^2}{\varepsilon} \left[\frac{\partial \bar{u}_k}{\partial x_k} + \frac{\partial \bar{u}_k}{\partial x_j} \right] \quad (9)$$

III. Finite Element Penalty Algorithm

For the dependent variable set $\bar{q}(x_i) = \{\bar{u}_j, k, \varepsilon, p_p, p_c, u_i u_j\}$, equations 2, 3 + 7, 4, 5, 8, 6 + 9 represent a well-posed, initial-boundary value problem description on the three dimensional domain $\Omega = R^2 \times x_1 = \{x_2, x_3 : x_2$

$\in R^2$ and $x_1 \in [x_1, x_1]\}$. There is the additional fundamental requirement that equation 1 be rigorously satisfied, since it governs first order phenomena. The problem statement is completed with a polytropic equation of state for determination of \bar{p} for the isenergetic flow.

As the consequence of the PNS reformulation, each of the first six members of the set \bar{q} are eligible for constraint, on the boundary ∂R of R^2 , by a linear combination of Dirichlet and Neumann boundary conditions. The first five of these members are also required specified as an initial-condition on the plane $R^2 \times x_1$. No boundary conditions are appropriate for the algebraic equations governing $u_i u_j$.

The finite element penalty algorithm, for determination of the semi-discrete approximation $\bar{q}^h(x_j)$ to $\bar{q}(x_j)$, is based on classical concepts for differential constraints in the statement of variational boundary value problems⁷. These concepts are extended to the very non-linear PNS problem class using a Galerkin weighted-residuals formulation. Deferring details⁸, the transverse plane domain R^2 is discretized into the union of non-overlapping subdomains R_e^2 , wherein the functional form for the x_1 dependence of the semi-discrete approximation \bar{q}^h is assumed a priori specifiable. A convenient form is the cardinal basis $\{N_k(x_i)\}$, the members of which are polynomials on x_2 complete to degree k . Hence, the semi-discrete approximation becomes the union of elemental approximations,

$$\bar{q}(x_j) \approx \bar{q}^h(x_j) \equiv U_e \bar{q}^e(x_j) \quad (10)$$

$$\bar{q}^e(x_j) \equiv \{N_k(x_i)\}^T \{QI(x_1)\}_e \quad (11)$$

where subscript and/or subscript e denotes pertaining to the (finite element) domain R_e^2 . Further, $\{QI\}_e$ represents the values taken by \bar{q}^e at the nodes of the domain R^2 , and $1 \leq i \leq 13$ is a tensor index denoting the appropriate (nodal) vector dependent variable set of \bar{q}^h .

With definition of \bar{q}^h , equations 10-11 permit direct evaluation of the semi-discrete approximation error $L(\bar{q}^h)$ in each of the PNS governing differential equations. The basic concept in the calculus of a discretized variational boundary value problem is to render this error extremum in some norm. In the Galerkin weighed-residuals extension of this concept, this is accomplished by requiring this error to be orthogonal to the space of functions $\{N_k\}$ selected to define the semi-discrete approximation, i.e.

$$\int_{R^2} \{N_k\} L(\bar{q}^h) d\tau = \sum_e \int_{R_e^2} \{N_k\} L(\bar{q}^e) d\tau \equiv \{0\} \quad (12)$$

The middle expression in equation 12 emphasizes that the actual calculus operations are performed on the elemental domains R_e^2 . The resultant element (column) matrices are projected to the matrix structure of the global domain using the assembly operator S_e , which is simply matrix addition by rows⁸.

Equation 12 defines the numerical solution algorithm for the complete set \bar{q}^h with the exception of the combined equations 3 and 7 for \bar{u}_k . Here, the definition of the extremum must be augmented (penalized) such that the continuity equation is also satisfied. The functional form for this statement, which is an extension of the classical concept⁸, is

$$\int_{R^2} \{N_k\} \left[L(\bar{u}_k^h) + L^\delta(\bar{u}_k^h) \right] d\tau - \lambda \int_{R^2} \frac{\partial \{N_k\}}{\partial x_2} L(\bar{p}^h) d\tau \equiv \{0\} \quad (13)$$

The actual calculus operations defined in equation 13 are again performed on an elemental basis and assembled, and λ is an (arbitrary) parameter penalizing the statement of semi-discrete error orthogonalization for \bar{u}_k^h .

Equations 12-13 define the finite element penalty algorithm for the PNS equation system. The theoretical arbitrariness remaining is solely the degree k of the cardinal basis $\{N_k\}$, spanning either three-sided or four-sided element domains R^2 , the penalty parameter λ and the functional form for $L(\bar{p}^h)$. However, equations 12-13 are definitions of non-linear matrices, and resolution of the resultant problem definitions in linear algebra remains. For the semi-discrete approximations $\{\bar{u}_k^h, \bar{e}^h\}$, equations 12-13 are matrix statements expressing the x_1 -ordinary derivative of the appropriate elements of $\{QI\}_e$, equation 11. A Taylor series defines the matrix algebra statement for the assembly of these elements of $\{QI\}$, $1 \leq l \leq 5$, as.

$$\{FI\} \equiv \{QI\}_{j+1} - \{QI\}_j - \Delta x \{QI\}_{j+\theta} - \dots \equiv \{0\} \quad (14)$$

In equation 14, $\{QI\}_{j+1}$ represents this ordinary derivative evaluated at some location on the interval $x_{j+1} - x_j = \Delta x$ as defined by the parameter $0 \leq \theta \leq 1$.

Equation 12, evaluated for p_C^h , p_p^h and \bar{u}_k^h , yields directly the appropriate column matrix statement $\{FI\} = \{0\}$, $6 \leq l \leq 13$. Combined with equation 14, the resultant linear algebra statement of the finite element penalty algorithm for the PNS equation system, becomes

$$\left\{ FI(k, \lambda, \theta, \Delta x, \{QI\}) \right\} = \{0\} \quad (15)$$

Equation 15 is a highly non-linear algebraic equation system, the character of which is largely determined by the choice of the arbitrary solution parameters k , λ , θ , and Δx . Equation 15 does not readily admit a useful linearization, even for $\theta = 0$ which corresponds to explicit integration. Hence, the appropriate solution statement is the (Newton) matrix solution form,

$$\left[J(\{FI\}) \right]_{j+1}^p \{\delta QI\}_{j+1}^{p+1} = -\{FI\}_{j+1}^p \quad (16)$$

where p is the iteration index at step x_{j+1} , and

$$\{QI\}_{j+1}^{p+1} \equiv \{QI\}_{j+1}^p + \{\delta QI\}_{j+1}^{p+1} \quad (17)$$

$$\left[J(\{FI\}) \right] \equiv \frac{\partial \{FI\}}{\partial \{QI\}} \quad (18)$$

Equation 17 defines the fully-discrete approximation to the dependent variable set at the nodes of UR^2 , hence also $\bar{q}^h(x_i)$ throughout R^2 , see equation 10. Equation 18 defines the (Newton) Jacobian of the non-linear algebraic equation system, equation 15.

IV. Some Basic Decisions

Equation 15 delineates the basic decisions to be made regarding implementation of the finite element penalty algorithm into a computer code. In addition, for $\theta > 0$, a decision is required regarding approximate construction of the Newton algorithm Jacobian $[J]$, equation 18, since its size for the thirteen dependent-variable PNS statement is unwieldy on present computers. The decision on k , equation 11, of course impacts considerably on the "size" of $[J]$.

The aerodynamics analyses, documenting the theory as summarized herein, have been conducted using the CMC:3DPNS computer program.⁹⁻¹¹ Each of the cited basic decisions has therefore been made, as implemented for this code. In light of the resultant understanding of how the algorithm functions, as well as advances made in vector computer architectures, some of these decisions should and will eventually become modified. This in no way detracts from the proof of theory and practice that has resulted using this code.

Bearing this in mind, the discretization of R^2 is defined as the union of triangular cross-section finite elements spanned by the linear ($k=1$) natural coordinate cardinal basis. The trapezoidal rule is employed for the integration algorithm, $\theta = 1/2$ in equation 14. The penalty parameter λ , following extensive numerical experimentation, has been defined as the diagonal matrix,

$$\lambda^p \Rightarrow [\lambda]^p \equiv C \Delta x [U1]_{j+1}^p \quad (19)$$

where C is a constant of order unity, and the elements (on the diagonal) of $[U1]_{j+1}^p$ are $\{U1\}_{j+1}^p$, the nodal distribution of $\{QI\}$ computed at each iteration p at x_{j+1} .

The functional form of the penalty term, equation 13, involves definition of an auxiliary dependent variable $\bar{\phi}^h$, as

$$L(\bar{p}^h) = \frac{\partial}{\partial x_j} \left(\bar{p}^h \bar{u}_j^h \right) \equiv \frac{\partial^2 \phi^h}{\partial x_j^2} \quad (20)$$

The boundary conditions for ϕ are a linear combination of homogeneous Dirichlet and Neumann constraints, defined according to required flow porosity on various segments of ∂R . Hence, \bar{q}^h is augmented for one additional entry, the solution of

$$L(\phi^h) = \frac{\partial^2 \phi^h}{\partial x_j^2} - \frac{\partial(\bar{p}^h \bar{u}_j^h)}{\partial x_j} = 0 \quad (21)$$

The Galerkin weighted-residuals algorithm statement for equation 21 is the algebraic equation system $\{F1\} = \{0\}$, which is added to equation 15, hence equations 16-18. Therefore, the explicit form of the complete penalty term in equation 13 is.

$$\lambda \int_{R^2} \frac{\partial \{N_k\}}{\partial x_j} L(\bar{p}^h) d\tau \quad (22)$$

$$\equiv \int_{\bar{e}} \left[C \Delta x \right]_{R^2} \left[U1 \right]_e \frac{\partial \{N_1\}}{\partial x_j} \{N_1\}^T \{\phi\}_e d\tau$$

Regarding the Newton algorithm Jacobian, equation 18 has been replaced in CMC:3DPNS with two sparse matrices, yielding a corresponding compromise on overall convergence rate while significantly reducing the Jacobian matrix rank. The initial-valued dependent variables $\{\bar{u}_i^h, k, \epsilon\}$ are sequentially solved as multiple right side substitutions to equation 16, using the \bar{u}_1^h Jacobian, $\{J11\}_{j1}$, where

$$\{J11\} \equiv \frac{\partial \{F1\}}{\partial \{Q1\}} \quad (23)$$

The Poisson field variables $\{p_c^h, p_p^h, \bar{z}^h\}$ are solved sequentially as multiple right side substitutions using the p_c^h Jacobian $\{J66\}$. The scalar components of \bar{u}_i^h are determined using an elemental averaging and assembly procedure, equivalent to solving equation 16 using $\{J88\}$ for multiple right side substitutions. The algorithm timing utilizes the sequence $\{J11\}$, $\{J66\}$, $\{J88\}$, with update of the Jacobians occurring at every iteration. Details of the formation of these Jacobians is given in reference 8.

V. Documentary Results

A fairly voluminous library of documentary results has been generated and published on performance aspects of the PNS finite element penalty algorithm. The following synopsis emphasizes the essential points as a function of domain boundedness. All cited solutions were generated by the same code, the problem definition being completely contained within the general boundary condition statement.

$$i(\bar{q}^h) = a_1(\bar{q})\bar{q}^h + a_2(\bar{q}) \frac{\partial \bar{q}^h}{\partial x_j} \hat{n}_j + a_3(\bar{q}) = 0 \quad (24)$$

Semi-Bounded Solution Domain

This is the most typical aerodynamic specification, wherein the PNS equation system solution is sandwiched in between an exterior, three-dimensional potential flow solution and an aerodynamic configuration. Examples include three-dimensional boundary layers, juncture region flows and trailing edge wake flows among others. In each case, the exterior flow potential solution provides the PNS farfield boundary conditions for the complementary pressure solution p_c^h .

Figure 1a) illustrates an idealized wing-body junction region, and Figure 1b) defines the PNS solution domain R^2 and appropriate boundary condition specifications for \bar{q}^h , equation 24. Baker et.al.¹ document algorithm performance for the case of the

region defined by the right intersection of two, 10%-thick parabolic arc airfoils at zero angle of attack. Figure 2 compares the algorithm predictions of transverse plane velocity distributions $\bar{u}_1(x_1/C = 0.5, x_2)$, on the lower surface of the juncture region, for turbulent and laminar flow. The lateral flowfield reversal computed in the lower reaches of the laminar flow calculation are in qualitative agreement with the two-dimensional prediction of Rubin, et.al.¹² regarding this feature. The PNS algorithm solution converged to a stationary total pressure distribution, $\bar{p}(x_j) = p_c^h + p_p^h$, in three interaction sweeps. The Newton algorithm convergence limit was defined at $\epsilon = 3 \times 10^{-4}$, and the error in satisfaction of the continuity equation 1, measured in the energy norm of \bar{p} , was maintained of the order of 10^{-6} at the final iteration of each solution step.

As a second example, Figure 3a) shows the two-dimensional problem definition of a non-separated trailing edge wake flow, and Figure 3b) defines the associated algorithm boundary conditions. Figure 4 compares the results of the third interaction PNS solution with experimental data on the region, $1.0 \leq x_1/C \leq 1.10$, for turbulent flow¹³. The agreement on mean flow distributions $\bar{u}_1(x_j)$ is excellent, Figure 4a). Furthermore, similar agreement on components of the Reynolds stress tensor was achieved, including the various peaks and growth rates, see Figures 4b)-c). Similar levels of agreement have been documented for conventional laminar and turbulent boundary layer flows¹⁴.

Fully Bounded Solution Domain

The general aerodynamic problem class of flows in engine inlet and exhaust ducts exemplifies this problem class. The complementary pressure boundary conditions are derived from the duct curvature and inlet pressure, and the resultant complementary pressure axial gradient is augmented to conserve axial mass flux, cf. Patankar³. Figure 5a) illustrates a symmetric quarter plane PNS solution domain R^2 for flow in a straight duct of rectangular cross-section. Figure 5b) defines the corresponding distribution of boundary conditions. Baker et.al.¹ document comparisons between the PNS predictions and the experimental data of Melling and Whitelaw¹⁵ for the case of $Re = 10^4$. In Figure 6, the computed \bar{u}_1 isovel distributions indicate good agreement on level and inflection points, in the lower reaches of the wall layers, although the experimental data indicate a significantly more turbulent core region. Figure 7 compares the fully developed counter-rotating vortex patterns in \bar{u}_2 which indicate quite good qualitative and quantitative agreement. The PNS solutions confirm the causal mechanism to be non-isotropy of the Reynolds stress tensor, $\bar{u}_i^h \bar{u}_j^h$, and Figure 8 summarizes the comparison.

Aerodynamic ducts of general interest are typically of non-uniform cross-section, thus inducing axial pressure gradients. These gradients will reflect dominantly into the structure of the turbulent flow, especially near the walls. Figure 9 illustrates the essential aspect in a two-dimensional setting. Figure 10 compares the distributions of PNS predicted transverse velocities \bar{u}_2 for a simple diverging and converging cross-section with 20% area change. The correct mirror symmetries result, and the levels are quite small except in the transition region. Figures 11-12 compare the corresponding PNS prediction of k and ϵ , the principal distinctions being the larger peaks produced by the favorable pressure gradient associated with the converging duct. No experimental data are available for comparison, but these results do

emphasize the importance of sufficient discretization to resolve the wall layers along with a suitable low turbulence Reynolds number modification to the Reynolds stress equation.

Non-bounded Solution Domain

The aerodynamics problems of multiple free-jet interaction and wake vortex flows exemplify the non-bounded solution domain definition. For example, Figure 13a) illustrates a multiple jet configuration, and Figure 13b) defines the corresponding PNS domain boundary condition distribution. A key factor here is that the farfield boundary must be porous to cross-flow, such that influx/efflux can be admitted in response to the entrainment action of the jets. The farfield boundary condition on complementary pressure p_c is typically a homogeneous constant in this instance.

As an example, Figure 14 summarizes the symmetric half-plane PNS prediction¹⁶ of mixing and entrainment produced by a turbulent slot jet of half-width H_f on the region $0 \leq x_1/H_f \leq 1.0$. The gradual erosion of the potential core in \bar{u}_1 is evident, Figure 14a), as well as the distribution of entrainment (negative \bar{u}_2) from the farfield, Figure 14b). The sharp growth and resultant monotonic decay of both k and ϵ are also illustrated, Figures 14c)-d).

Figure 15 compares the PNS prediction¹⁶ of symmetric-half, transverse plane velocity distributions \bar{u} , one diameter downstream of a single, circular cross-section jet for laminar and turbulent flow. Both solutions document essentially radial entrainment, with diametric opposition along the circumference of the jet (recall Figure 14b)). The salient defining feature of this comparison is that the extremum normalized magnitude of \bar{u}_2 for the laminar case is $\bar{u}_2^m = 0.0017$, while $\bar{u}_2^m = 0.044$ for the turbulent case. Therefore, in comparison, the measure of entrainment is enhanced by a factor of 20 for the turbulent case. Finally, Figure 16 shows the PNS predicted distribution of transverse plane velocity \bar{u} , produced by a symmetric multiple-free-jet configuration, consisting of four jets each centered on the bisector intersection of each quadrant with the circle. A pattern of eight counter-rotating vortex pairs has been induced, by the rapid decay of this closely-coupled multi-jet geometry, with a complex pattern of influx/efflux on the farfield boundary. This prediction is in good qualitative agreement with smoke flow visualization experimental data, including a variety of parameter modifications and comparisons¹⁶.

VI. Conclusions

The spectrum of computational results generated using a finite element penalty numerical algorithm for approximate solution of the three-dimensional parabolic Navier-Stokes equations for steady, subsonic turbulent and laminar flows, serves to document the mathematical appropriateness and robustness of the construction. With addition of the energy equation, and identification of the linear momentum $\bar{m}_i \equiv \bar{\sigma}_{ij}$, the formal construction should be equally appropriate for supersonic flows. The theoretical concepts underlying the algorithm formulation are direct extensions of fundamental principals in constrained extremization of a variational boundary value problem. As such, the PNS application has verified the use and utilization of classical concepts in mechanics applied to the computational problem class. It is hoped that this may be the progenitor of a long and

fruitful association, that will focus computational fluid mechanics algorithm constructions within the robust framework of theoretical and applied mechanics, the very backbone of engineering analysis.

VII. References

1. Baker, A. J., and Orzechowski, J. A., "An Interaction Algorithm For Three-Dimensional Turbulent Subsonic Aerodynamic Juncture Region Flow," AIAA J., V. 21, 1983, to appear.
2. Dodge, P. R. and Lieber, L. S., "A Numerical Method For the Solution of Navier-Stokes Equation For a Separated Flow," Technical Paper AIAA-77-170, 1977.
3. Patankar, S. V., Numerical Heat Transfer and Fluid Flow, McGraw-Hill/Hemisphere, NY, 1980.
4. Briley, W. R., and McDonald, H., "Analysis and Computation of Viscous Subsonic Primary and Secondary Flows," Technical Paper AIAA-79-1453, 1979.
5. Mikhail, A. G. and Ghia, K. N., "Analysis and Asymptotic Solutions of Compressible Turbulent Corner Flow," Trans. ASME, J. Engr. Power, V. 104, 1982, pp. 571-579.
6. Cebeci, T., and Smith, A.M.O., Analysis of Turbulent Boundary Layers, Academic Press, New York, 1974.
7. Oden, J. T., "A Theory of Penalty Methods for Finite Element Approximations of Highly Nonlinear Problems in Continuum Mechanics," Comp. & Structures, V. 8, 1978, pp. 445-449.
8. Baker, A. J., Finite Element Computational Fluid Mechanics, McGraw-Hill/Hemisphere, NY, 1983.
9. Baker, A. J., "The CMC:3DPNS Computer Program For Prediction of Three-Dimensional, Subsonic, Turbulent Aerodynamic Juncture Region Flow - Volume I - Theoretical," NASA Technical Report CR-3645, 1982.
10. Manhardt, P. D., "The CMC:3DPNS Computer Program For Prediction of Three-Dimensional, Subsonic, Turbulent Aerodynamic Juncture Region Flow - Volume II - User's Manual," NASA Technical Report CR-165997, 1982.
11. Orzechowski, J. A., "The CMC:3DPNS Computer Program For Prediction of Three-Dimensional, Subsonic, Turbulent Aerodynamic Juncture Region Flow - Volume III - Programmer's Manual," NASA Report CR-165998, 1982.
12. Rubin, S. G., "Incompressible Flow Along a Corner," J. Flu. Mech., V. 26, Pt.1, 1966, pp. 97-110.
13. Baker, A.J., Yu, J.C., Orzechowski, J.A., and Gatski T.B., "Prediction and Measurement of Incompressible Turbulent Aerodynamic Trailing Edge Flows," AIAA J., V. 20, No. 1, 1982, pp. 51-59.
14. Baker, A. J., "A Penalty Finite Element Algorithm For Parabolic Flow Prediction," ASME, App. Mech. Div., AMD-Vol. 51, 1982, pp. 137-142.

15. Melling, A., and Whitelaw, J. H., "Turbulent Flow in a Rectangular Duct," J. Fluid Mech., V. 78, Pt. 2, 1976, pp. 289-315.

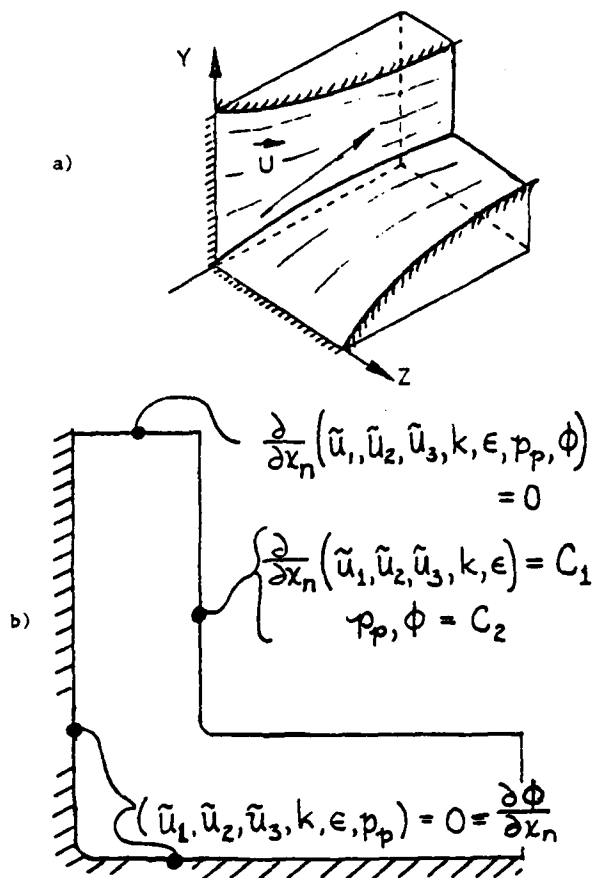


Figure 1. Characterization of a Semi-Bounded Aerodynamic Junction Region Flow, a) Geometry, b) Penalty Algorithm Boundary Conditions.

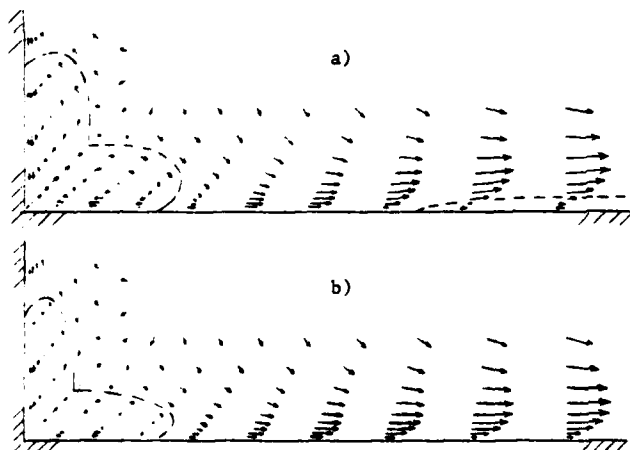


Figure 2. Penalty Algorithm Prediction of Parabolic Arc Junction Region Transverse Plane Velocity \tilde{u}_1 Distribution, $x_1/C = 0.5$, a) Laminar Flow, $u_1^m = 0.06$ b) Turbulent Flow, $u_1^m = 0.10$, from Ref. 1.

16. Baker, A. J., Orzechowski, J. A., and Stungis, G. E., "Prediction of Secondary Vortex Flowfields Induced By Multiple Free-Jets Issuing In Close Proximity," Technical Paper AIAA 83-0289, 1983.

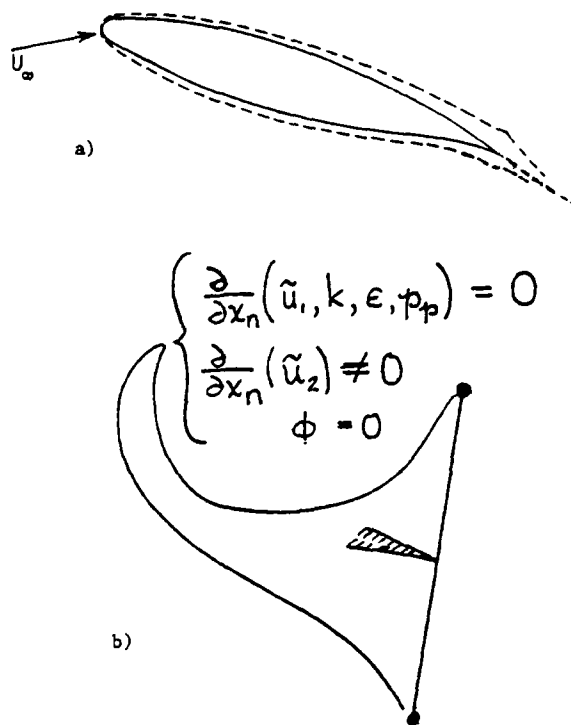


Figure 3. Characterization of a Semi-Bounded Aerodynamic Trailing Edge Wake Flow, a) Geometry, b) Penalty Algorithm Boundary Conditions.

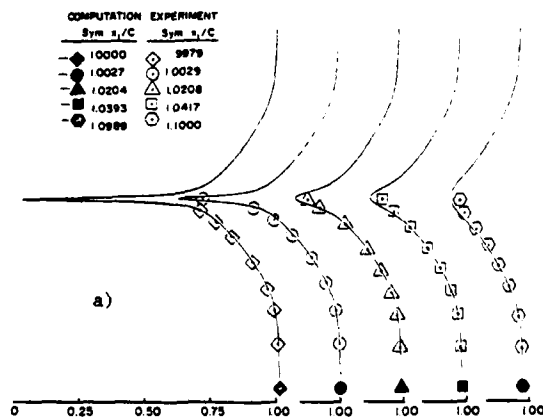


Figure 4. Comparison Between Penalty Algorithm Prediction and Experiment For Wake Region Flow, NACA 63-012 Airfoil, $\alpha = 0^\circ$, a) Mean Axial Velocity \tilde{u}_1 , b) Reynolds Shear Stress $\tilde{u}_1 \tilde{u}_2$, c) Reynolds Normal Stress $\tilde{u}_1 \tilde{u}_1$, from Ref. 13.

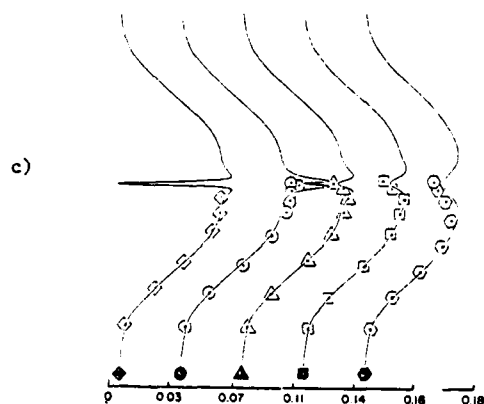
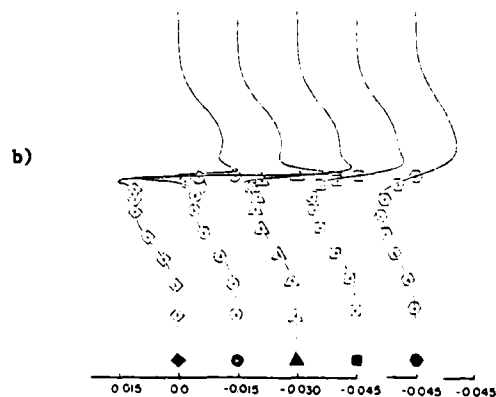
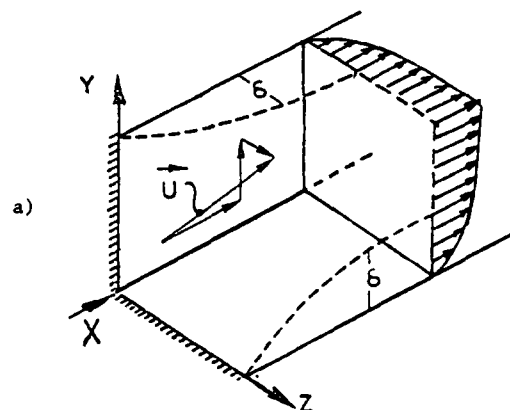


Figure 4. Comparison Between Penalty Algorithm Prediction and Experiment For Wake Region Flow, NACA 63-012 Airfoil, $\alpha = 0$, a) Mean Axial Velocity u_1 , b) Reynolds Shear Stress u_1u_2 , c) Reynolds Normal Stress u_1u_1 , from Ref. 13, Concluded.



a) $\frac{\partial}{\partial x_n} (\tilde{u}_3, k, \epsilon, p_p, \phi) = 0$

b) $\frac{\partial}{\partial x_n} (\tilde{u}_2, k, \epsilon, p_p, \phi) = 0$

$(\tilde{u}_1, \tilde{u}_2, \tilde{u}_3, k, \epsilon, p_p, \phi) = 0$

Figure 5. Characterization of a Fully Bounded Duct Flow, a) Geometry, b) Penalty Algorithm Boundary Conditions.

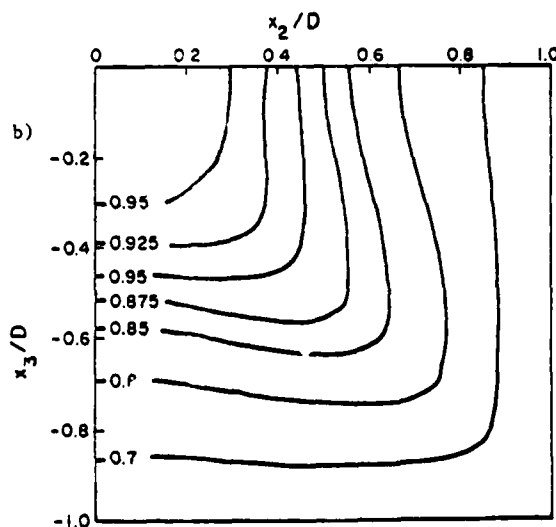
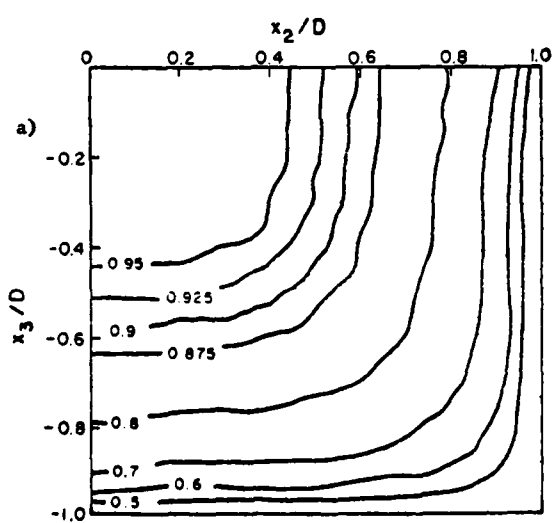


Figure 6. Comparison Between Penalty Algorithm Solution and Experimental Data, Axial Velocity \tilde{u}_1 Distribution, $x_1/D_H = 37$, a) PNS Prediction, from Ref. 1, b) Experimental Data, from Ref. 15.

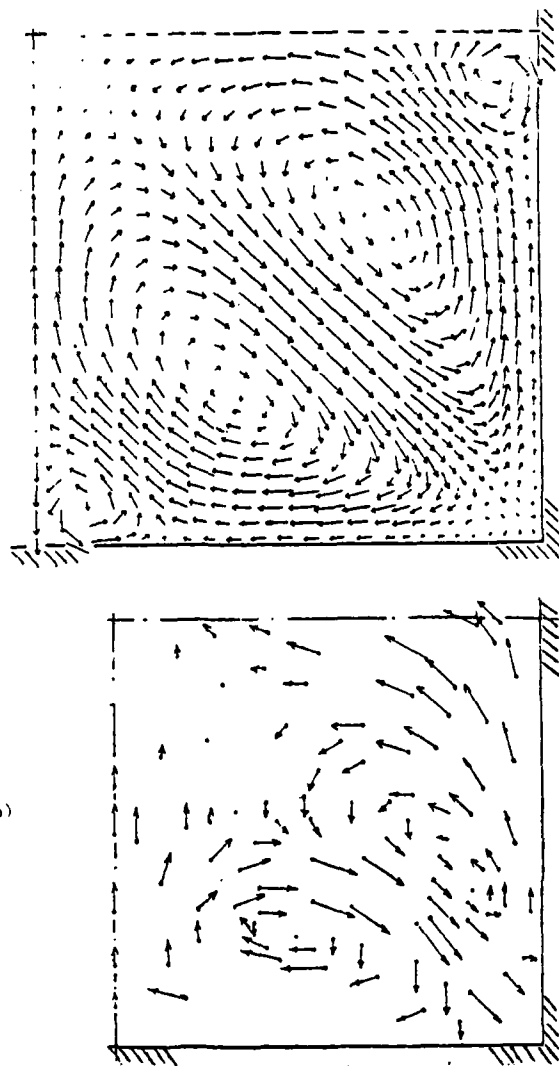


Figure 7. Comparison Between Penalty Algorithm Solution and Experimental Data, Transverse Plane \bar{u}_z Distribution, $x_1/D_h = 37$, a) PNS Prediction, from Ref. 1, b) Experimental Data, from Ref. 15.

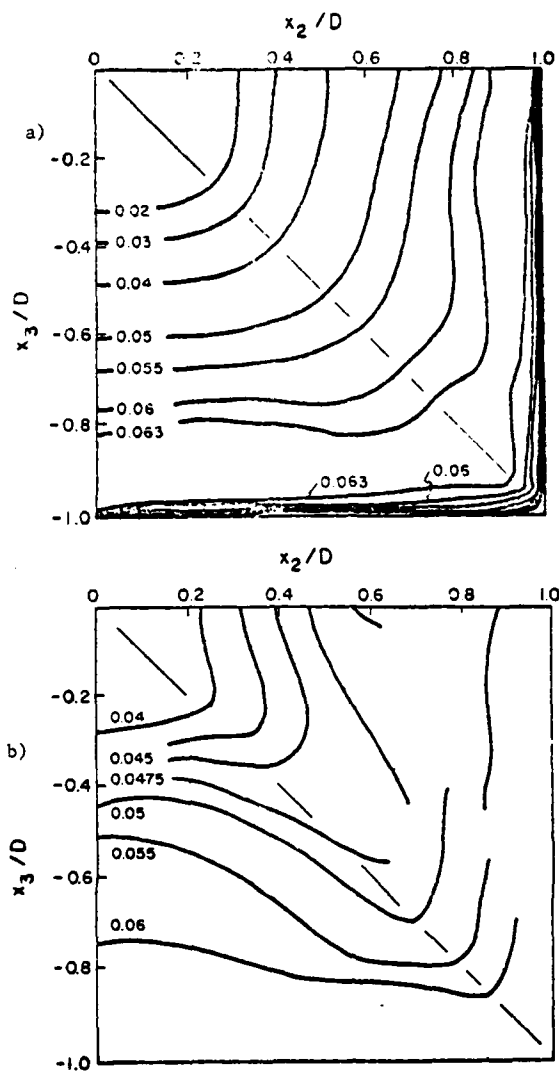


Figure 8. Comparison Between Penalty Algorithm Solution and Experimental Data, Transverse Reynolds Normal Stress $\bar{u}_z'u_z'$ Distribution, $x_1/D_h = 37$, a) PNS Prediction, from Ref. 1, b) Experimental Data, from Ref. 15.

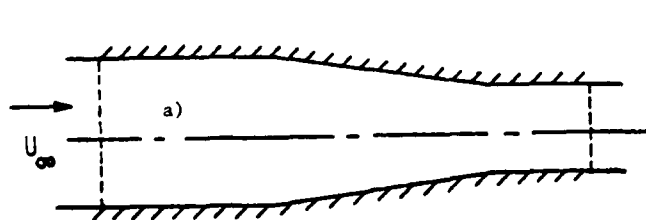
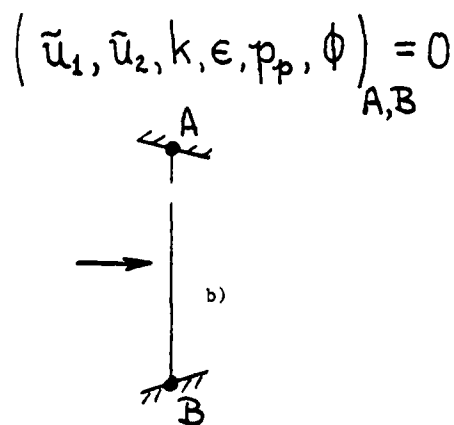


Figure 9. Characterization of a Fully Bounded, Variable Area Duct Flow, a) Geometry, b) Penalty Algorithm Boundary Conditions.



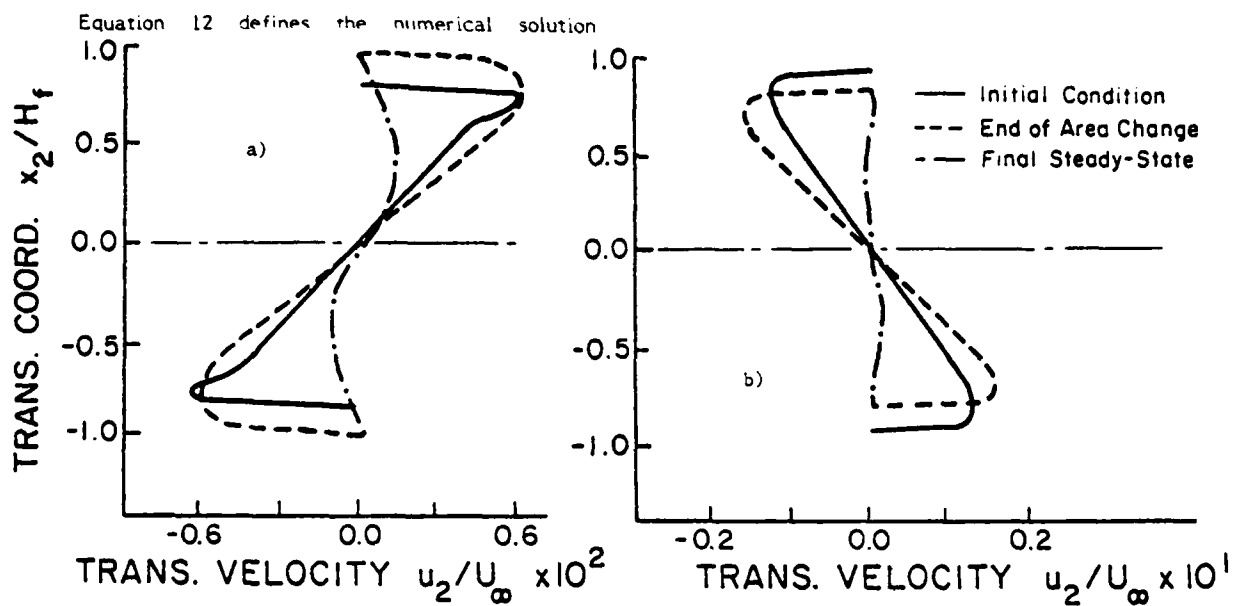


Figure 10. Penalty Algorithm Duct Flow Prediction of Transverse Velocity \bar{u}_2 Distributions, a) Diverging Cross-Section, b) Converging Cross-Section, from Ref. 14.

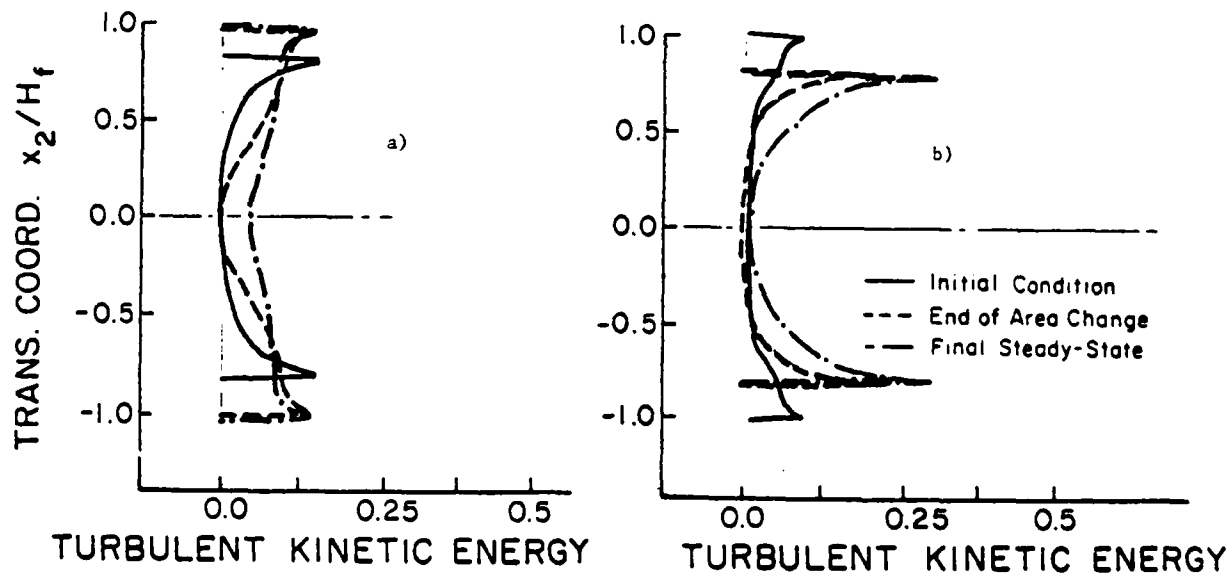


Figure 11. Penalty Algorithm Duct Flow Prediction of Turbulent Kinetic Energy k Distributions, a) Diverging Cross-Section, b) Converging Cross-Section, from Ref. 14.

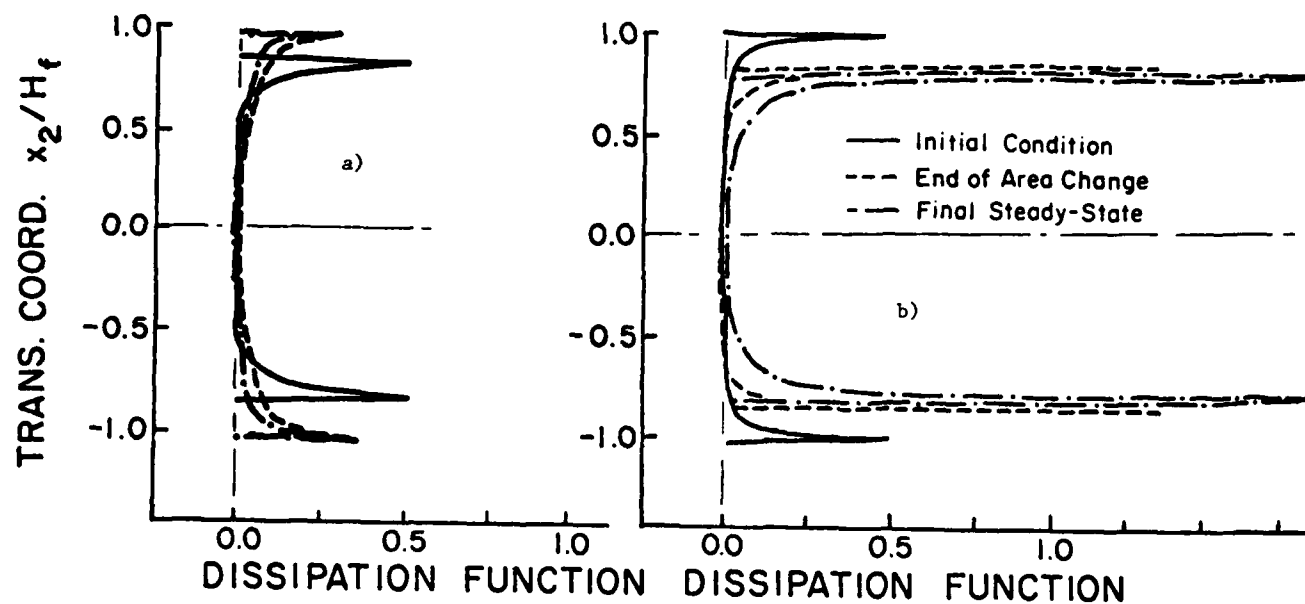


Figure 12. Penalty Algorithm Duct Flow Prediction of Isotropic Dissipation Function ϵ Distributions, a) Diverging Cross-Section, b) Converging Cross-Section, from Ref. 14.

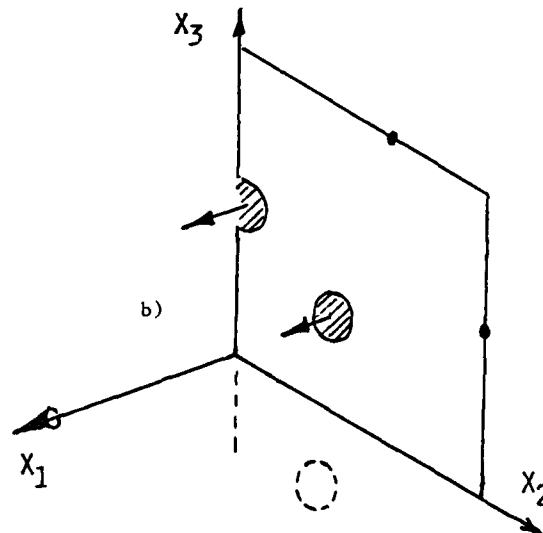
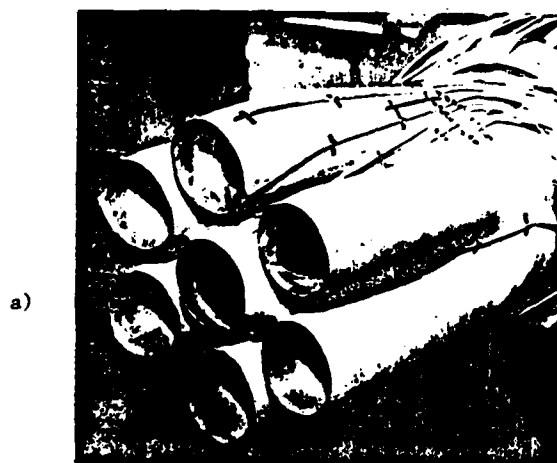


Figure 13. Characterization of an Unbounded Multiple Free-Jet Flow, a) Geometry, b) Penalty Algorithm Boundary Conditions.

$$\frac{\partial}{\partial x_n}(\tilde{u}_1, \tilde{u}_2, \tilde{u}_3, k, \epsilon, p_p, \phi) \equiv 0$$

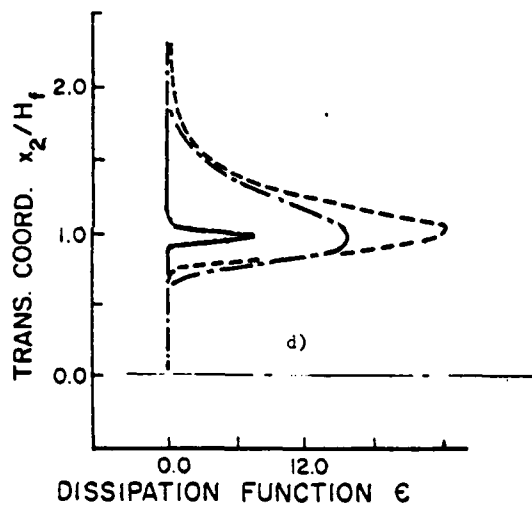
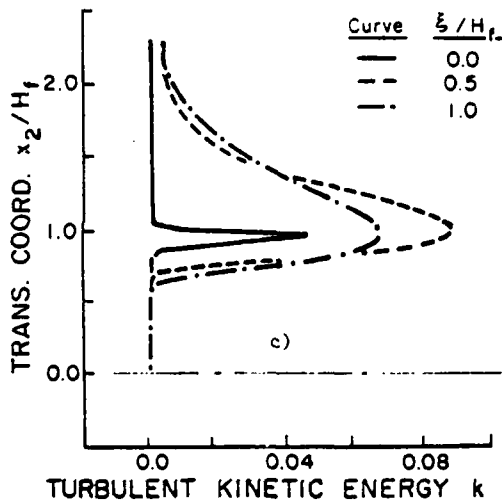
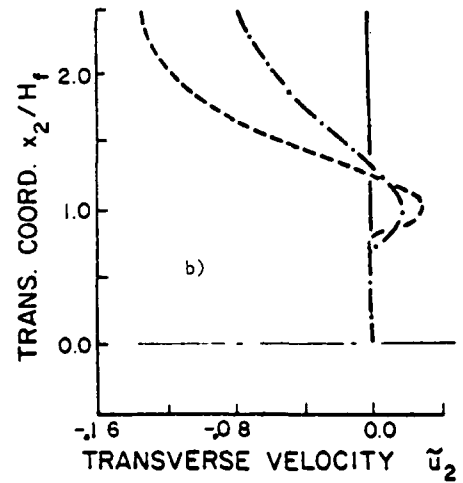
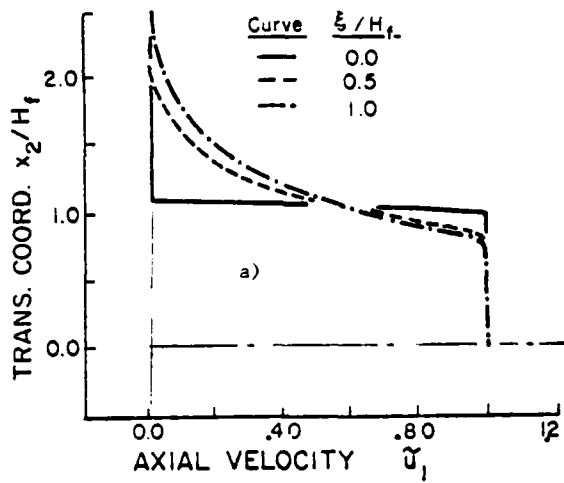


Figure 14. Penalty Algorithm Prediction of Symmetric Two-Dimensional Slot-Jet Flow, $x_1/D_h = 1.0$, a) Axial Velocity \bar{u}_1 , b) Transverse Velocity \bar{u}_2 , c) Turbulent Kinetic Energy k , d) Isotropic Dissipation Function ϵ , from Ref. 16.

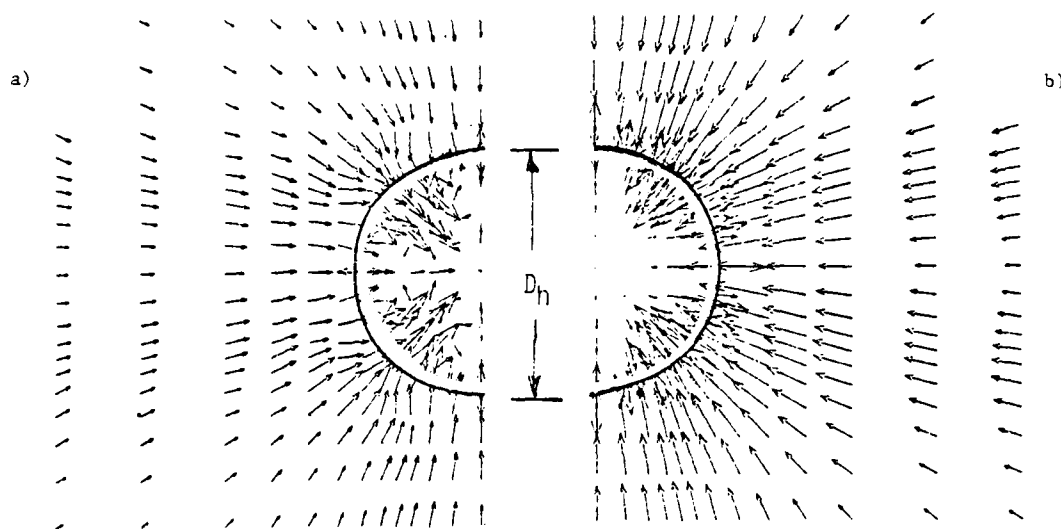
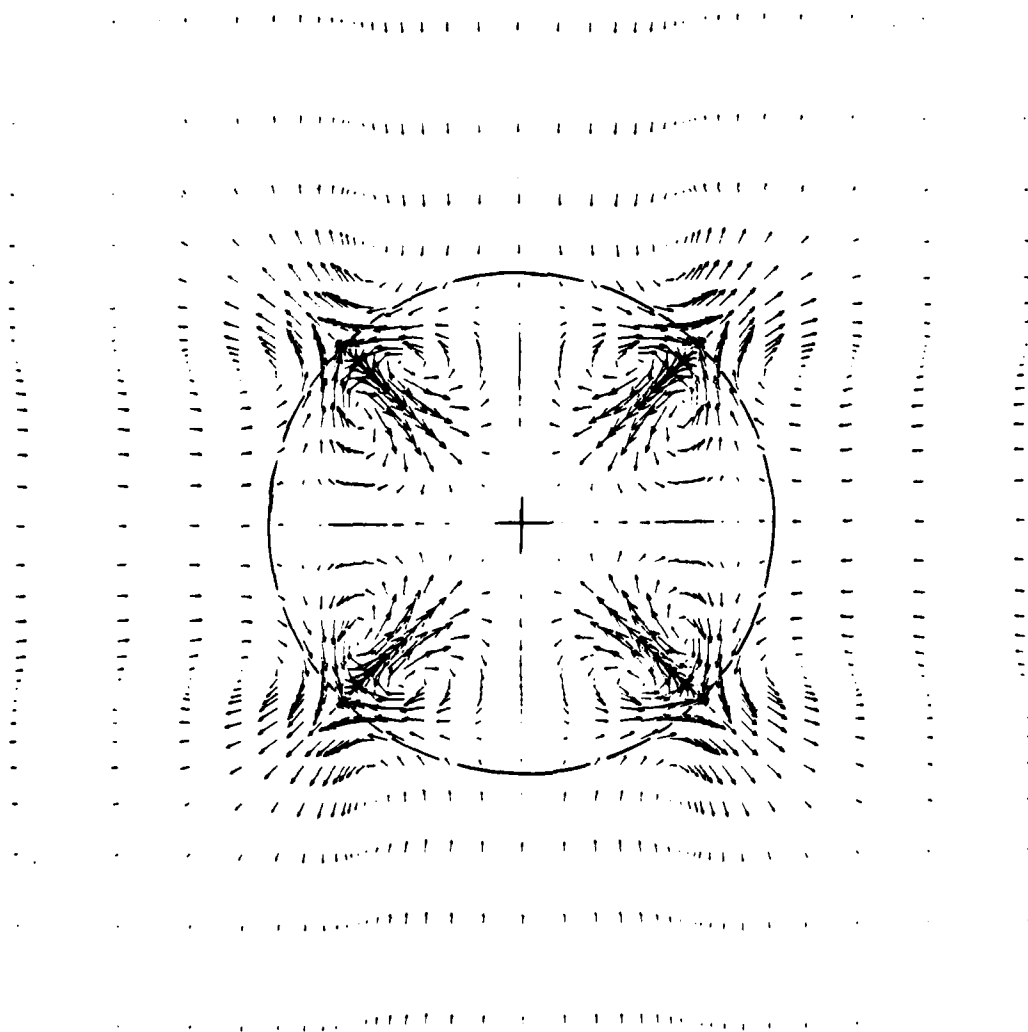


Figure 15. Penalty Algorithm Prediction of Transverse Plane Velocity \bar{u}_x Distributions, Isolated Circular Cross-Section Free-Jet, $x_1/D_h = 1.0$, a) Laminar Flow, $u_0^m = 0.0017$, b) Turbulent Flow, $u_0^m = 0.044$, from Ref. 16.

Figure 16. Penalty Algorithm Prediction of Transverse Plane Velocity \bar{u}_x Distributions, Four Free-Jets, $x_1/R = 1.5$, from Ref. 16.



KEYNOTE LECTURE 1

WING DESIGN AND ANALYSIS - YOUR JOB

by

A.M.O. SMITH

Douglas Aircraft Company, Retired

1.0 Introduction

Many years ago, about World War II, I believe, I learned the definition of an airplane. It is a device that almost won't work. A missile was defined slightly later. It is a device that almost will work. But perhaps now with all the advances in rockets and spacecraft, the airplane definition would be more appropriate.

These definitions characterize our problem because first-line airplanes are truly exceedingly complicated, very expensive devices; in fact, worth their weight in sterling silver. The "backbone" of an airplane is its wing, and this with its many nuances and complications is the subject of my lecture, in which I shall outline the aerodynamic problems and roughly indicate the status of solutions.

Compared with many other fields, the analysis of the fluid flow about a body such as a wing is in its infancy. In aerodynamics, many of the properties of a body are found by estimation, by interpolation between known answers, by calculation for a highly simplified approximation, and the like. But in some fields that is not so, at all. If we had to apply aerodynamic methods to finding some arithmetic product, say $(211 + 307i) \times (62.6 + 9.5i)$, we would likely work from a graph determined by some "beacon" values that could be calculated and then interpolate, because we did not really know how to evaluate this particular product.

To get a bit more complicated, weight estimation and calculation is a very important function in the design of aircraft. The word "estimation" comes from not knowing initially the exact size of some part such as a structural member, but if a shape is given and the material identified so that density is known, weight estimation becomes simply a process of calculating the volume, and I emphasize "calculating," not estimating. If one wishes to take the necessary pains, the volume can be calculated to any degree of accuracy. Unlike the aerodynamicist, who is said to assume everything but the responsibility, the weight man can precisely calculate the weight of any shape that he is given.

The same can be said for many parts of the structural problem. If a structures man is given any cross section, no matter how complicated, he can calculate the section modulus in a straightforward manner. Electrical circuit analysis is the same way. Given resistances, capacitances, impedances, etc. the analyst writes a differential equation that exactly indicates currents, transients, etc. at least to the accuracy known for the elements.

But until recently aerodynamics has had little of this true calculation. The art consisted of "beacon" type of answers - the flow about a sphere, or ellipsoid, a two-dimensional wing at low angle of attack, the boundary layer on a flat plate, etc. These known solutions would then be used as guide-points or beacons to go from them to the actual case by a process of estimation and correction.

For many years I considered one of my underlying goals in research was to develop methods of calculating the aerodynamic properties of bodies. An ordinary brick is really quite a simple shape, but can we calculate the lift, drag, moments, and pressure distribution for it, at all orientations? The weight man certainly can do his equivalent job. Looking at the broad problem like this makes me feel very humble, because from this viewpoint obviously aerodynamic analysis is in its infancy. Some people may reply that I am being too severe, but the brick is not that far from some aircraft problems. Consider a wing with a spoiler extended from the upper side.

In reality, due mainly to the electronic calculator we have progressed a long ways in the last forty years. Around 1940 calculation of flow around an arbitrary airfoil could indeed be done provided the shape was "easy" and quite fair. I am speaking of methods like Theodorsen's method. But calculation was almost a "stunt". I did it once and it took me most of two weeks as I remember. Of course there was thin airfoil theory, but this is more or less one of my "beacons". Nothing could be done on multi-element airfoils except for the special case of an infinite set of airfoils in cascade. Also, of course the analyses were essentially for $M=0$, the only effect of Mach number being accounted for by Prandtl-Glauert or Kármán-Tsien types of corrections.

The calculation of flow about bodies of revolution, even at zero angle of attack, was even less developed than the two-dimensional problem such as for airfoils. There was von Kármán's method originally developed for airships, Fuhrmann type bodies and of course the prolate spheroid family. But even so simple a body as a hemisphere-cylinder combination was quite beyond the existing analytic capability.

When dealing with the boundary layer problem, there were Pohlhausen and Thwaites's type of methods for low-speed adiabatic type of laminar flow. Some work on the integral method existed for heat transfer, but the methods were never developed very far. In

turbulent flows, with pressure gradient, everything depended on von Kármán's integral equation. The main accounting for the effect of pressure gradient for changes in skin friction was to use the local velocity instead of the freestream, together with the momentum thickness, θ . Also of course, the methods applied only at $M=0$, without heat transfer, and were only two dimensional.

But at the present time, thanks in great part to CFD, so long as the flow remains attached, we can calculate the inviscid flow for any reasonable shape when $M=0$, or is small, both two dimensional and three dimensional, whether internal or external. For instance, the flow has been calculated for the very complicated shape of the space shuttle mounted on the Boeing 747 airplane. The latest and very active development is calculation of transonic flow, complete with shocks, for three-dimensional wings of arbitrary shape. So you see we have progressed from barely being able to analyze a two-dimensional airfoil at $M=0$ to rather routine analysis of a three-dimensional wing at any Mach number.

In the field of turbulent boundary layers, I do not think the progress has been so great. Of course, now there are quite rational methods that can calculate the boundary layer flow for two-dimensional problems and arbitrary pressure gradients so long as separation does not set in. Also, heat transfer effects and Mach number are handled well, and in general, the accuracy as determined by experiment is good. Furthermore, a great many three-dimensional problems, including heat transfer and Mach numbers other than zero, can be handled, but this work has not settled to a routine. However, the progress has not been so great as for inviscid flow because basically we know little more of the real fundamentals of turbulent flow than we did many years ago. So our development of methods of analysis is based upon a weak foundation because the governing equations are really not known. Of course, many tests leading to better founded empiricism have been made since World War II, but the data is still empiricism of the type that led me to say that aerodynamics, at least in many ways, is just an involved interpolation process, working from beacon data.

But for laminar flow, the situation is considerably different. Here the governing equations are known, and because of the computer, great strides have been made in their solution. For two-dimensional problems, providing the input conditions are sufficiently well known, and again, providing the flow is attached, four-place accuracy can be obtained, if needed, for highly arbitrary conditions, including boundary-layer suction. Hence, questions of laminar boundary-layer flow can be answered by pure calculation, just as one finds the product of $(211 + 307i) \times (62.6 + 9.5i)$. Much can be done for three-dimensional flows as well, but calculations are not as routine as for two-dimensional because of crossflow and reverse-flow problems, three-dimensional separation, and the like. However, it should be noted that, at the Reynolds numbers of airplanes, the extent of laminar flow will be small unless some form of laminar flow control (LFC) is being used, and then, because it is sought only at low angles of attack, separation should not be a problem.

I have long been interested in flow-field calculations. My first attempt by other than classical methods was to use Southwell's relaxation method to calculate flow around a symmetrical "bumpy" airfoil

at zero angle of attack. We succeeded (I mean we got a sensible answer) after about two weeks of steady work. Later, I wished to study the boundary-layer flow into a suction slot. I wrote out equations that I thought covered the situation and put them into a finite difference form and asked for a time estimate from computing, which then had its first electronic calculator, the IBM 701. The estimate was 2000 machine-hours, so that put an end to that effort. My panel method for potential flow was more successful, but it is not really CFD.

Then, as better computers arrived, I tackled the ordinary laminar boundary-layer equations with success. This led me to see what could be done for turbulent boundary layers, and here we had luck because a very simple algebraic formulation for turbulent transport properties yielded considerable success.

So you see I have been periodically in and out of the field of CFD, but since 1975 when I retired, I have done no more work in the area. In preparation for this paper, I have reviewed many of the symposiums, papers, and books on the subject, and while I am generally aware of the state of the art, I find I have been left far behind technically. One can say that, at present, CFD is a leading style, and because it is relatively new, results leading to papers are rather easily obtained. Hence, many scientists have gravitated to the area. This is good because it is a natural and attractive way for a new field to get explored rapidly. Right after World War II, I observed the same phenomenon and rapid exploration, but then it was in linearized supersonic aerodynamics.

But although many are gravitating to this field, I do not mean it is simple. Far from it. There are exceedingly many subtleties - the numerical stability problem, questions such as whether a finite difference representation truly represents the differential equation in the limit, the boundary problem, grid systems, etc. For instance, a derivative somewhere in a net can be written in many ways, some of which are stable, others not, and each may have different truncation errors. With this wealth of detailed knowledge that has developed, including all the special nuances, I find I am quite unable to provide any authoritative discussion or review of the actual technical subject.

Instead, I shall try to point out the total job as applied to airplanes and show where we are, at the present moment.

But before proceeding, I wish to point out one very important fact. If computing can be done instead of testing, the lead time for obtaining useful answers is reduced tremendously. Depending on the problem and how well one is tooled up for it, a new answer can be found by CFD in from one day to a week; for example, a change in a wing design. Furthermore, there is little difficulty in getting access to a computer, at least for important problems. But if a model must be tested in a wind tunnel, even with numerical milling to make the model, the numerical description of the model must be put into the machine, then the model must be hand finished and checked, then mounted in the tunnel, and then tested. A month is substantially the minimum time to get test results on a new model. Furthermore, a good wind tunnel is usually involved with some other test, and immediate access is a rarity. Finally, with CFD, a

small change in shape, as of a wing, can often be made by modifying a few numbers. But a small change in shape of a wind tunnel model means either fastening on some added material, or machining some off, either process taking considerable time. So turnaround time is a tremendous advantage to CFD, and cost may compound that advantage.

2.0 A Few Comments About the Operation of Airplanes

A basic reason for continually trying to improve the design and accuracy of analysis of airplane components is to improve the airplane performance. Therefore, it seems proper to show basically and very briefly how drag, weight, aspect ratio, and other major parameters influence airplane performance. From the equations, one can then sense more directly the incentives for improvement.

Unless the ultimate in accuracy is sought, it is very satisfactory and useful to note that typically the drag of an airplane varies parabolically with C_L , or more specifically, the drag coefficient can be written as

$$C_D = C_{Df} + \frac{C_L^2}{\pi e A} \quad (1)$$

Here C_D is the total drag coefficient, C_{Df} is the drag coefficient at zero lift - the friction drag, or so-called parasite drag, A is the aspect ratio, and e the span-efficiency factor. That is, eA is the effective aspect ratio. Because of its simplicity, this formula is very easily manipulated to yield such results as

$$\left(\frac{L}{D}\right)_{\max} = \left(\frac{C_L}{C_D}\right)_{\max} = \frac{1}{2} \sqrt{\frac{\pi e A}{C_{Df}}} \quad (2)$$

Shortly, the term $(C_L^{1/2}/C_D)_{\max}$ will be used. Its formula is

$$\left(\frac{C_L^{1/2}}{C_D}\right)_{\max} = \frac{3}{4} \left(\frac{\pi}{3} \frac{eA}{C_{Df}^3}\right)^{1/4} \quad (3)$$

Equation (2) is more applicable for a conventional airplane, and Equation (3) is more applicable for a jet airplane. They are given here because they clearly and simply reveal the way the several measures of airplane characteristics affect airplane performance. $(L/D)_{\max}$ varies with $A^{1/2}$, hence gains from increased aspect ratio are fairly substantial. Also note that $(L/D)_{\max}$ improves as $C_{Df}^{-1/2}$, so reductions in drag help greatly. The span efficiency factor e is a lumped parameter that takes into account the deviations in induced drag from the ideal elliptical wing as well as the variations of skin friction and other drag with C_L . On typical airplanes, it lies in the 0.8 to 0.9 range.

For the jet airplane, the effects of these parameters are somewhat different. Now the gains from aspect ratio vary only as $A^{1/4}$ while gains from drag reduction vary as $C_{Df}^{-3/4}$. These tell us that, as compared with piston-propeller airplanes, the jet

will tend to have a lower aspect ratio and its aerodynamic cleanliness should be at a premium.

On many airplanes, range is one of the most important measures of performance. On commercial airplanes, it certainly is, and on many military airplanes the maximum combat radius is of major importance. For a piston engine, the fuel consumption is proportional to brake horsepower which is proportional to thrust times velocity. But for a jet engine, the fuel consumption is more nearly proportional to thrust. Then it is easy to show that the fundamental equation for range, R , of a jet airplane is

$$dR = V dt = \frac{-V}{c'} \frac{L}{D} \frac{dW}{W} \quad (4)$$

Here c' is the thrust specific fuel consumption of the engine, usually given as pounds per hour per pound of thrust, W is the instantaneous weight of the airplane, and dW is what is being used as fuel. Equation (4) also can be written in another form, bringing in Mach number and velocity of sound as

$$dR = \frac{-aM}{c'} \frac{C_L}{C_D} \frac{dW}{W} \quad (5)$$

In this form, since C_L/C_D is a function of Mach number, it is clear that for best instantaneous miles per gallon, the quantity MC_L/C_D should be maximized.

However, to keep it at its maximum value requires flight at variable altitude. In commercial operation, airplanes do climb as their fuel is used up, but only a mile or so in 2500 miles. Hence, for purposes of this paper, which is to bring out how parameters affect the performance of an airplane, we will present the range formula for a jet airplane that is flying at constant altitude. In Equation (4), the velocity enters directly. When it is eliminated in terms of C_L , etc. we get for the range in miles

$$R_{\max, \text{miles}} = \frac{2}{c'} \left(\frac{C_L^{1/2}}{C_D}\right)_{\max} \sqrt{\frac{391 W_0}{\sigma S}} \left[1 - \left(\frac{W_1}{W_0}\right)^{1/2}\right] \quad (6)$$

In this formula, W_0 is the initial weight or weight at the beginning of the range flight, and W_1 is the final weight. The term σ is the ratio of the air density at altitude to its value at sea level, and S is the wing area. This formula brings the main factors all together. First of all, notice that the range varies as $(c')^{-1}$, so any improvements in fuel consumption lead to large range gains or perhaps fuel savings. The range is also directly proportional to the maximum value of $C_L^{1/2}/C_D$. Equation (3) describes the maximum value and, in fact, could have been substituted in Equation (6), but as Equation (6) stands, the C_L - C_D polar does not have to be parabolic. $W_0/\sigma S$ is an effective wing loading, and obviously the higher the altitude, the better for range so long as drag rise due to Mach number does not reduce $(C_L^{1/2}/C_D)_{\max}$. At 35,000 ft, σ is about 0.3, so an airplane whose wing loading is 100 lb/ft² has an effective wing loading of 330 lb/ft²; by itself, σ indicates that flight should be at high altitude. The last term in (6) shows the effect of

the fuel carried. The weight ratio is to the $1/2$ power. If Equation (5) had been integrated, a logarithmic variation would have been obtained, but differences are not great so long as one does not go to extremes. In short, Equation (6) shows that range is proportional to $(C_L^{1/2}/C_D)_{\max}$, the effective wing loading, and $(W_1/W_0)^{1/2}$. In this form, it is interesting that the range is finite even if the airplane were 100% fuel so that $W_1 = 0$. The W_1/W_0 term shows the importance in design of keeping the airplane weight low. Therefore, greater wing thickness or stronger materials can directly affect the weight, or they may alter the optimum aspect ratio which is a direct factor in determining $C_L^{1/2}/C_D$, according to Equation (3).

Before closing this part, a few comments about e and its estimation are in order. We mention again that the product eA is the effective aspect ratio, and it arises in both Equations (2) and (3). Therefore, when engineers are estimating the performance of an airplane, attempts both to improve e and to make accurate estimates of it become quite important. For elliptic lift distribution, it is theoretically equal to unity. But in actuality, there are deviations from this ideal. Wing-fuselage junctures, small gaps, nacelles, flap brackets, unusual planforms, etc. essentially reduce e in an inviscid fashion. But e is affected by the boundary layer as well because the profile drag increases as C_L is increased. The main fact is that e helps describe the total variation of drag with C_L . Obviously, it is a function of Mach number.

In my years at McDonnell Douglas, I have witnessed several lengthy attempts to improve the accuracy of estimating e , which is poor. The work was a mixture of theory and correlation with test data. As you might expect, each new study yielded slightly different methods and results, but the studies really were down in the noise level of our knowledge, so no significant improvement ever was made. So as I see it, one part of your overall job is to produce a sound and accurate method of estimating e - or better still, the entire polar. Anyone who does indeed make a real advance in estimation of e or the polar will receive the undying gratitude of the aerodynamic performance engineers.

The design of an airplane involves two aspects - design and off-design features. Except for some military requirements, design properties are generally for relatively low lift coefficients, meaning attached flow. Here, thanks to various methods including CFD, aerodynamics is becoming reasonably capable of truly analyzing such flows. But to be a "well tempered airplane," the airplane must behave satisfactorily in a wide range of off-design conditions, including the stall and recovery from it.

Also of course, there is the possibility of engine failure. For multi-engine airplanes, failure should not lead to catastrophe - the airplane should have reasonable takeoff and flight qualities, including of course the ability to counter the adverse yaw due to asymmetric thrust.

Another condition that is called off-design here is the takeoff and landing condition. Here, wheels are extended. Sometimes, there might even be high-lift boundary-layer control. In these landing and take-off configurations, the airplane geometry, i.e., the boundary conditions, is vastly more complicated.

For maximum lift, the flows are very likely to be flows with partial separation. Furthermore, very near the ground, the ground acts as another boundary to the flow which must be taken into account. Fortunately, in landing and takeoff, speeds are low so that incompressible methods of analysis appear adequate. But the military are greatly concerned with transonic maneuverability. Here, lift enhancing devices may be extended and then the problem becomes one of transonic flow past slotted airfoils at high Mach number. So you see that, while the design condition is exceedingly important, it is only a small portion of the entire airplane design problem.

3.0 The Wind Tunnel

Before proceeding to my basic subject, some mention of the wind tunnel is in order, if for no other reason than that the general aim of groups like the present one is to reduce the need for wind tunnel tests and perhaps someday to eliminate them. So it is useful to study the competition.

While there are a few limits, the wind tunnel basically can supply answers to any airplane-aerodynamic problem or question that is put to it. In a sense, it is the ultimate in analogue calculation. The main requirement is first to make a properly shaped scale model, second to put it at the attitude of interest, and third to turn on the wind and measure forces, pressures, and other features of the flow that may be of interest. For example, a strake leaves a vortex trail. To analyze the flow theoretically is a formidable undertaking, but, to find its effect in the wind tunnel, nothing more need be done than to make the proper shape of strake, mount it on the model, measure its effect on balances, and perhaps do some flow visualization. The use of scale models is on an extremely fundamental foundation, as is easily shown by manipulating the Navier-Stokes equations.

As already noted, models are difficult, costly, and slow to build and test. Often, as the author has seen many times, many parts of a design are frozen well before the wind tunnel results are ever obtained. Then the tests are mainly a check on the decisions. When computed results are meaningful and believed, there is a tremendous gain in time. With all out company support, a wind tunnel result might arrive in a month, but a computer answer might arrive in a day, if changes from some previous configuration are not too great. But the wind tunnel has some operational advantages. If characteristics are to be measured over a range of Mach numbers and lift coefficients for a particular configuration, all that is necessary is to set the speed of the tunnel and the angle of attack and then measure the forces. Each data point takes only a few seconds, depending on the kind of wind tunnel being used. But if calculations are to supply the answers and if Mach number is involved, the governing flow equations are non-linear, and then each new data point requires a complete new calculation. So if results are sought for 5 Mach numbers and 10 C_L values the flow field problem must be solved anew 50 times. But in the wind tunnel, all 50 results can be obtained from one setup.

It was noted above that the use of scale models has an extremely sound foundation. But there are many side problems, and that is another reason why aerodynamicists are not entirely happy with wind tunnels. First of all, the flow is not truly matched

unless the Reynolds number is matched, and that is very hard to do. Furthermore, for a true scale model, all the boundary conditions on the model should be scaled as well. But that is often impossible or impractical to do. There may be visible butt joints in the solid model that do not exist in the full-scale airplane. Flap brackets and the like are probably only approximate representation of the flight article. Also, on an airplane, there is a certain amount of general airflow from one place to another because parts are not perfectly sealed. That kind of flow is certainly not matched on the model.

A new development is the cryogenic wind tunnel that will easily match full-scale Reynolds numbers with a small model. If the effective smoothness of the full-scale model were to be matched, the model would need the smoothness of plate glass. I look forward to seeing just how well flight results will be reproduced when flight Reynolds numbers are truly matched.

There are other differences. The model is in a wind tunnel and has wall effects. It has supports such as stings that affect results. The tunnel, being a moving stream, has a different level of turbulence compared with flight in the free air. The tunnel is very noisy and noise has a large effect on transition. All these factors can make the measured answers different from flight, even when the Reynolds number is matched exactly. An interesting possibility is foreseen, however. With the advance of CFD and other methods of analysis, calculations can be easily made with and without wall effects, with and without the sting support, with and without power effects, and with and without other factors. Such types of calculations may provide much more sophisticated wind tunnel corrections than those used at present. Then even though the wind tunnel remains the primary test instrument, a combination of CFD corrections plus the wind tunnel may lead to a hybrid method that provides data that is more accurate than that now yielded by conventional wind tunnel tests.

Work exists on reducing these drawbacks. Slotted walls now exist, and work is underway on adaptive walls. With the cryogenic tunnel, the magnetic support system begins to look feasible. With it, the model just floats in the middle of the tunnel and strut interference is entirely eliminated.

But in spite of these troubles, which may degrade the accuracy of the results or sometimes give entirely wrong ones, the wind tunnel must remain as the standard by which CFD is judged, not particularly for accuracy but for versatility. I have heard it stated that fluid dynamics calculation has progressed to the point where it can supply first-order answers, and the wind tunnel is used to supply answers to second-order effects. While not really an accurate statement it conveys the general idea. As one example of a first-order answer, we mention the drag, lift, and pressure distribution of airfoils that are less than about 15% thick at the lower lift coefficients and at low Mach numbers. With these qualifications, I believe the forces can be calculated as accurately as the wind tunnel will measure, provided the wind tunnel has low turbulence. But near and above the stall, the wind tunnel is the only sure way to obtain answers that have reasonable accuracy.

While I have not made any careful study, I am under the impression that the amount of wind tunnel test-

ing has not decreased one bit with time. This fact is true in spite of our considerable advance in analytical capability. What is happening, at least partially, is that our standards and demands are increasing fast enough to compensate for our gains in analytic capability. We wish for a better wing or a better moment curve or more detailed data, so more configuration changes and tests must be run. So the use of the wind tunnel is not fading out. I have been thinking of the wind tunnel as a development tool. Of course, it also has a major function as a research tool. For this function, I see no real inroads either.

For what it is worth, practically my first job after finishing college was to make the performance estimates for the Douglas DC-5 transport. This airplane was unusual in that it was built without any wind-tunnel tests at all. In my performance report, I remember that I predicted the high speed to be 220 mph. The final official flight tests showed that the high speed, indeed, to be exactly 220 mph! The best performance estimates are based strongly on flight test data of previous airplanes, because wind tunnel tests do not exactly duplicate many features of the airplane, such as Reynolds number, power plant installation effects, flow leakages, etc.

4.0 Wings - Clean as in Cruise

Originally, it was planned to discuss wings in two sections - one inviscid and the other viscous. But complications develop because the two kinds of flows are intimately connected. A more logical breakdown is wings with fully attached flow and wings with varying degrees of separated flow. In this section, we discuss the case of unseparated flow although that is not explicitly stated in the heading; of course, cruise should not involve separated flow.

On many aircraft wings, the clean condition is the design problem, for a most basic purpose of an airplane is to obtain good cruise performance which occurs at low lift coefficients and with attached flow. While lift coefficients may be low, any analysis must treat both variable Mach number and variable lift coefficient. But if there is some kind of inverse approach, a design point might be selected for a single lift coefficient - Mach number combination.

Before getting into specifics, the author would like to mention the problem of calculating drag. Profile drag is really a second-order effect. A typical lift coefficient is 1.0. A typical drag coefficient is 0.01 or two orders of magnitude less. There are mainly two ways of calculating the drag - directly by integrating the pressures and shears over the surface or by looking at the momentum defect far downstream. The author finds the situation exasperating. Except for very thin airfoils at low angles of attack, a pressure drag caused by the boundary layer displacement thickness develops, and the drag calculated by integrating pressures and shears is unsatisfactorily inaccurate.

The other way is to look at the momentum defect far downstream. For low angles of attack and attached flow, the boundary layer on a single surface can be calculated rather accurately almost to the trailing edge, but at this point the local pressures are not ambient and the wall boundary condition suddenly changes, so the boundary layer must be properly traced past the trailing edge into the wake and on

to infinity. While special studies have indeed been made, no reliable and production method of finding the momentum defect caused by the drag has yet been developed.

Up to this point, the writer has mainly been thinking of the simplest case - two-dimensional flow. But the real flow is three dimensional, as on a swept wing. Further, if one is to be concerned with the true problems, there are even worse kinds of three dimensionalities - corners, wing tips, under-slung nacelles and their pylons, not to mention miscellaneous effects such as fences, gaps at joints, etc.

While on this subject, it seems best to consider the worst problems although they properly belong in the next section. These are the problems of calculating the drag when there is partial separation as at high lift and when flaps and slats are extended to varying degrees. Consider an extended slat. Now the shears must be calculated on both airfoil elements. Pressure drag effects will be much greater because the boundary layers are much thicker and more complicated. Or if one tries to trace the wake defect to infinity, one must follow the slat wake along the side of the main airfoil through a strongly rising pressure region, then pick up the main airfoil wake at the trailing edge, and follow the development of both to infinity. The two boundary layers and wakes may or may not merge. If they do merge, the problem becomes even more complicated.

Again, this is two-dimensional thinking. The problem of really basic analysis on a real three-dimensional swept wing becomes far worse. There may be added complications such as slats. Often a slat is only part span, so it has a variable load distribution along its length, and at its ends, vortices are shed which trail back over the wing, further adding to the three dimensionality.

One noteworthy step in this area has been made. We now seem to be able to calculate the initial wave drag rise for an arbitrary clean wing, that is, the inviscid portion. But, shades of d'Alembert's paradox, the full problem of the viscous portion is with us nearly as much as it was forty years ago. So here is a very important problem, because the drag is such a key to airplane performance. Obviously, all this problem is directly connected to the estimation of the airplane efficiency factor, e . It is noted here that the general accuracy sought in all these problems is not really very high. It is about what can be read from an 8-1/2 x 11 in. graph whose zeros are not suppressed.

On the simple wing at low angle of attack, remarkable progress has been made in the last few years. Reasonably accurate direct and inverse methods for compressible flow have been developed. The basic full inviscid equations (the Euler) are known but have not been solved very much, so even though many good inviscid solutions of varying degrees of accuracy do now exist, further development of methods is clearly part of any long-range attack. Your job is to gradually develop efficient application of the more comprehensive equations.

But there are still uncertainties about some of the basic calculations, physical uncertainties that are not likely to be eliminated by one grand application of some very comprehensive equation. The exact process of circulation change across a fuselage is not

known very well. Perhaps a better theory of the lift of a body of revolution at angle of attack would help this problem. Nor is the flow physics fully known at a wing tip. On a gradually rounded wing tip, just when does the classical Kutta condition cease to exist?, and for the blunter portions of the trailing edge, how is the circulation determined? Much work has been done on the details of the final vortex rollup and buildup at the wing tip, but most is a kind of global analysis. A really detailed understanding is needed. Winglets and tip tanks complicate the problem. Also of course, Mangler and Smith have added to the confusion by showing that the flow for a swept wing must leave parallel to one side or the other, not the bisector of the airfoil. Here is another question to resolve. Another complication that must be handled, if we are ever to arrive at true design methods, is the problem of nacelles and underwing stores on military airplanes. These also affect the lift and lift distribution. At present, the only good way of determining the effects is to resort to the wind tunnel. Will we ever be able to make flat-out calculations? A feature common to some of these problems is longitudinal concave and convex corner problems. Work is being done on these, but there is much further to go.

Another problem that can be important, even at low-lift coefficients, is the effect of wing rigidity. The problem is largely structural, but deflections are brought on by aerodynamic loads, and accurate design of the flying machine must yield a good design under operating deflection and load conditions. One classic example of problems of this kind that must be kept in mind is aileron reversal. When an aileron is deflected down to lift a wing, moments are applied that may twist the entire wing to negative angles at high speed, thus negating the effect of the aileron. Currently many wind tunnel models are built to model the airplane in some loaded (and deflected) condition, rather than the unloaded condition, in order to obtain data that more accurately represents the loaded aircraft in flight.

CFD requires many coordinate points of the shape to be analyzed. These must be specified to a high degree of accuracy, because frequently differences between adjacent points are taken to get slopes. The problem of supplying them for a complicated shape such as a swept wing or wing-pylon combination has unexpectedly developed into a real nuisance. When several thousand coordinate points must be loaded into a computer, determination of them by conventional hand methods is a far longer job than the final flow calculation. So you see that a requirement for automated input is apparent. The entire airplane exterior must be defined by equations. Where parts were originally defined by flexible splines or by eye they must be converted into equations in order to be usable.

A viscous problem that should be answered is the question of transition. Here neither the wind tunnel or calculation does particularly well. Only flight test gives an authoritative answer. The best calculations of transition are really just estimates. The position of transition depends on the pressure distribution, amount of sweep, contamination from the fuselage, amount of surface roughness and irregularities, ambient noise, concave curvature as on some supercritical airfoil sections, and turbulence. However, in the atmosphere, turbulence is so low it does not seem to affect transition. Accounting for the effects of turbulence in a wind

tunnel is very important, but it is an artificial problem, because it arises only in connection with wind tunnel tests. Of course wing surface temperature conditions also affect transition, and then there is the entire subject of Laminar Flow Control which is receiving renewed emphasis with the present fuel situation. When laminar flow is sought, prediction of the transition point or the amount of suction needed to move it to a specified location become especially important because the extent of laminar flow now becomes large. On present day jet transports, that is not a problem because, due to the destabilizing effect of sweep, there will probably be only 1% laminar flow or less, so even if we miss the true transition point by 100%, the overall error in position is only 1% chord. In this connection a rough rule of thumb for drag calculations can be given. To determine drag, just ignore the part that is laminar and consider only the turbulent portion. That is, if the first 40% of an airfoil is laminar, the profile drag of the airfoil is about the same as if it were only 60% as large, but all turbulent. So you clearly see that the amount of laminar flow strongly affects the performance of an airplane.

Thus, another part of your job is to improve the methods of predicting transition for given conditions, or conversely, the conditions that are required to get a given amount of laminar flow must be specified more accurately. Theory for the problem, at present, is in the same sad state as that of turbulence, so a very long haul is seen, and for many years, prediction methods will be basically empirical but will be improved gradually by refinements here and there. But I repeat, if ever we are to do a good job of drag calculation, accurate prediction of transition is a necessary part of the job.

Another problem that can arise is that of the leading edge vortex flow that may occur on highly swept wings such as supersonic designs. Development of this vortex drastically affects the slope of the lift curve, so analysis is important. Good progress is being made on its analysis, but its prediction and the prediction of pressure distributions of wings having leading edge vortices is far from solved. The problem and conditions for its strength are far more complicated than the simple Kutta condition at the trailing edge, but the solution must be known accurately because it directly affects the lift and pressure distributions. Development of a leading edge vortex makes a first-order difference in wing characteristics, so the problem is definitely important. To complicate your job, sometimes the vortex bursts, and this bursting point too should be predicted, but the prediction of vortex bursting is in a far more primitive state than the prediction of transition.

While this section is mainly concerned with attached flow, it is well to mention another problem here - laminar bubbles and reattachment. If a laminar flow encounters an adverse gradient, it separates very easily. But the separation may not be extensive. It may just form a laminar bubble which is quite an unstable flow that can easily turn turbulent and then reattach before there is any catastrophic change in the flow pattern. Will the bubble cause major separation or not? Will it turn turbulent first and just remain as a bubble? Here is another problem of transition prediction. The bubble also may be caused by a shock. While considerable work

has been done on the problem and there are rules for predicting behavior, the problem can hardly be considered solved in any basic sense. The bubble of course affects the pressure distribution, the lift, and the drag. Predictions are not entirely satisfactory even for two-dimensional flow. The prediction of bubble bursting is in an even more primitive state if the bubble is three dimensional as on a swept wing.

Even though the flow is all essentially attached, your job has many problems. Most seem to involve viscous effects. For the inviscid portion, you know the proper equations and are making remarkable progress in solving them subject to the correct boundary conditions. Similar progress is being made on the exceedingly useful inverse problem. But there are nagging problems involving viscosity except perhaps where the flow is purely laminar, where here too we know the equations. But most flows are turbulent, so to beat the wind tunnel you must gain better knowledge of the basic turbulent processes, i.e., corner flows, bubbles, transition, and leading edge vortices. Except possibly for transition, the wind tunnel can provide answers very well. It is a wonderful analogue device, but one whose role in aerodynamics will slowly be reduced, we hope. Continuous improvements are being made in the inviscid calculations, but ominously in the background is the loss of accuracy due to viscous effects. The problem is aptly identified by the title of a recent paper by Lars Ericsson entitled "Viscous Flow-Nemesis of the Theoretician in Pursuit of Higher Order Accuracy."

5.0 Wings - Dirty as for High Lift

While design conditions as considered in the previous section are very important, the entire flight envelope covers a far greater range of conditions, and for them the airplane must still be a satisfactory flying machine. Hence, most of the problems of the previous section apply here too but under more complicated and more extreme conditions.

An obvious problem is that of stability. In the previous section, we hinted that the full three-dimensional boundary layer must be found, but there it was mainly for design and analysis purposes. Here it is needed especially for flying qualities determination, as for pitchup - and the analysis is mainly at the more extreme conditions. Stall patterns must be calculated. That means inviscid flow fields must be calculated at several high-lift coefficients, and then three-dimensional boundary layers must be calculated at these same lift coefficients in order to finally determine such relations as C_M - C_L curves. In symmetrical flight, if the tip of a swept-back wing loses its lift first, the tips will tend to drop, leading to the phenomena called pitchup, which is a highly undesirable stability characteristic. That is, the airplane tends to increase its angle of attack instead of reducing it by diving out of a stall. To really analyze this characteristic for a complete range of lift coefficients, it will be necessary to compute the complete distribution of lift, and at higher lifts, many wings will have partially separated flow. So the basic problem is three-dimensional lift with partial separation - certainly a formidable problem. Flow or shear patterns right on the surface will be interesting, but only as a guide as to what the force distribution will be.

Several configurations must be checked. First the clean condition, because the airplane normally flies that way, and both high and low Mach numbers must be checked. Furthermore, on combat airplanes, maneuverability at high Mach number is very important, so here especially the properties must be checked. Also of course, the airplane must take off and land. Here flaps and slats are used, and they are usually at different settings for the two conditions. Hence several more configurations are involved here, but mainly these conditions are only at low Mach number, so compressibility is only weakly involved.

More than symmetrical flight is involved, rolling and yawing stability for instance. For these, because the flows are highly nonlinear, flow fields and boundary layers must be calculated as a function of yaw, meaning several more calculations. Airplanes have roll rate requirements. When the wing is rolling, the relative onset flow is along a helix, so that the different portions of the wing are at different angles of attack. This causes a damping in roll which must be overcome by the ailerons if the roll rate is to be met. So in addition to symmetrical configurations involving flaps and slats at various settings, a complete calculational design procedure will involve span load analysis for an unsymmetrical wing with ailerons deflected - and this too must be over the Mach number range.

Finally in the range of conditions to be considered must be mentioned the ground, because the airplane must land. The ground affects the downwash and hence the lift pattern, and longitudinal and lateral stability here too must be satisfactory, so some further calculations are indicated, probably by approximating the ground with a reflection plane model. Also of course, if one is attempting to find the stability behavior at extreme lift coefficients, the configuration being analyzed must be complete. The fuselage must be included and nacelles certainly should be included because they can have strong effects on the lift distribution and local separation. There is no question about the necessity for checking this ground condition. It is so important that aerodynamicists are willing to spend considerable extra money in wind tunnel tests of this condition, including the construction of ground boards. Ground effect analysis can require numerous calculations. At each new height and attitude, the basic geometry is changed, thus requiring a new calculation. In the infinite atmosphere, a few primary calculations are enough for all cases because their results can be linearly combined if the Mach number is low.

Another challenging problem is the analysis of spoilers. If one tries to lift a wing by downward deflection of an aileron, a nose-down twisting moment is developed in the whole wing section. Depending on the elasticity of the wing, this can nullify the effect of the aileron as already noted. Therefore, spoilers often are now used as auxiliary controls because they do not introduce such adverse moments. A spoiler has separated flow behind it. So now you see there exists the problem of analyzing the three-dimensional flow and force distribution for a range of spoiler deflections, wing C_L values and Mach numbers. Unless shortcuts can be found, the number of calculations becomes very large. But wind tunnel tests easily solve this problem. For each spoiler setting, the C_L range is covered, and it in turn is checked at several Mach numbers. This problem is not too much different from my previously mentioned flow about a brick.

In the landing and takeoff condition, flaps and slats are extended varying amounts. The flap is likely to be at least a double-slotted type, and if so, together with the slat we have at least a four-element airfoil. If true analysis is ever to exist, the boundary layer and inviscid flow past the system must be calculated, and because we are now interested in the extremes, the flow must be analyzed for cases of partial separation. Partial separation may occur first on any one of the elements, and then unless the analysis is stopped right there, it must proceed in spite of the partial separation on to the maximum angle of attack. In fact, very interesting problems arise such as predicting the effect of Reynolds number or there may be partial separation in one of the flap gaps, and now we find a complicated problem of merging boundary layers or wakes and interactions. The problem of drag estimation was mentioned earlier. Here it is much worse, but very important because engineers not only want low-drag flap systems to go with the high lift but want to know their drag. Now in estimating the drag, we must trace the wake development of all the elements all the way to infinity, or must sum shear and pressure forces directly on the elements, if anything more than empirical relations are to be used.

The thinking to this point has been two dimensional. But flaps on a real airplane are quite three dimensional. So now modified span load analyses are indicated. A flap usually stops at the ailerons, but on many airplanes it can have changes in sweep angle and even breaks along its length. On many transports there is a portion directly behind the engines that is not deflected at all in order to keep it out of the jet blast. Furthermore, slats are not full span, so the three dimensionality must be considered for them too. Then from a design point, the question of their extent arises, because their stopping point helps determine the general stall behavior of the entire wing. So you see again the need for both the three-dimensional inviscid analysis and three-dimensional boundary layer and separation analysis, or else one grand analysis.

At this time, it is not known whether effects for the inviscid flow are linear, enabling superposition to be used, since Mach numbers are low, or whether the problem is nonlinear. The reason it may have to be handled as a nonlinear problem is that the downwash field is a function of lift coefficient, and because lift coefficients may be high, the downwash may be large. Then it may be insufficient to make some general assumption about the location of the trailing vortex system. Of course the viscous flow analysis is nonlinear anyway because of the nature of the equations.

One final point should be mentioned. Flaps and slats must be mechanically supported. Wind tunnel tests show that the support brackets substantially reduce the lift increments supplied by the flaps and slats. So in any ultimate system of calculation, the brackets too must enter as part of the configuration. Exactly how to do anything basic is quite a problem. In their cleanest form, the brackets introduce viscous corner flows in a strongly varying pressure field. Perhaps if the flow is all attached, the potential flow portion of the analysis can indeed be made, but because the brackets are a moving device, they are poorly streamlined, and so the flow past them will be one with partial separation for which a potential flow approximation is poor.

One good feature of the entire problem is mentioned here. Because the flow is for high angle of attack conditions, a slat probably exists, and it is extended so that we know that there will be no laminar flow. Hence, here prediction of transition is easy. But there still can be problems. If the wing has no slat and its accompanying joint, it may be sufficiently smooth to support laminar flow. In that case, the underside is at quite a favorable gradient, and long runs of laminar flow could exist if the wing is not beset with constructional roughness such as joints, flush rivets, inspection panels, and the like. Ignoring the extent of laminar flow in these cases will lead to poor accuracy in the drag calculations.

So far we have only considered questions and problems of the primary design. But there are add-on devices that can greatly improve some of the behavior at high-lift coefficients. A notable one is the strake, i.e., a small portion of the wing near the root that has much more sweep than the rest of the leading edge. A strake develops a leading edge type of vortex flow that travels down over the rest of the wing and thereby delays separation. The idea goes at least as far back as the DC-3 which used one in front of the vertical surface to delay its stall to high yaw angles. Because the strake is a very powerful device, combat aircraft have incorporated it from the very beginning, otherwise the wing would be significantly inferior competitively. So here is an added complication to your job. The inviscid analysis is not one of just treating the proper shape at high angle of attack, because a vortex of a strength to be determined must be added, and then afterward, the highly three-dimensional boundary layer must be calculated. How to handle the inviscid portion is being worked on, but it is not yet down to a science. But certainly, if calculations are to substitute for the wind tunnel, problems like this must be handled well. On a new model, probably several strake designs are tested in the wind tunnel to find the best. If CFD is ever to replace the wind tunnel, calculations predicting the effect of the different shapes become the necessary equivalent.

Vortex generators, that is, small wings placed at angle of attack on the main wing and perpendicular to it, may be used. In one sense, a vortex generator is a kind of crutch or a pair of eyeglasses to fix up a bad wing. But it is a very powerful device, and at times a better wing can be made by using it as a "tool" from the beginning. For instance, on the new 767 transport, Boeing has found that seven vortex generators on each wing can replace a complicated black-box stability augmentation device. Vortex generators shed vortices that trail over the surface and modify the boundary layer - thus, changing separation patterns and the accompanying force coefficients. The analysis problem is much like that for the larger strakes. But here, because of the small size of the generators, we are not much interested in details of the flow on the generator. The basic problem is to calculate the effect of the vortices on the flow field and then calculate what they do to the boundary layer. While they are quite small, their smallness is probably the least of the problems, because to obtain the necessary locally very fine grid system, one of the embedded mesh techniques can be used. In inviscid flow, it is easy to introduce a longitudinal vortex and find its effect on the flow field, but here the vortex is just at the edge of the boundary layer,

and it is not clear whether inviscid pressure calculations will suffice. Wind tunnel tests may be needed to show what modifications in theory are necessary before analysis can replace the wind tunnel.

Fences are another common "fix" device. They reduce the spanwise flow of the boundary layer. More basic knowledge of their operation is needed, and then, just as a wind tunnel can show the effect of the fence, the effect must be predicted if ever CFD becomes mature.

Of course there are many other problems; they are rarer but should be kept in mind. At times, blowing boundary layer control is used on flaps to get higher lift. It is used on the F-4 fighter. So the wall jet problem now becomes involved. STOL and VTOL aircraft are more complicated applications of powered lift. Sometimes the flap may be a blown flap, i.e., in the slipstream of the jet. Or the Coanda effect may be used as on the YC-14. Any sound analysis of these types must involve the three-dimensional effects. Another consideration is buffeting. Prediction of the buffet boundary is certainly important because it helps define the flight envelope of the airplane. While some really basic predictions exist, it is believed that the buffet boundary can be satisfactorily inferred from static calculations. That is what is now done, using steady state wind tunnel test results. Buffeting occurs at extreme conditions and can exist in some kind of transonic maneuvering condition, but usually the important configuration condition is the airplane clean. So in some senses, buffeting belongs in the previous section, but it is included here because it is for extremes and involves some separation.

If one searches, there are many more problems to be found, but they seem to be of lesser importance. To name one, I mention the landing and takeoff condition. In addition to the extended flaps and slats, the landing gear is down, and usually it comes out of the wing. Sometimes when the gear is extended, the landing gear door is returned to its original position to cover the cavity. Then the problem is simpler, just the bluff landing gear to account for. But often the door is left open. Then we are faced with analyzing the flow past a large three-dimensional cavity in a wing; drag and force coefficients being the items of interest. So you see, the problems seem endless, but all that I have mentioned are checked routinely in the wind tunnel, even spin characteristics, if the airplane is a fighter or some other kind that requires high maneuverability. Accurate analysis of a spinning airplane is close to the ultimate in complication, because the entire airplane must be considered and the flow is largely separated.

Occasionally unsteady flow problems arise, but usually they are not main line. The ordinary wind tunnel is principally a steady-state testing means, and analogously CFD methods aim mainly at steady state answers. But there are unsteady problems or even some flows that are unsteady but have long time average values. Of course, buffeting, dynamic stability, and flutter all involve unsteady flows. In many cases, it is probably not difficult to extend methods to handle the unsteady problem. For instance, one major method of analysis uses the full time-wise equations of motion to march forward in time through the transient until the steady state is well approximated.

6.0 Concluding Remarks

As you see, the complete analysis and design job is really formidable. It is really formidable even in the inviscid portions where we know the equations that apply - the Euler equations for the most general case. The viscous portions, especially flows involving some turbulent separation, are even worse, because the basic equations are not even known. The laminar viscous equations are known, but on airplanes, laminar flow is so rare that it is not very important. However, tests and thought should develop better relations such as turbulent transport properties, and so the viscous analysis should slowly follow the inviscid. But at the pace that methods and computers are being developed, it is likely that the viscous portions of analyses will be a major drag to real advances.

But the state of the art has undergone really remarkable progress. Even such problems as wings with nacelles beneath them are now being analyzed transonically, and methods are in sight for analyzing wings with stores or other small objects. The present state of analysis is especially applicable to the design condition which is the one that primarily determines the shape and size of the airplane. So the methods are becoming quite useful right now. We have gone a long ways from when all we could do was analyze a two-dimensional airfoil in incompressible flow or a symmetrical transonic shape at zero lift. But who flies two-dimensional airfoils? Flying one transonically at zero lift might be exciting, but the flight will not last long.

However, an airplane must have satisfactory behavior over a large range of conditions, and calculation of this behavior at these extremes is in its infancy, and I see a long haul of many years. It is now impossible to predict whether we will reach these extended objectives, or just end up on some plateau short of them. The computer has vastly extended our capability, but it will not extend it infinitely, and turbulence and separation problems are so complicated, that it is difficult to tell whether advanced computers and methods will have the needed capability. But the writer is fairly optimistic that methods for analyzing viscous problems for one kind of flow will be found, then slowly another, then another, etc.

Then we can expect the wind tunnel to suffer inroads. At this time, at low speed and low lifts, there often is no sense in running wind tunnel tests on two-dimensional airfoils, because we can calculate coefficients as accurately as we can measure them. Likewise, we are approaching that same state for practical three-dimensional wings. Therefore, the wind tunnel will be used less and less to search for optimums. The optimum will be found theoretically. Then it will be tested to make a cursory check that it is performing as predicted. But the main tests will be for the extremes of operation, moment breaks, stall patterns, drag at high lift, and the like. Or as already said, somewhat inaccurately, the wind tunnel mainly will be used to examine second-order effects. So gradually over the years, the use and purpose of the wind tunnel will change. Now it seems to be in a period of transition away from finding design point shapes. Later as the CFD and other calculational art progresses, inroads will be made on the prediction of extremes, and perhaps some day, only a few special checks will be needed. But the entire problem is really awful.

If CFD methods are ever to be used in a relatively routine method by engineers, there must be much automatic searching and testing for special flow features. Does a leading edge vortex exist or not? Do laminar bubbles exist? Where is transition? This kind of information cannot be loaded in ahead of time, so the computer must find whether some special flow exists or not, or its extent. Then to progress further, it must use a form of program that handles the special kind of flow that has been found. If it does not do this relatively automatically, the calculations must be in the hands of experts, but wind tunnel testing does not require fluid mechanics experts. So that state seems far in the future, and the author is reminded of a favorite saying of his - Thank God for the Wind Tunnel.

I have heard it stated that aerodynamics is a mature science, and support for its continued development should be at a low level. Before automatic computers arrived, it indeed was on a sort of plateau, but that plateau has been crossed, and we now are on an uphill climb again. So the statement is either true or not true, according to your viewpoint. If you never expect to make significant inroads into both the design and so called second-order analysis of shapes, then the statement is true. But if we do think we can finally analyze all or many of these fringe problems, then the discipline is really in its infancy, because at present, we can do hardly anything. Remember my reference to flow about a very simple shape - a brick?

While any really fundamental calculation of turbulence and its transport properties still seems out of the question, much of the rest of the problem seems much nearer attainment. Many problems, such as the wing design problem, now can be handled with the existing better state of the art computers. To be definite, the author would hazard a guess that, if our capability were increased by 1000 times, we could analyze most of these extremes, at least sufficiently well to be very useful. By 1000 times, I mean some kind of combination of computer speedup and capacity plus improved algorithms. I hope these viewpoints are interesting and of some help. It is significant that your calculational capability has progressed so far that there is some justification for a paper such as this. Forty years ago, this kind of paper would have been absurd.

Postscript

Since this paper is a general distillation of knowledge, obtained from innumerable sources, no references have been cited. But for anyone who wishes to know more about the workings, problems, design, and performance of airplanes, two books are cited. The first is Airplane Performance Stability and Control by C. D. Perkins and R. E. Hage, John Wiley & Sons 1949. This is an older book but contains very good presentations of all the basic problems of an aircraft, which have not changed much with time. The second is The Aerodynamic Design of Aircraft by D. Kuchemann, Pergamon Press 1978. It is a very up to date and excellent treatise on configuration design of aircraft for the several speed ranges. It emphasizes the aerodynamic problems and is especially concerned with gaining an understanding of the aerodynamics of the various parts. Kuchemann was one of the worlds leading experts in aerodynamic design and analysis.

SESSION 4

NUMERICAL VISCID-INVISCID INTERACTION IN STEADY AND UNSTEADY FLOWS

by

Jean-Claude LE BALLEUR

Office National d'Etudes et de Recherches Aéronautiques (ONERA)

BP 72, 92322 Châtillon Cédex (France)

Abstract

This paper surveys some recent progress which have been achieved to generate numerical methods based on Viscous-Inviscid Interaction, for lifting flows, with strong interaction phenomena and separations. The composite solution is deduced from a Defect Formulation of the viscous equations, approximately solved with a boundary-layer-like integral method, coupled with an overlapping inviscid problem, where the viscosity controls the boundary conditions.

Are summarized the concepts for the Viscous-Inviscid splitting, the detailed first order Thin-layer Defect equations, the allowance on the normal pressure gradient, the singularities in non-interactive viscous steady or unsteady solutions, the full upstream influence recovery in interacted solutions, the turbulent integral closure, based on new three-dimensional velocity profiles and on turbulent transport equations, the numerical relaxation techniques developed for the viscous-inviscid coupling.

Methods and applications are shown for 2D-flows on airfoils, in low speed, or transonic, or unsteady conditions, with multi-elements or spoiler devices, and for 3D-flows on wings. Separation is solved in steady 2D-flows and quasi-3D flows (infinite swept wing).

Introduction

Joint progress, both in Direct Navier-Stokes solvers as well as in Composite methods of solution, are now believed [1 to 5] to be determinant on further computing capability and numerical techniques.

This paper summarizes some developments and results for the Composite approach, with Viscous-Inviscid splitting and with overlapping computational domains. The Composite solution is based on a viscous Defect Formulation [5, 7, 15], coupled with a pseudo-inviscid problem where the viscosity controls the boundary conditions. The Defect formulation insures that the viscous solution is matched continuously with the outer pseudo-inviscid solution, and not simply patched.

From an integration normal to the surface, the Defect Formulation rationally provides inte-

gral equations, which interact the equivalent inviscid flow via differential and strongly coupled viscous-inviscid boundary conditions. A noteworthy point is that a first order approximation to the Defect Integral form of the Thin-layer Navier-Stokes equations may reduce to the usual integral form of the Prandtl equations without requiring that the normal pressure gradient vanishes. Consequently, if we assume that a few closure relations between the Defect Integral thicknesses can be extrapolated from a boundary-layer-like closure, based on velocity profiles modelling associated to a simplified model of turbulence, then a set of interacting integral equations, boundary-layer-like, may be deduced to close very simply the pseudo-inviscid problem, without involving the Prandtl assumptions.

Due to the viscid-inviscid interaction, the first order set of integral equations is free of separation singularities [6, 7], as well of the singularities observed in pressure-prescribed Prandtl solutions [8, 9, 7], in steady or unsteady flows. In separated or reverse flow regions, non-interactive and regular viscous solutions may be marched in the free stream direction, using inverse methods where the pressure is an unknown [10, 11, 6, 12, 13] both in steady or unsteady flows [8]. The upstream influence recovery is always present, at least because of the viscous-inviscid coupling, even in supersonic regions. This is due to the behaviour of the branching solutions, which are always subcritical [6, 14]. The removal of the supercritical interactions of Crocco-Lees illustrates that a normal pressure gradient is approximately taken into account with the Defect Formulation, or simply with the Defect integral continuity equation (wall-transpiration coupling).

Finally, the first order Defect integral form of the thin-layer Navier-Stokes equations, interacted with an outer equivalent inviscid flow, removes all major shortcomings of boundary layer theory, and provides a basis to compute the strong interaction phenomena in flows involving thin viscous layers, including separations, trailing-edges, wakes and shock-boundary layers interactions. Further investigation of higher order Defect integral equations is of course possible, either to improve the overall accuracy, as suggested by East [16], or to insure an asymptotically consistent approximation of the momentum equations at infinite Reynolds number, in turbulent flow, as pointed out by Melnik

[17]. Presently, only a second order modelling of the normal momentum equation, uncoupled from the tangential momentum equation, has been used to take into account the interaction effect of the wake curvature.

The first order approximation of the Defect form of the thin-layer Navier-Stokes equations may also be solved easily using finite difference techniques, in the same way as the Prandtl equations, as pointed by Carter [18]. Although the relative merits compared to the integral methods of solution are probably balanced, the interest of the integral method approach is based on two non-negative points. If the discretization tangent to the surface has still to resolve the viscous-inviscid interaction exactly as in Navier-Stokes solvers, the integral methods avoid a fine discretization normal to the surface, which may be determinant on computer resources for complex flows. On the other hand, if the integral methods are closed with a rather global turbulent modelling, where details are lost, the overall efficiency and robustness look rather good, for a wide range of shear layers, at the present state of the art.

We summarize in the following the detailed equations, the turbulent closures, the numerical relaxation techniques which have been developed for the viscous-inviscid coupling. Methods and a few results are shown for two-dimensional flows, low speed, or transonic, or unsteady, and in three-dimensional flows. Separation may be solved, via interacted inverse viscous solutions, in steady two-dimensional or quasi three-dimensional flows (infinite swept wings).

I. VISCOUS-INVISCID SPLITTING - DEFECT FORMULATION

I.1. Zonal solver approaches

The composite methods of solution involve basically the splitting of a global problem into several interacting ones, which requires a coupling algorithm. A first approach is a zonal splitting where coupled subdomains are patched [5, 7].

The subdomains may either be relevant of the same equations and numerical techniques, as frequently in patched inviscid computations, or dissociate viscous and inviscid domains, as for example the patching model of the interacting boundary layer theory [5, 14]. The coupling may be achieved either with a strict patching technique along the junction boundaries of the different subdomains, or with a small overlap of the subdomains.

The determinant concept is that a single set of equations is directly representative of the solution inside each zone or subdomain.

I.2. Composite solver approaches

On the contrary, the Defect Formulation assumes that the pseudo-inviscid domain fully overlaps the viscous regions, inside which both the pseudo-inviscid problem and the viscous problem contribute equally to determine the overall composite solution. The same concept is used to split a turbulent solution into an averaged problem plus a fluctuation problem. The splitting involves both the equations and the boundary conditions of the problem.

Considering a contour $z=0$, whose curvature is $K(x)$, denoting \bar{u} , \bar{w} the curvilinear velocity com-

ponents, $\bar{\rho}$ the density, \bar{p} the pressure, denoting u , w , p , p , the corresponding unknowns of the pseudo-inviscid problem, $\bar{\tau}$ the viscous stress terms, the Navier-Stokes equations may be written, with $h=i+\kappa z$:

$$\frac{\partial \bar{U}}{\partial t} + \frac{\partial \bar{F}}{\partial x} + \frac{\partial \bar{G}h}{\partial y} - \kappa \bar{H} = \bar{V} \quad (1)$$

$$\bar{U} = \begin{bmatrix} \bar{\rho} \\ \bar{\rho} \bar{u} \\ \bar{\rho} \bar{w} \end{bmatrix} \quad \bar{F} = \begin{bmatrix} \bar{\rho} \bar{u} \\ \bar{\rho} \bar{u}^2 + \bar{p} \\ \bar{\rho} \bar{u} \bar{w} \end{bmatrix} \quad \bar{G} = \begin{bmatrix} \bar{\rho} \bar{w} \\ \bar{\rho} \bar{u} \bar{w} \\ \bar{\rho} \bar{w}^2 + \bar{p} \end{bmatrix} \quad \bar{H} = \begin{bmatrix} 0 \\ -\bar{\rho} \bar{u} \bar{w} \\ \bar{\rho} \bar{u}^2 + \bar{p} \end{bmatrix} \quad (2)$$

$$O = \lim_{\bar{y} \rightarrow \infty} [\bar{p} - \bar{p}] \quad \bar{p} = \{u, w, p, p\} \quad (3)$$

Equations (3) correspond to the smooth matching conditions with the inviscid far field. Additional equations are necessary to determine the Pseudo-Inviscid problem. The choice is not unique and defines the Composite solver. For example, an irrotational pseudo-inviscid problem may be selected either with $\bar{p}=p$ as suggested by Dodge [19], or with $\bar{w}=w$ as suggested by Rubin, Khosla [20].

I.3. Defect Formulation

Here, the Pseudo-Inviscid problem is selected to satisfy the exact inviscid flow equations. The equation (1) is then split :

$$\frac{\partial \bar{U}}{\partial t} + \frac{\partial \bar{F}}{\partial x} + \frac{\partial \bar{G}h}{\partial y} - \kappa \bar{H} = 0 \quad (4)$$

$$\frac{\partial (\bar{U} - \bar{U})}{\partial t} + \frac{\partial (\bar{F} - \bar{F})}{\partial x} + \frac{\partial (\bar{G} - \bar{G})h}{\partial y} - \kappa (\bar{H} - \bar{H}) = -\bar{V} \quad (5)$$

The definitions of the inviscid fluxes in (4) are similar to relations (2). The equations (5) represent a Defect form of the Navier-Stokes equations. In addition to the matching conditions (3), denoting $\langle f(x, 0, t) \rangle = f(x, 0, t) - \bar{f}(x, 0, t)$ the discontinuities (when the line $z=0$ is the center of a wake), the viscous boundary conditions are :

$$\text{WALL} \quad \bar{u}(x, 0, t) = \bar{w}(x, 0, t) = 0 \quad (6)$$

$$\text{WAKE} \quad \langle \bar{u}(x, 0, t) \rangle = \langle \bar{w}(x, 0, t) \rangle = \langle \bar{p}(x, 0, t) \rangle = 0 \quad (7)$$

The pseudo-inviscid boundary conditions are deduced from an integration normal to the surface. The continuity equation provides the exact displacement effect :

$$\text{WALL} \quad \rho w(x, 0, t) = \frac{\partial}{\partial t} \int_0^\infty (\rho - \bar{\rho}) dz + \frac{\partial}{\partial x} \int_0^\infty (\rho u - \bar{\rho} \bar{u}) dz \quad (8)$$

$$\text{WAKE} \quad \langle \rho w(x, 0, t) \rangle = \frac{\partial}{\partial t} \int_{-\infty}^\infty (\rho - \bar{\rho}) dz + \frac{\partial}{\partial x} \int_{-\infty}^\infty (\rho u - \bar{\rho} \bar{u}) dz \quad (9)$$

The exact curvature effect of the wake is :

$$\langle \bar{p}(x, 0, t) \rangle = \int_{-\infty}^\infty - \frac{\partial (\bar{p} - \bar{p})}{\partial y} dz \quad (10)$$

II. APPROXIMATION TO THE THIN-LAYER NAVIER-STOKES EQUATIONS

From this point, the so-called Thin-Layer Navier-Stokes equations (or Parabolized equations) will be assumed. All the viscous terms are then removed, excepted the usual shear stress term of Prandtl in the x - momentum equation. The set of equations is a non-parabolic one.

II.1. First order approximation of the pressure.

Because of the previous non-asymptotic choice,

a first order expansion, based on the gauge $z = \delta z$. may be applied simply to the z-momentum equation of (5). We get then :

$$\begin{cases} \frac{\partial(p-\bar{p})}{\partial t} + \frac{\partial(\rho u - \bar{p}u)}{\partial x} + \frac{\partial(\rho w - \bar{p}w)}{\partial y} = 0 \\ \frac{\partial(\rho u - \bar{p}u)}{\partial t} + \frac{\partial(\rho u^2 - \bar{p}u^2)}{\partial x} + \frac{\partial(\rho u w - \bar{p}u w)}{\partial y} = -\frac{\partial(p-\bar{p})}{\partial x} + \frac{\partial \delta}{\partial y} \\ 0 = -\frac{\partial(p-\bar{p})}{\partial y} \end{cases} \quad (11)$$

The defect formulation (11)(3) provides then a first order pressure field with a non-zero and inviscid normal gradient $\bar{p}(x, z, t) = p(x, z, t)$.

II.2. First order Defect Integral equations

A z-integration of (11) provides exactly, if $\bar{w}(x, 0, t) = 0$ and $q^2 = u^2 + w^2$:

$$\left[\frac{1}{\rho q} \frac{\partial \rho \delta_0}{\partial t} + \frac{1}{\rho q} \frac{\partial \rho q \delta_1}{\partial x} \right]_{(x, 0, t)} = \left[\frac{w}{q} \right]_{(x, 0, t)} \quad (12)$$

$$\left[\frac{1}{\rho q^2} \frac{\partial \rho q \delta_0}{\partial t} + \frac{1}{\rho q^2} \frac{\partial \rho q \delta_1}{\partial x} + \frac{1}{\rho q^2} \frac{\partial \rho q^2 \theta_{11}}{\partial x} + \frac{\delta_1}{q} \frac{\partial q}{\partial x} \right]_{(x, 0, t)} = \frac{C}{2} \quad (13)$$

The Defect Integral thicknesses δ_0 , δ_1 , θ_{11} involve the z-variation of the overlapping inviscid field. Only the momentum equation (13) is an approximate one :

$$\begin{cases} \delta_0 \cdot \rho q(x, 0, t) = \int_0^\infty [\rho u(x, z, t) - \bar{p}u(x, z, t)] dz \\ (\delta_1 + \theta_{11}) \rho q^2(x, 0, t) = \int_0^\infty [\rho u^2(x, z, t) - \bar{p}u^2(x, z, t)] dz \\ \delta_0 \cdot \rho(x, 0, t) = \int_0^\infty [\rho(x, z, t) - \bar{p}(x, z, t)] dz \end{cases} \quad (14)$$

In addition to a few algebraic closure relations, at least one additional integral equation must be solved, for the integral method to fit the physics and mathematics of the local equations (11), for example the recovery of upstream influence in reverse flow regions, or the separation singularity in pressure-prescribed steady solutions. The kinetic energy equation :

$$\begin{aligned} & \left[\frac{1}{\rho q^3} \frac{\partial \rho q^3 (\delta_1 + \theta_{11})}{\partial t} + \frac{1}{\rho q^3} \frac{\partial \rho q^3 \delta_0}{\partial x} - \frac{2 \delta_{11}}{q^2} \frac{\partial q}{\partial t} \right]_{(x, 0, t)} \\ & + \left[\frac{1}{\rho q^3} \frac{\partial \rho q^3 \theta_{11}}{\partial x} + 2 \frac{\delta_1 \delta_{11}}{q} \frac{\partial q}{\partial x} \right]_{(x, 0, t)} = \phi + \phi_p \end{aligned} \quad (15)$$

$$\begin{cases} (\delta_1 + \theta_{11}) \rho q^3(x, 0, t) = \int_0^\infty [\rho u^3(x, z, t) - \bar{p}u^3(x, z, t)] dz \\ \delta_{11} \cdot q(x, 0, t) = \int_0^\infty [u(x, z, t) - \bar{u}(x, z, t)] dz \\ \phi(x, t) \cdot \rho q^3(x, 0, t) = \int_0^\infty 2 \bar{z} \frac{\partial \bar{u}}{\partial y} dz \\ \phi_p(x, t) \cdot \rho q^3(x, 0, t) = \int_0^\infty 2(u - \bar{u}) \left[\frac{\partial p}{\partial x}(x, 0, t) - \frac{\partial \bar{p}}{\partial x}(x, z, t) \right] dz \end{cases} \quad (16)$$

is presently used as a closure equation for laminar and transitional flows, with the assumption that $\phi_p = 0$. The entrainment equation, a collocation with the local x-momentum equation at a conventional edge $z = \delta(x, t)$ of the layer, is used for turbulent flows :

$$\begin{cases} \left[\frac{1}{u} \frac{\partial \delta}{\partial t} + \frac{\partial \delta}{\partial x} - \frac{w}{u} \right]_{(x, \delta, t)} = E(x, t) \\ \left[\frac{1}{\rho q} \frac{\partial \rho (\delta - \delta_0)}{\partial t} + \frac{1}{\rho q} \frac{\partial \rho q (\delta - \delta_1)}{\partial x} \right]_{(x, 0, t)} \approx E \end{cases} \quad (17)$$

$$E(x, t) = \left[\frac{\frac{\partial \delta}{\partial y}}{\rho u \frac{\partial(u - \bar{u})}{\partial y}} \right]_{(x, \delta, t)} \quad (18)$$

II.3. Second order pressure modelling - Wake Curvature Effect

We assume that a z-averaged curvature $K^*(x, t)$ of the interacting inviscid streamlines may be used according to :

$$\begin{cases} \frac{\partial(p-\bar{p})}{\partial y} = K^*(x, t) \cdot [\rho u^2(x, z, t) - \bar{p}u^2(x, z, t)] \\ [p-\bar{p}]_{(x, 0, t)} = -K^*(x, t) (\delta_1 + \theta_{11}) \rho q^2(x, 0, t) \end{cases} \quad (19)$$

$K^*(x, t)$ is a strongly coupled viscous-induced curvature, for example the displacement surface curvature, see East [16, 3] .

For a wake, the upper-lower dissymmetry must be taken in account, both for the curvature K^* and the thicknesses δ_1 , θ_{11} :

$$\begin{cases} \langle p(x, 0, t) \rangle = -K^*(x, t) (\delta_1^+ + \theta_{11}^+) \rho q^2(x, 0, t) \\ \quad + K^*(x, t) (\delta_1^- + \theta_{11}^-) \rho q^2(x, 0, t) \end{cases} \quad (20)$$

II.4. Viscous Upstream Influence-Singularities

The viscous (or non-interacting) upstream influence corresponds to a pressure prescribed solution of the first order equations. In the incompressible case, denoting $(\delta - \delta_1) = \bar{H} - \delta_{11}$, $\delta_1 = \bar{H} - \delta_{11}$, and the derivation with respect to \bar{H} , the integral set of equations based on mass (12), x-momentum (13) and entrainment (17) is :

$$\begin{cases} \frac{1}{q} \frac{\partial q}{\partial t} + A \frac{\partial q}{\partial x} = \frac{1}{\theta_{11}} B \\ p = \begin{bmatrix} \log \theta_{11} \\ H \\ \log q \end{bmatrix}_{(x, 0, t)} & B = \begin{bmatrix} w/q \\ C_{f/2} \\ E \end{bmatrix}_{(x, 0, t)} \\ C = \begin{bmatrix} 0 & 0 & 0 \\ H & 1 & H \\ H - \bar{H} & 1 - \bar{H} & 0 \end{bmatrix} & A = \begin{bmatrix} H & 1 & \bar{H} \\ 1 & 0 & H - 2 \\ \bar{H} & \bar{H} & \bar{H} \end{bmatrix} \end{cases} \quad (21)$$

For pressure-prescribed or q-prescribed solutions, θ_{11} , H , and w are computed from (21). A rank-2 system for \bar{H} , H is obtained from momentum and entrainment. The system is hyperbolic and the characteristic slopes in the (x, t) plane demonstrate that the upstream influence is only present in reverse flow regions, which may be identified with the condition $\bar{H} > 0$, see [6] . A singularity is present at separation ($\bar{H} = 0$) for the steady system, excepted when the pressure gradient satisfy a compatibility condition [6, 7] . Weak solutions of the unsteady hyperbolic system (21) may also provide unsteady singularities (discontinuities), see [8, 9] . Such discontinuities are not coincident with the beginning of upstream influence ($\bar{H} > 0$). They are also present in three-dimensional steady flows with pressure-prescribed solutions [9] .

Both steady and unsteady singularities may be removed in w-prescribed solutions, where θ_{11} , H , q are computed from (21). The compatibility condition at steady separation is automatically satisfied [6]. The weak solutions of the unsteady hyperbolic system are canceled [8]. In addition the characteristic slopes of the rank-3 hyperbolic system, in the (x, t) plane, indicate that the upstream influence is lost, even with reverse flow ($\bar{H} > 0$), and that the solution may be marched in the outer flow direction (analogy with the FLARE approximation), see [8] . Of course the upstream influence is included inside $w(x, 0, t)$ and is recovered from the viscous-inviscid coupling.

II.5. Interacting Upstream Influence - Subcritical branching

The recovery of the viscous upstream influence before separation (from the inviscid coupling) is however not automatic in supersonic regions. The elimination of the viscous variables in the steady system (21) provides the influence operator associated to the viscous layer for the coupling :

$$\tilde{H} w_{(x,0)} = D \left[\frac{dq}{dx} \right]_{(x,0)} + d \quad (22)$$

The perturbation of a given solution (w_0, q_0) then satisfy :

$$w - w_0 = B^* \frac{d(q - q_0)}{dx} \quad \tilde{H} B^* = D \quad (23)$$

and corresponds to a subcritical branching solution, which is unstable when marching in free stream direction and which is also equivalent to an upstream influence recovery, so long as $B^* < 0$. The analysis demonstrates that the Defect Form of the continuity equation (the wall-transpiration coupling) insures this property to be always satisfied, see [6, 7, 14, 5].

II.6. Wall-transpiration velocity in Three-Dimensions.

The same Defect Formulation as (3)(4)(5) may be written in three dimensions. With an appropriate selection of the Defect Integral thicknesses, the Defect Integral form of the first order Thin-Layer Navier-Stokes equations, with $\bar{p}(x, y, z, t) = p(x, y, z, t)$, reduces to the usual momentum integral equations. The Defect continuity equation is free of approximations. Considering non-orthogonal (x, y) coordinate-lines on the surface, z along the normal, we get in the steady case :

$$\left\{ \begin{aligned} \frac{\partial}{\partial x} \left[\frac{J}{h_1} (\rho u - \bar{\rho} \bar{u}) \right] + \frac{\partial}{\partial y} \left[\frac{J}{h_2} (\rho v - \bar{\rho} \bar{v}) \right] + \frac{\partial}{\partial z} \left[\frac{J}{h_3} (\rho w - \bar{\rho} \bar{w}) \right] &= 0 \\ ds^2 &= h_1^2 dx^2 + h_2^2 dy^2 + dz^2 + 2h_1 h_2 \cos \lambda dx dy \\ J &= h_1 h_2 \sin \lambda \end{aligned} \right. \quad (24)$$

The Defect Integral Continuity equation is exactly :

$$\left[\frac{1}{J \rho q} \frac{\partial}{\partial x} \left(\frac{J \rho q \delta_1}{h_1} \right) + \frac{1}{J \rho q} \frac{\partial}{\partial y} \left(\frac{J \rho q \delta_2}{h_2} \right) \right]_{(x,y,0)} = \left[\frac{w}{q} \right]_{(x,y,0)} \quad (25)$$

$$\left\{ \begin{aligned} q^2 &= u^2 + v^2 + w^2 + 2uv \cos \lambda \\ \delta_1(x,y) \rho q(x,y,0) &= \int_0^{\infty} [\rho u(x,y,z) - \bar{\rho} \bar{u}(x,y,z)] dz \\ \delta_2(x,y) \rho q(x,y,0) &= \int_0^{\infty} [\rho v(x,y,z) - \bar{\rho} \bar{v}(x,y,z)] dz \end{aligned} \right. \quad (26)$$

III. TURBULENT INTEGRAL CLOSURE

It is noteworthy that the closure of the entrainment integral method, which solves equations (12)(13)(17), requires only three auxiliary relations, determining the variable δ, C_f, E , from the computed Defect thicknesses δ_1, δ_{M1} , and the local Mach and Reynolds numbers. The three unknowns δ, C_f, E are strongly connected to the turbulence. We assume here simply that the relations between δ, C_f, E and $\delta_1, \delta_{M1}, M, Re_{M1}$ are exactly the same as in a boundary layer analysis, which would be based on a modelling of the velocity profiles, and of the turbulence.

III.1. Three dimensions velocity profiles modelling

A one-sided cross flow modelling is used, Fig. 1, based on a vectorial description of the viscous velocity profile $\vec{q}(\delta, C_2, C_3)$. δ is the thicknesses of the layer, C_2 and C_3 are two free shape parameters. We denote \vec{x} and \vec{y} the unit vectors, respectively tangent and normal to the inviscid velocity \vec{q} .

The suggested description combines a Wake vector \vec{W} and a logarithmic shear stress vector $\vec{\tau}$ along two different planes. An important point is that the Wake Component describes a plane Defect profile. If $z = \delta \cdot \eta$:

$$\left\{ \begin{aligned} \vec{q} &= \vec{q} - \vec{W} \tilde{F}(\eta) + \vec{\tau} \log \eta \\ \vec{W} &= q (C_2 \vec{x} + C_3 \vec{y}) \\ \vec{\tau} &= q \frac{C_1}{C_4} [(1-C_2) \vec{x} - C_3 \vec{y}] \end{aligned} \right. \quad (27)$$

The universal law of the Wall is assumed to provide the skin-friction and C_1 :

$$\left\{ \begin{aligned} C_4 &= \sqrt{(1-C_2)^2 + C_3^2} \quad C_1 = \frac{1}{0.41} \sqrt{\frac{C_2}{2}} \\ C_4 &= \sqrt{\frac{C_2}{2}} \left[\frac{1}{0.41} \log \left(Re_{\delta} \sqrt{\frac{C_2}{2}} \right) + 5.25 \right] \end{aligned} \right. \quad (28)$$

The Wake function $\tilde{F}(\eta)$ is the same as previously used in two-dimensions, see [15], and involves a rather empiric relation $\eta^* (5.4 \eta^*)$, in order to dissociate the shear layer from the Wall in extensive separations, and to control the maximum reverse flow velocities (η^* is zero for attached flows or incipient separations) :

$$\left\{ \begin{aligned} \tilde{F}(\eta) &= F \left[\frac{\eta - \eta^*}{1 - \eta^*} \right] \quad F(\eta) = (\eta^{\frac{3}{2}} - 1)^2 \end{aligned} \right. \quad (29)$$

As a first approximation, the wall shear stress may be assumed colinear to the vector $\vec{\tau}$. At large Reynolds numbers, C_1 decreases, and the polar velocity profile is roughly a triangular one. In two-dimensions ($C_3 = 0$), the profile becomes similar to the description of Coles [23], excepted for the wake function selection.

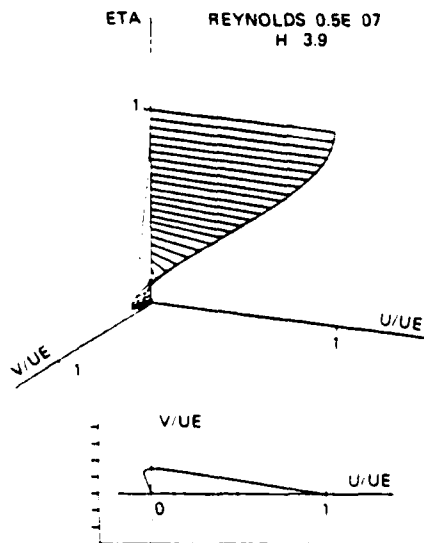


Fig. 1 - Three-dimensional turbulent velocity profiles modelling.

The same profiles are used in compressible or unsteady flows. The density is deduced from the local inviscid total enthalpy. The formulae (27) with $C_f = 0$ provide also at least a modelling of the upper or lower half-wake velocity profiles.

III.2. Equilibrium turbulent modelling

For an equilibrium boundary layer, the modelling of the entrainment E_{eq} and global dissipation Φ_{eq} may be deduced from the velocity profiles using an algebraic closure, for example the mixing length model of Michel [21], or the Debeauville-Smith model [22], with a length scale connected to the outer shear layer, defined as $\delta^* = \delta^*_{eq}$, in case of extensive separation. An adequate analytical approximation is in two-dimensions [15]:

$$\begin{cases} \tilde{\omega}_w = 1 - \frac{2.222}{1+1.222\alpha^2} \frac{\delta^*_{eq}}{\delta} \\ E_{eq} = [0.053(1-\tilde{\omega}_w) - 0.162 \frac{\delta^*_{eq}}{(\delta^*_{eq})^2}] \lambda_1 \lambda_2 \lambda_3 \\ \Phi_{eq} = [C_f / |\tilde{\omega}_w| + 0.048(1-\tilde{\omega}_w)^3] \lambda_1 \lambda_2 \lambda_3 \end{cases} \quad (30)$$

The constants of (30) are deduced from a best fit with the results of Michel [21] in attached flows at large Reynolds number. The correction terms are such that $\lambda_1 = \lambda_2 = \lambda_3 = 1$ for usual boundary layers. For wakes, we assume $\lambda_1 = 2$ and $C_f = 0$. The terms λ_2, λ_3 are used in case of curvature, or in case of free stream turbulence, see [15]. A smooth intermittency function is used at last to weight the turbulent closure relations, and the laminar closure of similar solutions, in transitional regions.

III.3. Out-of-Equilibrium modelling

The velocity profiles are assumed to be unchanged. In two-dimensions for example, the departure of the shear stress $\tau(x, z)$ from the equilibrium model $\tau_{eq}(x, z)$ is assumed to be only x-dependent. We deduce then from (16)-(18):

$$\begin{cases} \tilde{\tau}(x, z) = \lambda(x) \cdot \tilde{\tau}_{eq}(x, z) \\ E(x) = \lambda(x) \cdot E_{eq}(x) \\ \Phi(x) = \lambda(x) \cdot \Phi_{eq}(x) \end{cases} \quad (31)$$

In order to compute $\lambda(x)$, denoting $k(x, z)$ the turbulent kinetic energy, $\varepsilon(x, z)$ the unit dissipation of energy, we assume at last an approximate model $\tilde{\tau}(x)$, $k(x)$, $\varepsilon(x)$ for the turbulent transport of averaged quantities across the shear layer:

$$\tilde{\tau}(x) = \lambda(x) \cdot \tilde{\tau}_{eq}(x) \quad (32)$$

The transport equations of Launder, Hanjalic are simplified in the following way, see [15]:

$$\begin{cases} \frac{D\tilde{\tau}}{Dt} = \frac{\tilde{\tau}}{\tilde{\tau}_{eq}} \Phi_{eq} \frac{q^2}{2} - \tilde{\varepsilon} \tilde{\tau} \\ \frac{D\tilde{\varepsilon}}{Dt} = 1.5 \frac{\tilde{\varepsilon}}{\tilde{\tau}} \left[\left(\frac{\tilde{\tau}}{\tilde{\tau}_{eq}} \right)^2 \frac{\tilde{\varepsilon}_{eq}}{\tilde{\varepsilon}} \tilde{\tau}_{eq} - \tilde{\tau} \right] \\ \frac{\tilde{\varepsilon}}{\tilde{\tau}_{eq}} = \left(\frac{\tilde{\tau}}{\tilde{\tau}_{eq}} \right)^{3/2} \end{cases} \quad (33)$$

using averaged equilibrium levels $\tilde{\tau}_{eq}(x)$, $\tilde{\varepsilon}_{eq}(x)$, $\tilde{\tau}_{eq}(x)$ deduced from the velocity profiles modelling:

$$\begin{cases} \tilde{\varepsilon} \tilde{\tau}_{eq} = 0.5 \Phi_{eq} q^2 \\ \tilde{\tau}_{eq} = [0.045 \lambda_1 \lambda_2 \lambda_3 (1-\tilde{\omega}_w) \Phi_{eq}]^{1/2} q^2 \\ \tilde{\varepsilon}_{eq} = \lambda_1 \lambda_2 \lambda_3 [0.09 (1-\tilde{\omega}_w)]^2 q^2 \end{cases} \quad (34)$$

IV. NUMERICAL COUPLING ALGORITHMS

The following results were computed with different numerical methods, where the viscous-inviscid coupling is however always based on explicit relaxation techniques. This relaxation procedure couples the viscous and inviscid calculations, each of them being solved separately at a given iteration. The coupling iteration may be a fixed point one, or a more complex one, but the correction process at each coupling node is only dependent on the coupling error at this node, or in a restricted environment. This explicit-like approach is very flexible with respect to the interchangeability of the inviscid solver, but generates a problem of stability control.

For steady two-dimensional or quasi three-dimensional flows (infinite swept wing), a linear stability analysis is developed to control the relaxation techniques at each node, both with or without separation, for a boundary layer or a wake.

For two-dimensional unsteady or three-dimensional flows, only preliminary studies without separation have been achieved, using an arbitrary and uniform underrelaxation, deduced from trial and error. Converged coupled solutions are then however obtained, numerically fully consistent (or time-consistent) with a strong viscous-inviscid interaction, without inconsistent smoothing, with a coupling discretization allowing always for a possible interacting upstream influence.

IV.1. Steady attached flow-Direct Relaxation

The viscous layer is solved pressure-prescribed. Denoting n the iteration index, the viscous coupling operator of equation (22) is written:

$$[\tilde{w}^{n+1} - \tilde{w}^n] = D^{n+1} \frac{dq^n}{dx} + d^{n+1} \quad (x, 0) \quad (35)$$

The inviscid distribution q^n at $z=0$ is deduced from a w^n -prescribed inviscid solution. A fixed point iteration with under or over-relaxation is generated:

$$[\tilde{w}^{n+1} - \tilde{w}^n] = \omega(x) (\tilde{w}^{n+1} - \tilde{w}^n) \quad (x, 0) \quad (36)$$

Consistent centered or downwind discretizations of dq^n/dx insure the viscous upstream influence recovery.

IV.2. Linear stability - Local relaxation control

Denoting with prime the small perturbations of the solution, in two-dimensions, we get from (35) the viscous operator at wave number α :

$$\tilde{w}' = i \alpha B^* q' \quad \tilde{H} B^* = D \quad (37)$$

From an approximate linearized analysis of the inviscid stability with respect to the boundary conditions at $z=0$, we get at wave number α , see [24, 7, 15]:

$$w' = i \beta q' \quad \beta = \sqrt{1-M^2} \quad (38)$$

Within this assumptions, we may deduce the amplification $\mu_D(\alpha)$ of the iteration (36) before relaxation, real at subsonic nodes, imaginary at supersonic nodes, and the optimum relaxation at wave number α . Finally, stability is achieved with the over-relaxation-like technique [24]:

$$\begin{cases} \mu_D(\alpha) = \frac{\alpha B^*}{\beta} = R + iI \\ \omega_{opt}(\mu_D) = \frac{1-R}{(1-R)^2 + I^2} \\ \omega(x) = \omega_{opt}[\mu_D(\alpha_{max})] \\ 0 < \omega < 2 \end{cases} \quad (39)$$

We notice that $\omega_{opt}(\alpha_{max})$ decreases with the mesh refinement, the viscous layer thickness, the proximity of separation or sonic points.

IV.3. Steady Semi-Inverse Relaxation

In separating or separated flow regions, the viscous solution is still marched in free stream direction, usually with an implicit integration scheme, using a w^n - prescribed inverse method, which provides a first guess of the inviscid velocity q . The usual w^n - prescribed inviscid solution provides a second guess q^n , which is compared to q in order to iteratively correct w^n . The technique is Semi-Inverse [24] because only the viscous solver is an inverse one.

In Fourier space, at wave number α , we get from (38) that the usual inverse coupling iteration (inverse-viscous and inverse-inviscid successive calculations) may be simulated, at least for small perturbations, with the following semi-inverse correction :

$$\{w^{n+1} - w^n = \frac{\beta}{\alpha} \left[\frac{d\tilde{q}}{dx} - \frac{d\tilde{q}^n}{dx} \right] - \frac{i\beta}{\alpha^2} \left[\frac{d^2\tilde{q}}{dx^2} - \frac{d^2\tilde{q}^n}{dx^2} \right]\}_{(x,0)} \quad (40)$$

With some additional analysis, a stable and over-relaxation-like correction may be written, see [24, 7, 15]:

$$\{w^{n+1} - w^n = \omega_1 \frac{\beta}{\alpha} \left[\frac{d\tilde{q}}{dx} - \frac{d\tilde{q}^n}{dx} \right] + \omega_2 \frac{\beta}{\alpha^2} \left[\frac{d^2\tilde{q}}{dx^2} - \frac{d^2\tilde{q}^n}{dx^2} \right]\}_{(x,0)} \quad (41)$$

$$\begin{cases} 0 < \omega < 2 \\ \omega_3 = \omega_{opt}[\mu_I(\alpha_{max})] \\ \beta = \sqrt{1-M^2} \\ \mu_D(\alpha) / \mu_I(\alpha) = 1 \end{cases} \quad (42)$$

As originally suggested [24], we use presently $\omega_1 = \omega_3$ and $\omega_2 = 0$ at subsonic nodes, $\omega_1 = 0$ and $\omega_2 = \omega_3$ at supersonic nodes. At supersonic nodes, a theoretical improvement of the selection may be $\omega_1 \cdot \alpha_{max} = 8 \omega_3$, $\omega_2 = \omega_3$, as more recently suggested by Wigton, Holt [25]. The optimal convergence rate is however only obtained at a single wave number, α_{max} , which presumably is not determinant in the global convergence rate.

A switch between the Direct Relaxation (36) and the Semi-Inverse Relaxation (41) along the contour $z=0$ is used. The switching is based on the viscous calculation, and is controlled with the incompressible shape parameter of the viscous layer.

IV.4. Steady wakes coupling

The displacement effect of symmetrical wakes calculations may be coupled using Direct and Semi-Inverse Relaxation techniques which are very similar to (36)(41), excepted we consider now the normal-velocity jump of the inviscid flow along the cut.

The wake calculation may also be asymmetrical, either to reach the correct positioning of the cut (minimal velocity locus), either because of an inviscid dissymmetry ($q^+ \neq q^-$), or to get an asymmetrical estimate of the half-wakes thicknesses

(turbulent modelling, wake curvature effect). The mutual interference of the upper-lower viscous-inviscid interactions changes mainly the viscous coupling operator of (37) in the following way, see [15] :

$$\begin{cases} \frac{\partial}{\partial x} \begin{bmatrix} q^+ \\ q^- \end{bmatrix} = L \begin{bmatrix} w^+ \\ w^- \end{bmatrix} \\ \frac{\partial}{\partial x} [q^+ - q^-] = 0 \end{cases} \quad (43)$$

The second relation of (43) corresponds to solve the displacement coupling with a frozen curvature effect, and provides :

$$\tilde{w}'_{\pm} = i \alpha B_{\pm}^* q' \quad (44)$$

The coefficients B_{\pm}^* may be used to compute $\omega_{\pm}^+(x)$ and $\omega_{\pm}^-(x)$ in the Semi-Inverse Relaxation (41). The Direct Relaxation becomes :

$$\{w^{n+1} - w^n = \omega_{opt}(\mu_D^{\pm}) [\tilde{w} - w^n \pm R]\}_{(x,0 \pm)} \quad (45)$$

The residual R in relation (45) is the local angular error of the wake geometry positioning.

The exact positioning of the wake geometry may be achieved iteratively. After converging the displacement coupling along an approximate geometry, the residual R provides an improved update of the wake geometry, which may be converged within a few cycles, without noticeable stability problem, see [15].

The interacting curvature effect of the wake (10), even with the modelling (19)(20), is more complex than in the boundary layer theory, because the local averaged curvature $K^*(x)$ is no more issued from a preliminary and purely inviscid calculation, and requires the "induced" curvature of the coupled inviscid flow (strong-interaction). In the same way as for the displacement coupling, an iterative update of the pressure jump across the wake-cut generates a fixed point iteration for the induced curvatures K_{\pm}^* and raises a stability problem. The stability control depends on the mesh size, see [15], and may become impossible on a fine mesh, even when using an underrelaxation technique. We use in this case an inconsistent smoothing to estimate numerically the local curvature K_{\pm}^* .

IV.5. Progress in Unsteady and 3D-flows

The Direct and Semi-Inverse relaxation techniques have been extended to the quasi-three dimensional calculation of infinite swept wings, with or without separation, see section V. On the contrary, the fully three-dimensional calculations are performed with a uniform underrelaxation, with the Direct technique, without separation.

In unsteady flows, the time marching integration probably increases the efficiency of weak coupling techniques where the viscous set of equations (12)(13)(17), which controls $w(x,0,t)$ is not coupled to the derivatives of $\rho(x,0,t)$, $q(x,0,t)$ with a fully consistent discretization. An inconsistent coupling may be consequent, for example, to a solution procedure where viscous and inviscid problems are computed successively, at a given time-step, without fully converging the mutual compatibility before marching in time. Of course, a weak coupling is always consistent with the boundary layer theory, and may become irrelevant only with respect to the strong viscous-inviscid interaction, at trailing-edge for example. The stability control, when marching in time with an implicit inviscid solver

and a large time step, without a time-consistent coupling, has also to be considered.

Time consistent solutions without separation are here simply achieved in converging a Direct Relaxation technique at each time step. The viscous equations are solved marching and pressure-prescribed, with an implicit technique. The coupling underrelaxation is uniform and empirical.

V. RESULTS AND APPLICATIONS

We consider here a few typical results taken from different methods developed for airfoils and wings. They are based on potential solutions of the pseudo-inviscid problem. They strongly couple Defect Integral methods, which are issued from a unique closure (excepted for 3D-wings).

V.1. Two-Dimensions Transonic Solver - Low speed

The full viscous-inviscid solver depicted in sections II-III-IV is used for steady compressible flows around airfoils. Laminar or turbulent boundary layers and dissymmetrical wake calculations are strongly interacted, with possibly displacement, curvature and wake positioning effects. Separation bubbles or important trailing-edge separations may be resolved, approximately until maximum lift. The full potential equation is assumed for the inviscid flow, which is solved with the finite difference relaxation technique of Chattot, Coulombeix [26], in conservative or non-conservative form, with simultaneous relaxation of the viscous coupling.

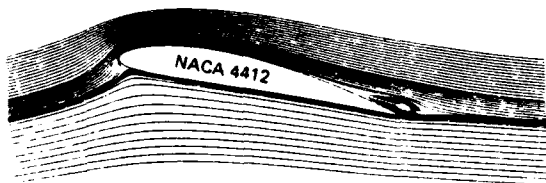


Fig. 2 - Transonic solver at Low speed and High lift : Composite viscous solution with trailing-edge separation (NACA 4412, $\alpha = 13.6^\circ$, $R = 1.5 \times 10^6$, $V = 20$ m/s).

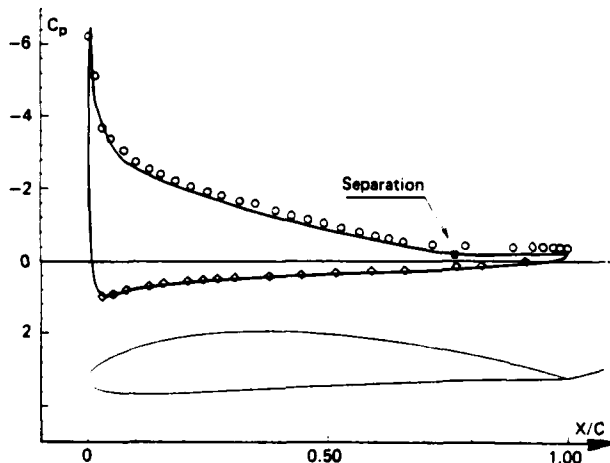


Fig. 3 - Pressure distribution from the transonic viscous solver (NACA 4412, $\alpha = 13.6^\circ$, $R = 1.5 \times 10^6$, $V = 20$ m/s).

The solver may be used at low speed and high lift, without extensive stall. An example of this limit is given on fig. 2 and Fig. 3. The flow is the so-called "Stalled airfoil case" of the 1980-81 AFSOR-Stanford Conference, and corresponds approximately to the maximum lift of the NACA 4412 section. The composite solution of fig. 1 is deduced from the velocity field $q(x,z)$ of the interacted inviscid flow, and from the velocity profiles of the Defect Integral method. The viscous velocity field $\bar{q}(x,z)$ is written :

$$\bar{q}(x,z) = q(x,z) \left[1 - C_2(x) \tilde{F}(\eta) + C_1(x) \log \eta \right], \quad z = \eta \delta(x) \quad (46)$$

The computed trailing edge bubble shows approximately a separation at 75 % chord, with a rear stagnation point in the wake. A fully dissymmetrical calculation of the wake with converged positioning is used. The non-equilibrium turbulent modelling and the wake curvature correction are however switched off.

V.2. Two-Dimensions Panel Solver - Multi Elements airfoils

This study has been developed jointly with M. Néron [27]. The direct-inverse viscous solver of the transonic airfoils codes, still connected with the same Direct and Semi-Inverse coupling algorithms, has been interacted with the accurate panel solver developed by Néron, for incompressible flows around single or multi-elements airfoils. The method is valid so long as the boundary layers and wakes are not confluent.

The influence matrix of the panel set is used to converge the viscous coupling iteration. Separations bubbles at trailing-edges, cove, slat, or flap may be resolved automatically so long as the mesh resolution on the panels is fine enough, with respect to local viscous effects.

The fig. 4 shows an Aerospatiale RA16SCL section with flap and slat, numerically investigated by Néron for a High-lift Garteau group. In such a difficult case, the high concavity of the slat on the lower side, jointed to a discontinuous geometry which separates a very thin boundary layer at a sharp corner, has required to modify empirically the slat geometry inside the well-separated region as shown on fig. 4, in order to remove a cavity-like configuration. The reattachment process is however computed with the exact geometry. At the present time, a symmetrical wake calculation is still used, without curvature correction, and without a full turbulent modelling. Computed pressure coefficients are compared on fig. 5 with the ONERA experiments of J.J. Thibert.

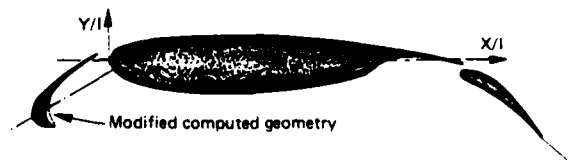


Fig. 4 - RA16SCL airfoil with slat and flap (40°)

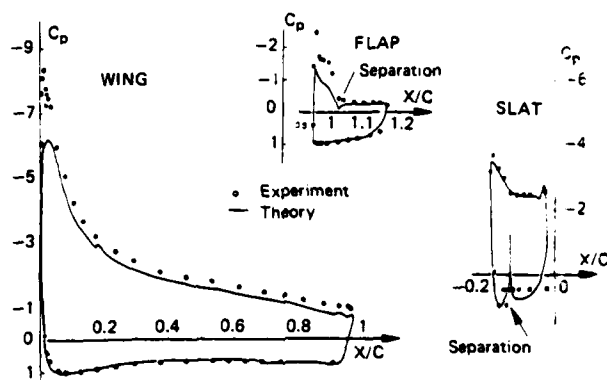


Fig. 5 - Pressure distributions on the multi-elements airfoil of fig. 4 from the interacted panel solver ($\alpha = 12^\circ$, $\alpha_{FLAP} = 40^\circ$).

V.3. Two-Dimensions Transonic Solver - Supercritical airfoils

The transonic solver of section V.1. may be used at supercritical conditions, with possibly bubbles or trailing-edge separations. The fig. 6 shows a typical result in attached flow, with the full viscous model and the conservative inviscid solver, for a RAE 2822 test case of the 1980-81 Stanford Conference. At the present time, the major limitation is the shock-induced separation, which would require a spatial resolution of very fine scale at the beginning of turbulent interactions, beyond the scope of the present potential solver robustness, see [15]. In attached flow, a small overprediction of the pressure recovery at the shock, sensible on fig. 6, illustrates probably the same effect when using the conservative inviscid technique.

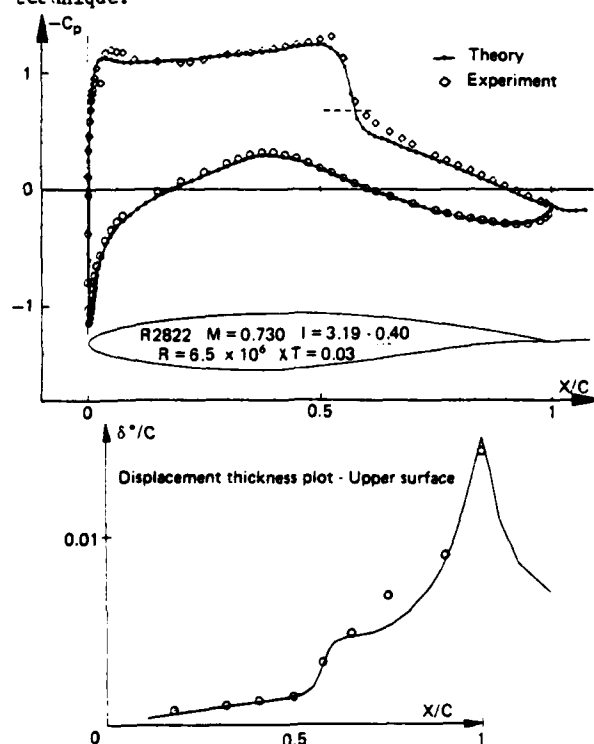


Fig. 6 - Transonic viscous solver at supercritical conditions (RAE 2822, $M = 0.730$, $\alpha = 2.79^\circ$, $R = 6.5 \times 10^6$, $x_t = 0.03$).

A recent improvement was recently achieved for computation of the airfoils for which a small base is present at the trailing-edge. The slight modification in the geometry of the section, usually involved to close the airfoil, has been here associated to an equivalent wall-transpiration technique, firstly designed for modelling the flows with spoilers [28]. The technique cancels approximately the error of the computed geometry near the trailing-edge, and is connected to the control volume balance at trailing-edge, via an increase of the wake displacement thickness, equal to the base height. The fig. 7 compares with experiments the pressure distribution over the CAST7 section at supercritical conditions, and illustrates the results obtained with the non-conservative inviscid solution. The full two-equations turbulent modelling and wake curvature corrections are used. The computation without base modelling assumes simply a geometrical closure of the section near the trailing-edge. The full model provides a noticeably improved agreement with experiments. The base thickness is 0.5 percent chord.

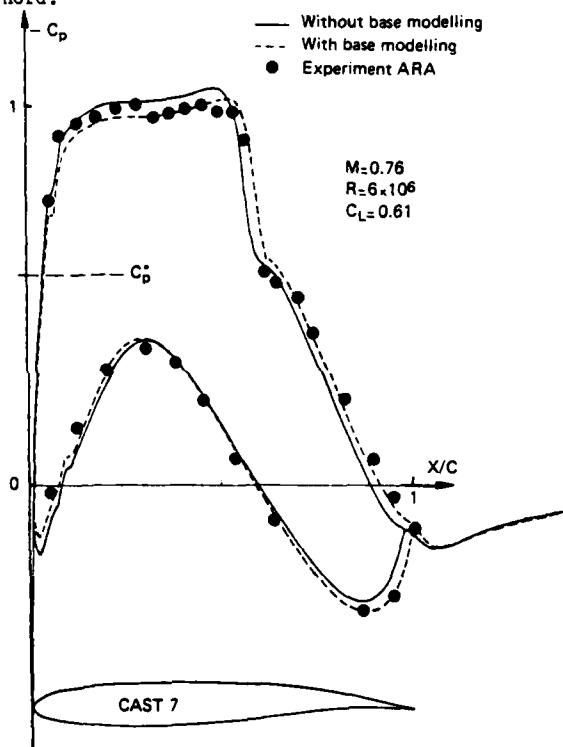


Fig. 7 - Influence of the trailing-edge base modelling - Transonic viscous solver (non-conservative option).

V.4. Two-Dimensions Transonic Solver - Spoiler flap modelling

The deflection of a spoiler flap, hinged on the wall on the upper surface, see fig. 8, is simply assumed to provide a new solid airfoil section where a discontinuity, similar to a backward-facing step, is present at the trailing-edge of the spoiler. This geometry (G), however, cannot be used directly for the computation, and an approximate geometry (G'), which may be for example the original airfoil, is substituted to (G). At each station along the contour, the angular error between (G) and (G') is approximately canceled with an equivalent wall-transpiration velocity, see [28], superimposed to the

viscous effect. The viscous contribution to the wall transpiration velocity, is still deduced from the defect Integral method interacted with the inviscid field. The strong coupling allows to deal with the separation of the viscous layer, at the spoiler hinge or downstream the spoiler. A control volume balance increases suddenly the displacement thickness at the station of the spoiler trailing-edge.

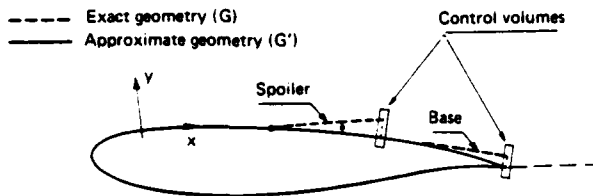


Fig. 8 - Spoiler or base modelling.

The Aerospatiale RA16SC1 airfoil has been computed with a 10° spoiler flap on the upper surface fig. 9, 10, 11. The agreement with the ONERA experiments of Consigny, Philippe is promising, although the wall-interference corrections are not optimal. The separation is induced just downstream the spoiler, and the calculated separated boundary layer does not reattach before the trailing-edge. An acceptable plateau-pressure is predicted. The two-equations turbulent modelling, the dissymmetrical wake calculation and positioning are used, with the conservative technique, without wake curvature corrections. A trailing-edge base is present. The negative lift due only to the spoiler, with a supercritical lower-surface, is predicted. Streamlines and Mach-lines contours of the composite solution are displayed on fig. 10-11.

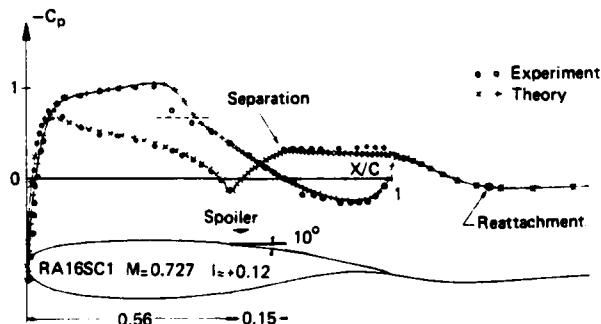


Fig. 9 - Pressure on the supercritical RA16SC1 airfoil with a spoiler flap ($M = 0.727$, $\alpha = 0^\circ$, $R = 4.2 \times 10^6$, $\alpha_{\text{SPOILER}} = 10^\circ$).



Fig. 10 - Composite viscous solution on RA16SC1 airfoil with spoiler - Streamlines contours.

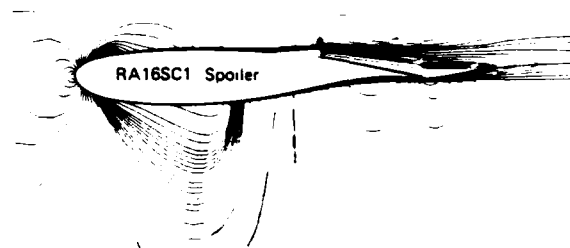


Fig. 11 - Composite viscous solution on RA16SC1 airfoil with spoiler - Mach-lines contours.

V.5. Quasi-three dimensional Transonic Solver-Infinite Swept wing.

This work was developed jointly with D.Blaise for a thesis dissertation [29]. The 3D-velocity profiles modelling of section III.1 is involved in a 2D-numerical technique, along the direction normal to the leading edge. Both the stability control in the Direct Relaxation Technique for coupling, and the Semi-Inverse Relaxation Technique have been extended to infinite swept flows. Quasi-three dimensional separations, with wall streamlines accumulation can be computed with inverse solutions procedures, and may be interacted, exactly as in two-dimensions.

The present calculations of fig. 12-13 are assumed fully turbulent and are performed with the equilibrium closure. A symmetrical wake calculation is used. The inviscid potential solver is conservative. The inviscid solution is compared on fig. 12 to the viscous calculation for an ONERA-D section, with a 30° swept angle, at supercritical conditions. The flow is attached. The comparison with the 3D ONERA experiments of Schmitt, Manie [32] on a finite wing is only indicative, because of the tip effect. A comparison between the quasi-three dimensional viscous calculation and the purely two-dimensional approximation of the viscous flow is shown on fig. 13.

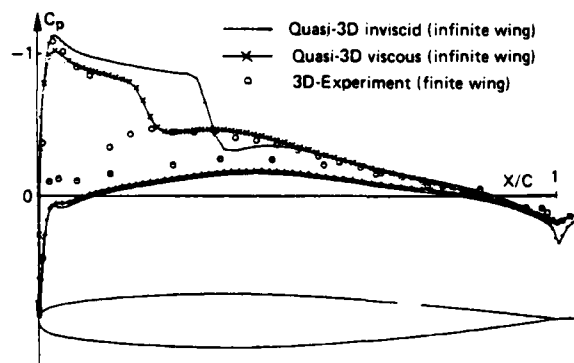


Fig. 12 - Quasi-3D transonic viscous solver - Infinite swept wing (ONERA-D, $M = 0.84$, $\alpha = 2^\circ$, $R = 2.5 \times 10^6$, $\phi = 30^\circ$).

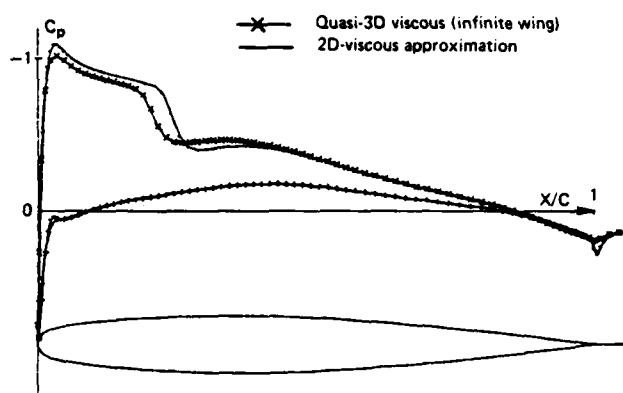


Fig. 13 - Comparison of 2D and Quasi-3D viscous solutions over an infinite swept wing (ONERA-D, $M = 0.84$, $\alpha = 2^\circ$, $R = 2.5 \times 10^6$, $\phi = 30^\circ$).

V.6. Two-Dimensions Unsteady Transonic Solutions

Time-consistent unsteady viscous solutions have been developed jointly with P. Girodroux-Lavigne for unsteady airfoils [30]. The inviscid part of the calculation was designed by Couston, Angelini for aeroelasticity problems, and assumes a transonic small perturbations approximation of the unsteady potential equation. The inviscid equations are solved at each time level with a two-step implicit ADI technique, where high frequency unsteady terms are included. The second Step (z - implicit) is interacted with the viscous wall-transpiration boundary condition, and is solved iteratively with the viscous calculation, until converging the coupling at a given time level.

The unsteady Defect Integral equations are solved with the turbulent integral closure used for steady flows. At each time level, the viscous equations are solved pressure-prescribed, with a nonlinear implicit integration in the (x, t) plane. A box scheme discretization [30] allows however to march the solution in the free stream direction. At the present time, only the equilibrium turbulent closure has been used, and the laminar calculation has been switched off. A symmetrical wake calculation has also been assumed for simplicity, although the theoretical upper-lower asymmetry of the inviscid velocities along the wake makes this approximation only valid at low reduced frequencies. The wake curvature corrections, which are not believed significant within the present approximations, have been neglected.

The fig. 14 compares to the NASA Ames experiments of Davis, Malcolm [31] the calculation results on unsteady pressure distributions, for the NACA64A010 airfoil at supercritical conditions, oscillating in pitch at 25 percent chord, with a reduced frequency $k = 0.40$ based on the chord length. The orders of magnitude used in the calculation are about 10 for the local Courant number, and about 10 cycles per time-step for the viscous-inviscid iterations. The fig. 15-16 shows a similar comparison to experiment for a supercritical ACTTA airfoil with an oscillating flap. The rear-loading, which may be seen on the steady pressure distribution, fig. 15, generates viscous effects close to separation. The separation calculation is not possible however, due to the present numerical technique.

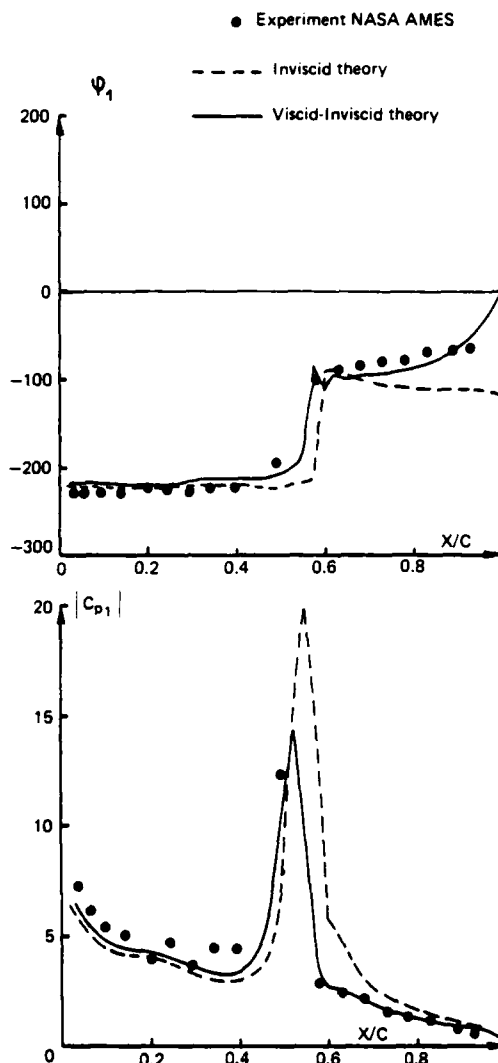


Fig. 14 - Time-consistent unsteady solution - First harmonic - Pitch oscillation (NACA 64A010, $M = 0.8$, $\alpha = 0^\circ$, $R = 12 \times 10^6$).

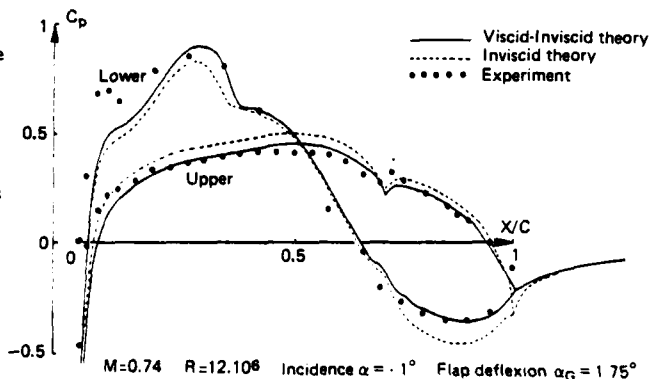


Fig. 15 - Time-consistent unsteady calculation - Steady asymptotic solution over ACTTA airfoil with flap.

$M = 0.74$ $\alpha = 1^\circ$ $\alpha_G = 1.79^\circ$ $\delta_G = 1^\circ \sin \omega t$
 $k = 0.475$ $R_\theta = 12.10^\circ$

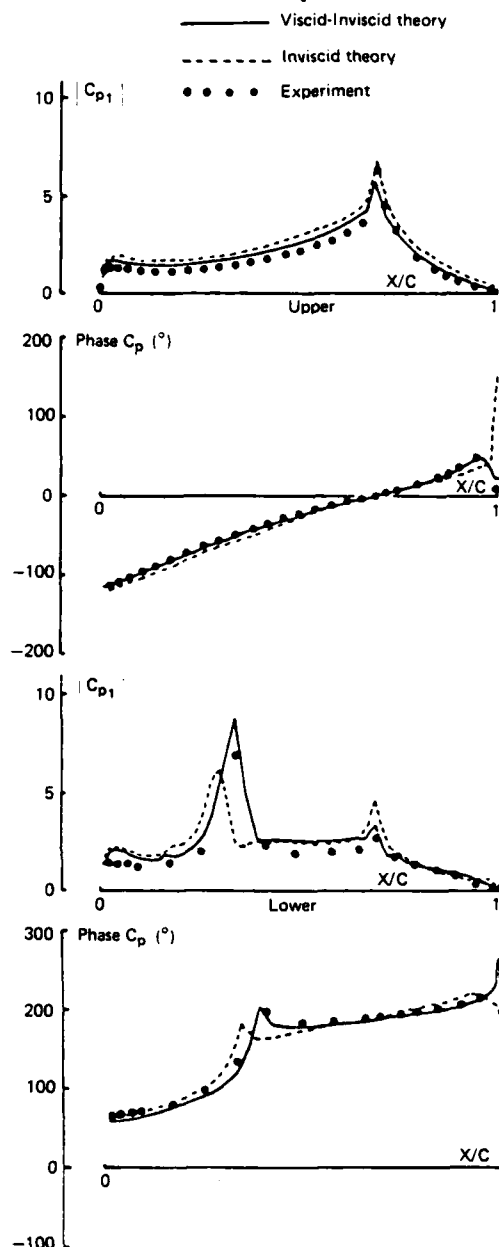


Fig. 16 - Time-consistent solution - First harmonic ACTTA airfoil - Flap oscillation.

V.7. Three-dimensions transonic Wings Solutions

A preliminary study of three-dimensional viscid inviscid interaction has been performed jointly with M. Lazareff. The transonic wing configuration, without tip effects, has been selected as a first tractable step in three-dimensions, before investigation of interactive boundary layer calculations over slender bodies (fuselage, missiles, with free vortex sheets).

On the contrary of the previous sections, the three-dimensional viscous integral method has here been reduced to the usual integral boundary layer

method of Cousteix, Aupoix [33], with an equilibrium turbulent closure, without separation capability. Some improvements, restricted to the numerical technique, have been developed by Lazareff to interact the method with the full potential equation solver (SLOR, non-conservative) of Chattot, L  , Coulombeix [26].

The viscid-inviscid interaction is performed with the inviscid grid. When necessary, especially at the laminar leading-edge region, and adaptive subgrid is used only for the viscous momentum equations (and entrainment). The integral method is solved with the inviscid velocity field prescribed, marching along the chord on the upper and lower surface. The wall-transpiration velocity is then computed with the continuity equation. Extrapolation techniques may be used in case of very small separated areas. The viscous wake is presently ignored. The coupling is achieved via a uniform underrelaxation, without any smoothing, in case of attached flow. The coupling relaxation is simultaneous with the inviscid relaxation.

The fig. 17 shows an example of pressure distribution over the F4-wing investigated by ONERA and the AEROSPATIALE* company for a Garteur Group.

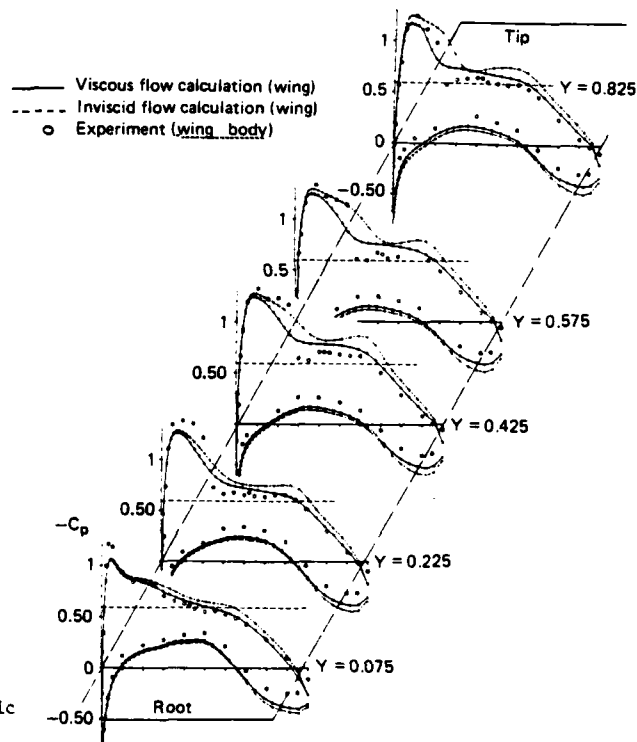


Fig. 17 - Three-dimensional viscous transonic solution. Pressure on the supercritical F4 - Wing ($M = 0.75$, $\alpha = 0.1^\circ$, $R = 3 \times 10^6$).

The flow is supercritical and attached. Although an improvement with respect to the inviscid solution is obvious on fig. 17, the comparison to the ONERA experiments of Schmitt [34] is only indicative, due to the body interference. The computed wall shear directions on the lower surface are shown on fig.18.

[*] The author is grateful to the AEROSPATIALE company, for providing its financial support to the present preliminary study on three-dimensional viscous-inviscid interaction over wings, and for giving permission to reproduce the present results.

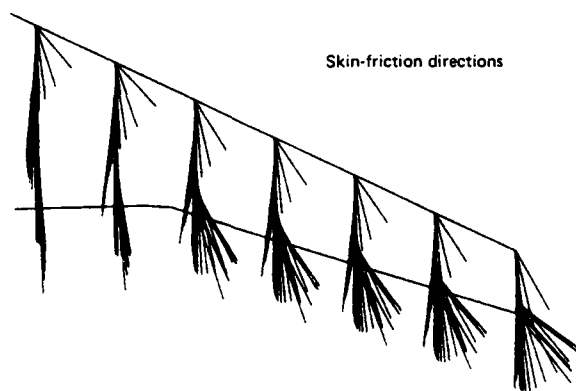


Fig. 18 - 3D - transonic viscous solution. (F4 - Wing, $M = 0.75$, $\alpha = 0.1^\circ$, $R = 3 \times 10^6$).

VI. CONCLUSIONS

The Defect Formulation of the Navier-Stokes problem, with respect to an overlapping Pseudo-Inviscid one, has been considered to generate a composite viscous solver. The viscous boundary conditions which control the pseudo-inviscid field may be written exactly, and the wall-transpiration concept is made free of any boundary-layer-like or thin-layer assumption.

The selection of an integral method of solution may be used either to decrease the required computer resources, or to increase the computable flow-complexity, when thin viscous layers are present. This is found to be consistent not only with the Prandtl equations, but also with an approximation of the Thin-layer Navier-Stokes equations, in Defect Formulation, with a non-zero normal pressure gradient.

For simplicity, the algebraic closure used in the Defect Integral equations may assume to extrapolate the usual boundary layer techniques. Determinant improvements are however achieved, both with a velocity profile modelling including reverse flow, and with an out-of-equilibrium turbulent modelling using two transport equations to control the entrainment.

The steady and unsteady boundary-layer-like singularities of the viscous solutions (separation, weak solutions) are removed via interaction with the inviscid flow, in Defect Formulation. The singularities of the interacting boundary layer theory (supercritical layers of the Crocco theory) are also removed in the Defect Formulation, where a full viscous upstream influence is always recovered in the supersonic zones. Although higher-order approximations, or a full solution of the Defect Formulation may be numerically investigated, the major shortcomings of boundary layer theory are removed as soon as the first order Defect Integral equations are strongly couple, with an inviscid solver. The approach, which includes separation bubbles, shock-boundary layer interactions, trailing-edge and wake phenomena, is then a wide scope and powerful technique in high Reynolds number flows.

A few coupling algorithms, based on explicit-like relaxation techniques, have been considered to get the interacted solution from dissociated viscous and inviscid solvers. Basically, the theoretical

analysis of the coupling techniques defines the stability of an inviscid potential solution with respect to perturbed boundary conditions. The results may be used also for coupling subdomains calculations, in inviscid patching techniques.

In case of viscous-inviscid interaction, the inviscid perturbation operator is coupled to the viscous layer influence operator. This may provide the local stability control at each coupling node in the fixed-point relaxation techniques. This may also provide Semi-Inverse relaxation techniques, which couple the usual Direct inviscid problem (Neuman Conditions) with inverse viscous solutions, which are required to march inside reverse flow regions. These coupling techniques are not restricted to the integral solutions of the viscous layer.

Results have been shown for two-dimensional flows, low speed, or transonic, or unsteady, and for three-dimensional flows. Presently, separated flows are solved only in steady two-dimensional and quasi-three dimensional lifting flows, including spoiler-induced separations.

Further investigations are especially required on coupling algorithms, relaxation-like or time-dependent, in unsteady or three-dimensional separated flows, in order to compute wings and fuselages at high incidence.

Further developments of the numerical viscous-inviscid techniques will at last provide new Composite solvers, for viscous flows equations, as soon as the Defect Integral equations will be replaced by a finite difference solution of the full Defect equations.

Acknowledgments :

The author wishes also to thank here many colleagues of ONERA who have contributed to the results which are presented here, and especially M. NERON, P. GIROUDROUX-LAVIGNE, M. LAZAREFF and D. BLAISE.

References

- 1 METHA U., LOMAX H. - Reynolds-averaged Navier-Stokes computations of transonic flows. The state of the art. Proc. Symp. Transonic Perspective, ed. D. Nixon, Progress in Astronautics vol. 81 (1982).
- 2 Mc CROSKEY W. - Unsteady airfoils - Annual Review of Fluid Mech., 14, p. 285-311 (1982).
- 3 LOCK R.C., FIRMIN M.C.P. - Survey of techniques for estimating viscous effects in external aerodynamics - RAE Techn. Memo. Aero. 1900 (April 1981).
- 4 CAMBIER L., GHAZZI W., VEUILLLOT J.P., VIVIAND H. - Une approche par domaines pour le calcul d'écoulements compressibles. Proc. Fifth. Int. Symp. on Computing Methods in Applied Sciences and engineering, Versailles (Dec. 1981).
- 5 LE BALLEUR J.C. - Calcul des écoulements à forte interaction visqueuse au moyen de méthodes de couplage. AGARD-CP-291, General Introduction Colorado-Springs, (1981), or ONERA-TP 1980-121.

- 6 LE BALLEUR J.C.-Couplage visqueux-Non-visqueux Analyse du problème incluant décollements et ondes de choc. La Recherche Aerosp. 1977-6, p. 349-358 (nov. 1977). English translation ESA-476.
- 7 LE BALLEUR J.C. - Viscid-Inviscid coupling calculations for two- and three-dimensional flows. VKI Lecture Series 1982-04, Computational Fluid Dynamics (1982). or ONERA TP.
- 8 COUSTEIX J., LE BALLEUR J.C., HOUDEVILLE R. - Calculation of unsteady turbulent boundary layers in Direct or Inverse mode, including reverse flows. Analysis of singularities. La Recherche Aerosp. 1980-3, English edition, p. 3-13 (May 1980).
- 9 COUSTEIX J., HOUDEVILLE R. - Singularities in three-dimensional turbulent boundary layer calculation and separation phenomena - AIAA J., vol. 19, n° 9, p. 976-985 (Aug. 1981).
- 10 CARTER J.E. - Inverse solutions for laminar boundary layers flows with separation and re-attachment - NASA-TR-447 (Nov. 1975).
- 11 CEBECI T., KELLER H.B., WILLIAMS P.G.-Separating boundary layer flow calculations. J. of Comput. Physic 31, p.363-378, (1979).
- 12 WORNOM S.-Application of higher-order numerical methods to the boundary layer equations-Proc. First Conf. on Num. Methods in laminar and Turbulent flows, Swansea (July 1978).
- 13 FORMERY M., DELERY J. - Méthode aux différences finies pour le calcul en mode inverse de la couche limite turbulente tridimensionnelle. La Rech. Aérop. 1981-5, p. 303-313 (July 1978).
- 14 LE BALLEUR J.C., PEYRET R., VIVIAND H. - Numerical studies in high Reynolds number aerodynamics. Computers and Fluids, Vol. 8, n° 1, p. 1-30 (March 1980).
- 15 LE BALLEUR J.C. - Strong matching method for computing transonic viscous flows including wakes and separations - Lifting airfoils. La Recherche Aérop. 1981-3, English edition, p. 21-45, (May 1981).
- 16 EAST L.F. - A representation of second-order boundary layer in the momentum integral equation and in viscous-inviscid interactions. RAE TR-81002 (1981).
- 17 MELNIK R.E. - Turbulent interactions on airfoils at transonic speeds. Recent developments. AGARD-CP-291, Paper 10, Colorado-Springs, (1981).
- 18 CARTER J.E., VATSA V.N. - Analysis of separated boundary layers flow. Proc. Eight Int. Conf. on Num. Meth. in Fluid Dyn., Aachen (June 1982).
- 19 DODGE P.R. - Numerical method for 2D and 3D flows. AIAA J., Vol. 15, n° 7, p. 961-965 (July 1977).
- 20 KHOSLA P.K., RUBIN S.G. - A composite velocity procedure for the compressible Navier-Stokes equations. AIAA Paper n° 820099 (Jan. 1982).
- 21 MICHEL R., QUEMARD C., DURANT R. - Application d'un schéma de longueur de mélange amélioré à l'étude des couches limites d'équilibre. Note Technique ONERA 154 (1969).
- 22 CEBECI T., SMITH A.M.O. - Analysis of turbulent boundary layers. Academic Press, New-York (1974).
- 23 COLES P.E. - The law of the wake in turbulent boundary layer - JFM, Vol. 1, part 2, (1956).
- 24 LE BALLEUR J.C. - Couplage visqueux-non visqueux : Méthode numérique et applications aux écoulements bidimensionnels transsoniques et supersoniques. La Recherche Aérop. 1978-2 p. 67-76 (March 1978).
- 25 WIGTON L.B., HOLT M. - Viscous-Inviscid interaction in transonic flow. Fifth Comput. Fluid Dyn. Conf., AIAA Paper n° 81-1003, Palo Alto (June 1981).
- 26 CHATTOT J.J., COULOMBEIX C., TOME C. - Calcul d'écoulements transsoniques autour d'ailes. La Recherche Aérop. n° 1978-4, p. 143-159, English translation ESA-TT-561.
- 27 LE BALLEUR J.C., NERON M. - Calcul d'écoulements visqueux décollés sur profils d'ailes par une approche de couplage. AGARD-CP-291, Paper 11, Colorado-Springs (1981).
- 28 LE BALLEUR J.C. - Calculation method for transonic separated flows over airfoils including spoilers effects. Proc. Eighth Int. Conf. on Num. Meth. in Fluid Dyn., Aachen (June 1982), or ONERA-TP-1982-66.
- 29 BLAISE D. - Mise en oeuvre et développement d'une méthode de couplage fort pour le calcul d'écoulements autour d'ailes en flèche infinies. Doct. Thesis 3rd Cycle, Lille 1 Univers. (1982), Note Technique ONERA (to be published 1983).
- 30 COUSTON M., ANGELINI J.J., LE BALLEUR J.C., GIRODROUX-LAVIGNE P. - Prise en compte d'effets de couche limite instationnaire dans un calcul bidimensionnel transsonique. AGARD-CP-296, Aix-en-Provence (1981).
- 31 DAVIS S., MALCOLM G. - Transonic shock-wave/boundary layer interactions on an oscillating airfoil. AIAA J., Vol. 18, n° 11, p. 1306-1312, (1979).
- 32 SCHMITT V., MANIE F. - Ecoulements subsoniques et transsoniques sur une aile à flèche variable. La Recherche Aérop. 1979-4, p. 219-237, (July 1979).
- 33 COUSTEIX J. - Analyse théorique et moyens de prévision de la couche limite turbulente tridimensionnelle. Note Technique ONERA n° 157 (1974), English translation ESA-TT-238.
- 34 SCHMITT V. - Aérodynamique d'un ensemble voilure-fuselage du type avion de transport. 18 th Colloque Aero. Appl. AAAF, Poitiers (1981), ONERA TP-1981-122.

COMPUTATION OF TRANSONIC VISCOUS-INVISCID
INTERACTING FLOW**

D. L. Whitfield[~]
Department of Aerospace Engineering
Mississippi State University
Mississippi State, MS 39762

J. L. Thomas⁻⁻⁻
NASA Langley Research Center
Hampton, VA 23665

A. Jameson⁺⁺⁺
Department of Mechanical and Aerospace Engineering
Princeton University
Princeton, NJ 08544

W. Schmidt⁺⁺⁺⁺
Dornier GmbH
Friedrichshafen, West Germany

Abstract

Transonic viscous-inviscid interaction is considered using the Euler and inverse compressible turbulent boundary-layer equations. Certain improvements in the inverse boundary-layer method are mentioned, along with experiences in using various Runge-Kutta schemes to solve the Euler equations. Numerical conditions imposed on the Euler equations at a surface for viscous-inviscid interaction using the method of equivalent sources are developed, and numerical solutions are presented and compared with experimental data to illustrate essential points.

I. Introduction

Viscous-inviscid interaction is an important and difficult problem in transonic aerodynamics. Unfortunately, numerical solutions of the Navier-Stokes equations are not presently a practical method for routinely solving such problems due to computer resource requirements. Consequently, much research has been done and must be still going on with regard to coupling inviscid and viscous flow solvers for treating viscous-inviscid interaction. Lock⁽¹⁾ and Melnik⁽²⁾ have reviewed interaction methods. For the most part, these methods consist of using potential flow inviscid solution methods and attached flow viscous solution methods. Inverse boundary-layer methods are being used in some instances (see Le Balleur⁽³⁾ for a review) in order to include separated flow.

Computational fluid dynamics has recently matured to the point that numerical solution of the Euler equations can be considered for solving two- and three-dimensional flow problems.⁽⁴⁻⁶⁾ Because the Euler equations can handle rotational flow, these equations offer more information and an extended Mach number range compared to the potential flow equations. There has, as yet, not been a great deal of effort devoted to coupling

* This research was sponsored by the NASA Langley Research Center, Hampton, VA 23665

[~] Professor, Member AIAA

⁻⁻⁻ Ph.D. student on leave from NASA Langley, Member AIAA

⁺⁺⁺ Professor

⁺⁺⁺⁺ Supervisor, Computational Fluid Dynamics

the Euler equations with viscous flow solvers. The work that has been done includes Refs. 7-9, where the Euler equations were coupled with a compressible turbulent inverse integral boundary-layer method⁽¹⁰⁾ in order to handle rotational flow that may contain regions of separated flow. The purpose of this paper is to present further results of work involving the Euler and inverse boundary-layer equations. These results include: (1) improvements in the inverse boundary-layer method, (2) numerical experiments with regard to Euler equation boundary conditions, (3) experience using second-order Runge-Kutta schemes with various number of stages to solve the Euler equations, (4) numerical conditions imposed on the Euler equations at a surface and in a wake for viscous-inviscid interaction using the equivalent source method, (5) displacement surface versus the equivalent source method of interaction, and (6) numerical and experimental comparisons.

II. Viscous Method

The viscous flow solution method is an inverse (meaning the pressure distribution is obtained as part of the solution rather than being specified as in a direct method) integral compressible turbulent boundary-layer method. This inverse method is an extension of the direct method described in Ref. 11. Both methods solve the momentum and mean-flow kinetic energy integral equations. A fourth-order four-stage explicit Runge-Kutta scheme is used to solve the inverse equations.

A distinguishing feature of the direct and inverse integral methods in Refs. 11 and 7 was that the dissipation integral

$$D = \int_0^{\infty} \frac{1}{\tau_w} \frac{\partial(u/ue)}{\partial y} dy \quad (1)$$

was numerically evaluated at each streamwise location as opposed to using an empirical dissipation relation. This was accomplished by using a constant laminar plus turbulent shear stress in the region just at the wall, a Cebeci-Smith type model in the inner and outer regions, and the derivative of the velocity profile expression valid for $0 < y < \infty$.^(7, 12) Although this placed a stringent requirement on the accuracy of the velocity profile expression, the method gave good results, even better than finite difference methods for transonic flow over adiabatic surfaces.

However, the numerical evaluation of the dissipation integral at each streamwise location made this integral method relatively slow (with regard to computational time) as compared to other integral methods. The computational time was not a severe limitation for steady two-dimensional flow. However, with the extension of this method to unsteady two- and three-dimensional flow, it was desirable to eliminate the need for numerically evaluating Eq. (1) at each grid point. In this connection, Donegan (10) succeeded in correlating D , as given by Eq. (1), in terms of the local edge Mach number, shape factor, and skin friction coefficient (or shape factor and Reynolds number based on momentum thickness). Recently, Thomas⁽¹⁴⁾ has made improvements in the turbulence model used in Eq. (1), particularly near the separation point, and Donegan and Thomas have improved the correlation for D given in Ref. 10. The result of using an analytical correlation as opposed to numerically evaluating Eq. (1) is an increase in speed of 0(10).

III. Inviscid Method

Finite volume spatial discretization is applied to the integral form of the time-dependent Euler equations and the resulting equations were solved using second-order Runge-Kutta time-stepping schemes with various number of stages. Dissipative terms composed of a blend of second and fourth differences are used in this central difference scheme and these terms are held constant during each stage of the Runge-Kutta solution. Convergence to a steady state is accelerated by the addition of a forcing term that depends on the difference between the local total enthalpy and the freestream value of enthalpy. Convergence is also accelerated by using a local time step determined by the maximum Courant number. Far field boundary conditions are based on a characteristic combination of variables, and pressure at the wall is determined using the normal momentum relation. With the exception of the use of second-order Runge-Kutta schemes with various number of stages and frozen dissipation, the numerical method is that of Jameson, Schmidt, and Turkel.⁽⁶⁾

An advantage of this type of explicit scheme is that stability can be achieved for Courant numbers greater than one. By using different stage Runge-Kutta schemes, the stability region can be expanded (see Fig. 1) and the maximum attainable Courant number can be increased as shown in Table 1. Although a larger Courant number can be achieved by an increase in the number of stages, the increase in work associated with the increase in stages eventually reaches a point of diminishing returns. For example, a scheme with a small value of R (see Table 1) should probably be used in the early cycles and a scheme with a large value of R thereafter. Numerical experiments indicate that the four-stage scheme is a reasonable compromise. The use of a second-order accurate scheme in time as compared to a fourth-order scheme as used in Ref. 5 has the advantage of requiring slightly less storage. Also, because steady state solutions are of interest here, and because no noticeable improvement was found in the results using a fourth-order scheme as compared to a second-order scheme, the method used was the second-order four-stage scheme with a maximum Courant number of 2.2.

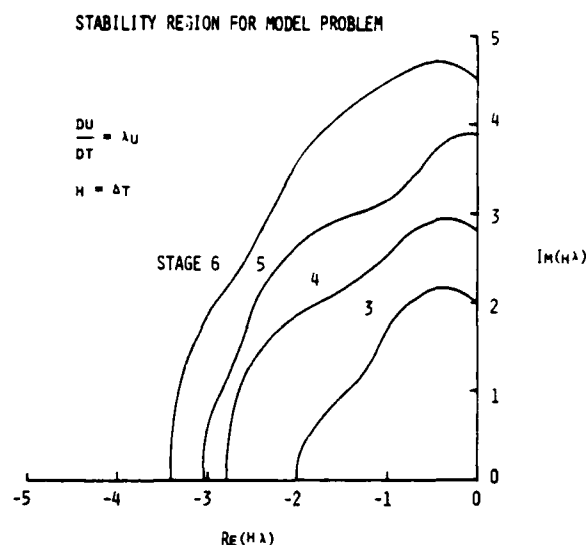


Fig. 1 Stability Region for Various Stage Second-Order Runge-Kutta Schemes

Table 1. Second-Order R-Stage Runge-Kutta (minimal storage)

R	(CFL) _{max}	η_1	η_2	$c_i, i = 1, R - 1$
1	unstable	--	--	--
2	unstable	--	--	--
3	2	.67	.50	1/2, 1/2
4	2.8	.70	.56	1/4, 1/3, 1/2
5	3.8	.76	.63	1/5, 1/5, 1/3, 1/2
6	4.5	.75	.64	1/7, 1/7, 1/4, 1/3, 1/2

$\eta_1 = \frac{CFL}{R}$ = efficiency for zero dissipation
 $\eta_2 = \frac{CFL}{R+1}$ = efficiency for frozen dissipation

IV. Viscous-Inviscid Coupling

The displacement surface concept where the inviscid solution is carried out on a grid that is displaced from the actual body by the amount of the boundary-layer displacement thickness, δ^* , is the most commonly used method of viscous-inviscid interaction. This approach, however, requires that a new grid be generated after each boundary-layer solution. A viscous-inviscid interaction approach that does not require a new grid to be generated after each boundary-layer solution is the method of equivalent sources of Lighthill.⁽¹⁵⁾ In this method, information from the viscous solution is used to specify a distribution of sources (either positive or negative) on the surface and in the wake, and this source distribution is used as a boundary condition in the inviscid solution. Assuming no attempt is made to align some portion of the grid with the wake, only one grid must be generated. Unlike a potential flow and boundary-layer interaction

method, an Euler equation and boundary-layer interaction method that uses the equivalent source concept requires that information be specified for the additional equations of momentum and energy. Development of the information necessary to use the equivalent source concept with an Euler equation and boundary-layer interaction method follows. This development is based on the work of Johnston and Sockol.⁽¹⁶⁾ Their work is reviewed and then specific relations for the elements of the \vec{g} vector of the Euler equations at a surface are obtained.

To illustrate the approach consider the steady two-dimensional Navier-Stokes equations in cartesian coordinates x, y

$$\frac{\partial \vec{F}}{\partial x} + \frac{\partial \vec{G}}{\partial y} = 0$$

and the steady two-dimensional Euler equations

$$\frac{\partial \vec{F}}{\partial x} + \frac{\partial \vec{G}}{\partial y} = 0 \quad (3)$$

where

$$\vec{F} = \begin{bmatrix} \rho u \\ \rho u^2 + p \\ \rho uv \\ (e + p)u \end{bmatrix} \quad \vec{G} = \begin{bmatrix} \rho v \\ \rho uv \\ \rho v^2 + p \\ (e + p)v \end{bmatrix}$$

$$e = \frac{p}{\gamma - 1} + \frac{1}{2} \rho (u^2 + v^2)$$

and u, v are velocity components in the x, y directions, and p, ρ , and e are the pressure, density and total energy per unit volume. An explicit description of the elements of \vec{F} and \vec{G} is not needed. Integrating Eqs. (2) and (3) with respect to y over $0 \leq y \leq h$, and considering the solution vectors \vec{g} and \vec{G} to coincide for $y > h$ (where h is taken outside the viscous region), the two integrals can be combined to obtain⁽¹⁶⁾

$$\vec{g}_0 = \vec{G}_0 + \frac{\partial}{\partial x} \int_0^h (\vec{F} - \vec{F}_0) dy \quad (4)$$

where the subscript 0 indicates $y = 0$. To avoid solving the Navier-Stokes equations, the exact solution \vec{F} is represented⁽¹⁶⁾ by a composite function \vec{F}_0 , where $\vec{F}_0 = \vec{F} + \vec{F} - \vec{F}$, and \vec{F} is a solution of the boundary-layer equations

$$\frac{\partial \vec{F}}{\partial x} + \frac{\partial \vec{G}}{\partial y} = 0 \quad (5)$$

where

$$\vec{F} = \begin{bmatrix} \rho u \\ \rho u^2 + p \\ \rho uv \\ (\bar{e} + \bar{p})u \end{bmatrix} \quad \vec{G} = \begin{bmatrix} \rho v \\ \rho uv \\ \rho v^2 + p \\ (\bar{e} + \bar{p})v - \bar{u}\tau - q \end{bmatrix}$$

and τ is the shear stress and q is the heat flux. Using the composite function for \vec{F} , and a similar one for \vec{G} (a point not mentioned in Ref. 16); Eq. (4) becomes

$$\vec{g}_0 = \vec{G}_0 + \frac{\partial}{\partial x} \int_0^h (\vec{F}_0 - \vec{F}) dy \quad (6)$$

Using Eq. (6) and the definitions of \vec{F} , \vec{g} , \vec{F} , and \vec{G} , the following conditions on the elements of \vec{g}_0 are obtained.

The term $(\rho v)_0$ is given by

$$(\rho v)_0 = (\bar{\rho} v)_0 + \frac{\partial}{\partial x} \int_0^h [(\rho u)_0 - \bar{\rho} u] dy \quad (7)$$

For no porosity in the boundary-layer solution $[(\bar{\rho} v)_0 = 0]$

$$(\rho v)_0 = \frac{d}{dx} [(\rho u)_0 s^*] \quad (8)$$

where s^* is defined as

$$(\rho u)_0 s^* = \int_0^h [(\rho u)_0 - \bar{\rho} u] dy \quad (9)$$

The term $(\rho uv)_0$ is given by

$$(\rho uv)_0 = (\bar{\rho} uv - \tau)_0 + \frac{\partial}{\partial x} \int_0^h [(\rho u^2 + p)_0 - (\bar{\rho} u^2 + p)] dy \quad (10)$$

For no-slip boundary conditions for the boundary-layer solution ($\bar{u}_0 = 0$), and taking the boundary-layer pressure equal to the pressure from the Euler solution at the surface

$$(\rho uv)_0 = -\tau_0 + \frac{d}{dx} [(\rho u^2)_0 (s^* + \theta)] \quad (11)$$

where θ is defined as

$$(\rho u^2)_0 (s^* + \theta) = \int_0^h [(\rho u^2)_0 - \bar{\rho} u^2] dy \quad (12)$$

As pointed out in Ref. 16 this approach will not provide the information necessary to obtain the pressure, and a specific approach to obtain the third element of \vec{g}_0 is not given in Ref. 16. The pressure is obtained here through an extension of the work of Rizzi⁽¹⁷⁾ by including a surface porosity term in Rizzi's normal momentum relation. This relation is derived by Thomas⁽¹⁴⁾ and the influence of including or neglecting the porosity term is demonstrated in the next section. The term $(\rho v^2 + p)_0$, therefore, is obtained by determining p_0 as mentioned, and determining $(\rho v^2)_0$ by Eq. (8) where the density is obtained from the previous time step.

The term $[(e + p)v]_0$ is given by

$$[(e + p)v]_0 = [(\bar{e} + \bar{p})v - \bar{u}\tau - q]_0 + \frac{\partial}{\partial x} \int_0^h [(\bar{e} + \bar{p})u]_0 - [(\bar{e} + \bar{p})\bar{u}] dy \quad (13)$$

Using no-slip and no porosity boundary conditions for the boundary-layer solution $\bar{u}_0 = \bar{v}_0 = 0$,

an adiabatic surface $[(q)_0 = 0]$, and the definition of total enthalpy $(h) = e + p$, Eq. (13) becomes

$$[(e + p)v]_0 = (\rho v H)_0 = \frac{d}{dx} \int_0^h [(\rho u H)_0 - \bar{\rho} \bar{u} \bar{H}] dy \quad (14)$$

The boundary-layer method (11) was developed for an adiabatic surface with variable total enthalpy across the boundary layer that takes into account total enthalpy overshoot and nonunity Prandtl number. (18) A correlation for the integral in Eq. (14) has not been developed as yet, hence the approximation $H_0 = \bar{H}$ is taken to prevent having to numerically evaluate Eq. (14) at each point. This approximation yields

$$[(e + p)v]_0 = (\rho v H)_0 = H_0 \frac{d}{dx} [(\rho u)_0 \delta^*] \quad (15)$$

which, by Eq. (8), is now simply an identity.

It is interesting to note that the combination of Eqs. (8) and (11) produces the von Kármán momentum integral equation. Hence, the results of this section can be summarized as

$$(\rho v)_0 = \frac{d}{dx} [(\rho u)_0 \delta^*] \quad (8)$$

$$(\rho u v)_0 = u_0 \frac{d}{dx} [(\rho u)_0 \delta^*] \quad (16)$$

$$(\rho v^2)_0 = \frac{1}{\delta_0} \left(\frac{d}{dx} [(\rho u)_0 \delta^*] \right)^2 \quad (17)$$

$$[(e + p)v]_0 = (\rho v H)_0 = H_0 \frac{d}{dx} [(\rho u)_0 \delta^*] \quad (15)$$

and the pressure, p_0 , is determined by the above mentioned extension of Rizzi's method. (17)

V. Results

Numerical results are compared in Refs. 8 and 19 with experimental data taken on the RAE 2822 airfoil (20) that show good agreement. The computations of Refs. 8 and 19 were carried out at the geometric angle of attack, α_2 , of the experiment as opposed to the corrected angle of attack, α_c , suggested in Ref. 20 to account for wall interference. Recent numerical experiments conducted to investigate the sensitivity of the solution to the grid, indicate a rather surprising sensitivity of lift to the location of the far field boundary as indicated in Fig. 2. The results in Fig. 2 were obtained by changing the location of the far field boundary, while maintaining the same far field boundary conditions (6) until there was no further change in the solution. Using the grid with the far field boundary located such that no change in the solution due to the grid would be expected, the computations for the RAE 2822 airfoil for $M_\infty = 0.734$, $\alpha = 3.19^\circ$, and Re_∞ (freestream Reynolds number based in chord) = 6.5×10^6 were repeated. These results are presented in Fig. 3 for both the geometric angle of attack ($\alpha = \alpha_2 = 3.19^\circ$) and the corrected angle of attack ($\alpha = \alpha_c = 2.78^\circ$) suggested by the experimenters. (20) As can be seen in Fig. 3, the agreement between the computations and the experimental data for $\alpha = \alpha_c = 2.78^\circ$ is better than for

$\alpha = \alpha_2 = 3.19^\circ$. The freestream Mach number correction of 0.004 used in Fig. 3 for the numerical solutions was that used by Lock. (1) It appears, therefore, that in view of the good agreement between numerical and experimental results obtained in Fig. 3 by accounting for the sensitivity of the far field boundary and using the corrected angle of attack, the good agreement obtained previously (8, 19) using $\alpha = \alpha_2 = 3.19^\circ$ was fortuitous. Further experimental results without wall interference, or with minimal wall interference and accurate far field measurements are needed.

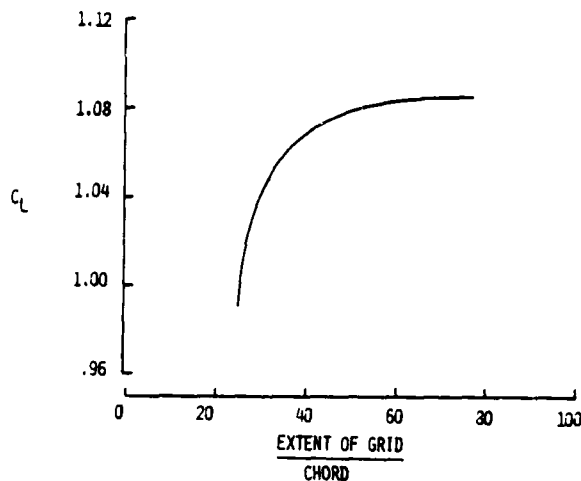


Fig. 2 Influence of the Far Field Boundary Location on the Lift Coefficient for the RAE 2822 Airfoil at $M_\infty = 0.734$ and $\alpha = 3.19^\circ$ (Inviscid)

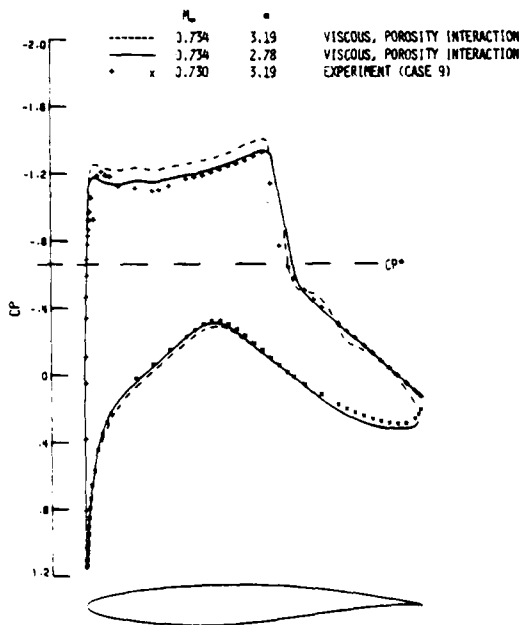


Fig. 3 Viscous-Inviscid Interaction Results for the RAE 2822 Airfoil Using Geometric (3.19°) and Experimenters' (20) Suggested Corrected (2.78°) Angle of Attack

The normal momentum relation derived by Rizzi⁽¹⁷⁾ to obtain surface pressure was based on an impermeable surface. Thomas⁽¹⁴⁾ has extended this work to include a permeable surface for viscous-inviscid interaction. The numerical results in Fig. 3 included this new normal momentum relation with a permeable surface. A comparison of numerical results obtained with and without the permeable surface term is given in Fig. 4 for the same flow conditions as Fig. 3. The results in Fig. 4 indicate that the influence of this term is small, although the influence the term does have is to improve the agreement with experiment slightly on the upper surface at the beginning of the shock and in the aft region of the lower surface.

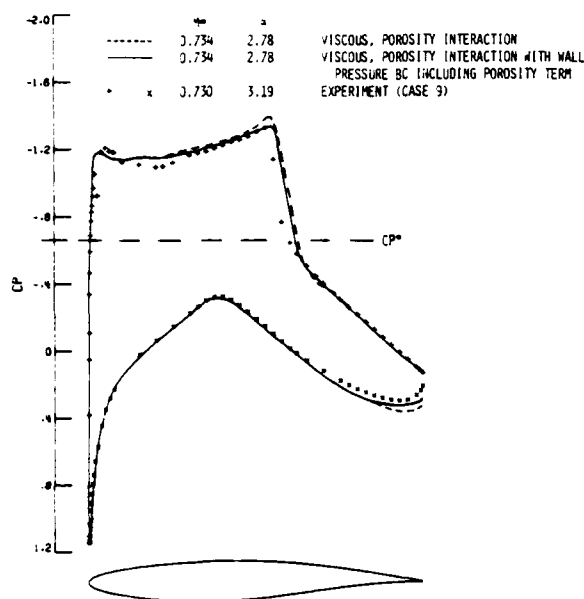


Fig. 4 Viscous-Inviscid Interaction Results for the RAE 2822 Airfoil With and Without the Porosity Term in the Surface Pressure Boundary Condition

Because the displacement surface method of viscous-inviscid interaction is the most commonly used method of calculation, a comparison is presented in Fig. 5 of the displacement surface method and the method of equivalent sources. The flow conditions used to obtain the results in Fig. 5 are the same as used to obtain the results in Figs. 3 and 4. Also, the normal momentum relation allowing for a permeable surface was used. There is some difference between the two methods of performing interaction computations as indicated in Fig. 5. The difference in shock location, for example, is of the order of the distance between grid points in this region. As mentioned, the method of equivalent sources requires that only one grid be generated, whereas, the displacement surface requires a new grid for each new boundary-layer displacement surface. The method of equivalent sources has been found the easiest to use once all the source relations are derived and coded.

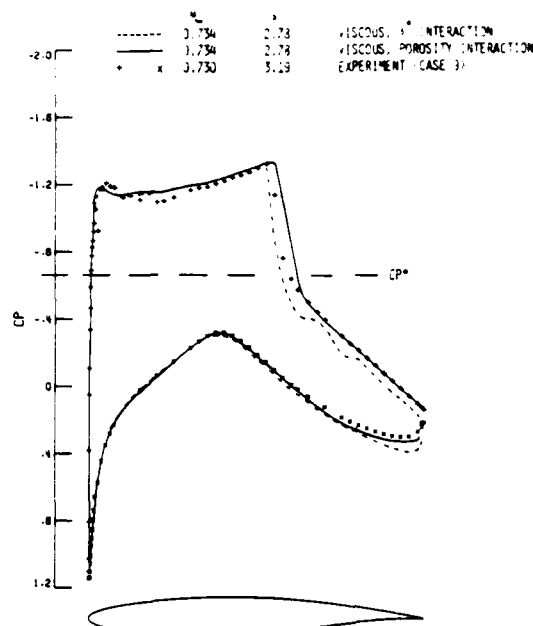


Fig. 5 Viscous-Inviscid Interaction Results for the RAE 2822 Airfoil Using Displacement Surface and Equivalent Source Methods of Interaction

VI. Concluding Remarks

The results presented involved improvements and experiences with previous work in using Euler and inverse boundary-layer equations for treating transonic viscous-inviscid interaction. Improvements in the inverse boundary-layer method included the handling of the turbulence modeling, particularly near separation, and a correlation for the dissipation integral which eliminated the need for numerical integration, and thereby reduced the computational time of the viscous solutions. Solutions of the Euler equations indicated a significant influence of the far field boundary on the lift of a supercritical airfoil with a reasonably strong shock on the upper surface. The computed lift did not change once the far field boundary was moved far from the airfoil. This observation is receiving further investigation. The use of second-order Runge-Kutta schemes with various number of stages indicated that a second-order four-stage scheme with a maximum Courant number of $2\sqrt{2}$ was a reasonable compromise for solving the Euler equations. Additional numerical surface conditions for the momentum and energy equations were developed and used in the Euler equations for the equivalent source method of viscous-inviscid interaction. Accounting for a permeable surface in the normal momentum relation used to obtain pressure produced a slight improvement in the results. Finally, numerical solutions indicated some difference between the displacement surface method and the equivalent source method of viscous-inviscid interaction, although the difference in shock location was approximately the same as the distance between grid points. The equivalent source method is the easiest to use and requires that only one grid be generated.

The present work was carried out on a CYBER 203 in 64-bit mode with only a small portion of the code vectorized. Typical run times were 208 seconds for 1000 Euler equation cycles on a 128 x 30 grid with 16 boundary-layer solutions. Experience indicates that a similar solution obtained on a CRAY-1S requires about half this amount of time.

References

(1) Lock, R. C. "A Review of Methods for Predicting Viscous Effects on Aerofoils and Wings at Transonic Speeds," AGARD-CPP-291, 1980.

(2) Melnik, R. E. "Turbulent Interactions on Airfoils at Transonic Speeds - Recent Developments," AGARD-CPP-291, 1980.

(3) Le Balleur, J. C. "Viscid-Inviscid Coupling Calculations for Two and Three Dimensional Flows." Lecture Series 1982-04, von Kármán Institute for Fluid Dynamics, March 29 - April 2, 1982.

(4) Jackocks, J. L. and Kneile, K. R. "Computation of Three-Dimensional Time-Dependent Flow Using the Euler Equations," AEDC-TR-80-49, Arnold Air Force Station, TN, October 1980.

(5) Rizzi, A. and Eriksson, L. E. "Transfinite Mesh Generation and Damped Euler Equation Algorithm for Transonic Flow Around Wing-Body Configurations," AIAA Paper No. 81-0999, June 1981.

(6) Jameson, A. Schmidt, W., and Turkel, E., "Numerical Solutions of the Euler Equations by Finite Volume Methods Using Runge-Kutta Time-Stepping Schemes," AIAA Paper No. 81-1259, June 1981.

(7) Whitfield, D. L., Swafford, T. W., and Jackocks, J. L. "Calculation of Turbulent Boundary Layers with Separation and Viscous-Inviscid Interaction," AIAA Journal, Vol. 19, No. 10, October 1981, pp. 1315-1322.

(8) Schmidt, W., Jameson, A., and Whitfield, D., "Finite Volume Solutions to the Euler Equations in Transonic Flow," J. of Aircraft, Vol. 20, 1983.

(9) Whitfield, D. and Jameson, A., "Three-Dimensional Euler Equation Simulation of Propeller-Wing Interaction in Transonic Flow," AIAA Paper No. 83-0236, January 1983.

(10) Whitfield, D. L., Swafford, T. W., and Donegan, T. L. "An Inverse Integral Computational Method for Compressible Turbulent Boundary Layers," in Transport Phenomena in Fluid Mechanics, Springer-Verlag, Berlin, 1982.

(11) Whitfield, D. L. "Integral Solution of Compressible Turbulent Boundary Layers Using Improved Velocity Profiles," Arnold Air Force Station, TN, AEDC-TR-78-42, December 1978.

(12) Whitfield, D. L. "Analytical Description of the Complete Turbulent Boundary-Layer Velocity Profile," AIAA Journal, Vol 17, No. 10, October 1979, pp. 1145-1147.

(13) Swafford, T. W. "Calculation of Skin

Friction in Two-Dimensional, Transonic Turbulent Flow," Arnold Air Force Station, TN, AEDC-TR-79-12, April 1979.

(14) Thomas, J. L. "Viscous-Inviscid Interaction Using Euler and Inverse Boundary-Layer Equations," Ph.D. Dissertation, Mississippi State University, 1983.

(15) Lighthill, M. J., "On Displacement Thickness," Journal of Fluid Mechanics, Vol. 4, Part 4, 1958, pp. 383-392.

(16) Johnston, W. and Sockol, P. "Matching Procedure for Viscous-Inviscid Interactive Calculations," AIAA Journal, Vol. 17, No. 6, June 1979, pp. 661-663.

(17) Rizzi, A., "Numerical Implementation of Solid-Body Boundary Conditions for the Euler Equations," ZAMM, Vol. 58, 1978, pp. 301-304.

(18) Whitfield, D. L. and High, M. D., "Velocity-Temperature Relations in Turbulent Boundary Layers with Nonunity Prandtl Numbers," AIAA Journal, Vol. 15, No. 3, March 1977, pp. 431-434.

(19) Whitfield, D., Jameson, A., and Schmidt, W., "1980-81 AFOSR-HTTM-Stanford Conference on Complex Turbulent Flows: Comparison of Computation and Experiment," Stanford, CA, September 1981.

(20) Cook, P. H., McDonald, M. A., and Firmin, M. C. P., "Aerofoil RAE 2822-Pressure Distribution, and Boundary Layer and Wake Measurements," in Experimental Data Base for Computer Program Assessment, AGARD-AR-138, 1979.

AIRFOIL FLOW FIELD CALCULATIONS WITH COUPLED BOUNDARY LAYER/POTENTIAL CODES

J. D. Murphy and L. S. King
NASA, Ames Research Center
Moffett Field, California

Abstract

In the proposed paper, the authors will consider the solution of airfoil flow fields by means of coupled boundary layer/full potential solutions, including the effects of separation.

The inviscid flow will be calculated using a conservatively differenced full potential code, which for the flows considered, should provide essentially the same flow field as a solution to the Euler equations.

The viscous flow will be obtained by solving the boundary-layer equations in either the direct or inverse mode as required.

The coupling will be carried out by means of a surface blowing and bleed distribution in the inviscid calculation modeling the viscous flow effects on the inviscid flow. Convergence is indicated when the pressure distributions in the viscous and inviscid solutions agree.

It is well established that substantial economies can be obtained in the computation of interacting flows by the use of zonal methods. It is less clear, however, what one pays for these solutions in terms of lost information or loss of

accuracy due to the approximation inherent in these methods.

A significant portion of the paper will be devoted to the assessment of the effects of the choices between:

1. Specification of δ^* (or equivalently stream-function at the edge), or of C_t , as a boundary condition for the inverse boundary-layer calculations.

2. The flare approximation or iterative sweeping in the separation bubble.

3. The choice of and definition of boundary conditions on the inviscid calculation to represent the viscous flow.

4. The selection of parameters of the viscous and inviscid calculations which are to be matched and the significance of the convergence criteria.

In each case above, the effects of the various choices available will be determined by comparing solutions under the various options and where significant differences are noted by comparing the solutions to the thin-layer equations and to experimental data.

COMPONENT PART NOTICE

THIS PAPER IS A COMPONENT PART OF THE FOLLOWING COMPILATION REPORT:

(TITLE): Symposium on Numerical and Physical Aspects of Aerodynamic Flows (2nd),
17 20 January 1983, California State University, Long Beach, California.

(SOURCE): California State Univ., Long Beach 389278

TO ORDER THE COMPLETE COMPILATION REPORT USE AD-A134 151.

THE COMPONENT PART IS PROVIDED HERE TO ALLOW USERS ACCESS TO INDIVIDUALLY AUTHORED SECTIONS OF PROCEEDINGS, ANNALS, SYMPOSIA, ETC. HOWEVER, THE COMPONENT SHOULD BE CONSIDERED WITHIN THE CONTEXT OF THE OVERALL COMPILATION REPORT AND NOT AS A STAND-ALONE TECHNICAL REPORT.

THE FOLLOWING COMPONENT PART NUMBERS COMPRISE THE COMPILATION REPORT:

AD#:	TITLE:
AD-P001 929	Time Dependent Finite-Difference Simulation of Unsteady Interactive Flows.
AD-P001 930	A Direct Method for the Solution of Unsteady Two-Dimensional Incompressible Navier-Stokes Equations.
AD-P001 931	Computation of Flow Past a Hypersonic Cruiser.
AD-P001 932	Interactive Separation from a Fixed Wall.
AD-P001 933	The Interaction Between a Steady Laminar Boundary Layer and an Oscillating Flap: The Condensed Problem.
AD-P001 934	Application of Unsteady Laminar Triple-Deck Theory to Viscous-Inviscid Interaction from an Oscillating Flap in Supersonic Flow.
AD-P001 935	A Study of Non-Unique Solution of the Two-Dimensional Boundary-Layer Equations at Laminar Separation and Reattachment Points.
AD-P001 936	Measurements and Calculations of a Separating Boundary Layer and the Downstream Wake.
AD-P001 937	Why? A Finite-Element Algorithm for the Parabolic Navier-Stokes Equations.
AD-P001 938	Wing Design and Analysis.
AD-P001 939	Computation of Transonic Viscous-Inviscid Interacting Flow.
AD-P001 940	Viscous-Inviscid Matching Using Higher-Order Shear-Layer Equations.
AD-P001 941	A Comparison Between the Predicted and Experimental Characteristics of a NACA 643-418 Aerofoil at Low Reynolds Numbers.
AD-P001 942	A Survey of Recent Work on Interacted Boundary Layer Theory for Flow With Separation.
AD-P001 943	An Interactive Approach to Subsonic Flows with Separation.

Acquisition For

AD-A134 151

AD-A134 151

AD-A134 151

AD-A134 151

AD-A134 151

AD-A134 151

AD-A134 151

AD-A134 151

AD-A134 151

AD-A134 151

AD-A134 151

AD-A134 151

AD-A134 151

AD-A134 151

AD-A134 151

AD-A134 151

AD-A134 151

AD-A134 151

AD-A134 151

AD-A134 151

AD-A134 151

AD-A134 151

DTIC

NOV 7 1983

A

COMPONENT PART NOTICE (CON'T)

AD#:

TITLE:

AD-P001 944	Prediction of Subsonic Separation Bubbles on Airfoils by Viscous-Inviscid Interaction.
AD-P001 945	Unsteady Viscous Transonic Flow Computations Using the LTRANZ-NLR Code Coupled with Green's Lag-Entrainment Method.
AD-P001 946	Viscous/Inviscid Interaction Analysis of Asymmetric Trailing-Edge Flows.
AD-P001 947	Measurements of Attached and Separated Turbulent Flows in the Trailing-Edge Regions of Airfoils.
AD-P001 948	Numerical Simulation of Turbulent Trailing Edge Flows.
AD-P001 949	Problems Associated with the Aerodynamic Design of Missile Shapes.
AD-P001 950	Theoretical and Experimental Dynamic Stall, Investigations on a Rotor Blade Tip.
AD-P001 951	Effect of Roughness on Three-Dimensional Turbulent Boundary Layers.
AD-P001 952	Transonic Small Disturbance Calculations Including Entropy Corrections.
AD-P001 953	The Efficient Solution of Transonic Wing Flow Fields.
AD-P001 954	Transonic Flowfield Computation Using a Modified Shock-Point Operator.
AD-P001 955	Viscous-Inviscid Interactions with a Three-Dimensional Inverse Boundary-Layer Code.
AD-P001 956	Store Separation at Transonic Speeds.
AD-P001 957	Development of Boundary Layers and Separation Patterns on a Body of Revolution at Incidence.
AD-P001 958	Calculation of Boundary Layers and Separation on a Spheroid at Incidence.
AD-P001 959	Stern Boundary-Layer Flow on Two Three-Dimensional Bodies Having Elliptical Transverse Cross-Sections.
AD-P001 960	Calculation of Three-Dimensional Boundary Layers Around Ship Hull Forms.
AD-P001 961	Calculations of Thick Boundary Layers Using a Streamline Curvature Method.

VISCOUS-INVISCID MATCHING USING HIGHER-ORDER SHEAR-LAYER EQUATIONS

P. Bradshaw, M.J. Kavanagh and D. Mobbs

Department of Aeronautics
Imperial College, London.Abstract

A progress report is given on three related projects, in all of which elliptic equations are used to describe shear layers with significant upstream influence, such as occurs near trailing edges or rapid changes in surface curvature. The large computing times usually required for iterative elliptic solutions are avoided, or disguised, by imbedding the shear layer iteration in the iteration loop required to match any shear layer solution to a solution for the outer "inviscid" flow. Programs for calculation of flow over single airfoils are running in incompressible and compressible flow (in the latter case with moderate shock induced separation) and extension to multi element airfoils is in hand.

1. Introduction

The conventional process of viscous inviscid matching involves the solution of an "inviscid" equation for the outer flow to provide the boundary condition for a solution of the parabolic thin shear layer equations ("boundary layer equations") in the viscous or turbulent part of the flow; the presence of the retarded viscous region in turn affects the inner boundary condition for the inviscid equation, and the two sets of boundary conditions must be matched iteratively (this description covers both "direct" and "inverse" calculations). It is well known that the thin shear layer equations are inaccurate, or even singular, in flows where the normal pressure gradient cannot be neglected: sometimes the normal pressure gradient can be related to the curvature of a solid surface or a known streamline (in which case the equations remain parabolic) but this is not a reliable procedure if the curvature is changing rapidly, as it does near a trailing edge.

Mahgoub and Bradshaw (1) described a method of combining the iterative scheme required to match a shear layer calculation to an inviscid flow calculation with the iterative scheme required to solve elliptic equations in the shear layer. Thus, the full Navier Stokes equations or any desired simplification of them could be solved for any shear layer, without incurring the large increase in computing time that would be required if the shear layer solution were iterated to convergence at each cycle of the viscous inviscid matching iteration. The object was to improve the accuracy of calculations in highly curved flows or near airfoil trailing edges, where large errors can result from trusting the thin shear layer approximation that the normal pressure gradient is negligible. Mahgoub and Bradshaw restricted their work to shear layers without reversed flow, and with a sufficiently high Reynolds number that normal stress gradients could be approximated; thus, two dimensional storage was required only for

the pressure field, and not for the velocity field or viscous stresses, because upstream influence was assumed to propagate only via the pressure and not via longitudinal gradients of viscous or turbulent stress or via flow reversal (Fig. 1).

In the numerical scheme for the shear layer, based on the BFA method, the x-component momentum equation, the continuity equation and the Reynolds stress transport equations are solved, at a given streamwise position, using the pressure field calculated on the last "sweep" of the shear layer calculation to evaluate dp/dx (which is allowed to vary with y): then, the y-component momentum equation is solved, trivially, for $p-pe$, given U , V and the Reynolds stresses. Actually, the y-component equation is solved at the previous x-position, so that the newly calculated values of V can be used in a central difference representation of the major term UdV/dx . The final station in the shear layer calculation is always chosen such that dp/dy is negligible - far downstream of an airfoil, for instance. At the end of the shear layer "sweep", the values of V calculated at the edge of the shear layer are used as the boundary condition for a calculation of the inviscid flow (using a surface source method in the case of incompressible flow) in the region outside the shear layer, which yields new values for pe . Note that a nominal, preferably generous, estimate of the shear layer thickness can be used at the first major iteration and improved as the calculation proceeds. The displacement surface concept is not used at all (it presents conceptual and practical difficulties if the external flow velocity varies significantly with y , as it is bound to do if dp/dy is significant). An improved estimate of the pressure field within the shear layer is now obtained from the new pe and the old $p-pe$ (i.e. that calculated in the last shear layer sweep), and the process repeated (Fig.2). The only major difficulty in this extension of boundary layer concepts is the need to use semi curvilinear (s,n) coordinates in the shear layer (axis curvature being negligible in the thin shear layer approximation): see Fig.3.

The present paper gives details of progress since the publication of Mahgoub and Bradshaw's paper. Complete airfoil calculations, including a laminar boundary calculation (assuming negligible dp/dy) and a full treatment of the wake have now been done in incompressible flow, using the Smith and Hess surface source method for the inviscid flow and Thwaites' method for the laminar boundary layer. In compressible flow, Jameson's FLO-11 program has been used, as an interim measure, for the inviscid flow, with the Cohen-Reshotko upgrade of Thwaites' method for the laminar boundary layer, and a simplified version of the wake routine in which the density is assumed to be constant across the wake, although streamwise variations are allowed for. (The incompressible wake program has now been

cleaned up and will be extended to compressible flow with a proper treatment of the density.) The (incompressible) program is being extended to multi element airfoils, where, at high lift, the rate of growth of the "boundary layer" over the rear flap can be of order unity (Fig. 8) and the traditional thin shear layer approximation breaks down completely. Extension to three dimensional flow is about to begin: the use of the V component velocity as the boundary condition for the inviscid flow avoids difficulties with the definition of displacement thickness in three dimensions. For development purposes, the inviscid flow calculation will be restricted to infinite yawed wings (when it becomes effectively two dimensional) in order to save computing time, but the shear layer calculation will treat fully three dimensional flows. The existing three dimensional boundary layer program can be extended to include the y-component momentum equation in much the same way as the two dimensional program. In a fully three dimensional flow, logic would be needed to control the direction of spanwise progress of the calculation according to the crossflow direction, as in the "characteristic box" method of Cebeci and Stewartson (2): an advantage of the BFA method is that the characteristics appear naturally.

2. Isolated airfoil calculation

2.1 Incompressible flow

The boundary layers on the upper and lower surfaces are solved independently (Fig.3). The laminar section of the boundary layer is solved by the Thwaites integral method; the point of transition is chosen arbitrarily but any standard criterion could be inserted. The turbulent solution using the BFA method continues up to points about two upper surface boundary layer thicknesses upstream of the trailing edge on each side. The dp/dy calculation is switched on if the surface curvature is large, but otherwise dp/dy is notionally set to zero and not stored.

Starting at this position just upstream of the trailing edge the coordinate system is transformed from the original (s,n) systems for each boundary layer to a curvilinear orthogonal coordinate system, (ϕ, ψ), which represents the streamlines and equipotentials of inviscid flow over a wedge with the same angle as the trailing edge (the surface is assumed flat in this region). This region extends the same distance downstream of the trailing edge; the dp/dy calculation remains switched on throughout the trailing edge region. Finally the original kind of (s,n) system, now referred to a nominal center line of the wake, is used in the rest of the wake region.

In this paper we concentrate on the improvements made in the last few years to the method of Mahgoub and Bradshaw, and readers are referred to their paper for a detailed description of the method. Introduction of a wake calculation requires two additions, (a) a wake turbulence model (b) special treatment of the coordinates in the trailing edge region.

(a) The wake turbulence model

The calculation of the two interacting shear layers, i.e. the upper and lower wake regions of the airfoil, by straightforward superposition was first

reported by Bradshaw, Dean and McEligot (3). It was postulated that any changes in the turbulent structure are likely to be small. It was pointed out that this approximation is not likely to be suitable for shear layers containing stress profiles of the same sign, e.g. an internal boundary layer. The physical justification of the superposition approach is that the flow structure in the interaction zone is of an intermittent nature with negatively and positively stressed fluid existing at the same point at different times. The basis of the method is that both shear stress profiles, τ_+ and τ_- , should be calculated independently; with the exception that the mean velocity profile is common.

The equations to be solved are slightly different from the original ones quoted in Ref. (4). In (x,y) coordinates - for simplicity - both shear stress equations are of the form:

$$\left\{ U \frac{\partial}{\partial x} + V \frac{\partial}{\partial y} \right\} \left(\frac{\tau}{\rho a_1} \right) = \tau \frac{\partial U}{\partial y} - \frac{\partial}{\partial y} \left(G \tau \frac{1}{\max} \right) - \frac{\tau^2}{L}$$

where:

$$\tau = \tau_+ \text{ or } \tau_-$$

The mean velocity is obtained from:

$$U \frac{\partial}{\partial x} + V \frac{\partial}{\partial y} U = \frac{\partial p}{\partial x} + \frac{\partial}{\partial y} (\tau_+ + \tau_-)$$

and

$$\frac{\partial U}{\partial x} + \frac{\partial V}{\partial y} = 0$$

The dimensionless parameters, a_1, G and L , which are defined above are evaluated in terms of τ_+ and τ_- separately. At the edges of the shear layer the flow velocity is prescribed to be equal to the external values, U_e .

The length scale of the wake region may be obtained either from an algebraic formula or by solving an additional transport equation. Fig. (4) illustrates how the two shear layers interact in the wake region. It is important to mention that the introduction of the extra shear stress into the equations does not affect their hyperbolicity since it may be considered simply as a body force term.

This approach was applied to flow in a duct (3) and later to a jet flow (5). The approximation was found to be successful for both cases. It is significant that although the turbulence levels in the jet are large the superposition assumption models the turbulence structure fairly successfully; for later results see Weir et al.(6).

(b) Trailing edge coordinate system

It is necessary to provide a smooth transition from the (s,n) coordinate system along the airfoil to the (s,n) coordinate system in the wake. A problem is caused by the singularity in geometry at the trailing edge (note that the Navier Stokes equations - as distinct from the thin shear layer equations - do not themselves generate singularities leading to unphysical behavior). The

original airfoil program changed from the two (s,n) coordinate systems used in the upper and lower boundary layers, to the single (s,n) system used in the wake, by simple interpolation of the former on to the s=0 line of the latter. However this proved to be unwieldy and inaccurate because of the wide variety of trailing edge geometries for which streamwise derivatives had to be evaluated. to choose a set of streamwise curves in the trailing edge region whose slope and curvature match the constant-n lines in the turbulent boundary layer region upstream and the wake region further downstream, and to produce an orthogonal set of curves to this streamwise set (the alternative being to use a non-orthogonal interpolation mesh which would have caused extra complication and suffered from many of the disadvantages of the first scheme). The main need is for a coordinate system which removes the trailing edge singularity. From potential theory a suitable system may be found based on a "wedge flow transformation".

Referring to Fig. (5) the entire ζ plane with a cut at $\theta = \pi$ is mapped onto a region $-\pi/n < \theta < \pi/n$ in the Z-plane, the transformation between the two planes being

$$Z = \zeta^{1/n}$$

This transformation is singular at $\zeta=0$ which maps on to $Z=0$.

The potential flow solution lines produced by the above transformation may be used here as an orthogonal curvilinear coordinate system in the Z-plane, where the streamlines of constant ψ are the lines of constant normal coordinate, and the equi-potential lines of constant ϕ are the lines of constant streamwise coordinate. The angle between these coordinate lines and the real-flow streamlines should at least be small enough to minimise false diffusion errors.

The Z-plane is described in terms of polar complex coordinates:

$$Z = re^{i\theta}$$

The potential field W is defined as:

$$\frac{\partial w}{\partial Z} = u - iv = \frac{\partial \zeta}{\partial Z} \frac{\partial \zeta}{\partial \zeta}$$

The potential flow in the ζ plane has unit velocity everywhere. Therefore:

$$\frac{\partial w}{\partial \zeta} = 1: \quad \frac{\partial w}{\partial Z} = \frac{\partial \zeta}{\partial Z} = nZ^{n-1}. \quad \text{Therefore } w(Z) = Z^n.$$

This potential flow is now described in terms of the streamwise variable ϕ - and the orthogonal variable ψ .

Thus:

$$w(Z) = Z^n = \phi + i\psi = r^n e^{in\theta}$$

Consequently the coordinate system may define as:

$$\phi = r^n \cos n\theta$$

and

$$\psi = r^n \sin n\theta$$

The trailing edge region extends about 2% of the chord length both upstream and downstream of the trailing edge.

The transformed "streamlines" all asymptote to the wedge surface at an infinite distance upstream of the trailing edge. Here it is necessary for the "streamlines" to become straight - or at least to match the constant-n lines - at a finite distance upstream. This is arranged by patching the (s,n) system of the turbulent boundary layer and the orthogonal curvilinear (ϕ, ψ) system of the trailing edge region together by using polynomial streamwise curves. For conformity with the constant-n lines of the turbulent boundary layer, they have to match slope and curvature at the upstream end. Similarly downstream they must have the same slope and curvature as the wake coordinate lines. A quartic is employed since it satisfies these minimum requirements. Care must be taken when deriving these curves to ensure that no turning points exist in the patching region, but the required quartic turns out to be highly degenerate and the whole trailing edge coordinate change is simple to program. At present the same size of wedge region is used on both sides of the airfoil (Fig. 3) which is slightly inefficient since the lower boundary layer is usually thinner: note that the viscous inviscid matching surface is not critical, but merely has to be outside the actual viscous region.

(c) Summary of calculation procedure.

(1) Estimate pressure field within boundary layers and wake (using a potential flow solution with the rear stagnation point smoothed out by eye and neglecting dp/dn within the shear layer, or otherwise).

(2) Calculate the laminar and turbulent boundary layers up to the start of the trailing edge region in (s,n) coordinates, and change via quartic patches to "wedge flow" coordinates for the flow up to the trailing edge. Retain wedge flow coordinates for the calculation of the shear layer interaction in the wake in the trailing edge region itself, and then change to a single (s,n) system for the downstream part of the wake.

(3) Use the V component velocity at the edges of the shear layers as the inner boundary condition for a new inviscid calculation for the flow outside the shear layer (i.e. outside the matching surface).

(4) Repeat step (2), deducing the pressure within the shear layer from the matching surface pressure derived from the inviscid calculation and the dp/dn in the shear layer obtained in the previous shear layer calculation. Repeat steps (2) and (3) until convergence occurs.

Convergence for an airfoil well below the stall takes no more than 10 iterations: although upstream influence of conditions near the trailing edge (say) can propagate far upstream, most of the propagation occurs via the external flow which - in incompressible flow - is solved "exactly" at each cycle, so that the number of iterations required is far smaller than the number of streamwise steps in the shear layer, in contrast to the usual situation with line relaxation solutions of elliptic

equations. This is one of a number of occasions on which the calculation scheme takes advantage of the fact that most shear layers, although not "thin" according to the traditional requirements of the thin shear layer approximation, are at least "fairly thin".

2.2 Compressible flow

The compressible flow program is described, and results including shock waves without separation are presented, by Chen (7). The basic scheme for attached flow is the same as in incompressible flow, except that the surface singularity method for the external flow is replaced by the field method necessary to solve the non linear equations of inviscid compressible flow. All the programs are written with separate overlays for the different parts of the calculation, communicating only via disc files, so that it is very easy to replace - say - the inviscid flow routine. We have therefore used a rather old code which happened to be conveniently available to us (8), and we have not yet tried to optimise the number of inviscid routine iterations executed per cycle of the whole matching program.

The alterations to the shear layer routines amount to a merging of the elliptic incompressible flow program and the incompressible thin shear layer program described in (4) but now extensively modernized; thus the development of a compressible flow program including the dp/dy calculation was relatively straightforward. (As mentioned above, the wake program available at the start of work on the compressible problem was inefficiently coded so, as an interim measure, compressibility effects were allowed for only approximately.) In transonic flow, pressure gradients in the x and y directions tend to be larger than in low speed flow, and in the early stages of convergence of the calculation scheme the streamwise position of regions of large dp/dy - e.g. below shock waves - may change considerably from one iteration to the next, leading to instability. (This has nothing to do with a change of type of the equations at a sonic line.) Iteration of the V and p solution has been inserted at each streamwise step, and the newly calculated pressure values are used as soon as available in the evaluation of dp/dx within the shear layer. Thus dp/dx is first obtained as the difference between a newly calculated value at x and the value from the previous sweep at $x+dx$: the value of p at $x+dx$ is then updated and dp/dx recalculated. We originally avoided this "Gauss Seidel" strategy because we thought it likely to lead to instability, but it appears to have no ill effects, whatever the sign of the pressure change from one sweep to the next. Typical results for attached flow are given in Fig. 6.

In and near separation regions, an inverse boundary layer method is used, with the "Box" algorithm. At present Carter's correction formula is used, with the true displacement thickness (undefinable from the velocity profile if dp/dy is appreciable) replaced by an arbitrary but self consistent integral of the velocity defect up to the matching surface; since the scheme is required merely to indicate the change in external flow velocity needed to reduce the error in shear layer displacement, any reasonable representation of the displacement effect will do although convergence may not be optimal. Further details of the

compressible flow calculation method for the "inverse" case are given by Chen (9) and sample results are given in Fig. (7).

3. Multi-element airfoils

3.1 General approach

The general approach to the multi element airfoil problem in incompressible flow is similar to that for the single airfoil, i.e. the flow field is split into viscous and inviscid regions with the viscous flow calculated by a finite difference "field" method and the inviscid flow by a boundary integral method: however in agreement with the general strategy of matching the viscous and inviscid regions at the edge of the shear layer, the inviscid calculation can be performed outside the simply connected shear layer edge, thus avoiding entirely the multi-body inviscid flow problem which has occupied the minds of previous workers (Fig. 8). However, the wake/boundary layer and wake/wake interactions which can occur, together with the more complicated geometry of the problem, demand a more generalized numerical implementation of the basic scheme.

Matching surface and mesh generation

The initial construction of the "matching surface" (MS) is more difficult in the multi airfoil case since the position of the shear layers is now harder to predict, and it is only when the MS has been defined that a suitable mesh can be constructed for the viscous flow calculation. In order to define a MS that is close to the edge of the shear layers, the MS, and therefore the mesh, is now constructed as part of the shear layer marching procedure. The mesh has to cope with trailing edges and shear layer mergers as well as simple boundary layers so a generalised ($s-n$) curvilinear system has been adopted.

To minimise the number of terms in the governing equations an orthogonal mesh is desirable, but its generation would strictly require the solution of an elliptic system with boundary conditions specified around the whole domain. In terms of the present problem this involves prior knowledge of the complete MS before the mesh can be set up. However, a general orthogonal mesh can be set up by a marching procedure providing the boundaries do not vary too quickly, i.e. providing the ellipticity of the problem is weak. At trailing edges the ellipticity is not weak and parabolization of the problem can lead to mesh crossover. A cure for this is the adoption of a non-orthogonal mesh which can legitimately be constructed by a marching procedure, albeit with the introduction of extra terms into the governing equations.

At trailing edges there is a singularity in the boundary conditions and hence a singularity in the mesh, as discussed above. Another singularity could occur where two shear layers merge; this would not be satisfactory because it would lead to a singularity in the velocity components. Using the mesh shown in Fig. 9(a), or a special case of the same (Fig. 9(b)), avoids this problem by merging the two coordinate systems together smoothly. The cusped mesh may be preferable for potential flow considerations because it eliminates a sudden change in the velocity component normal to the MS.

In addition to the above, the mesh generation scheme features the following:

- (1) Calculation stations are input, rather than being chosen by an internal step limit like CFL
- (2) The MS is a coordinate line
- (3) Metric evaluation is simple
- (4) The centre of a calculation cell is coincident in s- and x-y space. Since the s- mesh is arbitrary this simply means that a mesh node is defined to be at the x-y centre of the surrounding calculation nodes and not vice versa. Note that the x-y computational mesh is rectangular by definition.

Fig.10 summarises the basic scheme and Fig.11 shows its application to a trailing edge.

Non-orthogonality is confined to a small percentage of the domain and does not lead to a large increase in computing time: evaluations of metric coefficients can be bypassed when not required. After the first sweep of the viscous calculation it would be possible to construct an orthogonal mesh throughout, but this would be time-consuming and the lack of control over mesh spacing would probably lead to an unsatisfactory node distribution around trailing edges.

For every calculation cell, the nodes available are as shown in Fig.12. Centering on O, the metrics and their first derivatives with respect to s and η (and therefore the Christoffel symbols) can be determined easily from this arrangement, particularly since the increments in s and η are defined to be unity.

3.2 Viscous flow solution

The governing equations to be solved are:

Continuity: $\partial_i u^i = 0$

TKE: $u^k (\partial_i \bar{u}^i)_{,k} = g_{ij} \partial_j u^i - \frac{p' u^k}{\rho} + i q^2 u^k \}_{,k} - \epsilon$

Momentum: $(u^i u^j)_{,j} = - g^{ij} \frac{p'_{,j}}{\rho} - i j_{,j} + \text{viscous terms}$

Subject to the following boundary conditions:

$U = V = 0$ at a solid wall
 $U = U_e$ at a free stream edge
 $U^* = (1/K) \ln y^* + C$ at the first mesh point from the surface.

These are expanded, using physical variables and turbulence modeling similar to the single airfoil program. Since the coordinate system is always aligned roughly in the direction of the mean flow, s-wise turbulent diffusion can still be neglected. The resulting equations are solved, in primitive variable form, using the "Box" method. In order to eliminate numerical "wiggles" the V-nodes are staggered half a mesh width in the s direction with respect to the U- and η -nodes.

The superposition approach to modeling interaction regions is implemented by the simultaneous solution

of s-momentum, continuity and two TKE equations, leading to 4x4 blocks in the block tri-diagonal formulation. Subsidiary equations (e.g. turbulence length scale) can be solved within the Newton iteration loop without resorting to larger blocks providing convergence is not adversely affected. The extra terms introduced into the coefficients by non-orthogonality are by-passed if the mesh is orthogonal and similarly the extra algebra involved in the 4x4 formulation is by-passed if there is no interaction. In this way, although the code is written for any number of interacting shear layers, a simple boundary layer can still be computed with very few redundant operations.

The static pressure variation through the shear layer is obtained by integrating the η -momentum equation using the converged values of velocity and shear stress. Because of the position of the v-nodes, the integration is centered half a step behind the main calculation: this also produces values of pressure in the required positions for the next sweep, so no interpolation is necessary.

3.3 Inviscid flow solution and matching

The static pressure array is initialised by a Smith and Hess inviscid calculation applied to the multi-airfoil configuration using solid body boundary conditions. Then, after one sweep of the viscous calculation, the complete MS and the velocities normal to it are available. These boundary conditions are fed into the inviscid calculation and a "direct" iterative procedure as used in the single body case continues to convergence. The MS is not altered after the first sweep unless the position of the shear layers changes significantly, so neither the influence matrix nor the metrics of the mesh need to be re-computed.

The calculation nodes which define the discretised MS are also taken to define the linear "panels" of the inviscid calculation (Fig.13). Because the box scheme enables arbitrary step lengths to be taken, a satisfactory distribution of the viscous calculation stations gives a satisfactory distribution of panels with very simple matching of the two regimes. The matching is also accurate because the centres of the panels coincide with the positions of second order accurate viscous quantities.

3.4 Current status

At the present time a single airfoil is being used for preliminary tests on the code. The mesh generation scheme appears to have no difficulty tracking the development of the shear layers, and the boundary layer results agree with those obtained from the single airfoil program. Runs will begin shortly with flapped airfoil geometry; these will reveal any difficulties in predicting wake/boundary layer interaction and may prove to be a severe test for the inviscid code.

Conclusions

Further developments of the viscous inviscid matching scheme introduced by Mahgoub and Braunschweig have been presented. It is shown that combination, in the same iteration cycle, of an inviscid flow calculation and one sweep of a "line

relaxation" solution of elliptic equations for the shear layer, yields an efficient way of overcoming the deficiencies of the thin shear layer approximation without going to a full Navier Stokes solution with storage of all variables in part or all of the flow field. Complete airfoil calculations have been performed in incompressible flow and in compressible flow with shock waves strong enough to cause limited regions of separation (although turbulence modeling for the separated region is not yet satisfactory). Extension to three dimensional flow and to multi element airfoils is in hand, and it is hoped that the ability to perform inexpensive calculations for some of the complex shear layers measured by the authors' past and present associates will lead, by trial, error and inspiration, to improvements in turbulence modeling.

References

1. Mangoub, H.E.H. and Bradshaw, P., "Calculation of turbulent inviscid flow interactions with large normal pressure gradients", AIAA J., Vol. 17, 1979, p. 1025.
2. Cebeci, T. and Stewartson, K., see "Engineering Calculation Methods for Turbulent Flow" by P. Bradshaw, T. Cebeci and J.H. Whitelaw, Academic Press, London, 1981.
3. Bradshaw, P., Dean, R.B. and McEligot, D.M., "Calculation of interacting turbulent shear layers. Duct flow", J. Fluids Engg, Vol. 95, 1973, p. 214.
4. Bradshaw, P., Ferriss, D.H. and Atwell, N.P., "Calculation of boundary layer development using the turbulent energy equation", J. Fluid Mech. Vol. 28, 1967, p. 593.
5. Morel, T. and Torda, T.P., "Calculation of free turbulent mixing by the interaction approach", AIAA J., Vol. 12, 1974, p. 533.
6. Weir, A.D., Wood, D.H. and Bradshaw, P., "Interacting turbulent shear layers in a plane jet", J. Fluid Mech., Vol. 107, 1981, p. 237.
7. Chen, Z.B. and Bradshaw, P., "Calculations of viscous transonic flow over aerofoils", AIAA-82-0997, 1982.
8. Jameson, A., "Numerical computation of transonic flows with shock waves", Symposium Transonicum, II, p. 384.
9. Chen, Z.B., "Calculations of transonic viscous flows over aerofoils", Ph. D. thesis, Imperial College, London, 1982.

Acknowledgements

We are grateful to Drs Z.B. Chen, I. Kullar and H.E. Mangoub for their help and to MoD(PE) for support.

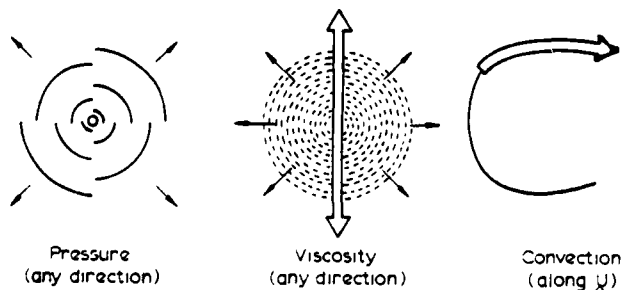


Fig. 1 Transport of information

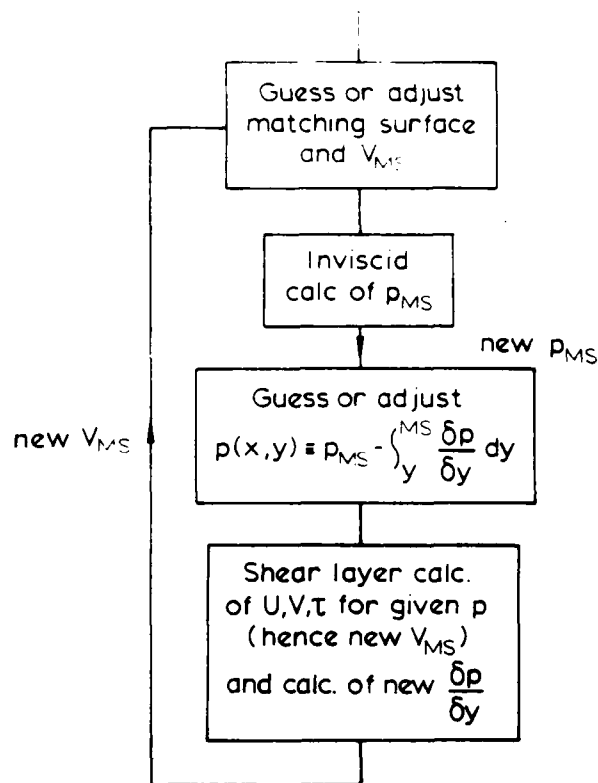


Fig. 2 Flow chart of matching process

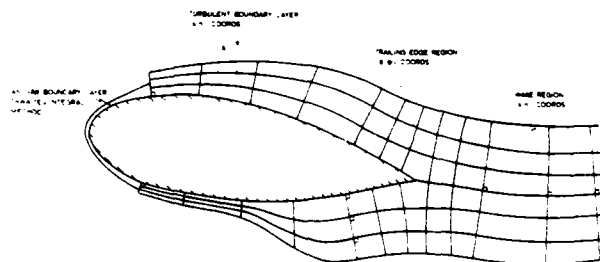


Fig. 3 Shear layer coordinates (vertical scale enlarged).

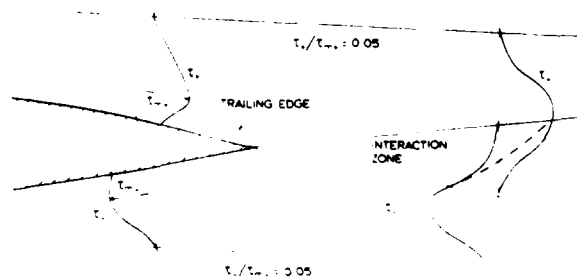


Fig. 4 Shear layer superposition in wake

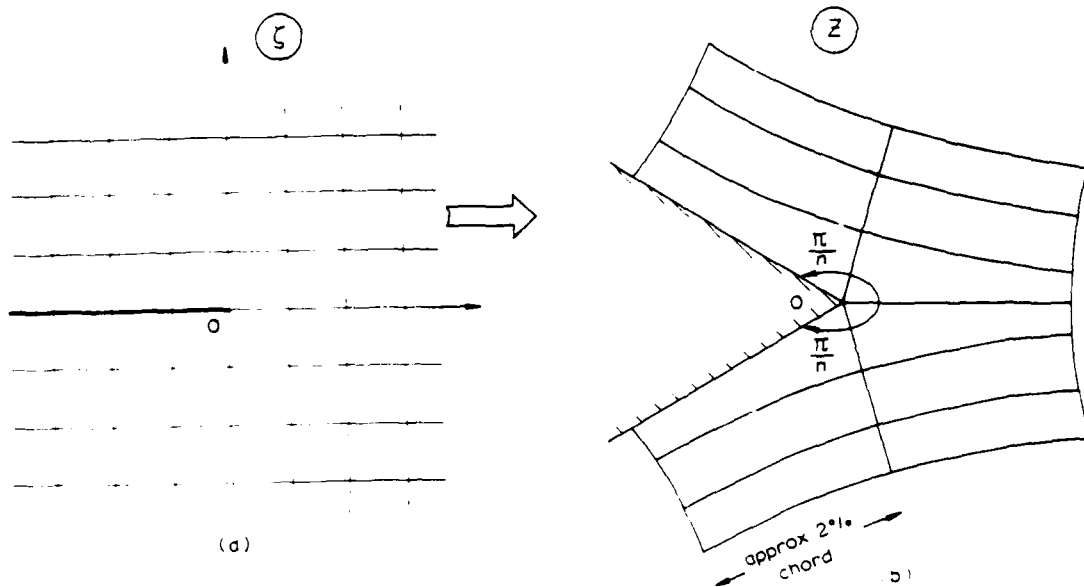


Fig. 5 Trailing edge transformation

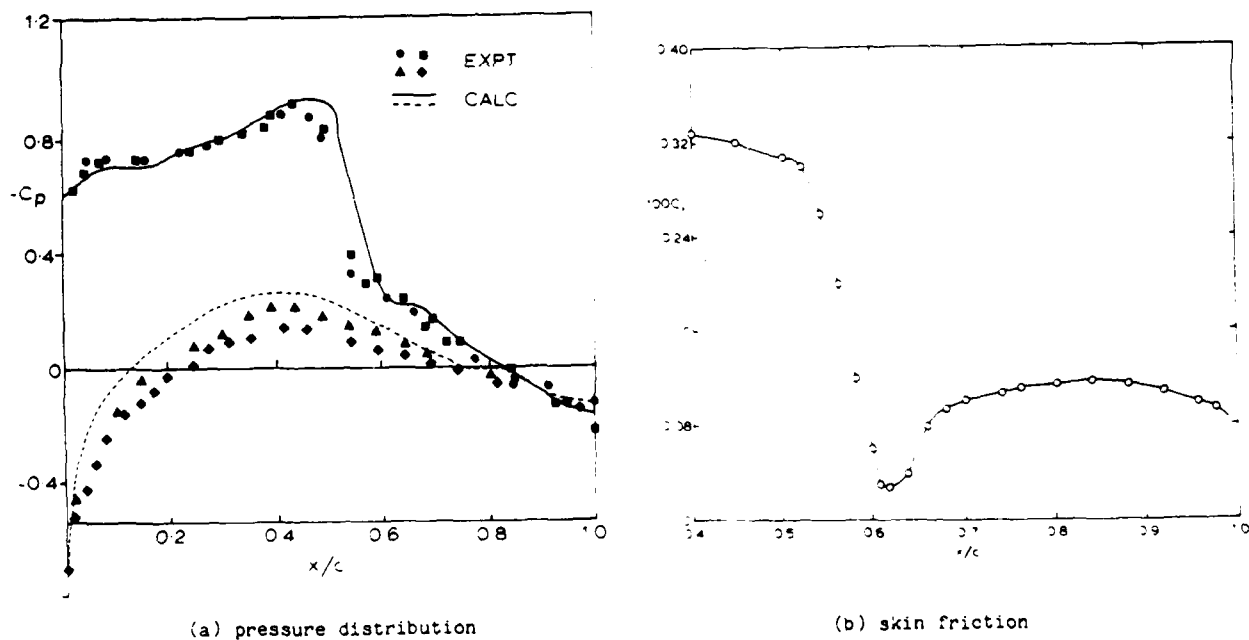
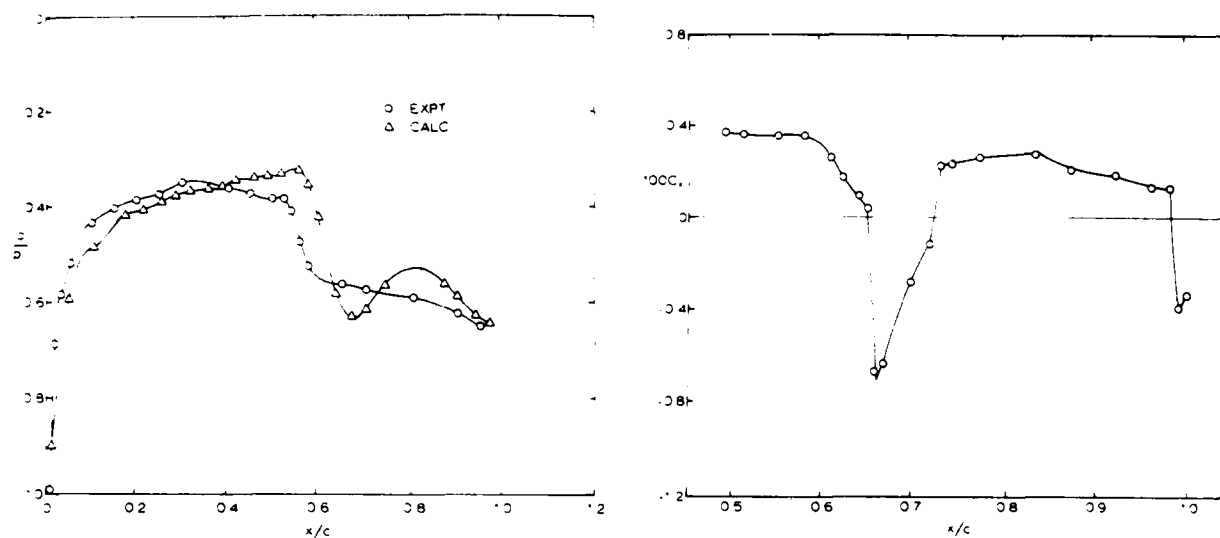


Fig. 6 Results for NACA 64A010, $M=0.8$, $Re=2$



(a) pressure distribution

(b) skin friction

Fig. 7 Results for NACA 0012, $M=0.864$, $z=0$

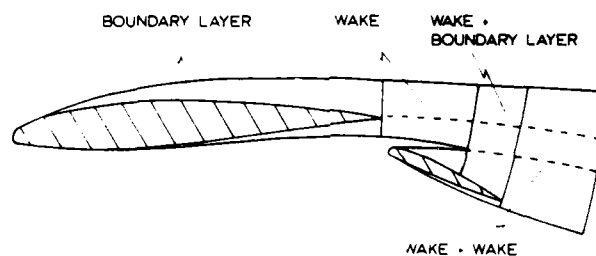
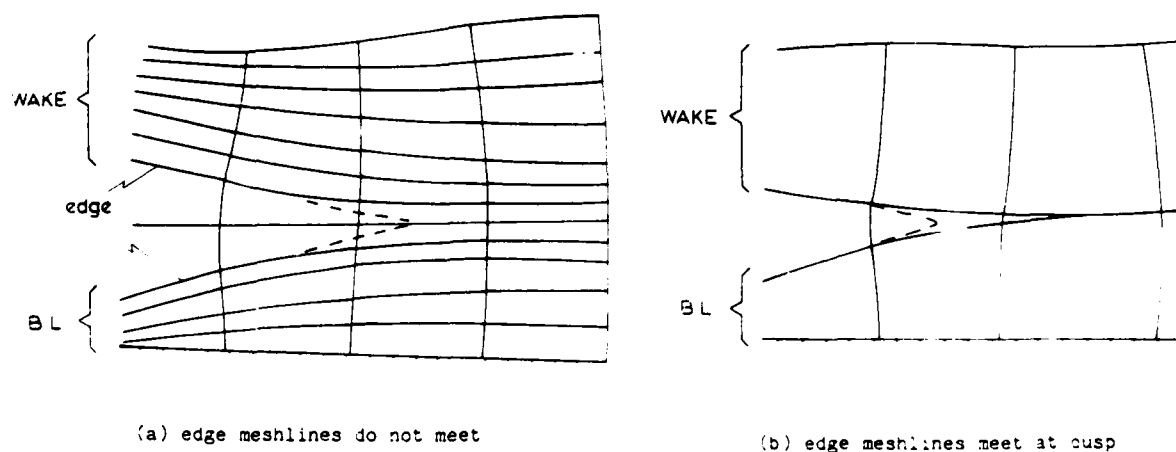


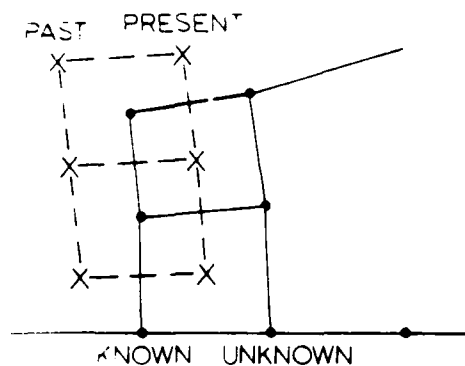
Fig. 8 Airfoil with flap



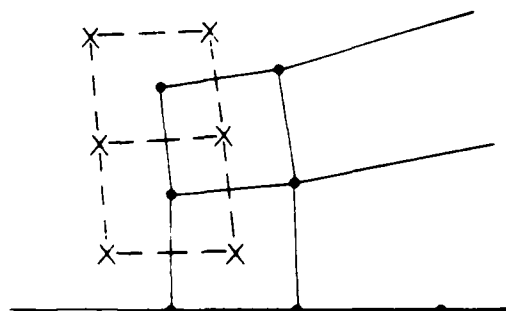
(a) edge meshlines do not meet

(b) edge meshlines meet at cusp

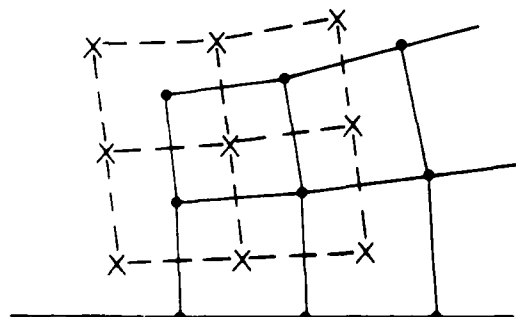
Fig. 9 Avoidance of meshline singularity
in merging shear layers



(i) From edge values at known station, compute $d\psi/ds$ and construct next step of MS



(ii) Set up ψ -constant lines from surface or LMS to UMS



• CALCULATION NODE

X MESH NODE

(iii) Set up orthogonal s -constant line at downstream station checking mesh spacing to avoid cross-over. If spacing is unsatisfactory introduce non-orthogonality and continue up to the UMS.

Fig. 10 Non-orthogonal mesh generation

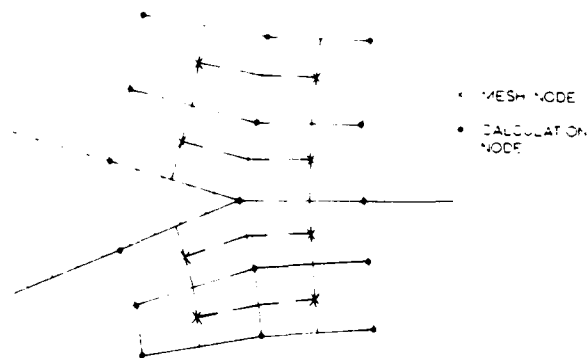


Fig. 11 Non-orthogonal mesh near trailing edge.

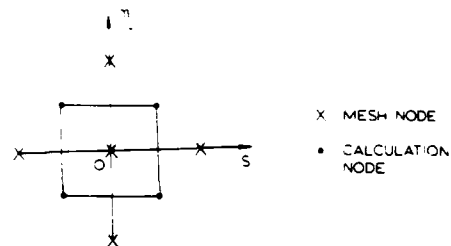
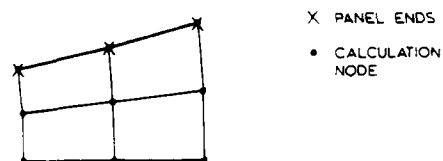


Fig. 12 Centering of calculation node.



X PANEL ENDS

• CALCULATION NODE

Fig. 13 Definition of panels for calculation of inviscid external flow.

A COMPARISON BETWEEN THE PREDICTED AND EXPERIMENTAL
CHARACTERISTICS OF A NACA 64₃-418 AEROFOIL AT LOW
REYNOLDS NUMBERS.

P.M.RENDER and J.L.STOLLERY
CRANFIELD INSTITUTE OF TECHNOLOGY
CRANFIELD, BEDFORD, ENGLAND.

Notation

A	aspect ratio
c	chord
C_D	drag coefficient
C_{D_0}	zero-lift drag-coefficient
C_L	lift coefficient
C_{Lmax}	maximum lift coefficient
C_P	pressure coefficient
$dC_L/d\alpha$	lift curve slope
H_{12}	boundary layer shape factor, $^{1/2}$
H_{12sep}	boundary layer shape factor at separation
H_{12te}	boundary layer shape factor at trailing edge
H_{12}^*	modified boundary layer shape factor for the calculation of section profile drag coefficient.
H_{32}	boundary layer shape factor, $^{3/2}$
K	constant in induced drag equation
R	roughness factor
Re_{δ_2}	Reynolds number based on local conditions and boundary layer momentum thickness
S_{sep}	arc length along which boundary layer is separated
U_∞	freestream velocity
U_{sep}	velocity at separation
U_{te}	velocity at trailing edge
X	chordwise aerofoil co-ordinate
X_{sep}	chordwise position of separation
Y	aerofoil co-ordinate normal to chord
α_0	zero lift incidence
α_c	incidence relative to chord line
γ	slope of trailing edge relative to chord line
δ	trailing edge angle
δ_{us}	slope of aerofoil surface near trailing edge
δ_1	boundary layer displacement thickness
δ_2	boundary layer momentum thickness
δ_{2sep}	boundary layer momentum thickness at separation
δ_{2te}	boundary layer momentum thickness at trailing edge
δ_3	boundary layer energy thickness
$\Delta\alpha$	incidence correction due to separation
ΔC_L	section lift coefficient correction due to separation
δ_{st}	correction of location of stagnation point near trailing edge

Abstract

This paper uses the computer program of Eppler & Somers (5) for low speed aerofoil design to obtain theoretical results for a NACA 64₃-418 aerofoil in the Reynolds number range 3×10^5 to 1×10^6 . These predictions are compared with our recent experimental results. So far the agreement is poor for the lift and drag coefficients. The predicted positions of laminar separation are shown to agree reasonably well with experiment, although the predicted positions of turbulent re-attachment and turbulent separation are in error. The program does have the facility to take account of aerofoil roughness and freestream turbulence. The predicted values appear to underestimate the measured effects of roughness.

The opportunity is also taken to compare the Eppler and Somers predictions with those obtained from the Delft University aerofoil design computer program (6) developed by Van Ingen. There is good agreement between the two programs.

1. Introduction

During recent years there has been considerable interest in the possibility of using Remotely Piloted Vehicles (RPV's) for surveillance and reconnaissance. These RPV's are usually considerably smaller than conventional manned aircraft, and are often required to operate at low speeds. Therefore, the operational Reynolds numbers of RPV's are lower than those associated with conventional manned aircraft. For example, a small general aviation aeroplane will usually cruise at a Reynolds number of about 3×10^6 , whilst many RPV's are required to operate at Reynolds numbers in the range of 1×10^5 to 1×10^6 .

The effects of reducing Reynolds number to such low values have been appreciated for many years. One significant effect is the increase in drag coefficient, C_D , as the Reynolds number is reduced. A typical variation is shown in Fig.1 for a NACA 64₃ - 418 aerofoil. The effects of Reynolds number on the lift curve slope, $dC_L/d\alpha$, and the maximum lift coefficient, C_{Lmax} , are not necessarily so pronounced, but in general terms a decrease in both parameters as the Reynolds number is reduced would be expected. However, combining the effects of Reynolds number on the lift and drag coefficients can

produce significant changes in the lift/drag ratio (Fig. 2.)

The influence of Reynolds number on aerofoil performance necessitates the RPV designer making a careful choice of aerofoil section. Unfortunately, data on aerofoils at low Reynolds numbers is not readily available. Aerofoil catalogues such as Abbott and Von Doenhoff (2) and Althaus (3) don't consider Reynolds numbers below about 3×10^6 , so the designer is forced to seek out reports on the low Reynolds number characteristics for individual aerofoils. However, there is now good reason to doubt the accuracy of much pre-war data (Swan (4)) and most of the limited recent low Reynolds number aerofoil work concerns sailplane-type aerofoils. Generally these advanced sections are more complicated and perhaps more expensive than is desired for RPV manufacture, where the designer is looking for a simple and robust section.

With due regard to the requirements of the RPV designer, a programme is now under way to develop a low-Reynolds-number aerofoil design and analysis method. To date the first of three aerofoil sections suitable for RPV applications has been tested in Cranfield's 8' x 6' low speed wind tunnel. The results are being used to evaluate two existing low speed aerofoil computer programs. One of these, written by Eppler and Somers (5), is available on the Cranfield computing facility. The other program written by Van Ingen (6), is based at Delft University in the Netherlands, but free access to the program has been granted to the authors.

2, The Computer Programs

2.1 Computing Facilities

The computing facilities at Cranfield are presently being extended by installing an additional DEC VAX 11/782 computer. All the work included in this paper has been carried out on the existing DEC VAX 11/780 computer. The VAX runs under the Virtual Memory operating system and can be accessed via terminals sited in individual departments. The present work has been carried out using Fortran 77 and the Gino-F graphics software.

2.2 The Eppler and Somers Program

The low-speed-aerofoil-design computer program written by Eppler and Somers is fully described in Reference 5, and to date no alterations have been made to the program other than those necessary to allow the program to run on the VAX computer. The program has three constituent parts :

- 1) Potential-flow aerofoil design method
- 2) Potential-flow aerofoil analysis method
- 3) Viscous corrections.

To date, the work has concentrated on the last two parts of the program.

The potential flow analysis procedure is a panel method, with the geometry of the panels being determined by a spline fit of the aerofoil co-ordinates. The end points of the panels are those co-ordinates input by the operator into the program. The condition that the inner tangential velocity is zero is satisfied at the end of each panel. Two incidences are analysed and the flow for any other incidence is derived by superposition from these two solutions.

The potential flow analysis is then used to determine the necessary viscous corrections. The method used is an integral method involving the solution of the integral momentum and energy equations.

For the laminar boundary layer some Hartree profiles have been selected as velocity distributions. The numerical integration of the momentum and energy equation yields the momentum and energy thicknesses at each point along the chord, and hence gives a value for the boundary layer shape factor H_{32} . The shape factor is used in determining laminar separation which is assumed to occur when $H_{32} = 1.52$.

Transition is taken to occur when the inequality

$$\ln Re_{\frac{1}{2}} \geq 18.4H_{32} - 21.74 - 0.36R \quad (1)$$

is satisfied. The constants were empirically derived by Eppler (7). A roughness factor $R = 0$ corresponds to natural transition on a smooth surface with no freestream turbulence. A value of $R=4$ represents a rough surface or a turbulent freestream. The value of R only affects the position of transition, it does not affect the boundary layer development.

For the turbulent boundary layer, the empirical expressions of Wieghardt, Ludwig-Tillman and Rotta as modified by Eppler (8) are used. Unlike the laminar boundary layer a single value of H_{32} cannot be used to predict separation. It can only be stated that for $H_{32} > 1.58$ there will be no separation, and for $H_{32} < 1.46$ there will be separation (5). Eppler and Somers argue that their method produces lower values of H_{32} for adverse pressure gradients than most other turbulent boundary layer methods. Therefore their program assumes turbulent separation at $H_{32} = 1.46$.

The Eppler and Somers program makes no attempt to simulate the behaviour of laminar separation bubbles. When laminar separation is predicted before the transition criteria is satisfied, the computation continues by assuming turbulent flow.

Having computed the boundary layer development, the program then modifies the potential flow section characteristics. The drag coefficient is calculated from a modified Squire-Young formula (9) to take account of the high values of the shape factor H_{12} that occur when the flow at the trailing edge is near separation. This empirical modification is :

$$C_D = 2s_{2te} \left(\frac{u_{te}}{u_\infty} \right)^{\frac{5+H_{12}^*}{2}} \quad (2)$$

where $H_{12}^* = H_{12te}$ for $H_{12te} \leq 2.5$
 $= 2.5$ for $H_{12te} > 2.5$.

If boundary layer separation is predicted, no more boundary layer calculations are made, but the momentum thickness, δ_2 , is corrected by :

$$\delta_{2te} = \delta_{2sep} \left(\frac{u_{sep}}{u_{te}} \right)^{\frac{5+H_{12sep}}{2}} \quad (3)$$

The lift and pitching moment coefficients are determined from the potential flow by means of some simple viscous corrections. Without separation the lift-curve slope is assumed to be 2- such that

$$C_L = 2\pi(\alpha_c + \alpha_0) \quad (4)$$

Separation is accounted for by an incidence correction (Fig.3) of the form:

$$\Delta\alpha = \frac{-\delta_{2sep}}{C} (\alpha_{us} + \alpha_c) \quad (5)$$

which is used to correct the lift coefficient by :

$$\Delta C_L = 2\pi\Delta\alpha = -\pi \frac{\delta_{2sep}}{C} (\alpha_{us} + \alpha_c) \quad (6)$$

2.3 The Van Ingen Program

Like the Eppler and Somers program the Van Ingen program uses an integral method to calculate the viscous corrections. The program is under continuous development but recent descriptions are available (6) (10). The program takes the aerofoil co-ordinate input and obtains a Karman-Trefftz type aerofoil (18). The potential flow analysis is then completed using Timman's conformal transformation method (19). For the laminar boundary layer a Thwaites(11) type method is used. This method has been modified by Van Ingen to improve the prediction of separation. Transition is predicted using the e^N method (12), and turbulent boundary layer calculations are carried out using Head's entrainment method (13).

Unlike the Eppler and Somers program, Van Ingen does attempt to simulate laminar

separation bubbles. This simulation is described in references 14 and 15, where the shape of the separation streamline is prescribed. The angle at which the flow leaves the aerofoil surface is determined from an empirical relationship, and a linearly varying shape factor is then used in the separated region. The flow is required to satisfy the momentum integral equation, a wall condition and certain relations which follow from Stewartson's second branch solutions of the Falkner-Skan equations.

In the Van Ingen program the drag coefficient is calculated from the Squire-Young formula without any modification. The lift coefficient is corrected by an empirical relation which attempts to adjust the circulation round the aerofoil by adjusting the position of the rear stagnation point, θ_{st} in the conformal transformation. The present modification for a cambered aerofoil is :

$$\theta_{st} = 5 \tan^{-1} \left(\frac{\alpha_c + \alpha_0}{C_D} \right) \quad (7)$$

2.4 Comparison between the Eppler and Somers, and Van Ingen programs.

The opportunity has been taken to compare the theoretical predictions of the Van Ingen program with those of Eppler and Somers. For this purpose the theoretical co-ordinates of NACA 643-418 were taken from Abbott and Von Doenhoff, along with some extra points in the nose region. These extra points were calculated by transforming the NACA 64-018 thickness envelope into a Karman-Trefftz type aerofoil using the Van Ingen program. The program gives the x and y co-ordinates of the transformed aerofoil at 101 points. These co-ordinates were taken for the first ten per cent of the chord, and using the appropriate camber line further NACA 643-418 co-ordinates were calculated. The resulting total of seventy x,y co-ordinate pairs were used as the input for both the Van Ingen and the Eppler and Somers programs.

The results obtained from the two programs are shown in Figs. 4 - 7. The two Reynolds numbers correspond to the highest and lowest Reynolds numbers obtained in the wind tunnel program. It should also be noted that the results plotted in Figs. 6 and 7 have been corrected for the effective aspect ratio as measured in the experimental work. This is further described in the following section.

The Van Ingen program allows a variable turbulence level input, and the results shown have been computed using a turbulence level of 0.13 which is similar to the level measured in the wind tunnel. The maximum lift coefficient is not calculated directly by the Van Ingen program, but following the suggestion of Riegels (16)

C_{Lmax} is taken to occur when the point of turbulent separation reaches 90° of the chord (from the leading edge).

With the exception of C_{Lmax} and the incidence at which it occurs it is interesting that, in spite of the differences in approach and the more complete boundary layer analysis of the Van Ingen method, the two programs agree so closely.

3. Wind Tunnel Tests

The experimental data used to evaluate the computer programs were obtained using Cranfield's 8' x 6' low speed wind tunnel. The experimental arrangement is shown in Fig.8. An almost full span NACA 643-418 section wing of 0.343m (13.5ins) chord is mounted vertically from the six-component balance above the tunnel. The span of the model is 1.816m (71.5"). The difference between the span of the wing and the 1.828m (6') height of the tunnel is accounted for by the reflection plate at the tunnel roof, and a small gap (approx.3mm) at the tunnel floor. This gap is necessary to permit balance measurements.

It is recognised that this small gap will mean that the test arrangement will not permit two-dimensional conditions to be attained. However, an estimate of the effective aspect ratio can be made. The bottom 0.293m (11.5") of the wing is removable to give a known finite aspect ratio. Knowing the induced drag equation :

$$C_D = C_{D0} + \frac{K}{\pi A} C_L^2 \quad (8)$$

and the aspect ratio, it is possible to calculate the value of K. Assuming this value also applies for the higher aspect ratio case it is possible to determine the effective aspect ratio. The effective aspect ratio was found to be approximately 38 over the Reynolds number range tested.

All force and moment measurements were made using the balance. Pressure tappings were located at the mid-span of the wing, and the pressure measurements were made by two scanivalves controlled by a Commodore PET microcomputer. The profile of the model and the positions of the pressure tappings are shown in Fig.9.

4. Comparison between theory and experiment

Before testing commenced, the co-ordinates of the model were accurately determined, as were the positions of all the pressure tappings. Except where stated, the measured model co-ordinates were used as input to the Eppler and Somers program. Using the model co-ordinates rather than theoretical co-ordinates for the computer program input, resulted in a slight change in the predicted characteristics of the aerofoil. The largest change occurred

at the lowest Reynolds number i.e. 3×10^5 . This change is illustrated in Fig.10. In addition, all the computations have been carried out using a value of $R = 2$ (equation 1) unless otherwise stated.

As the change in the predicted results brought about by using the model co-ordinates is slight it is acceptable and convenient to plot some of the experimental results on the figures already used to compare the Eppler and Somers program with Van Ingen's. A comparison of the C_L - α curves for the highest and lowest Reynolds numbers are shown in Figs.4 & 5.

For the Eppler and Somers program the predicted C_{Lmax} for both Reynolds numbers is greater than those achieved experimentally. This program also predicts a noticeable change in C_{Lmax} as the Reynolds number is decreased. Such a significant variation was not apparent in the experiments. It can also be seen that the predicted lift-curve slopes are lower than those derived experimentally, and there are obvious differences in the predicted zero lift angles. The "kink" in the predicted curves is connected with the rapid forward movement of transition for a small increase in incidence. No such kink was noticed during the experiments. For both Reynolds numbers the C_{Lmax} predicted by the Van Ingen program agrees closely with the experimental results but occurs at a lower incidence. There is also good agreement between the lift curve slope predicted by the program and those derived experimentally. However there is an obvious difference on the zero lift angle.

The lift-drag polars for the same Reynolds numbers are shown in Figs.6 & 7.

The theoretical curves shown in these figures have been corrected from the two-dimensional case to the experimental aspect ratios by adding the induced drag term :

$$\frac{K}{\pi A} C_L^2$$

For the results shown the aspect ratios were 38.4 for the lowest Reynolds number and 37.5 for the highest. The programs predict the right trend in C_D ; i.e. increasing C_D with decreasing Reynolds number, but the predicted increases are significantly less than was achieved experimentally. At the lowest Reynolds number the predicted C_D 's are substantially lower at low C_L 's than the experimental results. At higher C_L 's the C_D 's predicted by the Eppler and Somers program increase more rapidly than was found in the wind tunnel experiments. At a Reynolds number of 1×10^6 the errors in the low C_D region are not as pronounced as for the lower Reynolds number. However, in percentage terms the errors can be significant.

The version of Eppler and Somers' program being used for the present work does not modify pressure distributions

for viscous effects. However, it can be instructive to compare measured pressure distributions with those derived from potential theory. Figs. 11a and 11b compare the measured pressure distributions at a Reynolds number of 3.1×10^5 with potential theory, for incidences of 4° and 8° respectively. Even at this low Reynolds number the shape of the measured pressure distribution follows closely the shape of the potential distribution. If an allowance is made for the difference in the predicted zero lift angle shown in Fig. 5 by reducing the theoretical incidence, an even closer agreement between the two sets of distributions can be achieved (Figs. 12a & b).

Pressure distributions were measured throughout the entire Reynolds number range. Two typical sets of pressure distributions for Reynolds numbers of 3.1×10^5 and 8.9×10^5 are shown in Figs. 13 and 14. Any program that takes account of viscous effects on pressure distributions would be expected to simulate the separated regions which are apparent from the experimental results.

Flow visualisation tests using titanium oxide paste, were used to determine separation and re-attachment positions. These tests served to verify that the flow over a large part of the span was two-dimensional. At the lowest Reynolds number laminar separation bubbles were present on both surfaces over a large part of the incidence range. A comparison of the predicted and experimental positions of laminar separation on the upper surface is shown in Fig. 15. There is reasonable agreement between the two sets of results. This is not the case for the predicted and measured positions of turbulent re-attachment which are shown on Fig. 15. The program does not give the position of turbulent re-attachment, but Eppler and Somers suggest that a laminar separation bubble would be expected to exist to at least $H_{32} = 1.58$. For Fig. 15 re-attachment has been assumed at $H_{32} = 1.58$.

The predicted and measured positions of turbulent separation are shown in Fig. 16. Beyond 6° and up until the aerofoil stalls the agreement between theory and experiment is disappointing.

The Eppler and Somers program does attempt to take some account of roughness and freestream turbulence in the transition criteria (equation 1). The effect of varying R between 0 and 4 at a Reynolds number of 3×10^5 is shown in Fig. 17. Again these results have been corrected to an aspect ratio of 38.4 to permit comparison with the experimental results shown in Fig. 17. The experiments were made with a $0.015''$ (0.381mm) transition wire placed at 2.5% chord on both the upper and lower surfaces. As with the smooth aerofoil the agreement is disappointing.

5. Discussion of results.

The comparison between the predicted results of the Eppler and Somers program and experiment for the force coefficients has proved to be poor. This was not altogether unexpected because prior to the wind tunnel tests the program was evaluated for a number of different aerofoils using experimental data from a number of sources. In all but a few cases the results proved to be disappointing. The Eppler and Somers program corrects the lift coefficient for viscous effects by means of an incidence correction which is determined by the extent of separated flow on the aerofoil (Fig. 3). However Fig. 16 shows that the program is inaccurate in predicting the position of turbulent separation. This inaccuracy may be completely responsible for the failure of the program to predict the viscous effects on the lift coefficient. When the program can be modified to accurately predict the position of turbulent separation, it will be possible to evaluate the viscous correction to the lift coefficient. From the experimental results for the lift curve slope it is clear that the assumption made by the Eppler and Somers program, concerning the potential flow thickness effects being offset by the boundary layer displacement effects, is unfounded. This assumption results in the lift curve slope being reduced to 2π but, as can be seen from Figs. 4 and 5 this is less than the experimentally derived values.

Adding the displacement thickness to the aerofoil surface, calculating a new pressure distribution and hence boundary layer development, and repeating the process until a solution is reached, is often suggested as a likely method to take account of viscous effects. However, these effects as described by Van Dyke (17) are of second order, and it is necessary to include other second order effects; e.g. pressure gradient normal to the surface within the boundary layer.

It would probably be more profitable to consider and improve the existing boundary layer development routines. To date, the investigation has shown that laminar separation can be predicted with a reasonable degree of accuracy (Fig. 15). However, this is not the case for turbulent re-attachment and separation. Until the re-attachment criteria can be accurately determined, the starting conditions for the turbulent boundary layer will always be in error. Consequently all subsequent calculations for the turbulent boundary layer will be open to question, and it is not surprising that the position of turbulent separation is poorly predicted.

Acknowledgement

This research has been funded by the Ministry of Defence through the Royal Aircraft Establishment, Farnborough and monitored enthusiastically by Dr.P.D.Smith.

References

1. Loftin, L.K. Smith H.A. Aerodynamic characteristics of 15 NACA airfoil sections at seven Reynolds numbers from 0.7×10^6 to 9×10^6 NACA TN1945. 1949
2. Abbott, I.H. Von Doenhoff, A.E. Theory of wing sections, Dover. 1959.
3. Althaus D, Wortmann F.X. Stuttgarter Profilkatalog. Vieweg, 1981.
4. Swan, P. The Aerodynamics of small RPV's 3rd Bristol International RPV Conf. 1982.
5. Eppler R, Somers D.M. A computer program for the design and analysis of low speed airfoils. NASA TM80210, 1980.
6. Van Ingen, J.L. Advanced computer technology in aerodynamics. A program for airfoil section design utilizing computer graphics. AGARD LS-37, 1970.
7. Eppler, R. (Francesca Neffgen Translation) Laminar airfoils for Reynolds numbers greater than 4×10^6 . B-819-35, 1969.
8. Eppler, R. Practical calculation of laminar and turbulent bleed-off boundary layers. NASA TM75328, 1978.
9. Squire H.B. Young A.D. The calculation of the profile drag of aerofoils. ARC R & M 1838, 1938.
10. Van Ingen J.L. Boermans, L.M.M. Blom, J.J.H. Low speed airfoil section research at Delft University of Technology ICAS-80-10 1980.
11. Thwaites, B. Approximate calculation of the laminar boundary layer. Aeronautical Quarterly Vol.1 1949.
12. Van Ingen, J.L. A suggested semi-empirical method for the calculation of the boundary layer transition region. Delft University of Technology, Dept. of Aerospace Eng. Report VTH-74, 1956.
13. Head, M.R. Entrainment in the turbulent boundary layer. R & M. 3152, 1958.
14. Van Ingen, J.L. On the calculation of laminar separation bubbles in two-dimensional incompressible flow. AGARD CP-168, 1975.
15. Dobbinga, E. Van Ingen J.L. Kooi, J.W. Some research on two dimensional laminar separation. AGARD CP-102, 1972.

16. Riegels, F.W. Aerofoil Sections. Butterworths, 1961.
17. Van Dyke, M. Perturbation methods in fluid mechanics. Academic Press 1964.
18. Clancy, L.J. Aerodynamics, Pitman, 1975.
19. Timman, R. The direct and inverse problem of airfoil theory. A method to obtain numerical solutions NLL Amsterdam Report Fl6, 1951.

Authors' Note

The views expressed in this paper are those of the authors and do not necessarily represent those of the Royal Aircraft Establishment.

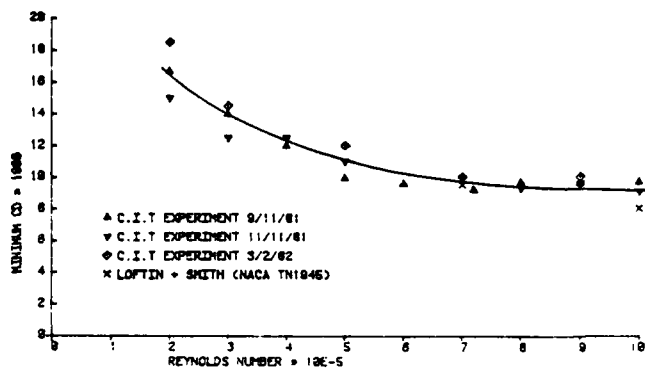


FIGURE 1

Variation of minimum drag coefficient with Reynolds number for NACA 64₃-418.

FIGURE 2

Lift/drag ratios at three Reynolds numbers for NACA 64₃-418.

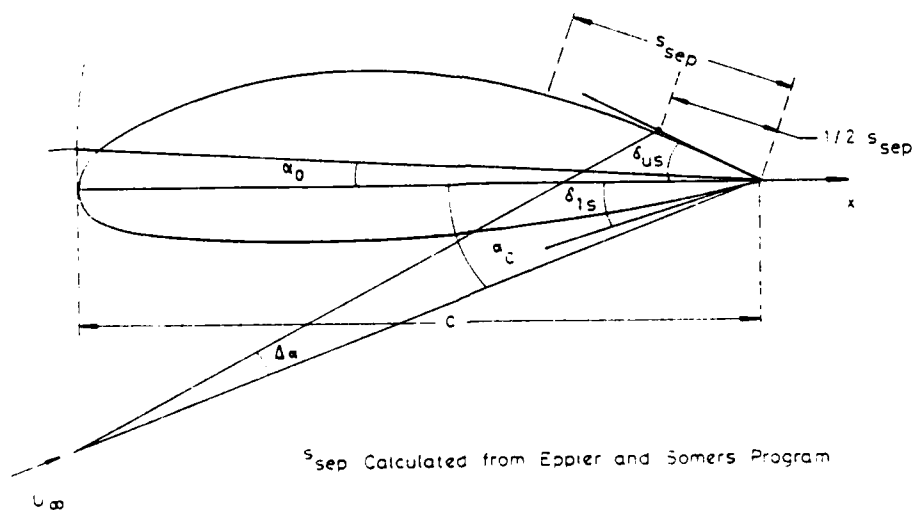
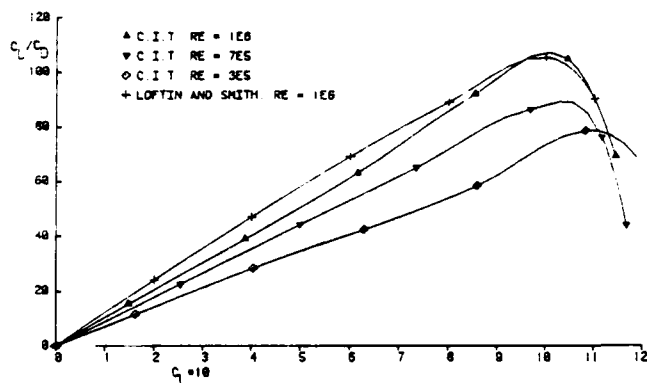


FIGURE 3

Incidence correction due to separation used by the Eppler & Somers computer program.

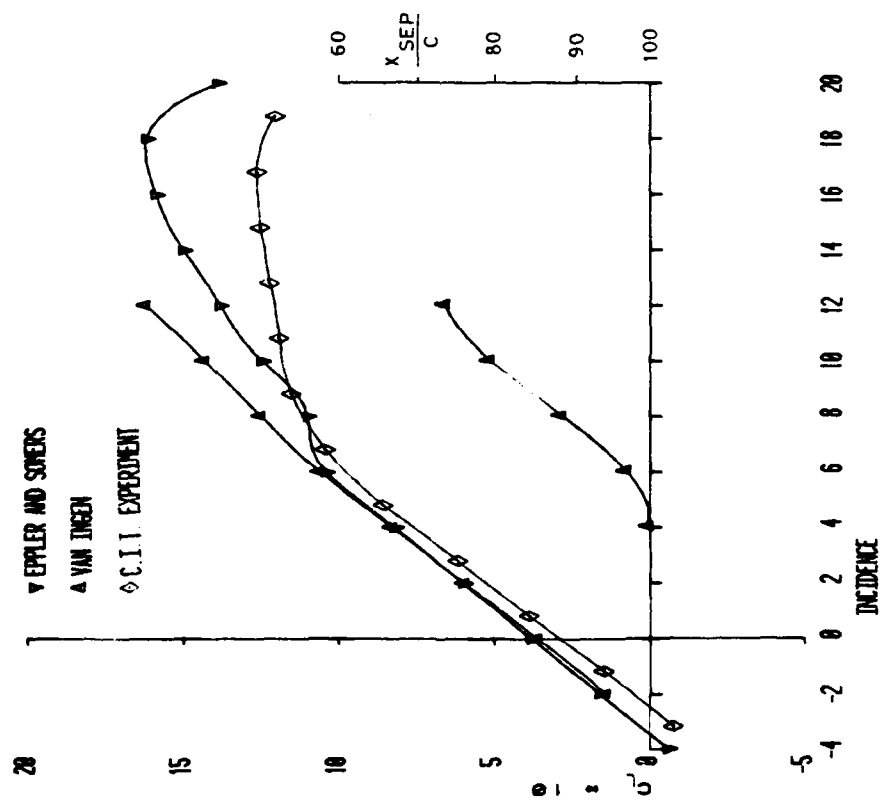


FIGURE 4
Theoretical and experimental $C_L - \alpha$ plots.
Reynolds number = 1×10^6

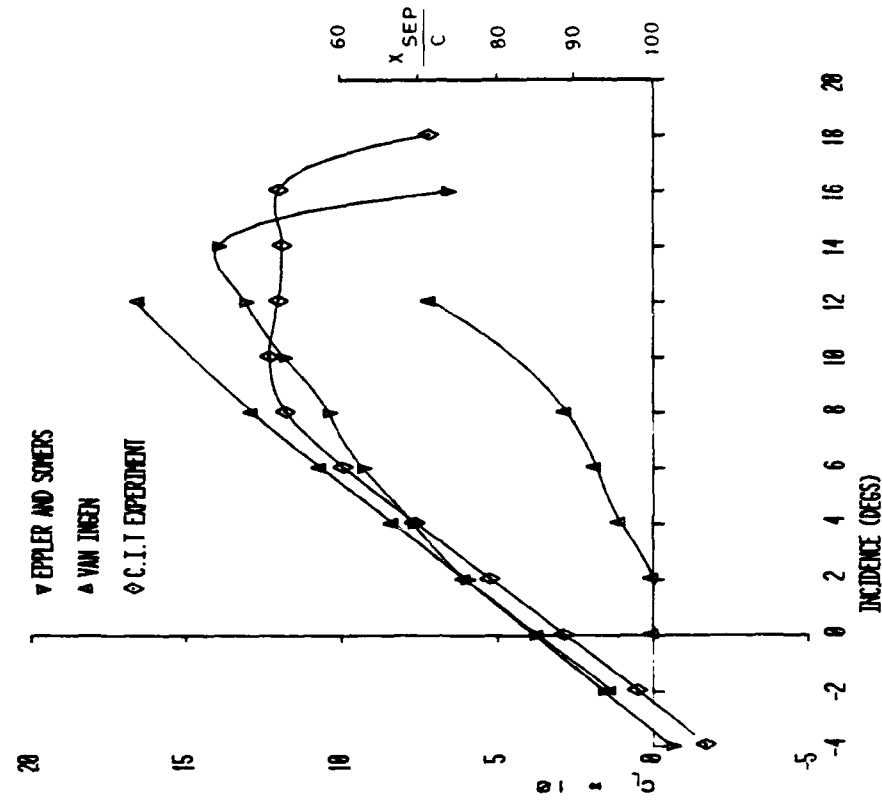


FIGURE 5
Theoretical and experimental $C_L - \alpha$ plots.
Reynolds number = 3×10^5

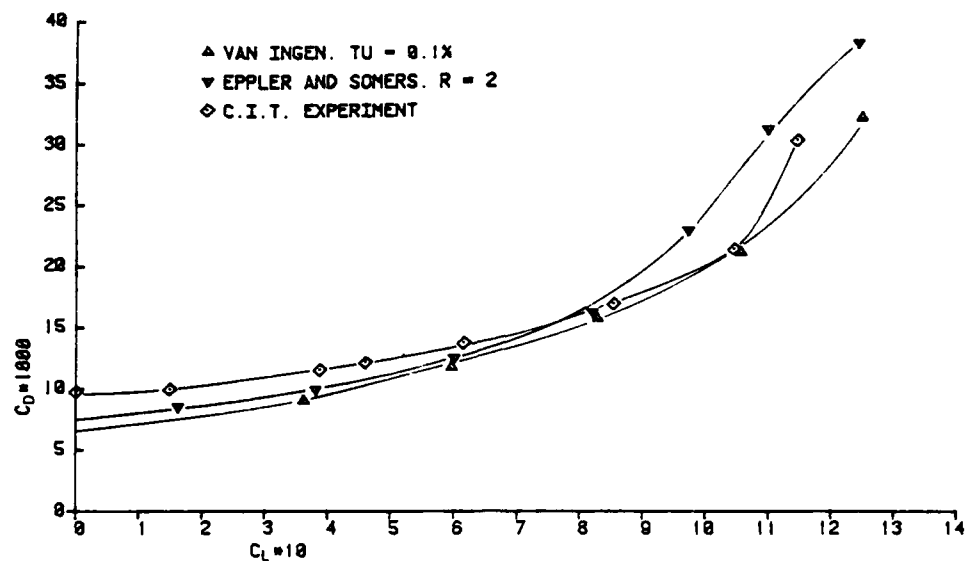


FIGURE 6

Theoretical and experimental $C_D - C_L$ plots.
Reynolds number = 1×10^6 .
Aspect ratio = 37.5

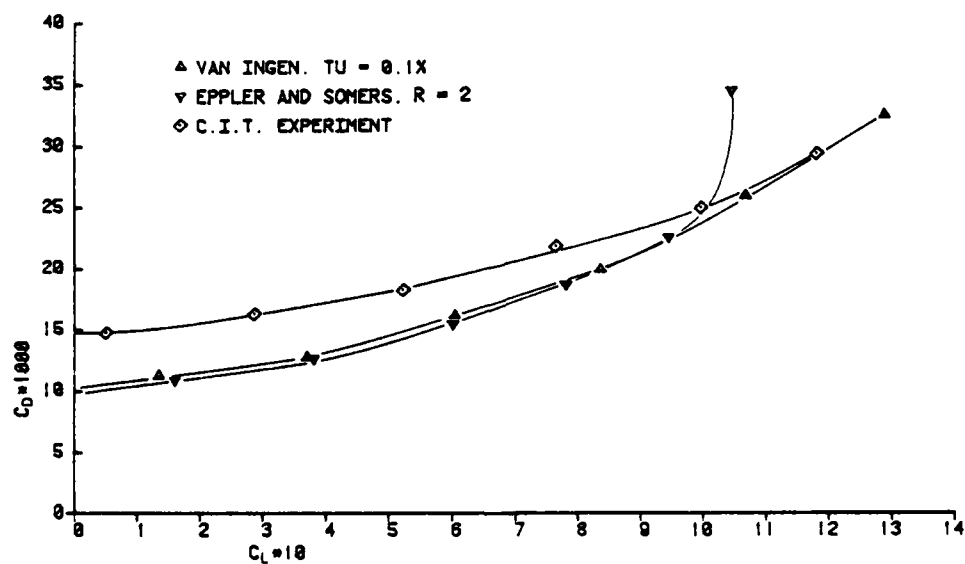


FIGURE 7

Theoretical and experimental $C_D - C_L$ plots.
Reynolds number = 3×10^5
Aspect ratio = 38.4

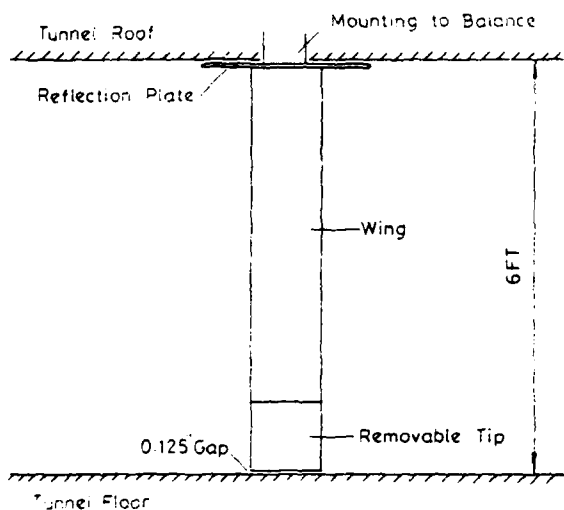


FIGURE 8

Experimental arrangement in 8' x 6' low speed wind tunnel

CHORDWISE POSITION OF PRESSURE TAPPINGS SHOWN BY DOTS

FIGURE 9

NACA 643 - 418 model profile

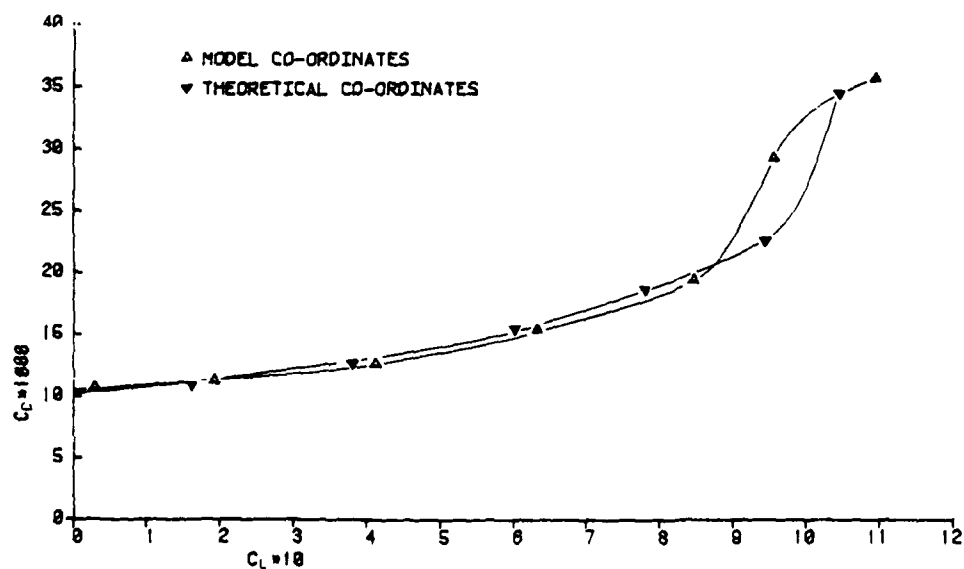
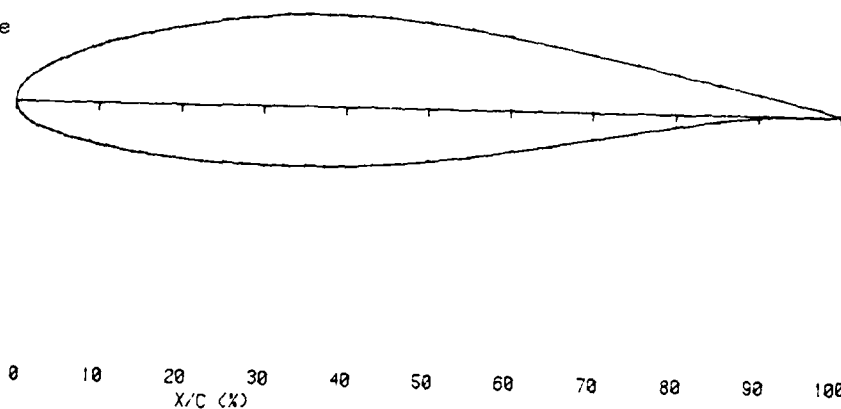
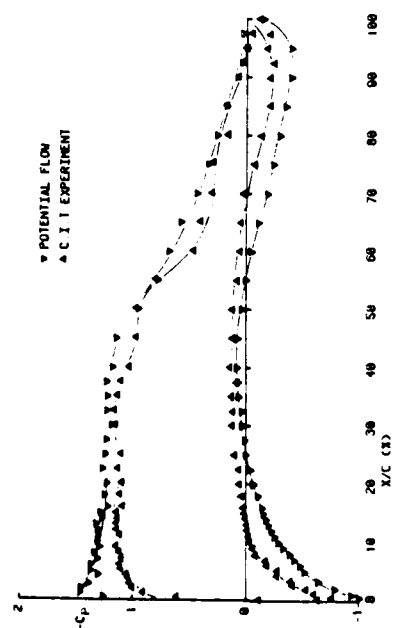
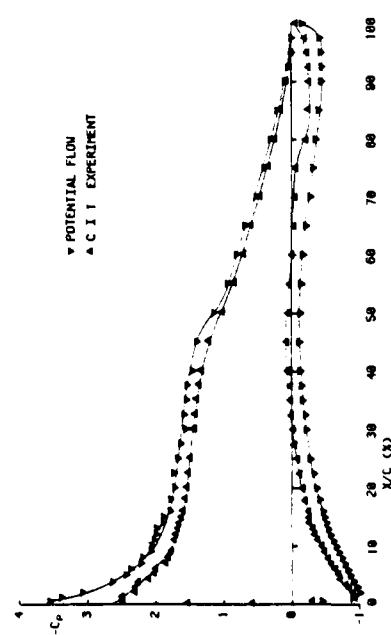


FIGURE 10

Predicted results from Eppler & Somers' program for model and theoretical co-ordinates. Reynolds number = 3×10^5 Aspect ratio = 38.4



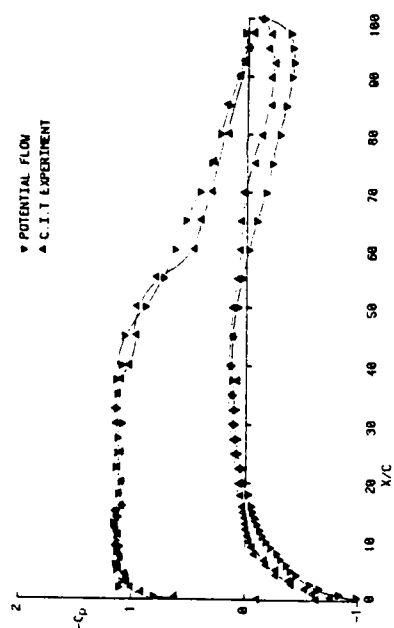
a) $\alpha = 4^\circ$



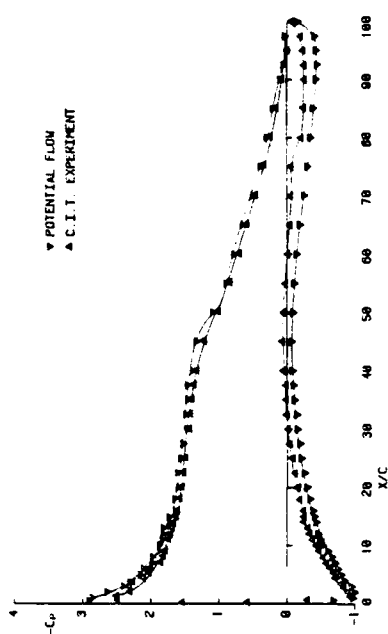
b) $\alpha = 8^\circ$

FIGURE 11

Comparisons between potential flow pressure distributions, and experimental pressure distributions measured at Reynolds number = 3.1×10^5



a) $\alpha = 4^\circ$



b) $\alpha = 8^\circ$

FIGURE 12

Comparisons between potential flow pressure distributions corrected for difference between predicted and experimental zero lift incidence and experimental pressure distributions measured at Reynolds number = 3×10^5 .

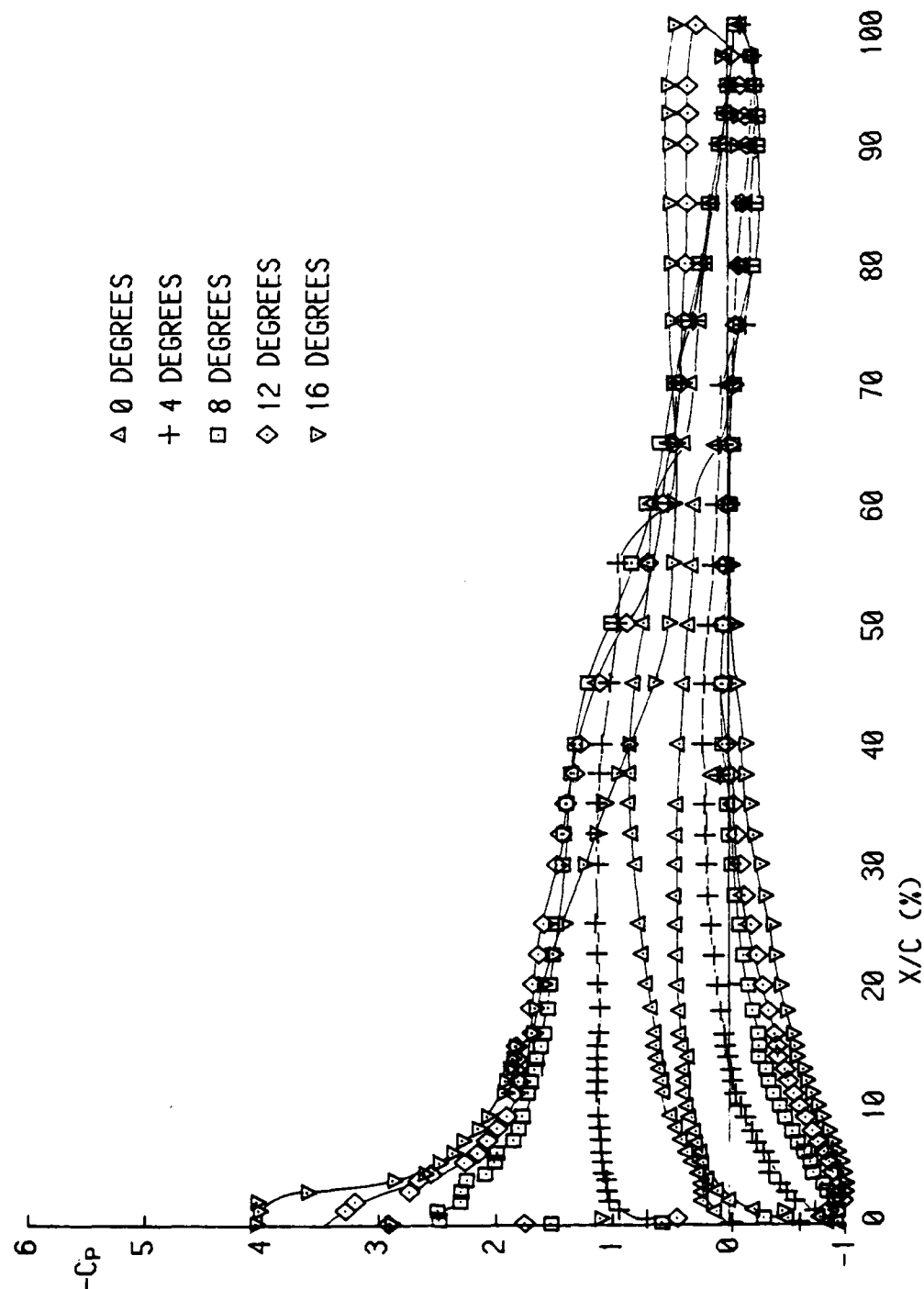


FIGURE 13

NACA 64₃ - 418 experimental pressure distributions.
 Reynolds number = 3.1×10^5

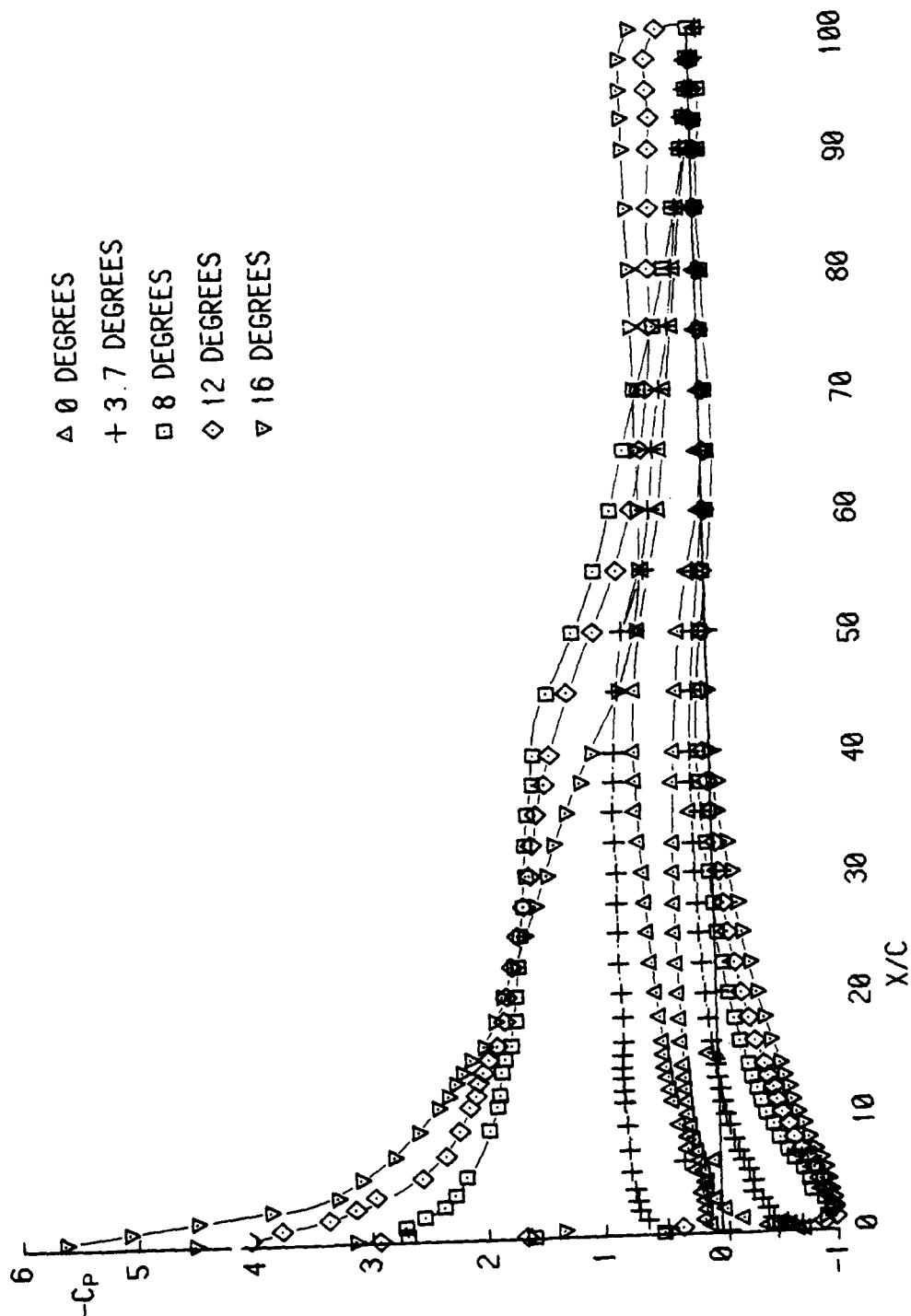


FIGURE 14

NACA 64₃ - 418 experimental pressure distributions.
 Reynolds number = 8.9×10^5

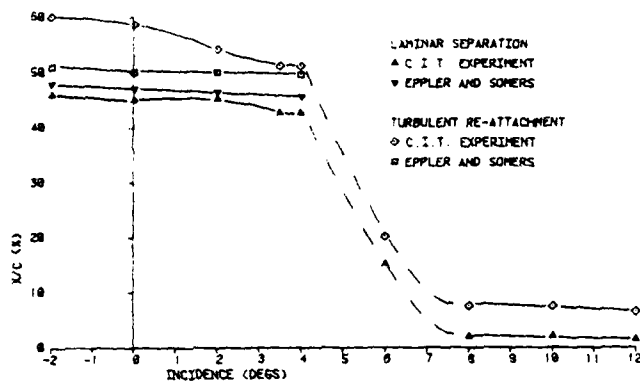


FIGURE 15

Theoretical and experimental positions of laminar separation and turbulent re-attachment. NACA 64₃ - 418 upper surface. Reynolds number = 3×10^5

FIGURE 16

Theoretical and experimental positions of turbulent separation NACA 64₃ - 418 upper surface. Reynolds number = 3×10^5

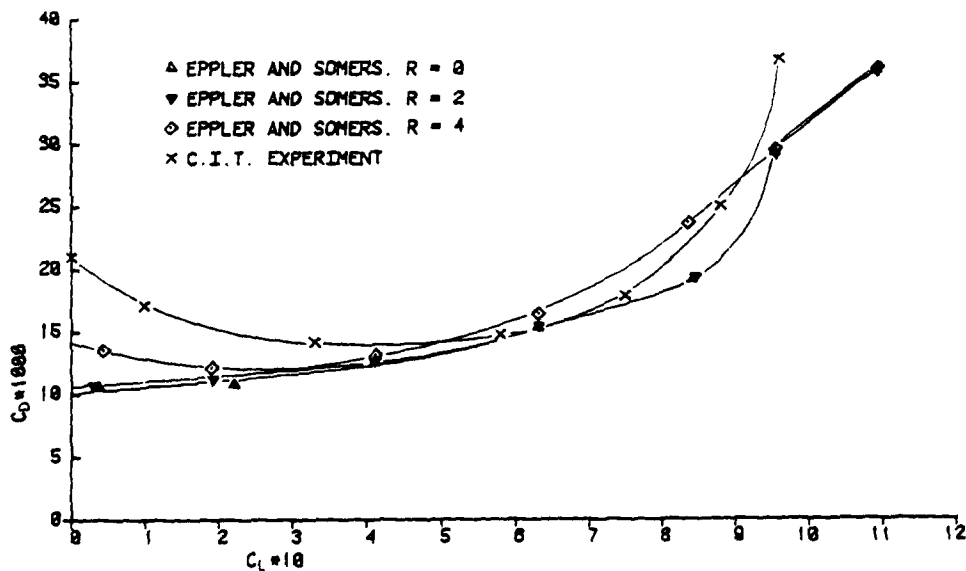
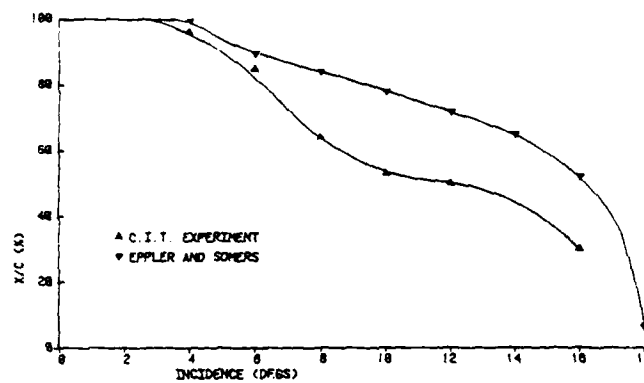


FIGURE 17

Effects of the Eppler and Somers roughness factor for NACA 64₃ - 418. Reynolds number 3×10^5 . Aspect ratio = 38.4

SESSION 5

A SURVEY OF RECENT WORK ON INTERACTED BOUNDARY LAYER THEORY FOR FLOW WITH SEPARATION

H. McDonald and W. R. Briley
Scientific Research Associates, Inc.
Glastonbury, CT

Abstract

It is now widely recognized that the steady boundary layer equations can be used to predict small regions of flow separations when the interaction with the outer inviscid flow is allowed for. A very close relationship between the formalism of the finite Reynolds number approach of treating the interacting boundary layer equations and the so-called triple deck approach to unravel the structure of asymptotic high Reynolds number interacting shear layers is also now widely accepted. The alternative procedure of approaching the problem numerically via the ensemble-averaged Navier-Stokes equations is possible, and the steady interacted boundary layer approach is attractive when numerical solutions of the interacted boundary layer equations are of sufficient generality and can be routinely obtained accurately and more efficiently than solutions of the Navier-Stokes equations. Thus, the numerical treatment of the interacted boundary layer approach is critical to ensure a net benefit is realized relative to the alternatives. Further, since there is now widespread agreement on the interacted boundary layer formulation, attention here is devoted to elucidating, comparing and contrasting some elements of the numerical approaches to solving the interacted system.

Introduction

High Reynolds number shear flows often lead to the development of multiple length scales in problems of practical interest. One solution approach would be to resolve all these important length scales in one analysis which would contain the necessary generality, and then apply it throughout the flow - even to those regions of the flow where the generality was not required and some simplification was possible.

In an effort to be more efficient and perhaps even improve and make use of the basic understanding of such flows, alternative approaches have been explored. Here the multi-scale problem of interest involves small regions of separated flow. For this problem, physical models of the various flow regions have been established and linked together by means of boundary conditions. The simplified governing equation systems appropriate to each flow region are then solved efficiently making use of the (valid) approximations and linked together (interacted) through the appropriate boundary conditions. This approach encompasses three distinct areas: a model formulation including interface boundary conditions, validation of the model, and computation of the solutions. Although here we will be primarily concerned with computational aspects i.e. the third area mentioned, the numerical problems cannot be addressed without an understanding of the formulation and validation.

Considering the model formulation, it is known that a potential i.e. inviscid irrotational, outer

flow gives valid high Reynolds number force and moment distributions over bodies operating in unseparated flow conditions. Viscous effects dominate loss levels and set the operational limits of the device by determining separation and stall. Conventional boundary layer theory provides the first level at which viscous effects can be allowed for, given the pressure distribution, and has in the past been limited to unseparated flow. The question addressed by a number of investigators was, given the possible utility of such an analysis, would it be possible to extend boundary layer theory into limited regions of separated flow? Considerable encouragement for these efforts came on the one hand from the importance of the practical applications which would be within reach of an extended boundary layer theory and on the other from experimental studies. These experimental studies have indicated that in many small but important regions of separated flow, the boundary layer invoked approximations were valid, notably that v , a normal velocity, remained small compared to a streamwise velocity u , and that across these separation regions the normal static pressure gradient was negligible. Since away from the small separation region the outer flow remained inviscid, it was natural to retain these approximations and attempt to construct a flow model to adequately predict these small separation regions thereby enlarging the region wherein inviscid and boundary layer calculations can provide accurate predictions of the flow. Having constructed such a flow model, the next question would be its validation and finally to ascertain that the resulting system of approximate governing equations could be solved more efficiently for the entire domain than, say, the Navier-Stokes equations.

In order to understand the numerical aspects, the construction of such a model is first examined, then its validation to ensure that the essential physical elements are retained and finally the numerical solution procedures are examined, to ensure that the use of flow approximations, however valid, have resulted in a net savings in computational effort.

The Interacted Boundary Layer Formulation and Its Validation

Construction of a suitable model for small regions of separated flows has its roots in the work of Crocco and Lees (1952) who investigated the interaction of a laminar wake with an inviscid supersonic outer flow. In this case a boundary layer momentum integral technique was used to describe the shear layer and a simple local Prandtl-Meyer wave relationship used to relate the free stream pressure at the edge of the shear layer to the local displacement effect of the shear layer. This approach was relatively successful although a singularity caused a great deal of difficulty with the solution implementation. In this approach, the boundary layer or the shear layer development and the free stream are independently governed by

spatially parabolic and hyperbolic systems of equations respectively. Rather remarkably Garvine (1968) later showed that a model of this problem was improperly posed as an initial value problem in space and should be approached as a boundary value problem. The boundary value nature was present although each individual flow regime was governed by a system which could be solved by itself as an initial value problem in space; however, the boundary condition representing interaction of the two regions produced a boundary value problem. Garvine's observations explained much of the difficulty experienced in solving the problem as formulated by Crocco and Lees.

The next series of developments occurred almost simultaneously with Stewartson and Williams (1969), Neiland (1969) and Messiter (1970) developing very similar asymptotic theories of shear layers interacting with external inviscid flows. In these analyses, valid for $R \rightarrow \infty$, Stratford's (1959) concept of a two-layer boundary layer was used in conjunction with an analysis by Lighthill (1953) to produce a rational, self-consistent structure for these interacting shear flows. Solved now as a boundary value problem, much of the previously elusive structure of this class of interacting flows emerged. These important results led to further developments and widespread application of what has become known as triple deck theory [e.g., Stewartson (1974)].

On a parallel development, work continued on the finite Reynolds number behavior of interacting shear layers. In the case of supersonic external stream, Werle and Vatsa (1974) successfully and routinely obtained solutions to the laminar shock wave boundary layer interaction problem, essentially as formulated by Crocco and Lees, by using an iteration procedure and solving the boundary layer equations by an implicit finite difference scheme. Subsequently, very favorable comparison between triple deck results and those of Werle and Vatsa were obtained in the limit as $Re \rightarrow \infty$ by Burggraf, Werle, Rizzetta and Vatsa (1979). However, Davis (1976), Burggraf, et al (1979) and Davis and Rubin (1980) pointed out the rather slow approach of these composite solutions at finite Reynolds numbers to the asymptotic limits of triple deck, at least for this particular problem of a supersonic corner flow. This slow approach to the asymptotic limit has provided one justification for continued development of the 'composite' interacted boundary layer theories. Additional justification for the numerical treatment of the boundary layer as one region interacting with some external inviscid flow, is to be found in the desire not to be bound by the various assumptions of the asymptotic approach when applying the interaction concepts to less simple configurations.

In view of the elliptic nature of the external flow, in the case of a subsonic flow the boundary value nature of the interaction problem is not as surprising as it was in supersonic flow. However, important to the development of a computationally efficient composite approach was the recognition that at finite Reynolds numbers in subsonic flow for small separation regions, the interaction was localized and could be represented as a perturbation of the exterior flow and determined by the particularly simple displacement body of linearized thin airfoil theory (the Hilbert integral). Briley and McDonald (1975) used linearized subsonic thin air-

foil theory in this manner to provide the change to the external flow resulting from the boundary layer interaction. With this formulation, Briley and McDonald were able to predict the development of transitional separation bubbles on airfoils and obtained a favorable comparison with experimental data. Subsequently, Kwon and Pletcher (1979) and Cebeci and Schimke (1982) used this same formulation, but with quite different numerical solution algorithms and turbulent transition models and obtained good agreement with the data and with the earlier predictions of Briley and McDonald. A related study has recently been performed by Carter and Vatsa (1982) for leading edge bubbles.

While the interaction with both the subsonic and the supersonic external flow can be well represented very simply for many problems using linearized flow theory, the mixed elliptic-hyperbolic nature of the transonic problem raises obvious problems. LeBalleur (1978) and Carter (1979, 1981) eliminated these problems in a straightforward manner by iteratively computing the external flow using an efficient transonic potential flow solver. Thus, the interacting boundary layer analysis has been formalized and applied for localized separations in incompressible, transonic, supersonic and hypersonic flow. Attention will now be given to results which validate the general approximations introduced in this analysis.

As mentioned earlier, order of magnitude estimates, experimental measurements and comparisons between predictions and measurements all gave encouragement to the view that for small separation regions boundary layer approximations would remain valid. Early work on the supersonic interaction problem, in spite of being troubled by singularities such as the Crocco-Lees point, did give much encouragement and more than a hint of the potential of this approach to the problem. Werle and Vatsa (1974) compared favorably with both data and the Navier-Stokes solution obtained by Carter (1972) for a compression ramp. Rizzetta, Burggraf and Jensen (1978) using triple deck theory compared favorably with data and with Werle-Vatsa solutions for corner flow. Very direct tests of the validity of the boundary layer approximations for subsonic flow were made by Briley and McDonald (1975) and Ghia, Ghia and Tesch (1975). These comparisons are of special significance since the same algorithms, codes and grids were used. In these instances, flow solutions were obtained using the Navier-Stokes equations and then the terms in the Navier-Stokes equations but not in the conventional boundary layer equations were deleted and the results compared. Briley and McDonald (1975) examined the previously mentioned transitional separation bubbles and found only a small effect of the terms neglected in the incompressible interacted boundary layer formulation. K. Ghia, U. Ghia and W. Tesch (1975) examined the effect of a wide range of approximations upon the incompressible flow over a slab with varying degrees of nose bluntness and upon the flow over a circular cylinder with a rear splitter plate. They conclude that interacted boundary layer type approximations are valid in many instances of separated flow. Murphy, Presley and Rose (1975) compared solutions from the Navier-Stokes to those obtained from a scheme using boundary layer approximations in both laminar and turbulent supersonic shock wave boundary layer interaction. They concluded that in these cases, as long as the flow angle remained small, the neglect of the appropriate terms did not produce a significant discrepancy between the boundary layer

and Navier-Stokes predictions. Vatsa and Carter (1982) compared interacted boundary layer solutions with solutions obtained by a Navier-Stokes solver for turbulent flow over a boattail with a sting, where a small separation zone occurred at the boattail sting juncture. Relatively good agreement was obtained between these two sets of predictions. Thus it has been demonstrated, at least for the flow problems examined above, that use of the boundary layer approximation does not lead to major errors compared to the Navier-Stokes solutions.

Structure of Proposed Solution Procedures

It is at this point that details of the numerical schemes must be introduced, since it can be concluded from the foregoing that a validated approximate flow model for small separated flow regions interacting with an essentially inviscid outer flow region has been firmly established. The basic structure of this flow model leads one to expect considerable economy of computation relative to solving, for instance, the full Navier-Stokes equations with appropriate multi-scale resolution. In the simplest of formats, the steady inviscid external flow around the geometry in question is computed once. If the external flow can be assumed irrotational, a single scalar potential equation may be used with obvious computational savings. The correction perturbation to this inviscid outer flow may be obtained from linearized flow theory and at worst in transonic flow with small separations some perturbation potential would have to be solved throughout the flow. For subsonic flow, the correction can be obtained from the simple Hilbert line integral of thin airfoil theory. For supersonic flow, the correction can be obtained on a pointwise basis using for instance the linearized wave theory of Prandtl and Glauert. The remaining issue is the computation of the interacted boundary layer. The conventional boundary layer approach leads one to think in terms of a parabolic system of equations in space and prior experience indicates that this system can be solved very rapidly and efficiently. Unfortunately, the boundary value nature of the interaction problem described earlier indicates that the interacted boundary layer is not well posed as an initial value problem in space and, if a forward-marching solution algorithm is to be used for solving this boundary value problem, then multiple iterations through the parabolic system are required. Unless a sufficiently economical approach to the boundary value problem is adopted, the resulting effort of solving the boundary value problem will seriously degrade the overall apparent computational efficiency of the formulation and, hence, the numerical approach adopted is of some importance.

Two subsidiary points emerge when the boundary value nature of the problem is addressed, particularly via iterated spatial forward marching approaches. The first point is the steady separation singularity commonly termed the Goldstein singularity, and the second is the reversed flow streamwise velocities that are encountered after the separation. Each of these points will be addressed in more detail subsequently, together with their impact on the solution algorithm. For the present, it is noted that it is now widely accepted that the Navier-Stokes equations are regular at separation while the Goldstein singularity arises in the steady (uninteracted) boundary layer equations when the streamwise pressure gradient is specified as a boundary condition and the equations are solved as

an initial value problem by forward marching in the streamwise direction. Convincing numerical evidence for the regularity of the Navier-Stokes equations at separation has been presented for instance by Briley (1971), Leal (1973), Ghia and Davis (1974). Clear numerical evidence of the presence of the separation singularity in the steady boundary layer equations when the streamwise pressure gradients are prescribed has been given by Werle and Davis (1972), and Klineberg and Steger (1974) for instance. However, it has been established, and is now widely accepted, that the steady interacted boundary layer/inviscid flow solutions both from the composite equations and from triple deck agree with the corresponding Navier-Stokes solutions, as discussed in the previous validation section, and hence are regular at separation. Thus, the Goldstein singularity in interacting flows may have a very considerable impact on the calculation efficiency and strategy, but it is a matter for the solution algorithm, not of the formulation, and will be discussed in that context later. Insofar as the difficulties associated with reverse flow velocities are concerned, these too are features of the solution algorithm, not of the problem formulation, as can be seen for instance from the work of Klineberg and Steger (1974), Carter (1975), and Williams (1974). The problems here are rather obvious and arise from forward marching in space against the mean flow velocity direction. Such problems clearly affect certain types of solution algorithms, but again the elliptic boundary value nature of the interaction and its recognition in the formulation support the contention that the presence of reverse flows is not a difficulty of formulation, but of solution technique.

In the light of the foregoing, we examine some aspects of the numerical algorithms which have been and are being used to solve the steady composite equations of interacting boundary layer theory.

Development of the Numerical Methodology

As mentioned above, the emphasis here will be elucidating some of the numerical aspects of the various approaches adopted to solve the composite interacting boundary layer equations. The governing equations can be written in the form:

$$(\rho u)_x + (\rho v)_y = 0 \quad (1)$$

$$\rho u u_x + \rho v u_y = -p_x + (\mu_T u_y)_y \quad (2)$$

where μ_T is the sum of the laminar and turbulent effective viscosity and an x or y subscript denotes differentiation. For turbulent compressible flow, the dependent variables will be assumed to have been mass averaged following Favre. The governing equations are subject to the impermeable wall and free stream boundary conditions.

$$y = 0, \quad u = v = 0 \quad y = \delta \quad p = p_e(x) \quad (3)$$

The imposed pressure gradient is related to the streamwise velocity U_e

$$p_x = -\rho_e U_e (U_e)_x \quad (4)$$

and the streamwise velocity is decomposed into the imposed and perturbation velocity $U_e = U_e^0 + U_c$ where U_c is the perturbation to the imposed inviscid velocity field U_e^0 due to the interaction. For incompressible flow, this airfoil theory defines the perturbation velocity by the so-called Hilbert integral wherein

$$U_c = \frac{i}{\pi} \oint_{-\infty}^{+\infty} \frac{(U_e \delta^*) \xi}{x - \xi} d\xi \quad (5)$$

where the symbol \oint denotes that the Cauchy principle part of this singular integral is taken, and δ^* is the usual boundary layer displacement thickness. An even simpler relationship between the local rate of change of displacement thickness and the perturbation velocity U_c can be derived in supersonic flow relative to a perturbation flow angle α ,

$$(U_c)_x / U_e = (M_e^2 - 1)^{-1/2} \alpha_x \quad (6)$$

$$\alpha = (v/u)_y \delta^* = \delta_x^* \quad (7)$$

In the supersonic literature some minor variation in this type of expression can occur depending on where the flow angle match point is taken and on the specifics of the linearization approximation. With this slight exception, the formulation given above is remarkably standard and in addition to being part of the basic structure of triple deck [Stewartson, (1974)] has been used as the appropriate system of governing equations describing composite interacting boundary layer flows at finite Reynolds number. For instance, in subsonic flows precisely this formulation has been used by Briley and McDonald (1975), Carter (1979), Carter and Wornom (1975), Kwon and Pletcher (1979), Veldman (1981), Cebeci and Stewartson (1982), Cebeci and Schimke (1982) and Carter and Vatsa (1982). In supersonic flows, the composite formulation is essentially that used for instance by Crocco and Lees (1952) and Baum and Denison (1966) for a wake and Werle and Vatsa (1974) for boundary layers. In view of the wide acceptance of the formulation, the distinction between the various approaches can be made on this basis of the numerical solution algorithm, and/or the turbulence model adopted.

It is instructive to briefly review the evolution of the numerical methods used to solve the composite equations. It is apparent that the widespread availability of computer codes embodying efficient and accurate numerical schemes which solve the previously given boundary layer equations as an initial-boundary value problem in the streamwise direction, have greatly influenced the numerical development. In approaching the boundary value problem arising from the composite system, it is natural to attempt to utilize these existing computer codes within an iterative technique. This is, of course, a perfectly legitimate approach if upon convergence the appropriate solution is obtained satisfying the necessary interacted boundary

conditions. In this mode, the streamwise forward marching iterates can encounter the two previously mentioned problems of the separation singularity and forward marching into regions of reverse flow. Cathaler and Mangler (1966) demonstrated that changing a boundary condition on the boundary layer equations from specified $U_e(x)$ to specified (smooth) $\delta^*(x)$ was sufficient to ensure regular behavior near zero skin friction. Introduction of a specified displacement thickness as a boundary condition is a minor and easily introduced modification to these existing computer codes and the resulting schemes have been termed the inverse mode of solving the boundary layer equations. Carter (1975), and Ghia, Ghia and Tesch (1975) have demonstrated that specifying a smooth skin friction distribution also served to produce a smooth solution of the boundary layer equation in the vicinity of separation. Once past the immediate vicinity of the separation point, these initial value schemes encountered the problem of marching against the streamwise velocity. Here, iterative schemes have been constructed and demonstrated by Klineberg and Steger (1974), Carter (1975), Williams (1974), Ghia, Ghia and Tesch (1975) which remove the reverse flow problem without further approximation to the governing equations. An approximate noniterative technique proposed by Flügel-Lotz and Reyhner (1968) termed 'FLARE' has also been shown to permit forward marching into regions of reverse flow. The technique involves either neglecting the streamwise convective term in the axial momentum equation or replacing the streamwise convective velocity in the equation by its modulus. The stabilizing effect of this modification is obvious and the approximation valid so long as the streamwise convective term is negligible. Carter (1975) has shown that noticeable errors could arise from use of this approximation when the negative convective velocity exceeds about 10% of the free stream value. Since high reverse flow velocities (>10%) are observed, experimentally and theoretically, in the vicinity of reattachment in turbulent flow, some concern over the widespread use of the FLARE approximation must be expressed.

Given now that the iterative approaches can be developed to streamwise march through the separation region by operating in the inverse mode, it now becomes necessary to complete the iteration and satisfy the external interacted boundary conditions. Here some subtlety is required since the edge velocity deduced from the inverse solution of the boundary layer equations must eventually be the same, to within satisfactory numerical error levels, as that arising from the displacement surface as given by the external flow calculation. The various investigators have devised systematic ways of performing the correction to ensure rapid convergence, in general. Thus, this type approach can be evaluated numerically in four categories. One, how the boundary layer equations are solved; two, how the separation singularity is dealt with; three, how the problem of marching into the reverse flow is treated, and four, how the interacted external flow boundary conditions are satisfied. As will be shown subsequently, once this is done a high degree of uniformity is observed in the algorithm's structure used to solve the problem by the iterative or shooting approach.

The boundary value problem could be formulated numerically as a large matrix inversion problem as solved by a combination of Newton iteration and direct elimination. This has, as yet, not been done. In other fluid dynamics problems governed by elliptic

equations, various time-dependent approaches to solving steady boundary value problems as the large time asymptote of a time or pseudo-time integration process have gained widespread acceptance. For the present interaction problem, a time-dependent approach can be attractive, although to date it has not been widely used in spite of the availability of computer codes which can efficiently solve the time-dependent boundary layer equations. Here an attempt will be made to explain this somewhat anomalous result. In a time-dependent approach, the problem is recast into an initial/boundary-value problem in time or a pseudo-time variable with a two-point boundary value problem in space satisfied at each time step. Since the problem is marched in time, not in space, no difficulty with sign of the streamwise velocity is encountered. As Phillips and Ackerberg (1973) and Cebeci (1978) point out, an unsteady separating and reattaching boundary layer with specified free stream velocity as a boundary condition (the direct mode) does not encounter a Goldstein type of singularity. Since the interacted formulation ensures that the Goldstein singularity is not present in the steady solution, one is led to the expectation that if steady solutions are obtained by an unsteady approach, these will be singularity free both in the transient and at steady state, otherwise the results could not constitute (unique) solutions.

A physical time-dependent approach was used by Briley and McDonald (1975) to generate solutions to the steady interacted boundary-layer equations subject to the interacted freestream boundary-condition and also to generate solutions of the Navier-Stokes equations for this same problem, subject to the same boundary conditions. Subsequently, it was questioned by Carter (1975) and Kwon and Fletcher (1979) whether this time-dependent approach had removed the separation singularity. Although an incomplete streamwise mesh refinement study prevented a firm conclusion at that time that the separation singularity was absent in the steady solutions, in light of the current unanimity that the steady interaction formulation is nonsingular following convergence, any doubt concerning these particular solutions can only encompass behavior of the algorithm itself prior to convergence, and not the interacted boundary-layer formulation itself. Stated another way, if unique solutions exist the singularity obviously cannot be absent for a solution obtained by one particular numerical technique and not by another. If any particular solution technique produces steady results which show evidence of singular behavior then this implies that convergence to the (nonsingular) interacted solution has not been obtained.

Concern for the adequacy of time-dependent approaches in general may have been engendered by the previously mentioned study of Werle and Vatsa (1974), who used a pseudo-time formulation for the purpose of iteration to satisfy the interaction equation. In the Werle-Vatsa formulation, a pseudo-time derivative of displacement thickness is added to the steady form of the momentum equation. As Werle and Vatsa point out, during each spatial marching interaction this pseudo-time term (which is independent of y) behaves essentially as an imposed pressure gradient, and since freestream velocity is imposed during each forward-marching iteration sweep, this particular algorithm is thus subject to the separation singularity and reverse flow problems unless special solution techniques are introduced. To eliminate these problems Werle and Vatsa modified

the pseudo-time term to give it a functional dependence on the streamwise derivative of displacement thickness, based on the observed behavior of displacement thickness at the separation singularity. With this modification, Werle and Vatsa were apparently able to forward march through separation with an imposed freestream velocity without encountering singular behavior. The reverse flow problem was treated by introducing the FLARE approximation mentioned earlier. The difficulties encountered and dealt with in the Werle-Vatsa pseudo-time formulation (for use as an iterated spatial forward-marching algorithm) must be contrasted with a formulation based on physical time dependence, wherein the time derivatives represent local physical time accelerations. Since the physical time accelerations vary with all spatial coordinates, they cannot be equivalent to an imposed pressure gradient which is independent of the normal coordinate y . In fact, the particular time-dependent algorithm applied by Briley and McDonald to the unsteady boundary layer equations was a conventional Douglas-Gunn ADI scheme in which each of the two steps is implicit in only one coordinate direction. Consequently, although the freestream velocity was imposed as a (direct) boundary condition in one of the ADI sweeps, the terms treated implicitly (as a two-point boundary value problem) in each sweep do not constitute the steady boundary layer equations, and thus the algorithm does not encounter the separation singularity.

Another early use of a physical time-dependent formulation to solve an interaction problem is that of Rizzetta, Burggraf and Jenson (1975, 1978) who solved the triple-deck equations for steady hypersonic flow past a corner. The unsteady equations were solved using a semi-implicit algorithm, and these results were examined quite extensively for numerical errors by the authors, and in the vicinity of separation compared very well with the previous triple deck results of Stewartson and Williams (1969) for free interactions. No evidence of the separation singularity was encountered, and upwind differencing of the streamwise convective term was sufficient to maintain stability in the reversed flow region. Although the implementation of boundary conditions during the transient and the effect of unwinding on the tridiagonal structure of the semi-implicit algorithm were not discussed in detail, these details are immaterial once convergence is obtained. Since Rizzetta, Burggraf and Jenson were able to perform a complete streamwise mesh refinement near separation, their findings provide rather convincing evidence that the separation singularity is absent in the physical time-dependent formulation for solving the incompressible boundary layer equations subject to the interacted freestream boundary conditions of triple deck theory.

As a final observation on avoiding the separation singularity during iteration procedures for solving the nonsingular steady interaction formulation, it appears that at least three distinct approaches have now been suggested. Each is consistent with the observation that the singularity seems to occur only when the steady boundary layer equations are solved (by any method) subject to an imposed freestream velocity or pressure gradient (i.e., "direct" boundary conditions). In one approach, the singularity is avoided during iteration by retaining the steady equations but changing to "inverse" boundary conditions (i.e., a specified displacement thickness or wall shear stress). In

another approach, the direct boundary conditions are used during iteration but the equations themselves are changed to the unsteady form. The third approach is that of Werle and Vatsa which apparently succeeded by retaining the direct boundary conditions but changing the pressure gradient term perceived by the equations to a special form dependent on the streamwise derivative of displacement thickness.

Having discussed the various numerical strategies for solving the interacted boundary layer equations, attention is now devoted to examining some aspects of the numerical implementation of the interaction boundary condition. In the main, the subsonic problem resulting from the Hilbert integral is addressed, this being a more difficult problem than the supersonic interaction.

The Interaction Boundary Condition

Since for subsonic flows the interacted boundary condition represented by the Hilbert integral, Eq. 5, cannot be conveniently treated as fully implicit at the advanced $n+1$ iteration or time level, alternative strategies are adopted in both time dependent and spatial approaches. In the main, the interactive boundary condition has been applied explicitly at the n level iterate or time level. In the time-dependent approach where the freestream velocity can be imposed directly as a boundary condition without encountering a singularity, the $n+1$ interaction contribution to the freestream velocity may be obtained from the integration of the known n level displacement thickness via the Hilbert integral and applied as a direct boundary condition through the specification of U_e . In the inverse approaches, the interaction contribution to the streamwise velocity, U_c^{n+1} , may be computed from n -level quantities as before and then used to deduce a new guess at the displacement thickness (or skin friction) at the $n+1$ level, δ^{n+1} . This displacement thickness δ^{n+1} is then imposed as the boundary condition on the $n+1$ level solution. When the freestream velocity U_e^{n+1} obtained by integration of the boundary layer equations with the prescribed displacement thickness δ^{n+1} is sufficiently close to the freestream velocity given by the sum of the Hilbert integral contribution and the imposed inviscid distribution $U_e^n = U_e^0 + U_c^n$, the iteration is terminated and interaction boundary condition has been satisfied. Note that both here and subsequently the effect on the inviscid flow is viewed from the Hilbert integral correction point of view. However most of the arguments carry over at least in principle to the case where the inviscid flow is recomputed in its entirety.

It is observed from Eq. 5 that the far field contributions to the velocity perturbation from the Hilbert integral eventually decay as x^{-1} . The interaction perturbation to the freestream velocity gradient decays even more rapidly, in fact as x^{-2} . This rapid decay supports the localized view of the small separation bubble interaction effect, and as a result it is attractive to attempt to improve the iterative convergence of the interaction by taking as much as possible of the Hilbert integral implicitly at the advanced iteration level. In a recent development, Veldman (1981) has suggested a semi-implicit evaluation of the Hilbert integral during the spatial forward marching iteration procedure, as a means of improving the convergence

rate. This approach is termed "quasi-simultaneous" because it provides a (partial) simultaneous coupling between viscous and inviscid flow regions during the iteration. The stability of forward marching and convergence of the overall iteration are of interest. The results of Veldman demonstrate that this treatment of boundary condition was both stable during the forward marching iterations and led to rapid convergence of the overall iteration to satisfy the Hilbert integral. Given that the forward-marching iterates are stable, the improvement in convergence behavior observed by Veldman might be related to the highly localized behavior of the Hilbert integral. Veldman's results are intriguing in light of Garvine's analysis indicating that the interacted simultaneous treatment of the freestream boundary condition is ill-posed for the supersonic case when posed as an initial value problem in space. The stability or well-posedness of the subsonic case is explored here by relating a model problem, representing forward marching for a subsonic interaction, to Garvine's analytical result for the supersonic case. The subsonic case is found to have a close resemblance to the supersonic case except for the sign of the exponent controlling the exponential growth or decay in the solution. The exponent can be made negative for the subsonic case, thus producing a well-posed initial value problem. In order to develop the analysis, it is necessary to perform some preliminaries and discretize the Hilbert integral. This will be done and the relationship to Garvine's supersonic result established.

Consider the principal part of the Hilbert integral of linearized thin airfoil theory. The Hilbert integral is singular at $\xi = x$, and outside a region $x_a < x < x_b$ surrounding the singularity, it can be supposed that the integral is well behaved, and may be integrated by some convenient quadrature formula. Here, a uniform mesh of spacing $\Delta\xi$ is adopted for simplicity, and a trapezoidal rule is used. The quadrature is evaluated for a given value of x such that $x_a < x < x_b$ as follows:

$$\begin{aligned} U_c &= \int_{x_a}^{x_b} g(x, \xi) d\xi \\ &= \Delta\xi \left[\frac{1}{2} g_0 + g_{a-1} + \frac{1}{2} g_a \right] + \\ &\quad \int_{x_a}^{x_b} g(x, \xi) d\xi + \Delta\xi \left[\frac{1}{2} g_b + g_{b-1} + \frac{1}{2} g_c \right] \end{aligned} \quad (8)$$

where $g(x, \xi) \equiv h(\xi)/(x-\xi)$, and $h(\xi) \equiv (i\pi U_e)_{\xi}/\pi$. The principal part of the singular integral is defined by

$$\begin{aligned} \int_{x_a}^{x_b} g(x, \xi) d\xi &= \lim_{\epsilon \rightarrow 0} \frac{1}{\pi} \int_{x_a}^{x-\epsilon} \frac{(U_e \delta^*)_{\xi}}{(x-\xi)} d\xi + \\ &\quad \frac{1}{\pi} \int_{x+\epsilon}^{x_b} \frac{(U_e \delta^*)_{\xi}}{(x-\xi)} d\xi \end{aligned} \quad (9)$$

Note that although the integrand of the integral is singular at $\xi = x$, the variation of $h(\xi)$ is regular. To illustrate a point, assume $h(\xi)$ may be described by some polynomial consistent with the spatial difference operator of the boundary layer finite difference scheme. For the present, a linear distribution consistent with the previous use of the trapezoidal rule is written as follows:

$$h(\xi) \equiv (\delta^* u_e)_\xi / \pi \approx q + r\xi \quad (10)$$

and of course the values for the constants q and r follow from the function values of the argument at x_a, x_b . The required integration can now be performed and the limit of $\epsilon \rightarrow 0$ taken. If now the singularity at x is placed at the mid point between x_a and x_b (denoted x_s), a logarithmic term which arises in the definite integral disappears and the very simple result is obtained that the Cauchy principal part of the singular integral is given by

$$\int_{x_a}^{x_b} g(x_s, \xi) d\xi = (x_a - x_b)r \quad (11)$$

Replacing r by the appropriate function values, and noting that $g_a \equiv h_a/(x_s - x_a)$ and $x_s \equiv (x_a + x_b)/2$, Eq. (11) can be written as

$$\begin{aligned} \int_{x_a}^{x_b} g(x_s, \xi) d\xi &= -(x_b - x_a) [h(x_b) - h(x_a)] / (x_b - x_a) \\ &= \frac{\Delta \xi}{2} (g_b + g_a) \end{aligned} \quad (12)$$

With each half of the principal part inserted into the appropriate trapezoidal rule, the overall result is

$$\begin{aligned} \int_{x_0}^{x_c} g(x, \xi) d\xi &= \\ \Delta \xi \left[\frac{1}{2} g_0 + \dots + g_a + g_b + g_{b+1} + \dots + \frac{1}{2} g_c \right] \end{aligned} \quad (13)$$

which is identical to a straightforward application of the trapezoidal rule to the Hilbert integral without special treatment of the singularity. With this particular quadrature, which has an equally spaced mesh, and the singularity located at the mesh center, the correction for the singularity is zero. This particular quadrature of the Hilbert integral was used by Briley and McDonald (1975), and other quadratures properly allowing for non-uniform meshes and other positions of the singularity are easily developed. Note here that the

discrete form of the integral given by the trapezoidal rule, Eq. 13, can be written

$$\begin{aligned} U_c &= \int_{x_0}^{x_c} g(x, \xi) d\xi \\ &= \frac{1}{2} \left[\frac{h(x_c)}{m+1/2-n} + \frac{h(x_0)}{m+1/2} \right] \\ &\quad + \sum_{j=1}^{j=n-1} \frac{h(\xi_j)}{m+1/2-j} \\ &= \alpha_{nm} + \sum_{j=1}^{j=n-1} \beta_{jm} h(\xi_j) \end{aligned} \quad (14)$$

with $x_0/\Delta \xi = 0, \quad x_c/\Delta \xi = n$

$$x/\Delta \xi = m + 1/2 \quad \xi/\Delta \xi = j$$

Most quadratures can be written in the form of a discrete sum, Eq. 14, but this sum will be different for different quadrature formulae, particularly in the weights β_{jm} . It will be shown later that the sign of the weights, particularly the weight at $j = m$, can have a considerable impact on the stability of certain iterative algorithms. To develop this point, it is necessary to introduce a model problem, and here we follow Garvine (1968) and introduce the Oseen linearized boundary layer equations.

The boundary layer equations given in Eqs. 1 and 2 are now normalized by a reference length l and velocity U_{ref} , and subsequently all lengths and velocities should be considered non-dimensionalized accordingly. This introduces a Reynolds number R based on U_{ref} , l and the turbulent effective viscosity ν_T . From the point of view of the development, little is lost by considering the turbulent effective viscosity ν_T as a constant. The solution variation from the n to $n+1$ iterate or time level is examined. The velocity increments are expressed

$$\begin{aligned} u^{n+1} &= u^n + \Delta u \\ v^{n+1} &= v^n + \Delta v \end{aligned} \quad (15)$$

Neglecting the product of increments and introducing the Oseen simplifications a model linear system is obtained which yields an approximation to the increment Δu which is now a perturbation about the (non-dimensional) constant velocity U_0 . This model equation is

$$U_0 (\Delta u)_x = U_0 (\Delta u)_x + R^{-1} (\Delta u)_{yy} \quad (16)$$

Consistent with the Oseen approximation, the interaction boundary condition obtained from the

Hilbert integral is

$$\Delta u_c = \Delta u_c(x) = \frac{1}{\pi} \int_{x_0}^{x_c} \frac{(u_0 \delta^*)_{\xi}}{x - \xi} d\xi \quad (17)$$

and

$$\delta^* = \int_0^{\delta} \left(1 - \frac{\Delta u}{U_0}\right) dy \quad (18)$$

Some initial profile is to be specified together with the usual no-slip and boundary condition at large y . Following Garvine, the algebra is considerably simplified if the boundary layer thickness δ is taken sufficiently large and constant with x . From the continuity equation, and the definition of the displacement thickness δ^* it follows that

$$(u_0 \delta^*)_{\xi} = - \int_0^{\delta} (\Delta u)_{\xi} dy$$

and

$$(u_0 \delta^*)_{\xi\xi} = - \int_0^{\delta} (\Delta u)_{\xi\xi} dy \quad (19)$$

Now the stability of semi-implicit interacting spatial marching algorithms will be examined. The solutions are to be spatially marched from some station x_m to x_{m+1} . The time or iteration level is advancing from the known n level to the $n+1$ level. For the evaluation of the spatial behavior of the sweep, the steady Oseen approximation with appropriate boundary conditions will serve as an approximate model of the governing equations. In obtaining the contribution of the interaction to the freestream velocity gradient, it is convenient first to integrate the Hilbert integral by parts with due allowance for the Cauchy principle part. This yields

$$\begin{aligned} \pi \Delta u_c &= \int_{x_0}^{x_c} \frac{(u_0 \delta^*)_{\xi}}{(x - \xi)} d\xi \\ &= - \left[\log |x - \xi| \cdot (u_0 \delta^*)_{\xi} \right]_{x_0}^{x_c} + \\ &\quad \int_{x_0}^{x_c} \log |x - \xi| (u_0 \delta^*)_{\xi\xi} d\xi \end{aligned} \quad (20)$$

If it is assumed that at $x = x_c$ and $x = x_0$ the boundary layer has returned to some relatively undisturbed state, consistent with the local view of the interaction, it is permissible and convenient to neglect the first term in the integral. If this is not acceptable, then this same term may be dropped after differentiation to obtain the velocity gradient by making sure that x_0 and x_c are far from the point of interest. Proceeding to obtain the velocity gradient

$$(\Delta u_c)_x \approx \frac{1}{\pi} \int_{x_0}^{x_c} \frac{(u_0 \delta^*)_{\xi\xi}}{(x - \xi)} d\xi \quad (21)$$

and this integral can be represented by the same quadrature formula as that developed previously for the velocity perturbation Δu_c , Eq. 13, by redefining $g(x, \xi)$.

In the quadrature of the Hilbert integral, all the required values of δ^* and U_0 are supposed known except one, which is to be evaluated implicitly at the advanced spatial location x_{m+1}^{n+1} when marching from the known solution at x_m^{n+1} . Recall that the superscript denotes the iteration level. The contribution to Hilbert integral for x less than x_{m+1} is known at the $n+1$ level having been determined as the solution is forward marched. The contribution for $x > x_{m+1}$ is taken from the n level solution, that is the integral is split between n and $n+1$ levels and thus evaluated semi-implicitly. This results in the integral for the velocity gradient being expressed at the midpoint $x = (x_{m+1} + x_m)/2$ as

$$\begin{aligned} (\Delta u_e)_x &= \alpha_{nm} + \sum_{\substack{j=n-1 \\ j=1 \\ j \neq m}} \beta_{jm} (u_0 \delta^*)_{\xi\xi} + \beta_{mm} (u_0 \delta^*)_{\xi\xi} \quad (22) \\ &= I - \beta_{mm} \int_0^{\delta} (\Delta u)_{xx} dy \\ \beta_{mm} &= +2/\pi \end{aligned}$$

and the second derivative of the displacement thickness in the latter expression is to be evaluated at $x = x_m$. (This would cause δ_{m+1}^{n+1} to appear if a central difference at $x = x_m$ were used for $d^2 u_0 \delta^* / dx^2$).

The model interaction equation is rewritten

$$\Delta u_{yy} + b \int_0^{\delta} \Delta u_{xx} - a \Delta u_x = S \quad (23)$$

$$\text{where } b = -\beta_{mm} R U_0 \quad a = U_0 R \quad S = -I R U_0$$

This equation may be solved subject to the required boundary conditions by writing the dependent variable in the form

$$\Delta u = \tilde{u}(x, y) + w(y) \quad (24)$$

with w defined as $w_{yy} = S$ subject to the boundary conditions $w(0) = w(\delta) = 0$. This results in the quadratic profile

$$w = -\frac{S y}{2} (\delta - y) \quad (25)$$

Note that the w profile does not satisfy a zero gradient outer edge condition, but that this could be imposed without changing the subsequent results significantly. However giving up on this gradient condition leaves \bar{u} subject to precisely the same governing equation and boundary equations as Garvine's model problem for a supersonic interacting boundary layer, and hence his solution may be taken over in its entirety to represent \bar{u} . In view of the rather complex structure of Garvine's solution, we will not present it here. Instead we note Garvine's observation that his solution contains an exponential term operating on a function of the initial profile and this term either decays or diverges with the sign of the coefficient b which scales the integral in the model interaction equation. With the coefficient b positive, the solution diverges exponentially with increasing x . Obviously, the addition in subsonic flow of the quadratic profile for $w(y)$ to define our perturbation velocity $\Delta u = \bar{u} + w$, does nothing to correct the exponential spatial amplification. With the particular quadrature and also the location of the chosen implicit term in the semi-implicit interaction integral boundary condition, it turns out that b is negative and the forward marching solution contains no exponentially growing terms with increasing x . The supersonic case is recovered by setting the source term S in Eq. 23 to zero, and thus dropping the quadratic profile for w . As Garvine points out with a simple linearized wave approach to the external flow, the sign of b in the supersonic situation is positive, in fact $b = R/2(M_\infty^2 - 1)^{-1/2}$, and the well known phenomenon of branching is observed in the model problem, resulting from the presence of the exponentially growing component in the solution. Branching is, of course, a well known problem in supersonic interacting shear flows when solved by forward marching, e.g. Baum and Dennison (1966). The absence of exponentially growing spatial modes in the linearized Oseen approximation to the interacted boundary layer equations is obviously not a sufficient condition to ensure a well posed iterated forward marching approach to the interacted boundary layer equations. However, any spatially exponentially growing modes in the Oseen approximation to the interacted boundary layer equations would give considerable concern and while the absence of such modes is not a proven necessary condition in generating well behaved forward marching iterates to the interacted boundary layer equations, it would seem a good working hypothesis to ensure such modes were absent.

Note also that the sign of b determines the presence or absence of the growing mode, and this sign can readily be altered. As mentioned earlier a different quadrature formula used to represent the Hilbert integral could give rise to a different sign, as could the correction for the Cauchy principal part. Further changing the form of the various spatial derivatives involved, for example by forward differencing in space and then taking the downstream unknowns at the prior iteration (i.e. the terms within the difference molecule are taken at the implicit $n + 1$ level where possible and the known n -level otherwise) is an effective way to change the sign of b .

Some feel for the behavior of spatial marching with a local interaction contribution can be obtained from very simple considerations. In subsonic

flow a local increase in displacement thickness creates a local flow acceleration over the resulting 'bump'. This acceleration tends to thin the boundary layer thus reducing the displacement thickness 'bump', and a stable situation arises. This can be contrasted with supersonic flow where an increase in displacement thickness creates a local deceleration. The resulting deceleration further intensifies the thickening of the boundary layer and increases the displacement thickness, and an unstable situation could arise. The argument in both the subsonic and supersonic cases remains the same if a decrease in the displacement thickness is postulated. Considerable caution must be used when applying these arguments, however, since in reality a supersonic flat plate turbulent boundary layer is not unstable to small disturbances. The key missing physical element in the foregoing argument is the global effect of the perturbation. In a real subsonic or supersonic flow problem, the reaction to the perturbation is not independent of upstream and downstream effects. The arguments given earlier concerning the local reaction to the displacement thickness change were based on an interpretation of the behavior of the governing equations viewed as an initial value problem in space. The interpretation given is relevant in explaining the behavior of iterative schemes for solving the interacted equations which make repeated initial value spatial marching sweeps using the conventional steady boundary layer equations. Since only the converged solutions need to represent real flows, the behavior of the interactions is of no real concern so long as the algorithm converges to the correct solution and is computationally efficient. These stability concepts are well known and are discussed in detail by Weinbaum and Garvine (1969), and more recently by LeBalleur (1978) and LeBalleur, Peyret and Viviani (1980). The sign of parameter b shown to determine the presence or absence of the growing spatial modes in the linearized model interaction indeed, represents the sign of the relationship between the induced edge velocity and the boundary layer displacement thickness. Thus the intuitive arguments given above, can readily be placed on a firm quantitative footing at least for the model problem. The earlier remarks of the usefulness of changing the sign of b can be carried over into the qualitative model by noting for instance a forward and backward difference of pressure gradient have a different sign in their local response to a change in displacement thickness.

As a final comment on the solution behavior in iteration space, it is not sufficient to ensure that the solutions sweep at each iteration be stable, as was investigated here and by Garvine. It must also be demonstrated that the iterations, complete with iterated interacted boundary conditions, converge and that the rate of convergence be measured and adequate. Since the iterated boundary layer formulation is now standard and widely accepted, the numerical solution algorithm and its convergence rate become critical discriminatory features of the proposed schemes. To date, very little has been accomplished in developing a thorough theoretical understanding of the convergence properties of the various schemes. A major difficulty in this regard appears to be the observed crucial role of the interaction boundary conditions [e.g. Veldman (1964)] and the theoretical difficulties of determining the convergence rate when the boundary conditions are included.

This discussion of iteration space convergence brings up the subject of FLARE, once again, since the FLARE approximation changes the governing equations, i.e. one is no longer solving the interacted boundary layer equations, but some approximation thereto. Further, the FLARE approximation to the governing equation system apparently does have quite different convergence properties than the unapproximated system. Thus, a brief discussion of the FLARE approximation will be given.

Some Remarks on the FLARE Approximation

First of all, it should be recalled that there are at least two published variants of the FLARE approximation. For instance, in their original proposal Reyhner and Flugge-Lotz (1968) showed that when u was less than zero setting the convection term $\rho u u_x$ to zero in the boundary layer streamwise momentum equation, Eq. 2, allowed them to obtain stable finite difference solutions of the resulting approximation to the boundary layer equations by the usual procedure of forward marching even in the presence of separated flow. Some authors, e.g. Kwon and Pletcher (1979) have adopted a slightly different approach and replace the convective term $\rho u u_x$ by $\rho |u| u_x$ with $c=1$ when $u>0$ and with c a small positive number, e.g., $<.2$, when $u<0$, and again were able to obtain stable finite difference solutions of the resulting approximation to the boundary layer equations by forward marching into regions of separated flow.

The use of the FLARE approximation, for the expense of the resulting error, eliminates the need to perform an inner iteration to allow for reverse flow velocities. It also eliminates the need to store the various levels of the field of iterates which would be used to obtain the solution with reverse flow. Since this inner iteration usually occurs within the outer iteration to satisfy the interacted boundary condition, elimination of this inner iteration is attractive and would be very beneficial from an efficiency point of view if the resulting errors were acceptable. Various methods of merging the inner and outer iterations suggest themselves, the inner iteration to allow for the reverse flow velocities being in some sense performed simultaneously with the outer iteration to satisfy the interacted boundary condition. To date little has been done to investigate such proposals.

The question of the accuracy of a FLARE type of approximation for thin incompressible laminar separation bubbles was investigated by Carter (1975). Using an inverse boundary layer procedure and a global iterative scheme Carter obtained solutions of the laminar boundary layer equations in a separation bubble without invoking a FLARE approximation. Two bubbles involving maximum reverse flow velocities of $-.05U_\infty$ and $-.10U_\infty$ where U_∞ is the free stream velocity, were examined. In each case a prescribed displacement thickness boundary condition was applied. The interaction boundary condition was not enforced in this test and the prescribed displacement thickness remained unaltered during the iterations. The solutions thus obtained were compared with solutions obtained by neglecting the streamwise convection of vorticity in the separated flow region. For the case where the maximum reverse flow velocity did not exceed $-.05U_\infty$ the predicted skin friction distributions with and without the FLARE approximation were in quite good agreement. For the case where the maximum reverse flow velocity was in

the region of $-.10U_\infty$ the maximum skin friction upstream of reattachment was different with and without FLARE by about 11% of the Blasius skin friction at the upstream boundary. The FLARE approximation to the boundary layer equations resulted in a smaller value of skin friction. It was observed by Carter that the error was localized to the region of the boundary layer reattachment and that the same reattachment point was predicted with and without the FLARE approximation. The solutions were essentially unaltered beyond the reattachment point. In the context of the triple deck approach for supersonic free interactions, Williams (1975) has noted that use of a FLARE approximation introduced more error into the reverse flow velocity profile than into the computed skin friction. These results of Carter and Williams provide a useful calibration of FLARE accuracy for a laminar flow.

Several items are worth noting if Carter's observations are extrapolated to justify the use of a FLARE approximation for transitional/turbulent separation bubbles for finite Reynolds number flows with interaction. First, it is not known whether incorporating the interaction boundary condition alters the sensitivity to the FLARE approximation. Second, characteristically transitional/turbulent bubbles show a sharp dip in the skin friction in the region of reattachment, consistent with a rapid decrease in displacement thickness during reattachment and evidence of local high reverse flow velocities, commented upon experimentally by Gaster (1966). Reverse flow velocities of about $.13U_\infty$ were observed in the transitional separation bubble calculations of Briley and McDonald (1975). As mentioned previously, by virtue of the time dependent approach the Briley-McDonald calculations did not require a FLARE type approximate form of the boundary layer equations. Had such an approximate form been used the predicted reverse flow velocities might have been lower if the trend observed by Carter were followed, so caution must be exhibited in the justification and use of a FLARE type approximation to the boundary layer equations.

The point is often made that use of the FLARE approximation might be very beneficial in aiding rapid convergence of the interacted boundary layer equations if used during the initial iterations. These iterations are required and undertaken in any event to satisfy the interaction boundary conditions, and during the later phases the iteration to remove the FLARE type approximation could be folded in. Although not yet rigorously demonstrated, nor even routinely performed, such a computational strategy would seem to have considerable potential. However, most investigators who use the FLARE type approximation to the interacted boundary layer equations do not remove the approximations as the solution converges and hence the approximation induced errors remain in the converged solutions. As has been noted earlier, depending on the problem these errors could be quite significant. Comparing Carter's solutions and the solutions of Briley and McDonald (1975), Kwon and Pletcher (1979) and Cebeci and Schimke (1982) for transitional separation bubbles, it seems plausible that the FLARE approximations could introduce errors of the same order as those resulting from the variations in the turbulence model.

In some instances, it has been possible to obtain numerical results by forward marching downstream of separation without introducing the FLARE approximation. Further justification would be

needed for general use of this approach, since a numerical stability analysis for simple linear model equations usually indicates instability when u is negative. For example, the two-point backward difference scheme applied to the linear model equation $u\phi_x = \phi_{yy}$ has an amplification factor $A = (1 + 4c \sin^2 \omega/2)^{-1}$, where $c = \Delta x / \Delta y^2$. Since $|A|$ exceeds unity for sufficiently small negative c , this algorithm is unstable for negative u when the mesh is refined. In forward marching their inverse boundary layer solutions into regions of reverse flow without using a FLARE type of approximation, Catherall and Mangler (1966) noted difficulty in obtaining solutions at some finite distance downstream of separation. This finite distance to produce observable problems with marching the boundary layer equations into reverse flow regions is consistent with the very reasonable notion of a spatial amplification rate depending not only on the sign of the convective velocity but also on the spatial mesh size.

As a final observation on the use of a FLARE type of approximate form of the interacted boundary layer equations, as has been noted earlier, most investigators do not remove the approximation as the solution converges. On the other hand, in those cases where spatial marching is performed into the separated flow and the FLARE approximation is removed, the iteration to enforce the interaction boundary condition has not yet been performed in the published literature. The only demonstrated procedure to date to successfully treat the interacted boundary layer equations, both applying the interaction boundary conditions and allowing for reverse flow velocities, is the physical time dependent approach. Although the observed convergence rates of some of the spatial forward marching iteration procedures appear very promising for solution of the FLARE approximation to the interacted boundary layer equations, these equations are not directly comparable to the unapproximated formulation solved for example by the time-dependent approaches, and thus relative efficiency of the two approaches has not yet been established.

Computational Efficiency and Related Topics

In discussing the interaction formulation in subsonic flow, it was assumed that for efficiency the Hilbert integral perturbation would be the method of choice to obtain the interacted potential flow. In transonic flow this no longer seems adequate and a more extensive inviscid flow calculation seems mandatory. As mentioned earlier for separated flow, LeBalleur (1978) and Carter (1979, 1981) have initiated such approaches. It is noted that a number of efficient iterative transonic potential flow solvers have become available and that it is possible that the boundary layer interaction could be incorporated into the iteration that would be required in any event to produce the basic uninteracted potential flow. Such a prospect is obviously interesting and much remains to be explored in this regard. The point remains that deleting the Hilbert integral in and of itself should not affect in any substantial way the various stability problems mentioned earlier. The stability problems arise from the interactive response of the numerical system representing the potential flow and boundary layer, the potential flow being approximated by a basic flow and a linearized correction. Improving the inviscid flow representation even to the extent of using the Euler equations, should not

fundamentally alter the interaction numerical stability unless the numerical interaction algorithm is changed.

The same is true for the boundary layer calculation. Also, it has been presumed in the preceding development that an (implicit) finite difference calculation of the boundary layer would be performed, as most investigators in recent years have elected to do. Treating the boundary layer by a momentum integral spatial marching approach does not remove the numerical problems concerned with branching, and although the Goldstein singularity and the reverse flow problems are not apparent, other singularities arise [Green (1965), Shamroth (1969), Cousteix, LeBalleur and Houdeville (1980)]. To this is added the need to characterize the mean velocity profile in some suitably general manner. In addition, for turbulent flow inherently the same basic information on the turbulent structure must be supplied, even if only in some moment form. Thus while boundary - layer momentum - integral calculation schemes have much to recommend them by way of computational efficiency, they do not by themselves present a solution to the interaction computational problems referred to earlier.

In reviewing the literature to try and establish the relative efficiencies of various numerical approaches, considerable difficulty is encountered. Often algorithms and codes are not optimized in view of their research nature, run times are available on dissimilar computers with unknown resource cost/time algorithms and/or relative efficiency. Only some rather general comments on efficiency can be made, in spite of its critical role. Taking the individual components of the formulation, the labor of computing each boundary-layer iteration or time step could be much less for an integral scheme which is comprised of a small system of ordinary differential equations. If it were necessary to remove or improve on the additional approximations required to construct the integral boundary layer approach, then a finite difference solution of the boundary-layer partial differential equations could be undertaken. From numerical studies in the literature on solution methodologies for the boundary layer equations, the computational efficiencies of the various possible approaches may be obtained. For the multiscale problem, highly efficient implicit finite difference schemes have been developed and currently generally require of order one CPU second on a CDC 7600 per thousand grid points to compute a solution or time step in either the direct or inverse mode. It should be possible to obtain solutions via boundary layer integral techniques using one to two orders of magnitude less computation. Insofar as the inviscid potential flow is concerned, fast iterative transonic solvers have been developed which require about five CPU secs per thousand mesh points on a CDC 7600 to achieve a suitably converged solution. For accuracy levels sufficient to define the drag of fairly conventional transonic airfoils, the present schemes require about five to ten thousand mesh points, distributed wisely, for the inviscid flow and about the same for the airfoil boundary layers (excluding the wake).

The situation becomes very fuzzy when the interactive coupling between the boundary layer and inviscid flow is allowed for. If one remains with the Hilbert integral as defining the inviscid flow perturbation, the required numerical evaluation introduces

AD-A134 151

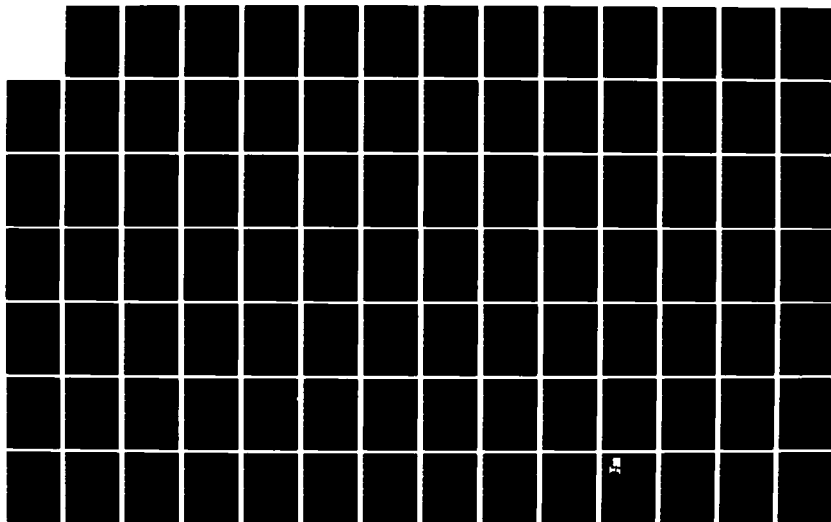
SYMPOSIUM ON NUMERICAL AND PHYSICAL ASPECTS OF
AERODYNAMIC FLOWS (2ND) 17-20 JANUARY 1983(U)
CALIFORNIA STATE UNIV LONG BEACH T CEBECI 1983

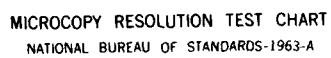
3/5

UNCLASSIFIED

F/G 20/4

NL





MICROCOPY RESOLUTION TEST CHART
NATIONAL BUREAU OF STANDARDS-1963-A

no significant computational labor relative to say a finite difference solution advancement of the complete boundary layer. Computing the boundary layer solution with interaction requires iteration, since boundary conditions cannot yet be applied fully implicit, and the number of iterations through the boundary layer equations can vary widely. In the time-dependent approach, the early variants with explicit interaction took up to three hundred time steps to achieve satisfactory convergence. More recent compressible time- and pseudo-time dependent linearized block implicit schemes for solving viscous flows have been able to substantially reduce the number of time steps to achieve the same degree of convergence by about a factor of five by applying the boundary conditions in a fully implicit manner, using time-step cycling and pseudo-time matrix conditioning. Thus, one could hope eventually to achieve a satisfactory overall solution for an interacted airfoil using an implicit finite difference solution for both the inviscid and viscous flow in about three to five minutes of CDC 7600 CPU time if the Hilbert integral approach were used. If the boundary layer were treated by a time dependent momentum integral technique, then it is conceivable that the required run time would be reduced by about an order of magnitude to virtually that of the computation of the uninteracted potential flow.

If the inverse forward-marching iteration approach is used, together with a FLARE approximation, recent developments have led to convergence being obtained in fifty or less iterations. Some authors report having developed displacement thickness correction schemes which result in satisfactory convergence being achieved in about twenty iterations. The achieved convergence rate appears to depend critically on the algorithm for correcting the imposed distribution of displacement thickness from a computed boundary-layer deduced free stream velocity. The use of a semi-implicit imposition of the coupling boundary condition appears beneficial. With this number of iterations, the run time would be similar to that which could be expected from a modern time-dependent approach. If the flow problems addressed required the removal of the FLARE approximation, then with the finite difference approach, it would appear that a nested inner iteration might have to be performed and the existing evidence is that this would result in a significant increase in computation effort.

If the Hilbert integral perturbation approach is not suitable, it does not appear that a converged inviscid flow solution would be required for each time or iteration advancement of the boundary layer equations. It does appear both feasible and advantageous to incorporate the boundary layer solution advancement into the basic iteration used to determine the potential flow. At present no studies are available which would give an indication if significant degradation of the inviscid flow calculation convergence would result.

As a final observation, with the Hilbert integral approach it appears at present that at least about one order of magnitude in computational effort is being saved by adopting the interacted boundary layer approach as opposed to treating the entire flow by efficiently solving the averaged Navier-Stokes equations.

REFERENCES

- Baum, E. and Denison, M.R.: "Interacting Supersonic Laminar Wake Calculations by a Finite Difference Method", AIAA Paper 66-454 (1966).
- Briley, W.R. and McDonald, H.: "Numerical Prediction of Incompressible Separation Bubbles", J. Fluid Mech., Vol. 69, Part 4 (1975) pp. 631-656.
- Briley, W.R.: "A Numerical Study of Laminar Separation Bubbles Using the Navier-Stokes Equations", J. Fluid Mech. 47 (1971) pp 713-736.
- Burggraf, O.R., Rizzetta, D., Werle, M.J. and Vatsa, V.N.: "Effect of Reynolds Number on Laminar Separation of a Supersonic Stream", AIAA Journal, Vol. 17, (April 1979) pp. 336-343.
- Carter, J.E.: "Numerical Solutions of the Navier-Stokes Equations for the Supersonic Laminar Flow Over a Two-Dimensional Compression Corner", NASA TR R-385 (July 1972).
- Carter, J.E.: "Inverse Solutions for Laminar Boundary Layer Flows With Separation and Attachment", NASA TR R-447 (1975).
- Carter, J.E. and Wornom, S.F.: "Solutions for Incompressible Separated Boundary Layers Including Viscous-Inviscid Interaction", NASA SP347 (1975).
- Carter, J.E.: "A New Boundary-Layer Inviscid Iteration Technique for Separated Flow", AIAA Paper 79-1450 (July 1979).
- Carter, J.E.: "Viscous-Inviscid Interaction Analysis of Transonic Turbulent Separated Flow", AIAA Paper 81-1241 (June 1981).
- Carter, J.E. and Vatsa, V.N.: "Analysis of Airfoil Leading Edge Separation Bubbles", NASA Contractor Report 165935, Contract NAS1-16585 (May 1982).
- Catherall, D. and Mangler, K.W.: "The Integration of the Two-Dimensional Laminar Boundary-Layer Equations Past a Point of Vanishing Skin Friction", J. Fluid Mech., Vol. 26 (1966) pp. 163-182.
- Cebeci, T.: "An Unsteady Laminar Boundary Layer with Separation and Reattachment", AIAA Journal, Vol. 16, No. 12, (Dec. 1978) pp. 1305-1306.
- Cebeci, T. and Schimke, S.: "The Calculation of Separation Bubbles in Interactive Turbulent Boundary Layers", (1982) To be published.
- Coisteix, J., LeBalleur, J-C. and Houdeville, R.: "Calculation of Unsteady Turbulent Boundary Layers in Direct or Inverse Mode, Including Reverse Flows-Analysis of Singularities", Rech. Aerosp. No. 1980-3 May-June.
- Crimi, P. and Reeves, B.L.: "Analysis of Leading-Edge Separation Bubbles on Airfoils", AIAA Journal, Vol. 14, (Nov. 1976) pp. 1548-1555.
- Crocco, L. and Lees, L.: "A Mixing Theory for the Interaction Between Dissipative Flows and Nearly Isentropic Streams", J. Aero. Sci., Vol. 19, No. 10 (1952).
- Davis, R.T.: "Numerical and Approximate Solution of the High Reynolds Number Small Separation Problem", Univ. of Cincinnati Dept. of Aero. Eng. Report No. AFL 76-8-24 (1976).
- Davis, R.T. and Rubin, S.G.: "Non-Navier Stokes Viscous Flow Computations", Computers and Fluids, Vol. 8, (1980) pp. 101-131.

- Garvine, R.W.: "Upstream Influence in Viscous Interaction Problems", *The Physics of the Fluids*, Vol. 11 (1968) pp. 1413-1423.
- Gaster, M.: "The Structure and Behavior of Laminar Separation Bubbles", *AFARD Conf. Proc. 4*, (1966) pp. 819-854.
- Ghia, U. and Davis, R.T.: "Navier-Stokes Solutions for Flow Past a Class of Two-Dimensional Semi-infinite Bodies", *AIAA Journal*, Vol. 12 (1974) pp. 1659-1665.
- Ghia, K.N., Ghia, U., Tesch, W.A.: "Evaluation of Several Approximate Models for Laminar Incompressible Separation by Comparison with Complete Navier-Stokes Solutions", *AGARD Conf. Proc. No. 168*, Flow Sep. (1975) pp. 6-1 to 6-15.
- Green, J.E.: "Two-Dimensional Turbulent Reattachment as a Boundary-Layer Problem", presented at AGARD Specialists Meeting on Separated Flows, Rhode-Saint-Genese, Belgium (May 1965).
- Jenson, R., Burggraf, O.R., and Rizzetta, D.P.: "Asymptotic Solution for Supersonic Viscous Flow Past a Compression Corner", *Proc. 4th Int. Conf. on Num. Meth. in Fluid Mech.*, Springer-Verlag, Lecture Notes in Physics (1975).
- Klineberg, J.M., Steger, J.L.: "On Laminar Boundary-Layer Separation", *AIAA Paper 74-94* (1974).
- Kwon, O.K. and Fletcher, R.H.: "Prediction of Incompressible Separated Boundary Layers Including Viscous-Inviscid Interaction", *J. Fluids Eng.*, Vol. 101, No. 4 (1979) pp. 466-472.
- Leal, L.G.: "Steady Separated Flow in a Linearly Decelerated Free Stream", *J. Fluid Mech.*, Vol. 59, (1973) pp. 513-535.
- LeBalleur, J.C.: "Couplage visqueux-non visqueux: methode numerique et applications aux ecoulements bidimensionnels transoniques et supersoniques", *Rech. Aerosp.*, Vol. 183 (1978) pp. 65-76. English translation ESA TT496.
- LeBalleur, J.C., Peyret, R. and Viviani, H.: *Numerical Studies in High Reynolds Number Aerodynamics*, Computers and Fluids, Vol. 8 (1980) pp. 1-30.
- Lighthill, J.: "On Boundary Layers and Upstream Influence. I. A Comparison Between Subsonic and Supersonic Flows", *Proc. Roy. Soc., A*, Vol. 217 (1953).
- Messiter, A.F.: *SIAM, J. Appl. Math.*, Vol. 18 (1970) p. 241.
- Murphy, J.D., Presley, L.L., and Rose, W.C.: "On the Calculation of Supersonic Separating and Reattaching Flows", *NASA SP 347* (1975).
- Neiland, V.Y.: *Mekh. Zh. i., Gaza* 4, 40 (1969)
- Phillips, J.H. and Ackerberg, R.C.: "A Numerical Method for Integrating the Unsteady Boundary-Layer Equations When There Are Regions of Backflow", *J. Fluid Mech.*, Vol. 58 (1973) p. 561.
- Reyhner, T.A. and Flugge-Lotz, I.: "The Interaction of a Shock Wave with a Laminar Boundary Layer", *Int. J. on Non-linear Mech.*, Vol. 3, No. 2 (1968) pp. 173-199.
- Rizzetta, D.P., Burggraf, O.R., and Jenson, R.: "Triple-deck Solutions for Viscous Supersonic and Hypersonic Flow Past Corners", *J. Fluid Mech.*, Vol. 89, Part 3 (1978) pp. 535-552.
- Shamroth, S.J.: "On Integral Methods for Predicting Shear Layer Behavior", *J. of App. Mech.*, Vol. 36 (Dec. 1969).
- Stewartson, K. and Williams, P.G.: "Self-Induced Separation", *Proc. of the Roy. Soc. of London, Ser. A*, Vol. 312 (Sept. 1969) pp. 181-206.
- Stewartson, K.: "Multistructured Boundary Layers on Flat Plates and Related Bodies", *Adv. in Appl. Mech.*, Vol. 14 (1974) pp. 145-239.
- Stratford, B.S.: "The Prediction of Separation of the Turbulent Boundary Layer", *J. Fluid Mech.*, Vol. 5, Part 1, (1959) pp. 1-16.
- Vatsa, V.N., Carter, J.E. and Swanson, R.C.: "Comparison of Solutions of the Navier-Stokes and Interacting Boundary-Layer Equations for Separated Turbulent Flow", Paper presented at ISCME Int. Conf. on Comp. Meth. and Exper. Meas., Wash., D.C., June 30-July 2, 1982.
- Veldman, A.E.P.: "New, Quasi-simultaneous Method to Calculate Interacting Boundary Layers", *AIAA Journal*, Vol. 19, No. 1 (Jan. 1981) pp. 79-85.
- Weinbaum, S. and Garvine, R.W.: "On the Two Dimensional Viscous Counterpart of the One Dimensional Sonic Throat", *J. Fluid Mech.*, Vol. 39, Part 1, (1969) pp. 57-85.
- Werle, M.J. and Davis, R.T.: "Incompressible Laminar Boundary Layers on a Parabola at Angle of Attack: A Study of the Separation Point", *J. of App. Math.*, Vol. 7 (March 1972).
- Werle, M.J. and Vatsa, V.N.: "New Method for Supersonic Boundary-Layer Separations", *AIAA Journal*, Vol. 12, No. 11 (Nov. 1974) pp. 1491-1497.
- Williams, P.G.: "A Reverse Flow Computation in the Theory of Self-Induced Separation", *Proc. 4th Int. Conf. Numer. Meth. Fluid Mech.*, Lecture Notes in Phys., Vol. 35 (1975) p. 445.

AN INTERACTIVE APPROACH TO SUBSONIC FLOWS WITH SEPARATION

Tuncer Cebeci
California State University, Long Beach

and

R. W. Clark
McDonnell Douglas Aircraft Company
Long Beach, California

Abstract

A viscous-inviscid interaction procedure is presented for computing incompressible separation bubbles in two-dimensional flow over lifting airfoils. The scheme consists of an inviscid-flow method, based on the technique of conformal mapping, together with an inverse boundary-layer method which makes use of the Cebeci-Smith algebraic eddy-viscosity formulation together with the Mechul-function approach. The coupling between the viscous and the inviscid calculations is achieved through the use of a set of interaction coefficients computed using the conformal mapping method. These coefficients define the relationship between the boundary-layer thickness, represented by means of a blowing-distribution on the airfoil surface, and the external inviscid velocity distribution. Results are presented for the calculation of separation bubbles occurring at the leading edge and midchord of the NACA 663-018 airfoil at both lifting and nonlifting conditions.

I. Introduction

An accurate calculation of the lift on an airfoil requires a modeling of the interaction between the inviscid flow away from the airfoil and the viscous flow close to the surface. In many cases of interest the boundary-layer flow may separate upstream of the trailing edge, causing a strong interaction between the viscous and the inviscid flow. For such cases if a boundary-layer method is used to account for the viscous effects, the solution obtained for the prescribed pressure distribution will break down at the point of separation where the equations become singular. On the other hand, if the boundary-layer method is reformulated as an inverse procedure so that the pressure distribution is not prescribed but computed as part of the solution, the singularity at separation can be avoided¹, and flows with small separation can be computed. This paper presents an interactive method for combining such an inverse boundary-layer procedure with an incompressible potential-flow calculation.

In addition to the separation near the trailing edge, small separation bubbles are observed on airfoils. They occur as the laminar boundary layer begins to separate from the surface, transition takes place, flow becomes turbulent and at a short distance downstream, it reattaches as a turbulent boundary layer. Such transitional bubbles have been observed in the midchord regions of comparatively thick airfoils at small angles of attack, as well as near the leading-edge of airfoils at higher angles of attack^{2,3}.

A review of the earlier work on separation bubbles was provided by Taniguchi⁴, and there are several more recent experimental studies such as the low Reynolds number work of Arena and

Mueller⁵ and Mueller and Batill⁶. An important theoretical contribution was provided by Briley and McDonald⁷ who combined a Navier-Stokes calculation in the separation region with a boundary-layer calculation elsewhere. An interactive boundary-layer approach was used by Kwag and Pletcher⁸, and also by Crimi and Reeves⁹ who used an integral boundary-layer method with the interaction effects confined to the immediate vicinity of the separation bubble.

Recently a new interactive approach was proposed by Veldman¹⁰ in which the viscous perturbation to the inviscid velocity distribution is computed by a thin airfoil approximation. This approach was used by Cebeci, Stewartson and Williams¹¹ to study separation bubbles near the leading edge of a thin airfoil and by Cebeci and Schimke¹² in an investigation of mid-chord separation bubbles at small angles of attack. However, at higher angles of attack the thin airfoil approximation, as implemented in references 11 and 12, does not account for the change in lift on an airfoil due to the viscous effects. This paper therefore presents a generalization of this approach in which the thin airfoil approximation is replaced by a surface singularity method.

The new method has been applied to the calculation of the flow over the NACA 663-018 airfoil, at both lifting and nonlifting angles of attack, and the results are compared with the experimental data obtained by Gault³. For small angles of attack the results are in agreement with those obtained by Cebeci and Schimke¹². At higher angles of attack, converged solutions are obtained for flows involving both separation bubbles and trailing-edge separation. The comparison of the computed pressure distribution with the experimental data around the nose indicates that the method does not fully account for the viscous effects, particularly as the angle of attack increases. This discrepancy is believed to be due to the fact that the effect of the viscous wake on the external velocity distribution has been neglected. Further work is planned to extend the interactive boundary-layer calculation into the near-wake region.

II. Governing Equations

The boundary-layer equations for steady incompressible flow are well known and with the concept of eddy viscosity (ϵ_m), they can be written in the form

$$\frac{\partial u}{\partial x} + \frac{\partial v}{\partial y} = 0 \quad (1a)$$

$$u \frac{\partial u}{\partial x} + v \frac{\partial u}{\partial y} = u_e \frac{du_e}{dx} + \frac{\partial}{\partial x} \left(b \frac{\partial u}{\partial y} \right) \quad (1b)$$

while $b = \nu + \epsilon_m$.

Eqs. (1) are subject to the boundary conditions given by

$$y = 0; u = v = 0, \quad y = \delta; u = u_e(x) \quad (2)$$

In Eq. (2), the external velocity distribution $u_e(x)$ is obtained either from experiment or from inviscid flow theory. In the latter case it is often necessary to consider the viscous effects on the calculated external velocity distribution. One convenient way of doing this is to write the edge boundary condition with $u_e^0(x)$ denoting the inviscid velocity distribution and δu_e the perturbation velocity due to the viscous effects as

$$u_e(x) = u_e^0(x) + \delta u_e \quad (3)$$

The perturbation velocity δu_e can be computed in several ways. In the scheme used by Yeldman¹⁰, Cebeci et al.¹¹, and Cebeci and Schimke¹², this is done by using a thin airfoil approximation,

$$\delta u_e = \frac{1}{\pi} \int_{x_a}^{x_b} \frac{d}{d\xi} (u_e \delta^*) \frac{d\xi}{x - \xi} \quad (4)$$

Here $d/dx (u_e \delta^*)$ denotes the blowing velocity used to simulate the boundary layer in the interaction region (x_a, x_b) . However, for airfoils at higher angles of attack, this approach becomes less accurate. Under such conditions the boundary-layer separation at the trailing-edge can cause significant changes to the airfoil circulation which is not accounted for by this approach. This paper presents an alternative formulation to Eq. (4) in which the interaction effects are calculated in terms of a surface singularity distribution on the airfoil surface. In this way the change in lift due to the viscous effects can be incorporated into the interaction procedure. The approach described here makes use of the conformal mapping techniques, developed by Halsey¹³, to calculate the perturbation velocity. Thus, if $|dz/d\zeta|$ is the modulus of the derivative of the function which maps the airfoil to a circle, the perturbation velocity on the airfoil can be written as

$$\delta u_e(\theta) = \frac{\int_0^{2\pi} V_n(\theta') [\cot \frac{1}{2}(\theta - \theta') + \cot \frac{1}{2} \theta'] d\theta'}{2\pi |dz/d\zeta|} \quad (5)$$

Here $V_n(\theta)$ denotes the blowing velocity in the circle plane given by

$$V_n(\theta) = \frac{d}{ds} (u_e \delta^*) \left| \frac{dz}{d\zeta} \right| \quad (6)$$

Introducing a discrete approximation into Eqs. (5) and (6), the external velocity distribution at a point on the airfoil, Eq. (3), can be written as

$$u_e = u_e^0 + \sum_{j=1}^n c_{ij} [(u_e \delta^*)_j - (u_e \delta^*)_j] \quad (7)$$

where $[c_{ij}]$ is a matrix of interaction coefficients, and where the computed velocity distribution u_e corresponds to the displacement thickness δ^* obtained in each sweep as we shall discuss later. The interaction coefficient matrix depends on the airfoil geometry and on the boundary-layer spacing used around the airfoil, but it can be computed once and for all at the start of the calculation.

III. Turbulence Model

The boundary-layer equations outlined above make use of the eddy-viscosity concept which requires a turbulence model. This present study uses the algebraic eddy-viscosity formulation developed by Cebeci and Smith¹⁴. Two separate formulas are used to compute the eddy viscosity, ϵ_m . In the inner region of the boundary layer, $0 \leq y \leq y_c$, we use

$$(\epsilon_m)_i = \{0.4y[1 - \exp(-y/A)]\}^2 \left| \frac{\partial u}{\partial y} \right| \gamma_{tr} \quad (8)$$

where

$$A = 26\nu_\tau^{-1} [1 - 11.8p^+]^{-1/2}, \quad u_\tau = \left(\frac{\tau}{\rho} \right)^{1/2}_{\max}$$

$$p^+ = \frac{\nu u_e}{u_e^3} \frac{du_e}{dx} \quad (9)$$

In the outer region, $y \geq y_c$, we use

$$(\epsilon_m)_o = 0.0168 \left| \int_0^\infty (u_e - u) dy \right| \gamma_{tr} \quad (10)$$

The value of y_c is defined by the condition that $(\epsilon_m)_i = (\epsilon_m)_o$ which ensures the continuity of the eddy-viscosity across the boundary layer.

The intermittency factor γ_{tr} accounts for the transition which exists between the laminar and turbulent. The formula used here is that suggested by Chen and Thyson¹⁵,

$$\gamma_{tr} = 1 - \exp \left[-G(x - x_{tr}) \int_{x_{tr}}^x \frac{dx}{u_e} \right] \quad (11)$$

where x_{tr} defines the location of the start of transition. The empirical factor G is given by

$$G = \frac{1}{1200} \frac{u_e^3}{\nu^2} R_{x_{tr}}^{-1.34} \quad (12)$$

with $R_{x_{tr}}$ corresponding to the transition Reynolds number, $(u_e x / \nu)_{tr}$.

IV. Solution Procedure

When the boundary-layer equations are coupled to the external inviscid-flow equations, two distinct regions are identified. The first is the weakly interacting region in which the boundary layer remains thin and attached. In this region the boundary-layer equations are solved with the specified external velocity distribution, a procedure which we will refer to as the standard problem. In a region of strong viscous-inviscid interaction with flow separation, the standard problem breaks down and as a result we employ an inverse boundary-layer method and compute the external velocity as part of the boundary-layer solution.

In order to improve the behavior of the solutions near the leading-edge stagnation point and reduce the sensitivity of the solutions to the x-spacing, we use similarity variables for the standard problem¹⁶. Thus, with the definition of stream function ψ and the Falkner-Skan transformation,

$$\eta = \left(\frac{u_e}{\sqrt{x}}\right)^{1/2} y, \quad \psi = (u_e \sqrt{x})^{1/2} f(x, \eta), \quad (13)$$

Eqs. (1) can be written as

$$(bf'')' + \frac{m+1}{2} ff'' + m[1 - (f')^2] = x(f' \frac{\partial f'}{\partial x} - f'' \frac{\partial f}{\partial x}) \quad (14)$$

Here the primes denote differentiation with respect to η , and m is a dimensionless pressure gradient parameter defined by $m = (x/u_e)(du_e/dx)$. The boundary conditions given by Eq. (2) can also be written as

$$\eta = 0; \quad f = f' = 0; \quad \eta = \eta_e; \quad f' = 1 \quad (15)$$

In the interaction region, the inverse boundary-layer method is formulated in terms of primitive variables in which a dimensionless normal coordinate Y and the dimensionless stream function, F , are defined by

$$Y = \left(\frac{u_0}{\sqrt{L}}\right)^{1/2} y, \quad \psi = (u_0 \sqrt{L})^{1/2} F(x, Y) \quad (16)$$

Here L and u_0 denote the reference length and velocity, respectively. In terms of these variables and with primes now denoting differentiation with respect to Y , Eqs. (1) and (2) can be written as

$$(bF'')' + \bar{u}_e \frac{d\bar{u}_e}{dx} = F' \frac{\partial F'}{\partial x} - F'' \frac{\partial F}{\partial x} \quad (17)$$

$$Y = 0; \quad F = F' = 0; \quad Y = Y_e; \quad F' = \bar{u}_e \quad (18)$$

where $\bar{u}_e = u_e/u_0$.

To perform the inverse boundary-layer calculations at $x = x_i$, in addition to the boundary conditions given by Eq. (18), another condition is derived from Eq. (7) which contains the unknowns u_{e1} and δ_1^* . Rearranging Eq. (7), we get

$$u_{e1}(1 - c_{11}\delta_1^*) = g_1, \quad (19)$$

where

$$g_1 = u_{e1}^{\kappa} + \sum_{j=1}^{i-1} c_{1j}[(u_e \delta^*)_j - (u_e \delta^{\kappa})_j] \quad (20)$$

In terms of dimensionless variables defined by Eq. (16), Eq. (19) can be written as

$$F_e' - c_{11} \left(\frac{\sqrt{L}}{u_0}\right)^{1/2} (Y_e F_e' - F_e) = \bar{g}_1 \quad (21)$$

where $\bar{g}_1 = g_1/u_0$.

The solution of the system for the inverse problem given by Eqs. (17), (18) and (21) is obtained in an iterative manner by performing several sweeps for both the upper and lower surfaces of the airfoil. For the first sweep where $\kappa = 0$, u_e is the inviscid velocity distribution. However, after each complete sweep, this velocity u_e^{κ} is recomputed for the next sweep.

Kellers' box method is used to solve both the standard and the inverse problems with the Mechul function approach being used for the inverse problem. A full account of this method is given in several references, for example, see ref. 16. When computing separated flow, the FLARE approximation is applied so that the convective term $F'(\partial F'/\partial x)$ in Eq. (17) is set equal to zero in the recirculating region of the flow. For cases involving small separated regions, this is an adequate approximation although for flows involving larger regions of separation, it can be improved as described in refs. 16 and 17.

V. Results and Discussion

The method described in previous sections has been applied to the calculation of the viscous flow over the symmetric airfoil, NACA 663-018, for which experimental data was obtained by Gault³. The results presented here are for the nonlifting case ($\alpha = 0^\circ$) and for two lifting cases, ($\alpha = 7^\circ$ and $\alpha = 12^\circ$) for a Reynolds number $R_c = 2 \times 10^6$ based on the airfoil chord.

The experimental data indicates that for low angles of attack the flow remains laminar until the midchord region. The flow then separates, becomes transitional and reattaches as a turbulent boundary layer. At higher angles of attack, a separation bubble forms near the leading edge which also reattaches as a turbulent boundary layer.

The midchord separation bubble case has been examined in detail by Cebeci and Schimke¹² using the thin airfoil approximation for the interaction coefficients based on Eq. (4). For low angles of attack, the boundary layer remains attached at the trailing edge, and the viscous perturbation to the external flow is small. Equation (4) is therefore a good approximation to this viscous perturbation. The current method has therefore been compared with this earlier method for the nonlifting case and these results are presented first before discussing the results for the higher angles of attack.

Our calculations and those of Cebeci and Schimke¹² indicate that the specification of the transition location has a significant effect on the computed boundary-layer behavior. If the transition location is specified a very short distance upstream of the laminar separation point, then the extent of the separation bubble is reduced or eliminated entirely. On the other hand, if the transition is specified a little downstream of this point, then the separated flow region grows with each sweep, eventually extending to the trailing edge, without any signs of numerical difficulties. In subsequent sweeps, the solutions, however, become unstable and the calculations break down. An empirical formula has therefore been used to compute the transition location for this midchord separation bubble. The relationship used is that proposed by Crimi and Reeves⁹ which indicates that, at the transition point

$$y_{u=0} = 10^6 / [\delta^*(u_e/\nu)^2]_s \quad (22)$$

where $y_{u=0}$ is the distance from the wall at which the streamwise velocity is zero, while the subscript s denotes the values computed at the separation point. Thus, when a laminar separation is encountered, the right-hand side of Eq. (22) is computed. The left-hand side is then evaluated at

each station, and the turbulent flow calculation is started at the point at which Eq. (22) is satisfied.

Figure 1 shows the computed wall shear parameter F_w for the converged solution plotted versus the airfoil surface distance measured from the leading edge. This figure also shows the values computed by Cebeci and Schimke¹². The two methods can be seen to agree well through the separation bubble, although they differ nearer the trailing edge. This is due to the fact that the current method takes into account the airfoil geometry in that region. Gault's experimental data indicates that the separation bubble extends from $(s/c) = 0.62$ to 0.725 . The calculated results can be seen to predict the length of the separation bubble well, although its location is further downstream than that measured by Gault³.

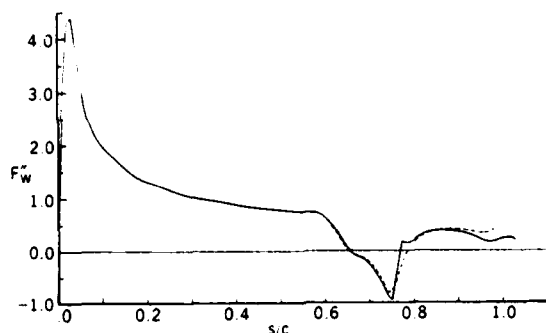


Fig. 1. Computed wall shear parameter, F_w , for $\alpha = 0^\circ$, $R_c = 2 \times 10^6$. Comparison of present method (solid line) and ref. 12 (dashed line).

The calculated velocity profiles are very close to the results of thin airfoil method used by Cebeci and Schimke¹². Figure 2 shows the computed velocity profiles compared with the experimental data at several stations through the separation bubble. The agreement is again good upstream of about $(s/c) = 0.72$ after which the measured boundary layer reattaches.

Figure 3 compares the computed pressure distribution over the airfoil with the experimental values measured by Gault³. The computed pressures

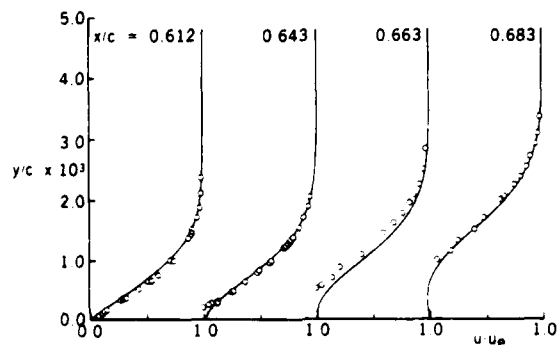


Fig. 2 Comparison of computed (solid line) and measured (symbols) velocity profiles for $\alpha = 0^\circ$, $R_c = 2 \times 10^6$.

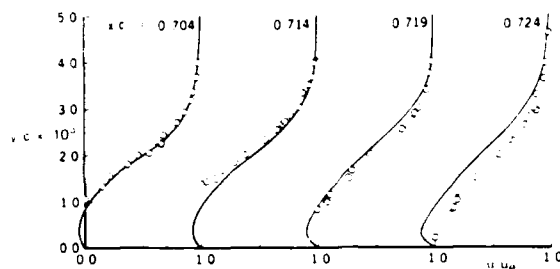


Fig. 2 Continued.

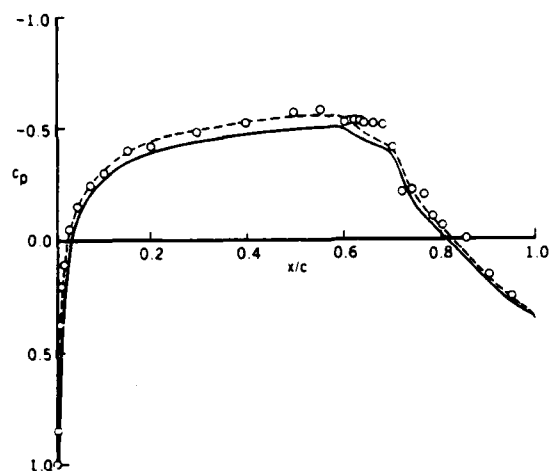


Fig. 3 Comparison of measured pressure distribution (symbols) and computed viscous solution with (dashed line) and without (solid line) tunnel wall correction for $\alpha = 0^\circ$, $R_c = 2 \times 10^6$.

are seen to be too low even forward of the separation bubble where the viscous effects are small. This discrepancy is mainly due to wind-tunnel blockage effects present in the experimental data. A purely inviscid calculation was therefore performed to evaluate the effects of the wind tunnel corresponding to the model size used by Gault. This was achieved using the multielement mapping method, developed by Halsey¹³, in which the upper and lower tunnel walls are simulated by two flat plates aligned with the freestream, and extending fore and aft of the airfoil. For this particular calculation, the flat plates were located one chord above and below the airfoil, and extending one chord fore and aft of the leading and trailing edges. Figure 4 shows the pressure distribution with and without this tunnel correction. This figure also shows the measured pressures obtained for a Reynolds number of 10^7 , showing that the tunnel interference does account for most of the discrepancy observed in the inviscid solution. This same wind-tunnel correction has been applied to the computed pressure distribution in Fig. 3. There is still, however, some difference between the computed and the measured pressures through the separation bubble, particularly at the reattachment point.

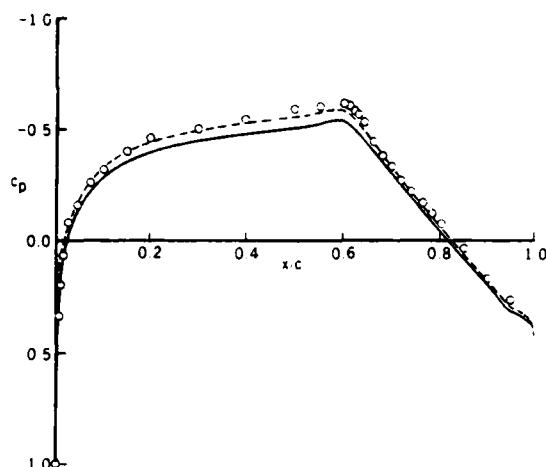


Fig. 4. Comparison of measured pressure distribution (symbols) and inviscid solution with (dashed line) and without (solid line) tunnel wall correction for $\alpha = 0^\circ$, $R_c = 10^7$.

This method has also been applied to the same airfoil at two angles of attack, 7° and 12° , for which there is a leading-edge separation bubble. For both of these cases solutions were obtained through the boundary-layer separation and reattachment, and also in the separated region close to the trailing edge.

As in the calculation of midchord separation bubbles, the transition location has a very important influence on the size of the leading-edge separation bubble. It is interesting to note that Eq. (22) is an empirical criterion based on data from leading-edge separation, including the two lifting cases considered here. However, attempts to use this formula for the calculation of leading-edge bubbles have not been successful since the size of the separation region is too small. For these cases there is a very sharply defined pressure peak near the leading edge. The transition location was therefore taken to be at the pressure peak for a number of iterations until the boundary-layer solution near the trailing edge had stabilized. The transition point was then moved downstream in order to compute the leading-edge separation.

Figures 5 and 6 show the computed wall shear parameter for the upper surface at 7° and 12° , respectively. At 7° , the computed leading-edge separation bubble is very small, with a larger bubble being computed at 12° . However, for both cases the method is able to compute a converged solution through the boundary-layer separation and reattachment, as well as through the trailing-edge separation. Figure 7(a) shows the computed pressure distribution for 7° for the inviscid and the viscous calculations, for which the computed lift coefficients are 0.87 and 0.73, respectively. The pressure distribution around the leading edge is shown in figure 7(b), along with the measured pressure distribution obtained by Gault³. At 12° , the computed lift coefficients for the inviscid and the viscous calculations are 1.49 and 1.22, respectively, and the pressure distributions are shown in Figs. 8(a) and (b). For the lower angle of attack, the agreement between the computed and the

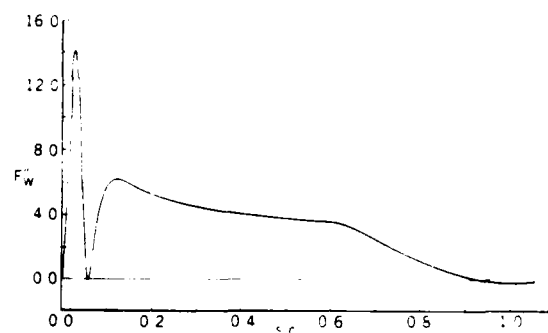


Fig. 5. Computed wall shear parameter, F_w'' , for $\alpha = 7^\circ$, $R_c = 2 \times 10^6$.

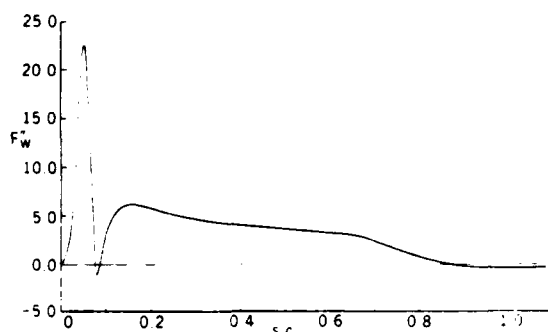


Fig. 6. Computed wall shear parameter, F_w'' , for $\alpha = 12^\circ$, $R_c = 2 \times 10^6$.

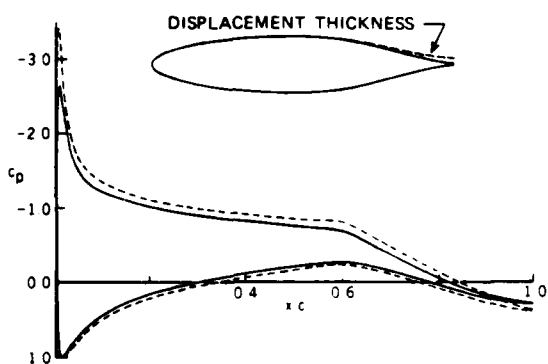


Fig. 7a. Comparison of computed viscous (solid line) and inviscid (dashed line) pressure distributions for $\alpha = 7^\circ$, $R_c = 2 \times 10^6$.

experimental pressure distribution is reasonable although at 12° , the computed results account for only about half of the difference between the inviscid pressure and the measured values. Also, the computed results do not pick up the rapid pressure rise which occurs with the reattachment of the leading-edge bubble.

There are two additional factors which must be accounted for in order to improve the computed results. As for the nonlifting case, we can expect there to be some significant effect due to the wind tunnel blockage effect, which would increase the

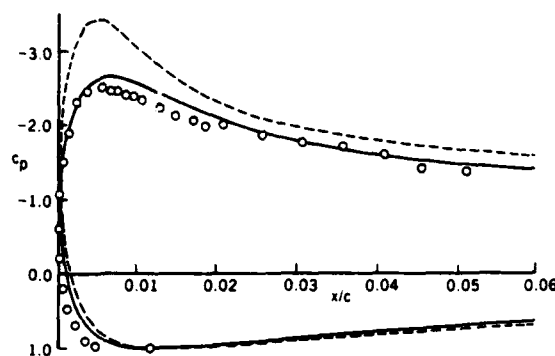


Fig. 7b. Comparison of measured pressure distribution (symbols) with computed viscous (solid line) and inviscid (dashed line) solutions for $\alpha = 7^\circ$, $Re = 2 \times 10^6$.

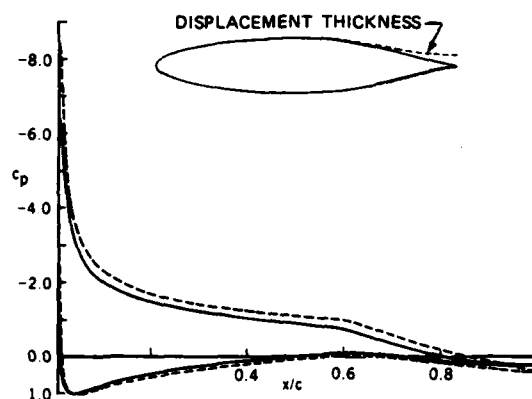


Fig. 8a. Comparison of computed viscous (solid line) and inviscid (dashed line) pressure distributions for $\alpha = 12^\circ$, $Re = 2 \times 10^6$.

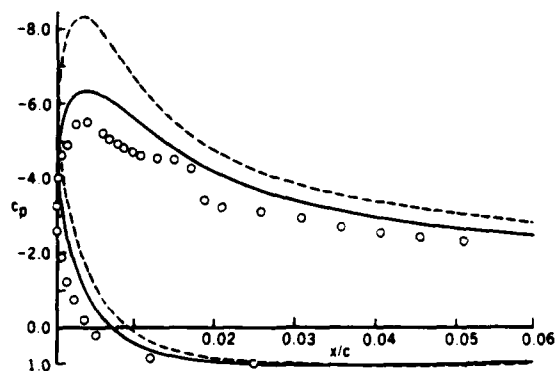


Fig. 8b. Comparison of measured pressure distribution (symbols) with computed viscous (solid line) and inviscid (dashed line) solutions for $\alpha = 12^\circ$, $Re = 2 \times 10^6$.

pressure peak for the inviscid solution. On the other hand, the current calculation does not include the effects of the viscous wake, and in order to compute the airfoil circulation it is important to model the flow correctly in the trailing-edge region. The method will therefore be extended to

include the effects of the viscous interaction on the wake. Currently the approach described here is being also extended to the calculation of interacting flows on multielement airfoils. This code will also be used to simulate the wind tunnel wall effects as outlined above.

Acknowledgments: This research was supported under the National Science Foundation Grant No. MEA-8018565.

VI. REFERENCES

1. Catherall, D. and Mangler, K.W.: The Integration of the Two-Dimensional Laminar Boundary-Layer Equations Past the Point of Vanishing Skin Friction. *J. Fluid Mech.* **26**, pp. 163-183, 1966.
2. Burshall, W.J. and Loftin, L.K.: Experimental Investigation of Localized Regions of Laminar-Boundary-Layer Separation. NACA TN 2338, 1951.
3. Gault, D.E.: An Experimental Investigation of Regions of Separated Laminar Flow. NACA TN 3505, 1955.
4. Tani, I.: Low-Speed Flows Involving Bubble Separations. *Progress in Aeronautical Sciences*, Vol. 5, Pergamon Press, NY, pp. 70-103, 1964.
5. Arena, A.V. and Mueller, T.J.: On the Laminar Separation, Transition, and Turbulent Reattachment of Low Reynolds Number Flows Near the Leading Edge of Airfoils. *AIAA J.* **18**, pp. 747-753, July 1980.
6. Mueller, T.J. and Batill, S.M.: Experimental Studies of Separation on a Two-Dimensional Airfoil at Low Reynolds Numbers. *AIAA J.* **20**, pp. 457-463, Apr. 1982.
7. Briley, W.R. and McDonald, H.: Numerical Prediction of Incompressible Separation Bubbles. *J. Fluid Mech.* **69**, Pt. 4, pp. 673-686, 1975.
8. Kwon, O.K. and Pletcher, R.H.: Prediction of Incompressible Separated Boundary Layers Including Viscous-Inviscid Interaction. *J. Fluids Eng.*, **101**, pp. 466-472, 1979.
9. Crimi, P. and Reeves, B.L.: Analysis of Leading-Edge Separation Bubbles on Airfoils. *AIAA J.* **14**, pp. 1548-1555, Nov. 1976.
10. Veldman, A.E.P.: New, Quasi-Simultaneous Method to Calculate Interacting Boundary Layers. *AIAA J.* **19**, pp. 79-85, Jan. 1981.
11. Cebeci, T., Stewartson, K. and Williams, P.G.: Separation and Reattachment Near the Leading Edge of a Thin Airfoil at Incidence. Presented at AGARD Symp. on Computation of Viscous-Inviscid Interacting Flows, Colorado Springs, 1980.
12. Cebeci, T. and Schimke, S.M.: The Calculation of Separation Bubbles in Interactive Turbulent Boundary Layers. Submitted for publication.
13. Halsey, N.D.: Potential Flow Analysis of Multielement Airfoils Using Conformal Mapping. *AIAA J.* **17**, pp. 1281-1288, Dec. 1979.

14. Cebeci, T. and Smith, A.M.O.: Analysis of Turbulent Boundary Layers. Academic Press, NY, 1974.
15. Chen, K.K. and Thyson, N.A.: Extension of Emmons' Spot Theory to Flows on Blunt Bodies. AIAA J. 5, pp. 821-825, May 1971.
16. Bradshaw, P., Cebeci, T. and Whitelaw, J.H.: Engineering Calculation Methods for Turbulent Flows. Academic Press, London, 1981.
17. Cebeci, T. and Chiu, J.: An Inverse Boundary-Layer Method for Compressible Unsteady Laminar and Turbulent Flows. NASA Report in press, 1983.

A CALCULATION METHOD OF LEADING EDGE SEPARATION BUBBLES

by

C. GLEYZES, J. COUSTEIX, J.L. BONNET

ONERA/CERT
2 avenue Edouard Belin
31055 TOULOUSE CEDEX, FRANCE

ABSTRACT

This paper is devoted to the method we have developed for the calculation of transitional separation bubbles at the leading edge of an airfoil at incidence.

This method is mainly based on :

- the solution in inverse mode, of global boundary layer equations ;
- a viscous-inviscid interaction scheme ;
- the solution, in inverse mode too, of a local inviscid problem.

The experimental study we have performed at the same time is also briefly reported. In fact, we have emphasized the different points which strongly guided us in the choice of the assumptions we have introduced in this method. In particular, the detailed study of transition in a separation bubble gave us the physics of the phenomenon and was at the origin of the transition criterion we have developed and introduced in the boundary layer calculation.

INTRODUCTION

The positive pressure gradient, downstream of the suction peak at the leading edge of an airfoil at incidence, may, under some conditions, induce large perturbations on the general pattern of the flow.

If Reynolds number (for instance $Re_c = U_\infty c / \nu$ where c is the chord of the airfoil) is large, the boundary layer becomes rapidly turbulent and is not much affected by this gradient. On the opposite, if Re_c is low enough for the boundary layer to remain laminar, separation may occur, followed generally by a transitional bubble.

Previous studies have already shown that the effect of this bubble upon the downstream turbulent boundary layer is important and that it must be taken into account to be able, for instance, to predict the possible separation at the rear of the airfoil.

In this purpose, we have developed a calculation method which deals with short separation bubbles, in two-dimensional subsonic compressible flows.

In parallel, an experimental study [1] has been carried out, which strongly helped in the choice of the assumptions we have introduced in the method.

Before presenting the calculation method, we will give a brief summary of this experimental study.

1. EXPERIMENTAL STUDY

1.1. Global results

A first series of experiments has been carried out on a 200 mm chord ONERA LC100D peaky profile.

Wall pressure distribution has been obtained for a range of Reynolds number Re_c between $8 \cdot 10^4$ and 10^6 and incidence between 3° and 8° .

The corresponding velocity distributions are presented in figure 1, for an incidence of $7^\circ 30'$.

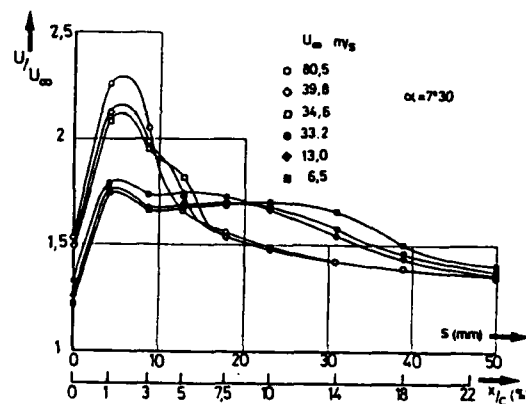


Fig. 1 - LC100D profile-Velocity distributions in the leading edge region

The main results of this study are :

- a) for short bubbles (here, for $Re_c > 0.45 \cdot 10^6$), the velocity distribution is close to the high Reynolds number velocity distribution, except in a small domain around the bubble, where the difference is however small ;
- b) for a given incidence, exists a Reynolds number for which a sudden change in the velocity distribution occurs, corresponding to the classical bursting of a short bubble in a long bubble.

An important remark about this bursting point is that no discontinuity in the physical size of the separation region seems to exist /Ref. 2/. This can be seen in figure 2 where momentum thickness at 75 % of the chord is plotted, versus upstream velocity. For the corresponding bursting point, there is a change in the slope of the curve, but continuity in the evolution. The increase in momentum thickness is also shown, compared with a calculation assuming transition at separation, with continuity of momentum thickness. This increase is very large for long bubbles and is far from negligible for short bubbles.

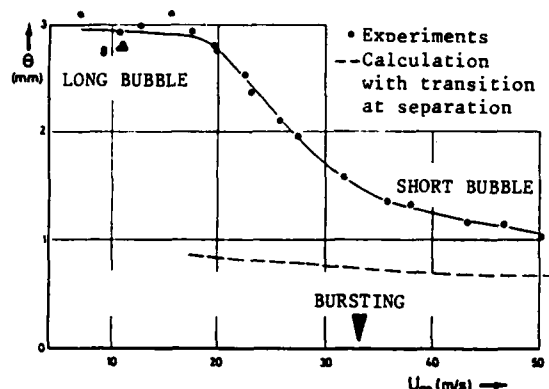


Fig. 2 - LC100D profile-Momentum thickness at $x/c = 75\%$ ($\alpha = 7^\circ 30'$)

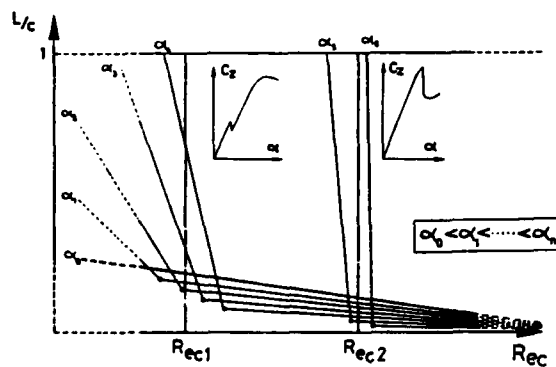


Fig. 3 - Schematic evolution of the length of leading edge separation bubbles

A global result, collecting various information about the different types of bubbles /Ref. 2, 3, 4/ is presented in figure 3.

We have schematically plotted the evolution of a characteristic length L/c of the separated region, for different incidences, versus chord Reynolds number. Below a given incidence (here α_0), no separation occurs and boundary layer remains laminar up to natural transition.

For a moderate incidence α_2 (between 5 and 10° depending upon the airfoil), the evolution of L/c , when decreasing Reynolds number, is characterized by a continuous increase, with a much higher rate below bursting Reynolds number, leading progressively to a complete separation. The change in the slope of the curves increases when incidence increases.

If we look at the evolution of L/c for a given Reynolds number, two major schemes exist :

- If Re_c is low (Re_{c1} for instance), increasing angle of attack induces first decrease in the size of the short bubble, up to $\alpha = \alpha_2$. With a further increase, bubble bursts and the size of the long bubble now increases with incidence, leading to a progressive stalling. The lift coefficient curve may or not present a break at the bursting incidence, according to the airfoil.
- If Re_c is high (Re_{c2} for instance), the evolution is similar up to the bursting point, but due to the higher pressure gradient, an increase in incidence causes boundary layer not to reattach, and stalling is then sudden.

1.2. Detailed results about short separation bubbles

A study of the short leading edge separation bubbles has then been carried out on a special model, called "enlarged leading edge". This model, presented in figure 4, corresponds to a 2.5 m chord ONERA D airfoil, truncated and fitted with a blown flap. Position of stagnation point and consequently velocity distribution in the leading edge region could be set by changing incidence, flap angle or blowing rate /Ref. 4/.

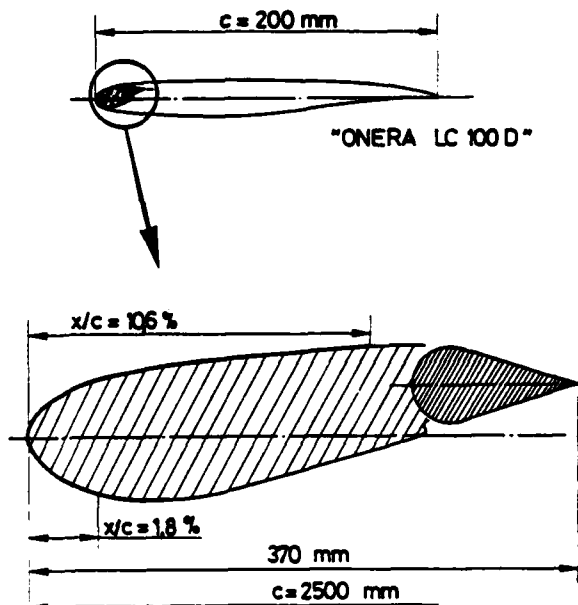


Fig. 4 - Experimental apparatus

These experiments consisted of :

- pressure distribution measurements ;
- hot wire and LDA boundary layer surveys (mean and longitudinal fluctuation velocity profiles) ;
- oil surface and smoke visualization (using the laser light sheet technique) ;
- hot wire signal spectral analysis ;

for a wide range of Reynolds number ($10^6 \leq Re_c \leq 8.10^6$) and two different levels of turbulence ($Tu_e = 0.4\%$ and $Tu_e = 2.5\%$).

In the presentation of the method, we will point out the assumptions deduced from these results.

2. PRELIMINARY REMARKS

In a classical "direct" boundary layer method, the external flow is the imposed input, the evolution of the different characteristic quantities of the viscous flow being the output of the calculation.

For the present problem, this technique leads to a singularity in the vicinity of the zero skin friction point /Ref. 5/, even if the experimental pressure distribution is the data of the calculation. A simple analysis of global boundary layer equation and of the related turbulent closure relationships /Ref. 6/ has shown that the system is singular at separation, except if the pressure gradient fills up a compatibility relation, in which case the system remains however undeterminate. The same conclusions are valid for a laminar separation, due to a similar behaviour of closure relationships in the neighbourhood of separation.

The adjustment of the pressure distribution to the compatibility condition leads to the inverse mode formulation of the problem /Ref. 7, 8/. The external velocity is then the solution of the boundary layer equations, a distribution of a boundary layer parameter (δ_1 or $Cf/2$ for instance) being the input of the calculation.

If one wants to predict the evolution of the boundary layer through a separated region, an inviscid calculation must be associated, through a viscous-inviscid interaction procedure. The inviscid calculation may be done in direct or inverse mode. We have chosen this second solution in spite of a strong under-relaxation necessary to the stability of the method.

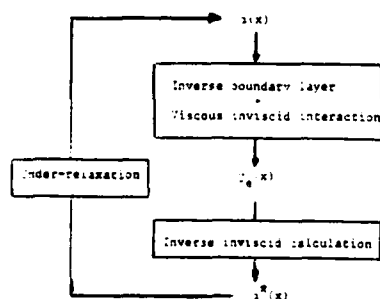


Fig. 5 - Flow-chart of the complete method

A simple flow-chart is presented in figure 5, where α is the quantity involved in the viscous-inviscid interaction.

3. BOUNDARY LAYER EQUATIONS

Because it is fast and satisfactorily accurate, it is an integral method which has been chosen for the boundary layer calculation.

The main equation is the streamwise momentum equation ; in some methods, the auxiliary equation may change with the nature of the boundary layer :

- global continuity (entrainment) equation in turbulent flow ;
- global kinetic energy equation in laminar flow.

For the present purpose, we have to deal successively with a laminar, transitional and turbulent boundary layer. To avoid numerical difficulties which could arise from a change in the equations, we have been brought to keep the same auxiliary equation all along the calculation domain : the entrainment equation.

Consequently, the system to be solved is :

$$\begin{cases} \frac{Cf}{2} = \frac{d\theta}{dx} + \theta \left[(H+2) \frac{1}{U_e} \frac{dU_e}{dx} + \frac{1}{\rho_e} \frac{d\rho_e}{dx} \right] \\ C_E = \frac{1}{\rho_e U_e} \frac{d}{dx} (\rho_e U_e (\delta - \delta_1)) \end{cases} \quad (3.1.)$$

δ_1 being known through the viscous-inviscid interaction relationship. Equations (3.1.) form a system of two equations for the five unknown quantities : $Cf/2$, C_E , θ (or H), δ and U_e .

Three closure relationships are needed.

4. CLOSURE RELATIONSHIPS

We will just give here the general guideline of these relationships. Detailed formulation can be found in /Ref. 9/.

4.1. Incompressible laminar flow

4.1.1. Similarity solutions

FALKNER-SKAN self-similarity solutions are a classical way of getting closure relationships for attached laminar boundary layers. They provide a family of velocity profiles, depending upon a pressure gradient parameter β ; $\beta = -0.199$ is the minimum value of this parameter and corresponds to the separation.

For boundary layers with reverse flows, the same equations can provide a family of velocity profiles, depending upon the same parameter. It can be shown that for negative values of β ($-0.199 \leq \beta \leq 0$), the solution is not unique and two profiles can be obtained for the same value of β : the classical solution and a separated one, obtained by setting $\frac{\partial U}{\partial y} < 0$ at wall.

These solutions, calculated for example by CHRISTIAN and HANKEY /Ref. 10/ provided the separated self-similarity profiles, complementary to the attached profiles we already had /Ref. 11/.

4.1.2. Closure relationships

It is then easy, for each velocity profile, to get the characteristic boundary layer quantities needed to close the system.

These closure relationships have finally to be represented in terms of an adequate pressure gradient parameter. In spite of its wide variations for separated flows, the shape parameter H seemed to be adequate. Closure relationships could then be :

$$\frac{Cf}{2} R_0 = \frac{Cf}{2} R_0(H), \quad C_E R_0 = C_E R_0(H) \text{ and } H^* = H^*(H)$$

In fact, the definition of δ would be included in both the two last relationships. However, a simple analysis of the entrainment equations shows that these two relationships are equivalent to the following ones :

$$\frac{C_E R_0}{H^*} = \frac{C_E R_0}{H^*}(H) \text{ and } H = H(\delta_1/\delta)$$

In this form, the first one is independent of the arbitrary definition of δ . We will see at § 4.4 how has been solved this problem for the last relationship.

4.2. Incompressible turbulent flow

Self-similarity solutions proposed by MICHEL-QUEMARD-DURANT /Ref. 12/, provided closure relationships for attached flows. They have been extended to the case of moderate separated flows ($H \leq 10$) ; however, due to the formulation of these relationships, they could not provide negative values of $Cf/2$. We have therefore used a relation proposed by EAST et al. /Ref. 13/, which is in good agreement with the one proposed by MICHEL et al. for the attached flows. To remain homogeneous with the laminar closure relationships, the set of turbulent ones is :

$$\frac{Cf}{2} = \frac{Cf}{2}(H, R_0) \quad \text{deduced from /Ref. 13/,}$$

$$\frac{C_E}{H^*} = \frac{C_E}{H^*}(H, R_0) \quad \text{deduced from /Ref. 12/,}$$

$$H^* = H(\delta_1/\delta) \quad \text{deduced from /Ref. 12/.}$$

Let us note that in this case, δ is a parameter of the self-similarity solution and is consequently completely defined.

4.3. Extension to compressible flows

For laminar /Ref. 11/ as well as for turbulent /Ref. 14/ flows, it has been shown that the use of transformed quantities allows to extend the incompressible closure relationships to compressible flows.

4.4. Treatment of the transition region

We have assumed that, in this region, two fictitious boundary layers, laminar and turbulent, could be defined. At this stage, we have hence arbitrarily defined δ for laminar flows, so that incompressible laminar and turbulent zero pressure gradient flows correspond, through the relationships $H(\delta_1/\delta)$ to the same value of δ_1/δ .

The two fictitious boundary layers are then assumed to correspond, in the transition region, to a common value of δ_1/δ . Closure relationships provide therefore respective characteristic quantities of these two boundary layers, quantities which are weighted through an "intermittency function" ϵ , to provide the transitional boundary layer following characteristic quantities :

$$H = (1 - \epsilon) H_L + \epsilon H_T$$

$$\frac{Cf}{2} = (1 - \epsilon) \frac{Cf_L}{2} + \epsilon \frac{Cf_T}{2}$$

$$C_E = (1 - \epsilon) C_{E_L} + \epsilon C_{E_T}$$

This method has been successfully used for attached flows and is based on the experimental observation of intermittency between laminar flow and turbulent spots in a flat plate boundary layer transition.

In fact, our experiments /Ref. 1/ have shown that for separation bubbles, transition process no more involves turbulent spots, but is due to the bursting of vortices, born in the laminar separated shear layer. However, this transition is very fast and the use of an intermittency function provides satisfactory results.

5. VISCOUS-INVISCID INTERACTION

The interaction relationship can be written in terms of the direction, relative to the wall, of the velocity vector at the boundary between viscous and inviscid flows.

LE BALLEUR /Ref. 6/ has shown that it could also be written in terms of vertical velocity at a given distance of the wall. An expansion through the boundary layer of the inviscid velocity normal to the wall, associated with the boundary layer global continuity equation, provides this relation.

If it is written at $y = 0$, one can see that the boundary layer is equivalent to a transpiration at wall, the magnitude of which is given by :

$$\left(\frac{v}{U_e}\right)_0 = \epsilon = \frac{1}{U_e} \frac{d}{dx} (U_e \delta_1)$$

5.1. INVISCID PROBLEM EQUATIONS

The inverse boundary layer calculation could be introduced in a complete flow calculation through this viscous-inviscid interaction relationship. In fact, our purpose was not to develop such a complex code, but rather to obtain a practical and easy to use method.

5.1.1. Incompressible flow

The flow around the airfoil being assumed irrotational, we can first define a potential ϕ , so that :

$$\vec{v} = \nabla \phi \quad \text{and} \quad \nabla^2 \phi = 0$$

where subscript e corresponds to the actual external flow with a bubble.

If we define ϕ_{FP} as the potential of the flow around the geometric airfoil, we have also :

$$\Delta \phi_{FP} = 0$$

with $U_{FP} = \frac{\partial \phi_{FP}}{\partial x}$ and $V_{FP} = \frac{\partial \phi_{FP}}{\partial y}$

We can then define the velocity $U_i(x)$ induced by the separation bubble as :

$$U_i(x) = U_e(x) - U_{FP}(x)$$

Because of the linearity of POISSON equation, it is easy to define the potential ϕ_i so that :

$$\Delta \phi_i = 0$$

$$U_i = \frac{\partial \phi_i}{\partial x} \quad \text{and} \quad v_i = \frac{\partial \phi_i}{\partial y}$$

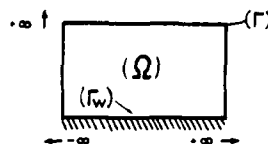
subscript i corresponding to the perturbation induced by the bubble.

Once ϕ_{FP} is known, the solution of the complete inviscid flow is then equivalent to the solution for the perturbation potential ϕ_i .

In fact, looking at the available experimental results, it appeared that we could reasonably assume that the velocity perturbation U_i was small and vanished outside the vicinity of the bubble.

Neglecting the wall curvature effects, the problem is then :

$$\begin{cases} \Delta \phi_i = 0 & \text{in } (\Omega) \\ \phi_i = 0 & \text{on } (\Gamma) \\ \frac{\partial \phi_i}{\partial x} = U_i & \text{on } (\Gamma_w) \end{cases}$$



In fact, the determination of ϕ_i is not necessary and the problem is practically to determine $v_i = \frac{\partial \phi_i}{\partial x}$ on (Γ_w) .

This result is easily obtained with a GREEN's function which provides :

$$v_o(x) = v_i(x,0) = \frac{1}{\pi} \int_{-\infty}^{\infty} \frac{U_i(\xi)}{(\xi-x)} d\xi$$

In fact, experiments showing that U_i is negligible out of the vicinity of the bubble, the integral is taken on an adequate finite domain around the bubble. The results we obtain provide subsequent validation of these assumptions.

6.2. Compressible subsonic flows

To keep the same formulation, we use a PRANDTL-GLAUERT approximation for the linearized potential flow equation :

$$(1 - M_o^2) \frac{\partial^2 \phi}{\partial x^2} + \frac{\partial^2 \phi}{\partial y^2} = 0$$

With the use of coordinate transformation $Y = y \sqrt{1 - M_o^2}$, the same assumptions lead to :

$$v_o(x) = v_i(x,0) = \frac{\sqrt{1-M_o^2}}{\pi} \int_{-\infty}^{\infty} \frac{U_i(\xi)}{(\xi-x)} d\xi$$

7. SOLUTION OF THE INVERSE VISCOUS PROBLEM

The system of the two global boundary layer equations, associated with the viscous-inviscid interaction relationship is the following :

$$\frac{Cf}{2} = \frac{d\theta}{dx} + \theta \left[(H+2) \cdot \frac{1}{U_e} \frac{dU_e}{dx} + \frac{1}{\rho_e} \frac{d\rho_e}{dx} \right]$$

$$C_E = \frac{1}{\rho_e U_e} \frac{d}{dx} (\rho_e U_e (\delta - \delta_1))$$

$$\alpha = \frac{1}{\rho_e U_e} \frac{d}{dx} (\rho_e U_e \delta_1)$$

On a quasi-conservative form, it can be written as :

$$\frac{d}{dx} (\rho_e U_e^2 (\delta_1 + \theta)) = \rho_e U_e^2 \left(\frac{Cf}{2} + \alpha \right)$$

$$\frac{d}{dx} (\rho_e U_e \delta) = \rho_e U_e (C_E + \alpha)$$

$$\frac{d}{dx} (\rho_e U_e \delta_1) = \alpha$$

where $\alpha = \frac{v_o}{U_e}$ is given by the previous inviscid calculation.

The integration of this system in x_{m-1} gives $\rho_e U_e \delta$, $\rho_e U_e \delta_1$ and $\rho_e U_e^2 (\delta_1 + \theta)$ in x_m .

Figure 6 gives a brief description of the method.

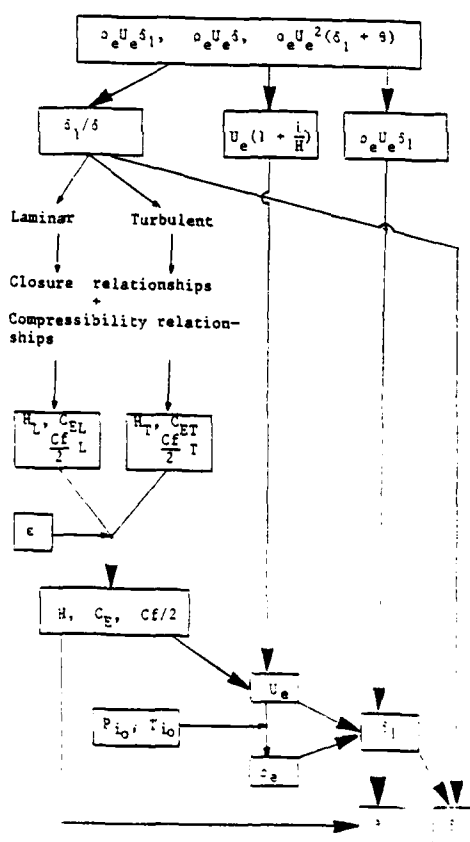


Fig. 6 - Flow-chart of the inverse boundary layer calculation

8. TRANSITION

The problem of transition (practically, the determination of the beginning of transition and its extent) is one of the main points of the method.

A delayed transition would cause the bubble not to reattach and the calculation would fail. On the other hand, with a too early transition, the increase in momentum thickness would be too small and the downstream turbulent calculation would not be significant.

Before going through our transition calculation method, we would like first to have a quick look at some of the existing methods.

8.1. Examples of existing transition criteria

One of these separation bubble transition criteria has been established by HORTON /Ref. 15/ and modified by VINCENT DE PAUL /Ref. 16/ and ROBERTS /Ref. 17/.

Once the separation point S has been found, through a direct laminar calculation method, they assume there is a sudden transition at a point T, defined as follows :

$$X_T - X_S = L \quad \text{with} \quad \frac{U_S \cdot L}{S} = \frac{K}{R_{\theta S}}$$

where subscripts S and T respectively correspond to separation and transition point.

- K is : - a constant for HORTON ($K = 4.10^4$)
 - a function of $R_{\theta S}$ for VINCENT DE PAUL
 - a function of Tu_∞ for ROBERTS.

Another criterion is used by KWON and PLETCHER /Ref. 18/, where the onset of transition is given by :

$$R_{XT} = 1.059 R_{\theta S} + 44720$$

The transition develops downstream of T with an intermittency function ϵ given by :

$$\epsilon = 1 - \exp(-C_T (x - x_T)^2)$$

$$\text{where } C_T = 0.025/\delta_{1S}^2$$

We have tried to introduce these different criteria in our boundary layer calculation, but the results were very poor, and that can perhaps be explained by the following remarks :

The influence of the turbulence intensity level is generally not taken into account (except by ROBERTS). If this parameter is not essential, it has a non negligible influence on the length of the laminar separated region. In our experiments for instance, a change in upstream turbulence intensity from 0.45 % to 0.65 % reduces the "equivalent constant" K from 7.10^4 to 4.10^4 . GAULT /Ref. 19/ and ROBERTS /Ref. 17/ find such a qualitative effect of this parameter. In fact, recent experiments we have performed with turbulence generating grids show that for a local turbulence intensity of 2.5 %, transition happens practically at separation and no bubble appears while, however, an increase in momentum thickness has been found. In addition, none of these criteria are able to take into account the physical phenomena which lead to the onset of transition.

Next paragraph will explain the way we have tried to introduce these two major points in our criterion.

8.2. Present transition calculation method for incompressible flows

From our experiments /Ref. 1/, we could point out that transition is initiated by the amplification of laminar instability waves, similar to TOLLMIEN-SCHLICHTING waves observed on a flat plate. This amplification proceeds from a critical point (point where Reynolds number reaches a critical value below which no disturbance can be amplified), which is generally upstream of separation.

In fact, ARNAL et al. /Ref. 20/ have shown that for attached flows, an important parameter characteristic of this amplification is the difference between local and critical momentum thickness Reynolds number. We have hence tried to develop, for transition in separated flows, a criterion similar to the one proposed by ARNAL et al. for attached flows, and which would intend to take into account the previous remarks.

We will briefly give the principles of this criterion.

8.2.1. Stability calculation

ARNAL and HABIBALLAH /Ref. 21/ have studied within the framework of spatial theory and for parallel flows, the stability of attached laminar self-similar velocity profiles. We have extended this study to the separated profiles used for the closure relationships as described in § 4.1..

These calculations provide, for a given profile, the amplification coefficient $\alpha_i (F, R\delta_1) = -\frac{1}{A} \frac{\partial A}{\partial x}$ of a sinusoidal disturbance, whose magnitude is A and whose reduced frequency is F ($F = 2\pi f\nu/Ue^2$ with f, physical frequency), for a wide range of $R\delta_1$.

A sweep in frequency provides then the stability diagrams. An example is presented in figure 7. On this diagram, iso-amplification lines are plotted, versus reduced pulsation ω and Reynolds number $R\delta_1$. The $\alpha_i = 0$ curve is the boundary between amplified and damped domains and is called neutral curve. The shape of this curve clearly shows that we can define a critical Reynolds number (subscript CR) below which any disturbance is damped.

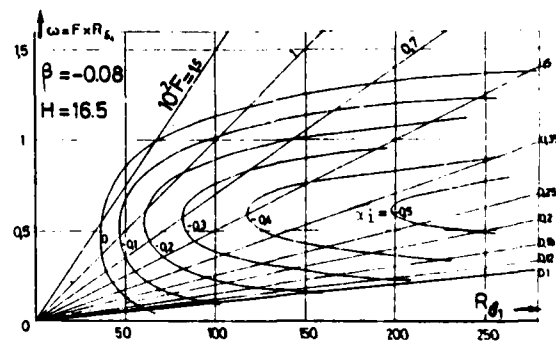


Fig. 7 - Example of stability diagram

Neutral curves, with the corresponding critical Reynolds number, are presented in figure 8. The great instability of these profiles is characterized by low values of $R_{\delta_1 CR}$, as well as by large aperture of neutral curves, indicating a wide range of amplified frequencies. Flat plate neutral curve has been reproduced as reference.

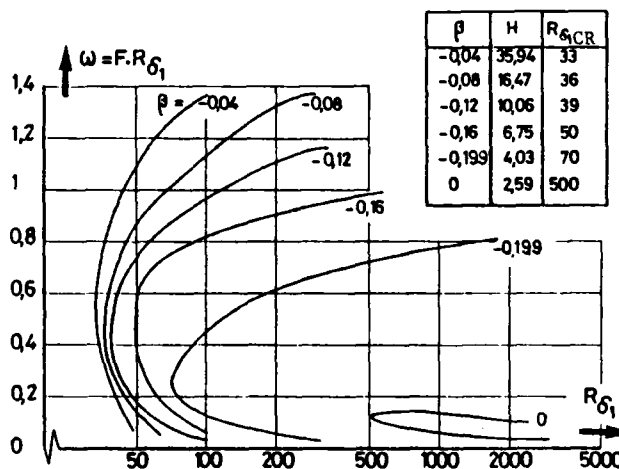


Fig. 8 - Neutral curves

8.2.2. Determination of the onset of transition

If we consider on figure 7 the evolution with R_{δ_1} of the amplification coefficient α_i of a disturbance of frequency F , the representative point lays on a straight line coming from the origin. For low R_{δ_1} , this disturbance is damped, up to the first crossing point with the neutral curve. Let A_0 be the magnitude of this disturbance at this point x_0 . From there, the disturbance is then amplified, up to the second intersection point with the neutral curve.

For each disturbance, at a given point x where Reynolds number is R_{δ_1} , we can define the local amplification $a(H, F, R_{\delta_1})$ as follows :

$$a(H, F, R_{\delta_1}) = \ln \left(\frac{A}{A_0} \right) = \int_{x_0}^x \alpha_i(x) \cdot dx$$

An example of this procedure is presented in figure 9, for a pressure gradient parameter of -0.08 ($H = 16.5$). The dash line corresponds to the envelope of the local amplification curves for the different values of the parameter F . This envelope gives the so called total amplification $n(H, R_{\delta_1})$ or also $n(H, R_{\delta_1})$, corresponding to the amplification of the most unstable frequency, for any Reynolds number greater than the critical Reynolds number $R_{\delta_1 CR}$.

For $n > 2$, the shape of the curve leads to a simple analytical representation :

$$n(\Pi, R_{\delta_1}) = A(\Pi) \cdot [R_{\delta_1} - R_{\delta_1 CR}(\Pi) + B(\Pi)] \quad (8.1)$$

where Π is an adequate pressure gradient parameter.

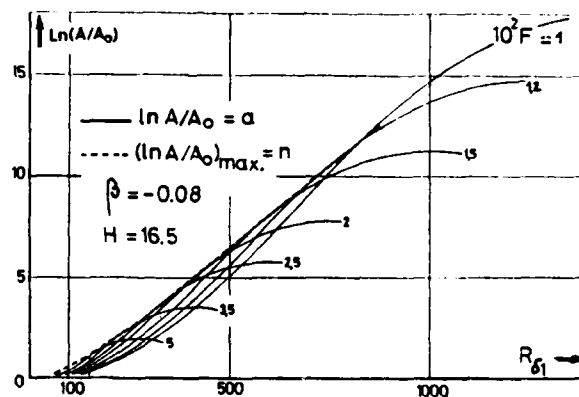


Fig. 9 - Example of amplification curves.

For attached flow, the choice of a mean POHLHAUSEN parameter gives fairly good results. In our case, due to the non uniqueness of the velocity profiles for negative values of this parameter, the choice of the shape parameter H seemed to be the most adequate. In addition, and for better convenience, relation (8.1) has been used in its differential form :

$$\frac{dn}{dR_{\delta_1}}(H, R_{\delta_1}) = A(H) \quad (8.2)$$

For self-similarity solutions, the integration of equation (8.2) from the critical point gives back relation (8.1).

For practical use, two problems arise :

- the determination of the critical point, where $n = 0$;
- the determination of the evolution of n for non self-similar flows.

For the first point, self-similarity solutions provide the evolution of the critical Reynolds number versus pressure gradient parameter. Presented in terms of shape parameter, this gives the relation :

$$R_{\delta_1 CRF} = R_{\delta_1 CRF}(H) \quad (8.3)$$

plotted in figure 10.

At each station, the integration of the boundary layer equation system provides local Reynolds number R_{δ_1} and local shape parameter H . For this calculated value of H , we deduce the fictitious critical Reynolds number $R_{\delta_1 CRF}$ by using equation (8.3) : this fictitious Reynolds number is the theoretical critical Reynolds number of a self-similar flow whose shape parameter would be H . We assume then that the critical point of the flow is obtained when local R_{δ_1} is equal to this fictitious $R_{\delta_1 CRF}$.

For the second point, we simply assume that the slope of the curve $n(R_{\delta_1})$ at a given station x , is only function of the local calculated shape parameter and is given by the corresponding self-similarity solution.

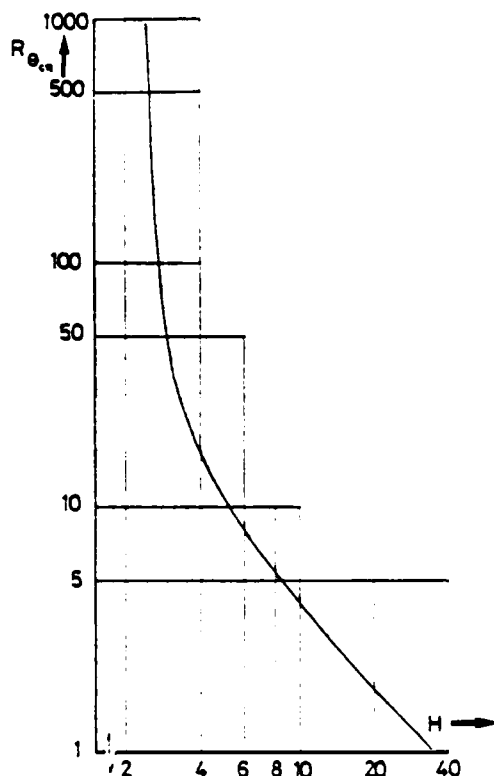


Fig. 1 - Critical Reynolds number $R_{\theta_{CR}}$ for self-similarity solutions

The integration leads then to :

$$n(x) = \int_{R_{\theta_{CR}}}^{R_{\theta}} \frac{dn}{dR_{\theta}} (H) dR_{\theta}$$

where : - R_{θ} and H are local Reynolds number and shape parameter at station x ,
- $R_{\theta_{CR}}$ is the critical Reynolds number previously defined.

The onset of transition is finally assumed to occur when the total amplification reaches a given value n_T , function of the local turbulence level through a relation proposed by MACK /Ref. 22/ :

$$n_T(\text{Tue}) = -8.43 - 2.4 \ln(\text{Tue})$$

8.3. Extension to subsonic compressible flows

At the present time, we have not yet performed a detailed study of the stability of laminar compressible boundary layers, which would allow us to develop the corresponding transition criterion. However, we have, as a first approximation, tried to extend the present calculation method to subsonic compressible flows, according to the following remarks :

- A review of experimental results /Ref. 21/ showed that, for an airfoil, critical point is generally located close to the suction peak, at a point where pressure gradient is close to zero ; on the other hand, stability

calculations relative to zero pressure gradient flows /Ref. 21/ exhibit a fairly weak influence of Mach number on critical Reynolds number. Consequently, we have, in a first step, determined the beginning of the amplification by the same way as for incompressible flows, using the incompressible parameters of the boundary layer :

$$H_i = \int_0^{\delta} \left(1 - \frac{u}{u_e}\right) dy / \int_0^{\delta} \frac{u}{u_e} \left(1 - \frac{u}{u_e}\right) dy$$

$$R_{\theta i} = \frac{u_e}{\nu_e} \int_0^{\delta} \frac{u}{u_e} \left(1 - \frac{u}{u_e}\right) dy$$

already used in the closure relationships transformations.

- Calculations by MACK /Ref. 23/ indicate that, if compressibility has a stabilizing effect, this effect becomes significant when reaching transonic regime.

In so far as no more specific results have been obtained, we have finally calculated the total amplification n , by introducing the incompressible parameters of the boundary layer, so that :

$$n = \int_{R_{\theta i CR}}^{R_{\theta i}} \left(\frac{dn}{dR_{\theta}}\right)_i dR_{\theta i}$$

where $\left(\frac{dn}{dR_{\theta}}\right)_i$ is the value of $\frac{dn}{dR_{\theta}}$ corresponding to the local incompressible shape parameter H_i .

The onset of transition is then obtained through MACK's relation.

8.4. Intermittency function

Formulation of ϵ from Chapter 8.1. has been tested, starting from our definition of beginning of transition. Sudden transition as well as other definition appeared not to fit with the experimental rapid but not punctual transition.

For attached flows, ARNAL et al. /Ref. 20/ found that intermittency function was fairly well correlated by the quantity θ/θ_T , where θ is momentum thickness at a given point in the transition region, as θ_T is the momentum thickness at the beginning of transition.

We have consequently tried to use the same type of relation and the best results were obtained with :

$$\epsilon = 1 - \exp \left(-2.5 \cdot \left(\frac{\theta}{\theta_T} - 1 \right) \right)$$

very close to the relation used by ARNAL et al. /Ref. 20/.

9. COMPARISON WITH EXPERIMENTS

9.1. Preliminary remarks

The present method deals with short leading edge separation bubbles, in subsonic compressible flows, and only needs :

- a) a velocity distribution without bubble,
- b) the local external turbulence intensity ($< 5\%$),
- c) condition for H and θ at the first grid point.

The following remarks are to be done, relative to these data :

- The velocity distribution can be either a potential or an experimental high Reynolds number one. If Reynolds number is far enough from bursting range, it is even possible to use a "smoothed" experimental velocity distribution. Results so obtained for boundary layer evolution remain quite significant, though calculated velocity distribution is of course slightly different from experimental one.
- Concerning point b), it is generally sufficient to know the upstream turbulence intensity. The local one can be obtained, assuming a constant turbulence kinetic energy by :

$$T_{ue} = T_{u\infty} \cdot \frac{u_{\infty}}{u_{em}}$$

where u_{em} is a mean value of the external velocity in the transition region. This assumption is no more valid for high turbulence intensities, where turbulence decay may be high (turbulence generated by a grid, in particular) and the knowledge of local turbulence intensity is important, otherwise, increase in momentum thickness may be underestimated through the previous assumption.

- About the last point, an integral laminar boundary layer calculation from stagnation point gives correct conditions.

9.2. ERLICH experiments /Ref. 4/

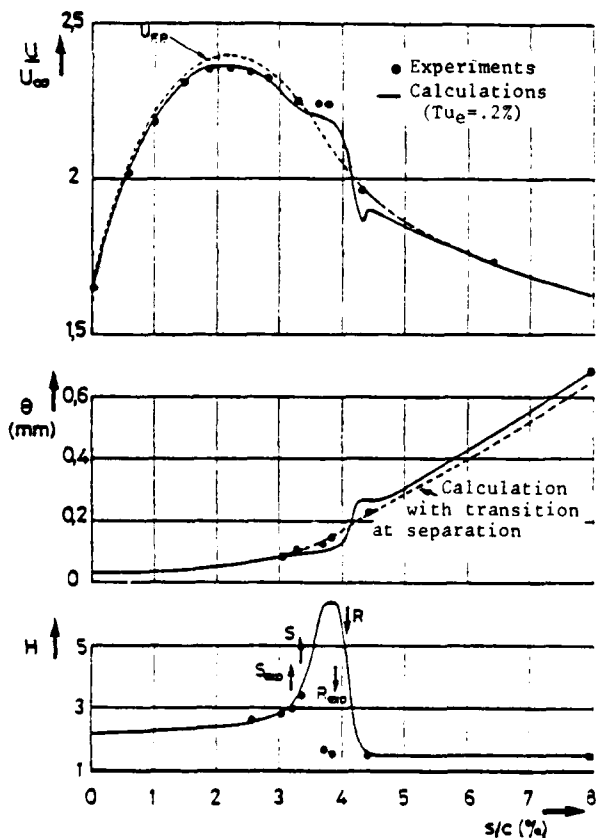


Fig. 11 - Comparison with OAGPI model

These experiments have been carried out at ONERA on another "enlarged leading edge", corresponding to a 2.85 m chord airfoil. Pressure distributions and boundary layer surveys obtained for $Re_c = 8 \cdot 10^6$ are compared to our calculation results in figure 11. Undisturbed velocity distributions have been obtained by "smoothing" the experimental values, while local turbulence level is deduced from mean upstream turbulence level of the wind tunnel ($T_{u\infty} = 0.4$ to 0.5%).

Here also, a slight shift exists between experimental and calculated separation regions ; in addition, the level of the pressure plateau is underestimated. The definition of the undisturbed velocity is probably one of the main reasons of these discrepancies. In spite of that, as it has been noted at § 9.1, if one is mainly interested in the initial conditions for the downstream boundary layer, this approximation allows to predict the correct level for momentum thickness.

9.3. Experiments on OAGPI model

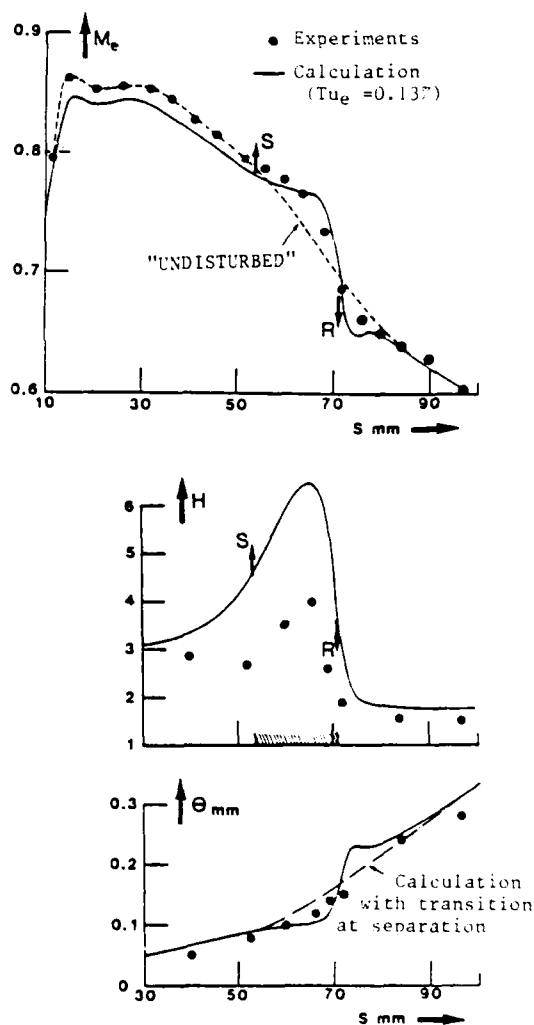


Fig. 12 - Comparison with OAGPI model

These experiments have been performed at ONERA, to provide additional data about the flow around compressor blades. The OAGPI model is a kind of "enlarged leading edge", the shape of which has been designed to reproduce, at a large scale, the pressure distribution at the upper surface of a cascade blade. Upstream Mach number is .707 and total pressure is 25 340 Pa. Reference chord of the model is 333 mm. Results relative to this test case are presented in figure 12.

A first remark, which, in fact, was the main reason for our method to be used, is that a calculation assuming transition at separation point, predicted momentum thicknesses downstream of the bubble, greater than the experimental values. These results were, however, questionable, because measured integral quantities were probably affected with some incertitudes because of the size of the boundary layer.

For this model, neither undisturbed inviscid, nor high Reynolds number velocity distributions were available. Consequently, the smoothed experimental distribution was used as the undisturbed one. Local turbulence intensity was deduced from the upstream value ($Tu_\infty = 0.15\%$).

Results seem to confirm that, effectively, this separation bubble does not induce increase in momentum thickness. A more accurate calculation would however need a better definition of the undisturbed velocity distribution.

9.4. GAULT experiments /Ref. 19/

These experiments correspond to a separation bubble at mid-chord of a NACA 63018 at low angle of attack ($\alpha = 2^\circ$), for a Reynolds number $Re_c = 2 \cdot 10^6$. Boundary layer surveys have been carried out in the region around the bubble but, in the separated domain, the velocity profiles were limited to the positive values of U . Consequently, we have only plotted the integral quantities for $s/c = .592$ (about 30 mm upstream of separation) and $s/c = .714$ (nearly at reattachment).

In our calculation, undisturbed velocity distribution has been taken for $Re_c = 10^7$, while local turbulence intensity has been deduced from the upstream value ($Tu_\infty = 0.15$ to 0.20%). Initial conditions have been adjusted to fit experimental boundary layer integral thicknesses at $s/c = .592$.

Figure 13 presents the comparison between these experiments and our calculation results (full line). In addition, two other calculations have been plotted :

- in dash line, a turbulent calculation initiated at the experimental reattachment point (case /A/);
- in dotted line, a direct calculation, laminar up to the calculated separation point S_D , turbulent downstream of it, and assuming continuity of θ at S_D (case /B/).

We can immediately note that the calculated separation region ($S - R$) is relatively far downstream of the experimental one ($S_{exp} - R_{exp}$). Let us however note that, as in GAULT report, the separation point S_D , calculated through a direct laminar

method, is also downstream of S_{exp} . In spite of that, the effect of the bubble on the downstream turbulent boundary layer seems fairly well predicted, if we compare our calculation to calculation /A/, for s/c greater than 0.8. Another noticeable fact is that our calculation, as well as calculation /A/, predict, downstream of the bubble, a momentum thickness lower than momentum thickness given by calculation /B/, as it has already been noted in § 9.3.

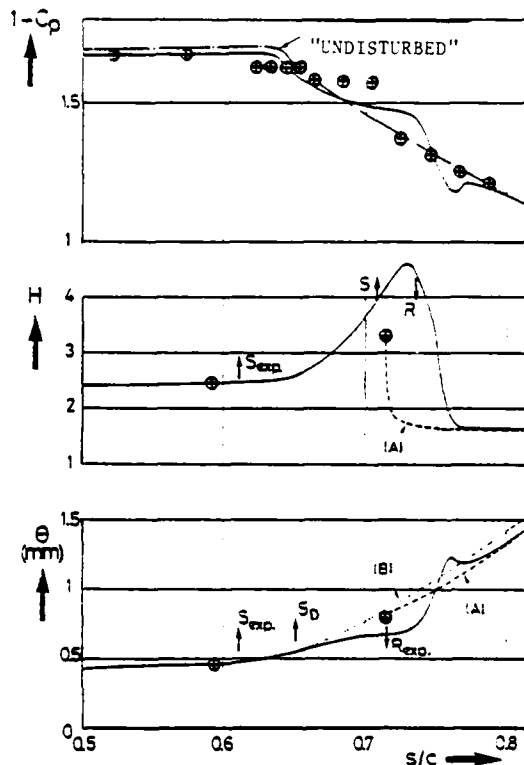


Fig. 13 - Comparison with GAULT experiments

9.5. Comparison with our experiments

9.5.1. Low turbulence level experiments

In figure 14 is presented one set of results obtained for $Re_c = 2.2 \cdot 10^6$ and a local turbulence intensity of 0.4% . The undisturbed velocity distribution has been obtained for the highest Reynolds number experimental case. Local turbulence intensity has been deduced from the upstream one. The choice of a few grid points in the constant pressure gradient region, provided good boundary conditions for H and θ through similarity solutions.

Open circles correspond to hot wire results while, in the separated region, closed circles correspond to LDA measurements. The agreement between calculation and experiments is quite satisfactory. In particular, the validity of the transition criterion seems good, owing to the correct prediction of either the size of the pressure plateau or the evolution of the shape parameter in the vicinity of reattachment. Compared with a calculation assuming transition at separation (see dotted line), the increase in momentum thickness is well predicted.

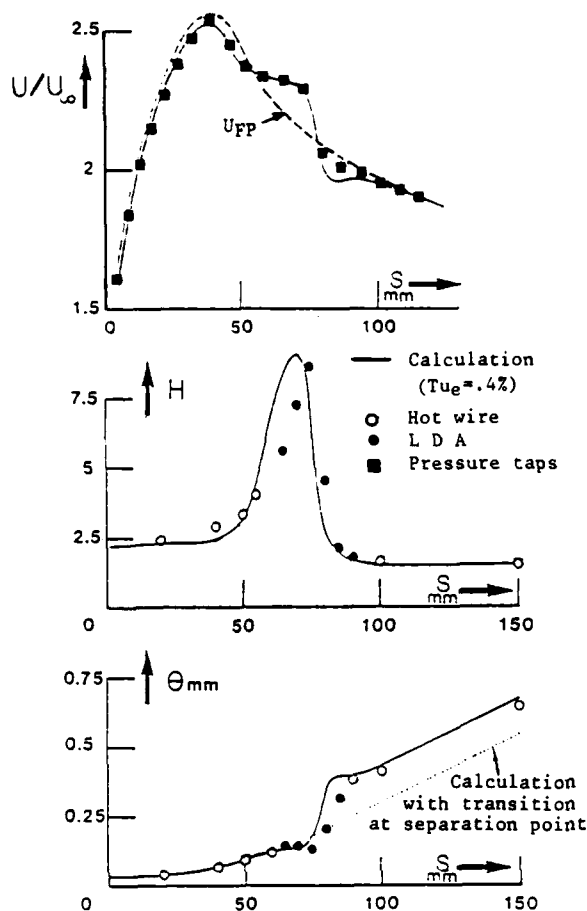


Fig. 14 - Comparison with our experiments on enlarged leading edge - low turbulence level case

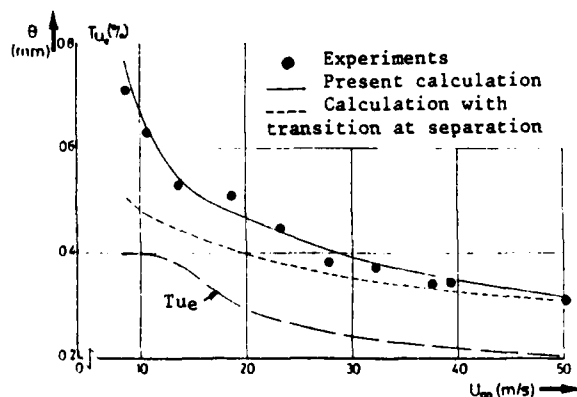


Fig. 15 - Evolution of momentum thickness at $s = 126$ mm

Figure 15 shows an other representation of this phenomenon, with the evolution of experimental and calculated momentum thickness at a fixed point downstream of reattachment, versus tunnel speed. Calculation with transition at separation has also been plotted, as well as local turbulence intensity (this data is slightly function of tunnel speed). Agreement is here also very satisfactory. Note that even for $U_{\infty} = 50$ m/s (i.e. $Re_c = 8.0 \cdot 10^6$), a bubble still exists.

9.5.2. Moderate turbulence level experiments

On the same model, turbulence has been generated by setting a grid at the beginning of the test section. Here, local turbulence intensity has been measured at the outer edge of the boundary layer, in the bubble region.

Figure 16 presents one set of experiments, corresponding to the same Reynolds number of $2.2 \cdot 10^6$ for a turbulence level of 2.5 %. A comparison between figures 14 and 16 immediately shows the influence of turbulence level on the position of transition and, consequently, on the size of the bubble.

In fact, for the high turbulence case, no more separated region seems to exist, transition beginning before theoretical laminar separation and shape parameter (experimental as well as calculated) reaches values of about 3.5. However, an increase in momentum thickness still exists.

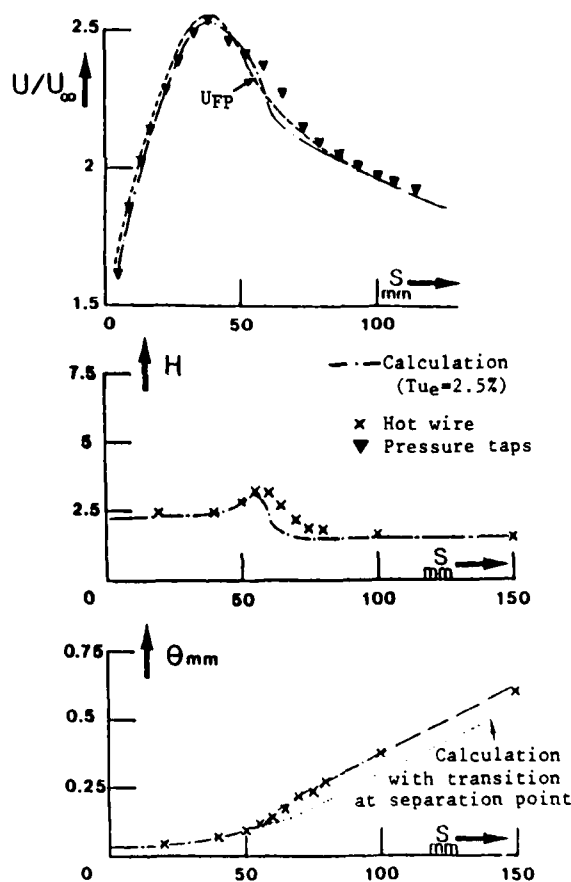


Fig. 16 - Comparison with our experiments on enlarged leading edge - High turbulence level case

CONCLUSION

The method we have presented here has been designed to take into account the effects of leading edge separation bubbles on the downstream turbulent boundary layer. This initial purpose led us to the various assumptions we made in the choice of the method. Previous experiments, as well as the detailed study we have carried out on the phenomenon have been widely responsible in this choice. The results obtained for this type of bubbles show a good general agreement, in regards to the cost and the simplicity of the method.

Considering mid-chord separation bubbles, the assumption of local viscous-inviscid interaction is perhaps questionable. The difficulties in the determination of the separation point through a high Reynolds number velocity distribution are probably significant of a non negligible influence of the bubble on the position of stagnation point. In spite of that, the results obtained by the calculation method seem fairly significant, provided that some care is taken in the definition of the "undisturbed" velocity distribution. In this case, a simple smoothing of the experimental distribution is no more sufficient.

In all the cases, the criterion we have developed seems to give a correct prediction of the onset of transition. In our opinion, it is the best compromise between the first generation of empirical criterion and the next one, where for instance stability of the boundary layer would be studied at each station, for each iteration. At a lower cost, the present criterion is however able to take into account the "history" of the laminar boundary layer, in a simplified but fairly efficient way.

REFERENCES

- /1/ BONNET J.L., GLEYZES C. "Etude expérimentale de la transition dans les bulbes de décollement laminaires au bord d'attaque de profils d'ailes" - Internal Report (To be published)
- /2/ GASTER M. "The structure and behaviour of laminar separation bubbles" - AGARD CP.4 (1969)
- /3/ HERRING R.N., ELY W.L. "Improved prediction of laminar leading edge separation" - NASA Conference Publication 2045, Paper 20 Advanced Technology Airfoil Research, March 7-9, 1978
- /4/ ERLICH E. "Contribution expérimentale à la recherche de la portance maximale des profils en subsonique" - Internal Report, ONERA (1970)
- /5/ GOLDSTEIN S. "On laminar boundary layer flow near a position of separation" Quart. J. of Mech. and Appl. Math., 1-43, (1948)
- /6/ LE BALLEUR J.C. "Couplage visqueux-non visqueux : analyse de problèmes incluant décollements et ondes de choc" - La Recherche Aérospatiale 1977-6
- /7/ CARTER J. "Solution for laminar boundary layer with separation and reattachment" - AIAA Paper 74-583
- /8/ KLINEBERG J.M., STEGER J.L. "On laminar boundary layer separation" - AIAA Paper 74-94
- /9/ GLEYZES C. "Calcul des bulbes de bord d'attaque de type court sur des aubes de turbomachines en écoulement subsonique compressible" - R.T. DERAT n° 8/5014 DN (Juillet 1982)
- /10/ CHRISTIAN J.W., HANKEY W.L. "Similar solutions of the attached and separated compressible boundary layer with heat transfer and pressure gradient" - ARL 70-0023 (1970)
- /11/ COUSTEIX J., GLEYZES C. "Couches limites laminaires bidimensionnelles avec flux de chaleur" N.T. ONERA/CERT-DERAT n° 8/5005 DN (1974)
- /12/ MICHEL R., QUEMARD C., DURANT C. "Application d'un schéma de longueur de mélange à l'étude des couches limites d'équilibre" - N.T. ONERA n° 154 (1969)
- /13/ EAST L.F., SMITH P.D., MERRYMAN P.J. "Prediction of the development of separated turbulent boundary layers by the lag-entrainment method" R.A.E., T.R. 77046 (1977)
- /14/ HOUEVILLE R., COUSTEIX J. "Couches limites turbulentes bidimensionnelles avec flux de chaleur. A) Etablissement et analyse des solutions de similitude" N.T. ONERA/CERT-DERAT n° 4/5005 DN (1974)
- /15/ HORTON H.P. "A semi empirical theory for the growth and bursting of laminar separation bubbles" - ARC, CP n° 1073 (1969)
- /16/ VINCENT DE PAUL M. "Prévision du décrochage d'un profil d'aile en écoulement incompressible" - AGARD CP 102 (1972)
- /17/ ROBERTS W.B. "Calculation of laminar separation bubbles and their effect on airfoil performance" AIAA 17th. 79-0285 (Jan. 1979)
- /18/ KWON O.K., PLETCHER R.H. "Prediction of incompressible separated boundary layer including viscous-inviscid interaction" - AIAA Paper A 79-38909
- /19/ GAULT D.E. "An experimental investigation of regions of separated laminar flow" - NACA TN 3505 (Sept. 1955)
- /20/ ARNAL D., HABIBALLAH M., DELCOURT V. "Synthèse sur les méthodes de calcul de la transition développées au DERAT" - R.T. DERAT n° 11/5018 AYD (1980)
- /21/ ARNAL D., HABIBALLAH M. "Résolution numérique des équations de stabilité de la couche limite. Comparaison aux résultats expérimentaux obtenus" R.T. ONERA/CERT-DERAT n° 10/5018 AYD (1979)
- /22/ MACK L.M. "Transition and laminar instability" Jet Prob. Lab., Publication 77-15 (1977)
- /23/ MACK L.M. "On the stability of the boundary layer on a transonic swept wing" - 17th Aerospace and Science Meeting, NEW-ORLEANS (Jan. 15-17, 1979)

PREDICTION OF SUBSONIC SEPARATION BUBBLES ON AIRFOILS BY VISCOUS-INVISCID INTERACTION

O. K. Kwon
Detroit Diesel Allison Division
General Motors Corporation
Indianapolis, Indiana

and

R. H. Pletcher
Department of Mechanical Engineering
Iowa State University
Ames, Iowa

Abstract

An iterative viscous-inviscid interaction calculation procedure is used to predict leading edge and midchord separation bubbles on airfoils in steady subsonic flow. The procedure utilizes an inverse finite-difference boundary layer calculation scheme to predict the viscous flow and a direct Hilbert integral formulation for the inviscid flow. Three models for laminar-turbulent transition are discussed. Predictions are compared with experimental measurements for several transitional separation bubble flows at angles of attack up through 7° .

Nomenclature

A function of Mach number (see Eq. 1b)
C constant
c airfoil chord
 C_p pressure coefficient, $1 - (u_e/u_\infty)^2$
 C_T function of displacement thickness
D damping function
 ℓ mixing length
L characteristic length
M Mach number
p pressure
 q intensity of line source or sink
 x_r reattachment point
 Re_x Reynolds number based on x
 Re_{θ} Reynolds number based on momentum thickness
 x_s separation point
 s distance along upper surface of airfoil measured from stagnation point

s' distance along surface measured from leading edge
 u x component of velocity
 u_τ friction velocity
 v y component of velocity
 x coordinate along the surface
 x' variable of integration in Eqs. (24) and (26)
 x_1 interaction starting point
 x_2 interaction end point
 Δx length of transition region
 y coordinate normal to surface
 α angle of incidence
 γ intermittency function
 δ boundary layer thickness
 δ^* displacement thickness, $\int_0^{\infty} (1 - u/u_e) dy$
 κ von Kármán constant
 λ extent of transition region
 μ viscosity
 ν kinematic viscosity
 ξ normalized streamwise coordinate in transition zone, $(x - x_{tr})/\lambda$
 ρ density
 τ shearing stress

Subscripts

BL	denotes boundary layer
c	indicates value of correction
e	evaluated at outer flow boundary
FT	evaluated for fully turbulent flow
INV	denotes inviscid flow
in	denotes inner region
L	evaluated at downstream flow boundary
max	evaluated at maximum condition
n	denotes iteration level
o	denotes reference quantity
ot	denotes outer region
s	denotes evaluation at separation point
T	denotes turbulent flow quantity
t	denotes turbulent flow quantity or transition end point
tr	denotes transition initiation point
∞	denotes evaluation at freestream conditions far upstream of airfoil

Superscripts

- ($\bar{}$) bars on dependent variables denote time mean quantities
- ()' prime on dependent variables denotes fluctuations

1. Introduction

The prediction and control of turbulent flow separation and reattachment continue to be important in many engineering applications. Subsonic flow separation occurs or can occur on airfoils, helicopter blades, near the tail of axisymmetric bodies, ship hulls, and in diffusers, compressors, and engine inlets. In many applications it is desirable to avoid separation entirely. In others, some separated regions must be tolerated over some range of the operating conditions; and it is highly desirable to be able to predict performance even with regions of recirculation present. Although progress is being made in the understanding and prediction of these flows, the accurate and economical calculation of turbulent flows containing regions of recirculation still remains one of the major challenges in the field of computational fluid dynamics.

Most recent investigators dealing with separated flows have been optimistic that the boundary layer equations may provide a suitable mathematical description for at least thin separ-

ated regions at moderate or high Reynolds numbers.¹⁻³ However, the solution of boundary layer equations alone provides only part of the answer to the problem posed by separation in applications because information from, or at least compatible with the outer inviscid flow is needed to establish the outer boundary conditions for this boundary layer calculation. In the neighborhood of separation, the inviscid flow solution over the displacement surface of the viscous flow differs significantly from the inviscid flow over the solid body alone. Neither the correct inviscid solution nor the correct viscous flow solution can be obtained independently. The two problems must be solved simultaneously or iteratively until the solutions "match" through a common streamwise pressure gradient at the solid surface. Thus, a practical calculation scheme based on boundary layer equations must include provisions for the viscous-inviscid interaction.

There have been only a few reports of viscous-inviscid interaction schemes being applied to subsonic separated turbulent flow. These computational studies have employed both integral and differential procedures for the solution of the viscous flow. Integral procedures have been applied to fully stalled turbulent flow in diffusers by Wooley and Kline⁴ and to the flow over a reward-facing step by Kim et al.⁵ Crimi and Reeves⁶ and van Ingen⁷ also used integral analyses in developing prediction schemes for separation bubbles on airfoils. Gerhart and Chima⁸ reported only partial success in their use of an integral boundary layer scheme in a viscous-inviscid interaction procedure for subsonic turbulent flows.

Differential solutions to the boundary layer equations were used in the interaction schemes applied to subsonic turbulent flow by Briley and McDonald,⁹ Carter,¹⁰ Cebeci et al.¹¹ and Kwon and Pletcher.¹² The Briley and McDonald study utilized a time-dependent analysis, whereas the others employed inverse boundary layer procedures. Only Refs. 9 and 12 included comparisons with experimental data.

In Ref. 12, an inverse boundary layer method was combined with a Hilbert integral formulation for the inviscid flow to predict a midchord transition bubble on an airfoil at zero angle of attack. Two models for laminar-turbulent transition were evaluated and both were found to perform satisfactorily for this flow. In the present paper, the generality of the computational method and transition models of Ref. 12 are tested by comparing predictions with experimental measurements for midchord and leading edge bubbles on airfoils at angles of attack ranging up to 7°. During the course of the study, turbulence and transition models were found to play a crucial role in determining the accuracy of the predictions. Three transition models are evaluated and discussed. The key features of the calculation method and turbulence modeling are given below. Further details on the method may be found in Refs. 12 and 13.

Analysis

Viscous Flow

The flow is assumed to be two-dimensional, steady, and incompressible. Any separated regions are assumed to be sufficiently thin so that the

boundary layer form of the momentum and continuity equations provides an adequate mathematical model for viscous regions. In any region of reversed flow, the streamwise convective derivative is also assumed to be negligibly small. Neglecting turbulent normal stresses, the governing conservation equations are

Continuity

$$\frac{\partial u}{\partial x} + \frac{\partial v}{\partial y} = 0 \quad (1)$$

Momentum

$$C \left| u \right| \frac{\partial u}{\partial x} + v \frac{\partial u}{\partial y} = - \frac{1}{\rho} \frac{dp}{dx} + \frac{1}{\rho} \frac{\partial \tau}{\partial y} \quad (2)$$

where $C = 1.0$ when $u > 0$, and $C = a$ small (≤ 0.2) positive constant when $u \leq 0$ and

$$\tau = \mu \frac{\partial u}{\partial y} - \rho \overline{v'u'} \quad (3)$$

The inner boundary conditions are

$$u(x,0) = v(x,0) = 0 \quad (4)$$

For attached flows some distance from the separation point, the standard direct finite-difference method was employed for which the outer boundary condition was

$$\lim_{y \rightarrow \infty} u(x,y) = u_e(x) \quad (5)$$

For the inverse method, the second boundary condition satisfied by the streamwise component of velocity was

$$\int_0^{\infty} \left(1 - \frac{u}{u_e} \right) dy = \delta^*(x) \quad (6)$$

where $\delta^*(x)$ is a prescribed function.

Equation (2) deviates from the conventional momentum equation in the treatment (FLARE approximation¹⁴) of the streamwise derivative term,

$C \left| u \right| \frac{\partial u}{\partial x}$. The form used permits marching the solution through regions of reversed flow by avoiding a negative coefficient for the streamwise derivative term. The boundary layer equations were solved by the implicit finite-difference scheme described in Ref. 1.

Turbulence and Transition Modeling

The Reynolds stress was assumed to be related to the rate of mean strain according to

$$-\rho \overline{u'v'} = \mu_T \frac{\partial u}{\partial y} \quad (7)$$

where μ_T is a turbulent viscosity. External flows which give rise to thin separation bubbles invariably separate in the laminar state and undergo transition to turbulent flow prior to or coincident with reattachment. Unfortunately, there are no known practical procedures for computing the details of laminar-turbulent transition from first principles. In the present study, the value of μ_T was determined as the product of a viscosity for fully turbulent flow, μ_{FT} , and an empirical intermittency factor, γ :

$$\mu_T = \gamma \mu_{FT} \quad (8)$$

Such an approach has proven useful for natural transition on flat surfaces and airfoils.¹⁵

The fully turbulent viscosity was evaluated according to Model D of Ref. 1. In this model,

$$\mu_{FT} = \rho \ell^2 \left| \frac{\partial u}{\partial y} \right| \quad (9)$$

where ℓ is a mixing length evaluated differently for the inner and outer regions of the boundary layer. For the region closest to the wall, the mixing length is specified as

$$\ell_{in} = \kappa Dy \quad (10)$$

$$\text{with } D = 1 - \exp \left[\left(\frac{1}{\gamma} \left| \frac{\partial u}{\partial y} \right|_{\max} \right)^{1/2} \frac{y}{26} \right] \quad (11)$$

Here κ was taken as 0.41. For the outer region, the mixing length was evaluated as

$$\ell_o = 0.12 L \quad (12)$$

where L was determined from

$$u_e \frac{dL}{dx} = 1.2 \left| u_t \right| \left[\frac{L}{\delta} - \left(\frac{L}{\delta} \right)^2 \right] \quad (13)$$

The motivation for the transport equation for L was given in Ref. 1. In the present predictions, $\ell_{ot} = 0.089 \delta$ was used to establish initial values for L . The inner expression for ℓ was used from the wall outward until $\ell_{in} = \ell_{ot}$. At that point the switch was made to the outer formulation.

Three schemes for evaluating γ have been applied in the present study.

Transition Model A: This model is based on existing correlations for natural transition on flat plates and airfoils. Transition was assumed to start when Re_θ equaled or exceeded the value given by Cebeci et al.¹⁵

$$Re_{\theta, tr} = 1.174 \left[1 + \frac{22400}{Re_x} \right] Re_x^{0.46} \quad (14)$$

for

$$0.1 \times 10^6 \leq Re_x \leq 40 \times 10^6$$

For the calculation of the extent of the transition region, the correlation suggested by Chen and Thyson¹⁶ was used:

$$Re_{\Delta x, tr} = A Re_{x, tr}^{0.67} \quad (15)$$

where A is the function of Mach number expressed by

$$A = 60 + 4.68 M_e^{1.92} \quad (16)$$

Thus, the extent of the transition region is

$$\Delta x = x_t - x_{tr} = \frac{A x_{tr}}{Re_{x, tr}^{0.33}} \quad (17)$$

The intermittency function was evaluated using the correlation presented by Dhawan and Narashima.¹⁷ The correlation was obtained based on the source density function of Emmons¹⁸,

$$\gamma = 1 - \exp(-0.412 \xi^2) \quad (18)$$

where

$$\xi = \frac{x - x_{tr}}{\lambda} \quad (19)$$

for $x_{tr} \leq x \leq x_t$. λ is a measure of the extent of the transition region determined in the present study by letting $\gamma = 0.999$ and $x = x_t$ in Eqs. (18) and (19).

Transition Model B: This model is based on correlations for separation bubble transition. According to the studies of Ward¹⁹ and Horton²⁰, the pressure distribution from the separation point to the point where the displacement thickness reaches a maximum is characteristically nearly uniform. Transition has frequently been associated with this point of maximum δ^* where the flow "turns down" to reattachment, and experiments tend to confirm that transition is well advanced or completed when reattachment occurs. This point, which marks the end of the constant pressure region in transitional bubbles from several experiments, has been correlated in Ref. 12 against the Reynolds number at separation. In transition Model B, transition was assumed to start at the point where the constant pressure region ends, which is reasonably well correlated by

$$Re_{x, tr} = 1.0607 Re_{x, s} + 33185 \quad (20)$$

where $Re_{x, s}$ is based on the distance along the surface from the airfoil stagnation point. Having established the point where transition is initiated by Eq. (20), the intermittency function is evaluated by the form suggested by Crimi and

Reeves⁶:

$$\begin{aligned} \gamma &= 0, \quad x < x_{tr} \\ &= 1 - \exp \left[-C_T (x - x_{tr})^2 \right], \\ &\quad x \geq x_{tr} \end{aligned} \quad (21)$$

where

$$C_T = 0.025 / \delta_s^{*2}$$

Transition Model C: This model assumes that transition occurs instantaneously at the point indicated by Eq. (20). Although the model gave surprisingly good results, its use was ultimately discontinued in the present study because the concept of "instantaneous" transition was thought to be physically unacceptable. Transition is expected to occupy a finite, although possibly very short, region.

Inviscid Flow

It is assumed that the inviscid flow is two-dimensional and irrotational, permitting the use of superposition to develop the potential flow solution. Letting $u_{e,0}$ denote the tangential component of velocity of the inviscid flow over the solid body without separation and u_c the velocity on the displacement surface induced only by the sources and sinks distributed on the surface of the body due to the displacement effect of the viscous flow in the interaction region, the x-component of velocity of a fluid particle on the displacement surface can be written as

$$u_e = u_{e,0} + u_c \quad (22)$$

Following Lighthill,²¹ the intensity of the line source or sink displacing a streamline at the displacement surface of the viscous flow can be evaluated as

$$q = \frac{d(u_e \delta^*)}{dx} \quad (23)$$

Using a small disturbance approximation valid for small values of δ^* , $u_c(x)$ can be evaluated as the Hilbert integral:

$$u_c(x) = \frac{1}{\pi} \int_{-\infty}^{\infty} \frac{d(u_e \delta^*)}{dx'} \frac{dx'}{(x - x')} \quad (24)$$

Further details on the calculation of $u_{e,0}$ (the inviscid surface velocity on the body without separation) will not be given here. $u_{e,0}$ can be obtained by conventional methods, such as the Hess and Smith²² procedure, or from experimental data. This distribution does not change during the interaction calculation.

For the numerical computation of u_c , it was assumed that strong interaction was limited to the region $x_1 \leq x \leq x_2$ in Fig. 1. The intensity of the source and/or sink was assumed to be significant in this region and to approach zero as x approaches $\pm\infty$. Consequently, q was only calculated in the region $x_1 \leq x \leq x_2$ using the boundary layer solution. Outside of this region, the source and/or sink distribution was extrapolated by

$$q'(x) = \frac{b}{x^2} \quad (25)$$

where b was computed to match q obtained from Eq. (23) at $x = x_1$ and $x = x_2$.

Equation (24) can be rewritten as

$$u_c = \frac{1}{\pi} \int_{-\infty}^{x_1} \frac{q'(x')}{(x-x')} dx' + \int_{x_1}^{x_2} \frac{q(x')}{(x-x')} dx' + \int_{x_2}^{\infty} \frac{q'(x')}{(x-x')} dx' \quad (26)$$

The first and third integrals can be evaluated analytically using Eq. (25). The second integral is evaluated numerically using the trapezoidal rule,

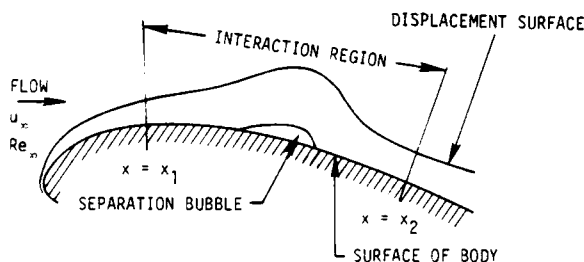


Fig. 1. Schematic diagram of interaction region on a two-dimensional body.

where the singularity at $x = x'$ is isolated in the manner employed by Jobe.²³ Further details of the procedure can be found in Ref. 24.

Viscous-Inviscid Interaction Procedure

A distribution of $u_{e,0}$ is first obtained as indicated in the previous section. Next, in order to verify the expectation of separation and to help determine the location and extent of the required interaction region, an attempt is made to calculate the entire viscous flow in the direct mode using $u_{e,0}(x)$ as a boundary condition. In a flow in which viscous-inviscid interaction is required, this calculation will end with a prediction of separation. Based on the results of this first viscous flow calculation, the interaction zone is established and a trial distribution of $\delta^*(x)$ is specified throughout the interaction zone. The

viscous flow calculation is repeated over the interaction zone in the inverse mode using the specified $\delta^*(x)$. The outer edge velocity, $u_{e,BL}$, is obtained as part of the output of this calculation. The same distribution of $\delta^*(x)$ is used to calculate the correction to the inviscid velocity, $u(x)$, as indicated by Eq. (26). A new inviscid surface velocity, $u_{e,INV}$, can now be computed. The edge velocities from the two calculations (viscous and inviscid) will not agree until convergence has been achieved.

The boundary layer calculation is repeated using a new δ^* distribution obtained from

$$\delta_{n+1}^* = \delta_n^* \left(\frac{u_{e,BL,n}}{u_{e,INV,n}} \right) \quad (27)$$

The form of Eq. (27), used previously by Carter¹⁰ and Kwon and Pletcher,¹² has been justified on the basis of a local continuity concept¹² and from a simplified momentum integral equation.¹⁰

It should be noted that Eq. (27) only serves as a basis for correcting δ^* between iterative passes, so no formal justification is required as long as the iterative procedure converges. At convergence, $u_{e,BL} = u_{e,INV}$ and Eq. (27) represents an identity, thereby having no effect on the nature of the final solution. One of the main advantages of this method is that the need to use "smoothing" or under-relaxation can be avoided; in fact, successive over-relaxation (SOR) can be used.

Results

Comparisons have been made with the experimental measurements of Gault^{25,26} and McCullough and Gault²⁷ obtained on two symmetric NACA airfoils at angles of attack.

In the study of Ref. 12, both transition models A and B were observed to satisfactorily predict the midchord separation bubble on an NACA 66₂-018 airfoil at zero angle of attack. When Model A was used to predict the flow on the same airfoil at the same Reynolds number but at two degrees angle of attack in the present study, the model predicted the onset of transition prior to the experimentally observed separation point and the predicted flow did not separate at all. Transition Model A utilizes elements developed for natural transition with very small pressure gradients and was evaluated in order to establish a baseline comparison through which the differences between bubble and natural transition might become evident. Apparently the model predicts an early (compared to experimental results) onset of transition in some cases, which can permit the transitional-turbulent flow to overcome the locally adverse pressure gradient and remain attached, counter to the experimental measurements. Because of this shortcoming, not shared by Models B and C, Model A was not used for further predictions in the present study.

Figure 2 compares the pressure coefficients predicted by Models B and C with the measurements of Gault²⁵ for the NACA 66₂-018 airfoil at $\alpha = 2^\circ$ and $Re_c = 2 \times 10^6$. Predicted separation and reattachment points are shown in the figure. The

bubble is seen to form somewhat downstream of mid-chord. Velocity profile comparisons are presented in Fig. 3 for this flow. Both transition Models B and C are seen to provide fairly good predictions although the velocity profiles predicted by Model C can be seen to be in slightly better agreement with the measurements.

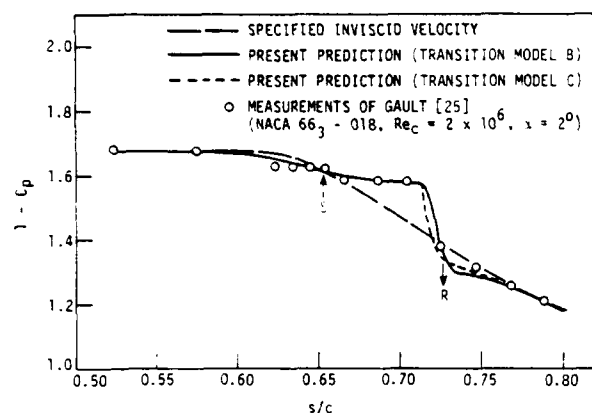


Fig. 2. Comparison of predicted pressure distribution with experimental data on NACA 66₃-018 airfoil, $\alpha = 20^\circ$.

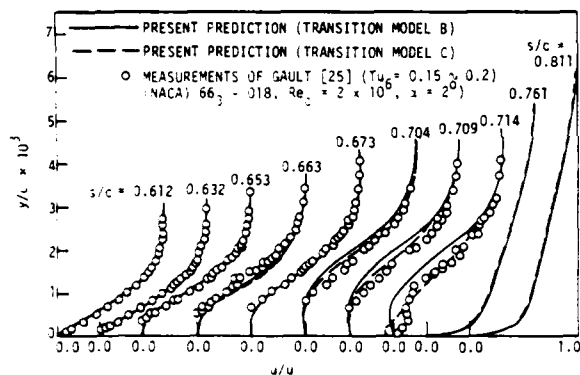


Fig. 3. Comparison of predicted mean velocity profiles with experimental data for NACA 66₃-018 airfoil, $\alpha = 20^\circ$.

The remaining comparisons are for the NACA 63-009 airfoil at $Re_c = 5.8 \times 10^6$ and angles of attack of 4, 5, and 7 degrees. Leading edge bubbles were observed to form under these flow conditions. An overview of the effect of increasing angle of attack can be seen in Fig. 4 where the predicted displacement surfaces and separation and reattachment points are presented for the three flows. The separation bubble can be seen to move toward the leading edge as the angle of attack increases. This same trend can be observed in the experimental measurements, although no displacement thickness was measured to allow a comparison in Fig. 4. Predictions were only obtained using transition Model B for these three flows. Earlier comparisons had indicated that both Models B and C gave acceptable and similar predictions. Model C was dropped from further consideration only because the idea of instantaneous transition was thought to be physically unrealistic.

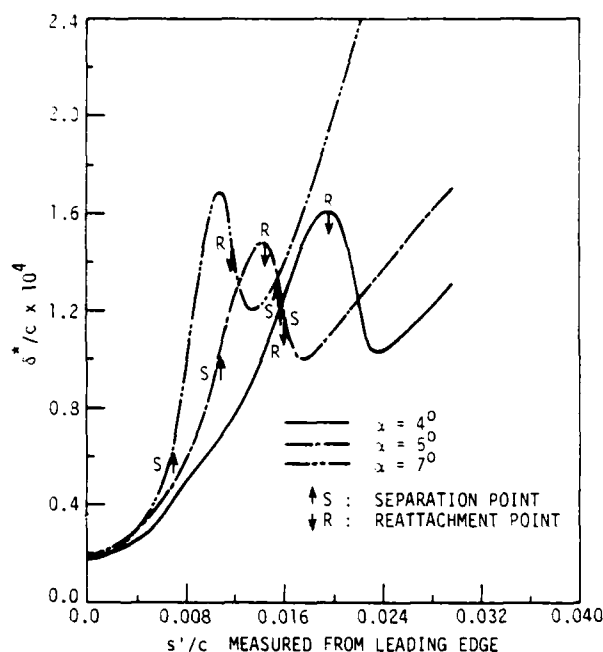


Fig. 4. Variation of displacement thickness distribution with angle of attack on NACA 63-009 airfoil, $Re_c = 5.8 \times 10^6$.

Figures 5-7 compare the predicted and measured^{26,27} pressure coefficients for the NACA 63-009 airfoil flows. The predictions which Crimi and Reeves obtained by an interaction scheme that calculated the viscous flow by an integral method are also shown in Fig. 7. The predicted separation and reattachment points are indicated in the figures. The agreement between the predicted and the measured pressure coefficient appears to be generally good.

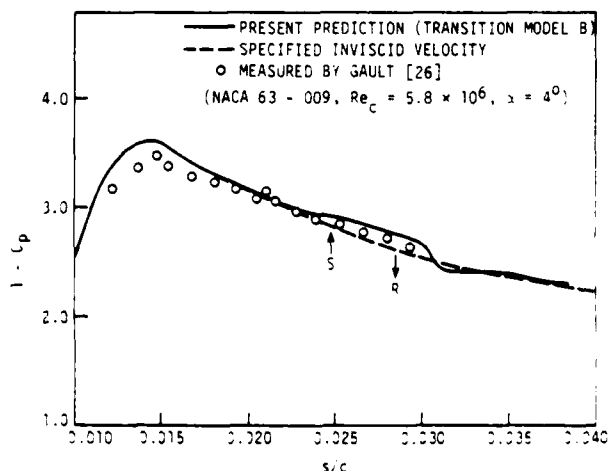


Fig. 5. Comparison of predicted pressure distribution with experimental data on NACA 63-009 airfoil, $\alpha = 4^\circ$.

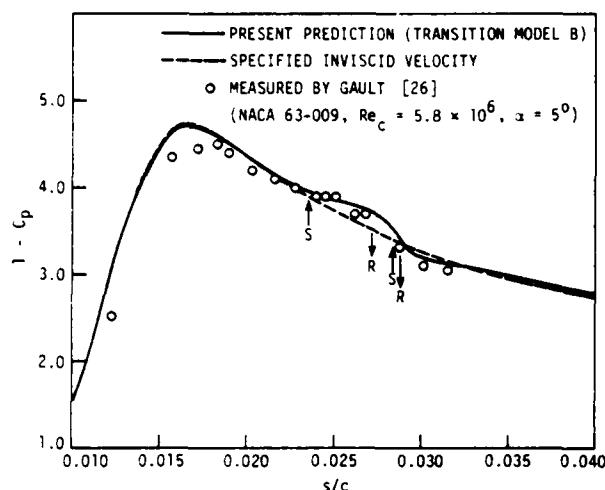


Fig. 6. Comparison of predicted pressure distribution with experimental data on NACA 63-009 airfoil, $\alpha = 5^\circ$.

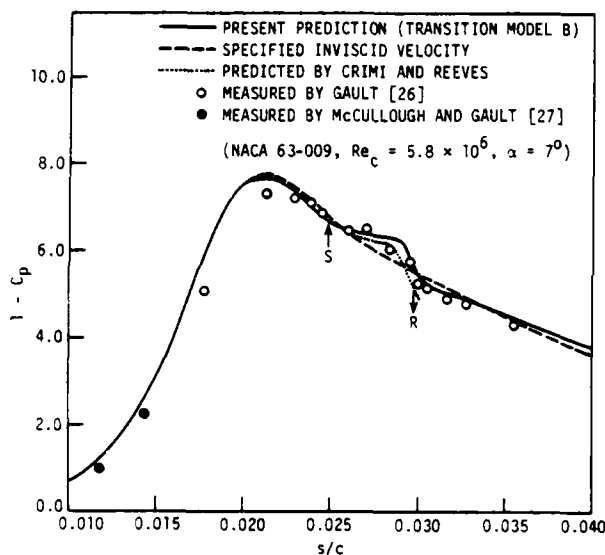


Fig. 7. Comparison of predicted pressure distribution with experimental data on NACA 63-009 airfoil, $\alpha = 7^\circ$.

Predicted velocity profiles in and near the separated regions are compared with measurements for the NACA 63-009 airfoil flows in Figs. 8-10. The agreement between predictions and measurements appears reasonable, except perhaps for the NACA 63-009 airfoil at $\alpha = 7^\circ$. The difficulty of obtaining accurate velocity measurements with conventional pressure probes in and near separated flows is well known. Predicted velocity profiles near reattachment are extremely sensitive to the location of the predicted transition point. For $\alpha = 7^\circ$, especially, the predicted transition occurred slightly downstream of that indicated by the experimental measurements. Here, the steepening of the velocity profiles is taken as evidence of transition from laminar to turbulent flow. Generally, the velocity profiles suggest that the flow separates laminarily and remains essentially

laminar until after the local peak in the displacement surface has occurred, indicating that the outer portion of the flow is turning toward the airfoil and that the reversed flow region is shrinking. In one computed case, the NACA 63-009 airfoil at $\alpha = 5^\circ$, the predicted flow reattached laminarily, separated a second time, underwent transition to turbulent flow, and then reattached a second time. Despite this unusual predicted flow pattern, the predicted pressure coefficients and velocity profiles are in fairly good agreement with the measurements. It should be remembered that the actual flow near separation and reattachment points is frequently quite complex, with certain portions of the flow fluctuating in time between the separated and attached state.²⁸

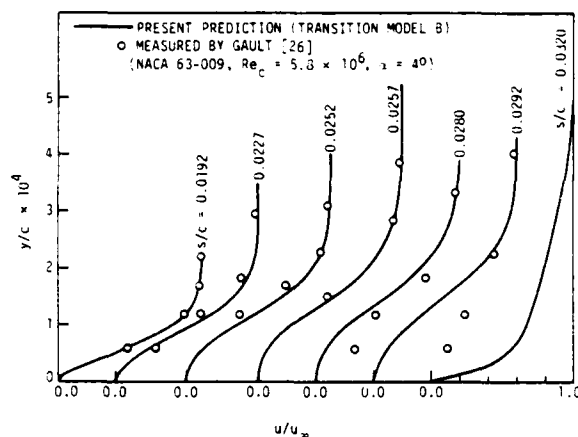


Fig. 8. Comparison of predicted mean velocity profiles with experimental data for NACA 63-009 airfoil, $\alpha = 4^\circ$.

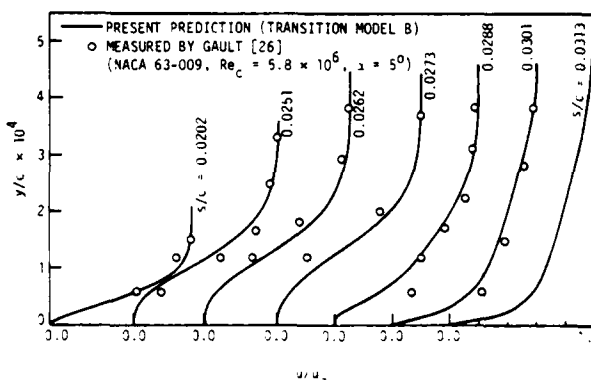


Fig. 9. Comparison of predicted mean velocity profiles with experimental data on NACA 63-009 airfoil, $\alpha = 5^\circ$.

The inviscid surface velocity distribution for unseparated flow, $u_{e,0}(x)$, needed in the present viscous-inviscid interaction procedure was obtained by the Hess and Smith procedure.²² From ten to fifteen iterations through the viscous and inviscid calculations were needed for convergence, as determined by the requirement that the maximum change in the inviscid edge velocity be less than 0.6% between two successive iterations. The maximum difference between $u_{e,BL}$ and $u_{e,INV}$ was less than 2%.

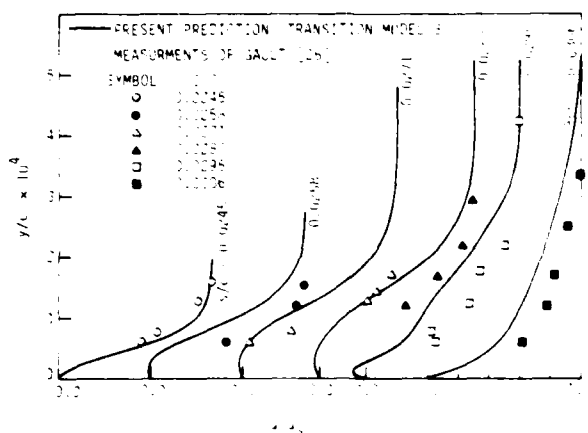


Fig. 10. Comparison of predicted mean velocity profiles with experimental data on NACA 63-009 airfoil, $\alpha = 7^\circ$, $Re_c = 5.3 \times 10^5$.

Concluding Remarks

The present viscous-inviscid interaction calculation procedure was seen to provide predictions in fairly good agreement with experimental data for both midchord and leading edge transitional separation bubbles on airfoils at angles of attack. The predictions appeared quite sensitive to the model used for laminar-turbulent transition. Model A, which is based on correlations for natural transition, proved unsatisfactory in the present study because early transition was predicted for some flows which prevented separation altogether. Both Models B and C gave good results for the NACA 63-018 airfoil flow at $\alpha = 2^\circ$. The main difference between the models was the way in which the length of the transition region was determined. Model C assumed that transition occurred instantaneously. This model was abandoned on physical grounds during the latter stages of the study in favor of Model B which made use of a transition zone of finite length.

The purpose of the present study has been to predict flows in which separation bubbles occurred, and for this purpose transition Model B has proven reasonably satisfactory for both midchord and leading edge bubble flows at several angles of attack. Unfortunately, this transition model uses the separation point as a parameter; consequently, it provides no information on transition for flows which do not separate. Further work is needed to establish a more generally useful transition model which would reliably predict no separation when none occurs. Laminar separation on airfoils in subsonic flow has been observed to occur at local Reynolds numbers up to about 7×10^5 . There would be no experimental basis for Eq. (20) beyond that point. In using transition Model B, it is tentatively suggested that transition be initiated according to Model A if separation does not occur before the local Reynolds number reaches 7×10^5 .

Acknowledgment

This work was supported by the Engineering Research Institute, Iowa State University, through funds provided by the U.S. Army Research Office.

References

1. Pletcher, R. H., "Prediction of Incompressible Turbulent Separating Flow," *Trans. ASME, J. Fluids Eng.*, **100**:427-433 (1978).
2. Carter, J. E., "Solutions for Laminar Boundary Layers with Separation and Reattachment," *AIAA Paper No. 74-583* (1974).
3. Cebeci, T., Keller, H. B. and Williams, P. G., "Separating Boundary-Layer Flow Calculations," *J. Comput. Phys.*, **31**:363-378 (1979).
4. Wooley, R. L. and Kline, S. J., "A Procedure for Computation of Fully Stalled Flows in Two-Dimensional Passages," *Trans. ASME, J. Fluids Eng.*, **100**:180-186 (1978).
5. Kim, J., Kline, S. J. and Johnston, J. P., "Investigation of Separation and Reattachment of a Turbulent Shear Layer: Flow Over a Backward Facing Step," Report MD-37, Dept. of Mech. Engr., Stanford University (1978).
6. Crimi, P. and Reeves, B. L., "Analysis of Leading-Edge Separation Bubbles on Airfoils," *AIAA J.*, **14**(11):1548-1555 (1976).
7. van Ingen, J. L., "On the Calculation of Laminar Separation Bubbles in Two-Dimensional Incompressible Flow," AGARD Conference Proceedings No. 168, Flow Separation, Paper No. 17 (1975).
8. Gerhart, P. M. and Chima, R. V., "Development of a Method for Predicting Subsonic Turbulent Separating Boundary Layers," Final Report, Dept. of Mech. Engr., University of Akron, Akron, Ohio (1978).
9. Briley, W. R. and McDonald, H., "Numerical Prediction of Incompressible Separation Bubbles," *J. Fluid Mech.*, **69**(4):631-656 (1975).
10. Carter, J. E., "A New Boundary-Layer Interaction Technique for Separated Flows," *NASA Tech. Mem. 78690* (1978).
11. Cebeci, T., Stewartson, K. and Williams, P. G., "Separation and Reattachment Near the Leading Edge of a Thin Airfoil at Incidence," *Proceedings of AGARD Conference on Computation of Viscous-Inviscid Interactions*, AGARD-CP-291, pp. 20-1 to 20-13 (1981).
12. Kwon, O. K. and Pletcher, R. H., "Prediction of Incompressible Separated Boundary Layers Including Viscous-Inviscid Interaction," *Trans. ASME, J. Fluids Eng.*, **101**:466-472 (1979).
13. Pletcher, R. H., Kwon, O. K., and Chilukuri, R., "Prediction of Separating Turbulent Boundary Layers Including Regions of Reversed Flow," Final Technical Report HTL-22, ISU-ERI-Ames-80112 (1980).
14. Reyhner, T. A. and Flügge-Lotz, I., "The Interaction of a Shock Wave with a Laminar Boundary Layer," *Int. J. Non-Linear Mech.*, **3**(2):173-199 (1968).

15. Cebeci, T., Mosinskis, G. J. and Smith, A. M. O., "Calculation of Viscous Drag and Turbulent Boundary-Layer Separation on Two-Dimensional and Axisymmetric Bodies in Incompressible Flows," Report No. MDC J0973-01, Douglas Aircraft Co., Long Beach, California (1970).
16. Chen, K. K. and Thyson, N. A., "Extension of Emmons' Spot Theory to Flows on Blunt Bodies," AIAA J., 9(5):821-825 (1971).
17. Dhawan, S. and Narashima, R., "Some Properties of Boundary Layer Flows during the Transition from Laminar to Turbulent Motion," J. Fluid Mech., 3(4):418-436 (1958).
18. Emmons, H. W., "The Laminar-Turbulent Transition in a Boundary Layer-Part I," J. Aerosp. Sci., 18(7):235-246 (1951).
19. Ward, J. W., "The Behavior and Effects of Laminar Separation Bubbles on Aerofoils in Incompressible Flow," J. R. Aeronaut. Soc., 67:783-790 (December 1963).
20. Horton, H. P., "A Semi-Empirical Theory for the Growth and Bursting of Laminar Separation Bubbles," United Kingdom Aeronautical Research Council, Current Paper No. 1073 (1969).
21. Lighthill, M. J., "On Displacement Thickness," J. Fluid Mech., 4:383-392 (1958).
22. Hess, J. L. and Smith, A. M. O., "Calculation of Potential Flow About Arbitrary Bodies," Progress in Aeronautical Sciences, 3:1-138 (1967).
23. Jobe, C. E., "The Numerical Solution of the Asymptotic Equations of Trailing Edge Flow," Tech. Report AFFDL-TR-74-40, Air Force Flight Dynamics Laboratory (1974).
24. Kwon, O. K., "Prediction of Incompressible Boundary Layers Including Viscous-Inviscid Interaction," MS Thesis, Iowa State University, Ames (1978).
25. Gault, D. E., "An Experimental Investigation of Regions of Separated Laminar Flow," NACA TN-3505 (1955).
26. Gault, D. E., "Boundary Layer and Stalling Characteristics of the NACA 63-009 Airfoil Section," NACA TN-1894 (1949).
27. McCullough, G. B. and Gault, D. E., "Examples of Three Representative Types of Airfoil Section Stall at Low Speed," NACA TN-2502 (1951).
28. Simpson, R. L., Strickland, J. H. and Barr, P. W., "Laser and Hot Film Anemometer Measurements in a Separating Turbulent Boundary Layer," Technical Report WT-3, Southern Methodist University, Thermal and Fluid Sciences Center (1974).

SESSION 6

UNSTEADY VISCOUS TRANSONIC FLOW COMPUTATIONS USING THE LTRAN2-NLR CODE
COUPLED WITH GREEN'S LAG-ENTRAINMENT METHOD *

R. Houwink*
National Aerospace Laboratory NLR
Amsterdam, The Netherlands

List of Symbols

A	amplitude
c	chord
C_L	lift coefficient
C_M	moment coefficient (about 0.25 c, positive nose down)
C_H	hinge moment coefficient (positive trailing edge up)
C_p	pressure coefficient
$C_{p,u}$	unsteady pressure coefficient (Eq. 4)
δ	displacement thickness input in airfoil and wake boundary conditions (Eqs. 4 and 5, dimensionless, relative to chord)
f	frequency (Hz)
h	s coordinate of instantaneous airfoil contour (dimensionless, relative to chord)
k	reduced frequency based on semi-chord, $k = \frac{\pi c f}{U_\infty}$
k_u	unsteady lift coefficient (Eq. 11)
m	unsteady moment coefficient (about 0.25 c, positive nose down, Eq. 12)
M_∞	free-stream Mach number
n	unsteady hinge moment coefficient (positive trailing edge up, Eq. 13)
r_{bd}	relaxation factor on displacement thickness input in airfoil and wake boundary conditions (Eq. 7)
Re	Reynolds number based on chord
Re_δ	Reynolds number based on momentum thickness
t	time (dimensionless, relative to c/U_∞)
t	airfoil thickness
T	time, $T = kt$
Δt	time step in unsteady flow computation
U_∞	local flow velocity (dimensionless, relative to U_∞ , $U_\infty = 1 + \frac{1}{2}k$)
U_∞	free-stream velocity
x	coordinate in free stream direction (dimensionless, relative to chord)
x_t	transition point location
z	coordinate normal to x axis (dimensionless, relative to chord)
α	angle of attack (deg)
β	flap deflection (deg)
δ^*	displacement thickness (dimensionless, relative to chord)
δ_u^*	unsteady displacement thickness (Eq. 10)
γ	ratio of specific heats
ϕ	perturbation potential (dimensionless)
ϕ_0	phase shift (deg) (Eq. 3)
<u>Subscripts</u>	
a	pitching motion
f	flap motion
s	mean steady state
1	first harmonic component

Summary

Results of unsteady inviscid and viscous transonic flow computations are presented and compared with experimental data for the NACA-0012 airfoil with oscillating flap, for the NACA-0012 airfoil and for a supercritical airfoil oscillating in pitch. The computations were performed using the NLR version of the NASA-Ames computer code LTRAN2, coupled with the lag-entrainment method of Green for a turbulent boundary layer. The computed effect of the boundary layer on the unsteady airloads (reduction of the magnitude and a positive phase shift) generally leads to a better agreement with experimental data. The remaining differences may be due to the low frequency small perturbation potential approximation, the weak interaction modelling and wall interference effects. For various cases considered, in comparison with the unsteady boundary layer methods developed at ONERA the steady method of Green predicts an about similar effect of the boundary layer on the unsteady airloads.

1. Introduction

Recently various unsteady transonic small perturbation methods have been coupled with boundary layer integral methods to improve the prediction of unsteady airloads on airfoils oscillating in attached transonic flow. Results of these methods have been reported in, for instance, Refs. 1 to 6. The two-dimensional methods developed at ONERA (Refs. 1 and 2) employ versions of the unsteady boundary layer method of Cousteix, Houdeville and Desoppe (Ref. 6), whereas the LTRAN2-NLR version of the two-dimensional NASA-Ames code LTRAN2 (Refs. 4, 5) and the three-dimensional code developed at Boeing (Ref. 3) are coupled with the steady lag-entrainment method of Green (Ref. 7). The methods described in Refs. 2 and 3 employ different models of strong viscous-inviscid interaction, whereas the methods described in Refs. 1 and 5 employ a weak interaction model.

The present paper contains a short description of the LTRAN2-NLR code coupled in weak interaction with Green's method ("LTRANV" program) and a comparison of calculated results for various oscillating airfoils with experimental data and results of other theories. The aim of the paper is twofold: first, to verify the expected improvement in accuracy by taking into account boundary layer effects both for conventional and supercritical oscillating airfoils, and second, to investigate the prediction of these effects by Green's lag-entrainment method in comparison with the unsteady boundary layer methods employed at ONERA. The latter comparison is justified, because the inviscid flow methods used at NLR and ONERA have the same

* This investigation has been carried out under contract with the Netherlands Agency for Aerospace Programs (NIVR).

* Senior Research Engineer, Department of Fluid Dynamics

theoretical basis (transonic small perturbation theory).

An outline of the LTRANV code is given in section 2. A summary of the transonic flow computations and a definition of results are given in section 3. In section 4 results are presented for the NACA64A006 airfoil with oscillating flap, for the NACA64A010 airfoil pitching about 0.25 chord and for a supercritical airfoil pitching about 0.45 chord.

2. Outline of the LTRANV computer program

The basis of LTRANV is the LTRAN2-NLR computer program (Ref. 8), an improved version of the LTRAN2 code developed by Ballhaus and Boorjian (Ref. 9). This program computes the time history of the inviscid transonic flow about a 2D airfoil in unsteady motion. It is based on the low frequency transonic small perturbation potential equation:

$$[1 - M_\infty^2 - (\gamma + 1) M_\infty^2] \phi_{xx} + \phi_{zz} - 2M_\infty^2 \phi_{xt} = 0 \quad (1)$$

where $\gamma^* = 2 - (2 - \gamma) M_\infty^2$. For an instantaneous airfoil contour defined by $z = h(x, t)$, the boundary condition on the airfoil is given by:

$$\phi_z = h_x + h_t \quad (2)$$

Across the wake the pressure jump is required to be $\Delta C_p = 0$, which results in the boundary condition:

$$\Delta(\phi_x + \phi_t) = 0 \quad (3)$$

In the unsteady flow computation the motion is subdivided into a number of time steps, and at each time step equation (1) is solved by a conservative alternating direction implicit (ADI) finite difference scheme.

In practical applications, first a steady state solution is computed. In the LTRAN2-NLR program this is performed by a separate relaxation method. Starting from this steady state, the unsteady flow is usually calculated for a few periods of sinusoidal motion. Fourier analysis of the unsteady airloads during the last period yields the unsteady aerodynamic coefficients which can be used for aeroelastic analyses.

For viscous computations the boundary condition (2) is modified by adding the displacement thickness effect to the airfoil boundary conditions:

$$\phi_z = h_x + d_x + h_t \quad (4)$$

To account for the displacement thickness of the wake, the wake condition (3) is supplemented by the condition:

$$\Delta(\phi_z) = d_x \quad (5)$$

The displacement thickness of the turbulent part of the boundary layer and the wake are computed using Green's lag-entrainment method, of which a full description is given in Ref. 7. The three ordinary differential equations underlying this method are the momentum integral equation, the entrainment equation (based on conservation of mass) and the lag equation (derived from the turbulent kinetic energy equation). In the LTRANV program these equations are integrated using a fourth-order Runge-Kutta method. Secondary influences such as curvature are neglected, and no special care is taken to treat the effect of

shock waves. Initial conditions and the transition point location can be prescribed (e.g. in case of forced transition), or they are calculated using the laminar boundary layer method of Thwaites (Ref. 10) with Illingworth - Stewartson transformation (Ref. 11) and the transition point prediction method of Granville (Ref. 12). The latter method was implemented in the form described by Cebeci and Smith (Ref. 13).

The coupling with the boundary layer computation is carried out according to the weak interaction model: at each time step, the displacement thickness distribution is computed for the local velocity distribution $U(x)$ at the old time level T^n , and is used subsequently as input (through equations (4) and (5)) for the inviscid flow computations at the new time level T^{n+1} . In order to suppress divergence in the iteration process relaxation factors have to be applied to U_e and to d_x in Eqs. (4) and (5):

$$U_e^n = 1 + 0.5 (\phi_x^n + \phi_x^{n-1}) \quad (6)$$

$$d_x^n = \pm r_{bl} \delta_x^n + (1 - r_{bl}) d_x^{n-1} \quad (7)$$

In Eq. (7) the minus sign for $r_{bl} \delta_x^n$ is used for the lower side of the airfoil. In practice, $r_{bl} = 0.33$ gives a converging unsteady flow computation. It should be noted that the above relaxation factors introduce a phase shift in the viscous displacement term d_x in the boundary conditions, which for harmonic motions is approximately given by:

$$\Delta\phi = \frac{360}{2\pi r_{bl}} \Delta T \text{ (deg)} \quad (8)$$

The resulting error in the phase angle of the unsteady airloads depends on the computed effect of the boundary layer, and therefore usually is a small fraction of $\Delta\phi$ in Eq. (8).

The above viscous-inviscid interaction was implemented both in the steady (line-relaxation) and in the unsteady (ADI) computation. By accounting for the effect of only the boundary layer on the airfoil the computational cost are increased by about 30 % relative to an inviscid flow computation; accounting for the displacement effect of boundary layer and wake leads to a 50 % increase.

In order to improve the accuracy and applicability of the code, in the near future the weak interaction model will be replaced by a simultaneous solution of flow equation and boundary layer equation as formulated by Oldman (Ref. 14). A rather similar coupling procedure was implied in the method described by Rizzetta in Ref. 15. This type of coupling should eliminate instability in the computed interaction near separation, and consequently reduce the need to apply underrelaxation factors to the displacement thickness variation.

3. Computations and definition of results

Both inviscid and viscous flow computations were carried out for the following cases:

- (a) NACA64A006 airfoil with oscillating flap with a hinge at 0.75 c (experimental data from Tijdeman and Schippers, Ref. 16);
mean steady: $M_\infty = 0.85$, $\alpha_\infty = 0$ deg, $Re = 2.4 \times 10^7$,
 $x_t = 0.10$;
unsteady: $\delta_f = 1$ deg, $k = 0.004, 0.18, 0.24$

- (b) NACA64A010 airfoil (NASA Ames model)
oscillating in pitch about 0.25 c (experimental data from Davis and Malcolm, Ref. (17);
mean steady: $M_\infty = 0.8$, $\alpha_0 = 0$ deg, $Re = 12.5 \times 10^6$,
transition point assumed at 0.10 c;
unsteady: $\alpha_1 = 1$ deg, $k = 0.05, 0.1, 0.2$
- (c) NLR supercritical airfoil with relative thickness $t/c = 0.12$, oscillating in pitch about 0.45 c (experimental data from Horsten, Ref. 18, and partly unpublished);
mean steady: $M_\infty = 0.6$ to 0.75, incidence matched to obtain approximate agreement with pressure distributions measured at $\alpha = 0.75$ deg, $Re = 2.2 \times 10^6$, $x_t = 0.10$;
unsteady: $\alpha_1 = 0.5$ deg, $f = 40$ Hz ($k = 0.09$ to 0.11).

In the viscous flow computations for cases (a) and (b) the displacement thickness of the wake was not taken into account; in case (b) at $k = 0.2$, and case (c) this effect was accounted for.

The unsteady flow was computed during two cycles of oscillation at 120 time steps per cycle. The initial conditions for the turbulent boundary layer computation (θ and x_t) were obtained by the laminar boundary layer and transition point computations, with the transition strip location as downstream boundary for x_t , and the Reynolds number based on momentum thickness $Re_\theta = 320$ as lower boundary for the initial value of Re_θ .

The unsteady pressure and displacement thickness distributions are presented in the following form, where A indicates the amplitude of the sinusoidal motion and subscript 1 indicates the first harmonic component:

$$\text{pressure: } \Delta C_p = \Delta C_p' + i \Delta C_p'' = \frac{C_{p1}}{A} \quad (9)$$

$$\text{displacement thickness: } \Delta \delta^* = \Delta \delta^{*'} + i \Delta \delta^{*''} = \frac{\delta_1^*}{A} \quad (10)$$

The overall airloads are presented as follows, where the index α or c indicates a pitching motion or a flap motion, respectively:

$$\text{lift: } k_{\alpha,c} = k' + ik'' = \frac{1}{\pi} \frac{C_{l1}}{A} \quad (11)$$

$$\text{moment (about 0.25 c): } m_{\alpha,c} = m' + im'' = \frac{2}{\pi} \frac{C_{m1}}{A} \quad (12)$$

$$\text{hinge moment: } n_c = n' + in'' = \frac{2}{\pi} \frac{C_{n1}}{A} \quad (13)$$

The reduced frequency is based on semi-chord and defined as:

$$k = \frac{\pi c f}{U_\infty} \quad (14)$$

4. Results and discussion

4.1 The NACA64A006 airfoil

Figures 1, 2 and table 1 show some results for the NACA64A006 airfoil with oscillating flap. The mean steady pressure distribution (Fig. 1a) exhibits a weak shock wave near midchord. Addition of the boundary layer leads to a more forward shock location and a lower trailing edge pressure,

resulting into a better agreement with the experimental result. In the real and imaginary part of the pressure distribution at $k = 0.24$ (Figs 1b and 1c) similar remarks apply. The peaks in ΔC_p near mid-chord are associated with the shock wave motion, whereas the peak in the real part of ΔC_p at 0.75 chord is generated by the discontinuity in surface slope at the flap hinge.

The effect of the boundary layer on the lift, moment and hinge moment coefficients is shown in figure 2 for $k = 0$ to 0.24. Except for the phase angle of the hinge moment coefficient the effect of the boundary layer (reduction of magnitude and a positive phase shift) leads to a better agreement with the experimental data. The boundary layer effect is opposite the effect of thickness, which illustrates the often acceptable performance of linear theory at transonic conditions. The viscous transonic flow computation gives the best results for the moment coefficients. For the lift coefficient the predicted phase angle is too negative and, for low frequencies, the magnitude is overestimated.

This may indicate an underprediction of the boundary layer effect on the shock wave motion, inaccuracy of the TSP theory and the presence of wall interference effects at low frequencies. The significance of the latter effects is illustrated by the quasi-steady wall-interference correction to k_c at $k = 0$ in figure 2. In general it should be remarked that the presence of wall-interference effects prohibits a definite conclusion about the accuracy of the theories investigated.

Also in figure 2, for $k = 0.24$ a comparison is made with results of a rather similar TSP method in use at ONERA, which is coupled with an unsteady boundary layer method (Desoppe and Grenon, Ref. 1). Compared with this method the method of Green predicts a slightly stronger, though rather similar effect of the boundary layer. Taking into account the effect of the use of relaxation factors (in equations 6 and 7, causing a slight positive phase shift of about 1 deg in k_c to 3 deg in n_c) it can be concluded that the steady boundary layer method is equally well applicable, compared to the unsteady method. The same conclusion can be drawn from a comparison of results of the present method and data from Couston et al (Ref. 2) for a slightly different case ($M_\infty = 0.854$, $k = 0.18$), presented in table 1. Couston et al. also employ a TSP method, coupled with an unsteady boundary layer method approximately similar to that of reference 1.

4.2 The NACA64A010 airfoil (NASA Ames model)

An example of the computed mean steady and unsteady pressure and displacement thickness distributions (without viscous wake computation) is given for $k = 0.2$ in figure 3. In the mean steady pressure distributions (Fig. 3a) there is a reasonable agreement between the experimental and theoretical results. Accounting for the boundary layer leads to a more upstream and weaker shock wave, and to a lower pressure at the tail, like in the case of the airfoil with oscillating flap discussed in section 4.1. These effects can be associated with a local increase of the displacement thickness at the shock wave ("viscous wedge") and at the trailing edge. The theoretical results at the shock wave exhibit a lower gradient than the measured data, which is likely due to the coarseness of the computational grid.

The corresponding unsteady pressure and displacement thickness distributions are shown in figure 3b (real part) and figure 3c (imaginary part). For the real part a good agreement is found

between experimental and theoretical results. As to the boundary layer effect the same remarks apply as in the steady case. This leads to a better agreement with the experimental data. Like the steady case the unsteady pressure peak at the shock is smeared out, compared to the experimental result. A strong gradient in the displacement thickness reflects the gradient in the pressure distribution at the shock wave.

Again, similar remarks apply to the imaginary parts shown in Figure 3c. However, here the unsteady pressure level upstream of the shock wave is somewhat underpredicted, which leads to significant differences in the phase angle of experimental and theoretical airloads discussed next.

A comparison of unsteady lift and moment coefficients is made in figure 4. The results are presented as magnitude and phase angle. For reference, also results of linear theory are shown. Like the airfoil with oscillating flap, the effects of the boundary layer on lift and moment is a reduction in magnitude and a positive phase shift, compared to the effect of thickness. For $k = 0.2$ the observed underprediction of ΔC_p upstream of the shock wave (Fig. 3c) leads to a considerable difference in the phase angle of both lift and moment coefficients; the magnitude of these quantities is reasonably well predicted. The error in phase angle probably indicates inaccuracy of the low frequency small perturbation potential equation (1) for the present case. However, also a possible unsteady displacement of the transition point in the experiment (not accounted for) may contribute to the observed difference between experimental and theoretical results. It is not known to what extent also wall-interference effects play a role.

For $k = 0.2$ also results are shown where the displacement effect of the wake is taken into account. This effect reduces the effect of the boundary layer by about 25 % in magnitude and 50 % in phase angle. The explanation is that the wake displacement thickness reduces the pressures at the trailing edge, which results in a thinner boundary layer and a smaller influence of the boundary layer on the unsteady airloads.

4.3 The supercritical airfoil

In Figures 5 and 6 results are presented for an oscillating supercritical airfoil (relative thickness 12 % chord) developed at NLR. To obtain stable viscous flow solutions for this airfoil, the distribution of U_e near the trailing edge was modified in the following way before each boundary layer computation. The trailing edge velocity was prescribed ($U_e = 0.9$) and a smooth distribution of U_e was matched between this value and the values of U_e at 90 % and 110 % chord.

Figure 5a shows the mean steady pressure distribution for the experimental shock-free condition ($M_\infty = 0.75$, $\alpha_0 = 0.75^\circ$). The shock-free theoretical results were obtained at a lower Mach number ($M_\infty = 0.731$) at different angles of attack ($\alpha_0 = -0.2^\circ$ deg for the inviscid case, and $\alpha_0 = 0.25^\circ$ deg for the viscous case). The difference in α_0 relative to the experimental incidence was necessary largely to account for wall-interference effects ($\Delta\alpha \approx 0.5^\circ$ deg), and additionally for the inviscid case, for viscous effects ($\Delta\alpha \approx 0.5^\circ$ deg). The reduction in Mach number was probably required to account for the small perturbation potential approximation and (possibly) again some wall-interference effects. The viscous results show clearly the best agreement with the experimental data. The steady effect of the boundary layer is a reduction

of the rear loading and of the trailing edge pressure level.

The corresponding unsteady results are shown in figure 5b (real part) and figure 5c (imaginary part). The real and imaginary parts of ΔC_p show the same order of agreement with the experimental results. The pressure distribution on the lower surface is predicted satisfactorily. It shows a typical subsonic behaviour, except for the peaks at the weak shock wave near the nose. The boundary layer and wake hardly affect the pressure distribution.

On the upper surface a broad peak near 10 % chord indicates the typical character of a shock-free mean steady state, which is predicted reasonably well by both viscous and inviscid theory. The broad peak is due to the sensitivity of the pressure distribution for small incidence variations about the shock-free mean steady state. The computed displacement thickness shows wedge-type changes at the unsteady pressure peaks and at the trailing edge, which cause some reduction of the pressure peaks and the loading on the rear part of the airfoil. The strong peak in the experimental unsteady pressure distributions near midchord is not predicted. This may be due to strong shock wave-boundary layer interaction, not accounted for in the theoretical results.

For $M_\infty = 0.6$ to 0.8 unsteady lift and moment coefficients for a constant frequency $f = 40$ Hz ($k = 0.09$ to 0.11) are shown in figure 6. A comparison is made of results of linear theory, the present inviscid and viscous transonic flow computations and experimental results. The experimental mean steady state conditions range from subsonic at $M_\infty = 0.6$ through the shock-free transition condition at $M_\infty = 0.75$ to separated transonic flow at $M_\infty = 0.8$. The mean steady incidences for the computation were chosen such that an approximate matching was obtained between theoretical and experimental mean steady pressure distributions.

Compared to the results of linear theory, which exhibit smoothly increasing airloads with increasing Mach number, both the theoretical transonic results and the experimental data exhibit a stronger and qualitatively different effect of M_∞ . Typical transonic effects on the lift are a larger magnitude and a more negative phase angle. These thickness effects are reduced by the boundary layer and the wake. The strong change of m_1 near $M_\infty = 0.74$ reflects the displacement of the shock wave and, correspondingly, the unsteady pressure peaks from upstream the quarter-chord point to a more downstream location. Up to flow separation, these effects on m_1 are satisfactorily predicted by the LTRANV program.

The predicted effect of the boundary layer is rather similar to that on the NACA64AC10 airfoil. Contrary to the latter airfoil, however, the phase angles of the lift coefficient on the supercritical airfoil are predicted more negative compared with the experimental data. This may be due to stronger wall interference and viscous effects in the experimental results for the supercritical airfoil. Finally it is interesting to note that the difference between experimental and theoretical viscous results in figure 6 indicates a difference in effective free-stream Mach number of about 0.02. This difference also exists between the theoretical and experimental shock free results shown in figure 5. As mentioned before both wall-interference effects and the small perturbation potential approximation may contribute to the observed difference.

The above results demonstrate that the

combination of the LTRAN2-NLR code with the steady lag-entrainment method of Green can provide a reasonably realistic prediction of unsteady air loads at an oscillating supercritical airfoil at attached flow conditions. However, they also indicate limitations to the accuracy of the low frequency small perturbation formulation, and of the weak viscous-inviscid interaction model. In view of the unknown effects of wall interference it is difficult to draw a definite conclusion about the accuracy of the present LTRANV program.

5. Conclusions

Unsteady transonic flow computations were carried out using the LTRAN2-NLR code coupled in weak interaction with the steady lag-entrainment method of Green. Applications were made for the NACA64A006 airfoil with oscillating flap, the NACA64A010 airfoil and a supercritical airfoil oscillating in pitch.

A comparison of results of this programme with inviscid results and experimental data demonstrates the generally improved accuracy as compared to the inviscid method. For the cases considered, the use of a steady boundary layer method yields an almost similar effect on the unsteady airloads as unsteady boundary layer methods developed at ONERA.

The still existing differences relative to the experimental data may indicate limitations in accuracy of LTRANV, in particular the low frequency transonic small perturbation theory, and the weak interaction coupling procedure. Definite conclusions about the accuracy of the LTRANV code cannot be made due to unknown effects of wall interference.

6. References

- Desopper, A. and Grenon, R.: Couplage fluide parfait-fluide visqueux en écoulement instationnaire bidimensionnel incompressible et transsonique. AGARD-CP-291, 1980.
- Couston, M., Angelini, J.C., Le Balleur, J.C. and Girodroux-Lavigne, P.: Prise en compte d'effets de couche limite instationnaire dans un calcul bidimensionnel transsonique. AGARD-CP-291, 1980.
- Fizzetta, D.P. and Borland, C.J.: Numerical solution of three-dimensional unsteady transonic flow over wings including inviscid/viscous interaction. AIAA paper 82-0352, Orlando, Florida, January 1982.
- Houwink, R.: Some remarks on boundary layer effects on unsteady airloads. AGARD-CP-296, paper 5, Aix-en-Provence, France, Sept. 1980.
- Houwink, R.: Results of a new version of the LTRAN2-NLR code (LTRANV) for unsteady viscous transonic flow computations. NLR TR 81078 U, July 1981.
- Costeix, G., Houdeville, P. and Desopper, A.: Résultats expérimentaux et méthodes de calcul relatives aux couches limites turbulentes en écoulement instationnaire. AGARD-CP-227, Paper 17, 1977.
- Green, J.E., Weeks, D.J. and Brooman, J.W.F.: Prediction of turbulent boundary layers and wakes in compressible flow by a lag-entrainment method. ARC R and M No. 3791, 1973.
- Houwink, R. and van der Vooren, J.: Improved version of LTRAN2 for unsteady transonic flow computations. AIAA Journal, Vol. 18, no. 6, pp. 1005-1010 (August 1980).

- Salinas, W.D. and Salas, L.M.: Explicit finite difference computations of unsteady transonic flows over airfoils, including the treatment of irregular shock wave motions. AIAA paper 82-0352, 1982.
- Detoni, T. and Bradshaw, P.: Momentum transfer in boundary layers. Hemisphere Publishing Corporation, 1977.
- Penikent, D.: Boundary Layer Theory. McGraw-Hill, 1968.
- Granville, P.J.: The calculation of the viscous drag of bodies of revolution. David Taylor Model Basin Rep. 144, 1959.
- Detoni, T. and Smith, A.M.: Analysis of turbulent boundary layers. Academic Press, 1971.
- Veliman, A.E.P.: The calculation of incompressible boundary layers with strong viscous-inviscid interaction. AGARD-CP-291, 1980.
- Fizzetta, D.P.: Procedures for the computation of unsteady transonic flows including viscous effects. NASA CP-166049, August 1981.
- Tijdeman, H. and Schippers, P.: Results of pressure measurements on an airfoil with oscillating flap in two-dimensional high subsonic and transonic flow (zero incidence and zero mean flap position). NLR TR 73078 U, 1973.
- Davis, S.S. and Malcolm, J.N.: Experimental unsteady aerodynamics of conventional and supercritical airfoils. NASA-TM-51221, August 1980.
- Horsten, J.J.: Recent developments in the unsteady pressure measuring technique at NLR. Paper presented at the International Symposium on Aeroelasticity, Nuremberg, Germany, October 1981.

TABLE 1

Comparison of theoretical and experimental unsteady airloads

NACA64A006 airfoil with flap $M_\infty = 0.8$ $\alpha_0 = 4^\circ$, $\alpha_1 = 2^\circ$ $Re = 1.5 \times 10^6$, $K_1 = 0.01$ $K_2 = 0.04$	UNSTEADY AIRLOADS					
	LIFT		MOMENT		HINGE MOMENT	
	K_{L1}	arg K_{L1}	M_1	arg M_1	H_1	arg H_1
INVISCID						
LTRAN-NLR	1.00	1.00	1.00	1.00	1.00	1.00
EXPERIMENT	1.00	1.00	1.00	1.00	1.00	1.00
ADDITIONAL EFFECTS						
BOUNDARY LAYER	1.00	1.00	1.00	1.00	1.00	1.00
LTRANV	1.00	1.00	1.00	1.00	1.00	1.00
EXPERIMENT	1.00	1.00	1.00	1.00	1.00	1.00

NACA64A006 AIRFOIL WITH OSCILLATING FLAP

MACH = 0.85 K = 0.24
 ALPHA = 0 DEG AMP = 1 DEG
 RE = 2.4E06 F = 120 HZ
 XT = 0.10

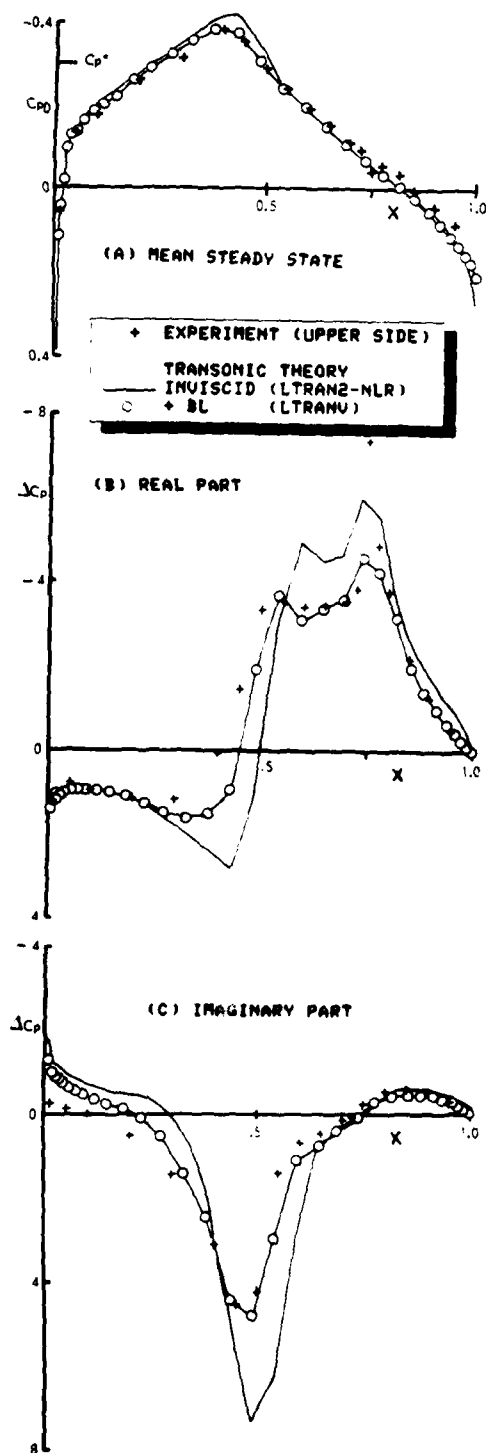


Fig. 1 Mean steady and unsteady pressure distributions on the NACA64A006 airfoil with oscillating flap

NACA64A006 AIRFOIL WITH OSCILLATING FLAP

MACH = 0.85
 ALPHA = 0 DEG
 RE = 2.4E06
 XT = 0.10
 AMP = 1 DEG

+ EXPERIMENT (± CORRECTED FOR WALL INTERFERENCE)

THEORY
 LINEAR
 TRANSONIC (INVISCID)
 LTRAN2-NLR
 DESOPPER/GRENON
 TRANSONIC (+ BL)
 LTRANU
 DESOPPER/GRENON

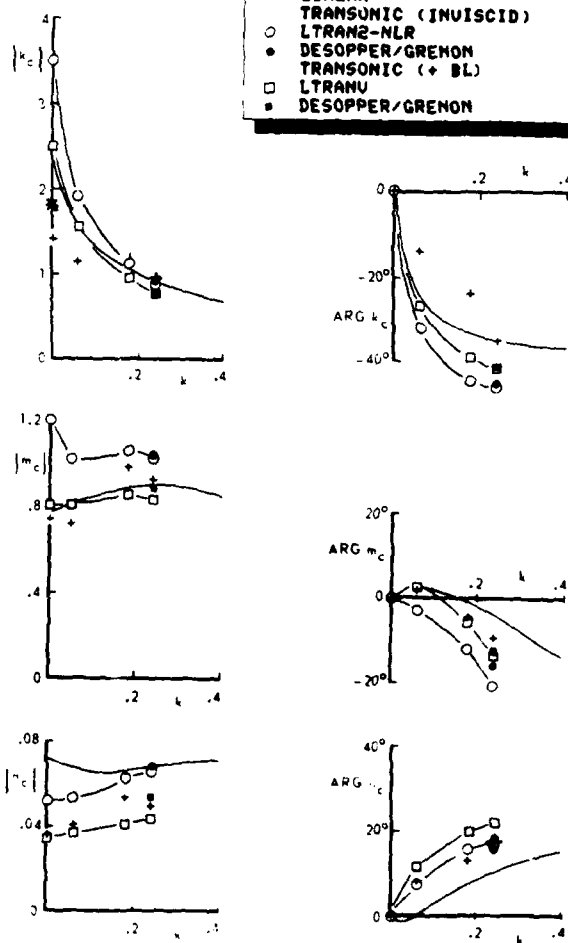
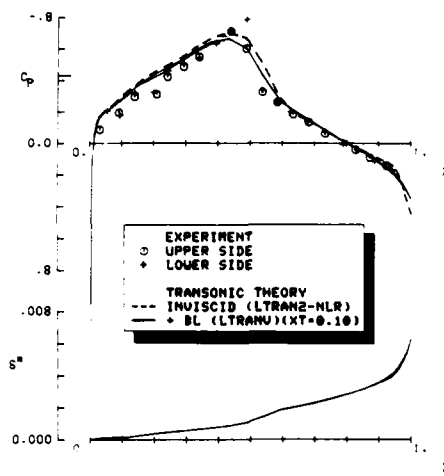


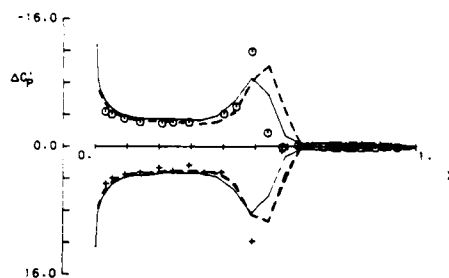
Fig. 2 Unsteady lift, moment and hinge moment coefficients on the NACA64A006 airfoil with oscillating flap

NACA64A010 AIRFOIL PITCHING ABOUT 0.25 CHORD

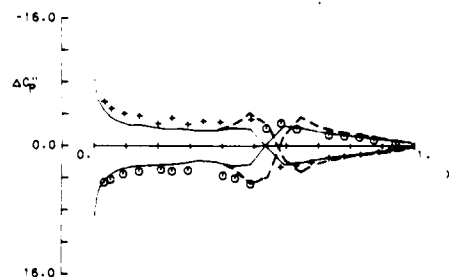
MACH = 0.80 K = 0.2
 ALPHA = 0 DEG AMP = 1 DEG
 RE = 12.5E06



(A) MEAN STEADY STATE



(B) REAL PART



(C) IMAGINARY PART

Fig. 3 Mean steady and unsteady pressure and displacement thickness distributions on the NACA64 A010 airfoil pitching about 0.25 C

NACA64A010 AIRFOIL PITCHING ABOUT 0.25 CHORD

MACH = 0.8
 ALPHA = 0 DEG
 RE = 12.5E06
 AMP = 1 DEG

+ EXPERIMENT
 --- LINEAR THEORY
 TRANSONIC THEORY
 ○ INVISCID (LTRAN2-NLR)
 + BL (LTRANU)
 △ + BL + WAKE (LTRANU)

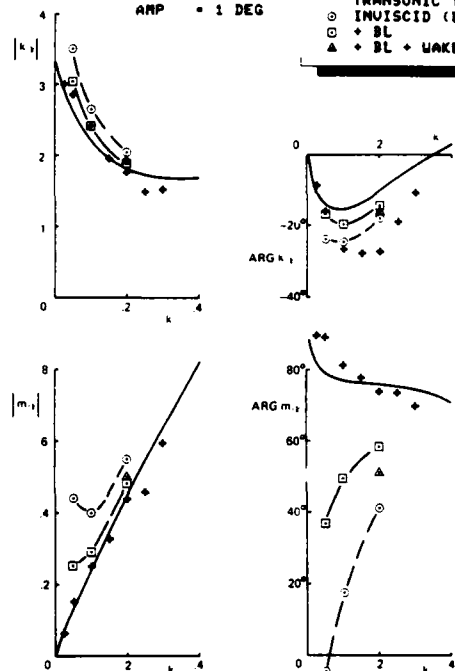
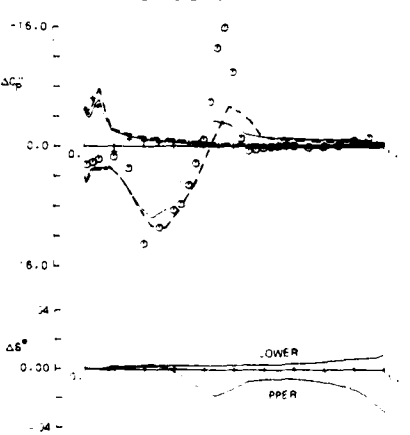
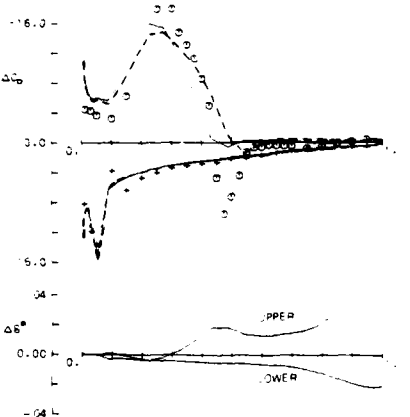
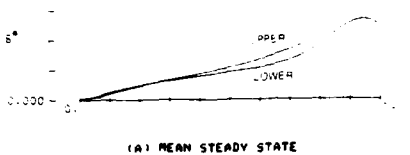
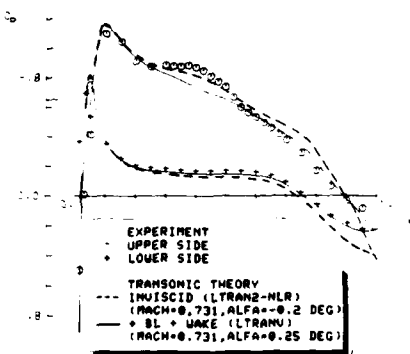


Fig. 4 Unsteady lift and moment coefficients on the NACA64 A010 airfoil pitching about 0.25 C

SUPERCritical AIRFOIL PITCHING ABOUT 0.45 CHORD

RACH = 0.75 K = 0.09
 ALPHA = 0.75 DEG AMP = 0.5 DEG
 RE = 2.2E06 F = 40 HZ
 XT = 0.10



(C) IMAGINARY PART

Fig. 5 Unsteady pressure and displacement thickness distributions on a shock-free supercritical airfoil pitching about 0.45 C

SUPERCritical AIRFOIL PITCHING ABOUT 0.45 CHORD

ALFA = 0.75 DEG
 RE = 2.2E06
 XT = 0.10

K = 0.1
 AMP = 0.5 DEG
 F = 40 HZ

+ EXPERIMENT
 — LINEAR THEORY
 — TRANSONIC THEORY
 ○ INVISCID (LTRAN2-NLR)
 □ BL + WAKE (LTRANU)

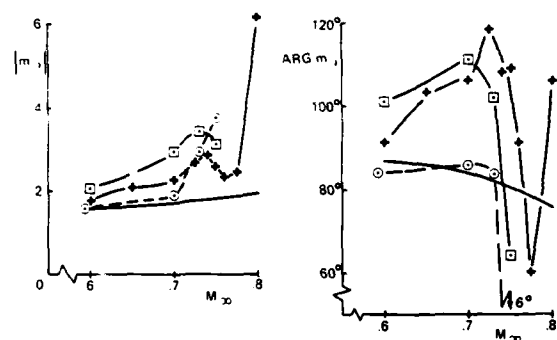
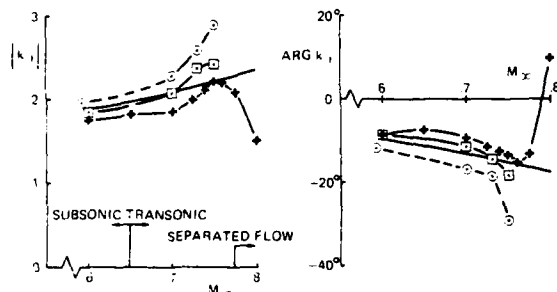


Fig. 6 Unsteady lift and moment coefficients on a supercritical airfoil pitching about 0.45 C

Viscous-Inviscid Interaction Analysis
of Asymmetric Trailing-Edge FlowsVeer N. Vatsa and Joseph M. Verdon
United Technologies Research Center
East Hartford, CT 06108Abstract

Contributions are made to finite Reynolds number, viscous/inviscid interaction theory for laminar, subsonic flow past a thin-airfoil trailing edge. In particular, an analytical/computational technique is developed for predicting high Reynolds number, attached or separated, trailing-edge and near-wake flow. The analysis is based on interacting boundary-layer theory in which the outer inviscid and the inner viscous flows are solved simultaneously to determine the complete flow past the displacement body. Inviscid solutions are based on linear airfoil theory and viscous solutions are determined by a finite difference approximation to the boundary-layer equations cast in Levy-Lees variables. A semi-inverse viscous/inviscid iteration procedure is employed in which viscous and inviscid solutions are repeatedly determined until the inviscid pressure distribution at the displacement surface match the viscous pressure distribution. This approach is assessed through comparisons with previous solutions for incompressible flow past a modified flat plate airfoil at an angle of attack. In addition, results of parametric studies are presented to illustrate the effects of angle of attack, Reynolds number, Mach number and wake curvature on trailing-edge flow behavior.

Introduction

The ultimate goal of the present research program is to employ viscous/inviscid interaction concepts to develop a reliable analytical/numerical method for predicting viscous effects in subsonic to low supersonic cascade flows at high Reynolds numbers. The approach to be followed is similar to that being successfully applied to high Reynolds number external aerodynamic flows wherein viscous/inviscid interaction concepts are used to construct the full flow field using locally relevant component flow solvers^{1,2}. Thus, for the case of high Reynolds number flow in a cascade the full flow field is broken down into the four major categories to represent 1) the inviscid flow; 2) attached boundary-layer flow; 3) wake flow; and 4) locally interacting (possibly separated) flow such as occurs at a blade trailing edge. Construction of a general cascade flow solver involves first, the development of component flow solvers, and second, the matching of these component solvers into an overall computational procedure to produce a reliable and efficient general flow solver. Therefore, the utility and reliability of this cascade solver is critically dependent on the level of development of its component members. The first

three components which deal with the inviscid flow, the boundary-layer flow, and the wake flow are well understood fluid dynamically, and solution methods are at a relatively mature state^{3,4}. Work on the fourth component, the local interaction solver, is the subject of the present paper. Here solution techniques are developed and demonstrated for laminar, asymmetric trailing-edge flow.

This effort is a continuation of the work initiated by Werle and Verdon⁵ in which separated trailing-edge flows were calculated based on asymptotic triple-deck concepts. This approach was subsequently extended to treat finite Reynolds number flows, and solutions were obtained for symmetric flows past thin flat-plate and elliptic-section trailing edges⁶. Flat-plate solutions were found to be in very good agreement with those of other investigators⁷⁻⁹ for finite Reynolds number (Re), and with asymptotic triple-deck solutions in the limit as $Re \rightarrow \infty$. Under the present effort this finite Re interaction analysis has been further developed and applied to calculate asymmetric flows past the trailing edge of a thin cambered airfoil, and results have been determined for both attached and separated flows. Comparisons with Veldman's¹⁰ recent incompressible results have been made, and a detailed parametric study has been conducted to illustrate the effects of angle of attack, Reynolds number, Mach number, and wake curvature on flow behavior in the vicinity of a loaded airfoil trailing edge.

General Concepts

For flows of practical interest in either external or internal aerodynamics the Reynolds number is usually sufficiently high so that the flow past an airfoil or blade can be divided into two regions: an "inner" dissipative region consisting of the boundary layer and the wake, and an "outer" inviscid region. The principal interaction between the viscous and inviscid regions arises from the displacement thickness which leads to a thickened semi-infinite equivalent body with corresponding changes in surface pressures. If the interaction is "weak", the viscous effect on the pressure is small (i.e., of $O(Re^{-1/2})$ in laminar flow or of $O(\ln Re)^{-1}$ in turbulent flow); then the complete flow problem can be solved in a hierarchical manner¹⁰. The first step is to determine the inviscid flow past the airfoil. The resulting pressure distribution is then imposed on the viscous layer calculation to determine the displacement thickness due to viscous dissipation and hence, the effective shape of the body. The displacement effect on the inviscid flow is then estimated by computing the inviscid pressure distribution over the displacement body.

The foregoing method for calculating the interaction between the viscous and inviscid parts of the flow is based on a direct hierarchy between the viscous and inviscid regions which applies as long as the disturbances to the inviscid flow due to viscous displacement effects are small. However, the flow over an airfoil involves both a weak overall interaction arising from standard displacement effects and also from wake curvature effects, and local "strong" interactions arising, for example, from boundary-layer separation, shock boundary-layer interaction, or the rapid flow acceleration immediately aft of the trailing edge. In such situations viscous displacements cause substantial changes in the local inviscid pressure field. The concept of an inner viscous region and an outer inviscid region still applies, but the classical hierarchical structure of the flow breaks down. In a strong interaction region the hierarchy changes from direct (i.e., pressure determined by the inviscid flow) to inverse (pressure determined by the viscous layer), and this change must be accommodated in developing a complete solution¹⁰.

The approach taken here employs an interacting boundary-layer model in which the flow in the outer inviscid region is potential and the viscous flow is governed by Prandtl's boundary-layer equations. At an airfoil trailing edge the strong interaction arises from the abrupt change in the slip condition that the boundary layer experiences at the termination of the airfoil surface. This leads to a singularity in the classical boundary-layer solution and subsequent local breakdown of a weak interaction procedure. However, strong viscous/inviscid interaction solutions can be determined by an iterative procedure which requires successive solutions for the viscous and inviscid regions. Here an efficient semi-inverse solution procedure using Carter's¹¹ iterative technique is applied to the local strong interaction region at an airfoil trailing edge. Thus both the "inner" viscous and "outer" inviscid flows are repeatedly solved for a prescribed displacement thickness distribution until inviscid pressures at the displacement surface match viscous pressures.

We consider high Reynolds number ($Re = \frac{\rho_\infty U_\infty L}{\mu_\infty}$), adiabatic, laminar flow with negligible body forces of a perfect gas with constant specific heats and unit Prandtl number past the trailing edge of a two-dimensional airfoil (Fig. 1). In

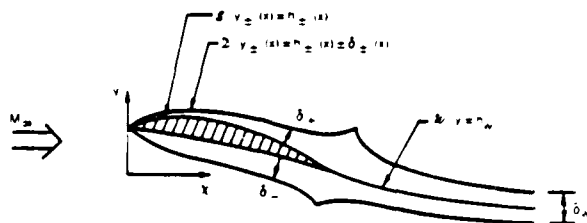


Fig. 1 High Reynolds Number Flow Around a Thin Airfoil

the present analysis, viscous displacement thickness effects at the trailing edge are regarded as strong, while wake curvature effects are regarded as weak. This treatment is in accordance with the triple-deck scaling requirements for laminar flow at asymptotically large Reynolds number¹². Thus, iterative solutions of the inviscid and viscous equations will be determined to account for strong displacement interactions and the resulting outer inviscid solutions will then be corrected to account for wake curvature interactions.

In the following discussion flow variables and spatial coordinates have been made dimensionless. Lengths have been scaled with respect to the length of the airfoil (L^*), density, velocity and viscosity with respect to their freestream values (ρ_∞^* , u_∞^* and μ_∞^* , respectively), pressure with respect to twice the freestream dynamic pressure ($\frac{1}{2} \rho_\infty^* u_\infty^{*2}$), and temperature with respect to the square of the freestream speed divided by the specific heat at constant pressure (u_∞^{*2}/c_p^*). Here the superscript * denotes a dimensional quantity and the subscript ∞ refers to the flow conditions at infinity.

Inviscid Region

Consider two dimensional, subsonic flow in the x, y plane with freestream velocity, u_∞ , in the direction of the positive x -axis around a thin, slightly cambered airfoil at small angle of attack relative to the freestream direction (Fig. 1). The airfoil is located along the interval $[0, 1]$ of the x -axis and the location of the upper and lower surfaces of the airfoil and wake displacement body are defined by

$$\begin{aligned} y_{\pm}(x) &= h_{\pm}(x) \pm \delta_{\pm}(x), & x \in [0, 1] \\ &= h_w(x) \pm \delta_{\pm}(x), & x > 1 \end{aligned} \quad (1)$$

where h_+ and h_- define the upper and lower surfaces of the airfoil and h_w defines the location of the reference wake streamline, i.e., the streamline which emanates from the airfoil trailing edge and δ is the viscous displacement thickness. The functions h_+ and h_- are prescribed, but h_w and δ must be determined as part of the solution. Under the stated assumptions concerning airfoil shape and orientation, the projection of the airfoil and wake displacement body on the y -axis will be small. In addition, if the outer inviscid flow is assumed to be isentropic and irrotational, a velocity potential, $\phi(x, y)$ exists which can be expressed in terms of an asymptotic series, i.e.,

$$\phi = \phi_0 + \epsilon \phi_1 + O(\epsilon^2) = \phi_0 + \phi + O(\epsilon^2) \quad (2)$$

where ϵ is a small parameter. The disturbance potential, $\phi(x, y)$ is then governed by the linear equation

$$(1 - M_\infty^2) \phi_{xx} + \phi_{yy} = 0 \quad (3)$$

To within first order (in ϵ) the inviscid flow properties are given by

$$\gamma M_\infty^2 P = \rho^\gamma = \left[(\gamma - 1) M_\infty^2 T \right]^{\gamma/(\gamma-1)} \quad (4)$$

$$\approx 1 - \gamma M_\infty^2 \phi_x$$

where P is the pressure, ρ is the density, T is the temperature, M_∞ is the freestream Mach number, and γ is the specific heat ratio. Note that the pressure is related to the disturbance potential by

$$P = P_0 + p = \frac{1}{\gamma M_\infty^2} - \phi_x \quad (5)$$

The inviscid flow is determined as a solution of Eq. (3) and is subject to a flow tangency condition at the airfoil surface, jump conditions on normal velocity and pressure across the wake, and the uniform flow condition in the far field. To account for the effect of viscous displacement thickness at the airfoil surface, the inviscid solution must satisfy the following form of the flow tangency condition

$$\phi_y|_{y=0\pm} = [h_\pm(x) \pm \delta_\pm(x)]', \quad x \in [0,1] \quad (6)$$

where the prime denotes the differentiation. In addition, two conditions arise from the formal asymptotic matching of the viscous and inviscid solutions along the wake¹. The first condition accounts for the wake displacement effects and requires that the inviscid solution for the normal component of velocity must be discontinuous across the wake with a jump given by

$$[[\phi_y]] = \delta_w'(x), \quad x > 1 \quad (7)$$

Here $[[\]]$ denotes the difference in a quantity (upper minus lower) across the wake and δ_w is the displacement thickness of the complete wake. The second condition accounts for the wake curvature effect which arises from the turning of the low momentum flow along the curved wake streamlines which generates a pressure difference across the wake. The requirement that the outer inviscid flow match this pressure difference leads to the following jump condition on the inviscid pressure

$$[[p]] = -[[\phi_x]] = \kappa(x) [\delta_w(x) + \theta_w(x)], \quad x > 1 \quad (8)$$

where θ_w is the momentum thickness of the complete wake and κ is the curvature of the reference wake streamline which is taken as positive when the reference wake streamline is concave upwards. A complication arises in that the location of the reference wake streamline is unknown apriori; however, to lowest order in Re , the wake conditions

can be referenced to any arbitrary curve which emanates from the trailing edge and lies within the wake. Note that for symmetric flows, the reference wake streamline (centerline) lies in the plane of the symmetry ($y = 0$) and condition (6) can be applied for $x > 0$ to determine the inviscid solution in the upper half plane. Finally, the disturbance velocity must vanish in the far-field, i.e.,

$$\nabla \phi \rightarrow 0 \text{ as } |\vec{x}| \rightarrow \infty \quad (9)$$

where \vec{x} is a position vector in the x, y -coordinate frame.

Symmetric and Asymmetric Flows

It is convenient to write the solution to the foregoing problem as the sum of two terms; a symmetric term, ϕ^S , giving the flow due to thickness effects and an asymmetric term, ϕ^A , giving the flow due to loading effects. Both ϕ^A and ϕ^S must satisfy the differential equation (3) and the far-field condition, Eq. (9). In addition, the symmetric component of the potential must satisfy the tangency condition

$$\phi_y^S|_{y=0\pm} = \pm D_T'(x), \quad x > 0 \quad (10)$$

where D_T is one-half the displacement body thickness; i.e.,

$$D_T = (y_+ - y_-)/2 = (h_+ - h_- + \delta_+ + \delta_-)/2, \quad x \in [0,1] \quad (11)$$

$$= (\delta_+ + \delta_-)/2 = \delta_w/2, \quad x > 1$$

The symmetric solution does not produce a pressure difference across the airfoil or its wake, and therefore,

$$[[p^S]] = 0 \quad (12)$$

The asymmetric component of the potential must satisfy the following requirements

$$\phi_y^A|_{y=0\pm} = D_c'(x), \quad x \in [0,1] \quad (13)$$

$$[[\phi_y^A]] = 0, \quad x > 1 \quad (14)$$

$$[[p^A]] = -[[\phi_x^A]] = \kappa(\delta_w + \theta_w), \quad x > 1 \quad (15)$$

where $y = D_c(x)$ defines the location of the airfoil and wake "camber" line, i.e.,

$$D_c = (y_+ + y_-)/2 = (h_+ + h_- + \delta_+ - \delta_-)/2, \quad x \in [0,1] \quad (16)$$

$$= h_w + (\delta_+ + \delta_-)/2, \quad x > 1$$

Clearly then, the sum

$$\phi^s + \phi^A = \phi \quad (17)$$

is a solution of the original inviscid boundary value problem.

A further decomposition of the disturbance velocity potential will be used in the present study to distinguish between displacement thickness and wake curvature effects on the outer inviscid flow. Thus we set $\phi^A = \phi_D^A + \phi_{wc}^A$ where the asymmetric potential, ϕ_D^A , due to airfoil geometry and viscous displacement effects must satisfy conditions (13) and (14) but it does not contribute to the pressure jump across the wake, i.e.,

$$[\rho_D^A] = 0, \quad x > 1 \quad (18)$$

while the asymmetric potential due to wake curvature effects, ϕ_{wc}^A , must satisfy conditions (14) and (15), but it does not contribute to the normal velocity at the airfoil surface, i.e.,

$$\left. \frac{d\phi_{wc}^A}{dy} \right|_{y=0^\pm} = 0, \quad x \in [0, 1] \quad (19)$$

Inviscid Pressure Distributions

Solutions to the foregoing boundary value problems can be conveniently determined using complex variable theory and, in particular, Cauchy's integral formula¹³. It follows that the symmetric component of the pressure acting on the airfoil and wake can be determined in terms of a prescribed thickness distribution $D_T(x)$ by evaluation of a Cauchy principal value integral, i.e.,

$$p^s(x, 0^\pm) = -\phi^s(x, 0^\pm) = -\frac{1}{\pi(1-M_\infty^2)^{1/2}} \int_0^\infty \frac{D_T'(\xi)}{x-\xi} d\xi \quad (20)$$

The asymmetric component of the pressure, $p^A(x, 0^\pm) = \pm [\rho^A]/2$, acting on the airfoil surface is determined from the solution of an integral equation given by

$$D_c'(x) = \frac{(1-M_\infty^2)^{1/2}}{2\pi} \left[\int_0^1 \frac{[\rho_D^A(\xi)]}{x-\xi} d\xi + \int_1^\infty \frac{\kappa(\xi)[\delta_w(\xi) + \theta_w(\xi)]}{x-\xi} d\xi \right] \quad (21)$$

Both displacement and wake curvature effects contribute to this pressure jump. To determine the jump due to displacement effects alone $[\rho_D^A]$, the second term on the right-hand side is set equal to zero. Analytical techniques (c.f., Ref. 13) can be used to invert the resulting singular integral equation and provide the following direct solution for the pressure jump due to displacement effects

$$[\rho_D^A] = \frac{2}{\pi(1-M_\infty^2)^{1/2}} \left(\frac{1-x}{x} \right)^{1/2} \int_0^1 \frac{D_c'(\xi)}{x-\xi} \left(\frac{\xi}{1-\xi} \right)^{1/2} d\xi \quad (22)$$

The pressure jump across the airfoil due to wake curvature is then determined as a solution of the integral equation

$$\int_0^1 \frac{[\rho_{wc}^A(\xi)]}{x-\xi} d\xi = - \int_1^\infty \frac{\kappa(\xi)[\delta_w(\xi) + \theta_w(\xi)]}{x-\xi} d\xi \quad (23)$$

In the present study of viscous, inviscid interactions near the trailing edge of an airfoil, displacement interactions are regarded as strong whereas the wake curvature interactions are regarded as weak. Thus, an inviscid solution for the potential $\phi^s + \phi_D^A$ is determined by simultaneously solving inviscid and viscous-layer equations for prescribed viscous displacement thickness distributions until inviscid pressures on the airfoil surface and on the wake streamline match the viscous pressures. Once a converged solution to the strong-displacement interaction problem is achieved, the resulting inviscid pressure will be corrected to account for wake curvature effects. For this purpose the wake curvature is taken to be the curvature of the inviscid wake "camber" line as determined by the strong displacement interaction inviscid solution, i.e.,

$$\kappa(x) = D_c''(x) = \frac{(1-M_\infty^2)^{1/2}}{2\pi} \frac{d}{dx} \int_0^1 \frac{[\rho_D^A(\xi)]}{x-\xi} d\xi, \quad x > 1 \quad (24)$$

Finally, the pressure acting on the airfoil and reference wake streamline is given by

$$p(x, 0^\pm) = p^s(x, 0) \pm [\rho^A]/2, \quad x \in [0, 1] \\ = p^s(x, 0) \pm \kappa(\delta_w + \theta_w)/2, \quad x > 1 \quad (25)$$

Viscous Layer Region

The flow in the inner or viscous region is assumed to be governed by Prandtl's boundary-layer equations expressed in s and n coordinates which are directed along and normal to the airfoil surface and wake streamline, respectively, and u and v which are the velocity components in the s and n directions. These equations are then recast in Levy-Lees variables to minimize the growth of the viscous layer in the computational domain. The new independent variables are defined by

$$\xi = \xi_1 + \int_{s_1}^s \rho_e \mu_e u_e ds \quad (26a)$$

$$\eta = \frac{u_e \sqrt{Re}}{\sqrt{2\xi}} \int_0^n \rho_e dn \quad (26b)$$

where subscript e refers to the edge of viscous layer. With dependent variables, $F(\xi, \eta)$, and $\psi(\xi, \eta)$, defined by

$$F = u/u_e \quad (27)$$

$$v = 2\xi \left[F \frac{\partial \eta}{\partial s} + \rho_e \sqrt{Re} (2\xi)^{-1/2} \right] / \frac{d\xi}{ds}$$

the boundary layer equations for adiabatic flow at unit Prandtl number reduce to the familiar form

Continuity

$$2\xi \frac{\partial F}{\partial \xi} + \frac{\partial v}{\partial \eta} + F = 0 \quad (28)$$

ξ - momentum

$$2\xi F \frac{\partial F}{\partial \xi} + v \frac{\partial F}{\partial \eta} + \beta(F^2 - 1) - \frac{\partial}{\partial \eta} \left(\lambda \frac{\partial F}{\partial \eta} \right) = 0 \quad (29)$$

where

$$\begin{aligned} \lambda &= \rho \mu / (\rho_e \mu_e) \\ \beta &= \frac{2\xi}{u_e} \frac{du_e}{d\xi} \left(1 + \frac{u_e^2}{2T_e} \right) \end{aligned} \quad (30)$$

In addition, one requires the equation of state, i.e.,

$$p = (\gamma - 1) \rho T / \gamma \quad (31)$$

for relating pressure, density and temperature. In the present study the viscosity is assumed to vary linearly with temperature, and hence, it follows from Eqs. (30) and (31) that $\lambda = 1$ since the normal pressure gradient is zero across the boundary layer.

Boundary conditions for the foregoing equations are as follows

Edge conditions ($\xi \rightarrow \infty$)

$$F \rightarrow 1 \quad (32)$$

Airfoil surface conditions ($\xi = \xi_{TE}, \eta = 0$)

$$F = v = 0 \quad (33)$$

Wake streamline condition ($\xi \rightarrow \xi_{TE}, \eta = 0$)

$$v = 0 \quad (34)$$

For symmetric flow, the additional condition

$$\frac{\partial F}{\partial \eta} = 0 \quad (35)$$

can be applied at the wake centerline to restrict the solution domain to either the upper or lower half-plane. Fluid properties at the edge of the boundary layer (i.e., inviscid properties at the displacement surface, 0) can be expressed in terms

of the freestream and edge Mach numbers. It follows from Bernoulli's equation that

$$\begin{aligned} (M_\infty u_e / M_e)^2 &= (M_\infty A_e)^2 = (\gamma M_\infty^2 \rho_e)^{(\gamma-1)/\gamma} \\ &= \rho_e^{(\gamma-1)} = (\gamma-1) M_\infty^2 T_e \\ &= \left(1 + \frac{\gamma-1}{2} M_\infty^2 \right) / \left(1 + \frac{\gamma-1}{2} M_e^2 \right) \end{aligned} \quad (36)$$

and therefore

$$\beta = \frac{2\xi}{M_e} \frac{dM_e}{d\xi} \quad (37)$$

In addition, it follows from the definition of the displacement, δ , and momentum, δ^* , thicknesses that

$$\rho_e u_e \delta (Re/2\xi)^{1/2} = \int_0^\infty \left[1 - F + \frac{(\gamma-1)}{2} M_e^2 (1 - F^2) \right] d\eta \quad (38a)$$

$$\rho_e u_e \delta^* (Re/2\xi)^{1/2} = \int_0^\infty (1 - F) d\eta \quad (38b)$$

Finally, the surface skin friction coefficient, C_f , is defined by

$$C_f = \frac{\tau_w}{\frac{1}{2} \rho_\infty u_\infty^2} = \frac{u_e^2 \sqrt{2}}{(\xi Re)^{1/2}} \left(\rho \mu \frac{\partial F}{\partial \eta} \right)_{\eta=0} \quad (38c)$$

Viscous/Inviscid Iteration

The complete flow field is determined by matching the solutions of the inviscid and viscous equations. The inviscid flow is determined subject to the conditions of flow tangency at the airfoil displacement surface and jump conditions due to viscous displacement and wake curvature effects across the wake. The solution of the viscous layer equations must approach the inviscid conditions on the airfoil surface and on the reference wake streamline at the outer edge of the viscous layer. For weak viscous/inviscid interactions, flow properties at the edge of the viscous layer can be determined from the zeroth order inviscid solution and the solution for the complete first-order flow field can be determined sequentially. For strong interactions, flow properties at the edge of the viscous layer depend on the first order inviscid solution. In this case inviscid and viscous equations must be solved simultaneously. Since neither the pressure gradient at the edge of the boundary layer nor the displacement and momentum thickness of the viscous layer are known apriori, iterative procedures are required to determine the complete solution.

In the present study displacement effects at the trailing edge of the airfoil are regarded as strong while wake curvature effects are regarded as weak. Thus, simultaneous solutions of the inviscid and viscous equations are determined to account

for strong displacement interactions and the resulting inviscid solution is then modified to account for wake curvature interactions. It has been found that a semi-inverse calculation procedure using underrelaxation provides a relatively efficient method for determining the flow in strong viscous/inviscid interaction regions¹¹. In this approach the inviscid and viscous equations are solved for a prescribed nth displacement thickness distribution, $\delta^n(s)$, to determine the (n+1)th inviscid pressure distribution, $p_{inv}^{n+1}(s)$, at the displacement surface and the (n+1)th viscous pressure distribution, $p_{visc}^{n+1}(s)$, in the viscous layer. The (n+1)th estimate for the displacement thickness is then obtained by underrelaxation, i.e.,

$$\delta^{n+1}(s) = \delta^n(s) \left[1 + \omega [p_{inv}^{n+1}(s) - p_{visc}^{n+1}(s)] \right] \quad (39)$$

where ω is the relaxation parameter.

Equation (39) is applied to update the calculated displacement thickness of the boundary layers on the upper and lower surfaces of the airfoil and the complete wake. The process is repeated until the maximum change in δ satisfies the relation

$$|\delta^{n+1}(s) - \delta^n(s)|_{\max} < \epsilon_\delta \quad (40)$$

where ϵ_δ is a small positive number.

Numerical Solution Procedure

Inviscid Region

The numerical integration procedure developed by Napolitano, et al.¹⁴ has been extended to accommodate a variable streamwise mesh spacing and applied to determine the symmetric component of the pressure acting on the airfoil and wake streamline. Thus, the integral appearing in Eq. (20) is approximated in the strong-interaction region by the following second-order accurate expression

$$\begin{aligned} \int_{\bar{x}_{IB-1}}^{\bar{x}_{IE}} \frac{D'_T(\zeta)}{x_i - \zeta} d\zeta &= \sum_{j=IB-1}^{IE-1} \int_{\bar{x}_j}^{\bar{x}_{j+1}} \frac{D'_T(\zeta)}{x_i - \zeta} d\zeta \\ &\approx \sum_{j=IB-1}^{IE-1} D'_T(x_{j+1}) I_1(x_i; \bar{x}_j, \bar{x}_{j+1}) + \\ &\quad \sum_{j=IB-1}^{IE-1} D''_T(x_{j+1}) I_2(x_i; \bar{x}_j, \bar{x}_{j+1}) \end{aligned} \quad (41)$$

where

$$I_1(x_i; \bar{x}_j, \bar{x}_{j+1}) = \int_{\bar{x}_j}^{\bar{x}_{j+1}} \frac{1}{x_i - \zeta} d\zeta \quad (42a)$$

$$I_2(x_i; \bar{x}_j, \bar{x}_{j+1}) = \int_{\bar{x}_j}^{\bar{x}_{j+1}} \frac{\zeta}{x_i - \zeta} d\zeta \quad (42b)$$

and i and j are streamwise mesh point indices, IB and IE refer to the mesh stations at the beginning and end of the strong interaction region, respectively, and $\bar{x}_j = (x_{j+1} + x_j)/2$. The integrals I_1 and I_2 in Eq. (42) are evaluated analytically. Contributions to the local (at $x = x_i$) pressure due to thickness effects upstream ($0 < \bar{x}_{IB-1}$) and downstream ($> \bar{x}_{IE}$) of the strong interaction region are determined by analytical or numerical (using trapezoidal rule quadrature) integration depending on the assumed functional form of the thickness distribution, $D_T(x)$ (c.f., Ref. 6).

Asymmetric Pressure - Displacement Effects

It is somewhat more difficult to determine the asymmetric pressure component, p_D^A , because of the singular term $[\cdot/(1-\cdot)]^{1/2}$ which appears inside the integral on the right-hand side of Eq. (22). However, a first-order accurate approximation to this integral has been determined and is given by

$$\begin{aligned} \int_0^1 \frac{D'_C(\zeta)}{x_i - \zeta} \left(\frac{\zeta}{1-\zeta} \right)^{1/2} d\zeta &= \int_0^{\bar{x}_0} \frac{D'_C(\zeta)}{x_i - \zeta} \left(\frac{\zeta}{1-\zeta} \right)^{1/2} d\zeta \\ &\quad + \int_{\bar{x}_{IT-1}}^1 \frac{D'_C(\zeta)}{x_i - \zeta} \left(\frac{\zeta}{1-\zeta} \right)^{1/2} d\zeta \\ &\quad + \sum_{j=0}^{IT-2} \int_{\bar{x}_j}^{\bar{x}_{j+1}} \frac{D'_C(\zeta)}{x_i - \zeta} \left(\frac{\zeta}{1-\zeta} \right)^{1/2} d\zeta \\ &\approx D'_C(0) I_3(x_i; 0, \bar{x}_0) \\ &\quad + D'_C(1) I_3(x_i; \bar{x}_{IT-1}, 1) \\ &\quad + \sum_{j=0}^{IT-2} D'_C(x_{j+1}) I_3(x_i; \bar{x}_j, \bar{x}_{j+1}) \end{aligned} \quad (43)$$

where 0 and IT refer to the leading and trailing edge mesh lines, respectively. The integral term I_3 is given by

$$I_3(x_i; \bar{x}_1, \bar{x}_2) = \int_{\bar{x}_1}^{\bar{x}_2} \frac{1}{x_i - \zeta} \left(\frac{\zeta}{1-\zeta} \right)^{1/2} d\zeta \quad (44)$$

and is evaluated in closed form.

Asymmetric Pressure-Wake Curvature Effects

Once a converged solution to the strong-displacement interaction problem is achieved, the inviscid pressure distribution must be corrected to account for wake curvature effects. The curvature of the wake streamline is determined by a

numerical approximation to Eq. (24). Since $\phi(x)$ must only be determined for $x \leq 1$, the integral on the right-hand side of Eq. (24) can be evaluated by a simple trapezoidal rule. The asymmetric pressure difference across the airfoil due to wake curvature effects $[p_{wc}^A]$ is then determined by a numerical solution of the integral equation, Eq. (23). This equation can be solved by first transforming the interval $[0, 1]$ on the x -axis to the interval $[0, \pi]$ on the unit circle and then invoking certain properties of Chebychev polynomials (c.f., Ref. 15). Thus with the transformation

$$\begin{aligned} x &= (1 - \cos \chi)/2 \\ \zeta &= (1 - \cos \psi)/2 \end{aligned} \quad (45)$$

and the use of a trapezoidal rule quadrature, Eq. (23) can be approximated by

$$\begin{aligned} \int_0^1 \frac{[p_{wc}^A(\zeta)]}{x_1 - \zeta} d\zeta &= \int_0^\pi \frac{[p_{wc}^A(\psi)]}{\cos \psi - \cos \chi_1} \sin \psi \\ &\approx \frac{\pi}{N} \sum_{k=1}^N \frac{[p_{wc}^A(\psi_k)] \sin \psi_k}{\cos(\psi_k) - \cos \chi_1} = g(\chi_1), \\ i &= 0, 1, \dots, N-1 \end{aligned} \quad (46)$$

where

$$\begin{aligned} \chi_i &= i\pi/N, & i &= 0, \dots, N \\ \psi_k &= \frac{(2k-1)\pi}{2N}, & k &= 1, \dots, N \end{aligned} \quad (47)$$

and the source term $g(\chi_i)$ refers to the right-hand side of Eq. (23). The system of difference equations, Eq. (46), is solved by a standard matrix inversion. To retain pressure continuity at the trailing edge, the following condition must be imposed

$$[p_{wc}^A]_{TE} = [\kappa(\delta_w + \theta_w)]_{TE} \quad (48)$$

Viscous Region

For strong displacement interactions, the inviscid and viscous flows are determined by an iterative procedure which is continued until the inviscid pressure ($p = P_0 + p^S + p_{\delta}^A$) at the displacement surface matches the viscous pressure (p_e) at the edge of the viscous layer. At each step of this process the viscous layer equations are solved numerically for prescribed displacement thickness distributions. Solutions for the boundary layers on the upper and lower surfaces of the airfoil and the complete wake are determined separately. In each case the continuity and momentum equations are replaced by a set of linear algebraic equations using a finite difference approximation in which the nonlinear terms in the momentum equation are linearized around the solution at the previous iteration and the δ and θ

derivatives are replaced by one-sided and central difference expressions, respectively. For the δ -derivatives, an upwind differencing scheme is used, i.e., backward difference is used if the local streamwise velocity, F , is positive and forward difference is used if local velocity, F , is negative. This results in a stable numerical algorithm in the presence of reverse flow which is more accurate than the commonly used FLARE approximation in which the streamwise convection terms are set to zero in reverse flow regions¹⁶.

The set of linear difference equations are then solved using Davis coupled scheme⁴ via a superposition technique developed by Werle and Verdon⁵. Essentially, the dependent variables, F and V , are decomposed into two components such that one component depends on the pressure gradient parameter δ whereas the other component has no δ dependence. As a result of this decomposition, two sets of linear algebraic equations are obtained. Final closure is achieved by determining the value of the pressure gradient parameter, δ , such that the resulting solutions satisfy the prescribed value of displacement thickness. It should be pointed out that the procedure briefly described here yields an extremely efficient numerical algorithm because of its noniterative nature. Complete details of this viscous layer solution procedure are available in Ref. 17.

Results

The analytical and numerical approach outlined above has been applied to predict high Reynolds number laminar flow, past the trailing edge of a thin lifting airfoil. Following Veldman¹⁰, the inviscid pressure distribution p_A^A , due to the airfoil alone, is assumed to be constant on the upper and lower surfaces of the airfoil upstream of the point $x = x_c$ and equal to those acting on a flat plate inclined at an angle α relative to the uniform stream for $x_c < x < 1$. Thus,

$$\begin{aligned} p_A^A(x, 0^\pm) &= \mp \frac{\alpha}{(1-M_\infty^2)^{1/2}} \left(\frac{1-x_c}{x_c} \right)^{1/2}, & 0 < x < x_c \\ &= \mp \frac{\alpha}{(1-M_\infty^2)^{1/2}} \left(\frac{1-x}{x} \right)^{1/2}, & x_c < x < 1 \\ &= 0, & x > 1 \end{aligned} \quad (49)$$

The foregoing pressure distribution ensures that the oncoming boundary layers remain attached until (or shortly before) the trailing edge and corresponds to a thin cambered airfoil (modified flat plate) which more closely approximates an inclined flat plate as $\alpha \rightarrow 1$.

Since attention is being focused on local viscous/inviscid interaction phenomena at the trailing edge of the airfoil, viscous displacements and wake curvatures upstream ($x < x_i$) and downstream ($x > x_f$) of the strong-interaction region

are assumed to have a negligible impact on pressures near the trailing edge. Thus, for the calculations presented here, u' for $x = x_1$ and w' and $-(w' + w)$ for $x = x_2$ are set equal to zero when evaluating the integrals in Eqs. (20), (22) and (23). Unless stated otherwise x_1 and x_2 have been set at 0.5 and 1.5, respectively. Further, the extent of the viscous solution domain normal to the airfoil and wake streamline has been taken to be $7\delta_{BL}$ where δ_{BL} is the Blasius boundary-layer thickness. Inviscid and viscous solutions have been repeatedly determined for prescribed displacement thickness distributions until the maximum difference between the (n+1)th values of the displacement thickness over the strong interaction solution interval was within 10^{-7} . The corresponding maximum difference between the viscous and inviscid pressures was approximately 10^{-4} . This level of convergence required approximately 15 iterations for the attached flow solutions and approximately 30 iterations for the separated flow solutions.

Present results for a flow at $M_\infty = 0.1$ and $Re = 10^6$ past the trailing edge of the modified flat plate airfoil described above with $\alpha = 0.07$ are shown in Figs. 2 and 3. First-order pressure (or pressure coefficient) distributions due to (1) the airfoil alone as given by Eq. (49), (2) the airfoil and viscous displacement effects, and (3) the airfoil, viscous displacement and wake curvature effects are given in Fig. 2. It can be seen that strong displacement interactions at the trailing edge cause a rather substantial reduction in the pressure acting on the lower (or pressure) surface of the airfoil and a somewhat smaller change in the upper (or suction) surface pressure except for the reduction in the immediate vicinity of the trailing edge. In addition, displacement effects cause a reduction in near wake pressures. For this example (i.e., $Re = 10^6$), the effect of wake curvature on pressure is generally smaller than the effect of viscous displacement. The former provides a reduction in pressure on the

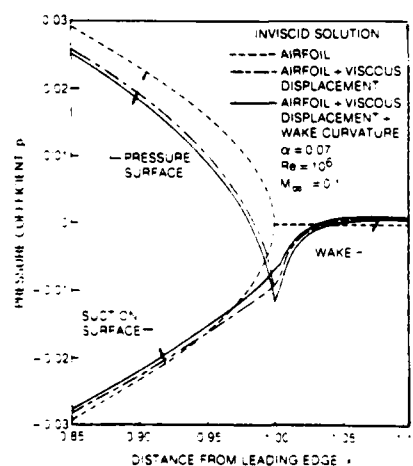


Fig. 2 Effect of Viscous Displacement and Wake Curvature on Airfoil and Wake Pressure Distributions

lower side of the airfoil and wake streamline, and an increase in pressure on the upper surface. Both viscous displacement and wake curvature tend to decrease the loading on the airfoil, and the wake curvature effect gives rise to a negative loading in the immediate vicinity of the trailing edge. Finally, both effects contribute to a more favorable suction-surface pressure gradient at the trailing edge which would tend to delay separation of the suction surface boundary layer.

The present results for $M_\infty = 0.1$, $Re = 10^6$ and $\alpha = 0.07$ are compared with Veldman's incompressible predictions in Fig. 3. In this comparison only displacement interaction effects are considered. Comparisons are provided for pressure distributions (Fig. 3a), displacement thickness distributions (Fig. 3b), and skin friction and wake streamline velocity distributions (Fig. 3c). The results obtained from the two different solution procedures are observed to be in very good agreement.

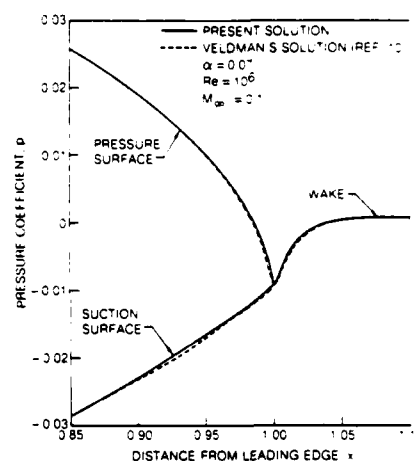


Fig. 3 Asymmetric Trailing-Edge Flow
a) Comparison of Pressure Distributions

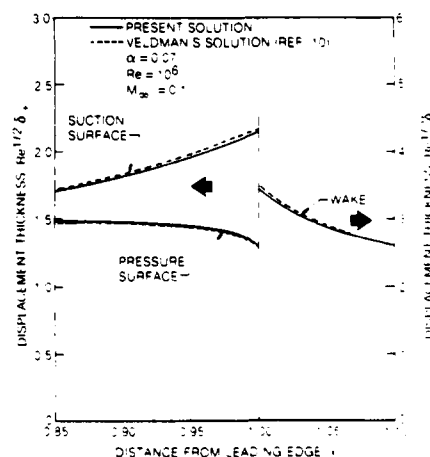


Fig. 3 Asymmetric Trailing-Edge Flow
b) Comparison of Displacement Thickness Distributions

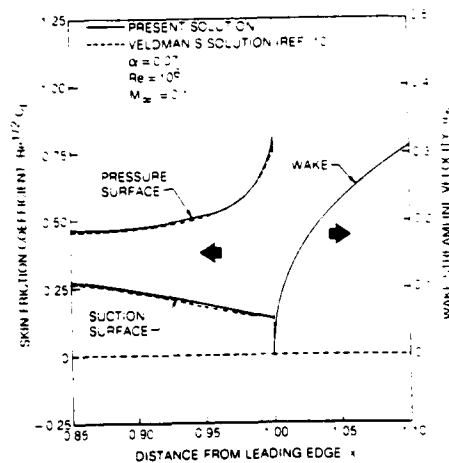


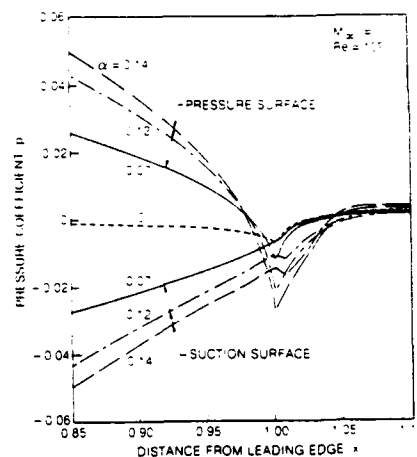
Fig. 3 Asymmetric Trailing-Edge Flow
c) Comparison of Skin Friction and Wake Streamline Velocity Distributions

Parametric Studies

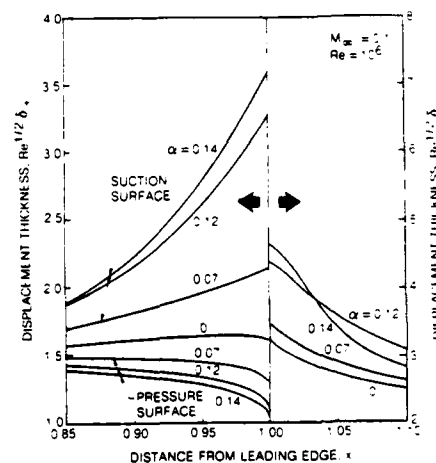
Having partially illustrated the effects of viscous displacement and wake curvature on pressures in the trailing-edge region and having established the accuracy of the present solution procedure, we proceed to present results from parametric studies. These studies were conducted to illustrate the effects of angle of attack or trailing edge loading parameter (α), Mach number (M_∞) and Reynolds number (Re) on the flow behavior in the trailing-edge region.

Solutions for a flow at $M_\infty = 0.1$ and $Re = 10^6$ and values of α of 0, 0.07, 0.12 and 0.14 are shown in Figs. 4 and 5. These solutions indicate that flow separates from the suction surface at $x = 0.12$ and $x = 0.14$. In the separated flow cases it was found necessary to modify the linearization procedure for the streamwise convection term in the momentum equation in order to achieve a converged solution. In particular, this term was linearized relative to the solution at the previous streamwise station rather than the solution at the previous iteration level. The pressure distributions depicted in Fig. 4a reveal, as expected, an increased loading on the airfoil with increasing angle of attack over most of the trailing-edge region (i.e., $x > 0.85$); however, both pressure (lower) and suction (upper) surface pressures, particularly the former, tend to decrease with increasing α in the immediate vicinity of the trailing edge. Further, there is a strong adverse pressure gradient in the near wake which increases with increasing angle of attack. The slight pressure plateau just aft of the trailing edge for $\alpha = 0.12$ and $\alpha = 0.14$ arises from the small reversed flow regions which occur at these angles.

Boundary-layer and wake displacement thicknesses (Fig. 4b) generally increase with increasing angle of attack, particularly on the suction surface of the airfoil. However, there is a



a) Pressure Distributions



b) Displacement Thickness Distributions

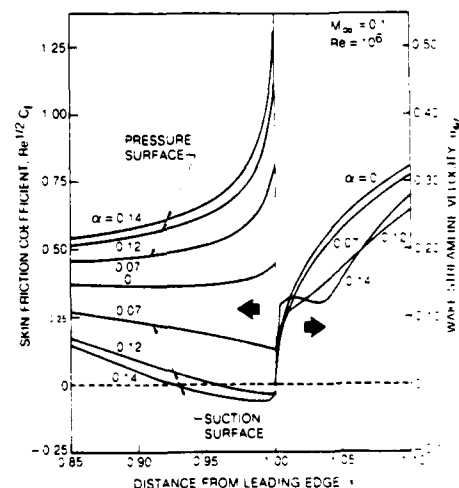


Fig. 4 Asymmetric Trailing-Edge Flow: Effect of Angle of Attack
c) Skin Friction and Wake Streamline Velocity Distributions

rapid thinning of the wake for the separated flow at $\alpha = 0.14$. The skin friction distributions (Fig. 4c) indicate that the flow separates from the suction surface at approximately $x = 0.96$ and $x = 0.93$ for $\alpha = 0.12$ and $\alpha = 0.14$, respectively. It should be mentioned that the case $\alpha = 0.12$ has also been investigated by Veldman¹⁰. Since only the symmetric components of the displacement thickness and the pressure were presented in Ref. 10, a detailed comparison with Veldman's solutions cannot be made here for this case. However, the skin friction distributions of Fig. 4c and the predicted location of the separation point on the suction surface compare very well with Veldman's results. The wake streamline velocity distributions shown in Fig. 4c reveal a very rapid flow acceleration just aft of the trailing edge generally followed by a gradual acceleration to the freestream velocity. For the separated flow at $\alpha = 0.14$ the wake streamline velocity is approximately constant in the near wake region (from $x \approx 1.01$ to $x \approx 1.05$) after undergoing a rapid acceleration just aft of the trailing edge, and then it gradually accelerates to the freestream value. The behavior of the wake displacement thickness and wake streamline velocity distributions for the $\alpha = 0.14$ case is somewhat surprising and will be interrogated in more detail in our future work. The important point to be made here is that converged strong viscous/inviscid interaction solutions have been achieved for separated, laminar, asymmetric, trailing-edge flow.

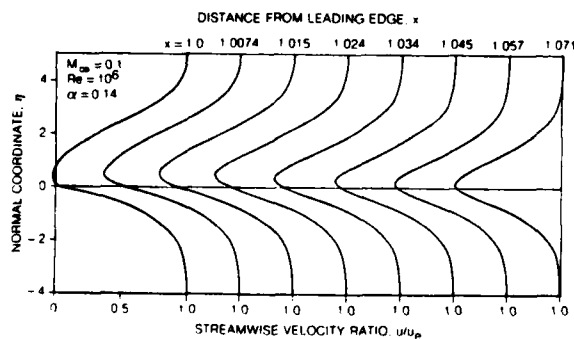
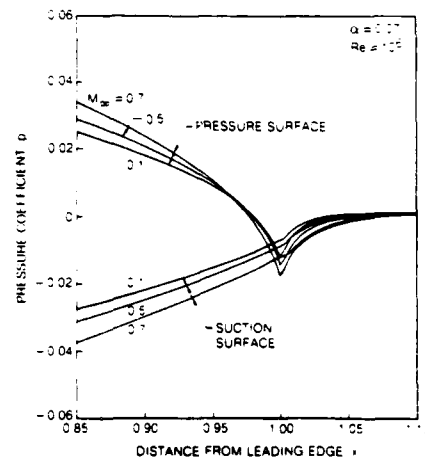


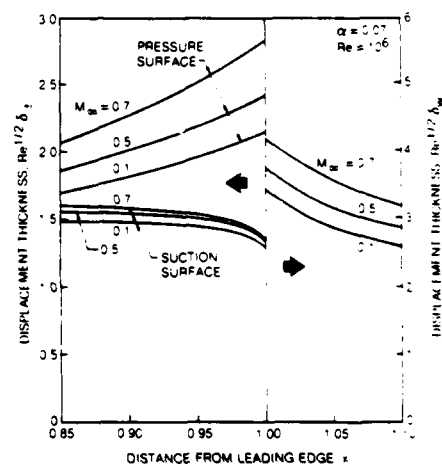
Fig. 5 Velocity Profiles in the Near Wake Region for Separated Asymmetric Flow

Velocity profiles in the near wake region are shown for the $\alpha = 0.14$ case in Fig. 5. A small reverse flow region is apparent in the profiles at $x = 1$ (i.e., at the trailing edge), $x = 1.0074$ and $x = 1.015$. The minimum values of the streamwise velocity occur on the suction surface at the trailing edge and above the wake streamline in the near wake. Further downstream the location of the minimum streamwise velocity tends to coincide with the wake streamline.

The effect of Mach number is depicted in Fig. 6. Here $\alpha = 0.07$, $Re = 10^6$ and freestream Mach numbers of 0.1, 0.5 and 0.7 are considered. The pressure distributions (Fig. 6a) reveal an increase in airfoil loading with an increase in Mach number except in the immediate vicinity of the trailing



a) Pressure Distributions



b) Displacement Thickness Distributions

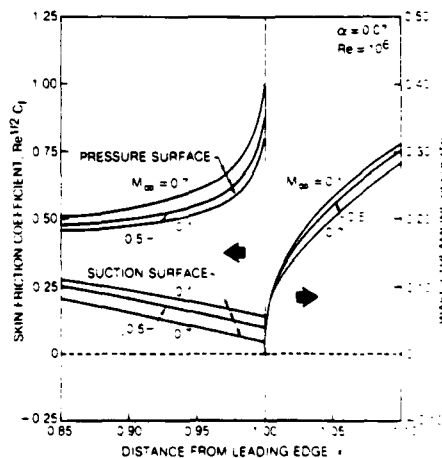


Fig. 6 Asymmetric Trailing-Edge Flow: Effect of Mach Number
c) Skin Friction and Wake Streamline Velocity Distributions

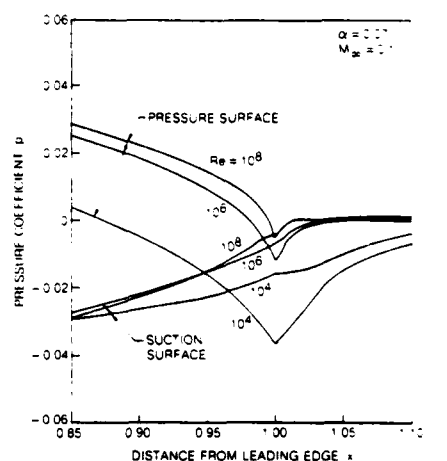
edge. In addition, there is a thickening of the suction-surface boundary layer and the wake and a thinning of the pressure-surface boundary layer with increasing Mach number (Fig. 6b). Finally, the skin friction increases on the pressure surface and decreases on the suction surface of the airfoil, and the streamwise acceleration in the wake decreases with increasing Mach number (Fig. 6c). The trends for suction-surface skin friction and wake streamline velocity depicted in Fig. 6c suggest that an increase in freestream Mach number would tend to promote flow separation in the trailing-edge region.

The effect of Reynolds number on trailing-edge flow behavior is examined in Fig. 7 for $M_\infty = 0.1$ and $\alpha = 0.07$. The inviscid pressure distribution (i.e., due to the airfoil only) for this case is shown in Fig. 2. Viscid/inviscid interaction results have been determined for $Re = 10^4$, 10^6 and 10^8 , respectively. The extent of the strong interaction solution interval was varied with Reynolds number and set at 1.5, 1.0 and 0.5 for $Re = 10^4$, 10^6 and 10^8 , respectively. The results in Fig. 7 indicate that the streamwise length scale of the strong-interaction phenomena in the immediate vicinity of the trailing edge decreases with increasing Reynolds number. Hence, at high Reynolds number a very fine mesh is required to accurately resolve flow gradients near the trailing edge.

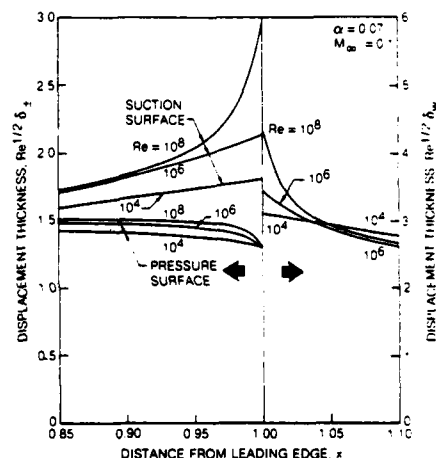
The pressure distributions in Fig. 7a reveal that the interaction between the viscous and inviscid flows tends to reduce airfoil loading with decreasing Re , particularly at lower Re . In addition, wake curvature effects become stronger with decreasing Reynolds number. Note that for $Re = 10^8$, wake curvature has a negligible impact on pressure. The corresponding displacement thickness distributions are shown in Fig. 7b. The larger displacement thicknesses on the suction surface tend to "uncamber" the airfoil and reduce lift. This effect as well as the wake curvature effect becomes more pronounced with decreasing Reynolds number since boundary layer and wake displacement thicknesses generally scale with $Re^{-1/2}$. The skin friction (Fig. 7c) decreases with increasing Re on both the pressure and suction surfaces of the airfoil. In addition, the predicted skin friction distribution for $Re = 10^8$ indicates that there is a small region of separated flow adjacent to the suction surface of the airfoil. Such a trend is anticipated on intuitive grounds since a smaller disturbance (or angle of attack) is needed to separate the flow as Reynolds number is increased.

Concluding Remarks

An efficient analytical/numerical approach has been developed to determine high Reynolds number, laminar flow in the trailing-edge region of a lifting airfoil. Here strong viscous/inviscid interactions arise from the change in boundary condition experienced by the fluid as it leaves the airfoil surface and accelerates into the wake.



a) Pressure Distributions



b) Displacement Thickness Distributions

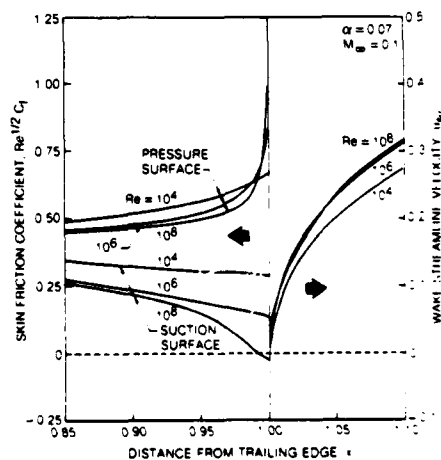


Fig. 7 Asymmetric Trailing-Edge Flow: Effect of Reynolds Number
c) Skin Friction and Wake Streamline Velocity Distributions

In the present study the inviscid flow has been determined by the methods of classical linear theory and an inverse numerical solution procedure has been used to calculate the flow in the viscous layer. Thus, both inviscid and viscous solutions are determined for a prescribed displacement thickness distribution. For strong-displacement interactions, simultaneously determined inviscid and viscous solutions are underrelaxed until the computed pressure distribution converges. The resulting inviscid solution is then corrected to account for the weak-interaction effect of wake curvature.

The capability for computing the flow in the trailing-edge region has been demonstrated for a thin lifting airfoil (modified flat plate). Results of the present analysis have been shown to be in very good agreement with Veldman's¹⁰ incompressible predictions. In addition, a brief parametric study has been conducted to illustrate the effects of trailing-edge loading, Mach number, and Reynolds number on trailing-edge/near-wake flow. Converged solutions with a small reverse flow region adjacent to the trailing edge on the suction surface of the airfoil and extending into the near-wake region have been obtained. In future work, the analysis described herein will be extended to include thickness effects and a more detailed study of flow separation in the trailing-edge region will be conducted.

Acknowledgements

This research was sponsored by the Naval Air Systems Command under Contract N00019-81-C-0295. The assistance provided by Dr. M. F. Platzer, NASC Program Manager for this contract, is gratefully acknowledged.

References

1. Melnik, R. E., "Turbulent Interactions on Airfoils at Transonic Speeds-Recent Developments," AGARD Symposium on Computation of Viscous-Inviscid Flows, AGARD-CPP-291, Chapter 10, 1980.
2. Melnik, R. E., Chow, R., and Mead, H. R., "Theory of Viscous Transonic Flow Over Airfoils at High Reynolds Number," AIAA Paper No. 77-680, presented at the Tenth Fluid and Plasma Dynamics Conference, Albuquerque, New Mexico, June 27-29, 1977.
3. McNally, W. D., and Sokol, P. M., "Computational Methods for Internal Flows with Emphasis on Turbomachinery," NASA Technical Memorandum 82764, November 1981.
4. Blottner, F. G., "Computational Techniques for Boundary Layers," AGARD Lecture Series 73 on Computational Methods for Inviscid and Viscous Two- and Three-Dimensional Flow Fields, presented at the von Karman Institute, February 17-22, 1975.
5. Werle, M. J., and Verdon, J. M., "Solutions for Laminar Subsonic Trailing Edge Flows at Asymptotically Large Reynolds Numbers," paper presented at the International Conference on Boundary and Interior Layers, held at Trinity College, Dublin, Ireland, June 3-6, 1980.
6. Vatsa, V. N., Werle, M. J., and Verdon, J. M., "Viscid/Inviscid Interaction at Laminar and Turbulent Symmetric Trailing Edges," AIAA Paper No. 82-165, presented at the AIAA 20th Aerospace Sciences Meeting, Orlando, Florida, January 11-14, 1982.
7. Veldman, A. E. P., "A New Calculation of the Wake of a Flat Plate," Journal of Engineering Mathematics, Vol. 9, pp. 65-70, 1975.
8. Veldman, A. E. P., "Boundary Layer Flow Past a Flat Plate," Ph.D. Thesis, Mathematical Institute, University of Groningen, The Netherlands, 1976.
9. Davis, R. T., and Werle, M. J., "Progress on Interacting Boundary Layer Computations at High Reynolds Number," paper presented at the Conference on Numerical and Physical Aspects of Aerodynamic Flows, California State University, Long Beach, CA, January 19-21, 1981.
10. Veldman, A. E. P., "The Calculations of Incompressible Boundary Layers with Strong Viscous-Inviscid Interaction," AGARD Symposium on Computation of Viscous-Inviscid Flows, AGARD-CPP-291, Chapter 12, 1980.
11. Carter, J. E., "A New Boundary Layer Interaction Technique for Separated Flows," AIAA Paper No. 79-1450, presented at the 4th Computational Fluid Dynamics Meeting, Williamsburg, VA, July 23-24, 1979.
12. Brown, S. N. and Stewartson, K., "Wake Curvature and Kutta Condition in Laminar Flow," The Aeronautical Quarterly, Vol. 26, pp. 275-280, 1975.
13. Ashley, H., and Landahl, M., "Aerodynamics of Wings and Bodies," Addison-Wesley Publishing Company, 1965, pp. 88-97.
14. Napolitano, M., Werle, M. J., and Davis, R. T., "A Numerical Technique for the Triple-Deck Problem," AIAA Paper No. 78-1133 presented at the 11th Fluid and Plasma Dynamics Conference, Seattle, WA, July 10-12, 1978.
15. DeJarnette, F. R., "Arrangement of Vortex Lattices on Subsonic Wings," presented at the Workshop on Vortex-Lattice Utilization, NASA Langley Research Center, Hampton VA, NASA-SP-405, pp. 301-323, May 17-18, 1976.
16. Reyhner, T. A., and Flügge-Lotz, I., "The Interaction of a Shock Wave with a Laminar Boundary Layer," Report No. 163, Division of Engineering Mechanics, Stanford University, November 1966.
17. Vatsa, V. N., Werle, M. J., and Verdon, J. M., "Analysis of Laminar and Turbulent Symmetric Blunt Trailing-Edge Flows," UTRC Report No. R31-914986-5, prepared for Naval Air Systems Command under Contract N00019-80-C-0057, 1981.

MEASUREMENTS OF ATTACHED AND SEPARATED TURBULENT FLOWS IN THE TRAILING-EDGE REGIONS OF AIRFOILS

A. Nakayama
Douglas Aircraft Company, McDonnell Douglas Corporation
Long Beach, California

Summary

Measurements of incompressible turbulent flows near the trailing edge have been made in three different configurations: (1) a conventional airfoil at zero incidence with near-symmetric flow, (2) a supercritical airfoil at an angle of attack of 4 degrees with strongly asymmetric but attached flow, and (3) supercritical airfoil at a high angle of attack of 12 degrees with upper-surface boundary-layer separation.

Mean flow and turbulence including three Reynolds stress components, four triple correlations and some frequency spectra were obtained using pressure and hot-wire probes as well as a laser-doppler velocimeter. Selected results are presented to show the features of viscous-inviscid interaction and characteristics of turbulence in the trailing-edge region.

I. Introduction

There are mainly two problems in the calculation of the trailing-edge flow for which no unanimously accepted satisfactory solution method has yet been given. The first one is how to account for the viscous-inviscid interaction. It is trivial that one way or another an interactive approach is necessary in order to avoid the stagnation pressure predicted by the potential-flow theory at a finite-angle trailing edge. The second one is how to model the turbulent stresses in the case of practical high Reynolds number flows. The present paper presents some experimental evidences that may suggest a better way of calculation and modeling method, test existing methods and help understand underlying turbulence mechanism in a few cases of asymmetric lifting airfoils with or without separation under incompressible conditions.

In recent years, while the present investigation has been in progress, a number of experimental studies have been published that are related to the trailing-edge flows. Many of them¹⁻³ are concerned with the near wake of flat plates, for which the problem of viscous-inviscid interaction is very small and the main concern is the structure of turbulence. Airfoil flows have also been studied by a number of investigators. Perhaps the most detailed data were obtained by Yu⁴ with a non-lifting symmetrical airfoil. Measurements with lifting airfoils have been reported by Hoad et al.⁵, Johnson and Spaid⁶, and Hah and Lakshminarayana⁷ under unseparated conditions. Separated flows were measured by Coles and Wadcock⁸ and Young et al.⁹. Some simulated trailing-edge flows were studied by Salignac¹⁰ and Viswanath et al.¹¹. These experimental data have increased the understanding of the turbulent flow near the trailing edge of a streamlined body but by no means are they adequate. The sets of data that contain details near the trailing edge are only in the simpler symmetric cases. The measurements of asymmetric airfoil flow with or without separation are either sketchy or incomplete in terms of quantities measured. Detailed measurements of turbulence quantities are important since

simpler turbulence models are not expected to be able to predict the complex flow accurately, and development of more advanced turbulence models require detailed data.

The present results contain extensive mean-flow and turbulence data including all one-point velocity correlations up to the third-order and the frequency spectra (from which the rate of energy dissipation was reduced) in the regions near the trailing edge, in the upstream boundary layers and the downstream wake of two practical airfoil models. One of the models is designated by Model A and is a conventional airfoil and the measurements with this model were made at zero incidence. The second model is a supercritical airfoil Model B. Measurements with this model were made at two angles of attack. The first one is at 4 degs which represents a highly asymmetric case but without any flow separation and the second one is at 12 degs which includes a small trailing-edge separation. Since the volume of data is very extensive, samples will be presented to illustrate important results that are discussed.

II. Experimental Arrangements and Techniques2.1 Wind Tunnel

The experiments were conducted at the 38 x 54 x 120-inch low-speed wind tunnel at DAC Long Beach facilities. For the present experiments it was operated at a fixed speed of 30m/s with a honeycomb and six screens to keep the freestream turbulence level smaller than 0.05 percent. Over the portion of the test section (2m) used for the present experiments the total streamwise pressure variation was only one-percent of the dynamic pressure. Over most of the cross-section the cross-stream nonuniformity was less than 0.1 percent per inch.

All pressure data were measured relative to p_{ref} , the tunnel piezometer pressure, which can be regarded as the freestream pressure. All velocity data were normalized by

$$U_{ref} = \sqrt{\frac{2(p_o - p_{ref})}{\rho}}$$

where p_o is the pressure in the settling chamber and ρ is the air density.

No flow control was used to maintain the two-dimensionality of the flow even in the separated-flow measurements. However, since the separated region is small, relatively good two-dimensionality over the center-span region was confirmed by measurements of spanwise variations of surface pressure, skin friction, mean velocity and Reynolds stresses.

2.2 Models

The two airfoil models used for the measurements were Model A and Model B. The former is a 10-percent-thick conventional airfoil and the

latter is a 14-percent-thick supercritical airfoil with a large camber near the trailing edge. The included angles of the two surfaces meeting at the trailing edge of the two airfoil models are nearly the same and about 10 degrees. For the present tests, two-foot chord, 54-in. span models of the airfoils were used. They were equipped with a total of 72 pressure orifices, most of them arranged along the midspan and some were arranged in four spanwise arrays. A flat shaped orifice was installed at the trailing edge where the thickness of Model A was 0.6mm and that of Model B was 0.18mm; these backward facing pressure holes dictate the "base pressure." The trailing-edge thickness of Model A is comparable to the viscous sublayer thickness at the trailing edge. Circular wires of diameters 0.5mm and 1.3mm, respectively, were placed at 5-percent chord on the lower surface and 16-percent chord on the upper surface to insure the transition.

The blockage effects due to the tunnel walls were not negligible in the sense that the minimum surface static pressure is lowered by about 10 percent of the dynamic pressure and the wake trajectory was found to be slightly upwards at downstream positions. Other than the fact that these effects can influence the way the viscous and inviscid parts of the flow interact, the direct effects of walls on quantities such as turbulence can be regarded as negligible.

2.3 Measurements of Unseparated Region

In all flow configurations, pitot and static tubes were traversed throughout the flow field to obtain the distributions of total and static pressure separately. The pitot tube used was either a flattened tube of thickness 0.76mm or a round one of outside diameter 1.6mm. The static pressure data were obtained with a standard NPL-type tube with side holes and with a wedge-shaped tube.

Turbulence measurements in the unseparated regions were made with two TSI 1050 hot-wire anemometers operated in the constant temperature mode and 3.8um tungsten wire sensors in a cross array. At most measurement stations, the probe was placed in the flow such that the plane of sensors was parallel to the x,y-plane. At a few selected stations the probe was placed parallel to the x,z-plane to measure the spanwise fluctuation w^2 .

The anemometer outputs were analyzed with on-site analog averaging methods and off-site digital averaging techniques. For the digital averaging, the signals were first recorded on magnetic tapes and reproduced later at a slower speed for sampling, digitizing and averaging. Analog linearizers were not used but the calibration curve was approximated by a parabola locally fitting the King's law for the on-site analog averaging and the digital analysis included the inversion of the nonlinear calibration relation. The mean velocities and Reynolds stresses obtained by the analog and digital methods agreed well with maximum discrepancies less than 5 percent, and the Reynolds stress results reported here are the analog-averaged results but the averages of triple products and the frequency spectra used to obtain the rate of dissipation of the turbulent kinetic energy, are the digitally-averaged results.

All the probe data were obtained by traversing the probes normal to the airfoil surface in the boundary layers and in the vertical direction in the wake. Figure 1 shows the coordinates used.

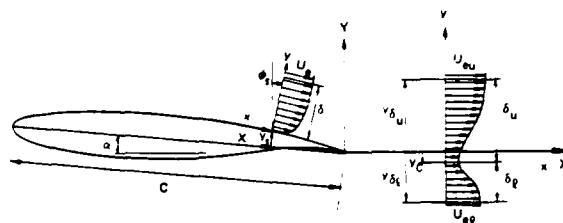


Fig. 1. Definition of coordinates.

2.4 Laser Doppler Velocimeter Measurements in the Separated and Near-Wake Region

Measurements of mean and fluctuating velocity components in the region where the flow can reverse its direction (upper-surface boundary layer near the trailing edge and the near wake of DSMA 671 model at $\alpha = 12$ degs) were made using a directionally sensitive two-component laser-doppler velocimeter. The velocimeter consisted of an argon-ion laser of maximum power 4 watt, a TSI series 900 two-color dual-beam backscatter optics equipped with two Bragg-cell frequency shifters modified for an off-axis (about 10 degs) forward-scatter operation and TSI 1990 two-channel counter-processor system.

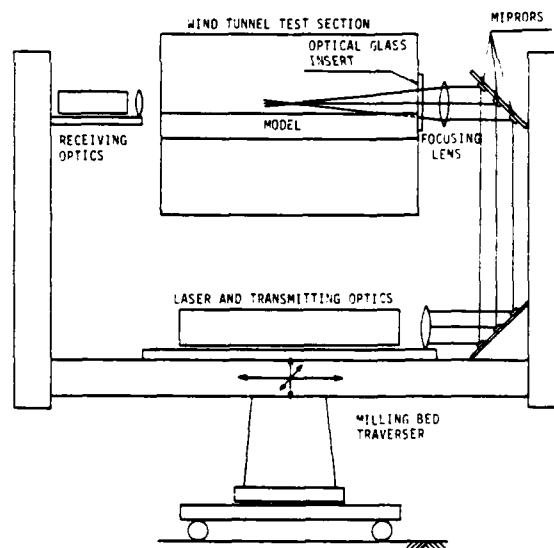


Fig. 2. Laser anemometer optical system and traverse mechanism.

Figure 2 depicts the optical system and the traverse mechanism. All optical components, both transmitting and receiving, were attached to a large U-shaped frame and to a milling table which allowed translation in the three orthogonal directions. The laser, a color-separating prism, beam splitters, frequency shifters and a beam expander were mounted under the wind tunnel test section. The beams coming out of the beam expander were

deflected upwards to the level of the measurement position and then into the test area by eight mirrors. The green beams (514.5nm line) were aligned to form a vertical set of fringes, which moved downstream with a velocity greater than the maximum flow speed to measure the horizontal component of the velocity while the blue beams (488nm line) were arranged to form a horizontal set of fringes moving upwards.

To make measurements close to the airfoil surface, the axis of the incident beams was inclined approximately 5 degrees towards upstream so that the velocity component u_h measured by the vertical fringes of the blue beams corresponds to

$$u_h = (U + u) \cos \phi_h - w \sin \phi_h \quad (1)$$

where $\phi_h (\approx 5^\circ)$ is the angle of inclination of the fringes in the horizontal plane.

In the measurements of the upper-surface boundary layer, the beam axis was inclined downwards, by $\phi_v (\approx 5^\circ)$, so that the velocity component u_v measured by the blue beams was

$$u_v = [(V + v) \cos \phi_s - (U + u) \sin \phi_s] \cos \phi_v - w \sin \phi_v \quad (2)$$

where ϕ_s is the angle between the vertically-upward direction and the direction normal to the surface. In the data analyses, however, the contribution from w was ignored since the mean spanwise velocity and correlations involving w are small in the flow very close to two dimensional and $\sin \phi_v$ is small. Table 1 summarizes the characteristics of the optical and geometrical configurations.

Table 1. Laser Anemometer Optical and Geometrical Data

Laser Operating Power 1-2W	
Focal Length	1219mm (theoretical)
Beam Crossing Angle	6.26° (theoretical)
Measuring Volume, length diameter	2.8mm (based on e-2) 0.15mm
Fringe Spacing, green (514.5nm) blue (488nm)	4.71µm (theoretical) 4.47µm
Number of Fringes	32 (based on e-2)

The signal processing and data acquisition system is shown in Figure 3. The signals from the photomultiplier systems were high-pass filtered to remove the pedestals and downmixed with 30 MHz signals before being processed by the counters. The relation between the velocity components and the frequencies of the downmixed signals $f_0^{(1)}$ and $f_0^{(2)}$, considering the frequency shift, can be expressed by

$$f_0^{(1)} = (f_s - u_h/d_f^{(1)}) - f_m \quad (3)$$

$$f_0^{(2)} = (f_s + u_v/d_f^{(2)}) - f_m \quad (4)$$

where f_s is the shift frequency fixed at 40 MHz,

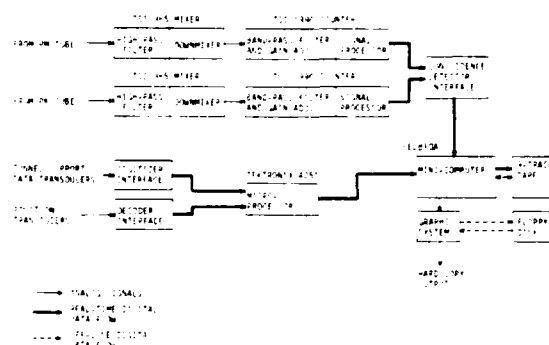


Fig. 3. Signal processing and data acquisition system.

f_m is the mixing-signal frequency fixed at 30 MHz and $d_f^{(1)}$ and $d_f^{(2)}$ are the spacings of the green and blue fringes, respectively.

The expected ranges of the velocity components are

$$-5\text{m/s} \leq u_h \leq 35\text{m/s}$$

$$-10\text{m/s} \leq u_v \leq 10\text{m/s}$$

and the corresponding ranges of $f_0^{(1)}$ and $f_0^{(2)}$ are

$$2.5\text{MHz} \leq f_0^{(1)} \leq 11\text{MHz}$$

$$8\text{MHz} \leq f_0^{(2)} \leq 12\text{MHz}$$

since both $d_f^{(1)}$ and $d_f^{(2)}$ are about 5µm (see Table 1). The estimated minimum number of doppler cycles per burst is at least 8 if the signals are produced by particles traversing near the center of the measuring volume at any speed within the expected range. On these assumptions, the downmixed signals were band-pass filtered between 1 MHz and 20 MHz for the green channel and between 5 MHz and 20 MHz for the blue channel and the counters were operated in a fixed 8-cycle mode.

The data sampled by the two counters were passed to the data acquisition system only if the time delay between the two channels was less than 20 µsec which is smaller than to the smallest turbulent time scale. The data acquired by the minicomputer were first written on a 1/2 in. magnetic tape by a single-buffering method and later transferred to a Tektronix graphic system for averaging.

The data were averaged by weighting the individual sample by

$$w^2(u_h, u_v) = (u_h^2 + u_v^2 + (b/a)^2 \bar{w}^2)^{-1/2} \quad (5)$$

where b/a is the ratio of the length and the diameter of the measuring volume, and \bar{w}^2 is the spanwise squared turbulent intensity which was estimated from the first 100 samples by

$$\bar{w}^2 = \frac{1}{2} (u_h^2 + u_v^2) \quad (6)$$

The usual "two dimensional" bias correction (ref. 12) is a particular case of Eq. (5) with $b/a = 0$.

In the present measurements where the instantaneous velocity can reverse, this two-dimensional weight which assumes infinitely long measuring volume, is unrealistic since $u_H \approx 0$ and $u_V \approx 0$ can be realized with a finite probability. The above weighting is based on the fact that the sampling probability is proportional to the product of the total velocity and the projected area of the measuring volume in the direction of the velocity vector (see Refs. 12 or 13) and that the instantaneous w^2 in the derivation may be approximated by the average w^2 . This weight does not take into account the fact that a single particle may produce more than one sample. Since this multiple sampling is likely to occur only when $u_H \approx u_V \approx 0$ and the effect can be partly reflected by using the value of b/a larger than the actual value. $b/a = 8$ was used for all the data shown. The difference between the two-dimensional bias correction method and the present one is very small unless u_H and u_V can become very small simultaneously, and practically no difference was found when the instantaneous velocity does not reverse directions.

The mean values and correlations up to the third order involving u_H and u_V were obtained by the averaging and then the mean velocities U and V and correlations up to the third order involving u and v , the fluctuating velocity components parallel and perpendicular to the local surface, were reduced by coordinate transformation. A nominal total of about 4000 samples were used (2400 in the low - turbulent - intensity region but 4800 in the high intensity region) for each average with an average data rate which was 100 per second at the best.

Results of hot-wire measurements and the laser measurements are presented in Figures 4(a,b), for unseparated and separated cases, respectively, and indicate maximum discrepancies in U and V for the unseparated case are of less than about 5% and about 10% in the turbulent intensities excluding near the edges of the wake. The hot-wire cannot respond to flow reversals and the averages are erroneous in the region $-0.05 < y/C < 0.15$. It is noted that in the rest of the flow, where the velocity is likely to be in the downstream direction all the time, the agreement is good.

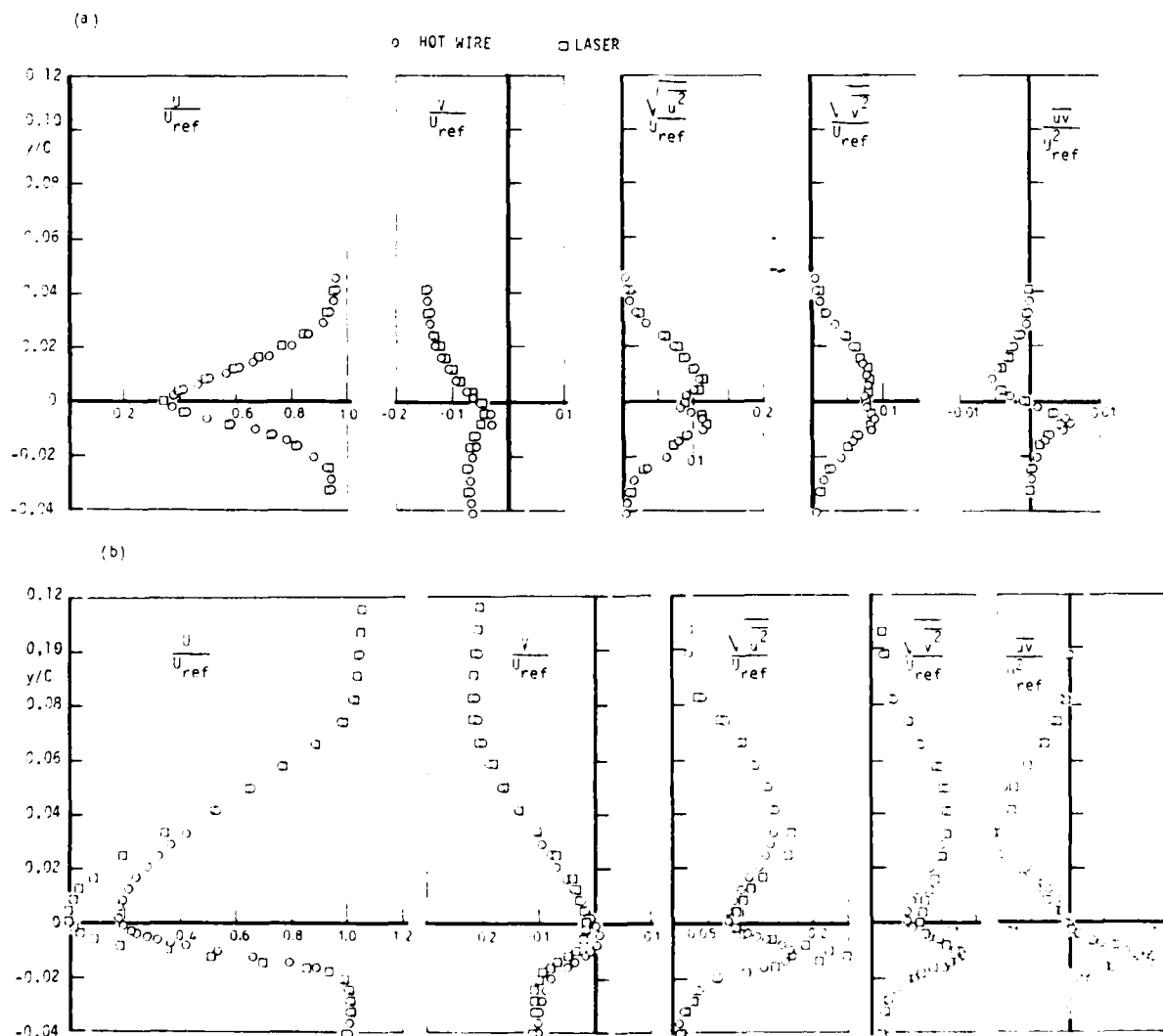


Fig. 4. Comparison between hot-wire and laser anemometer data. (a) Unseparated flow at $X/C = 1.05$ in the wake of Model B, $\alpha = 4^\circ$, (b) Separated flow at $X/C = 1.05$ in the wake of Model B, $\alpha = 12^\circ$.

III. Results

3.1 Overall Flow Fields

Two dimensionality and stationarity of the flow was very good in the unseparated cases. Even in the separated case, the entire flow was found to be free from quasi-periodic low-frequency unsteadiness and the flow near the center span was found to be fairly uniform in spite of the fact that the lower-surface boundary layer undergoes a natural transition at about $X/C = 0.75$.

The spanwise nonuniformity of the flow in the separated case was investigated extensively. The surface static pressure variation was no more than 3 percent of the freestream dynamic pressure over the mid-6 inches of the span. The spanwise variation of the skin-friction coefficient just upstream of the separation was within 0.00015 over the same range. The spanwise distributions of mean velocity and the shear stress in the boundary layer near separation were also measured. Over about two-boundary-layer thicknesses near the center span, velocity changed only about 5% and the shear stress about 10% which are about the ranges of expected errors.

Figures 5(a,b,c) through 7(a,b,c) show the overall flow fields of the three cases investigated. These plots (a), (b) and (c) in each figure correspond to the near-symmetric flow about the conventional airfoil at $\alpha = 0$, the strongly asymmetric attached flow about the supercritical airfoil at $\alpha = 4$ degs, and the separated flow about Model B at $\alpha = 12$ degs, respectively. The isobar contours shown in Figure 6 were generated from the static-tube data. The actual data points are shown in the accompanying cross-sectional plots at a few stations and compared with the integration of the y-momentum equation including all significant terms. The agreement is generally good in spite of uncertainties in the static-tube data. The mean velocity vectors are plotted in Figure 7 together with the displacement thickness added to the airfoil contours. The mean velocities shown in Figure 7(c) for the separated case are the laser data except for the first and the last stations and the lower-surface station. The positions of the shear layer edges were taken to be the points where the total-pressure defect is one percent of the maximum defect across the layer. The edge velocities shown in Figure 5 were calculated from the measured total and the static pressures at the edges. Strictly speaking, they represent the total velocity rather than the x-direction component.

In Figure 8, the distributions of the skin-friction coefficient C_f and the momentum thickness θ are shown. Except for the separated and the laminar region, C_f was determined by fitting the log-linear portion of the mean velocity profile by

$$\frac{U}{u_\tau} = 5.6 \log \frac{u_\tau y}{\nu} + 5.2 \quad (7)$$

In the separated region, the measured total shear stress $(-\rho uv + \mu \partial U / \partial y)$ was extrapolated to the surface. Figure 12 represents the closeness to the separation in the form of the Sandborn correlation¹⁴ between the shape parameter $H = \delta^*/\theta$ and δ^*/δ .

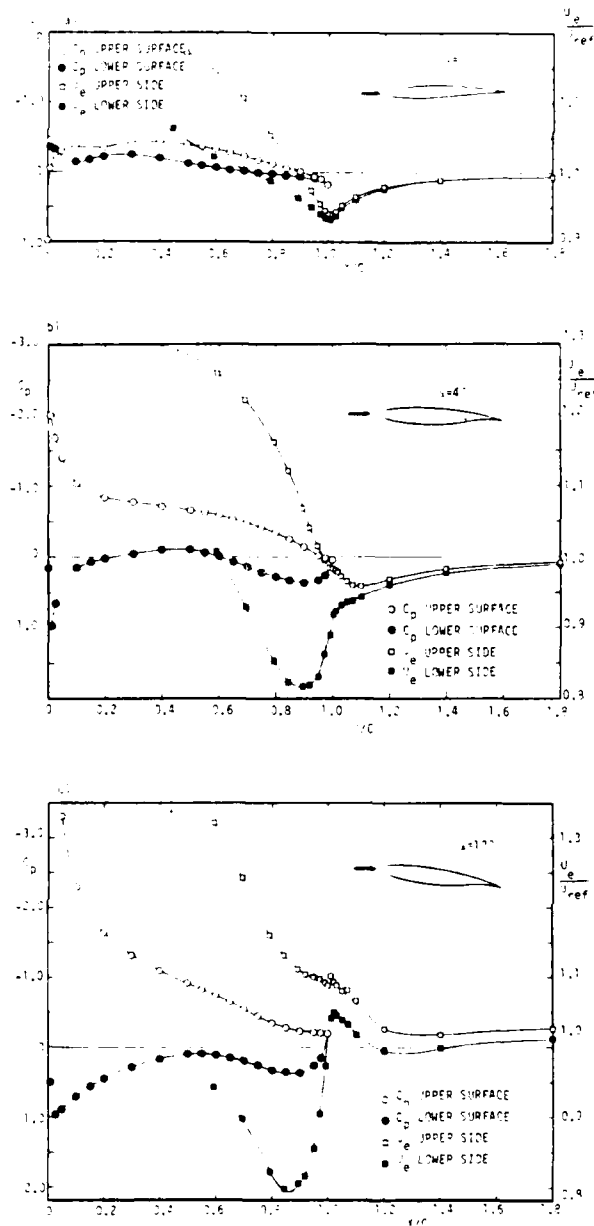


Fig. 5. Surface pressure and edge velocity distributions. (a) Conventional airfoil Model A at $\alpha = 0^\circ$, (b) Supercritical airfoil Model B at $\alpha = 4^\circ$, (c) Separated flow about Model B at $\alpha = 12^\circ$.

In the case of the conventional airfoil, the pressure rises on both surfaces towards the trailing edge. Figure 5(a) indicates that the pressure is highest at the trailing edge and it decreases in all directions. The boundary-layer experiences positive pressure gradient and the wake is accelerated. These pressure gradients are mild and the streamlines curve mildly. The boundary-layer and wake developments are expected to be only a small perturbation of flat-plate flows and similar to the trailing-edge flows of symmetric airfoils with wedge-shaped trailing edges like those measured by Yu⁴.

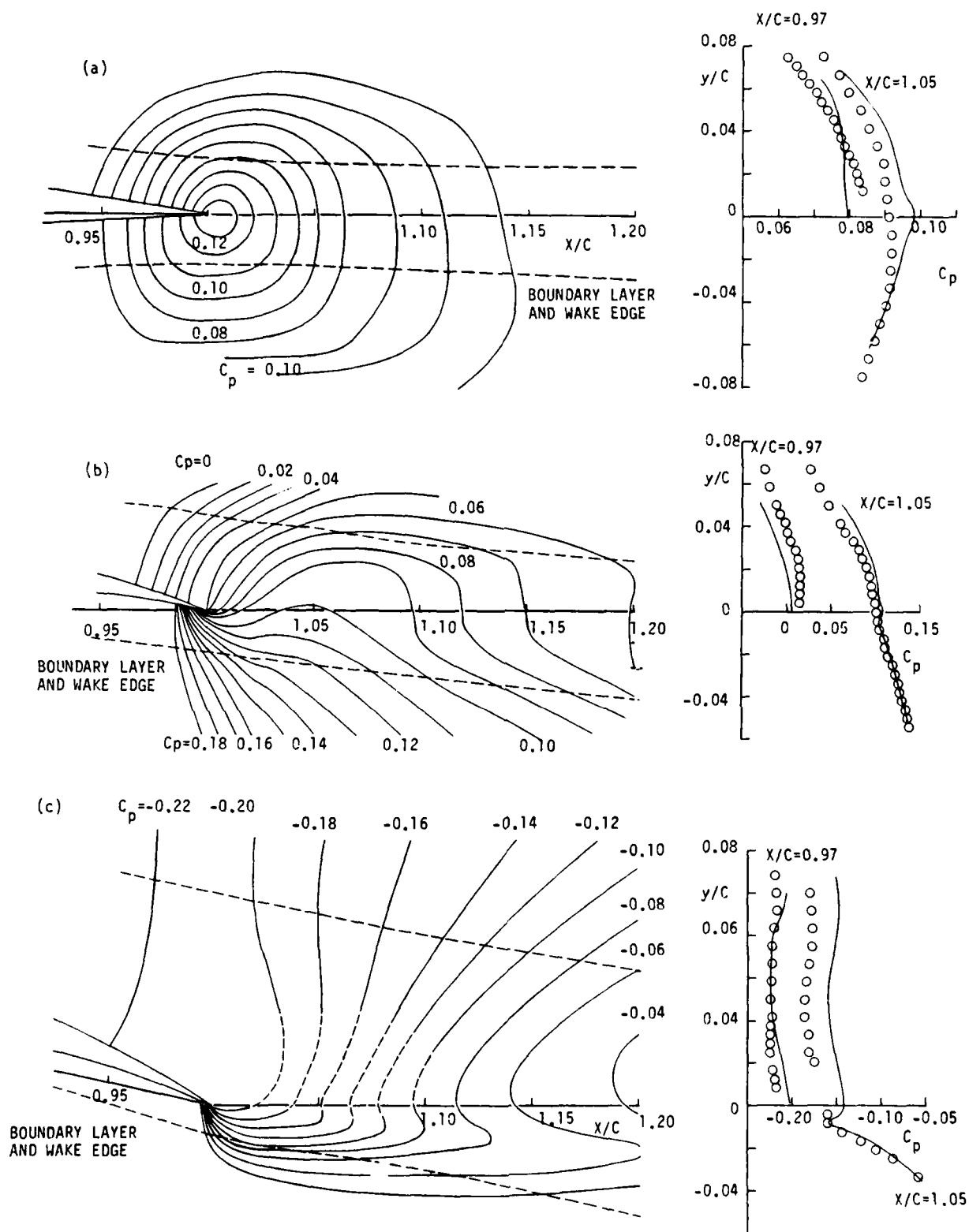


Fig. 6. Static pressure distribution in the trailing-edge region. (a) Conventional airfoil Model A at $\alpha = 0^\circ$, (b) Supercritical airfoil Model B at $\alpha = 4^\circ$, (c) Separated flow about Model B at $\alpha = 12^\circ$.

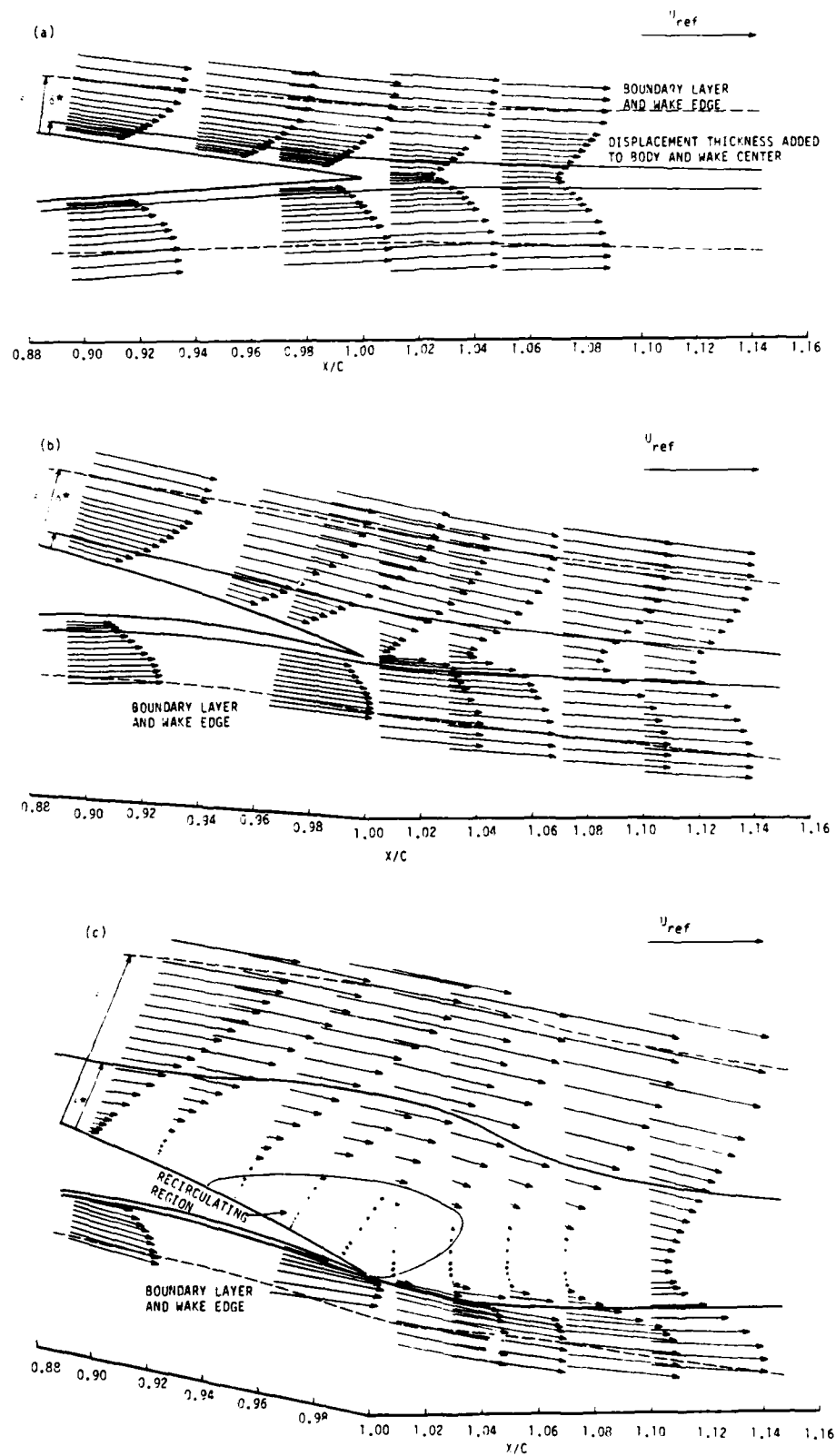


Fig. 7. Mean velocity distribution in the trailing-edge region. (a) Conventional airfoil Model A at $\alpha = 0^\circ$, (b) Supercritical airfoil Model B at $\alpha = 4^\circ$, (c) Separated flow about Model B at $\alpha = 12^\circ$.

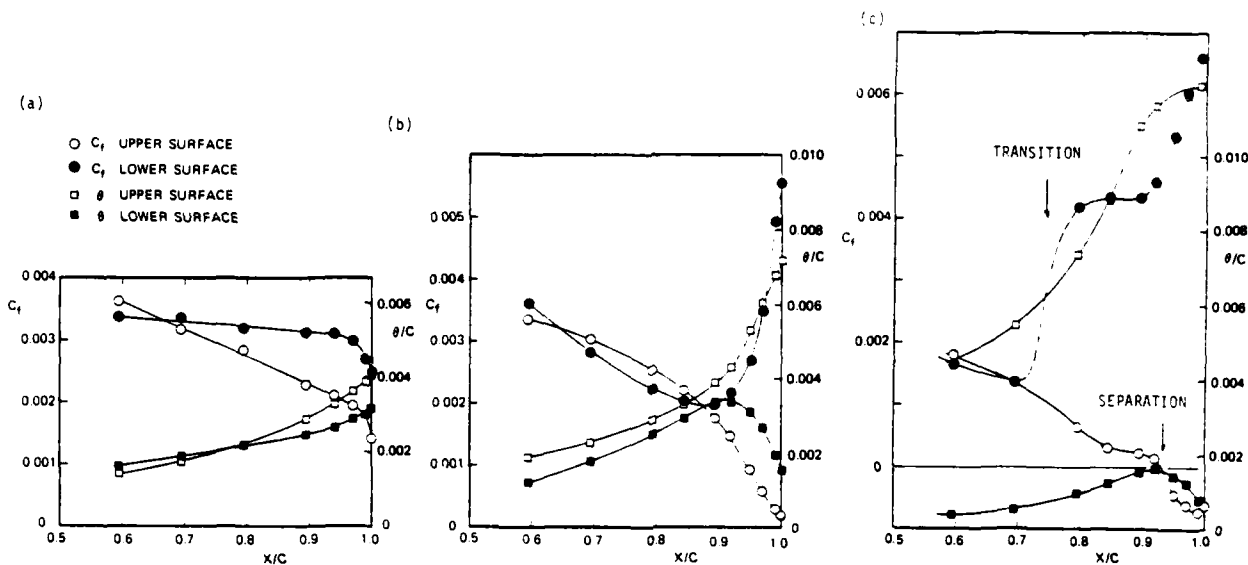


Fig. 8. Skin-friction coefficient and momentum thickness in boundary layers. (a) Conventional airfoil Model A at $\alpha = 0^\circ$, (b) Supercritical airfoil Model B at $\alpha = 4^\circ$, (c) Separated flow about Model B at $\alpha = 12^\circ$.

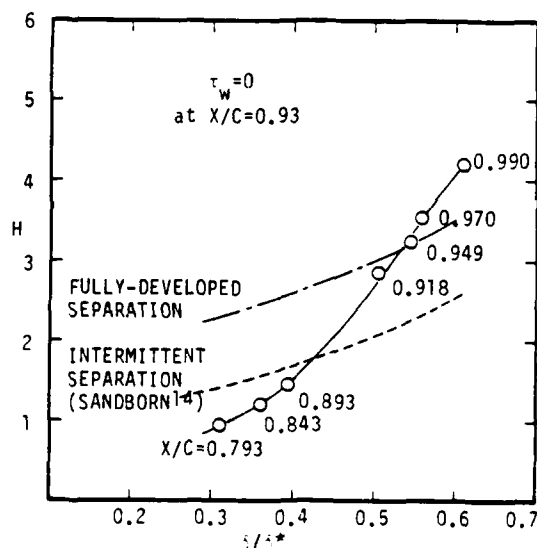


Fig. 9. Sandborn-Kline separation correlation.

In the case of the supercritical airfoil at $\alpha = 4$ degs, the highest pressure point moves upstream about 10-percent chord on the lower surface and the pressure within the flow decreases in the counter-clockwise direction around the trailing edge. The pressure difference between the upper and lower edges of the wake is sufficient to cause nearly 6% difference in the edge velocities. The boundary-layers experience opposite and strong pressure gradients and the upper-surface boundary layer is about 2.5 times thicker. The upper half of the initial part of the wake up to about $X/C = 1.07$ is still decelerated while the lower half is accelerated. The streamlines near the trailing-edge curve very accurately. The lower half of the

flow which has the larger momentum, deflects the streamline upwards just downstream of the trailing edge. In the thicker boundary layer on the suction side, the curvature and even the sign of the streamlines change.

At $\alpha = 12$ deg, the mean flow is in the upstream direction in the region $0 < y/C < 0.03$ between $X/C = 0.93$ and 1.07 . The backflow is small and at no place was the instantaneous velocity backward all the time, as is seen in figure 9 which shows the maximum fraction of time, y_p , the flow is backwards. The values of y_p were reduced from the laser-anemometer data which were taken downstream of $X/C = 0.918$ where y_p is already 0.35. Following Simpson's¹⁵ terminology, the incipient detachment is the position where $y_p = 0.01$ and it appears, by extrapolating backwards, to be in the region $X/C = 0.85 \pm 0.02$. The intermittent transitory detachment where $y_p = 0.2$ occurs around $X/C = 0.90$ with transitory detachment at $X/C = 0.93$ where $y_p = 0.5$. The position where $\tau_w = 0$, from Figure 8, is also at $X/C = 0.93$ which is very close to the point where the mean flow starts reversing. Figure 10 shows that Sandborn separation correlation agrees well with the present data.

Figure 6(c) shows that the pressure on the suction side further reduces to $C_p = -0.2$ and is very uniform over the recirculating region. On the lower side, however, the pressure changes very rapidly and mainly in the vertical direction. The edge velocity distribution implies deceleration on both sides as far downstream as $X/C = 1.25$ and may be compared with the case of the conventional airfoil where the entire wake is accelerated and with the case of the supercritical airfoil with $\alpha = 4$ deg where only the upper half of the initial wake is decelerated. Both upper and lower side edge velocities in this case approach asymptotic value which is slightly higher than the freestream velocity, due to the increased displacement thickness of the wake.

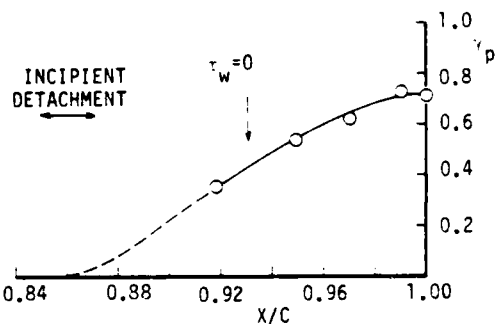


Fig. 10. Maximum fraction of time flow is backward near the trailing edge of supercritical airfoil Model B at $\alpha = 12^\circ$.

3.2 Mean Velocity and Reynolds Stress Data

The mean velocity profiles in the upper-surface boundary layers, $X/C < 1.0$ are plotted in semi-log coordinates in Figures 11(a,b). The mean velocity distributions in the trailing-edge region are already well represented by the vector plots in Figure 9.

The development of the wake minimum velocity is shown in Figure 12 together with flat-plate data¹⁻³ and the symmetric airfoil data of Yu⁴. Although there is a considerable range where the minimum velocity increases logarithmically, the slope can depend very much on the degree of asymmetry. The asymmetric case of Andreopoulos and Bradshaw⁴ which is obtained by roughening one surface of the flat plate is somewhat different from the present asymmetric wake flows. Although the ratio of the thicknesses of boundary layers at the trailing edge is large, the ratio of the time scale δ/u_τ is nearly one. In the case of asymmetric trailing-edge flow, however, the ratio of the time scale δ/u_τ is very large since the suction-side boundary layer is decelerated with smaller u_τ and larger δ but the pressure-side is less decelerated or accelerated with larger u_τ and smaller δ .

In the case of the conventional airfoil at $\alpha = 0$, the velocity profiles retain the logarithmic similarity up to the trailing edge. Although not very clear from the present set of data, there is an extension of this inner layer into the wake with changing velocity scale u_τ and the origin of the distance y . The Reynolds stress distributions in the boundary layers were found to be consistent with known characteristics in mild adverse pressure gradients. In the near wake, the effects of these adverse pressure gradients in the upstream boundary layers make the distributions closer to and approach faster to those in the far wake than in the wake behind a flat plate.

In the case of unseparated flow about the supercritical airfoil, the pressure gradients are so large that at the trailing edge there is hardly any semi-log portion left in the velocity profiles. In the near wake, there is only one sharp velocity gradient, as opposed to two opposite sharp gradients in the symmetric or near symmetric case. Since this single sharp gradient that occurs just below the wake centerline is so strong that the initial part of the wake presents locally mixing-

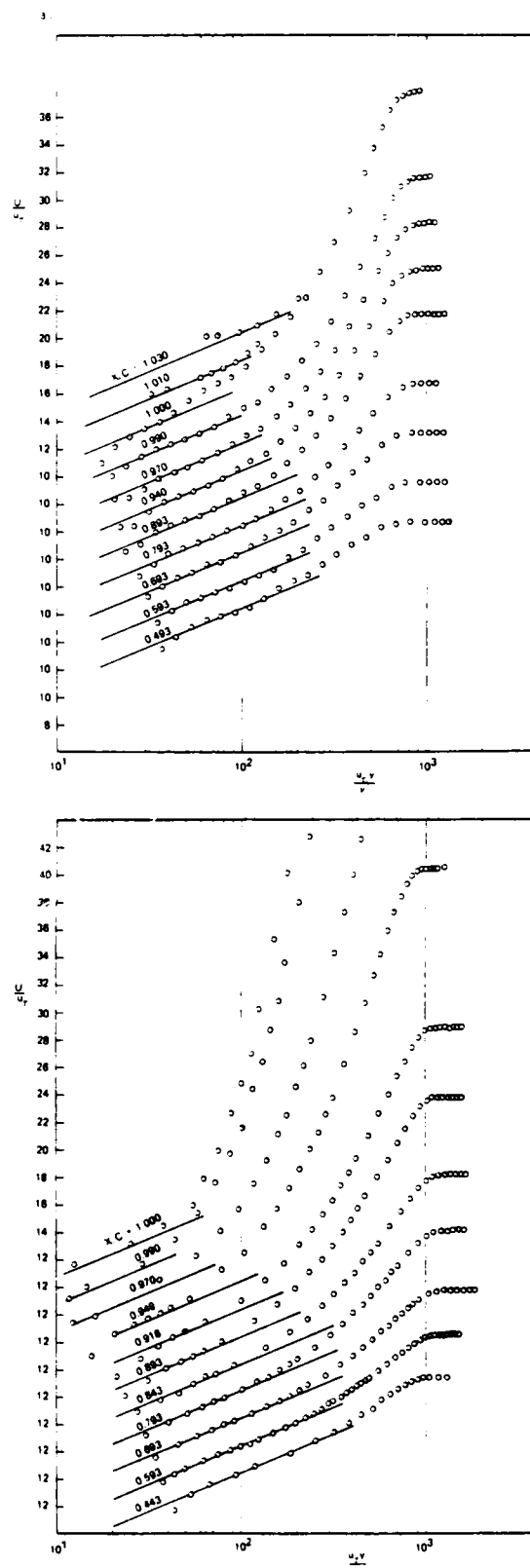


Fig. 11. Semi-logarithmic plot of upper-surface boundary-layer velocity profiles. (a) Conventional airfoil at $\alpha = 0^\circ$, (b) Supercritical airfoil at $\alpha = 4^\circ$.

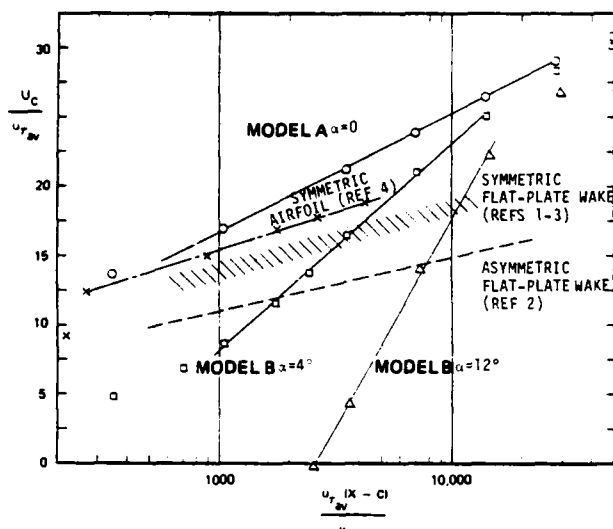


Fig. 12. Growth of wake minimum velocity.

layer like characteristics and large Reynolds stresses are generated (see Figure 4(b)).

At the angle of attack of 12 deg. the upper-surface boundary layer separated at about $X/C = 0.93$ and the lower-surface boundary layer remains laminar up to about $X/C = 0.75$. The turbulent intensities and the shear stress in the upper boundary layer are now very large. The boundary-layer thickness on the separated side is as much as 8 times thicker than the pressure-surface one. The initial part of the wake is dominated by the mixing between almost stagnant upper half and the high velocity flow in the lower side where the existence of the thin upstream boundary layer is almost insignificant. Consequently, the stress distributions have only two peaks, one is a broad one in the upper half the other other is a very sharp peak in the mixing-layer region.

IV. Discussion

4.1 Effects of Normal Pressure Gradient and Normal Stresses

It was seen in the pressure-field plots of Figure 6 that there are some normal pressure variations across the boundary layer and the wake near the trailing edge. The importance of this variation in connection with the viscous-inviscid interaction is discussed here. The question is whether or not the boundary-layer equations are sufficient to describe and to be used to calculate the flows near the trailing edge.

The momentum equation, if written in the streamline coordinates (s, n), may be integrated to give

$$\frac{1}{2} Q^2 + \frac{p}{\rho} + \overline{u^2} - \int_0^s \frac{\partial}{\partial n} \left(\frac{\tau}{\rho} \right) ds = \frac{1}{2} Q_0^2 + \frac{p_0}{\rho} \quad (8)$$

where Q is the total velocity, the subscript 0 indicates the quantity at the upstream station and $\overline{u^2}$ is the turbulent normal stress in the streamline direction. The turbulent stress terms associated with the streamline curvature is ignored being of smaller magnitude. Similarly, if the boundary-layer equation, which assumes the pressure

is constant across the layer and equal to the edge pressure p_e and does not consider the turbulent normal stress, is integrated to

$$\frac{1}{2} (Q + \Delta Q)^2 + \frac{p_e}{\rho} - \int_0^s \frac{\partial}{\partial n} \left(\frac{\tau + \Delta \tau}{\rho} \right) ds = \frac{1}{2} Q_0^2 + \frac{p_e}{\rho} \quad (9)$$

where ΔQ and $\Delta \tau$ are the deviations from the "true" velocity and the shear stress or the "errors" due to the neglect of the normal pressure gradient and the turbulent normal stress. If, for the purpose of the present discussion, the shear stresses in Eq. (9) are correct ($\Delta \tau = 0$) and if the differences in the paths of the integrations in Eq. (8) and (9) are small, the error ΔQ in the solution of the boundary-layer equation is, to the first order,

$$\frac{\Delta Q}{U_e} = \left(\frac{p - p_e}{\rho U_e^2} + \frac{\overline{u^2}}{U_e^2} \right) \frac{U_e}{Q} \quad (10)$$

if the local flow direction deviates mildly from the x -direction, Q may be set equal to U and Eq. (10) may be converted to

$$\frac{\Delta U}{U_e} = \left(\frac{p - p_e}{\rho U_e^2} + \frac{\overline{u^2}}{U_e^2} \right) \frac{U_e}{U} \quad (11)$$

Eqs. (10) and (11) may be used to evaluate whether or not the presently observed normal pressure gradient and the normal stress are significant. In the case of the conventional airfoil at zero incidence U_e/U never exceeds 3 outside the viscous sublayer. The pressure variation across the upper-surface boundary layer is at most $(p - p_e)/\rho U_e^2 = 0.015$ (Figure 6(a)). The normal stress $\overline{u^2}/U_e^2$ was found only 0.005 at its maximum. Even if all these occur at the same point, the error ΔU is 6 percent of U_e . Since the largest values of $(p - p_e)/\rho U_e^2$, $\overline{u^2}/U_e^2$ and U_e/U do not occur at the same point, the actual error would be smaller.

If similar analysis is made with the data in the upper-surface boundary layer of the supercritical airfoil at $\alpha = 4$ deg, it was found that $\Delta U/U_e$ can be as large as 15 percent, the region where the estimated error exceeds 5 percent extends over $0.95 < X/C < 1.0$. In the lower-surface boundary layer, although the pressure variation $(p - p_e)/\rho U_e^2$ can be much larger than in the upper-surface boundary layer, U_e/U is very small due to strong acceleration and the signs of $p - p_e$ and $\overline{u^2}$ are opposite tending to cancel each other so that the implied error is small.

In the separated case, it is obvious, because mean velocity can become zero, that the normal pressure gradient and normal stresses are very important.

Comparing the three cases measured, it is interesting to note that the pressure variation across the layer becomes less near separation or in the separated flow, but its importance in the calculation is greater. It may be said that the normal pressure gradient and the normal stress terms are unimportant in the pressure-surface boundary layer where the boundary layer is accelerated or decelerated very mildly. In the case of

the near symmetric case of the conventional airfoil, these effects are small on both surfaces. In the suction-surface boundary layers of more asymmetric flows about the supercritical airfoil, the normal pressure gradient and the normal stresses do play an important role.

In the near wake in any case the difference of the upper- and lower-edge velocities can only be accounted by the variation of the static pressure across the wake, which is also important in the prediction of the curving of the wake.

The contributions to the normal pressure variations from different terms in the y-component momentum equation were examined when the results of its integration shown in Figure 6 were obtained. Although the detailed results are not shown, the conclusion agrees partially with the conclusion of Simpson et al.¹⁵, namely that: the convective acceleration terms are unimportant where the velocity is small in the region near and inside separation and the turbulence term $\partial^2 v^2 / \partial y^2$ is more important. Outside the separated region and in the near wake, convective terms are significant. In the intense mixing regions found just downstream of the trailing edge in the highly asymmetric cases, the streamwise gradient of the shear stress was found to be non-negligible, but this region is confined in a relatively small region. It may be concluded that the boundary-layer approximation used in an interactive approach may be sufficient for calculating near symmetric flow about the conventional airfoil but an extension allowing the normal pressure variation and the normal stress would be required for an accurate prediction of more asymmetric flows about the supercritical airfoil.

4.2 On the Turbulence Modeling Near the Trailing Edge

In this section, implications of the present data on the modeling of turbulence is discussed. Detailed analyses of the data of the separated case are still in progress and discussion in this case is made only briefly.

In Figures 13(a,b,c) the distributions of the eddy-viscosity coefficient in the upper surface boundary layer are shown. In the boundary layer of the conventional airfoil, the level and the

shape of the distributions change very little. In the case of the supercritical airfoil at $\alpha = 4^\circ$, the level normalized by $U_\infty \delta^*$ decreases markedly to only 0.003 at $X/C = 0.99$, which is considerably smaller than the value 0.0168 used in the extensively-tested (in variety of situations) model of Cebeci and Smith¹⁶. It is remarkable that the eddy viscosity reduces further and becomes negative in the separated case. The region where the eddy viscosity is negative extends much further away from the surface than the minimum velocity point. The negative eddy viscosity in this region, however, does not imply the reversal of the energy from turbulence to mean flow since there is a significant production by the normal stresses. The distributions of the mixing length are similar (not shown) to those of the eddy viscosity. Modifications, if eddy viscosity model is to be used in the empirical constants may be required for an accurate prediction.

The distributions of the eddy viscosity and the mixing length in the near wake are complicated. They have minima at the locations of maximum velocity gradient and not at the minimum-velocity points where the mixing length quickly becomes infinity. The eddy viscosity assumes local minima at these points and at maximum mean velocity gradient points. The maximum value of the mixing length was found to grow linearly with streamwise distance in the region where the minimum velocity increased logarithmically.

In Figure 14, various length scales of turbulence and combination of mean and turbulence are shown at $X/C = 1.05$ of the supercritical airfoil model at $\alpha = 4^\circ$. The integral scale of the correlation of the fluctuating streamwise velocity L_u and the dissipation length, both of which are the scales of the large eddies, are nearly proportional. However, the mixing length and Prandtl-Kolmogoroff length scale are not proportional to the former two length scales: they have dips near the point where the mean velocity gradient takes maximum value.

V. Conclusions

From the three sets of data obtained with the two airfoils, the following conclusion may be extracted.

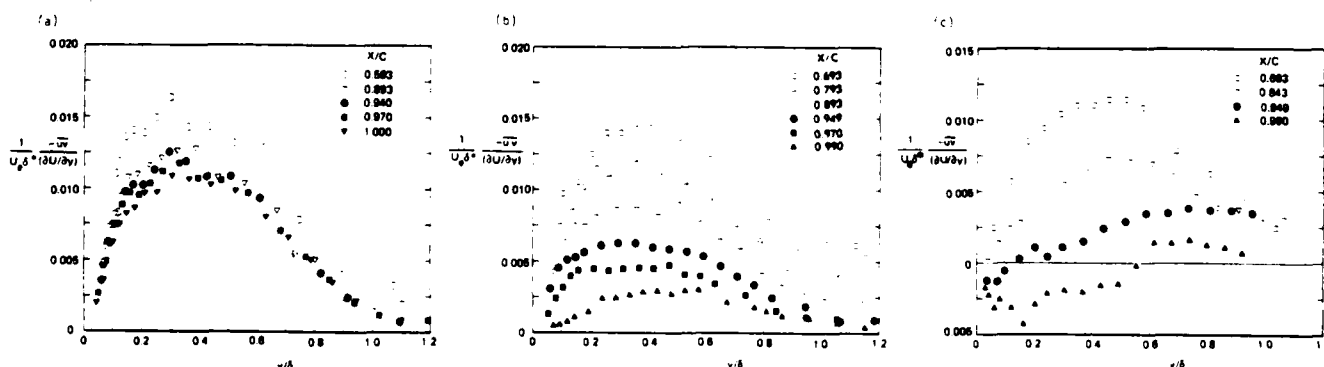


Fig. 13. Eddy-viscosity distributions in the upper-surface boundary layer. (a) Conventional airfoil Model A at $\alpha = 0^\circ$, (b) Supercritical airfoil Model B at $\alpha = 4^\circ$, (c) Separated flow about Model B at $\alpha = 12^\circ$.

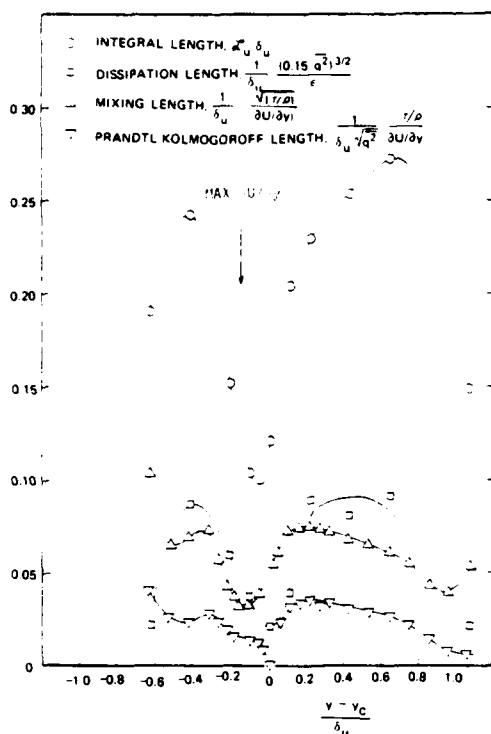


Fig. 14. Various length scales in the near wake of supercritical airfoil at $\alpha = 4^\circ$.

If the flow is near symmetric and the pressure gradients in the boundary layers are mild, the pressure gradient across the trailing-edge region is not very important and the viscous-inviscid interaction is weak. The turbulent stresses in the boundary layers are not very much different from those in mild pressure gradients and the same turbulence models may be used.

In the highly asymmetric case, with or without separation, small normal pressure gradient and increased normal stress in the suction-surface boundary layer are important. The shear stress level does not increase proportionately with the kinetic energy and the eddy-viscosity coefficient decreases significantly. In the region just downstream of the trailing edge, the mixing of the two merging boundary layers control the turbulence mechanism. Very large generation of the turbulent stresses and their transport are crucial in stress or kinetic energy modeling.

Acknowledgment

The present work was carried out under the Independent Research and Development Project Line Item 126061 at Douglas Aircraft Company, Long Beach. The author is indebted to Professor J. H. Whitelaw for his encouragement, suggestions and criticisms obtained at various stages of the work, especially during the preparation of this paper.

References

1. Pot, P.J.: A Wake Boundary Layer Mixing Experiment. Proc. 2nd Conf. on Turbulent Shear Flows, Imperial College, London, 1979.

2. Andreopoulos, J. and Bradshaw, P.: Measurements of Interacting Turbulent Shear Layers in the Near Wake of a Flat Plate. *J. Fluid Mech.*, **100**, pp. 639-668, 1980.
3. Ramaprian, B.R. and Patel, V.C.: The Symmetric Turbulent Wake of a Flat Plate. *AIAA J.*, **20**, pp. 1228-1235, 1982.
4. Yu, J.C.: Mean-Flow and Turbulence Measurements in the Vicinity of the Trailing Edge of a NACA 631-012 Airfoil. NASA TP 1845, 1981.
5. Hoad, D.R., Meyers, J.F., Young, W.H., Jr., and Hepner, T.E.: Correlation of Laser Velocimeter Measurements Over a Wing with Results of Two Prediction Techniques. NASA TP-1168, 1978.
6. Johnson, D. and Spaid, F.W.: Measurements of the Boundary Layer and Near Wake of a Supercritical Airfoil at Cruise Conditions. AIAA Paper 81-1242, 1981.
7. Hah, C. and Lakshminarayana, B.: Measurements and Prediction of Mean Velocity and Turbulence Structure in the Near Wake of an Airfoil. *J. Fluid Mech.*, **115**, pp. 251-282, 1982.
8. Coles, D. and Wadcock, A.J.: Flying-Hot-Wire Study of Flow Past NACA 4412 Airfoil at Maximum Lift. *AIAA J.*, **17**, pp. 321-329, 1979.
9. Young, W.H., Jr., Meyers, J.F., and Hood, D.R.: A Laser Velocimeter Flow Survey Above a Stalled Wing. NASA TP 1266, 1978.
10. Salignac, J-L.: Experimental Study of the Separation at the Trailing Edge of an Axisymmetrical Contoured After-Body. *Rech. Aérosp.* No. 1980-3, pp. 65-71, 1980.
11. Viswanath, P.R., Clearly, J.W., Seegmiller, H.L. and Horstman, C.C.: Trailing-Edge Flows at High Reynolds Number. AIAA Paper 79-1503, 1979.
12. Hoesel, W., and Rodi, W.: New Biasing Elimination Method for Laser-Doppler Velocimeter Counter Processing. *Rev. Sci. Instrum.* **48**, pp. 960-919, 1977.
13. McDougall, T.J.: Bias Correction for Individual Realization LDA Measurements. *J. Phys. E. Sci. Instrum.*, **13**, pp. 53-60, 1980.
14. Sandborn, V.A. and Kline, S.J.: Flow Models in Boundary-Layer Stall Inception. *ASME J. Basic Eng.* **83**, pp. 317-327, 1961.
15. Simpson, R.L., Chow, Y.-T. and Shivaprasad, B.G.: The Structure of a Separating Turbulent Boundary Layer. Part 1. Mean Flow and Reynolds Stresses. *J. Fluid Mech.*, **113**, pp. 23-51, 1981.
16. Cebeci, T. and Smith, A.M.O.: Analysis of Turbulent Boundary Layers. Academic Press, New York, 1974.

NUMERICAL SIMULATION OF TURBULENT TRAILING EDGE FLOWS

C. C. Horstman
NASA Ames Research Center
Moffett Field, California

Abstract

Numerical simulations of the time-dependent, Reynolds-averaged, Navier-Stokes equations, employing a two-equation turbulence model, are presented and compared with measurements from a series of trailing edge experiments at transonic Mach numbers. The test flows include an asymmetric flow with no separation, an asymmetric flow with a small region of separation and a symmetric flow with a large shock-wave induced separated zone. Comparisons are made for mean surface quantities as well as for mean and fluctuating flow-field quantities. For the trailing-edge flows with little or no separation, the solutions correctly predict all the major features of the flow field. Treatment of the viscous-inviscid interaction was found to be important for predicting these test cases. Two-equation eddy-viscosity turbulence models were found to be adequate for these flows. However, for the shock-wave induced separation case, these turbulence models were inadequate to predict this flow field. Modifications of the turbulence model to correct these deficiencies are discussed.

Nomenclature

c	= airfoil chord
C_{f_e}	= skin-friction coefficient based on boundary-layer edge conditions
C_p	= pressure coefficient
k	= turbulent kinetic energy
p	= pressure
t	= time
u	= velocity in x direction
u_o	= sonic (reference) velocity
v	= velocity in y direction
w	= velocity normal to u and v
x	= streamwise coordinate parallel to model centerline measured from model trailing edge for test cases I and II and from airfoil leading edge for test case III
y	= vertical coordinate normal to model centerline measured from model surface and in the wake from the extension of the model trailing edge
δ^*	= boundary-layer displacement thickness

ϵ	= turbulence energy dissipation
θ	= boundary-layer momentum thickness
μ	= molecular viscosity
ρ	= density
τ	= shear stress
ω	= turbulent dissipation rate

Subscripts

RET	= reattachment point
SEP	= separation point
t	= turbulent
T	= total
w	= wall conditions
∞	= free stream conditions

Superscripts

$()'$	= fluctuating quantity
$\langle () \rangle$	= rms value

Introduction

In the past several years, considerable advances have been made in the prediction of transonic trailing-edge flows. For modern supercritical airfoils the trailing edge region is dominated by viscous-inviscid interaction. In the near wake the flow field is complicated by streamline curvature and due to the interaction of the merging of two significantly different shear layers. Integral boundary-layer methods coupled with an inviscid flow-field solution have been successfully applied to both symmetric and asymmetric trailing-edge flows provided there is no boundary layer separation.¹⁻³ These methods are not satisfactory for flows with strong adverse pressure gradients leading to significant separated regions.^{2,4} Differential methods employing either a boundary-layer code coupled with an inviscid solution or the mass-averaged Navier-Stokes equations throughout the flow field have also been successful provided separation was not present.^{3,5} Recently an asymmetric trailing-edge flow with a small separated zone was successfully predicted using the Navier-Stokes equations.⁶ The ability to calculate trailing-edge flows with large separated zones remains to be tested.

For flows with no trailing-edge separation and moderate pressure gradients, the viscous-inviscid interaction effects are dominant and turbulence modeling may play a secondary role.^{3,5} For flow fields where separated regions are present,

turbulence modeling becomes important.^{3,6} Further progress in calculating separated trailing-edge flows relies heavily on extracting information relevant to turbulence modeling from well planned experiments involving turbulence measurements. Several recent experimental investigations performed at NASA Ames Research Center⁷⁻⁹ have provided excellent test cases for symmetric and asymmetric trailing-edge flows ranging from attached flows to flows with large shock-wave-induced separated zones. The measurements included both mean and fluctuating flow-field quantities in sufficient detail to allow a proper assessment of the turbulence modeling employed in the calculation method.

This paper presents a detailed comparison between numerical calculations and experimental results for the trailing-edge flows described above. The computed results are solutions of the time-dependent, Reynolds averaged, Navier-Stokes equations using variations of a two-equation eddy-viscosity turbulence model. By employing the Navier-Stokes equations throughout the flow field, the near-wake merging process is properly calculated and the effects of normal pressure gradient, viscous-inviscid interactions and ellipticity of the flow are automatically included. The emphasis of this paper is to assess the ability of a two-equation eddy-viscosity turbulence model with no special corrections for trailing-edge regions to predict these complex flows.

Description of Experiments

The experiments were performed in the Ames High Reynolds Number Facility (38.1-by 25.4-cm). A sketch of the flow geometries is shown in Fig. 1. For models I and II, the test configurations consisted of forebody spanning the test section with two trailing-edge geometries. For model I the cross section of the trailing-edge region is a 12.5° wedge with the lower surface aligned with the forebody. Data were obtained at a nominal Mach number of 0.4 and a free-stream unit-Reynolds number of $2.5 \times 10^7/\text{m}$.⁵ The resulting flow field remained attached for this case. For model II the cross section of the trailing-edge region is the upper rear quadrant of an 18% thick, circular-arc airfoil; the arc has a radius of 40.4 cm and the trailing-edge angle of the flap is 20.4°. Data were obtained at a nominal Mach number of 0.7 and a free-stream unit Reynolds number of $4.0 \times 10^7/\text{m}$.⁷ A small separated zone was obtained over the final 2 cm of the upper surface. For both cases the test section walls were straight.

Model III is an 18% thick, circular-arc airfoil at zero incidence spanning the test section. The data used for comparison in this paper were obtained at a free-stream Mach number of 0.785 and a Reynolds number, based on model chord, of 11×10^6 .^{8,9} The flow field includes an extensive shock-induced separation extending from $x/c = 0.65$ to 1.26. For this case the test section walls were contoured to minimize wall interference effects.

For the three test flows, two-dimensionality was verified with surface oil-flow patterns and spanwise-surface pressure measurements. Additional verification was obtained for models I and II with spanwise flow-field measurements and momentum integral balances using the measured data. The

measurements included surface pressure, skin friction, mean flow-field pressure and velocity distributions, and fluctuating velocity and shear stress data throughout the flow field in trailing-edge and near-wake regions of each test model. A two-color laser Doppler velocimeter was used to measure both the mean and fluctuating flow field. Further details of the experimental techniques, accuracy of the measurements, and results are contained in Refs. 5, 7-9.

Solutions to the Navier-Stokes Equations

The partial differential equations used to describe the mean flow field are the time-dependent Reynolds averaged Navier-Stokes equations for two-dimensional flow of a compressible fluid. Restrictions on the equations include the perfect gas assumption, constant specific heats, the Sutherland viscosity law, and zero bulk viscosity. For the turbulence closure, the k - ϵ eddy-viscosity model¹⁰ was used.

$$\frac{\partial \rho k}{\partial t} + \frac{\partial (\rho u k + q_{kx})}{\partial x} + \frac{\partial (\rho v k + q_{ky})}{\partial y} = P_k - \rho \epsilon \quad (1)$$

$$\frac{\partial \rho \epsilon}{\partial t} + \frac{\partial (\rho u \epsilon + q_{\epsilon x})}{\partial x} + \frac{\partial (\rho v \epsilon + q_{\epsilon y})}{\partial y} = C_1 \frac{\epsilon}{k} P_k - \frac{C_2 \rho \epsilon^2}{k} \quad (2)$$

The turbulent eddy viscosity is given by

$$\mu_t = C_\mu \rho \frac{k^2}{\epsilon} \quad (3)$$

P_k represents the production term for the kinetic energy of turbulence and q_{kx} , q_{ky} , $q_{\epsilon x}$, and $q_{\epsilon y}$ are the flux vectors associated with the turbulence field variables. Modifications to these equations proposed by Chein¹¹ to model the low Reynolds number near wall terms are also employed to permit integration to the wall. The constants employed are $C_1 = 1.35$, $C_2 = 1.8$ and $C_\mu = 0.09$. The complete equations are described in Refs. 11 and 12. Additional computations are performed which show that the solutions for the experimental test flows investigated here are essentially independent of the choice of near-wall treatment of the low Reynolds number terms and of the inclusion of corrections for streamline curvature.

The numerical procedure used here is the basic explicit second-order, predictor-corrector, finite difference, time-splitting method of MacCormack, modified by an efficient implicit algorithm.¹³

The computational domain extended in the streamwise direction from $x = -50$ to 65 cm for cases I and II and from $x/c = -5$ to 3 for case III. A mesh was developed that allowed a variable point spacing in each coordinate direction. One set of grid lines was placed normal to the free-stream direction and the other parallel to the model surface and wake centerline. Total mesh sizes were 79 points in the streamwise direction and 82 points normal to the model surface (41 points on each side) for cases I and II and 134×48 for case III (centerline symmetry was assumed). In the streamwise direction mesh spacing varied from 0.08 cm near the trailing edge to 12.5 cm at the downstream boundary for cases I and II and from $x/c = 0.005$ near the shock wave to $x/c = 1$ at the upstream

boundary for case III. In the direction normal to the surface, first an exponentially stretched spacing was used near the wall after which a uniform spacing was used. The distance of the first y mesh point from the model wall was selected small enough such that the solutions are independent of spacing (typically within $y_{\min} \approx y\sqrt{\tau_w \rho_w} / u_w < 1.0$).^{5,6}

The upstream boundary conditions were prescribed by uniform freestream conditions and for cases I and II combined with the result of a boundary-layer computation along the model surface. For cases I and II the downstream boundary was positioned far enough aft so that all of the gradients in the streamwise direction could be set to zero. This boundary condition was verified by the lack of any substantial change in the numerical results when the location of the downstream boundary was changed. For case III a constant static pressure condition was used at the downstream boundary ($x/c = 3$) which matched the experimental data at that location. At the model surface, no-slip boundary conditions were applied along with a constant wall temperature. The turbulent kinetic energy k and dissipation rate ϵ were set equal to zero at the wall. At the upper and lower boundaries (the wind tunnel walls), inviscid solid-wall boundary conditions were used.

Results and Discussion

Solutions have been obtained for the three flow fields described above. These solutions, which used the $k-\epsilon$ turbulence model¹⁰ with Chien's low Reynolds number terms,¹¹ will be compared in detail with the experimental results. Additional solutions were obtained using the Jones-Launder low Reynolds number terms,¹⁰ a correction to C_μ for streamline curvature and the $k-\omega^2$ eddy-viscosity turbulence model.¹⁴ Only minor differences were discovered between these additional solutions and the ones presented. In addition to the Navier-Stokes solutions, results obtained using boundary-layer codes¹⁴ and viscous-inviscid interaction codes¹⁵ will be compared with the present calculations and the data. Finally a solution using an ad hoc modification to $k-\epsilon$ model will be presented for the massive separation case (test model III) to demonstrate the influence of turbulence modeling on large separated flows.

The computed and experimental wall pressure distributions for the attached trailing-edge flow (test model I) are compared in Fig. 2. The agreement is very good. Figures 3, 4 and 5 compare the mean velocity, turbulent shear stress and turbulent kinetic energy profiles in the trailing-edge and near-wake regions. To compare the kinetic energy profiles it is necessary to convert the measured values $\langle u'^2 + v'^2 \rangle$ to the computed value k or vice versa. For the three test cases presented here, it was assumed that $\langle w'^2 \rangle = 1/2 \langle u'^2 + v'^2 \rangle$. Good agreement is observed between the computed and measured mean velocity profiles (Fig. 3). Also good qualitative agreement is seen for the turbulent shear-stress (Fig. 4) and kinetic-energy (Fig. 5) comparisons. The largest differences are noted in the wake at $x = 14$ cm.

For the airfoil designer who uses interactive procedures, the displacement thickness on the airfoil is the most critical viscous parameter to

correctly predict. This displacement thickness is necessary to predict the pressure distribution and thus predict the lift and drag. Comparisons of the present computations with experimental values of displacement thickness are shown in Fig. 6. The boundary-layer edge is defined at the first grid point where the computed total pressure was 99% of the free-stream value. Also shown are the computed displacement thicknesses from a boundary-layer code.¹⁴ The Navier-Stokes computations are in good agreement with the data while the boundary-layer results substantially underpredict the data. Reasons for these differences will be discussed later.

The computed and experimental wall-pressure distributions for the trailing-edge flow with a small separated zone (test model II) are compared in Fig. 7. The agreement is very good. Note that the computed pressure is slightly higher than the measured pressure on the upper surface ahead of the hinge line. When computing this flow field it was found that the upper surface free-stream Mach number had to be lowered to 0.85 from the quoted experimental value of 0.87 to prevent a shock wave forming on the flap. The maximum Mach number in the flow field is 1.00 for the solution shown, which occurs near the hinge line. The experimenters⁷ found that a 0.02 increase of the free-stream Mach number also produced a shock wave on the flap.

Figures 8, 9, and 10 compare the mean velocity, turbulent shear stress and turbulent kinetic-energy profiles in the trailing-edge and near-wake regions. An excellent agreement is observed between the computed and measured mean-velocity profiles (Fig. 8). Also, good qualitative agreement is seen for the turbulent shear-stress (Fig. 9) and kinetic energy (Fig. 10) comparisons. For the wake at $x = 5.08$ and 12.07 cm the magnitude of the computed shear-stress and kinetic-energy profiles are slightly less than and do not fill out as fast as the measured values. Although the present results do not extend into the far wake, the trends shown here suggest that the turbulence model employed will not predict the correct asymptotic growth rate of the far wake.

Comparisons of the present computations with experimental values of displacement and momentum thickness for the upper model surface are shown in Fig. 11. These comparisons show good agreement. Also shown are results from a boundary-layer code¹⁴ using the measured pressure distribution and a viscous-inviscid interaction method coupling the Euler and momentum and mean-flow kinetic-energy inverse-integral turbulent boundary-layer equations described by Whitfield.¹⁵ The viscous-inviscid interaction results are in good agreement with the data as opposed to the separate boundary-layer results which underpredict the data by 60% at the trailing edge.

Previous Navier-Stokes solutions⁶ for this flow field have shown that the present results are independent of the choice of the low Reynolds number near-wall terms, the inclusion of various streamwise curvature corrections, and the choice of the two-equation turbulence model itself. However, when an algebraic eddy-viscosity model with special near-wake treatment was used, the solutions were not as good as those employing the two-equation models. For example, the computed algebraic model results underpredict the experimental displacement thickness by 30% at the trailing edge. In addition,

several boundary-layer solutions have been obtained^{6,7} for this flow field. Both algebraic and two-equation turbulence models with and without curvature corrections were used. Also, solutions were obtained using both the measured wall and boundary-layer edge pressure distributions. None of these solutions differed significantly from the boundary-layer solution shown.

It was suggested⁶ that the failure of the boundary-layer code to predict the measured data was either the result of the boundary-layer assumption (neglecting normal-pressure and streamwise-turbulent-normal stress gradients) or the strong viscous-inviscid interaction process and ellipticity of the flow field. The present results show the latter to be valid. Evidently for a strong interaction flow such as the present trailing-edge flow field the boundary-layer solution is extremely sensitive to the streamwise flow gradients and hence both the viscous and inviscid portions of the flow field must be solved interactively. The turbulence model used in the integral boundary-layer equations¹⁵ is based on correlations of experimental data and would be expected to correctly model flow fields where these correlations are valid. The present case with a small separated zone is such a flow field. However, the extension of this method to flow fields with large separated zones will require additional data correlations not yet available.¹⁵

The computed skin-friction distribution on the test model is compared with the experimental values in Fig. 12. The scatter bars on the experimental data points represent experimental uncertainty. The computed Navier-Stokes values are in fair agreement with the data. The measured separated zone extended from -2 cm on the flap to 0.4 cm in the wake. The computed separation extended from -0.25 to 0.1 cm. The results from the interactive solution described above did not predict separation but elsewhere the results were in close agreement with the present computations.

The computed and experimental wall-pressure coefficient distributions for the circular arc airfoil with a large shock induced separation (test model III) are compared in Fig. 13. The predicted shock location ($x/c = 0.73$) is significantly downstream from the measured location ($x/c = 0.64$). Also the calculated size of the separation ($x/c = 0.73$ to 1.15) is much smaller than the experimental size ($x/c = 0.65$ to 1.26). As a test to determine the relative importance of turbulence modeling for this test flow, a small modification was made to the turbulence model to increase the size of the separation. This modification lowered the constant C_2 in Eq. (2) by 15% for all values of y at the computed separation point and with a linear variation in x to the original value of C_2 at the computed reattachment point.

$$C_2 = C_2[1 - 0.15(x_{RET} - x)/(x_{RET} - x_{SEP})]$$

This increased the dissipation rate ϵ in and above the separated zone thus lowering the eddy-viscosity and increasing the size of the separated zone. The correction was applied interactively such that x_{SEP} and x_{RET} were determined from the computed solution at each time step. The results from this modified solution show improved agreement with the data (Fig. 13). The computed shock location moved forward to $x/c = 0.66$ and the separated zone

increased to $x/c = 0.67$ to 1.25 . When changes to C_2 larger than 15% were tried, the solution became unsteady.

Coakley¹⁶ has also solved the above circular-arc airfoil flow field employing the Navier-Stokes equations with the Wilcox-Rubesin two-equation turbulence model.¹⁴ Although a splitter plate was used in the near wake it was also found that significant modifications had to be made to the turbulence-model constants to predict the experimental shock-wave location.

Figures 14, 15 and 16 compare the mean velocity, turbulent shear stress and turbulent kinetic-energy profiles over the aft portion of the airfoil and in the near wake. While the unmodified computation is in fair agreement with the measured mean velocity profiles (Fig. 14), the computed results with the modified turbulence model show a marked improvement. Neither computation shows much agreement with the measured shear stress (Fig. 15) or turbulent kinetic-energy profiles (Fig. 16). In fact, the modified results are not as good as the original computations for $x/c = 0.8$ and 0.9 . The measured high levels of shear stress and kinetic energy in the shear layer were not computed. One possibility for this disagreement is that the shock wave unsteadiness on the airfoil produces these high energy levels which the computations do not capture.¹⁷ A detailed experimental investigation of shock-wave unsteadiness and its effects on the flow field would be required to resolve this issue. The present computations did not indicate any significant shock-wave unsteadiness.

The predicted displacement thickness distributions are compared with the data on Fig. 17. As expected from the mean-velocity profile comparisons, the computation using the modified model is in good agreement with the data.

Computed Mach contours are shown in Fig. 18 for both solutions. For the computation using the original turbulence model, the shock wave extends far into the flow field and the sonic line intersects the wind-tunnel wall (near $y/c = 1$). When the modified model was used both the extent of the shock wave and sonic zone are significantly reduced. Experimental data showed that the flow near the wind-tunnel wall remained subsonic. These results indicate the important role that the turbulence model plays for flows with large separated zones.

Conclusions

Three transonic trailing-edge flow fields have been calculated and compared with detailed experimental results. The three test cases included an asymmetric attached flow, an asymmetric flow with a small separated zone, and a symmetric flow field with a massive shock-wave induced separation. When employing the mass-averaged Navier-Stokes equations with a two-equation turbulence model we found that the solutions correctly modeled all the major features of the flow field for the two asymmetric test cases. Present turbulence-modeling concepts seem to be adequate for trailing edge flows with little or no separation. (Previous work^{5,6} has shown that algebraic eddy-viscosity models are not adequate for these flow fields.) However, for the flow field with a large separated zone, the computed results did not predict the proper size of the separation or the location of the shock wave.

By modifying the turbulence model in an ad hoc fashion, the improved agreement was obtained. This shows the importance of turbulence modeling for the computation of flow fields with large separation. Improved turbulence models are necessary before we can compute these flow fields.

Large differences were obtained between the Navier-Stokes solutions and for boundary-layer predictions for the flow fields with little or no separation. These differences were not due to the boundary-layer assumptions or turbulence modeling, but due to the strong viscous-inviscid interaction process and ellipticity present in trailing-edge flows.

References

- ¹Melnik, R. E., Chow, R., and Mead, H. R., "Theory of Viscous Transonic Flow Over Airfoils at High Reynolds Number," AIAA Paper 77-680, Albuquerque, N.M., June 1977.
- ²Collyer, M. R., and Lock, R. C., "Prediction of Viscous Effects in Steady Transonic Flow Past an Airfoil," *Aero. Quart.*, Vol. 30, Aug. 1979, pp. 485-505.
- ³The 1980-81 AFOSR-HTTM-Stanford Conference on Complex Turbulent Flows: Comparison of Computation and Experiment, Stanford, CA, Sept. 1981.
- ⁴Spaid, F. W. and Hakkinen, R. J., "On the Boundary Layer Displacement Effect Near the Trailing-Edge of an Aft-Loaded Airfoil," *Journal of Appl. Math and Physics*, Vol. 28, 1977, pp. 941-950.
- ⁵Viswanath, P. R., Cleary, J. W., Seegmiller, H. L., and Horstman, C. C., "Trailing-Edge Flows at High Reynolds Number," *AIAA Journal*, Vol. 18, Sept. 1980, pp. 1059-1065.
- ⁶Horstman, C. C., "Prediction of Separated Asymmetric Trailing Edge Flows at Transonic Mach Numbers," AIAA Paper 82-1021, St. Louis, MO, June 1982.
- ⁷Viswanath, P. R. and Brown, J. L., "Separated Trailing-Edge Flow at a Transonic Mach Number," AIAA Paper 82-0348, Orlando, FL, Jan. 1982.
- ⁸McDevitt, J. B., Levy, L. L., Jr., and Deiwert, G. S., "Transonic Flow About a Thick Circular-Arc Airfoil," *AIAA Journal*, Vol. 14, May 1976, pp. 606-613.
- ⁹Seegmiller, H. L., Marvin, J. G., and Levy, L. L., Jr., "Steady and Unsteady Transonic Flow," *AIAA Journal*, Vol. 16, Dec. 1978, pp. 1260-1270.
- ¹⁰Jones, W. P. and Launder, B. E., "The Prediction of Laminarization With a Two-Equation Model of Turbulence," *Int. Journal of Heat and Mass Transfer*, Vol. 15, 1972, pp. 301-314.
- ¹¹Chien, K-Y., "Predictions of Channel Boundary-Layer Flows with a Low-Reynolds-Number Turbulence Model," *AIAA Journal*, Vol. 20, Jan. 1982, pp. 33-38.
- ¹²Viegas, J. R. and Horstman, C. C., "Comparison of Multiequation Turbulence Models for Several Shock Boundary-Layer Interaction Flows," *AIAA Journal*, Vol. 17, Aug. 1979, pp. 811-820.
- ¹³MacCormack, R. W., "A Numerical Method for Solving the Equations of Compressible Viscous Flow," *AIAA Journal*, Vol. 20, Sep. 1982, pp. 1275-1281.
- ¹⁴Wilcox, D. C. and Rubesin, M. W., "Progress in Turbulence Modeling for Complex Flow Fields, Including Effects of Compressibility," NASA TP-1517, Apr. 1980.
- ¹⁵Whitfield, D. L., Swafford, T. W., and Jacocks, J. L., "Calculation of Turbulent Boundary Layers with Separation and Viscous-Inviscid Interaction," *AIAA Journal*, Vol. 19, Oct. 1981, pp. 1315-1322.
- ¹⁶Coakley, T. J., "Numerical Method for Gas Dynamics Combining Characteristic and Conservation Concepts," AIAA Paper 81-1257, Palo Alto, CA, June 1981.
- ¹⁷Johnson, D. A., Horstman, C. C., and Bachalo, W. D., "Comparison Between Experiment and Prediction for a Transonic Turbulent Separated Flow," *AIAA Journal*, Vol. 20, June 1982, pp. 737-744.

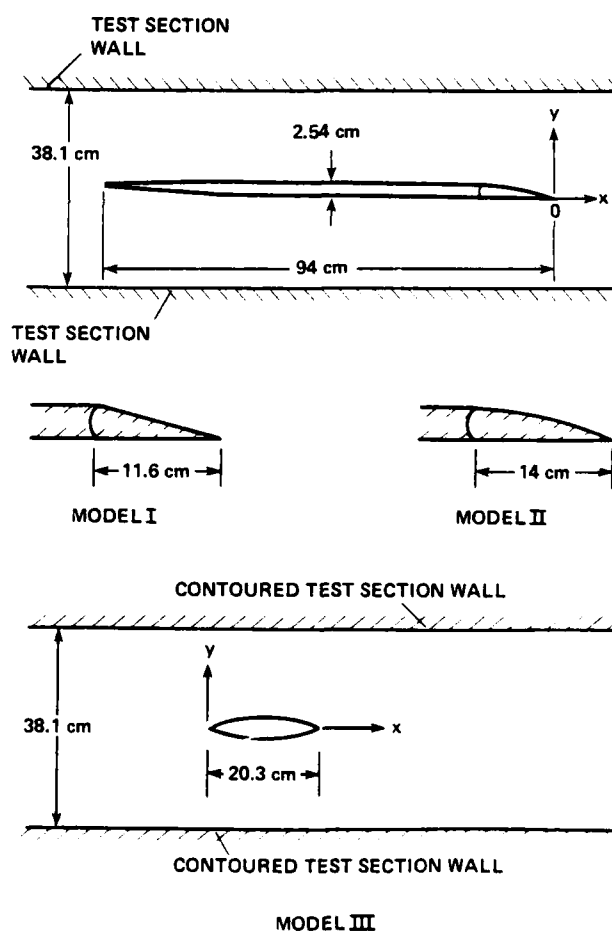


Fig. 1 Flow Geometries

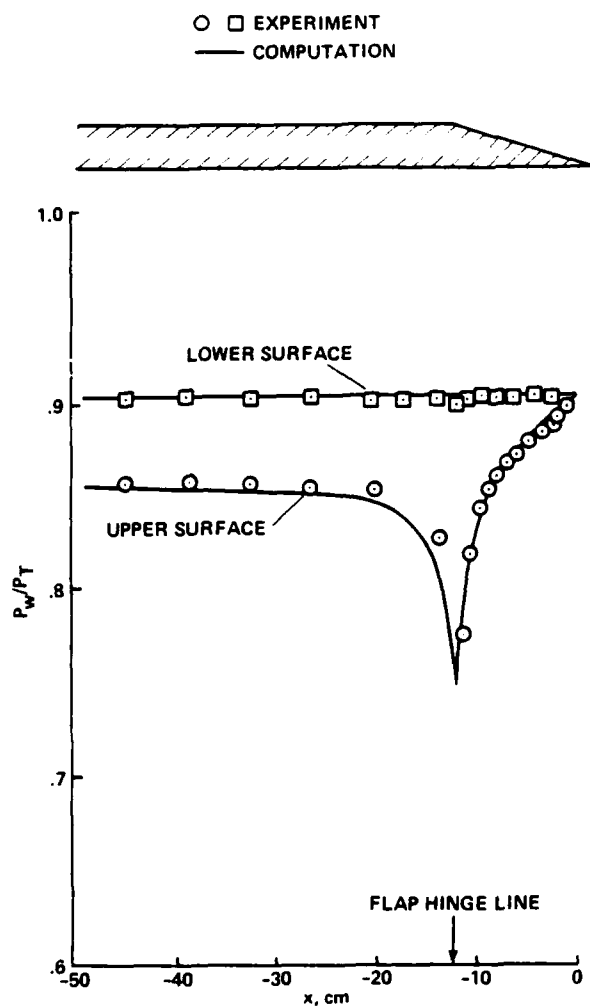


Fig. 2 Surface pressure distributions in the trailing-edge region, test model I.

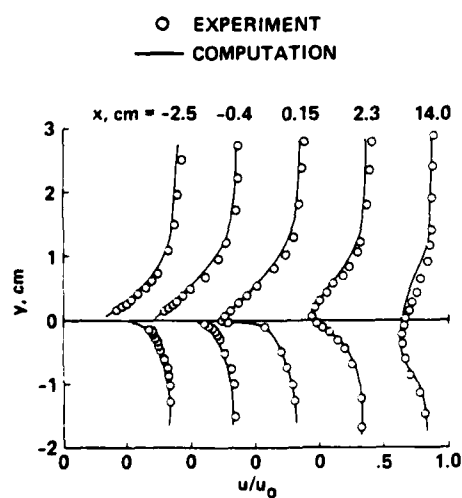


Fig. 3 Mean velocity profiles in the trailing-edge and near-wake regions, test model I.

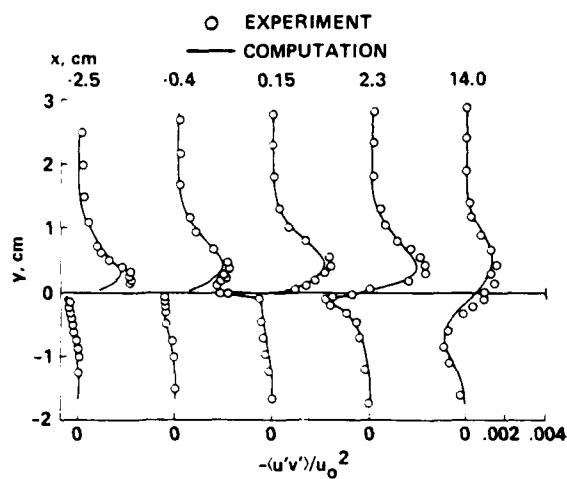


Fig. 4 Turbulent shear-stress profiles in the trailing-edge and near-wake regions, test model I.

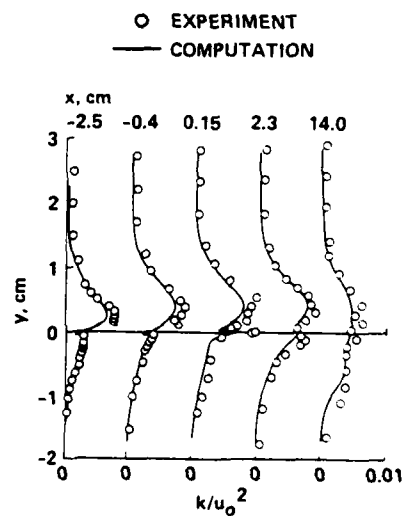


Fig. 5 Turbulent kinetic energy profiles in the trailing-edge and near-wake regions, test model I.

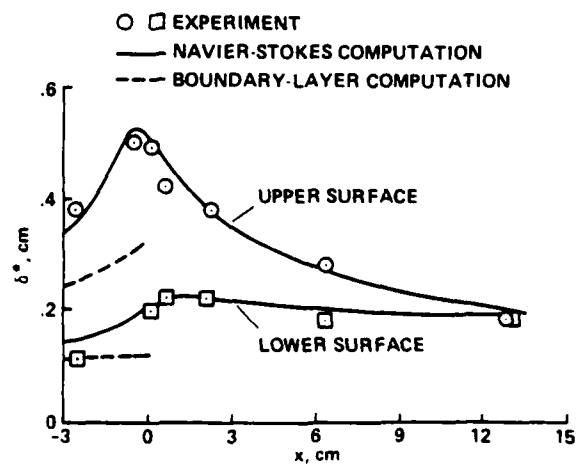


Fig. 6 Displacement thickness distributions in the trailing-edge and near-wake regions, test model I.

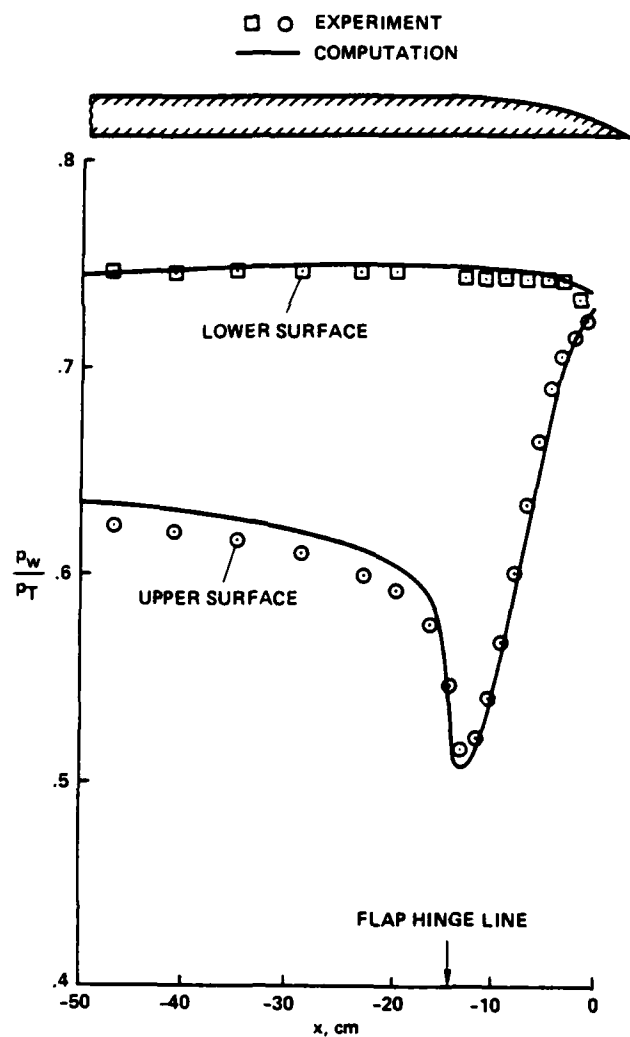


Fig. 7 Surface pressure distributions in the trailing-edge region, test model II.

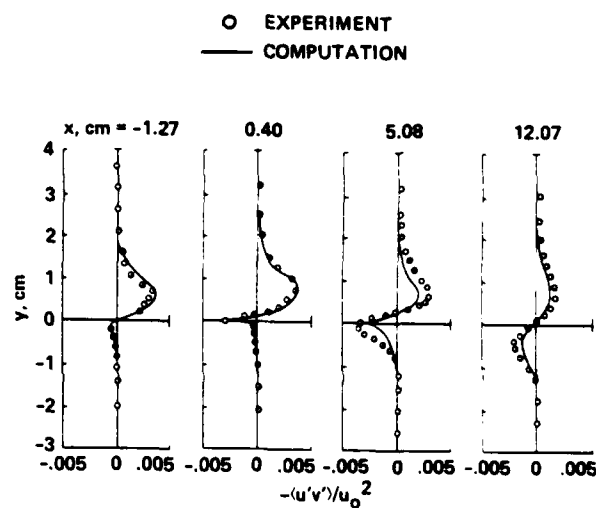


Fig. 9 Turbulent shear-stress profiles in the trailing-edge and near-wake regions, test model II.

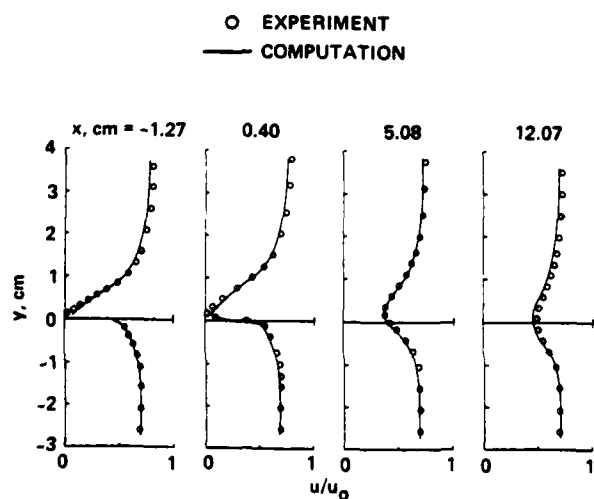


Fig. 8 Mean velocity profiles in the trailing-edge and near-wake regions, test model II

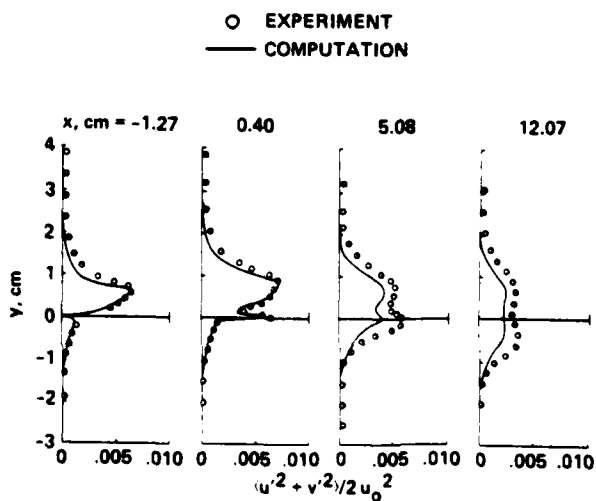


Fig. 10 Turbulent kinetic energy profiles in the trailing-edge and near wake regions, test model II.

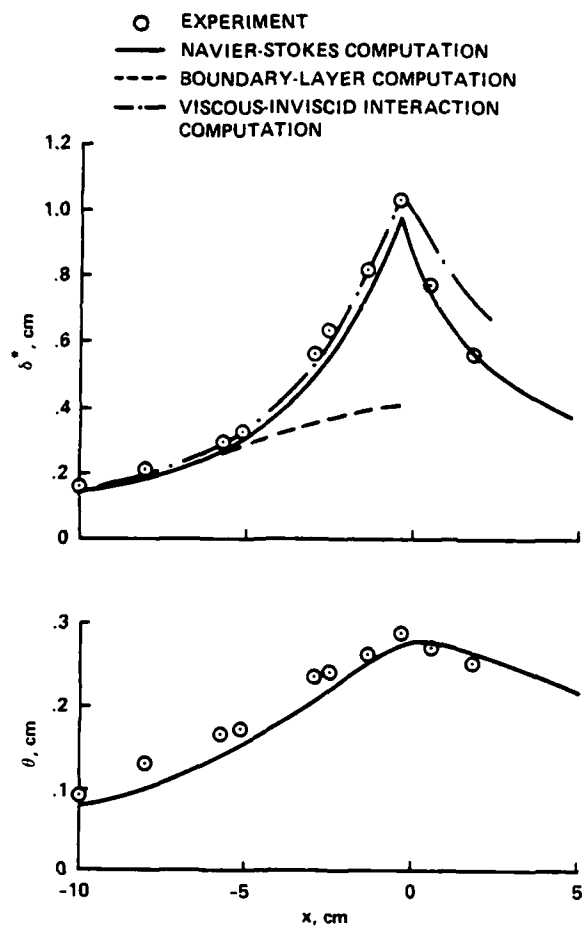


Fig. 11 Displacement and momentum thickness distributions in the trailing-edge regions, test model II.

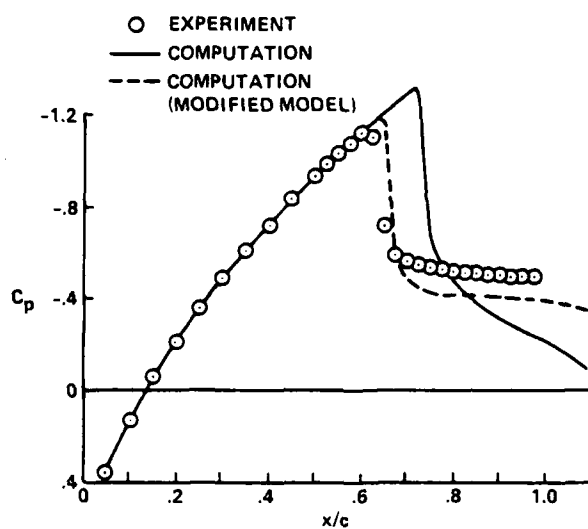


Fig. 13 Surface pressure coefficient distribution over the airfoil, test model III.

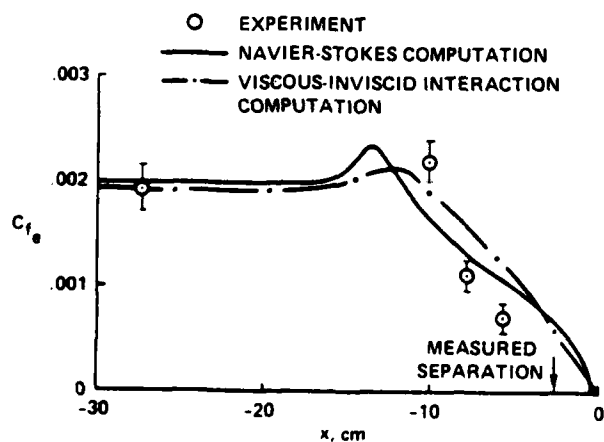


Fig. 12 Skin-friction distribution in the trailing-edge region, test model II

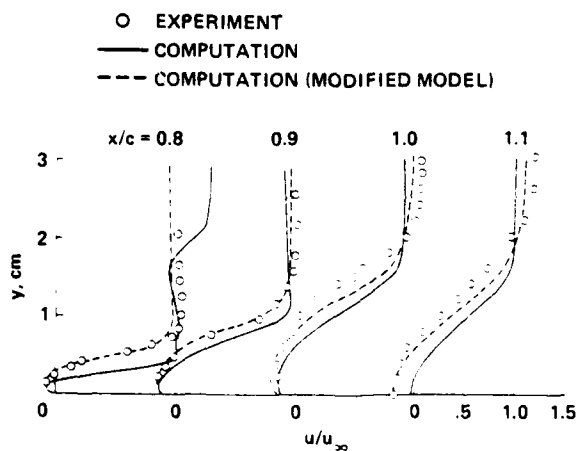


Fig. 14 Mean velocity profiles in the trailing-edge and near-wake regions, test model III.

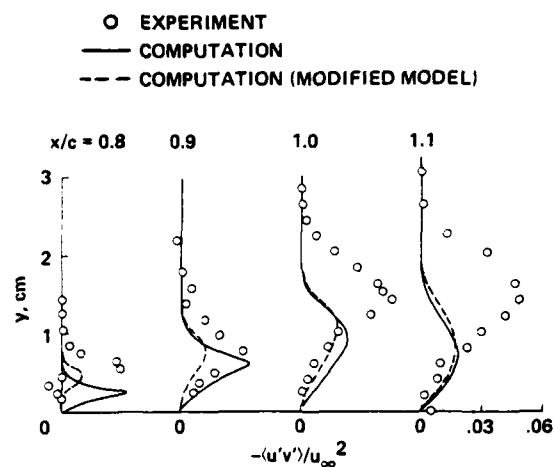


Fig. 15 Turbulent shear-stress profiles in the trailing-edge and near-wake regions, test model III.

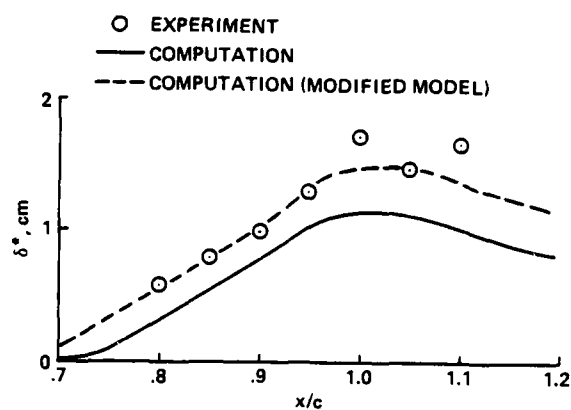


Fig. 17 Displacement thickness distributions in the trailing-edge and near-wake regions, test model III.

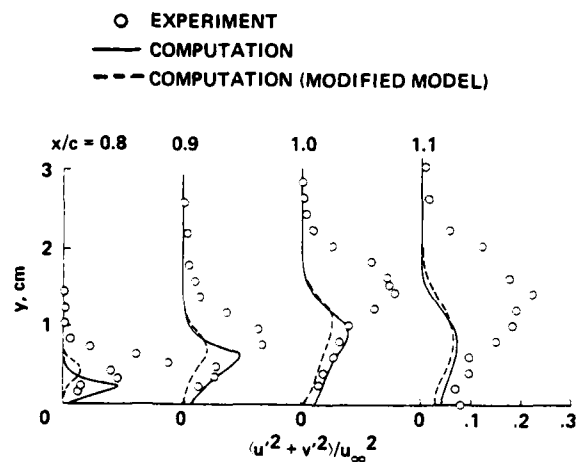


Fig. 16 Turbulent kinetic energy profiles in the trailing-edge and near-wake regions, test model III.

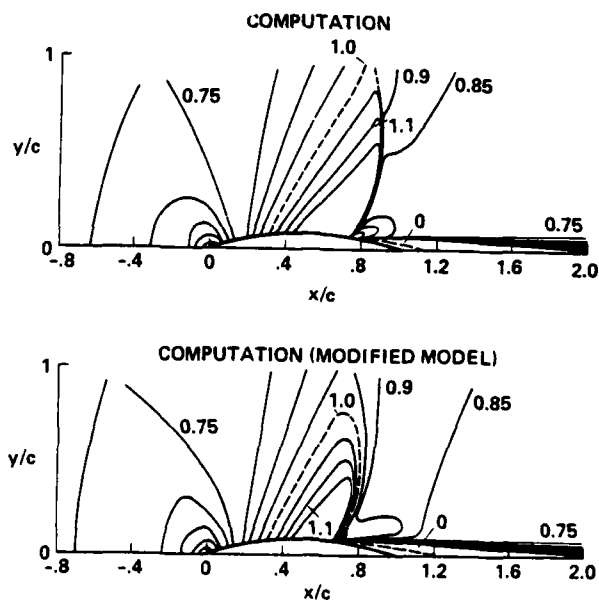


Fig. 18. Computed Mach contours over the airfoil, test model III.

KEYNOTE LECTURE 2

PROBLEMS ASSOCIATED WITH THE AERODYNAMIC
DESIGN OF MISSILE SHAPES

Jack N. Nielsen
Nielsen Engineering & Research, Inc.
Mountain View, CA 94043

Abstract

The purpose of the paper is to discuss various trends in the design of tactical missiles which influence the future directions of missile aerodynamics. Some of the subjects discussed include airframe-inlet interference, high angle of attack problems, waveriders, efficient hypersonic missiles, computational fluid dynamics applied to missile aerodynamics, aerothermal design and supersonic stores. A number of specific areas where increased emphasis is needed in missile aerodynamics are suggested.

1. Introduction

The purpose of this paper is the review of aerodynamic problems involved in the design of tactical missiles, both present and future. Many of the subsystems of missiles interact with the complete missile aerodynamic characteristics in ways which determine the important trends in the evolution of missile aerodynamics. One important subsystem is propulsion wherein the type of propulsion, airbreathing or non-airbreathing, is the significant parameter. The warhead size necessary to effect kill based on the CEP from the guidance and control sets the basic diameter of the missile. The guidance sensor characteristics such as frequency bandwidth, tolerable boresight error slope, and needed aperture influence the size and shape of the seeker dome. The launching platform usually imposes certain constraints on missile dimensions such as wing span. Nonlinearities in lateral-directional control and control cross-coupling interact strongly with the autopilot performance, or alternatively constrain the configuration or its responsiveness. Also, the structure and its vibration are strongly influenced by aerodynamics as a source of steady and unsteady loads as well as coupling between bending, vibration, and loads.

Some specific subjects of present and future interest are of particular importance in future missile designs. Since airbreathers are now receiving increased attention in the quest for battle space and for intercepting standoff targets, problems of interference between inlet and airframe arise. Hypersonic missiles are of great interest as a means of quickly neutralizing standoff targets, and achieving high L/D at high speeds through such devices as waveriders is receiving renewed emphasis. The carriage and delivery of stores at supersonic speed is of increased importance for penetration.

High angle of attack aerodynamics has received much attention over the past several years, particularly as applied to enhance maneuverability of missiles, and many problems impacting aerodynamic design need more attention in this area. Improved accuracy of prediction methods for angles of attack greater than 20° is needed.

One discipline which can be brought to bear more heavily on missile design problems is computational fluid dynamics. It seems that missiles have not received the attention they deserve in this area, but there are signs of increased activity in this field. Applications of CFD to subregions of the missile flow field are frequently made at the present time, but applications to the complete missile flow fields are lagging.

There is a changing role of the missile aerodynamicist in missile design. In the past it has frequently been the practice to test the final design over the entire operating range in wind tunnels. It is now possible to do conceptual and trade-off studies up to angles of attack of about 20° using existing predictive methodology since more confidence is now placed in these methods than formerly. However, wind-tunnel tests for angle of attack above 20° are still required. As predictive methodology and CFD continues to improve, hopefully the amount of expensive wind-tunnel testing will be reduced although this can be argued. However, it is certain that missile aerodynamicists are making more extensive use of analytical tools.

In the following sections we will discuss in greater detail some of the subjects mentioned above. The treatment will necessarily be in breadth rather than depth.

A number of investigators have reviewed missile aerodynamics or special areas of it in References 1 to 7, and their work has been very helpful in preparing the present paper.

2. Problems in Airbreathing
Missile Design

2.1 Introductory Remarks

Solid fuel rockets are the principal propulsion means of existing tactical missiles, and it is well known that the range of such missiles is limited by the fact that they must carry their own oxidizers. Increased missile range is needed to enlarge the battle space and to

AD P 001949

engage the enemy further out. It is also needed to counter stand-off jammers and to deny close-in airspace to reconnaissance aircraft. In addition there is a need to get out to the limits of the battle space quickly. These requirements lead to the future importance of the hypersonic air-breathing missile. Existing and developmental supersonic airbreathing missiles appear to operate with critical or supercritical flow in the inlet for simplicity. By-passing the extra airflow to avoid spillage or varying compression ramp angle to avoid subcritical operation is avoided for the most part. The basic problems of importance are the effects of airframe on the inlet, the installed inlet forces, and the effects of the inlet on the airframe which includes flow changes at downstream lifting surfaces. Operation over wide ranges of angle of attack, angle of bank and Mach number will provide many aerodynamic problems for future airbreathing missiles.

2.2 Mutual Interference Between Inlet and Airframe

Consider first the interference effect of the airframe on the inlet. Inlets are often tested alone with uniform onset flow, but when they are mounted on a body the onset flow is not uniform. The onset flow can vary in Mach number, flow direction and magnitude, and it may possess vorticity and total pressure losses. A basic problem is to locate the inlet in a region of high mass flow rate per unit area and high total pressure to keep the inlet small. Inlet placement from the viewpoint of stealth is also important but at odds with inlet performance considerations.

The effect of the inlet on the airframe is complicated and important and it depends very much on the quantity of air flowing through the inlet. Data illustrating this effect are available from Reference 8 on the drag of the F-15 airplane with two-dimensional inlets forward of the wings. The inlets have three ramp angles. Tests were performed of the inlet installed on the airplane but mounted on a balance independent of the airplane. Airplane and inlet forces and moments were individually measured as a function of angle of attack and mass flow through the inlet. The inlet mass flow was controlled by choking the flow in a tube into which the flow exhausts at the rear of the aircraft. Figure 1 shows how the airplane drag varies with capture area ratio (mass flow ratio) at various angles of attack. The quantity A_C is the streamtube capture area for $\alpha = 0$ with the shock at the throat of the inlet. Data were not obtained to $A/A_C = 1$ because of choking in the tube. Significant increase in drag occurs in the low angle of attack range as a result of the reduced mass flow ratio.

Figure 2 shows how the inlet drag and lift coefficients vary with angle of attack

and mass flow ratio for the same case as Figure 1. The reference area is now the capture area A_C . Note that reduction of capture area ratio at constant angle of attack increase the inlet lift and drag substantially. The drag of two inlets at $\alpha = 0^\circ$ varies from 29% of the total airplane drag at $A/A_C = 0.4$ to 15% at $A/A_C = 0.7$, illustrating increase in drag due to off-design operation of the inlet. We have used this airplane case since comparable data for a missile are not available.

The variable mass flow into an inlet has an influence on the stability and control of the airframe. In subcritical operation, more flow will go around the inlet (spill) and the pressures on the fuselage and tail will be influenced. Not only is the trim of the airframe influenced by spillage, but so also is tail control effectiveness. There does not seem to be a good data base on this subject, nor do any reliable prediction methods for missiles appear to exist.

2.3 State of Prediction Methodology for Flow Fields

Let us consider the role of finite-difference methods, panel methods, and hybrid methods in treating inlet-airframe flow fields including flow at the tail. With regard to Euler codes, it is possible at this time to solve a two-dimensional or axisymmetric problem for interaction between an internal and external flow⁹. In such solutions both the internal and external flows must be covered by the mesh and the solution developed in time from some assumed initial conditions. The mass flow ratio for the inlet is controlled by the downstream boundary condition of the internal flow and is generally not directly controllable. The type of downstream boundary condition to use is not clear. An achievable back pressure may be specified with a uniform flow as an approximate boundary condition. A large number of time steps are required before the wave system stabilizes so the calculation is lengthy. The subcritical case takes longer than the supercritical case. For the supercritical case the external flow up to the normal shock can be carried out by time marching in the streamwise direction. However, for the subcritical case the three-dimensional calculation appears beyond the state of the art. Euler codes should be good for matching internal and external flows and thus getting the external aerodynamics well. However, the internal aerodynamics may be inaccurate if viscous effects are large.

The application of supersonic panel methods to predicting loads on complete configurations without inlets is an accomplished fact^{10,11}. An approximate panel method accounting for flow into the inlet has been used by Dillenius¹² in a supersonic external store separation

program. In this approach panels which permit variable nonzero normal velocity are placed across the streamtube entering the inlet. In this fashion the effect of mass flow ratio on the external flow is accounted for. The method appears to have the potential for accounting for subcritical flow as well as supercritical flow. It is also possible to control the mass flow ratio as a parameter in the panel method.

A third approach to flow-field analysis is to use approximate equations in the regions where they are valid and to patch the solution together in an attempt to reduce computer time. As an example, a marching code might be used up to the inlet normal shock, a Navier-Stokes code in the region of the shock, and some code such as a parabolic NS code in the diffuser.

A handbook of experimental data for the effects of inlets on airbreathing missile external aerodynamics is embodied in Reference 13.

3. Vertically Launched Missile With Transonic Turn-Over

There is a need for a vertically launched missile that can turn over horizontally at low altitude very quickly after launch. Such a need arise for defense from low-flying threats such as missiles, RPV's, helicopters, and airplanes. Also, such a missile and launcher are required to eliminate the need for trainable missile launchers that are frequently pointed in the wrong direction. Vertical launch is required because the threat may come from any direction for combat at the forward edge of the battle area.

The requirements for vertical launch are very severe. The missile must get aloft and turn over as quickly as possible. This means that it will be subject to large normal accelerations and must have a short time constant in pitch. An example of the variation with time of the predicted flight parameters is shown in Figure 3 as taken from Reference 14 for a range of nine nautical miles. Angles of attack of up to 30° are experienced with corresponding high normal accelerations. For shorter ranges, higher angles of attack will be met.

A number of interesting problems arise in connection with the design of such a missile, a partial list of which follows.

1. Over the transonic/supersonic range of high angle of attack operation how can we achieve a high turn rate; that is, powerful pitch control.

2. To what extent should aerodynamic or thrust vector control be used?

3. What type of aerodynamic control is best?

4. Will asymmetric vortices complicate the design of the control system?

If wings are used to obtain the high normal accelerations, planforms which have small shift in axial center-of-pressure location with Mach number and angle of attack such as delta wings should be used. A body-alone might be used together with thrust-vector control.

In a study of the type of control systems for a vertically launched missile, the authors of Reference 14 arrived at a combined system utilizing a body-tail configuration plus an ejectable jet-vane control. The jet-vane control is particularly useful during the low dynamic pressure part of the trajectory. The combination of controls increases the available maneuverability.

With regard to aerodynamic controls, one might consider canard controls, wing controls, or tail controls of the all-movable kind. Canard and wing controls are known to stall at lower angles of attack than tail controls since their control deflections are additive to angle of attack. Canard and wing controls however show poor roll control because of interference effects on the tail (the exceptional case occurs when the wing control fin span is much greater than the tail fin span). Control by a tail alone has the well-known disadvantage that it puts the trimming force in the opposite direction to the desired maneuver and thereby increases the missile time constant. It's hinge moments are influenced by body vortices and are nonlinear. In selecting the fin planform and airfoil section special attention should be paid to the transonic regime where control effectiveness can be very low and hinge-moments high due to transonic nonlinearities. Figure 4 from Reference 15 illustrates the effectiveness of pitch control at high angles of attack at two transonic Mach numbers. The factor k_w is basically the ratio of the normal force developed by the all-movable control panel to half of that developed by the wing alone at an angle of attack equal to $\alpha + \delta$. These data are for canard fins with an aspect ratio of 3.53, a taper ratio of 0.06, and ratio of body radius to fin semi-span of 0.4. The problem of good all-movable controls for large $\alpha + \delta$ at transonic speeds is an unsolved one. Control effectiveness and hinge moment are strongly influenced by both planform and airfoil sections. Neither a good data base nor a good predictive method exist for selecting the control.

The well-known subject of "induced yaw," the appearance of large side forces and yawing moments on a body of revolution at large angles of attack, could be a limitation on the amount of controllable

normal acceleration available to a transonic missile. The onset of such asymmetric forces is determined by body fineness ratio and nose bluntness for bodies of revolution. For a fineness ratio of about 10, an angle of attack of about 25° to 30° marks the onset of asymmetry. Asymmetry starts to disappear when shock waves form on the sides of the body for crossflow Mach numbers above the critical speed which is about 0.4 for a circular cylinder. From $M_c = 0.4$ to 0.8 the magnitude of the side force as a fraction of the lift or normal forces decreases until it essentially disappears at $M_c = 0.8$. Figure 5, from an article by Wardlaw and Morrison¹⁶, exhibits data showing this trend. If these limits for the transition of asymmetric vortices to symmetric vortex regions are adopted, and if $\alpha = 25^\circ$ is taken as the boundary between concentrated symmetric and asymmetric vortices, then the diagram shown in Figure 6 results. By plotting the same data of Figure 5 against free-stream Mach number, Wardlaw and Morrison¹⁶ show that the induced yaw is greatly reduced at supersonic speeds and disappears for Mach numbers greater than 1.3 except in a few instances.

There are several other ways of alleviating the asymmetric vortex switching problem besides avoiding the region $\alpha > 25^\circ$ and $M_\infty < 1.3$. The use of vortex generators on the nose has been shown by Clark, Peoples, and Briggs¹⁷ to eliminate induced yaw. An approach to harnessing induced yaw is fixing the asymmetry with a nose strip or proturbance and simultaneously controlling the roll attitude of the missile. If this is done, it is possible to fly at an increased maneuvering load equal to $\sqrt{C_L^2 + C_Y^2}$. In this case one would want to maximize the square root for maximum maneuverability. Innovative ideas for controlling induced yaw are still needed.

4. The Search for High L/D at High Speeds; Waveriders

4.1 Introductory Remarks

The need for ground-launched or air-launched missiles which fly out far and fast and intercept launch platforms beyond the range of their attacking missiles has lead to the studies of the hypersonic airbreathing missile. A number of feasibility studies have been made to determine aerodynamically efficient missile shapes which meet this mission. Hunt, et al.¹⁸ have proposed a mid-inlet concept; Krieger¹⁹ has proposed a noncircular body concept and a lifting body concept; Rasmussen²⁰ and Schindel²¹ have adapted the waverider airplane concept to hypersonic missiles. We will briefly describe these concepts and then discuss waveriders in greater detail.

4.2 Genesis of High Speed Configurations

Current rocket-powered missiles developed in the USA employing cruciform fins mounted on bodies of revolution have been designed principally for maneuverability or other characteristics, not for high lift/drag ratio or long range. Accordingly, it is not surprising that their lift/drag ratios at Mach numbers greater than 3 are low and become lower with increasing Mach number.

The mid-inlet concept of Hunt, et al.¹⁸ for a hypersonic missile is shown in Figure 7. This is a sketch of the proposed design of a missile to fit a U.S. Navy vertical launching system (VSL), to be boosted to $M_x = 4$ by a booster, and to cruise at $M_\infty = 6.0$. One of the aerodynamic considerations in the design is to make use of the high air density on the windward side of the missile to give sufficient thrust to maneuver at angle of attack. Another point is that the boundary layer is sufficiently thin on the windward meridian that boundary-layer diverters may not be required for the inlet. (The question of the shock layer still remains.) By specially tailoring the nose and forebody to make it flatter in front of the inlet, the inlet flow can be improved and its lateral divergence lessened.

The Air Force Flight Dynamics Laboratory over the past years has pursued a line of investigation to exploit the aerodynamic potential of supersonic missiles to achieve significant improvements in performance for tactical long-range air-to-air missions. The concepts which have emerged are termed "aerodynamic configured missile" (ACM). One concept taken from Krieger¹⁹ is a "noncircular body cruiser" as shown in Figure 8. One novel aerodynamic feature of this design is the spatula nose and flat bottom which produce high L/D ratio and neutral stability to $\alpha = 20^\circ$. The high wing and twin vertical tails provide good lateral-directional stability characteristics. An L/D ratio of 5 to 8 at $M_\infty = 4.0$ is quoted. Because of the large range of operating conditions, a two-dimensional inlet with variable internal contraction ratio is needed to maintain high pressure recovery during cruise and climb. A two-dimensional variable geometry nozzle provides the capture area necessary for cruise and climb. In seeking the highest L/D configuration, it was found that C_{Dmin} was a controlling parameter. Since for a symmetric parabolic drag curve (C_D vs. C_L),

$$\left(\frac{L}{D}\right)_{\max} = \frac{1}{2} \sqrt{\frac{C_{Dmin}}{C_{D1} C_{D2}}} \quad (1)$$

with

$$C_{D1} = C_D - C_{Dmin}$$

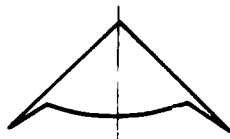
control of both minimum drag and drag-rise factor (C_{D_i}/C_L^2) is needed for maximum L/D ratio.

Another efficient aerodynamically configured missile emerging from the study is the lifting body missile shown in Figure 9. This configuration used a triangular body with wing tips and an inlet on the lower surface. It is noted that both of these missiles tend to look like airplanes. The lack of radomes in the design is noteworthy.

Another type of hypersonic missile design which is receiving current consideration is the waverider. The most elementary form of waverider is due to Nonweiler²² and has the form shown in Figure 10. It is also termed the caret wing because of its similarity to the proofreader's mark. At the design condition the upper surface of the wing is streamwise and has no pressure drag. A planar shock stretches across the lower surface between the wing leading edges, producing a uniform pressure between them. The wing thus rides the wave and hence the term waverider. At off-design conditions the leading edges can be subsonic or supersonic.

The waverider concept has been extensively studied in Great Britain for its potential application to hypersonic aircraft. The late Dietrich Küchemann in his delightful book "The Aerodynamic Design of Aircraft"²³ has an extensive discussion of waverider technology. In this country, Rasmussen²⁰ and Schindel²¹ have started to exploit this technology by applying it to the hypersonic missile.

A large number of waverider concepts are available. A simple way to obtain the on-design shape of a waverider is to consider, for example, a conical flow as over a circular cone or elliptical cone at angle of attack. Many streamsurfaces exist between the cone surface and the shock wave. The cross-section of a conical waverider is then formed by the body, the shock wave, and two such streamtube surfaces. This is possible since the flow above and below the streamtube surfaces cannot communicate pressure effects except possibly through the boundary layer. Examples of waveriders derived from cones by Rasmussen²⁰ are given in Figures 11 and 12. The wave rider shapes studied by Schindel²¹ are of the following cross-sectional shape. At $M_\infty = 5.9$



Schindel gets an L/D of 4. Higher values are predicted for caret wings²³.

When a waverider with conical flow on design goes off design, either by changes

in angle of attack or Mach number, the aerodynamic surface pressures show smooth variations with these variables. It is possible to derive efficient waveriders using nonconical flow at the design point. The primary problem in conical or nonconical design is to get good volume into the waverider with high L/D ratio. One interesting question concerns the general lack of axisymmetric noses or leading-edge bluntness with waveriders. Axisymmetric noses are desirable to minimize radome bore-sight error and bluntness is needed for aerodynamic heating reasons. It appears that such waveriders can be constructed using Euler codes coupled with blunt nose starting solutions. The penalties for bluntness need assessing.

There are a number of problems that need attention for waveriders. First, the questions of integrating the airframe with the engine needs attention. Some ideas for incorporating inlets have been advanced by Rasmussen²⁴. Good ideas for incorporating controls are needed. Base drag is a problem for waveriders, and the use of boattail to lessen base drag is feasible²³.

There are a number of viscous problems concerning waveriders of which friction drag is one. All present methods of deriving waveriders shapes ignore separation, yet probably most waveriders will experience separated flow at the sharp leading edges for some Mach numbers. At high Mach numbers transition is delayed to high Reynolds number, and a large part of a waverider might encounter laminar flow. At reattachment lines the heat transfer rates can be high even if the location is on the leeward side of the missile. The art of estimating heat transfer rates is well developed and can be applied to waveriders. However, there are still problems of heat transfer as influenced by separation, reattachment, and shock-wave intersections.

One problem that has arisen with respect to waveriders is how to calculate their characteristics at off-design conditions. It appears that Euler codes can be applied fruitfully to this problem although they have not been so far.

5. High Angle of Attack Aerodynamics

5.1 Introductory Remarks

The aerodynamic problems of missiles at high angles of attack have received much attention in the last few years, but the problems are only partially solved. The importance of high angles of attack arises primarily from the need for greater maneuverability to intercept targets or to perform evasive action. The problems are mostly associated with nonlinearities which are induced either by

vorticity effects or compressibility effects or both. A recent survey of high α nonlinearities and means for calculating them is given in Reference 25. There are fundamental differences between some of the nonlinear phenomena at transonic speeds and those at supersonic speeds that are a consequence of stall and vortex behavior.

5.2 Transonic Versus Supersonic Problem Areas

One of the high α nonlinearities, which occurs at transonic speed but not at supersonic speed, is wing stall. An example of effects of wing stall on normal-force coefficient and axial center-of-pressure position are shown in Figures 13 and 14, respectively. Results are shown for two wings of $AR = 2.0$ and $\lambda = 0.5$ for $M_\infty = 0.8$. Wing P8 has a thickness ratio of 8.85 percent at the root chord and is a wing of uniform thickness except for 30° wedge angles normal to all edges. Wing T₂₃ on the other hand has a root chord thickness ratio of 4.9 percent increasing to 9.7 percent at the tip. The sections are double wedges in the tip region and modified double wedges inboard. These data are taken from Reference 26 wherein their original sources are quoted. Note the stall of the thicker wing in Figure 13 and the larger center-of-pressure travel of the thinner wing in Figure 14. There is no stall at $M_\infty = 1.2$ and the curves coincide up to 20° but differ as much as 0.2 in C_N at higher angles of attack.

The point I want to make is that airfoil section effects are important on transonic wing normal force and center of pressure at high angle of attack due to stall, and this effect is absent at $M_\infty = 1.2$ and above. This makes a prediction method for transonic wing-body or wing-body-tail combination difficult for high angle of attack since it must account for the effects of airfoil section on stall. Present predictive methods are data-base methods^{27,28} and apply strictly only to the airfoil sections used in the tests. While this difficulty is present, it is usually ignored in preliminary design. Areas where it cannot be ignored is in control effectiveness (fig. 4), hinge moments, and control cross-coupling. Predictive methodology is largely lacking in these important areas.

Returning now to the important transonic problem of induced yaw, Brian Hunt has summarized the present state of knowledge in Reference 29. It is known from vortex-cloud theory that the separation points on bodies of revolution at transonic speed can be estimated by the Stratford criterion based on adverse pressure gradients. However, for supercritical crossflow the asymmetric vortex effects are achieved or eliminated with the appearance of strong shock waves in the crossflow. What is interesting in this case is that separation occurs at nearly uniform pressure for some

reason, possibly due to forward influence of the shock wave.

5.3 Some Supersonic/Hypersonic High α Problems

5.3.1 High α wing theory

While a large body of theory exists for the design of subsonic and supersonic wings at low angles of attack, there is no general method for wings at high angles of attack. This fact probably results from the complexity of the viscous phenomena including separation at high angles of attack. Examples of the various types of leeward flow over a thick delta wing are shown in Figure 15 as taken from Reference 30. In this figure the Mach number in a plane normal to the leading edge is the abscissa and the angle of attack in that plane is the ordinate. Without describing the various flows in detail, it is sufficient to say that six different cases are differentiated. Four of these cases involve leading-edge separation which can be handled by a Kutta condition. This lends some promise to the hope that the Euler equations can be used to develop a general theory of supersonic wings at high angles of attack²⁵. Eventually, the Navier-Stokes equations will prevail.

5.3.2 Wing-body interference at high α

Most airplanes and missiles encounter favorable wing-body interference at low angles of attack through most of the speed range as a result of increased wing lift due to body induced upwash. However, at high angles of attack and high speeds the strong nose shocks significantly reduce the dynamic pressure at a wing position. In fact, the interference can turn from highly favorable to highly unfavorable. This result is for conventional fins mounted on a body of revolution. A number of ways of improving high M and α wing-body interference include wing blending, and unconventional configurations (waveriders). Other concepts are needed.

Fin problems at high angles of attack, in addition to adverse wing-body interference, include loss of control effectiveness, control cross-coupling, and induced rolling moments. A simple example will illustrate all three problems. Consider a cruciform wing-body at high angles of attack such that the density on the leeward side of the body is very low, approaching a vacuum. With the configuration in the $+$ position, call for a yaw command by equally deflecting the upper and lower fins. The normal force on the upper fin is far less than that on the lower fin so that a large rolling moment is induced as a result of yaw control. If the missile rolls so that the upper fin is in the body vortex, a further rolling moment is induced. These severe nonlinearities greatly complicate the stability and control of cruciform configurations at high angle of attack. The

nonlinearities can be greatly reduced by utilizing a monoplane bank-to-turn configuration. One wonders to what limits cruciform missiles can be operated before reaching their ultimate capability.

5.3.3 Wing-body-tail interference

For wing-body-tail configurations, wing-tail interference is an important cause of nonlinearities in the range up to about 20° angle of attack. Both roll angle and wing deflection contribute to the nonlinearities. These nonlinearities include loss of longitudinal stability, large induced rolling moments, and loss of fin normal force. At higher angles of attack, depending on the distance between the wing trailing edges and the empennage, the wing and forebody vortices pass well above the tail, and cause much diminished nonlinearities. However, now the afterbody section between wing and tail sheds its own vortices which impinge on the tail. These afterbody vortices are not necessarily symmetric since the missile may be rolled or the wings deflected to cause asymmetric flow over the afterbody. A powerful new series of nonlinearities thus come into play for angles much above 20°. One scheme for handling these nonlinearities does a fair job of predicting longitudinal characteristics²⁷ but needs improvement in calculating lateral/directional characteristics. The problem area is a difficult one which needs more attention.

5.3.4 Vorticity effects; noncircular bodies

There are a number of reasons that missiles will use noncircular bodies to a greater degree in the future. Airbreathing missiles will have noncircular bodies because of inlets and ducts; bank-to-turn missiles do not require round bodies. Also, the use of square bodies to enhance internal packaging and submunition deployment is under active development³¹. They may also be of importance because of radar crosssection. It is not possible to predict the high angle-of-attack aerodynamics of these noncircular bodies in supercritical crossflow using any theory but that of Navier-Stokes because of flow separation. For subcritical crossflow, where separation is still controlled by adverse pressure gradients, it is possible to apply vortex-cloud theory with some success. An example of such a calculation is shown in Figure 16 following Mendenhall³².

5.3.5 Status of engineering prediction methods

A number of engineering prediction methods exist for defining the forces and moments acting on wing-body and wing-body-tail combinations from subsonic to hypersonic speeds. Ten of these methods are reviewed by Williams in Reference 33. All apply to cruciform configurations, about half to lifting bodies, and several to

airbreathers. While most have angle of attack capabilities to $\alpha = 40^\circ$, the accuracies of the methods are not good to such high angles, particularly for lateral/directional characteristics which about half do not treat. Most do not have all-movable control capability, and none handles control characteristics accurately through the entire range of applicability. There is a need for better design tools for high angles of attack, both for conventional cruciform missiles and other advanced configurations, including lifting body types and airbreathers. Reliable prediction methods for lateral/directional stability and control parameters for angles of attack greater than 20° remain to be accomplished.

6. Some Observations on the Application of CFD To Missile Aerodynamics

6.1 Methods Other Than Navier-Stokes

In Reference 34, Klopfer and Nielsen survey the application of CFD to missile aerodynamics. Some of the applications noted in that paper are listed in Figure 17(a) for methods other than the Navier-Stokes methods and in Figure 17(b) for the Navier-Stokes methods. References 35-59 are covered in the figure. Figure 17(a) shows that the inviscid methods of transonic small disturbance theory and of full potential theory have been applied by several investigators to bodies and fins with no flow separation. In addition, three cases of application of the Euler equations are considered. The first case is that of the straight Euler equations with no boundary layer and the second case is with boundary layer displacement thickness included. The third case is the case of the Euler equations in which the separation lines are specified as input data and a Kutta-like condition is introduced at the separation lines. This latter approach yields good results for those cases where convection of vorticity overshadows any effects of diffusion of vorticity.

A few words on the Kutta condition are in order. It was found in Reference 44 that at the sharp subsonic leading edges of missile fins five boundary conditions can be specified without over-determining the problem, and the choice of these conditions involves some arbitrariness. Some of these arbitrary boundary conditions have only a small effect which is confined locally to the neighborhood of the edge. The dominant boundary condition that determines the vorticity shedding rate at the edge is the requirement that the flow leaves the edge in a plane tangent to the extended chord plane, a Kutta-like condition. A set of boundary conditions can also be specified for a separation line on a body of revolution which properly predicted the vortex shedding rate from the body as shown in Figure 18. Fair agreement

between the flow field as predicted and as measured was obtained except near the top of the body where secondary separation was ignored.

This experience appears to be contradictory to that of Schmidt, Jameson, and Whitfield⁵² who found that they did not have to impose a Kutta condition when applying the Euler equation to an airfoil with a sharp trailing edge. Also, Eriksson and Rizzi⁶⁰ has a similar experience when applying the Euler equations to airfoils and a delta wing with sharp subsonic leading edges.

A simple explanation can resolve these differences. We must differentiate between distinguished separation locations like sharp trailing edges the location of which are known a priori and other separation locations like the separation line on a body of revolution which are not known a priori and which are Reynolds number, Mach number, and angle of attack dependent. It is known that the action of viscosity is to make a sharp trailing edge a separation location. However the potential equations cannot handle the trailing vortex sheet explicitly because it is rotational. The Euler equation, which can support a rotational flow, might be expected to recognize a Kutta condition if viscous effects could be introduced into them. It is probable that the artificial viscosity introduced by the algorithm provides the necessary mechanism for the Euler equations to do this, and separation will appear at the distinguished location since its position is not Reynolds-number dependent.

The Euler equations are also known to produce separation on cones and other bodies of revolution⁴⁴. However, the separation does not appear at the correct position since the effective Reynolds number due to artificial viscosity is usually incorrect and it is also grid-dependent. Accordingly it is necessary to introduce a separation line based on experiment and Kutta-like boundary conditions to get good results for separated flow on bodies which do not have distinguished separation locations.

6.2 Navier-Stokes Methods

In figure 18(b) three different versions of the Navier-Stokes equations are listed for both laminar and turbulent flow. The thin-layer Navier-Stokes equations are obtained by neglecting viscous terms in the streamwise and/or spanwise direction. This is justified on the grounds that gradients in the boundary layer normal to the wall are much greater than in the other directions. No wing-body combinations have been attempted using these to the best of our knowledge.

The parabolized Navier-Stokes equations are a simplification of the full Reynolds-averaged Navier-Stokes equation

by neglecting the unsteady terms and by modifying the streamwise convective flux vector. This makes the equations hyperbolic/parabolic in the streamwise direction. For steady supersonic flow, this permits marching in the streamwise direction. It is possible to get solutions for many cases of interest within present computer resources. The method is stable if the subsonic part of the flow (boundary layer) is small. Large-scale separation generally cannot be handled by the PNS equations, not only because of stability, but because of the lack of a good turbulence model.

The full Navier-Stokes equations are applicable to missiles at any speed or angle of attack. However, their general application is limited by computer resources and turbulence modeling. The only application to a wing-body combination was made by Shang⁵⁴, for zero angle of attack, but no angle-of-attack cases seem to have been run to date.

6.3 Future Directions

It is of interest to speculate on the application of CFD to complete missile configurations in the future. It is probable that panel methods and Euler equations will be the principal tools for complete configurations for some time to come. The Euler equations are just emerging in this connection, and a great deal of work is needed in all areas from mesh generation to finding better ways of treating separation. The limits of applicability and the accuracy of the Euler equations in various cases need to be determined. It will be a long time before Navier-Stokes equations will be used routinely in conceptual design. While the size of existing computers is a limiting factor, it may not be so limiting as the lack of understanding of turbulent modeling for separated compressible flow.

Some specific advancements which could aid future applications of CFD aerodynamics include both calculative and experimental efforts. These include:

1. Special data to help formulate the Euler equation boundary conditions for separated flow near sharp edges.
2. Experimental separation-line data on noncircular bodies.
3. Starting solutions for the Euler equations for spatula noses.
4. Starting solutions for blunt nonspherical noses with detached shocks.
5. Prediction of vortex bursting at high Mach numbers.
6. Method of predicting vortex formation in wing-body junctures.

7. Other Areas Impacting Future Missile Design

A number of other areas influencing future missile design will be mentioned but will not be discussed in any detail for lack of time. The areas are supersonic carriage and separation of stores, aerothermal design, and radar cross-section.

It is well-known that an airplane with a load of external stores mounted on pylons has too much drag to fly at supersonic speed. This has led to a multitude of concepts for other methods of carrying and launching "external" stores, including the following ones:

1. Conformal
2. Semi-submerged
3. Cavities and open bays
4. Internal carriage
5. Topside carriage
6. In pod with salvo launch

Work needs to be done to determine which of these concepts or other ones are the most promising, and then research needs to be concentrated on the promising ones. The impact on missile design comes about from constraints for carrying the stores and for providing safe launch.

With regard to aerothermal design, the general problem areas are well known for ICBM and space shuttle technology. Also the methods for predicting heat transfer are fairly well developed. Special problems exist for missiles with regard to fin-body junctures on windward sides, and with hot spots near separation and reattachment regions and in the neighborhood of shock impingement. In addition, IR seekers are limited by self noise as well as thermal shock of their brittle ceramic materials. When boundary layer transition occurs on the seeker dome, the resulting increase in heating at the dome base leads to hoop stresses that may cause failure of the material. There are similar thermal problems with radomes and leading edges which may require large radii at the expense of drag.

Since the total temperature at Mach 6, 100,000 ft. altitude is about 3400° R, airbreathing engine and air inlet components must be fabricated from refractory metals and insulated with nonablative materials such as Zirconia. In such design, thermal control via radiation losses becomes an important factor.

In applications where radar cross-section must be minimized, there could be a definite impact both on the design of the missile and on its carriage position on the aircraft. Providing minimum radar cross-section with high aerodynamic efficiency will be a definite problem in certain applications. In RCS minimization,

the emphasis is upon bodies with multiple differing diffraction paths, leading to noncircular cross-sections, rounded bases, and non-cruciform fins to avoid corner reflectors.

8. Concluding Remarks

A number of trends in future missile design have been discussed with respect to the ways in which they influence aerodynamic design. Among the subjects discussed are:

- a. Airframe-inlet interference in airbreathing missiles.
- b. Transonic aerodynamic problems for vertically launched missiles with quick turn-over.
- c. Obtaining high L/D at hypersonic speeds.
- d. Waveriders; aerodynamically configured missiles.
- e. High angle-of-attack problems.
- f. Status of CFD applied to missile aerodynamics.
- g. Supersonic carriage and launch of stores.
- h. Aerothermal design.
- i. Radar cross-section.

A number of specific suggestions have been made where more work is required in the above areas including the following ones.

1. Methods for determining the effects of airframe-inlet interference on drag and stability and control are inadequate. Panel methods may be helpful in this area.
2. For missiles which must operate at high angles of attack in the transonic range, special nonlinearities need attention. These include better control systems and control prediction methodology, elimination or harnessing of induced yaw, and higher normal accelerations.
3. Better aerodynamic efficiency at hypersonic speeds (high L/D) is needed.
4. While waveriders are promising in connection with 3, much more work is needed to provide radomes and inlets for waveriders. Also methods for predicting their aerodynamic characteristics at off-design are generally lacking.
5. Methods for predicting control effectiveness, hinge moments, and control cross-coupling for large angles of attack and control deflection are needed for all-movable controls and other control types.

6. Ideas for producing favorable hypersonic wing-body interference with high lift-drag ratio configurations are needed.

7. Methods for predicting vortex behavior for noncircular bodies are needed for supercritical crossflow.

8. Missile engineering prediction method for lateral/directional characteristics for $\alpha > 20^\circ$ need improvement.

9. The application of the Euler equations to complete missile configurations needs to be extended especially with respect to flow separation phenomena.

10. CFD application to missile aerodynamics needs more attention.

11. Supersonic carriage and launch, radar cross-section, and aerothermal design need increased emphasis.

REFERENCES

1. Knoche, G. H.: Trends in Missile Development and Their Corresponding Requirements with Respect to Aerodynamics. Invited Paper presented at AGARD Fluid Dynamics Panel Symposium on "Missile Aerodynamics," Trondheim, Norway, Sep. 1982.
2. McGehee, R. M.: Bank-to-Turn (BTT) Technology. AIAA Paper 79-1752, Aug. 1979.
3. Froning, H. D., Jr.: Aerodynamic Design of Slender Missiles for Bank-to-Turn Flight at High Angles of Attack. AIAA Paper 81-0289, Jan. 1981.
4. Sawyer, W. C. and Jackson, C. M., Jr.: An Overview of NASA's Role in Maneuvering Missile Aerodynamic Technology. Invited Paper, AIAA Paper 82-0247, Jan. 1982.
5. Carlson, D. R.: The Changing Role of the Aerodynamicist in Tactical Missile Design. AIAA Paper 82-0315, Jan. 1982.
6. Cronvich, L. L. and Liepman, H. P.: Advanced Missile Technology - A Review of Technology Improvement Areas for Cruise Missiles. NASA CR 3187, Oct. 1979.
7. Nielsen, J. N.: Missile Aerodynamics - Past, Present, Future. AIAA Paper 79-1819, Aug. 1979 (also J. Spacecraft and Rockets, Vol. 17, No. 3, May/June 1980, pp. 165-176).
8. Kamman, J. H. and Wallace, H. W.: Assessment of Installed Inlet Forces and Inlet/Airframe Interactions. AFFDL Rept. No. AFFDL-TR-76-62, Jul. 1976.
9. Biringen, S. H. and McMillan, O. J.: An Implicit Method for the Calculation of Inlet Flow Fields. NASA CR 3413, Jun. 1981.
10. Rubbert, P. E. and Saaris, G. R.: Review and Evaluation of a Three-Dimensional Lifting Potential Flow Analysis Method for Arbitrary Configurations. AIAA Paper 72-188, Jan. 1972.
11. Dillenius, M. F. E. and Nielsen, J. N.: Computer Programs for Calculating Pressure Distributions Including Vortex Effects on Supersonic Monoplane or Cruciform Wing-Body-Tail Combinations with Round or Elliptical Bodies. NASA CR 3122, Apr. 1979.
12. Goodwin, F. K., Dillenius, M. F. E., and Mullen, J.: Prediction of Supersonic Store Separation Characteristics Including Fuselage and Stores of Non-circular Cross Section. Vol. I - Theoretical Methods and Comparisons With Experiment. AFWAL-TR-80-3032, Vol. I, Nov. 1980.
13. Perkins, S. C., Jr. and McMillan, O. J.: A Handbook of Experimental Data for the Effects of Inlets on Air-breathing Missile External Aerodynamics (U). NWC TP 6147, Jul. 1981. Vol. I - Overview and Summary (U) (CONFIDENTIAL). Vol. II - Configuration Data: Inlet Type Effects (U) (UNCLASSIFIED). Vol. III - Data Classified by Inlet Type: Part 1 (U) (CONFIDENTIAL). Vol. III - Data Classified by Inlet Type: Part 2 (U) (CONFIDENTIAL).
14. Giragosian, P.: Aerodynamic Considerations in the Design of a Vertically Launched Advance Interdiction Missile. AIAA Paper 82-1340, Aug. 1982.
15. Smith, C. A. and Nielsen, J. N.: Non-linear Aerodynamics of All-Movable Controls. Paper 25, AGARD CP 262, Aerodynamic Characteristics of Controls, Sep. 1979.
16. Wardlaw, A. B., Jr. and Morrison, A. M.: Induced Side Forces at High Angles of Attack. J. Spacecraft and Rockets, Vol. 13, No. 10, Oct. 1976, pp. 589-593.
17. Clark, W. H., Peoples, J. R., and Briggs, M. M.: Occurrence and Inhibition of Large Yawing Moments During High Incidence Flight of Slender Missile Configurations. AIAA Paper 72-968, Sep. 1972.
18. Hunt, J. L., Johnston, P. J., Cabbage, J. M., Dillon, J. L., Richie, C. S., and Marcum, D. C., Jr.: Hypersonic Airbreathing Missile Concepts Under Study at Langley. AIAA Paper 82-0316, Jan. 1982.

19. Krieger, R. J.: Summary of Design and Performance Characteristics of Aerodynamic Configured Missiles. AIAA Paper 81-0286, Jan. 1981.
20. Rasmussen, M. L.: Waverider Configurations Derived from Inclined Circular and Elliptic Cones. J. Spacecraft and Rockets, Vol. 17, No. 6, Nov./Dec. 1980, pp. 537-545.
21. Schindel, L. H.: Design of High Performance Hypersonic Missiles. AIAA Paper 82-0391, Jan. 1982.
22. Nonweiler, T. R. F.: Delta Wing Shapes Amenable to Exact Shock Wave Theory. J. Roy. Aero. Soc., Vol. 67, No. 39, 1963.
23. Küchemann, D.: The Aerodynamic Design of Aircraft. Pergamon Press, 1978.
24. Rasmussen, M. L., Daniel, D. C., and Jischke, M. C.: Supersonic Aerodynamics of a Class of Cone-Derived Waveriders. Proc. of the Twelfth Navy Symposium on Aeroballistics, Vol. 1, May 1981.
25. Nielsen, J. N.: Nonlinear Flow Phenomena at High Angles of Attack and Recent Advances in Their Prediction. Invited Paper presented at AGARD Fluid Dynamics Panel Symposium on "Missile Aerodynamics," Trondheim, Norway, AGARD Conf. Preprint No. 336, 20-22 Sep. 1982.
26. Nielsen, J. N. and Goodwin, F. K.: Preliminary Method for Estimating Hinge Moments of All-Movable Controls. Nielsen Engineering & Research, Inc. TR 268, Mar. 1982.
27. Nielsen, J. N., Hensch, M. J., and Smith, C. A.: A Preliminary Method for Calculating the Aerodynamic Characteristics of Cruciform Missile to High Angles of Attack Including Effects of Roll Angle and Control Deflection. Report ONR-CR215-226-4F, Nov. 1977.
28. Baker, W. B., Jr.: An Aerodynamic Coefficient Prediction Technique for Slender Bodies with Low Aspect Ratio Fins at Mach Numbers from 0.6 to 3.0 and Angles of Attack from 0 to 180 Degrees. AEDC TR-77-97, Mar. 1978.
29. Hunt, B. L.: Asymmetric Vortex Forces and Wakes of Slender Bodies. Invited Paper, AIAA Paper 82-1336, Aug. 1982.
30. Szodroch, J. C. and Ganzer, U.: On the Leaside Flow Over Delta Wings at High Angle of Attack. AGARD CP No. 247, Paper 21, Fluid Dynamics Panel Symposium, Sandefjord, Norway Oct. 1978.
31. Daniel, D. C., Yechout, T. R., and Zollars, G. J.: Experimental Aerodynamic Characteristics of Missiles With Square Cross Sections. J. of Spacecraft and Rockets, Vol. 19, Mar./Apr. 1982, pp. 167-172.
32. Mendenhall, M. R. and Allen, J. M.: Prediction of Vortex Shedding From Noncircular Bodies at High Angles of Attack in Supersonic Flow. Paper presented at AGARD Fluid Dynamics Panel Symposium on "Missile Aerodynamics," Trondheim, Norway, 20-22 Sep. 1982, AGARD Conf. Preprint No. 336.
33. William, J. E., Jr.: Evaluation of Supersonic Missile Aerodynamic Prediction Technique. AIAA Paper 82-0390, Jan. 1982.
34. Klopfer, G. H. and Nielsen, J. N.: Computational Fluid Dynamic Applications to Missile Aerodynamics. Paper presented at AGARD Fluid Dynamics Panel Symposium on "Missile Aerodynamics," Trondheim, Norway, Conf. Preprint No. 336, 20-22 Sep. 1982.
35. Bailey, F. R. and Ballhaus, W. F.: Relaxation Methods for Transonic Flow About Wing-Cylinder Combinations and Lifting Swept Wings. Lecture Notes in Physics, Vol. 19, Springer-Verlag, 1972, pp. 2-9.
36. Caughey, D. A. and Jameson, A.: Numerical Calculations of Transonic Potential Flow About Wing-Body Combinations. AIAA J., Vol. 17, No. 2, Feb. 1979, pp. 175-214.
37. Caughey, D. A. and Jameson, A.: Progress in Finite-Volume Calculations for Wing-Fuselage Combinations. AIAA J., Vol. 18, No. 11, Nov. 1980, pp. 1281-1288.
38. Deiwert, G. S.: Numerical Simulation of Three-Dimensional Boattail Afterbody Flowfields. AIAA J., Vol. 19, No. 5, May 1981, pp. 582-588.
39. Graham, J. E., Hankey, W. L., and Shang, J. S.: Navier-Stokes Solution of a Slender Body of Revolution at Large Incidence. AIAA Paper 80-0190, Jan. 1981.
40. Hankey, W. L. and Shang, J. S.: Analysis of Self-Excited Oscillations in Fluid Flows. AIAA Paper 80-1346, Jul. 1980.
41. Hung, C. M.: Numerical Solution of Supersonic Laminar Flow Over an Inclined Body of Revolution. AIAA J., Vol. 18, No. 8, Aug. 1980, pp. 921-928.

42. Hung, C. M. and Chaussee, D. S.: Computation of Supersonic Turbulent Flows Over an Inclined Ogive-Cylinder-Flare. AIAA J., Vol. 19, No. 9, Sep. 1981, pp. 1139-1144.
43. Klopfer, G. H. and Nielsen, J. N.: Euler Solutions for Wing and Wing-Body Combinations at Supersonic Speeds with Leading-Edge Separation. AIAA Paper 80-0126, Jan. 1980.
44. Klopfer, G. H. and Nielsen, J. N.: Euler Solutions of the Body Vortices of Tangent Ogive Cylinders at High Angles of Attack and Supersonic Speeds. AIAA Paper 81-0361, Jan. 1981.
45. Lin, T. C. and Rubin, S. G.: A Numerical Model for Supersonic Viscous Flow Over a Slender Reentry Vehicle. AIAA Paper 79-0205, Jan. 1979.
46. Marconi, F. and Koch, F.: An Improved Supersonic Three-Dimensional, External, Inviscid Flow Field Code. NASA CR 3108, 1979.
47. Minailos, A. N.: Calculation of Supersonic Flow Past Wings with Consideration of Tangential Discontinuities Shed from the Edges Within the Scope of a Model Using a System of Euler Equations. Fluid Dynamics, Vol. 13, No. 1, Sep. 1978, pp. 57-66.
48. Pulliam, T. H. and Lomax, H.: Simulation of Three-Dimensional Compressible Viscous Flow on the Illiac IV Computer. AIAA Paper 79-0206, Jan. 1979.
49. Pulliam, T. H. and Steger, J. L.: On Implicit Finite Difference Simulations of Three Dimensional Flow. AIAA Paper 78-10, Jan. 1978.
50. Rakich, J. V., Vigneron, Y. C., and Agarwal, R.: Computation of Supersonic Viscous Flows Over Ogive-Cylinders at Angle of Attack. AIAA Paper 79-0131, Jan. 1979.
51. Schiff, L. B. and Sturek, W. B.: Numerical Simulation of Steady Supersonic Flow Over an Ogive-Cylinder-Boattail Body. AIAA Paper 80-0066, Jan. 1980.
52. Schmidt, W., Jameson, A., and Whitfield, D.: Finite Volume Solution for the Euler Equations for Transonic Flow Over Airfoils and Wings Including Viscous Effects. AIAA Paper 81-1265, Jun. 1981.
53. Shang, J. S.: Numerical Simulation of Wing-Fuselage Interference. AIAA Paper 81-0048, Jan. 1981.
54. Shang, J., Smith, R., and Hankey, W.: Flow Oscillations of Spike-Tipped Bodies. AIAA J., Vol. 20, No. 1, Jan. 1982, pp. 25-26.
55. Siciari, M. J.: Investigation of Cross Flow Shocks on Delta Wings in Supersonic Flow. AIAA Paper 79-0345, Jan. 1979.
56. Sturek, W. B., Mylin, D. C., and Bush, C. C.: Computational Parametric Study of the Aerodynamics of Spinning Slender Bodies at Supersonic Speeds. AIAA J., Vol. 19, No. 8, Aug. 1981, pp. 1023-1024.
57. Tannehill, J. C., Venkatapathy, E., and Rakich, J. V.: Numerical Solution of Supersonic Viscous Flow Over Blunt Delta Wings. AIAA Paper 81-0049, Jan. 1981.
58. Wardlaw, A. B., Jr., Baltakis, J. P., Solomon, J. M., and Hackerman, L. B.: An Inviscid Computations Method for Tactical Missile Configurations. NSWC TR 81-457, 1981.
59. Wardlaw, A. B., Jr., Solomon, J. M., and Baltakis, F. P.: Supersonic Inviscid Flowfield Computations of Missile Type Bodies. AIAA J., Vol. 19, No. 7, Jul. 1981, pp. 899-906.
60. Eriksson, L. and Rizzi, A.: Computations of Vortex Flow Around Wings Using the Euler Equations. Proc. of the 15th CMM Conf. on Numerical Methods in Fluid Mech., Paris, Oct. 1981.

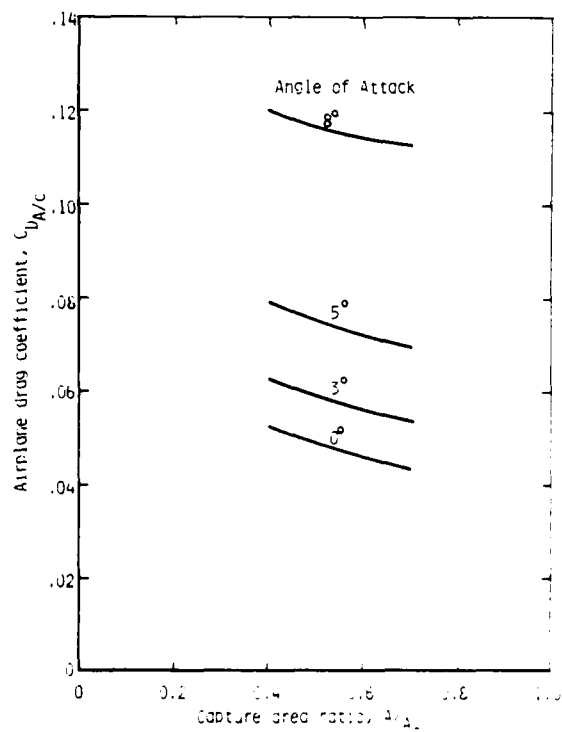


FIGURE 1.- EFFECT ON AIRPLANE DRAG COEFFICIENT OF MASS FLOW THROUGH INLET AND ANGLE OF ATTACK.

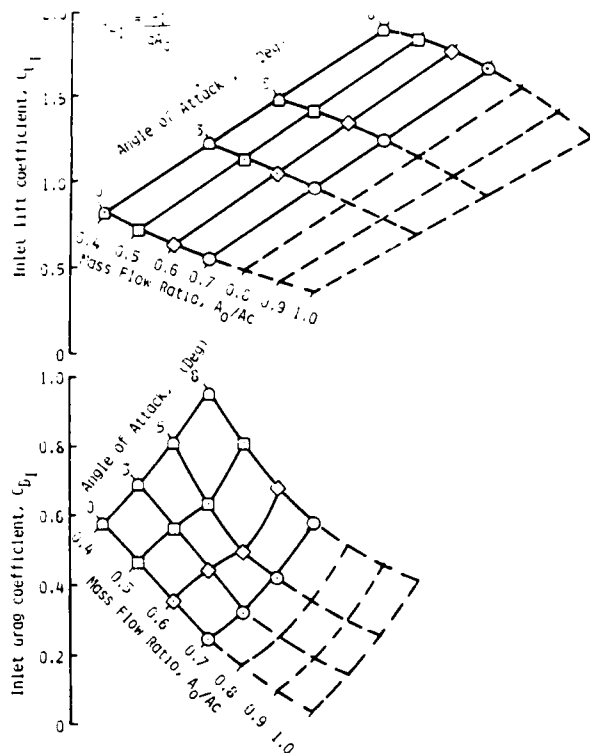


FIGURE 2.- INLET LIFT AND DRAG COEFFICIENTS AS AFFECTED BY ANGLE OF ATTACK AND MASS FLOW RATIO (A_0/A_C), F-15 INLET AT $M_\infty = 1.5$, ON-DESIGN, ZERO COWL DROOP.

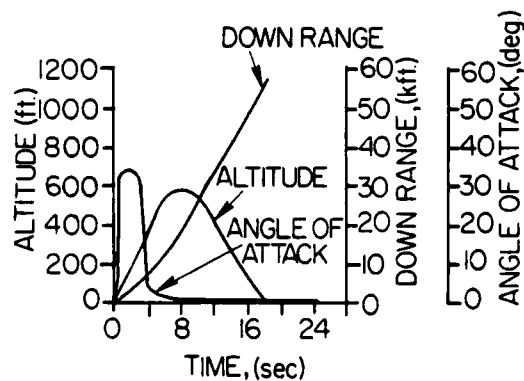
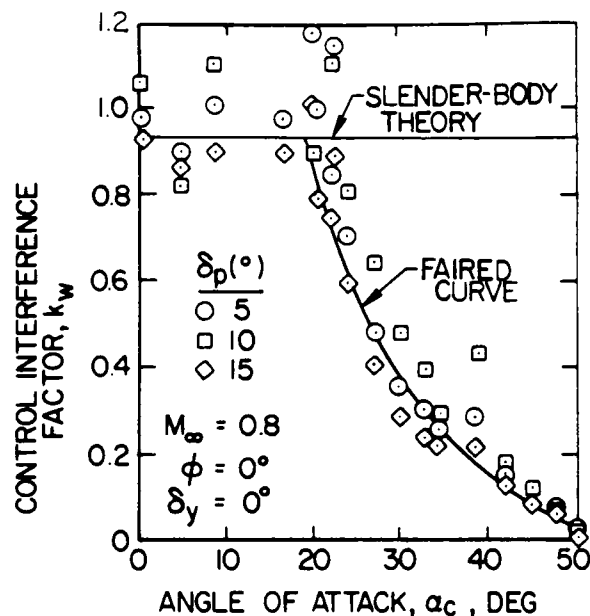
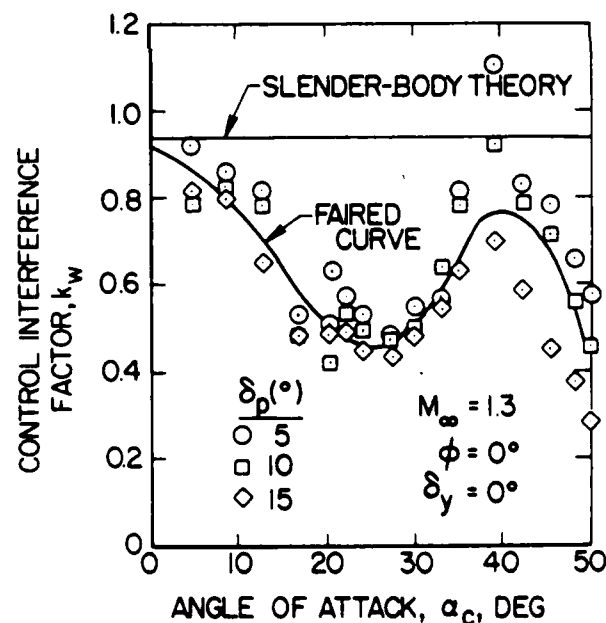


FIGURE 3.- TRAJECTORY QUANTITIES FOR A VERTICALLY LAUNCHED MISSILE WITH A RANGE OF 9 n.m.



(a) $M_\infty = 0.8$

FIGURE 4.- EFFECT OF ANGLES OF ATTACK AND CONTROL DEFLECTION ON PITCH-CONTROL EFFECTIVENESS.



(b) $M_\infty = 1.3$

FIGURE 4.- CONCLUDED.

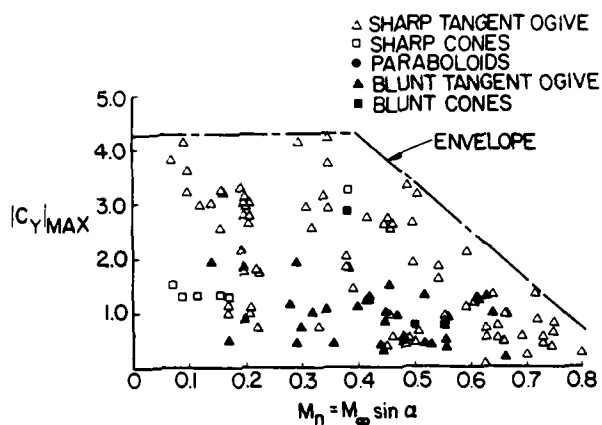


FIGURE 5.- EFFECT OF CROSSFLOW MACH NUMBER ON VORTEX-INDUCED SIDE FORCE.

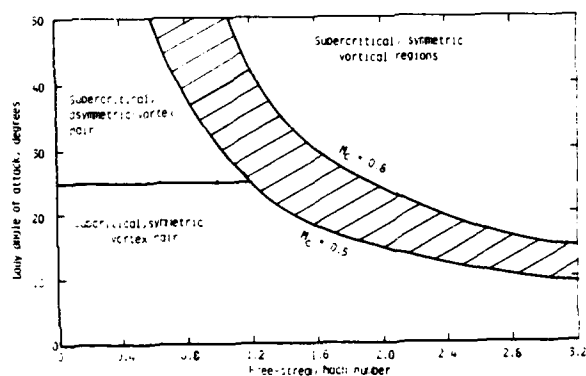


FIGURE 6.- APPROXIMATE REGIONS FOR VARIOUS TYPES OF BODY VORTICES.

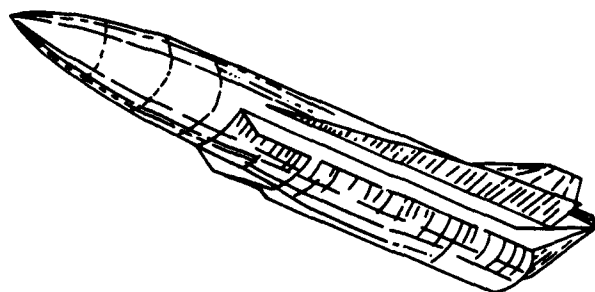
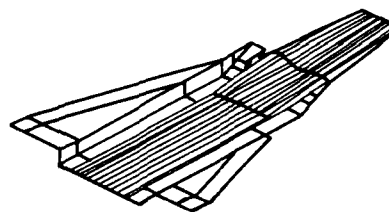
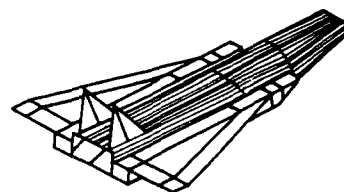


FIGURE 7.- MID-INLET CONCEPT.

- SPATULAR NOSE
- HIGH WING
- TWIN VERTICALS
- FLAT BOTTOM



- ELLIPTIC COMBUSTOR
- 2-D VARIABLE GEOMETRY NOZZLE
- 2-D VARIABLE GEOMETRY INLET
- SUPER PLASTIC FORMED STRUCTURE

FIGURE 8.- NONCIRCULAR BODY CRUISER USING ADVANCED TECHNOLOGIES.

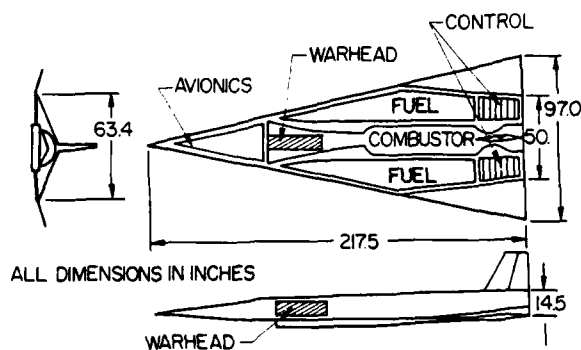


FIGURE 9.- LIFTING BODY MISSILE.

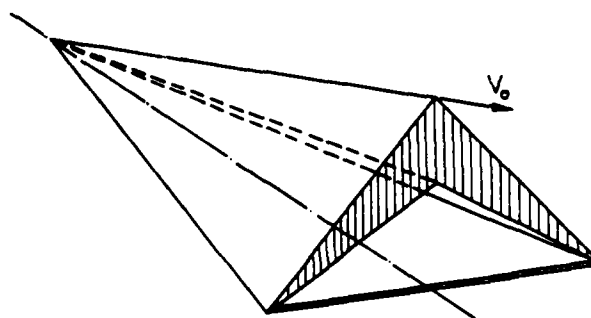
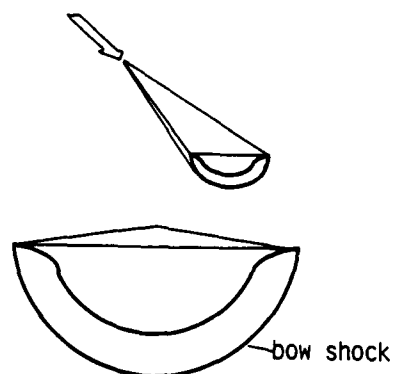
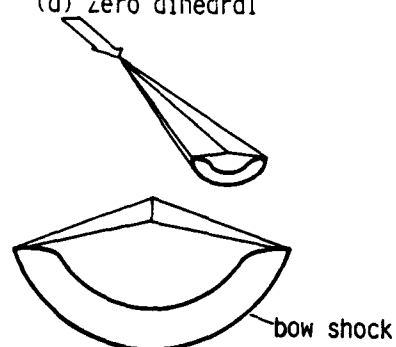


FIGURE 10.- CARET WING SUPPORTING AND CONTAINING A PLANE SHOCKWAVE. AFTER NONWEILER (1963).

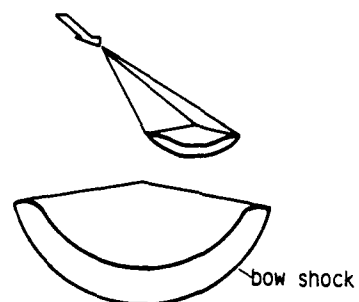


(a) Zero dihedral

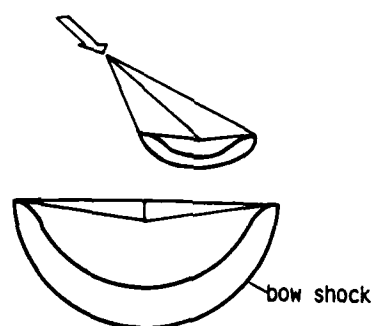


(b) Negative dihedral

FIGURE 11.- INCLINED CIRCULAR-CONE WAVE-
RIDERS WITH FREESTREAM UPPER SURFACES.



(a) Positive dihedral



(b) Negative dihedral

FIGURE 12.- INCLINED ELLIPTICAL-CONE
WAVERIDERS WITH FREESTREAM
UPPER FACE.

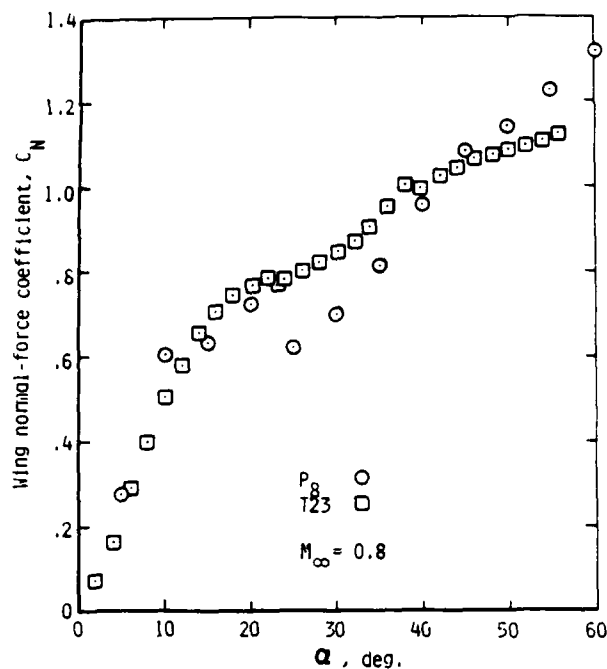


FIGURE 13.- EXPERIMENTAL NORMAL-FORCE CURVES FOR TWO WINGS OF ASPECT RATIO 2 AND TAPER RATIO 0.5 DIFFERING IN AIRFOIL SECTIONS.

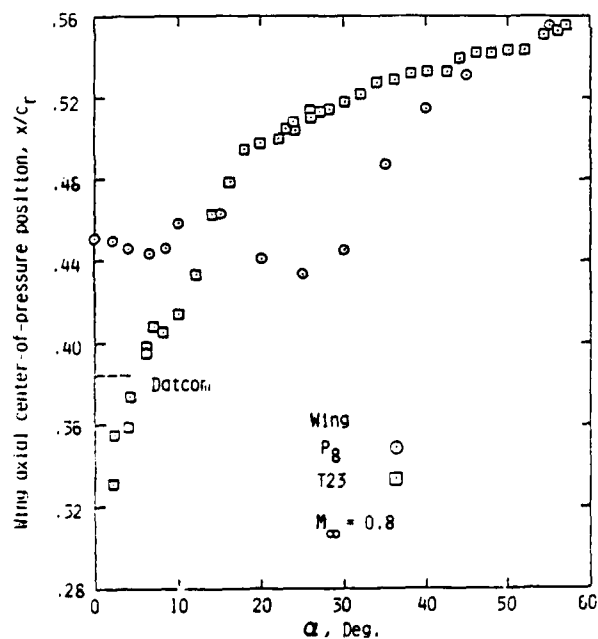


FIGURE 14.- EXPERIMENTAL CENTER-OF-PRESSURE POSITIONS FOR TWO WINGS OF ASPECT RATIO 2 AND TAPER RATIO 0.5 DIFFERING IN AIRFOIL SECTIONS.

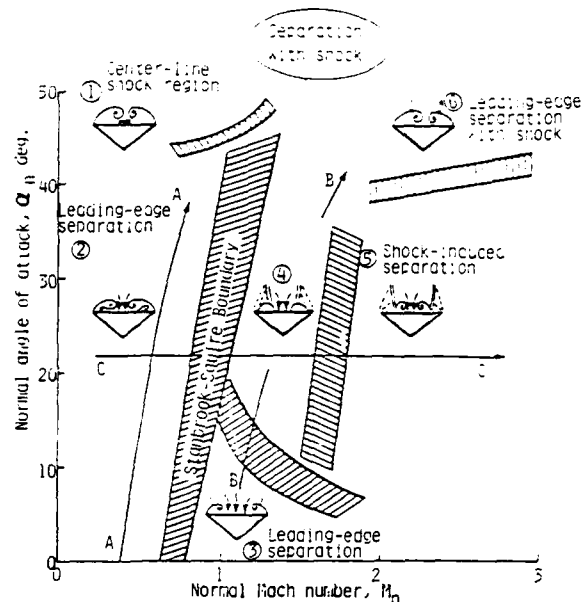


FIGURE 15.- LEE SIDE FLOW REGIMES OVER THICK DELTA WINGS AT SUPERSONIC SPEEDS. (SZODRUCH, 1978).

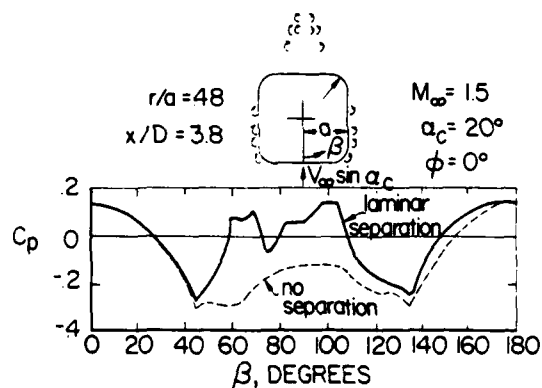


FIGURE 16.- PREDICTED PRESSURE DISTRIBUTION AND VORTEX WAKE ON A SQUARE CROSS SECTION BODY, $M = 1.5$, $\alpha_c = 20^\circ$.

Flow Configuration Equations	Bodies With Flow Separation	Bodies & Fins No Flow Separation	Bodies & Fins Flow Separation	Unsteady Flows
Transonic Small Disturbance (TSD)		Bailey (35)		
Full Potential		Caughey (37) Caughey (36)		
TSD & BOUNDARY Layer Correction				
Euler		Siclari (55) Marconi (46) Hardlow (59)		
Euler & Boundary Layer	Schmidt (52)		Schmidt (52)	
Euler & Kutta Condition	filnailos (47) Kloofler (44)		Kloofler (43)	

(a) Non Navier-Stokes Codes

Flow Configuration Equations	Bodies With Flow Separation	Bodies & Fins No Flow Separation	Bodies & Fins Flow Separation	Unsteady Flows
Thin Layer Navier- Stokes, Laminar	Pulliam (40) Hung (41)			
Thin Layer Navier- Stokes, Turbulent	Pulliam (40) Schiff (51) Deiwert (38) Hung (42)			
Parabolized Navier- Stokes, Laminar	Rakich (50) Tannehill (57) Lin (45)			
Parabolized Navier- Stokes, Turbulent	Rakich (50) Sturek (56) Schiff (51)			
Full Navier-Stokes, Laminar	Graham (39)			
Full Navier-Stokes, Turbulent	Graham (39)	Shang (53)		Shang (53) Hankey (40)

(b) Navier-Stokes Codes

Figure 17.- SURVEY OF CFD IN MISSILE AERODYNAMICS.

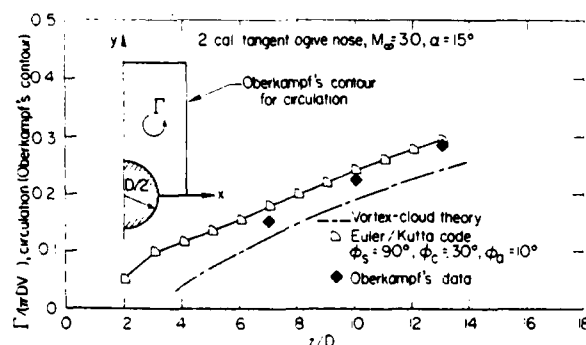


FIGURE 18.- COMPARISON OF CIRCULATION FOR EULER/KUTTA CODE, VORTEX CLOUD THEORY, AND EXPERIMENTAL DATA.

SESSION 7

THEORETICAL AND EXPERIMENTAL DYNAMIC STALL INVESTIGATIONS ON A ROTOR BLADE TIP.

U. Geissler
DFVLR, West Germany/NASA Ames Research Center, USA

Summary

Theoretical and experimental investigations have been carried out on oscillating blade tips at moderate and high steady mean incidences and oscillation amplitudes.

Some selected data of these tests are compared with a previously developed prediction method based on potential theory to investigate the main effects of viscosity in different domains of dynamic stall. A simple correction procedure is described to take into account the main effects of viscosity on the unsteady airloads. To get a more detailed insight into the beginning of unsteady separation on oscillating profiles a finite-difference procedure has been developed to calculate the unsteady boundary-layer equations. This method has been applied to the oscillating flat plate problem as a first step. The application to problems of more practical interest like profiles under pitching motion is straightforward.

I. Introduction

The flow about a retreating helicopter rotor blade is highly affected by viscous phenomena like dynamic stall and unsteady tip vortex and wake interactions. These complicated unsteady flows are still far from satisfactory analytical solutions. Details of unsteady flow separation, transition from laminar to turbulent flow and turbulence itself are still not understood well enough such that numerical methods can take these complicated problems sufficiently into account.

For the investigation of viscous phenomena on oscillating helicopter rotor blade tips, measurements of steady and unsteady (first harmonic components) pressure distributions have been carried out in the low speed 3-m wind tunnel of the DFVLR in Göttingen, West Germany. These experiments were done within the scope of a cooperative agreement between NASA, Langley Research Center and the DFVLR, Institute of Aeroelasticity in Göttingen. The measurements included variations of frequency ($f = 0.4/8/12$ Hz), steady mean incidences: $0^\circ \leq \alpha_0 \leq 20^\circ$ and oscillation amplitudes: $1^\circ \leq \Delta \alpha \leq 8^\circ$.

In addition to the experimental investigations, a panel-type method to calculate the inviscid steady and unsteady pressure distributions about three-dimensional wing configurations undergoing plunging, pitching or control-surface oscillations has been developed¹.

The following discussion will concentrate on a comparison of measured and calculated pressure distributions for a rectangular blade tip at various incidences and oscillation amplitudes. The results are given in a similar manner as has been proposed in ref. 2. The discussions will show the effects of viscosity at the beginning of separation as well as in the deep dynamic stall region. It will be shown that a simple correction procedure for the calculated inviscid results within the separated

region leads to remarkable improvement compared to the experimental data.

It is assumed that the information needed for such a phenomenological correction procedure can be obtained by a detailed unsteady boundary-layer investigation before flow separation. The unsteady behavior of the boundary-layer characteristics and the mechanism of unsteady separation itself are necessary problems for investigation.

Therefore a numerical method to calculate two-dimensional unsteady boundary layers has been developed and first of all applied to the oscillating flat-plate problem. This finite-difference procedure, working in the time-domain, will then be applied to oscillating profiles taking into account the unsteady boundary conditions obtained by the panel method described in ref. 1.

II. Experimental Investigations

Figure 1a shows the rectangular blade tip model in the open test section of the 3-m low-speed wind tunnel of the DFVLR in Göttingen. The model with a NACA 0012 airfoil section was mounted vertically on a ground plate and allowed to oscillate about its quarter-chord axis. The chord reference length was $c = 400\text{mm}$ and the span $s = 2c = 800\text{mm}$ ($\Lambda = 4^\circ$). The model was equipped with a tubing system connecting about 150 pressure orifices within 8 spanwise sections over four scanning valves with a pressure transducer below the ground plate. The experiments have been performed at a tunnel speed of 50 m/s leading to a Reynolds number of $Re = 1.2 \times 10^5$ based on c . Further details of the model and measuring technique as well as the experimental results are given in ref. 3.

III. Calculation Procedures (Panel Method)

The potential theoretical method applied for calculating the steady and unsteady pressures on the real surface of an oscillating 3-D-wing configuration has been given in ref. 1. Figure 1b shows the arbitrary wing geometry with the corresponding panel arrangement, control point locations and the wake surface divided into wake strips. Each panel is represented by a source/sink and doublet distribution, each of constant strength. The wake is represented by doublets alone. The wake geometry is prescribed and not changed during the calculation.

The panel method has been applied to a variety of problems including three-dimensional swept wings and wings with oscillating control surfaces. Comparisons with other methods and, in particular with experimental data, show quite satisfactory correspondence in cases where viscous effects are small. Influences of steady boundary layers on the steady as well as unsteady pressure distributions have also been taken into account and give an improvement of the steady and real-part unsteady pressures. The imaginary parts, however, are not influenced properly by this simple correction procedure.

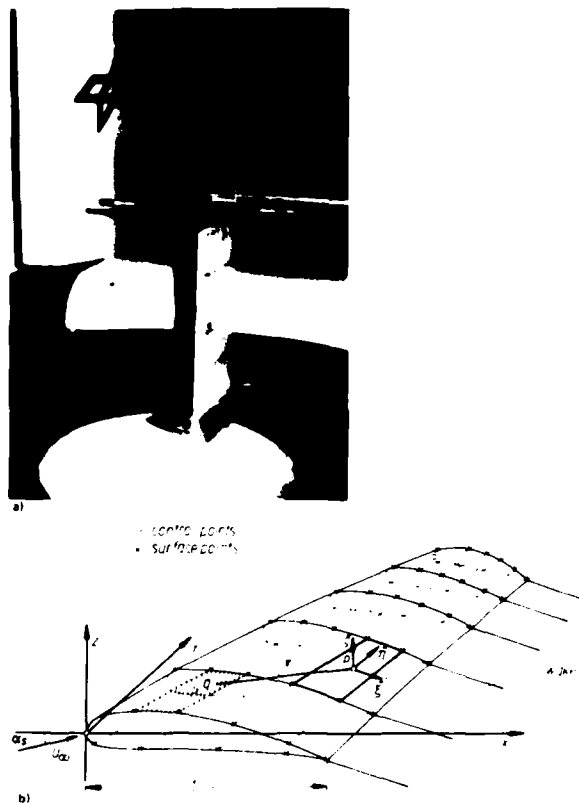


Fig. 1 (a) Photo of the rectangular blade tip in the test section of the 3m-low speed wind tunnel of the DFVLR/Göttingen. (b) Panel-method: wing geometry, panel arrangement.

IV. Results

In the following series of figures (figures 2-4), some selected steady and unsteady pressure distributions are given for small ($\bar{\alpha} = 1^\circ$) as well as for higher ($\bar{\alpha} = 8^\circ$) oscillation amplitudes about $\alpha_0 = 8^\circ$ and 16° steady mean incidence. The plots always give calculated and measured steady as well as real and imaginary parts of the unsteady pressures and, in addition, amplitude and phase angle distributions for complete information. The pressure data are plotted versus \sqrt{x}/c instead of x/c in order to expand the leading edge region of the profile. Several additional results are discussed in ref. 5.

4.1 Stall Onset

Figure 2a shows steady as well as real and imaginary part of the unsteady pressure distribution at the inboard station ($\eta = y/c = 1.5$ with $y = 0$ at the wing tip). The steady mean incidence is $\alpha_0 = 8^\circ$ and the experimental results are obtained for $\bar{\alpha} = 1.05^\circ$ and 7.37° oscillation amplitude. The unsteady pressures C_p and C_p^* are referred to the amplitude. The measured steady and real part unsteady pressures show only a small reduction compared to theory which must be referred to boundary-layer displacement effects. Figure 2b shows the amplitude and phase angle distributions for the same case. Only the phase angles on the upper surface of the wing show a remarkable

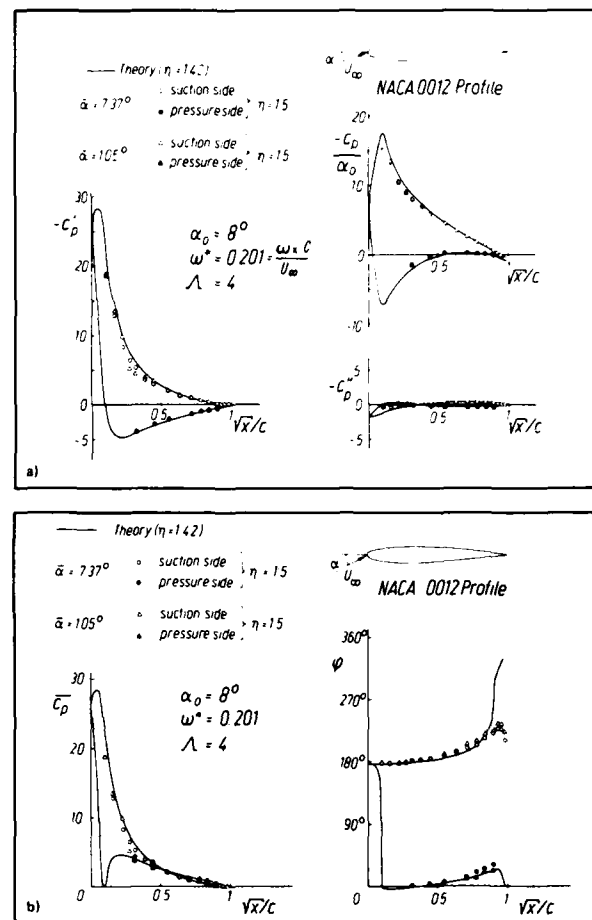


Fig. 2 NACA 0012: $\alpha = 8^\circ + 1^\circ/7.37^\circ \sin \omega t$, inner section ($\eta = 1.5$). (a) Steady, real and imaginary pressures. (b) Amplitude and phase.

reduction close to the trailing edge. This effect must be attributed to the beginning of a trailing-edge separation, because these effects on the phase angle distribution are similar to cases of higher incidence where separation is obviously apparent, as will be discussed in the next section.

4.2 Deep Dynamic Stall

Figure 3 displays results for the high incidence case of $\alpha_0 = 16^\circ$ with $\bar{\alpha} = 1^\circ$ and 8.14° oscillation amplitude (inboard station, $\eta = 1.5$). In the small amplitude case there is still a good correspondence between inviscid theory and experiment. Again the phase angles in Fig. 3b show larger deviations from the calculated results which must be referred to the beginning of a turbulent trailing-edge separation. The situation changes, however, completely for the high amplitude case: On the suction side the leading edge pressure peak of C_p (Fig. 3a) is now considerably reduced. At the same location a strong peak is built up in the imaginary pressures. Further on the C_p -values remain on a nearly constant level compared to theory over large parts of the upper wing surface. The phase angles in Fig. 3b show a quite contrary behavior on the wing suction side. These phase differences between theory and experiment are responsible for the strong shift of the unsteady real-part pressure peak into the imaginary part.

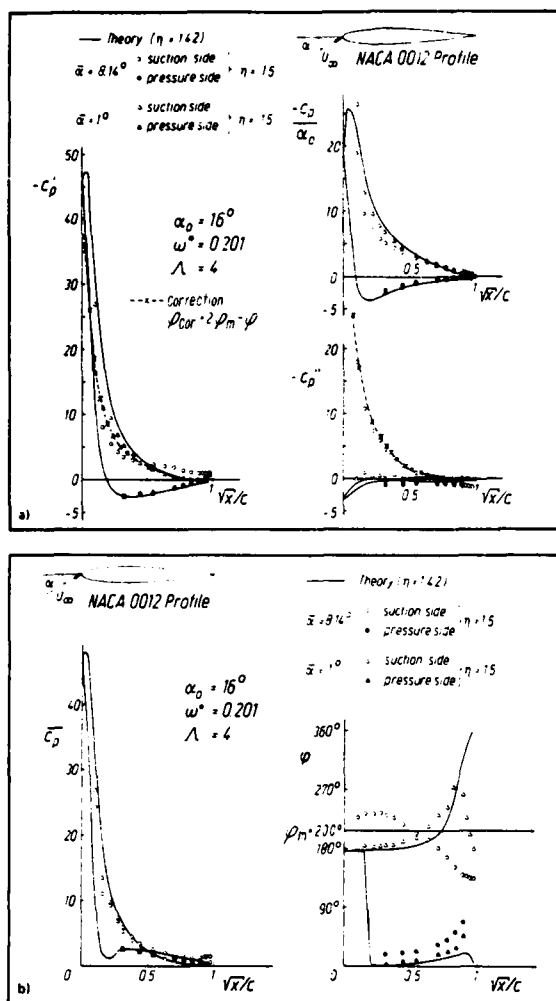


Fig. 3 NACA 0012: $\alpha = 16^\circ + 1^\circ/8.14^\circ \sin \omega t$, inner section ($\eta = 1.5$).
(a) Steady, real and imaginary pressures.
(b) Amplitude and phase.

In this high amplitude case the flow obviously separates from the leading edge over a part of the cycle. Due to this leading-edge separation, large vortex-like disturbances are created which propagate downstream over the upper side of the wing. The separation mainly affects the phase angle of the unsteady pressures whereas the amplitudes remain nearly constant within the separated region.

4.3 Effects on Outboard Sections

For the very tip region of the wing, the situation is completely changed. Figure 4 shows the corresponding results at $\eta = 0.1$ ($y/c = 0.1$ measured from the wing tip). Now the leading-edge region is only affected slightly by viscous effects even in the high amplitude case. On the other hand, characteristic effects of the tip-vortex near the trailing edge can be observed in the steady and real part pressures. The imaginary pressures, however, remain nearly unchanged.

4.4 Unsteady Separation on a Profile Section with Oscillating Control

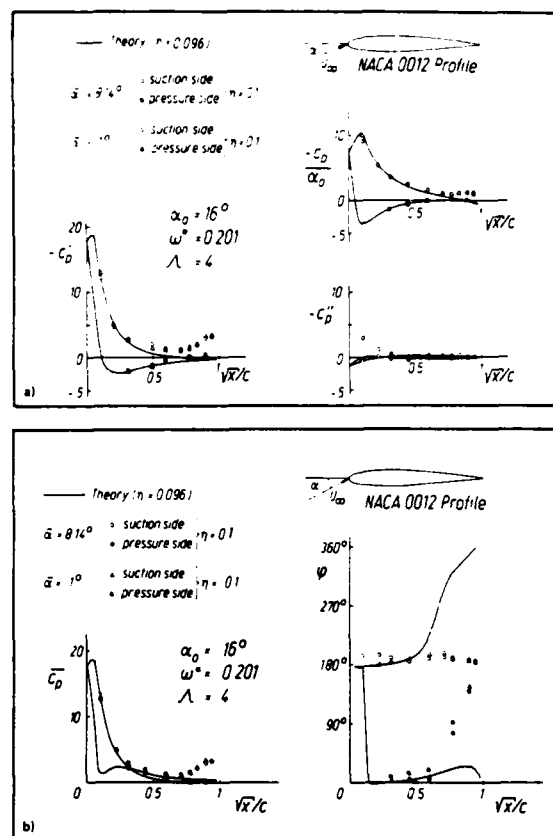


Fig. 4 NACA 0012: $\alpha = 16^\circ + 1^\circ/8.14^\circ \sin \omega t$, outer section ($\eta = 0.1$).
(a) Steady, real and imaginary pressures.
(b) Amplitude and phase.

The results shown in Figures 2-4 are a few typical examples of the flow situation on oscillating wings under separated flow conditions. Further examples are discussed in ref. 5. To show that the separation effects on the unsteady pressures are not a feature of the special wing configuration, Figure 5 shows results of a supercritical wing-section (Va-2 supercritical airfoil) with oscillating trailing-edge control. The steady mean flap deflection in this case is $\delta = 10^\circ$ and the oscillation amplitude $\bar{\alpha} = 1^\circ$ (frequency $f = 9$ Hz). The results in Fig. 5a show again steady, real and imaginary parts of the unsteady pressures and Fig. 5b displays amplitude and phase angle distributions. The inviscid theoretical results are corrected by a simple procedure taking into account the displacement effect of the steady boundary layer. This correction improves the steady and real part unsteady pressures but does not have the right influence on the imaginary parts. Strong deviations between theory and experiment can again be observed on the suction side of the oscillating flap which must be referred to turbulent separation. The real part pressure peak at the control leading edge is now considerably reduced and shifted into the imaginary part. This is again due to the contrary behavior of the phase angle inside the separated region (Fig. 5b). In the following section it is shown how a simple correction procedure is able to take care of these viscous effects.

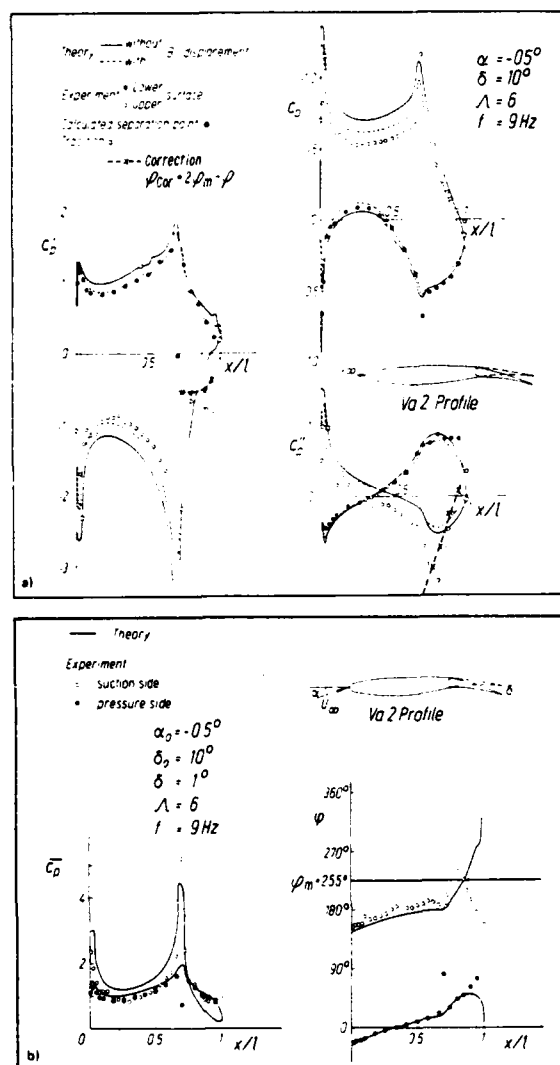


Fig. 5 Va2 supercritical airfoil section with oscillating control: $\delta = 10^\circ + 1^\circ \sin \omega t$
 (a) Steady, real and imaginary pressures.
 (b) Amplitude and phase.

4.5 Viscous Correction Procedure

In Fig. 3b, for the wing case, as well as in Fig. 5b, for the profile with oscillating control, the phase distribution in the separated region can simply be corrected by

$$\phi_{cor} = 2\phi_m - \phi$$

where ϕ_m is given in the corresponding figures. Comparing inviscid theoretical with experimental phase-angle distributions inside the separated regions, ϕ_m serves as an "image line."

The effects of the corrected theoretical ϕ -distributions on the real and imaginary pressures are given in Figs. 3a and 5a. The shift of the pressure peak from the real part into the imaginary part is in surprisingly good agreement with the experimental data. Deviations in the real parts of Fig. 5a must be referred to amplitude differences which have not been taken into account.

Viscous correction procedures of this type have, of course, the disadvantage that the correction factor, in this case the image value ϕ_m , can only be found by comparison between theory and experiment. To change this unsatisfactory situation, calculation procedures must be developed to take into account unsteady viscous effects which at least give more insight into the phase and amplitude behaviors at separation or inside the separated regions.

V. Unsteady Boundary-Layer Calculations - Oscillating Flat Plate Problem

One possibility to obtain some detailed information of unsteady viscous flows before and close to separation can be achieved by the investigation of unsteady boundary layers. As a first step towards this goal, a finite-difference procedure has been developed to calculate the unsteady laminar boundary layer by a time-marching procedure. This method, which is described in detail in Ref. 5, has first of all successfully been applied to the well-known problem of a flat plate oscillating in its own plane. The flat-plate problem is on one hand very suitable to check a numerical procedure against various results existing already in the literature and make comparisons with low and high frequency solutions which can be found in Ref. 7. On the other hand some characteristic features of unsteady boundary layers, which differ considerably from their two-dimensional steady counterparts, can already be studied.

The most remarkable feature, which can be found in Figs. 6a-c, is the appearance of reversed flow regions over a part of the oscillation cycle. The implicit numerical calculation procedure of a Crank-Nicolson type, which has been applied here, does not show any difficulties in marching through these reversed flow regions. This is, of course, only possible as long as the numerical stability condition limited by the zone of influence of the flow characteristics is not violated. In Figs. 6a-c the results of a high frequency solution obtained from a simple system of ordinary differential equations are used for comparison. The results fit extremely well with the numerical data giving a lot of confidence in the validity of the numerical procedure.

Two other important features of the unsteady boundary layers can also be studied in Figs. 6a-c. Figure 6c shows the large amount of unsteadiness during a cycle of oscillation which makes it difficult to choose a suitable family of profiles for a simpler integral procedure. Figure 6b finally displays the behavior of the boundary-layer displacement thickness: δ_1 shows an unsymmetric behavior (low minimum, larger maximum) during a cycle which is mainly influenced by the oscillation amplitude ϵ . τ_w , as well as δ_1 show considerable phase shifts with respect to the movement of the plate.

VI. Extension of the Unsteady Boundary-Layer Method to Oscillating Profiles

With the experience from the flat plate problem, the numerical calculation procedure can now be applied to the more complicated problem of oscillating airfoils. In this case, suitable initial

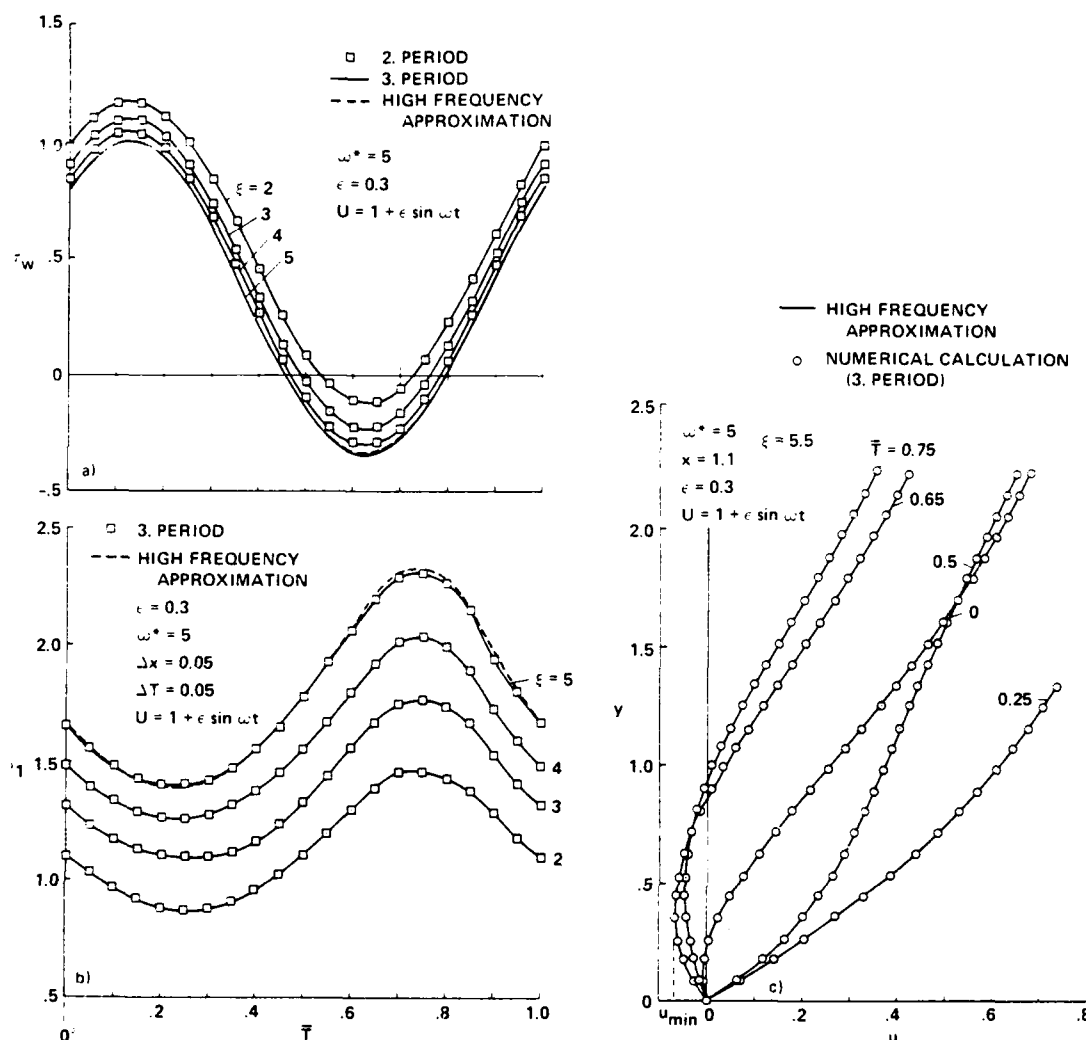


Fig. 6 Unsteady flat plate boundary layer $U = 1 + \epsilon \sin \omega t$, $\omega^* = 5$, $\epsilon = 0.3$.
 (a) Wall shear stress-distribution.
 (b) Boundary-layer displacement thickness.
 (c) Boundary-layer profiles.

and boundary conditions must be determined before the calculation can start.

Results from the unsteady panel method described in Section 3 serve as useful boundary conditions at the outer edge of the boundary layer. Initial conditions along the profile at $t = 0$ can be calculated by the solution of the steady-state boundary layer. Initial conditions close to the front stagnation point can be determined by using a stagnation point fixed frame of reference, i.e. a system which moves harmonically with the stagnation point. The same finite-difference procedure can then be applied as before, but care must be exercised with respect to the numerical stability condition. Due to the very high pressure gradients, the step sizes in the x -direction must be very small, leading to even smaller time steps to fulfill numerical stability requirements.

VII. Conclusion

Theoretical and experimental investigations have been carried out on a rotor blade tip oscillating in pitch about its quarter-chord axis. Comparisons between an inviscid, panel-type theory and experiment show the effects of viscosity on the steady and, in particular, on the unsteady pressure distributions on the wing surface. Special features which seem to be common have been found to influence the unsteady airloads under separated flow conditions. Simple correction procedures are suitable to take care of these effects, but for this type of correction, experimental data are necessary. More insight into unsteady viscous flows may be obtained by the study of unsteady boundary layers. Therefore, a finite-difference procedure has been developed to solve the unsteady boundary-layer equations. This method has first of all been applied to the

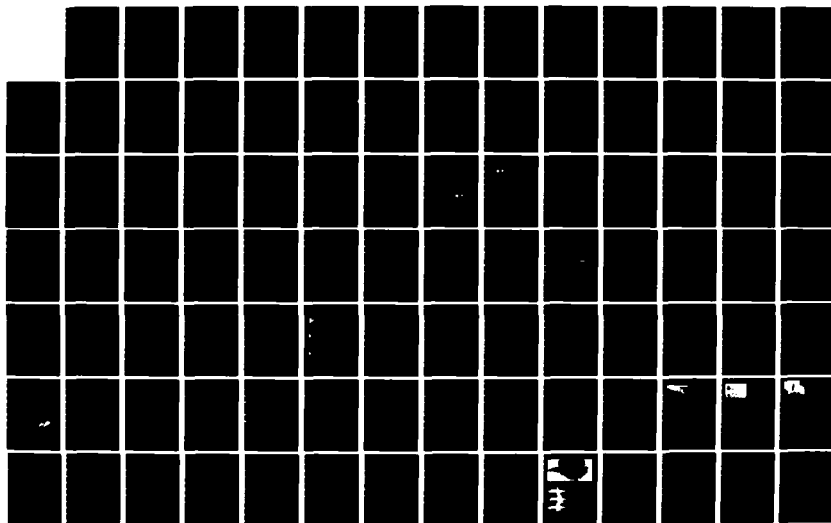
AD-A134 151

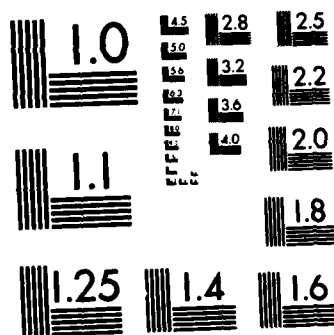
SYMPOSIUM ON NUMERICAL AND PHYSICAL ASPECTS OF
AERODYNAMIC FLOWS (2ND) 17-20 JANUARY 1983(U)
CALIFORNIA STATE UNIV LONG BEACH T CEBECI 1983

4/5

UNCLASSIFIED

F/G 20/4 NL





MICROCOPY RESOLUTION TEST CHART
NATIONAL BUREAU OF STANDARDS-1963-A

oscillating flat-plate problem. Results from these calculations already give a lot of insight into the special features of unsteady viscous flow. The method can then be applied to the more complicated problem of oscillating profiles.

VIII. Acknowledgment

Parts of these investigations have been carried out while the author stayed at the NASA, Ames Research Center. The support of the National Research Council is very much acknowledged.

IX. References

1. Geissler, W.: Nonlinear Unsteady Potential Flow Calculations for Three-Dimensional Oscillating Wings. AIAA Journal, Vol. 16, No. 11, pp. 1168-1174, Nov. 1978.
2. McCroskey, W.J. and Pucci, S.L.: Viscous-Inviscid Interaction on Oscillating Airfoils. AIAA 18th Aerospace Sciences Meeting, St. Louis, MO. 12-15 Jan 1981.
3. Kienappel, K.: Einfluss der Blattspitzen geometrie auf die instationaere Druckverteilung an einem Rotorblatt. Teil I: Rechteckblattspitze, DFVLR-FB March 1982, in preparation.
4. Geissler, W.: Viscous Effects on Unsteady Airloads of Oscillating Configurations. AGARD-CP-296, pp. 4-1/4-11, 1980.
5. Geissler, W.: Dynamic Stall Investigations on a Rectangular Blade Tip. DFVLR IB232-82J04, 1982.
6. Geissler, W.: Unsteady Laminar Boundary Layer Calculations on Oscillating Configurations Including Backflow. Part I: Flat Plate Oscillating in Its Own Plan. DFVLR-FB, in preparation.
7. Lighthill, M.J.: The Response of Laminar Skin Friction and Heat Transfer to Fluctuations in the Stream Velocity. Proc. of the Royal Society, Ser. A, Vol. 224, pp. 1-23, June 1954.

AD P 001951

EFFECT OF ROUGHNESS ON THREE-DIMENSIONAL
TURBULENT BOUNDARY LAYERS

P.A. Krogstad* and T.K. Fanneløp**

Abstract

The paper describes a three-dimensional boundary layer experiment on a rough surface. The data obtained are compared to a reference experiment having the same geometry and flow conditions but with a smooth surface. The boundary layer data are compared using scaling criteria developed from two-dimensional flows. It is found that the results, in terms of scaled variables, agree well in regions where pressure gradients are the dominant cause of three-dimensionality. In regions where shear stresses are more important, significant deviations in profile characteristics appear. A possible interpretation is that the degree of anisotropy is greater in three-dimensional rough boundary-layer flows than in the corresponding smooth-wall case.

I. Introduction

During the last few decades a large number of boundary layer experiments on rough surfaces have been conducted in two-dimensional flows both with and without pressure gradients (ref. 1 to 9). This has provided invaluable information to the development of computational methods (ref. 10 to 15) which seem to be able to predict the 2D rough boundary layer flows successfully. However, to our knowledge, no experimental information is available on 3D, rough boundary layers.

Recently, Ryhming and Fanneløp¹⁶ published a 3D law-of-the-wall formulation including surface roughness effects. The results of their analysis show, that in 3D boundary layer flows, the effects of roughness on the velocity profiles cannot fully be accounted for by a downward shift Δy^+ of the wall coordinate. Additional terms, proportional to y^+ or $y^+ \log y^+$ appear, which would seem to be of increasing importance away from the wall. These terms are related to the curvature and convergence/divergence of the wall streamline and would therefore not be present in 2D flows. The theory presumes the existence of the law-of-the-wall and no conclusions can be drawn concerning the flow outside the logarithmic region.

*) SINTEF, The foundation of scientific and industrial research, Trondheim, Norway.

**) Norwegian Institute of Technology, Trondheim, Norway

From a physical point of view roughness could affect the 3D in two different ways. The increase in transverse friction would tend to reduce the crossflow. On the other hand, the increase in streamwise wall friction also tends to slow down the fluid, making it more sensitive to the lateral pressure gradient and therefore increases the production of crossflow. Which one of these two opposing effects is dominant is not quite clear but in their sample computation of the infinite swept wing experiment documented in reference 17, substantial differences in crossflow was noted when a small amount of roughness was specified. If this is a physically significant effect it should be discernable when the same 3D boundary layer experiment were repeated with a rough and a smooth test surface.

In this paper we discuss some of the results obtained by repeating a previously documented boundary layer experiment performed at our institute (ref. 18) with sand paper roughness added to the test surface. The data from the smooth surface tests will be used as a reference in analyzing the data.

II. Experimental setup
and instrumentation

The experiment for the smooth surface case is fully documented in reference 18. The model consists of a semi-infinite blunt body mounted on a flat surface extending 3.34 m upstream of the model. The shape of the blunt body is produced by computing the potential flow contour of a line source in a uniform flow. After taking into account the effect of the wind tunnel walls by the method of mirror images it is shown in ref. 18 that very good agreement between the analytical and measured pressure distribution was obtained. Figure 1 shows the model with the coordinate system, the computed inviscid streamlines and the surface streamlines obtained for the smooth case by means of oil flow visualization. The measurement stations are also indicated. Unfortunately no surface streamlines are obtainable for the rough surface so the exact position of the separation line could not be established for this case.

Figure 4 and 5 show law-of-the-wall and wake plots of the rough and smooth surface boundary layer profiles at station 11 for the same Re_x ($3.76 \cdot 10^6$). G was found to be 6.73 in the smooth case which is somewhat higher than the values normally specified for flat plate boundary layers, confirming the presence of a slight adverse pressure gradient. The logarithmic region is seen to be well developed in both cases and the wake components collapse on the same curve.

VI. Experimental results

Figure 6 shows the wake profiles for the measurement stations along the line of symmetry. It is seen that the data for rough and smooth surfaces collapse at each station supporting the assumption of a constant G -function. The law-of-the-wall plots in figure 7 show an increasing wake function as separation is approached. For station 18 the logarithmic region has disappeared in the smooth case which most likely is also the case for the rough surface flow making the estimate of c_f questionable. (The solid line is the van Driest formulation of the law-of-the-wall for a smooth surface).

Figure 8 shows the wake profiles for the second streamline. (The profiles for station 21 have been omitted because they are practically identical to those of profile 11). Some deviations are seen at station 28. Possibly it is the result of "forcing" the data to produce a larger logarithmic region than what is physically correct (fig. 9) with results similar to those illustrated in figures 2 and 3. As discussed previously, the method relies on the existence of at least a small but recognizable logarithmic region in the law-of-the-wall plot.

Assuming that the proper length scale for the lateral velocity component in the outer flow is the same as that characterizing the streamwise velocity defect, the crossflow angle has been plotted against $y u_\tau / \delta^* U_e$ as shown in fig. 10. It should be pointed out however, that it is not obvious that the shift of origin should be the same for the streamwise and lateral velocity profiles, as ϵ could depend on the shear velocity in the respective directions. The figure indicates that the magnitude of the crossflow angle close to the wall is not much affected by the surface roughness. In this region the flow angle is primarily determined by a balance of local pressure gradients and the turbulent shear stresses. Further out the crossflow for the rough surface experiment is considerably reduced. Because the extent and shape of the separated region seems to be influenced very little

by the addition of roughness, the height of the separation vortex relative to the boundary layer thickness of the oncoming flow is much reduced in the rough wall case. This will reduce the effective normal pressure gradient which in turn could influence the crossflow angle. Figure 11 shows a polar plot of the same data which clearly shows the differences in the outer flow but agreement near the wall.

Figure 12 shows wake plots for the streamline furthest out from the line of symmetry. The wakes are seen to collapse for rough and smooth surfaces at all stations. The estimated skin friction coefficients along this streamline are considered reliable as all profiles show extensive logarithmic regions (fig. 13). At station 37 the pressure gradient is favourable which results in a wake part that drops below the logarithmic line.

Crossflow angles have been plotted in figure 14 and polar plots are shown in figure 15. The flow along this line differs from that along the other streamline because the pressure gradients are weak and the shear forces relatively more important. This will influence the flow most significantly in the region outside the viscous sublayer extending to about the middle of the boundary layer, where the shear forces have been strongly reduced. It is seen from the crossflow plots that the most significant differences between the smooth and rough data is found up to $y u_\tau / \delta^* U_e$ of about 0.1 corresponding to y / δ of approximately 0.3. For profile 35 the crossflow is increased by almost 50% in this region compared to the smooth case. It has been shown in numerical experiments that these effects can occur if the turbulent shear stresses are anisotropic (Fanneløp and Humphreys²⁵). By reducing the eddy viscosity in the lateral direction substantially more crossflow can be produced. A parametric study of the 3D law-of-the-wall by Ryming and Fanneløp¹⁶ also supports this. For the flow closest to the wall the differences are minor although for profile 37 the rough surface crossflow comes out slightly negative at the wall whereas the smooth data show a small positive angle.

VII. Conclusions

A 3D boundary layer experiment is described where smooth and rough wall data have been obtained for the same geometry and flow conditions.

A method for comparing rough and smooth surface boundary layer data has been described. It is believed that the method gives reliable estimates of the wall skin friction coefficient as well as of the shift in origin, which is required to obtain correct values of the integral length scales.

Because it is impossible to use common surface flow visualization techniques on the rough wall, precise information on the wall flow direction is not available. However, there was little indication that the flow direction in the inner layer is much affected by the surface roughness.

VIII. References

1. Nikuradse, J., NACA TM 1292, 1950.
2. Schlichting, H., Ingenieur-Archiv, Vol. VII, No. 1, 1936.
3. Moore, W.F., Ph.D. dissertation, State Univ. of Iowa, 1951.
4. Perry, A.E., Joubert, P.N., J. Fluid Mech., Vol. 17, 1963.
5. Scottron, V.E., Power, J.L., David Taylor Model Basin, Rep. 2115, 1965.
6. Perry, A.E., Schofield, W.H., Joubert, P.N., J. Fluid Mech., Vol. 37, 1969.
7. Antonia, R.A., Luxton, R.E., J. Fluid Mech., Vol. 48, 1971.
8. Karlson, R.I., Proc. Int. Symp. on Ship Viscous Resistance, 1978.
9. Aswatha Narayana, P.A., Aeronautical Quarterly, 1980.
10. Rotta, J.C., Progress Aeronautical Sciences, Vol. 2, 1962.
11. Dvorak, F.A., AIAA J., Vol. 7, No. 9, 1969.
12. Chan, Y.Y., Nat. Research Council Canada, Aero. Rep. LR-546, 1971.
13. Antonia, R.A., Wood, D.H., Aeronautical Quarterly, 1975.
14. Cebeci, T., Chang, K.C., AIAA J., Vol. 16, No. 7, 1978.
15. Krogstad, P.A., SINTEF Rep. STF 15 A81014, 1981.
16. Ryhming, I.L., Fannelöp, T.K., Proc. IUTAM Symp. Berlin, 1982.

17. Fannelöp, T.K., Proc. IUTAM Symp. Berlin, 1982.
18. Fannelöp, T.K., Ingénierie Navale Arch. Mécanique, Vol. 62, 1951.
19. Clauser, L.H., J. Aeronautical Sci., 1954.
20. Patel, V.C., J. Fluid Mech., Vol. 23, No. 1, 1965.
21. Brown, K.C., Joubert, P.N., J. Fluid Mech., Vol. 35, No. 4, 1969.
22. Winter, K.G., Prog. Aerospace Sci., Vol. 18, 1977.
23. van Driest, E.R., J. Aeronautical Sci., 1956.
24. Fannelöp, T.K., Humphreys, D.A., FFA Rep. 126, 1975.

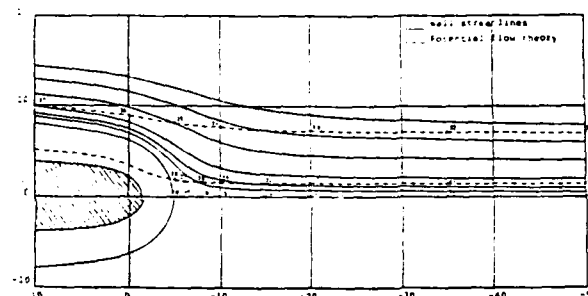


Fig. 1 - Geometry of experiment.

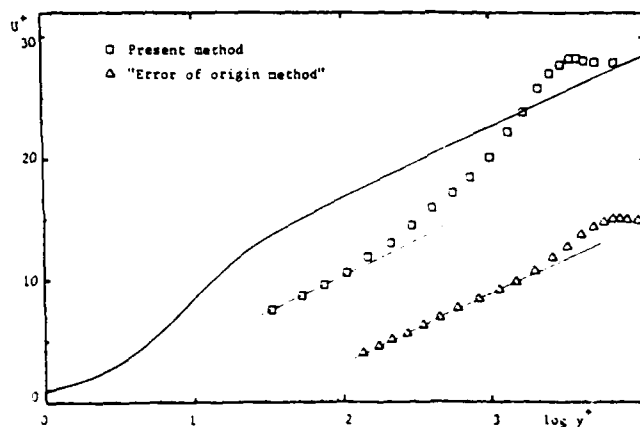


Fig. 2 - Law-of-the-wall plot of profile 16.

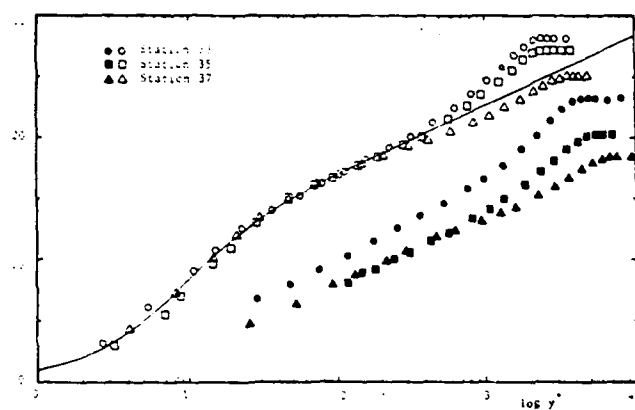


Fig. 13 - Law-of-the-wall plots along outer streamline.

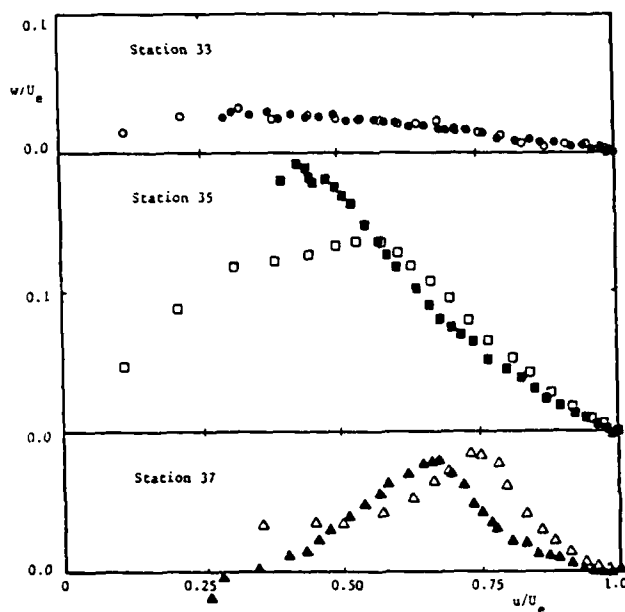


Fig. 15 - Polar plots of profiles 33, 35 and 37.

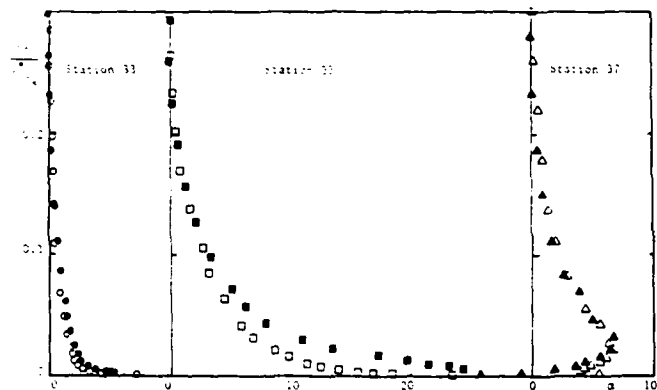


Fig. 14 - Crossflow angles along outer streamline.

THREE-DIMENSIONAL WAKE OF A SWEEP WING

BY

J. COUSTEIX, G. PAILHAS AND B. AUPOIX

ONERA/CERT
2, avenue Edouard Belin
31055 TOULOUSE CEDEX, FRANCE

Abstract

The properties of a turbulent three-dimensional wake behind a swept wing are analyzed. The sweep angle and the incidence have been chosen to generate very dissymmetric initial conditions of the wake. One of the aims of the experiment is to study the relaxation of this initial dissymmetry. The experiment is also aimed at providing a detailed set of data for testing calculation methods and turbulence schemes. For this, detailed measurements of mean velocity profiles and of Reynolds stresses profiles have been carried out. Particular attention has been paid to Reynolds stress measurements. These have been carried out by using several types of hot wire probes (45° slanting sensor probe, X-wire probe and four-wire probe) and the various results are compared.

Two calculation methods have been applied. The first is an integral method and the second is a field method in which the turbulence scheme is a transport equation model. The results are presented and discussed with special emphasis on the turbulence model.

1. INTRODUCTION

The objective of the present experimental study of a turbulent three-dimensional wake is many-sided. First it is aimed at providing a set of data on a flow which has been rarely studied /Ref. 1, 2/. From a fundamental point of view, this flow is interesting because it is a relaxed flow : the initial conditions at the trailing edge, which are very dissymmetric and three-dimensional, are generated on the airfoil by a rather strong adverse pressure gradient which becomes very small in the wake. Therefore, knowledge of turbulence behaviour is valuable for comparison with turbulence modelling. Another aspect of the interest of such data is that more and more calculation procedures of the flow field around an airfoil are taking into account the wake and the three-dimensionality of the flow. Therefore, these data should be useful for validating the calculation methods. Finally such an experiment is also a good opportunity for testing measurement techniques of turbulent three-dimensional flow especially if the Reynolds stress components are considered.

2. EXPERIMENTAL CONDITIONS

The wake is generated by a swept wing mounted between the lateral walls of a subsonic wind tunnel of the EIFFEL type (Fig. 1). The wing section is an ONERA D profile. The chord length is constant and equal to 200 mm. The sweep angle is 22,5°. The angle

of attack is 8° (normal incidence). The free-stream velocity is 35 m/s so that the Reynolds number based on the chord length is $4,7 \cdot 10^5$. The free-stream turbulence level is $\sqrt{u'^2}/U_\infty = 0,7 \%$.

On the suction side, the transition is natural and is caused by a leading edge bubble. On the pressure side, the transition has been tripped by using a wire parallel to the leading edge.

The boundary layers developing on the pressure side and on the suction side have been measured in detail but the results are not given here. They are reported in /Ref. 3/.

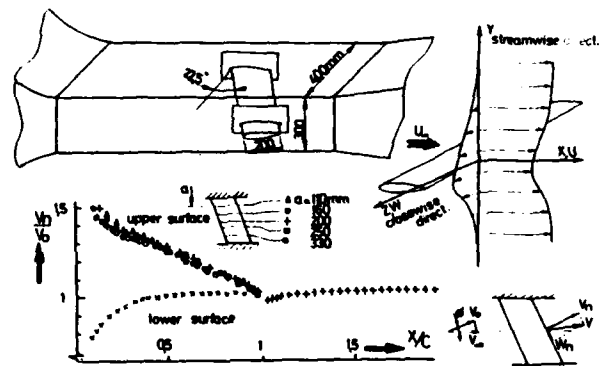


Fig. 1 - Experimental set-up

The static pressure distribution has been measured by using a static pressure probe. From these measurements, an "inviscid velocity" distribution has been deduced and is given in Fig. 1. This figure shows that the suction side boundary layer develops under the effect of an adverse pressure gradient leading to a boundary layer which is almost separated at the trailing edge. Therefore, the three-dimensional effects are very strong : at the trailing edge, the deviation between the wall streamlines and the boundary layer edge streamlines is about 35°. On the contrary, the pressure side boundary layer develops in presence of a favourable pressure gradient so that the three-dimensional effects are very small. Moreover, the thicknesses of the suction side- and pressure side-boundary layers are very different : at the trailing edge, they are respectively about 20 mm and 5 mm ; the shape parameters of the streamwise velocity profiles are also very different : respectively 1.75 and 1.5.

Therefore, it follows that the initial conditions of the wake are strongly dissymmetric. One of the purposes of the experiment is precisely to analyze the evolution and the relaxation of this dissymmetry.

For this, measurements of the mean velocity and of the Reynolds stresses have been performed.

These measurements have been carried out mainly in the vertical median plane of the wind tunnel up to a distance of 1.24 chord length downstream from the trailing edge. However, due to the rather small ratio between the wing chord and the wing span, the flow is not exactly invariant in the spanwise direction. In order to produce a set of data useful for comparison between calculation and experiment, wake measurements have also been performed in off median plane. A total of five planes has been investigated (Fig. 2). The distance between the two extreme planes is 100 mm. All the data are tabulated in /Ref. 3/. In this paper, only characteristic results are given.

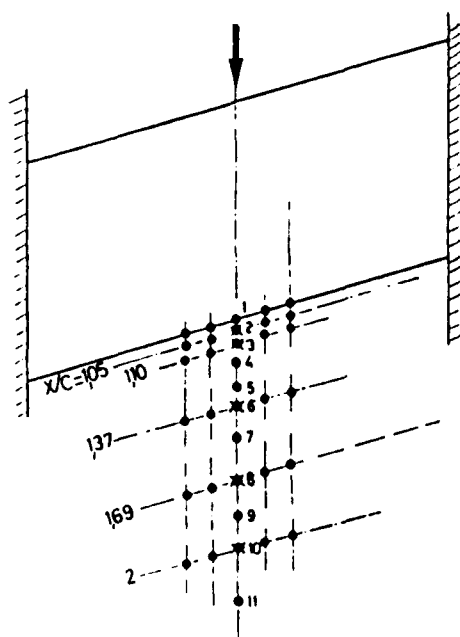


Fig. 2 - Measurement stations
• mean velocity profiles
X Reynolds stress profiles

3. MEAN VELOCITY MEASUREMENTS

The mean velocity has been measured by using a clinometric three tube probe. The probe can rotate about its axis and the velocity direction is known when the two lateral tubes (which are symmetrically 45°-chamfered) indicate the same pressure. In this way, the probe is aligned with the mean velocity, the magnitude of which is known from the pressure measured with the central tube.

The mean velocity is decomposed into streamwise and crosswise components (Fig. 1). The evolution of these components is given in Fig. 3 at several stations located along the vertical median plane of the wind tunnel. In this figure, $y = 0$ represents an horizontal plane containing the trailing edge.

At the trailing edge, the suction side and pressure side-boundary layers lead to very dissymmetric profiles of the streamwise component and of the crosswise component as well. Gradually, there is a symmetrization of these profiles which results in particular in a transfer of three-dimensionality from the upper side to the lower side. At the same time, a flattening of the velocity profiles is observed. It should be noted that the time scales of symmetrization and of flattening of crosswise and streamwise profiles have the same order of magnitude.

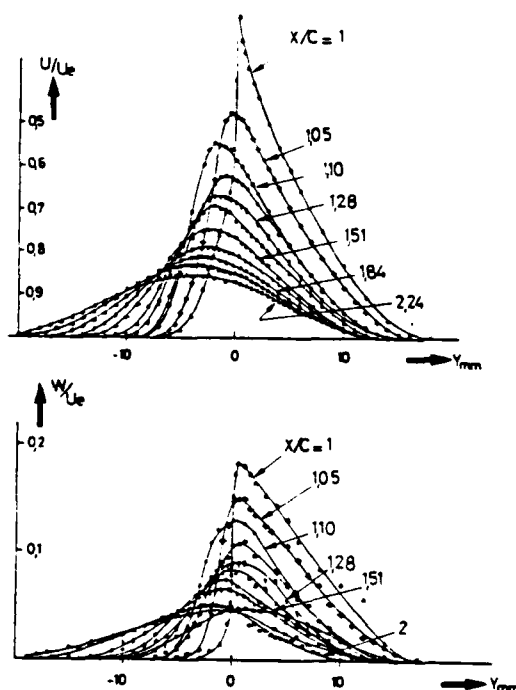


Fig. 3 - Streamwise and crosswise velocity profiles

These evolutions can also be analyzed in the hodograph plane (Fig. 4). Just downstream from the trailing edge, the polar plot becomes a simple closed loop, the pattern of which is very different from that obtained just upstream from the trailing edge: this is due to the sudden removal of the no-slip condition.

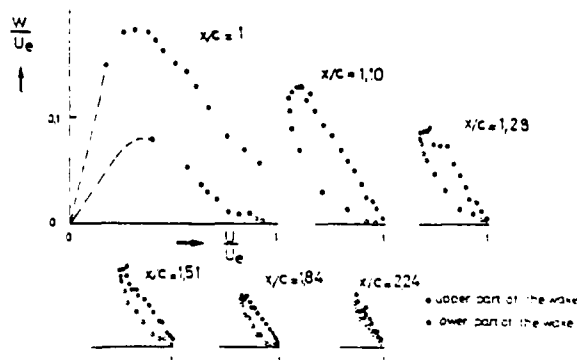


Fig. 4 - Polar plots

It is noted that the points representing the upper side and the lower side become closer and closer because of the symmetrization of the profiles. However, it is difficult to tell if the symmetrization is achieved before or after the limit form is reached (the limit form is defined by the point such that $\frac{u}{u_e} = 1$ and $\frac{W}{U_e} = 0$). In fact, it seems that all these phenomena develop with the same time scale.

The static pressure has also been measured within the wake at several stations (Fig. 5). At stations close to the trailing edge, the static pressure has a maximum near the point of minimum velocity and a normal pressure gradient is observed. Outside the wake, the static pressure is not constant either; it should be noted however that even in inviscid flow, there would be a static pressure variation which is generated by the airfoil. Further downstream, say half a chord length, the normal static pressure gradient becomes negligible.

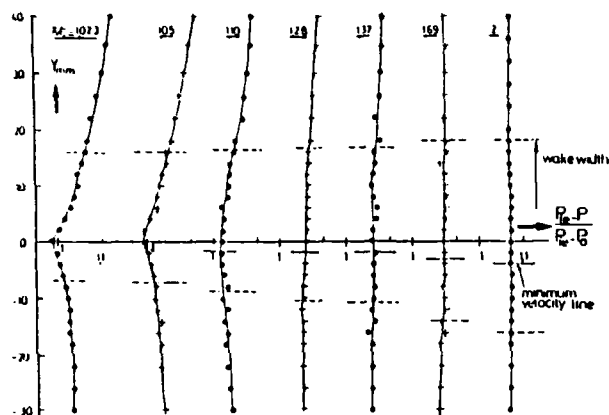


Fig. 5 - Static pressure variations across the wake (P_{ie} : external stagnation pressure - P : local static pressure - P_0 : reference static pressure)

4. REYNOLDS STRESS MEASUREMENTS - EXPERIMENTAL TECHNIQUES

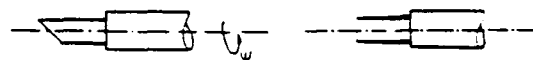
The Reynolds stresses have been measured by using constant temperature hot wire anemometry. Three types of hot wire probes have been used and compared (Fig. 6).

4.1. Method 1 : 45° slanting sensor probe

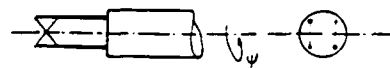
In this case, the probe is placed in the direction of the mean velocity vector at each measurement point, this direction being known from clinometric three tube probe measurements.

It is assumed that the fluctuation of voltage applied to the wire is a linear function of the velocity fluctuations /Ref. 4/.

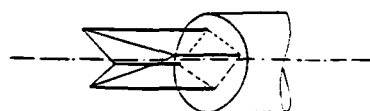
$$(1) \quad e' = k(u' + r(w' \cos \psi + v' \sin \psi))$$



Method 1 : 45° slanting sensor probe (rotating probe) and straight probe



Method 2 : X-wire probe (rotating probe)



Method 3 : four-wire probe (non rotating probe)

Fig. 6 - Hot wire probes

In this formula, ψ is the roll angle of the probe; u' is the velocity fluctuation in the probe-axis direction; v' and w' are velocity fluctuations in a plane orthogonal to the probe-axis; k is the magnitude sensitivity coefficient and r is a directional sensitivity coefficient. These coefficients k and r are determined from calibration.

To get the Reynolds stresses, the r.m.s. values $\overline{e'^2}$ are measured. For any value ψ , the quantity $\overline{e'^2}$ is a function of the six components of the Reynolds stress tensor. Then, $\overline{e'^2}$ must be measured for six different values of ψ . However, this is not sufficient because the system so obtained is indeterminate and it is necessary to perform an extra measurement. The simplest consists of measuring $\overline{u'^2}$ with a straight probe aligned with the mean velocity vector.

This procedure is very time-consuming since three steps are needed: the mean velocity is first measured; then, $\overline{u'^2}$ is determined with a straight probe and finally the five other components of the Reynolds stress tensor are calculated from the r.m.s. values of $\overline{e'^2}$ measured for five ψ angles. In fact, to improve the accuracy, $\overline{e'^2}$ has been measured for eight values of ψ and the Reynolds stresses have been calculated by using a least square method.

4.2. Method 2 : X-wire probe

The second method which has been tested uses a X-wire probe (Fig. 6). In this case also the probe has been aligned with the mean velocity vector and measurements are performed for several values of the ψ angle.

However, there is a difference with the method described previously. In effect, for each value of Ψ , in addition to the r.m.s. values of the voltages applied to each wire, an additional independent piece of information is available: this is the correlation between each voltage. Moreover, this method no longer needs the independent measurement of u'^2 .

4.3. Method 3 : four-wire probe

The third method uses a four-wire probe which consists of a set of two X-wire probes (Fig. 6). The four wires are electrically independent. With this probe, it is possible to measure the six components of the Reynolds stress tensor without rotating the probe. To define a quite efficient procedure, it is interesting to measure the mean velocity and the Reynolds stresses in the same single operation. This means that the direction of the probe with respect to the mean velocity vector is a priori unknown. In this case, it becomes necessary to use a hot wire law containing two directional sensitivity coefficients.

$$(2) \quad e^2 = e_o^2 + B U_{eff}^{1/m}$$

e_o is the zero velocity voltage and B and m are coefficients determined from calibration. U_{eff} is an effective velocity defined as :

$$(3) \quad U_{eff}^2 = U_n^2 + k_1^2 U_t^2 + k_2^2 U_s^2$$

where U_n is the velocity component parallel to the wire, U_t is orthogonal to the wire (in the plane of the wire and the prongs) and U_s is orthogonal to U_n and U_t . k_1 and k_2 are directional coefficients determined from calibration.

With this kind of probe, the instantaneous values of the voltages applied to the four wires are measured. From them, the three components U_n , U_t , U_s are calculated by using a least square method. After, the mean velocity components are calculated from a statistical treatment of a sampling of a great number of values of U_n , U_t , U_s . The next step consists of calculating the fluctuations u'_n , u'_t , u'_s and a statistical treatment enables us to know the Reynolds stresses.

Obviously, this method is much more attractive than the first two methods since the instantaneous values of fluctuations are known. It can, therefore, be imagined that a lot of turbulence characteristics can be deduced, such as, for example, spectra, time correlations...

5. REYNOLDS STRESS MEASUREMENTS - RESULTS

5.1. Comparisons of measurements techniques

The various techniques have been compared at several stations. Here, only a sample of these comparisons is given. Figure 7 shows the comparison of mean velocity profiles measured either with the clinometric three-tube probe or with the four-wire probe. The agreement is pretty good even for the crosswise velocity which is rather small compared with the streamwise velocity. This demonstrates the good directional sensitivity of the four-wire probe.

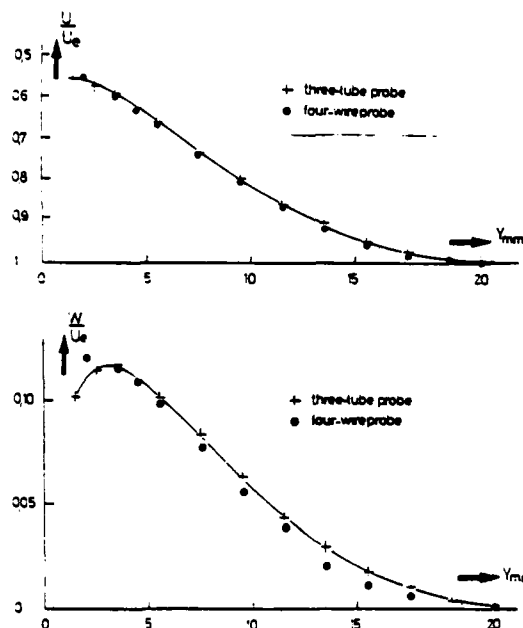


Fig. 7 - Comparison of streamwise and crosswise velocity profiles ($X/C = 1.10$)

Figure 8 shows comparisons of v'^2 , $u'v'$ and $v'w'$ measured either with the 45° slanting sensor probe or with the four-wire probe at stations $x/c = 1.10$.

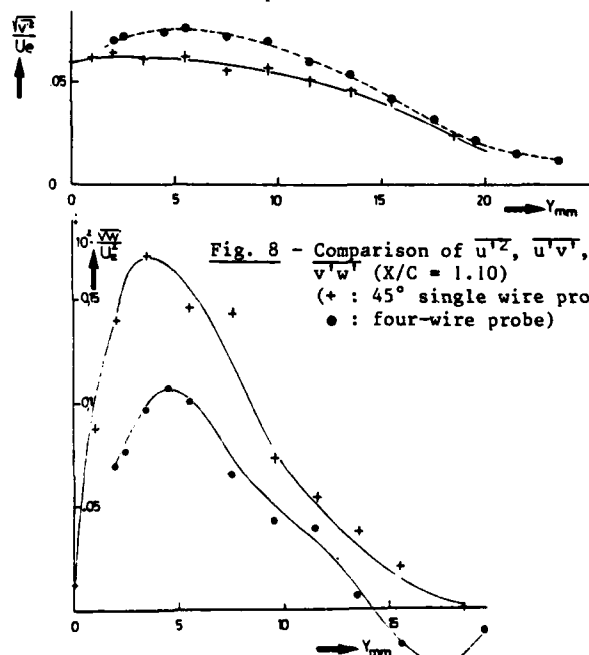
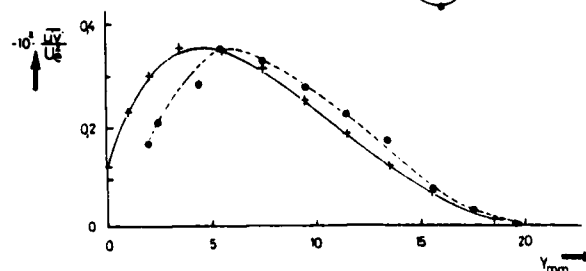


Fig. 8 - Comparison of u'^2 , $u'v'$, $v'w'$ ($X/C = 1.10$)
(+ : 45° single wire probe
• : four-wire probe)



The overall agreement seems acceptable. The largest discrepancies are obtained on the $\overline{v'w'}$ component. It should be noted, however, that $\overline{v'w'}$ is smaller than the other five Reynolds stress components. In addition $\overline{v'w'}$ is the most difficult correlation to measure. In the case of the technique using the 45° slanting sensor probe, the measurements of $\overline{e'^2}$ for two values of ψ ($\psi = 0$ and $\psi = 180^\circ$) enable us to determine $\overline{u'w'}$ if $\overline{u'^2}$ is known. Indeed, we have :

$$(4) \overline{e'^2}(\psi = 0^\circ) = k^2 (\overline{u'^2} + r^2 \overline{w'^2} + 2r \overline{u'w'})$$

$$(5) \overline{e'^2}(\psi = 180^\circ) = k^2 (\overline{u'^2} + r^2 \overline{w'^2} - 2r \overline{u'w'})$$

On the contrary, $\overline{v'w'}$ can be determined only from equations containing the six components of the Reynolds stress tensor. Therefore, all the inaccuracies are accumulated on $\overline{v'w'}$.

Figure 9 shows comparisons of $\overline{v'^2}$, $\overline{u'v'}$ and $\overline{v'w'}$ measured either with the 45° slanting sensor probe or with the X-wire probe at station $x/c = 1.69$. The overall agreement between the two techniques seems slightly better than that observed in figure 8 between the 45° slanting sensor probe and the four-wire probe. Possibly, this is due to the fact that there is a closer resemblance between methods 1 and 2 than between methods 1 and 3.

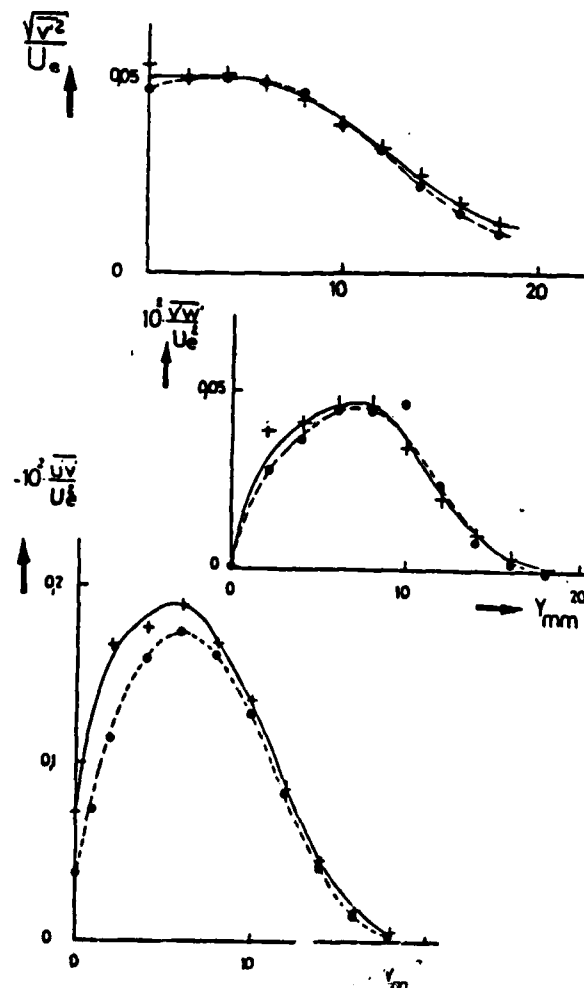


Fig. 9 - Comparison of $\overline{v'^2}$, $\overline{u'v'}$, $\overline{v'w'}$ (+ : X-wire probe - o : 45° slanting sensor probe)

5.2. Results

Figure 10 gives the evolutions of $\overline{u'^2}$, $\overline{u'v'}$, $\overline{v'w'}$ and $\overline{u'w'}$ at several stations located in the median vertical plane of the wind tunnel. Let us specify that these stresses are expressed in a local axis system. This means that u' is aligned with the mean local velocity, v' is orthogonal to u' such that the plane (u' , v') is vertical and w' is orthogonal to u' and v' .

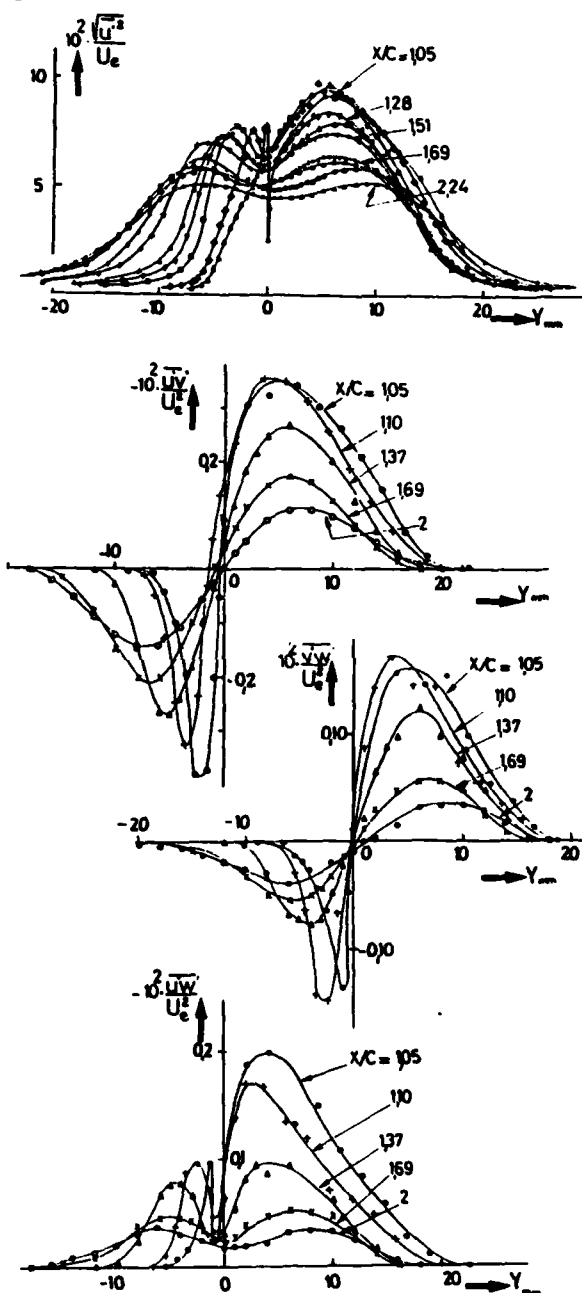


Fig. 10 - Evolution of $\overline{u'^2}$, $\overline{u'v'}$, $\overline{v'w'}$ and $\overline{u'w'}$ ($X/C = 1.69$)

The component $\overline{u'^2}$ has been measured with a straight probe aligned with the mean velocity vector.

At the trailing edge, the profile is very dissymmetric. On the lower side ($y < 0$), the profile has a peak near $y = 0$ and it looks like a flat plate boundary layer profile. On the upper side ($y > 0$), the profile has a bump located at one third of the thickness of the boundary layer; this reflects the existence of a positive pressure gradient on the suction side of the airfoil. Downstream, a progressive symmetrization is observed. At $\bar{x}/c = 2.24$, the overall feature is that of a classic two-dimensional wake but the profile is still significantly dissymmetric.

The profiles of $\overline{u'v'}$, $\overline{v'w'}$ and $\overline{u'w'}$ are also very dissymmetric at the trailing edge and become more symmetric downstream. More precisely, the profiles of $\overline{u'v'}$ and $\overline{v'w'}$ tend to be antisymmetric whereas $\overline{u'w'}$ tends to be symmetric. It is noted that the magnitude of $\overline{u'w'}$ is of the same order as the one of $\overline{u'v'}$ and $\overline{v'w'}$.

5.3. Analysis of the cross correlations

The evolution of the cross correlations can be analyzed by considering a turbulence model as the one proposed by LAUNDER-REECE-RODI /Ref. 5/.

If the modelled Reynolds stress equations are simplified by neglecting the convection and diffusion terms and if only the components $\frac{\partial U}{\partial y}$ and $\frac{\partial W}{\partial y}$ of the velocity gradient are considered, simple expressions of Reynolds stresses are obtained. In a cartesian coordinate system, these are :

$$(6) - \overline{u'v'} = v_t \frac{\partial U}{\partial y}$$

$$(7) - \overline{w'v'} = v_t \frac{\partial W}{\partial y}$$

$$(8) - \overline{u'w'} = +2 \frac{C_2 - 3}{11C_1} \frac{k}{\epsilon} v_t \frac{\partial U}{\partial y} \frac{\partial W}{\partial y}$$

where the index l means that the velocity components are defined in a cartesian system. In the local streamline coordinate system, the Reynolds stresses are :

$$(9) - \overline{u'v'} = v_t \frac{\partial u}{\partial y}$$

$$(10) - \overline{w'v'} = v_t u \frac{\partial \gamma}{\partial y}$$

$$(11) - \overline{u'w'} = +2 \frac{C_2 - 3}{11C_1} \frac{k}{\epsilon} v_t \frac{\partial u}{\partial y} u \frac{\partial \gamma}{\partial y}$$

where γ is the direction of the mean velocity with respect to any given axis (for example, γ can be defined as $\gamma = \tan^{-1}(W_1/U_1)$). Proposed values of constants are $C_1 = 1.5$ and $C_2 = 0.4$.

In the above expressions, k and ϵ are the turbulent kinetic energy and its dissipation rate and v_t is the eddy viscosity coefficient.

Figure 10 shows that $\overline{u'w'}$ is negative in the whole thickness of the wake. This is coherent with formula 8 because both quantities $\frac{\partial u}{\partial y}$ and $\frac{\partial \gamma}{\partial y}$ change their sign at almost the same location in the wake. In fact, it could be that there is a thin region where $\overline{u'w'}$ is positive but this has not been detected from experiments.

The formulae 9, 10 show that $\overline{u'v'}$ and $\overline{w'v'}$ resp.

are zero when U and γ resp. are extrema. This property is not exactly verified in experiments because the zeros of $\overline{u'v'}$ and $\overline{w'v'}$ are slightly shifted with respect to the extrema of u and γ . However, not too close to the points where $\overline{u'v'}$ and $\overline{w'v'}$ are zero, the signs of these correlations are in agreement with the ones given by formulae 9, 10. In addition, expressions 9, 10 show that the vector of components $(\overline{u'v'}, \overline{w'v'})$ is aligned with the y -derivative of mean velocity. To check this, the parameter N defined as :

$$(12) N = \frac{\tan(\gamma_t - \gamma)}{\tan(\gamma_g - \gamma)}$$

is plotted in figure 11. In this definition (12) of N , the quantities $(\gamma_t - \gamma)$ and $(\gamma_g - \gamma)$ define respectively the directions of vector $\vec{\tau}(\overline{u'v'}, \overline{w'v'})$ and of the y -derivative $\frac{\partial \vec{V}}{\partial y}$ of the mean velocity with respect to the direction of mean velocity.

The parameter N is equal to 1 if $\vec{\tau}$ and $\frac{\partial \vec{V}}{\partial y}$ are aligned. Figure 11 shows that N is around 1 but there is a rather large scatter in experimental values which is due to the difficulty in measuring the Reynolds stresses $\overline{v'w'}$ and $\overline{u'v'}$.

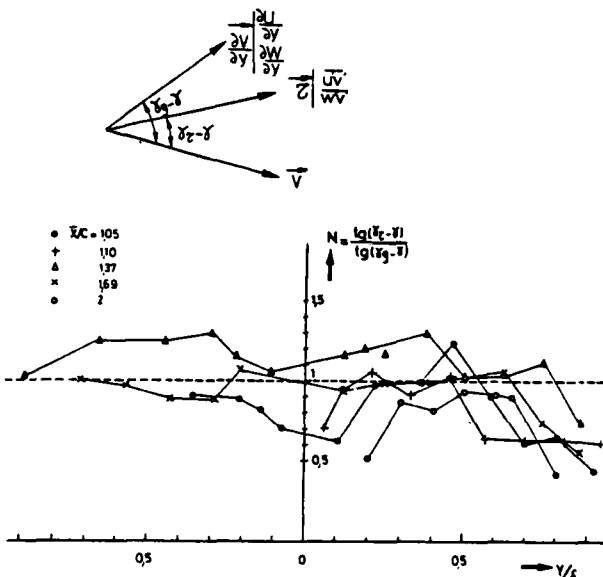


Fig. 11 - Evolution of N

6. CALCULATION METHODS

Two calculation methods have been implemented : the simpler method consists in solving the global equations of the wake and the more elaborate uses the partial differential equations by introducing a transport equation model.

6.1. Integral method

The integral method is based on the solution of global equations which are the momentum equations and the continuity equation integrated with respect to y between the lower and the upper boundaries of the wake. The main unknowns of the equations are characteristic thicknesses between which closure relationships are needed to solve the system of equations. To obtain these relationships,

a representation of the velocity profiles is needed. For this, rather crude hypotheses have been made. The streamwise velocity profile is divided into two parts : 1) one between the minimum velocity point and the lower boundary of the wake ; 2) the other between the minimum velocity point and the upper boundary of the wake.

Each part is represented by a profile used in two-dimensional flow :

$$(13) \quad \frac{U_e - u}{U_{\min} - u} = \left[\left(\frac{y}{\delta} \right)^{3/2} - 1 \right]^2$$

The crosswise velocity profile is determined by using a simplified representation of the polar plot which is assumed to be a triangle as shown in figure 12.

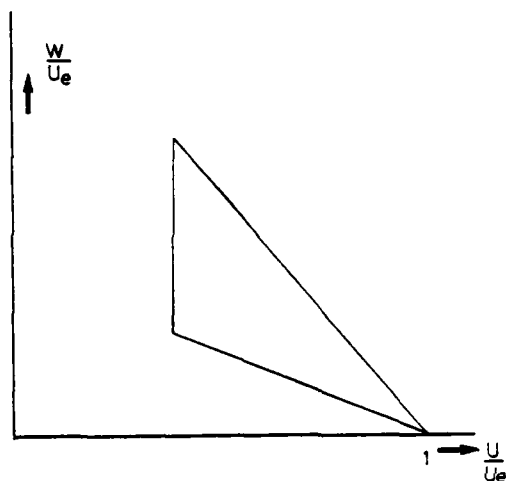


Fig. 12 - Simplified representation of polar plot in a wake

The continuity equation also needs the specification of the entrainment coefficient for each half part of the wake. This coefficient is :

$$(14) \quad C_E = \frac{\partial \delta}{\partial s} - \frac{v_e}{U_e}$$

where δ is the thickness of the lower (or upper) part of the wake, s is the coordinate along the external streamlines, U_e is the velocity magnitude at the wake boundary and v_e is the normal velocity component at the wake boundary. This coefficient is calculated by a formula used in two-dimensional flow :

$$(15) \quad C_E = 0,14 \frac{U_e - U_{\min}}{U_e}$$

In the method which has been developed, the upper and lower points of the wake are calculated separately. For this, global equations are written for each part of the wake and further hypotheses are introduced : 1) the points of minimum streamwise velocity and of maximum crosswise velocity are assumed to be at the same location ; 2) at this point, the shear stress components are assumed to be equal to zero.

Obviously, all the hypotheses introduced in the integral method are very crude but this method has been developed with the aim of providing a simple and practical tool.

6.2. Transport equation model

The partial differential equations of the wake have been solved by using either a two-equation model or a four-equations model. In both cases, the equations for the turbulent kinetic energy and its dissipation rate are used. In a cartesian coordinate system, they are :

$$(16) \quad \frac{Dk}{Dt} = - \overline{u'v'} \frac{\partial U}{\partial y} - \overline{v'w'} \frac{\partial W}{\partial y} - \epsilon + \frac{\partial}{\partial y} \left(\frac{\nu_T}{\sigma_k} \frac{\partial k}{\partial y} \right)$$

$$(17) \quad \frac{D\epsilon}{Dt} = - C_{\epsilon 1} \frac{\epsilon}{k} \left(\overline{u'v'} \frac{\partial U}{\partial y} + \overline{v'w'} \frac{\partial W}{\partial y} \right) - C_{\epsilon 2} \frac{\epsilon^2}{k} + \frac{\partial}{\partial y} \left(\frac{\nu_T}{\sigma_\epsilon} \frac{\partial \epsilon}{\partial y} \right)$$

$$\text{with } \nu_T = C_\mu \frac{k^2}{\epsilon}$$

The modifications proposed by ROTTA /6/ for calculating $\overline{u'v'}$ and $\overline{v'w'}$ have been tested. If four-equation model is used, the $\overline{u'v'}$ - and $\overline{v'w'}$ -equations are :

$$(18) \quad \frac{D}{Dt} \overline{u'v'} = -k \left(a_{pxx} \frac{\partial U}{\partial y} + a_{pxz} \frac{\partial W}{\partial y} \right) - C_1 \frac{\epsilon}{k} \overline{u'v'} + \frac{\partial}{\partial y} \left(\frac{\nu_T}{\sigma_\tau} \frac{\partial}{\partial y} \overline{u'v'} \right)$$

$$(19) \quad \frac{D}{Dt} \overline{v'w'} = -k \left(a_{pzx} \frac{\partial U}{\partial y} + a_{pzz} \frac{\partial W}{\partial y} \right) - C_1 \frac{\epsilon}{k} \overline{v'w'} + \frac{\partial}{\partial y} \left(\frac{\nu_T}{\sigma_\tau} \frac{\partial}{\partial y} \overline{v'w'} \right)$$

$$(20) \quad \text{with } a_{pxx} = C_{\tau 1} \frac{U^2 + W^2}{U^2 + W^2}$$

$$(21) \quad a_{pzx} = a_{pxz} = C_{\tau 1} (1 - T) \frac{UW}{U^2 + W^2}$$

$$(22) \quad a_{pzz} = C_{\tau 1} \frac{TU^2 + W^2}{U^2 + W^2}$$

If a two-equation model is used, $\overline{u'v'}$ and $\overline{v'w'}$ are calculated from :

$$(23) \quad -\overline{u'v'} = \frac{\nu_T}{C_{\tau 1}} \left(a_{pxx} \frac{\partial U}{\partial y} + a_{pxz} \frac{\partial W}{\partial y} \right)$$

$$(24) \quad -\overline{v'w'} = \frac{\nu_T}{C_{\tau 1}} \left(a_{pzx} \frac{\partial U}{\partial y} + a_{pzz} \frac{\partial W}{\partial y} \right)$$

In these models, a new parameter T has been introduced. Formulae (23) and (24) clearly show the effect of this parameter : when $T = 1$, a classic model is obtained, in which the vector $\vec{\tau}$ of components $(\overline{u'v'}, \overline{v'w'})$ is aligned with the vector $\frac{\partial \vec{v}}{\partial y}$ of components $(\frac{\partial U}{\partial y}, \frac{\partial W}{\partial y})$; when $T \neq 1$, $\vec{\tau}$ is no longer aligned with $\frac{\partial \vec{v}}{\partial y}$. In fact, when $\overline{u'v'}$ and $\overline{v'w'}$ are calculated from equations (23), (24), the parameter T is exactly identifiable with the parameter N defined by equation (12) ; this is no longer true when $\overline{u'v'}$ and $\overline{v'w'}$ are calculated from transport equations (18), (19).

6.3. Results

The integral method and the transport equation models have been applied to the previously described experiments. The partial differential equations

have been solved by assuming invariance in the direction parallel to the trailing edge (infinite swept wing hypothesis). This is not exactly true in particular because initial conditions of the wake (at the trailing edge) are not invariant in the spanwise direction. The influence of the initial conditions has been studied by using the integral method. For this, two calculations have been performed : one takes into account the variations of initial conditions, the other does not. The differences between the results are not absolutely negligible but they are rather small.

A sample of results obtained from the various calculation methods is given in figures 13, 14, 15. The shape factor H is defined from streamwise velocity profiles ($H = \int (1 - \frac{u}{u_e}) dy / \int \frac{u}{u_e} (1 - \frac{u}{u_e}) dy$) and the thicknesses δ_2 and θ_{12} are defined from cross-wise velocity profiles ($\delta_2 = \int -\frac{w}{u_e} dy$; $\theta_{12} = \int \frac{w}{u_e} (1 - \frac{u}{u_e}) dy$).

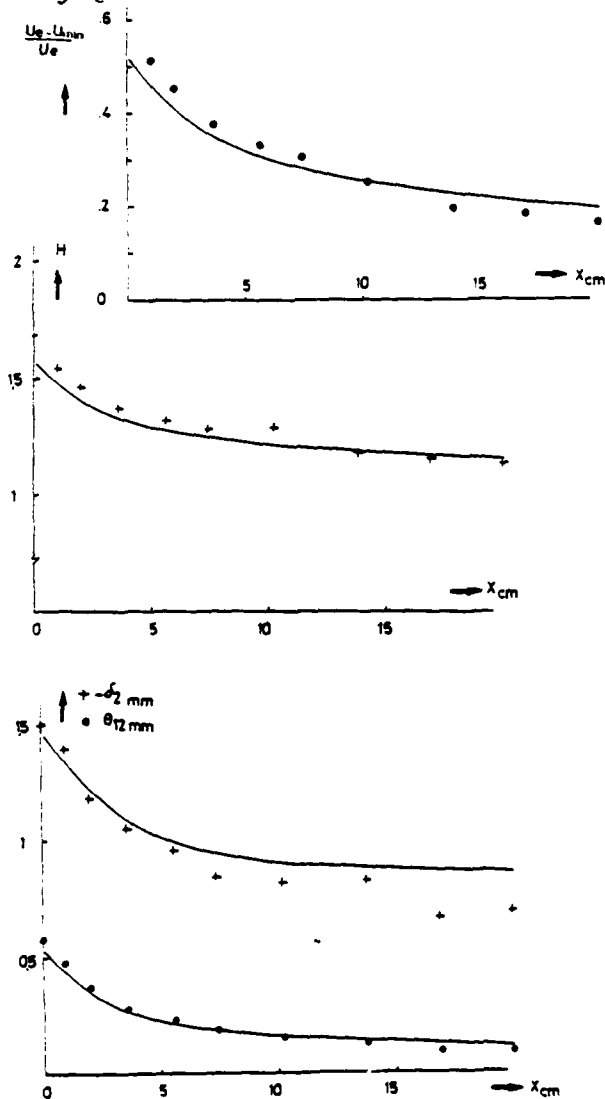


Fig. 13 - Comparisons between experiments and calculations : • + experiment
— integral method

The various methods give nearly the same overall agreement on the evolutions of the shape factor H , the minimum streamwise velocity and the thicknesses θ_{12} and δ_2 . The transport equation model gives, however, better results in the immediate vicinity of the trailing edge. The results obtained from the two-equation model, not represented here, are practically the same as those obtained from the four-equation model.

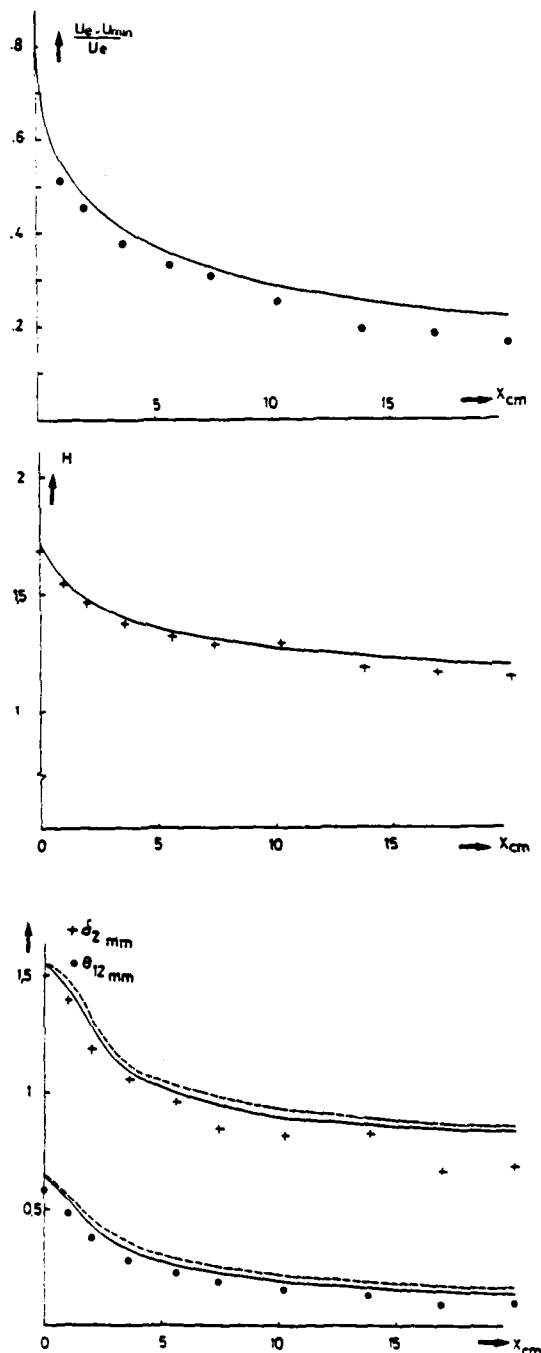


Fig. 14 - Comparisons between experiments and calculations : • + experiment
— four-equation model $T = 1$
--- four-equation model $T = 0.5$

With the transport equation model, two values of T have been tested: $T = 1$ and $T = 0.5$. The influence of this variation of T on the shape factor and on the minimum streamwise velocity is negligible whereas small variations of the thicknesses δ_2 and θ_{12} are observed. Nevertheless, the effect of T on δ_2 and θ_{12} is not representative of its effect on the crosswise velocity profiles (Fig. 15). It can be said that T plays the role of a time constant for the decay of the crosswise velocity. With $T = 0.5$, the evolution of the crosswise velocity profiles is too slow: the decay and the symmetrization of this profile are not fast enough. The value $T = 1$ gives a reasonable agreement with experiments.

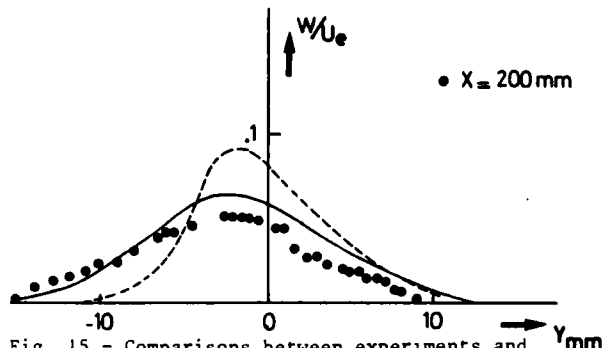


Fig. 15 - Comparisons between experiments and calculation • experiment — four-equation model $T=1$ --- four-equation model $T=0.5$

It appears, therefore, that a simple hypothesis leading to an alignment between $\vec{\tau}$ and $\frac{\partial \vec{v}}{\partial y}$ is acceptable for calculating such a three-dimensional wake flow. This is at variance with certain other cases of boundary layer flow [Ref. 4]. In fact, it is believed that the validity of the hypothesis that $\vec{\tau}$ and $\frac{\partial \vec{v}}{\partial y}$ are aligned depends on the nature of the

flow, more precisely if extra rate of strain terms are important or not. Let us explain this. The main feature of the present experiment is that the flow is a relaxed flow. This implies that, except near the trailing edge, the evolution of any characteristic is slow and parameters such as streamline curvature or longitudinal derivatives of mean velocity have negligible effects. Then, the dominant terms of the velocity gradient are the y -derivatives $\frac{\partial U}{\partial y}$ and $\frac{\partial W}{\partial y}$. This hypothesis, introduced in the Reynolds stress equations modelled by LAUNDER et al., leads to the results given in section 5.3: the vector $\vec{\tau}$ is aligned with the y -derivative of mean velocity. On the contrary, in three-dimensional boundary layers submitted to strong pressure gradient (as is the case of Ref. 4), parameters such as streamline curvature are certainly not negligible and terms other than $\frac{\partial U}{\partial y}$ and $\frac{\partial W}{\partial y}$ (i.e. $\frac{\partial U}{\partial x}$, $\frac{\partial U}{\partial z}$, $\frac{\partial W}{\partial x}$, $\frac{\partial W}{\partial z}$...) should be retained in the complete Reynolds stress equations modelled by LAUNDER et al.. This would lead to a non-alignment between $\vec{\tau}$ and $\frac{\partial \vec{v}}{\partial y}$. In fact, ELSENAAR-BOELSMA's measurements indicate that $\vec{\tau}$ and $\frac{\partial \vec{v}}{\partial y}$ are not aligned. This is why ROTTA tried to develop his model by introducing the parameter T . Unfortunately, the value of T is certainly not universal: to get a good agreement with ELSENAAR-BOELSMA's experiments, a value of T of the order 0.7 is needed,

whereas the comparisons with the present experiments show that a value $T = 1$ is more appropriate. It is believed that the right way for obtaining a good model for calculating three-dimensional thin shear layers is not the use of the parameter T . Possibly, the solution could be to keep in the modelled Reynolds stress equations extra rate of strain terms, i.e.

terms in $\frac{\partial U}{\partial x}$, $\frac{\partial U}{\partial z}$, $\frac{\partial W}{\partial x}$, $\frac{\partial W}{\partial z}$... This means that the boundary layer hypotheses, even if they are acceptable for momentum equations, are not necessarily valid for the Reynolds stress equations: a small extra rate of strain term in the Reynolds stress equation can have a strong effect on the calculation of Reynolds stresses.

7. CONCLUSION

The experimental study of a three-dimensional turbulent wake has led to a set of data consisting of mean velocity profiles and of the six components of the Reynolds stress tensor profiles. Since the flow is not invariant in the spanwise direction, the investigation has not been restricted to a single plane of measurements.

Three different hot wire techniques of Reynolds stresses measurements have been tested and compared. The agreement between the various results is not perfect but is sufficiently good to credit the measurements with a certain level of confidence. In particular, it is interesting to note that the four-wire probe works quite well. As discussed in section 4.3., it can be hoped that it could be used for measuring turbulence characteristics other than the Reynolds stresses.

A simple integral technique for calculating the wake development has been elaborated. Comparing the results with experimental data shows that the integral properties of the wake are rather well determined and therefore, it can be thought, such a method could be fruitfully included in an interactive technique for calculating the three-dimensional flow field around a wing.

If more details about wake development are wanted, the partial differential equations are solved. In this case, a turbulence scheme is needed. Comparisons with experiments have shown that a simple model in which the shear stress is assumed to be aligned with the y -derivative of mean velocity works quite well. Therefore, the model including a prescribed value of T different from 1 is not correct. It is believed that a model capable of describing a large variety of thin shear layers should include extra rate of strain terms such as those reflecting the curvature of streamlines.

REFERENCES

- /1/ FIRMIN, "Measurements of the mean flow in three-dimensional turbulent boundary layers near the rear of the swept wing at subsonic speeds and moderate Reynolds numbers" - Lecture at Euromech 33, BERLIN, 1972
- /2/ NOVAK C.J., RAMAPRIAN B.R., "Measurements in the wake of an infinite airfoil" - IOWA Institute of Hydraulic Research, IIHR Report n° 240, April 1982

- /3/ COUSTEIX J., PAILHAS G., "Measurements of mean velocity and Reynolds stress tensor within a wake of a swept wing" - Rapport Technique OA 41/2259 AYD, Octobre 1980
- /4/ ELSENAAR A., BOELSMA, "Measurements of the Reynolds stress tensor in a three-dimensional boundary layer under infinite swept wing conditions" - NLR, TR 74095 U (1974)
- /5/ LAUNDER B.E., REECE G.J., RODI W., "Progress in the development of a Reynolds stress turbulence closure" - Journal of Fluid Mech., Vol. 68, Part 3, pp. 537-566 (1975)
- /6/ ROTTA J.C., "A family of turbulence models for three-dimensional thin shear layers" - First Symposium on Turbulent Shear Flows, 1977, Penn. State University

THREE-DIMENSIONAL BOUNDARY-LAYER CALCULATIONS ON WINGS, STARTING FROM THE FUSELAGE

J.P.F. Lindhout, B. van den Berg, A.C. de Bruin
National Aerospace Laboratory NLR
Amsterdam, The Netherlands

Abstract

Computation of a Wing Boundary Layer

To compute the three-dimensional turbulent boundary layer on wings, it is required by many methods to prescribe initial data on a line of constant chord percentage and data at the lateral boundaries of the computational domain. At NLR a method is developed which requires a minimum amount of data to be prescribed at initial lines or boundaries. For a general configuration, the boundary-layer flow is computed in the region of determinacy of the initial data. A point is situated in the region of determinacy if all the streamlines through the corresponding normal can be traced back to the line of initial data. If we consider the pattern of edge- and wall-streamlines for attached flow on a wing, it is clear that almost the complete wing is covered by streamlines emerging from the wing-body junction near the leading edge. Therefore, the flow in the covered region can be computed from initial data given at that very position. The calculations are performed in three stages: the computation marches from the leading-edge-wing-body junction between two lines of constant chord. Data are found by this computation on the lateral boundaries. Then the program continues with the upper and lower surfaces employing the data at the chord lines as initial conditions.

Description of the Method

The general features of the method (1) are given below: An eddy viscosity turbulence model is implemented. Although there exist much more advanced turbulence models, it is difficult to do

better than simple eddy viscosity models, especially for pressure driven flow. The equations are dealt with in a general nonorthogonal coordinate system. For each new configuration a subroutine has to be written with which the geometric quantities are computed. An expanding library of configuration subroutines can be considered as a part of the method.

A hybrid difference scheme is used combining the simpleness and stability properties of first-order schemes and the accuracy of second-order schemes. These difference approximations are contained in implicit as well as explicit difference molecules. Explicit difference molecules suffer from stability restrictions on the stepsizes in marching direction. A computational sequence is adopted exploiting implicit molecules as much as possible.

The boundaries of the computational domain are treated mathematically correct: no redundant information is required for outflow boundaries neither data is found on it by extrapolation for inflow conditions. The boundaries are constructed such that only outflow can occur across the boundaries. This requires difference molecules which are not aligned along the coordinate lines.

Reference

1. Lindhout, J.P.F., Moek, G., de Boer, E. and van den Berg, B.: A method for the calculation of 3-D boundary layers on practical wing configurations. Joint ASME/CSME Applied Mechanics Fluids Engineering and Bioengineering Conf., Niagara Falls, 1979.

THE QUASI-SIMULTANEOUS CALCULATION OF STRONGLY INTERACTING VISCOUS FLOW AROUND AN INFINITE SWEEP WING

A. E. P. Veldman and J.P.F. Lindhout
National Aerospace Laboratory NLR
Amsterdam, The Netherlands

Abstract

Introduction

The "classical" way of calculating boundary layers and wakes, by prescribing a pressure distribution, gives rise to (large) difficulties in regions where a strong interaction exists between the viscous and inviscid parts of the flow field. Using inverse techniques, in which displacement thickness or wall shear is prescribed, these difficulties can be overcome. However, sufficiently accurate starting values for these quantities are generally not available. The appropriate values have to be obtained, as part of the overall problem, from the interaction between the viscous layer and the external flow; thus a method which iterates frequently between the viscous and inviscid parts of the flow field is required.

A semi-inverse method has been introduced a few years ago by le Balleur (ref. 1). In regions with strong interaction he solves the viscous flow equations with prescribed displacement thickness; the regions where the interaction is weak are treated in the "classical" (direct) way.

A somewhat different numerical strategy is being followed by NLR (ref. 2). Here the viscous flow equations are solved using a boundary condition which prescribes, essentially, a linear combination of pressure and displacement thickness. This combination, called the interaction law, is chosen such that it gives an approximate (but adequate) description of the outer flow. As the interaction law is treated simultaneously with the viscous flow equations we have termed the method quasi-simultaneous.

Treatment of the Interaction

Briefly, the quasi-simultaneous method can be sketched as follows. For ease of presentation, let the coupling between the viscous region and the external flow region be performed in terms of pressure p and displacement thickness δ^* . Then in each part of the flow field a relation exists between p and δ^* . In operator notation we will write these as

$$\text{external flow region: } p = P\delta^*, \quad (1)$$

$$\text{boundary-layer/wake: } p = B\delta^*, \quad (2)$$

In order to facilitate a simultaneous numerical treatment of viscous and inviscid flow, the exter-

nal flow description is approximated by a simplified version

$$\text{interaction law: } p = I\delta^* \quad (3)$$

The equations (2) and (3) are treated simultaneously (for details see ref. 2). The external flow description (1) is incorporated by means of an outer iterative process

$$p(k) - I\delta^*(k) = p\delta^*(k-1) - I\delta^*(k-1)$$

$$p(k) - B\delta^*(k) = 0$$

such that upon convergence ($k \rightarrow \infty$) the solution satisfies the exact relations (1) + (2).

Choice of Flow Equations

The above description allows a large flexibility with regards to the choice of the viscous and inviscid flow equations. At the conference we will present results for two-dimensional flow past an infinite swept wing. The flow equations are chosen as follows:

- The viscous part of the flow is described by compressible boundary-layer equations. Normal pressure gradients can be included. Turbulence is incorporated by means of a zonal mixing length model.
- The matching with the external flow is performed by means of a higher-order outflow concept.
- The interaction law is based on thin-airfoil theory with leading-edge separation.
- The external flow is taken to be incompressible.

References

1. le Balleur, J.C.: Calcul des écoulements a forte interaction visqueuse au moyen de methods de couplage. AGARD-CP 291, Computation of viscous-inviscid interactions, Paper 1, 1980.
2. Veldman, A.E.P.: The calculation of incompressible boundary layers with strong viscous-inviscid interaction. AGARD-CP 291, Computation of viscous-inviscid interactions, Paper 12, 1980.

SESSION 8

TRANSONIC SMALL DISTURBANCE CALCULATIONS INCLUDING ENTROPY CORRECTIONS

M. Hafez and D. Lovell
The George Washington University/NASA-Langley Research Center
Hampton, Virginia

Abstract

Murman's fully conservative mixed type finite-difference operators are first modified. A special sonic point operator with an iterative damping term is introduced which helps the convergence and does not affect the spatial conservative differences. Reliable calculations with second order supersonic schemes are obtained using two sonic operators, the regular sonic point operator followed by a first order supersonic scheme. Also, shock point operator is shown to be equivalent to fitting a locally normal shock terminating the supersonic region.

The potential calculations are then modified to account for the non-isentropic jump conditions using a simple shock fitting procedure based on Prandtl relation. The entropy increase across the shock is calculated in terms of the Mach number upstream of the shock and the effect of the generated vorticity is estimated via Crocco relation. Different examples are calculated and extensions to the full potential equation are discussed.

Introduction

In 1971, Murman and Cole⁽¹⁾ introduced an iterative type dependent finite difference method for transonic flow calculations. Their pioneering work triggered an intensive effort in this field.

In 1974, Murman⁽²⁾ introduced the fully conservative operators and recently conservative boundary conditions are used⁽³⁾. Convergence acceleration is achieved by the use of Extrapolation⁽⁴⁾, Fast Solver⁽⁵⁾, Approximate Factorization⁽⁶⁾, and finally Multi-Grid⁽⁷⁾ methods.

Jameson extended Murman's work to solve the full potential equation^(8,9). For complex geometries, accurate treatment of boundary conditions are needed and finite elements (finite volumes⁽¹⁰⁾) are successfully applied for calculations of transonic flows around practical configurations, with fast iterative methods⁽¹¹⁾.

For high Mach number flows with shocks, the irrotationality assumption is questioned and efforts are directed towards efficient methods to solve the full Euler equations.

There are two main entropy corrections to the potential calculations, namely, the nonisentropic jump conditions and the vorticity generated due to the shock. Both corrections are studied within the small disturbance assumptions and extensions to the full equations are discussed.

In the following, modifications of Murman's fully conservative operators are introduced first, and then methods to implement entropy corrections

are presented.

I. Potential Equations

For 2-D flows, the continuity equation in Cartesian coordinates is:

$$(\rho u)_x + (\rho v)_y = 0 \quad (1)$$

Assuming inviscid irrotational flows, there exists a potential function ϕ , such that $u = \phi_x$, and $v = \phi_y$. Moreover, the density can be determined uniquely in terms of the speed via the energy equation:

$$\rho = [1 - \frac{\gamma-1}{2} M_\infty^2 (u^2 + v^2 - 1)]^{\frac{1}{\gamma-1}} \quad (2)$$

where M_∞ is the free stream Mach number. The x- and y- momentum equations are automatically satisfied for smooth flows. Equation (1) admits a weak solution conserving mass. If the potential function is continuous across the shock, the tangential momentum is conserved but not the normal momentum. The entropy increase across the shock is, in terms of shock strength, of third order and hence can be neglected for moderate transonic flows.

Equations (1) and (2) can be combined in a single nonlinear partial differential equation in ϕ and together with the impermeability, wake and far field boundary conditions, the formulation of the problem is complete.

Equation (1) can be written in the form

$$(a^2 - u^2)\phi_{xx} - 2uv\phi_{xy} + (a^2 - v^2)\phi_{yy} = 0$$

where

$$a^2 = \frac{1}{M_\infty^2} - \frac{\gamma-1}{2} (u^2 + v^2 - 1) \quad (3)$$

Equation (3) can be rearranged as follows:

$$(1 - M^2)\phi_{ss} + \phi_{nn} = 0$$

where

$$\frac{\partial^2}{\partial s^2} = \frac{u^2}{q^2} \frac{\partial^2}{\partial x^2} + 2uv \frac{\partial^2}{\partial x \partial y} + \frac{v^2}{q^2} \frac{\partial^2}{\partial y^2}$$

and

$$\frac{\partial^2}{\partial n^2} = \frac{v^2}{q^2} \frac{\partial^2}{\partial x^2} - 2uv \frac{\partial^2}{\partial x \partial y} + \frac{u^2}{q^2} \frac{\partial^2}{\partial y^2} \quad (4)$$

s and n are interpreted as the natural coordinates (along the stream line direction and normal to it).

Assuming small disturbances, the streamlines are almost parallel to the axis and Equation (4) reduces to the transonic small disturbance equation (in terms of ϕ ; $\phi = U_\infty x + \phi$):

$$(1 - M^2)\phi_{xx} + \phi_{yy} = 0 \quad (5)$$

Furthermore, a consistent approximation of $(1 - M^2)$ is:

$$(1 - M^2) \sim (1 - M_\infty^2) - (\gamma + 1)M_\infty^2 \phi_x \quad (6)$$

Combining Equations (5) and (6) gives

$$(1 - M_\infty^2 - (\gamma + 1)M_\infty^2 \phi_x)\phi_{xx} + \phi_{yy} = 0 \quad (7)$$

or, in conservative form,

$$((1 - M_\infty^2)\phi_x - \frac{\gamma + 1}{2}M_\infty^2 \phi_x^2)_x + (\phi_y)_y = 0 \quad (8)$$

Bailey and Ballhaus⁽¹²⁾ used a modified version of (8),

$$((1 - M_\infty^2)\phi_x - \frac{\gamma + 1}{2}M_\infty^n \phi_x^2)_x + (\phi_y)_y = 0 \quad (9)$$

where n is determined such that either the sonic condition matches the exact potential condition or the jump conditions at the shock are matched.

Newman and Klunker⁽¹³⁾ used a more general form:

$$((1 - M_\infty^2)\phi_x + c_1 \phi_x^2 + c_2 \phi_x^3)_x + (\phi_y)_y = 0 \quad (10)$$

where c_1 and c_2 can be chosen to match both the sonic and shock conditions.

The two terms between brackets in Equation (8) are an approximation for the mass flux in x and y directions. Different approximations are given by van der Vooren et al⁽¹⁴⁾ by expanding the flux directly in terms of the velocity.

The linearized boundary condition usually associated with Equation (8) for a symmetric airfoil at zero angle of attack is

$$\phi_y = f'(x) \quad (11)$$

where $f(x)$ is the shape of the airfoil. The flux conservative boundary condition⁽³⁾ is

$$\phi_y = f'(x) \cdot [(1 - M_\infty^2)\phi_x - \frac{\gamma + 1}{2}M_\infty^2 \phi_x^2] \quad (12)$$

II. Modification of Murman Sonic Point Operator

Murman's fully conservative operators are sketched in figure (1). A test function (based on centered differences everywhere) is used to check whether the flow at a point is subsonic or supersonic. The first point in the supersonic region is called sonic point and the first point downstream of the supersonic region is called shock point. Centered differences are used for subsonic points, and backward differences are used for supersonic points.

At the sonic point, the flow based on the test function is supersonic, hence if backward differences were used, the coefficient of ϕ_{xx} term at that point would be positive. To avoid such inconsistency, Murman used the following equation:

$$\phi_{yy} = 0 \quad (13)$$

If the coefficient of the ϕ_{xx} term at the sonic point is small and if ϕ_{xx} is finite, Equation (8) reduced to Equation (13).

Enquist and Osher⁽¹⁵⁾ and Georgian and Van Buskirk⁽¹⁶⁾ claim that Equation (13) admits a local expansion shock and propose a Godunov-type scheme to overcome this difficulty.

A simple remedy is suggested here by introducing an iterative damping term at the sonic point, without upsetting mass conservation at steady state. Equation (13) is replaced by:

$$\epsilon \phi_x = \phi_{yy} \quad (14)$$

where ϵ vanishes with iteration. For example, ϵ is chosen to be proportional to error, where error is $\max |\phi_{1,j}^n - \phi_{1,j}^{n-1}|$. Results based on Equation

(14) where backward differences are used for ϕ_x and centered differences for ϕ_{yy} are shown in figure (2). The convergence history compares favorably with calculations based on Murman's scheme. In both cases, the subsonic points are overrelaxed and the relaxation factor for supersonic points is one.

III. A Second Order Scheme for Smooth Supersonic Flows

Murman used a first order scheme for supersonic points. Second order schemes^(1,17) are found to be unreliable. Second order schemes have three upstream points and switching across the sonic line from centered differences to backward differences may lead to inconsistency at both the sonic point and the point after. In Reference (18), two sonic points are introduced, the first is the regular sonic point followed by the first order supersonic scheme and then second order schemes are used for the rest of the supersonic points. These modifications are sketched in figure (3), and the corresponding results are shown in figure (4).

Second order accuracy is dependent on the number of supersonic points but it is achieved for moderate supersonic regions in spite of the first order schemes at the sonic boundary.

Finally, the first sonic point operator can be based on Equation (14) rather than Equation (13).

IV. Murman Shock Point Operator

At the shock point, Murman used centered differences of ϕ_{yy} but for the x -term he used the sum of centered and backward differences. It is shown that mass is thus conserved across the shock. Non-conservative calculations produce weak shocks which are usually displaced upstream. Shock jump conditions are not satisfied and artificial sources are generated at the shock⁽¹⁹⁾.

More precisely, let

$$\xi = (1 - M_\infty^2)x - (\gamma + 1)M_\infty^2 \phi \quad (15)$$

Equation (8) in terms of ξ reads

$$\frac{1}{2} (\xi_x^2)_x + (\xi_y)_y = 0 \quad (16)$$

At a shock point (i,j), Murman's operator is

$$\begin{aligned} & \frac{\frac{1}{2} (\xi_x^2)_{i+\frac{1}{2},j} - \frac{1}{2} (\xi_x^2)_{i-\frac{1}{2},j}}{\Delta x} + \\ & \frac{\frac{1}{2} (\xi_x^2)_{i-\frac{1}{2},j} - \frac{1}{2} (\xi_x^2)_{i-\frac{3}{2},j}}{\Delta x} + \\ & + \frac{(\xi_y)_{i,j+\frac{1}{2}} - (\xi_y)_{i,j-\frac{1}{2}}}{\Delta y} \end{aligned} \quad (17)$$

or simply,

$$\begin{aligned} & \frac{\frac{1}{2} (\xi_x^2)_{i+\frac{1}{2},j} - \frac{1}{2} (\xi_x^2)_{i-\frac{3}{2},j}}{\Delta x} + \\ & \frac{(\xi_y)_{i,j+\frac{1}{2}} - (\xi_y)_{i,j-\frac{1}{2}}}{\Delta y} = 0 \end{aligned} \quad (17')$$

In Equation (17'), differencing across the shock in the x-direction is avoided and it is clear that the flux (ξ_x^2) is conserved across a locally normal shock between i and i-1 points.

Hafez and Cheng (20) treated the shock as an internal boundary with Neuman boundary condition derived from the shock jump relation, namely,

$$(\xi_x)^+ = -(\xi_x)_{i-\frac{3}{2}} \quad (18)$$

where $(\xi_x)^+$ is ξ_x downstream of the shock.

The finite difference equation at the shock point with the derivative boundary condition (18) is identical to Murman's shock point operator Equation (17'). Results may differ slightly due to different linearization procedures as shown in figure (5).

Equation (18) is the isentropic jump condition admitted by the weak solution of Equation (16) and represents conservation of mass under the transonic small disturbance assumptions.

V. Entropy Corrections

An inviscid flow is governed, in general, by Euler equations where mass, momentum and energy are conserved. For steady state, pressure can be eliminated and three conservative equations in ρ , u , and v are solved simultaneously.

Nonconservative equations in u and v in terms of a^2 are easily derived, namely

$$(a^2 - u^2)u_x - uv u_y - uv v_x + (a^2 - v^2)v_y = 0 \quad (19)$$

$$u_y - v_x = -\omega \quad (20)$$

In this case, jump conditions (Rankine-Hugoniot) must be imposed across the shock.

*We notice that the nonisentropic correction in equation (23) is $O(\epsilon^2)$ or $(\tau^{1/3})$ where τ is the thickness, while the vorticity in equation (28) is $O(\tau^{1/3})$;

Obviously, there are two main corrections to isentropic (irrotational) calculations:

a) Non-isentropic Jump Conditions:

A jump condition across a normal shock is given by Prandtl relation:

$$(1+u_1)(1+u_2) = a^{*2} = \frac{2}{\gamma+1} a_0^2 \quad (21)$$

$$\text{since } \frac{1}{2} + \frac{a_\infty^2}{\gamma-1} = \frac{a_0^2}{\gamma-1} \quad (22)$$

Equation (21) becomes:

$$u_1 u_2 + u_1 + u_2 = 2 \frac{(1-M_\infty^2)}{(\gamma+1)M_\infty^2} \quad (23)$$

If the term $u_1 u_2$ is neglected, Equation (23) reduces to Equation (18).

Equation (23) is easily implemented using the simple shock fitting procedure discussed earlier where a derivative boundary condition is used downstream of the shock. For an oblique shock, Prandtl relation reads

$$q_1 q_2 = a^{*2} - \frac{\gamma-1}{\gamma+1} v^2 \quad (24)$$

where q_1 and q_2 are the normal velocity components upstream and downstream of the shock and v is the tangential component.

b) Vorticity Generated by the Shock:

If the vorticity, ω , is neglected in Equation (20), Equation (19) reduced to the potential Equation (3). Some transonic flow fields of interest, are, however, associated with strong shock waves of variable strength with a variable entropy from one streamline to another and according to Crocco's theorem, vorticity is generated due to the differences in entropy:

$$\omega = T\rho \frac{ds}{d\psi} = \frac{T}{q} \frac{ds}{dn} \quad (25)$$

The jump in entropy across a shock is given by:

$$\begin{aligned} \frac{\Delta s}{R} = & \ln \left[1 + \frac{2\gamma}{\gamma+1} (M_1^2 \sin^2 \beta - 1) \right] \frac{1}{\gamma-1} \\ & \times \left[\frac{(\gamma+1)M_1^2 \sin^2 \beta}{(\gamma-1)M_1^2 \sin^2 \beta + 2} \right] \frac{\gamma}{\gamma-1} \end{aligned} \quad (26)$$

where β is the shock inclination to the upstream flow direction.

For a weak normal shock, Equation (26) reduced to:

$$\frac{\Delta s}{R} \approx \frac{2\gamma}{3(\gamma+1)^2} (M_1^2 - 1)^3 \quad (27)$$

According to small disturbance assumptions, streamlines are almost parallel to the axis and Equations (19), (20) and (25) reduce to:

$$[(1-M_\infty^2) - (\gamma+1)M_\infty^2] u_x + v_y = 0 \quad (28)$$

$$u_y - v_x = -\frac{1}{\gamma M_\infty^2} \left(\frac{\Delta s}{R} \right)_y$$

where $\Delta s/R$ is assumed to be a function of y only. Hence Equation (29) can be written in the form:

$$(u + \frac{1}{\gamma M_\infty^2} \frac{\Delta s}{R})_y - v_x = 0 \quad (30)$$

and consequently a potential function is defined such that Equation (30) is automatically satisfied, namely,

$$(u + \frac{1}{\gamma M_\infty^2} \frac{\Delta s}{R}) = \phi_x, \quad v = \phi_y \quad (31)$$

substituting Equation (31) in Equation (28) yields:

$$[(1-M_\infty^2) + \frac{(\gamma+1)}{\gamma} \frac{\Delta s}{R} - (\gamma+1)M_\infty^2 \phi_x] \phi_{xx} + \phi_{yy} = 0 \quad (32)$$

or

$$[(1-M_\infty^2)(\phi_x - \frac{1}{\gamma M_\infty^2} \frac{\Delta s}{R}) - \frac{1}{2}(\gamma+1)M_\infty^2(\phi_x - \frac{1}{\gamma M_\infty^2} \frac{\Delta s}{R})^2]_x + \phi_{yy} = 0 \quad (33)$$

According to Equation (32), the transonic similarity parameter K is modified with a second order quantity

$$\tilde{K} = K + \frac{1}{\gamma M_\infty^2} \frac{\Delta s}{R} \epsilon M_\infty^2 (\gamma+1) \quad (34)$$

where $K = (1-M_\infty^2)/\epsilon M_\infty^2 (\gamma+1)$; $\epsilon = O(\tau^{2/3})$

and in terms of scaled variables:

$$\frac{\Delta s}{R} \sim \frac{-\gamma(\gamma+1)}{1-\gamma} [\phi_x]^3 \begin{matrix} \text{downstream of} \\ \text{the shock} \\ \text{elsewhere} \end{matrix} \quad (35)$$

($[\phi_x]$ is the jump of ϕ_x across the shock)

Equations (32,34) call for a fuller and consistent treatment of second and third order terms in deriving a higher order transonic small disturbance equation. For example, terms like $\phi_x \phi_{yy}$ and $\phi_y \phi_{xy}$ appear in second order equations and are neglected here. In this study, the entropy term is singled out and its effects are shown numerically.

In passing, the drag can be calculated in terms of entropy production via Oswatitsch relation (21):

$$D = \frac{T_\infty}{q_\infty} \int_{\text{shock}} \rho q_n \Delta s \, dl \quad (36)$$

Murman and Cole⁽²²⁾ obtained an estimate of the drag based on (35) and (36) and it is indeed consistent with surface pressure integration.

Results based on modifications of small disturbance calculations according to Prandtl and Crocco relations are shown in figure (6). Convergence rate and computational work are hardly affected by such modifications.

VI. Extension to Full Equations

The full potential calculations can be similarly modified to account for entropy corrections where the small disturbance assumptions are relaxed at least in deriving the governing equations. The exact equations are:

$$(\rho u)_x + (\rho v)_y = 0 \quad (1)$$

*It is assumed that, at the foot of the shock, the rotational flow is no more singular than the potential and even the shock curvature may be infinite there, the vorticity is finite.

$$u_y - v_x = -\frac{T}{q} \frac{ds}{dn} \quad (25)$$

where the density is given by

$$\rho = \rho_i e^{-\Delta s/R} \quad (37)$$

ρ_i is the isentropic density (Equation (2)).

In general, a velocity vector (u, v) can be decomposed into a gradient of a potential plus another vector (u', v') :

$$u = \phi_x + u', \quad v = \phi_y + v' \quad (38)$$

Different choices of (u', v') are discussed:

a) u' and v' can be chosen such that

$$u' = \psi_y; \quad v' = -\psi_x \quad (39)$$

Hence Equation (25) becomes

$$\psi_{xx} + \psi_{yy} = -\frac{T}{q} \frac{ds}{dn} \quad (40)$$

It should be mentioned that $\psi = \text{constant}$ is not a streamline. The streamline direction is

$$\left(\frac{dy}{dx}\right)_{\text{stream}} = \frac{\phi_y - \psi_x}{\phi_x + \psi_y} \quad (41)$$

On the body surface, if we choose

$$\phi_n = 0 \quad (42)$$

the corresponding boundary condition for ψ is

$$\psi = 0 \quad (42')$$

Similarly across the shock, the jump condition is

$$\left(\frac{dy}{dx}\right)_{\text{shock}} = \frac{-[u]}{[v]} = \frac{[\phi_x] + [\psi_y]}{[\phi_y] - [\psi_x]} \quad (43)$$

If ϕ is chosen to be continuous across the shock, the corresponding shock boundary condition for ψ is, (assuming ψ vanishes upstream of the shock)

$$\psi_n = 0 \quad (44)$$

The boundary conditions of ψ -problem are sketched in figure (7).

b) Without loss of generality, v' in Equation (38) can be chosen identically zero, and Equation (40) reduces to a simple ordinary differential equation:

$$u'_y = -\frac{T}{q} \frac{ds}{dn} \quad (45)$$

where u' vanishes in the far field where the flow is irrotational. The right hand side of Equations (40) or (45) has to be evaluated downstream of the shock. The entropy across the shock is first computed based on shock relations and since the entropy is constant along a streamline, it can be easily calculated everywhere else. The choice of the grid may simplify the calculations. For sake of simplicity, it is assumed here that $\frac{T}{q} \frac{ds}{dn}$ is approximately

equal to $\frac{1}{\gamma M^2} \frac{d\Delta s/R}{dy}$ as in small disturbance calculations. Preliminary numerical results using artificial compressibility method(23,24) are shown in Figure (8).

Concluding Remarks

Transonic small disturbance calculations are revisited and Murman's fully conservative operators are modified. The sonic point operator is augmented by an iterative damping term and a reliable second order supersonic scheme is used with two sonic operators. Shock point operator is shown to be equivalent to fit a locally normal shock terminating the supersonic region.

Entropy corrections to potential calculations are studied including nonisentropic jump conditions and vorticity generated due to shocks. Modifications based on Prandtl and Crocco relations are introduced and numerical results are obtained. Extensions to the full equations are discussed and preliminary results are presented. The effects of such modifications on convergence rate and computational effort are minor.

In general, Euler corrections lead to weaker shocks which are usually located upstream of those obtained from potential calculations. For high Mach numbers, conservative potential calculations result in a fish tail shock while with Euler corrections, a normal shock occurs at the trailing edge.

Although in this paper, only steady flows are discussed, the above corrections can be easily extended and implemented to unsteady potential calculations(25).

Acknowledgement

This work was supported in part by NASA-Langley Research Center. The first author wishes to thank Jerry South of Theoretical Aerodynamic Branch for helpful discussion.

References

1. Murman, E. M., and Cole, J. D. "Calculation of Plane Steady Transonic Flow," AIAA Journal, Vol. 9, No. 1, 1971, pp. 114-121.
2. Murman, E. M. "Analysis of Embedded Shock Calculated by Relaxation Methods," AIAA Journal, Vol. 12, No. 5, 1974, pp. 626-633.
3. Schmidt, W. "A Self-Consistent Formulation of the Transonic Small-Disturbance Theory" in "Recent Developments in Theoretical and Experimental Fluid Mechanics," Muller, Y. (ed.), Springer Verlag, New York, 1979.
4. Hafez, M. M., and Cheng, H. K. "Convergence Acceleration of Relaxation Solution for Transonic Flow Computations," AIAA Journal, Vol. 15, No. 3, 1977, pp. 329-336.
5. Martin, E. D. "A Fast Semidirect Method for Computing Transonic Aerodynamic Flows," AIAA 2nd Computational Fluid Dynamics Conference, Connecticut, June, 1975.
6. Ballhaus, W. F., Jameson, A., and Albert, A. "Implicit Approximate Factorization Schemes for the Efficient Solution of Steady Transonic Flow Problems," AIAA 3rd Computational Fluid Dynamics Conference, New Mexico, June 1977.
7. South, J. C. and Brandt, A. "The Multi-Grid Method: Fast Relaxation for Transonic Flows," Advances in Engineering Science, NASA CP-2001, Vol. 4, 1976, pp. 1359-1369.
8. Jameson, A. "Iterative Solution of Transonic Flows Over Airfoils and Wings," Comm. Pure Appl. Math., Vol. 27, 1974, pp. 283-309.
9. Jameson, A. "Transonic Potential Flow Calculations Using Conservative Form," AIAA 2nd Computational Fluid Dynamics Conference, Connecticut, June 1975.
10. Jameson, A., and Caughey, D. A. "A Finite Volume Method for Transonic Potential Flow Calculations," AIAA 3rd Computational Fluid Dynamics Conference, New Mexico, June 1977.
11. Jameson, A. "Acceleration of Transonic Potential Flow Calculations on Arbitrary Meshes by the Multiple-Grid Method," AIAA Computational Fluid Dynamics Conference, Virginia, July 1979.
12. Bailey, F. R. and Ballhaus, W. F. "Comparison of Computed and Experimental Pressure for Transonic Flows About Isolated Wings and Wing-Fuselage Configurations," NASA SP-347, Part II, 1975, pp. 1213-1231.
13. Newman, P. A. and Klunker, E. B. "Computation of Transonic Flow About Finite Lifting Wings," AIAA Journal, Vol. 10, No. 7, 1972, pp. 971-973.
14. Van der Vooren, Sloof, J. W., Huizing, G. H., and VanEssen, A. "Remarks on the Suitability of Various Transonic Small Perturbation Equations to Describe Three Dimensional Transonic Flows," Symposium Transonicum II, Oswatitsch (ed.) Springer Verlag, New York, 1976.
15. Enquist, B., and Osher, S. "Stable and Entropy Satisfying Approximations for Transonic Flow Calculations," Math. of Comp. Vol. 34, 1980, pp. 45-75.
16. Goorjian, P. M., and Van Buskirk, R. "Implicit Calculations of Transonic Flows Using Monotone Methods," AIAA Paper 81-0331.
17. Warming, R. F., and Beam, R. M. "Upwind Second-Order Difference Schemes and Applications in Unsteady Aerodynamic Flows," AIAA 2nd Computational Fluid Dynamic Conference, Connecticut, June 1975.
18. Hafez, M. M., Wellford, L. C., Merkle, C. L., and Murman, E. M. "Numerical Computation of Transonic Flows by Finite-Element and Finite-Difference Methods," NASA Contractor Report 3070, December 1978.
19. Hafez, M. M., and Murman, E. M. "A Shock Fitting Algorithm for the Full Potential Equation," AIAA 3rd Computational Fluid Dynamics Conference, New Mexico, June 1977.

20. Hafez, M. M. and Cheng, H. K. "Shock Fitting Applied to Relaxation Solutions of Transonic Small Disturbance Equations," AIAA J., Vol. 15, No. 5, 1977, pp. 786-793.

21. Oswatitsch, K., Gas Dynamics, Academic Press, 1956.

22. Murman, E. M., and Cole, J. D. "Inviscid Drag at Transonic Speeds," AIAA Paper 74-540.

23. Hafez, M. M., South, J. C., and Murman, E. M. "Artificial Compressibility Methods for Numerical Solution of Transonic Full Potential Equation," AIAA Journal, Vol. 17, No. 8, 1979, pp. 836-844.

24. South, J. C., Keller, J. D., and Hafez, M. M. "Vector Processor Algorithms for Transonic Flow Calculations," AIAA Journal, Vol. 18, No. 7, 1980, pp. 786-792.

25. Ballhaus, W. F. and Goorjian, P. M. "Implicit Finite-Difference Computations of Unsteady Transonic Flows about Airfoils," AIAA Journal, Vol. 15, No. 12, 1977, pp. 1728-1735.

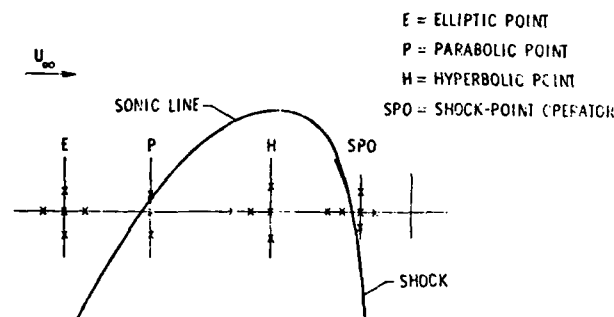


Figure (1) A sketch of Murman's fully conservative operators

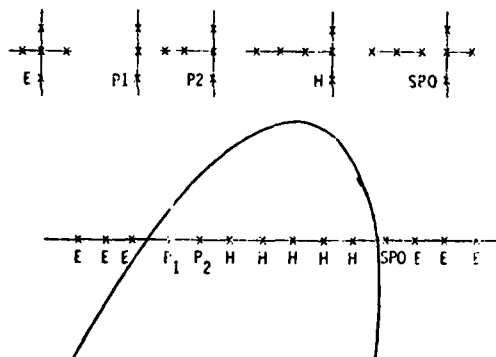


Figure (3) A sketch of modified Murman's Operators including the present Second Order Supersonic Scheme

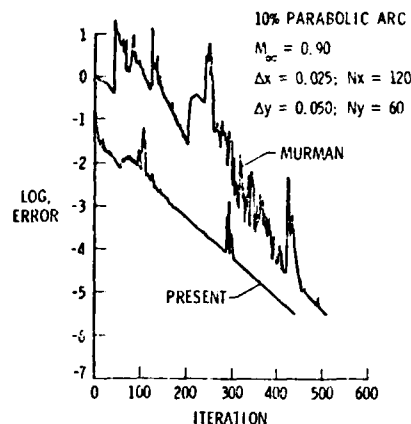


Figure (2) Convergence History of calculations based on Murman's Sonic Point Operator and present Parabolic Point Operator

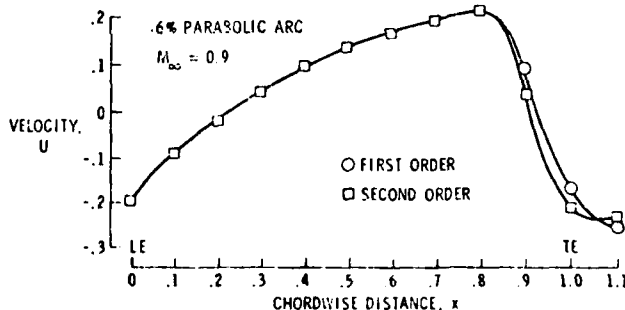


Figure (4) Comparison of Surface Pressure of First Order and Second Order calculations

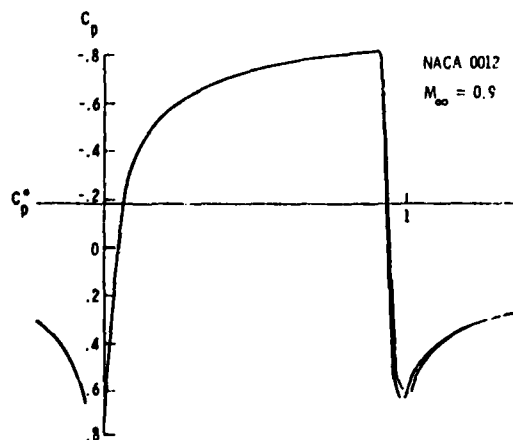
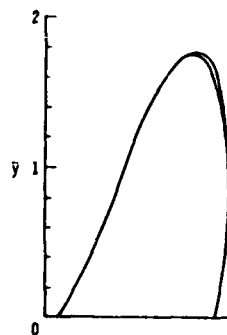


Figure (5) Comparison of results based on Murman's Shock Point Operator and present local by normal shock fitting procedure



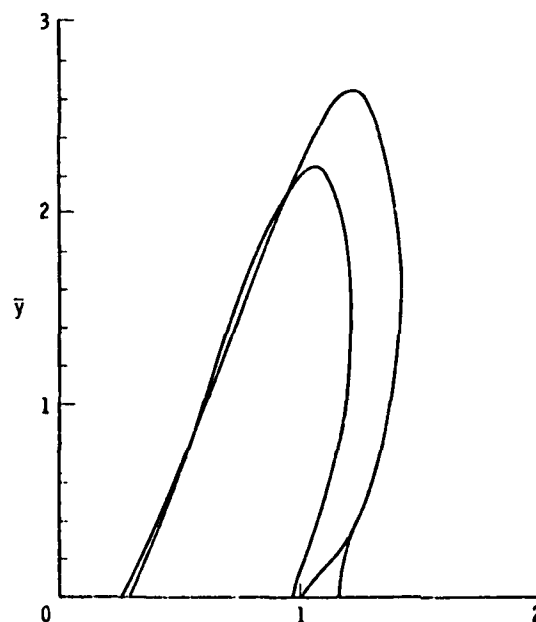
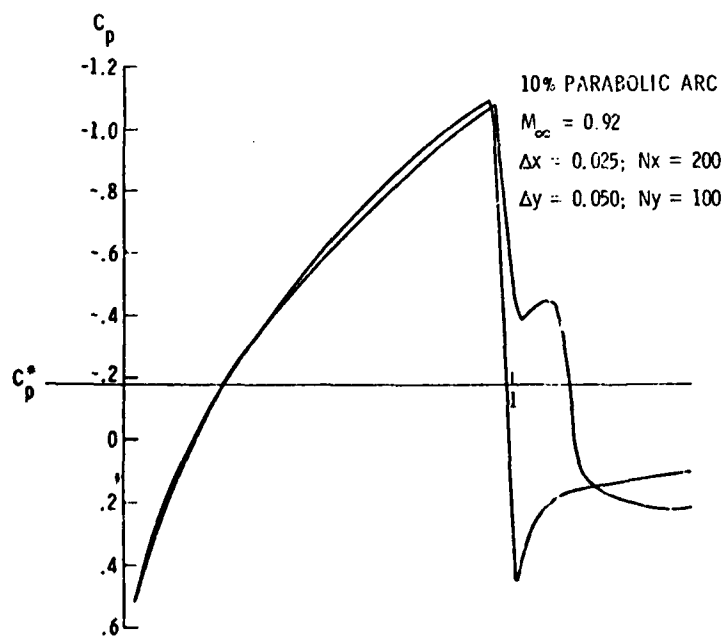
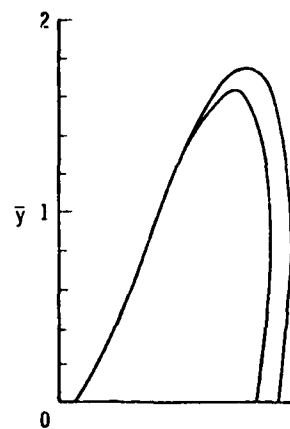
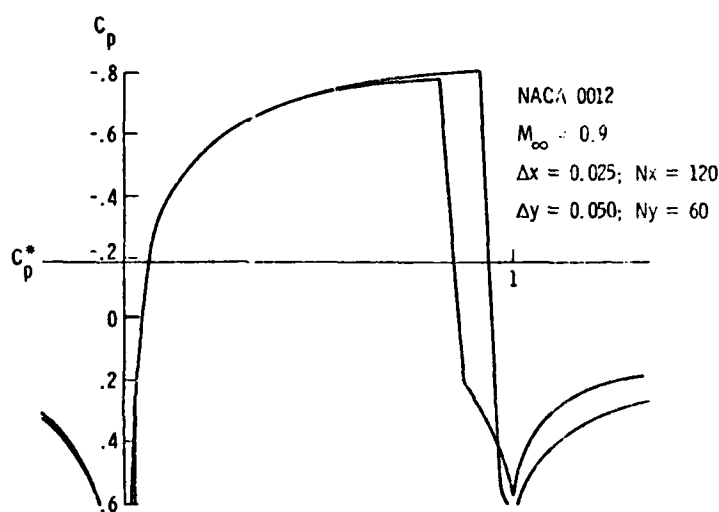
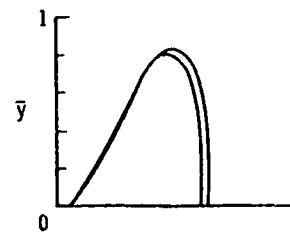
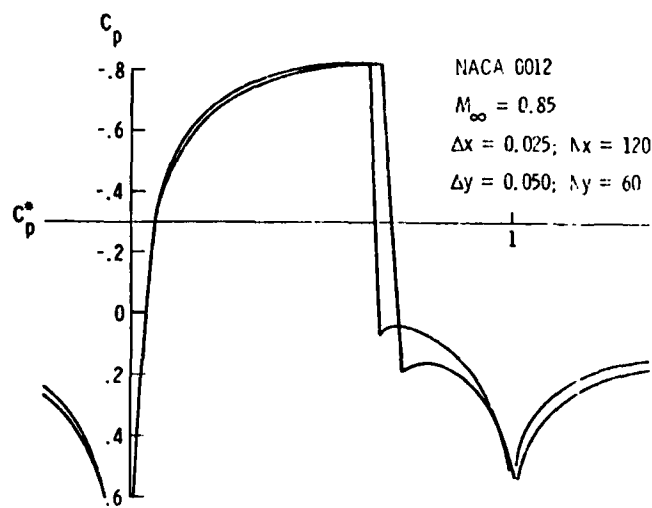


Figure (6) Results of Euler Corrections to Transonic Small Disturbance calculations

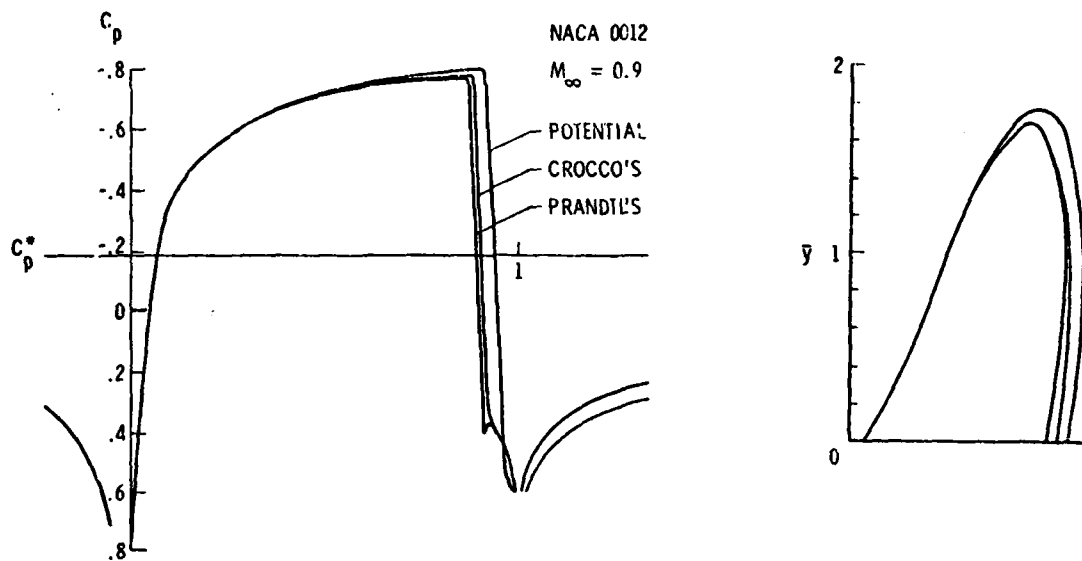


Figure (6) Continued

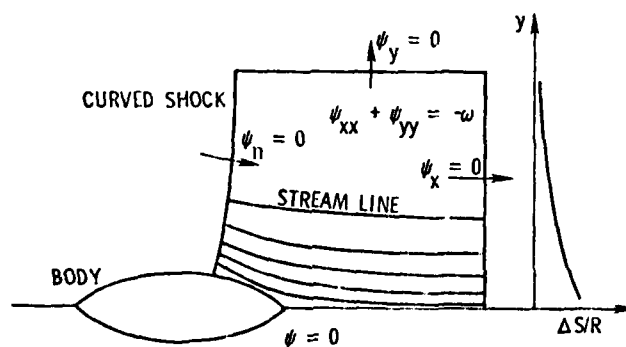


Figure (7) A sketch of ψ -problem

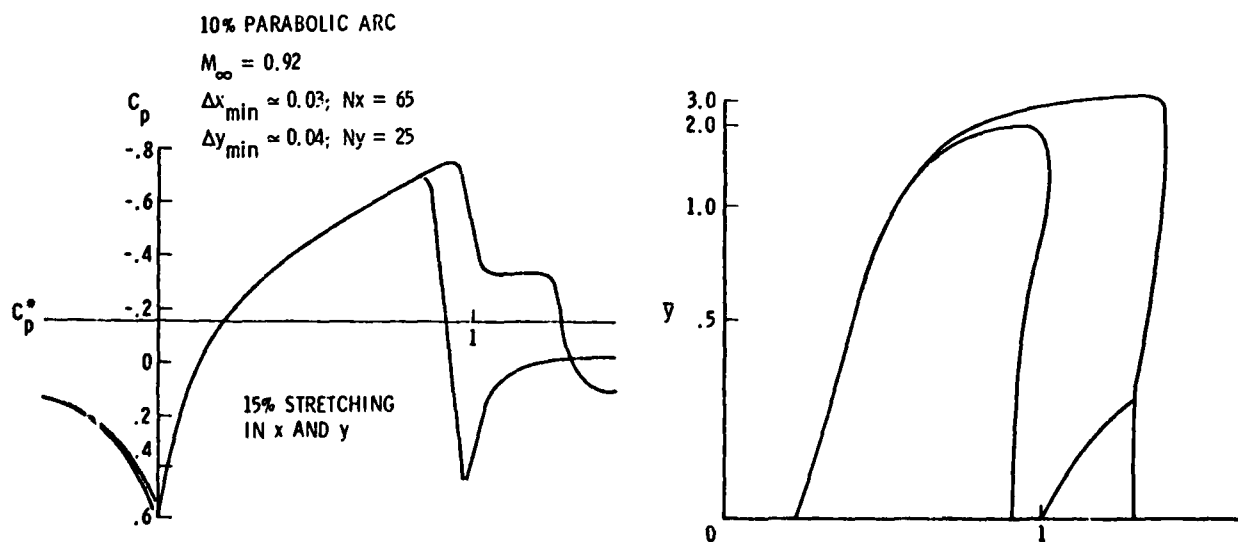


Figure (8) Results of Euler corrections to Transonic full potential calculations

AD P001953

THE EFFICIENT SOLUTION OF TRANSONIC WING FLOW FIELDS

Terry L. Holst* and N. R. Subramanian†
NASA Ames Research Center, Moffett Field, California

and

Scott D. Thomas*
Informatics General Corporation, Palo Alto, California

Abstract

An evaluation of the transonic-wing-analysis computer code TWING is presented. TWING utilizes a fully implicit, approximate-factorization iteration scheme to solve the full-potential equation in conservative form. A numerical elliptic-solver grid-generation scheme is used to generate the required finite-difference mesh. Several wing configurations have been analyzed, and comparisons of computed results have been made with available experimental data. Results indicate that the code is robust, accurate (when significant viscous effects are not present), and efficient. TWING generally produces solutions an order of magnitude faster than other conservative, full-potential codes using successive-line overrelaxation. The present method is applicable to a wide range of isolated wing configurations, including high-aspect-ratio transport wings and low-aspect-ratio, high-sweep, fighter configurations.

I. Introduction

During recent years, inviscid transonic flow computations have been obtained using two formulations: 1) the transonic small disturbance (TSD) formulation and 2) the full-potential (FP) formulation. The TSD formulation is valid for isentropic, irrotational flows involving thin bodies at small angles of attack and for transonic conditions. Flow-tangency boundary conditions are imposed on mean geometrical surfaces, for example, wing "slits" or fuselage "boxes." Thus, simplified grids can be used, usually involving sheared, stretched Cartesian coordinates. This is the primary reason why the TSD formulation was introduced before the FP formulation and why more complete geometrical configurations have been solved using the TSD approach.

The worst problem associated with the TSD formulation occurs at the wing leading edge where the stagnation region generally causes the small-disturbance assumption to break down. However, this formulation yields results that are generally better than expected. Indeed, good correlations with experiment have been obtained for a wide variety of applications. Example applications using the TSD formulation can be found in Refs. 1-5. Although the TSD formulation is capable of computing flows for relatively sophisticated geometries, the FP formulation is generally desired when an accurate solution near the wing leading edge is required.

The FP formulation is valid for isentropic, irrotational flows ranging from incompressible to transonic conditions. The flow-tangency boundary

condition is prescribed in an exact manner (relative to the TSD approach) at the geometry surface. Thus, a more complex mapping procedure is required with this approach. Example applications using the FP formulation are given in Refs. 6-10. In addition, a survey of computational transonic methods in which the TSD and FP formulations are compared and contrasted is presented in Ref. 11.

Recently, a large number of researchers have investigated various ways of improving solution convergence. This research has been largely necessitated by the slow rate of convergence associated with the standard relaxation algorithm, successive-line overrelaxation (SLOR). Some of the new algorithms investigated include multigrid,¹²⁻¹⁶ the strongly implicit procedure (SIP),¹⁷ and various approximate-factorization schemes.^{3,18-24}

In this study, the TWING computer code (Transonic Wing analysis) is described and evaluated. This code uses the AF2 fully implicit, approximate-factorization scheme to solve the FP equation in conservative form.²⁴ Supersonic regions of flow are stabilized in the spatial-differencing scheme by using an upwind bias in the density evaluation.^{19,25,26} This causes the spatial differencing scheme to be first-order accurate in supersonic regions and second-order accurate in subsonic regions. A variety of isolated wing geometries with variations in wing aspect ratio, taper ratio, sweep, twist, and airfoil cross section have all been investigated. Correlations with experimental results are included for most of the cases presented.

II. Numerical Algorithm

Governing Equations

The three-dimensional, full-potential equation written in strong conservation-law form is given by

$$(\rho\phi_x)_x + (\rho\phi_y)_y + (\rho\phi_z)_z = 0 \quad (1a)$$

$$\phi = \left[1 - \frac{\gamma - 1}{\gamma + 1} (\phi_x^2 + \phi_y^2 + \phi_z^2) \right]^{1/(\gamma - 1)} \quad (1b)$$

The density ρ and velocity components ϕ_x , ϕ_y , and ϕ_z are nondimensionalized by the stagnation density ρ_s and the critical sound speed a_∞ , respectively; x , y , and z are Cartesian coordinates in the streamwise, spanwise, and vertical directions, respectively, and γ is the ratio of specific heats.

Equation (1) is transformed from the physical domain (Cartesian coordinated) to the computational domain by using a general independent variable transformation. This transformation (see Fig. 1), indicated by

*Research Scientist.

†Senior NRC Associate.

This paper is declared a work of the U.S. Government and therefore is in the public domain.

$$\begin{aligned} \xi &= \xi(x,y,z) \\ \eta &= \eta(x,y,z) \\ \zeta &= \zeta(x,y,z) \end{aligned} \quad (2)$$

maintains the strong conservation-law form of Eq. (1) (see Ref. 27). The full-potential equation written in the computational domain ($\xi = 0$ to $\xi = 1$, coordinate system) is given by

$$\left(\frac{\partial U}{\partial \xi}\right)_{\xi} + \left(\frac{\partial V}{\partial \eta}\right)_{\eta} + \left(\frac{\partial W}{\partial \zeta}\right)_{\zeta} = 0 \quad (3a)$$

$$U = \left[1 - \frac{1}{\gamma + 1} (U^2 + V^2 + W^2)\right]^{1/(\gamma + 1)} \quad (3b)$$

where

$$\begin{aligned} U &= A_1 \xi_{\xi} + A_2 \xi_{\eta} + A_3 \xi_{\zeta} \\ V &= A_4 \xi_{\xi} + A_5 \xi_{\eta} + A_6 \xi_{\zeta} \end{aligned} \quad (4a)$$

$$W = A_7 \xi_{\xi} + A_8 \xi_{\eta} + A_9 \xi_{\zeta}$$

$$\begin{aligned} A_1 &= \xi_x^2 + \xi_y^2 + \xi_z^2 \\ A_2 &= \xi_x \xi_y + \xi_y \xi_x \\ A_3 &= \xi_x \xi_z + \xi_z \xi_x \\ A_4 &= \xi_x \xi_x + \xi_y \xi_y + \xi_z \xi_z \\ A_5 &= \xi_x \xi_y + \xi_y \xi_x + \xi_z \xi_z \\ A_6 &= \xi_x \xi_z + \xi_z \xi_x + \xi_y \xi_y \end{aligned} \quad (4b)$$

$$A_7 = \xi_x \xi_x + \xi_y \xi_y + \xi_z \xi_z$$

$$A_8 = \xi_x \xi_y + \xi_y \xi_x + \xi_z \xi_z$$

$$A_9 = \xi_x \xi_z + \xi_z \xi_x + \xi_y \xi_y$$

and

$$\begin{aligned} J &= \xi_x \eta_y \zeta_z + \xi_z \eta_x \zeta_y + \xi_y \eta_z \zeta_x \\ &\quad - \xi_z \eta_y \zeta_x - \xi_y \eta_x \zeta_z - \xi_x \eta_z \zeta_y \\ &= 1/(x_{\xi} y_{\eta} z_{\zeta} + x_{\eta} y_{\zeta} z_{\xi} + x_{\zeta} y_{\xi} z_{\eta} \\ &\quad - x_{\zeta} y_{\eta} z_{\xi} - x_{\eta} y_{\xi} z_{\zeta} - x_{\xi} y_{\zeta} z_{\eta}) \end{aligned} \quad (5)$$

Note that this formulation for the FP equation is more general than the formulation of Ref. 24. The simplification that all $\eta = \text{constant}$ surfaces coincide with $y = \text{constant}$ planes has been removed. Thus, completely general orientations of the $\xi - \eta - \zeta$ mesh can be supported with the present formulation. For more discussion of the details of this transformation procedure see Ref. 24.

Grid Generation

The grid-generation scheme used in the present three-dimensional formulation is a simple extension of the two-dimensional scheme presented in Ref. 28. The finite-difference mesh is generated using a standard two-dimensional algorithm. This requires solution of two Laplace equations in each spanwise plane used as a defining station. These equations are transformed to the computational domain and

solved using a fast approximate-factorization relaxation algorithm.

This establishes values for x and z in each spanwise plane used as a defining station. Coordinate values (x and z) for computational planes between the defining stations are obtained via linear interpolation. For the case of a wing with no taper or section variation, only two defining stations are required, one at the root and one outboard of the tip in the wing-extension region. The root station is user-specified, but the wing-extension station is always chosen as a flat plate. In addition, wing taper, twist, thickness, and sweep variations can be specified at each defining station.

The coordinate values in the spanwise direction (y values) are computed from a stretching formula, which in its simplest form gives equal spacing over the wing with relatively rapid stretching beyond the tip. The x and z values generated for the first station outboard of the tip are used for each wing extension station. Then a smoothing step for the two $y = \text{constant}$ planes on either side of the tip is implemented to remove grid discontinuities, which may arise in the transition from an airfoil of positive thickness to one of zero thickness. An example grid generated using the procedure just discussed will be presented in the section on computed results.

Spatial Differencing

A finite-difference approximation for Eq. (3) suitable for both subsonic and supersonic flow regions is given by

$$\begin{aligned} \bar{\xi}_{\xi} (SU/J)_{i+1/2,j,k} + \bar{\xi}_{\eta} (SV/J)_{i,j+1/2,k} \\ + \bar{\xi}_{\zeta} (SW/J)_{i,j,k+1/2} = 0 \end{aligned} \quad (6)$$

where the operators $\bar{\xi}_{\xi}(\cdot)$, $\bar{\xi}_{\eta}(\cdot)$, and $\bar{\xi}_{\zeta}(\cdot)$ are first-order-accurate, backward-difference operators in the ξ , η , and ζ directions, respectively. The density coefficients $\bar{\xi}$ and $\bar{\xi}$ are defined by

$$\begin{aligned} \bar{\xi}_{\xi} &= \left\{ \begin{aligned} &[(1 - \epsilon)]_{i+1/2,j,k} \\ &+ [(1 - \epsilon)]_{i+1/2,j,k}^{i+r+1/2,j,k} \end{aligned} \right\} \\ \bar{\xi}_{\eta} &= \left\{ \begin{aligned} &[(1 - \epsilon)]_{i,j+1/2,k} \\ &+ [(1 - \epsilon)]_{i,j+1/2,k}^{i,j+s+1/2,k} \end{aligned} \right\} \end{aligned} \quad (7)$$

where

$$\begin{aligned} r &= \pm 1 \quad \text{when} \quad U_{i+1/2,j,k} \neq 0 \\ s &= \pm 1 \quad \text{when} \quad V_{i,j+1/2,k} \neq 0 \end{aligned} \quad (8)$$

and

$$\begin{aligned} i+1/2,j,k \\ = \begin{cases} \max\{M_{i,j,k} - 1, 0\} & \text{for } U_{i+1/2,j,k} \neq 0 \\ \max\{M_{i+1/2,j,k} - 1, 0\} & \text{for } U_{i+1/2,j,k} = 0 \end{cases} \end{aligned} \quad (9)$$

The quantity $M_{i,j,k}$ is the local Mach number; C is a user-specified constant (usually between 1.0 and 2.0); and the quantities U , V , and W are the contravariant velocity components computed using standard, second-order-accurate, finite-difference formulas. The density ρ is computed from the second-order-accurate discretized version of Eq. (3b) and is stored at half points in the finite-difference mesh (i.e., at $i + 1/2, j, k$). Values needed at $i, j + 1/2, k$ or $i, j, k + 1/2$ are obtained using simple four-element averages.

The spatial differencing scheme given by Eqs. (6)-(9) is centrally differenced and second-order accurate in subsonic regions. In supersonic regions, the differencing is a combination of 1) the second-order-accurate central differencing used in subsonic regions and 2) the first-order-accurate upwind differencing resulting from the upwind evaluation of the density coefficients (ρ and τ). In the present formulation, upwind evaluations of the density have been used along only the i and j indices (wraparound and spanwise directions, respectively). Thus, the fully rotated form of the spatial difference scheme has not been used. This has not adversely affected convergence for any of the cases presented herein. However, other cases involving large regions of supersonic flow at the wing trailing edge may require the fully rotated difference scheme with all three values of density in Eq. (6) biased in the upwind direction.

AF2 Iteration Scheme

The AF2 fully implicit iteration scheme used in the present study can be expressed in a three-step format.

Step 1:

$$\left(1 - \frac{1}{A_k} \bar{\tau}_k A_j \bar{\tau}_j\right) g_{i,j}^n = \alpha L \rho_{i,j,k}^n + \alpha A_{k+1/2} f_{i,j,k+1/2}^n \quad (10a)$$

Step 2:

$$\left(A_k + \bar{\tau}_k \bar{\tau}_j - \frac{1}{\alpha} \bar{\tau}_k A_j \bar{\tau}_j\right) f_{i,j,k}^n = g_{i,j}^n \quad (10b)$$

Step 3:

$$(\alpha + \bar{\tau}_k) c_{i,j,k}^n = f_{i,j,k}^n \quad (10c)$$

where the n superscript is an iteration index; α is an acceleration parameter; $L \rho_{i,j,k}^n$ is the n th iteration residual [defined by the left-hand side of Eq. (6)]; $\bar{\tau}_k$ is a relaxation factor, equal to 1.8 for all cases presented; $g_{i,j}^n$ is an intermediate result stored at each grid point in a given k plane and $f_{i,j,k}^n$ is an intermediate result stored at each point in the finite-difference mesh. The A_i , A_j , and A_k coefficients are defined by

$$\begin{aligned} A_i &= (CA_i/J)_{i-1/2,j,k}^n \\ A_j &= (CA_j/J)_{i,j-1/2,k}^n \\ A_k &= (CA_k/J)_{i,j,k-1/2}^n \end{aligned} \quad (11)$$

and the density coefficients ρ and τ are defined by Eq. (7).

The quantity τ appearing in Eq. (10) can be considered as τ^{-1} . The best choice for τ is to use a sequence of values. The small values are particularly effective for reducing the low-frequency errors, and the large values are particularly effective for reducing the high-frequency errors. The τ -sequence given in Ref. 19 has been used for the computations presented herein.

A ρ_{eff} -type term has been added inside the brackets of step 2 [see $A_k \bar{\tau}_k$ in Eq. (10b)]. This term is necessary to provide time-like damping to the iteration scheme. The parameter ρ_{eff} is user-specified and usually ranges between 0.05 and 0.3. Larger values are generally required for cases with larger regions of supersonic flow.

In step 1, the g -array is obtained by solving a tridiagonal matrix equation for each $k = \text{constant}$ line in the k th plane. In step 2, the f -array is obtained from g by solving a tridiagonal matrix equation for each $k = \text{constant}$ line, again for just the k th plane. Next, step 1 is used to obtain the g -array for the $k - 1$ plane, and then step 2 is used to obtain the f -array for the $k - 1$ plane, etc. This process continues until all values of f in the three-dimensional mesh are established. Then, by using step 3, the correction array is obtained from the f -array by solving a simple bidiagonal matrix equation for each i, j line in the entire finite-difference mesh. Other aspects of the present spatial differencing and iteration schemes are discussed in more detail in Ref. 24.

Boundary Conditions

The wing-surface boundary condition in the body-fitted coordinate system is implemented by applying

$$\left(\frac{\partial W}{\partial J}\right)_{i,j,NK+1/2} = -\left(\frac{\partial W}{\partial J}\right)_{i,j,NK-1/2} \quad (12)$$

where NK is the wing surface. A similar reflection condition is used for the symmetry plane ($y = 0$). Along the free-stream and outer boundaries, the initial free-stream distribution of ρ is fixed for nonlifting conditions. For lifting wings, the outer boundary is updated by the usual compressible vortex solution with circulation Γ_j . A user-specified relaxation parameter (RGAM) is used to control the circulation build up. Details describing the circulation algorithm are given in Ref. 24.

III. Computed Results

In this section several results computed from the TWING computer code are presented. In each case the solution procedure started with the numerical generation of the finite-difference mesh. An example grid is shown in Figs. 2-7 for the wing-C geometry obtained from Ref. 29. The x/c , y/c , and z/c Cartesian coordinates used in these figures are based on an origin at the wing-root midchord and are normalized by root chord c . This grid contains $127 \times 27 \times 20 = 68,580$ points (wraparound, spanwise, and near-normal directions, respectively), and is typical of the grids used for the results presented herein. Note that with this grid $127 \times 17 = 2159$ points are used to define the wing-surface geometry.

This configuration is a high-sweep ($\Delta LE = 45^\circ$), high-taper ($TR = 0.3$) wing with 8° of twist. The amount of taper and twist is apparent from Figs. 2-4 which show blowups of the root and tip airfoil sections and the wing-extension station outboard of the tip plotted to the same scale. Note the efficiency with which the "O mesh" topology clusters points around the airfoil-section geometry regardless of its position in the span (root or tip). For this particular grid, a special clustering procedure has been used to cluster grid points at the wing leading edges. This is especially useful for wings with sharp leading edges. The wing planform including the surrounding mesh is shown in Fig. 5, and the grid in the $\xi = \text{constant}$ plane corresponding to the wing half-chord position (i.e., the wing on edge) is shown in Fig. 6. Apparent in these views is the wing-tip grid topology and the stretching rates used above and below the wing, as well as outboard of the wing tip. Finally, Fig. 7 is a perspective view of the three-dimensional grid which consists of the symmetry plane, wing surface, and vortex-sheet grid distributions. This view very much represents the view of the wing mounted in the wind tunnel (except for the vortex sheet) and presents a good picture of the overall grid topology.

This wing grid was generated with three airfoil defining stations. The first two stations were user-specified and served to define the wing-root and tip airfoil sections. Through interpolation, these two stations were then used to define the entire wing. The third station was the internally specified, flat-plate section used to define the wing extension outboard of the wing tip. The entire wing grid-generation procedure for this configuration required 1.3 sec of CPU time on the Cray 1S computer.

The first transonic-wing calculation presented consists of the wing-C geometry just discussed (see Refs. 29 and 30). This geometry represents a difficult test for any transonic analysis procedure because of the large sweep ($\Delta LE = 45^\circ$), twist (8.17°), and taper ($TR = 0.3$). A comparison of the wing surface-pressure distribution with two different experiments (Refs. 29, 31) is shown in Fig. 8. The nominal conditions for these experimental and computational results are $M_\infty = 0.82$ and $\alpha = 5^\circ$. Results are shown at five semispan stations, $\eta = 0.1, 0.3, 0.5, 0.7$, and 0.9 . The agreement between the three results at all stations is generally good for the lower surface. The agreement between the three results on the upper surface is good at the first station ($\eta = 0.1$) but deteriorates toward the tip. The Keener data³¹ and the TWING results are in reasonable agreement but the Hinson-Burdges data²⁹ underpredict the leading-edge expansion and the shock position at $\eta = 0.5, 0.7$, and 0.9 .

The substantial difference between the two experimental results shown in Fig. 8 is one of the difficulties facing code developers. How can the accuracy of a code be established with the uncertainties that exist in experimental results? One technique is to assume Mach-number and angle-of-attack corrections suitable to match experimental lift. A wing-surface comparison using this philosophy establishes the basic physics-capturing capability of a computational technique. The Mach-number and angle-of-attack corrections attempt to serve two purposes: 1) the removal of experimental error owing to wind-tunnel-wall interference, flow

angularity effects, etc., and 2) the removal of numerical error owing to inadequate modeling of viscous effects, etc. Obviously, this procedure does not always work. For instance, when viscous effects are moderately strong, the local errors at shock waves cannot be simulated by such global effects as Mach-number or angle-of-attack corrections. However, in the code validation phase, such simplistic corrections can be quite useful. More details regarding the categorization of error in a numerical/experimental comparison are presented and discussed in Refs. 11 and 32.

The foregoing procedure requires an a priori experimental value of lift and therefore is not totally predictive. Having the accuracy of an absolutely predictive technique is a noble goal but may not in every case be a necessity. In a preliminary design stage, sometimes the only question of importance is whether a shock exists at the design point. If it does, then other more quantitative details about the solution are irrelevant.

More sensitive details about a given design can also be investigated. First, the experimental and numerical error associated with a particular facility and a given configuration can be "calibrated" out of the solution. This is accomplished by applying "adjustments" or "corrections" to the angle of attack, free-stream Mach number, and, if necessary, the wing twist distribution, until a good numerical/experimental correlation is achieved.

After the results are calibrated, geometry perturbations are sought either by trial and error or by using a suitable design approach to force desirable characteristics into the solution; for example, reduction in shock, strength at constant lift or a reduction in the isentropic pressure gradient also at constant lift to avoid separation. With this kind of approach, the use of numerical methods is most attractive. A large number of geometry perturbations can be examined quickly and efficiently. Once the optimal configuration is found numerically it can then be verified experimentally. As a result of this type of approach, much larger design spaces can be explored in the time available to the designer. This ultimately translates into more efficient aircraft designs obtained more cost effectively.

The results of a "calibration study" are presented in Fig. 9. The pressure coefficient distributions at two span stations for the wing-C configuration of Ref. 29 ($\eta = 0.3$ and 0.7) are compared with the Hinson-Burdges²⁹ experimental results for several conditions: 1) the experimental conditions with both the angle of attack and Mach number corrected ($M_\infty = 0.8, \alpha = 4.0^\circ$), 2) the experimental conditions with the angle of attack corrected ($M_\infty = 0.82, \alpha = 4.0^\circ$); and 3) the uncorrected experimental conditions ($M_\infty = 0.82, \alpha = 5.0^\circ$). As seen from Fig. 9, the results with corrected Mach number and angle of attack are in excellent agreement with experiment (upper surface). The result with only the angle of attack corrected is, by itself, in good agreement with experiment, thus indicating the importance of the α -correction.

Adjustment of these two parameters (M_∞ and α) has greatly improved the experimental/numerical correlation on the upper surface while producing slightly poorer agreement on the lower surface. This indicates that the less sensitive lower surface

solution has been (to an extent) sacrificed. That is, a significant portion of the $\Delta\alpha$ used in this calculation has been used to model viscous corrections or wind-tunnel wall interference.

Two additional comparisons utilizing the wing-C geometry and experimental results from Ref. 29 are presented in Figs. 10 and 11. Figure 10 shows a weakly supercritical case, $M_\infty = 0.7$ and $\alpha = 4.949^\circ$, and Fig. 11 shows the supercritical condition for which this wing was designed, $M_\infty = 0.85$ and $\alpha = 5.9^\circ$. For the first case, the experimental Mach number was matched and the angle-of-attack correction was -0.55° . Except for a slight over-prediction of the minimum pressure at the leading-edge upper surface, the overall agreement is excellent.

For the wing-C design case ($M_\infty = 0.85$, $\alpha = 5.9^\circ$) the Mach-number and angle-of-attack corrections were $\Delta M = -0.02$ and $\Delta\alpha = -0.9^\circ$. The agreement for this case is quite good everywhere except at the tip, where the need of viscous corrections is apparent. Of particular note in this calculation is the ability of the TWING code to predict the oblique shock which exists at both the third ($\eta = 0.5$) and fourth ($\eta = 0.7$) span stations. The differencing scheme in this region is entirely first-order accurate and yet little shock smearing is exhibited.

The wind-tunnel-wall interference study conducted in Ref. 29 produced similar, but smaller corrections for the wing-C design case ($\Delta M = -0.005$ and $\Delta\alpha = -0.9^\circ$). The angle-of-attack correction of Ref. 29 was determined from the FLO 22 computer code³³ by varying the computational angle of attack until the computed upper and lower surface pressures in the wing leading-edge region matched experiment. Then the difference between the experimental and computational angles of attack was taken as the desired angle-of-attack correction $\Delta\alpha$. After $\Delta\alpha$ was obtained, the Mach-number correction (ΔM) was determined by using the Bailey-Bailhaus TSD computer code.³⁴ Experimentally measured wind-tunnel-wall pressures were imposed as boundary conditions on the outer boundary of the computational domain (set to model the wind-tunnel-wall position). Next, free-air solutions were computed with variations in the Mach number to produce a "best match" free-air solution with the wind-tunnel solution. The difference in Mach number (if sufficiently small) between the wind-tunnel-wall case and the "best-match" free-air case was taken to be ΔM .

This wind-tunnel correction procedure seems to be a good one, for it includes nonlinear, three-dimensional effects; however, it could suffer from numerical uncertainties arising from viscous modeling, as well as other numerical errors, for example, nonconservative differencing and mesh effects. It should be noted that the corrections determined in Ref. 29 for the wing-C geometry, as well as other geometries not discussed herein, produced good agreement for comparisons between FLO22 and experiment, but not good agreement between other computer codes and experiment. The probable reason is that this correction procedure removes both experimental errors and the numerical errors associated with the FLO22 computer code. This suggests that separate corrections tailored to each individual computer code may be required.

The effects of the angle-of-attack ($\Delta\alpha$) and Mach-number (ΔM) corrections used for the wing-C design case just discussed are shown in Fig. 12. The pressure coefficient distributions at two span stations ($\eta = 0.30$ and 0.70) are compared with the Hinson-Burdges experiment for several conditions: 1) the corrected experimental conditions using the present corrections ($M_\infty = 0.83$, $\alpha = 5.0^\circ$); 2) the corrected experimental conditions using the corrections cited in Ref. 29 ($M_\infty = 0.845$, $\alpha = 5.0^\circ$); and 3) the uncorrected experimental conditions ($M_\infty = 0.85$, $\alpha = 5.9^\circ$). As seen from Fig. 12, the angle-of-attack correction is again more important than the Mach-number correction. The conditions cited in Ref. 29 yield a reasonable solution in the present case, primarily because both angle-of-attack corrections are the same.

The moderate sweep, taper, and aspect ratio case presented in Ref. 29 (wing B) is discussed next ($\Lambda_{LE} = 35^\circ$, $TR = 0.4$, and $AR = 3.8$). Pressure coefficient comparisons with experiment are presented for wing B at $M_\infty = 0.9$, and $\alpha = 3.9^\circ$ (experimental conditions) in Fig. 13. The ΔM and $\Delta\alpha$ corrections used in the TWING results were -0.02 and $+1.7^\circ$. The corresponding ΔM and $\Delta\alpha$ corrections computed in Ref. 29 were -0.005 and -1.0° . Overall, the agreement between experiment and TWING is good at every span station. The aft shock position near the root is about 5%-10% too far downstream, but moves into good agreement outboard of the midchord position.

Figures 14 and 15 present the results of an interesting study to determine the ability of TWING to handle both positive and negative sweep. The shock sonic line has been plotted in each figure on a normalized planform of the wing. This configuration consisted of a parallelogram NACA 0012 wing (i.e., $TR = 1.0$) at $M_\infty = 0.8$, $\alpha = 3^\circ$. The aspect ratio was 6. Figure 14 shows results for positive, or aft, sweep (sweep = 0° , 20° , 30° , 50° , and 60°), and Fig. 15 shows results for negative or forward sweep (sweep = 0° , -20° , -30° , -50° , -60° , and -70°). A case involving $+70^\circ$ of sweep was also obtained, but because it was entirely subcritical, no result at $\Lambda = 70^\circ$ appears in Fig. 14. As expected, the shock position moves forward and decreases in strength for increasing sweep (either positive or negative). For all cases the shock approaches the symmetry plane wall ($2y/b = 0$) in a normal fashion (i.e., in the physical domain), as it must to satisfy inviscid tangent-flow boundary conditions. This causes the variation in position of the shock/symmetry-plane intersection, as shown in Figs. 14 and 15.

Of particular interest in these calculations is the robustness displayed by the TWING code. The TWING grid mapping becomes singular as the sweep angle approaches 90° . In addition, cross-derivative terms in the transformed FP equation grow as the sweep increases. Since these cross-derivative terms are not represented in an implicit fashion in the AF2 iteration scheme, instability might be expected to develop for even moderate levels of sweep. However, as indicated by the present results, very large values of sweep ($-70^\circ \leq \Lambda \leq 70^\circ$) can be accommodated, in a stable fashion, by the TWING computer code.

A summary of computer times obtained from the TWING computer code for a range of computed examples

is shown in Table 1. The convergence for each of these cases is generally nonoptimal. The iteration number corresponds to the number of iterations required to reduce the initial maximum residual by two orders of magnitude. Computation times based on this measure of convergence range from 18 sec to 55 sec. Essentially converged results are obtained when the lift is bounded by a 1% band about the final value of lift. This level of convergence yields computational times ranging from 13 sec to 18 sec. The grid-generation time is also shown in Table 1; it is 1.3-1.4 sec (three defining stations).

These computational times are generally an order of magnitude smaller than other conservative full-potential codes using SLOR on the same computer (see Ref. 24 for a comparison of FLO28 and TWING). In addition, the advantage of vectorization, as provided by the Cray-1S vector computer, produces over an order of magnitude improvement in computational speed for TWING relative to the slower CDC 7600 computer. Other algorithms, such as SLOR, would not be so efficiently vectorized because of inherently recursive operations. See Ref. 35 for more discussion of this point.

IV. Conclusions

The TWING three-dimensional, transonic, full-potential computer program was evaluated using a wide range of test examples, and calculated pressure distributions were compared with experiment for most of the cases presented. The major conclusions of this study are as follows:

- 1) Good correlation with experimental pressure distributions were obtained in generally all cases when viscous effects were not important (that is, when strong shocks and the associated shock/boundary-layer interaction effects are not present).
- 2) The TWING computer program proved to be computationally efficient (even without optimizing each individual run for minimum run time) and robust (no convergence problems were encountered for the cases presented herein).
- 3) The TWING computer program proved to be geometrically general for isolated-wing calculations, in that a wide range of geometries has been run including high-aspect-ratio, low-taper transport-type configurations and low-aspect-ratio, high-taper fighter-type configurations.

References

- ¹Mason, W., Mackenzie, D. A., Stern, M. A., and Johnson, J. K., "A Numerical Three-Dimensional Viscous Transonic Wing-Body Analysis and Design Tool," AIAA Paper 78-101, Jan. 1978.
- ²Albone, C. M., Hall, M. G., and Joyce, G., "Numerical Solutions for Transonic Flows Past Wing-Body Configurations," Symposium Transonicum II, Gottingen, Sept. 1975, Springer-Verlag, 1976.
- ³Boppe, C. W. and Stern, M. A., "Simulated Transonic Flows for Aircraft with Nacelles, Pylons, and Winglets," AIAA Paper 80-130, Jan. 1980.
- ⁴van der Haagen, H., Bilitz, E., van Halbeek, H. H., and van Essen, A., "Remarks on the Suitability of Various Transonic Small Perturbation Equations to Describe Three-Dimensional Transonic Flow Examples of Computations Using a Fully-Conservative Rotated Difference Scheme," Symposium Transonicum II, Gottingen, Sept. 1975, Springer-Verlag, 1976.
- ⁵Wai, T. C., Yoshihara, H., and Abevanis, W. K., "Transonic Perturbation Analysis of Wing-Fuselage-Nacelle-Pylon Configurations with Powered Jet Exhausts," AIAA Paper 82-0255, Jan. 1982.
- ⁶Jameson, A., "Iterative Solution of Transonic Flows Over Airfoils and Wings, Including Flows at Mach 1," Communications on Pure and Applied Mathematics, Vol. 27, 1974, pp. 183-209.
- ⁷Caughey, D. A. and Jameson, A., "Numerical Calculation of Transonic Potential Flow About Wing-Body Combinations," AIAA Journal, Vol. 17, No. 2, Feb. 1979, pp. 175-181.
- ⁸Caughey, D. A. and Jameson, A., "Progress in Finite-Volume Calculations for Wing-Fuselage Combinations," AIAA Journal, Nov. 1980, pp. 1281-1288.
- ⁹Chattot, J. J., Coulombeix, C., and da Silva Tome, C., "Calculs d'écoulements Transsoniques Autour d'ailes," La Recherche Aérospatiale, No. 4, 1978, pp. 143-159.
- ¹⁰Yu, N. J., "Transonic Flow Simulations for Complex Configurations with Surface Fitted Grids," AIAA Paper 81-1258, June 1981.
- ¹¹Holst, T. L., Slooff, J. W., Yoshihara, H., and Ballhaus, W. F., Jr., "Applied Computational Transonic Aerodynamics," AGARDograph No. 266, 1982.
- ¹²Jameson, A., "Acceleration of Transonic Potential Flow Calculations on Arbitrary Meshes by the Multiple Grid Method," AIAA Paper 79-1458, July 1979.
- ¹³McCarthy, D. R. and Reyhner, T. A., "A Multi-Grid Code for Three-Dimensional Potential Flow About Axisymmetric Inlets at Angle of Attack," AIAA Paper 80-1365, July 1980.
- ¹⁴Shmilovich, A. and Caughey, D. A., "Application of the Multi-Grid Method to Calculations of Transonic Potential Flow About Wing-Fuselage Combinations," Multigrid Methods, NASA CP-2202, 1981.
- ¹⁵Boerstoeel, J. W., "A Multi-Grid Algorithm for Steady Transonic Potential Flows Around Aerofoils Using Newton Iteration," Multigrid Methods, NASA CP-2202, 1981.
- ¹⁶Deconinck, H. and Hirsch, C., "A Multigrid Method for the Transonic Full Potential Equation Discretized with Finite Elements on an Arbitrary Body Fitted Mesh," Multigrid Methods, NASA CP-2202, 1981.
- ¹⁷Sankar, N. L., Malone, J. B., and Tassa, Y., "An Implicit Conservative Algorithm for Steady and Unsteady Three-Dimensional Transonic Potential Flows," Proceedings of the AIAA 5th CFD Conf., Palo Alto, Calif., June 1981.

¹¹Ballhaus, W. F., Jr., Jameson, A., and Albert, J., "Implicit Approximate Factorization Schemes for the Efficient Solution of Steady Transonic Flow Problems," AIAA Journal, Vol. 16, 1978, pp. 573-579.

¹²Holst, T. L. and Ballhaus, W. F., Jr., "Fast Conservative Schemes for the Full Potential Equation Applied to Transonic Flows," AIAA Journal, Vol. 17, No. 2, Feb. 1979, pp. 145-152.

¹³Holst, T. L., "A Fast, Conservative Algorithm for Solving the Transonic Full-Potential Equation," AIAA Journal, Vol. 18, No. 12, Dec. 1980, pp. 1431-1439.

¹⁴Baker, T. J., "Potential Flow Calculation by the Approximate Factorization Method," Journal of Computational Physics, Vol. 42, 1981, pp. 1-19.

¹⁵Baker, T. J. and Forsey, C. R., "A Fast Algorithm for the Calculation of Transonic Flow Over Wing/Body Combinations," Proceedings of the AIAA 5th CFD Conf., Palo Alto, Calif., June 1981.

¹⁶Benek, J., Steinhoff, J., and Jameson, A., "Application of Approximate Factorization to the Three-Dimensional Transonic Potential Flow Calculations," Presented at the AIAA 5th CFD Conf., Palo Alto, Calif., June 1981.

¹⁷Holst, T. L. and Thomas, S. D., "Numerical Solution of Transonic Wing Flow Fields," AIAA Paper 82-0105, Jan. 1982.

¹⁸Hafez, M., South, J., and Murman, E., "Artificial Compressibility Methods for Numerical Solutions of Transonic Full Potential Equation," AIAA Journal, Vol. 17, No. 8, Aug. 1979, pp. 838-844.

¹⁹Eberle, A., "A Finite Volume Method for Calculating Transonic Potential Flow Around Wings from the Pressure Minimum Integral," NASA TM-75324, Translated from MBB UFE 1407(0), Feb. 1978.

²⁰Steger, J. L., "Implicit Finite Difference Simulation of Flow About Arbitrary Geometries with Application to Airfoils," AIAA Journal, Vol. 16, July 1978, pp. 679-686.

²¹Holst, T. L., "An Implicit Algorithm for the Conservative, Transonic Full Potential Equation Using an Arbitrary Mesh," AIAA Journal, Vol. 17, Oct. 1979, pp. 1038-1045.

²²Hinson, B. L. and Burdges, K. P., "Acquisition and Application of Transonic Wing and Far-Field Test Data for Three-Dimensional Computational Method Evaluation," AFSOR-TR-80-0421, Mar. 1980.

²³Hinson, B. L. and Burdges, K. P., "An Evaluation of Three-Dimensional Transonic Codes Using New Correlation-Tailored Test Data," AIAA Paper 80-0003, Jan. 1980.

²⁴Keener, E., Ames Research Center, private communication, 1982.

²⁵Hicks, R. M., "Transonic Wing Design Using Potential-Flow Codes - Successes and Failures," SAE Paper 810565, 1981.

²⁶Jameson, A. and Caughey, D. A., "Numerical Calculation of the Transonic Flow Past a Swept Wing," COO-3077-140, ERDA Math. and Comput. Lab., New York U., June 1977 (also available as NASA CR-153297).

²⁷Ballhaus, W. F., Jr., Bailey, F. R., and Frick, J., "Improved Computational Treatment of Transonic Flow About Swept Wings," NASA CP-2001, Nov. 1976.

²⁸Thomas, S. D. and Holst, T. L., "Numerical Computation of Transonic Flow About Wing-Fuselage Configurations on a Vector Computer," AIAA Paper 83-479, Jan. 1983.

Table 1 TWING convergence times on the Cray-1S computer (nonoptimal convergence), all times are for a $127 \times 27 \times 20$ (68,580) grid with 127×17 (2159) surface points

Wing	M_∞	α , deg	CPU time grid generation, sec	Number of ² iterations	CPU time, sec	CPU time for 98% lift, sec
C	0.7	4.4	1.4	90	27.6	17.2
C	0.8	4.0	1.4	90	27.5	17.4
C	0.83	5.0	1.4	99	30.9	18.1
B	0.88	2.2	1.3	170	54.9	12.9

²Two-order of magnitude reduction in the maximum residual.

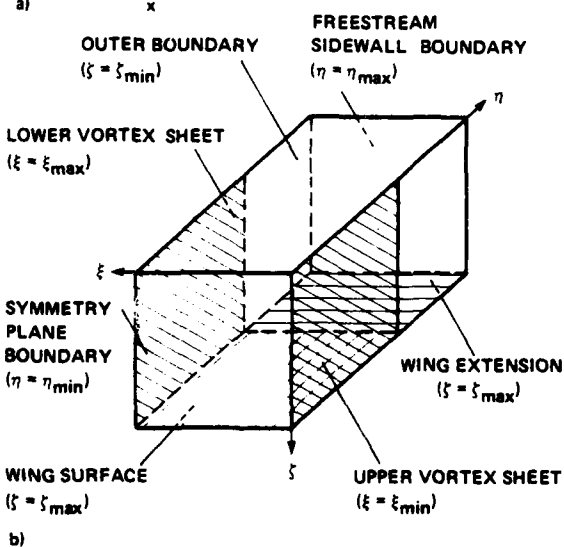
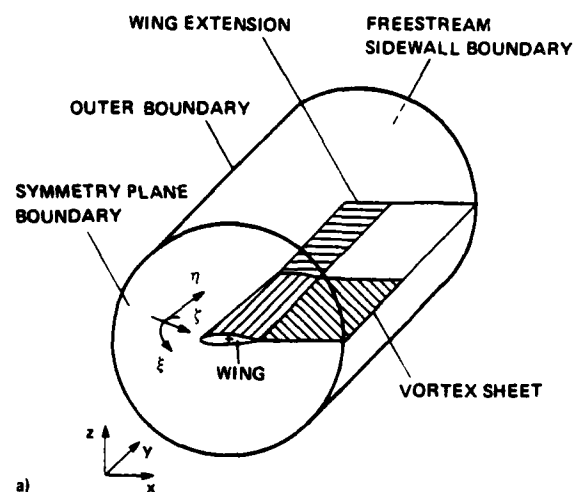


Fig. 1 Schematic of general $(x, y, z) \leftrightarrow (\xi, \eta, \zeta)$ transformation: a) physical domain; b) computational domain.

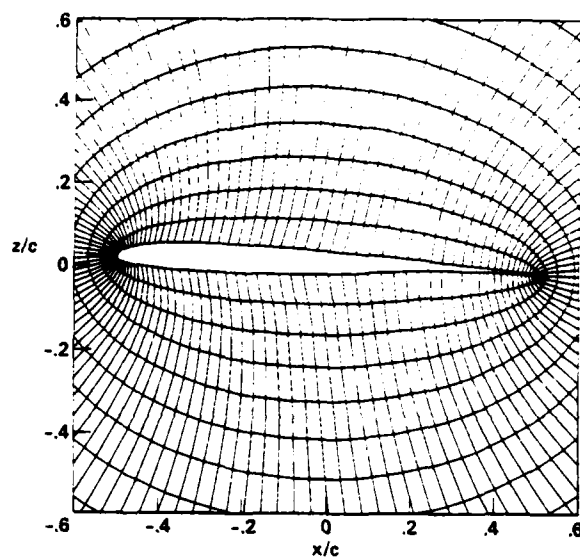


Fig. 2 Numerically generated finite-difference mesh about wing C configuration (Ref. 29), root station (127×20 grid points).

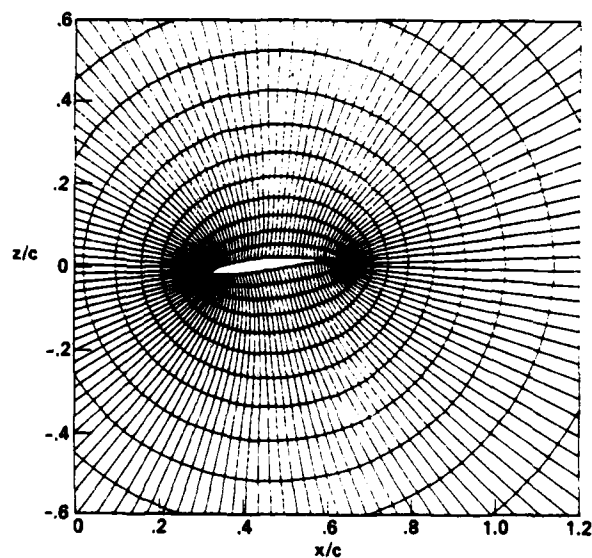


Fig. 3 Numerically generated finite-difference mesh about wing C configuration (Ref. 29), tip station (127×20 grid points).

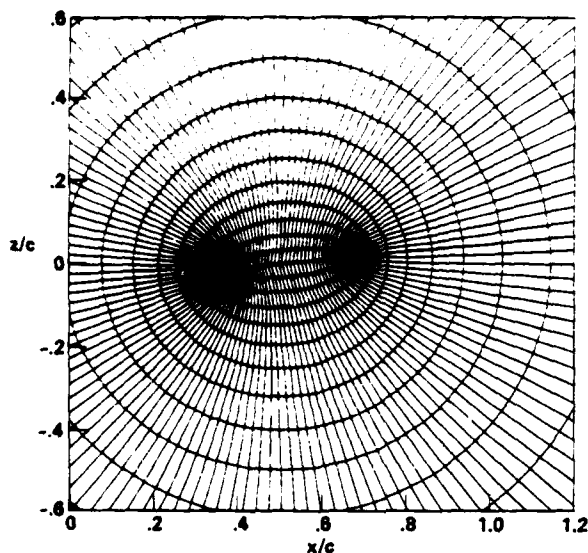


Fig. 4 Numerically generated finite-difference mesh about wing C configuration (ref. 29), station out-board of the tip (127×20 grid points).

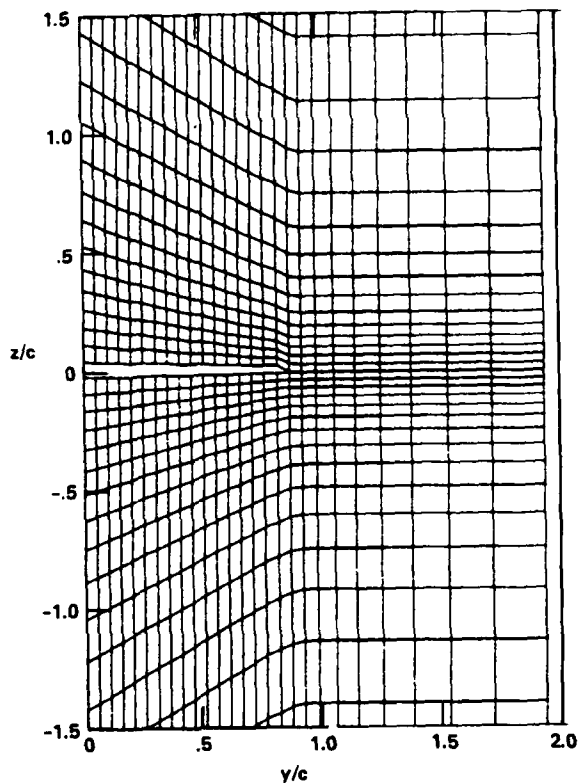


Fig. 6 Three-dimensional grid about wing C configuration (Ref. 29), half-chord view, 27×20 grid points.

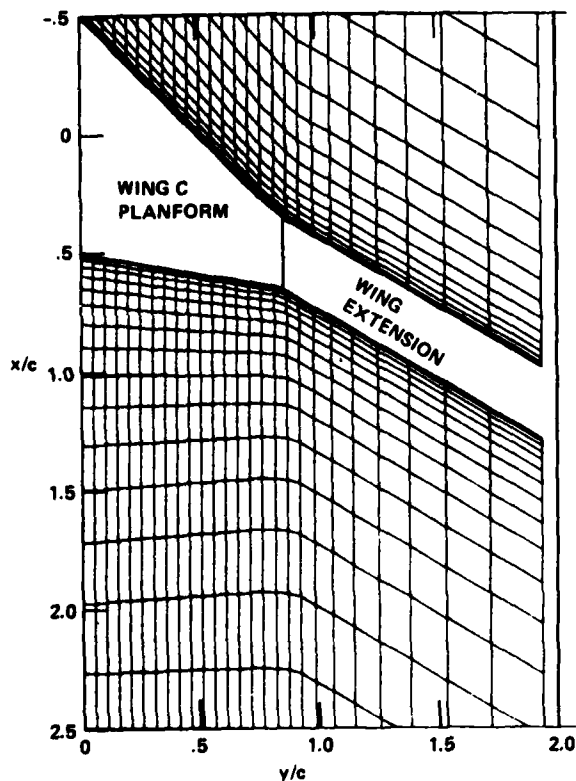


Fig. 5 Three-dimensional grid about wing C configuration (Ref. 29), planform view, 27×20 grid points.

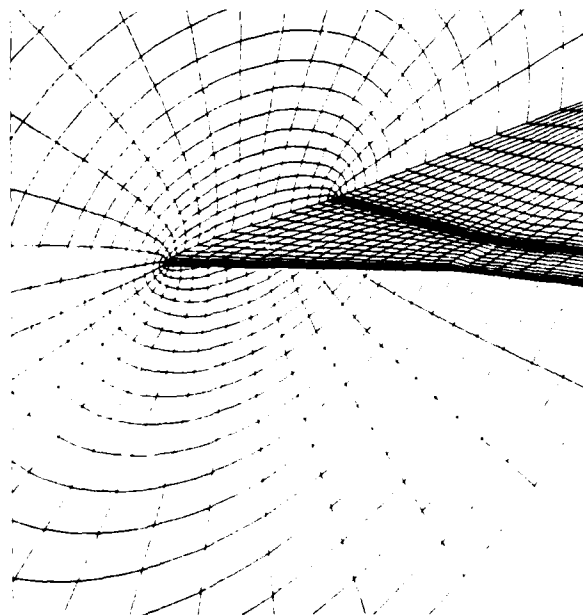


Fig. 7 Perspective view of the grid about wing C configuration, $127 \times 27 \times 20$ grid points (only every fourth point plotted in the wraparound direction).

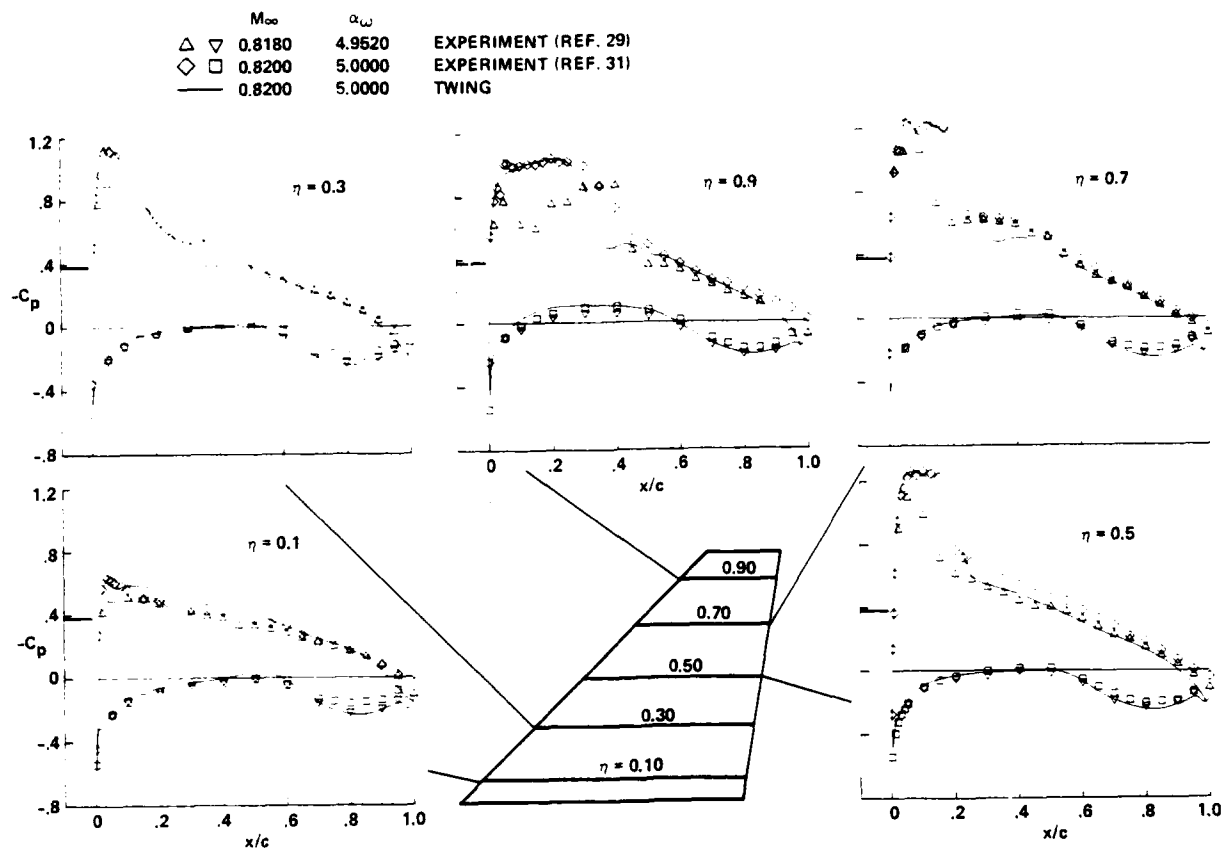


Fig. 8 Comparison of pressure coefficient distributions, wing C configuration, $\alpha_{LE} = 45^\circ$, $TR = 0.3$, $R = 2.6$.

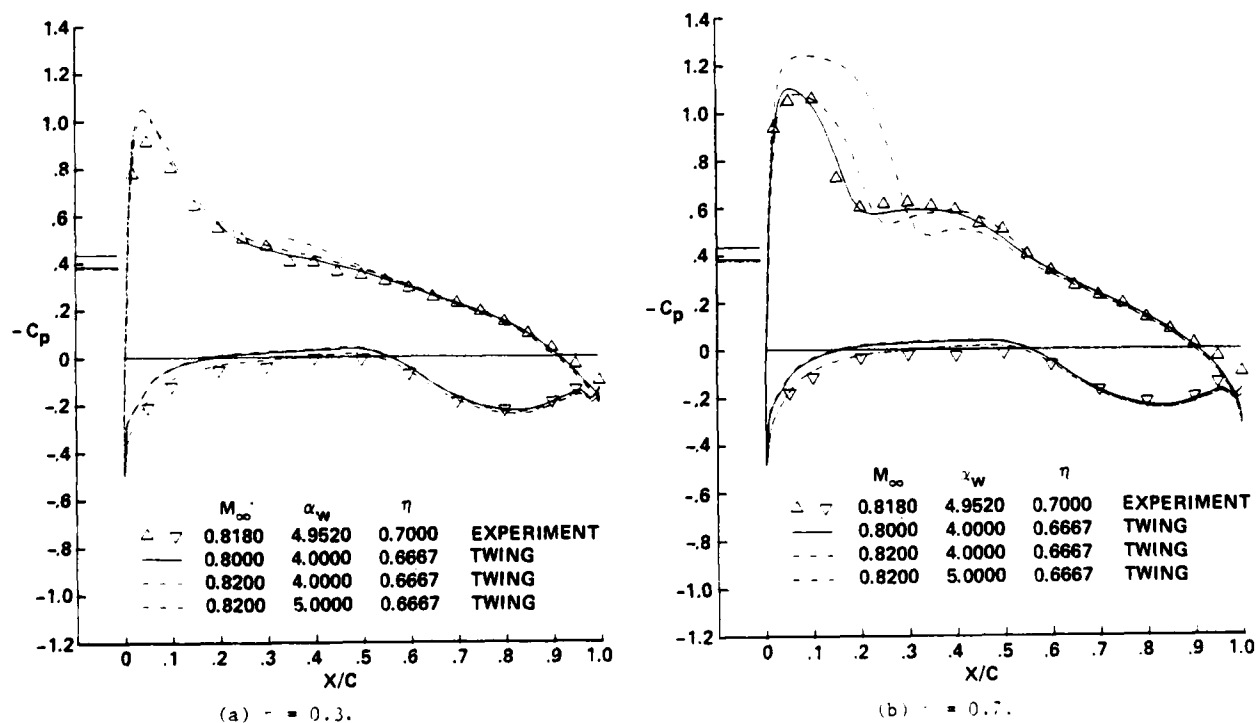


Fig. 9 Effect of Mach number and angle-of-attack corrections on the pressure coefficient distribution, experiment taken from Ref. 29: wing C, $\alpha_{LE} = 45^\circ$, $TR = 0.3$, $R = 2.6$.

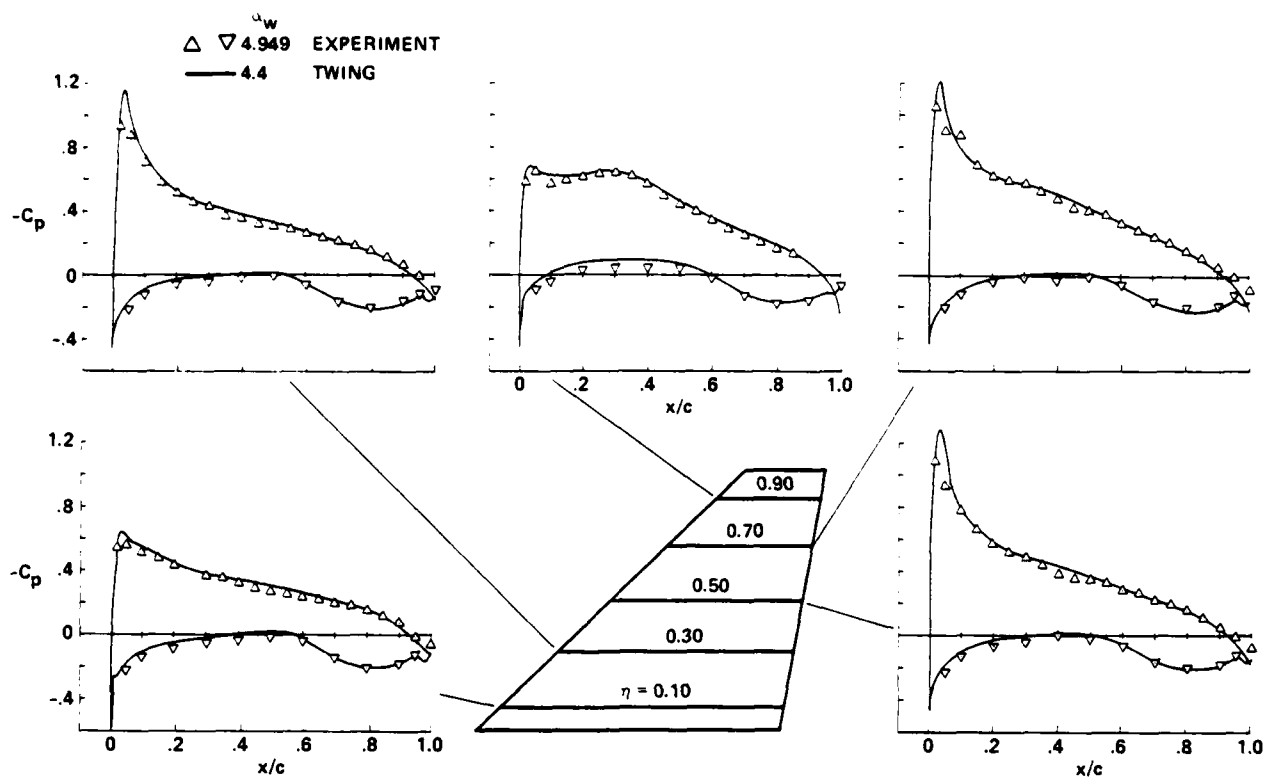


Fig. 10 Comparison of pressure coefficient distributions; weakly supercritical case; experiment taken from Ref. 29, wing C configuration, $\alpha_{LE} = 45^\circ$, $TR = 0.3$, $R = 2.6$.

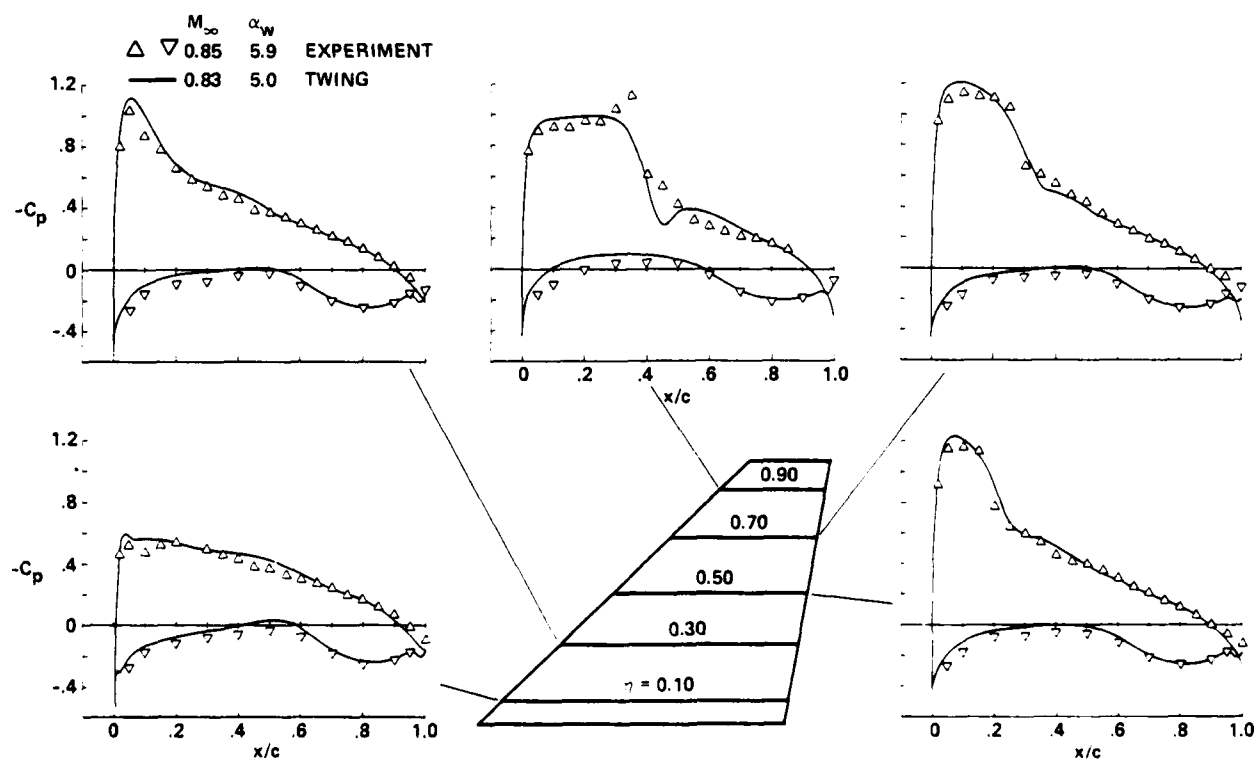


Fig. 11 Comparison of pressure coefficient distributions; design condition; experiment taken from Ref. 29, wing C configuration, $\alpha_{LE} = 45^\circ$, $TR = 0.3$, $R = 2.6$.

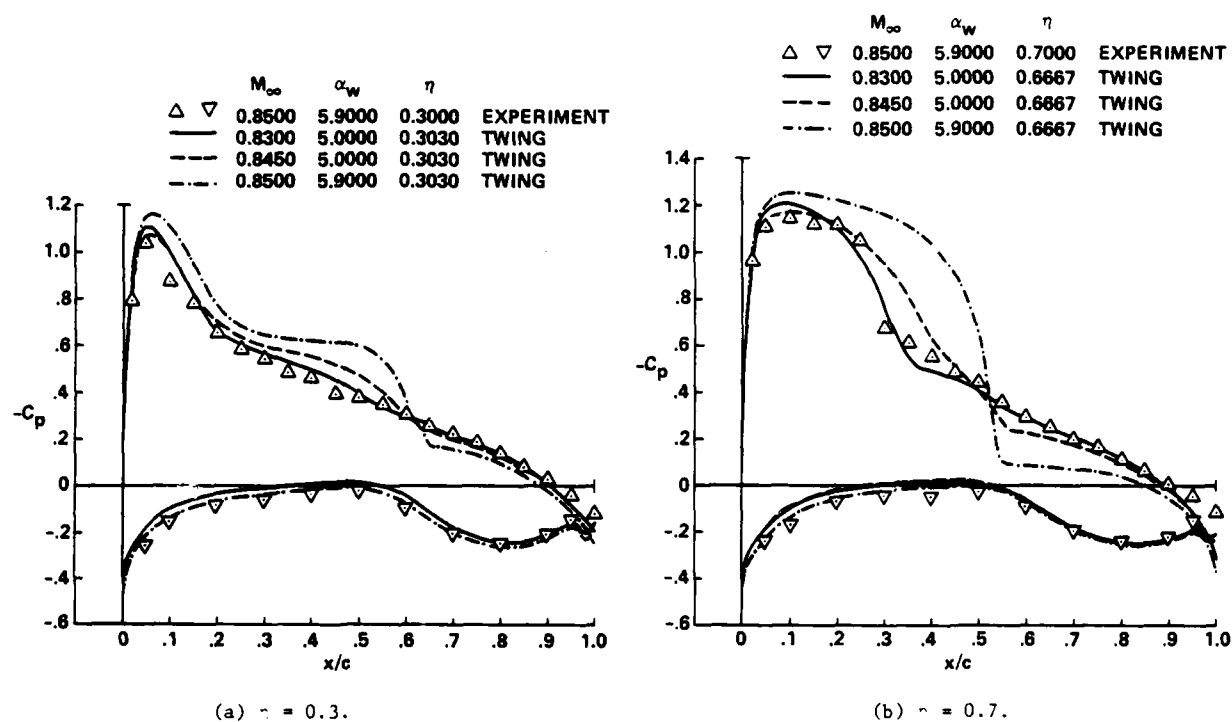


Fig. 12 Effect of Mach number and angle of attack corrections on the pressure coefficient distribution, experiment taken from Ref. 29, wing C configurations, $\Delta_{LE} = 45^\circ$, $TR = 0.3$, $R = 2.6$.

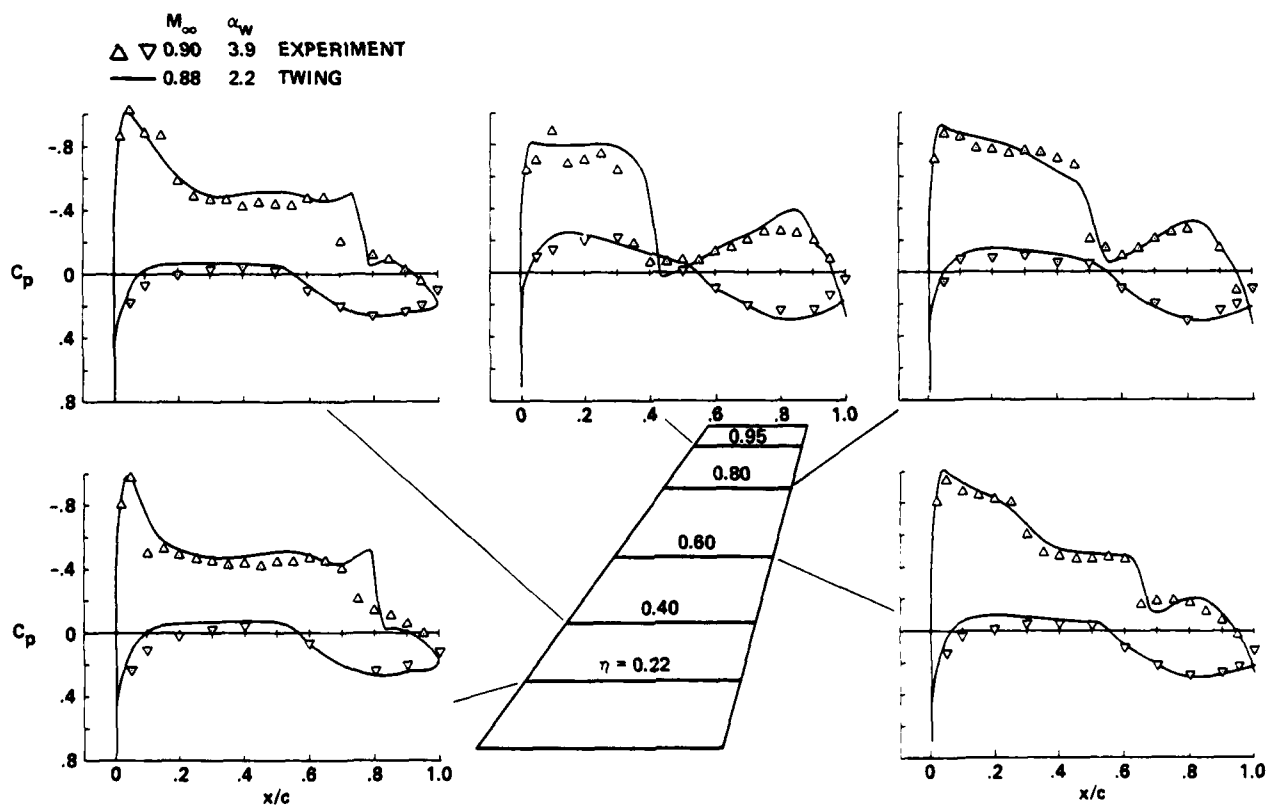


Fig. 13 Comparison of pressure coefficient distributions, experiment taken from Ref. 29, wing B configuration, $\Delta_{LE} = 35^\circ$, $TR = 0.4$, $R = 3.8$.

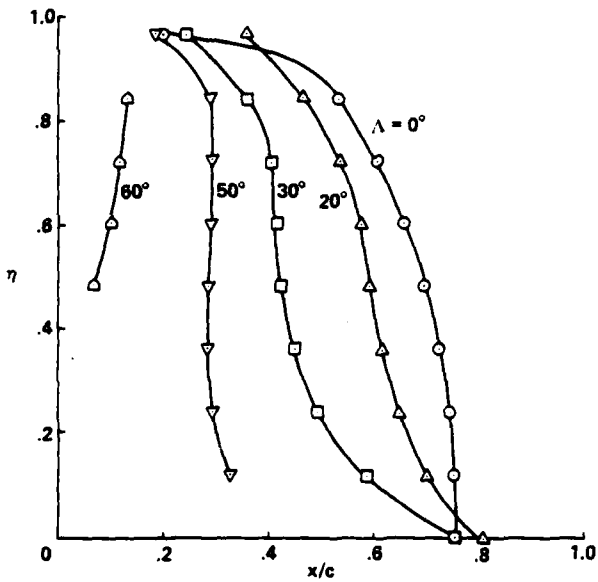


Fig. 14 Variation of shock sonic line with sweep: aft sweep (NACA 0012 airfoil sections, $M_\infty = 0.8$, $\alpha = 3^\circ$, $R = 6$, $TR = 1.0$).

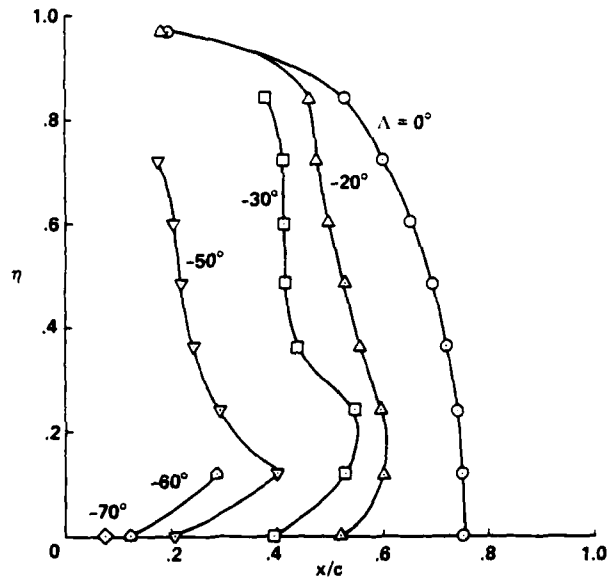


Fig. 15 Variation of the shock sonic line with sweep: forward sweep (NACA 0012 airfoil sections, $M_\infty = 0.8$, $\alpha = 3^\circ$, $R = 6$, $TR = 1.0$).

TRANSONIC FLOWFIELD COMPUTATION USING
A MODIFIED SHOCK-POINT OPERATOR

L. T. Chen

McDonnell Douglas Research Laboratories
St. Louis, Missouri 63166

Abstract

The development of higher-order finite-difference schemes for application to transonic wing-body flow calculations is described. These schemes treat supersonic flows and shocks more accurately than most existing schemes. A transformed full potential equation in a general curvilinear coordinate system is derived, and higher-order operators are introduced. A new shock-point operator produces Mach number jumps at a shock that agree reasonably well with Rankine-Hugoniot values. Second- and third-order, quasi-conservative, and fully conservative schemes are thereby developed for general geometries where flow directions can be approximately aligned with coordinate lines in supersonic regions. The fully conservative schemes are developed by modifying an existing finite-volume algorithm, while the quasi-conservative schemes are developed by solving the transformed full potential equation directly with the addition of the second- and third-order artificial viscosities at supersonic points, and the corresponding first- and second-order shock-point operators at shock points.

To evaluate the proposed shock-point operators, a model problem was studied, consisting of flow through a converging-diverging planar channel, with a shock in the diverging section. The computed shock locations and strengths were compared with a one-dimensional analysis including Rankine-Hugoniot shocks. These methods were successfully extended to three-dimensional flowfield computations. Computed results are presented for an ONERA-M6 wing on a vertical wall and on a semi-infinite fuselage, and compared with corresponding experimental data.

Nomenclature

a	speed of sound
a_0	stagnation speed of sound
a_∞	speed of sound at $M = 1$
\underline{A} , \underline{B} , \underline{C}	transformation matrices defined in Eqs. (3), (4), and (5)
c_1, c_2, \dots, c_9	coefficients defined in Eqs. (9)–(17) and (38)–(42)
D	determinant of Jacobian transformation matrix defined in Eqs. (33) and (47)
G	reduced velocity potential defined in Eq. (69)
h_1, h_2, \dots, h_9	coefficients defined in Eqs. (21)–(29)
H	artificial viscosities at supersonic points defined in Eqs. (53) and (56)
H_s	artificial viscosities at shock points defined in Eqs. (55), (57), (64), and (65)
\dot{m}	mass flow rate defined in Eq. (68)
M	local Mach number
M^*	normalized Mach number $= u/a_\infty$
P_m	partially conservative parameter defined in Eqs. (55) and (57)
P_x, P_y, P_z	second-order transformation derivatives defined in Eqs. (30)–(32) and (48)–(49)
s	coordinate in streamwise direction

u, v, w	velocity components in x, y , and z directions defined in Eqs. (34)–(36)
U, V, W	velocity components defined in Eqs. (18)–(20)
x, y, z	coordinates in physical space
x_s	location of shock in the channel axis
μ	switch function defined in Eq. (54)
ρ	local flow density
ρ^*	flow density at $M = 1$

Introduction

Shock structures on supercritical wings are generally complex so that the conventional first-order schemes¹⁻⁵ may not be accurate enough to capture their subtle changes. It is therefore desirable to develop higher-order schemes to improve the solution accuracy in supersonic regions. It has also become clear that prediction of shock strength and location in potential flow calculations depends almost entirely on the so-called shock-point operator, i.e., the equation solved at the first subsonic point downstream of the shock. Therefore, it is important to formulate an adequate shock-point operator so that the predicted shocks are in good agreement with physical shocks.

Several second-order schemes⁶⁻⁹ have been introduced for airfoil and cascade flowfield calculations. Jameson¹⁰ and Chen⁷ demonstrated that second-order fully conservative and quasi-conservative schemes, respectively, are capable of predicting double shocks on an airfoil surface, which cannot be accurately resolved using a first-order scheme without a large number of grid points. Chen⁷ also demonstrated that his second-order quasi-conservative scheme provides better resolution of a double shock than the second-order fully conservative scheme. Ives and Liutermoza⁸ showed that their second-order nonconservative scheme provides better resolution for transonic cascade flows than first-order nonconservative schemes. A discussion of first- and second-order nonconservative schemes has also been given in Ref. 7. A study of artificial viscosities and conservative shock-point operators of different orders was provided in Ref. 11 by Chen and Caughey, who also introduced a third-order quasi-conservative scheme. In the present study, second- and third-order artificial viscosities are first introduced for transonic potential flowfield computations about wings and wing-body combinations.

Methods for differencing the small disturbance equation at shocks were investigated by Murman¹² and Hafez.¹³ Methods for treating shocks in a full potential formulation were studied by Jameson⁶ and Chen and Caughey.¹¹ Fully conservative schemes for treating the potential equation conserve mass flux isentropically across shocks; therefore, the predicted shocks are always stronger than Rankine-Hugoniot shocks.² In the present study, a shock-point operator is derived from an approximate one-dimensional flow analysis. Use of this operator results in Mach number jumps at shocks that are in reasonable agreement with Rankine-Hugoniot values. Methods for differencing at shocks are evaluated using a model problem consisting of flow through a converging-diverging planar channel, with a shock in the diverging section. In flowfield calculations about wings, par-

tially conservative shock-point operators provide results that are in better agreement with experiment than a conservative scheme.

To the author's knowledge, this result is the first demonstration of a successful third-order scheme applied to solution of the full potential equation, the first presentation of both second- and third-order solutions for transonic potential flowfield computations about wings and wing-body configurations, and the first attempt to formulate a shock-point operator that produces Mach number jumps in a potential flow that are in reasonable agreement with Rankine-Hugoniot values.

Full Potential Equation

Quasi-conservative schemes are used to solve finite-difference approximations of the full potential equation. Therefore, it is convenient to first formulate the full potential equation in computational coordinates. By applying the chain rule, derivatives of the potential function ϕ in physical coordinates (x, y, z) can be related to its derivatives in an arbitrary curvilinear coordinate system (X, Y, Z) as follows:

$$\begin{bmatrix} \phi_x \\ \phi_y \\ \phi_z \end{bmatrix} = \underline{A} \begin{bmatrix} \phi_X \\ \phi_Y \\ \phi_Z \end{bmatrix} \quad (1)$$

$$\begin{bmatrix} \phi_{xx} \\ \phi_{yy} \\ \phi_{zz} \\ \phi_{xz} \\ \phi_{yz} \end{bmatrix} = -\underline{B} \underline{C} \underline{A} \begin{bmatrix} \phi_X \\ \phi_Y \\ \phi_Z \end{bmatrix} + \underline{B} \begin{bmatrix} \phi_{XX} \\ \phi_{YY} \\ \phi_{ZZ} \\ \phi_{XZ} \\ \phi_{YZ} \end{bmatrix} \quad (2)$$

where

$$\underline{A} = \begin{bmatrix} x_X & y_X & z_X \\ x_Y & y_Y & z_Y \\ x_Z & y_Z & z_Z \end{bmatrix}^{-1}$$

$$\underline{B} = \begin{bmatrix} x_X^2 & y_X^2 & 2x_X y_X & z_X^2 & 2x_X z_X & 2y_X z_X \\ x_Y^2 & y_Y^2 & 2x_Y y_Y & z_Y^2 & 2x_Y z_Y & 2y_Y z_Y \\ x_X x_Y & y_X y_Y & x_X y_Y + x_Y y_X & z_X z_Y & x_X z_Y + x_Y z_X & y_X z_Y + y_Y z_X \\ x_Z^2 & y_Z^2 & 2x_Z y_Z & z_Z^2 & 2x_Z z_Z & 2y_Z z_Z \\ x_X x_Z & y_X y_Z & x_X y_Z + x_Z y_X & z_X z_Z & x_X z_Z + x_Z z_X & y_X z_Z + y_Z z_X \\ x_Y x_Z & y_Y y_Z & x_Y y_Z + x_Z y_Y & z_Y z_Z & x_Y z_Z + x_Z z_Y & y_Y z_Z + y_Z z_Y \end{bmatrix}^{-1} \quad (4)$$

and

$$\underline{C} = \begin{bmatrix} x_{XX} & x_{YY} & x_{XY} & x_{ZZ} & x_{XZ} & x_{YZ} \\ y_{XX} & y_{YY} & y_{XY} & y_{ZZ} & y_{XZ} & y_{YZ} \\ z_{XX} & z_{YY} & z_{XY} & z_{ZZ} & z_{XZ} & z_{YZ} \end{bmatrix}^T \quad (5)$$

The full potential equation to be solved is

$$(a^2 - u^2)\phi_{xx} + (a^2 - v^2)\phi_{yy} + (a^2 - w^2)\phi_{zz} - 2uv\phi_{xy} - 2vw\phi_{yz} - 2uw\phi_{xz} = 0, \quad (6)$$

where u, v, w are the x, y, z components of the flow velocity, respectively, and a is the local speed of sound determined from the energy equation

$$a^2 = a_0^2 - \frac{\gamma - 1}{2} (u^2 + v^2 + w^2), \quad (7)$$

where γ is the ratio of specific heats for the assumed calorically perfect gas and a_0 is the stagnation speed of sound.

Substituting Eqs. (1) and (2) into Eq. (6), and after performing matrix inversion, multiplication, and careful algebraic manipulation, a full potential equation multiplied by the determinant of the Jacobian transformation matrix, D , in arbitrary curvilinear coordinates can be derived as

$$c_1\phi_{XX} + c_2\phi_{YY} + c_3\phi_{ZZ} + c_4\phi_{XY} + c_5\phi_{YZ} + c_6\phi_{XZ} + c_7\phi_X + c_8\phi_Y + c_9\phi_Z = 0, \quad (8)$$

where

$$c_1 = [a^2(h_1^2 + h_2^2 + h_3^2) - U^2]/D \quad (9)$$

$$c_2 = [a^2(h_4^2 + h_5^2 + h_6^2) - V^2]/D \quad (10)$$

$$c_3 = [a^2(h_7^2 + h_8^2 + h_9^2) - W^2]/D \quad (11)$$

$$c_4 = [2a^2(h_1 h_4 + h_2 h_5 + h_3 h_6) - 2UV]/D \quad (12)$$

$$c_5 = [2a^2(h_4 h_7 + h_5 h_8 + h_6 h_9) - 2VW]/D \quad (13)$$

$$c_6 = [2a^2(h_1 h_7 + h_2 h_8 + h_3 h_9) - 2UW]/D \quad (14)$$

$$c_7 = (h_1 p_X + h_2 p_Y + h_3 p_Z)/D \quad (15)$$

$$c_8 = (h_4 p_X + h_5 p_Y + h_6 p_Z)/D \quad (16)$$

$$c_9 = (h_7 p_X + h_8 p_Y + h_9 p_Z)/D, \quad (17)$$

U, V, W are velocity components defined as

$$U = h_1 u + h_2 v + h_3 w \quad (18)$$

$$V = h_4 u + h_5 v + h_6 w \quad (19)$$

$$W = h_7 u + h_8 v + h_9 w, \quad (20)$$

(4) coefficients h_1, h_2, \dots, h_9 are first-order transformation derivatives defined as

$$h_1 = y_Y z_Z - y_Z z_Y \quad (21)$$

$$h_2 = z_Y x_Z - z_Z x_Y \quad (22)$$

$$h_3 = x_Y y_Z - x_Z y_Y \quad (23)$$

$$h_4 = y_Z z_X - y_X z_Z \quad (24)$$

$$h_5 = z_Z x_X - z_X z_Z \quad (25)$$

$$h_6 = x_Z y_X - x_X y_Z \quad (26)$$

$$h_7 = y_X z_Y - y_Y z_X \quad (27)$$

$$h_8 = z_X x_Y - z_Y x_X \quad (28)$$

$$h_9 = z_X y_Y - x_Y y_X, \quad (29)$$

and coefficients p_X, p_Y , and p_Z are second-order transformation derivatives defined as

$$p_X = c_1 x_{XX} + c_2 x_{YY} + c_3 x_{ZZ} + c_4 x_{XY} + c_5 x_{YZ} + c_6 x_{XZ} \quad (30)$$

$$p_Y = c_1 y_{XX} + c_2 y_{YY} + c_3 y_{ZZ} + c_4 y_{XY} + c_5 y_{YZ} + c_6 y_{XZ} \quad (31)$$

$$p_Z = c_1 z_{XX} + c_2 z_{YY} + c_3 z_{ZZ} + c_4 z_{XY} + c_5 z_{YZ} + c_6 z_{XZ} \quad (32)$$

The determinant of the Jacobian transformation matrix is defined as

$$D = h_1 x_X + h_4 x_Y + h_7 x_Z. \quad (33)$$

The velocity components u , v , w are defined as

$$u = (h_1 \phi_X + h_4 \phi_Y + h_7 \phi_Z) / D \quad (34)$$

$$v = (h_2 \phi_X + h_5 \phi_Y + h_8 \phi_Z) / D \quad (35)$$

$$w = (h_3 \phi_X + h_6 \phi_Y + h_9 \phi_Z) / D. \quad (36)$$

Equation (8) can be reduced to a two-dimensional equation given in Ref. 7.

After the physical coordinates of grid points have been prescribed, the transformation derivatives $x_X, x_Y, x_Z, y_X, \dots, x_{XX}, x_{XY}, x_{YY}, \dots$ can be computed at each control point within a local mesh element. A second-order-accurate, finite-difference approximation of the transformed full potential equation thus can be obtained by applying a second-order element (Fig. 1). Within the element, X , Y , and Z vary from -1 to 1 from nodal point to nodal point. Therefore the mesh element is uniformly spaced in the computational space. Second-order shape functions can be constructed that relate the function at any point p within the element to the values of the function at 27 nodal points. If the control point is chosen to be $X = Y = Z = 0$, then the well-known second-order, centered, finite-difference formulations^{14,15} are obtained.

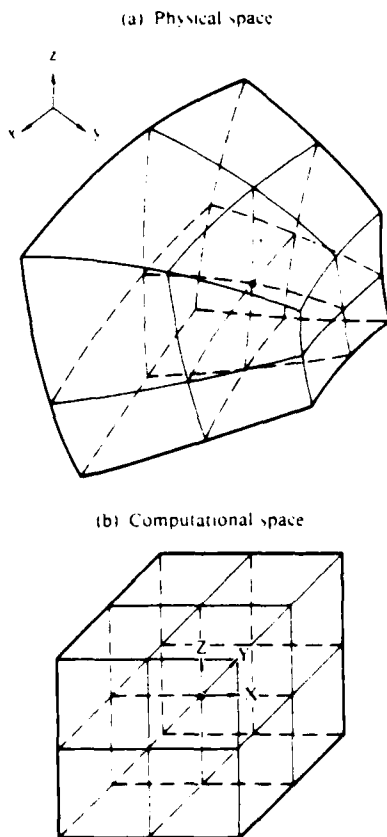


Fig. 1 Transformation of a second-order element.

Supersonic Flow and Shocks

The finite-difference approximation to the full potential equation discussed thus far is adequate for flows that are entirely subsonic. To treat transonic flows, proper artificial viscosities or densities are normally added to the finite-difference approximation of the potential equation solved at supersonic points. The directional bias of supersonic flows can thus be reflected in the governing equation.

The so-called fully conservative and quasi-conservative schemes conserve the artificial viscosities or densities along streamlines; in other words, the total summation of artificial viscosities or densities added to the potential equation at all points along the streamline is exactly zero. Naturally the shocks thus predicted are consistent with isentropic mass-conserving shocks, which do not simultaneously conserve momentum and therefore are stronger than the Rankine-Hugoniot shocks.

In the nonconservative schemes, the total summation of artificial viscosities or densities added along the streamline is not zero. In the limit of the finite-difference approximation, this unbalanced summation term appears as a nonzero source term on the right side of the potential equation solved at certain points along the streamline generally at the shock point, the first subsonic point downstream of the shock. This source term in the equation represents a mass source in the flowfield. Therefore, the solutions thus obtained deviate from the isentropic mass-conserving solutions. Since the potential formulation does not permit simultaneous conservation of mass and momentum flux at shocks, errors in the jumps in fluid properties are inevitable. A desirable method from an engineering point of view is one in which errors in the properties of primary interest are minimized. As a matter of fact, it has been consistently shown that the shocks computed by these nonconservative schemes agree better with experiment than those computed by the conservative schemes.¹⁶ The nature of the nonzero source term was understood to be related to the addition of mass flux; however, an adequate mathematical explanation of its effect has not been given. An attempt to explain the nonzero source term will be given in the form of a simple one-dimensional flow analysis, following introduction of artificial viscosities.

Artificial Viscosities and Partially Conservative Shock Point Operators

The second derivative of the potential function in the streamwise direction, s , is given as

$$\phi_{ss} = \frac{a^2}{q^2} (u^2 \phi_{xx} + v^2 \phi_{yy} + w^2 \phi_{zz} + 2uv \phi_{xy} + 2vw \phi_{yz} + 2uw \phi_{xz}). \quad (37)$$

Substituting Eqs. (1) and (2) into Eq. (37) yields

$$\phi_{ss} = \frac{1}{q^2} (U^2 \phi_{XX} + V^2 \phi_{YY} + W^2 \phi_{ZZ} + 2UV \phi_{XY} + 2VW \phi_{YZ} + 2UW \phi_{XZ}). \quad (38)$$

where U , V , W are given in Eqs. (18)–(20).

The directional bias of supersonic flows can be properly simulated by performing an upwind differencing or adding artificial viscosities in the approximate streamwise direction. If $Y = \text{constant}$ lines are in the approximate s direction, the principal part of ϕ_{ss} can be approximated by

$$\phi_{ss} = \frac{U^2}{q^2} \phi_{XX}. \quad (39)$$

A second-order artificial viscosity can be expressed as

$$H = \left[\frac{(\Delta X)^2 \mu U^2 \phi_{XX}}{D} \right]_{XX} = \left(\frac{\mu U^2 \phi_{XX}}{D} \right)_{i-2} - 2 \left(\frac{\mu U^2 \phi_{XX}}{D} \right)_{i-1} + \left(\frac{\mu U^2 \phi_{XX}}{D} \right)_i \quad (40)$$

where

$$\mu = \max \left(1 - \frac{a^2}{q^2}, 0 \right) \quad (41)$$

H is then added to the finite-difference representation of Eq. (8) at supersonic points. At shock points, i.e., the first downstream subsonic points after the shocks, the following first-order artificial viscosity H_s is added with p_m controlling the nonconservative differencing:

$$H_s = (p_m - 1) \left[\frac{(\Delta X) \mu U^2 \phi_{XX}}{D} \right]_X = \left[\left(\frac{\mu U^2 \phi_{XX}}{D} \right)_{i-1} - \left(\frac{\mu U^2 \phi_{XX}}{D} \right)_{i-2} \right] (p_m - 1) \quad (42)$$

If $p_m = 0$, the quantity $\mu U^2 \phi_{XX}$ is conserved along $Y = \text{constant}$ lines, implying that the added artificial viscosities are conserved along approximate streamlines. If $p_m > 0$, a numerical mass flux is introduced at shocks, modifying the locations and strengths of the shocks. The effect of p_m on the captured shocks will be discussed later. Although μ is a ramp function, both H and H_s reduce to zero as the mesh size goes to zero. The solution is second-order accurate at both subsonic and supersonic points and first-order accurate at shock points. The scheme is second-order quasi-conservative. In the so-called quasi-conservative schemes, only the differencing of artificial viscosities is in divergence form; the differencing of the governing potential equation is not. A second-order fully conservative scheme also can be constructed by incorporating H and H_s into the existing finite-volume algorithm.

Third-order, quasi-conservative and fully conservative schemes can be developed by adding the following third-order artificial viscosity at supersonic points:

$$H = \left[\frac{(\Delta X)^3 \mu U^2 \phi_{XXX}}{D} \right]_{XXX} = \left(\frac{\mu U^2 \phi_{XXX}}{D} \right)_i - 3 \left(\frac{\mu U^2 \phi_{XXX}}{D} \right)_{i-1} + 3 \left(\frac{\mu U^2 \phi_{XXX}}{D} \right)_{i-2} - \left(\frac{\mu U^2 \phi_{XXX}}{D} \right)_{i-3} \quad (43)$$

and adding the following second-order artificial viscosity at shock points:

$$H_s = (p_m - 1) \left[\frac{(\Delta X)^3 \mu U^2 \phi_{XXX}}{D} \right]_{XX} = \left[\left(\frac{\mu U^2 \phi_{XXX}}{D} \right)_{i-3} - 2 \left(\frac{\mu U^2 \phi_{XXX}}{D} \right)_{i-2} + \left(\frac{\mu U^2 \phi_{XXX}}{D} \right)_{i-1} \right] (p_m - 1) \quad (44)$$

If p_m is set to zero, the quantity $\mu U^2 \phi_{XXX}$ is conserved along $Y = \text{constant}$ lines. If p_m is set to be greater than zero, a numerical mass flux is added at shocks, as in the second-order schemes.

A Simple One-Dimensional Flow Analysis and a Shock-Point Operator

An alternative new method to formulate a shock-point operator is described in the following paragraphs. This method is based on an approximate one-dimensional analysis in which information from the Rankine-Hugoniot relations is incorporated.

The flows upstream and downstream of the shock can be considered as relating to two branches of isentropic flows. Because of the entropy increase across the shock, the stagnation density decreases, while the stagnation speed of sound remains unchanged because the process is adiabatic. The continuity equation can therefore be written as

$$\rho_1^* M_1 \left(1 + \frac{\gamma-1}{2} M_1^2 \right)^{-3} = \rho_2^* M_2 \left(1 + \frac{\gamma-1}{2} M_2^2 \right)^{-3} \quad (45)$$

or

$$\int_{x_1}^{x_2} \left[\rho^* M \left(1 + \frac{\gamma-1}{2} M^2 \right) \right]_X dx = 0, \quad (46)$$

where x_1 and x_2 are the axial positions just upstream and downstream of the shock and ρ_1^* , ρ_2^* , M_1 , and M_2 are sonic densities and Mach numbers of the flows just upstream and downstream of the shock. If the Mach number is assumed to change smoothly across the shock, as it does in most finite-difference solutions, the integration followed by the differentiation of the term inside the bracket can be performed to give the following approximate equation.

$$(1 - M^{*2}) (M_2^* - M_1^*) = - \left(1 - \frac{\gamma-1}{\gamma+1} M^{*2} \right) M^* \left(1 - \frac{\rho_2^*}{\rho_1^*} \right) \quad (47)$$

where $M^* = u/a_* = \phi_x/a_*$ and a_* is the sonic speed at $M = 1$. Two approximations have been made: the $(1 - M^{*2})$ term on the left side and the $[1 - (\gamma-1)/(\gamma+1)M^{*2}]M^*$ term on the right side are treated as constants during integration, and the relative change in ρ^* is assumed to be small. In a fully isentropic flow, ρ^* is constant, the right side of Eq. (47) is therefore zero, and the left side can be rewritten as the familiar one-dimensional potential equation

$$(a^2 - u^2) \phi_{XX} = 0. \quad (48)$$

A change in ρ^* occurs across a shock in a real flow. The right side of Eq. (47) should be related to the error incurred at a shock in a potential flow calculation. M^* on the right side of Eq. (47) is the average value of M_1^* and M_2^* , and therefore a reasonable approximation is $M^* = 1$. If this approximation is made and the left-side notation of Eq. (48) is retained for clarity,

$$(a^2 - u^2) \phi_{XX} = - a_*^2 \left(1 - \frac{\rho_2^*}{\rho_1^*} \right) / \Delta x, \quad (49)$$

where Δx is the axial spacing across the shock. Numerical values for the right side of Eq. (49) can be obtained by introducing a Rankine-Hugoniot relation,

$$\frac{\rho_2^*}{\rho_1^*} = M_1^{2\gamma/(\gamma-1)} \left[\left(1 - \frac{\gamma-1}{\gamma+1} M_1^{*2} \right) / \left(M_1^{*2} - \frac{\gamma-1}{\gamma+1} \right) \right]^{1/(\gamma-1)} \quad (50)$$

where ρ_1^* and ρ_2^* are values of ρ^* upstream and downstream of shocks, respectively, and M_1 is the normalized shock Mach number upstream of the shock.

This result is used to modify the conservative first- and second-order artificial viscosities at shock points as follows (see Eqs. (42) and (44)):

$$H_x = - \left[\frac{(\Delta X) \mu U^2 \phi_{xx}}{D} \right]_x + a_1^2 \left(1 - \frac{\rho_2^*}{\rho_1^*} \right) / \Delta x_s \quad (51)$$

and

$$H_y = - \left[\frac{(\Delta X)^2 \mu U^2 \phi_{xx}}{D} \right]_{xx} + a_1^2 \left(1 - \frac{\rho_2^*}{\rho_1^*} \right) / \Delta x_s \quad (52)$$

where ΔX_s is the distance between the shock point and its upstream supersonic point in the streamwise direction.

Relaxation Strategies

The finite-difference approximation to Eq. (8) can be solved by a line-relaxation scheme with the boundary conditions described in the previous section. To ensure that the relaxation scheme corresponds to a convergent process, the old and updated values of the potential functions, ϕ and ϕ^+ , must be mixed properly. The basic relaxation strategies developed for the present method are similar to the ones described in Refs. 14 and 17, except for careful treatments of artificial viscosities at supersonic and shock points.

In the second-order quasi-conservative scheme, the old and new values of ϕ contributing to the terms $(q^2 - a^2)\phi_{ss} + H$ (or H_y) of the relaxation equation are chosen to ensure a convergent process in the $i = \text{constant}$ line sweep according to

$$\begin{aligned} (q^2 - a^2) \phi_{ss} + H = & \left[\left(\frac{\mu U^2}{D} \right)_{i,j,k} + 4 \left(\frac{\mu U^2}{D} \right)_{i-m,j,k} \right. \\ & \left. + \left(\frac{\mu U^2}{D} \right)_{i-2m,j,k} \right] \times (c_{i,j,k} - c_{i-m,j,k}) \\ & - 2 \left[\left(\frac{\mu U^2}{D} \right)_{i-m,j,k} + \left(\frac{\mu U^2}{D} \right)_{i-2m,j,k} \right] \\ & \times (c_{i,j,k} - c_{i-2m,j,k}) + R_{ss} \end{aligned} \quad (53)$$

for supersonic points, and

$$\begin{aligned} (q^2 - a^2) \phi_{ss} + H_y = & 2 \left[\left(\frac{\mu U^2}{D} \right)_{i-m,j,k} + \left(\frac{\mu U^2}{D} \right)_{i-2m,j,k} \right] \\ & \times (1 - p_m) (c_{i,j,k} - c_{i-m,j,k}) - \left[\left(\frac{\mu U^2}{D} \right)_{i-m,j,k} \right. \\ & \left. - 2 \left(\frac{\mu U^2}{D} \right)_{i-2m,j,k} \right] \\ & \times (1 - p_m) (c_{i,j,k} - c_{i-2m,j,k}) + R_{ss} \end{aligned} \quad (54)$$

for shock points, where $c_{i,j,k} = \phi_{i,j,k}^+ - \phi_{i,j,k}$ is the correction to the potential function, m is equal to 1 or -1 if $U > 0$ or $U < 0$, respectively, and R_{ss} is the residual of the finite-difference approximation to $(q^2 - a^2)\phi_{ss}$ evaluated using old values of ϕ . The second-order fully conservative scheme applies the same

strategy to treat the artificial viscosities at supersonic and shock points. A similar strategy can also be developed for the third-order quasi-conservative and fully conservative schemes.

Analysis of Shocks in Channel Flows

A model problem, consisting of flow through a planar, symmetric converging-diverging channel (Fig. 2) was used to evaluate various methods for treatment of shock waves in potential flow. This configuration provides a relatively simple, inexpensive framework for evaluation of numerical methods prior to incorporation into a three-dimensional method.

The flow becomes sonic at the throat, x_t , and shocks occur in the diverging section extending from x_t to x_e . The slope of the diverging wall can be adjusted so that the predicted shock Mach numbers range from 1.0 to 2.0. Values of p_m vary from -0.6 to 0.8 , and mass flux across each x station is computed to check the mass flux conservation.

A previously developed inlet program¹⁴ was modified to compute the flows with shocks in the channel by incorporating the second- and third-order artificial viscosities and the partially conservative shock-point operators described previously. A typical grid system is presented in Fig. 3. In the calculation, two meshes were used; the coarse mesh had 50 mesh elements in the unwrapped X -direction, 12 mesh elements in the surface normal direction, and 20 equally spaced streamwise mesh elements in

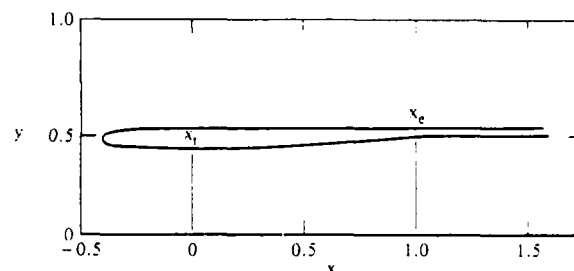


Fig. 2 A converging-diverging channel.

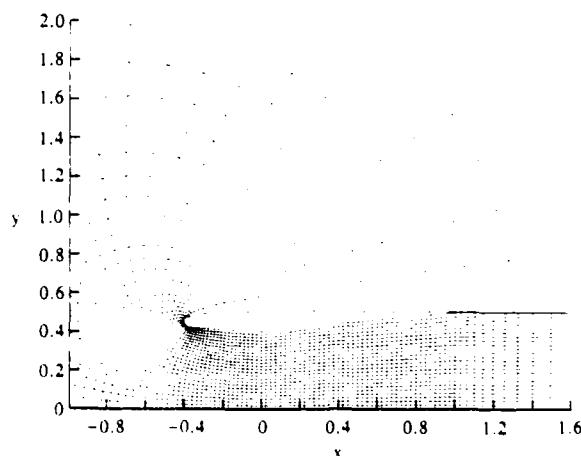


Fig. 3 Grid distribution about nozzle C.

the diverging section. The fine mesh had twice as many mesh elements in both directions. To ensure that a converged solution in the fine mesh existed and to improve the convergence rate, the potential function at the downstream outer boundary was frozen after 300 iterations, while the procedure continued to a total of 600 iterations. The number of supersonic points usually ceases to change in the last 50 to 200 iterations. Solutions were obtained for various slopes of the diverging wall and various inlet and exit conditions. After each flowfield computation, the total mass flux across each cross-section was computed by numerical integration:

$$\dot{m} = \int \rho u dy$$

or

$$\frac{\dot{m}}{\rho^* a^*} = \int_{\text{axis}}^{\text{wall}} M_x \left(1 + \frac{\gamma-1}{2} M^2 \right)^{-\frac{\gamma}{\gamma-1}} dy \quad (55)$$

where M_x is the component of the Mach number parallel to the nozzle axis. The nozzle flow differs from an external flow with a shock in that the flow downstream of the shock in the channel can be regarded as a potential flow with $\rho^* = \rho_2^* = \text{constant}$, since the variation in shock strength across the channel is relatively small. For each flowfield computation, the mass flow rate and a^* were assumed constant, and the change of the integral upstream and downstream of the shock was interpreted as a change in ρ^* across the shock.

Table 1 presents a summary of results. Channels A, B, C, D, E, and F have values of diverging wall slopes of 0.15, 0.20, 0.25, 0.40, 0.50, and 0.875, respectively; H represents the order of artificial viscosity; p_m is the parameter, first introduced in Eq. (42), controlling the degree of nonconservative differencing; RH in the p_m column means that the shock-point operators defined in Eqs. (51) or (52) were used, and x_s is the shock location. M_{exit} is the average Mach number at the channel exit; $x_s = 1.475$ for all cases considered here. M_1 and M_2 are the average Mach numbers upstream and downstream of the shock. By assuming $M = 1$ at the throat ($x = 0$), the channel area ratio can be used to find a one-dimensional value of M_1 at the shock. Similarly, the area ratio (between $x = x_s$ and $x = x_e$) and M_{exit} can be used to determine a corresponding value of M_2 . The Mach number downstream of the shock is M_2 ; RH given by the Rankine-Hugoniot relation. $(\rho_2^*/\rho_1^*)_c$ is the stagnation density ratio across the shock, computed by numerically integrating the function given in Eq. (55). $(\rho_2^*/\rho_1^*)_{RH}$ is the analytical stagnation density ratio across a Rankine-Hugoniot shock given by Eq. (53), and ϵ is the relative error of $(\rho_2^*/\rho_1^*)_c$ to $(\rho_2^*/\rho_1^*)_{RH}$. As p_m increases from 0 to 0.8, $(\rho_2^*/\rho_1^*)_c$ decreases from near unity to a value less than $(\rho_2^*/\rho_1^*)_{RH}$. Smaller values of ϵ generally mean better agreement between M_2 and M_2 RH .

Figure 4 compares computed shock Mach numbers, M_1 and M_2 , with Rankine-Hugoniot shocks and Mach numbers obtained from isentropic, mass-conserving relations. Solutions obtained by setting $p_m = 0$ always lie below the isentropic, mass-conserving shock curve. Solutions obtained by setting $p_m = 0.6$ to 0.8 give reasonable agreement with the Rankine-Hugoniot

Table 1. Summary of channel flow calculations.

Case	H	Channel	p_m	x_s	M_1	M_2	M_2 RH	M_{exit}	$\rho_2^*/\rho_1^*)_c$	$\rho_2^*/\rho_1^*)_RH$	ϵ (%)
1	2	A	-0.6	0.475	1.312	0.709	0.780	0.617	1.014	0.977	3.7
2	2	A	-0.3	0.475	1.312	0.713	0.780	0.621	1.011	0.977	3.4
3	2	A	0	0.475	1.312	0.713	0.780	0.620	1.011	0.977	3.4
4	2	A	0.6	0.475	1.312	0.760	0.780	0.651	0.383	0.977	0.6
5	2	A	0	0.900	1.435	0.626	0.725	0.612	1.022	0.946	7.6
6	2	C	0	0.725	1.508	0.577	0.699	0.530	1.025	0.927	9.8
7	2	D	0	0.600	1.587	0.515	0.672	0.435	1.059	0.900	15.9
8	2	D	0	1.000	1.763	0.464	0.625	0.464	1.007	0.829	17.8
9	2	B	0.6	0.150	1.200	0.792	0.843	0.580	0.992	0.993	-0.1
10	3	A	0.8	0.450	1.303	0.766	0.785	0.650	0.977	0.979	-0.2
11	3	B	0.8	0.475	1.364	0.737	0.755	0.615	0.971	0.967	0.4
12	3	B	0.8	0.575	1.402	0.788	0.739	0.665	0.930	0.958	-2.8
13	2	D	0.8	0.375	1.460	0.716	0.716	0.511	0.936	0.942	-0.6
14	2	C	0.7	0.875	1.560	0.712	0.681	0.675	0.888	0.910	-2.2
15	3	D	0.8	0.575	1.574	0.704	0.676	0.559	0.885	0.904	-1.9
16	2	E	0.8	0.725	1.726	0.656	0.634	0.558	0.826	0.845	-1.9
17	2	E	0.8	0.950	1.832	0.623	0.609	0.606	0.782	0.798	-1.6
18	2	F	0.8	0.725	1.961	0.545	0.584	0.450	0.768	0.739	2.9
19	2	F	0.8	0.975	2.110	0.568	0.560	0.558	0.660	0.670	-1.0
20	2	A	RH	0.550	1.336	0.743	0.768	0.653	0.982	0.973	0.9
21	3	B	RH	0.550	1.393	0.707	0.742	0.610	0.975	0.960	1.5
22	2	B	RH	0.550	1.393	0.708	0.742	0.610	0.973	0.960	1.3
23	3	B	RH	0.725	1.454	0.691	0.718	0.632	0.953	0.944	0.9
24	2	C	RH	0.675	1.490	0.662	0.704	0.589	0.954	0.932	2.2
25	3	D	RH	0.475	1.527	0.635	0.692	0.496	0.945	0.921	2.4
26	2	C	RH	1.000	1.602	0.655	0.668	0.657	0.896	0.894	0.2
27	2	D	RH	0.875	1.719	0.608	0.636	0.577	0.856	0.848	0.8

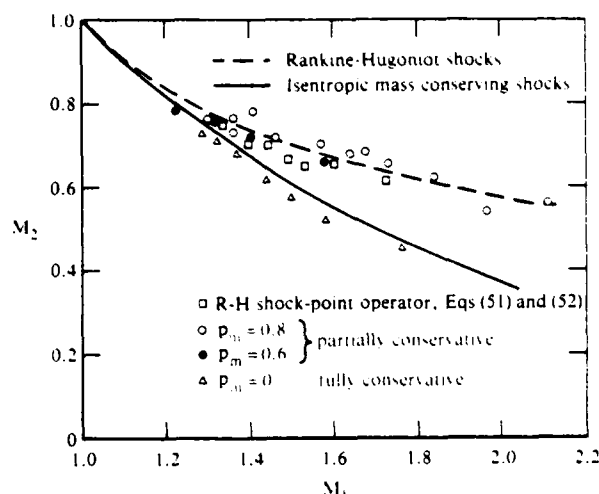


Fig. 4 Comparison of computed average shock Mach number with analytical solutions.

curve over a wide range of M_1 . Solutions obtained by applying Eqs. (51) or (52) depend on the determination of M_1^* in Eq. (50). However, in the solution process, M_1^* is chosen to be the largest value of M^* at the last two supersonic points upstream of the shock. The value of M_1^* so chosen is always smaller than the exact M_1^* because of the smearing of the shock over a few mesh spacings. Therefore, M_2^* is in general, overpredicted. In case 26, the shock occurred at the end of the diverging section, and the prediction of M_1^* agrees with the Rankine-Hugoniot value almost exactly; flowfield gradients upstream of the shock were small, resulting in a more accurate value of M_2^* . The scatter in the computed solutions is believed to depend on the variation of Mach number across the channel height, i.e., the two-dimensionality of the channel flow and the effect of mesh spacing relative to the shock orientation.

Figure 5 presents computed values of ρ_2^*/ρ_1^* compared with the exact Rankine-Hugoniot solution. The exact solution for ρ_2^*/ρ_1^* for an isentropic, mass-conserving shock is unity. Solutions obtained with $p_m = 0$ are all slightly greater than unity. Figures 4 and 5 are actually alternative methods of presenting the same information because of the unique relation between M_2^* and ρ_2^*/ρ_1^* for a particular value of M_1^* . Figures 6-11 present tables and line-printer plots of computed Mach number distributions on the wall and along the axis of symmetry, and Rankine-Hugoniot Mach number distributions for various cases. The columns labeled MACH-RH present the analytical one-dimensional Mach number distribution; columns labeled MACH-AXIS and MACH-WALL are computed Mach numbers distributions along the axis of symmetry and along the wall, respectively.

The preceding channel-flow calculations demonstrate that, in this instance, it is possible to obtain solutions from a potential formulation that closely approximates solutions to the Euler equations. In the flow about an airfoil or wing, the shock strength is maximum near the surface and decreases to zero with increasing distance normal to the surface. Vorticity, which is neglected in the potential formulation, is thereby introduced into the real flow. Although the vorticity effect in transonic flowfields is second-order,¹⁸ potential flows with variable-strength shocks contain errors which can be minimized, from an engineering standpoint, but not eliminated. A good example of this is shown by Lock¹⁹ who applied a partially conservative

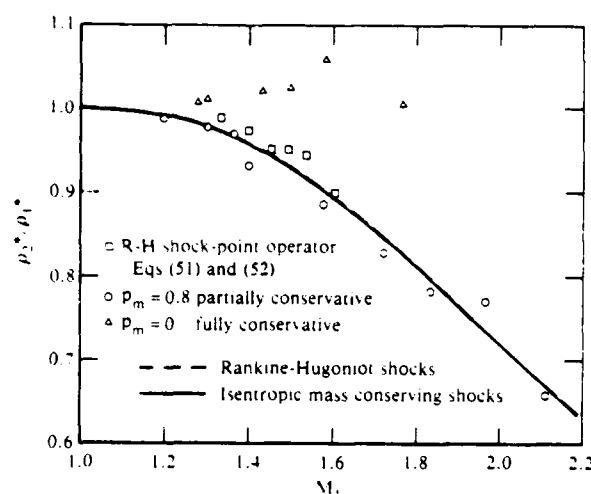


Fig. 5 Comparison of computed stagnation density changes across shocks with analytical solutions.

shock-point operator to compute airfoil flows. In the nonlifting case, his partially conservative solutions agree reasonably well with Euler solutions, while in the lifting case, a discrepancy persists. Since the present work gives a shock-capturing technique resulting in Mach number jumps that are close to the Rankine-Hugoniot values, it is possible to interpret the computed velocity potential distribution downstream of the shock using the Rankine-Hugoniot values of stagnation pressure or density at each streamline, rather than with the conventional isentropic assumption. This interpretation would have the effect of carrying the inherent error in the solution from the immediate vicinity of the shock wave, where mass and momentum are now conserved, to the region downstream of the shock. Comparisons of potential flowfield computations with numerical solutions of the Euler equations are needed to evaluate the usefulness of this interpretation because comparisons involving experimental data are usually complicated by wind-tunnel wall effects and viscous-inviscid interactions.

Wing-Body Flowfield Computations

Grid Generation and Computational Domain

The finite-difference approximation of the governing equation obtained in the previous section can be constructed with the knowledge of mesh-point locations. The coordinate transformation derivatives are found at each control point within a local second-order element shown in Fig. 1. Any scheme that generates a grid system in a regular computational domain can be incorporated with the finite-difference equation solver.

In the present study, a grid-generation scheme developed in Ref. 20 is applied. The transformation of the physical space to the computational space is shown in Fig. 12. The computational space is truncated at a finite distance from the wing surface. For the results presented here, the farfield boundary is placed approximately five to six root-chord lengths from the wing surface in the streamwise and surface normal directions, and the spanwise farfield is located two to three semi-span lengths from the wing tip and the outboard farfield. C-type meshes are generated which wrap around the fuselage nose and wing leading edge. Outboard of the wing tip, the mesh wraps around a surface extending from the wing tip to the outboard farfield. Details of the grid-generation scheme can be found in Ref. 20.

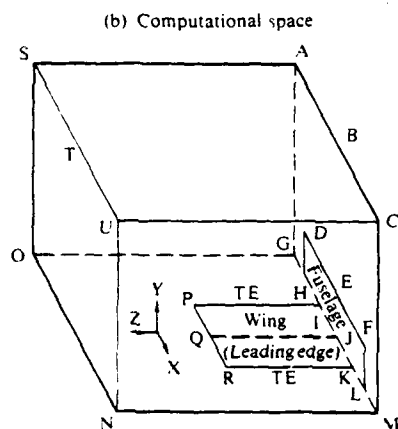
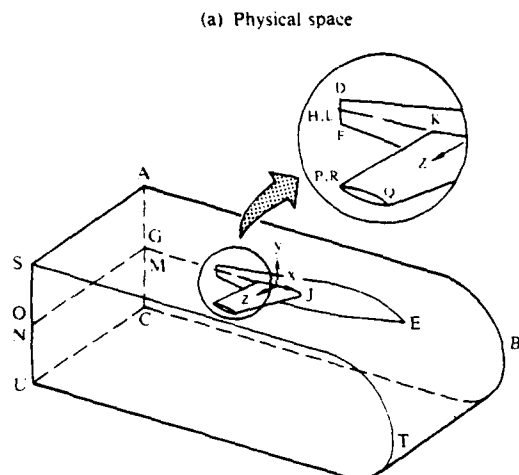


Fig. 12 Physical and computational domain for a wing-fuselage configuration.

Typical grids used in the present calculation are presented in Figs. 13 and 14. Figure 13 shows the grid distribution on an ONERA-M6 wing on a vertical wall, and Fig. 14 shows the grid distribution on the same wing on a semi-infinite fuselage.

Boundary Conditions

The necessary boundary conditions include the impermeability condition on the wing and fuselage surfaces, the Kutta condition along the trailing edge, the zero streamwise variation on the downstream Trefftz plane, and the freestream condition on the other farfield boundaries. For easy implementation of the far-field freestream condition, a reduced potential, G , representing a perturbation from the freestream, is introduced according to

$$\phi = U_{\infty} (x \cos \alpha + y \sin \alpha + G), \quad (56)$$

where U_{∞} is the freestream velocity and α is the angle of attack.

On the boundary cross-planes, ACUSA and SUNOS, G is set to zero, representing the freestream condition. On the Trefftz plane or the boundary cross-plane AGOSA and CMNUC, the streamwise variations are assumed to be zero; therefore, the following two-dimensional equation is applied:

$$c_2 \phi_{YY} + c_3 \phi_{ZZ} + c_5 \phi_{YZ} + c_8 \phi_Y + c_9 \phi_Z = 0. \quad (57)$$

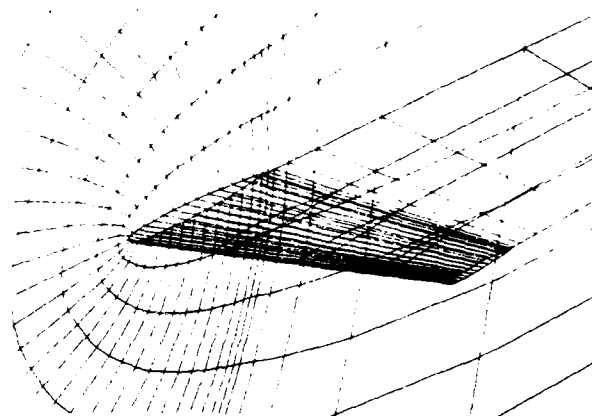


Fig. 13 Grid distribution on an ONERA-M6 wing and a vertical wall.

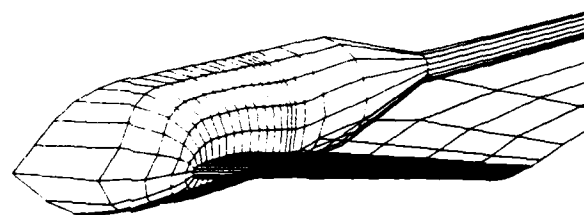


Fig. 14 Grid distribution on an ONERA-M6 wing and a simplified fuselage.

Equation (57) is obtained from Eq. (8) by neglecting all derivatives in the X -direction.

On the fuselage and wing surfaces, the impermeability condition is applied:

$$V = 0, \text{ on the wing surface,} \quad (58)$$

and

$$W = 0, \text{ on the fuselage surface.} \quad (59)$$

Exact surface-boundary conditions can be enforced at boundary points by substituting Eqs. (19) and (20) into Eqs. (58) and (59), respectively, and solving the equations for the value of the potential function at boundary points. One-sided differencing is used in the surface-normal direction so that there is no need to extrapolate the potential to imaginary points inside the wing or fuselage surfaces. However, Eq. (59) may not be suitable for highly distorted grids near the fuselage and wing intersection. Boundary conditions obtained from the finite-volume algorithm¹ give better results near the intersection. Therefore, all solutions presented in the following section were obtained by applying the finite-volume surface-boundary condition in the cross-plane AC-MG.

Along the trailing edge, the linearized equation

$$(h_1^2 + h_2^2 + h_3^2) \phi_{XX} + (h_4^2 + h_5^2 + h_6^2) \phi_{YY} + (h_7^2 + h_8^2 + h_9^2) \phi_{ZZ} = 0 \quad (60)$$

is assumed to hold. Equation (60) is obtained from Eq. (8) by neglecting the nonlinear velocity contribution and the cross- and first-derivative terms. This linearized equation is approximately

valid along the trailing edge only for wing cross-sections having a finite trailing-edge angle where zero flow velocity can be approximately assumed; Eq. (60) can be regarded as an interpolation operator when the wing trailing edge is cusped. The circulation Γ at each spanwise location is determined iteratively as the solution proceeds. Constant discontinuities in potential across the cut downstream of the trailing edge are enforced along the streamwise coordinate lines extending from the trailing edge to the downstream farfield. The value of the discontinuity in each spanwise plane is computed at the trailing edge by satisfying Eq. (60) at both the upper and lower trailing edges.

Beyond the wing tip, the continuity of the potential function across the surface about which the mesh is unwrapped can be approximated by solving $\phi_{YY} = 0$ at points on this surface and just next to the tip. The same condition is applied in the FLO-22 code²¹ to solve for the potential function at points lying on the vortex sheet.

Numerical Results

Typical solutions obtained using the second- and third-order, quasi-conservative and fully conservative schemes are presented in this section. Two meshes are used in all calculations. The coarse mesh contains 44 mesh cells in the X-direction, 10 mesh cells in the Y-direction, and 7 mesh cells in the Z-direction, where 32×5 mesh cells are on the unwrapped wing surface. The fine mesh has double the number of mesh cells in each direction. Two-hundred relaxation sweeps were performed on the coarse mesh, followed by two-hundred relaxation sweeps on the fine mesh.

Figures 15 and 16 present comparisons of first- and second-order fully conservative solutions obtained for the ONERA-M6 wing on a semi-infinite fuselage shown in Fig. 14. The fuselage has a constant radius of 0.2 semi-span length, measured from the wing root to wing tip, in the section of the wing-fuselage intersection. There are no experimental data for this configuration; however, experimental data are available for the same wing on a vertical wall in Ref. 22. Computed solutions at 20% and 65% semi-span locations are presented in Figs. 15 and 16, respectively, for $M_\infty = 0.84$ and $\alpha = 3.06^\circ$, where α is the angle of attack and also the angle of incidence between the wing and fuselage. The fuselage effect is not pronounced in this case, and agreement between the computed solutions and experiment is generally good. At the 20% semi-span location, the first-order solution agrees with the second-order solution except for minor differences in suction peaks and details at the shocks. At the 65% semi-span location, experimental data show a distinct double shock on the upper surface. The second-order solution obviously resolves this double shock better than the first-order solution, although there are still small discrepancies between the second-order solution and experiment, presumably because the mesh used for the computation is relatively coarse.

In Figs. 17-21 pressure distributions obtained for an ONERA-M6 wing on a wall, Fig. 16, are shown and compared with experimental data.²² The freestream Mach number is 0.84 and the angle of attack is 3.06° . Second-order quasi-conservative and first- and second-order fully conservative solutions were obtained at the 20%, 65%, and 95% semi-span locations and are shown in Figs. 17-19. At the 20% semi-span location, numerical solutions predict lower suction peaks. The plateau pressures at the 20% and 65% semi-span locations are slightly overpredicted, while the pressures downstream of the shocks are slightly higher than the experimental data. The locations of shocks are predicted accurately by the numerical solutions. Although the mesh used is still relatively coarse, the overall agreement between the numerical and experimental results is satisfactory. The quasi-conservative solutions predict a more positive pressure at the trailing edge and yield better agreement

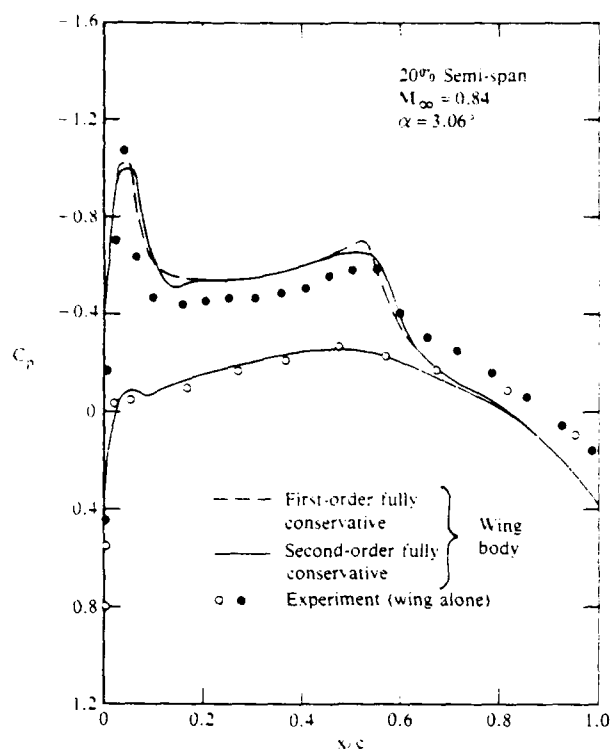


Fig. 15 Comparison of first- and second-order fully conservative solutions.

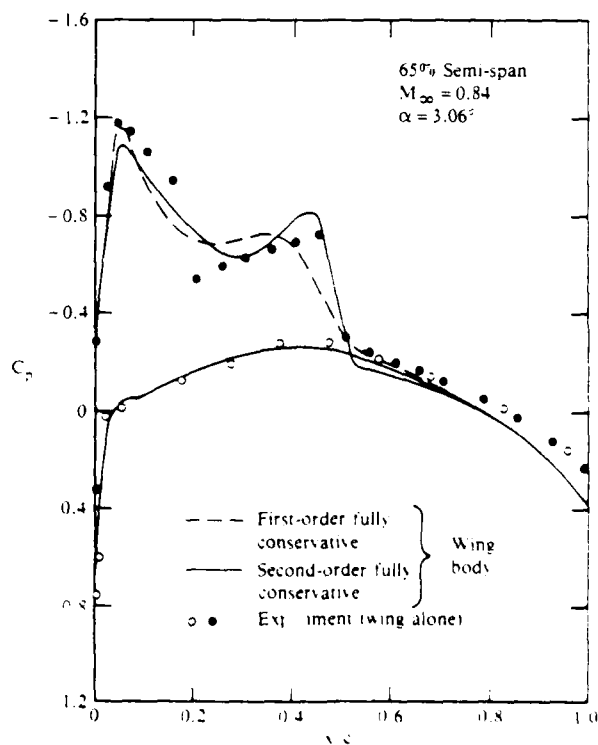


Fig. 16 Comparison of first- and second-order fully conservative solutions.

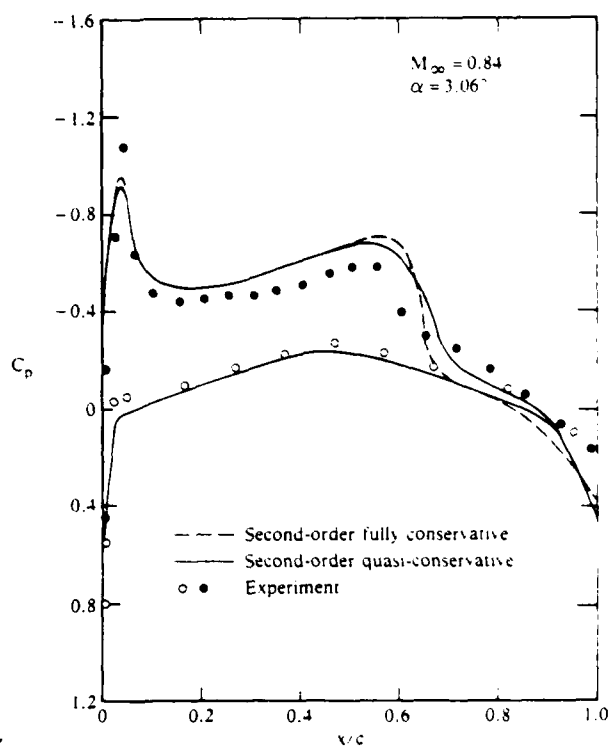


Fig. 17 Pressure distributions on the upper and lower surfaces of an ONERA wing on a wall at the 20% semi-span location.

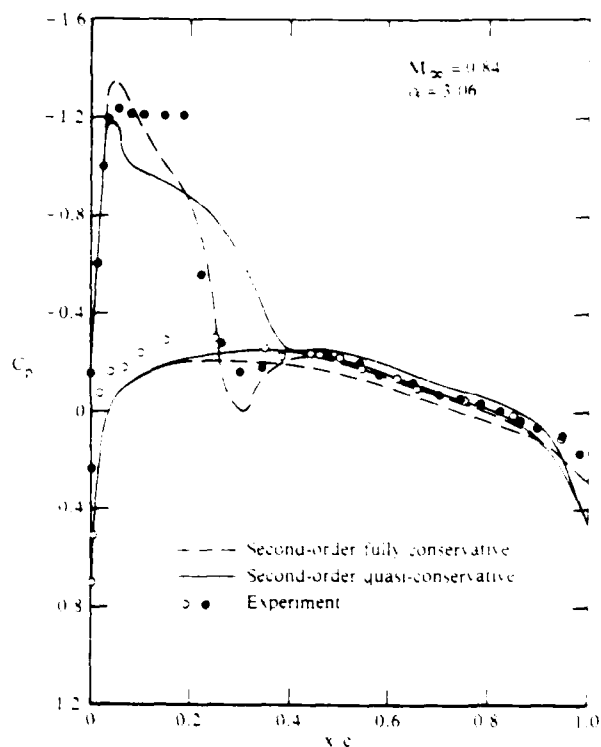


Fig. 19 Pressure distribution on the upper and lower surfaces of an ONERA-M6 wing on a wall at the 95% semi-span location.

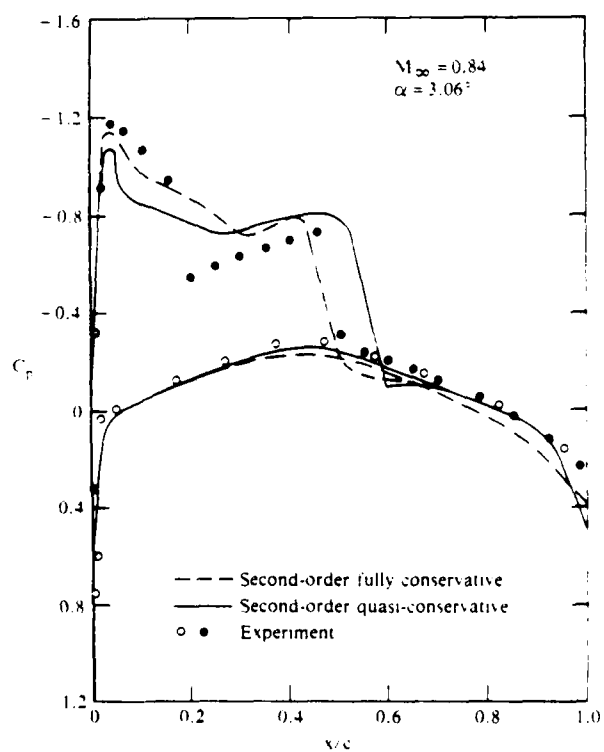


Fig. 18 Pressure distributions on the upper and lower surfaces of an ONERA-M6 wing on a wall at the 65% semi-span location.

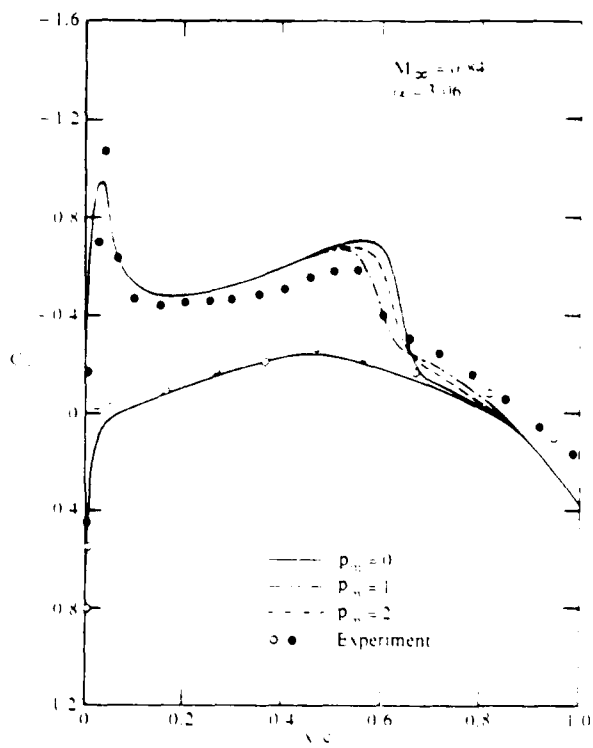


Fig. 20 Study of partially conservative shock-point operators at 20% semi-span location on an ONERA-M6 wing.

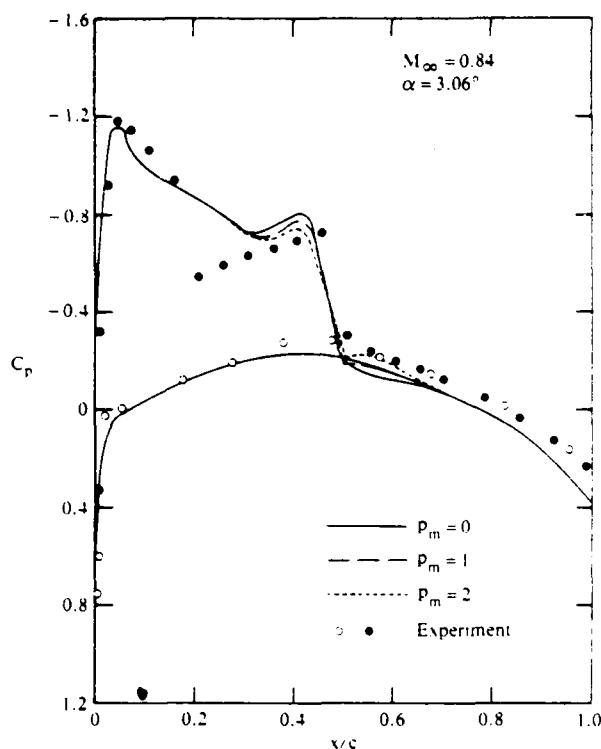


Fig. 21 Study of partially conservative shock-point operators at 65% semi-span location on an ONERA-M6 wing.

with experimental data upstream of the trailing edge. This result is apparently attributable to enforcement of the exact surface boundary condition and the linearized equation, Eq. (72), which approximately simulates a flow stagnation condition for finite trailing-edge angles, as mentioned previously. However, the quasi-conservative solutions predict a more-downstream shock location at a 65% semi-span location and do not resolve the suction peak as well as the fully conservative scheme. The poor resolution of the suction peak is caused by the second-order element not resolving the surface curvature and potential gradient near the leading edge as the exact surface-boundary condition is enforced. The leading-edge resolution can be significantly improved by using a third-order element as shown in Ref. 7.

A study of the shock-point operator for the same ONERA-M6 wing on the wall at $M_\infty = 0.84$ and $\alpha = 3.06^\circ$ is shown in Figs. 20 and 21. As mentioned previously, p_m is the parameter controlling the nonconservative differencing of the shock-point operators in Eqs. (61) and (64). Solutions are obtained for $p_m = 0, 1$, and 2 at 20% and 65% semi-span locations by using the second-order artificial viscosity at supersonic points. A second-order fully conservative solution is obtained as $p_m = 0$. As p_m increases, the amount of nonconservative differencing increases, and the additional mass flux introduced at the shock increases. By adjusting the value of p_m , part of the shock-induced boundary-layer displacement effect can be simulated. By increasing the value of p_m , the shock moves upstream, the shock strength decreases, and agreement of the computed pressure with experimental data is significantly improved both upstream and downstream of the shocks. Solutions obtained by setting $p_m = 2$ seem to yield best agreement with experiments.

Third-order, quasi-conservative and fully conservative solutions were obtained by using the mesh used to obtain the

previous results, and a triple shock pattern was found in the results.²³ However, this triple shock pattern may be the result of a numerical oscillation. To study the characteristics of the third-order solutions, finer-mesh solutions were obtained. In the finest mesh, there are 128 mesh elements in the unwrapped chordwise direction, 24 mesh elements in the surface normal direction, and 12 mesh elements on the wing in the spanwise direction. First-, second- and third-order partially conservative solutions were obtained and presented in Figs. 22-24. The partially conservative parameter $p_m = 0.7$ was used. The second-order solution agrees better with experimental data than the first-order solution. However, the third-order solution shows unreasonable oscillations at various semi-span locations. The cause of these oscillations is unknown; it may be related to the fact that artificial viscosities were not used in the cross-flow direction.

Conclusions

Second- and third-order, fully conservative and quasi-conservative schemes have been developed to compute flowfields about transonic wings and wing-body configurations. The quasi-conservative scheme was developed by solving a finite-difference representation of a transformed full potential equation formulated in this report and enforcing an exact body surface-boundary condition.

The second-order solutions obtained have been shown to provide better resolution for a double shock than the conventional first-order schemes. The third-order solutions show a triple-shock pattern. Additional study will be required to determine whether this pattern is a real flowfield characteristic or a feature of the numerical scheme. The enforcement of an exact surface-boundary condition in the quasi-conservative scheme provides solutions with better agreement with experiments upstream of the trailing edge.

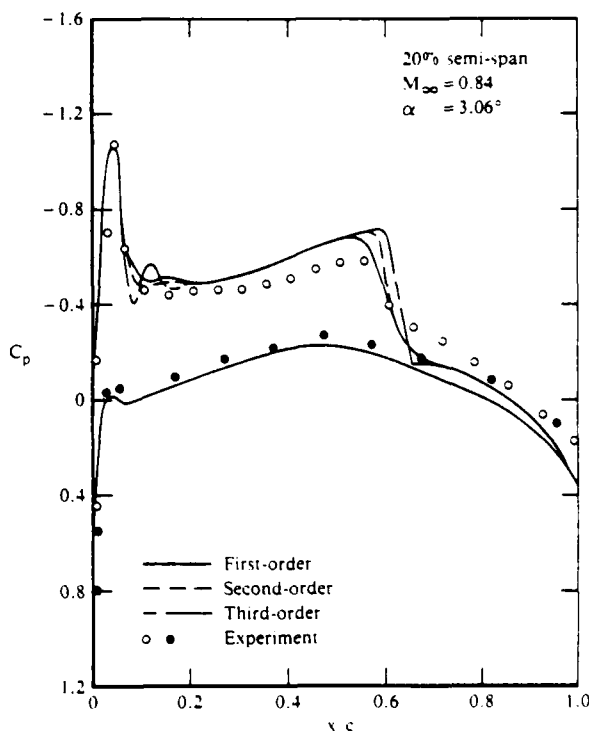


Fig. 22 Comparison of first-, second-, and third-order partially conservative solutions obtained with a finer mesh.

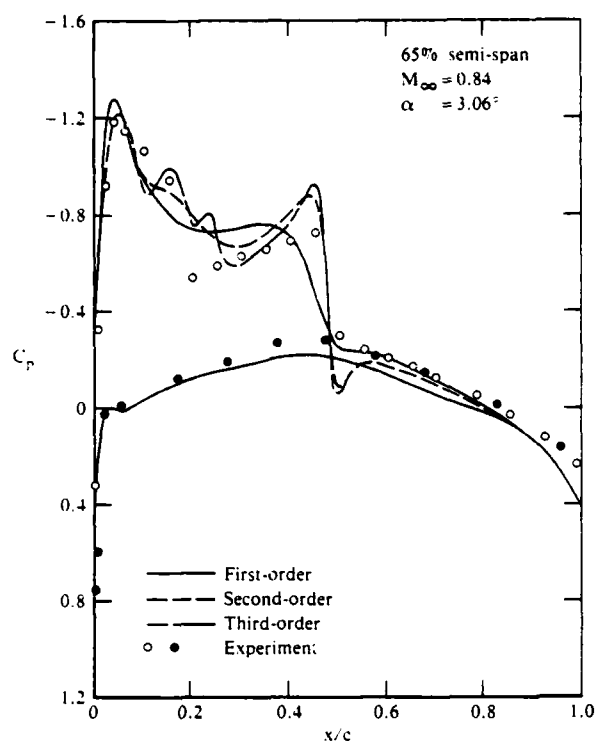


Fig. 23 Comparison of first-, second-, and third-order partially conservative solutions obtained with a finer mesh.

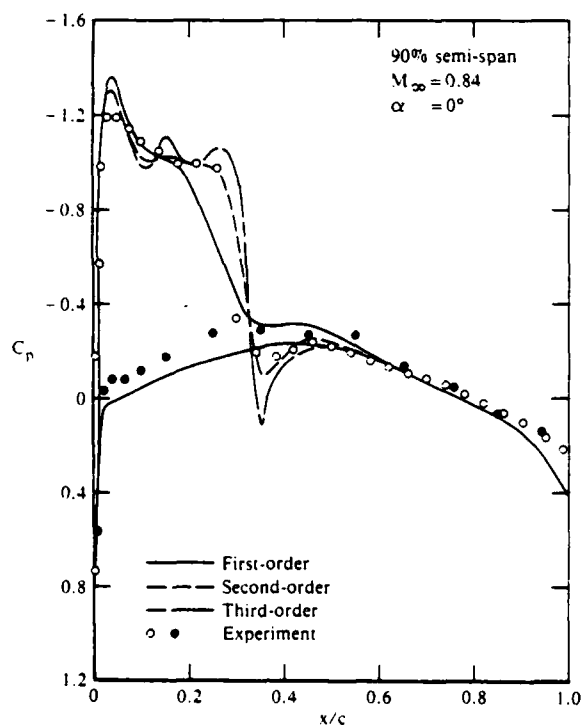


Fig. 24 Comparison of first-, second-, and third-order partially conservative solutions obtained with a finer mesh.

A partially conservative shock-point operator is introduced to control the amount of nonconservative differencing at shock points and thus modify the location and strength of shocks. Proper choice of the shock-point operator significantly improves the agreement of computed pressure distribution with experimental data near the shocks. A new shock-point operator is derived from an approximate one-dimensional flow analysis that properly considers the stagnation density change across the shock and predicts shocks in reasonable agreement with Rankine-Hugoniot shocks.

Acknowledgement

This report was supported in part by the Naval Air Systems Command (D. Kirkpatrick, monitor) and by the David Taylor Naval Ship Research and Development Center (T. C. Tai, monitor) under contract No. N000167-81-C-057 and in part by the McDonnell Douglas Independent Research and Development program.

References

1. Jameson, A., and Caughey, D. A., *A Finite-Volume Method for Transonic Potential Flow Calculations, Proceedings of AIAA 3rd Computational Fluid Dynamics Conference*, (AIAA, New York, 1977), pp. 35-54.
2. Caughey, D. A., and Jameson, A., *Progress in Finite-Volume Calculations for Wing-Fuselage Combinations*, *AIAA J.* 18, 1281 (1980).
3. Chmielewski, G. E., *Transonic Wing/Body Flow Analysis Using Non-Surface-Fitted Coordinates*, *AIAA Paper No. 81-0384* (1981).
4. Bailey, F. R., and Ballhaus, W. F., *Relaxation Methods for Transonic Flow About Wing-Cylinder Combinations and Lifting Swept Wings, Lecture Notes in Physics*, (Springer-Verlag, 1972) Vol. 19.
5. Boppe, C. W., *Computational Transonic Flow About Realistic Aircraft Configurations*, *AIAA Paper No. 78-104* (1978).
6. Jameson, A., *Transonic Potential Flow Calculations Using Conservative Form, Proceedings of AIAA 2nd Computational Fluid Dynamics Conference*, (AIAA, New York, 1975), pp. 148-161.
7. Chen, L. T., *Improved Finite-Difference Scheme for Transonic Airfoil Flowfield Calculations*, *AIAA J.* 20, 218 (1982).
8. Ives, D. C., and Liutermoza, J. F., *Second-Order-Accurate Calculation of Transonic Flow Over Turbomachinery Cascades*, *AIAA J.* 17, 870 (1979).
9. Caughey, D. A., and Jameson, A., *Basic Advances in the Finite Volume Method for Transonic Potential Flow Calculations, Proceedings of Symposium on Numerical and Physical Aspects of Aerodynamic Flows*, T. Cebeci, ed. (Springer-Verlag, in press).
10. Jameson, A., *Acceleration of Transonic Potential Flow Calculations on Arbitrary Meshes by the Multiple Grid Methods, Proceedings of AIAA 4th Computational Fluid Dynamics Conference*, (AIAA, New York, 1979), pp. 122-146.
11. Chen, L. T., and Caughey, D. A., *On Various Treatments of Potential Equations at Shocks, Symposium on Numerical Boundary Condition Procedures and Multi-Grid Methods*, NASA Ames Research Center, Moffett Field, CA, 19-22 Oct. 1981.

12. Murman, E. M., *Analysis of Embedded Shock Waves Calculated by Relaxation Method*, AIAA J. 12, 616 (1974).
13. Hafez, M. M., and Cheng, H. K., *Shock-Fitting Applied to Relaxation Solutions of Transonic Small Disturbance Equations*, AIAA J. 15, 786 (1977).
14. Chen, L. T., and Caughey, D. A., *Calculation of Transonic Inlet Flowfields Using Generalized Coordinates*, J. Aircraft 17, 167 (1980).
15. Chen, L. T., and Caughey, D. A., *Higher-Order Finite-Difference Scheme for Three-Dimensional Transonic Flowfields About Axisymmetric Bodies*, J. Aircraft 17, 668 (1980).
16. Lynch, F. T., *Recent Applications of Advanced Computational Methods in the Aerodynamic Design of Transport Aircraft Configurations*, Douglas Paper No. 6639, 11th Congress of ICAS, Lisbon, Portugal, 1978.
17. Jameson, A., *Iterative Solution of Transonic Flows Over Airfoils and Wings, Including Flows at Mach 1*, Comm. Pure Appl. Math. 27, 283 (1974).
18. Hayes, W. D., *La seconde approximation pour les écoulements transsoniques non visqueux*, J. Mécanique 5, (1966).
19. Lock, R. C., *A Modification to the Method of Garabedian and Korn, Notes on Numerical Fluid Mechanics, Numerical Methods for the Computation of Inviscid Transonic Flows with Shock Waves*, ed. A. Rizzi and H. Viviand, (Friedr. Vieweg & Sohn, Braunschweig/Wiesbaden, 1979), Vol. 3.
20. Chen, L. T., Caughey, D. A., and Verhoff, A., *A Nearly Conformal Grid-Generation Method for Transonic Wing-Body Flowfield Calculation*, AIAA Paper No. 82-108, (1982).
21. Jameson, A., and Caughey, D. A., *Numerical Calculation of the Transonic Flow Past a Swept Wing*, ERDA Research and Development Report COO-3077-140, Mathematical Sciences, New York University, June 1977.
22. Schmitt, V., and Charpin, F., *Pressure Distributions on the ONERA-M6 Wing at Transonic Mach Numbers; in Experimental Data Base for Computer Program Assessment*, AGARD-AR-138, May 1979.
23. Chen, L. T., *Higher-Order Computational Methods for Transonic Wing/Body Flowfields*, McDonnell Douglas Report MDC Q0773, Sept. 1982.

VISCOUS-INVISCID INTERACTIONS WITH A THREE-DIMENSIONAL INVERSE BOUNDARY-LAYER CODE

L. Wigton and H. Yoshihara
The Boeing Company
Seattle, Washington

Abstract

Consideration of three-dimensional inverse boundary-layer codes to treat separated flow is motivated by the success enjoyed by two-dimensional inverse boundary-layer codes. Indeed, as was first shown by Catherall and Mangler¹, the separation singularity which occurs in the direct mode (integrating the boundary-layer equations with a prescribed inviscid outer edge velocity u_{inv}) can be eliminated by using an inverse mode. With an inverse mode some other quantity such as displacement thickness δ^* is prescribed, and the outer edge velocity which we call u_{vis} is generated by the boundary-layer calculation. A coupling scheme must then be devised to insure that the velocity u_{inv} from the outer inviscid flow agrees with u_{vis} from the boundary layer. Recently several efficient coupling schemes have been developed (e.g. Carter², Le Balleur³, Wigton and Holt⁴) which have led to successful calculations of viscous-inviscid interactions, including those involving flow separation. In view of these successes in two-dimensional calculations, we attempt in this paper to extend inverse boundary-layer methods to the three-dimensional case.

The present investigation starts with the integral three-dimensional compressible turbulent boundary-layer method developed by Peter Smith⁵. The velocity profiles in the streamwise direction are assumed to be those used in Green's Lag Entrainment method⁶. The Mager representation of the crossflow velocity profile is used. The dependent variables used to describe the boundary layer include:

- θ momentum thickness of streamwise profile
- H incompressible shape parameter of streamwise profile
- B angle between external streamline and the limiting wall streamline
- C_E entrainment coefficient
- U_E magnitude of velocity at outer edge of boundary layer
- α angle between x axis and the external streamline.

The dependent vector $p = (\theta, H, B, C_E, U_E, \alpha)^T$ satisfies the x -momentum, y -momentum, continuity and the lag entrainment equations. These equations can be cast in the form:

$$A = \frac{\partial p}{\partial x} + B \frac{\partial p}{\partial y} = r \quad (1)$$

where A and B are 4×6 matrices, r is a vector and x and y are nonorthogonal curvilinear coordinates in a body surface. The formidable algebra involved in generating the code for evaluating the entries in A , B and r was performed on the computer using REDUCE 2⁷ and a specially designed FORTRAN program. This enabled the boundary-layer code to be written much faster and with a far greater assur-

ance of correctness than would otherwise have been possible.

In the usual direct mode used in the attached case we prescribe U_E and α so that (1) may be written:

$$C \frac{\partial p'}{\partial x} + D \frac{\partial p'}{\partial y} = r' \quad (2)$$

where $p' = (\theta, H, B, C_E)^T$ and C and D are 4×4 matrices. The eigenvalues of the matrix C^{-1} are all real, so that the system (2) is hyperbolic. This enables us to solve (2) as an initial value problem using a marching procedure (say in the x -direction). Unfortunately, just as in the two-dimensional case, near flow separation the matrix C becomes ill-conditioned which disrupts our calculation. In order to avoid the singularities associated with flow separation, we consider the use of inverse boundary-layer methods.

Variables other than U_E and α may be prescribed in equation (1) leading to other equations of the form (2) with different matrices C and D . Additional inverse modes can be found by adjoining the equation for the transpiration velocity and that for the irrotationality of inviscid edge flow. All these methods lead to equations of the form (2). A program which is capable of operating in any of these modes has been written, and the corresponding eigenvalues and nature of the singularities have been analyzed. In many cases, including those used by other investigators, some of the eigenvalues of the matrix $C^{-1}D$ are complex. In this case the system of equations (2) is not hyperbolic and cannot be solved as an initial value problem unless the derivatives in the y direction happen to be 0. Such methods may be used for two-dimensional or infinite yawed wing calculations but are not suitable for general three-dimensional boundary-layer calculations for which one expects to use a marching procedure. Accordingly, attention is directed towards methods for which the eigenvalues of the matrix $C^{-1}D$ are all real and for which the matrix C remains well-conditioned for as large a range of input variables as possible.

After selecting promising inverse boundary-layer methods we next consider coupling schemes with the outer inviscid flow. The coupling schemes introduced by Carter and Le Balleur are generalized to the three-dimensional case. A successful calculation involving flow separation around a nacelle-sting combination at angle of attack is presented.

It appears that in the general case involving flow separation and large cross-flow angles, a coupling scheme based on a strictly local analysis is inadequate. Thus, generalizations of the Carter algorithm and that introduced by Le Balleur are not always effective in the three-dimensional case. Therefore, a new global coupling scheme is now being developed and applied to the case of a swept wing with shock-induced separation. Here the in-

viscid code used is the exact potential code FLO 30 with multigrid developed by Caughey.

References

1. Catheral, D., Mangler, K.W.: The Integration of the Two-Dimensional Laminar Boundary-Layer Equations Past The Point of Vanishing Skin Friction. J. of Fluid Mech., Vol. 26, pp. 163-182, 1966.
2. Carter, J.E.: A New Boundary-Layer Inviscid Interaction Technique for Separated Flow. AIAA Computational Fluid Dynamics Conf., July 1979, Williamsburg, VA.
3. Le Balleur, J.C.: Couplage Visqueux-Non Visqueux: Methode Numerique et Applications Aux Ecoulements Bidimensionnels Transsoniques et Supersoniques. La Recherche Aerospatiale, Mar.-Apr., 1978.
4. Wigton, L.B. and Holt, M.: Viscous-Inviscid Interaction in Transonic Flow. AIAA Computational Fluid Dynamics Conf., June 1982, Palo Alto, CA.
5. Smith, P.D.: An Integral Prediction Method for Three-Dimensional Compressible Turbulent Boundary Layers. British Aeronautical Research Council Reports and Memoranda, No. 3739, 1974.
6. Green, J.E., Weeks, D.J. and Brooman, J.W.F.: Prediction of Turbulent Boundary Layers and Wakes in Incompressible Flow by a Lag-Entrainment Method. British Aeronautical Research Council Reports and Memoranda, No. 3791, 1977.
7. Hearn, A.C.: REDUCE 2 User's Manual. Mar. 1973.

SESSION 9

AN INVISCID COMPUTATIONAL METHOD FOR TACTICAL MISSILES

A. B. Wardlaw, F. P. Baltakis, J. M. Solomon and L. B. Hackerman
Naval Surface Weapons Center
White Oak, Silver Spring, Maryland 20910

Abstract

Several methods for numerically calculating the inviscid flow field about tactical missile configurations are discussed. An approach based on the thin fin assumption is outlined which treats body and fin geometry separately. Comparisons between calculation and experiment are provided and problems associated with applying this method to configurations of design interest are given. Deficiencies in the state-of-the-art are summarized and possible remedies are suggested.

I. Introduction

A practical means of predicting the nonlinear, inviscid, supersonic shock layer on missile configurations is to numerically solve the steady, three-dimensional inviscid equations using an efficient finite difference method. Several computer programs are currently available for calculating flow fields about arbitrary bodies in supersonic flow.¹⁻⁷ However, their application to practical wing-body-tail configurations presents some serious computational problems. The primary focus of the present study is the development of a more efficient numerical technique for treating finned bodies. To achieve this, the approach used here departs from the basic computational strategy used in Refs. 1-7 when fin surfaces are present. Instead of considering the cross-sectional body-fin geometry as a single entity, the present method considers the body alone (i.e., the body with all fin surfaces removed) and the fin geometries separately. The computational grid is generated using normalizing transformations^{1,4,5,7} applied to the body alone configuration. The fin surfaces are allowed to extend into the computational region and can be adequately resolved within a relatively coarse computational grid. In order to treat the complex flow in the immediate vicinity of fin leading and trailing edges, appropriate local analyses are built into the program which depend strongly on the local Mach number of the flow component normal to the edge. These local analyses can range from locally exact, when the edge is sharp and the normal velocity component is sufficiently supersonic, to ad hoc or semi-empirical in other situations. It is possible to exercise the above computational procedure without recourse to a special leading edge analysis. However, such a procedure is not as robust and does not resolve the leading edge region as accurately.

A detailed description of the computational method developed during this study for treating missile configurations can be found in Refs. 8 and 9. Included in these reports are a number of sample cases in which calculation and experiment are compared. Although fairly versatile and efficient, this computational method does have areas in which improvement is desirable. In this paper we will describe possible methods for setting up tactical missile computations, outline the unique aspects of our current computational procedure and present several sample calculations.

Existing computational capabilities and shortcomings are then discussed along with possible remedies.

II. Strategies for Computing Inviscid Flow Fields

In the current study flow field calculations are implemented by marching the steady three dimensional Euler equations in the Z-direction (Figure 1), from an initial data plane near the

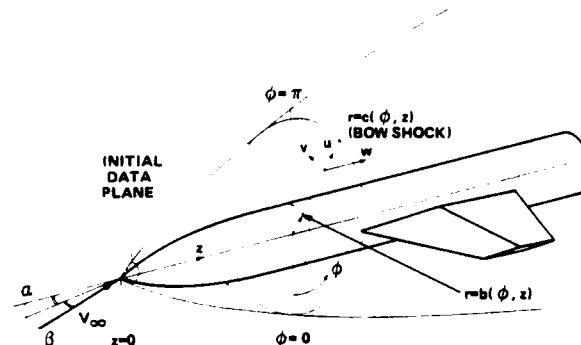


Fig. 1 Cylindrical coordinates used for inviscid calculations.

missile nose. One of the principal issues in this type of calculation is the selection of a transformation which at each step maps the cross-sectional plane under consideration into a rectangular computational domain. One of the most direct approaches is to use the simple grid of Figure 2a which maps into a square computational domain with a stretching in the radial direction and a clustering about the fin surfaces in the circumferential direction. In the resulting computational domain the body and fin surfaces lie along the bottom edge while the bow shock is positioned along the top. The primary advantage of this approach is its simplicity. However, the skewness of the mesh in the vicinity of the fins causes computational problems and a large number of mesh points are needed to resolve cross-sections with several fins present. An improvement on this approach is to use a more sophisticated transformation that maps the computational domain onto a more nearly rectangular mesh in the crossflow plane. Generalized conformal transformation methods exist which can accomplish this.^{6,10} As depicted in Figure 2b, the resulting mesh in physical space is qualitatively appropriate since it clusters points about the fin tips. Such methods have been applied in Refs. 6 and 11 and are viable for tackling many missile computations. Possible drawbacks to this approach are solution sensitivity to small variations in the transformation and difficulty in controlling mesh point locations throughout the flow field on complicated configurations. When a complicated transformation

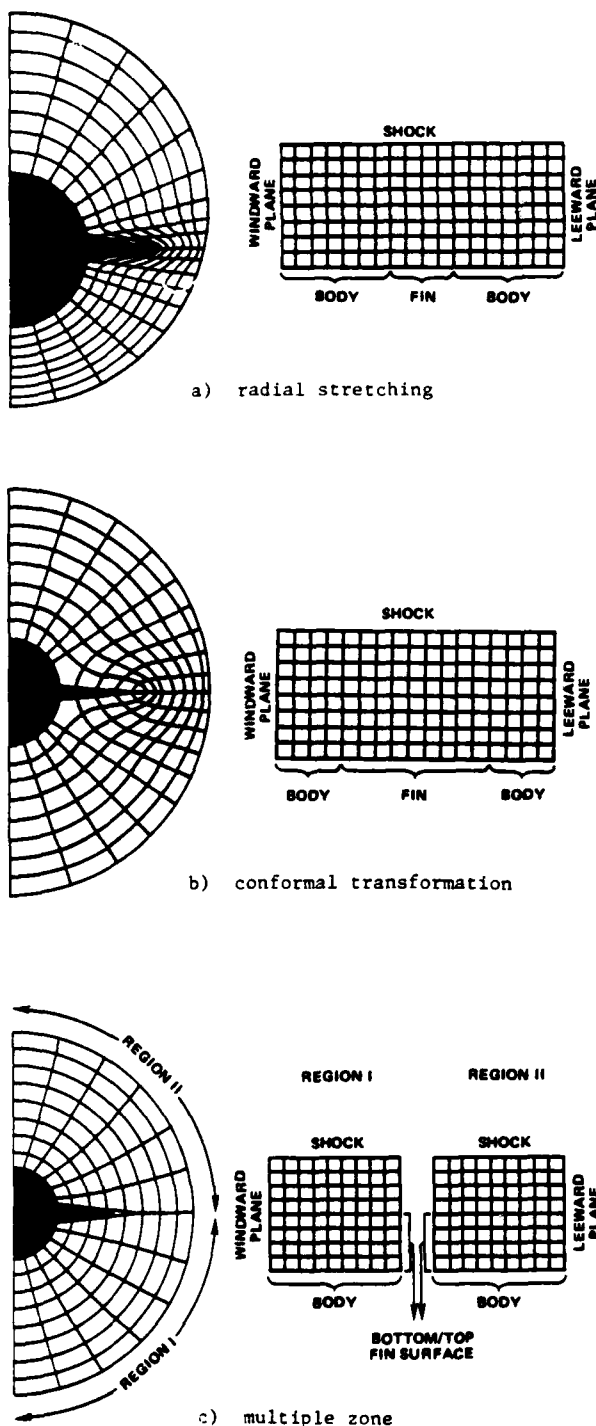


Fig. 2 Possible mappings for missile cross sections

is used, a significant portion of the computation is associated with its implementation.

In the current study a multiple zone approach is used. The concept of the multiple zone approach entails dividing the flow field up into several regions as shown in Figure 2c. As originally applied (e.g. Refs. 6 and 12) the boundary of the zones are taken to coincide with shock waves. Along the zonal boundaries two computational points are associated with each location in space, one with each of the two adjacent regions. The availability of two mesh points along the shock front allows the shock to be fitted, with upstream conditions stored at one point and downstream conditions in the other. In the current study all interior shocks are captured and zone boundaries are based on missile geometry and the bow shock location. A fin or inlet cow becomes a convenient interface with boundary mesh points from one of the adjacent regions describing one side of this surface and boundary mesh points from the adjacent region the other side. In the most general application of the multiple zone method a separate mapping is applied to each zone. Since zones can be constructed to ensure relatively simple geometries, the resulting transformations are also simple. A sample of a missile cross-section treated with the multiple zone approach is illustrated in Fig. 2c. The great advantage of the multiple zone approach is its flexibility and relative ease of application. Its disadvantage is that it requires a more complicated computer program to implement. This is primarily because of the bookkeeping and special numerical techniques required to treat points along the interfaces between adjacent zones.

To simplify development of computational methods for the current study, an abbreviated version of the multiple zone approach has been applied. The analysis is restricted to relatively thin fins with sharp leading edges which lie approximately along constant ϕ planes. A thin fin approximation is employed which neglects fin thickness but retains the actual fin slopes. The resulting location of the body, shock and fin surfaces in the computational plane is shown in Figure 3. Use of the thin fin approximation makes it convenient to treat the computational domain

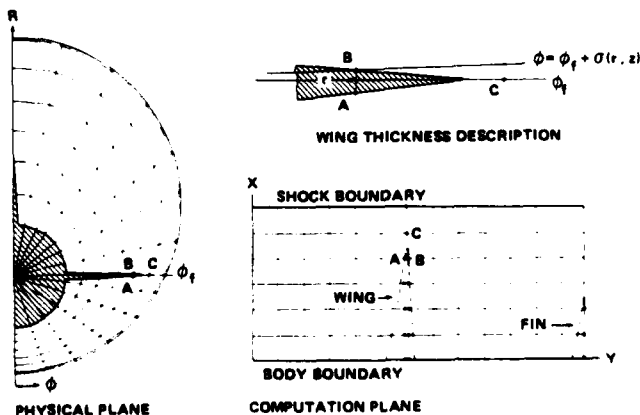


Fig. 3 Thin fin approximation in physical and computational coordinates.

as one region. Along planes on which fins are located, cuts are placed and two points are carried, one describing each surface of the fin. For many configurations, only a stretching in the radial direction is necessary, even though improved local resolution can be obtained with ϕ or r clustering. The current computational algorithm admits transformations of the form:

$$Z = z; X = X(r, \phi, z); Y = Y(\phi, z) \quad (1)$$

where X, Y, Z are the computational coordinates.

A disadvantage of the thin fin approach as outlined above is an absence of mesh clustering near the wing tip where large gradients in flow properties occur. Clearly, these areas are not being accurately resolved. However, viscous effects are important near fin tips and accurate resolution of these regions with an inviscid computational method seems of dubious pragmatic value. Furthermore, resolution of the fin tip region with a highly clustered mesh is computationally expensive. Smaller marching steps must be used to satisfy the CFL condition of explicit methods. Implicit schemes, while allowing larger time steps, also feature a greatly increased amount of work per step. Retaining accuracy in the marching direction places a limit on the allowable step size and thus application of implicit schemes also results in an expensive calculation.

III. The Computational Algorithm

The algorithm for advancing the inviscid flow field quantities from $Z = Z^k$ to the next axial station $Z = Z^k + \Delta Z$ depends on the location of the individual mesh points in the shock layer. These are divided into the following four types: interior, body surface, shock, and fin surface points. The numerical procedures used to treat the first three types of points are essentially the same as those given in Ref. 7. The only difference is that the inviscid, weak conservation equations have been recast to simplify the source term. For interior points the MacCormack predictor-corrector scheme is applied directly to the associated conservation form of these equations in the X, Y, Z space. The points on the body and bow shock surfaces are treated using predictor-corrector methods applied to certain characteristic compatibility relations for each surface along with the appropriate flow boundary conditions. See Refs. 7 and 8 for details. A complete discussion of various techniques for treating fin surface points is given in Refs. 8 and 13. In the remainder of this section these procedures are outlined along with certain special procedures used when fins are present.

III.1 Fin Surfaces

THE THIN FIN APPROXIMATION. The thin fin approximation is applicable to fins with surfaces that lie close to a constant ϕ plane, say $\phi = \phi_f$, which is defined as the fin plane. The fin geometry is assumed to be represented by two surfaces, the upper and lower surfaces, each described independently by relations of the form

$$\phi = \phi_f + \mathcal{J}(r, z) \quad (2)$$

In the cross-section $Z = \text{constant}$, the actual fin surfaces will lie within the computational mesh as

shown in Fig. 3. The thin fin approximation assumes that σ is small and thus places the fin surfaces along the fin plane corresponding to $Y = Y_f$ in each $Z = \text{constant}$ plane. Although the fin is approximated by a zero thickness plane lying on $\phi = \phi_f$, the surface slopes are described to $O(|\sigma|)$. The fin surface is prescribed by specifying $\theta(r, z)$, $\nu(r, z)$, $L(z)$ and the first derivatives of these quantities. Here θ and ν are the angles between the fin surface tangency plane and the fin planes in the r and z directions respectively, and the quantity L is the radial location of the fin edge. In terms of θ, ν the derivatives of σ correct to $O(|\sigma|)$ are given by:

$$r\sigma_r = \tan \theta, \quad r\sigma_z = \tan \nu, \quad (3)$$

$$r\sigma_{rr} = \sec^2 \theta (\theta_r - \sigma_r)$$

$$r\sigma_{zz} = \nu_z \sec^2 \nu - \sigma_r \tan^2 \nu, \quad r\sigma_{rz} = \sec^2 \theta (\theta_z - \sigma_z)$$

Within the restriction that $|\sigma|$ be "small", the thin fin approximation can be applied to arbitrary fin geometries including surfaces with discontinuous slopes and fins with "small" deflections, camber, and variations in dihedral.

The numerical algorithm for treating fins by the thin fin approximation requires that the computational mesh be chosen so that each fin plane is coincident with a computational mesh plane, $Y = Y_f$. Two sets of computational points are carried on the $Y = Y_f$ plane to describe the flow properties on the upper and lower surfaces as is illustrated in Fig. 3. As the calculation is marched down the length of the body, fin surfaces are encountered on $Y = Y_f$. Thus a point at some X may at one axial location be an interior flow field point and in the next axial step move onto the fin. Here the interior point is split into two points corresponding to the upper and lower fin surfaces. The fin points thus created are referred to as leading edge points. For a fixed X , a pair of points which are on the fin at one axial step can in the next step move off the fin and become a single interior flow field point. Such a point will be referred to as a trailing edge point. The flow variables at leading and trailing edge points are determined from an appropriate local analysis which is described in the following subsections. The adjustment for the presence of a leading and trailing edge is made immediately after the completion of the step in which the edge is encountered. The values of the flow variables prior to the adjustment are termed upstream while the adjusted values are termed downstream. Note that the locations of leading and trailing edge points are within one ΔZ of the physical edges of the wing.

FIN SURFACE BOUNDARY CONDITIONS. On a fin surface, the velocity component normal to the surface must vanish: i.e.,

$$v/r - \sigma_z w - \sigma_r u = 0 \quad (4)$$

The numerical methods used to advance the fin surface points are based on the appropriate characteristic compatibility relations associated with the Euler equations which are derived in Ref. 8. Both the upper and lower fin surfaces, although

considered separately, are treated using the same techniques. For fin surface points not on the fin body junction ($X=0$), three compatibility relations are used to advance s , $V_3 = u + r\sigma_T v$ and $P = \ln p$ along the fin surface.

The fin body junction is assumed to be a sharp corner. At this corner both fin and body tangency conditions are satisfied and thus flow is directed along the corner. This implies that entropy is constant along the corner except at compressive discontinuities in body or fin slope and at leading and trailing edges. Since the stagnation enthalpy is also constant only one additional relation is needed to completely determine the flow variables along the junction. This is given by a characteristic compatibility condition. However, an ambiguity arises in the choice of an appropriate characteristic condition. Two possible equations are derived in Ref. 8. Both equations appear to produce similar results except when large pressure gradients occur in the vicinity of the junction (i.e., close to a leading edge or surface discontinuity).

LEADING EDGES. Several different strategies are available for treating leading edge points. The simplest approach is to switch from the interior point advancement scheme to the fin surface scheme. This is referred to as option 0 and represents a formal discretization of the various applicable equations without recourse to additional modeling at the leading edge.

An alternative approach is to apply locally an analysis which models the flow very near to the leading edge. This is designated as option 1. The justification for this option is that in most calculations, for reasons of computational efficiency, the mesh spacing in the vicinity of the edge is not sufficiently fine for option 0 to yield satisfactory results. The computational algorithm proceeds by completing the step in which a leading edge is encountered without taking the fin surface into account. The resulting flow properties are then taken as the conditions immediately upstream of the leading edge. An appropriate local analysis is then used to determine the flow quantities immediately downstream of the edge for both the upper and lower fin surfaces.

The downstream flow properties at leading edge points are determined by a local analysis based on the computed flow upstream of the edge and the prescribed local fin geometry. Using this information, the Mach number normal to the leading edge, M_n , is determined. If $M_n > 1$ an attached shock or expansion fan occurs in most cases which permits a local analysis. The velocity component tangent to the edge, is unaffected by the edge and all other downstream flow quantities are determined by turning the normal flow component using either an oblique shock or a Prandtl-Meyer expansion. A similar procedure for the case of an attached oblique shock has also been used in Ref. 6. In Ref. 6, the leading edge shocks are "tracked" downstream of the edge whereas in the present work these shocks are "captured" using the conservation

and dissipative properties of the interior point scheme without additional numerical smoothing.

At the leading edges where a compression turn is required, the condition $M_n > 1$ does not guarantee the existence of an oblique shock and for sufficiently large turns, a detached shock wave will be present. If $M_n < 1$ neither oblique shock nor Prandtl-Meyer expansion can be applied. Under these conditions use of a purely local analysis is at best an approximation. However, it has been possible to formulate empirical rules for determining leading edge conditions that give satisfactory results when compared to experiment. This empirical procedure is described in detail in Ref. 8.

If M_n is significantly less than unity, the jump conditions assigned by option 1 often do not give satisfactory results. This is particularly true on the expansion surfaces when the local analysis produces extremely low pressures. The condition $M_n \ll 1$ occurs on highly swept wings which feature leeside separation and a large leeside vortex. Under these circumstances, the streamlines on the upper and the lower wing surfaces are directed outward at locations near the edges. The conditions at the leading edge are thus strongly influenced by the flow on the fin surface. To handle this situation, option 2 is introduced. When an interior point (X_n, Y_m) moves onto the fin, the leading edge pressure and density is determined by averaging values at (X_{n-1}, Y_m) and (X_n, Y_m).

For the leading edge points at the fin-body junction a special procedure is required. The flow in the vicinity of these points features a complicated shock interaction pattern which cannot be resolved within the relatively coarse mesh used in the present calculations. Accordingly, a simple heuristic procedure is used to determine the flow variables immediately downstream of the leading edge corners. The upstream velocity vector on the body lies in the body tangency plane which also contains the corner direction. The flow downstream of the leading edge corner is obtained by rotating the velocity vector within the body tangency plane and aligning it with the corner using either the oblique shock or the Prandtl-Meyer turning relations.

TRAILING EDGES. At a trailing edge the two points on $Y = Y_f$ representing the upper and lower fin surfaces, are coalesced into a single interior flow field point using a local analysis. The computational algorithm proceeds by completing the step in which a trailing edge is encountered without taking the fin edge into account. The resulting flow properties on the upper and lower fin surfaces are the upstream values and represent the flow properties on the two fin surfaces immediately upstream of the trailing edge.

The trailing edge local analysis is dependent on the Mach number normal to the trailing edge. If the flow component normal to the trailing edge on both surfaces is sufficiently supersonic, the streamlines from the upper and lower sides of the

fin will turn onto a slip surface by means of a system of oblique shocks and/or expansions which are attached to the trailing edge. The orientation of this surface is such that the final pressures on both sides will be the same. Reference 13 describes an iterative procedure for determining the plane orientation. Unfortunately this scheme is cumbersome to apply and convergence cannot be guaranteed. Thus, this procedure has been discarded in favor of a simpler method that turns both of the surface streamlines onto the fin plane. The coalesced property values for p , ρ , u , v are then determined by averaging the results on the upper and lower surface streamlines. The velocity component w is solved by requiring that the coalesced trailing edge point has the correct total enthalpy.

If the flow component normal to the trailing edge on either wing surface are subsonic, a different algorithm is applied. At a trailing edge point (X_n, Y_m) , flow properties are assigned to be those at (X_{n+1}, Y_m) , unless this point is a fin point. In that case properties at (X_{n-1}, Y_m) are used. If both of these points are on the fin, the upper and lower surface properties are set to the average values at points (X_n, Y_{m+1}) and (X_n, Y_{m-1}) .

III.2 Special Procedures

The presence of fin surfaces in the interior of the computational domain requires the introduction of some special differencing procedures. In addition, physical considerations have motivated other adjustments to the differencing used at both fin and interior points located next to the fin edge.

ALTERATION OF X DIFFERENCING FOR FIN AND INTERIOR POINTS ADJACENT TO THE FIN TIP. The types of points under consideration in this subsection are A, B, C of Figure 3. Selection of appropriate schemes for advancing these points depends on the Mach number normal to the leading edge and the applied leading edge treatment. Several differencing strategies are available.

Option 0 for the fin points such as A, B and interior points such as C is similar to the computational algorithm applied elsewhere in the flow field. Fin points A, B are advanced using the usual fin surface point algorithm. The MacCormack scheme for advancing point C must be modified since there are two adjacent sets of flow values (i.e., points A and B) corresponding to the upper and lower fin surfaces. Point C is advanced in two separate calculations using first the lower fin surface values at A and then the upper fin surface values at B. The resulting two conservation vectors are then averaged.

A second strategy, option 1, advances the fin edge points A, B without using the information at point C, and interior points such as C without recourse to the information at points A, B. To advance point C using this option, X differences are taken in the direction away from the fin in both the predictor and corrector steps. Using one-sided X differences to advance points A, B has been found to produce unsatisfactory results. Instead, X derivatives calculated from flow properties at A and C or B and C are set to zero. The computational algorithm has been constructed

with sufficient generality to allow C to be advanced using either A and B, A only or B only.

SUPPRESSION OF Y DERIVATIVES NEAR THE LEADING EDGE. Fig. 4 illustrates the calculated surface pressures on a fin in uniform flow. The calculated results should exhibit a constant pressure downstream of the leading edge, but in fact overshoot the leading edge value. The excessive pressure values aft of the leading edge are a consequence of the numerical procedure and the error becomes more severe as the magnitude of the pressure jump at the leading edge increases. Such inaccuracies at the leading edge can have a strong influence on the total vehicle aerodynamics. The calculated pressure overshoot at the leading edge may be suppressed by damping the Y derivatives occurring in the relations that advance the fin and corner pressures. Such a procedure is automatically implemented on leading edges which feature a pressure rise.

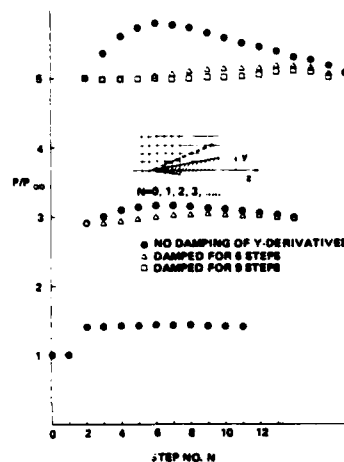


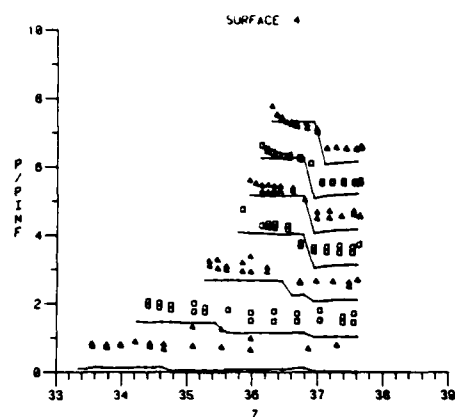
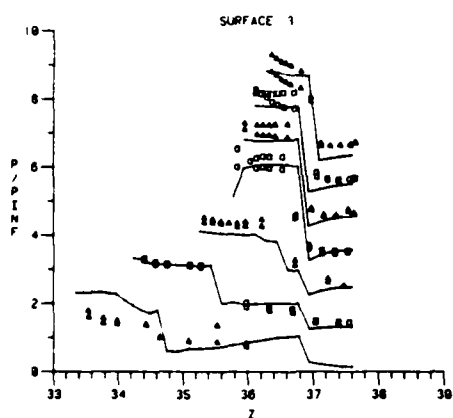
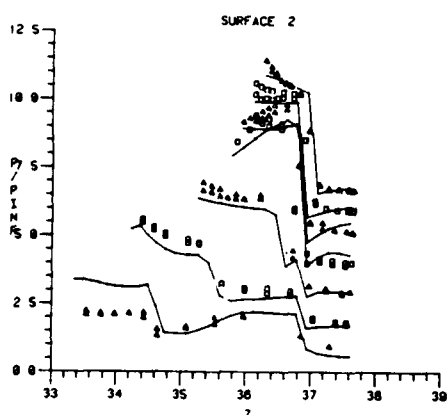
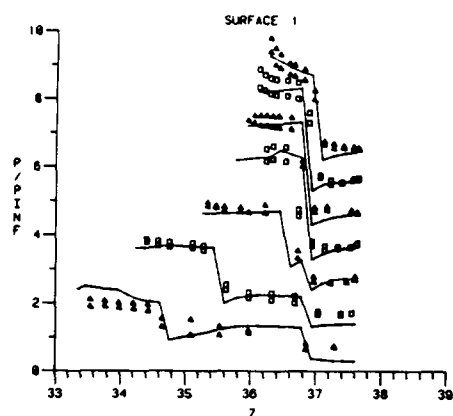
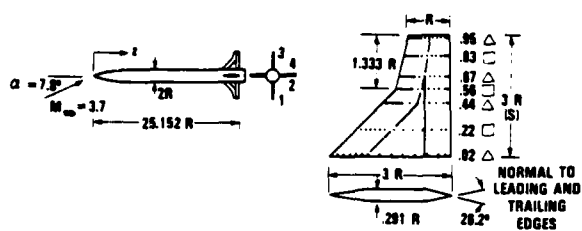
Fig. 4 Effect of suppressing Y derivative for various strength jumps.

APPLICATION OF SMOOTHING TO INTERIOR, BODY AND FIN POINTS. In computations featuring body separation, and on highly swept wings with subsonic normal Mach numbers at the leading edge, large vortex structures develop in the flow field. In such circumstances it is often necessary to smooth the calculated flow field. This is accomplished by applying a switched Schuman filter¹⁴ with a density switch after the completion of each corrector step, prior to decoding. (The use of the Schuman filter is one way of introducing artificial viscosity.) For interior points smoothing is applied to the conservation vector U , while at the body and fin surfaces it is applied along the surface to the advanced quantities. A non-Schuman type smoothing of the fin tip points can also be applied which averages advanced fin tip quantities with those of adjacent fin points.

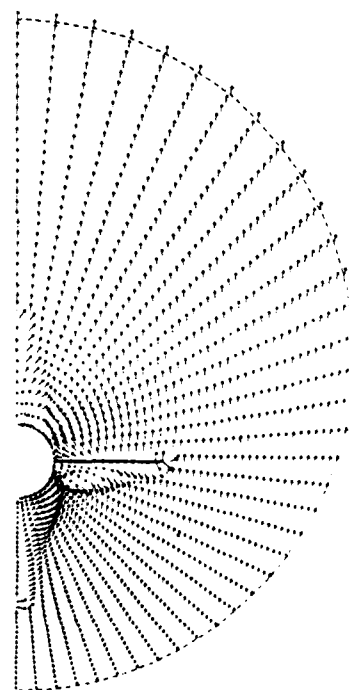
IV. Application of the Computational Method to Missile Configurations

IV.1 TYPICAL RESULTS

Computed results have been compared to experiment for a large number of cases in Ref. 4. The three examples shown in Figs. 5, 6 and 7 have



a) surface pressures (zero reference shifted by 1 for each successive curve). Data from Ref. 15.



b) Cross flow velocity vectors at upstream of fin trailing edge.

Fig. 5 Calculated and measured results on a cranked delta fin configuration in + roll orientation.

been selected from this report to indicate the general capabilities of the computational method. These cases are representative of wings with leading edge normal velocity components which are supersonic transonic and subsonic. Fig. 5 exhibits fin surface pressures on a body tail configuration in which the velocity component normal to the fin leading edge is supersonic and leading edge conditions are determined using oblique shock and Prandtl-Meyer relations. Body surface pressures are shown in Fig. 6 for a body-wing configuration with transonic leading edges. Here empirical relations are used to specify leading edge conditions. The wing shown in Fig. 7 has a subsonic normal velocity component and on the windward surface the solution was directly marched through the leading edge without applying a local analysis (option 0), while option 2 was applied (c. f. Sec. 3) on the lee side.

An examination of the predicted and measured surface pressures indicates satisfactory agreement in most areas, however, there are clearly a few locations where discrepancies exist. Three such regions are the body-wing junction, the lee surface of a wing with supersonic normal components and body pressure near the 90° meridian (e. g. Fig. 6). In these areas viscous effects are expected to play an important role and it is not surprising that an inviscid model leads to poor agreement with experiment. For further discussion of these problem areas see Ref. 8.

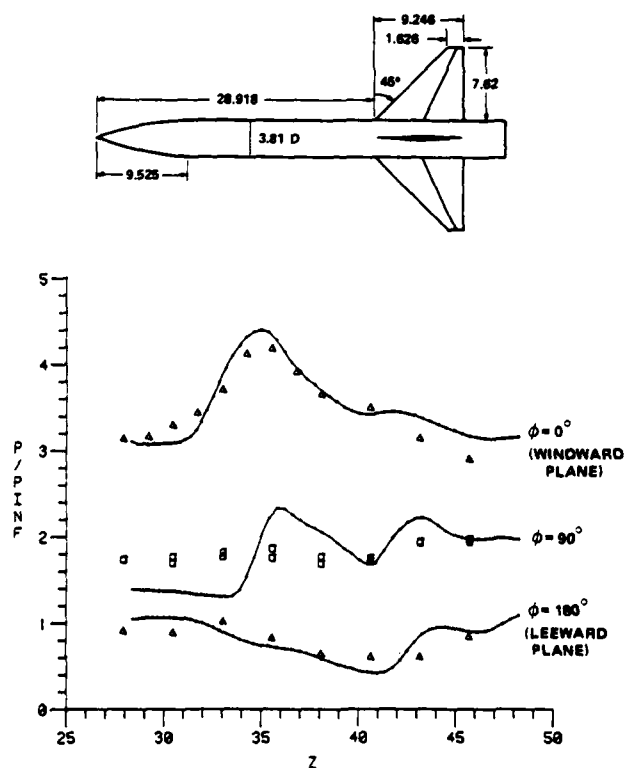
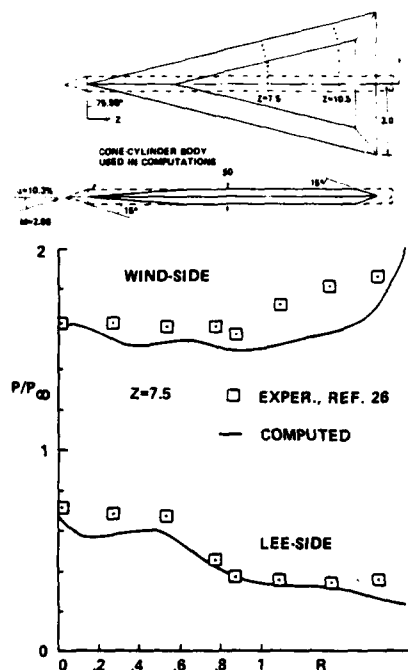
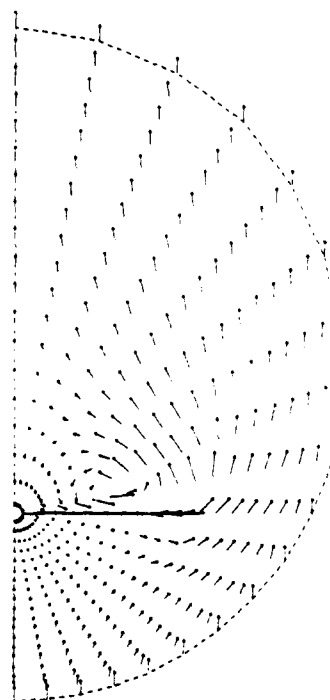


Fig. 6 Calculated and measured surface pressures along body in "X" roll position at $M = 2.7$, $\alpha = 10^\circ$. Data from Ref. 16.



a) surface pressure at $Z = 7.5$
Data from Ref. 17.



b) computed cross flow velocity vectors upstream of trailing edge.

Fig. 7 Calculated and measured results on a delta wing.

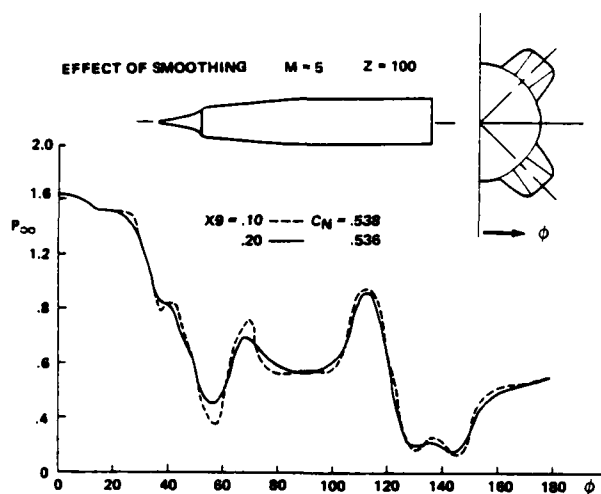


Fig. 8 Influence of smoothing on circumferential pressures for a body of non-circular cross section at $M_\infty = 5$, $\alpha = 8^\circ$.

IV.2 PRACTICAL PROBLEMS IN APPLICATION OF THE COMPUTATIONAL METHOD

Figs. 5, 6 and 7 illustrate the general quality of results that have been obtained to date on missile type configurations. It is, however, relevant to discuss the practical problems encountered when applying this computational method to new configurations. The current computational method is most robust for configurations with wings that feature leading edges with supersonic normal velocity components. Here relatively few problems are encountered to completing calculations and there is little ambiguity associated with setting up the calculation. The standard procedure is to apply a Prandtl-Meyer expansion or oblique shock at the leading edge (i.e. Option 1). Differencing at the fin tip and at the adjacent interior point is accomplished using option 1. As pointed out in Sec. 3.2 the number of steps for which the Y derivatives are to be suppressed following the occurrence of a leading edge is controlled by an algorithm built into the code.

More serious problems are encountered when applying the computational method to wings or fins having subsonic leading edges. In particular, the computation is not robust in the vicinity of the fin tip. In Ref. 8 a set of leading edge and fin differencing options are recommended. The current practice differs from this and consists of marching through the leading edge without using a local analysis (i.e. option 0). The interior point adjacent to a fin tip (i.e. point C of Fig. 3) is differenced across the tip onto both surfaces (option 0) while the tip point is advanced using one sided differencing on the lee side (option 1) and differencing across the tip on the windward side (option 0). This prescription is generally adequate as long as the wing geometry and flow conditions do not result in the formation of strong vortices. When such vortices form, the computation tends to break down unless artificial viscosity or smoothing is introduced. This tendency and the need for smoothing generally increases with the angle of incidence. Low aspect ratio wings also tend to form stronger vortices at lower incidences. Here the effective incidence of the wing is increased due to the body upwash. Recommended values of artificial viscosity for interior and surface points are given in Ref. 8. If the computation breaks down at an interior point the interior artificial viscosity is increased and similarly for the surface points. In severe cases (i.e., incidences $> 10^\circ$ on low aspect ratio wings) it may be necessary to apply smoothing to the fin tip point also (see Sec 3.2).

The current computational method also requires special attention when applied to bodies of highly non-circular cross-sections such as the one shown in Fig. 8. Here vortices tend to form leeward of protrusions and the calculated flow field in this area becomes ill-behaved. This behavior can be controlled through addition of artificial viscosity.

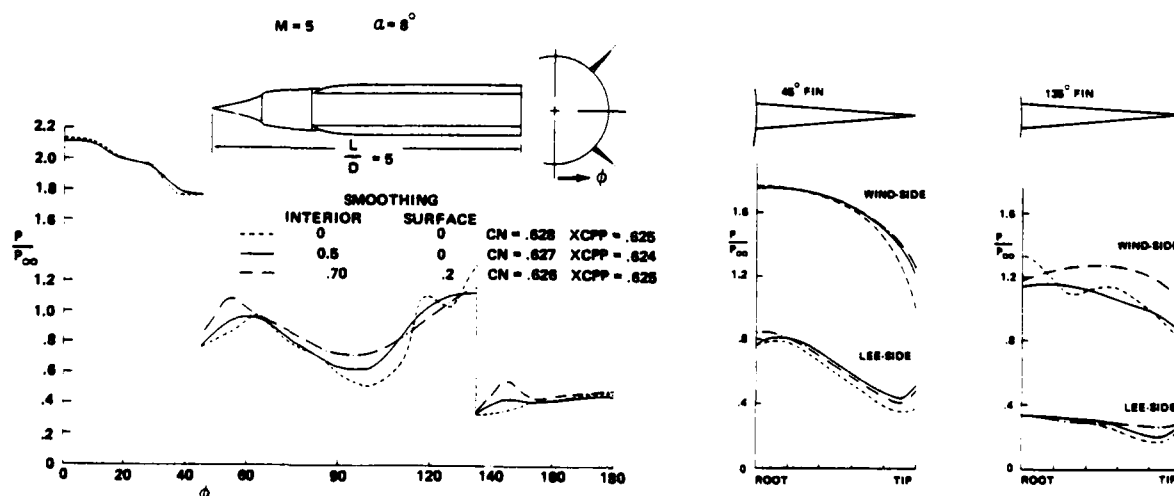


Fig. 9 Influence of smoothing on circumferential pressures for a body-wing configuration.

The effect of artificial viscosity has been investigated to some extent. In Figs. 8 and 9 surface pressures are shown on a body with cross flow plane protrusions and on a body with low aspect ratio wings featuring subsonic leading edges. These figures indicate that the variation in the level of artificial viscosity principally influences only surface pressures in the regions featuring large pressure gradients. However, as may be noted in Fig. 9, a high level of interior smoothing may significantly alter the surface pressure levels. The normal force and center of pressure for both of the cases shown in Figs. 8 and 9 are insensitive to the level of smoothing.

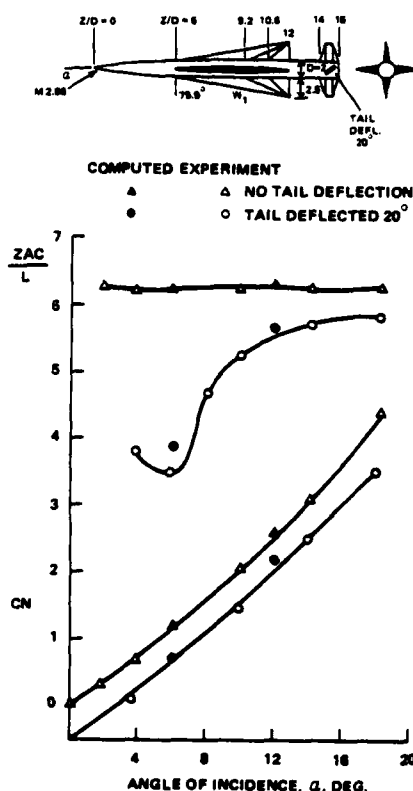


Fig. 10 Normal force coefficient and center of pressure for a body-wing-tail configuration with and without fin deflection. Data from Ref. 18.

IV.3 TREATING COMPLICATED GEOMETRIES

The present computational method is limited to the following types of configurations:

- (i) The body alone surface, $b(z, \phi)$, must be single valued in ϕ . This precludes a direct treatment of geometries containing items such as detached inlets.
- (ii) Fins must be relatively thin and lie near constant ϕ planes. By moving the coordinate origin, it is often possible to position fins along constant ϕ planes.

- (iii) Fin edges must be sharp and the radial location of the fin edge, $L(z)$ must be single or double valued in z . This allows wings with forward or backward sweep to be treated.
- (iv) Fins cannot extend through the bow shock.
- (v) The velocity component in the axial direction must remain supersonic throughout the entire calculation. This precludes bodies with blunt protrusions which feature upstream subsonic flow.

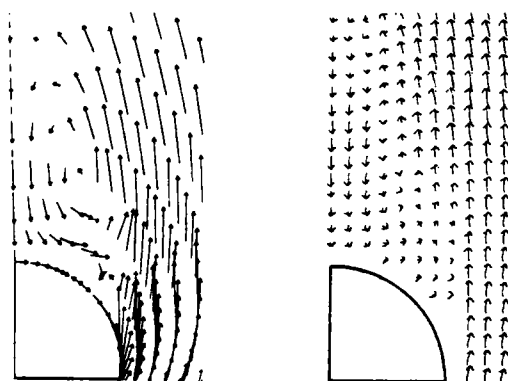
Configurations which do not strictly meet these requirements can often be treated using a slightly altered geometry. The feasibility of such modeling is dependent on the type of results desired from the computation. If such results are aerodynamic coefficients then significant latitude is possible. For example, fin deflection can be simulated by increasing the fin slope by the angle of incidence on one side of the fin and decreasing it by the same amount on the other. This misplaces the location of the shocks and expansions generated by the fin, but generally produces a reasonable pressure values on the fin. The integrated effect on the overall aerodynamic coefficients is adequately modeled, as illustrated in Figure 10. Ref. 8 is suggested for additional illustrations and comparisons.

IV.4 MODELING OF SEPARATED CROSS FLOWS

It is well known that at incidences above a few degrees the flow over a delta wing with subsonic leading edges separates to form lee side vortices. As can be seen in Fig. 7, the calculated flow field contains the appropriate vortex structure. At incidences greater than about 5 degrees, the flow over circular bodies also separates and forms vortices. The resulting cross flow separation has a large effect on the lee side pressure of the body and on the body upwash experienced by the lifting surfaces. Unfortunately, inviscid solutions on circular bodies do not adequately predict flow field vortices. Generally, a cross flow shock occurs with little or no separation. It has been shown in Refs. 8, 21 and 22 that by the application of a Kutta condition, a flow field vortex structure can be generated which approximates what has been observed experimentally. Application of a Kutta condition entails prescribing a separation line along the body surface and a velocity direction along the separation line. In the current procedure the velocity vector is aligned with the separation line, which differs from the method used in Ref. 15 and 16. A comparison of the calculated and measured surface pressures and flow field velocities are shown in Fig. 11. Qualitatively, the correct vortex structure is captured in this solution. Computed surface pressures are satisfactory for calculating normal force and pitching moment although there is substantial disagreement between measured and computed pressure profiles near the separation line.

In Table 1 calculated normal force coefficients and centers of pressure on bodies with several different cross sectional shapes have been compared to experiment. Each configuration was calculated in three modes: as a smooth body, with a Kutta

condition and with a low aspect ratio wing located at estimated separation lines. In the case of the circular body the separation line was determined using the empirical correlation of Ref. 8 while in the remaining cases separation was assumed to occur at the corners. On the square shaped body two separation points were thus prescribed. Application of the low aspect ratio wing to the circular body required the use of a separation line with constant angular orientation. An examination of Table 1 indicates that all three types of calculations produced the correct trends with variation in cross-sectional shape. Best results for normal force were obtained using the low aspect ratio wing approach. However, application of the Kutta condition yielded the closest center of pressure comparisons. The flow field calculated on the diamond body is shown in Fig. 12, and appears to exhibit the correct qualitative structure.



a) cross flow velocities. Data from Ref. 19.

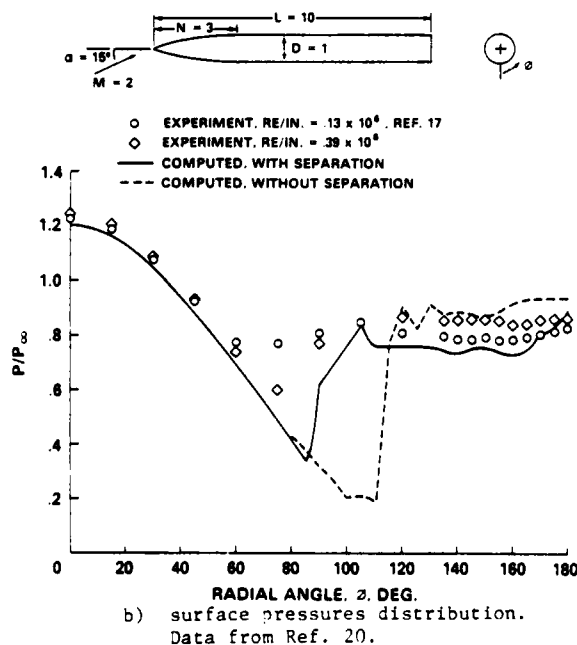


Fig. 11 Computed results on a circular body using a Kutta condition

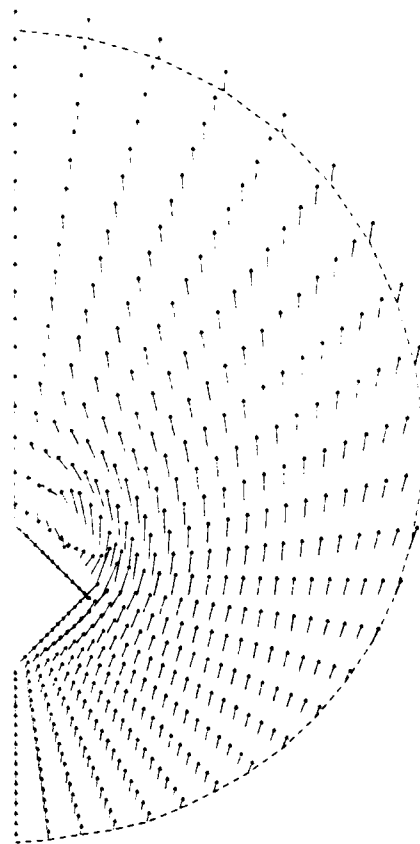


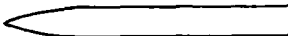




Fig. 12 Cross flow velocity vectors for a tangent-ogive-cylinder body of diamond cross section at $M = 3.88$, $\alpha = 10^\circ$.

V. Discussion of Results and Conclusions

An examination of the test cases described in the preceding sections indicates three notable deficiencies in the current predictive capabilities: accounting for viscous effects; treating arbitrary geometries typical of the next generation of low cross-section, airbreathing missiles; and a lack of computational robustness.

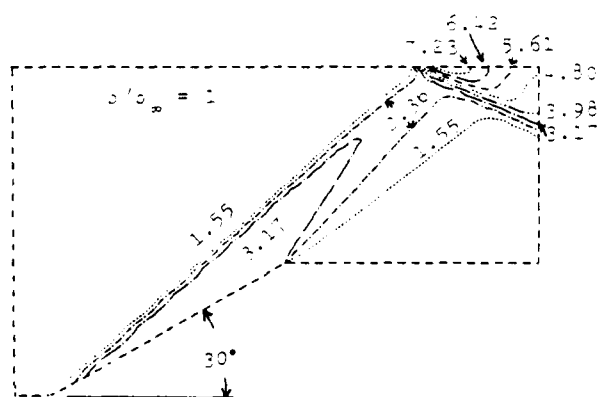
Clearly, viscous effects cannot be directly treated with an inviscid code. However, as may be noted in the last section, the most important influence of viscosity from the point of view of predicting vehicle aerodynamic characteristics, is accounting for body cross flow separation. This is of paramount importance since the occurrence of large body vortices alters the flow field surrounding lifting surfaces. As shown by the work of NEAR (Refs. 21 and 22) and the results of Ref. 8, application of a Kutta condition along a prescribed separation line gives a correct qualitative description of flow field vortices. In the case of a circular cylinder the predicted pressure levels on the lee side of the body are adequate for accurate determination of body normal force and pitching moment. However, it remains to be shown through additional comparisons between calculation and experiment on winged bodies that application of the Kutta condition quantitatively accounts for cross flow separation.

TABLE 1

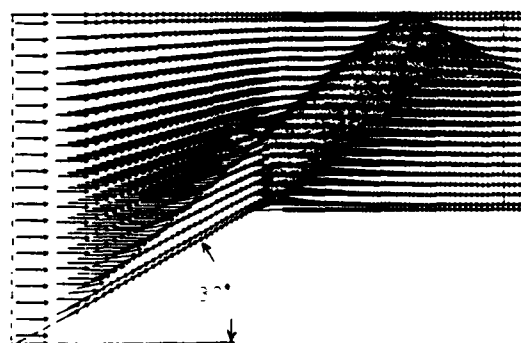
	+ $2/D = 10$ +		Normal Force and Center of Pressure at Mach 3.88 at 10° Incidence					
								
	C_n	X_{cp}	C_n	X_{cp}	C_n	X_{cp}	C_n	X_{cp}
Experiment	.934	.425	1.126	.425	1.376	.465	1.720	.465
Separation not Simulated	.967	.433	.932	.395	1.250	.464	1.306	.407
Kutta Condition	1.022	.448	1.05	.437	1.287	.479	1.55	.461
Fin at Separation Point	.960	.431	1.187	.458	1.420	.494	1.62	.456

A second major deficiency of the described computational method is its inability to handle unconventional missile geometries. This shortcoming can be removed by further extending the multiple zone approach, described in Sec. 2, or by applying a generalized transformation procedure. The multiple zone approach appears to provide a more flexible framework but at the expense of increased complexity of the resulting computational method.

A final deficiency in the current computational method is a lack of robustness in the numerics. As discussed in the previous section, the formation of large vortices in the flow field leads to computational difficulties which are currently resolved by an ad hoc addition of artificial viscosity. Recently robust methods have been developed for unsteady inviscid flow which can capture strong discontinuities in only a few steps. Of particular interest here are the methods based on Godunov's scheme. These methods treat boundary points as well as interior points in conservation form using a control volume formulation. Aside from increased robustness, application of such schemes to steady flow problems may improve resolution of wing shocks and eliminate the problem of the pressure over-shoot on compression surfaces. To investigate the possible application of robust schemes to the steady supersonic problem, Godunov's method has been extended to this case. Fig. 13 illustrates the ability of this method to capture a strong shock and expansion in a two dimensional internal duct with a ramp. Of course the robustness of Godunov's method when large variations of vorticity are present or its ability to properly convect vorticity downstream have yet to be tested.



a) density ratio



b) velocity vectors

Fig. 13 Computed flow field in a two dimensional duct using an extension of Godunov's method to steady flow at $M_\infty = 5$.

REFERENCES

1. Thomas, P. D., Vinokur, M., Bastianon, R. and Conti, R. J., "Numerical Solution for Three-Dimensional Inviscid Supersonic Flow," AIAA J. Vol. 10, No. 7, 1972, pp. 887-894.
2. Moretti, G., Grossman, B. and Marconi, F., "A Complete Numerical Technique for the Calculation of Three-Dimensional Inviscid Supersonic Flow," AIAA Paper 72-192, San Diego, CA 1972.
3. Marconi, F. and Salas, M., "Computation of Three Dimensional Flows About Aircraft Configurations," Computers and Fluids, Vol. 1, 1973, pp. 185-195.
4. Kutler, P., Reinhardt, W. A. and Warming, R. F. "Multishocked, Three-Dimensional Supersonic Flowfields with Real Gas Effects," AIAA J., Vol. 11, No. 5, 1973, pp. 657-664.
5. Kyriakos, C. L. and Harris, T. B., "A Three-Dimensional Flow Field Computer Program for Maneuvering and Ballistic Re-entry Vehicles," Tenth USN Sym. on Aeroballistics, July 1975.
6. Marconi, F., Salas, M. and Yaeger, L., "Development of a Computer Code for Calculating the Steady Super/Hypersonic Inviscid Flow Around Real Configurations, Vol 1 Computational Techniques", NASA CR 2675, Apr. 1976.
7. Solomon, J. M., Ciment, M., Ferguson, R. E., and Bell, J. B., "Inviscid Flowfield Calculations for Reentry Vehicles with Control Surfaces," AIAA J., Vol. 15, No. 12, 1977, pp. 1742-1749.
8. Wardlaw, A. B., Baltakis, F. P., Solomon, J.M. and Hackerman, L. B., "An Inviscid Computational Method for Tactical Missile Configurations" NSWC TR 81-457, Dec. 1981.
9. Wardlaw, A. B., Hackerman, L. B. and Baltakis, F. P., "An Inviscid Computational Method for Supersonic Missile Type Bodies - Program Description and Users Guide" NSWC TR 81-459, Dec. 1981.
10. Moretti, G., "Conformal Mappings for Computation of Steady, Three-Dimensional, Supersonic Flows," Numerical/Lab. Computer Methods in Fluid Dynamics, ASME, 13, 1976.
11. Klopfer, G. H., Nielsen, J. N., "Euler Solutions for Wing and Wing-Body Combination at Supersonic Speeds with Leading-Edge Separation," AIAA Paper No. 80-0126, Jan. 1980.
12. Hindman, R. S., Kulter, P. and Anderson, D., "A Two-Dimensional Unsteady Euler Equation Solver for Flow Regions with Arbitrary Boundaries," AIAA Paper 1465, Williamsburg, VA 1979.
13. Wardlaw, A. B., Solomon, J. M. and Baltakis, F. P., "Supersonic Inviscid Flow Field Computations of Missile Bodies" AIAA J., 19, 7, July 1981, pp. 899-906.
14. Harten, A. and Zwas, G., "Switched Numerical Shuman Filters for Shock Calculations," Journal of Engineering Mathematics, 6,2, April 1972, pp. 207-216.
15. Lamb, M., Sawyer, W. C., Wassum, D. L. and Babb, C. D., "Pressure Distributions on Three Different Cruciform Aft-Tail Control Surfaces of a Wingless Missile at Mach 1.60, 2.36 and 3.780," vol. II and III, NASA TM 80097, Aug. 1979.
16. Stallings, R. L., Lamb, M., Watson, C. B., "Effect of Reynolds Number on Stability Characteristics of a Cruciform Wing-Body at Supersonic Speeds," NASA TP 1683, July 1980.
17. Stallings, R. L. and Lamb, M., "Wing Alone Aerodynamic Characteristics for High Angles of Attack at Supersonic Speeds," NASA TP 1889, July 1981.
18. Jorgensen, L. H., "Inclined Bodies of Various Cross Sections at Supersonic Speeds" NASA Memo 10-3-58A, Nov. 1958.
19. Oberkampf, W. L. and Bartel, T. J., "Supersonic Flow Measurements in the Body Vortex Wake of an Ogive Cylinder," AFATL-TR-78-127, Nov. 1978.
20. Perkins, E. E. and Jorgensen, L. H., "Comparison of Experimental and Theoretical Normal Force Distributions (Including Reynolds Number Effects on an Ogive Cylinder Body at Mach 1.98)", NACA TN 3716, May 1956.
21. Klopfer, G. H. and Nielsen, J. N. "Euler Solutions of the Body Vortices of Tangent Ogive Cylinders at High Angles of Attack and Supersonic Speeds," AIAA Paper 81-0361.
22. Nielsen, J. N., Kuhn, G. D. and Klopfer, G. H., "Euler Solutions of Wing Body Interference at High Incidence Including Vortex Effects" NEAR TR 263, Aug. 1982.

STORE SEPARATION AT TRANSONIC SPEEDS

Stephen S. Stahara*
Nielsen Engineering & Research, Inc.
Mountain View., CA

Abstract

A review is provided of the state of the art of methods currently employed for predicting store separation at transonic speeds. Both experimentally- and theoretically-based methods are surveyed. A discussion of the various underlying aspects of the store separation problem, in particular, those most crucial at transonic speeds is provided. Future developments required for these methods to become usable in a design mode are identified, and a possible next plateau of theoretical modeling development is suggested.

Introduction

The safe and controllable separation of external stores from modern fighter-bomber aircraft throughout their flight envelope is a problem of current significant military importance. The ability to carry and deliver externally-mounted weapons with a minimum of detriment to speed and performance basically defines the mission effectiveness of attack aircraft. Placement of external stores on aircraft has two major effects. First, unless attention has been given to an integrated design, there is a large increase in drag as shown schematically in Fig. 1, resulting in both lower operating and delivery speeds¹. Even more important, however, is the necessity of imposing restrictive operating limitations because of dangerous store release or jettison characteristics, thereby compromising the entire weapon delivery capability². The ability to establish weapon system designs which alleviate these effects depends upon the development and use of accurate and reliable methods of predicting store separation characteristics.

Mission requirements of ever higher operational and delivery speeds have resulted in the occurrence of either local or global transonic environments for the separating external store. Prediction of separation characteristics in the linear subsonic and supersonic regimes is a complex, difficult, and presently incomplete task. The corresponding prediction in the transonic regime is severely compounded by the essential non-linearity of the basic flow field. Nevertheless, it is in this regime that separation problems become most severe. At this time, much effort both experimentally and analytically has lead to advances in the understanding of the underlying physical phenomena and in the preliminary prediction of these characteristics.

The purpose of this paper is to provide a review of the state of the art of current methods employed for predicting store separation in the transonic regime. As a prelude to that discussion, we provide a description of the store separation

problem in general including a brief discussion of the various factors involved, the sequence of operations necessary to determine a store trajectory, and some particular problems created by a transonic environment. Next, we review the complete problem of store separation prediction, some of the simplifications generally adopted, and the predictive methods in current use. Finally, we discuss some future developments required for these methods.

The Store Separation ProblemCategories of and Parameters Effecting Separation

The most basic subdivision of the store separation problem arises from store type². This classifies the problem into the following three categories:

- Jettison
- Delivery
- Launch Transient

The first category involves those classes of stores (fuel tanks, pods, etc.) which are released under either emergency or normal conditions with no requirement for accurate delivery but only for safe separation. This is the most hazardous of the three categories. The second involves stores such as unguided general purpose bombs and munitions released for target delivery, and requires both a safe and benign separation to maintain accuracy. The third category involves those classes of stores (optically guided bombs, radar directed missiles, etc.) which lock onto target prior to release, and usually have active controls during launch to avoid target breaklock. These are the most difficult to analyze, but they normally do not pose a danger to the launch aircraft in either the jettison or normal launch mode unless control failure results in abnormal control deflection.

Because there are three separate geometric components involved (parent aircraft, ejector rack, and store) having a first-order influence on separation characteristics, there exists a large number of both aerodynamic and physical parameters that must be accounted for. The most significant of these² are depicted in Fig. 2. All of these parameters are coupled to and interact with each other with varying degrees of importance. Much work has been done to investigate the relative importance of these parameters on store separation characteristics, for example, ref. 3. The general conclusions of these studies² are that the most significant parameters are:

- store stability
- aircraft flow field as a function of $(M_\infty, \alpha_\infty)$
- aircraft acceleration at release
- ejector induced moments

* Senior Research Scientist, Associate Fellow AIAA

Complicating, or rather adding another dimension to these parameters, is the necessity of current military aircraft to carry a variety of different weapons in a multiplicity of combinations and configurations. Fig. 3 illustrates just several of the various store carriage possibilities for an F-16⁴.

Particular Problems at Transonic Speeds

At transonic speeds, the mutual coupling between the various aerodynamic and physical parameters intensifies. New high-gradient regions are created in the parent aircraft flow field, and those already existing at lower speeds usually become more severe. The store itself will begin to generate its own transonic effects, and these can interact with and intensify those of the parent. Additionally, store stability generally reaches its minimum in this regime. Unsteady effects can occur both in the flow field (buffeting, etc.) and in the aircraft structure (flutter). The store separation problem in general reaches its most critical stage in this speed regime. This is due primarily to the rapid lateral propagation of disturbances in the flow field which enhances the interaction between the various geometric components involved.

Sequence of Operations for Store Trajectory Calculation

To perform a store trajectory calculation, a sequence of operations is required. The first step is the simulation and description of the flow field about the parent aircraft. The simulation can be accomplished either experimentally in a wind tunnel or analytically via a computational model. The resultant description can be provided in the form of local velocity components or more commonly in terms of flow field angularities. Next is the determination of the forces/moments acting on the store in this nonuniform flow field. This also can be accomplished either directly through experimental measurements on a model or determined analytically from surface pressures predicted from a flow field simulation or by using a sectional loading procedure. Finally, using the determined aerodynamic forces acting on the store together with gravitational and any other forces (ejector impulse, engine thrust), the six-degree-of-freedom rigid body Euler equations of motion of the store are integrated to determine the trajectory. By far the most time consuming and expensive operation is the definition of the parent aircraft flow field.

Transonic Store Separation Prediction

The General Problem

In order to solve the complete transonic store separation problem, it would be necessary to describe the unsteady, nonlinear, three-dimensional interference flow field about such formidably complex parent aircraft/multiple store configurations such as shown in Fig. 3, simultaneously accounting for all of the aerodynamic and physical parameters indicated in Fig. 2. Even at the inviscid, steady, small-disturbance level, this is not presently possible. Fortunately, for most separation applications such a complete description

is not necessary. Many features of store trajectory calculations can be well approximated by relatively simple analytic considerations. The essential art in these applications is to identify those aspects most critical for a particular problem and, because of the requirement for many repetitive calculations, to simulate them with as simple an analytical model as possible while retaining the required accuracy.

Rational Simplifications Possible

Perhaps the most important simplification usually introduced into the separation problem is the time-dependent quasilinearization or quasi-steady assumption. This replaces consideration of the store's unsteady motion through the nonuniform flow field with a sequence of steady states. The quasi-steady approach is valid only if the time variation of forces acting on the store occurs sufficiently slowly when compared to the characteristic time associated with the store's motion so as to be negligible. The characteristic time of the store's motion can be taken as the store length divided by its instantaneous speed. If this variable time increment is used in the trajectory calculation and is short compared to that taken for the force variations on the store to occur, then the quasi-steady assumption is valid. The crucial force variations on the store inevitably occur during release, and this is when the sensitivity to time steps in the trajectory calculation is greatest. Fig. 4 illustrates the effect of selecting an improper time step in the initial portion of a store trajectory (dashed line) compared with corresponding results for the proper time step⁵. In that figure, store inclination has been plotted versus flight time, and the result of too large of a time step along the dashed portion of curve 1 results in the prediction of the store alternatively undergoing large pitch-up/pitch-down oscillations which result in the high-drag deceleration of the store and the prediction of a much reduced flight time and range than for the correct result indicated by the completely solid line of curve 2.

In addition to the quasi-steady assumption, the remainder of the important simplifications relate to the treatment of the various interference effects on the separating store. In terms of decreasing importance, these effects classify as follows⁵:

- 1st order - steady interference on the attached store due to the parent aircraft, ejector rack, and adjacent attached stores
- 2nd order - store motion and aircraft motion effects on the effective angles of attack and sideslip (α, β) incident on the store
- 3rd order - unsteady effects on store due to motion of nearby stores during multiple release/jettison
- higher order - mutual interference on the separated store due to reciprocal interaction of the store with the parent

An ideal interference procedure would solve the quasi-steady motion of the store, accounting for all of the above interference effects at each time step along the trajectory. This would require a new determination of the 3-D multi-component interference flow field at each of those steps. Since

typical trajectory calculations require several hundred time steps, such a procedure is not practical.

Various approximations to this procedure have been proposed and developed to various degrees. In what can be considered indicative of the current state of the art realization of the ideal method (although restricted to subcritical speeds), NWC⁶ is currently extending a method originally developed by Dillenius, et. al.⁷ which will ultimately embody the following interference effects: 1st order effects due to parent aircraft, ejector rack, and other attached stores, 2nd order effects of store motion on effective store (α, β), and higher order mutual interference on the store due to reciprocal interactions between store, wing pylon, triple ejector rack, and the other attached stores. The effects neglected include: flow field changes as store is displaced through it, unsteady aircraft motions, and unsteady effects of nearby stores during multiple release.

The most important of the effects neglected in that method⁶ as well as all other separation methods commonly in use is the assumption that the parent-generated nonuniform flow field so determined, as shown in Fig. 5, remains unchanged as the store is released and displaces through it. Within this assumption, there are two alternative approximations. In the first, the parent-generated flow field is determined with the store whose trajectory is to be tracked mounted in the carriage position. In the second alternative, the parent flow field is determined with the store to be tracked absent. This approach assumes that the flow field through which the store moves is generated only by the adjacent stores and parent aircraft structure. Neither alternative is correct. The first properly accounts for mutual interference between the store and the parent with the store in the carriage position, but not thereafter. The second neglects this mutual interference altogether. To date, these two alternatives have not been systematically compared against each other. The one currently favored is the first, since it is known that the store/parent mutual interference is strongest in the carriage position and then rapidly decays as the store moves away.

The final simplification of the trajectory calculation concerns the determination of the aerodynamic loads acting on the store. The obvious choice of determining and then integrating surface pressures over the store at each time increment along the trajectory can easily be the most time consuming operation of the entire trajectory calculation⁷. Many of the currently based schemes, therefore, employ a sectional loading concept as illustrated in Fig. 6 whereby loads along segments of the store are determined based upon the local flow angles at that section. The number of sections employed in these procedures vary from as few as two⁸, to the order of 10^5 ,⁹ to the continuous loading distribution methods⁷. Both experimental and analytical flow fields have been employed with the sectional loading concept. Since the methods are all similar in concept, we briefly consider the continuous loading distribution methods described in detail in ref. 7. With the parent generated flow field with store absent available (Figs. 5, 6), the store loading distribution is determined by locally applying apparent mass concepts to individual cross

sectional slices of the store together with the nonuniform parent-generated crossflow velocity components at the locus of points corresponding to the position that the longitudinal axis of the store would occupy in the flow as shown in Fig. 7. The procedure can directly account for buoyancy due to streamline curvature as well as local slender-body loading, and a viscous crossflow correction to account for vortex separation can also be easily included. Such procedures avoid the computationally expensive integration of surface pressures at each time increment, and have proven to be quite accurate for the many subsonic applications carried out to date^{7,10-15}. At transonic speeds, these concepts must be modified in order to account for the presence of shock waves on the store¹⁶.

Methods Currently In Use

The methods currently available for predicting store separation characteristics at transonic speeds can be broadly categorized according to whether they are primarily experimentally or theoretically based. Several of these methods, however, such as the influence function method have been used with both experimental and theoretical flow field results, and could be placed into either classification.

In this country, for the prediction of store separation characteristics there has been and continues to be a broad reliance by government agencies on experimental methods based on wind tunnel results. In particular, the flow angularity method⁹ in conjunction with wind tunnel data for parent aircraft flow fields is heavily used in store certification programs by the U.S. Air Force. European approaches also currently favor the flow angularity method but usually coupled with theoretically predicted aircraft flow fields⁵. A major incentive to develop theoretical methods capable of accurate transonic store separation simulation occurs at the preliminary conceptual design stage where tunnel testing is often not practical. Understandably, much of the current transonic method development detailed below is occurring in the industrial arena. In the following subsections, we provide a summary of those experimental and theoretical techniques in current use.

Experimentally Based

There are four major experimental techniques used today to predict store separation characteristics. These are²

- Captive Trajectory System
- Grid
- Flow Angularity
- Freedrop

A fifth, the influence function method mentioned previously, is under current development. Although it has not yet reached the stage of completeness of the other methods, we discuss it here in view of its future potential as an alternative method.

Detailed descriptions of the first four methods have been provided in the open literature, for example refs. 17-20. Here we provide a summary

discussion of these methods to provide background for the theoretically-based methods to follow.

The Captive Trajectory System (CTS) is considered the most versatile and accurate of all the experimentally-based methods and is often used as a benchmark for evaluating the other techniques. The operation of the CTS method, as shown in a typical installation in Fig. 8, proceeds as follows. Using the wind tunnel flow about the parent model together with a six-degree-of-freedom store model support system controlled by a closed-loop computer system, it solves the Euler equations of motion using the measured aerodynamic forces and the mass, inertia and other characteristics of the store. Based on these solutions at a particular time increment, the store is moved to its next position along the trajectory where the process is repeated. The principle advantage of the CTS method is accuracy, while its main disadvantage is cost.

In addition to cost, however, other factors have led to consideration of alternative methods. For example, the continuing trend to develop guided weapons having autopilot and control systems that are active during launch has provided a major incentive for developing the grid method. Since it is not feasible to remotely control and accurately model the control surfaces of store models this size, some technique for simulating the trajectories of guided weapons having active controls during the launch sequence was necessary. The grid method accomplishes this by using the CTS to traverse the store through a predetermined grid in the vicinity of the store carriage location. The forces/moments acting on the store are then measured. This information, obtained as a function of Mach number and parent aircraft attitude, is then used off-line in six-degree-of-freedom trajectory simulations of the weapon which incorporate the characteristics of the weapon flight control system². It has been found that in many circumstances^{18,21,22} the primary dependence of the store aerodynamic coefficients is with vertical displacement with weak dependence on lateral and longitudinal displacement. This has led to use of the 'limited grid' concept in which data is obtained only as a function of vertical displacement, Mach number, and aircraft attitude. Comparisons²²⁻²⁴ with CTS and full scale results have indicated that reasonably accurate correlations can be obtained in certain flight regimes. The primary advantages of the grid method are tunnel time savings and the ability to simulate trajectories for conditions beyond those obtained in the tunnel, such as simulation of store active controls and store release while the parent aircraft is in a climb/dive or accelerated flight condition. However, grid results are limited to the particular store configuration tested. Applications to other stores require the local flow angularities to be inferred from force/moment data and this is not always accurate.

The flow field or flow angularity method was evolved primarily to eliminate this configuration dependence. With the flow angularity technique, a data bank of local flow angles is obtained for a particular aircraft as a function of Mach number and attitude over a predetermined grid in the vicinity of the carriage station of interest. Next, using the free stream aerodynamics of the store, interference aerodynamic coefficients are determined for the various forces/moments acting on the store, separately accounting for the local

flow angles acting at the center of pressure of the body and fins. Those interference coefficients are then used together with the flow angularity data and the free stream characteristics of the store in a six-degree-of-freedom calculation of the trajectory. Although of all the preceding methods, the flow angularity method is the least accurate, comparisons⁸ with CTS and full scale flight tests have generally been reasonably good. The method's main advantage is that it can be used to predict trajectories for weapon configurations not tested.

The freedrop method involves the release or ejection of dynamically scaled store models from the parent, and the subsequent determination of separation characteristics by photographic means. Three different scaling laws, termed 'heavy', 'light', and 'Froude', are currently in use and differ depending upon how the aerodynamic, static, and inertial characteristics of the store are scaled^{17,20,23-26}. Unlike the previous methods, the freedrop technique can be employed to study long trajectories of simultaneous multiple releases without sting interference effects. However, while it is well suited to flow-down tunnels, it is much slower than the other methods for continuous flow tunnels.

The influence function method^{9,27-29} is the most recently developed store separation technique. The method employs conventional grid survey force/moment data to identify the local flow angularities. As illustrated in Fig. 9, the method proceeds by assuming that the normal force and pitching moment coefficients of any store can be expressed as a linear combination of local influence function coefficients associated with finite axial segments of the store multiplied by the local flow angles acting on each of those segments, together with the zero-lift angle of attack α_0 and zero-lift pitching moment coefficient C_{m_0} . The local influence coefficients and (α_0, C_{m_0}) are determined by placing the store in a known calibration flow field. With that information, the local angle of attack along the grid survey is identified in a least-squared sense. With the flow angularity known, the force/moment characteristics for any other store in that parent flow field can then be determined once that store's influence coefficients and (α_0, C_{m_0}) are known.

The method was originally developed for supersonic flows^{9,27-28} for which the calibration flow field used to determine the influence function coefficients were simple wedge flows. The method has since been applied to subsonic/transonic flows²⁹ and has employed both experimental and theoretical PANAIR flow fields⁹ to determine the influence coefficients. The method has not yet incorporated side force/moment characteristics nor has it been employed in a complete trajectory determination. Consequently, final comparison of the method with other techniques cannot be made at this time. In Fig. 10, comparisons are shown of normal force coefficient results and data along a fuselage centerline location at $Z/D = 4.67$ for a GBU-15 store in the presence of an F-15 at $M_\infty = 0.95$ and display reasonably good agreement²⁹.

Analytically-Based

Historically, due to the absence of reliable 3-D transonic solvers, the initial theoretical transonic store separation predictions were based on panel method flow field simulations. The methods used and applications reported have included among others the following:

- NEAR subsonic/supersonic codes³¹⁻³³
- MMB codes⁵
- PANAIR derivative codes²⁸
- Northrop/NEAR codes³³

Although it was recognized that deficiencies existed in the predictions due to neglected nonlinear effects, many features of these calculations were found to compare favorably with data - for example, the extensive comparisons of store loading distributions made in ref. 31 - and were correct for reasons that will be discussed below. As an example of these results for a trajectory calculation, Fig. 11 displays comparisons of panel method results using the Northrop/NEAR subsonic code³³ with data for the normal force coefficient for an MK-83 bomb separating from an outboard wing/pylon location of an F-18 at the transonic flight condition, $M_\infty = 0.95$. These comparisons are reasonably typical of panel method results at transonic conditions in that trends are generally predicted but magnitudes and displacement of maxima/minima peaks are usually in error. Consequently, use of panel methods, which are widely available, for initial transonic calculations continues, with the results used as guidelines for certain preliminary analyses. Clearly, however, accurate simulation of store separation characteristics at transonic speeds can only be realized with full 3-D nonlinear transonic flow methods. Those nonlinear methods currently under development are identified below.

The earliest systematic investigations^{30,31} aimed at establishing a routinely-usable predictive method capable of determining the nonlinear transonic separation characteristics of stores from fighter-bomber aircraft are summarized by Stahara in ref. 32. One of the primary objectives of the study reported in ref. 32 was to investigate methods that were capable of predicting with sufficient accuracy the essential nonlinearities of the non-uniform parent-generated 3-D transonic flow field surrounding the store, while requiring a minimum of computational resources. Three different methods summarized below

- Classical transonic equivalence rule
- Extended transonic equivalence rule
- Nonlinear 3-D correction procedure

were investigated and compared with data from an extensive parallel experimental program^{34,5} involving the simplified F-16 wing-body/pylon/store configuration shown in Fig. 12. The conclusions drawn were that neither the classical equivalence rule nor the extended version in which the classical 2-D crossflow solutions are replaced by 3-D linear paneling method solutions are capable of adequately predicting the 3-D spanwise variations of shocks or other high-gradient regions that occur near the wing trailing edges of these configurations.

At least one nonlinear 3-D finite-difference solution is required to simulate such effects, although it is not necessary for that solution to be for the complete geometrically complex configuration. In the nonlinear 3-D correction method proposed, the effect of the wing pylons is simulated by invoking the hypothesis that the addition of geometric complexities to a basic configuration can be treated with differences between appropriate 3-D paneling method solutions. The primary nonlinear transonic effects generated by these configurations are due to the wing and can be adequately accounted for by computing the 3-D transonic small-disturbance (TSD) flow about a simpler basic configuration. For pylon addition to a basic wing-body, we then have

$$\phi = \phi_{WBP}^L - \phi_{WB}^L + \phi_{WB}^{NL} \quad (1)$$

where ϕ_{WBP}^L and ϕ_{WB}^L denote linear paneling method solutions for the wing-body/pylon and wing-body alone configurations, and ϕ_{WB}^{NL} denotes a nonlinear 3-D TSD finite-difference solution for the wing-body alone.

The basis for this hypothesis was derived from extensive comparisons of 3-D paneling method solutions with the data^{34,35} from this program at flow conditions throughout the transonic range. It was found that surprisingly good predictions of the lateral velocity components (upwash and sidewash), but not the axial component, could be obtained from paneling method solutions for these configurations at Mach numbers throughout the transonic regime even in the vicinity of shock waves. A similar solution decomposition has been employed with success in ref. 36 to model geometrically complex fuselage effects on wing pressures of the F-111 at transonic speeds. The primary point is that as long as detailed transonic effects are not required on the modeled component, then such a procedure is capable of providing good representations of the primary lift and volume effects of the modeled component upon the remainder of the flow.

In Fig. 13, we illustrate the effect of the 3-D nonlinear correction where a comparison is provided of theoretical and experimental results for local upwash and sidewash for the wing-body of Fig. 12 with wing pylon at a flow survey location directly under the wing pylon. The theoretical result with the nonlinear correction is shown as the solid curve, while the corresponding paneling method result is shown as the dashed curve. Both predictions compare quite well with data, with the nonlinear results somewhat superior.

The importance of these favorable lateral velocity component predictions to the store loading determination is paramount. The loading distribution on external stores in the presence of parent aircraft depends primarily on the lateral velocity components (see Fig. 7) and secondarily on the axial velocity component. The exception is regions where parent-generated shocks or other high-gradient regions impinge on the store. These effects are illustrated in Fig. 14 where normal force loading distribution results based on the procedure described in Fig. 7 are provided based

on the flow field results given previously in Fig. 13. The theoretical results indicate little difference in loading when employing the 3-D nonlinear corrected flow field or the linear paneling method flow field - presumably since the loading method only makes use of the lateral velocity components for which Fig. 13 indicated no substantial differences. Comparison of the theoretical results with data indicates generally good agreement except in the vicinity of the large axial gradient near the pylon trailing edge.

These loading comparisons serve to identify two deficiencies of the loading calculation procedure outlined in Fig. 7: (1) the procedure as constituted cannot accurately handle steep axial gradients in the parent-generated flow field, and (2) the method does not account for store-induced transonic effects. A modification to the loading calculation method that is capable of accounting for both of these effects has been reported in ref. 16. The method proceeds by applying the transonic equivalence rule to the store alone and accounting for store-induced transonic effects on the crossflow velocity components. Details of the procedure are given in ref. 16 together with results for a variety different body shapes at conditions throughout the transonic regime.

An indication of the magnitude of this improvement is given in Fig. 15 which displays a comparison of the difference in the pitching-moment coefficient $C_{m\alpha}$ variation throughout the transonic regime when including and not including store-generated transonic effects. The results indicated in the bottom plot are for an ogive/cylinder store similar to that shown in Fig. 14, but of 5 caliber rather than 8.5 caliber length. These results were carried out for free air flow past the store alone, for which the loading method shown in Fig. 7 without parent-generated flow field curvature reduces to the slender-body result. The effect of the improvement to the loading calculation has an even more dramatic effect when boattailing (and/or fins) are employed on the rear of the store. That change in pitching moment for a boattail addition is also indicated in Fig. 15 for a 1/2 caliber 7° conical boattail.

In addition to the 3-D methods described in refs. 30-32, 3-D TSD simulations of the combined parent plus store have been reported in refs. 37 and 38. Both of those methods are based on the modified transonic 3-D small-disturbance potential equation solver of Ballhaus, et al³⁹ later refined by Mason, et al⁴⁰. In ref. 37, the flow field about a simple fuselage-wing-pylon-store configuration is discretized about convenient computational support surfaces, as shown in Fig. 16. A fine grid is employed about a rectangular region encompassing the computational configuration with a coarser grid exterior to that region. Image points are used to simulate the boundary conditions on the pylon and store computational surfaces. Wing surface pressure results for a modified F-5 wing/pylon/store configuration have been determined and compared with the clean wing, as shown in Fig. 17, and provide a preliminary validation of the procedure. Additionally, a parametric study of a wing-fuselage-pylon-store configuration has been made. Both results are for the store in the carriage position. No trajectory calculations have yet been reported, but a sectional load procedure for

store separation applications was suggested.

In ref. 38, a similar fine mesh/coarse mesh is employed for the wing-body but with the addition of a third mesh about the store to facilitate treatment of store fins. Preliminary results have been reported³⁸ for several isolated stores, and also for a F-16 wing-body and B-16 store combination for which the wing pylon has not yet been incorporated. Future work is being directed toward pylon addition and separation simulation.

Future Developments and Concluding Remarks

With the continuing advances in 3-D computational flow simulations, theoretically-based method development is capable of contributing significantly to reducing the cost/time involved in both wind tunnel and full scale store certification programs. Because primary usage of theoretical store separation methods will be in a high-frequency repetitive use environment, any basic procedure must be capable of both accurately simulating the flow and providing some means of performing repetitive calculations without major computational demands.

Broadly speaking, the improvements and advancements necessary for such methods to become a usable design tool can be categorized under two major subdivisions:

I. Improved realism of simulation

* Parent related

- Noncircular fuselages
- Inlets
- Multiple pylons
- TER & MER's

* Store related

- Canards
- Tail fins
- Blunt noses

* Combined parent/store

- Mutual interference

II. Computational efficiency

- Rapid 3-D solvers
- Combination with nonlinear approximation methods

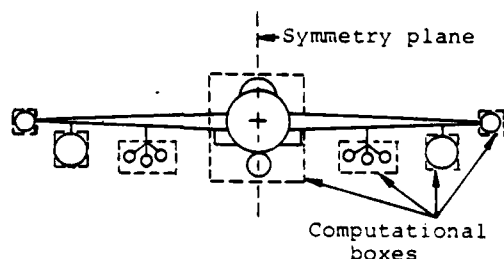
Increasing the realism of the simulation by more accurate modeling of the geometric details of the parent and store is clearly achievable with the current state of computational procedures. Of the various components listed above related to parent, store, and combined parent/store, all can be accounted for at the TSD level given the development effort. Increasing the level of solution accuracy beyond small-disturbance does not appear to be warranted at this time. Perhaps the single, most serious impediment to the use of these methods is their potential massive computational demands when used in the design mode. Before these methods will be accepted for routine use, some means must be available to reduce substantially their computational requirements. In this regard, an important technique has recently been developed which can be coupled with the nonlinear 3-D parent flow field solvers to provide such a means. The technique is a rapid

approximation method for predicting nonlinear flows and allows minimization of the actual number of 3-D nonlinear finite-difference solutions required to perform a store separation certification study. The method has been applied to a variety of 2- and 3-D transonic problems^{41,42} and ref. 42 provides a summary of a large number of nonlinear transonic flow applications.

In relation to the store separation problem, Fig. 18 displays an application of the method to prediction of 3-D transonic flow fields about the simplified F-16 wing-body/pylon combination for which results were previously provided in Fig. 13. In Fig. 18, we have used the 3-D nonlinear correction solutions [see Eq. (1)] for the local upwash u_L at $M_\infty = 0.95$ and $\alpha = 0^\circ$ and 5° , given by the dashed and dash-dot curves, respectively, to predict the corresponding result throughout a range of angles of attack without need for further finite-difference solutions. The predicted result for $\alpha = 2^\circ$ is given by the solid curve and is meant to be compared with the data points indicated by the crosses. Agreement is excellent.

Given the present status of computational technology and theoretical store separation methodology, together with the current and future needs for predictive transonic store separation methods, it is of interest to project the next plateau of theoretical modeling development in this area. In what follows, we describe a possible near-term transonic store separation computational model applicable to externally-carried stores that is both achievable within present technology and configured so as to be usable in the design environment.

The primary simplifications discussed in Section 3.2, i.e., quasi-steady motion, parent flow field invariance to store displacement, and store continuous sectional loading concept are employed. The parent aircraft flow field will be obtained via a 3-D TSD solver, with separate computational boxes surrounding the fuselage and the various pylon/stores as sketched below.



These separate boxes will allow either more or less accuracy at more or less computation expense to be attained in the simulation of the particular component (store, pod, etc.) under study. At each computational box, then, the boundary conditions imposed will be optionally approximated by either (1) transferral of the boundary condition from the actual component surface to the computational box using slender-body methods^{37,40}, or more accurately by (2) use of locally-normal lateral velocity components at the box obtained from a separate 3-D linear panel method solution for the actual geometrically-complete parent/store configuration³⁶.

For a given parent/store configuration, a series of these 3-D TSD calculations with the store in the carriage location will be determined as a function of $(M_\infty, \alpha_\infty)$ to fill a certain sparse data base matrix (defined below) of these parent flow fields. Those flow field results throughout the spatial volume encompassing the anticipated flight corridor of the store would then be archived in a data bank.

The store loading procedure would employ a transonic modification⁵ of the continuous sectional loading concept⁷; and would simultaneously account for high axial-gradient flow field effects on the store due to the parent flow field and store-generated transonic effects. Since this procedure would involve, as a component calculation, several axisymmetric TSD finite-difference calculations about the store alone at various M_∞ 's, those finite-difference results on the surface of the store would also be archived.

Next, with the 3-D nonlinear approximation method of refs. 41-42 configured so as to account for simultaneous changes in $(M_\infty, \alpha_\infty)$, that method together with the archived parent aircraft flow field results would be used to predict aircraft flow fields throughout the entire $(M_\infty, \alpha_\infty)$ flight range desired. If the flow topology within the desired $(M_\infty, \alpha_\infty)$ range does not change fundamentally, then only three independent parent-aircraft flow field solutions are needed to determine all the required flow fields. If the flow topology does change, for example if additional shock waves are generated or other high gradient regions created, then additional parent flow field solutions are needed, generally one for each topology change. For the axisymmetric TSD store-alone component solutions required in the loading determination, the 2-D version of the approximation method would also be used with the archived store-alone results to predict those required solutions. This combined parent aircraft/store loading solution procedure would then provide the aerodynamic forces/moments acting on the store as input to the six-degree-of-freedom store trajectory calculations throughout the $(M_\infty, \alpha_\infty)$ flight range.

Acknowledgments

The support of this survey paper was provided under the Nielsen Engineering & Research, Inc. Independent Research & Development Program.

References

1. Haines, A. B.: Prospects for Exploiting Favourable and Minimising Adverse Aerodynamic Interference in External Store Installations. AGARD-CP-285, Sept. 1980.
2. Mathews, C. B.: Drag and Other Aerodynamic Effects of External Stores. AGARD Manual AR-107, Nov. 1977, Chap. 5.
3. Marshall, J. C. and Summers, W. E.: An Analysis of the Relative Importance of Parameters Required for the Simulation of Store Separation Trajectories. Aircraft/Stores Compatibility Symposium Proceedings, Vol. 2, Dec. 1971.

4. Bradley, R. G.: Practical Aerodynamic Problems - Military Aircraft, Transonic Aerodynamics, Edited by D. Nixon, Progress in Astronautics and Aeronautics, Vol. 81, 1982.
5. Deslandes, R.: Evaluation of Aircraft Interference Effects on External Stores at Subsonic and Transonic Speeds. AGARD-CP-285, Sept. 1980.
6. Smith, R. E.: Private Communication, Naval Weapons Center, China Lake, CA, Nov. 1982.
7. Dillenius, M. F. E., Goodwin, F. K., and Nielsen, J. N.: Extension of the Method for Predicting Six-Degree-of-Freedom Store Separation Trajectories at Speeds Up to the Critical Speed to Include a Fuselage with Noncircular Cross Section. Vol. I - Theoretical Methods and Comparisons with Experiment. Technical Report AFFDL-TR-74-130, Vol. I, Nov. 1974.
8. Korn, S. C.: Use of the Flow Angularity Technique for Predicting Store Separation Trajectories. AFATL-TR-71-140, Oct. 1971.
9. Cenko, A. and Waskiewicz, J. P.: Recent Improvements in Prediction Techniques for Supersonic Weapon Separation. AIAA Paper No. 82-0170. Jan. 1982.
10. Spahr, H. R.: Theoretical Store Separation Analyses of a Prototype Store. J. of Aircraft, Vol. 12, No. 10, Oct. 1975, pp. 807-811.
11. Spahr, H. R., Everett, R. N., and Kryvoruka, J. K.: A Multifaceted Store Separation Analysis. Proc. of the AIAA 9th Aerodynamic Testing Conf., Arlington, TX, June 7-9, 1976, pp. 292-300.
12. Goodwin, F. K. and Smith, C. A.: Theoretical Separation Characteristics of Two Conceptual Solid Rocket Booster Parachute Test Units from the B-52 Aircraft. Nielsen Engineering & Research, Inc. TR 114, Aug. 1976.
13. Maddox, A. R., Dix, R. E., and Mattasits, G. R.: In-Flight Measurements of Captive Loads on a Store as Compared with Wind Tunnel and Mathematical Simulation. NWC TP 6026, Apr. 1978.
14. Pugh, P. G., Ilott, G. P., Peto, J. W., and Wood, M. B.: Development of the Raenear Method and Associated Facilities. Royal Aircraft Establishment Rept. No. TTCP-W2-KTA4-WP/UK5, Sept. 1979.
15. Goodwin, F. K. and Nielsen, J. N.: Experimental and Theoretical Study of Flow Fields and Store Forces in Close Proximity to a Triple Ejection Rack at Transonic Speeds. NWC TP 6210, Sept. 1980.
16. Stahara, S. S., Elliott, J. P., and Spreiter, J. R.: Transonic Flow Past Axisymmetric and Nonaxisymmetric Boattail Projectiles. AIAA Journal, Vol. 20, No. 10, Oct. 1982, pp. 1329-1337.
17. Binion, T. W., Jr.: Special Wind Tunnel Test Techniques Used at the AEDC. AGARD Fluid Mechanics Symposium, Flight/Ground Testing Facilities Correlations. Valloire, France, June 1975.
18. Little, R. E.: A Parametric Method of Aerodynamic Flow Field Investigation. Aircraft/Stores Compatibility Symposium, Vol. 3, Sacramento, CA, Sept. 1973.
19. Korn, S. C.: Validation and Expansion of the Flow Angularity Technique for Predicting Store Separation Trajectories. AFATL-TR-72-164, Sept. 1972.
20. Moore, S. B.: Advanced Wind Tunnel Simulation System and Techniques for Aircraft Store Carriage and Delivery Studies. Aircraft/Stores Compatibility Symposium Proceedings, Vol. 6, Eglin AFB, FL, Nov. 1969.
21. Studwell, V. E.: Experimental Aerodynamics of Multiple Weapon Carriage, AFATL-TR-71-5, Jan. 1971.
22. Mathews, C. B., Cason, R. D., McGinn, P. G., Carreras, E. M.: A Technique for Investigating the Launch and Separation of Guided Weapons. Aircraft/Stores Compatibility Symposium, Vol. 1, Arlington, VA, Sept. 1975.
23. Brooks, D. L.: Weapon Separation Clearance Procedures for the F-111 Aircraft. Aircraft/Stores Compatibility Symposium Proceedings, Vol. 2, Dayton, Ohio, Dec. 1971.
24. Reed, J. F. and Curry, W. H.: Aircraft Separation Problems Associated with Nuclear Ordnance - A Survey. Aircraft/Stores Compatibility Symposium Proceedings, Vol. 6, Eglin AFB, FL, Nov. 1969.
25. Cox, G. A.: Mathematical Modeling of External Store Jettison Trajectories Including Comparison with Flight Data. British Aircraft Corp. LTD Report, June 1975.
26. Marshall, J. C.: Analytical Evaluation of the Limitations of the Various Scaling Laws for Freedrop Store Separation Testing. Fourth Aircraft/Stores Compatibility Symposium Proceedings, Vol. 1, Fort Walton Beach, FL, Oct. 1977.
27. Meyer, R., Cenko, A., and Yaros, S.: An Influence Function Method for Predicting Store Aerodynamic Characteristics During Weapon Separation. 12th Navy Symposium on Aeroballistics Proceedings, Vol. 1, May 1981.
28. Tessitore, F., Cenko, A., Meyer, R., Dyer, R., and Waskiewicz, J.: A New Approach to Weapon Separation Aerodynamics. AIAA Paper No. 81-1654, Aug. 1981.
29. Dyer, R., Stepheson, S., Cenko, A., Tessitore, F., and Lijewski, L.: Influence Function Method - A New Technique for Predicting Subsonic, Transonic, and Supersonic Store Separation Characteristics. Sixth Biennial Aircraft/Stores Compatibility Symposium Proceedings, Oct. 1982.
30. Crisalli, A. J., Stahara, S. S., Nielsen, J. N., and Spreiter, J. R.: The Development of Rapid Predictive Methods for Three-Dimensional Transonic Flow Fields About Fighter Bomber Aircraft. AFOSR-TR-79-1281, 1979.

31. Crisalli, A. J., Stahara, S. S., and Hemsch, M. J.: The Rapid Prediction of Aircraft Store Loading Distributions at Transonic Speeds. AFOSR-TR-79-1282, Oct. 1979.
32. Stahara, S. S.: Study of Transonic Flow Fields About Aircraft: Application to External Stores. AGARD-CP-285, Sept. 1980.
33. Nadir, S. and Wedan, B. W.: The Northrop-NEAR Subsonic Store Separation Prediction Method. Sixth Biennial Aircraft/Stores Compatibility Symposium Proceedings, Oct. 1982.
34. Perkins, S. C., Jr., Stahara, S. S., and Hemsch, M. J.: Data Report for a Test Program to Study Transonic Flow Fields About Aircraft with Application to External Stores. Vols. I to VI, AFOSR-TR-78-1485 to 1490, July 1977.
35. Stahara, S. S. and Crisalli, A. J.: Data Report for a Test Program to Study Transonic Flow Fields About Wing-Body/Pylon/Store Combinations. Vols. I to III, AFOSR-TR-79-1070 to 1072, Jan. 1978.
36. Chen, A., Tinoco, E., and Yoshihara, H.: Transonic Computational Design Modifications of the F-111 TACT. AIAA Paper No. 78-106, Jan. 1978.
37. Shankar, V. and Malmuth, N. D.: Computational and Simplified Analytical Treatment of Transonic Wing-Fuselage-Pylon-Store Interactions. AIAA Paper No. 80-0127, Jan. 1980.
38. Thompson, D. S.: A Mesh Embedding Approach for Prediction of Transonic Wing/Body/Store Flow Fields. Presented at Numerical Boundary Condition Procedures Symposium, Moffett Field, CA, Oct. 1981.
39. Ballhaus, W. F., Bailey, F. R., and Frick, J.: Improved Computational Treatment of Transonic Flow About Swept Wings. NASA CP-2001, 1976.
40. Mason, W. H., MacKenzie, D. A., Stern, M. A., Ballhaus, W. F., and Frick, J.: An Automated Procedure for Computing the Three-Dimensional Transonic Flow Over Wing-Body Combinations, Including Viscous Effects. Vol. I, AFFDL-TR-77-122, Oct. 1977.
41. Nixon, D.: Perturbations in Two- and Three-Dimensional Transonic Flows. AIAA Journal, Vol. 16, No. 7, July 1978.
42. Stahara, S. S., Elliott, J. P., and Spreiter, J. R.: A Rapid Approximation Procedure for Nonlinear Solutions: Application to Aerodynamic Flows. AIAA Journal, Vol. 20, No. 8, Aug. 1982.

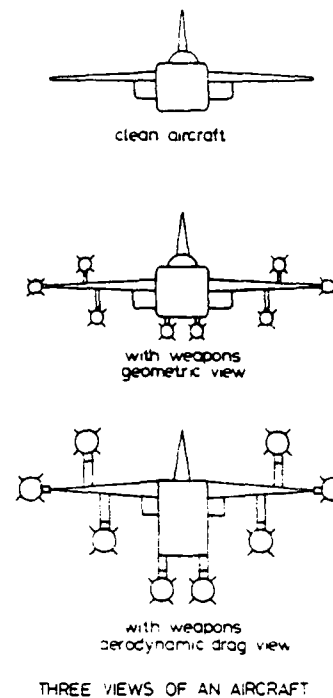


Fig. 1 Schematic illustration of detrimental drag increase due to external store addition¹

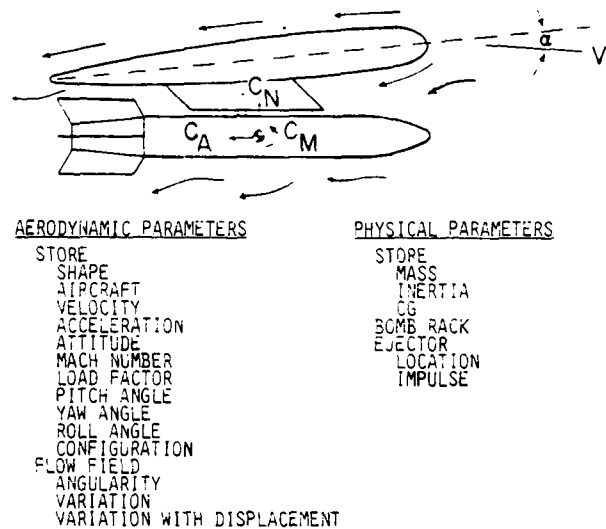


Fig. 2 The many aerodynamic and physical parameters affecting store separation²



Fig. 3 Illustration of several of the numerous store carriage possibilities typical of modern military aircraft⁴

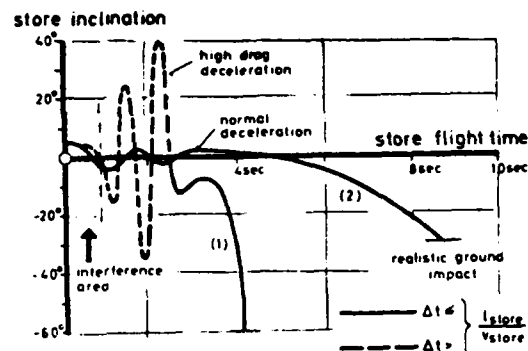


Fig. 4 Effect of time-step increment on predicted store separation characteristics⁵

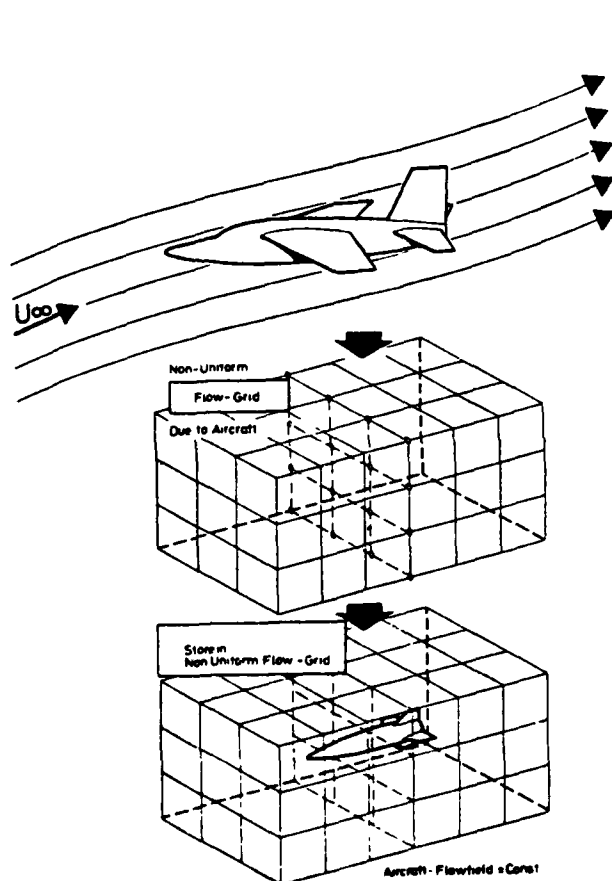


Fig. 5 Illustration of parent aircraft flow field invariance to store motion approximation⁵

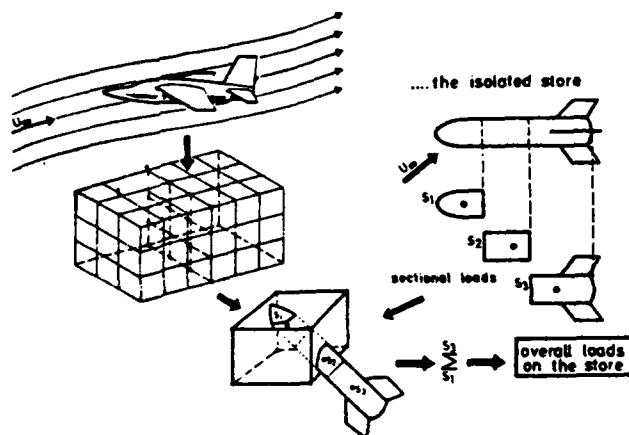


Fig. 6 Store sectional load concept in nonuniform parent flow field⁵

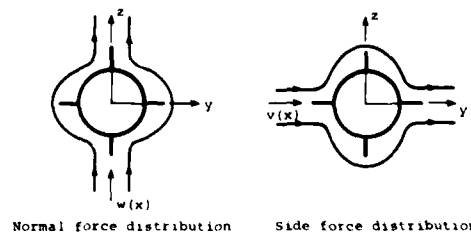
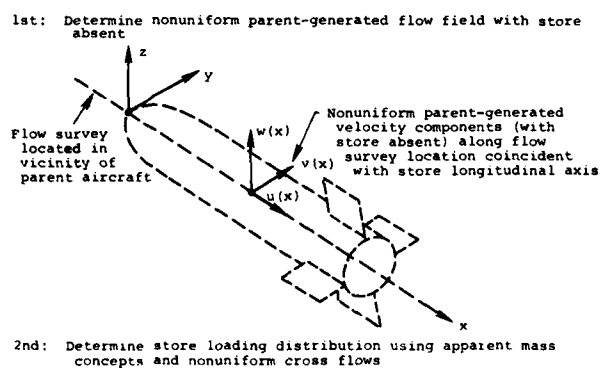


Fig. 7 Illustration of continuous store loading analytic model based on nonuniform crossflow theory⁷

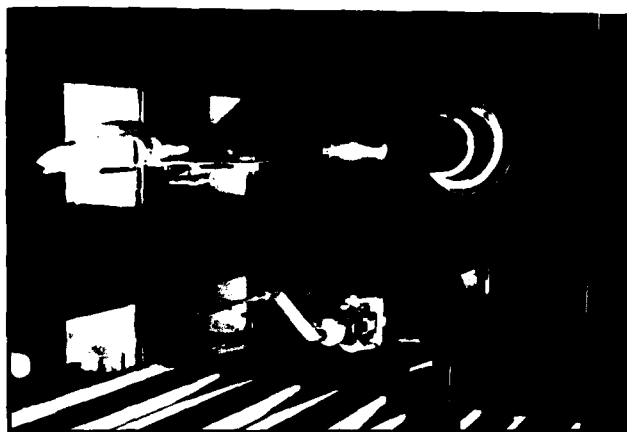


Fig. 8 Typical CTS system: 7x10 ft. transonic wind tunnel facility at DTNSRDC²

$$C_N = \sum_{i=1}^N A_i (\alpha - \alpha_0)$$

$$= A_1 \alpha_1 + A_2 \alpha_2 + \dots + A_N \alpha_N - C_{N_0} \alpha_0$$

$$C_m = \sum_{i=1}^N B_i (\alpha - \alpha_0) + C_{m0}$$

$$= B_1 \alpha_1 + B_2 \alpha_2 + \dots + B_N \alpha_N + C_{m0} - C_{m_0} \alpha_0$$

ELEMENT $i = 1 \quad 2 \quad 3 \quad \dots \quad N$

WHERE

A_i C_N INFLUENCE COEF FOR i TH ELEMENT

α_i LOCAL α AT i TH ELEMENT

B_i C_m INFLUENCE COEF FOR i TH ELEMENT

C_{N_0} ISOLATED STORE NORMAL FORCE SLOPE

C_{m0} ISOLATED STORE C_m ZERO LIFT PITCHING MOMENT

Fig. 9 Basis of Influence Function Method²⁷

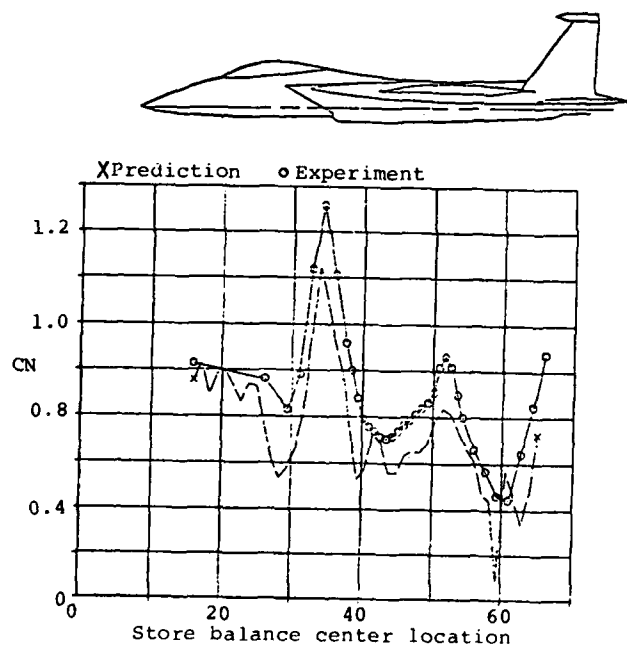


Fig. 10 Comparison of Influence Function Method predictions of C_N for a GBU-15 along a fuselage centerline location under a F-15 at $M_\infty = 0.95$ ²⁹

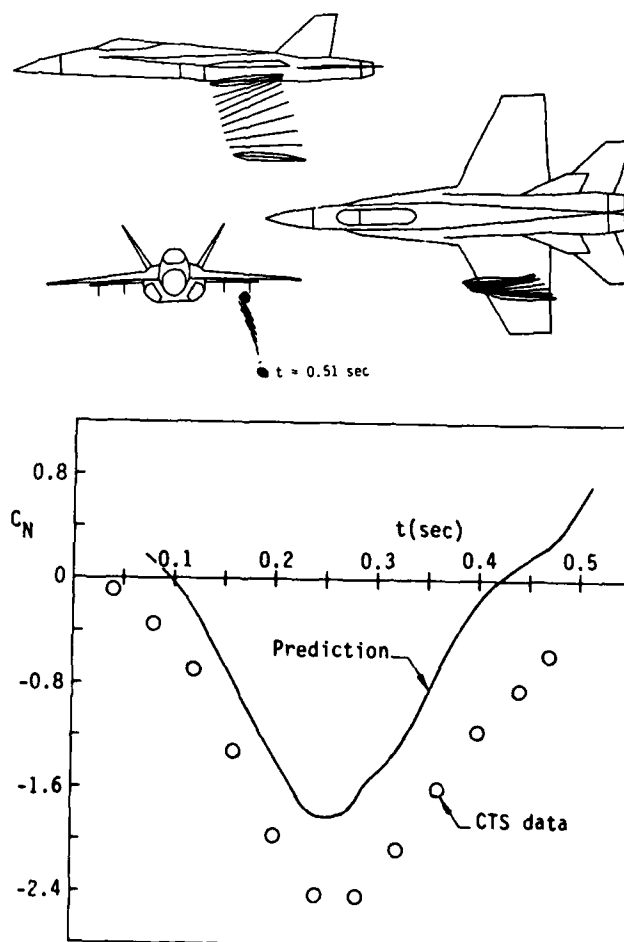


Fig. 11 Comparison of Northrop/NEAR panel method C_N predictions with data for an MK-83 separating from an F-18 at transonic conditions, $M_\infty = 0.95$ ³³

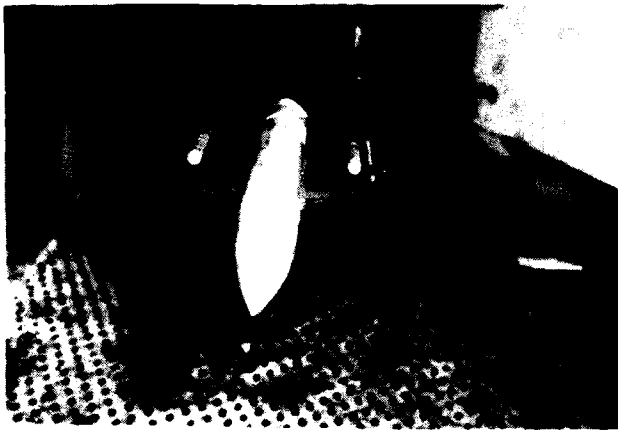


Fig. 12 Simplified F-16 wing-body/pylon/store configuration used in theoretical/experimental store studies³²

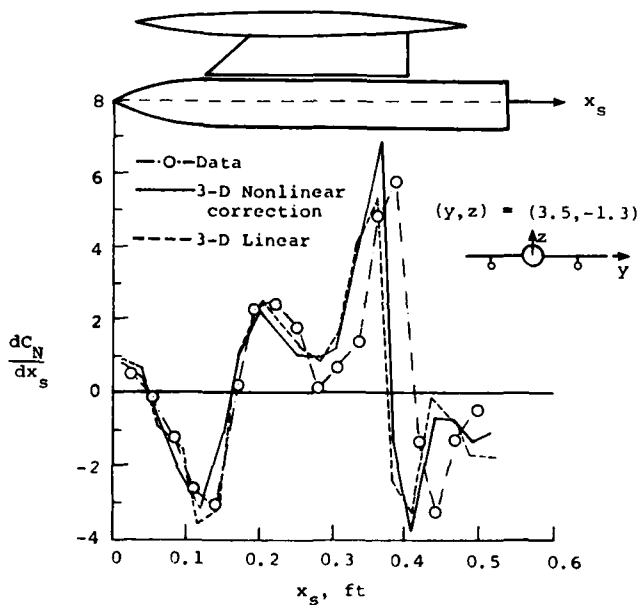


Fig. 14 Comparison of theoretical and experimental store normal loading distribution for a store location directly under wing pylon at $M_\infty = 0.95$ and $\alpha = 5^\circ$ ³²

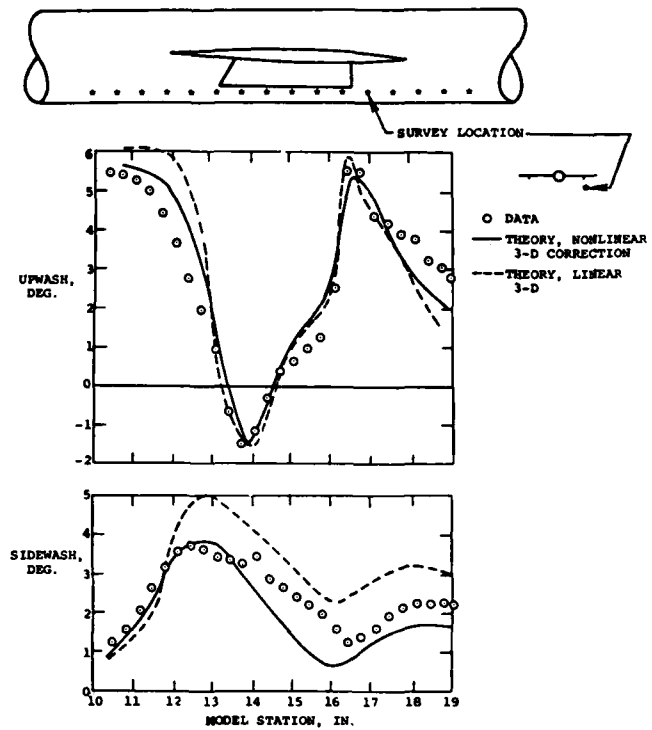


Fig. 13 Comparison of theoretical and experimental results for the local upwash and sidewash angles for the F-16 wing-body/pylon model directly under the wing pylon at $M_\infty = 0.95$ and $\alpha = 5^\circ$ ³²

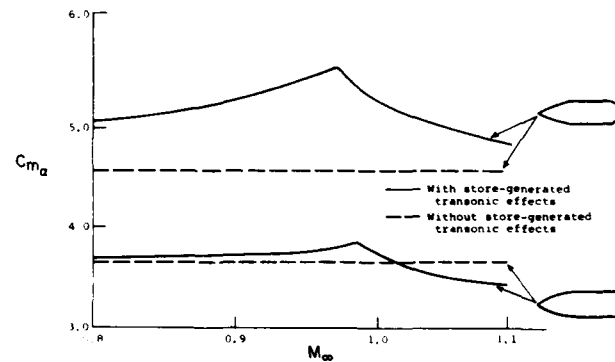


Fig. 15 Comparison of C_{m_α} variation throughout the transonic regime with and without store-generated transonic effects for two different store shapes³²

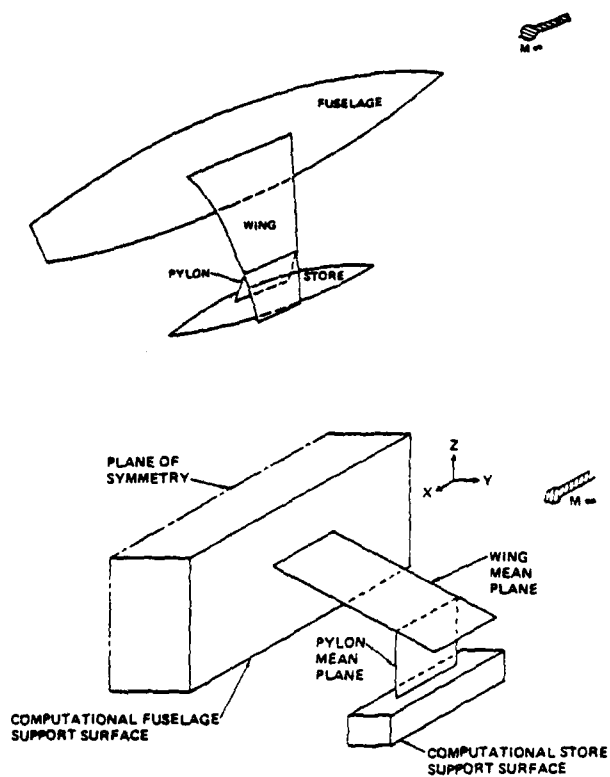


Fig. 16 Illustration of simple wing-fuselage-store configuration and corresponding computational support services for 3-D TSD method³⁷

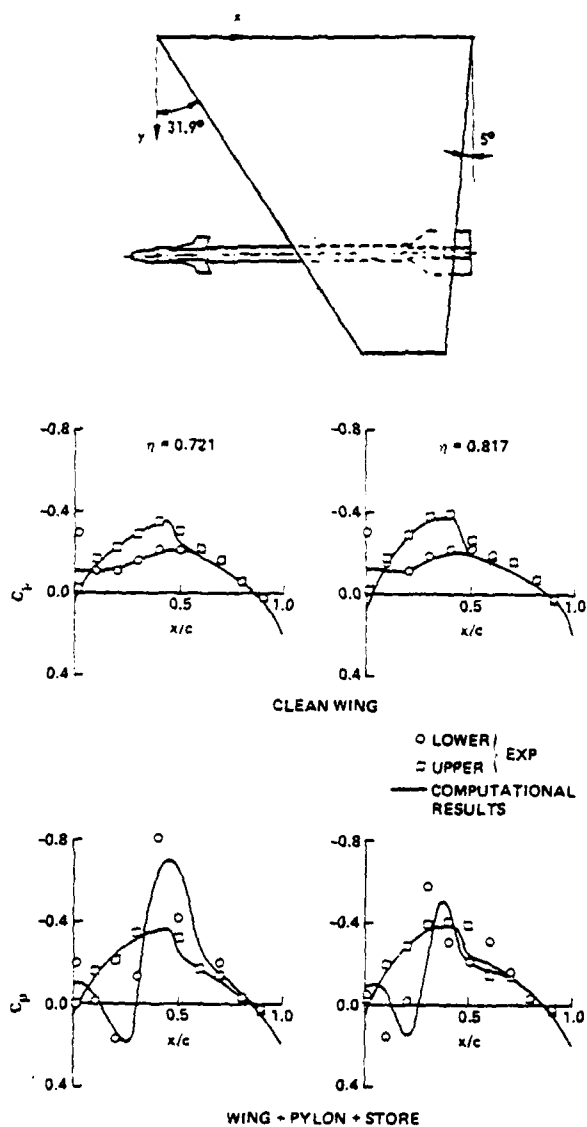


Fig. 17 Comparison of theoretical and experimental wing surface pressures for a modified F-5/pylon/store configuration with and without the store-pylon at $M_\infty = 0.9$, $\alpha = 0.5^\circ$ ³⁷

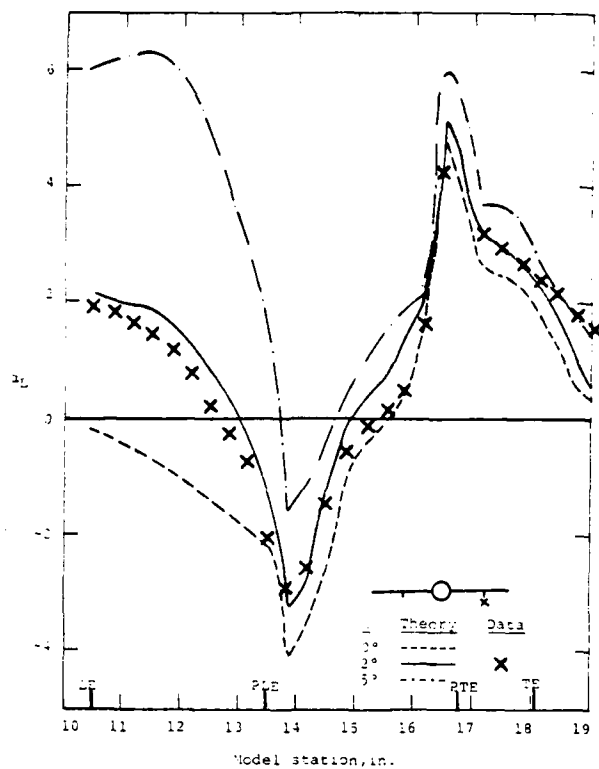


Fig. 18 Comparison of nonlinear approximation method and data for local upwash directly under wing pylon of the simplified F-16 wing-body/pylon configuration at $M_\infty = 0.95$ and $\alpha = 2.32^\circ$

Navier-Stokes Computational Study of the Influence of Shell Geometry on the Magnus Effect at Supersonic Speeds

Walter B. Sturek*
Donald C. Mylin**
Bernard Guidos***
Charles J. Nietubicz****

U.S. Army Ballistic Research Laboratory, ARRADCOM
Aberdeen Proving Ground, Maryland 21005

Abstract

Recent papers have reported the application of the thin-layer Parabolized Navier-Stokes (PNS) computational technique to predict the flow over spinning shell at supersonic speeds. This paper reports the results of a computational study using thin layer Navier-Stokes codes to examine the effects of shell nose tip and afterbody geometry. The geometries considered include sharp, hemisphere cap, and flattened nose configurations and a parametric variation of boattail shape. The results are presented primarily as the aerodynamic coefficient versus Mach number for $1.5 < M < 5$. The Magnus effect is shown to be strongly influenced by nose bluntness as well as the geometry of the shell afterbody.

Nomenclature

a	= speed of sound
CP	= center of pressure for normal force
CPY	= center of pressure for Magnus force
C_m	= pitching moment coefficient
$C_{M_{p\alpha}}$	= $d^2 C_m / [d(\frac{PD}{V}) - d\alpha]$, slope of Magnus moment coefficient evaluated at $PD/V = 0$, $\alpha = 0$
C_n	= Magnus (yawing) moment coefficient
C_N	= normal force coefficient
C_y	= Magnus (side) force
D	= diameter of model
e	= total energy per unit volume of fluid, normalized by $\rho_\infty a_\infty^2$
$\hat{E}, \hat{E}_s, \hat{F}, \hat{G}$	= flux vectors of transformed gasdynamic equation
J	= Jacobian of transformation between physical and computational coordinates
L	= reference length
M	= Mach number
p	= pressure normalized by $\rho_\infty a_\infty^2$
Pr	= Prandtl number, $\mu_\infty c_p / \kappa_\infty$
PD/V	= non-dimensional spin rate about model axis
Re	= Reynolds number, $\rho_\infty U_\infty L / \mu_\infty$
\hat{S}	= viscous flux vector
u, v, w	= Cartesian velocity components along the x, y, z axis, respectively,

normalized by a_∞

U, V, W	= contravariant velocity components
x, y, z	= physical Cartesian coordinate axes
α	= angle of attack
γ	= ratio of specific heats
κ	= coefficient of thermal conductivity, normalized by free-stream value κ_∞
μ	= coefficient of viscosity, normalized by free-stream value μ_∞
ξ, η, ζ	= computational coordinates in the axial, circumferential, and radial directions (Fig. 1)
ρ	= density, normalized by free-stream density ρ_∞

Subscripts

∞	= free-stream conditions
aw	= adiabatic wall
w	= body surface values
x	= based on axial distance from nose

I. Introduction

Recent papers^{1,2,3} have reported the development and application of the thin-layer Parabolized Navier-Stokes computational technique to predict the flow about slender bodies of revolution at supersonic velocities. Reference 3 showed the technique to be a viable computational tool for predicting Magnus effects for a six-caliber slender shell with a one-caliber, 7° boattail as verified by comparison to wind tunnel force measurements. The results of Reference 3 represent the first successful efforts to compute the Magnus effect for boattailed shell using sophisticated numerical computational techniques. In this paper, the ability of the PNS computational technique to predict normal and Magnus forces at angles of attack up to 10-degrees and the effects of nose and afterbody geometry on the aerodynamics of shell are examined. The influence of nose bluntness is determined using a starting solution generated by the unsteady Navier-Stokes (time marching) computational technique and then using the PNS (space marching) code to compute the flow over the remainder of the shell.

*Chief, Aerodynamics Research Branch

**Mathematician

*** Engineer Trainee

****Aerospace Engineer

II. Computational Technique

a. Space Marching Solution

The steady thin-layer Parabolized Navier-Stokes equations can be written for general spatial coordinates ξ, η, ζ as¹

$$\frac{\partial \hat{E}_S}{\partial \xi} + \frac{\partial \hat{F}}{\partial \eta} + \frac{\partial \hat{G}}{\partial \zeta} = \frac{1}{Re} \frac{\partial \hat{S}}{\partial \zeta} \quad (1)$$

where $\xi = \xi(x)$ is the streamwise (marching) coordinate
 $\eta = \eta(x, y, z)$ is the circumferential coordinate
 $\zeta = \zeta(x, y, z)$ is the normal coordinate

The inviscid flux vectors in Eq. (1) are

$$\hat{E}_S = J^{-1} \begin{pmatrix} \rho U \\ \rho U + \xi_x p_S \\ \rho V U \\ \rho W U \\ (e + p_S) U \end{pmatrix}, \quad \hat{F} = J^{-1} \begin{pmatrix} \rho V \\ \rho U V + \eta_x p \\ \rho V V + \eta_y p \\ \rho W V + \eta_z p \\ (e + p) V \end{pmatrix},$$

$$\hat{G} = J^{-1} \begin{pmatrix} \rho W \\ \rho U W + \zeta_x p \\ \rho V W + \zeta_y p \\ \rho W W + \zeta_z p \\ (e + p) W \end{pmatrix}$$

The vector $\hat{q}(\rho, \rho u, \rho v, \rho w, e)$ contains the dependent variables. Variations of body geometry are included in Eq. (1) through the presence of the metric terms η_x, η_y, η_z , etc., which appear in the flux vectors. The thin-layer viscous term, valid for high Reynolds No. flow, is

$$\hat{S} = J^{-1} \left\{ u(\zeta_x^2 + \zeta_y^2 + \zeta_z^2) u_\zeta + (u/3)(\zeta_x u_\zeta + \zeta_y v_\zeta + \zeta_z w_\zeta) \zeta_x \right. \\
+ u(\zeta_x^2 + \zeta_y^2 + \zeta_z^2) v_\zeta + (u/3)(\zeta_x u_\zeta + \zeta_y v_\zeta + \zeta_z w_\zeta) \zeta_y \\
+ u(\zeta_x^2 + \zeta_y^2 + \zeta_z^2) w_\zeta + (u/3)(\zeta_x u_\zeta + \zeta_y v_\zeta + \zeta_z w_\zeta) \zeta_z \\
+ ((\zeta_x^2 + \zeta_y^2 + \zeta_z^2) [(u/2)(u^2 + v^2 + w^2)]_\zeta \\
+ \kappa Pr^{-1} (\gamma - 1)^{-1} (a^2)_\zeta] + (u/3)(\zeta_x u \\
+ \zeta_y v + \zeta_z w)(\zeta_x u_\zeta + \zeta_y v_\zeta + \zeta_z w_\zeta) \}$$

Equation 1 is parabolic-like with respect to ξ and can thus be marched downstream in the ξ direction from an initial data plane (subject to appropriate body and free stream boundary conditions) under those conditions where the local flow is supersonic.

The numerical algorithm used to march Eq. (1) downstream is an approximately-factored, fully implicit, finite-difference scheme. The algorithm is conservative and of second-order accuracy in the marching direction. A two-layer, algebraic eddy viscosity model⁴ is included for the computation of turbulent flows. Details of the Parabolized Navier-Stokes assumption and the derivation of the algorithm are included in Reference 1.

The computations are started from a converged conical solution near the tip of the projectile. The full solution is then obtained by marching over the body in the streamwise (axial) direction. This marching technique is depicted in Figure 1 along with the coordinate system. A logarithmic stretching is used to achieve adequate grid resolution of the turbulent viscous layer. The grid generator employs an adaptive capability which insures that adequate resolution of the viscous layer is maintained over the full length of the model. The streamwise marching stepsize was adjusted to yield 500 to 800 computational steps for the full length of the shell. The computational grid consisted of 36 stations about the circumference of the model ($\Delta\phi = 10^\circ$) and 50 points between the body and the outer boundary.

b. Blunt Nose Solution

The solution for the flow over the blunt nose of the shell has been obtained using the three dimensional thin-layer Navier-Stokes solver recently reported by Chaussee, Kutler and Pulliam⁵. This is a fully implicit computational technique which solves for the entire flow field by converging to a steady flow solution. The outer boundary for this code employs a shock-fitting scheme. Since the solution is obtained for only a small flow field region near the nose, good grid resolution has been achieved. The grid used consisted of 30 points from the body to the outer boundary, 20 points axially along the surface of the shell, and 36 points circumferentially around the shell.

The nose region has initially been modeled as a hemisphere cone. The conical extension is of sufficient length to achieve a well established supersonic conical flow in order to apply the zero gradient outflow boundary condition with confidence. This modeling of the nose region is depicted schematically in Figure 2. The bluntness ratio is defined to be the ratio of the diameter of the cone at the forward tangency point to the maximum diameter of the shell.

In addition to the hemisphere blunt nose, several cases have been run for a flattened nose. The intent is to model as closely as possible the meplate (flat face) configuration of typical Army shell.

The time-dependent thin-layer Navier-Stokes equations can be written in strong conservation-law form as

$$\frac{\partial \hat{q}}{\partial \tau} + \frac{\partial \hat{E}}{\partial \xi} + \frac{\partial \hat{F}}{\partial \eta} + \frac{\partial \hat{G}}{\partial \zeta} = \frac{1}{Re} \frac{\partial \hat{S}}{\partial \zeta} \quad (2)$$

where $\tau = t$ is the time (marching)

$\xi = \xi(t, x, y, z)$ is the longitudinal coordinate

$\eta = \eta(t, x, y, z)$ is the circumferential coordinate

$\zeta = \zeta(t, x, y, z)$ is the near normal coordinate

The inviscid flux vectors are \hat{E} , \hat{F} , \hat{G} and contain terms for the conservation of mass, momentum, and energy in the three coordinate directions. The vector $\hat{q}(\rho, \rho u, \rho v, \rho w, e)$ contains the dependent variables. The \hat{S} matrix contains the viscous terms which are valid for high-Reynolds number flows.

The contravariant velocity components are

$$U = \xi_x u + \xi_y v + \xi_z w$$

$$V = \eta_x u + \eta_y v + \eta_z w$$

$$W = \zeta_x u + \zeta_y v + \zeta_z w$$

Variations of body geometry are included in Equation (2) through the presence of metric terms (ξ_x , η_x , etc.) and the Jacobian J , which appear in the flux vectors and contravariant velocities. A two-layer algebraic eddy viscosity model is used for the turbulent viscous solutions.

III. Results

a. Comparisons to Aerodynamic Force Measurements

In Reference 3 a series of results obtained for $\alpha = 2^\circ$ were compared to experimental measurements (Reference 6) of aerodynamic forces for $2 < M < 4$. The model configuration for this study is shown in Figure 3. The sign convention for the aerodynamic forces is shown in Figure 4. The results in Reference 3 indicated that the thin-layer PNS computational technique achieved excellent agreement in comparison to experimental measurements of aerodynamic forces including the Magnus effect. Comparisons of the PNS computed results to experiment have now been carried out for $\alpha < 10^\circ$. Computed results were obtained for $\alpha = 2^\circ, 4^\circ, 6^\circ$, and 10° .

Comparisons between computation and experiment are shown as a function of angle of attack for normal force for $M = 2$ and $M = 3$ in Figures 5 and 6, respectively. Results for two boattail configurations are shown. The notation SOCBT depicts the 7° , one caliber boattail model in Figure 3. The notation SOC depicts a model with a 0° boattail. Excellent agreement is achieved for $\alpha < 10^\circ$ for magnitude as well as the non-linear behavior of the normal force coefficient.

A similar comparison is shown for Magnus force for $M = 2$ and $M = 3$ in Figures 7 and 8, respectively. These results indicate very good agreement between computation and experiment for

$\alpha < 6^\circ$. However, the computed results for $\alpha = 10^\circ$ are not in close agreement with the trend of the experimental data for $\alpha > 6^\circ$. This is more clearly indicated in Figure 8. This discrepancy is not unexpected since, as shown in Reference 2 where comparisons between computation and experiment for surface pressure were made, good agreement was achieved at $\alpha = 6.3^\circ$ and significantly less satisfactory agreement was obtained at $\alpha = 10.4^\circ$. The discrepancy at $\alpha = 10.4^\circ$ was attributed to the inability of the computational technique to accurately model the significant development of lee-side vortical flow.

The ability of the computational technique to accurately predict Magnus for $\alpha < 6^\circ$ does represent a significant capability. This demonstrates that useful engineering results can be achieved for highly three-dimensional flow fields using a very simple turbulence model.

b. Effect of Boattail Geometry

1. Scope of Computational Effort

A series of computations have been accomplished for a parametric variation of boattail configuration. The geometries are shown in Figure 9 and include boattail lengths of one and two calibers for boattail angles of $0^\circ, 5^\circ, 7-1/2^\circ$, and 10° . This range of boattail length and angle effectively spans the range for practical shell application.

The computations were accomplished for standard atmospheric and wall temperature conditions commonly encountered in projectile firing tests. These conditions are summarized in Table 1.

TABLE 1. Summary of Boundary Conditions for Parametric Computations

MACH No.	α , degrees	PD/V	T_∞ , °K	P_∞ , atm	T_w , °K
2	2	.19	294	1	239,294,325
3	2	.19	294	1	239,294,325
4	2	.19	294	1	239,294,325
MACH No.	FREE STREAM REYNOLDS NO.				
2	$4.53 \times 10^7/m$				
3	$6.80 \times 10^7/m$				
4	$9.06 \times 10^7/m$				

2. Aerodynamic Forces versus Axial Position

The development of the normal force as a function of axial position is shown in Figure 10 for boattail angles of 0° and $7-1/2^\circ$. The normal force increases monotonically for the 0° boattail in contrast to the behavior for the $7-1/2^\circ$ boattails where the normal force reaches a

maximum and then decreases as the boattail length increases.

The development of the Magnus force as a function of axial position is shown in Figures 11 and 12 comparing the effects of boattail length (Figure 11) and boattail angle (Figure 12). Figure 11 shows that the length of the boattail strongly affects the magnitude of the Magnus force. Figure 12 shows that the Magnus force increases monotonically for increasing boattail angle for the cases considered here.

3. Aerodynamic Coefficients versus Mach No.

Parametric comparisons for pitch and yaw plane aerodynamic parameters are shown in Figures 13 and 14. These examples illustrate the ability of the computational technique to develop data which reflect the effects of body configuration and Mach number.

The effect of boattail angle and length for the slope of the pitching moment ($CG = 3.6$ calibers) is shown in Figure 13. These results show that both boattail length and angle have a significant effect on the pitching moment. The trends indicate that C_{M_α} is increased for increasing boattail angle and boattail length. This trend is accentuated for flow velocities near $Mach = 2$.

The slope of the Magnus moment coefficient ($CG = 3.6$ calibers) is shown in Figure 14. The effect of boattail length is seen to strongly affect the Magnus moment coefficient. The trend illustrated is that $C_{M_{p\alpha}}$ is increased as boattail length and angle are increased.

c. Effects of Nose Bluntness

A spark shadowgraph of an artillery shell at a speed of approximately $Mach = 2.25$ taken in the BRL Transonic Range is shown in Figure 15. This shadowgraph shows the detached bow shock that occurs for supersonic flow over artillery shell. Note the presence of a shock at the sharp corner of the flattened nose. This shock is caused by the local flow separation that is induced by the strong expansion at the sharp corner.

A recent wind tunnel test⁷ was performed in which aerodynamic force measurements were made for spinning models with sharp, hemisphere, and flattened nose tips. A Schlieren photograph of the flow over these nose tips at $Mach = 3$ is shown in Figure 16. It is obvious that the bow shock pattern is different for each of these configurations. The inner shock at the nose tip that is very distinct in Figure 15 also occurs at the sharp corner of the flattened nose in Figure 16. This shock is not visible for the hemisphere nose. The shock waves starting about one diameter downstream of the model nose are generated by a boundary layer trip.

In this portion of the study, the significance of the technique for modeling the nose region of spinning shell on the predicted aerodynamic behavior at supersonic velocities is examined. The model geometry used is the ogive-

cylinder-boattail (SOCBT) shape shown in Figure 3. Figure 2 shows the nose tip geometries in detail. Flow field computations have been obtained for wind tunnel test conditions and for free flight atmospheric conditions. The wall temperature boundary condition has been modeled as an adiabatic wall for the wind tunnel tests and as a constant wall temperature equal to the atmospheric temperature for the atmospheric flight conditions.

Examples of u-velocity profiles at the starting plane for sharp and blunt noses are shown in Figure 17. The profile for the blunt nose cases are significantly distorted in the inviscid flow region compared to the sharp nose case which has a comparatively flat profile. An interesting comparison is shown in Figure 18 which illustrates Mach contours for the blunt starting solutions. The more severe flow expansion around the flattened nose compared to the hemisphere nose is clearly illustrated. Figures 19 and 20 show the distribution of surface pressure for windward and leeward rays for the two blunt nose shapes.

Additional examples of u-velocity profiles for the different nose configurations are shown in Figure 21 for a longitudinal station near the start of the boattail. Small but distinct differences are apparent upon comparison of these profiles indicating that the effect of the initial conditions does not wash out rapidly.

The wind tunnel test⁷ conducted recently for the BRL at the Naval Surface Weapons Center, White Oak Laboratory obtained measurements of the aerodynamic forces on the slender shell with sharp, hemisphere, and flattened nose configurations. Force balance measurements were obtained for pitch plane and Magnus forces. Computational results for sharp and hemisphere nose geometries have been obtained for comparison to these data. The computational and experimental results for Magnus force are compared in Figure 22. The experimental data indicate an increasing Magnus force for increasing nose flatness. The agreement between computation and experiment for the sharp and hemisphere nose configurations is quite good. However, there is substantial disagreement between computation and experiment for the flattened nose geometry. The computation for the hemisphere and the flattened nose yielded virtually identical results. This is in sharp contrast to the experimental results which yielded a substantially greater Magnus force for the flat nose case than that for the hemisphere cap. Further computations for which the boundary layer on the nose cap was laminar yielded results that were virtually identical to the results for which the boundary layer on the nose cap was turbulent. A possible cause for the discrepancy is the difference between the flatness of the nose for the computational model and the model used in the wind tunnel test. As shown in Figure 2, the flat part of the nose does not extend to the full diameter of the meplate. Additional computations are planned in which the actual flatness of the fuze configuration will be modeled more closely. It would also be useful to have experimental data for a wider range of free stream Mach number for comparison to the computations.

An example is shown in Figure 23 of the development of the Magnus force as a function of axial position comparing computational results for

sharp, hemisphere, and flattened nose configurations for atmospheric flight conditions. The results indicate a significant increase in the Magnus force for the blunt noses. The trend of increasing Magnus force for increasing nose flatness is observed. Examples of the Magnus force as a function of Mach number for the sharp and hemisphere blunt noses are shown in Figure 24. The blunt case is consistently greater in absolute magnitude than the sharp case.

The slope of the Magnus moment coefficient as a function of Mach number is shown in Figure 25 comparing results for sharp and hemisphere noses. Again, the blunt nose results are consistently greater than those for the sharp nose. The results also predict a greater influence of nose bluntness as the Mach number decreases. The behavior of the Magnus center of pressure is shown in Figure 26. These results indicate that the Magnus center of pressure is: (1) located well downstream of the CG location (3.6 calibers); (2) weakly sensitive to Mach number; and (3) not highly sensitive to the nose bluntness.

The slope of the pitching moment coefficient as a function of Mach number is shown in Figure 27. These results indicate that the pitching moment is not sensitive to small nose bluntness typical of artillery shell

IV. Summary

A computational study has been described in which thin-layer Navier-Stokes computational techniques have been employed to predict the aerodynamics of slender, spinning shell at supersonic velocity.

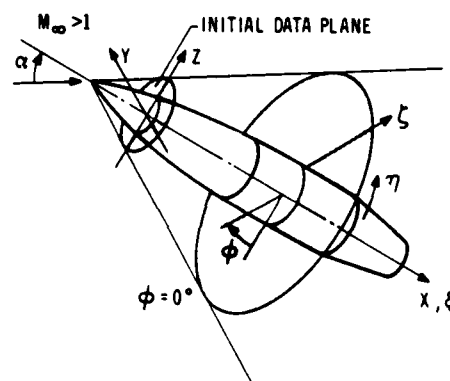
Results have been discussed which illustrate the ability of the computational technique to accurately predict Magnus and normal forces for angles of attack up to six degrees. Parametric results showing the effects of boattail length and boattail angle were discussed for pitching moment and Magnus moment.

Comparisons have been shown between results obtained in which the nose tip of the shell has been modeled as a sharp cone, a hemisphere-cone, and a truncated cone. The results indicate that small nose bluntness, typical of artillery shell, can significantly increase the Magnus moment. The results further indicate that the pitching moment is not strongly affected by the small nose bluntness considered in this study.

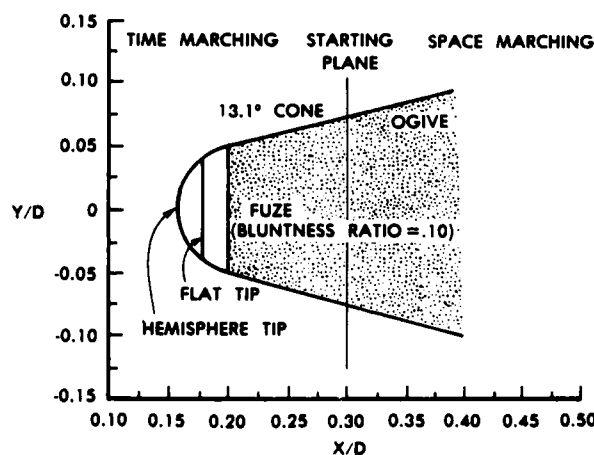
References

1. Schiff, L.B., and Steger, J.L., "Numerical Simulation of Steady Supersonic Viscous Flow", *AIAA Journal*, Vol. 18, No. 12, December 1980, pp. 1421-1430.
2. Schiff, L.B., and Sturek, W.B., "Numerical Simulation of Steady Supersonic Flow Over an Ogive-Cylinder-Boattail Body", AIAA Paper No. 80-0066, AIAA 18th Aerospace Sciences Meeting, January 1980.

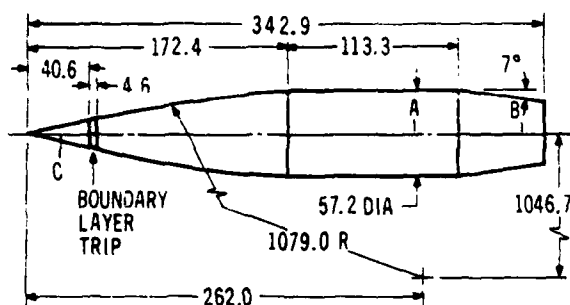
3. Sturek, W.B., and Schiff, L.B., "Computations of the Magnus Effect for Slender Bodies in Supersonic Flow", AIAA Paper No. 80-1586-CP, AIAA Atmospheric Flight Mechanics Conference, August 1980.
4. Baldwin, B.S., and Lomax, H., "Thin Layer Approximation and Algebraic Model for Separated Turbulent Flows", AIAA Paper No. 78-257, 1978.
5. Chaussee, D.S., Kutler, P., and Pulliam, T.H., "Three Dimensional Viscous Flow Field program; Part I: Viscous Blunt Body Program (Interim Report)", AFWL-TM-81-63-FIMG, March 1981.
6. Nietubicz, C.J., and Opalka, K., "Supersonic Wind Tunnel Measurements of Static and Magnus Aerodynamic Coefficients for Projectile Shapes with Tangent and Secant Ogive Noses", ARBRL-MR-02991, U.S. Army Ballistic Research Laboratory/ARRADCOM, Aberdeen Proving Ground, MD 21005, February 1980.
7. Unpublished Wind Tunnel Data. Test performed at the Naval Surface Weapons Center, White Oak Laboratory, Silver Spring, Maryland for the U.S. Army Ballistic Research Laboratory.



1. Coordinates and Notation.

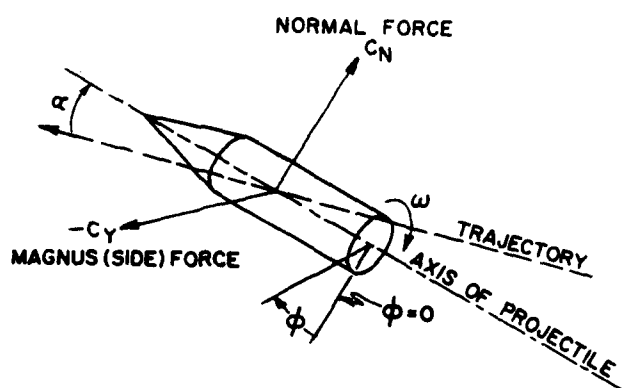


2. Illustration of Blunt Nose Modeling Geometries

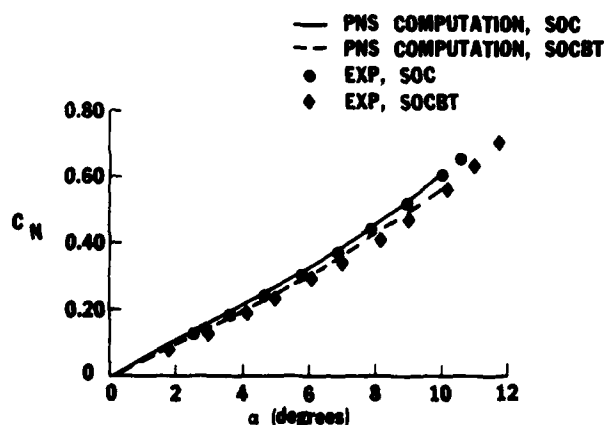


NOTE: DIMENSIONS ARE IN MILLIMETRES
A, B BOUNDARY LAYER SURVEY STATIONS
C CONICAL STARTING SOLUTION STATION

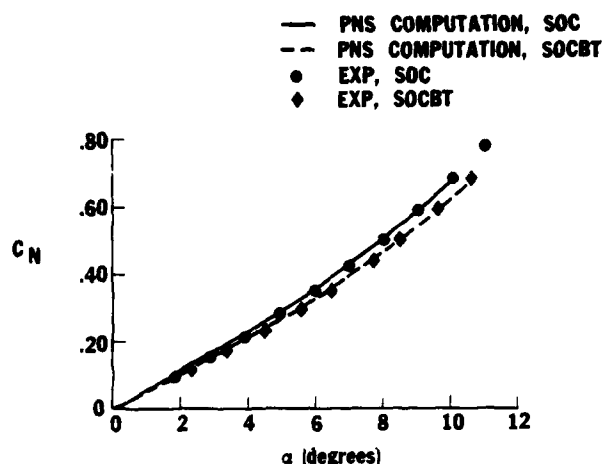
3. Model Configuration for Wind Tunnel Test



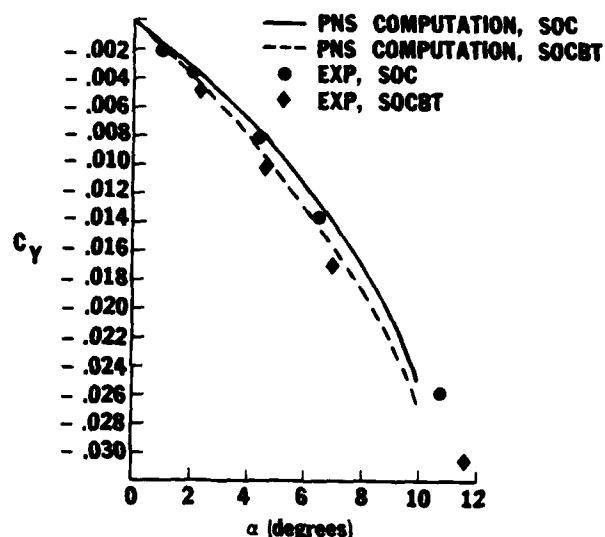
4. Sign Convention for Aerodynamic Forces



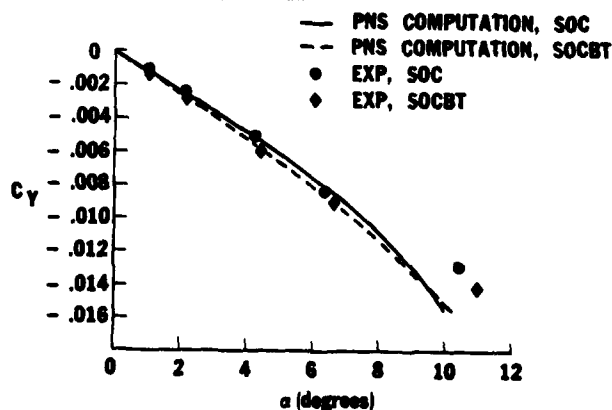
5. Normal Force Coefficient versus Angle of Attack, Computation Compared to Wind Tunnel Force Measurements, $M = 2$, $Re = 2.49 \times 10^7/m$



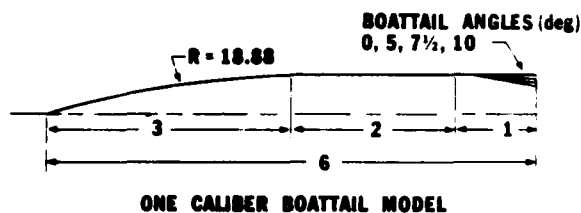
6. Normal Force Coefficient versus Angle of Attack, Computation Compared to Wind Tunnel Force Measurements, $M = 3$, $Re = 2.11 \times 10^7/m$



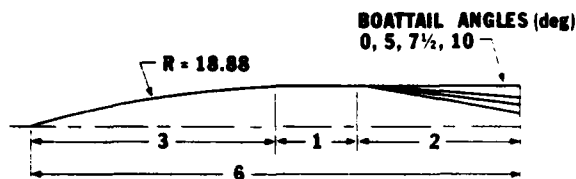
7. Magnus Force Coefficient versus Angle of Attack, Computation Compared to Wind Tunnel Force Measurements, $M = 2$, $Re = 2.49 \times 10^7/m$, $PD/V = .23$, $T_w = T_{aw}$



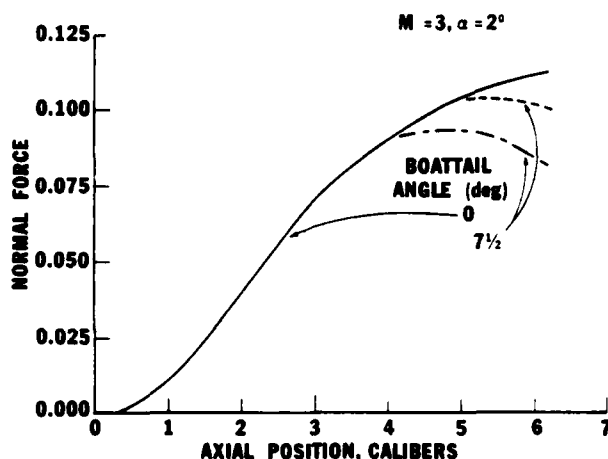
8. Magnus Force Coefficient versus Angle of Attack, Computation Compared to Wind Tunnel Force Measurements, $M = 3$, $Re = 2.11 \times 10^7/m$, $PD/V = .19$, $T_w = T_{aw}$



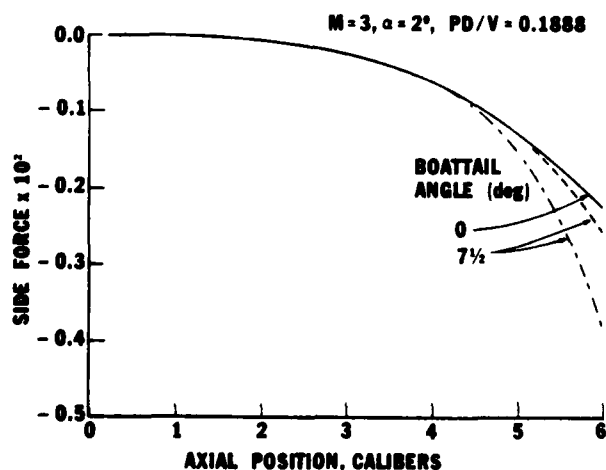
NOTE: All dimensions in calibers



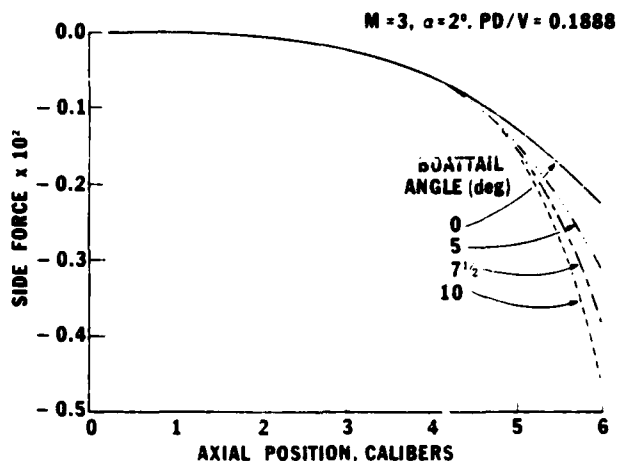
9. Model Configurations for Parametric Study



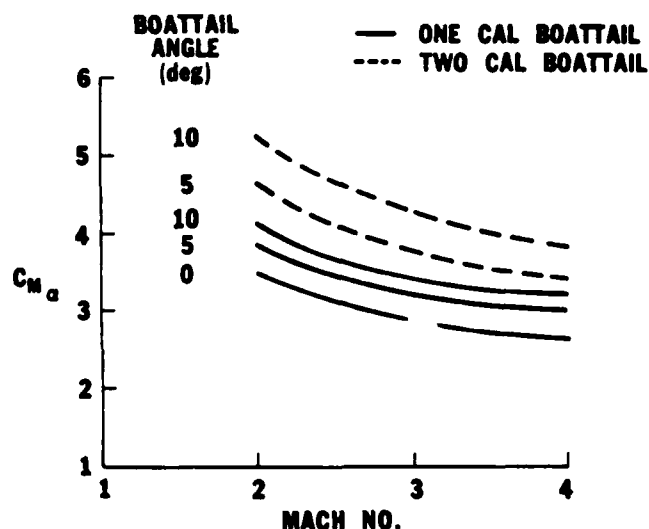
10. Normal Force Coefficient versus Axial Position, Parametric Comparison, $M = 3$, $\alpha = 2^\circ$, $T_w = T_{aw}$



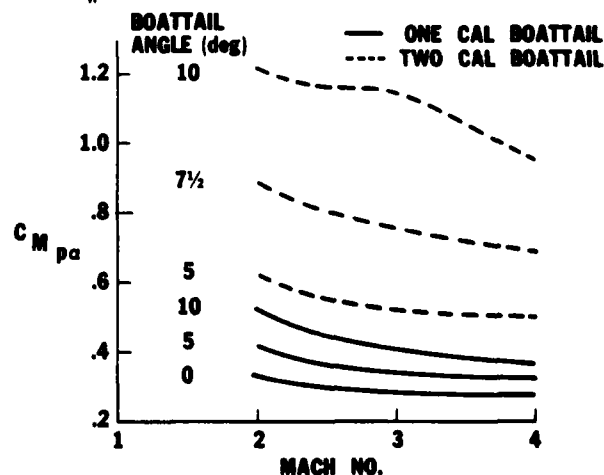
11. Magnus Force Coefficient versus Axial Position, Parametric Comparison, $M = 3$, $\alpha = 2^\circ$, $PD/V = .19$, $T_w = T_{aw}$, $Re = 6.80 \times 10^7/m$



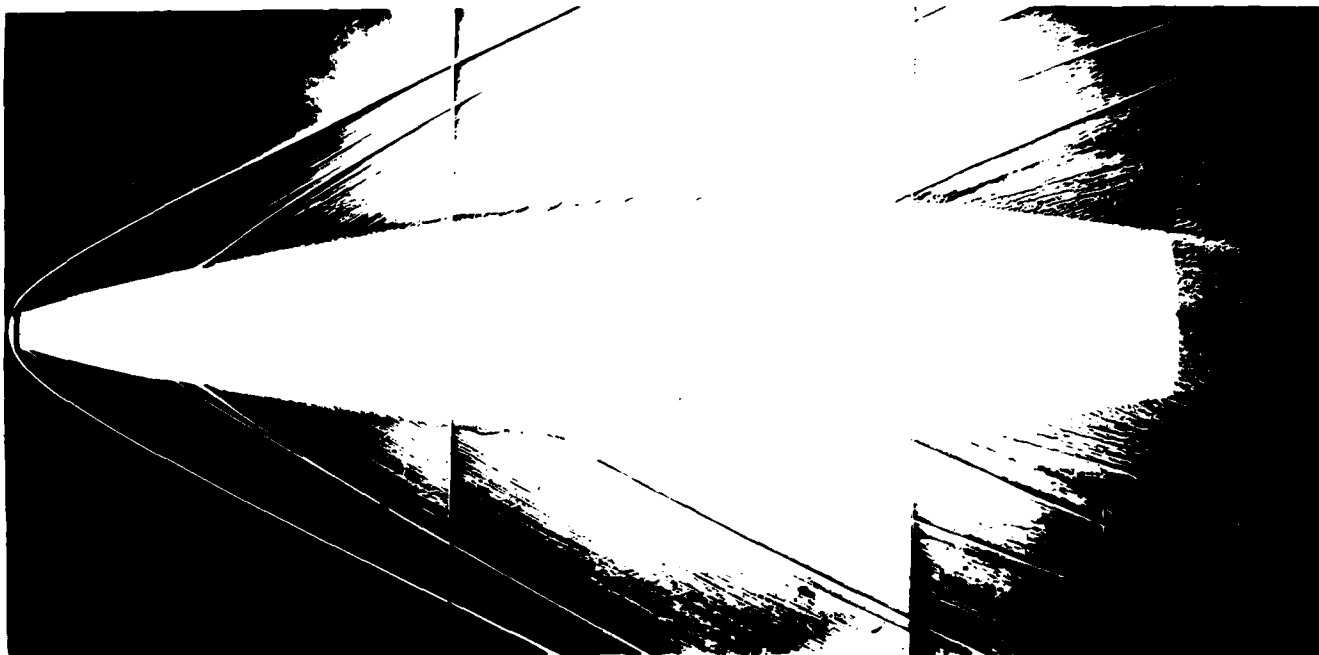
12. Magnus Force Coefficient versus Axial Position, Parametric Comparison, $M = 3$, $\alpha = 2^\circ$, $PD/V = .19$, $T_w = T_{aw}$, $Re = 6.80 \times 10^7/m$



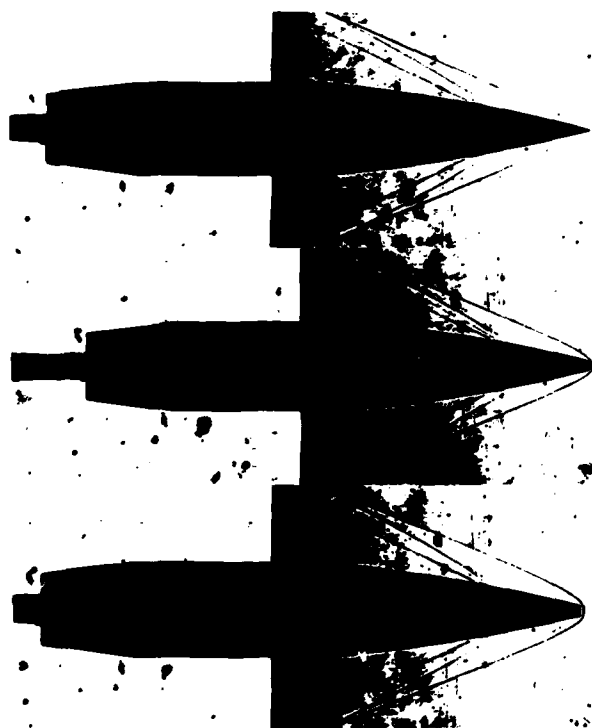
13. Slope of Pitching Moment Coefficient versus Mach No., Parametric Comparison, $T_w = 294K$, $CG = 3.6$ calibers



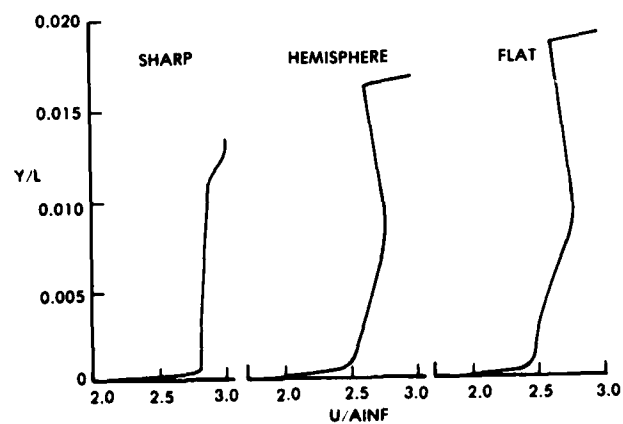
14. Slope of Magnus Moment Coefficient versus Mach No., Parametric Comparison, $T_w = 294K$, $CG = 3.6$ calibers



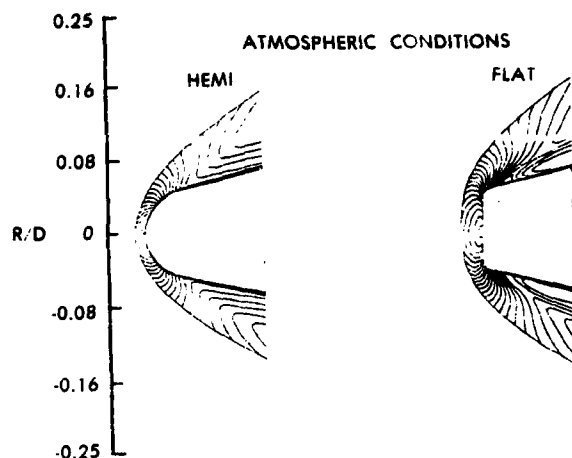
15. Aerodynamics Range Spark Shadowgraph of Artillery Shell at Supersonic Velocity, $M = 2.3$



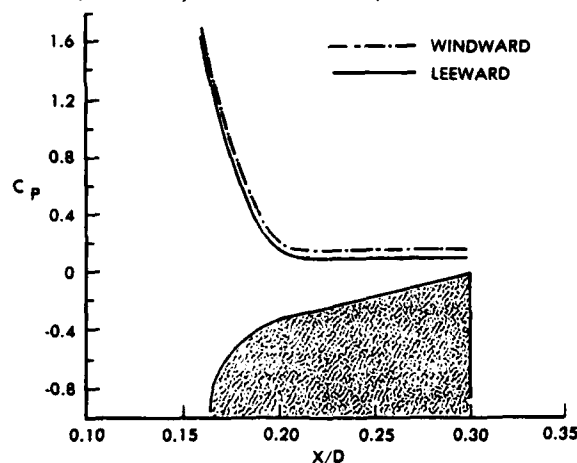
16. Schlieren Photographs of Wind Tunnel Flow over SOCBT Shell with Sharp, Hemisphere, and Flattened Nose Geometries, $M = 3$, $Re = 9.19 \times 10^6/m$



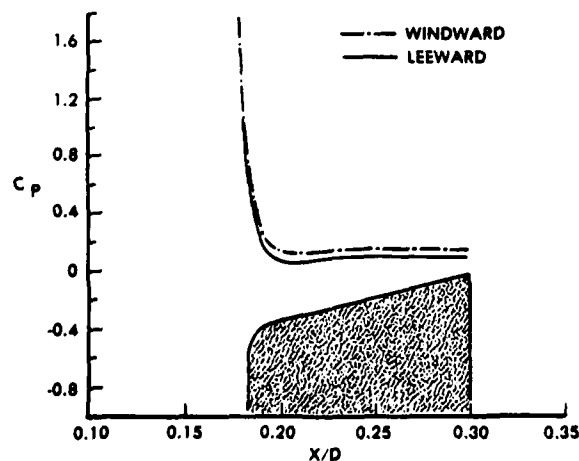
17. Lee Side U-Velocity Profiles at Starting Plane, $M = 3$, $\alpha = 2^\circ$, $PD/V = 0.19$, Atmospheric Flight Conditions, $Re = 6.80 \times 10^7/m$



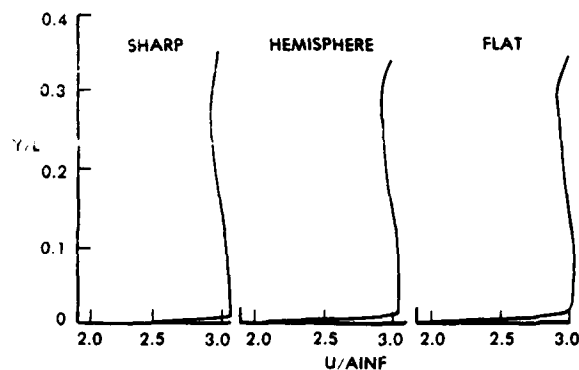
18. Mach Contours of Nose Region Flow for Hemisphere and Flattened Nose Geometries, $M = 3$, $\alpha = 2^\circ$, $PD/V = 0.19$, Atmospheric Flight Conditions, $Re = 6.80 \times 10^7/m$



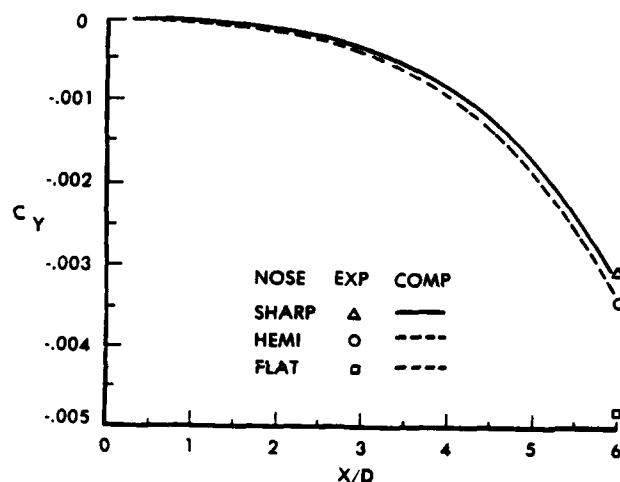
19. Surface Pressure on Hemisphere Nose, $M = 3$, $\alpha = 2^\circ$, $PD/V = 0.19$, Atmospheric Flight Conditions, $Re = 6.80 \times 10^7/m$



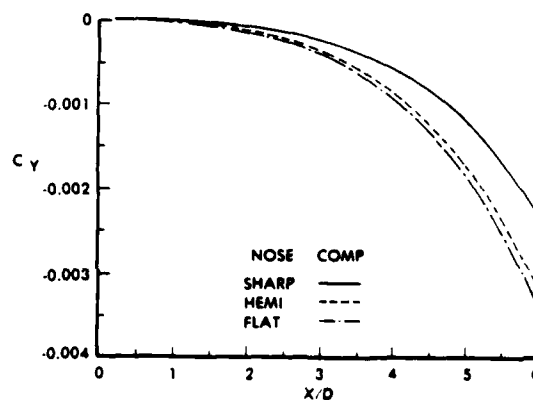
20. Surface Pressure on Flat Nose, $M = 3$, $\alpha = 2^\circ$, $PD/V = 0.19$, Atmospheric Flight Conditions, $Re = 6.80 \times 10^7/m$



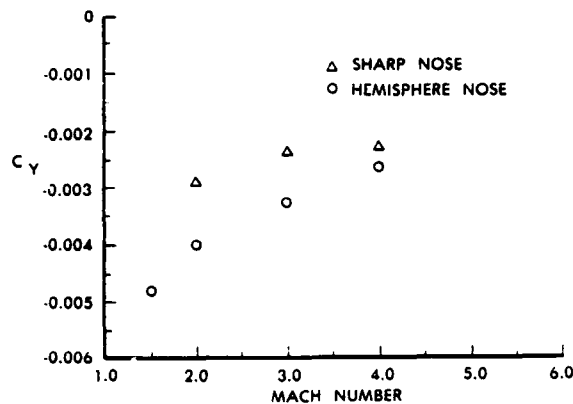
21. Lee Side U-Velocity Profiles at $X/D = 4.88$, SOCBT Model, $M = 3$, $\alpha = 2^\circ$, $PD/V = 0.19$, Atmospheric Flight Conditions, $Re = 6.80 \times 10^7/m$



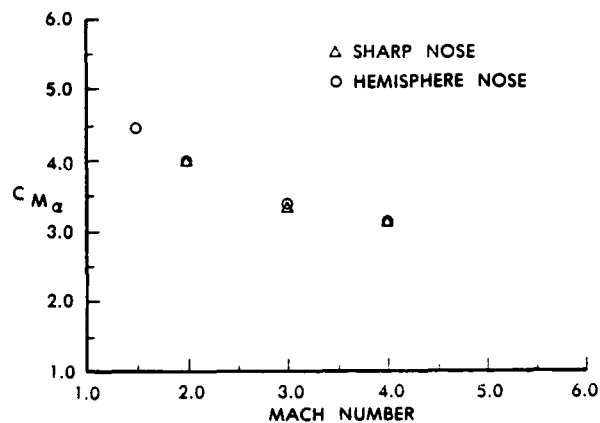
22. Magnus Force versus Axial Position, SOCBT Model, Computation Compared to Experimental Force Measurements, $M = 3$, $\alpha = 2^\circ$, $PD/V = 0.19$, Wind Tunnel Test Conditions, $Re = 9.19 \times 10^6/m$



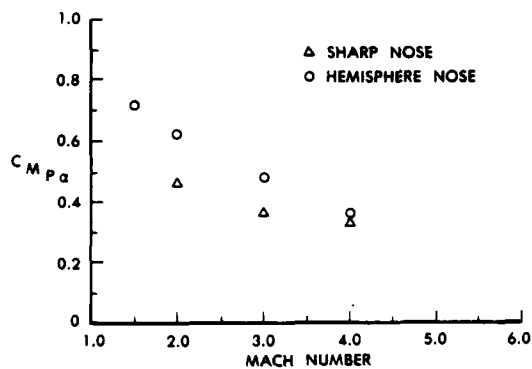
23. Magnus Force versus Axial Position, SOCBT Model, $M = 3$, $\alpha = 2^\circ$, $PD/V = 0.19$, Atmospheric Flight Conditions, $Re = 6.80 \times 10^7/m$



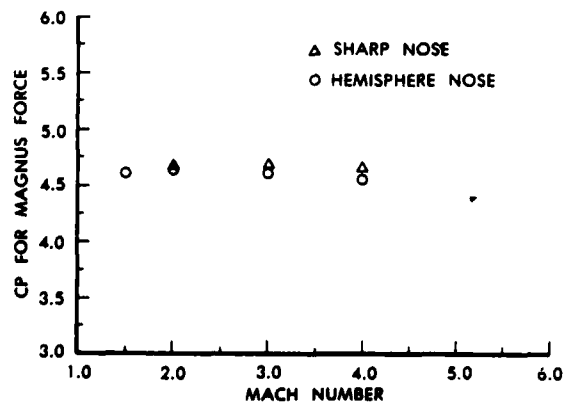
24. Magnus Force versus Mach Number, SOCBT Model, Comparison between Sharp and Hemisphere Noses, $\alpha = 2^\circ$, $PD/V = 0.19$, Atmospheric Flight Conditions



27. Slope of Pitching Moment Coefficient versus Mach Number, SOCBT Model, Comparison between Sharp and Hemisphere Noses, Atmospheric Flight Conditions



25. Slope of Magnus Moment Coefficient versus Mach Number, SOCBT Model, Comparison between Sharp and Hemisphere Noses, Atmospheric Flight Conditions



26. Magnus Force Center of Pressure versus Mach Number, SOCBT Model, Comparison between Sharp and Hemisphere Noses, Atmospheric Flight Conditions

DEVELOPMENT OF BOUNDARY LAYERS AND SEPARATION PATTERNS ON A BODY OF REVOLUTION AT INCIDENCE

Meier, H.U.*; Kreplin, H.-P.*; Vollmers, H.**

DEUTSCHE FORSCHUNGS- UND VERSUCHSANSTALT
FÜR LUFT- UND RAUMFAHRT E.V.
AERODYNAMISCHE VERSUCHSANSTALT GÖTTINGEN

*) Institut für Experimentelle Strömungs-
mechanik

**) Institut für Theoretische Strömungs-
mechanik

Abstract:

Detailed measurements in three-dimensional boundary layers and separated flow fields, developing on a prolate spheroid, are presented. The discussion is concentrated on the possible topological structure of separation patterns resulting from laminar or turbulent boundary layer flows. A hypothesis about the transition from an unsteady two-dimensional axisymmetric flow separation into a steady three-dimensional vortex flow is established.

I. Introduction

The calculation of the viscous subsonic flow around bodies of revolution at incidence has attracted much interest during the past. Most of the research activities have been concentrated on the calculation of three-dimensional laminar and turbulent boundary layers up to a region where the boundary layer concept is no longer valid. In this region e.g. the static pressure variation normal to the surface implies that such a shear layer cannot be described by parabolic equations. Therefore the determination of the "separation line" is not unequivocal because it may not be related to real physics. However, for low angles of incidence ($\alpha < 10^\circ$) the agreement between "separation lines" determined from calculations and experiments agree quite well. A detailed description of the state of the art as far as three-dimensional boundary layer calculations are concerned is given by T. Cebeci et al. in Ref. [1].

Methods which approximate the Navier Stokes equations encounter similar problems as long as the equations are parabolized. To date solutions of the full Navier Stokes equations require computer time and storage which are not acceptable. In addition to the problems discussed, the modelling of the turbulence in three-dimensional shear layers has not been investigated sufficiently - neither by experiment nor theory - in order to develop generally applicable calculation procedures.

The objectives concerning activities of the DFVLR, Institute for Experimental Fluid Mechanics, Göttingen, in this field of research are:

- to determine the laminar to turbulent boundary layer transition on bodies of revolution at incidence, which cannot be calculated at the present time,
- to provide experimental data for the examination of calculation procedures and physical models,
- to investigate by means of mean velocity distributions in three-dimensional boundary layers, separated flow fields, and flow visualizations the separation patterns on bodies of revolution at various angles of incidence and Reynolds numbers.

In this contribution we shall concentrate on physical aspects of the development of three-dimensional boundary layers, and the corresponding separation pattern if these laminar, transitional or turbulent boundary layers leave the surface and create vortex flows. It will be investigated whether the laminar or turbulent boundary layer separation on an axisymmetric body of revolution at zero incidence can lead to a meaningful interpretation of the separation pattern observed in the three-dimensional case.

II. Description of the Experiments

The model investigated in the 3m x 3m Low Speed Wind Tunnel of the DFVLR Göttingen is a sting-mounted prolate spheroid 1 : 6 (Fig. 1). The wind tunnel model was

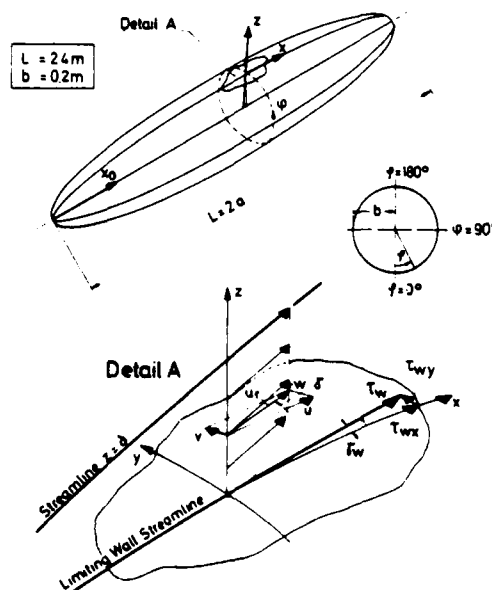


Fig. 1
Model and boundary layer co-ordinate system.

especially designed for the investigation of three-dimensional boundary layers and separated flow fields. The measuring techniques used, which are described in detail in Refs. [2, 3, 4], enable us to measure the following quantities at the surface

- pressure,
- shear stress (magnitude, direction and fluctuations),

and in the boundary layer or separated flow field

- components of the local velocity vectors.

The measurements of the velocity distribution in the inviscid flow field were carried out by the HNW*, cf. Ref. [5]. For flow field measurements the 3m x 3m Low Speed Wind Tunnel is equipped with a ten-hole-pressure probe mounted on a traversing mechanism, which is placed well outside of the open wind tunnel test section. The probe allows measurement of

Total pressure (1 hole)

Static pressure (4 holes)

Two directions of the flow (4 holes)

Reverse flow (1 hole).

Two of the four pressure tappings for the detection of the flow direction were connected to an electronic circuit. This arrangement allowed an automatic alignment of the probe in the (x,z)-plane of the wind tunnel Cartesian co-ordinate system (x = free stream flow direction). For each test run the position of the probe, the velocity of the probe displacement, and the integration time of the measurement were computer controlled and programmed in advance. The probe, together with the traversing mechanism, enabled us to determine 3 velocity components in an arbitrary flow field at defined positions. Despite the finite size ($d = 6$ mm) and the automatic alignment of the probe in one plane, errors due to strong velocity gradients in the neighbourhood of vortex cores or probe displacement effects cannot be avoided or corrected, because comparative measurements using non-intrusive methods were not available. The boundary layer measurements were carried out applying a three-hole-direction probe, which allows the determination of the magnitude and the direction of the local velocity in the (x,z)-plane. The calibration and data reduction procedure is described in detail in Ref. [6].

These quantitative measurements were supplemented by different flow visualization techniques like oil flow patterns, Laser

*) HNW = DFVLR Hauptabteilung Niedergeschwindigkeitswindkanäle (Department for Low Speed Wind Tunnels)

light sheets and the hydrogen bubble method in a water towing tank.

III. Results

The purpose of the qualitative flow investigations was to achieve a better insight into the development of three-dimensional boundary layers and the topology of the flow separation on such a body of revolution and to enable us to interpret the quantitative measurements. As an example the following test result is presented:

As found from surface hot film measurements, Ref. [4], the boundary layer flow over the prolate spheroid is completely laminar at an angle of incidence $\alpha = 10^\circ$ and a free stream velocity of $U_\infty = 10$ m/s. As demonstrated in [4] one can calculate wall streamlines from measured wall shear stress vectors. In Fig. 2 the derived wall streamlines and a typical example of wall

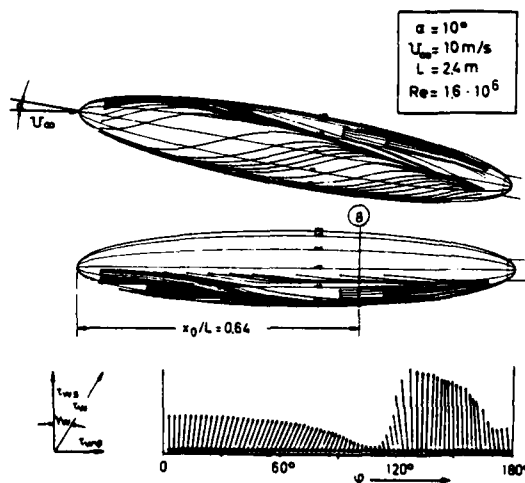


Fig. 2
Wall streamlines calculated from measured wall shear stress values in 12 cross sections. The wall shear stress vectors for laminar boundary layer flow in the cross section $x_0/L \approx 0.64$ are shown as an example.

shear stress vectors measured in the cross section $x_0/2a \approx 0.64$ for this flow case are shown.

This result clearly indicates two facts:

- 1) One obtains converging streamlines which merge to an envelope.
- 2) In the regime of the enveloping streamline the wall shear stress reaches a minimum and its circumferential component vanishes, if the co-ordinate system of Fig. 1 is applied.

AD-A134 151

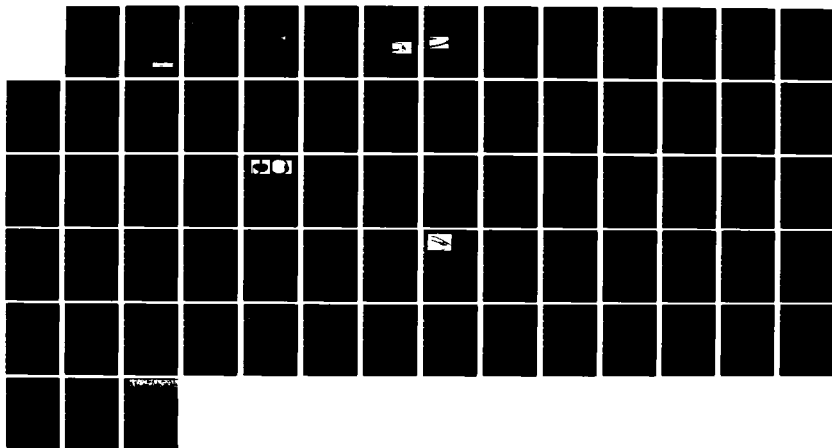
SYMPOSIUM ON NUMERICAL AND PHYSICAL ASPECTS OF
AERODYNAMIC FLOWS (2ND) 17-20 JANUARY 1983(U)
CALIFORNIA STATE UNIV LONG BEACH T CEBCI 1983

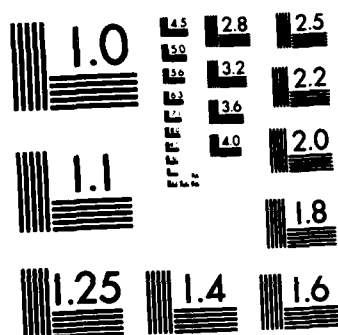
5/5

UNCLASSIFIED

F/G 20/4

NL





MICROCOPY RESOLUTION TEST CHART
NATIONAL BUREAU OF STANDARDS-1963-A

This wall streamline pattern is difficult to understand if the corresponding wall pressure distribution (Fig. 3) is considered. At a first glance the differences

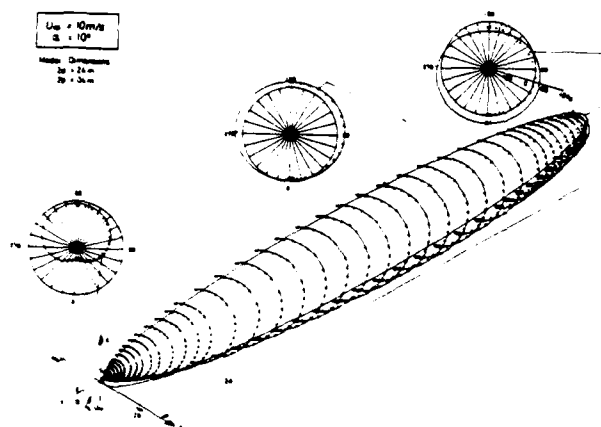


Fig. 3 Measured surface pressure distributions in comparison with calculated values based on potential flow theory (laminar boundary layer flow).

between the measured and the potential flow pressure distributions do not lead to the supposition that a vortex flow is created. The wall pressure measurements were carried out by means of pressure transducers (SETRA D239 SS) with a sufficiently high resolution at a range of $\pm 70 \text{ N/m}^2$. On the other hand, for a three-dimensional laminar boundary layer, all viscous effects are directly coupled with the difference between the actual and potential pressure field. In order to obtain more detailed information about the measured viscous wall pressure distribution, the first derivatives of the surface pressure with respect to the circumferential angle ϕ and the direction x_0 were calculated. In Figs. 4 a,b pressure gradients $\partial c_p / \partial \phi$ and $\partial c_p / \partial x_0$ derived from measurements are plotted for different cross-sections ($x_0 = \text{const.}$). They show small but systematic differences compared to those calculated from the potential flow. It is clearly indicated that in the regime where negative deviations between the derivatives $(\partial c_p / \partial \phi)_{\text{exp.}}$ and $(\partial c_p / \partial \phi)_{\text{pot.}}$ occur, an enveloped limiting streamline was found. That means, two different measurements - pressure and wall shear stress - lead to similar results. It can be concluded that at least a weak viscous-inviscid interaction exists. This implies that the cross flows induced from the vortex flow are still small compared to the longitudinal velocity component at this angle of incidence and Reynolds number. To check this result an oil flow pattern was performed at $\alpha = 10^\circ$. Because a laminar boundary layer flow on the 2.4 m long model could only be established at very low free stream velocities ($U_\infty \approx 10 \text{ m/s}$), a smaller model (scale 1 : 5) was built in order to allow flow visualizations by means of oil flow

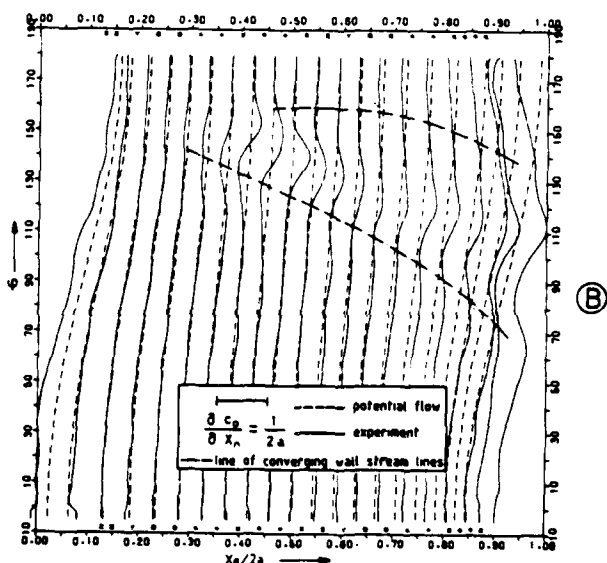
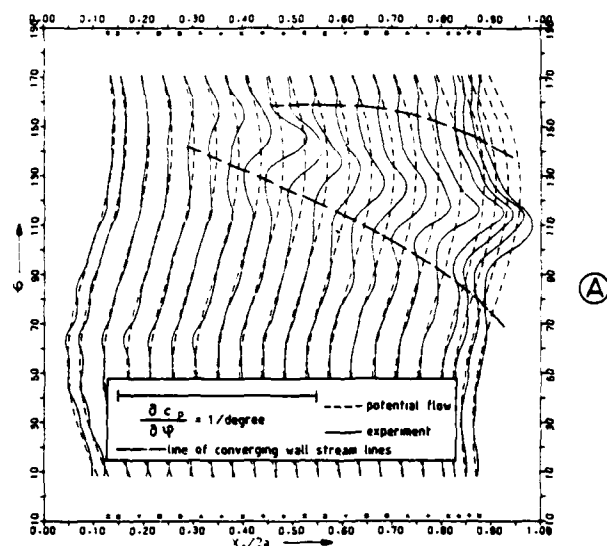


Fig. 4a,b Derivatives $\partial c_p / \partial \phi$ and $\partial c_p / \partial x_0$ for cross-section $x_0/L = \text{const.}$ ($\alpha = 10^\circ$, $U_\infty = 10 \text{ m/s.}$)

patterns at 50 m/s in the 1m Low Speed Wind Tunnel of the DFVLR Göttingen. The oil flow pattern obtained is in excellent agreement with the wall streamlines derived from measured wall shear stress values (Fig. 5). For comparison, the calculated

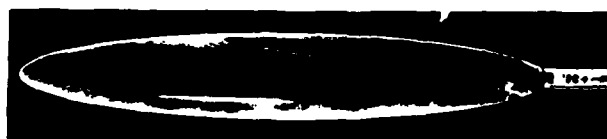


Fig. 5 Oil flow pattern for laminar boundary layer flow ($\alpha = 10^\circ$, $U_\infty = 50 \text{ m/s}$, model length $L = 50 \text{ cm} \rightarrow \text{Re} = 1.6 \times 10^6$).

line of boundary layer "separation"*) is shown in Fig. 6. This result published

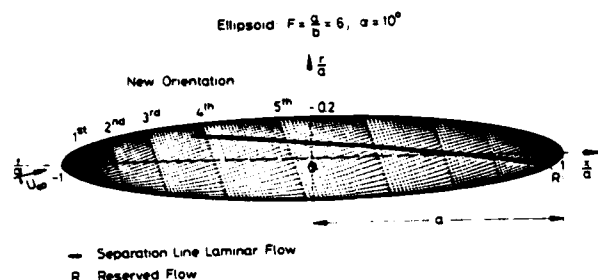


Fig. 6
Calculated "Separation Line" for laminar boundary layer flow at $\alpha = 10^\circ$ (Ref. 7).

in Ref. [7] would differ only slightly if other calculation methods (Refs. [1] and [8] to [10]) were applied. Differences in the calculated separation lines would mainly be caused by different numerical methods which result in different break downs of the calculations. The reason for the good agreement between the laminar boundary layer calculations - all based on the potential pressure distributions - with the experiment is simply due to the small differences in the potential and measured pressure distributions.

In order to obtain some more detailed information about the topology of the separated flow field the Laser light sheet technique in the 1m Wind Tunnel and the hydrogen bubble method in the DFVLR Water Towing Tank [11] were applied. Both flow visualization techniques lead to a flow pattern on the leeward side of the prolate spheroid which is shown in a systematical sketch in Fig. 7. In an attempt to describe

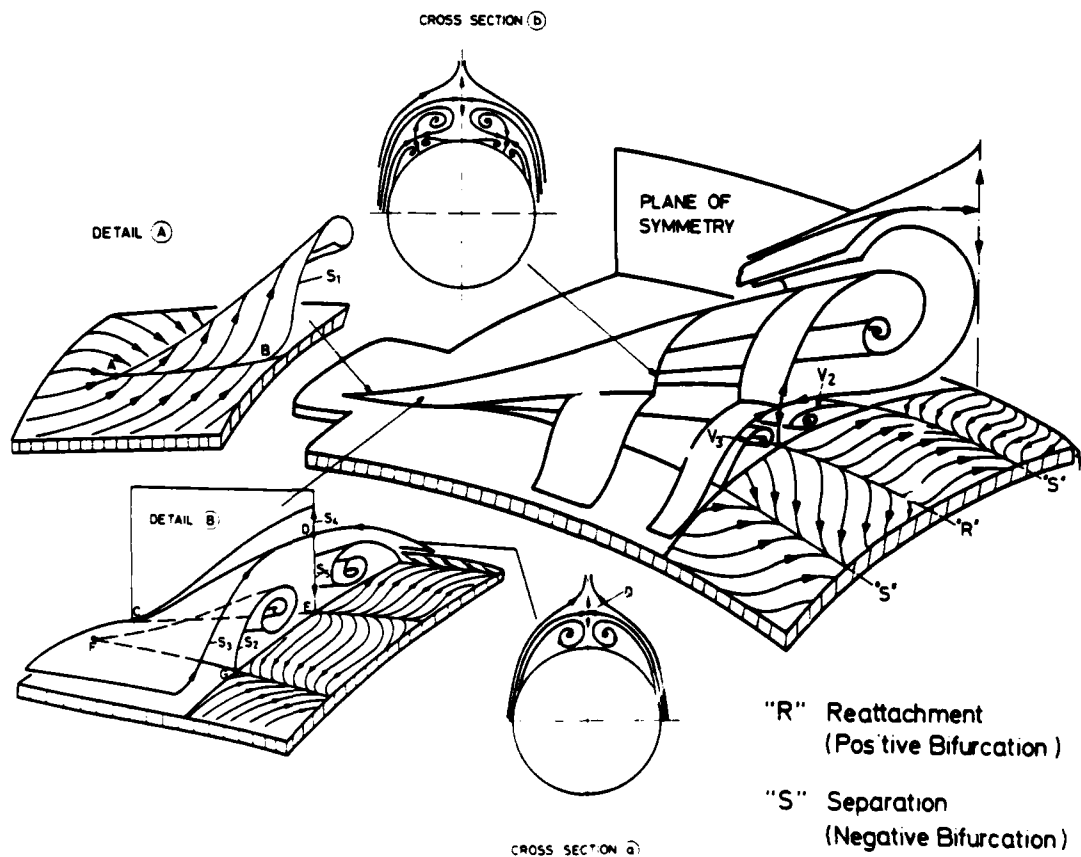


Fig. 7
Topological considerations of the separation pattern on an inclined prolate spheroid.

*) We put this word in quotation marks, because a proper definition of three-dimensional boundary layer separation is not yet offered here.

three-dimensional separated flows unambiguously, Hornung and Perry [12] introduce the concepts of streamsurface and streamsurface bifurcation. In this manner they avoid using the terminology of two-dimensional separation for three-dimensional flow, in which streamsurfaces (rather than streamlines) constitute the boundaries between distinct regions of space. As indicated in Fig. 7, Detail (A), two wall sheets result in one free sheet at a negative streamsurface bifurcation. The bifurcation line AB terminates at A, and does not form a closed curve. This pattern is defined in Ref. [12] as an open negative streamsurface bifurcation which is referred to as a separation line in the literature. The streamsurface S_1 rolls up into a vortex which induces a velocity field near the surface whose cross-flow component is opposite to that on the other side of the bifurcation line. A consequence of this is that a second streamsurface bifurcates positively at the wall and creates a surface streamline pattern which is known as a reattachment line. The corresponding possible crossflow pattern is shown in the schematic sketch of "Cross Section (a)" in Fig. 7 which describes a symmetric pair of open negative bifurcations in this plane. In Detail (B) it was tried to show the bifurcation of surface sheets in a perspective view, which can be interpreted in the following manner: The free vortex sheet S_1 shown in Detail (A) - issuing from the negative bifurcation line AB - and a similar symmetric one on the other side of the axisymmetric body roll up into two vortices S_2^* . These vortices induce a velocity field in the region of the plane of symmetry which results in two special streamsurfaces S_3 which bifurcate along the open free double bifurcation line CD (D corresponds to the saddle point shown in the "Cross Section (a)"). CD is a double bifurcation line because sheets S_4 and S_5 have to issue from the same line. Due to symmetry conditions the sheet S_4 has to be perpendicular to the sheet S_3 and consequently does not roll up. We will give some experimental evidence for that later. S_5 is the free sheet of a subsequent open positive bifurcation along the line CE. Considering bifurcation lines on the surface, the free vortex sheet S_2 issues from the negative bifurcation line FG. The virtual origins of the lines CD, CE, and FG are drawn as the points C, F, although they are, in general, regions of finite extent.

Due to the induced velocity field on the leeward surface a secondary boundary layer separation occurs. An oil flow pattern would indicate for such a flow case a reattachment line in the leeward line of symmetry and a separation line resulting from the positive and negative streamsurface bifurcations. In order to avoid a free shear layer in the flow field it is

*) Due to the symmetry conditions the streamsurfaces are only named on one side.

necessary to introduce a third vortex V_3 . The corresponding system of streamsurface bifurcations shown in Fig. 7 is similar to that described in Detail (B). As indicated in the "Cross Section (b)" we have in addition to the saddle point in the plane of symmetry one saddle point on each side due to the vortices V_2 and V_3 .

The schematic flow pattern of "Cross Section (b)" is confirmed by experiments shown in Figs. 8a and 8b, where measured

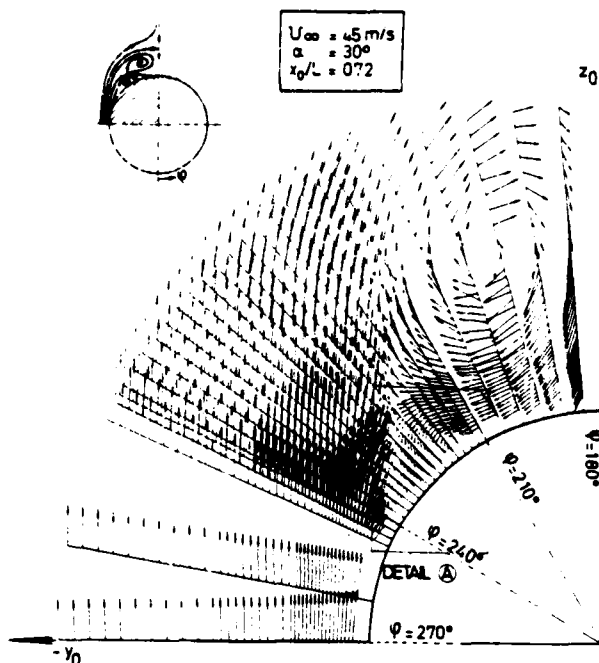


Fig. 8

a) Cross flow velocity components in the y_0 - z_0 -plane of the leeside flow field on an inclined prolate spheroid. (Turbulent boundary layer separation in the cross section $x_0/L = 0.72$ at $\alpha = 30^\circ$, $U_\infty = 45$ m/s.)

velocity vectors in the (y_0-z_0) -plane at $x_0/L = 0.72$ are shown. The measurements were carried out on the prolate spheroid at a free stream velocity of $U_\infty = 45$ m/s for an angle of incidence $\alpha = 30^\circ$ with the ten-hole-probe. As demonstrated in Ref. [3] the three-dimensional boundary layer is fully turbulent for the given flow conditions before separation. The measured velocity field (Fig. 8a) clearly indicates a strong vortex with a core at about $\varphi \approx 200^\circ$. An enlargement of the details between $\varphi = 210^\circ$ and $\varphi = 240^\circ$ (Fig. 8b) elucidates the existence of two additional vortices. The directions of rotation are identical with those shown in Fig. 7. Even a free saddle point is indicated, so that the supposed topology of the separation is clearly supported by experimental evidence. Unfortunately, we could not determine the velocity field

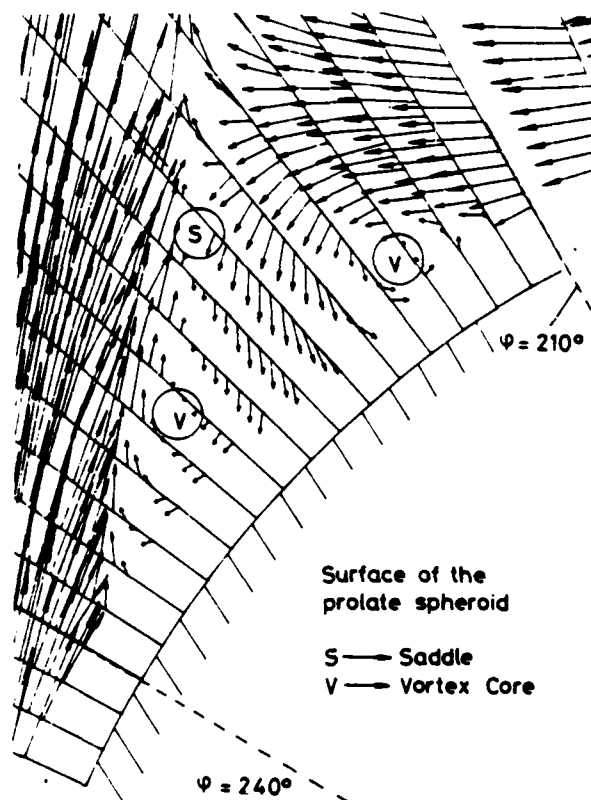


Fig. 8

b) Detail (A) of Fig. 8a) indicating two vortices and a saddle point, a topological structure as described in Fig. 7.

for the laminar case ($\alpha = 10^\circ$, $U_\infty \approx 10$ m/s, Figs. 3-6) by means of the ten-hole-probe. However, the expected result should have led to a similar topological structure, as we concluded from the limiting wall streamline pattern obtained by flow visualizations and wall shear stress measurements (Fig. 5 and 2). These wall streamline patterns are in fact very similar for the laminar and turbulent boundary layer flow (cf. Ref. [4]), even if the pressure distribution in the turbulent case differs considerably from corresponding values calculated by potential theory (Fig. 9). This implies that we have, in contrast to the laminar flow separation, a strong inviscid-viscous interaction on the leeward side flow field but a comparable topology of the separated flow field.

If we increase the free stream velocity U_∞ to 45 m/s, at an angle of incidence $\alpha = 10^\circ$ we can expect to have a separation of a three-dimensional turbulent boundary layer in the cross section $x_0/2a = 0.64$ (compare Ref. [4]). The surface pressure distribution for this flow condition is very similar to that shown in Fig. 3. However, the topological structure of the flow separation seems to differ considerably from that we found for the laminar case.

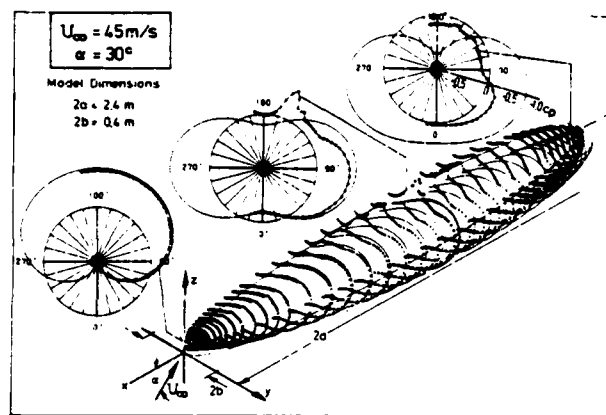


Fig. 9

Measured surface pressure distributions in comparison with calculated values based on potential flow theory (laminar, transitional and turbulent boundary layer flow).

In Fig. 10 the development of the limiting wall streamlines indicates a convergence only at the rear part. Following again the

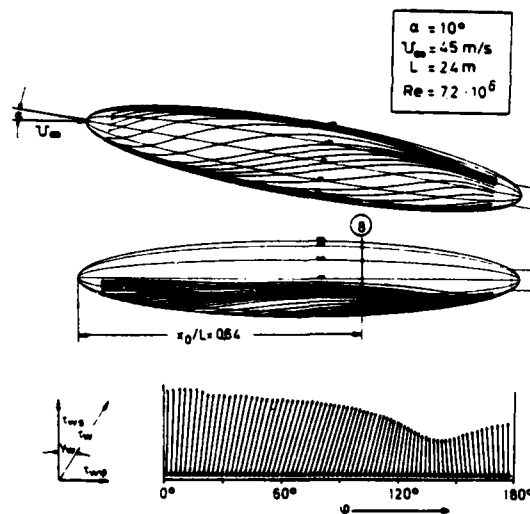


Fig. 10

Wall streamlines calculated from measured wall shear stress values in 12 cross sections. The wall shear stress vectors for laminar, transitional and turbulent boundary layer flow in the cross section $x_0/L = 0.64$ are shown as an example.

interpretation of the streamsurface bifurcation, Ref. [12], the surface flow pattern leads to a negative streamsurface bifurcation of the form shown in Fig. 7, Detail (B). That means we have only one pair of vortices at the rear part of the prolate

spheroid. These vortices do not cause a secondary boundary layer separation as it was determined in the laminar case (Fig. 2). In the body-orientated co-ordinate system (Fig. 1) the limiting streamlines which are nothing else but skin friction lines indicate in the cross section $x_0/L = 0.64$ a change of sign for the circumferential shear stress component at $\varphi \approx 140^\circ$.

Measured boundary layer profiles of the velocity components u, v at the angles $\varphi = 120^\circ, 140^\circ$ and 160° indicate the change of sign of the crossflows close to the surface (Fig. 11). As far as the boundary layer separation is concerned

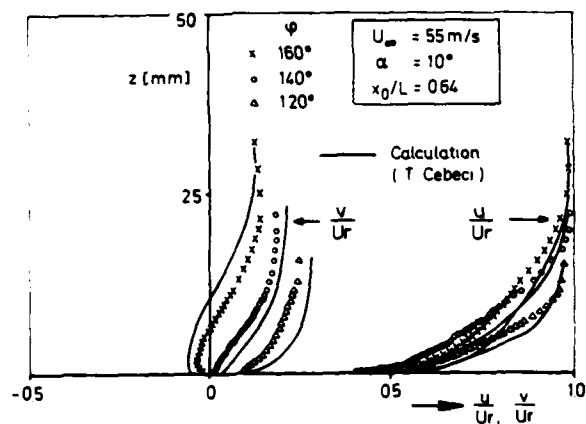


Fig. 11

Profiles of the velocity components u, v in three-dimensional turbulent boundary layers ($\alpha = 10^\circ, U_\infty = 55 \text{ m/s}$). Comparison of measurements with calculations by T. Cebeci [Ref. 13].

these boundary layer measurements do not lead to an answer as to where a negative streamsurface bifurcation occurs. The negative crossflow is certainly not an unequivocal identification of a flow separation, because its location depends only on the co-ordinate system chosen for the data reduction procedure. Consequently for the identification of separation other criteria should be applied which have to be independent of co-ordinate systems. These may be obtained by calculating the divergence of the wall shear stress and/or determining the eigen-values of the Jacobian matrix of the velocity field. The measured boundary layer data are compared with calculated results obtained by T. Cebeci [13]. The calculations, based on the potential pressure distribution, agree quite well with the measured results.

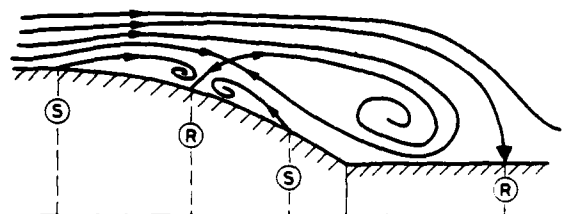
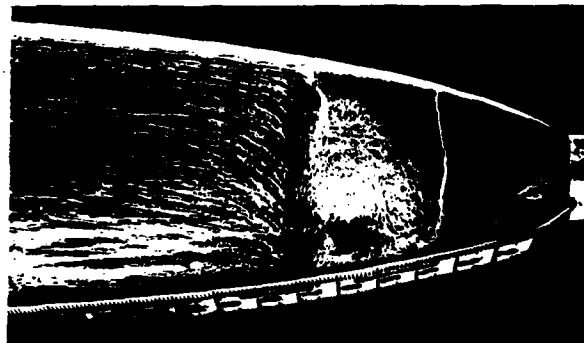
IV. A possible interpretation of the flow separation at small angles of incidence

So far we have considered the three flow cases summarized in

Case No.	$\alpha [^\circ]$	$U_\infty [\text{m/s}]$	Boundary Layer Separation
①	10	10	laminar
②	30	45	turbulent
③	10	45	turbulent

One fundamental result obtained was the similar topological structure of the separation patterns in cases No. ① and ②, which differ clearly from case No. ③. To study the Reynolds number effect at small angles of incidence we investigated the axisymmetric flow case by means of oil flow patterns. For this purpose a smaller model with $a = 240 \text{ mm}$ was investigated in the 1m Low Speed Wind Tunnel. At a free stream velocity of 50 m/s ($Re = 1.6 \times 10^6$) and axisymmetric flow conditions the boundary layer is fully laminar up to separation. This is confirmed by surface hot film measurements on the 2.4 m long prolate spheroid, [3], as well as by calculations applying J.C. Rotta's boundary layer programme [14].

The corresponding oil flow pattern obtained at $\alpha = 0^\circ$, (Fig. 12a) indicates



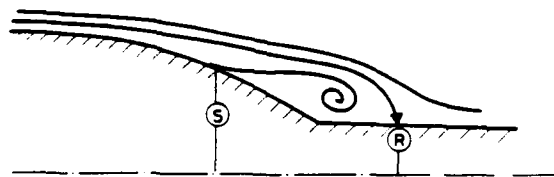
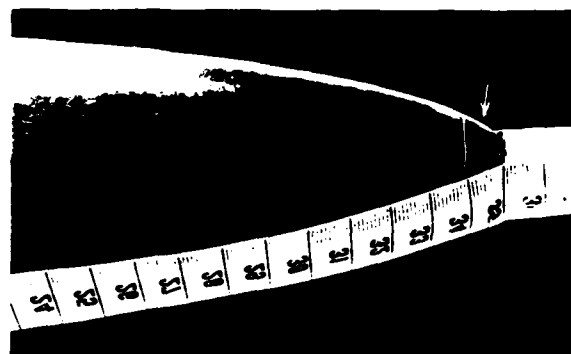
- Ⓢ Separation
- Ⓡ Reattachment

Fig. 12

- a) Oil flow pattern at $\alpha = 0^\circ$ for a laminar boundary layer separation.
- b) Possible topological structure for an unsteady laminar two-dimensional boundary layer separation.

a separation line at $x_0/2a = 0.86$. (The streamline deflection in this region is simply due to the extremely low wall shear compared to the gravity forces). A second separation line can be seen at $x_0/2a = 0.93$. Behind that line we observed reverse flow. In this region the colour dried out much faster compared to the region between the first and second separation line. The latter fact indicates that the flow is laminar in the first separated flow region and turbulent after the second separation line. Such flow conditions at the surface possibly can result from a separation pattern as described in Fig. 12b. This flow has to be unsteady because fluid is entrained in the vortices so that they grow and are transported downstream. This is not necessarily a periodic process because the exchange of the flow can be turbulent, too.

If we force the boundary layer flow to become turbulent by introducing an artificial disturbance at $x_0/L = 0.3$ the boundary layer separates at the very rear part of the prolate spheroid ($x_0/L = 0.98$) (Fig. 13a). This leads to simple separation patterns as it is described in Fig. 13b.



- (S) Separation
- (R) Reattachment

Fig. 13

- a) Oil flow pattern at $\alpha = 0^\circ$ for turbulent boundary layer separation.
- b) Possible topological structure for an unsteady turbulent two-dimensional boundary layer separation.

At high Reynolds number it appears to be true that separation is either unsteady or three-dimensional. On the other hand, a three-dimensional separated flow can be steady, because the entrained fluid is transported downstream by longitudinal vortices. If this consideration is accepted we can establish a hypothesis about the transition of an unsteady two-dimensional boundary layer flow separation into a steady three-dimensional one as the angle of incidence is increased from zero. The possible topological descriptions of the boundary layer separation in Figs. 12b and 13b are similar to those shown as crossflow patterns in Fig. 7 (Cross Sections (a) and (b)). Therefore it seems to be possible that the first axisymmetric separation line (Fig. 12b) changes into a negative three-dimensional streamsurface bifurcation line if the body of revolution is inclined to a small angle of incidence. In a series of oil flow patterns obtained on the small model we found a systematical change of the location of the negative bifurcation line (Fig. 14), if we increase the angle of

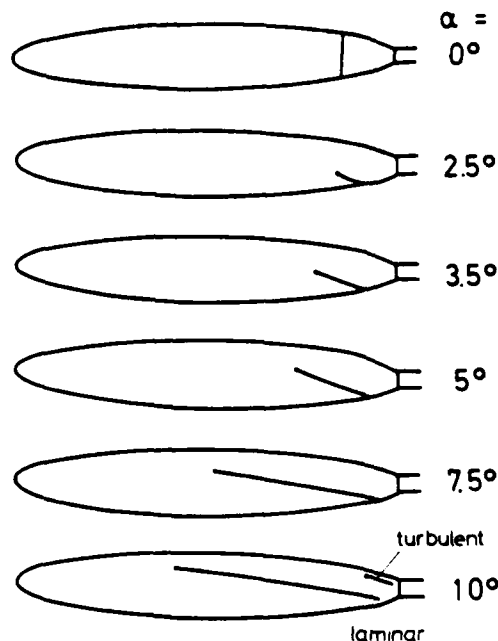


Fig. 14

Negative bifurcation lines derived from oil flow patterns of laminar boundary layers.

incidence up to $\alpha = 10^\circ$. At small angles of incidence ($\alpha < 10^\circ$) we found similar surface streamline patterns as we had found at $\alpha = 10^\circ$ (Figs. 2 and 5) but the spatial resolution was too poor to identify bifurcation lines. All these observations lead to the supposition that the unsteady two-dimensional boundary layer separation is preserved in its fundamental topological structure if the prolate spheroid is inclined. The main change in the separation pattern is the transition of an unsteady two-dimensional separation to a steady three-dimensional

vortex flow pattern. This consideration is underlined if we consider the turbulent separation at $\alpha = 0^\circ$ and 10° (Figs. 10 and 13). The unsteady two-dimensional turbulent boundary layer separation changes only at the very rear part of the model into a negative streamsurface bifurcation which forms one vortex on each side.

V. Summary

The investigations lead to the following results and conclusions:

- The topological structure of the separation patterns on the prolate spheroid indicates considerable differences at an angle of incidence $\alpha = 10^\circ$ between laminar and turbulent three-dimensional boundary layer flow.
- The viscous-inviscid interaction at $\alpha = 10^\circ$ is weak, thus only small cross flows compared to the longitudinal velocity components occur. For this reason differences between the measured and the calculated potential flow surface pressure c_p , which would indicate a flow separation, are not recognizable. The corresponding derivatives $\partial c_p / \partial \varphi$ and $\partial c_p / \partial x_0$ lead to systematical deviations in a region where flow visualizations and wall shear stress measurements indicate negative streamsurface bifurcations.
- The topological structure of the separation pattern at an angle of incidence $\alpha = 10^\circ$ for laminar boundary layer flow is similar to that observed at $\alpha = 30^\circ$ where a turbulent boundary layer separation occurs. This separation pattern is discussed in detail and compared with experimental results.
- Based on some experimental evidence it is shown how the transition from an unsteady two-dimensional axisymmetric flow separation to a steady three-dimensional vortex flow could be explained.

VI. References

- [1] Cebeci, T.; Khattab, A.K.; Stewartson, K.: Three-dimensional Laminar Boundary Layers and the OK of Accessibility. J. Fluid Mech. 107, pp. 57-87, 1981.
- [2] Kreplin, H.-P.; Meier, H.U., Maier, A.: Wind Tunnel Model and Measuring Techniques for the Investigation of Three-dimensional Turbulent Boundary Layers. Proc. AIAA 10th Aerodynamic Testing Conf., San Diego, Calif Paper 78-781, 1978.
- [3] Meier, H.U.; Kreplin, H.-P.: Experimental Investigation of the Boundary Layer Transition and Separation on a Body of Revolution. Z. Flugwiss. Weltraumforschung 4 Heft 2, pp. 65-71, 1980.
- [4] Kreplin, H.-P.; Vollmers, H.; Meier, H.U.: Measurements of the Wall Shear Stress on an Inclined Prolate Spheroid. Presented at the 5th US-FRG DEA Meeting, Annapolis, Maryland, 16-18 April 1980, AFFDL-TR-80-3088, pp. 315-332, 1980, Z. Flugwiss. Weltraumforschung 6, Heft 4, pp. 248-252, 1982.
- [5] Meier, H.U.; Kreplin, H.-P.; Vollmers, H.: Velocity Distributions in 3-D Boundary Layers and Vortex Flows Developing on an Inclined Prolate Spheroid. Presented at the 6th US-FRG DEA Meeting DFVLR-Göttingen, W.-Germany, 28-30 April 1981. DFVLR-AVA-Report IB 222 81 CP 1, 1981.
- [6] Meier, H.U.; Kreplin, H.-P.: Experimental Study of Boundary Layer Velocity Profiles on a Prolate Spheroid at Low Incidence. Presented at the 5th US-FRG DEA Meeting, Annapolis, Maryland, 16-18 April 1980, AFFDL-TR-80-3088, pp. 169-189, 1980.
- [7] Schneider, G.: Calculation of Three-dimensional Boundary Layers on Bodies of Revolution at Incidence. Presented at the 5th US-FRG DEA Meeting, Annapolis, Maryland, 16-18 April 1980, AFFDL-TR-80-3088, pp. 287-314, 1980.
- [8] Geißler, W.: Calculation of Threedimensional Laminar Boundary Layer Around Bodies of Revolution at Incidence and With Separation. AGARD CP 168, 1975.
- [9] Wang, K.C.: Boundary Layer Over a Blunt Body at Low Incidence With Circumferential Reversed Flow. J. Fluid Mech. 72, 49-65, 1975.
- [10] Patel, V.C.; Baek, J.H.: Calculation of Three-dimensional Boundary Layers on Bodies at Incidence. Presented at the 7th US-FRG DEA Meeting Army Ballistic Research Lab. Aberdeen, Proving Ground, Maryland, 26-27 May, 1982.
- [11] Bippes, H.; Maier, A.: Research Programme and Measurement Techniques in the Water Towing Tank of DFVLR in Göttingen. Proc. ICIASF Congr., Dayton, Ohio, 30 Sept. - 02 Oct. 1981, ICIASF '81 Record, pp. 53-60, 1981.
- [12] Hornung, H.; Perry, A.E.: Stream Surface Bifurcation, Vortex Skeletons and Separation. DFVLR-Report IB 222-82 A 25, 1982.
- [13] Cebeci, T.: Private Communication.
- [14] Rotta, J.C.: FORTRAN IV Rechenprogramm für Grenzschichten bei kompressiblen ebenen und achsensymmetrischen Strömungen. DLR-FB 71-51, 1971.

CALCULATION OF BOUNDARY LAYERS AND SEPARATION ON A SPHEROID AT INCIDENCE

V.C. Patel and J.H. Baek
Iowa Institute of Hydraulic Research
The University of Iowa
Iowa City, Iowa 52242

Abstract

Three-dimensional boundary layers on a 6:1 spheroid at an incidence of 10 degrees have been calculated at two Reynolds numbers and comparisons have been made with the corresponding data of Meier et al. The results clearly demonstrate the capabilities and limitations of first-order boundary-layer theory.

At the lower Reynolds number, the laminar boundary-layer calculations are in good agreement with the data on the windward side of the body and separation is predicted in the region where the experiments indicated near zero wall shear stress just before transition to turbulent flow. The solutions have been interpreted in the light of previous proposals concerning the topology of three-dimensional flow separation. Although the results support several alternative possibilities, it is concluded that boundary-layer calculations, by themselves, are insufficient to identify a clear choice.

The calculations at the higher Reynolds number involve laminar, transitional and turbulent flow. The results indicate the need for improvements in the turbulence model to better describe transitional flow. However, when the boundary layer is fully turbulent and thin, the calculations are in good agreement with experiments. Finally, the solutions with potential-flow as well as measured pressure distributions fail to provide an adequate description of the development of the vortical flow in the thick turbulent boundary layer on the leeside even though the flow is far from separation. This is attributed to the neglect of the strong viscous-inviscid interaction due to the thick boundary layer.

I. Introduction

The three-dimensional incompressible boundary layer on bodies of revolution has been the subject of many recent investigations. Among the experimental studies are those of Werle [1], Wilson [2], Peake, Rainbird and Atraghji [3], Han and Patel [4], Ramaprian, Patel and Choi [5], Hayashita [6] and Meier et al. [7-10]. Most of the early studies were restricted to flow visualization and, to date, much of the available information is concerned with flow at or close to the surface. Measurements within the boundary layer are quite limited [Refs. 5, 6-8]. On the other hand, there is an increasing number of numerical studies (see, for example, Refs. [11-22]) in which different methods are used to solve the boundary-layer equations for laminar as well as turbulent flows. These are of course able to generate much more information than can be

extracted from even the most detailed experiments. In a few instances where the results of the calculations have been compared with experimental data (e.g., Refs [15,18,21,22]), it is found that some of the observed features of the flow can be reproduced quite successfully while others remain unexplained. In particular, experiments on bodies of revolution as well as other shapes indicate different types of flow separation resulting in a wide variety of flow patterns, whereas most calculations terminate at an ill-defined separation point or line. Frequently, separation is said to occur when the particular boundary-layer calculation method meets with some numerical irregularity or catastrophe. Thus, the problem of identifying the type and location of separation of a three-dimensional boundary layer by numerical means remains controversial. This paper attempts to address this issue by means of detailed comparisons between boundary-layer calculations and experimental data.

The calculation method employed here has been described previously [15, 23] in some detail. For the present purposes, it suffices to note the major features. The method solves the usual thin boundary-layer equations in the body-fitted orthogonal coordinates shown in Figure 1 using an ADI (Alternating-Direction-Implicit) numerical scheme. The turbulence model is based on the turbulent kinetic-energy equation, a prescribed turbulence length-scale distribution and the assumption that the directions of the stress and rate-of-strain vectors are coincident. The method is capable of calculating laminar as well as turbulent boundary layers, transition being simulated by 'switching-on' the turbulence model along a prescribed transition line. No attempt has yet been made to tailor the model constants or functions for better representation of the development of turbulence over a finite transition length. Finally, for turbulent as well as laminar flow, the equations are solved numerically up to the wall without using any 'wall functions'.

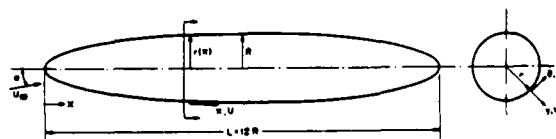


Figure 1. Notation

In the following, we shall consider the flow over a prolate spheroid of axes-ratio 6:1 which has been used in the detailed experimental investigations of Meier et al. [7-10]. Furthermore, we shall confine our attention to a moderate incidence of 10 degrees since it has been explored in greatest detail. The experimental

information is first reviewed to point out the most significant features. The results of the boundary-layer calculations are then presented and compared with the data. The comparisons lead to several important observations concerning the capabilities and limitations of thin boundary-layer theory, the role of viscous-inviscid interactions, and a plausible topology of flow separation and vortex formation.

II. Review of Experiments

In the experiments of Meier et al. [7-10], conducted in a large, low-speed wind tunnel at the DFVLR in Göttingen, a 6:1 prolate spheroid, 2.4 m long and 0.4 m maximum diameter, has been tested over a range of incidences and at two Reynolds numbers, namely $Re \equiv (U_\infty L/\nu) = 1.6 \times 10^6$ and 7.2×10^6 , corresponding to the reference freestream velocities, $U_\infty = 10\text{ m/s}$ and 45 m/s . As noted earlier, we shall consider the case $\alpha = 10^\circ$. The available measurements include the distributions of the pressure coefficient, $C_p = (p - p_\infty)/\frac{1}{2}\rho U_\infty^2$, and the magnitude and direction of skin-friction vector, $C_f = \tau_w/\frac{1}{2}\rho U_\infty^2$, at the surface at both Reynolds numbers. The longitudinal and circumferential components of mean velocity, U and

W , respectively, in the notation of Figure 1, were also measured across the boundary layer at two axial positions at the higher Reynolds number. Since a tripping device was not employed, the boundary layer is initially laminar, and transition, when present, occurs naturally.

The pressure distributions measured at the two Reynolds numbers are compared with that predicted by potential-flow theory in Figure 2(a) at several representative axial sections. The corresponding longitudinal and circumferential pressure gradients are shown in Figures 2(b) and 2(c), respectively. These are defined as follows:

$$(\nabla C_p)_x = \frac{\partial(2C_p)}{h_1 \partial(X/L)}, \quad (\nabla C_p)_\theta = \frac{\partial(2C_p)}{h_3 \partial\theta}$$

where $h_1 = \{1 + (dr/dX)^2\}^{1/2}$, $h_3 = r(X)$ and r is the transverse radius of the body. It should be noted that this is one of a few experiments in three-dimensional boundary-layer flows where the pressures have been measured at such closely-spaced intervals in both directions that the gradients can be evaluated without much uncertainty. Secondly, these and the other data discussed below have been taken from tapes and tables kindly made available by the experimenters through the auspices of the US-FRG Data Exchange Agreement.

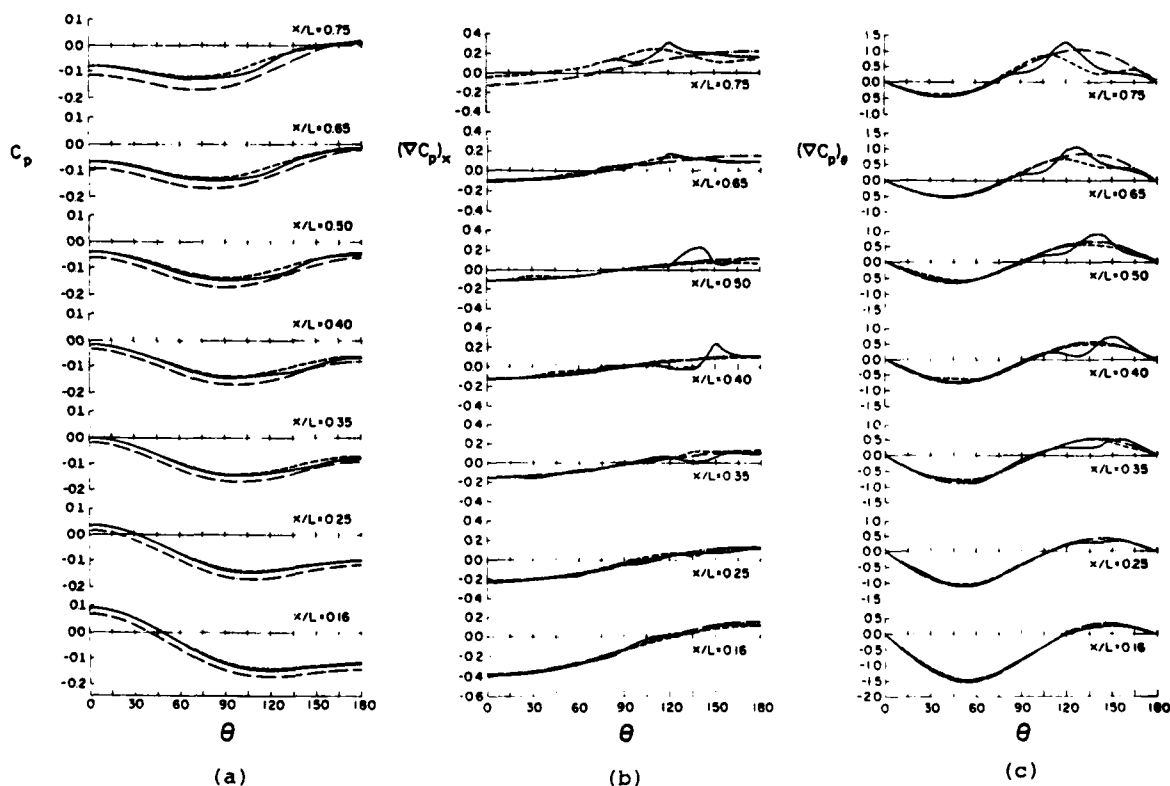


Figure 2. Potential-Flow and Measured Pressure Distributions and Gradients.
--- Potential Flow, — $Re = 1.6 \times 10^6$, -.- $Re = 7.2 \times 10^6$

Figure 2 indicates several interesting differences among the three pressure distributions. Over the windward side of the body the measured pressure distributions resemble that in potential flow but are consistently higher. This is presumably due to a 'negative blockage' usually encountered in an open-jet wind tunnel. As shown in Figures 2(b) and 2(c), however, the influence of these differences on the pressure gradients, which enter the boundary-layer equations, are quite small upto $X/L = 0.65$.

At the lower Reynolds number, the measured pressure distribution and gradients show marked departures from potential flow starting at approximately $X/L = 0.25$ in the region $120^\circ < \theta < 150^\circ$ and spreading to $80^\circ < \theta < 180^\circ$ by $X/L = 0.75$. The development of a short circumferential plateau of constant pressure at and beyond $X/L = 0.35$ is reflected in the positive (adverse) longitudinal and circumferential pressure gradients. The plateau is followed by a pressure rise towards the leeward side and associated with this are somewhat larger pressure gradients than in potential flow.

At the higher Reynolds number, Figure 2(a) shows that there is no constant-pressure plateau but there is a gradual reduction in the pressure coefficient on the leeward side, starting at $\theta = 180^\circ$ near $X/L = 0.40$ and spreading to $105^\circ < \theta < 180^\circ$ by $X/L = 0.75$. Significant departures of the experimental pressure gradients from potential flow are also not evident until about $X/L = 0.65$.

The observed pressure distributions have been described here in some detail since they are indicative of the level and extent of viscous-inviscid interactions and consequently of the limits of validity of the first-order boundary-layer approximations. Secondly, they will be used to confirm or support the occurrence of certain flow phenomena observed experimentally or indicated by calculations.

The measured wall shear-stress vectors at the two Reynolds numbers are shown in Figures 3 and 4. At the lower Reynolds number (Figure 3), we can distinguish a narrow region, starting at $\theta \sim 125^\circ$ at $X/L = 0.395$ and extending to $\theta \sim 90^\circ$ at $X/L = 0.825$, of rather small near-zero wall shear stress. The relationship between this and flow separation will be discussed later. Just beyond the near-zero stress region, in the circumferential direction, is a growing wedge of much larger stresses. This is believed to be due to transition to turbulent flow. The wedge grows from $140^\circ < \theta < 160^\circ$ at $X/L = 0.395$ to $105^\circ < \theta < 180^\circ$ at $X/L = 0.825$. The lower stresses along the leeward plane of symmetry ($\theta = 180^\circ$) upto $X/L \sim 0.74$ indicate that the flow continues to be laminar over a diminishing region on the leeside upto that station.

The shear-stress measurements at the higher Reynolds number, shown in Figure 4, are quite different since the flow over a large part of the body is turbulent. The location of the zone of transition from laminar to turbulent flow can be inferred from the relative magnitudes of the

stresses and is in accordance with the observations of Meier and Kreplin [7] on the basis of the surface hot-film signals. For later reference, the position of the transition line determined by Meier and Kreplin at this Reynolds number is shown in Figure 5. Finally, Figure 4 indicates a zone of near-zero stress at $X/L = 0.936$, which is close to the sting used to support the model in the wind tunnel.

As noted earlier, mean-velocity profiles were measured at several circumferential positions at $X/L = 0.64$ and 0.71 at the higher Reynolds number. From Figures 4 and 5 it is evident that the flow at these axial positions is turbulent although it may still be recovering from the delayed transition on the windward side.

The foregoing review of the available experimental information indicates the complexities of the flows to be addressed computationally. It is clear that the two cases provide ample opportunities to explore the

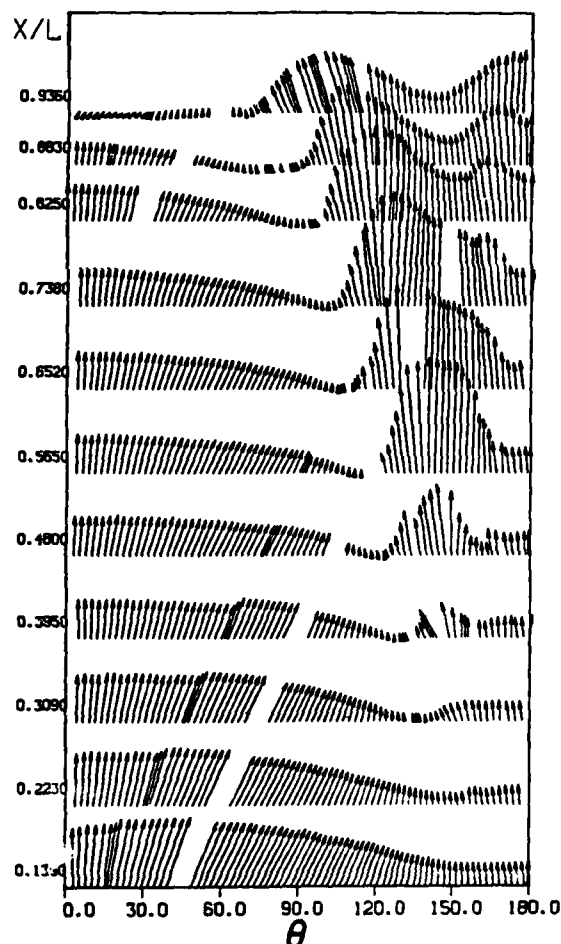


Figure 3. Measured Wall Shear Stress,
 $Re = 1.6 \times 10^6$

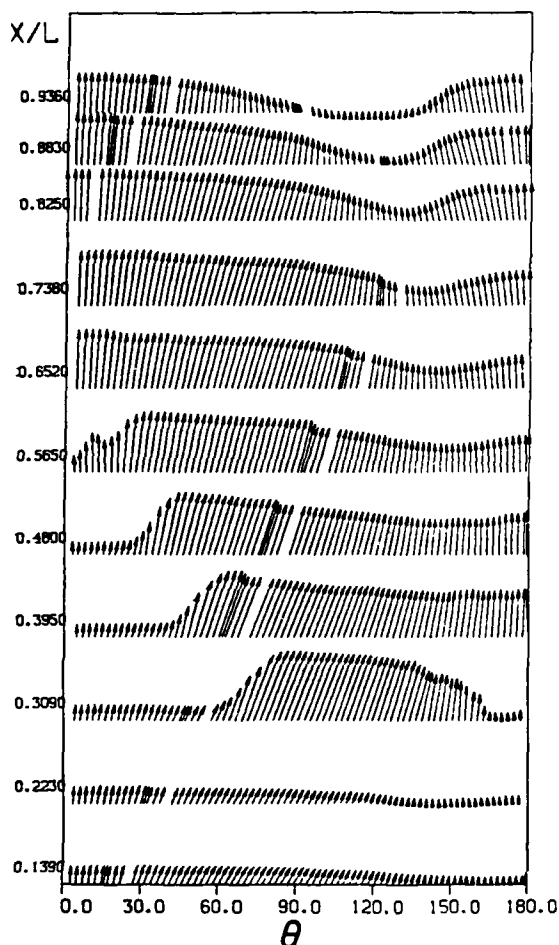


Figure 4. Measured Wall Shear Stress,
 $Re = 7.2 \times 10^6$

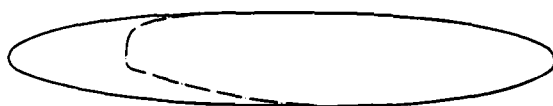


Figure 5. Transition Line at $Re = 7.2 \times 10^6$

performance and limitations of three-dimensional boundary-layer calculation methods.

III. Numerical Solutions

The calculations were started just downstream of the axial position containing the potential-flow stagnation point using the procedure described in Ref. [15]. The number of grid points across the boundary layer is 21. Some earlier solutions, reported in Ref. [22], were obtained with a circumferential step size $\Delta\theta = 15^\circ$. The results to be presented here were obtained with a

step size of 7.5° , primarily for better resolution of the flow in certain key areas. Detailed comparison between the two sets of calculations, with respect to the integral parameters as well as the velocity profiles, indicated grid dependence and lack of numerical convergence in regions where the magnitude of the wall shear stress became very small (typically $|C_f| < 0.0001$). Although we shall discuss the possible reasons for this, it should be emphasized that such regions have been excluded from the results presented in this section.

In view of the differences noted earlier between the potential-flow and experimental pressure distributions and pressure gradients, calculations have been performed using both. Since the experimental pressure distributions in the nose region indicated more scatter, the calculations in these cases were started at $X/L = 0.127$ using the solutions with the potential-flow pressures and scaling the velocity profiles for the difference between the measured and theoretical pressure coefficients. Note that the boundary layer is laminar at $X/L = 0.127$ at both Reynolds numbers. The subsequent solutions utilized the experimental pressures and gradients shown in Figure 2.

(a) $Re = 1.6 \times 10^6$

For this case, calculations were performed assuming laminar flow. Although these solutions were continued almost up to the tail of the body, we shall show the results only up to $X/L = 0.4$ since numerical problems were first encountered just downstream of this position over a region on the body roughly coincident with a line along which the wall shear stress became very small and the leeward plane of symmetry.

The main results of the calculations, with potential-flow and measured pressure distributions, are shown in Figures 6 through 8. To facilitate comparison with the experimental wall shear-stress data of Figure 3, the same scales have been used for the computed results in Figure 6, and calculations are shown at the axial locations corresponding to the measurement stations. Figure 7 shows the resultant of the circumferential (W) and normal (V) components of the velocity vector. For clarity, these profiles are shown only in the region $75^\circ \leq \theta \leq 180^\circ$, and the vertical scale has been expanded by a factor of five. The corresponding axial component of velocity is shown in Figure 8.

Consider first the calculated results by themselves. Figure 7 shows the development of a zone of circumferentially reversed flow starting on the leeward plane of symmetry just downstream of $X/L = 0.16$ and spreading outwards from there until, at $X/L = 0.4$, it occupies $120^\circ < \theta < 180^\circ$ in the calculations with potential flow pressure distribution, and $135^\circ < \theta < 180^\circ$ in those with the experimental pressure distribution. The boundary layer in this region is relatively thick. It is also possible to identify this region in Figure 6 from the changes in the direction of the wall shear stress relative to the axis of the body, and define a line on the body

that demarkates circumferential flow-reversal (CFR line). This line starts on the leeward symmetry plane and proceeds to more windward positions further downstream. Note that such a line is 'geometric' insofar as it is defined with respect to the geometry of the body and not that of the flow. Since the flow outside the boundary layer is known by virtue of the assumed pressure distribution, it is also possible to determine another line, namely the crossflow reversal line (XFR line, say), which indicates the reversal of the direction of wall shear stress relative to that of the external flow. This line lies a few degrees to the windward side of the CFR line.

Calculations with both pressure distributions indicate that there exists a point at $X/L = 0.4$ ($\theta = 120^\circ$ and 135° in Figures 6(a) and (b), respectively) at which the direction of the wall shear stress changes abruptly and its magnitude becomes very small. Within the resolution of the numerical grid, this point coincides with almost explosive growth in boundary layer thickness (see Figures 7 and 8) and with the beginning of the numerical difficulties noted earlier.

A comparison between the solutions obtained with the two pressure distributions indicates that they are qualitatively similar. The major difference lies in the extent of the

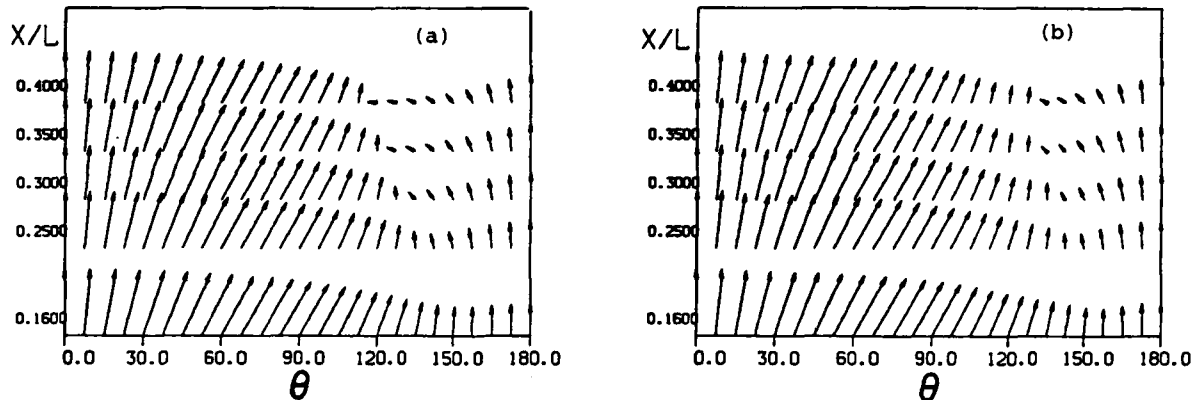


Figure 6. Calculated Wall Shear Stress, $Re = 1.6 \times 10^6$
(a) Potential-Flow Pressure Distribution
(b) Experimental Pressure Distribution

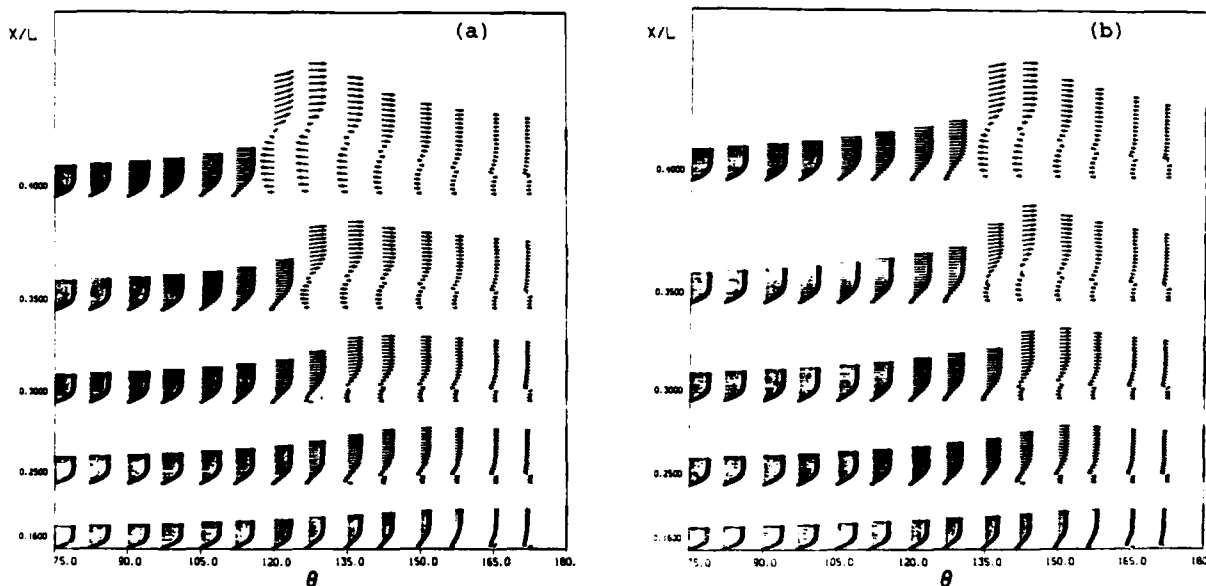


Figure 7. Velocity Vectors in the y - θ Plane, $Re = 1.6 \times 10^6$
(a) Potential-Flow Pressure Distribution
(b) Experimental Pressure Distribution

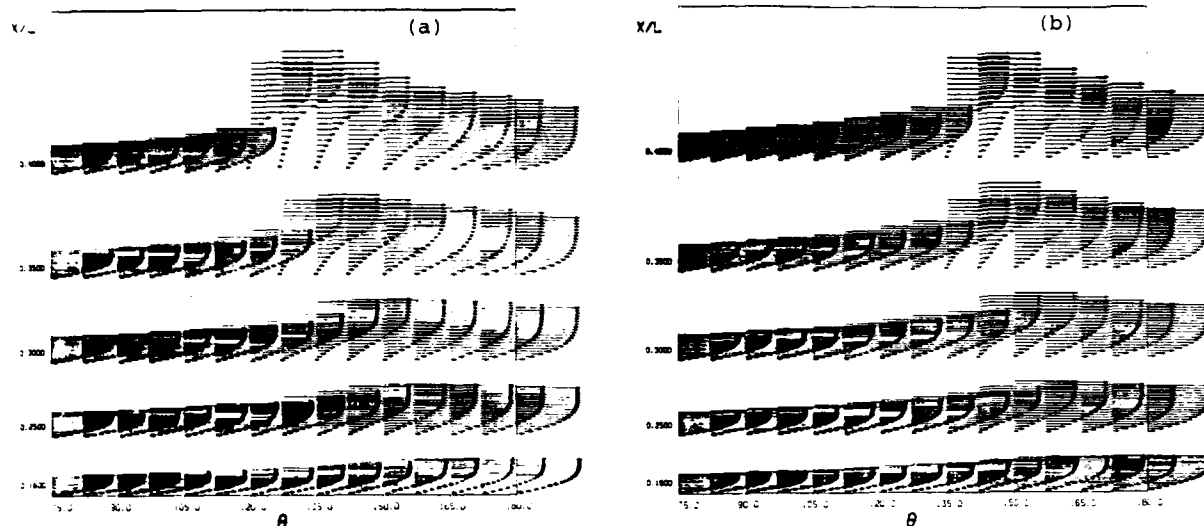


Figure 8. Axial velocity Profiles, $Re = 1.6 \times 10^6$
 (a) Potential-Flow Pressure Distribution
 (b) Experimental Pressure Distribution

circumferential flow reversal zone and the location of the point of minimum wall shear stress and abrupt changes in its direction. Both occur closer to the leeward plane of symmetry with the experimental pressure distribution.

Finally, a comparison can be made between the calculations shown in Figure 6 and the corresponding experimental data of Figure 3. The following observations can be made. (a) In the laminar flow upto $X/L = 0.3$, the calculations with potential-flow pressure distribution agree well with the data with respect to magnitude as well as direction (see also Figure 12) except in a small region around the CFR line, where the predicted stresses are larger. (b) As may be expected from the relief of the measured pressure gradients in this region, the use of the experimental pressure distribution leads to even higher stresses and therefore somewhat poorer agreement with the data. (c) Beyond $X/L = 0.3$, the two calculations agree over a large region ($\theta < 100^\circ$) on the windward side of the body with the measured stress directions but the predicted magnitudes are higher. However, the corresponding data indicate some irregularities in magnitude. (d) At $X/L = 0.4$, the experiments indicate transition just beyond the stress minimum and the CFR line. In this region both calculations predict very small stresses. However, the accompanying abrupt changes in the direction of the wall shear stress are not observed in the experiment. (e) The point of minimum stress in the experiment is located at $\theta = 127^\circ$, whereas the calculations with potential-flow and measured pressure distributions predict near-zero stress at $\theta = 122^\circ$ and 136° , respectively. (f) The calculated shear stress along the leeward plane of symmetry, $\theta = 180^\circ$, continues to agree well with the data upto $X/L = 0.4$, indicating laminar flow along that line. (g) Figures 6, 7, 8 and 2 show that the observed changes in the pressure distribution are

correlated with the zone of small wall shear and rapid boundary-layer growth.

(b) $Re = 7.2 \times 10^6$

For this case, the laminar boundary-layer calculations were continued upto the experimentally observed transition line shown in Figure 5 and the turbulence model was activated as this line was crossed along each meridian. Thus, for example, at $X/L = 0.3$ (see Figures 4 and 5), the computation domain includes laminar flow over the windward side, transitional and turbulent flow over the middle, and again laminar flow near the leeward plane of symmetry. The flow becomes turbulent over the entire circumference only beyond $X/L = 0.56$ where the transition line crosses the windward symmetry plane.

These calculations also indicated circumferential flow reversal in the upstream laminar boundary layer but due to transition to turbulent flow numerical difficulties were not encountered at $X/L = 0.4$ as in the previous case. The solutions failed to converge within the maximum 10 iterations allowed in the ADI cycles only beyond $X/L = 0.88$.

The results of the calculations with the potential-flow and measured pressure distributions are shown in Figures 9-11. As pointed out earlier in Figure 2, the measured pressure gradients at this higher Reynolds number are in substantial agreement with those in potential flow over a large region on the windward side of the body. Consequently, the two sets of calculations are essentially the same in this region. The calculated wall shear-stress plots of Figure 9, the cross-stream velocity vectors of Figure 10 and the detailed axial and circumferential velocity profiles of Figure 11 indicate that significant

differences between the results with potential-flow and measured pressure distributions are observed, as expected, on the leeward side. Also, as in the laminar case, the region of circumferential-flow reversal is smaller with the experimental pressure distribution.

Comparison of Figure 9 with Figure 4 shows that the calculations reproduce the major features observed in the experiments except in the neighborhood of transition. The agreement in this region can be improved by incorporating a damping or intermittency function in the turbulence model in order to accomplish a more gradual change from laminar to turbulent flow. The calculated shear stresses in the turbulent flow just after transition tend to be lower than those measured. This again may be due to the inadequacy of the turbulence model for transitional flows. Further downstream, where the flow has recovered from transition, both calculations show good agreement with the data over a large portion of the body on the windward side and over a somewhat smaller

region near the leeward plane of symmetry. However, substantial differences are observed in the region where the experimental data show a stress minimum, the calculated magnitudes being higher. Note that the data indicate almost zero stress at $X/L = 0.883$, $\theta \sim 120^\circ$ and at $X/L = 0.936$, $90^\circ < \theta < 130^\circ$, and the flow features are somewhat similar to those observed in the lower Reynolds-number case. As noted above, the present calculations indicated the first signs of numerical difficulties just beyond $X/L = 0.88$.

The reasons for the poor performance of the calculations in the zone of the stress minimum are not entirely evident from the wall shear stresses. The cross-stream velocity vectors shown in Figure 10 provide some explanation. It should be pointed out that, unlike the corresponding plot of Figure 7 for laminar flow, the vertical and horizontal length scales are nearly the same in Figure 10 and therefore it provides a picture of the variation of the boundary-layer thickness in the circumferential direction. Thus, for example,

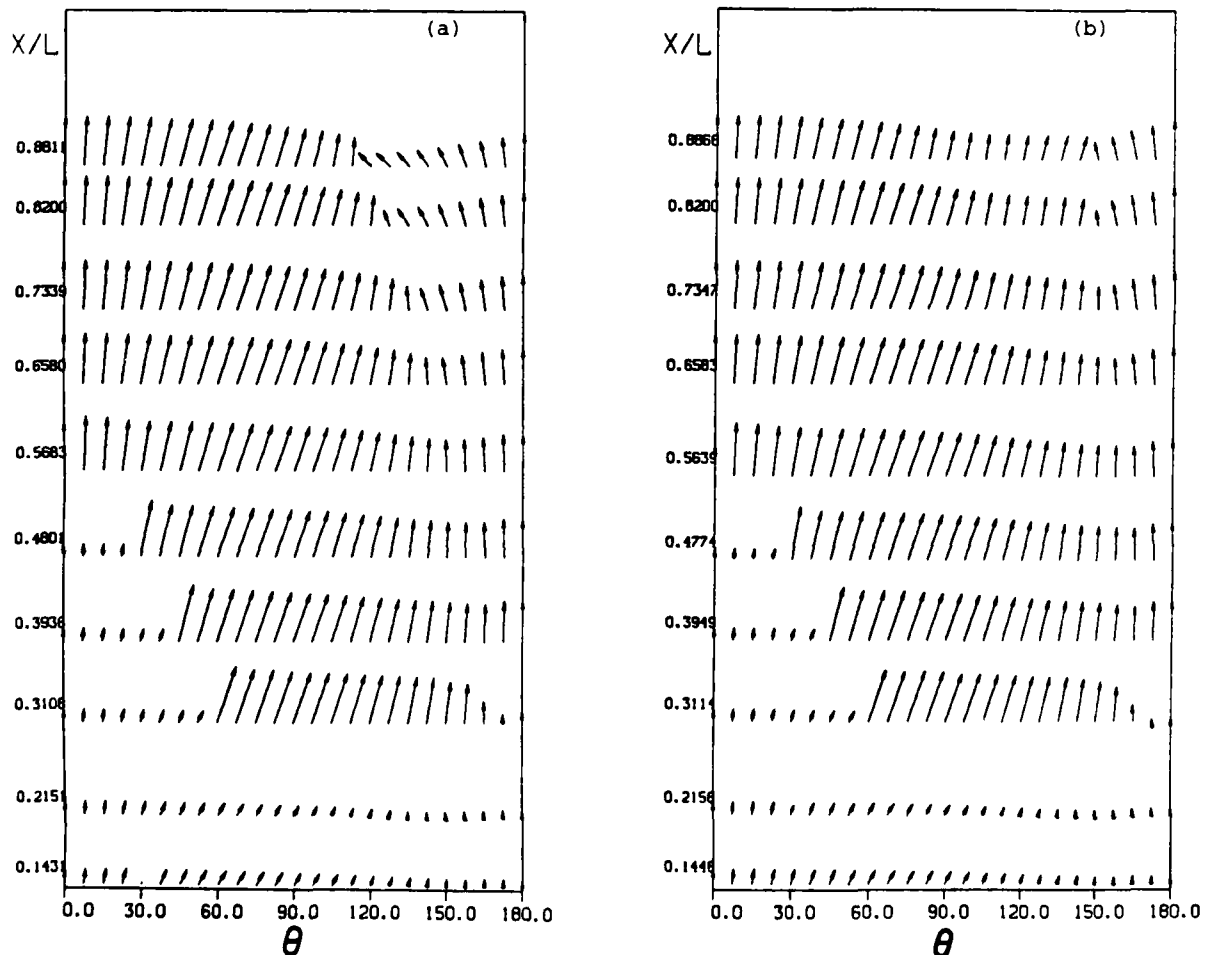


Figure 9. Wall Shear Stress Vectors, $Re = 7.2 \times 10^6$
 (a) Potential-Flow Pressure Distribution
 (b) Experimental Pressure Distribution

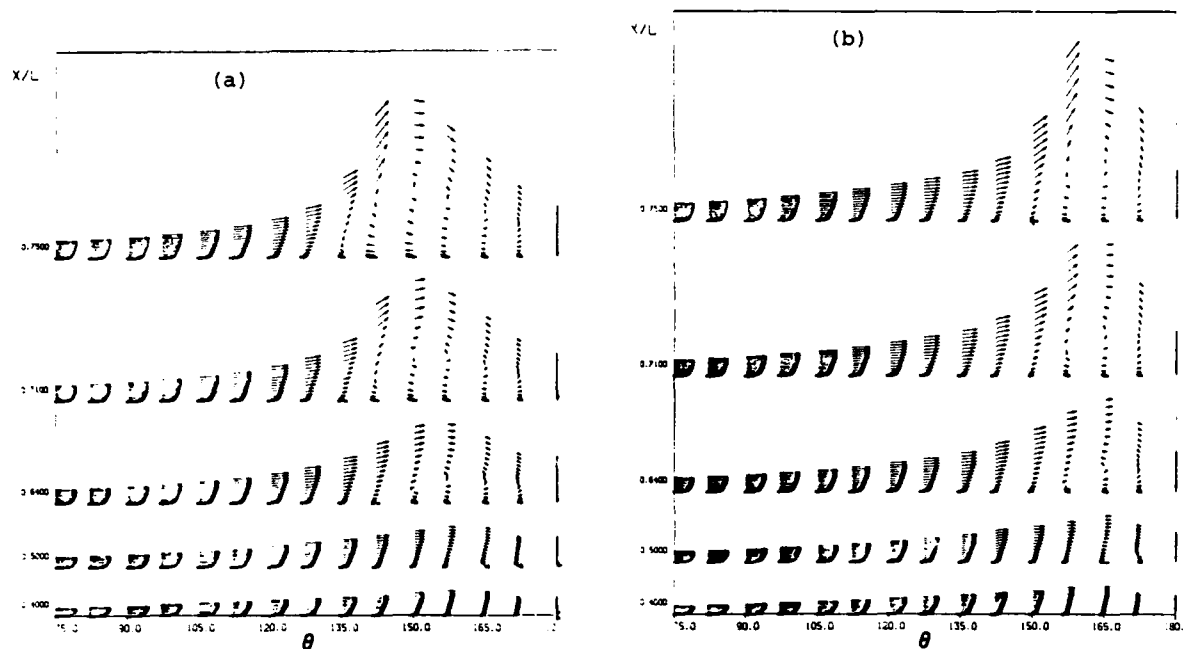


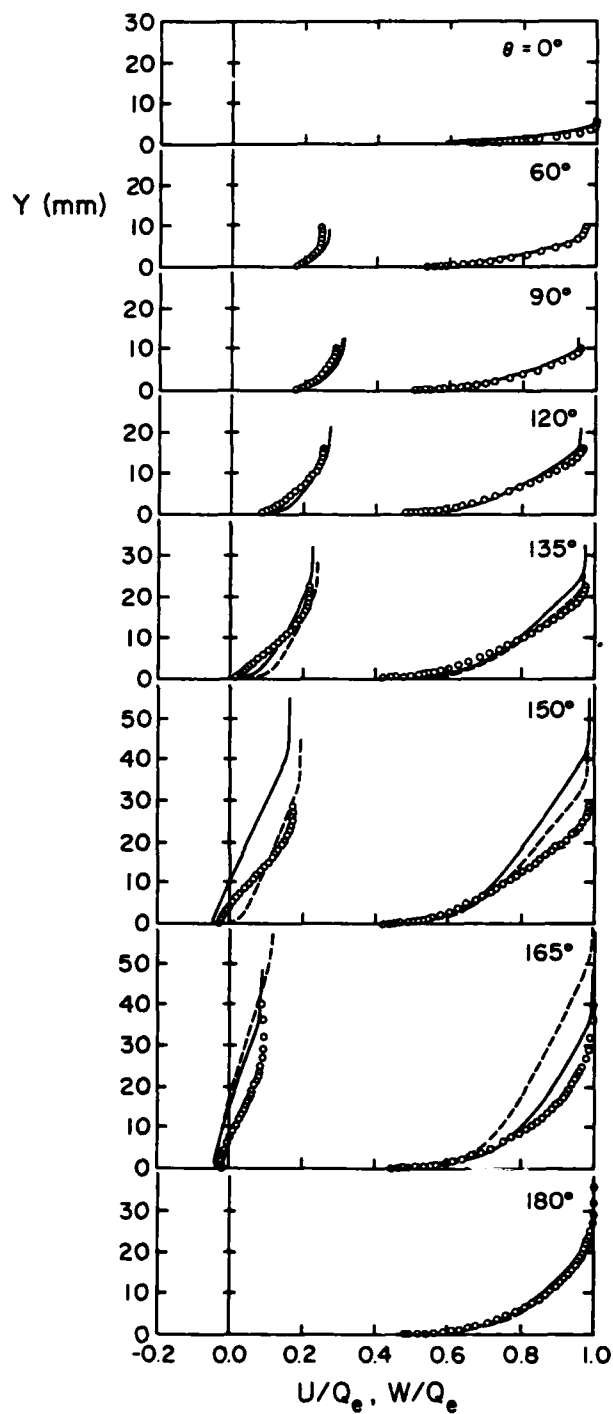
Figure 10. Velocity Vectors in the y - θ Plane, $Re = 7.2 \times 10^6$
 (a) Potential-Flow Pressure Distribution
 (b) Experimental Pressure Distribution

at $X/L = 0.75$, the ratio of the maximum boundary-layer thickness, which occurs at $\theta \sim 157.5^\circ$, to the local body radius is approximately 0.67. The rapid thickening of the boundary layer and the development of a vortical flow on the leeside is associated with the convergence of near-wall streamlines from both sides. The thick boundary layer implies a strong viscous-inviscid interaction even in the absence of separation, and it is not surprising that the use of the measured surface pressure distribution does not guarantee improved agreement with experiment in all respects.

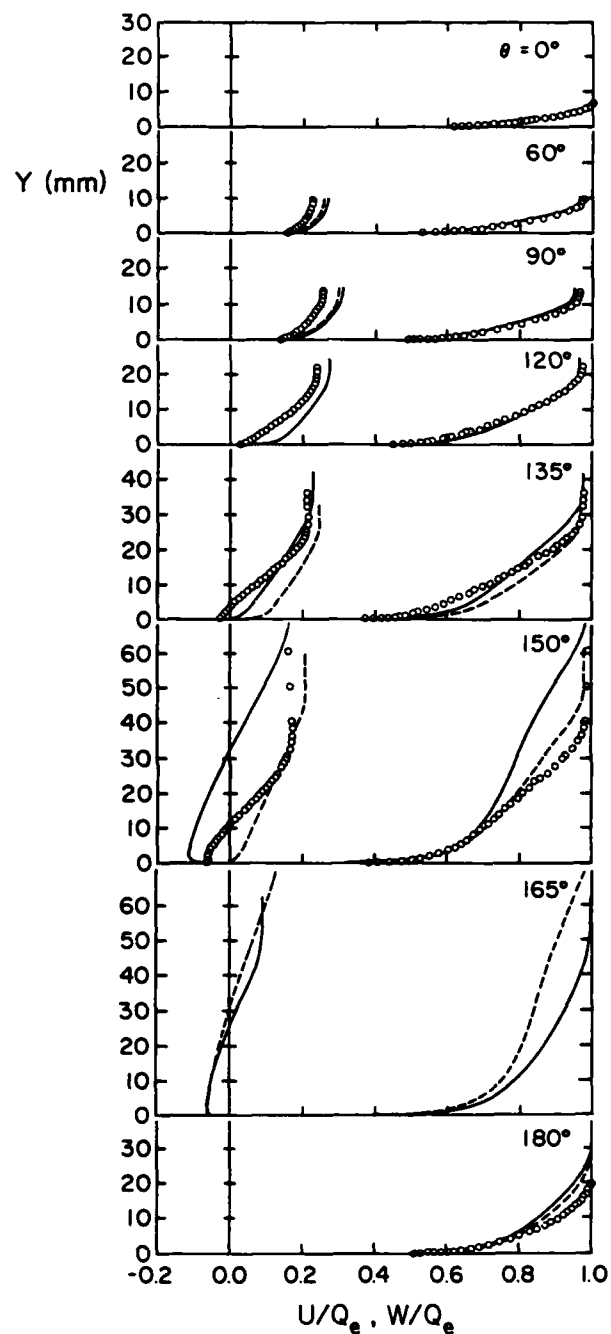
The detailed velocity-profile comparisons of Figure 11 show that there is little to choose between the two sets of calculations except in the region of viscous-inviscid interaction. At $X/L = 0.64$, the calculations are in good agreement with the data everywhere except in the zone $135^\circ < \theta < 165^\circ$, where Figure 2 first shows substantial differences in the pressure gradients and where Figure 10 indicates a thickening of the boundary layer. However, the measured boundary layer is thinner than that predicted by either calculation. The situation at $X/L = 0.71$ is quite similar but with one important difference, namely the measured velocity components at the edge of the boundary layer do not agree with those calculated with either the potential-flow or the experimental pressure distribution over a circumferential extent much larger than that in which the boundary layer is thick. In other words, the measured velocities and directions in

the external flow are not compatible with the pressure distribution measured at the surface. If systematic experimental errors of this magnitude are discounted, the differences imply not only a variation of pressure across the thick boundary layer but also significant changes in the direction of the external flow over regions quite remote from that where the boundary layer is thick. Thus, the peak in the displacement thickness associated with the thick boundary layer is responsible for a reorientation of the external flow over the entire circumference. The observed decrease in the measured transverse component of velocity on the windward side is compatible with this explanation.

Two other aspects of the calculations are also noteworthy. The first is that the boundary layer along the leeward plane of symmetry is predicted quite well, especially with the measured pressure distribution, almost up to $X/L = 0.71$. Secondly, the calculated axial or primary component of the mean velocity in the wall region is in good agreement with the measurements. These suggest that the turbulence model employed here is not a major source of the disagreements observed in the outer part of the boundary layer. Since the calculated distributions of the turbulent kinetic energy and the Reynolds stresses are readily available it would be informative to compare them with corresponding turbulence measurements in progress at the DFVLR.



(a)



(b)

Figure 11. Axial and Circumferential Velocity Profiles, $Re = 7.2 \times 10^6$
 (a) $X/L = 0.64$, (b) $X/L = 0.71$

---- Potential Flow Pressure, — Measured Pressure;
 ○ Experiment

IV. Separation

We shall now explore the reasons for, and the implications of, the numerical problems encountered in the laminar boundary-layer calculations at the lower Reynolds number. Continuation of the present calculations beyond $X/L = 0.4$ showed well behaved solutions over a diminishing domain on the windward side of the body upto a line just beyond the CFR line. As this line was approached, the magnitude of the wall shear stress became very small and its direction changed rapidly, the angle between the stress vector and the body axis changing from zero at the CFR line to values so large ($\sim 75^\circ$) that the wall crossflow angle (i.e., the angle between the wall shear stress and the external flow) became 90° . Note that the latter criterion is often invoked to pronounce separation, especially in integral calculation methods.

Solution features similar to those noted above have also been observed in previous calculations (see, for example, Wang [12, 13], Patel and Choi [15], Cebeci, Khattab and Stewartson [18], and Ragab [21]). It is generally agreed that the flow on the windward side, at least upto the CFR line, can be calculated with some confidence using a variety of numerical schemes since there is no difficulty in identifying the corresponding zone of dependence for this region. It is also acknowledged that the behaviour of the solutions in the neighborhood of the CFR line is related in some way to the imminence of separation. Another point of agreement is that the convergence of skin-friction lines, or the limiting streamlines at the wall, from both sides is a symptom of separation. Unfortunately, there is little consensus among researchers on the precise definition of separation.

Figure 12 shows the magnitude of the wall shear stress according to the present calculations with the potential-flow pressure distribution. This is the same information as in Figure 4(a) except that typical solutions beyond $X/L = 0.4$ have been added and it is now possible to make a direct comparison with the data. In order to explore the detailed behavior of the calculations, Figure 13(a) shows the variation of C_f . The recent results of Cebeci, Khattab and Stewartson [18] for a 4:1 spheroid at $\alpha = 6^\circ$ are presented in the same format in Figure 13(b) to show the remarkable similarity between the two sets of calculations for different spheroids and incidences.

It is evident from Figures 12 and 13(a) that, in the present case, the resultant wall shear stress approaches zero, within the uncertainties of numerical analysis, at $X/L = 0.4$ and $\theta \sim 122^\circ$. In fact, Figure 13(a) shows that C_f vanishes as the square-root of the distance from this point from both sides but at different rates, suggesting the presence of a Goldstein type of singularity (see also Cebeci et al. [18]). Thus, it is not surprising that numerical difficulties are first encountered there. It is reasonable to infer that this is the most upstream point on the separation

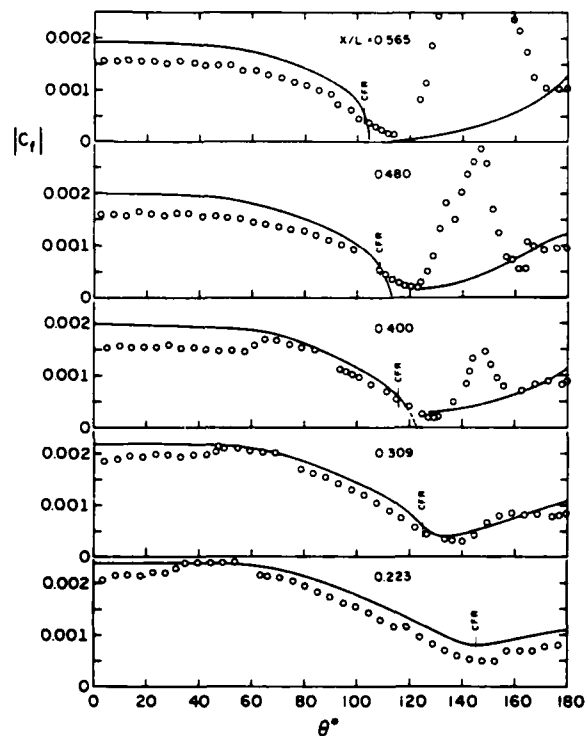


Figure 12. Wall Shear-Stress Magnitude, $Re = 1.6 \times 10^6$, \circ Experiment; — Calculation

line, regardless of how that line is defined or the shape it takes further downstream.

The solutions beyond $X/L = 0.4$ are quite well behaved on the windward side and show a very rapid decrease in the wall shear stress magnitude beyond the CFR line. It is tempting to infer, by very short extrapolations from the windward side, that the shear stress vanishes along some line lying a short distance to the lee of the CFR line. Although this would provide an unambiguous definition of separation, the numerical evidence is not sufficiently conclusive. Furthermore, such a definition would not be general enough to encompass certain special cases, such as the separation on an infinite swept wing. However, the present solutions, like those of Cebeci et al. and others, indicate a singular behavior in the boundary-layer equations and consequently we conclude that it is not possible to determine the flow properties at the line of separation from boundary-layer equations alone, regardless of the numerical scheme used to approach the separation line. Finally, it is interesting to note that between the CFR line and the extrapolated zero-stress line is a line that demarkates the vanishing of the streamwise component of wall shear-stress, which, as noted earlier, has often been used as a separation criterion. Unfortunately, it is also known to fail in the simple case of an infinite swept wing.

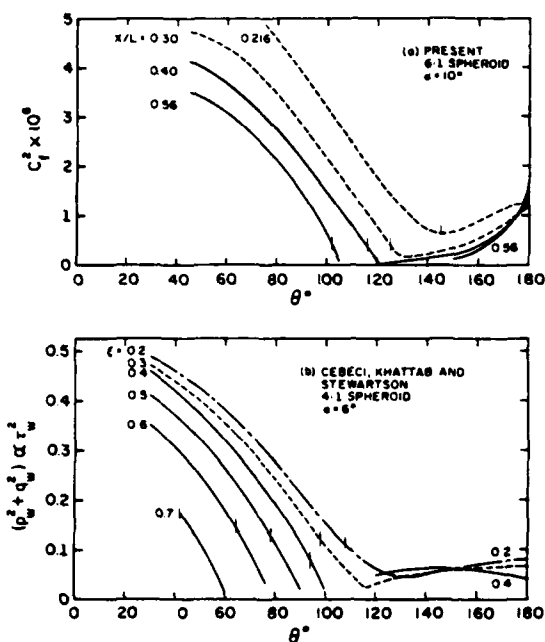


Figure 13. Transverse Variation of C_f^2

Yet another controversy concerns the origin of the separation line. The basic issue is whether the separation line on the windward side originates at the most upstream singular point, discussed above, or continues downstream on the leeward side. Wang [12, 13, 24] maintains that both possibilities exist, with the former occurring at higher incidences and the latter at lower incidences. From their solutions marching out of the leeward plane of symmetry, Cebeci et al. deduced a limiting line of 'accessibility' (to the upstream flow) and suggested that this is a continuation, on the leeside, of the separation line on the windward side (which they defined on the basis of certain irregularities in the numerical solutions). At the lower incidences they infer that this line is closed and terminates at the well-defined saddle point of separation on the leeward plane of symmetry. This is in agreement with the suggestion of Wang and the experiments of Han and Patel [4]. At the higher incidences, $\alpha = 15^\circ$ and 30° , Cebeci et al. suggest that the separation line also continues on the leeside but the problem of whether it is closed or open could not be resolved since the line of accessibility lay upstream of separation. However, the notion that the separation line continues on the leeward side appears to contradict the concept of 'open separation' of Wang [24], who maintains that the windward separation line can originate at a point on the body and does not need to bend back towards the leeside.

Figure 14 summarizes the various possibilities concerning the behavior of the skin-friction lines in the neighborhood of the origin

of separation. Of the three possibilities attributed to Cebeci et al., they favor the version (b). The fundamental differences between these and the open-separation idea of (a) due to Wang are quite obvious. Also shown in this figure is another possibility proposed originally by Legendre [25] and supported by Peake and Tobak [26] on the basis of the suggestion of Lighthill [27] that separation lines must originate at a saddle singularity.

The problem of determining which of these possibilities actually exists in a particular case is not a simple one since the available experimental evidence may be interpreted to support each pattern. The present calculations for laminar flow on a 6:1 spheroid at $\alpha = 10^\circ$ suggest that the most upstream point on the separation line is a singular point. According to Lighthill, this singularity must be connected to other singular points on the body. There are two possibilities. It may be connected to the saddle point of separation on the leeward plane of symmetry, by a continuation of the separation line on the leeside, thus producing a closed separation line, in agreement with Wang's suggestion and Cebeci et al.'s conclusion for low incidences ($\alpha \sim 6^\circ$ for a 4:1 spheroid). The second is that the point in question is itself a saddle point and is connected with another singularity, such as a spiral node or 'focus', as in Figure 14(c). According to Wang [24], this would constitute a special case of an open separation since it does not require the separation line to encircle the body. Also, this possibility is not at variance with the results of Cebeci et al. since the line of accessibility would lie ahead of the separation line. The directions of the calculated limiting streamlines at $X/L = 0.4$ shown in Figure 6 and the corresponding velocity field away from the body shown in Figure 7 and 8 are also compatible with the two possibilities discussed above and sketched in Figure 14(b) and (e) but they are not sufficient to enable a clear choice between them. The present results do not confirm the open

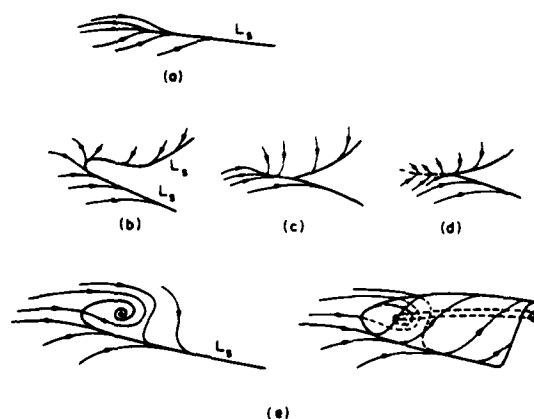


Figure 14. Possible Wall-Streamline Configurations at Origin of Separation Line (L_s)
(a) Wang; (b), (c), (d) Cebeci et al. (e) Legendre

separation as shown in Figure 14(a) and further calculations are required at high incidences to verify that such a possibility exists.

It is clear from the foregoing discussion that several issues concerning the topology of separation lines remain unresolved. It is unlikely that these can be settled on the basis of boundary-layer calculations alone since the irregularities observed in the solutions indicate singularities in the equations themselves. Note that the use of the experimental pressure distribution in the first-order boundary-layer equations leads to essentially the same behavior. Thus, further progress can be made only with the use of higher-order equations which take into account viscous-inviscid interaction and numerical techniques that can handle massive flow reversals. Secondly, experimental information which provides only the foot-print of the flow on the body, e.g., direction of the limiting streamlines on the surface without the magnitude of the wall shear stress, cannot by itself resolve the issues involved. In the one experiment where the stresses were measured (Figure 3 and 4) the flow became turbulent just beyond the line of very small stresses. Similar experiments are obviously needed at Reynolds numbers low enough for the flow to remain laminar beyond separation.

V. Conclusions

The calculations of the laminar boundary layer on a 6:1 spheroid at an incidence of 10° reproduce many of the features observed in the low Reynolds number experiments of Meier et al. [7-10]. The solutions fail close to and beyond a separation line on the body. In the experiments, separation is followed by transition to turbulent flow but no attempt has been made here to model this part of the flow.

The most upstream point on the separation line is identified by the vanishing of the wall shear stress but the flow features at the line of separation could not be defined. Also, whether the separation line on the windward side continues on the leeward side to become closed, or remains open either by originating at a point or at additional singularities, remains an issue open to debate. However, possible topological features of the flow associated with these alternatives have been examined and a few plausible ones have been identified. We believe that a clear choice among these cannot be made on the basis of boundary-layer calculations alone.

The solutions at the higher Reynolds number indicate that they are quite successful in predicting the observed characteristics of the boundary layer over a large part of the body where the boundary layer is thin. Some modifications of the turbulence model are needed to improve the representation of the flow in the neighborhood of transition. The calculations fail to provide an adequate description of the flow in the region on the leeward side where the boundary layer becomes thick. This region is quite extensive and well removed from separation.

The calculations using the potential-flow as well as experimental pressure distributions clearly demonstrate the limitations of first-order boundary-layer theory. In particular, it is shown that knowledge of the experimental pressure distribution on the surface does not lead to a dramatic improvement in the prediction of either separation or thick boundary layers. The latter observation is of considerable practical significance since extensive regimes of thick boundary layers may be present on bodies such as aircraft fuselages and ships (Patel [28]) without encountering separation. The results presented here suggest that such flows can be calculated only by recourse to higher-order equations which allow for the viscous-inviscid interaction through the relaxation of the pressure field. The data of Meier et al. at the higher Reynolds number provides an excellent test case for the validation of such calculation methods.

VI. Acknowledgements

This research has been supported by the U.S. Army Research Office and the U.S. Air Force Office of Scientific Research under Grant AFOSR-80-0148-B. The authors also acknowledge the timely assistance of Dr. A.W. Fiore of the AFFDL and Dr. H.U. Meier of the DFVLR, Project Officers of the United States and Federal Republic of Germany Data Exchange Agreement, in making available tabulated data from the DFVLR experiments.

VII. References

- 1) WERLE, H., "Separation on Axisymmetrical Bodies at Low Speed", *Rech. Aeron.*, No. 90, 1962, pp. 3-14.
- 2) WILSON, G.R., "Experimental Study of a Laminar Boundary Layer on a Body of Revolution", M. Sc. Thesis, Air Force Inst. Tech., Wright-Patterson AFB, No. GAM/AE/71-4, 1971.
- 3) PEAKE, D.J., RAINBIRD, W.J. and ATRAGHJI, E.G., "Three-Dimensional Flow Separation on Aircraft and Missiles", *AIAA Journal*, Vol. 10, No. 5, May 1972, pp. 567-580.
- 4) HAN, T.-Y. and PATEL, V.C., "Flow Separation on a Spheroid at Incidence", *Journal of Fluid Mechanics*, Vol. 92, 1979, pp. 643-657.
- 5) RAMAPRIAN, B.R., PATEL, V.C. and CHOI, D.H., "Mean Flow Measurements in the Three-Dimensional Boundary Layer over a Body of Revolution at Incidence", *Journal of Fluid Mechanics*, Vol. 103, 1981, pp. 479-504.
- 6) HAYASHITA, S., "Flow Around a Spheroid at Angle of Attack", *Trans. Society of Naval Architects of West Japan*, Vol. 63, No. 2, 1981, pp. 41-50.
- 7) MEIER, H.U. and KREPLIN, H.P., "Experimental Investigations of Boundary Layer Transition and Separation on a Body of Revolution", *Z. Flugwiss. Weltraumforschung*, Vol. 4, 1980, pp. 65-71.

8) MEIER, H.U. and KREPLIN, H.P., "Experimental Study of Boundary Layer Velocity Profiles on a Prolate Spheroid at Low Incidence in the Cross-Section $X/L = 0.64$ ", Proc. 5th USAF-FRG Data Exchange Agreement Meeting, AFFDL-TR-80-3088, 1980, pp. 169-189.

9) MEIER, H.U., KREPLIN, H.P. and VOLLMERS, H., "Velocity Distributions in 3-D Boundary Layers and Vortex Flows on an Inclined Prolate Spheroid", Proc. 6th USAF-FRG Data Exchange Agreement Meeting, DFVLR-AVA Report IB 22281 CP1, 1981, pp. 202-217.

10) KREPLIN, H.P., VOLLMERS, H., and MEIER, H.U., "Measurements of the Wall Shear Stress on an Inclined Prolate Spheroid", Z. Flugwiss. Weltraumforschung, Vol. 6, 1982, pp. 248-252.

11) WANG, K.C., "Separation Patterns of Boundary Layer Separation over an Inclined Body of Revolution", AIAA Journal, Vol. 10, 1972, pp. 1044-1050.

12) WANG, K.C., "Boundary Layer over a Blunt Body at High Incidence with an Open-Type of Separation", Proc. Royal Society, Vol. A340, 1974, pp. 33-55.

13) WANG, K.C., "Boundary Layer over a Blunt Body at Low Incidence with Circumferential Reversed Flow", Journal of Fluid Mechanics, Vol. 72, 1975, pp. 49-65.

14) GEISSLER, W., "Three-Dimensional Laminar Boundary Layer over a Body of Revolution at Incidence and with Separation", AIAA Journal, Vol. 12, No. 12, 1974, pp. 1743-45.

15) PATEL, V.C. and CHOI, D.H., "Calculation of Three-Dimensional Laminar and Turbulent Boundary Layers on Bodies of Revolution at Incidence", in Turbulent Shear Flows II, Selected Papers from the 2nd Intern. Symp., London, ed. by L.J.S. Bradbury, F. Durst, B.E. Launder, F.W. Schmidt, J.H. Whitelaw (Springer, New York), 1980, pp. 199-217.

16) CEBECI, T., KHATTAB, A.K. and STEWARTSON, K., "Prediction of Three-Dimensional Laminar and Turbulent Boundary Layers on Bodies of Revolution at High Angles of Attack", in Turbulent Shear Flows II, Selected Papers from the 2nd Intern. Symp., London, ed. by L.J.S. Bradbury, F. Durst, B.E. Launder, F.W. Schmidt, J.H. Whitelaw (Springer, New York), 1980, p. 189-198.

17) CEBECI, T., KHATTAB, A.K. and STEWARTSON, K., "Studies on Three-Dimensional Laminar and Turbulent Boundary Layers on Bodies of Revolution at Incidence. I. Nose Separation", AIAA Paper 79-0138, 1979.

18) CEBECI, T., KHATTAB, A.K. and STEWARTSON, K., "Three-Dimensional Laminar Boundary Layers and the OK of Accessibility", Journal of Fluid Mechanics, Vol. 107, 1981, pp. 57-87.

19) STOCK, H.W., "Laminar Boundary Layers on Inclined Ellipsoids of Revolution", Z. Flugwiss. Weltraumforschung, Vol. 4, 1980, pp. 217-224.

20) SCHNEIDER, G.R., "Calculation of Three-Dimensional Boundary Layers on Bodies of Revolution at Incidence", Proc. 5th USAF-FRG Data Exchange Agreement Meeting, AFFDL-TR-80-3088, 1980, pp. 287-305.

21) RAGAB, S.A., "A Method for the Calculation of Three-Dimensional Boundary Layers with Circumferential Reversed Flow on Bodies", AIAA Paper 82-1023, 1982.

22) PATEL, V.C. and BAEK, J.H., "Calculation of Three-Dimensional Boundary Layers on Bodies at Incidence", Iowa Institute of Hydraulic Research, Report No. 256, 1982.

23) NASH, J.F. and SCRUGGS, R.M., "An Implicit Method for the Calculation of Three-Dimensional Boundary Layers on Fuselage Configurations", Report LG76ER0199, Sybucon Inc., Atlanta, 1976.

24) WANG, K.C., "New Developments About Open Separation", San Diego State University, Report AE&EM TR-82-02, 1982.

25) LEGENDRE, R., "Lignes de Courant d'un Ecoulement Continu", Recherche Aerospatiale, No. 105, 1965, pp. 3-9.

26) PEAKE, D.J. and TOBAK, M., "Three-Dimensional Interactions and Vortical Flows with Emphasis on High Speeds", AGARDograph 253, 1980.

27) LIGHTHILL, M.J., "Aerodynamical Background", in Laminar Boundary Layers, ed. L. Rosenhead, Ch. 2, p. 79, Oxford University Press, 1963.

28) PATEL, V.C., "Some Aspects of Thick Three-Dimensional Boundary Layers", Presented at the 14th Symposium on Naval Hydrodynamics, Ann Arbor, Michigan, Aug. 23-27, 1982. To be published in the Proceedings.

SESSION 10

STRUCTURE OF THE TURBULENT SHEAR FLOW IN SHIP BOUNDARY LAYERS

A. Yücel Odabasi
The British Ship Research Association,
Wallsend, Tyne and Wear, England

Melvyn E. Davies
National Maritime Institute
Feltham, Middlesex, England

Abstract

This paper summarizes the findings of a research conducted on the behavior of turbulent shear layers around the aft-ends of ships during a recent project on Propeller-Hull Interactive Vibration Excitation (PHIVE) jointly undertaken by the British Ship Research Association (BSRA) and the National Maritime Institute (NMI).

The paper commences with a brief description of the full flow study within the PHIVE project where the research strategy and the aims are clearly outlined. To provide a suitable background a selective review of the assumptions commonly employed in turbulent shear flow calculations is provided and a critical evaluation of some commonly used turbulence models (e.g. algebraic eddy viscosity, $k-\epsilon$, and turbulent kinetic energy models) is made. Next, the flow around the aft-ends of ships is introduced as an example of nonhomogeneous and anisotropic complex shear flows with the aid of wind tunnel measurement made on scaled ship models by NMI. A brief description of the experimental setup, and measurement and calibration techniques is provided in an appendix.

To provide further insight into the flow structure, relative magnitudes and gradients of the elements of the Reynolds stress terms τ and of shear

transport velocities as well as typical mixing length, eddy viscosity and integral length scale distributions are presented. As a new phenomenon the concept of shear separation (see Figure) is introduced and its differences with respect to free vortex layer separation are brought out. The paper points out similar flow structures also exist in boundary layers with weak shock-wave interaction and in this respect a discussion is given on the roles of curvature and pressure gradient effects.

The following part of the paper is devoted to the numerical simulation and correlation studies undertaken by BSRA. Here a computer program suite developed to calculate the flow around the aft-ends and near wakes of ships is briefly described and a comparison of computed results with experimental data is presented. Conceptual and numerical difficulties associated with the calculation of flows after shear separation is discussed and a possible memory effect on the wall shear velocity is introduced. Initial results of a newly developed procedure are presented.

Finally the utility and usefulness of the results obtained so far are summarized and the need for further experimental and theoretical research is emphasized. Certain areas are offered for immediate attention.

STERN BOUNDARY-LAYER FLOW ON TWO THREE-DIMENSIONAL BODIES HAVING ELLIPTICAL TRANSVERSE CROSS-SECTIONS

T.T. Huang, N.C. Groves and G.S. Belt
David W. Taylor Naval Ship R&D Center
Bethesda, Maryland 20084

Abstract

A comprehensive set of experimental pressure, velocity and turbulence data are presented for two simple three-dimensional models having 2:1 and 3:1 elliptical transverse cross sections. The Lighthill displacement body concept is used to predict the pressure distributions over the models. The predicted pressure distributions are in good agreement with the measured pressure distributions. Around the corner regions over the major axes of the models the three-dimensional boundary-layer equations do not predict well the measured mean velocity distributions. In these regions the boundary layers are much thicker than the cross section dimensions and differences in curvatures between the flow and body surface are very large. However, over large areas of relatively flat body surfaces, the computed and measured mean velocity distributions are in good agreement. As was found in the axisymmetric case, the measured eddy viscosity and mixing-length parameters in the stern region are much smaller than those of a thin boundary layer.

I. Introduction

Many single-screw ship propellers operate inside of thick stern boundary layers. Satisfactory predictions of turbulent boundary-layer characteristics can be made for the forward portions of a body by solving the boundary-layer equations in either integral or differential forms. However, at the ship stern, the thickness of the boundary layer increases rapidly, mainly due to the diminishing cross-sectional area. The thickness of the stern boundary layer usually exceeds the thickness of the body. Detailed measurements of the turbulent boundary layer characteristics in the thick stern boundary layers of axisymmetric bodies have been made by Huang et al. [1,2] in order to gain insight into the physics of thick stern boundary layers. These measurements have been used to validate the displacement body concept as suggested by Lighthill [3] for solving viscous-inviscid flow interaction and to obtain an improved turbulence model for computing thick axisymmetric boundary-layers on two convex sterns and one concave stern [1,2]. The present work is an initial investigation into extending to three-dimensions the previous studies on axisymmetric bodies by Huang et al. [1,2].

Experiments have been made to measure the flow across the thick stern boundary layers of two simple three-dimensional bodies having 2:1 and 3:1 elliptical transverse cross sections. The 10.06 ft (3.07 m) fiberglass models were tested in the DTNSRDC Anechoic Flow Facility at a speed of 100 ft/sec (30.48 m/s), resulting in an overall Reynolds number based on length of 6.5×10^6 . Pressure taps, embedded in the models, were used to measure the pressure distributions on the surface. Velocity and turbulence characteristics were measured using a two-element hot-film sensor and were analyzed with an on-line computer. Measurements include mean velocity profiles, turbulence intensities, Reynolds stresses, eddy viscosity, and mixing-length.

Several experimental quantities are compared with data from existing theoretical methods using an iterative scheme. The potential flow distribution on the body surfaces is computed using an updated version of the Hess-Smith [4] Potential Flow Computer Program, known as the XYZ Potential Flow (XYZPF) computer code of Dawson and Dean [5]. Initial boundary-layer computations, using the McDonnell Douglas Corporation [6], Cebeci, Chang, Kaups (C²K) computer code, are made using the first potential-flow pressure distribution on original body. The potential and boundary-layer flow calculations are repeated once for a modified body and wake geometry, formed by adding the computed effective displacement thickness. Flow separation is predicted for both models by the C²K code at axial locations x greater than 89 percent of the body length L and angular locations greater than 80 degrees, based on the pressure distributions of the original bodies. Flow separation is predicted at $x/L = 0.93$ for the 2:1 elliptical model and at $x/L = 0.91$ for the 3:1 elliptical model if the pressure distributions of the displacement bodies are used in the boundary-layer calculations. Flow visualization indicated that flow separation occurred at $x/L = 0.91$ for the 2:1 elliptical model and at $x/L = 0.90$ for the 3:1 elliptical model. The region of separation is limited to angles between 80 and 90 degrees (See Figure 1 for geometric details). Comparison of predicted and measured results shows that this procedure predicts accurate values of pressure over most of the bodies and accurate mean velocity profiles in locations where the boundary layer is thin compared with cross-sectional area. The measured eddy viscosity distribution is compared with the thin boundary-layer model of Cebeci [6,7] and is found to be smaller than predictions.

In the following sections, the experimental techniques and model geometries are given in detail. The experimental data are presented and compared with theoretical predictions.

II. Wind Tunnel and Model

The experimental investigation was conducted in the DTNSRDC Anechoic Wind Tunnel Facility. The wind tunnel has a closed jet test section that is 8 ft (2.4 m) square and 13.75 ft (4.19 m) long. The corners have fillets which are carried through the contraction. The test section is followed by an acoustically-lined large chamber 23.5 ft (7.16 m) long. It was found previously, by Huang et al., [1] that the ambient free-stream turbulence levels are 0.075, 0.090, 0.100 and from 0.12 and 0.15 for free-stream velocities U_∞ of 24.4, 30.5, 38.1, and 45.7 m/s, respectively. Integration of the measured noise spectrum levels in the test section from 10 to 10,000 Hz indicated that the typical background acoustic noise levels at 30.5 m/s were about 93 dB re 0.0002 dyne/cm² (0.0002 Pa). These levels of ambient turbulence and acoustic noise were con-

sidered low enough so as not to unfavorably affect the measurement of boundary-layer characteristics. The maximum air speed that can be achieved is 200 ft/sec (61 m/s); in the present experiments the wind tunnel velocity was held constant at 100 ft/sec (30.48 m/s).

Two simple three-dimensional models having 2:1 and 3:1 elliptical transverse cross sections were chosen for investigation. The longitudinal distributions of the transverse cross-sectional areas of the two simple three-dimensional models are equal to that of the axisymmetric body 1 of reference 1. Thus, the three models have the same volume and longitudinal distribution of buoyancy. However, the 2:1 and 3:1 elliptical models have 9% and 23% more wetted surface area, respectively, than the axisymmetric body. The two models have the same bow entrance length of 1.667 ft (50.8 cm) and the same afterbody length of 3.949 ft (120.4 cm). The total model length is 10.06 ft (306.6 cm). The length of parallel middle body is 4.444 ft (135.4 cm). The 2:1 elliptical model has a maximum major axis of 1.296 ft (39.5 cm) and a maximum minor axis of 0.648 ft (19.8 cm). The 3:1 elliptical model has a maximum major axis of 1.588 ft (48.4 cm) and a maximum minor axis of 0.635 in (16.1 cm). A schematic of the two three-dimensional afterbodies with the 2:1 and 3:1 elliptical cross sections is shown in Figure 1. The major and minor elliptical axes are shown in Figure 1 as a and b, respectively.

The 3:1 elliptical model was initially supported by two streamlined struts separated by one-third of the model length. The struts are 0.5 in. (1.27 cm) thick with a 1.5 in. (3.81 cm) chord upstream and 2.25 in. (5.72 cm) thick with a 6.0 in. (15.24 cm) chord downstream. The model is designed to rotate 90 degrees radially about a center axis to permit vertical traversing normal to the surface. Pressure taps (see section on Instrumentation). The disturbances generated by the supporting struts were within the region below the horizontal center-plane. Therefore, all of the experimental data were taken above the model on the vertical center-plane along the upper meridian where there was no effect from the supporting struts. On both models, one-half of the model length protruded beyond the closed jet working section into the open-jet section. The ambient static pressure coefficients across and along the entire open-jet chamber (7.2 m x 7.2 m x 6.4 m) were found to vary less than 0.3 percent of the dynamic pressure. Tunnel blockage and longitudinal pressure gradient effects along the tunnel length were almost completely removed by testing the afterbody in the open-jet section.

A portion of the experiments on the 3:1 elliptical model were repeated with a second model support system. This second support system was also used with the 2:1 elliptical model. A streamlined strut located one foot (30.5 cm) downstream of the after end of the model, was attached to a 1.0-inch (2.54 cm) diameter supporting shaft which ran longitudinally through the center of the model. Three streamline guide wires were attached to the same shaft inside the model at the location $x/L = 4.5\%$ from the nose of the model. The differences in the measured axial velocity and the pressure coefficients between the two supporting systems were found to be less than the experimental accuracies of the measurements (one percent).

The disturbance generated by the supporting system is not significant. The models are shown in the Anechoic Wind Tunnel Facility in Figure 2.

The location of the boundary-layer transition from laminar to turbulent flow was artificially induced by a 0.024 in. (0.61 mm) diameter trip wire located at $x/L = 0.05$. Huang et al. [1] found that the trip wire effectively moved the location of the virtual origin to $x/L = 0.015$ for axisymmetric models at a length Reynolds number of 5.9×10^6 . The virtual origin [8] for the turbulent flow is defined such that the sum of the laminar frictional drag from the nose to the trip wire, the parasitic drag of the trip wire, and the turbulent frictional drag aft of the trip wire is equal to the sum of the laminar frictional drag from the nose to the virtual origin and the turbulent frictional drag from the virtual origin to the after end of the model. The virtual origin locations for the three-dimensional body are expected to be different for different streamlines. Due to the limited number of grid locations used in the present calculations, the location of the transition for the C^2K boundary-layer calculation is set at a constant value of $x/L = 0.030$. The computed differences in velocities using $x/L = 0.01$ and $x/L = 0.03$, for axisymmetric body 1, [1,2] are found to be less than 0.1 percent of the free-stream velocities in the tail region. Thus, the error of using the constant transition location of $x/L = 0.03$ for the present C^2K computation is expected to be negligible.

III. Instrumentation

A series of 0.031 in. (0.8 mm) diameter pressure taps were embedded normal to the surface of the stern at numerous locations. When a model was rotated about its axis, the pressure taps were at the upper meridian location. Additional taps were added for model alignment; see Figures 3a and 3b. A model was aligned by balancing the surface static pressure about a line of symmetry. From Figure 3b, a model is aligned when symmetrically located pressure taps at c and d, and at e and f, give equal pressures, i.e., $p(c) = p(d)$, and $p(e) = p(f)$. Each model was rotated to the test positions and the alignment was checked by the pressure balance technique. A Preston tube using a 0.072 in. (1.83 mm) inside diameter was attached and aligned with the flow at the pressure taps to measure the shear stress. The Preston tube was calibrated in a 1-in. (2.54 cm) diameter water-pipe flow facility described by Huang and von Kerczek [9]. These pressure taps were connected to a multiple pressure scanivalve system that takes one integral pressure transducer with its zeroing circuit and measures a single pressure in sequence along the stern upper meridian. The pressure transducer was designed for measuring low pressures of up to 1 psi (6.895×10^{-3} Pa). The zero-drift linearity, scanivalve hysteresis, and pressure transducer zeroing circuit were carefully checked and the overall accuracy was found to be within 0.5 percent of the dynamic pressure.

The mean axial and radial velocities and the turbulence intensities for the Reynolds stress calculations were measured by a TSI, Inc. Model 1241-20 "X" type hot-film probe. The probe elements are 0.002 in. (0.05 mm) in diameter with a sensing

length of 0.04 in. (1.0 mm). The spacing between the two cross elements is 0.04 in. (1.0 mm). A two-channel hot-wire and hot-film anemometer with linearizers was used to monitor the response of the hot-film probe. A temperature compensating sensor (probe) was used with each hot-film element to regulate the operating temperature of the sensor with changes in air temperature. The "X" hot film and its temperature-compensated sensor were calibrated together through the expected air temperature-range and supplied with their individual linearization polynomial coefficients at the factory.

The frequency response of the anemometer system, for reliable measurements claimed by the manufacturer, is 0 to 100 kHz. Calibration of the "X" hot film was made before and after each set of measurements. It was found that the hot-film anemometer system had a ± 0.5 percent accuracy, ± 0.75 ft/sec (± 0.23 m/s) accuracy at the free-stream velocity of 150 ft/sec (45.72 m/s), during the entire experiment. An estimate was made of the crossflow velocity by yawing the "X" hot-film probe in the free stream. It was found that the cross-flow velocities were about one percent of the free-stream velocity.

The linearized signals were fed into a Time/Data Model 1923-C real-time analyzer. Both channels of the analog signal were digitized at a rate of 128 points per second for 8 sec. These data were immediately analyzed by a computer to obtain the individual components of mean velocity, turbulence fluctuation, and Reynolds stress on a real time basis.

A traversing system with a streamlined strut was mounted on a guide plate that permitted the traverse to be locked in various stationary positions parallel to the longitudinal model axis.

IV. Viscous-Inviscid Interaction

Lighthill's displacement body concept [3] was used to compute the viscous-inviscid interaction of the two simple three-dimensional models. The potential flow is calculated by the Hess-Smith [4] potential flow computer program. The version used is the XYZ Potential Flow (XYZPF) computer code updated by Dawson and Dean [5]. The initial input offsets to XYZPF code are shown in Figure 1. The three-dimensional boundary layer over the body is calculated by the differential method of Cebeci, Chang, and Kaups (denoted C²K) [6].

The three-dimensional displacement thickness δ_{3D} derived by Lighthill [3],

$$\delta_{3D} = \delta_x - \frac{1}{U_e h_z} \frac{\partial}{\partial z} \int_0^x U_e h_x \delta_z dx \quad (1)$$

is used to calculate the boundary-layer displacement effect on the body. The streamwise and transverse "volume-flow thickness" δ_x and δ_z are

$$\delta_x = \frac{1}{U_e} \int_0^\infty (U_e - u) dy, \quad \delta_z = \frac{1}{U_e} \int_0^\infty v dy \quad (2)$$

and (x,z) form any orthogonal system of coordinates on the surface, such that the distance between the point (x,z) and (x + dx, z) is $h_x dx$ while that between (x,z) and (x, z + dz) is $h_z dz$, y is taken as

normal distance from the surface. The velocities in the x,y,z directions are u,v,w and the values of u and w just outside the boundary layer are U_e and W_e . On the symmetric lines of the major and minor axes, the transverse "volume-flow thickness" δ_z is zero.

An equivalent body of revolution is constructed to compute the displacement wake of the simple 3-D models. The computed distributions of the three-dimensional values of C_p and the local values of the offset at each meridian are used as the distributions of C_p and radius for the equivalent body of revolution. The integral relations of Granville [10] are used to calculate the displacement effect of the wake following the computation procedure given by Wang and Huang [11]. The differential equation for the momentum of an axisymmetric wake is

$$\frac{d\Omega}{dx} + (h+2) \frac{\Omega}{U_e} \frac{dU_e}{dx} = 0 \quad (3)$$

where $\Omega = \int_0^\delta (1 - \frac{u}{U_e}) \frac{u}{U_e} r dr$, momentum area

$\Lambda^* = \int_0^\delta (1 - \frac{u}{U_e}) r dr$, displacement area

$h = \frac{\Lambda^*}{\Omega}$, axisymmetric shape factor

At far wake ($x/L > 2$), the momentum loss of the flow should be equal to the total drag on the body. Therefore, the momentum area at far wake, Ω_∞ , is equal to $C_T S/2$, where C_T is the computed total drag coefficient and S is the surface area of the equivalent body of revolution. An empirical relation of Granville [10] for h

$$h = 1 + (1.42 - 1) \left[\frac{\ln(U_\infty/U_e)}{\ln(U_\infty/U_t)} \right]^{1/7} \quad (4)$$

is used. Here, U_∞ is the free stream velocity, U_e and U_t are the edge velocities on the surface of the displacement body at any point on the wake, and at the tail, respectively. Equations (3) and (4) can then be used to calculate Ω and Λ^* in terms of Ω_∞ and U_t . The wake thickness is given by

$$a^* = \sqrt{2\Lambda^*}$$

In the near wake region $x_u/L \leq x/L \leq x_d/L$, where neither the computed three-dimensional displacement surface nor the equivalent far wake equations (3) and (4) are accurate enough to generate a smooth surface for potential flow calculation, a fifth-degree polynomial is used to connect the upstream and downstream displacement surfaces. Usually, x_u/L is taken to be 0.93 and x_d/L is taken to be 1.05. However, for meridians having boundary layer separation, the matching points x_u/L must be moved a small distance upstream of the predicted separation point. At the upstream matching point, the offset and surface slope of the faired displacement surface are set equal to their respective values for the computed three-dimensional displacement surface, while these values at the downstream point are set equal to the computed displacement wake. The iteration process, consisting of calculating the pressure distribution over successive displacement bodies, continues until a given convergence criterion is met or until the prescribed number of iterations is exceeded. In the present

computation, only one iteration is used.

The C²K method consists of using Keller's two-point finite difference method [12] and Cebeci and Stewartson's procedure [6] for computing flows in which the transverse velocity component contains regions of reverse flow to solve three-dimensional boundary-layer equations. The governing equations for three-dimensional incompressible laminar and turbulent flows are given by

Continuity Equation

$$\frac{\partial}{\partial x} (u h_2 \sin \bar{\theta}) + \frac{\partial}{\partial z} (w h_1 \sin \bar{\theta}) + \frac{\partial}{\partial y} (v h_1 h_2 \sin \bar{\theta}) = 0 \quad (5a)$$

x-Momentum Equation

$$\begin{aligned} \frac{u}{h_1} \frac{\partial u}{\partial x} + \frac{w}{h_2} \frac{\partial u}{\partial z} + v \frac{\partial u}{\partial y} - K_1 u^2 \cot \bar{\theta} + K_2 w^2 \\ \csc \bar{\theta} + K_{12} u w = - \frac{\csc^2 \bar{\theta}}{h_1} \frac{\partial (p/\rho)}{\partial x} + \\ \frac{\cot \bar{\theta} \csc \bar{\theta}}{h_2} \frac{\partial (p/\rho)}{\partial z} + \frac{\partial}{\partial y} (v \frac{\partial u}{\partial y} - \overline{u'v'}) \end{aligned} \quad (5b)$$

z-Momentum Equation

$$\begin{aligned} \frac{u}{h_1} \frac{\partial w}{\partial x} + \frac{w}{h_2} \frac{\partial w}{\partial z} + v \frac{\partial w}{\partial y} - K_2 w^2 \cot \bar{\theta} + K_1 u^2 \csc \bar{\theta} + \\ K_{21} u w = \frac{\cot \bar{\theta} \csc \bar{\theta}}{h_1} \frac{\partial (p/\rho)}{\partial x} - \\ \frac{\csc^2 \bar{\theta}}{h_2} \frac{\partial (p/\rho)}{\partial z} + \frac{\partial}{\partial y} (v \frac{\partial w}{\partial y} - \overline{v'w'}) \end{aligned} \quad (5c)$$

where u , v , and w = velocity components in the x , y , and z directions, respectively

x, y , and z = nonorthogonal boundary-layer coordinates, as given in Reference 6

ρ = fluid density

p = pressure on the body

h_1, h_2 = metric coefficients

K_1, K_2 = geodesic curvatures of the curves $z = \text{constant}$ and $x = \text{constant}$, respectively

K_{12}, K_{21} = functions of the geodesic curvatures and metric coefficients

$\bar{\theta}$ = angle between the coordinates x and z

ν = kinematic viscosity of the fluid

$\overline{u'v'}, \overline{v'w'}$ = Reynolds stresses

The eddy-viscosity concept is used to relate the Reynolds stresses to the mean velocity profiles by

$$\overline{u'v'} = \begin{cases} \epsilon_1 \frac{\partial u}{\partial y}, & \text{inner region } 0 \leq y \leq y_c \\ \epsilon_0 \frac{\partial u}{\partial y}, & \text{outer region } y_c < y \end{cases} \quad (6)$$

$$\text{where } \epsilon_1 = \nu^2 \left[\left(\frac{\partial u}{\partial y} \right)^2 + \left(\frac{\partial w}{\partial y} \right)^2 + 2 \cos \bar{\theta} \left(\frac{\partial u}{\partial y} \right) \left(\frac{\partial w}{\partial y} \right) \right]^{1/2}$$

which is the eddy viscosity in the inner region

$$\text{with } \lambda = 0.4y \left[1 - \exp \left(-\frac{y}{A} \right) \right]$$

$$A = 26 \frac{\nu}{u_\tau}$$

$$u_\tau = \left(\frac{\tau_{tw}}{\rho} \right)^{1/2}$$

$$\tau_{tw} = \nu \left[\left(\frac{\partial u}{\partial y} \right)_w^2 + \left(\frac{\partial w}{\partial y} \right)_w^2 + 2 \cos \bar{\theta} \left(\frac{\partial u}{\partial y} \right)_w \left(\frac{\partial w}{\partial y} \right)_w \right]^{1/2}$$

$$\epsilon_0 = 0.0168 \left| \int_0^\infty (u_{te} - u_t) dy \right|$$

$$u_{te} = (u_e^2 + w_e^2 + 2u_e w_e \cos \bar{\theta})^{1/2}$$

$$u_t = (u^2 + w^2 + 2uw \cos \bar{\theta})^{1/2}$$

y_c = is the value of y at which $\epsilon_1 = \epsilon_0$

The characteristics of Lighthill's [3] three-dimensional thickness are demonstrated in Figures 4 and 5 for the 2:1 elliptical model and in Figures 6 and 7 for the 3:1 elliptical model. Figures 4 and 6 show the distributions of the streamwise integration of δ_z , while Figures 5 and 7 show the three-dimensional effect in terms of the ratios of the displacement thickness associated with the transverse "volume-flow thickness" δ_z to the streamwise "volume-flow thickness" δ_x . The importance of the three-dimensional nature of the displacement body is clearly demonstrated in Figures 4 through 7. At each longitudinal station, the computed distribution of the three-dimensional displacement δ_{3D} over the transverse cross section is used to generate a faired displacement body for the next potential-flow computation. Typical displacement surfaces after one iteration for the two elliptical models are shown in Figure 1.

V. Comparison of Experimental and Theoretical Results

All data are presented in the coordinate system used to experimentally measure the boundary-layer flow. The coordinate system, denoted $x-n_e-\theta$, is given in Figures 1 and 3. The axial coordinate x is measured from the nose of the body and passes through the center of the elliptic profile. The coordinates n_e and θ are defined along an axial cut normal to the x -axis, i.e., in the $y-z$ plane. The normal component n_e is measured from the model surface and is normal to the elliptic surface. The angular coordinate θ is defined as the angle, in degrees, measured from the z -axis to the line joining the surface offset and elliptic center.

Pressure Distribution

The steady pressure was measured along the stern surfaces using pressure taps. The pressure coefficient C_p is computed from the measured pressures by the relationship

$$C_p = \frac{p - p_o}{p_t - p_s} = \frac{-p_o}{\frac{1}{2} \rho U_o^2} \quad (7)$$

where p = measured local static pressure

p_o = measured ambient pressure

p_t = measured dynamic total pressure

P_s = measured static pressure
 ρ = mass density of the fluid
 U_o = free-stream velocity

The measured values of the pressure coefficients are compared in Figures 8 and 9 with two analytically-predicted distributions of pressure coefficient. The dashed curve, denoted by potential flow theory, represents the predictions of the XYZ potential flow method of Dawson and Dean [5] before using the displacement body concept. The solid curve shows C_p on the displacement body after one iteration of the displacement body procedure. The computed pressure coefficient is

$$C_p = 1 - \left(\frac{U_e}{U_o} \right)^2 \quad (8)$$

where U_e is the computed potential flow velocity on the displacement body and U_o is the free-stream velocity, 100 ft/sec (30.48 m/s).

After one iteration of the displacement procedure, overall agreement between theoretical and measured values of the pressure coefficient is considered reasonably good. No further iterations of the displacement method have been implemented at present.

Measured Mean Velocity and Turbulence Characteristics

Mean velocity and turbulence measurements were taken with an "X" hot-film sensor which was stepped away from the body in the n_e direction. Measurements of velocity in the axial x and normal n_e directions, u_x and v_n , respectively, were taken with the probe elements aligned vertically. The sensor elements were rotated 90 degrees to the horizontal position to measure the mean velocity w_θ in the θ direction. An on-line computer was used to collect data at a sample rate of 1024 data values in 8 sec. The root-mean-square values of turbulence velocity were recorded at each probe position and the eddy viscosity and mixing length values were computed from the measured Reynolds stresses and the measured mean velocity profiles.

Figures 10, 11, and 12 show the measured and predicted velocity profiles on the two models. The model surfaces are relatively flat and the rate of change in curvatures are small over the region of the minor axes of the models ($\theta = 0^\circ$). The boundary-layer equations are good approximations of the flow in this region. The agreement between the measured and predicted profiles are excellent along $\theta = 0^\circ$ for the entire length of the two models. The good agreement extends up to $\theta = 73^\circ$ for the 2:1 elliptical model and up to $\theta = 77^\circ$ for the 3:1 elliptical model. However, around the corner region over the major axes of the models ($\theta = 90^\circ$), the curvatures of the surfaces are relatively small and the curvatures undergo rapid change. The boundary-layer equations are not good approximations of the flow in this corner region. The poor agreement between the measured and predicted velocity profiles are anticipated. Typical discrepancy of the measured and predicted profiles is illustrated in Figure 12.

The distribution of the Reynolds stresses $-\overline{u'_x v'_n}$, $-\overline{u'_x w'_\theta}$, u'^2_x , v'^2_n , and w'^2_θ represent

the turbulence characteristics in the thick boundary layer. The mean-square turbulent velocity fluctuations u'^2_x in the axial direction and v'^2_n in the n_e direction, and the Reynolds stress $-\overline{u'_x v'_n}$ were measured with the "X" hot-film probe elements aligned vertically. The probe elements were rotated 90 degrees to the horizontal position to measure both the turbulent fluctuation w'^2_θ in the θ direction and the Reynolds stress $-\overline{u'_x w'_\theta}$. Linear interpolation was used to approximate w'^2_θ and $-\overline{u'_x w'_\theta}$ at the same off-body positions as the data measured in the vertical direction.

Eddy Viscosity and Mixing Length

The values of eddy viscosity and mixing length are not measured directly, but are obtained, as in the axisymmetric case [1,2], from the measured values of the Reynolds stress $-\overline{u'_x v'_n}$ and the mean velocity gradient $\partial u_x / \partial n_e$. The definitions used to compute these quantities are

$$\begin{aligned} \overline{u'_x v'_n} &= \epsilon \frac{\partial u_x}{\partial n_e} \\ &= \lambda^2 \left[\left(\frac{\partial u_x}{\partial n_e} \right)^2 + \left(\frac{\partial w_\theta}{\partial n_e} \right)^2 + 2 \left(\frac{\partial u_x}{\partial n_e} \right) \left(\frac{\partial w_\theta}{\partial n_e} \right) \cos \theta \right] \frac{\partial u_x}{\partial n_e} \end{aligned} \quad (9)$$

When the values of w_θ/u_x are less than 0.1 and the value of θ is 90 degrees for the present measurements, Equation (9) may be approximated by

$$\overline{u'_x v'_n} = \lambda^2 \left| \frac{\partial u_x}{\partial n_e} \right| \frac{\partial u_x}{\partial n_e} \quad (10)$$

A spline curve is used to fair the experimental data before the velocity gradient is obtained numerically.

The nondimensional distributions of the eddy viscosity $\epsilon / (U_o \delta^*)$ determined from the data of the 3:1 elliptical model are shown in Figure 13. The parameters U_δ and δ^* are defined as the potential flow velocity at the edge of the boundary layer and the planar displacement thickness, respectively, for the displacement body. The solid curve shown in these figures is the Cebeci and Smith [7] thin boundary layer formula, given by

$$\frac{\epsilon}{U_\delta \delta^*} = \frac{0.0168}{1 + 5.5 \left(\frac{n_e}{\delta^*} \right)^6} \quad (11)$$

All values of eddy viscosity for the 3:1 elliptical model are smaller than the experimentally-derived value recommended by Cebeci and Smith [7] for thin boundary layers.

The experimentally-determined distributions of the nondimensional mixing length, λ_p / δ^* , of the 3:1 elliptical model are shown in Figure 14. The solid curve in these figures represents the thin boundary-layer model of Bradshaw et al. [13]. Agreement between theory and measurements is, at best, fair for angular locations of 0 and 67 degrees; for angular locations greater than 67 degrees, the measured values of mixing length are much

smaller than the predictions.

For an axisymmetric turbulent boundary layer, Huang et al. [1,2] proposed a turbulence model relating the mixing length to the square root of the entire turbulence annulus area between the body surface and the edge of the boundary layer. The values of measured turbulence intensity, eddy viscosity, and intermittency across a turbulent boundary layer decrease from a maximum value at 60 percent of the boundary-layer thickness to zero at the outside edge of the boundary layer. The effective gross turbulence area relevant to the mixing length parameter is $[(a+0.6\delta_a)(b+0.6\delta_b)-(a+\epsilon_a)(b+\epsilon_b)]$; where ϵ_a and ϵ_b are the effective thicknesses of the separation bubble (low turbulence mixing) in the direction of the major and minor axes, a and b , respectively, of the elliptical cross-section, and δ_a and δ_b are the boundary-layer thicknesses along the a and b axes. A new empirical mixing length model is assumed to apply to a thick three-dimensional stern boundary layer. The schematic representation of effective turbulence areas, as determined by the areas between the body surfaces and the contours of $0.6\delta_r$ are shown in Figure 15. The outside edges of the effective turbulence areas are very close to the contours of $U_x^2/U_0 = 0.04$. Further outside of these edges, turbulence intensities reduce to 0.01 at the edge of the boundary layer. The mixing length parameter is assumed to be proportional to the square-root of these effective turbulence areas, e.g.,

$$l \sim \sqrt{(a+0.6\delta_a)(b+0.6\delta_b) - ab} = A(x)$$

where the value of ϵ_a is assumed to be small and will be neglected and the value of ϵ_b is zero since no separation occurs there. The values of ϵ_a and ϵ_b may not be negligible if the separation region is so large that the effective turbulence area is reduced significantly. However, in the inner region, the conventional mixing length in the wall region, Equation (2), is assumed to apply. The mixing length l is assumed to be the same at the intersection of the inner and the outer region, $y = y_c$ in Equation (6). Figures 16a through 16c show the normalized mixing length distributions for three axisymmetric bodies studied by Huang et al. [1,2]. These figures show that the measured values for the three axisymmetric models agree reasonably well; each peaking at a value of approximately 0.05. The values of l/A at various locations for the present three-dimensional models are shown in Figures 16d through 16i. The values of the nondimensional mixing length remain fairly constant over the stern with respect to both angular and axial positions.

The data in Figure 16 support the use of a revised empirical mixing length formulation. The existing thin turbulent boundary-layer method can be applied to the axisymmetric or three-dimensional elliptical body at locations forward of where the boundary layer thickness reaches 20 percent of the major or minor axis value.

Conclusions

The results of recent experimental investigations of the thick stern boundary layer on two simple three-dimensional bodies having 2:1 and 3:1 elliptic transverse cross sections are presented.

Comprehensive boundary layer measurements, including mean and turbulence velocity profiles and static pressure distributions are given in detail.

An initial attempt has been made to implement Lighthill's three-dimensional displacement body concept [3] to treat the viscous-inviscid stern flow interaction. The results of this initial investigation indicate that the use of the displacement model method significantly improves theoretical predictions of the measured pressure coefficients on the body surface. Theoretical predictions of the measured mean axial velocity profiles are excellent for the flat portion of the model surface, but are generally poor for the corner region over the major axes of the models, where model curvatures are relatively small and undergo rapid change.

Measured values of eddy viscosity and mixing length in the thick stern boundary layer were found to be smaller than values which have been proposed for thin boundary layers. Because eddy viscosity and mixing length models play an important role in boundary-layer calculations, a new empirical mixing length model is proposed and can be incorporated into the three-dimensional boundary layer computation.

Further work in this area is needed. Improvement of the flow computation method for the region where the curvatures of the body and the flow undergo rapid change are essential. A larger data base of experimental results on a variety of three-dimensional geometries will aid in the development of improved theoretical models to predict the viscous-inviscid stern flow interaction. The proposed new empirical mixing length formulation must be evaluated further.

Acknowledgments

The work described in this report was funded under the David W. Taylor Naval Ship Research and Development Center's Independent Research Program, Program Element 61152N, Project Number ZR 000 01, and DTNSRDC Work Unit 1542-103.

The authors would like to thank the staff at the DTNSRDC Anechoic Flow Facility for their co-operation during the testing and to express their gratitude to Dr. K.C. Chang for his many consultation sessions on the use of the C-K computer program.

References

1. Huang, T.T. et al., "Stern Boundary-Layer Flow on Axisymmetric Bodies," 12th Symposium on Naval Hydrodynamics, Washington, D.C. (5-9 Jun 1978). Available from National Academy of Sciences, Wash., D.C., pp. 127-147 (1979).
2. Huang, T.T. et al., "Boundary-Layer Flow on an Axisymmetric Body with an Inflected Stern," DTNSRDC Report 80/064 (1980).
3. Lighthill, M.J., "On Displacement Thickness," Journal of Fluid Mechanics, Vol. 4, pp. 383-392 (1958).
4. Hess, J.L. and A.M.O. Smith, "Calculation of

- Potential Flow About Arbitrary Bodies," Progress in Aeronautical Sciences, Vol. 8, Pergamon Press, Inc., New York (1966).
5. Dawson, C. and J. Dean, "The XYZ Potential Flow Program," NSRDC Report 3892 (1972).
 6. Cebeci, T. et al., "A General Method for Calculating Three-Dimensional Laminar and Turbulent Boundary Layers on Ship Hulls," McDonnell Douglas Corp. Report J7998 (1978). Also Ocean Engineering, Vol. 7, pp. 229-289, Pergamon Press, Great Britain (1980).
 7. Cebeci, T. and A.M.O. Smith, "Analysis of Turbulent Boundary Layers," Academic Press, New York (1974).
 8. McCarthy, J.H. et al., "The Roles of Transition, Laminar Separation, and Turbulence Stimulation in the Analysis of Axisymmetric Body Drag," 11th Office of Naval Research Symposium on Naval Hydrodynamics, London (1976).
 9. Huang, T.T. and C.H. von Kerczek, "Shear Stress and Pressure Distribution on a Surface Ship Model: Theory and Experiment," 9th Office of Naval Research Symposium on Naval Hydrodynamics, Paris (1972). Proceedings are available in U.S. Government Printing Office as ACR-203, Vol. 2.
 10. Granville, P.S., "The Calculation of the Viscous Drag of Bodies of Revolution," Report 849, David Taylor Model Basin, Bethesda, MD. July (1953).
 11. Wang, H.T. and T.T. Huang, "Calculation of Potential Flow/Boundary Layer Interaction on Axisymmetric Bodies," The American Society of Mechanical Engineers Symposium on Turbulent Boundary Layers, Niagara Falls, N.Y., pp. 47-57 (18-20 Jun 1979).
 12. Keller, H.B., "A New Difference Scheme for Parabolic Problems," Numerical Solution of Partial Differential Equations, II, J. Bramble (ed.), Academic Press, New York (1970).
 13. Bradshaw, P. et al., "Calculation of Boundary Layer Development Using the Turbulent Energy Equation," Journal of Fluid Mechanics, Vol. 28 (1967).

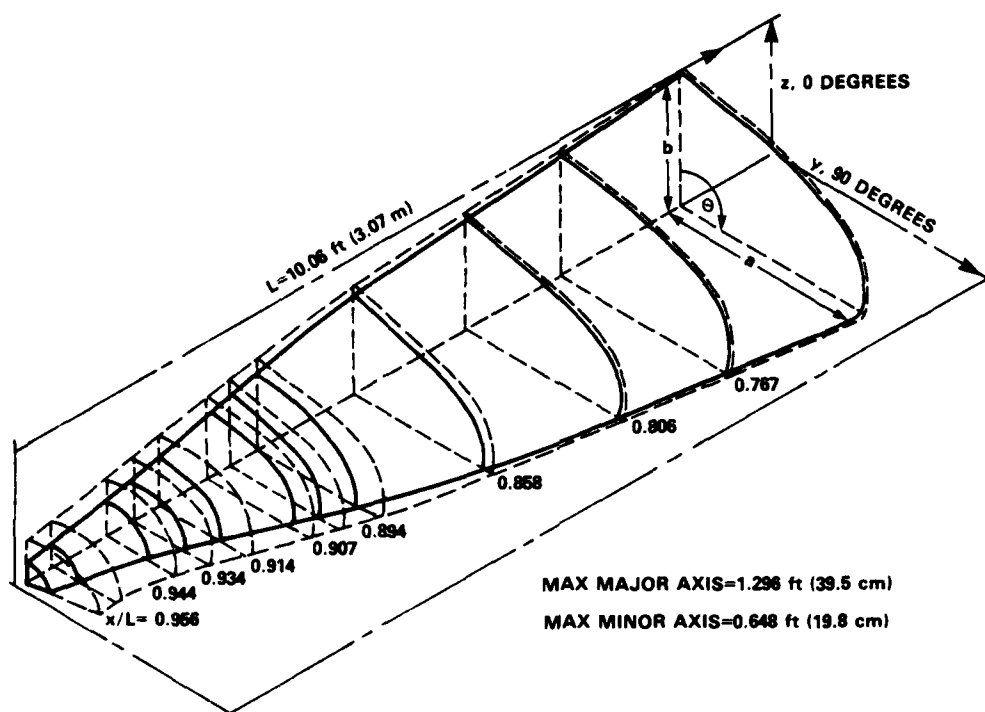


Figure 1a - Schematic of the Three-Dimensional Afterbody Having a 2:1 Elliptic Transverse Cross Section

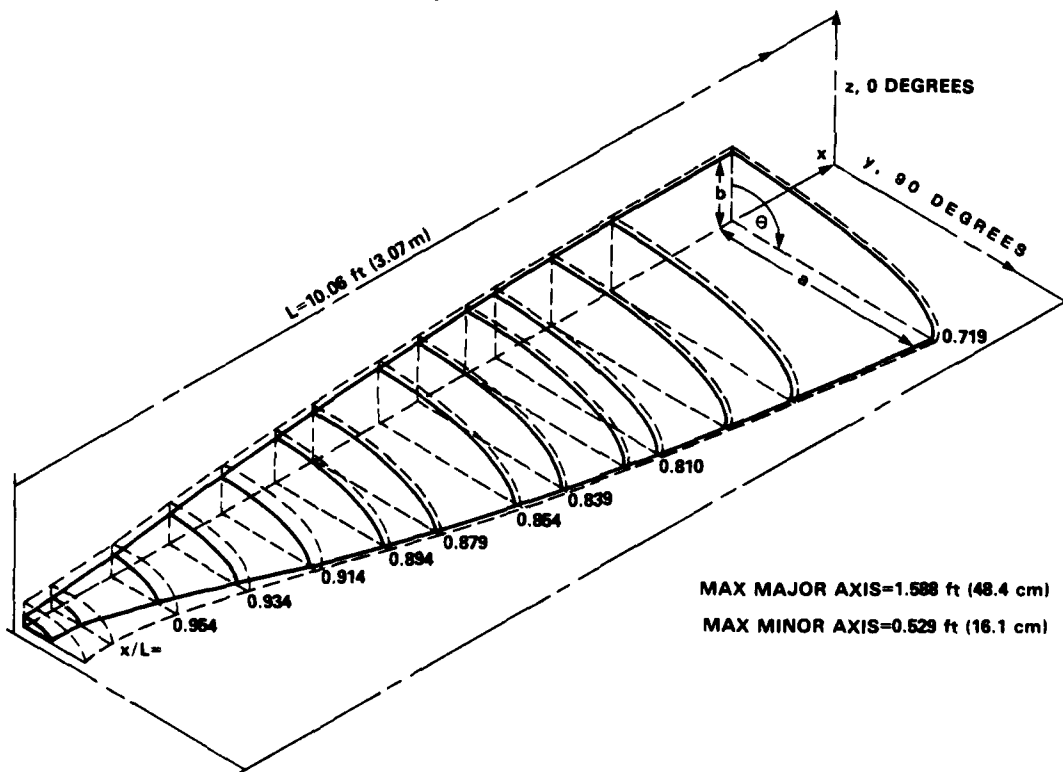


Figure 1b - Schematic of the Three-Dimensional Afterbody Having a 3:1 Elliptic Transverse Cross Section

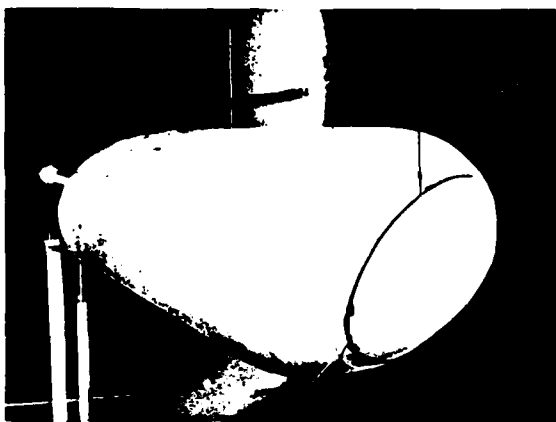


Figure 2a - The 2:1 Elliptical Model



Figure 2b - The 3:1 Elliptical Model

Figure 2 - Models Mounted in Anechoic Wind Tunnel

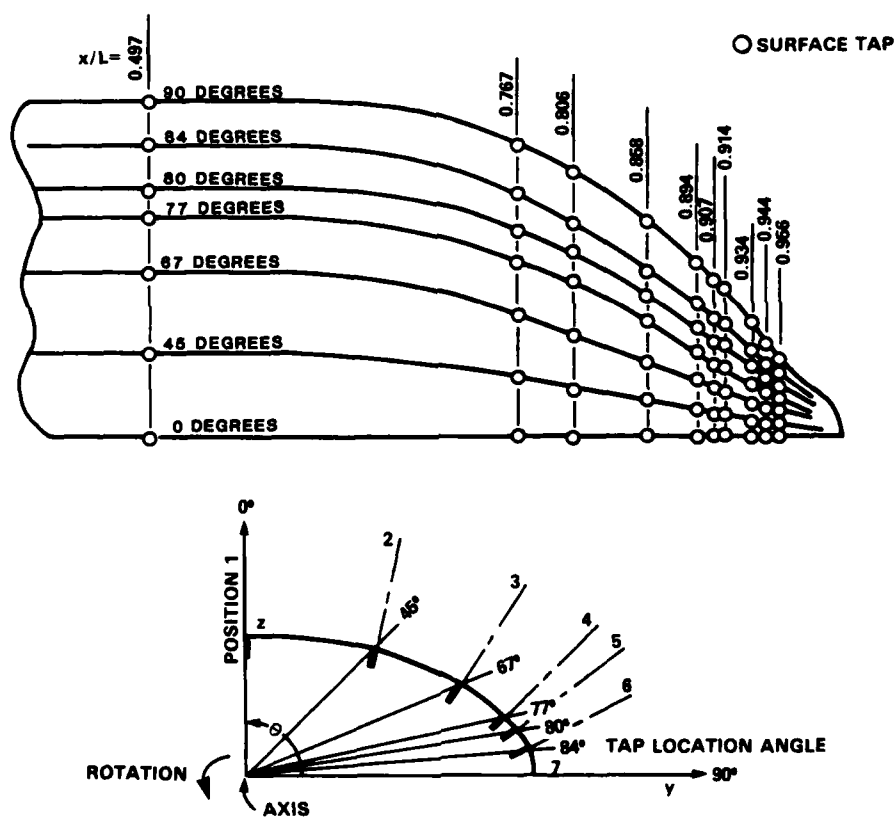


Figure 3a - Schematic of Surface Pressure Taps on the 2:1 Elliptical Model

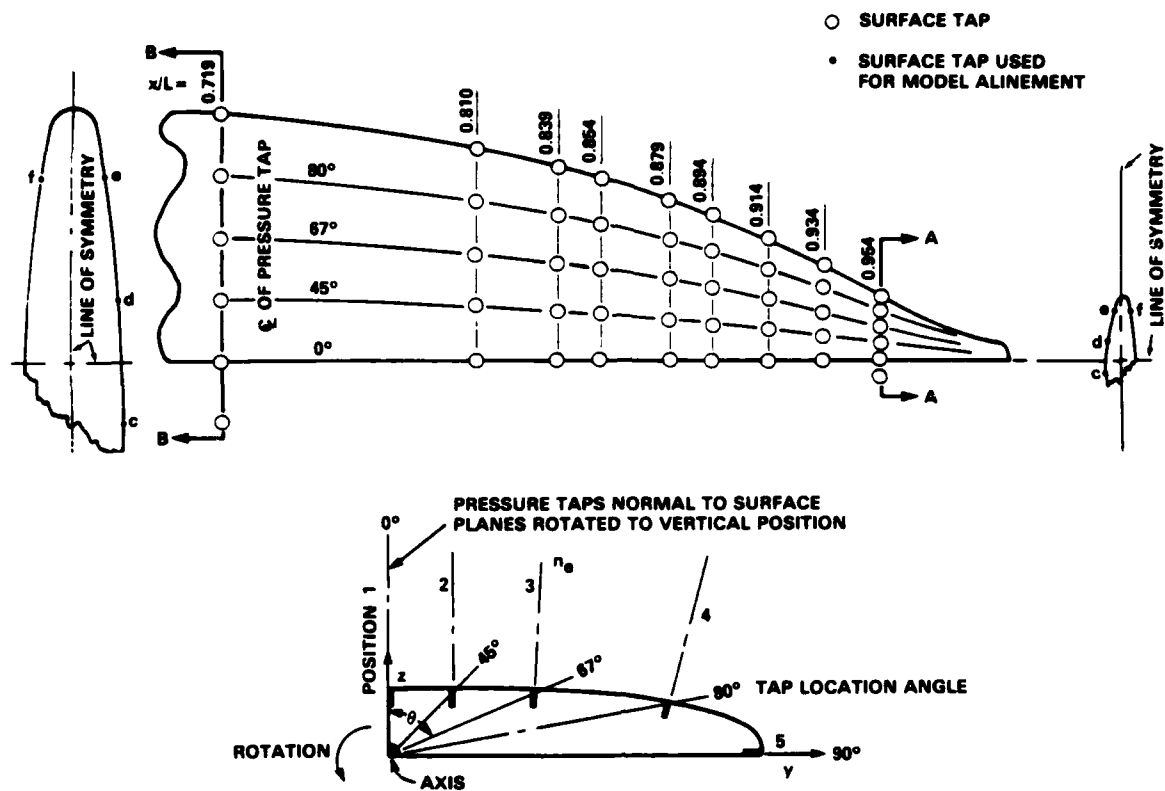


Figure 3b - Schematic of Surface Pressure Taps on the 3:1 Elliptical Model

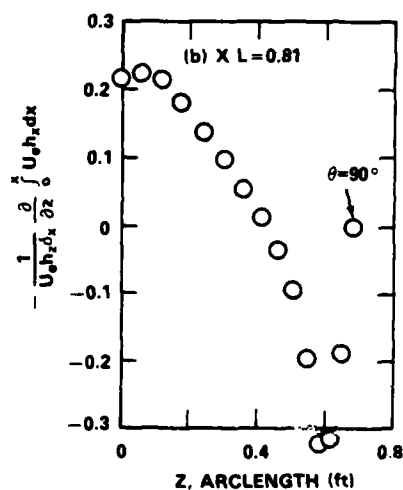
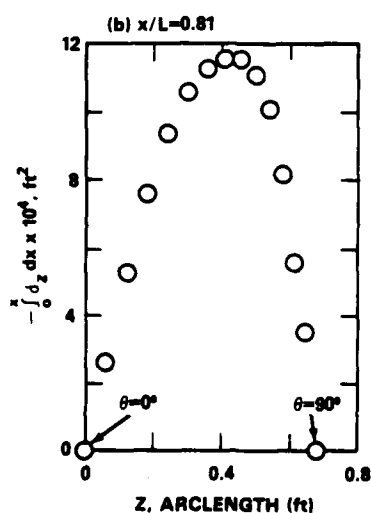
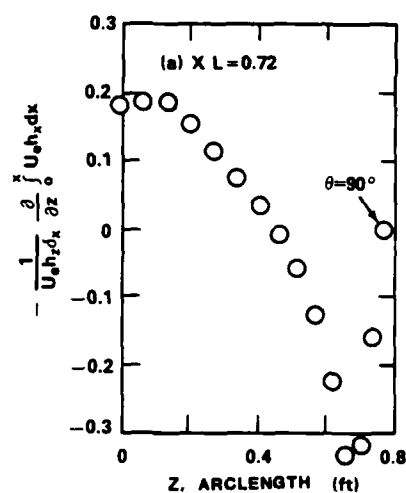
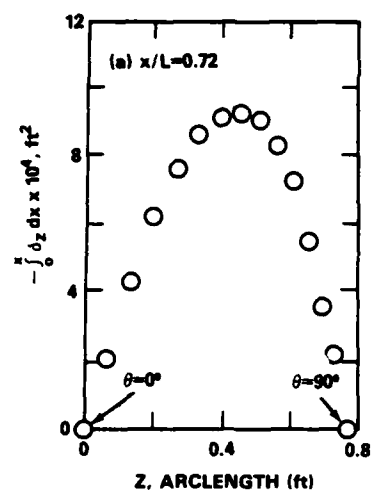


Figure 4 - Computed Distributions of $-\int_0^\pi \delta_z dx$ Over Two Transverse Cross Sections of the 2:1 Elliptical Model

Figure 5 - Computed Ratio of the Three-Dimensional Displacement Thickness Associated with δ_z to That of δ_x for the 2:1 Elliptical Model

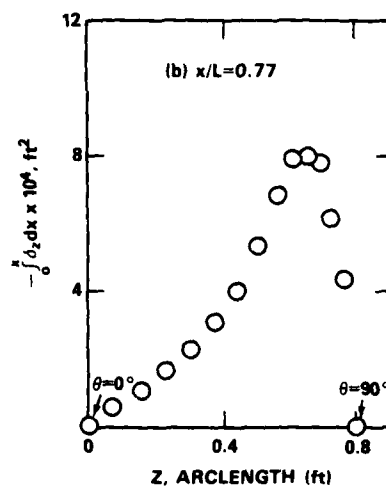
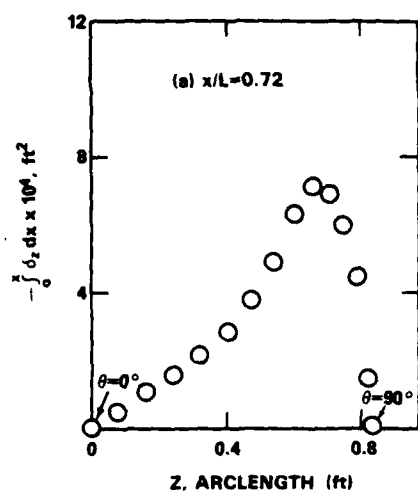


Figure 6 - Computed Distributions of $-\int_0^x \delta_z dx$ Over Two Transverse Cross Sections of the 3:1 Elliptical Model

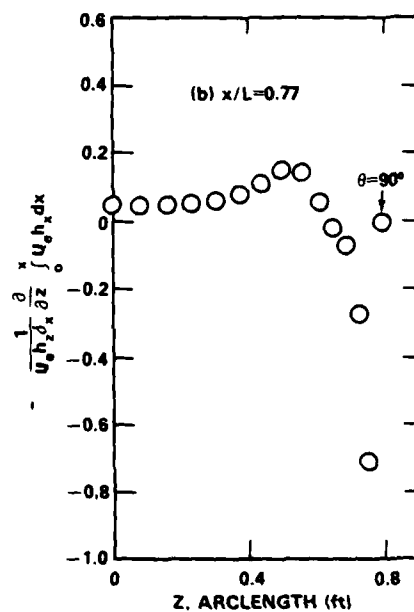
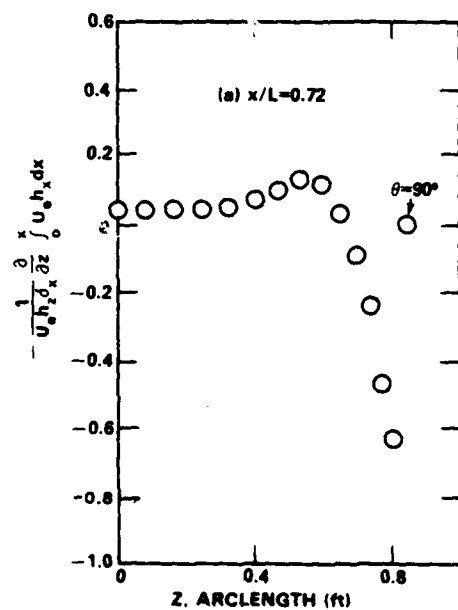


Figure 7 - Computed Ratio of the Three-Dimensional Displacement Thickness Associated with δ_z to that of δ_x for the 3:1 Elliptical Model

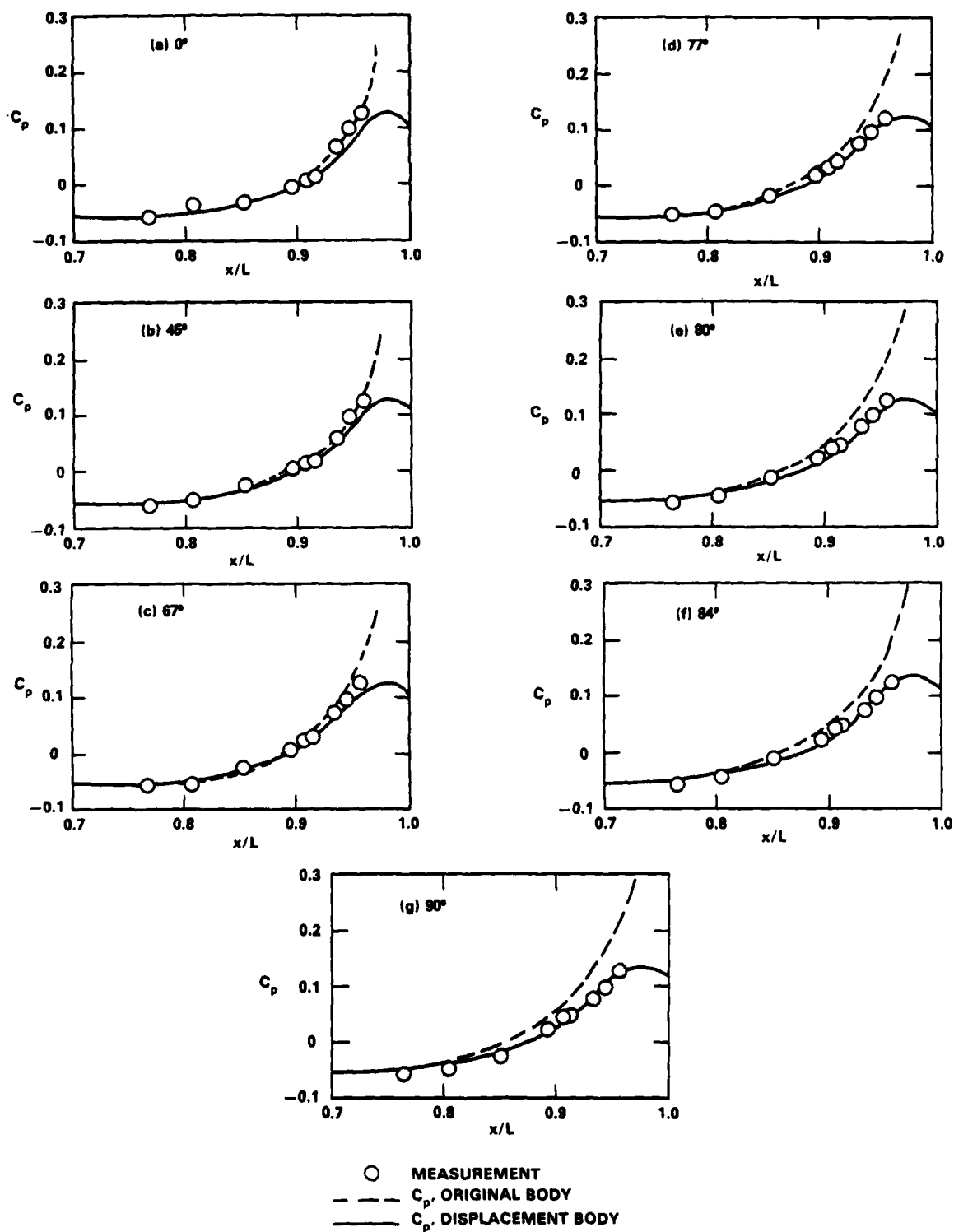


Figure 8 - Computed and Measured Stern Pressure Distributions for Seven Angular Locations on the 2:1 Elliptical Model

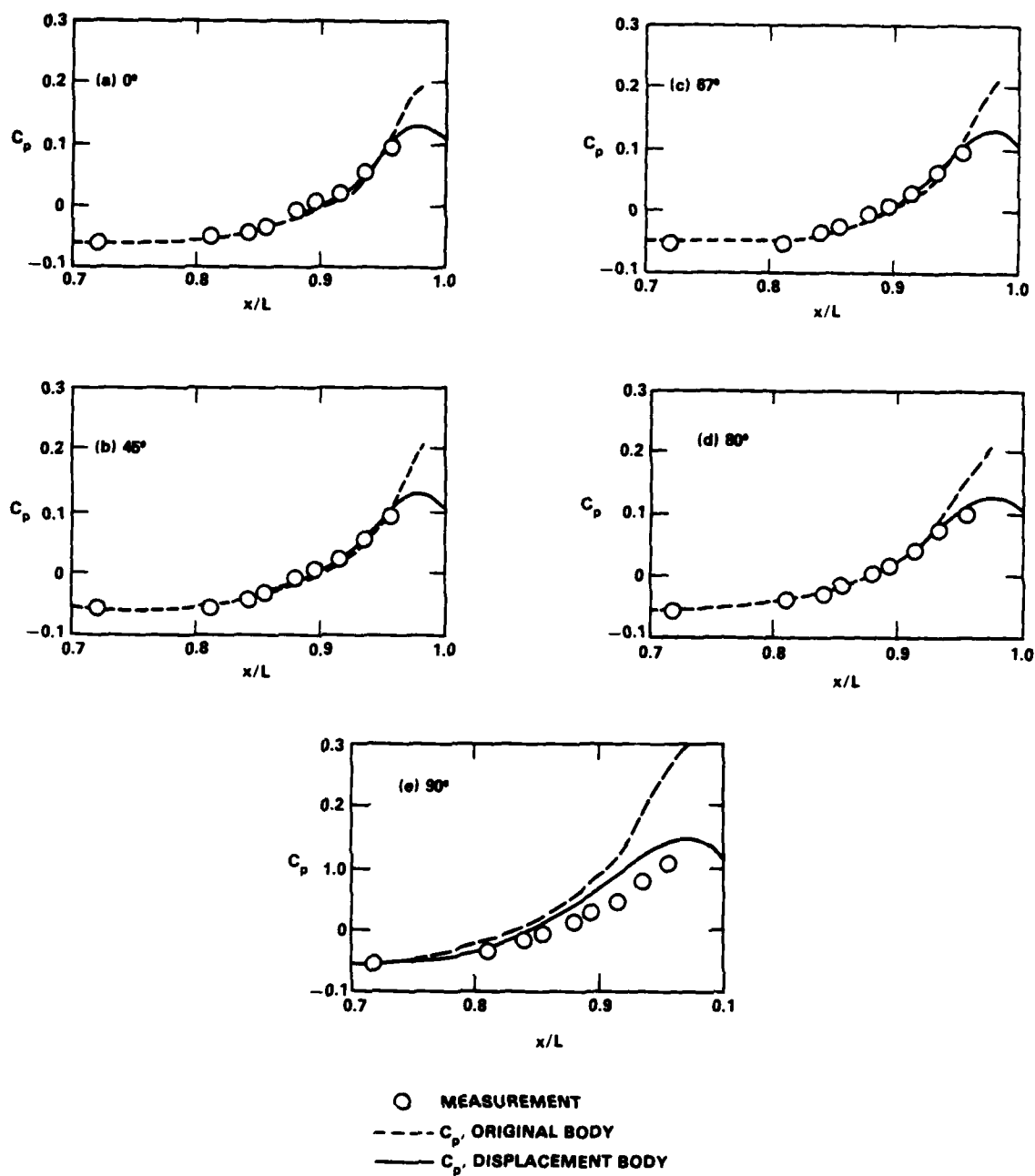


Figure 9 - Computed and Measured Stern Pressure Distributions for Five Angular Locations on the 3:1 Elliptical Model

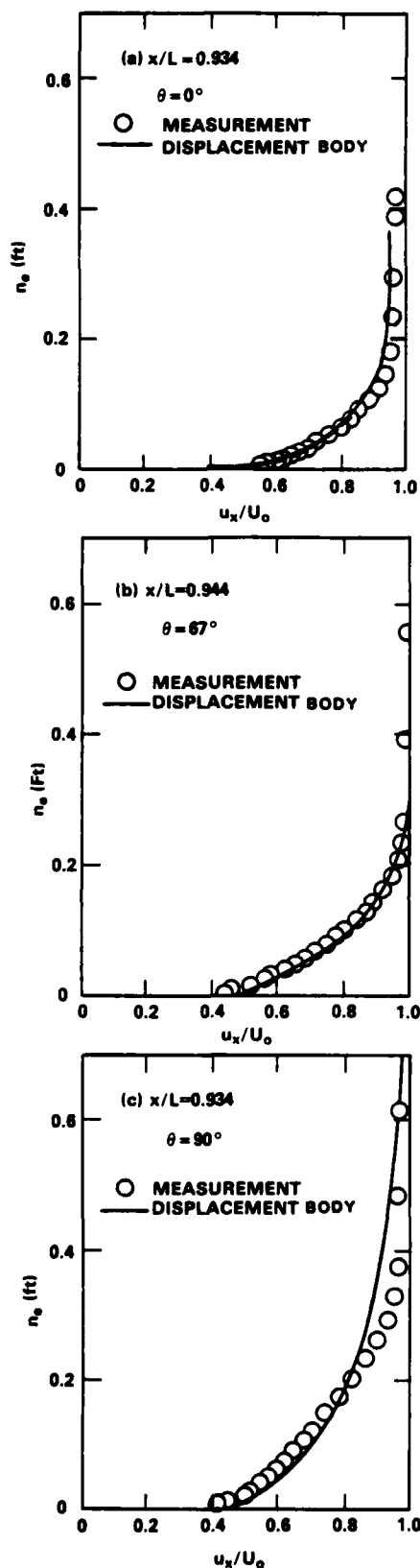


Figure 10 - Computed and Measured Mean Axial Velocity Distribution for the 2:1 Elliptical Model

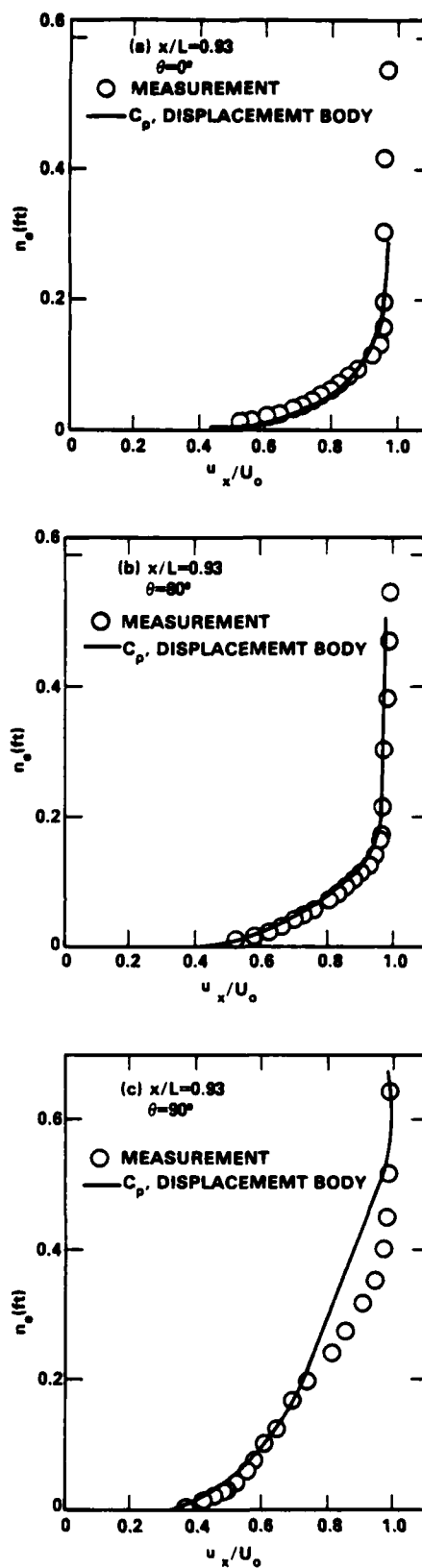


Figure 11 - Computed and Measured Mean Axial Velocity Distribution for the 3:1 Elliptical Model

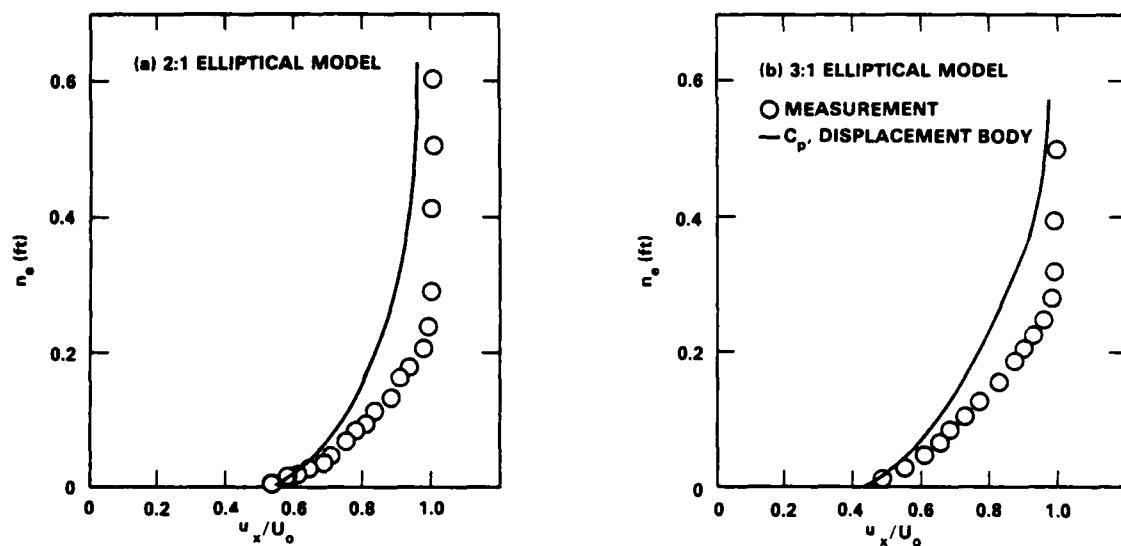


Figure 12 - Computed and Measured Mean Axial Velocity Distributions for the Models at $x/L=0.894$ and $\theta=90^\circ$

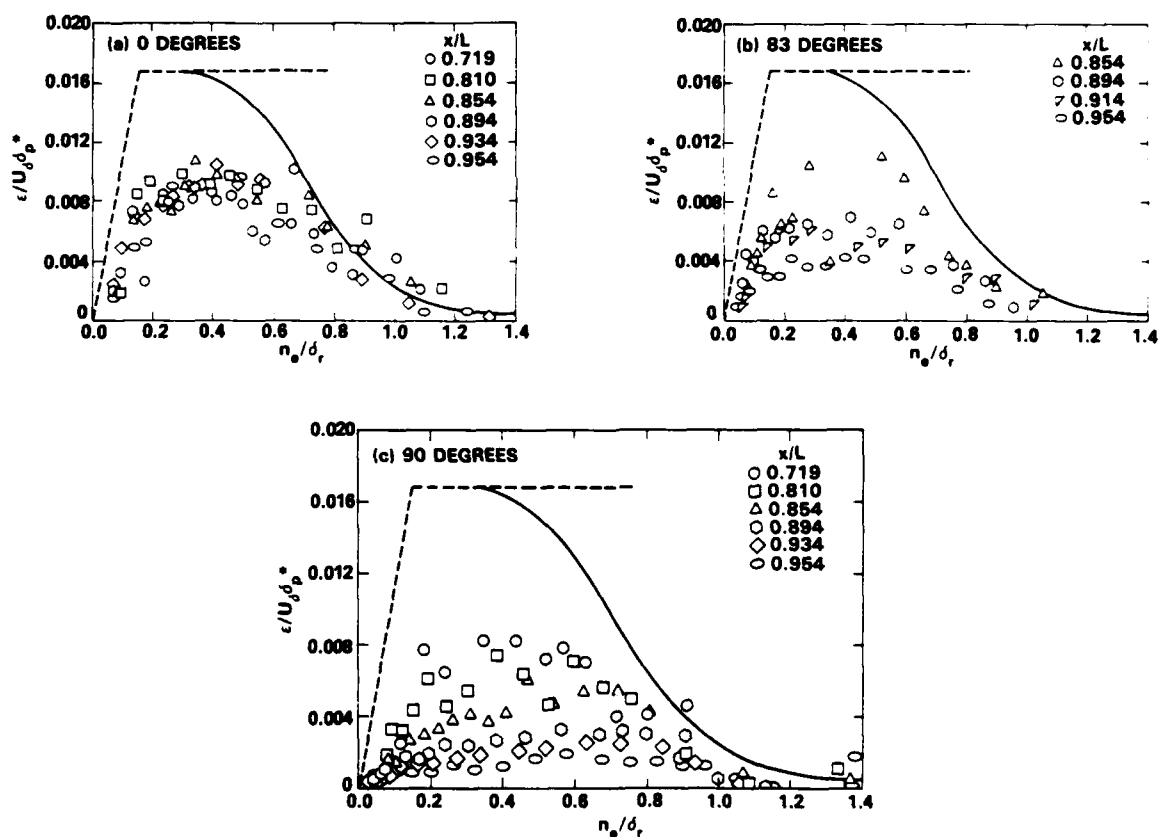


Figure 13 - Measured Distributions of Eddy Viscosity of the 3:1 Elliptical Model

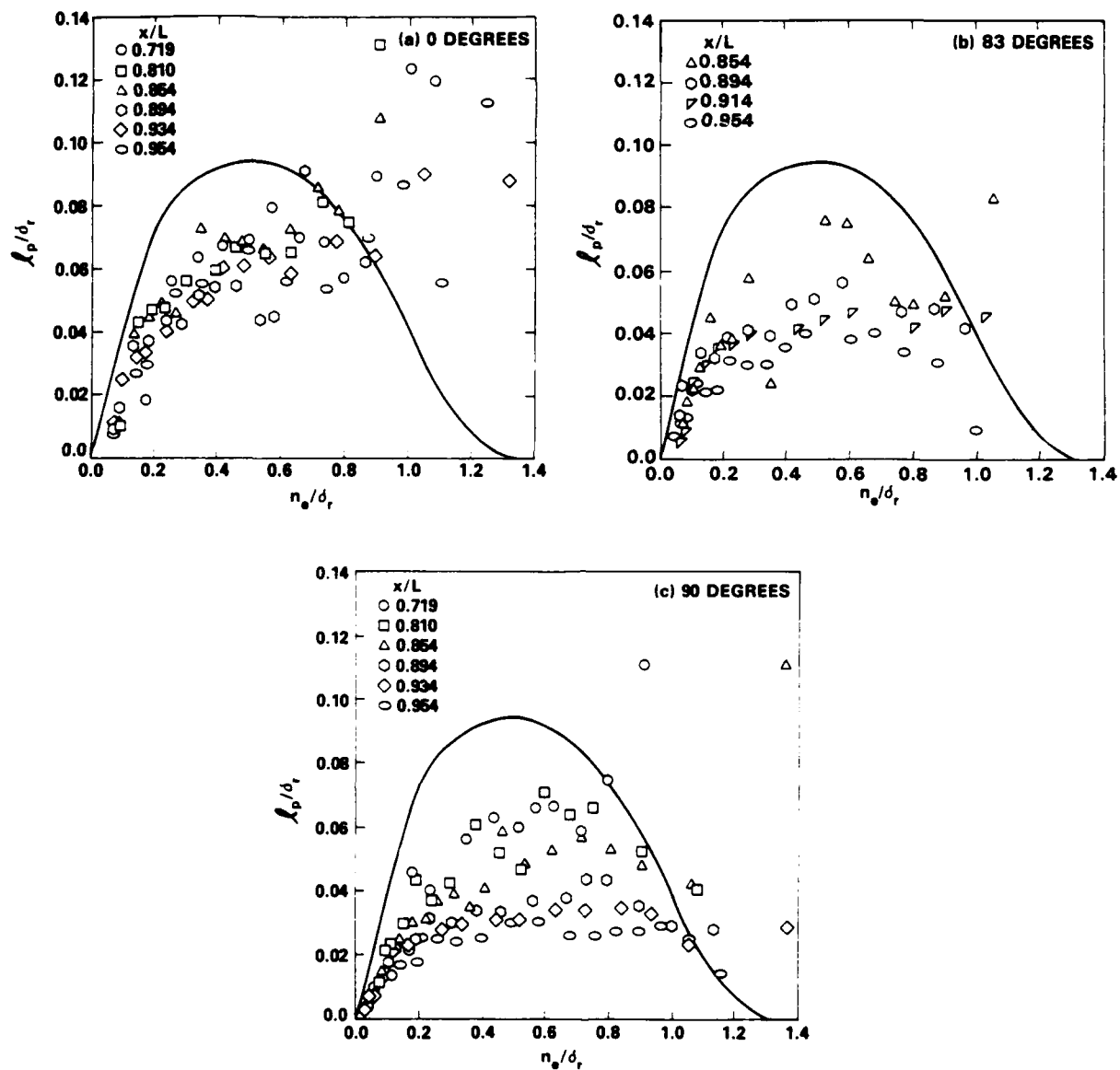
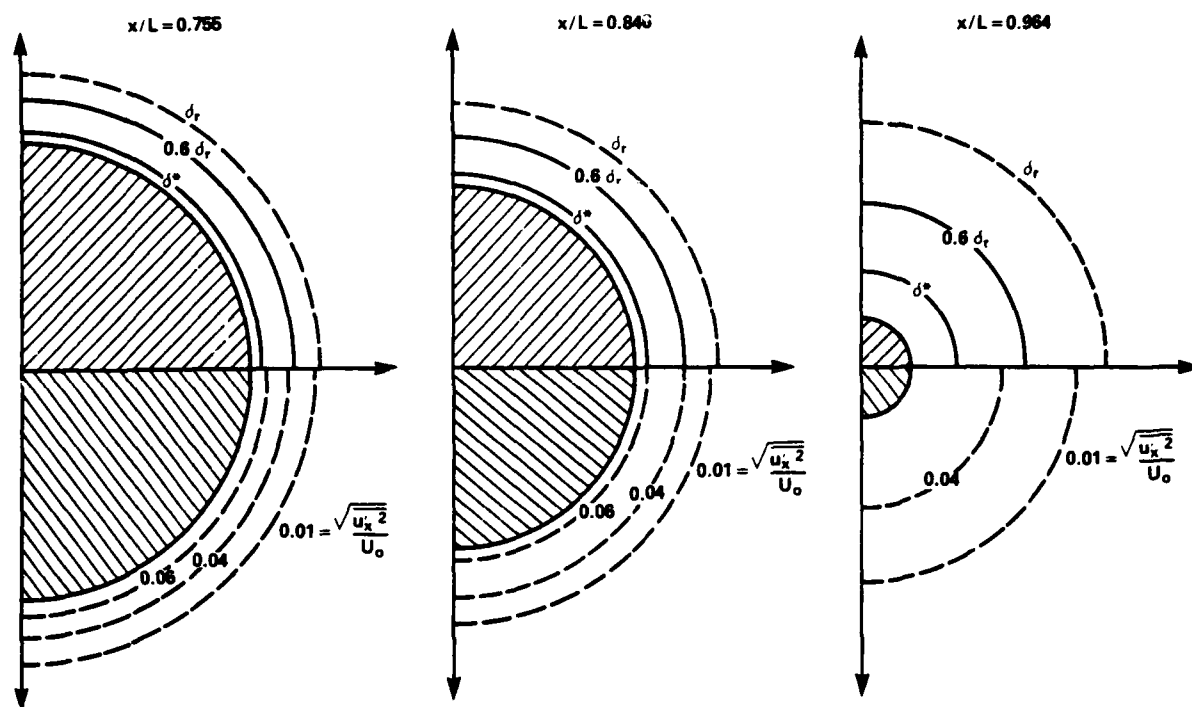
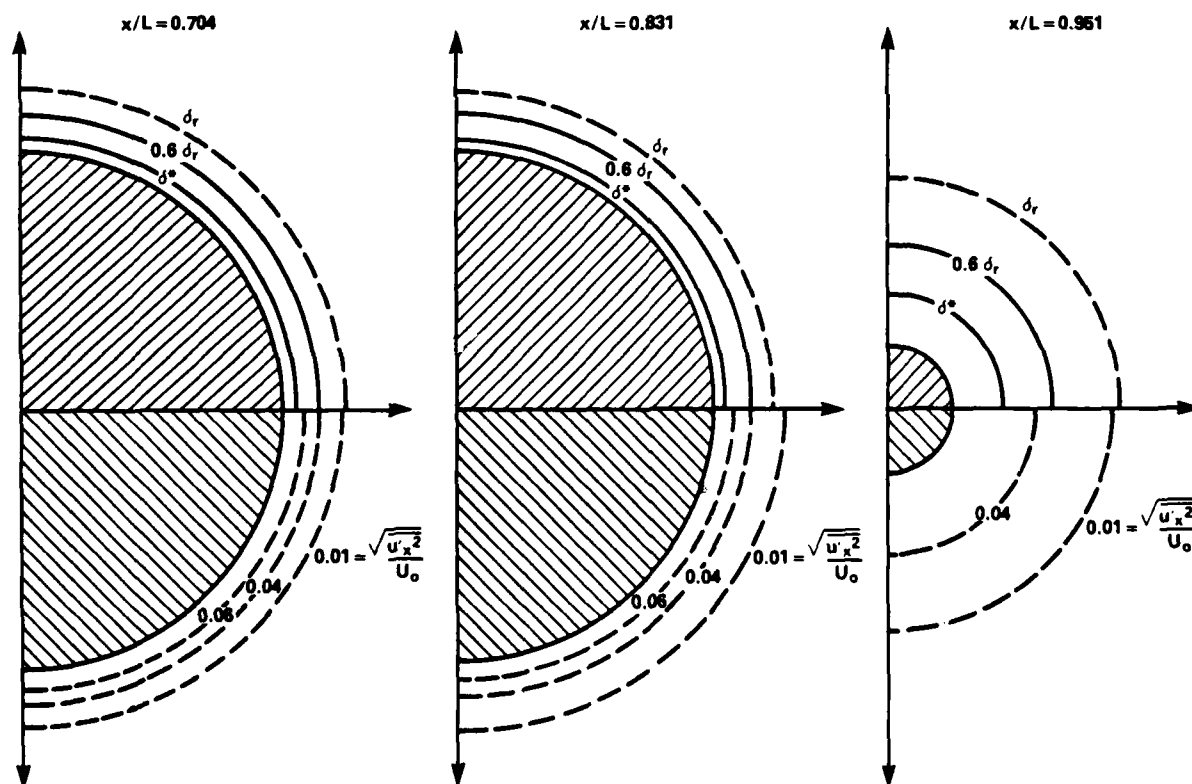


Figure 14 - Measured Distributions of Mixing Length of the 3:1 Elliptical Model

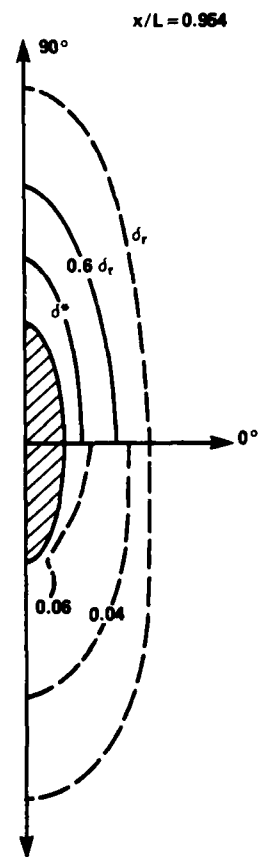
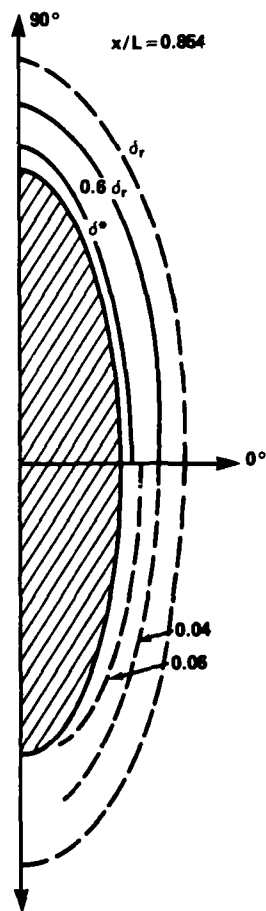
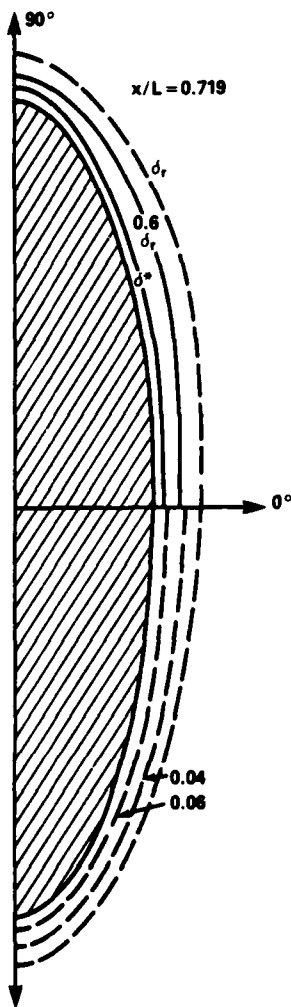


(a) Axisymmetric Afterbody 1¹

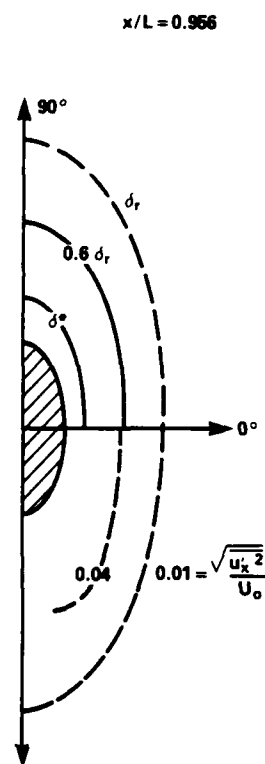
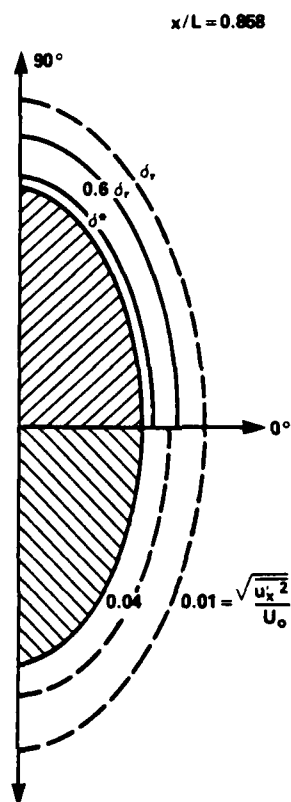
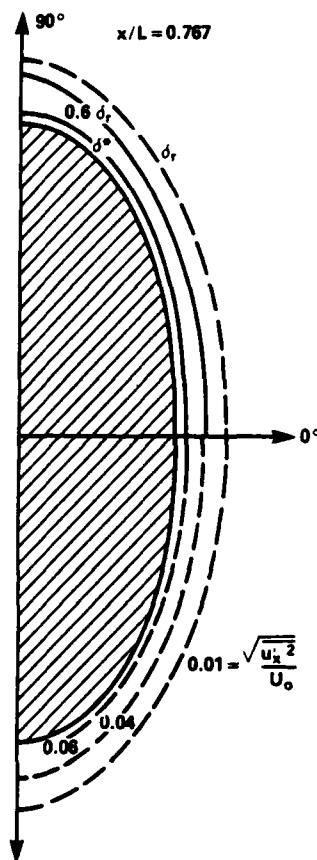


(b) Axisymmetric Afterbody 5²

Figure 15 - Representing the Mixing Length of the Stern Flow by the Square-Root of Turbulence Area



(c) The 3:1 Elliptical Model



(d) The 2:1 Elliptical Model

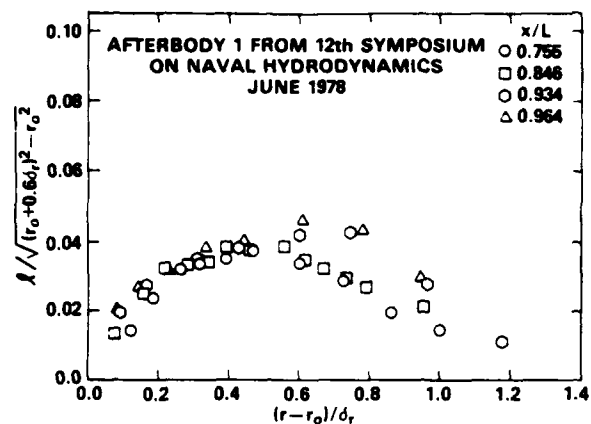


Figure 16a - Afterbody 1

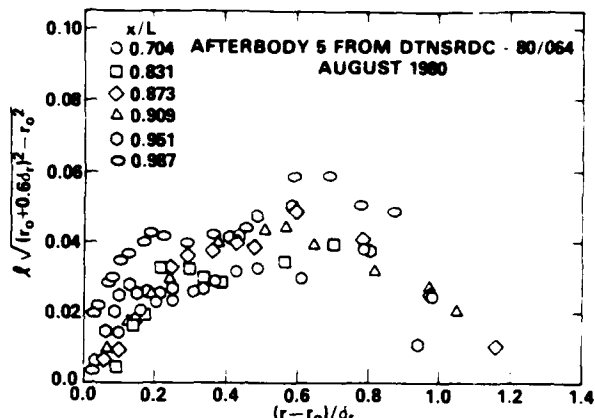


Figure 16c - Afterbody 5

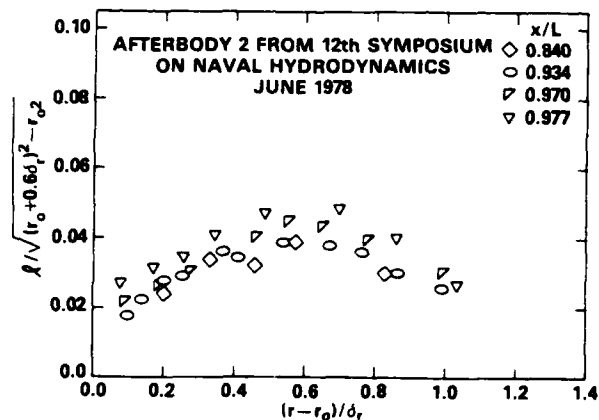


Figure 16b - Afterbody 2

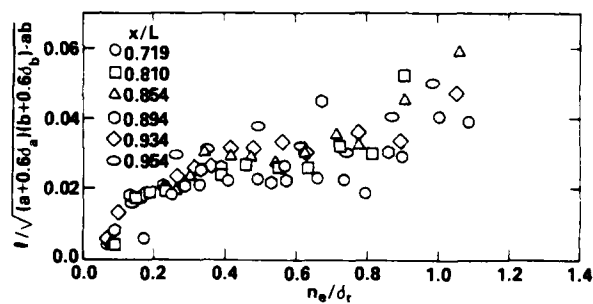


Figure 16d - The 3:1 Elliptical Model, 0 Degree Plane

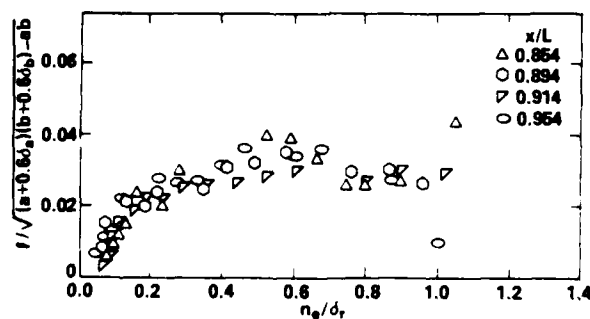


Figure 16e - The 3:1 Elliptical Model, 83 Degree Plane

Figure 16 - Proposed Similarity Concept for Mixing Length of Stern Turbulent Boundary Layer

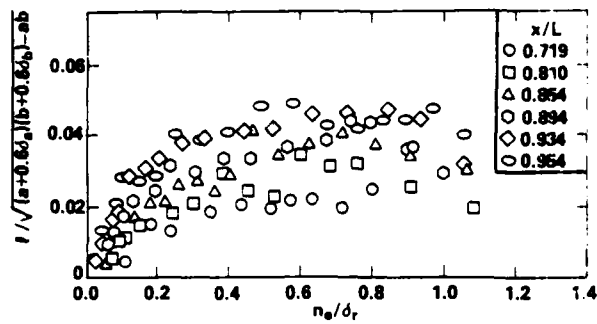


Figure 16f - The 3:1 Elliptical Model, 90 Degree Plane

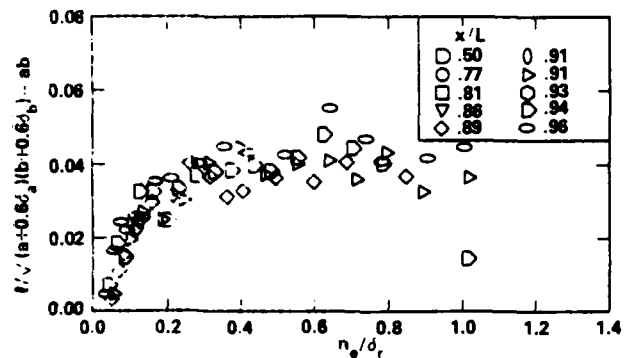


Figure 16h - The 2:1 Elliptical Model, 67 Degree Plane

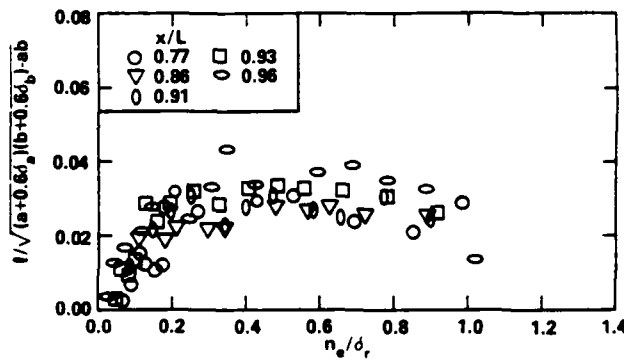


Figure 16g - The 2:1 Elliptical Model, 0 Degree Plane

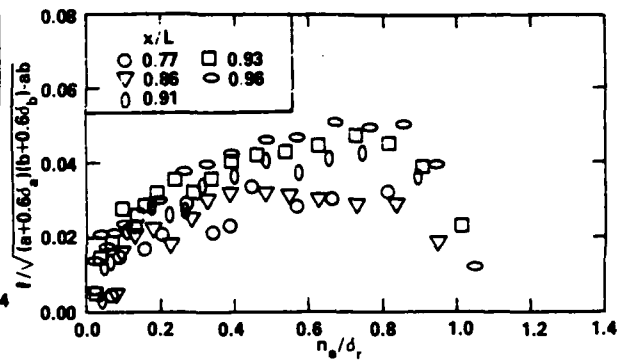


Figure 16i - The 2:1 Elliptical Model, 90 Degree Plane

Calculation of Three-Dimensional Boundary Layers
around Ship Hull Forms

Shunji Soejima
Mitsui Engineering & Shipbuilding Co., Ltd., Tokyo, Japan

Abstract:

Numerical investigations is made into complex three-dimensional boundary layers around ship hull forms.

At first, simple model of natural transition for boundary layers on ship fore-body surface is presented. Transitional boundary layer from laminar to turbulent calculated by using this model agreed very well with experimental results. Investigation is carried out about influence of the change of laminar boundary layer region and Reynolds number on the flow field around ship fore-body. The results shows that unstable flow pattern at bilge part is varied drastically due to above influence at comparatively low Reynolds number since turbulence intensity is smaller than that at high Reynolds number.

Investigation about calculation method of thick boundary layer on ship aft-body surface are also carried out by comparing measured results with calculated results by using a thick boundary layer equation. And it become clear that calculated velocity profile can be improved by taking account of curvature of body surface, viscid-inviscid flow interaction, and peculiar magnitude of Reynolds stress in thick boundary layers.

1. Introduction

Boundary layers around ship have complex characteristics since the ship hull surface has three-dimensional complex curvature. Namely, flow transits from laminar to turbulent, phenomena like three-dimensional separation occasionally occur and boundary layer on aft-body surface become very thick rapidly.

In case of actual ship, natural transition is estimated to occur near the fore end of ship. But, in case of model ship experiment in towing water tank, laminar boundary layer exists in wide range around ship fore-body due to comparatively low Reynolds number and existence of favorable pressure gradient. Therefore model ship is generally provided with turbulence stimulator at the position of about 5% Lpp from fore perpendicular to simulate the flow field of actual ship as far as possible. Laminar boundary layer still remains in the region of about 5% of ship surface in the case of most full hull form ship models. In such case, flow pattern behind turbulence stimulator should be different from the case of fore end transition although turbulence grew, and this difference may cause some difficulty in evaluation of resistance. Therefore it is important to investigate the influence of existence of laminar boundary layer on the flow field around ship fore-body in order to evaluate ship performance.

Prediction method of viscid flow field around ship hull forms has been developed rapidly, and thin boundary layers on the most part of ship hull surface became possible to be calculate with high accuracy by using conventional three-dimensional thin boundary layer equation as shown at workshop

on ship boundary layers in SSPA, 1980 1). Most calculation methods of boundary layer on ship surface neglect the laminar and transitional flow region and start their calculations from turbulent flow region.

Calculated examples of laminar and transitional flow region around ship model were reported by Soejima and Yamazaki 2) and Hoekstra 3). In these two papers, two models which predict occurrence of natural transition were used, however, examination about accuracy of these models was not conducted by taking account of Reynolds number effect. Soejima 4) tried comparative study about three models of laminar flow stability and three models of transition occurrence for boundary layers around ship fore-body taking account of effect of Reynolds number. The models of laminar flow stability indicate quite satisfactory results qualitatively in spite of the models for two-dimensional flows, and neutral stability line of laminar flow predicted by these models seemed to be actual starting line of transition. On the contrary, the three models of transition occurrence did not indicate satisfactory results.

In second chapter of this paper, simple natural transition model for ship boundary layers is presented and accuracy of this model is examined by comparing calculated results with experimental results. Then variation of boundary layer parameters on ship fore-body surface due to the change of transition starting position and Reynolds number is also investigated by boundary layer calculation.

It is very important to estimate viscid flow field around ship aft-body for prediction of ship performance. It is because viscous pressure resistance amount to 15 ~ 30% of all viscous resistance due to very thick boundary layer on ship aft-body surface and propulsor is located in this thick boundary layer and wake. But, such viscid flow field cannot be calculated accurately by using thin boundary layer equations because many neglected terms in thin boundary layer approximation become to have significant influence on this viscid flow fields.

Main phenomenological difference between thin and thick boundary layers can be summarized as follows.

- (1) Thickness of boundary layer become same order of magnitude with radius of body surface curvature.
- (2) There are strong interaction between inviscid and viscid flow.
- (3) Distribution and magnitude of Reynolds stress are different from that obtained by Reynolds stress model for thin boundary layer.

The above items cause some problems. From item (2), for example, pressure variation across boundary layer cannot be neglected and then pressure distribution on body surface is different from that obtained by potential flow calculation alone. Furthermore, in the case of full hull form ship, thick boundary layer problem becomes more complex due to the existence of large longitudinal vortex which is caused by open separation occurring at around 10% Lpp from aft perpendicular.

In third chapter, some discussion are made about numerical calculation method for thick boundary layers on ship aft-body surface by comparing measured data and calculated results by using thick boundary layer equations which include some higher order terms.

2. Thin Boundary Layer around Ship Fore-Body

2-1 3-D Thin Boundary Layer Equation

A three-dimensional curvilinear orthogonal coordinate system (ξ, η, ζ) is chosen so as to take ξ and η axes on the hull surface, and ζ axis is normal to the hull surface as shown in Fig. 1. The equations governing the turbulent thin boundary layer for incompressible three-dimensional flow are given as follows:

$$\frac{\partial}{\partial \xi}(h_2 u) + \frac{\partial}{\partial \eta}(h_1 v) + \frac{\partial}{\partial \zeta}(h_1 h_2 w) = 0 \quad (2-1)$$

$$\begin{aligned} \frac{u}{h_1} \frac{\partial u}{\partial \xi} + \frac{v}{h_2} \frac{\partial u}{\partial \eta} + w \frac{\partial u}{\partial \zeta} + K_{12} uv - K_{21} v^2 \\ = \frac{u}{h_1} \frac{\partial U}{\partial \xi} + \frac{v}{h_2} \frac{\partial U}{\partial \eta} + K_{12} UV - K_{21} V^2 + \frac{1}{\rho} \frac{\partial \tau_1}{\partial \zeta} \end{aligned} \quad (2-2)$$

$$\begin{aligned} \frac{u}{h_1} \frac{\partial v}{\partial \xi} + \frac{v}{h_2} \frac{\partial v}{\partial \eta} + w \frac{\partial v}{\partial \zeta} + K_{21} uv - K_{12} u^2 \\ = \frac{u}{h_1} \frac{\partial V}{\partial \xi} + \frac{v}{h_2} \frac{\partial V}{\partial \eta} + K_{21} UV - K_{12} U^2 + \frac{1}{\rho} \frac{\partial \tau_2}{\partial \zeta} \end{aligned} \quad (2-3)$$

where

$$\tau_1 = \mu \frac{\partial u}{\partial \zeta} - \overline{ou'w'}, \quad \tau_2 = \mu \frac{\partial v}{\partial \zeta} - \overline{ov'w'} \quad (2-4)$$

In these equations, U and V are velocity components in the ξ and η directions, respectively, at the outer edge of boundary layer. (u, v, w) and (u', v', w') are the components of time mean and fluctuating velocity, respectively. h_1 and h_2 are metric coefficient and K_{12} and K_{21} are defined by

$$K_{12} = \frac{1}{h_1 h_2} \frac{\partial h_1}{\partial \eta}, \quad K_{21} = \frac{1}{h_2 h_1} \frac{\partial h_2}{\partial \xi} \quad (2-5)$$

Boundary conditions for Eqs. (2-1) through (2-3) are given as

$$\begin{aligned} u = v = w = 0 \quad \text{at } \zeta = 0 \\ u = U, \quad v = V \quad \text{at } \zeta = \delta \end{aligned} \quad (2-6)$$

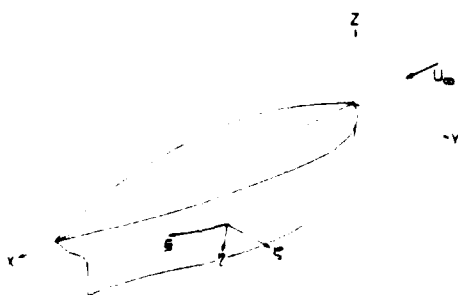


Fig. 1 Coordinate System

where δ is thickness of boundary layer.

In this paper, the eddy-viscosity concept for Reynolds stresses is used as

$$-\overline{ou'w'} = \rho \nu \frac{\partial u}{\partial \zeta}, \quad -\overline{ov'w'} = \rho \nu \frac{\partial v}{\partial \zeta} \quad (2-7)$$

According to Cebeci and Smith^{5,6} the eddy-viscosity of three-dimensional thin boundary layer is expressed as follows:

$$\nu_t = \begin{cases} \nu_{t1} & \text{for inner layer } (0 < \zeta \leq \zeta_c) \\ \nu_{t0} & \text{for outer layer } (\zeta_c \leq \zeta \leq \delta) \end{cases}$$

where

$$\begin{aligned} \nu_{t1} &= (0.4\zeta)^2 \cdot 1 - \exp\left(-\frac{\zeta}{A}\right)^2 \left\{ \left(\frac{\partial u}{\partial \zeta}\right)^2 + \left(\frac{\partial v}{\partial \zeta}\right)^2 \right\}^{1/2} \\ \nu_{t0} &= 0.0168 \int_0^\zeta U_s - (u^2 + v^2)^{1/2} d\zeta \cdot \left\{ 1 + 5.5 \left(\frac{\zeta}{\delta}\right)^6 \right\}^{-1} \end{aligned} \quad (2-8)$$

$$A = \frac{26\nu}{u_\tau (1 - 11.8p^+)^{1/2}}$$

$$u_\tau = \left[\nu \left\{ \left(\frac{\partial u}{\partial \zeta}\right)_w^2 + \left(\frac{\partial v}{\partial \zeta}\right)_w^2 \right\} \right]^{1/2} \quad (2-9)$$

$$p^+ = \frac{\nu U_s}{u_\tau} \frac{\partial U_s}{\partial s}, \quad U_s = (U^2 + V^2)^{1/2}$$

Here, U_s is velocity along a streamline at $\zeta = \delta$, and ds is a line element of this streamline. Further $(\)_w$ indicates a value at the wall, i.e. $\zeta = 0$. For laminar boundary layer, the above eddy-viscosity is zero.

The governing equations are solved by using the method based on Keller's box scheme and finite-difference approximation^{2,5}. Calculation is started from assumed leading edge which is positioned near the stagnation point and where flow is laminar and no cross flow exists².

2-2 Transition Model

Soejima⁴ tried to examine some models of natural transition for boundary layers around ship fore-body. However the predicted starting position of natural transition by using each model showed entirely different from each other at high Reynolds number and also seemed to be different from actual one. On the contrary, neutral stability position of laminar flow predicted by using three models^{7,8,9} shown in Fig. 2 seemed to be actual starting position of transition. Therefore, in this paper, neutral stability position predicted by using the above three models of laminar flow stability is used as the starting position of natural transition. These are the models for two-dimensional flows, and parameters in Fig. 2 are defined as follows:

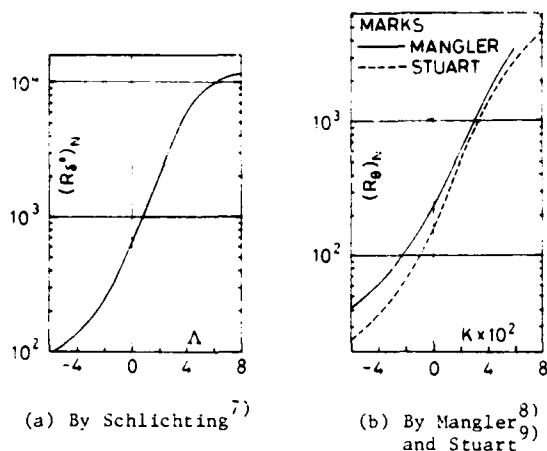


Fig. 2 Critical Reynolds Number of Laminar Boundary Layer Instability

$$\Lambda = \frac{\delta^2}{\nu} \frac{dU_s}{ds}, \quad K = \frac{\theta^2}{\nu} \frac{dU_s}{ds} \quad (2-10)$$

$$R_{\delta^*} = \delta^* U_s / \nu, \quad R_\theta = \theta U_s / \nu$$

where δ^* is displacement thickness and θ is momentum thickness. When the three models are applied for three-dimensional flows, δ^* and θ are replaced by δ_1^* and θ_{11} , respectively, where δ_1^* and θ_{11} are streamwise displacement thickness and streamwise momentum thickness defined by

$$\delta_1^* = \int_0^\delta (U_s - u_s) d\zeta / U_s \quad (2-11)$$

$$\theta_{11} = \int_0^\delta u_s (U_s - u_s) d\zeta / U_s^2$$

Region of transition is assumed to spread like a wedge which has half angle of 5 degree relative to the inviscid streamline even if each point in the wedge does not satisfy the above natural transition condition. And eddy viscosity model ν_{tr} in transition region is modified as follows:

$$\nu_{tr} = \nu_{tr} \cdot \nu_t$$

where ν_t is Cebeci and Smith's eddy viscosity model defined by eq. (2-8) and ν_{tr} is Chen and Thyson's intermittency factor¹⁰⁾ defined by

$$\nu_{tr} = 1 - \exp\{-G \cdot r_o \cdot (\int_{S_{tr}}^S \frac{dS}{r_o}) (\int_{U_s}^S \frac{dS}{U_s})\} \quad (2-12)$$

where

$$G = U_s^3 / 1200 \nu^2 R_{S_{tr}}^{1.34}$$

$$R_{S_{tr}} = S_{tr} \cdot U_s / \nu$$

$$r_o = (A_o / \pi)^{1/2}$$

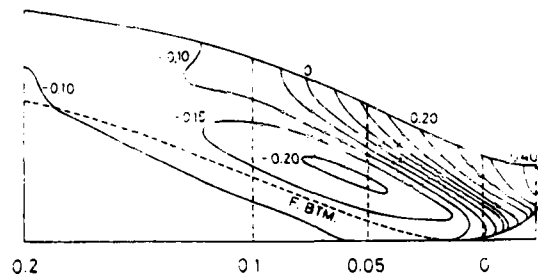


Fig. 3 Pressure Coefficient (C_p) Distribution on Ship Fore-Body Surface

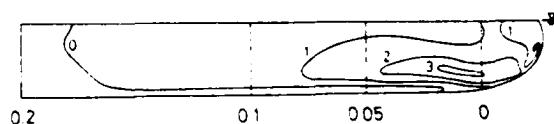


Fig. 4 Λ -Distribution on Ship Side Hull Surface

Here, A_o denotes a sectional area of the body at each section.

2-3 Calculated Results and Discussion

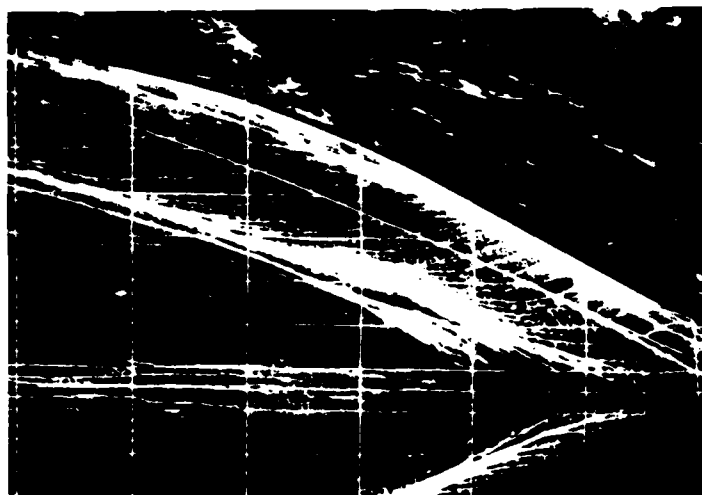
Calculation of the boundary layer around fore-body of a crude oil vessel ($L_{pp}/B = 6.52$, $C_B = 0.825$) was performed in order to examine the accuracy of the present transition model and also to investigate the effect of transition and Reynolds number on the flow pattern.

Pressure distribution on the hull surface calculated by using Hess and Smith method¹¹⁾ is shown in Fig. 3, and Λ -distribution on the side hull surface obtained by laminar boundary layer calculation is shown in Fig. 4. From these figures, it is understood that the hull form of this ship has strong stable laminar boundary layer region on the lower part of the side hull in front of $X/L = 0.05$. Such region where strong favourable pressure gradient and comparatively large Λ -value exists has a possibility of no transition or reverse transition even if turbulence stimulator fitted in front of this region, as reported by Asano et. al¹²⁾.

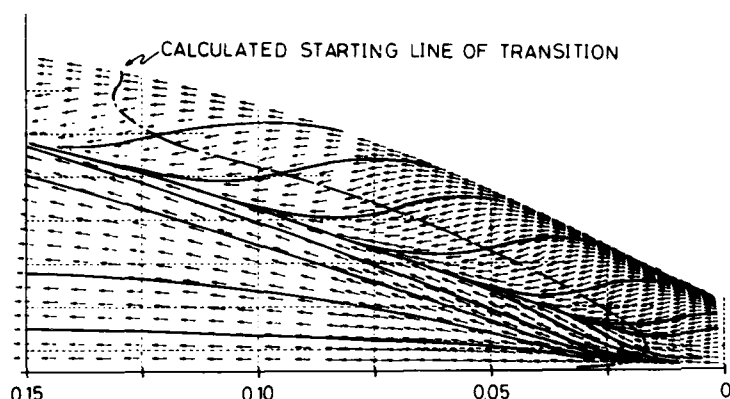
2-3-1 Comparison with Experiment

In this section, accuracy of the transition model is examined by comparing calculated results with experimental results.

Fig. 5-a shows a bottom view photograph of limiting streamlines observed in circulating water channel by using 2.5 M length model ship. Reynolds number was $R_{Lpp} (= L_{pp} \cdot U_\infty / \nu) = 2 \times 10^6$ and turbulence stimulator was not fitted. Calculated limiting streamlines are shown in Fig. 5-b in which calculated starting line of natural transition is also shown for reference. In Fig. 6 comparison of calculated and observed results is made about girthwise distribution of angle β_{wk} between X-axis and limiting streamline. The calculated peak of



(a) Oil-Flow Pattern Observed in Circulating Water Channel



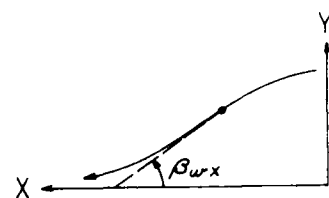
(b) Calculation

Fig. 5 Limiting Streamlines on Bottom Surface of Ship Fore-Body

β_{wx} and converged line of limiting streamlines are positioned a little towards the side hull compared with the observed results. But it is generally understood that the converged streamline at the bottom of bow observed by oil flow method is somewhat closer to the center line than actual one due to the effect of the outer flow. Therefore it can be said that calculated limiting streamline agreed very well with actual one.

Calculated limiting streamlines are very similar to the lee side surface flow pattern on body of revolution with high incidence case ($\alpha = 12^\circ$) reported by Wang¹³), called open separation or circumferential reverse flow. Furthermore longitudinal vortex is clearly indicated by the calculated tangential velocity distributions at $X/L = 0.10$ shown in Fig. 10-(b).

As another experiment to examine natural transition model, resistance measurement was also carried out in towing water tank for the cases without and with turbulence stimulator of rows of studs at $X/L = 0.05$. Difference of resistance between above two cases includes the difference of viscous resistance due to different starting position of transition and the own



MARKS
----- MEASURED
———— CALCULATION

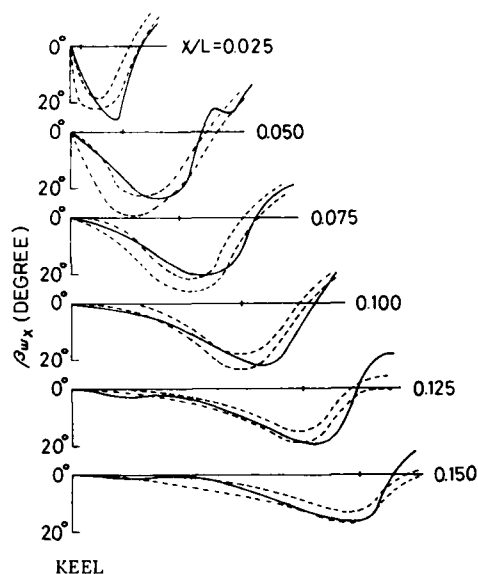


Fig. 6 β_{wx} Distribution on Bottom Surface of Ship Fore-Body

resistance of studs. To compare calculation with the above resistance measurement, additional boundary layer calculations were also carried out for three cases. Two are the cases that transition starts compulsorily at $X/L = 0.05$ under the conditions of $R_{Lpp} = 1 \times 10^6$ and 2×10^6 and another is the case of natural transition under the condition of $R_{Lpp} = 1 \times 10^6$. Frictional resistance R_F and viscous resistance R_V of the fore-body were calculated for each case by using following equations:

$$R_F = \frac{1}{2} \rho U_\infty^2 \int_S C_{fx} \left(\frac{U}{U_\infty} \right)^2 dS \quad (2-13)$$

$$R_V = \rho U_\infty^2 C_{V_s} \quad (2-14)$$

where

$$C_{fx} = \tau_w / \frac{1}{2} \rho U_s^2$$

R_{Lpp}	CALCULATION		EXPERIMENT
	$\Delta R_{F_{\infty}}$	$\Delta R_{V_{\infty}}$	ΔR_T
1×10^6	3.1	2.6	2 ~ 3
2×10^6	6.2	7.2	5 ~ 7

UNIT: GRAM

Table 1 Difference of Viscous Resistance between The Case of Natural Transition and The Case of Transition at $X/L = 0.05$

$$\Theta_{\infty} = \int_{\infty} \partial_{11} \left(\frac{U}{U_{\infty}} \right) d\ell$$

$$b = (H + 5)/2, \quad H = \frac{1}{\partial_{11}}$$

Here S_{∞} is the area of ship hull surface before $X/L = 0.50$, ℓ_{∞} is the girth length at $X/L = 0.5$, U_{∞} is model ship speed or uniform flow speed at infinity and $C_{f,x}$ is a X-component of local shearing stress C_f . The equation of $R_{V_{\infty}}$ is Squire and Young's relation for two-dimensional flow assuming that the flow at $X/L = 0.50$ is similar to two-dimensional flow. Comparison of calculated and measured difference of resistance is made in Table 1, in which measured ones are corrected by deducting the own resistance of studs calculated according to Tagori's study results¹⁴. The calculated results agree very well with the measured results at two different Reynolds numbers.

By Considering that the calculated results of above two examination agree very well with experimental results, it can be said that the present simple model of natural transition estimate very well actual transition around ship fore-body. Therefore present model is considered to be sufficient for the purpose of investigation about the influence of laminar boundary layer and the Reynolds effect on the flow pattern around ship fore-body.

2-3-2 Influence of Starting Point of Transition and Reynolds Effect

At first, calculated variation of starting position of natural transition by using present method due to the change of Reynolds Number is shown in Fig. 7. This figure shows that starting line of transition moves forward on the side hull and also moves gradually upwards from the bottom as Reynolds number increases. In the case of $R_{Lpp} = 10^8$, stable laminar boundary layer remains at the lower part of the side hull surface in front of $X/L = 0.05$, which coincides with the region of strong favourable pressure gradient and large Λ -value as shown in Fig. 3 and 4.

To investigate the influence of the change of laminar boundary region and Reynolds number on the flow field around ship fore-body, boundary layer calculations were carried out for three transition conditions, namely, natural transition, forced transition at $X/L = 0.05$ and at the fore end at five Reynolds numbers ($R_{Lpp} = 10^6, 2 \times 10^6, 10^7, 10^8, 10^9$).

Fig. 8 shows the calculated results of the

MARKS

R_{Lpp}
10^6
10^7
10^8
10^9

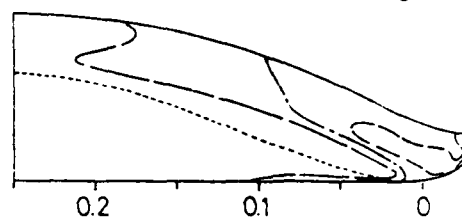
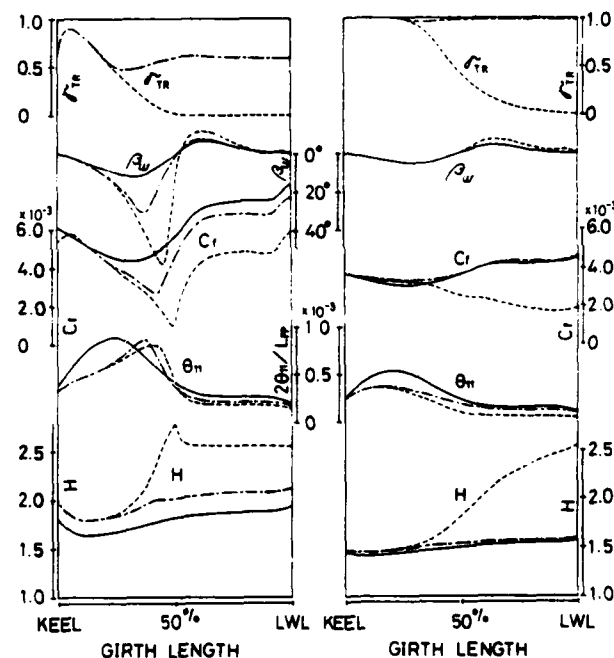


Fig. 7 Calculated Starting Line of Natural Transition

MARKS

---	NATURAL TRANSITION
---	TRANSITION AT $X/L=0.05$
---	TRANSITION AT FORE END



(a) $R_{Lpp} = 10^6$

(b) $R_{Lpp} = 10^7$

Fig. 8 Distribution of Boundary Layer Parameters at $X/L = 0.10$

influence of starting position of transition on girthwise distribution of boundary layer parameters at $X/L = 0.10$ for $R_{Lpp} = 10^6$ and 10^7 . As shown in this figure, degree of influence of transition condition on flow field around ship fore-body changes depending on Reynolds number.

In the case of $R_{Lpp} = 10^6$, variation of boundary layer parameters on the side hull surface between mid girth and LWL due to different

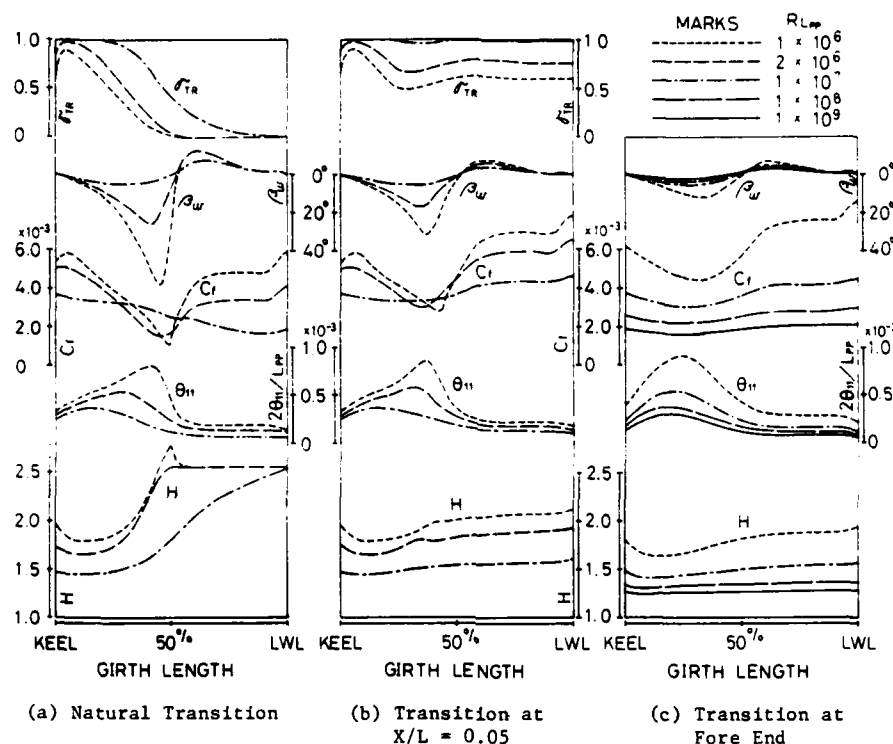


Fig. 9 Distribution of Boundary Layer Parameters at $X/L = 0.10$

transition condition is almost similar to flat plate case. On the bottom surface between keel to mid girth, variation is entirely different from the case of side hull. Judging from the distribution of boundary layer parameters in the case of natural transition, phenomenon called open separation or circumferential reverse flow occurs at mid girth. This tendency is gradually weakened as starting position of transition moves forward, and almost disappears at the case of fore end transition. Here, we have to pay attention to the fact that even if transition is stimulated at $X/L = 0.05$, flow pattern at $X/L = 0.10$ is still entirely different from the one of fore end transition case at low Reynolds number $R_{Lpp} = 10^6$ as shown in Fig. 8-(a).

At the case of $R_{Lpp} = 10^7$, on the other hand, variation of boundary parameters due to different transition condition is very small comparing with the case of $R_{Lpp} = 10^6$. Namely, the variation of β_w is very small. And similar to flat plate case, the variations of other parameters means only that velocity profile becomes the one of turbulent boundary layer from the one of laminar boundary layer as the starting position of transition moves forward, i.e. turbulence grows.

Next, calculated results about influence of Reynolds number variation on girthwise distribution of boundary layer parameters at $X/L = 0.10$ are shown in Fig. 9.

In the case of natural transition, the variations of boundary layer parameters for range of Reynolds number of $R_{Lpp} = 10^6 \sim 10^7$ are shown in Fig. 9-(a). In addition to Reynolds number effect, influence of starting position of natural

transition is also included in this case. Therefore, the variations of boundary layer parameters at mid girth where phenomenon called open separation occurs at low Reynolds number are very large as Reynolds number changes. In Fig. 10, calculated tangential velocity distributions for each Reynolds number of this case are shown. For reference, velocity profiles of streamwise, crosswise and normal component are also shown in Figs. 11 and 12. In these figures, longitudinal vortex is clearly shown at $R_{Lpp} = 10^6$, and with increase of Reynolds number, tangential velocity component decreases rapidly and finally longitudinal vortex become negligibly small at $R_{Lpp} = 10^7$.

In the next case of transition at $X/L = 0.05$ shown in Fig. 9-(b), the variations of boundary layer parameters are smaller than the case of natural transition. But tendency of phenomenon called open separation still remains at comparatively low Reynolds number of $R_{Lpp} = 10^6$ and 2×10^6 . Therefore it is clearly understood that flow pattern is considerably changed by Reynolds effect even if transition starts at same position in the range of $R_{Lpp} = 10^6 \sim 10^7$.

Boundary layer parameters in the case of fore end transition shown in Fig. 9-(c) show systematic variation entirely different from the above two cases. Especially in the range of $R_{Lpp} = 10^7 \sim 10^9$, the variations of β_w and θ_{11} due to the change of Reynolds number are in proportion to the variations of C_f . This results agrees very well with Tanaka and Himeno's conclusion¹⁵⁾ about scale effect which was derived from first order approximation to three-dimensional turbulent boundary layer.

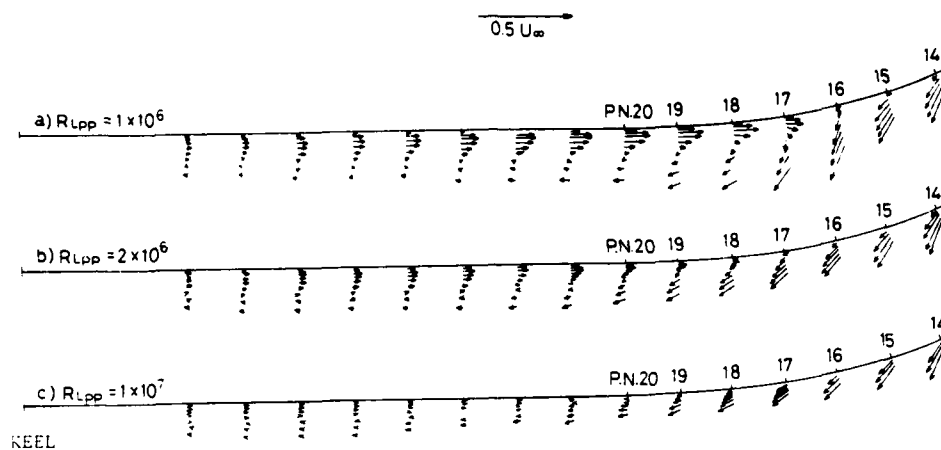


Fig. 10 Distribution of Tangential Velocity Component at $X/L = 0.10$, Natural Transition

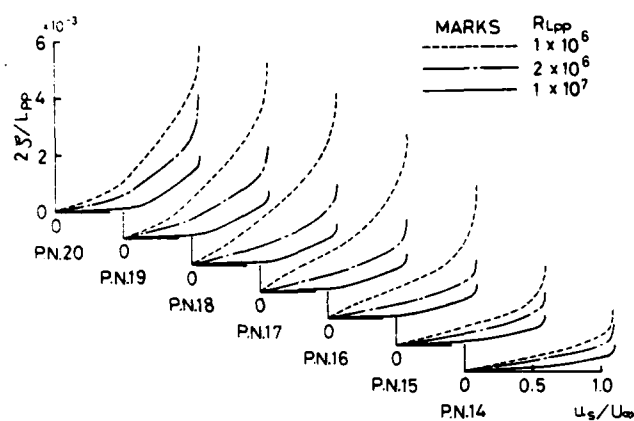


Fig. 11 Streamwise Velocity Profile at $X/L = 0.10$, Natural Transition

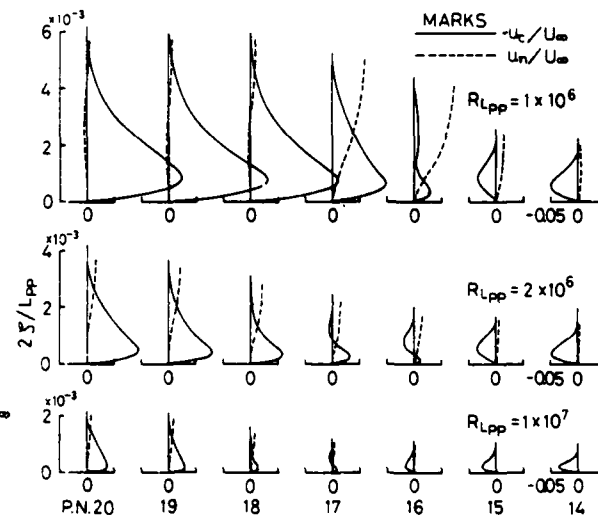


Fig. 12 Crosswise and Normal Velocity Profile at $X/L = 0.10$, Natural Transition

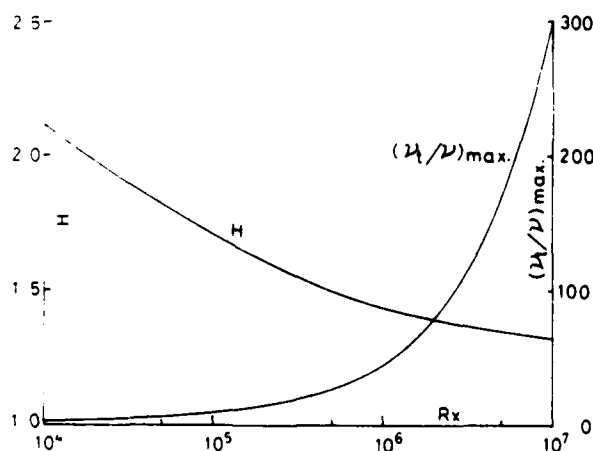


Fig. 13 Variation of ν_t/ν and H Flat Plate, $R_{xc} = 10^3$

On the other hand, in the range of $R_{Lpp} = 10^6 \sim 10^7$, a different relationship is found between β_w and C_f . This reason is considered as follows:

Shear stress included in turbulent boundary layer equations is expressed from Eqs. (2-4) and (2-7) as

$$\tau_1 = \rho \nu \left(1 + \frac{\nu_t}{\nu} \right) \frac{\partial u}{\partial z} \quad (2-15)$$

and ν_t/ν is generally proportional to $R_{\delta_1}^*$ ($= U_{\delta_1}^* \delta_1^*/\nu$). It means that with decrease of Reynolds number, ν_t/ν and Reynolds stress becomes small and solution of turbulent boundary layer equation approaches to solution of laminar boundary layer equation in which ν_t/ν is zero. For reference calculated ratio of ν_t/ν and shape factor H for flat plate case are shown in Fig. 13. From this figure, we can understand that shape factor H

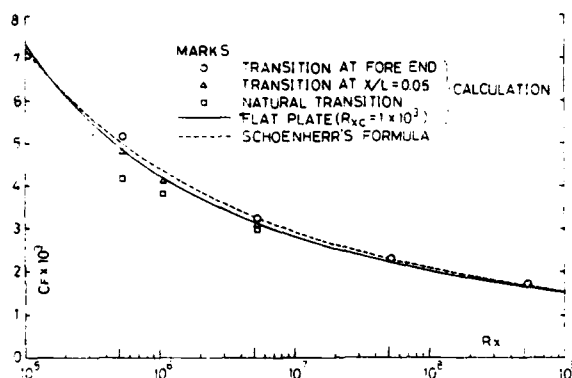


Fig. 14 Frictional Resistance Coefficient for Ship Fore-Body

increases rapidly below $R_x = 10^6$ and becomes close to the value of laminar boundary layer ($H = 2.6$). This implies that the tendency of unstable flow pattern still remains slightly even if turbulence is fully stimulated in case of a three-dimensional flow field which has very unstable flow pattern under laminar flow condition. Namely, the increase rate of β_w becomes large compared with that of C_f as Reynolds number decreases below 10^6 . Therefore, it can be concluded that scale effect derived from first order approximation to three-dimensional turbulent boundary layer can not be applied for unstable flow field at low Reynolds number.

Frictional resistance of fore-body before $X/L = 0.5$ for the above each case is calculated and is plotted in Fig. 14 on the basis of Reynolds number for the distance from fore end to $X/L = 0.5$. For a comparison purpose, Schoenherr's and calculated frictional resistance curves for flat plate are also shown in this figure. Furthermore, form factors K_p for frictional resistance are shown in Table 2.

In the case of natural transition, frictional resistance of the fore-body is lower than that of flat plate due to the existence of wide laminar boundary layer region, and gradually approaches to the level of flat plate as Reynolds number increases. On the other hand, in the case of transition at $X/L = 0.05$, frictional resistance is nearly equal to that of flat plate and form factor for frictional resistance is indicated to be almost constant for each Reynolds number.

In the case of fore end transition, form factor based on Schoenherr's frictional line varies for each Reynolds number, but form factor based on the calculated frictional resistance of flat plate is almost constant except the case of $R_{Lpp} = 10^6$. From this result, form factor for frictional resistance seems not to be influenced by the difference of Reynolds number under the condition that transition starts from ship fore end at sufficiently large Reynolds number.

2-4 Conclusion

Simple model of natural transition for boundary layer calculation was presented and calculated results by using this model agreed very well with experiments. And effects of transition

CASE	NATURAL TRANSITION		
R_{Lpp}	1×10^6	2×10^6	1×10^7
$1+K_{F\Box}$ (SCHOENHELL)	0.832	0.874	0.915
$1+K_{F\Box}$ (CALCULATION)	0.861	0.909	0.956

CASE	TRANSITION AT $X/L = 0.05$		
R_{Lpp}	1×10^6	2×10^6	1×10^7
$1+K_{F\Box}$ (SCHOENHELL)	0.960	0.947	0.947
$1+K_{F\Box}$ (CALCULATION)	0.993	0.986	0.989

CASE	TRANSITION AT FORE END			
R_{Lpp}	1×10^6	1×10^7	1×10^8	1×10^9
$1+K_{F\Box}$ (SCHOENHELL)	1.022	0.996	1.009	1.026
$1+K_{F\Box}$ (CALCULATION)	1.057	1.040	1.039	1.040

Table 2 Form Factor for Frictional Resistance

$$1+K_{F\Box} = C_{F\Box}/C_{F0}$$

C_{F0} : Frictional Resistance Coefficient of Flat Plate

$C_{F\Box}$: Frictional Resistance Coefficient of Ship Fore Body

starting position and Reynolds number for flow field around ship fore-body were investigated. The following conclusions are derived.

- (1) Present simple model of natural transition is considered to be sufficient for a purpose of studying the influence of laminar boundary layer and Reynolds effect on viscous flow field around ship fore-body.
- (2) Flow pattern called open separation or circumferential reverse flow observed on bow bottom surface of model ship is generally caused by the fact that turbulence does not sufficiently grow. And in the case of actual ship, such flow pattern will not appear or will be smaller scale even if appear than that on model ship.
- (3) At low Reynolds number, the influence of transition starting position on flow pattern is considerably large and there is a possibility that even if turbulence is stimulated at $X/L = 0.05$, flow pattern is entirely different from the one of actual ship.
- (4) At high Reynolds number greater than $R_{Lpp} = 10^7$, influence of transition starting position is almost similar to flat plate case, and resistance of actual ship can easily be estimated from model test results. Further study is necessary to investigate whether this can be applied for other ship hull form which has larger scale unstable flow pattern than

the one of the hull form in this paper.

- (5) Scale effect derived from first order approximation to three-dimensional turbulent boundary layer is applicable to boundary layer around ship fore-body, and form factor for frictional resistance of ship fore-body is considered not to be influenced by difference of Reynolds number under the condition that transition starts from ship fore end at sufficiently large Reynolds number.

3. Thick Boundary Layer on Ship After-Body

3.1 3-D Thick Boundary Layer Equations

General equations governing three-dimensional thick boundary layers are not established yet although several equations have been presented by many researchers. Here, the following equations¹⁶⁾ which take account of curvature of body surface and pressure variation across the boundary layer are examined.

$$\frac{\partial}{\partial \xi}(h_2 u) + \frac{\partial}{\partial \eta}(h_1 v) + \frac{\partial}{\partial \zeta}(h_1 h_2 w) = 0 \quad (3-1)$$

$$\begin{aligned} \frac{u}{h_1} \frac{\partial u}{\partial \xi} + \frac{v}{h_2} \frac{\partial u}{\partial \eta} + w \frac{\partial u}{\partial \zeta} + (K_{12} u - K_{21} v) v + K_{13} u w \\ + \frac{1}{h_1} \frac{\partial}{\partial \xi} \left(\frac{p}{\rho} \right) - \frac{1}{\rho} \frac{1}{h_1 h_2} \frac{\partial}{\partial \zeta} (h_1 h_2 \tau_1) = 0 \end{aligned} \quad (3-2)$$

$$\begin{aligned} \frac{u}{h_1} \frac{\partial v}{\partial \xi} + \frac{v}{h_2} \frac{\partial v}{\partial \eta} + w \frac{\partial v}{\partial \zeta} + (K_{21} v - K_{12} u) u + K_{23} v w \\ + \frac{1}{h_2} \frac{\partial}{\partial \eta} \left(\frac{p}{\rho} \right) - \frac{1}{\rho} \frac{1}{h_1 h_2} \frac{\partial}{\partial \zeta} (h_1 h_2 \tau_2) = 0 \end{aligned} \quad (3-3)$$

$$\begin{aligned} \frac{u}{h_1} \frac{\partial w}{\partial \xi} + \frac{v}{h_2} \frac{\partial w}{\partial \eta} + w \frac{\partial w}{\partial \zeta} - K_{13} u^2 - K_{23} v^2 + \frac{\partial}{\partial \zeta} \left(\frac{p}{\rho} \right) \\ + \frac{\partial}{\partial \zeta} (\overline{w'w'}) = 0 \end{aligned} \quad (3-4)$$

where

$$K_{13} = \frac{1}{h_1 h_3} \frac{\partial h_1}{\partial \zeta}, \quad K_{23} = \frac{1}{h_2 h_3} \frac{\partial h_2}{\partial \zeta}$$

Here, metric coefficient h_1 and h_2 are functions of ξ , η and ζ because curvature of body surface is considered. Eq. (3-4) express existence of static pressure gradient across boundary layers. In the process of numerical calculation, straight line distribution of static pressure across the layer is adopted instead of Eq. (3-4) by connecting the static pressure value on body surface and at boundary layer's outer edge. The static pressure at each point is obtained by potential flow calculation.

For assumption of the Reynolds stress, the eddy viscosity concept is used as in previous chapter, but following modification¹⁶⁾ is made from Cebeci and Smith's eddy viscosity model.

$$\nu_t = \begin{cases} \nu_{t_i} & \text{for inner layer } (0 < \zeta \leq \zeta_c) \\ C \cdot \nu_{t_o} & \text{for outer layer } (\zeta_c < \zeta < \delta) \end{cases} \quad (3-6)$$

where

$$C = \begin{cases} C_1 & \text{for } \zeta/\delta \geq 0.3 \\ C_1 \cdot C_2 & \text{for } \zeta/\delta < 0.3 \end{cases}$$

$$C_1 = \min. \begin{cases} (1 + 2R_o/\delta)/6 \\ 1.0 \end{cases}$$

$$C_2 = 3.33(1.0 - C_3)\zeta/\delta + C_3$$

$$C_3 = \max. \begin{cases} 2C_1 - 1.0 \\ 0.3 \end{cases}$$

$$R_o = \min. \begin{cases} \left(\frac{1}{K_{23} w} \right) & \text{for } (K_{23})_w > 0 \\ (A_o/\pi)^{1/2} \end{cases}$$

Here, ν_{t_i} and ν_{t_o} are expressed in Eq. (2-8). The above model is derived from the measured Reynolds stress distribution across axisymmetric thick boundary layer¹⁷⁾, and is very convenient to investigate the effect of Reynolds stress intensity on velocity distribution in boundary layer although this model has no physical explanation.

The governing equations can be solved by using the same method with thin boundary layer equations. Boundary layer on fore-body surface is calculated by using thin boundary layer equations mentioned in previous chapter.

3-2 Calculated Results and Discussion

In this section, calculated results about an axisymmetric body and three ship models are compared with measured data and discussions are made.

3-2-1 Calculated Results for An Axisymmetric Body

Calculation of thick boundary layers was performed for axisymmetric body which is named after body-1 by Huang et. al¹⁷⁾. The body length L is 3.066 m and the maximum radius R_{max} is 0.1397 m. In this case, static pressure distribution was corrected by taking account of displacement effect by iteration of potential flow and boundary layer calculation.

Calculated results of velocity profile at four sections are compared with the measured results in Fig. 15. Both results show very good agreement except radial velocity component near outer edge of boundary layer. Calculated eddy viscosity distributions at $X/L = 0.934$ and 0.964 are also agree very well with the measured results as shown in Fig. 16. From these results, it can be said that present method including eddy viscosity model estimate very well the characteristic of axisymmetric thick boundary layer.

Investigations were made into the influences of body surface curvature, static pressure gradient across the layers, and eddy viscosity magnitude on velocity distribution across the layer. This study was carried out by calculating boundary layer by using four different methods as shown in Table 3.

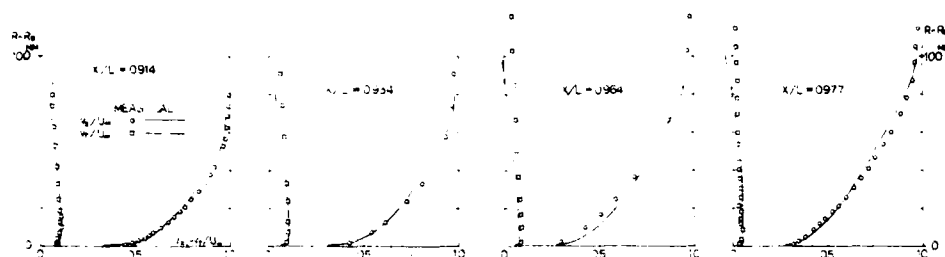


Fig. 15 Velocity Profiles across Axisymmetric Boundary Layer, Afterbody-1, Measurements Performed by Huang et.al.¹⁷⁾

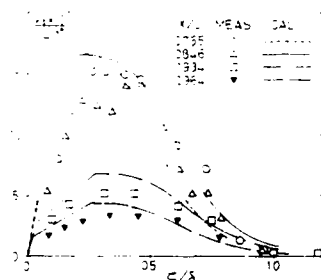


Fig. 16 Eddy Viscosity Distribution across Axisymmetric Boundary Layer, Afterbody-1, Measurements Performed by Huang et.al.¹⁷⁾

METHOD	COMMENT
1	$\frac{\partial p}{\partial x} = 0, v_t = (v_{t1}, v_{t0}')$, $K_{13}, K_{23} = 0$: THIN B.L.Eq.
2	$\frac{\partial p}{\partial x} = 0, v_t = (v_{t1}, v_{t0}')$, $K_{13}, K_{23} \neq 0$
3	$\frac{\partial p}{\partial x} = 0, v_t = (v_{t1}, C \cdot v_{t0}')$, $K_{13}, K_{23} \neq 0$
4	$\frac{\partial p}{\partial x} = 0, v_t = (v_{t1}, C \cdot v_{t0}')$, $K_{13}, K_{23} \neq 0$: THICK B.L.Eq.

Table 3 Calculation Method

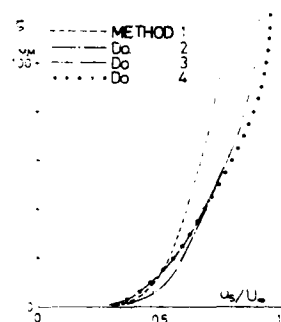


Fig. 17 Calculated Streamwise Velocity Profiles across Axisymmetric Boundary Layer at $X/L = 0.977$, Afterbody-1

In these calculations, static pressure distribution on the body surface corrected for displacement effect was used to clarify the effects of the above three items. Calculated velocity profiles at $X/L = 0.977$ are shown in Fig. 17. By comparing each velocity profile, influence of above each item can be summarized as follows.

- (1) Curvature of body surface plays an important role in estimating boundary layer thickness.
- (2) Velocity profile near wall is significantly influenced by the magnitude of eddy viscosity.
- (3) By taking account of pressure gradient across the layer, we can match the boundary layer with inviscid flow at the outer edge.

It is to be noted that the influence of viscous-inviscid flow interaction other than static pressure gradient in the layer are included in these calculated results.

From the above results, it is clear that curvature of body surface, viscous and inviscid flow interaction, and peculiar intensity of Reynolds stress in the thick boundary layer should be taken into account in order to calculate thick boundary layer accurately.

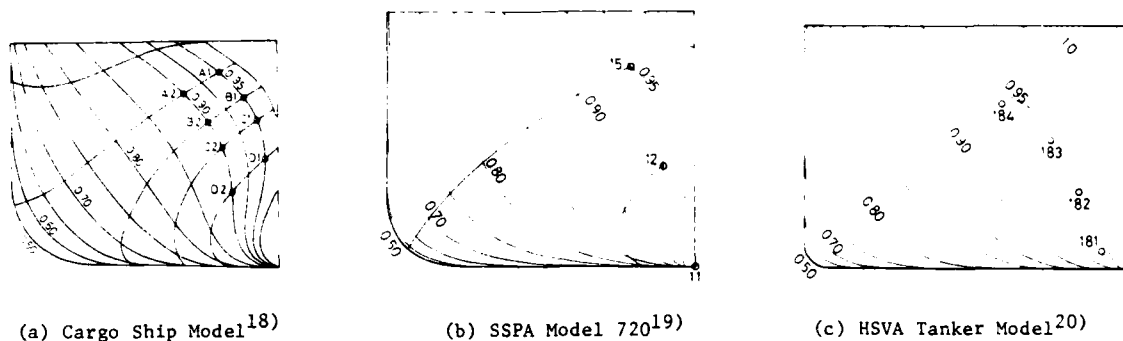
3-2-2 Calculated Results for Ship Models

Calculation of thick boundary layers was also performed for three ship models, namely, Cargo Ship Model¹⁸⁾, SSPA Model 720¹⁹⁾ and HSVA Tanker Model²⁰⁾. Body plans of these ship models are shown in Fig. 18. In these cases, static pressure distribution obtained from potential flow calculation alone was used, namely, viscous and

inviscid flow interaction was not taken into account.

Calculated streamwise and crosswise velocity profiles for each ship models are compared with the measured results in Fig. 19. For Cargo Ship Model shown in Fig. 19-(a), the calculated results by using thin boundary layer equations (Method 1) are also plotted only at $X/L = 0.90$ since the calculation did not converge at $X/L = 0.95$. The location of profile number (P.N.) in Fig. 19 is indicated in Fig. 18 (Body Plan).

From Fig. 19-(a), it is noted that calculated results by using Method 4 (i.e., thick boundary layer calculation) are improved from the results by using Method 1 in predicting thickness of boundary layer and cross flow velocity profile, especially, in predicting reverse cross flow. The improvements



by the present method were also shown on two ship models (i.e., SSPA Model 720 and HSVA Tanker Model) at SSPA-ITTC Workshop 1980¹).

Calculated wake contours for the three models are shown in Fig. 20 comparing with measured results. The calculated results estimates very well characteristic of the measured velocity distribution, especially location of swelled wake contour just above the bilge. In such region, calculated results in Fig. 21 show a flow pattern having concentrated limiting streamlines which is observed in the phenomenon called open separation.

But it is observed in Fig. 19 that the measured streamwise velocity near wall at such position of swelled wake contour (e.g., P.N.D1, P.N.12 and P.N.182) is smaller than calculated results. This tendency is also found in the velocity profiles on the body of revolution in Fig. 17 calculated by using Method 2 and Method 3 which showed the influence of magnitude of eddy viscosity. According to the results of turbulence measurements on Series 60 Model ($C_B = 0.8$) reported by Fukuda and Fujii²¹⁾, magnitude of eddy viscosity in a position of swelled wake contour is in a order of 15% of the value obtained by the CS Model as shown in Fig. 22. Considering the fact that the value of eddy viscosity for these three ship models calculated by using the present method is about 5 times of the above results, the overestimation of magnitude of eddy viscosity in the calculation may be one of causes of difference in velocity profiles at such position of swelled wake contour.

3-3 Conclusion

A method for three-dimensional thick boundary layer was presented and investigations were made into the influences of hull surface curvature, static pressure gradient in the layer, and magnitude of Reynolds stress on velocity profile by comparing calculated results with measured results. The following conclusions are derived.

- (1) In case of axisymmetric thick boundary layer, calculated velocity profiles by using present method agreed very well with measured data.
- (2) Hull surface curvature, viscid-inviscid flow interaction, and magnitude of Reynolds stress play different role each other for velocity profile. It is necessary to take account of all of the above items to calculate thick

boundary layers on three-dimensional body surface accurately.

- (3) In case of three-dimensional thick boundary layer on ship aft-body surface, calculated velocity profiles by using the present method were improved from those obtained by using thin boundary layer approximation, especially in estimating reverse cross flow.
- (4) With respect to Reynolds stress, it will be necessary to introduce more accurate turbulence model in order to improve the calculation of three-dimensional thick boundary layer around ship aft-body.

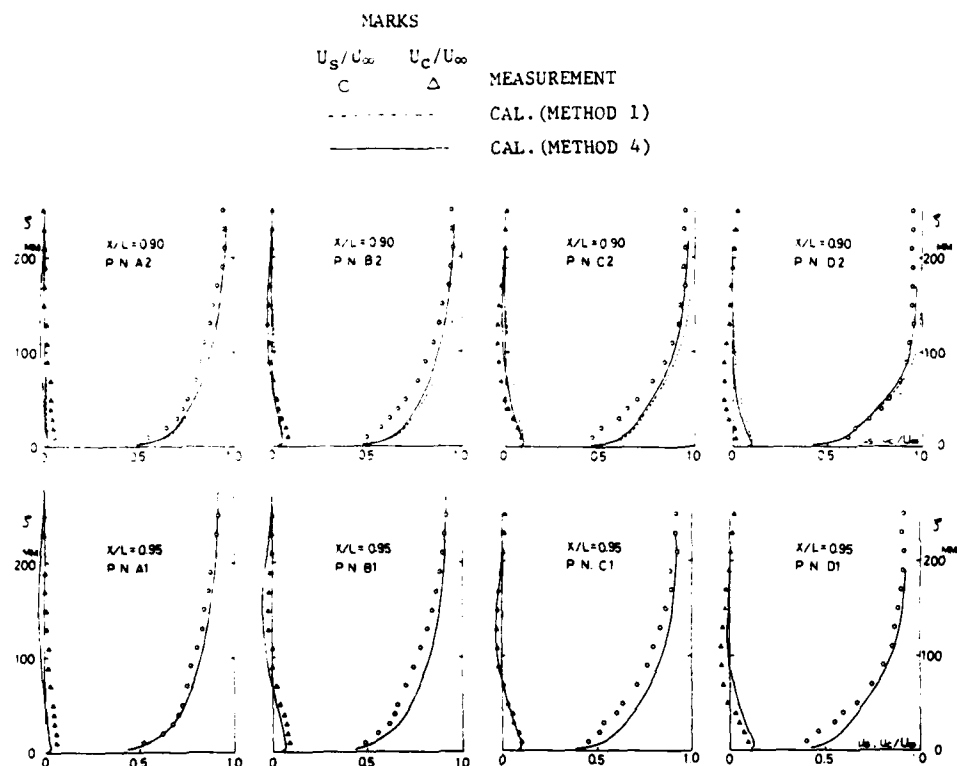
4. Acknowledgement

The author wishes to express his deep gratitude to Professor R. Yamazaki of Kyushu University and the members of Ship Turbulent Group for many usefull discussions and encouragement in writing this paper. He is grateful to Mr. M. Nito of Mitsui Engineering & Shipbuilding Co., Ltd. (MES) who assisted this work at initial stage and to the members of Akishima Laboratory of MES for their cooperation.

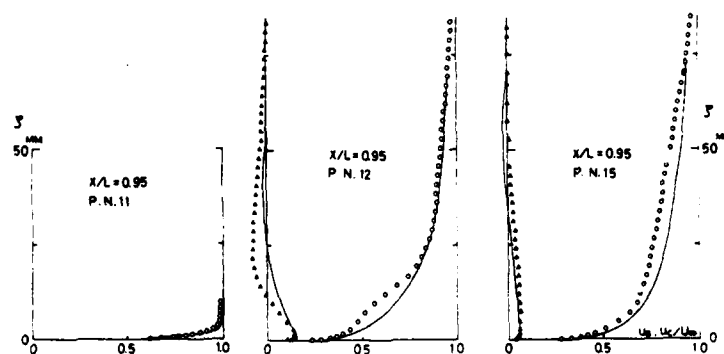
Finally, his thanks are also extended to Dr. H. Narita, Messrs. H. Yagi, K. Yoshida and M. Mizobe of MES for their assistance and encouragement.

References

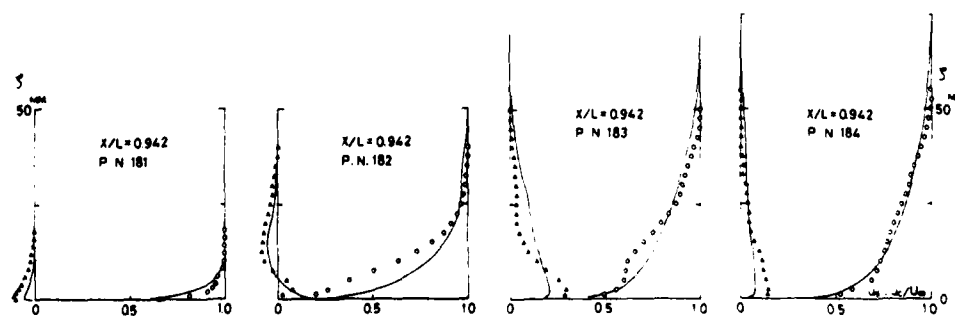
- 1) Larsson, L. (Editor), "Proceedings of SSPA-ITTC Workshop on Ship Boundary Layers 1980", SSPA, Nr.90, Goteborg, 1981.
- 2) Soejima, S. and Yamazaki, R., "Calculation of Three-Dimensional Boundary Layers on Ship Hull Forms", Trans. of The West-Japan Society of Naval Architects, No.55, March 1978.
- 3) Hoekstra, M., "Boundary-Layer Flow past a Bulbous Ship-Bow at Vanishing Froude Number", International Symposium on Ship Viscous Resistance, SSPA, Goteborg, 1978.
- 4) Soejima, S., "Calculation of 3-D Boundary Layer around Ship Fore-Body, 1'st Report: Reynolds Effect on Flow Pattern", Trans. of The West-Japan Society of Naval Architects, No.65, March 1983. (will be published)
- 5) Cebeci, T. and Smith, A.M.O., "Analysis of Turbulent Boundary Layers", Academic Press.



(a) Cargo Ship Model, Measurements Performed by Nagamatsu¹⁸⁾



(b) SSPA Model 720, Measurements Performed by Larsson¹⁹⁾



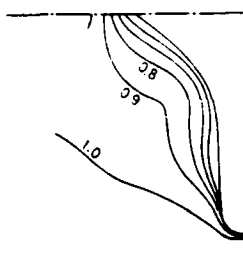
(c) HSVA Tanker Model, Measurement Performed by Hoffmann²⁰⁾

Fig. 19 Velocity Profile across Stern Boundary Layer of Three Ship Models

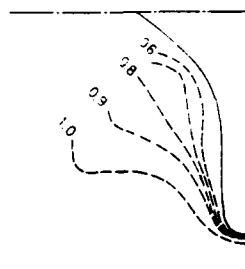


Calculation

(a) Cargo Ship Model, $X/L = 0.95$

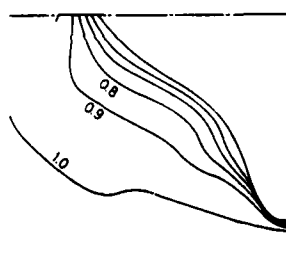


Calculation

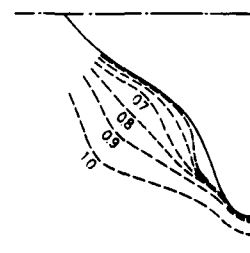


Measurement¹⁾

(b) SSPA Model 720, $X/L = 0.95$



Calculation



Measurement¹⁾

(c) HSVA Tanker Model, $X/L = 0.942$

Fig. 20 Wake Contour of Three Ship Models

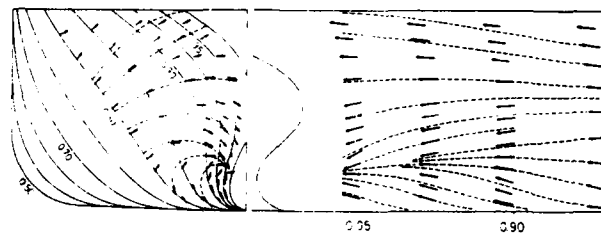
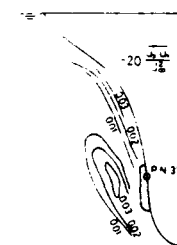


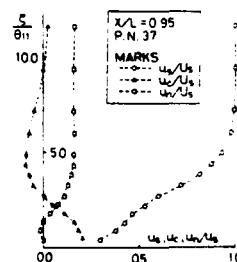
Fig. 21 Calculated Limiting Streamlines, Cargo Ship Model



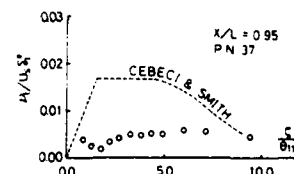
(a) Wake Contour



(b) Turbulence Component



(c) Velocity Profiles



(d) Distribution of Eddy Viscosity

Fig. 22 Measured Velocity and Turbulence Distribution in Stern Boundary Layer of Series 60 Model ($C_B = 0.8$), Measurements Performed by Fukuda and Fujii²¹⁾

- Inc., 1974.
- 6) Cebeci, T., Chang, K.C. and Kaups, K., "A General Method for Calculating Three-Dimensional Laminar and Turbulent Boundary Layers on Ship Hulls", 12th Symposium on Naval Hydrodynamics, Washington, DC, 1978.
- 7) Schlichting, H., "Boundary Layer Theory", 7th Edition, McGraw-Hill Book Comp., 1979.
- 8) Granville, P.S., "The Calculation of the Viscous Drag of Bodies of Revolution", Report No. 849, The David Taylor Model Basin, 1953.
- 9) Stuart, J.T., "Hydrodynamic Stability" in "Laminar Boundary Layers", Edited by L. Rosenhead, Oxford Univ. Press, 1963.
- 10) Chen, K.L. and Thyson, N.A., "Extension of Emmon's Spot Theory to Flows on Blunt Body", AIAA J., Vol. 9, No. 5, 1971.
- 11) Hess, J.L. and Smith, A.M.O., "Calculation of Non-Lifting Potential Flow about Arbitrary Three-Dimensional Bodies", J.S.R., Vol. 8, 1964.
- 12) Asano, S., Tsuda, T., Toya, M. and Ogawa, K., "Investigations on Turbulence Stimulators for Full Ship Models", Journal of The Kansai Society of Naval Architects, Japan, No. 175, Dec., 1979. (In Japanese)
- 13) Wang, K.C., "Separation Pattern of Boundary Layer over an Inclined Body of Revolution", AIAA J., Vol. 10, No. 8, 1972.
- 14) Tagori, T., "On the Effect of Various Shaped Turbulence Stimulators and Resistance of These Stimulators own", Journal of the Society of Naval Architects of Japan, Vol. 110, Dec. 1961. (In Japanese)

- 15) Tanaka, I. and Himeno, Y., "First Order Approximation to Three-Dimensional Turbulent Boundary Layer and Its Application to Model-Ship Correlation", Journal of the Society of Naval Architects of Japan, Vol. 138, Dec. 1975. (In Japanese)
- 16) Soejima, S., "Calculation of Thick Boundary Layers around Ship Stern", Trans. of the West-Japan Society of Naval Architects, No. 60, August, 1980.
- 17) Huang, T.T., Santelli, N. and Belt, G., "Stern Boundary Layer Flow on Axisymmetric Bodies", 12th Symposium on Naval Hydrodynamics, Washington, DC, 1978.
- 18) Nagamatsu, T., "Experimental Study on the Three-Dimensional Turbulent Boundary Layer of a Fine Ship Form Expressed by Means of Conformal Mapping", Trans. of the West-Japan Society of Naval Architects, No. 55, 1978.
- 19) Larsson, L., "Boundary Layers of Ships. Part III : An Experimental Investigation of the Turbulent Boundary Layer on a Ship Model", SSPA Report No. 46, 1974.
- 20) Hoffmann, H.P., "Investigation of a Three-Dimensional Turbulent Boundary Layer on a Double Model of a Ship in a Wind Tunnel", Institut fur Schiffbau, University of Hamburg, Report No. 343, 1976. (In German)
- 21) Fukuda, K. and Fujii, A., "Turbulence Measurements in Three Dimensional Boundary Layer and Wake around a Ship Model", Journal of the Society of Naval Architects of Japan, Vol. 150, Dec. 1981. (In Japanese)

AD-P002962

CALCULATIONS OF THICK BOUNDARY LAYERS USING A STREAMLINE CURVATURE METHOD *

Lars-Erik Johansson and Lars Larsson
Swedish Maritime Research Centre SSPA, Göteborg, Sweden

Abstract

The inability of ordinary boundary layer methods to compute the viscous flow close to the aft end of fat bodies, like ships, has been clearly demonstrated in several recent results, published in the literature. Such methods use approximations for the pressure, the stresses and the coordinate system. It is claimed in the paper that the most serious one of these approximations is the approximation for the coordinate system, which, if the surface of the body has a large curvature, may cause considerable errors, particularly in the continuity equation. It is also claimed that, while the pressure distribution may be quite important, the approximation for the stresses may not be too critical, provided the solution is matched to a wall function, which covers the region of high shear near the surface. The latter argument is based on experimental evidence. In the paper, a new method is described, which has shown results, considerably better than those obtained by ordinary boundary layer methods. Its most important feature is that the continuity is maintained exactly (within the numerical approximation) even if the surface has a considerable curvature. The equations are cast in a Cartesian coordinate system, whose x-axis is directed along the local streamline at every point in the thick boundary layer. In this way the equations become quite simple, the one in the x-direction expressing the change in total head due to shear forces, and the two in the other directions expressing the balance between the centrifugal force and the pressure and shear stress gradients. The solution is obtained by stepping streamlines downstream from an initial grid, and, apart from the momentum equations, the continuity equation is used for locating the streamlines. The first results of the method were presented at the 14th Symposium on Naval Hydrodynamics in August 1982. At that stage the computations were based on measured pressures. This restriction has now been removed and the pressure variation across the viscous region is considered.

1. Introduction

As a result of the rapidly increasing cost of oil it has become more and more important to design fuel-efficient ships. The possibilities of reducing the drag are therefore of great interest to ship builders and owners and at many ship research organizations considerable efforts are made to achieve this goal. Clearly, improved knowledge about the flow field might enable the scientists to develop calculation methods which could be used for parametric and optimization studies at the design stage, without huge expenses for model tests. The latter could then be used for the fine final tuning of the design, to obtain more efficient ships.

At SSPA, a program for fundamental ship flow studies, particularly the viscous part, has been in existence since the early seventies, the main

sponsor being the Swedish Board for Technical Development. The ultimate goal of the program is to develop calculation methods for the viscous flow around the hull and the viscous drag. Such theoretical work must be supported by experimental data, and the first project within the program was an experimental investigation of the turbulent boundary layer on a ship model, reported in 1974 [1]. Based on this information a three-dimensional turbulent boundary layer integral method was developed [2]. This method seemed to work well for the major part of the ship hull, but in the after region the results deteriorated considerably. The reasons for this were investigated [3] and in 1978 the research program was enlarged to include several different projects judged necessary to improve the prediction accuracy close to the stern. Thus, an extensive experimental investigation of the Reynolds stresses in the stern boundary layer on a ship model was initiated, and the development of calculation methods of three different kinds was outlined.

The first result of the enlarged program was reported in 1980 [4] when one of the new calculation methods was presented. It represents an extension to higher order of the original boundary layer integral method and incorporates such features as boundary layer - free surface potential flow interaction, pressure variation across the boundary layer and a coordinate system which is (at least approximately) fitted to the hull and the space occupied by the viscous region. In March of 1982 the first reports on the Reynolds stress measurements were published [5], [6], and in August a first version of the second calculation method, called the streamline curvature method, was presented [7]. This method is based on a new approach, especially designed for thick viscous regions, and does not necessarily have to rely on any boundary layer assumptions. The third method of the program, developed in cooperation between Chalmers University of Technology and SSPA, is still not ready for presentation, but it includes an analytical body fitted coordinate system and flow equations of the partially parabolic type. In the present paper the more recent development of the streamline curvature method will be described.

2. The Weak Points of the Boundary Layer Approximation

As mentioned in the introduction, the original boundary layer method could not predict the flow near the stern, and it was confirmed at the international workshop on ship boundary layer calculations, organized by SSPA in 1980 [8], that this is typical for all first order boundary layer methods. On this occasion 17 different calculation methods, some of them from the aircraft industry, participated in comparative calculations for two different hull forms, and the results were quite discouraging near the stern.

There seem to be three main reasons why boundary

* This research was sponsored by the Swedish Board for Technical Development, Contract No. 81-4113

layer methods cannot accurately predict a flow field of the kind found on the afterbody of a ship.

A. The coordinate systems which are used in boundary layer methods are assumed curvilinear only in the plane of the surface. The normals are thus assumed straight and parallel, so the metrics are not considered functions of the coordinate at right angles to the surface. Since in reality the normals may even intersect, see [7], within the boundary layer, this approximation is too crude. A major effect of this is that the continuity of the flow is not maintained downstream, so the volume flux may be quite unrealistic near the stern.

B. The pressure is assumed constant through the boundary layer and equal to that on the surface in a potential flow, without boundary layer displacement effects. In reality the boundary layer interacts with the potential flow, and the pressure may vary significantly across the layer. Matching between the two regions should be carried out at some surface on, or outside, the boundary layer edge.

C. Usually, only two Reynolds stresses are considered in the equations, and these stresses are computed using turbulence models, which may not be applicable in ship stern flows, mainly due to the strong effects of flow convergence and normal curvature.

Of these three approximations the first one seems to be least serious. Thus, all available information on Reynolds stresses close to the stern of ship hulls [5], [6], [9], [10], [11] and similar three-dimensional [12] and axisymmetric [13] bodies indicates that the magnitude of the stresses is very much reduced as compared with the thin boundary layer case. Since this holds also for the stress gradients, turbulence seems to play a fairly limited role in the flow close to the stern. Provided the stresses close to the surface could be handled properly, it might even be possible to use an essentially inviscid method in the stern region. The effects of the stresses would then be included through the initial velocity profiles, which are a result of stress actions further upstream.

3. The Basis of the Streamline Curvature Method

In the search for a method, in which the weak points of the boundary layer approximation could be removed, or at least reduced, the attention was directed towards a very original method for two-dimensional [14] and axisymmetric [15] flows, developed by Dyne. The basic feature of this approach is that the coordinate system is aligned with the local streamline, which is traced inside the boundary layer. In this way, the governing equations become quite simple, the longitudinal momentum equation being the Bernoulli equation and the equation in the normal direction representing the balance between the pressure gradient and the centrifugal force. A one-dimensional form of the continuity equation is used to compute the distance between neighbouring streamlines. The simplicity of the equations are of course obtained at the expense of having to trace the local streamlines.

Quite simple governing equations are obtained also if Dyne's method is extended to

three-dimensional flows. In principle the only difference is that one more pressure gradient - centrifugal force equation has to be introduced in the lateral direction. The one-dimensional continuity equation can still be used, but for individual stream tubes, which are formed by the streamlines traced downstream. Unfortunately the additional freedom for the streamlines to bend laterally causes huge difficulties in the streamline tracing, odd stream tube shapes, instabilities, etc, which make the development of a three-dimensional version of the approach considerably more difficult than the two-dimensional and axisymmetric ones. Nevertheless, in light of the very promising results obtained by Dyne, this is the approach chosen.

3.1 Governing Equations

The governing equations may be derived from the Reynolds equations, cast in a Cartesian coordinate system, (x, y, z)

$$\rho \left(u \frac{\partial u}{\partial x} + v \frac{\partial u}{\partial y} + w \frac{\partial u}{\partial z} \right) = - \frac{\partial p}{\partial x} + \mu \nabla^2 u - \rho \left[\frac{\partial \overline{u'^2}}{\partial x} + \frac{\partial \overline{u'v'}}{\partial y} + \frac{\partial \overline{u'w'}}{\partial z} \right] \quad (1a)$$

$$\rho \left(u \frac{\partial v}{\partial x} + v \frac{\partial v}{\partial y} + w \frac{\partial v}{\partial z} \right) = - \frac{\partial p}{\partial y} + \mu \nabla^2 v - \rho \left[\frac{\partial \overline{u'v'}}{\partial x} + \frac{\partial \overline{v'^2}}{\partial y} + \frac{\partial \overline{v'w'}}{\partial z} \right] \quad (1b)$$

$$\rho \left(u \frac{\partial w}{\partial x} + v \frac{\partial w}{\partial y} + w \frac{\partial w}{\partial z} \right) = - \frac{\partial p}{\partial z} + \mu \nabla^2 w - \rho \left[\frac{\partial \overline{u'w'}}{\partial x} + \frac{\partial \overline{v'w'}}{\partial y} + \frac{\partial \overline{w'^2}}{\partial z} \right] \quad (1c)$$

where ∇^2 is the Laplace operator, (u,v,w) the velocity vector, p the static pressure, μ the dynamic viscosity, ρ the density, and $\overline{u'^2}$, $\overline{u'v'}$ etc the Reynolds stresses.

If the system is locally oriented in such a way, that x is along the mean flow streamline, v and w are zero, although their gradients are not. Leaving the exact form of the stress terms for later discussion and denoting them s_1 , s_2 , s_3 , the equations may be written

$$\begin{aligned} \rho u \frac{\partial u}{\partial x} &= - \frac{\partial p}{\partial x} + s_1 \\ \rho u \frac{\partial v}{\partial x} &= - \frac{\partial p}{\partial y} + s_2 \\ \rho u \frac{\partial w}{\partial x} &= - \frac{\partial p}{\partial z} + s_3 \end{aligned} \quad (2)$$

Introducing the normal curvature, K_{12} , for a streamline

$$K_{12} = \frac{\partial (\tan^{-1} v/u)}{\partial x} = \frac{1}{u^2 + v^2} \left(u \frac{\partial v}{\partial x} - v \frac{\partial u}{\partial x} \right) = \frac{1}{u^2} \left(u \frac{\partial v}{\partial x} \right) \quad (3)$$

Since a corresponding relation holds for the lateral curvature, K_{13} , the equations may be written

$$\frac{\partial p_0}{\partial x} = s_1 \quad (4a)$$

$$\rho u^2 K_{12} = -\frac{\partial p}{\partial y} + s_2 \quad (4b)$$

$$\rho u^2 K_{13} = -\frac{\partial p}{\partial z} + s_3 \quad (4c)$$

where p_0 is the total head

$$F_0 = p + \frac{1}{2}\rho u^2 \quad (5)$$

4a is recognized as the Bernoulli equation with total head losses due to friction. 4b and c are the pressure gradient - centrifugal force equations also modified by friction. These are to be solved in connection with the one-dimensional continuity equation applied to each stream tube.

$$\dot{V} = u_m \cdot A = \text{const} \quad (6)$$

where \dot{V} is the volume flux, u_m the average velocity in the stream tube and A its cross-sectional area.

3.2 Outline of the Solution Procedure

The two coordinate systems used in the solution are defined in Figs 1 and 2. (X, Y, Z) is a global system with X backwards, Y to starboard and Z upwards. x, y, z is the local, also Cartesian, system with x along the streamline, z along a stream surface and y outwards.

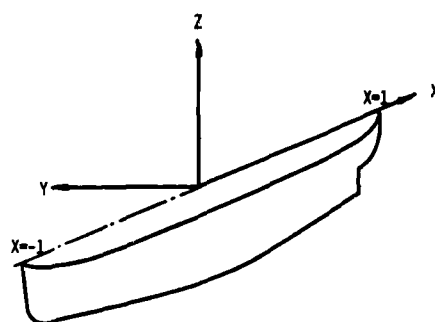


Figure 1. The global coordinate system X, Y, Z

Note that the index i runs in the X -direction, j outwards from the surface and k in the circumferential direction. A stream surface is formed by the streamlines having the same j .

By use of Fig 2 and the flow chart in Fig 3 the solution procedure may be outlined as follows

1. Solve the integral equation for the source strength on the hull in a potential flow, using the Hess & Smith method. Store the sources.
2. Define the starting points for all streamlines in a grid at $X=X_1$, generated by the projections in the plane $X=X_1$ of the normals to the surface, and a set of lines at constant fractions of the boundary layer thickness. Give initial data for the velocity vectors at all grid points. Compute the

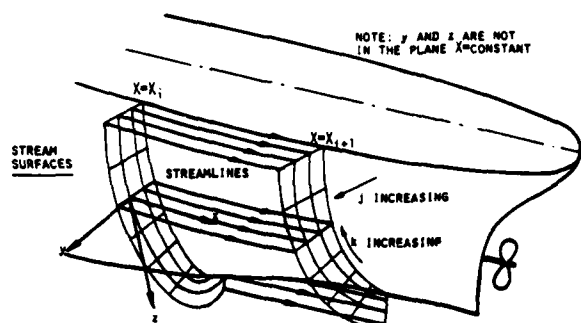


Figure 2. The local coordinate system x, y, z

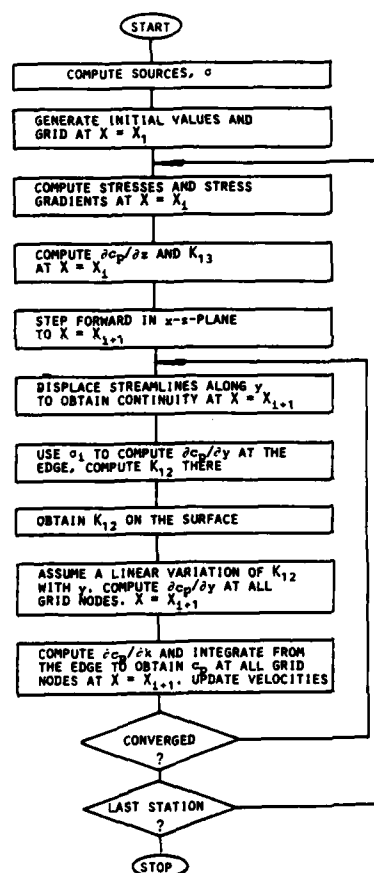


Figure 3. Schematic flow chart

velocity and pressure at the outermost stream surface, using the stored sources and assume (only in this plane) that the pressure is constant along each normal. Use the velocity and pressure at each grid point to calculate the total head and compute the volume flux through each stream tube, defined by a mesh in the grid, using the average velocity of the four corner streamlines. See Fig 4.

3. Compute the shear stresses in the plane $X=X_i$ using the given velocity distribution. (Mixing length theory used so far.) Compute necessary stress gradients neglecting longitudinal derivatives, i.e. determine s_1, s_2, s_3 .

4. Compute the lateral pressure gradient $\partial c_p / \partial z$ knowing the pressure at the grid points and the longitudinal pressure gradient $\partial c_p / \partial x$ (assumed zero in the first step). Use equation (4c) to obtain the lateral curvature K_{13} of each streamline.

5. Step forward each streamline to $X=X_{i+1}$, using the known streamline direction at $X=X_i$ and the lateral curvature K_{13} . Assume, as a first approximation, that the pressure can be obtained from the previous step, using a constant longitudinal pressure gradient. Compute the velocity, using (4a).

6. Start at the innermost stream surface (i.e. the hull) and displace the streamlines in the y-direction in such a way that the correct volume flux is obtained in each stream tube. (At the surface of the hull "limiting streamlines" are obtained from the projection of the streamlines next to the surface.) The first approximation for the location of the streamlines at $X=X_{i+1}$ is now obtained.

7. Use the stored sources to compute the pressure at the outermost two stream surfaces at $X=X_{i+1}$ and obtain the normal pressure gradient $\partial c_p / \partial y$ at the edge of the viscous region. Use (4b) to compute the normal curvature K_{12} at the edge.

8. Extrapolate the limiting streamlines to the station $X=X_{i+2}$ and compute the coordinates and the direction cosines after this step. Compute the normal curvature of the surface along the limiting streamlines, using the change in direction cosines compared with the previous step.

9. Assume a linear variation along the gridlines $k = \text{const}$ of the normal curvature of the streamlines, the boundary values being given by 7. and 8. Compute the normal pressure gradient $\partial c_p / \partial y$ at each grid point at $X=X_{i+1}$ from (4b).

10. Use the pressure gradients in the x, y and z directions to compute the gradient along each line $k = \text{const}$ and integrate from the known pressure at the edge to get the local pressure everywhere in the grid. Compute new velocities from (4a) and return to 6. Iterate until c_p changes less than 0.004 between two iterations. (Usually 2-3 iterations.)

11. Return to 3. and step to the next X.

Comparing the present approach with an ordinary boundary layer method it is seen that the most essential weak points of the latter have been removed. Thus, continuity is maintained exactly (within the numerical approximation), since the viscous region is correctly covered by the computational grid. Further, the pressure variation across the viscous region is considered, albeit approximately.

When starting the development of the method the intention was to compute the local pressure gradient across the boundary layer iteratively from the

normal streamline curvature obtained in a previous iteration. This approach turned out to be highly unstable, unfortunately. Even if considerable under-relaxation was applied when introducing the pressure change due to streamline curvature, the previous solution was disturbed to such an extent that the procedure became divergent in some regions. Therefore, the present approach was adopted. The pressure gradient is now almost independent of the solution, since at the outer edge the curvature is obtained from the potential flow, and at the surface from the curvature of the surface itself. Linear interpolation between these limits is used for all intermediate points. The direction of the limiting streamline, used for computing the normal curvature, has, however, to be found from the solution at a previous step.

As appears from the scheme outlined, no viscous-inviscid interaction is included so far. This is, admittedly, a serious limitation which will be removed in further work.

Although a considerable part of the present computer program is the same as the one described in [7] its logic has been changed. The main reason for this is that the input pressure is now taken from the edge of the viscous region (initially unknown), while in the previous approach a surface pressure distribution was used. As explained in [7] good results were obtained only if measured pressures were used as input. The objective of the present work is to enable calculations based on computed potential flow pressures.

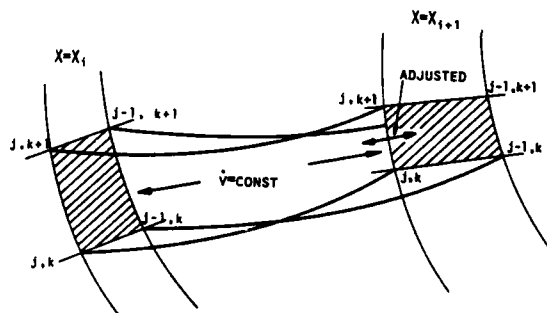


Figure 4. A stream tube

4. Details of the Streamline Curvature Method

Since a number of details in the present version of the method are similar to the ones described in [7] this description can be made relatively short. There is not much point in repeating all equations, so only brief descriptions will be given of features unchanged.

4.1 The Pressure at the Edge of the Viscous Region

The hull is represented by a large number of quadrilateral panels defined by the three space coordinates of a set of points on each section of the hull. On each panel the source strength, σ , is assumed constant. σ is solved by Gauss-Seidel iter-

ation from a set of simultaneous equations of the form

$$\sum_j A_{ij} \sigma_j = U_\infty \hat{n}_i \quad (7)$$

where U_∞ is the undisturbed velocity (usually put equal to unity), \hat{n}_i is the unit vector in the normal direction at panel i , and A_{ij} is a set of influence coefficients, defined by

$$A_{ij} = \iint_{S_j} \frac{\partial}{\partial n} \left(\frac{1}{r_{ij}} \right) dS \quad (8)$$

r_{ij} is the distance from a point on element j to the centre of panel i . Different numerical evaluations of the integral are used, depending on the distance between panels i and j .

Having solved the system of equations, the σ_i 's are stored. Once the pressure is needed at (or close to) the edge of the viscous region, a subroutine is called for computing the velocity components, using the following formulae

$$U = U_\infty + \sum_j X_j \sigma_j \quad (9)$$

$$V = \sum_j Y_j \sigma_j$$

$$W = \sum_j Z_j \sigma_j$$

where X_j, Y_j, Z_j represent influence coefficients for the three velocity components

$$X_j = \iint_{S_j} \frac{\partial}{\partial x} \left(\frac{1}{r_j} \right) dS$$

$$Y_j = \iint_{S_j} \frac{\partial}{\partial y} \left(\frac{1}{r_j} \right) dS$$

$$Z_j = \iint_{S_j} \frac{\partial}{\partial z} \left(\frac{1}{r_j} \right) dS \quad (10)$$

Knowing U, V, W the pressure is computed from Bernoulli's theorem.

4.2 Initial Values

As will be discussed later, the method is very sensitive to the initial values, so a good representation of the velocities at the initial plane is needed. For the longitudinal velocity u_1 , (along the streamline at the boundary layer edge) either the wall - wake law or the power law with a variable exponent is used, see [7].

The cross-flow, u_c , is assumed composed of two parts, one due to the potential flow variation across the region occupied by the viscous flow and the other due to the viscous cross-flow itself. The former is taken to be linear with y , while the latter is computed from Mager's formula, specifying a cross-flow boundary layer thickness, δ_c chosen so as to obtain a good fit to the initial data.

$$\frac{u_c}{u_e} = \frac{u_1}{u_e} \tan [k_1 \beta_p + \tan^{-1}(k_2 \tan \beta_v)]$$

$$k_1 = 1 - \frac{Y}{\delta}$$

$$k_2 = (1 - \frac{Y}{\delta_c}) \text{ for } Y \leq \delta_c; \quad k = 0 \text{ for } Y > \delta_c \quad (11)$$

β_p and β_v are the potential and viscous cross-flows resp. at the wall, and u_e is the velocity at the edge of the viscous region. In general, non-cross-over profiles are quite well represented in this way.

4.3 Stresses

Of the six Reynolds stresses only the two shear stresses in the plane of the stream surface are considered. As explained in [7] these are computed using the mixing length model, with Michel's et al representation of the mixing length across the viscous region and van Driest's damping factor close to the wall.

The turbulence model is thus of the common boundary layer type. This is not a very good approximation in the viscous region close to the stern, as appears from [5] and [6]. In a more complete model all six Reynolds stresses should be considered, and the effects of curvature and flow convergence should be included. The main effect of the approximation is that the two stresses computed become too large, yielding too large total head losses. However, as was shown in [7] viscous and inviscid calculations using the present method are not very much different, indicating that convection in this case is far more important than diffusion.

In [7] the details are also given on the computation of the necessary distance from the wall (which is not used otherwise), the computation of a shear velocity from the innermost streamlines and the evaluation of the necessary stress gradients from the grid points.

4.4 The step

The computation of the pressure gradient in the z -direction is fairly straightforward and this yields the lateral curvature K_1 , from (4c). Knowing this, the step may be taken from $X = X_i$ to $X = X_{i+1}$ in the plan $x-z$ (a stream surface), see Fig 2. The starting direction is then defined by the location of the streamline at $X = X_{i-1}$ and $X = X_i$, and the formula for computing its location at $X = X_{i+1}$, considering K_1 , is obtained by series expansion to second order about $X = X_i$ ($x = 0$), see [7].

4.5 Continuity

Once a layer of streamlines (corresponding to a stream surface, j say) has been stepped forward, the continuity is checked. Each pair of streamlines, j, k and $j, k+1$, form, together with the corresponding lines at the surface $j-1$ (i.e. $j-1, k$ and $j-1, k+1$), a stream tube, in which the continuity equation (6) should hold. Since \dot{V} is known from the entrance conditions, the necessary cross-sectional area at $X = X_{i+1}$ may be computed, taking u_m as the average velocity of the four corner streamlines. The outer edge (between j, k and $j, k+1$) is then adjusted so as to obtain the required area.

Now, since the stream surfaces should be continuous, the outer edges of the stream tubes cannot be moved independently. The procedure for satisfying

both the smoothness requirement and the flow continuity is described in [7].

4.6 Generation of New Grids

It was found, when testing the first version of the method, that the streamlines could not be traced all the way to the stern without difficulties. There are two main reasons for this. Firstly, in regions of large cross-flow, corresponding streamlines in adjacent stream surfaces may depart considerably from one another, creating very distorted stream tubes. Secondly, in regions of strong convergence, the streamlines tend to merge into one another, which, of course, makes the procedure blow up. It was therefore found necessary to introduce a special subroutine, for generating a new undistorted grid, whenever necessary. The new grid is generated by one-dimensional interpolation along the lines $j = \text{const}$ in the plane $X = X_i$ and the quantities interpolated are the velocity direction cosines, the pressure coefficient and the volume flux in the layer of stream tubes between the stream surfaces j and $j-1$. To avoid large local peaks in very convergent regions there are also two possibilities of smoothing the grid. Either the volume fluxes or the direction cosines of the streamlines can be adjusted.

Experience has shown that the smoothing parameters may be varied within fairly wide limits without changing the results, except locally.

4.7 Boundary Conditions

At the hull surface the no-slip condition is applied, and in the innermost layer of stream tubes either of two assumptions is made for the velocity distribution. When computing the volume flux a linear variation is assumed, while when computing the friction velocity, similarity functions are used [7].

Since the shear stresses cause a total head drop along each streamline, there will be a discontinuity at the outer edge of the computed region. To avoid this, new streamlines should be included as the calculation proceeds downstream. This is not done at present, so part of the viscous region is lost. Since, however, the total head drop is quite small, this is not considered a serious limitation. Symmetry conditions for velocities and pressures are applied at the lateral boundaries.

5. Results and Discussion

The two test cases presented in [7] have been recomputed using the new version of the method. The first one is the SSPA Model 720 experimentally investigated by Larsson [1] and Löfdahl [5], [6] and the second one is a tanker hull for which data by Hoffmann [16] and Wieghardt and Kux [17] are available. These are the two test cases used at the Ship Boundary Layer Workshop [8]. Comparisons will be made with some Workshop results.

5.1 The SSPA Model 720

The computations were started at $X = 0.5$, using input profiles according to section 4.2, based on measurements. In future calculations initial values will be generated by a boundary layer method, but to eliminate possible errors from this source, the

measured data were used.

5.1.1 Boundary Layer Parameters

Results from the present calculations at $R_n = 5 \cdot 10^6$ are compared with three other methods in Figs 5-10. The other methods are chosen to represent one typical boundary layer integral method (Larsson's [18]), one typical boundary layer differential method (Johansson's [19]), and the best of all methods participating in the Ship Boundary Layer Workshop (Muraoka's [20]). Muraoka's method is based on the partially parabolic approach by Spalding and his co-workers at Imperial College and is considerably more general than ordinary boundary layer methods.

In Fig 5 the distribution of the momentum thickness, θ_{11} , around the girth at $X = 0.7$ from keel to water-line is shown. Note that all lengths are normalized by the model half length according to Fig 1. It is seen that the present method and Muraoka's yield very good results, while the boundary layer results at this station (15 % of the length from the stern) are somewhat fluctuating, although the level is correct.

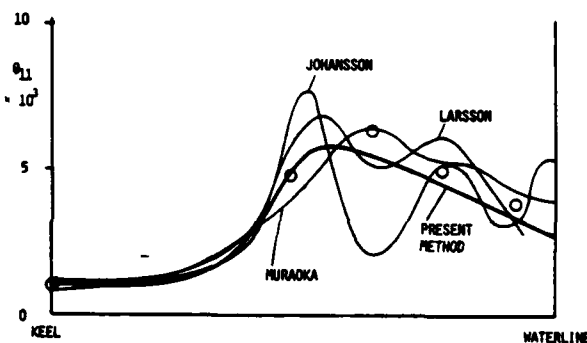


Figure 5. Momentum thickness. $X = 0.7$ (SSPA)

The velocity profile shape factor, H_{12} , at $X = 0.7$ is shown in Fig 6. The average deviation between the present results and the measurements is about 0.05, which must be considered satisfactory. Also in this case reasonable, but fluctuating, boundary layer results are obtained. Muraoka's method fails, probably due to bad grid resolution.

The fluctuations of the boundary layer methods are found also in the computed wall cross-flow angle, β_w . Both the present method and Muraoka's fail to predict the peak around mid-girth, but otherwise the results, at least for the present method, are quite good.

Turning to the results obtained at $X = 0.9$ (5 % of the length from the stern, the aftermost station where measurements are available) it is seen in Fig 8 that, except for a region near the keel, the present method and Muraoka's produce almost identical results. These are smooth and have the right trend but are about 25 % too low. Larsson's boundary layer method broke down (predicted separation) at $X = 0.88$, so no results are available at $X = 0.9$. The fluctuations in

Johansson's method are excessive at this station and quite unrealistic results are obtained in the upper region (outside the figure).

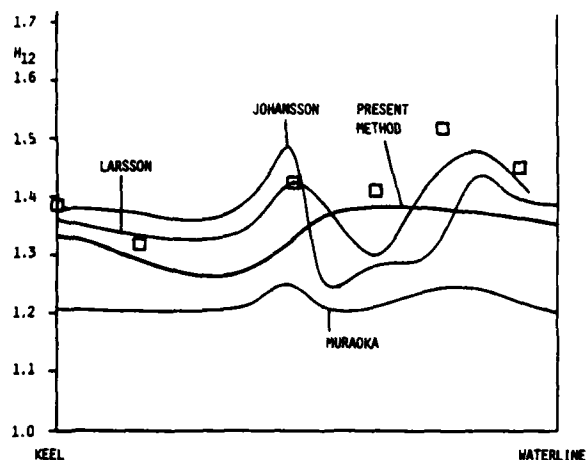


Figure 6. Shape factor. $X = 0.7$ (SSPA)

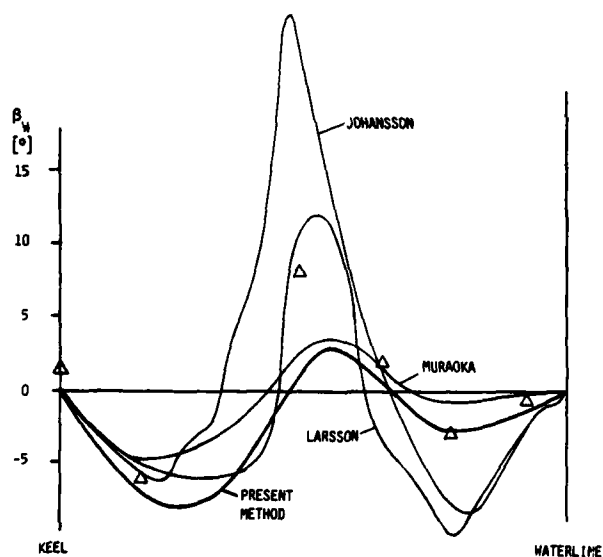


Figure 7. Wall cross-flow angle. $X = 0.7$ (SSPA)

The shape factor prediction by the present method in Fig 9 is reasonable, while the boundary layer results are again too irregular. Muraoka's shape factor is far too low at this station.

From Fig 10, finally, it appears that the wall cross-flow angles predicted by the present method are too low in the central region, where Muraoka's results are better. The opposite is true, however, near the keel.

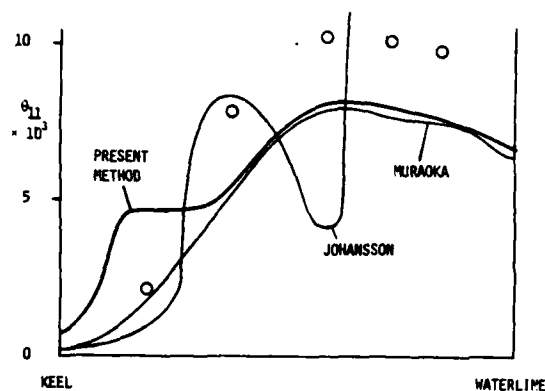


Figure 8. Momentum thickness. $X = 0.9$ (SSPA)

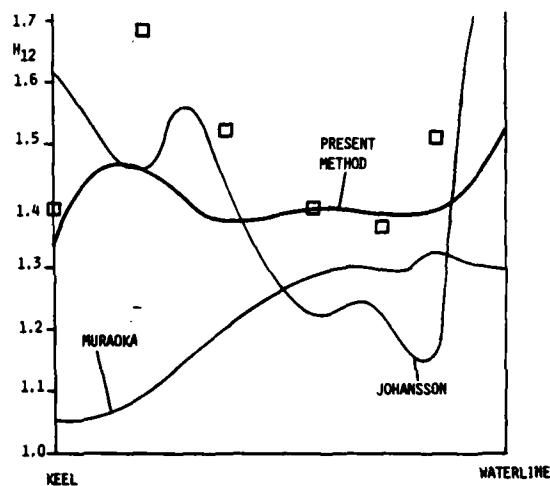


Figure 9. Shape factor. $X = 0.9$ (SSPA)

Summing the comparisons, the present method and Muraoka's seem to be equally accurate except in the prediction of the shape factor, where Muraoka's results are far too low. The boundary layer methods are clearly inferior in the computed region.

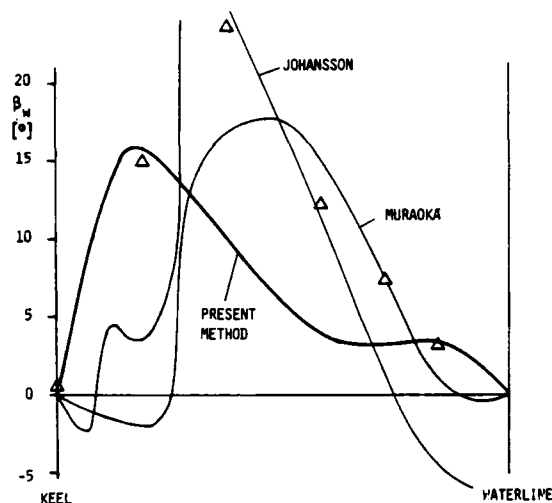


Figure 10. Wall cross-flow angle. $X = 0.9$ (SSPA)

5.1.2 Isovels

Wake contours (isovels) are shown in Figs 11 and 12. The upper figure represents the calculations, while the lower one is obtained from Larsson's boundary layer measurements [1].

Disregarding the fine details of the plots, it is seen that the predictions are quite good at $X = 0.7$. The thinning of the viscous region near the keel is realized, as is the concentration of momentum loss near midgirth.

At $X = 0.9$, Fig 12, the results are not so good. As could be seen in Fig 8, there is a concentration of momentum loss in the lower part of the vertical side. This effect is not found in the measurements. The reason for this is the pressure distribution, as will be discussed in the next paragraph.

The results presented in [7] were considerably better at $X = 0.9$. This is essentially due to the fact that the measured pressure distribution was used as input. Another reason is that the directions of the initial velocity vectors have been slightly changed. The present ones should be more accurate, but they seem to distribute somewhat too much momentum loss to the region near the water-line. Again this might be due to the neglect of viscoid-inviscid interaction and its effect on the direction of the velocity vectors at the edge of the viscous region. In Fig 13 the results of the previous calculations are shown for comparison.

5.1.3 The Pressure Distribution

Computed surface pressures at $X = 0.7$ and 0.9 are compared with measurements in Figs 14 and 15. Good results are obtained in the lower half of the girth at $X = 0.7$, while in the upper region the predictions are somewhat too high. It is interesting to note that the present predictions yield results very similar to the potential flow pressures on the surface. The same pressure variation (of the order of 0.05) is thus predicted by both methods across the region occupied by the

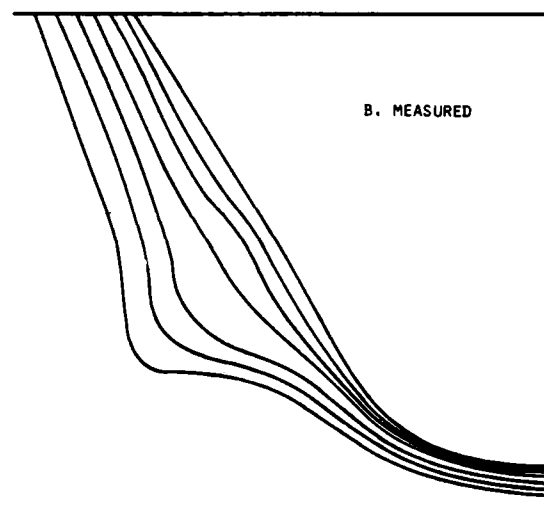
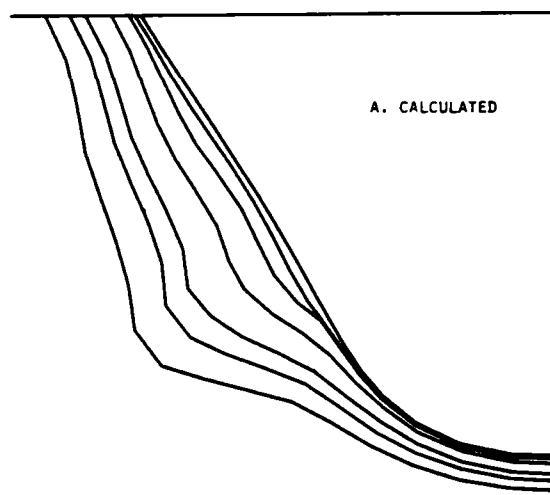
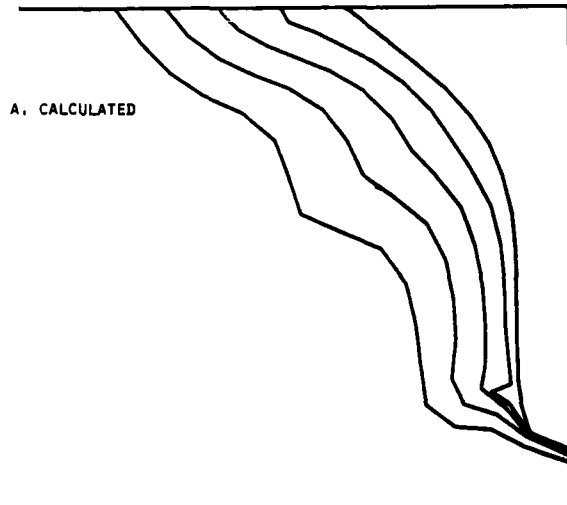


Figure 11. Isovels at $X = 0.7$. ($u/u_\infty = 0.6, 0.7, 0.8, 0.9, 0.95, 1.0$) (SSPA)

the viscous flow. This is a bit surprising since the velocities in the present method are lower, which would yield a smaller variation across the region.

Also at $X = 0.9$ the two methods produce similar results. A slightly better correspondence with measurements is however obtained in the upper region by the present method.

The too high computed pressures will push the low speed viscous flow downwards to the pressure minimum. This is the reason why the predicted isovels exhibit a bump in the lower region. Most probably the erroneous pressures are caused by the neglect of the viscoid-inviscid interaction.



B. MEASURED

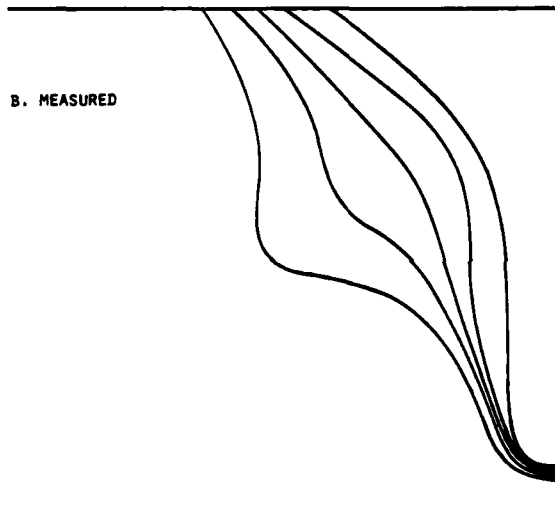


Figure 12. Isovells at $X = 0.9$. ($u/u_e = 0.6, 0.7, 0.8, 0.9$) (SSPA)

5.2 The HSVA Tanker Model

While the first test case is a relatively fine ship with a block coefficient of 0.675, the HSVA tanker is very bluff, having a block coefficient of 0.850. It might therefore be suspected that this case would be more difficult to compute, but this has turned out not to be the case. After trimming the method on the SSPA model, it has been quite simple to apply it to the second case.

Initial values based on measurements were specified at $X = 0.5$ and the computations were carried out at a Reynolds number of 6.8×10^6 . Boundary layer parameters and isovells will be presented.

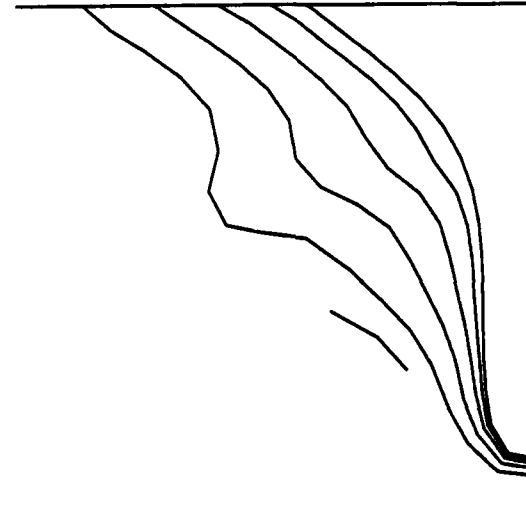


Figure 13. Isovells at $X = 0.9$. ($u/u_e = 0.6, 0.7, 0.8, 0.9, 0.95$). From [7]. (SSPA)

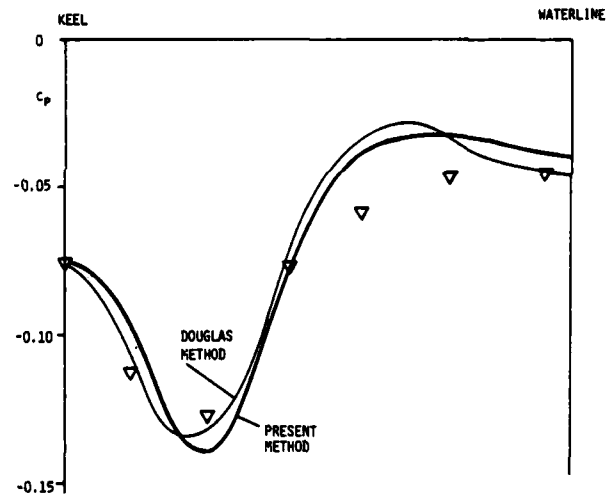


Figure 14. Pressure distribution at $X = 0.7$ (SSPA)

5.2.1 Boundary Layer Parameters

Since no measurements are available at $X = 0.7$, results will be given only at the aftermost station, $X = 0.9$. (The measured boundary layer parameters were however obtained at $X = 0.884$.) Unfortunately Johansson's method has not yet been applied to this case, so the comparisons will be made only with Larsson's and Muraoka's methods.

In Fig 15 the momentum thickness is given. Larsson's method could be used only in the lower half of the hull and as seen in the figure unrealistically high θ_{11} 's are predicted near mid-

girth. Muraoka's results are quite reasonable but a bit too high. The present results are a bit too low in the central region of the girth. A considerable part of the momentum loss has been pushed to the water-line and there is also a somewhat too large loss further down. The tendencies are thus the same as for the SSPA model.

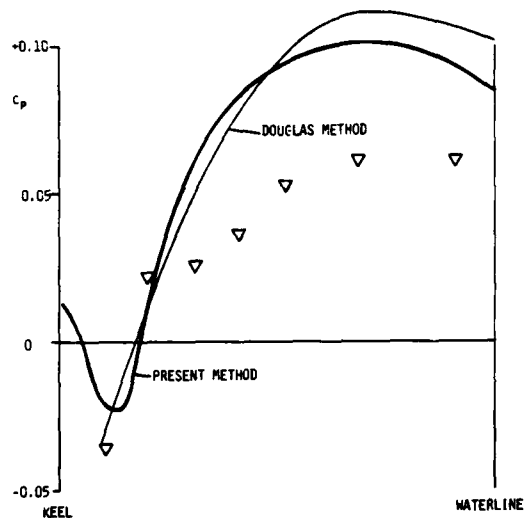


Figure 15. Pressure distribution at $X = 0.9$ (SSPA)

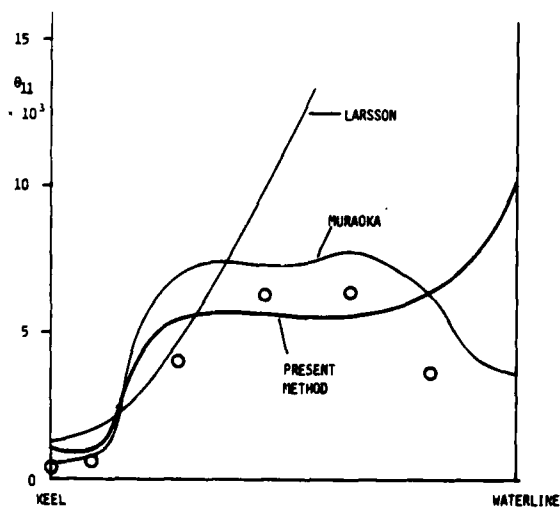


Figure 16. Momentum thickness $X = 0.9$ (HSVA)

The shape factor in Fig 17 is quite well predicted by the present method except at one location. Looking at the measured velocities, there is obviously a vortex at this position. This vortex has not been predicted by any of the methods. As in case of the SSPA model Muraoka's shape factors are too low.

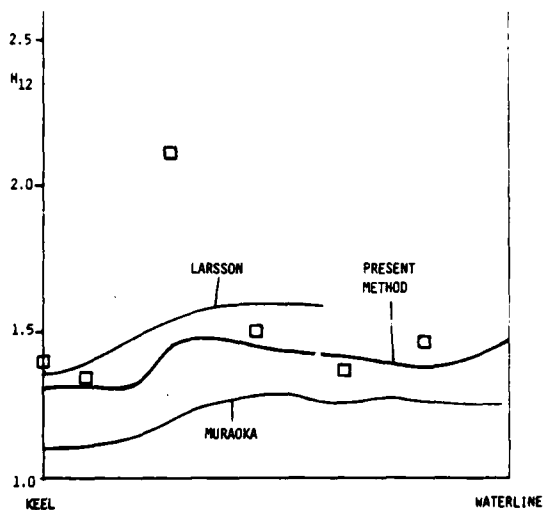


Figure 17. Shape factor $X = 0.9$ (HSVA)

The final boundary layer plot is the wall cross-flow angle, Fig 18. The best results are here obtained by Muraoka's method, since the drop near the keel is well predicted. On the other hand, the large angles near mid-girth are missed, as in the present method.

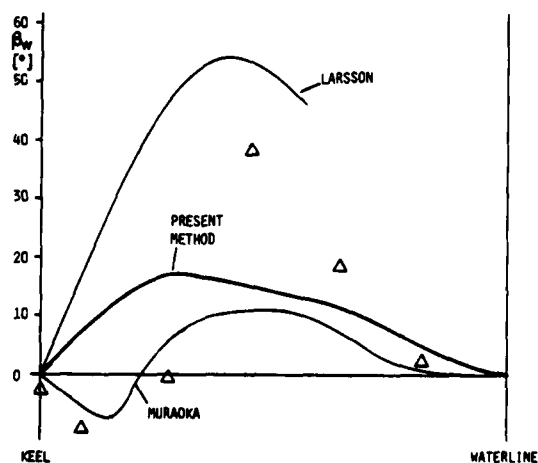


Figure 18. Wall cross-flow angle $X = 0.9$

5.2.2 Isovels

The features found in the boundary layer parameters are confirmed in the wake contours of Fig 19. Compared with measurements the momentum loss has been spread too much. For comparative purposes the results based on the measured pressure distribution are shown in Fig 20. The much better correspondence

indicates that the viscid-inviscid interaction has to be taken into account to obtain results of high quality.

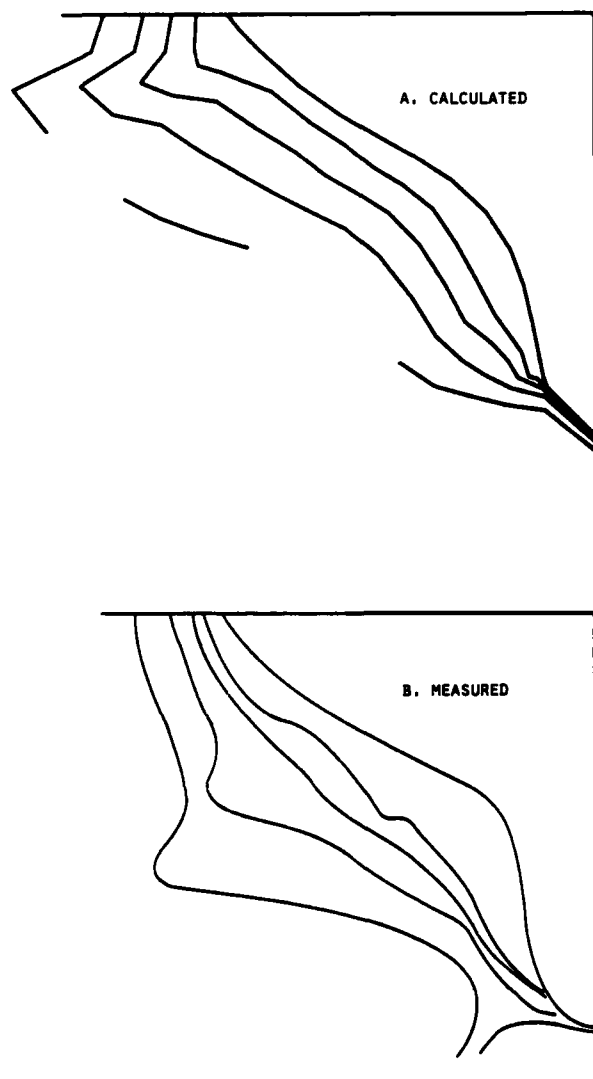


Figure 19. Isovels at $X = 0.9$. ($u/u_e = 0.6, 0.7, 0.8, 0.9$) (HSVA)

6. Conclusions

Results from the extended streamline curvature method have been presented for two ship hulls. Quite good predictions have been obtained for the first test case at a station 15 % of the length from the stern. At the aftermost station, however, the results deteriorate, most probably due to the fact that the viscid-inviscid interaction is neglected when computing the pressures at the edge of the viscous region. For the second case comparisons with measurements could be made only at the after station, but the trends are similar

to the ones from the first case.

Comparisons have also been made with results from two different boundary layer methods and a more general method for viscous flows based on Spalding's partially parabolic approach. It turned out that the latter and the present methods were fairly equal in accuracy, both superior to the boundary layer methods.

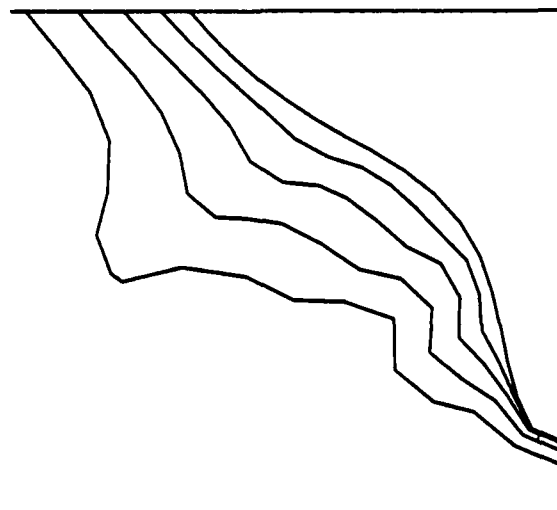


Figure 20. Isovels at $X = 0.9$. ($u/u_e = 0.6, 0.7, 0.8, 0.9$) From [7] (HSVA)

7. Acknowledgements

The authors are indebted to Miss Eira Samuelsson for great help in the coding and running of the program.

8. References

- [1] Larsson, L., "An Experimental Investigation of the Three-Dimensional Turbulent Boundary Layer on a Ship Model", Proceedings of the Eleventh Symposium on Naval Hydrodynamics, London, 1976.
- [2] Larsson, L., "A Calculation Method for Three-Dimensional Turbulent Boundary Layers on Ship-Like Bodies", Proceedings of the First International Conference on Numerical Ship Hydrodynamics, Washington DC, 1975.
- [3] Larsson, L., "Ship Viscous Resistance - a Survey", SSPA Report No. 57, 1978.
- [4] Larsson, L. and Chang, M.-S., "Numerical Viscous and Wave Resistance Calculations Including Interaction", Proceedings of the Thirteenth Symposium on Naval Hydrodynamics, Tokyo, 1980.
- [5] Löfdahl, L., "Measurements of the Reynolds Stress Tensor in the Thick Three-Dimensional Boundary Layer on a Ship Model", Ph D Thesis, Chalmers University of Technology, 1982.

- [6] Löfdahl, L. and Larsson, L., "Measurements of Reynolds Stress Profiles in the Stern Region of a Ship Model", Proceedings of the IUTAM-Symposium on Three-Dimensional Turbulent Boundary Layers, Berlin, 1982.
- [7] Larsson, L. and Johansson, L.-E., "A Streamline Curvature Method for Computing the Flow Near Ship Sterns", Proceedings of the 14th Symposium on Naval Hydrodynamics, Ann Arbor, 1982.
- [8] Larsson, L., "SSPA-ITTC Workshop on Ship Boundary Layers - Proceedings", SSPA Publication No. 90, 1981.
- [9] Hatano, S. and Hotta, T., "Turbulence Measurements in the Thick Boundary Layer and Near Wake of a 3-Dimensional Body", Sixth STG Meeting Tokyo, 1982.
- [10] Okuno, T. and Himeno, Y., "Turbulence Measurements in Ship Model Flow", Proceedings of the IUTAM Symposium on Three-Dimensional Turbulent Boundary Layers, Berlin, 1982.
- [11] Nagamatsu, T., "Flow Measurements Near the Stern of a Model of a Full Form Ship", Theoretical and Applied Mechanics, Vol 30, 1980.
- [12] Grooves, N., Belt, G. and Huang, T.T., "Stern Boundary Layer Flow on a 3-Dimensional Body of 3:1 Elliptic Cross Section", David W Taylor Naval Ship Research and Development Center, Ship Performance Department Research and Development Report DTNSRDC -82/022, 1982.
- [13] Patel, V.C., Nakayama, A. and Damian, R., "Measurements in the Thick Axisymmetric Turbulent Boundary Layer Near the Tail of a Body of Revolution", J of Fluid Mech, Vol 63, p 345, 1974.
- [14] Dyne, G., "A Streamline Curvature Method for Calculating the Viscous Flow Around Bodies of Revolution", Proceedings of the International Symposium on Ship Viscous Resistance, Göteborg, 1978.
- [15] Dyne, G., "A Streamline Curvature Method for the Calculation of the Boundary Layer and Wake of Two-Dimensional Symmetrical Airfoils", SSPA Report No. 2466-1, 1980.
- [16] Hoffmann, H.P., "Investigation of a Three-Dimensional Turbulent Boundary Layer on a Double Model of a Ship in a Wind Tunnel", (In German), Institut für Schiffbau, University of Hamburg, Report No. 343, 1976.
- [17] Wieghardt, K. and Kux, J., "Wind Tunnel Tests on the Stern Flow of a Double Model", (In German), Jahrbuch der Schiffbautechnischen Gesellschaft, Vol 74, 1980.
- [18] Larsson, L., "Small Cross-Flow and Fully 3-Dimensional Boundary Layer Calculations for Two Ship Models", in [8].
- [19] Johansson, L.-E., "Ship Boundary Layer Calculations Using an Alternating-Direction-Implicit Method", in [8].
- [20] Muraoka, K. and Shirose, Y., "Calculation of SSPA 720 and HSVA Tanker", in [8].

END

FILMED

11-83

DTIC